

12th Biennial SGA Meeting
12–15 AUGUST 2013, UPPSALA, SWEDEN

Mineral deposit research for a high-tech world



Proceedings

VOLUME 3



12th Biennial SGA Meeting
12–15 AUGUST 2013, UPPSALA, SWEDEN

**Mineral deposit research
for a high-tech world**



Proceedings

Volume 3

Edited by
Erik Jonsson et al.

The 12th Biennial Meeting was organised by the Geological Survey of Sweden with assistance from Uppsala University, Stockholm University, the Geological surveys of Finland and Norway, Luleå University of Technology and the Swedish Museum of Natural History.

Suggested citation for entire volume:

Jonsson, E. et al. (ed.), 2013: Mineral deposit research for a high-tech world. Proceedings of the 12th Biennial SGA Meeting, 12–15 August 2013, Uppsala, Sweden. ISBN 978-91-7403-207-9. 1882 pp.

Suggested citation for an individual paper:

Sundberg, N. & Karlsson, E., 2013: Metallogeny of the Fennoscandian Shield. Mineral deposit research for a high-tech world. Proceedings of the 12th Biennial SGA Meeting, 12–15 August 2013, Uppsala, Sweden, ISBN 978-91-7403-207-9, 1450–1452.

This publication cannot be reproduced in whole or in part without the permission of The Society for Geology Applied to Mineral Deposits (SGA).

A digital version of these volumes is available from the SGA website at www.e-sga.org

Cover photograph: View of the Aitik open pit copper mine in the very north of Sweden. Mining operations started in 1968 and the current mining depth is 430 m. The open pit is c. 3 km long and 1.1 km wide. The production in 2012 was 34,3 million tonnes of ore containing 67 100 tonnes of copper, 51 700 tonnes of silver and 1,9 tonnes of gold. Photo: Olof Martinsson, Luleå University of Technology.

ISBN 978-91-7403-207-9 set of 4 volumes

Layout: Jeanette Bergman Weihed, Kerstin Finn, Rebecca Litzell, SGU
Print: Elanders Sverige AB

VOLUME 3

Ore deposits associated with mafic and ultramafic rocks	929
Magma dynamics and the formation of magmatic sulfide deposits	930
Nicholas Arndt, Stephane Sobolev, Stephen Barnes & Jesse Robertson	
Platinum group elements in different types of Ni-laterite profiles from the northern Caribbean: a geochemical comparison	933
T. Aiglsperger, J.A. Proenza, J. F. Lewis, F. Zaccarini, G. Garuti, A. Rojas-Purón, F. Longo & A. Chang	
A new mineralogical method for the determination of metal tenors in Ni-Cu-PGE ores	937
Jens C. Ø. Andersen, Gavyn K. Rollinson & Duncan Pirrie	
The Ioko-Dovyren layered massif (Southern Siberia, Russia): fingerprints of an open magma chamber and compaction of original cumulates conjugated with sulphide percolation process	941
A.A. Ariskin, L.V. Danyushevsky, A.W. McNeill, G.S. Nikolaev & Yu.A. Kostitsyn	
Physical processes in magmatic ore formation: fluid dynamics of sulfide liquid droplets in sulfide-silicate emulsions	944
Stephen J. Barnes, Jesse Robertson & B�elinda Godel	
Cu-Ni-PGE mineralization of felsic dikes along the Grano fault in the Bathtub intrusion (Duluth Complex, Minnesota, USA)	948
Zsolt Benk�, Aberra Mogessie, Ferenc Moln�r, Mark Severson, Steven Hauck & Greg B. Arehart	
Cu-Ni-Au-PGE transport in the partially molten charnockitic footwall of the Spruce Road deposit, South Kawishiwi intrusion, Duluth Complex, Minnesota, USA	952
Zsolt Benk�, Aberra Mogessie, Ferenc Moln�r, Mark Severson, Steven Hauck & Greg B. Arehart	
Geochemistry of the Sakatti magmatic Cu-Ni-PGE deposit, northern Finland	956
Will Brownscombe, Richard J. Herrington, Jamie J. Wilkinson, Andrew J. Berry, Jim Coppard, Christian Ihlenfeld, Shephanie Klatt, Craig Hartshorne, Adrian J. Boyce & Rex N. Taylor	
Komatiite-associated Cr and Ni-Cu-(PGE) mineralisation in the Black Thor–Black Label ultramafic intrusive complex, McFaulds Lake greenstone belt, Ontario	960
Heather JE Carson, C Michael Leshner, Michel G Houli�, Riku T Metsaranta & David A Shinkle	
Ni-Cu-PGE mineralisation of the Riwaka Complex, Northwest Nelson, New Zealand	964
A.B. Christie & R.E. Turnbull	
Compositional diversity in chromitites from Eastern Rhodopes (SE Bulgaria): petrogenesis and tectonic implications	967
Vanessa Col�s, Isabel Fanlo, Fernando Gervilla, Jos� Maria Gonz�lez-Jim�nez & Thomas Kerestedjian	
The composition of spinels from Mongolia, Poland, Ukraine and Cyprus as an exploration tool for Cr-deposits – preliminary study	971
Tomasz �wiertnia, Adam Piestrzyński, Jadwiga Pieczonka & W�adys�aw Zygo	
Geochemistry of different ore-bearing intrusions in the Emeishan large igneous province	975
Xingxing Du, Jianmin Liu	
Petrogenesis of massive sulphides from the Lac-des-Iles palladium ore deposits, Western Ontario, Canada	978
Charley J. Duran, Sarah-Jane Barnes & John T. Corkery	
Estimates of redox conditions and temperatures of closure of the olivine-spinel system in cumulate rocks of the Ioko-Dovyren layered intrusion	982
I.S. Fomin, G.S. Nikolaev & A.A. Ariskin	
Olivine cumulates: Centrifuge experiments on the processes and time of formation	985
M�lanie Forien, Nick Bagdassarov, Max W. Schmidt & Guilio Solferino	
Reef disturbances of Critical Zone rocks of the eastern Bushveld Complex in the vicinity of the Steelpoort fault, South Africa – petrogenetic implications	989
C. Gauert, E. Kotz�, J.J. Beukes & R.J. Giebel	
Spatial distribution and geochemical characteristics of the talc-carbonate alteration of the Uitkomst Complex, Mpumalanga, South Africa	993
Christian G�nther & Christoph Gauert	
Geochemistry of ~2.45 Ga mafic dykes in northern Finland: constraints on the origin of PGE mineralization in coeval layered intrusions	997
Fang-Fang Guo, Wolfgang D Maier, Jouni Vuollo, Yann Lahaye, Hannu Huhma, Hugh O'Brien & Hanna Junttila	

Multi-stage emplacement and PGE-enrichment in the River Valley Intrusion, Ontario, Canada: implications for 'contact-type' PGE-Cu-Ni mineralization	1001
David A. Holwell, Emily A. Firth, Reid R. Keays & Jon Findlay	
The Platinova Reef, Skaergaard Intrusion, East Greenland: an example of the formation of low volume, high tenor magmatic PGE-Au mineralization in closed systems	1005
David A. Holwell & Reid R. Keays	
Temporal and spatial distribution of magmatic Ni-Cu-PGE, Cr, and Fe-Ti-V deposits in the Bird River-Uchi-Oxford-Stull-La Grande-Eastmain superdomain: a new metallogenic province within the Superior Province	1009
M.G. Houlié, C.M. Leshner, R.T. Metsaranta, J. Goutier, H.P. Gilbert & V. McNicoll	
Sulfur degassing and nickel sulfide ore forming process in Archean komatiite volcanoes	1013
Carissa Isaac, Marco L. Fiorentini & Boswell Wing	
The chromite-bearing ultramafic-mafic complexes of the Vizcaíno Peninsula (Baja California Sur, Mexico), re-visited for platinum-group minerals	1017
Luis A. Jiménez-Galindo, José M. González-Jiménez, Antoni Camprubí, Michelangelo Martini, Elena Centeno-García, Joaquín A. Proenza, William L. Griffin, Suzanne Y. O'Reilly & Norman J. Pearson	
Platinum-group-element and -mineral distribution and fine-scale chemical variation of chromite in the UG-2 chromitite, western Bushveld Complex, South Africa	1020
Malte Junge, Thomas Oberthür & Frank Melcher	
Magma mingling between sulphide-rich and carbonatite magmas to form a multi-commodity metal deposit: reconstruction using QEMSCAN® analysis	1024
Dora Kavecsanszki, Kathryn R. Moore, Gavyn K. Rollinson, Frances Wall & Paul A.J. Lusty	
Platinum mineralization at Owendale, NSW, Australia: new insights into the genesis of Pt mineralization in Alaskan-type ultramafic complexes	1028
Reid R. Keays, Hazel M. Prichard, Peter C. Fisher & Benjamin A. Sharp	
Variation in PGM within two orebodies in the Jinchuan intrusion, Gansu province, NW China	1032
Robert D. Knight, Hazel M. Prichard, Iain McDonald & Christina Y. Wang	
Dyumtaleyky massif, Taimyr, Russia: a magmatic derivative from a complex mantle source	1036
N.A. Krivolutskaya & B.I. Gongalskiy	
Catastrophic sulfide saturation and genesis of Ni-Cu-PGE mineralization in the Sudbury Igneous Complex	1040
CM Leshner	
Platinum-group element contents of kimberlites: constraints on mantle sources	1044
WD Maier, I McDonald & A Le Roex	
Processes affecting the massive sulphide lenses at the Delta deposit, Cape Smith Belt, Canada: implication for the distribution of PGE	1047
Pierre-Jean Misson, Sarah-Jane Barnes & Philippe Pagé	
Improved in-situ determination of PGE concentration of chromite by LA-ICP-MS: Towards a better understanding	1050
Philippe Pagé & Sarah-Jane Barnes	
Structure and dynamics of magmatic Ni-Cu sulphide deposits: theory, analogue modelling and insights from Voisey's Bay (Labrador, Canada)	1054
Benoit M. Saumur, Alexander R. Cruden, David Boutelier & Dawn Evans-Lamswood	
Petrology of low-sulphide PGE ores of the Norilsk region	1058
Sergey Sluzhenikin, Vadim Distler & Antonina Grigor'eva	
The emplacement and relative timing of PGE mineralisation within the northern Bushveld Complex	1061
Jennifer Smith, David Holwell, Adrian J. Boyce & Iain McDonald	
Formation of magmatic sulfide deposits in arcs	1065
Andrew G. Tomkins, Kyle C. Rebryna, Roberto F. Weinberg & Bruce F. Schaefer*	
Geology and stratigraphy of the Black Thor and Black Label chromite deposits, James Bay Lowlands, Ontario, Canada	1069
Ryan J. Weston & David A. Shinkle	
The structure of sulfide droplets zone in the "Rudniy" mafic intrusion (Tsagaan-Shuvuut ridge, NW Mongolia)	1072
Andrey Vishnevskiy, Maria Cherdantseva & Andrey Izokh	

Strontium isotope disequilibrium of plagioclase in the upper critical zone of the Bushveld complex: evidence for mixing of crystal slurries	1076
Shenghong Yang, Wolfgang Maier, Yann Lahaye & Hugh O'Brien	
Origin of Bushveld magmas via new constraints from Pb-Hf zircon systematics	1080
Marina Yudovskaya, Judith Kinnaird, Elena Belousova, Norman Pearson, Jan Kramers & Dmitry Kuzmin	
Orogenic gold deposits	1085
The orogenic gold mineral system	1086
T. Campbell McCuaig & Jon M.A. Hronsky	
The boron isotope composition of tourmaline from the Val-d'Or orogenic gold deposits, Québec, Canada	1090
Georges Beaudoin, Claire Rollion-Bard & Gaston Giuliani	
Various alteration stages in the Nalunaq gold deposit, south Greenland	1093
Robin-Marie Bell & Jochen Kolb	
World-class Mesozoic orogenic gold deposits, Jiaodong Peninsula, eastern China: constraints on timing, structural controls, and mineralization styles	1097
Hong-Rui Fan, Fang-Fang Hu, Kui-Feng Yang, Xiao-Chun Li & Ting-Guang Lan	
Mesozoic quartz-vein hosted Au (Ag-Pb-Zn-Cu) mineralisation at Mineral de Talca, Coastal Range, Chile: the role of felsic intrusives	1101
Emily A. Firth, David A. Holwell, Matthew P. Rovardi, Nick H. S. Oliver, Adrian J. Boyce & James K. Mortensen	
Multistage mineralization of the giant Obuasi gold deposit, Ghana	1105
Denis Fougerouse, Steven Micklethwaite, John Miller, T. Campbell McCuaig & Stanislav Ulrich	
Fluid inclusion and oxygen isotope constraints on gold mineralisation in the Senoufo Greenstone Belt, Côte d'Ivoire	1109
Lynnette Greyling, Chris Harris & Paul Harbidge	
Gold systems in the Lower Crustal Section ("bottom") of Greenstone Belts	1113
Steffen G. Hagemann, Kevin F. Cassidy & Walter Witt	
Gold and associated mineralisation in the Tyndrum area, Scotland: orogenic or intrusion-related?	1117
Nyree J. Hill, Gawen R.T. Jenkin & Christopher J.S. Sangster	
Mineralogical characteristics of a metasedimentary hosted Hosko gold deposit from the Archaean Hattu Schist Belt, eastern Finland	1120
Asko Käpyaho, Ferenc Molnár & Grigorios Sakellaris	
Hypozonal orogenic gold deposits: are they a myth?	1124
Jochen Kolb, Annika Dziggel & F. Michael Meyer	
The Velkua gold prospect in the high metamorphic grade area of south-western Finland	1128
Niilo Kärkkäinen, Asko Käpyaho, Raimo Lahtinen & Tuomo Törmänen	
Structural controls on orogenic gold mineralisation along the Dugbe Shear Zone, eastern Liberia	1132
R.G. Langdon, J.C.Ø. Andersen, R.K. Shail & D.A. Pelham	
Structural framework and evolution of the world class Siguiri orogenic gold district (Guinea, West Africa)	1136
Erwann Lebrun, John Miller, Nicolas Thébaud, T. Campbell McCuaig & Stanislav Ulrich	
Deep crustal-scale controls of orogenic gold mineral systems – Hodgkinson metallogenic zone, north Queensland, Australia	1140
Vladimir Lisitsin, Paul Donchak & Matthew Greenwood	
Depth variation characteristics at the Carruagem orebody, Archean BIF-hosted Lamego gold deposit, Quadrilátero Ferrífero, Brazil	1144
L.M. Lobato, B.S. Martins, C.A. Rosière, R.C. Figueiredo e Silva, A.M. Victória, L.H.A. Lemos, F.L.S.P. Villanova & L.F.S. Amaral.	
Zircon multi-isotopic mapping in Wabigoon Subprovince, western Superior Craton: implications for lithospheric architecture and controls on orogenic gold mineral systems	1148
Yong-jun Lu, T. Campbell McCuaig, Pete Hollings, Kirsty Ketchum, Robert Kerrich, Mark Smyk, John Cliff & Leon Bagas	
Structural setting and mineralisation of the carbonate-hosted Sadiola gold deposit, Mali, West Africa.	1152
Quentin Masurel, John Miller, Nicolas Thebaud, T.C. McCuaig & Stanislav Ulrich	

The amphibolite facies Lindsays deposit, Coolgardie Goldfield, Yilgarn Craton, Western Australia: a type example of the crustal continuum model?	1156
John Miller & Garry Adams	
Signatures of overprinting mineralisation processes in the orogenic gold deposit of the Pampalo mine, Hattu schist belt, eastern Finland	1160
Ferenc Molnár, Hugh O'Brien, Yann Lahaye, Asko Käpyaho & Grigorios Sakellaris	
Mineralization style and geochronology of the Sekisovka gold deposit, eastern Kazakhstan	1164
Evgeniy Naumov, Arkady Mizerny, Reimar Seltmann, Konstantin Kovalev & Andrey Izokh	
Gold-bismuth mineralisation in the orogenic gold occurrences of the Kuhmo greenstone belt (Finland)	1168
Konstantin Novoselov, Elena Belogub, Olga Ermolina & Alexandr Mikhailov	
Age constraints on host rocks for gold mineralisation in the Ashanti Belt, Ghana	1171
Luis A. Parra, Marco L. Fiorentini, John Miller, T. Campbell McCuaig, Yan Bourassa & Stéphane Perrouty	
The importance of black shales in the origin of the Amantaytau orogenic gold deposit in Uzbekistan: evidence from pyrite chemistry and sulfur isotope data	1174
Jan Pašava, Anna Vymazalová, Petr Dobeš, Hartwig Frimmel, Alexandr V. Jukov & Rustam I. Koneev	
Reaction mechanisms and gold mineralisation	1178
Mark A. Pearce, James S. Cleverley & Robert M. Hough	
Genesis of Archean batholith-hosted gold veins at the Lac Herbin deposit, Val-d'Or, Canada: mineralogical and fluid inclusion constraints	1182
Hervé Rezeau, Robert Moritz & Georges Beaudoin	
Geological setting of the Telfer gold-copper deposit and surrounding areas, Paterson orogen, Western Australia	1186
C. Schindler & S.G. Hagemann	
Geological, petrographical and geochemical characteristics of the granitoid hosted Amphibolite Ridge gold occurrence in south Greenland	1189
Denis Martin Schlatter, Alfons Berger & Ole Christiansen	
Svartliden gold mine: shear zone and BIF-hosted orogenic gold deposit, Gold Line, northern Sweden	1193
Katerina Schlöglova, Chris Gordon, Roman Hanes Henrik Ask & Curt Broman	
Fluid inclusion studies, and sulfur and oxygen isotope signatures at the Carvoaria Velha orogenic gold deposit, Quadrilátero Ferrífero, Brazil	1197
Rosaline C Figueiredo e Silva, Yuri Ribeiro, Lydia M Lobato, Steffen Hagemann & John Clifff	
The orogenic and not so orogenic gold deposits of the Agnew Gold Camp (Yilgarn Craton, Western Australia)	1201
Nicolas Thébaud, John Miller, Campbell McCuaig, Louise Fisher & Iris Sonntag	
A model for the Shuangwang hydrothermal breccia gold deposit, Taibai County, Shaanxi Province, China	1205
Wang Jianping, Liu Jiajun, Qi kaijing, Liu Zhenjiang, Wang Kexing, Liu Bizheng, Zeng Xiangtao & Wang Huan	
Structure of the Mick Adam gold deposit: Yilgarn Craton, Western Australia	1209
James Warren, Nicolas Thébaud & Steven Micklethwaite	
Ore genesis study of the shear zone-hosted Tianjingshan gold deposit, Anhui Province, China	1213
Yuling Xie, Yancen Jiang, Yanwen Tang, Simon C Dominy & Aiguo Wang	
Structural evolution and settings of orogenic gold and intrusion-related gold deposits in the central part of the Bohemian Massif, Czech Republic	1216
Jiří Zachariáš	
Re–Os age dating of the Hadamengou Au deposit, Inner Mongolia, China and its geological significance	1219
Wei-Bo Zhang, Wan-Rong Hou & Feng-Jun Nie	
Hydrothermal ore-forming processes	1223
Ag-Hg vein deposits hosted by Triassic dolostones from the Mina de la Guerra Antigua, Villahermosa del Rio (Castelló, Spain)	1224
Albert Acedo, Marina Galindos, Miriam Pastor, Ricard Segura, Sandra Amores & Joan Carles Melgarejo	
Hydrothermal ree rich minerals in granites from Lagoa Real uranium province Ba-Brazil	1228
Lucas Eustáquio Dias Amorim, Monica Elizetti Freitas, Francisco Javier Rios & Evando Carele de Matos	

Two types of non-conventional PGE mineralizations near Poblet, Catalonia (Spain): a possible metallogenic heritage?	1232
Carlos Arbiol-González, Núria Conesa, Àngels Canals, Joaquín A. Proenza, Joan Carles Melgarejo & Esteve Cardellach	
The Huanuni Sn-W-Pb-Zn-Ag vein deposits, Bolivia: structure and mineralogy	1236
Laia Arqués Farré, Andreu Cacho Amorós, David Artiaga Torres, Belén Torres Cueva, Lisard Torró i Abat, Joan Carles Melgarejo i Draper, Ramiro Condori, Néstor Guevara & Osvaldo Arce	
The Viloco Sn-W-Mo-As deposits, Bolivia: geology and mineralogy	1239
David Artiaga, Belén Torres, Lisard Torró, Esperança Tauler, Joan Carles Melgarejo & Osvaldo R. Arce	
Formation conditions of Hg-silver deposition at the Imiter deposit (Anti-Atlas, Morocco)	1243
A.S.Borisenko, A.A. Borovikov, G.G. Pavlova, Yu.A. Kalinin, P.A. Nevolko, L.V. Gushchina, V.I. Lebedev, L. Maacha & A.V. Kostin	
Proterozoic metallogeny in the NW border of Botswana	1247
Sergi Cardona, Lisard Torró, Marc Campeny, Eloi Andreu, Joan Carles Melgarejo, Joaquín A. Proenza, Mike C.J. De Witt, James M. Bruchs & John F. Lewis	
REEY characteristics in hydrothermal gangue carbonates within the sediment-hosted Nkana-Mindola Cu-Co deposit (Zambia) and in two polymetallic vein-type deposits (Kipushi and Dikulushi, Democratic Republic of Congo)	1251
David Debryne, Philippe Muchez, Lieve Balcaen & Frank Vanhaecke	
Understanding gold mineralisation: linking chemical and structural changes	1255
Angela Halfpenny, Louise Fisher, Robert Hough & James Cleverley	
Ore-forming processes in Reykjanes geothermal pipelines, Iceland	1259
V Hardardóttir, JW Hedenquist & MD Hannington	
Comparison of metals in seawater-dominated fluids of Reykjanes, Iceland, and seafloor black smoker systems	1263
V Hardardóttir, JW Hedenquist & MD Hannington	
Reactive fluid flow and integrated fluxes recorded by tin-bearing greisens, Krušné hory (Erzgebirge) Mts., central Europe	1267
Matylda Heřmanská & David Dolejš	
Hydrothermally induced fluorine enrichment in metagranitoids of the Felbertal scheelite deposit (Austria)	1271
Michael Kozlik & Johann G. Raith	
Cu-sulphides – native silver association in the Cu-Ag deposit, Lubin mine, Fore-Sudetic Monocline (SW Poland)	1275
Gabriela A. Kozub	
Potential role of a buoyant CO ₂ vapour phase in the formation of the Mount Isa copper ore deposit	1279
Michael Kühn & Klaus Gessner	
Cobalt-bearing structures of Tuva (Russia)	1283
Vladimir I. Lebedev & Irina G. Tretiakova	
T-P-X evolution path of ore forming fluid in Qiaogong polymetallic deposit, Tibet, China	1287
Yingxu Li, Guangming Li, Li Zhang, Yuling Xie, Baoshun Liu & Lamei Li	
Sulfur isotope composition of granite-molybdenum systems formed within a collided orogen setting: insights from the Newfoundland Appalachians, Canada	1291
Edward P. Lynch, Martin Feely, David Selby, Derek H.C. Wilton & Anthony E. Fallick	
Fault stepovers and gold mineralisation	1295
Steven Micklethwaite	
Pyrite trace element geochemistry of west and east Jiaodong gold district: insight into diverse metal sources in intrusion-hosted gold deposits	1299
Stephanie E. Mills, Andrew G. Tomkins & Roberto F. Weinberg	
The Mariana-San Marcos vein system: shallow features of epithermal Au-Ag deposits, Cerro Negro District, Deseado Massif, Argentina	1303
Conrado Permuy Vidal, Diego M. Guido, Sebastián M. Jovic & Gassaway Brown	
Primary and secondary deposits from the Crisoleja area (Pb-Zn-Ag-Sn), La Unión, Murcia, Spain	1307
Núria Pujol, Aleu Andreazini Sabaté, Stefania Schamuells, Sandra Amores Casals, Cristina Villanova-de-Benavent, Lisard Torró, Joan Carles Melgarejo & José Ignacio Manteca	
The mineral association in the Emilia and Brunita Pb-Zn-Ag-(Sn) deposits, La Unión, Murcia, Spain	1311
Lara Sanmartí Rodríguez, Anna Gaya Manós, Carlota Molina Treviño, Sandra Amores Casals, Cristina Villanovade-Benavent, Lisard Torró i Abat, Joan Carles Melgarejo i Draper & José Ignacio Manteca	

The San José and Gloria Pb-Zn-Ag-Sn deposits, La Union: An approach to the mineral sequence	1315
Júlia Soler, Júlia Farré, Lena Portell, Sònia Jou, Omar Corrales, Sandra Amores, Cristina Villanova, Lisard Torró, Joan Carles Melgarejo & José Ignacio Manteca	
Unconventional PGE mineralizations: a review	1319
Bernhard Stribny	
Structural constraints on the formation of Cu-rich mesothermal vein deposits in the Repparfjord Tectonic Window, northern Norway	1323
Espen Torgersen, Giulio Viola, Jan Sverre Sandstad & Holly Stein	
The Poopó Sn-Ag-Zn-Pb vein deposit, Bolivia: structure and mineralogy	1327
Belén Torres, David Artiaga, Lisard Torró, Esperança Tauler, Joan Carles Melgarejo & Osvaldo R. Arce	
Gold metallogenesis of The Novo Mundo granite, eastern sector of the Alta Floresta Gold Province (MT), Amazon Craton	1331
Verônica Godinho Trevisan, Roberto Perez Xavier, Rafael Rodrigues de Assis & Antônio João Paes de Barros	
Hydrothermal natrolite formation in the Fohberg phonolite, Kaiserstuhl volcanic complex, Germany	1335
Tobias Björn Weisenberger & Simon Spürgin	
The REE distribution patterns in altered rocks: implications for the genesis of orogenic gold deposits	1339
Olga V. Vikent'eva, Gennadii N. Gamyani & Nikolay S. Bortnikov	
Contrasting W and Sn mineralization events and related granitoids in Wangxianling-Hehuaping area, Nanling Range, South China	1343
Rongqing Zhang, Jianjuan Lu, Rucheng Wang, Xiancai Lu, Jichun Guo, Fuchun Li, Bernd Lehmann, Yuan Yao & Weiming Guo	
New developments in the understanding of IOCG deposits	1347
Vertical zoning and continuity in Fe oxide(-Cu-Au-Ag-Co-U-P-REE) (or 'IOCG') systems: Cordilleran insights	1348
Mark D. Barton, David A. Johnson, Douglas C. Kreiner & Eric P. Jensen	
The Merlin high grade Mo-Re deposit, Cloncurry District, Australia	1352
Joao Babo, Carl Spandler, Mike Rubenach, Nick Oliver & Mat Brown	
The geology of the giant Pampa de Pongo magnetite skarn (S Peru) and its relationship with IOCG systems	1355
Gustavo Calvo, Fernando Tornos & Francisco Velasco	
Age constraints on the Merlin molybdenum-rhenium deposit, Cloncurry District, Queensland, Australia: are we dealing with a unique addition to the IOCG family?	1359
Rob Duncan, Holly Stein, Murray Hitzman & Eric Nelson	
Skarn alteration in iron oxide-copper-gold systems, the Pocheon magnetite deposit, Korea	1363
Ji Su Go, Seon-Gyu Choi, Jieun Seo, Jung-Woo Park & Sang-Tae Kim	
Sulphur isotope geochemistry and ¹⁸⁷ Re- ¹⁸⁷ Os temporal constraints on the formation of polymetallic iron-oxide-dominated deposits in the Great Bear magmatic zone, NWT, Canada	1366
Pedro Acosta-Góngora, Sarah A. Gleeson, Robert Creaser, Bruce E. Taylor, Iain M. Samson, Luke Ootes & Louise Corriveau	
The Oued Belif breccia (northern Tunisia): a Miocene representative of the (IOCG)-IOU class of deposits	1370
Christian Marignac, Sophie Decrée, Thierry De Putter, Johan Yans, Norbert Clauer & Jean-Marc Baele	
A new perspective on the giant Salobo IOCG deposit, Carajás Province, Brazil	1374
Gustavo Henrique Coelho de Melo, Roberto Perez Xavier, Érika Suellen Barbosa Santiago, Lena Virginia Soares Monteiro, Antonio Fabricio Franco dos Santos, Axel Torres, Benevides Aires	
Metallogenetic evolution of the Archean and Paleoproterozoic Iron oxide Cu-Au systems in the southern copper belt, Carajás Province	1378
Carolina P. N. Moreto, Lena V. S. Monteiro, Roberto P. Xavier, Robert A. Creaser, Andy DuFrane, Wagner S. Amaral, Marco A. D. Silva & Gustavo H. C. Melo	
End-Permian Phreatomagmatic pipes of the Tunguska basin: IOCG deposits linked with the Siberian traps large igneous province	1382
Polozov A.G., Svensen H. & Planke S.	
Ore-forming brine-melts and fluids of the Karasug Fe-F-REE carbonatite deposit, Russia	1386
Ilya R. Prokopyev, Andrey A. Borovikov, Galina G. Pavlova & Alexander S. Borisenko	

The isotopic record of sulphur from Archean and Proterozoic Cu-Au deposits in the Carajás Mineral Province, northern Brazil	1390
Érika Suellen Barbosa Santiago, Roberto Perez Xavier, Lena Virginia Soares Monteiro, Steffen Hagemann & John Cliff	
In situ U-Pb and whole rock Nd data for the Kiruna iron oxide apatite deposits and their host rocks, Norrbotten, Sweden	1394
Anne Westhues, John M. Hanchar, Martin J. Whitehouse & Olof Martinsson	
Mineralogical and fluid characteristics of the Monakoff and El deposits, Cloncurry Region: implications for regional F-Ba-rich IOCG mineralisation	1398
Megan R. Williams, David A. Holwell, Richard M. Lilly, Iain McDonald & Adrian J. Boyce	
Sources of mineralizing fluids in Cu-Au systems from the Carajás Mineral Province (Brazil): constraints from in-situ microanalysis of hydrogen and boron isotopes in tourmaline	1402
Roberto Perez Xavier, Robert B. Trumbull, Michael Wiedenbeck & Lena Virginia Soares Monteiro	
Metallogenesis of collisional orogens in the tethyside domain	1407
Mineralization styles and orogen episodes in the Tethyan	1408
Jeremy P. Richards	
Bondar-e-Honza: An oldest and special porphyry copper (molybdenum) deposit in the Kerman porphyry copper belt, Iran	1412
Mehraj Aghazadeh, Zahra Badrzadeh & Zangqian Hou	
Hydrothermal alteration zones associated with Sargaz orebody, SE Iran	1416
Zahra Badrzadeh & Mehraj Aghazadeh	
Collision- and subduction-related porphyry Cu deposits in Tibetan orogen: a possible genetic linkage	1420
Zengqian Hou, Zhiming Yang, Yuanchuan Zheng, Juxing Tang & Zhusen Yang	
The giant Jinding Zn-Pb deposit: ore formation in an evaporite dome, Lanping Basin, Yunan, China	1424
David L. Leach, Yucai Song, Zengqian Hou, Tiannan Yang & Chuandong Xue	
Cu isotope fractionation during fluid evolution process in Qulong porphyry copper deposit, Tibet	1428
Zhenqing Li, Zhiming Yang, Xiangkun Zhu & Zengqian Hou	
Sediment-hosted Pb-Zn deposits controlled by facies transition in Tibetan orogenic belt: character and genesis – a case study of the Lalongla Pb-Zn deposit	1431
Yingchao Liu, Zengqian Hou & ZhuSen Yang	
Mineralization of the Dalucao REE deposit at Himalayan Mianning–Dechang REE belt in the Eastern Indo-Asian collision zone, SW China	1435
Yan Liu, Zengqian Hou, Zhusen Yang & Shihong Tian	
The sediment-hosted Pb-Zn polymetallic deposits in Zhaxikang ore district, northern Himalayan metallogenic belt, Tibet, China	1439
Guang-Ming Li, Yingxu-Li, Qing ZHOU, Sui-Liang DONG & Xiang-Biao XIA	
Genesis of fertile hydrous adakite-like melts in post-subduction porphyry Cu systems of Tibet	1443
Yong-jun Lu, Robert R. Loucks & Marco L. Fiorentini	
Jurassic to Tertiary metallogenic evolution of the southernmost Lesser Caucasus, Tethys belt	1447
Robert Moritz, Johannes Mederer, Maria Ovtcharova, Richard Spikings, Dave Selby, Rafael Melkonyan, Samvel Hovakimyan, Rodrig Tayan, Alexey Ulianov & Vagif Ramazanov	
Tectonic and structural setting of porphyry Cu-Au and epithermal Au mineralization of the Biga Peninsula, NE Aegean	1451
Matias G. Sanchez, Ken McClay & Adrian King	
Mineral deposit model of the Duolong gold-rich porphyry copper deposit cluster in Gaize County, Tibet: evidence from zircon U-Pb dating	1455
Guo Shuo, Zhao Yuanyi, Li Xiaosai, Xu Hong, Liu Xiaofei & Lü Lina	
Fluid inclusion and H, O, C, and Sr isotopes of Jinman-Liancheng vein Cu deposit in Lanping basin, Yunan, China: constraints on mineralization T-P-X conditions and source of the ore-forming fluid	1459
Yucai Song, Zengqian Hou, Wang Guanghui & Chuandong Xue	
Rb-Sr and Sm-Nd isochron ages of the Dongmozhazhua and Mohailaheng Pb-Zn ore deposits in the Yushu area, southern Qinghai and geological implications	1463
Shihong Tian, Zengqian Hou, Yingchao Liu, Yucai Song & Zhusen Yang	
Metallogenesis of the Au-Ag Middle Palaeozoic Kedon Volcanic Belt of the Omolon Cratonic Terrane (Northeast Russia)	1466
A. V. Volkov, A. A. Sidorov, V. Yu. Alexeev & N. E. Savva	

Geological and geochemical characteristics of Baiyangping lead-zinc polymetallic deposit in the Sanjiang Neo-Tethyan area, China	1469
Xiao-Hu Wang, Zeng-Qian Hou, Yu-Cai Song & Hong-Rui Zhang	
Increased magmatic water content — the key to Oligo-Miocene porphyry Cu-Mo±Au formation in the Gangdese belt, Tibet	1472
Rui Wang, Jeremy P. Richards, Zengqian Hou & Zhiming Yang	
A model for carbonatite hosted REE deposits: Mianning-Dechang REE belt in Western Sichuan province, China	1475
Yuling Xie, Yingxu Li, Zengqian Hou, Simon C. Dominy, David R. Cooke & Leonid Denyushevsky	
Sandstone- and conglomerate-hosted Urogen Zn-Pb deposit, Xinjiang, NW China	1479
Chunji Xue & Guoxiang Chi	
A preliminary study on geology of the post-collisional porphyry Mo-Cu deposit at Narigongma, Tibet	1483
Zhiming Yang	
Structural controls on carbonate-hosted Pb-Zn mineralization in the Dongmohazhua deposit, central Tibet	1487
Hongrui Zhang, Tiannan Yang, Zengqian Hou, Yucai Song, Yingchao Liu, Zhusen Yang, Shihong Tian, Fuchun Wang, Wanwen Xue & Yubao Zhang	
Magmatic-hydrothermal evolution of the Bolong porphyry copper deposit, Tibet, China	1491
Xiangping Zhu, Guangming Li, Huaan Chen & Dongfang Ma	
Miocene leucogranites, southern Tibet: geochemical characteristics and geodynamic significance	1493
Song Xiaoqin, Zhong Kanghui, Chen Bo & Gou Jie	

S 3.6

**Ore deposits associated with
mafic and ultramafic rocks**

SPONSORED BY CODMUR/IAGOD

Convenors:

Wolfgang Maier & Michael Lesher

KEYNOTE SPEAKER

Magma dynamics and the formation of magmatic sulfide deposits

Nicholas Arndt

IS Terre, Université de Grenoble, 38400 Grenoble, France, arndt@ujf-grenoble.fr

Stephane Sobolev

Deutsches GeoForschungsZentrum GFZ, Telegrafenberg, 14473, Potsdam, Germany

Stephen Barnes and Jesse Robertson

CSIRO earthscience and resource engineering, 26 Dick Perry Ave, Kensington, Perth, WA 6151

Abstract

Magmatic Ni-Cu sulfide deposits form when immiscible sulfide liquid separates from a mafic or ultramafic magma. The trigger is commonly assimilation of wall rocks, which adds sulfur and/or decreases sulfide solubility. When the segregated sulfide interacts with large volumes of magma, it scavenges chalcophile elements (Ni, Cu and PGE) to produce high-tenor ores. Such processes should operate in most or all magmatic systems, but ore deposits are found only in restricted parts of certain magmatic provinces. The restricted distribution might be explained by the craton-margin model, according to which deposits form when a mantle plume ascends at the sloping contact of cratonic lithosphere. The hypothesis that ore metals are derived from metasomatically enriched portions of the sub-continental lithospheric mantle (SCLM) receives little support when the compositions of ore-bearing magmas and samples from the SCLM are examined. A better understanding of the controls on ore formation will come from modelling of flowage of mixtures of silicate and sulfide liquid and solid phases (crystals and rock fragments) in the complex magmatic conduits that constitute contain the ore deposits.

Keywords. Ni sulfide deposit, craton margin, sub-continental lithospheric mantle, metasomatism, magma dynamics

1 The Ore-Forming Process

In broad terms we understand how a magmatic sulfide deposit forms. Mafic or ultramafic magma produced by relatively high degrees of partial melting in the mantle ascends to the upper parts of the continental crust where it interacts with granitic or sedimentary rocks. This interaction triggers the segregation of immiscible sulfide liquid, either by lowering the solubility of sulfide or by adding additional sulfur or a combination of both. Ore metals such as Ni, Cu and the PGE are strongly chalcophile and they become concentrated in the sulfide liquid. In some cases gravitative settling of dense sulfide droplets is sufficient to concentrate the sulfide in the lower part of an intrusion or lava flow, and if the tenor and tonnage is sufficient, an ore deposit is formed. Closer examination reveals that the process is more complicated. In many deposits, a small intrusion hosts a large amount of sulfide. The quantity of sulfide in the ore deposit is far higher than would be predicted on the

basis of our knowledge of the solubility of sulfide in mafic or ultramafic magma: an additional process must have extracted the sulfide from a volume of magma larger than that represented by the intrusion. In many cases the metal tenor (the concentration of metals in the sulfide) is greater than that expected if the sulfide had segregated from the small volume of magma; instead the sulfide must have interacted with, and extracted metals from, a much larger volume. Ore bearing intrusions normally are one of many units in large intrusive complexes: the intrusions that host the Norilsk-Talnakh ore bodies, for example, are restricted to a small part of a vast complex of sills that extends for thousands of kilometres around the lower margin of the Siberian flood basalts. The lithology, geochemistry and structure of the intrusions and the nature of their host rocks provide few clues as to why the Norilsk-Talnakh intrusions are the hosts of some of the world's richest ore bodies, while the other intrusions in the same intrusive complex seem to be barren.

2 The Craton-Margin Model

Various models have been proposed to explain the features discussed above. According to the "craton margin model" such deposits are located at the peripheries of Archean cratons (Begg et al. 2011). According to this model, the change in thickness of the continental lithosphere guides the ascent of the plume source, and/or the magmas themselves, so as to produce a high magma flux at the margin of the craton. When these magmas interact with sedimentary rocks in basins adjacent to the cratons, the assimilation of sedimentary sulfur could have triggered the segregation of sulfide. When these models are explored using numerical modelling of the impingement of a plume at a craton margin (Fig.1), some of the results are encouraging. Melting is indeed higher at the margin and high-flux magmas ascend at this junction. However high magma fluxes are distributed over a 500-km-wide zone and not immediately at the margin. Furthermore, when a plume ascends beneath the thin lithosphere beneath the West Siberian basin, which borders the Norilsk-Talnakh Ni-Cu sulfide deposits, the overall degree of melting is higher than at the craton-margin. In this situation as well, there is ample opportunity for the magma to interact with sediment. It is that ore deposits do not form in this context, because the melt is too widely dispersed across the entire melting zone.

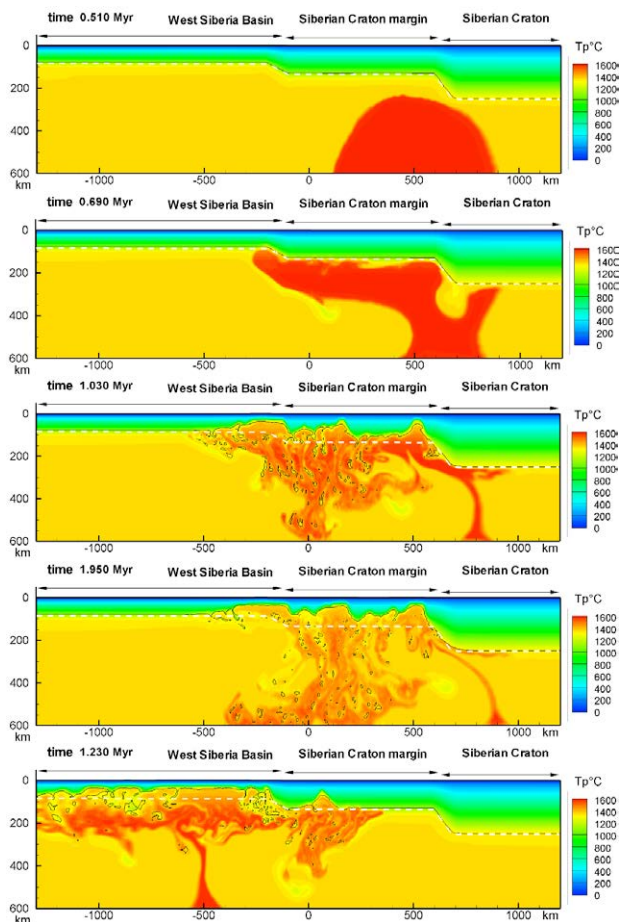


Fig 1. Images showing the temperature distributions in plumes rising at the boundary of an Archean craton, as at the margin of the Archean craton where the Norilsk-Talnakh deposits are localized. The top four diagrams show that the plume flows laterally towards to the thinner lithosphere, then upwards: as it ascends it partial melts and magma formation is thereby focussed near the craton margin. The lower diagram shows a plume ascending beneath thinner lithosphere beneath the West Siberian Basin where the plume produces high-degree melts dispersed over a wide area. Diagrams from S. Sobolev (unpublished) using techniques described by Sobolev et al. (2012)

3 A source in metasomatised sub-continental lithospheric mantle?

Another model calls on the generation of metal-enriched magmas from metasomatised parts of the sub-continental lithospheric mantle. Evaluation of the compositions of mantle xenoliths and of magmas derived from the lithosphere, however, provides little support for this model. As shown in Figure 2, there is little evidence that the metasomatised lithosphere is enriched in ore metals and little evidence that melting of any part of the lithospheric mantle produces the high-volume, high-flux magmas that yield magmatic ore deposits.

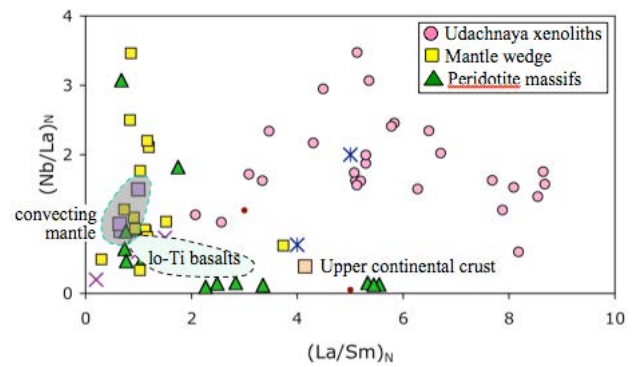


Fig. 2: Comparison between some critical trace-element ratios in samples from subcontinental lithosphere (xenoliths and peridotite massifs) and those of the parental magmas of magmatic ore deposits (labelled “lo-Ti basalts”). The samples from the lithosphere have compositions that do not coincide with those of ore-bearing magmas. In addition, their vast range of compositions is in marked contrast with the relatively uniform compositions of ore-bearing magmas (diagram from Arndt, 2013)

4 Dynamics of magma flow in sub-volcanic systems

A more fruitful line of investigation centres on the dynamics of magma flow in the conduit system that feeds the ore-bearing intrusions. There is evidence in some ore deposits (e.g. Norilsk, Jinchuan, Aguablanca) that the sulfides did not segregate from free-flowing magma but were forcefully injected as breccias or crystal mushes.

As magma ascends through the crust, it partially crystallizes because of pressure drop and heat loss. Once the proportion of phenocrysts exceeds 20-30%, the density of the crystal mush exceeds that of normal crustal rocks. If a sulfide liquid segregates, its presence further increases the density of the crystal mush. In inclined portions of the conduit system (for example in the rims of saucer-shaped intrusions), crystal-free melt continues to flow upwards while the mush stagnates at the lower contact. Periodically the dense mush will slump downwards, to be injected into the lower parts of the conduit system. Many puzzling features of magmatic sulfide deposits – the formation and migration of dense crystal-sulfide mushes, the taxitic textures, the evidence of injection into ore-bearing intrusions of multiple pulses of melt, crystals and sulfide liquid, the injection of sulfide liquid into floor rocks, the extensive interaction of sulfide with melt which boosts metal tenors – might result from the downward migration of crystals and sulfide that had accumulated higher in the system.

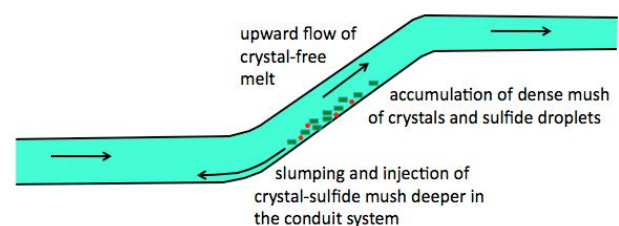


Fig. 3: Sketch showing how the accumulation, slumping and reinjection of dense crystal-sulfide mush can explain some features of magmatic sulfide deposits.

A better understanding of these processes – essential if we are to come to grips with the formation of, and exploration for, sulfide ore deposits – will come from detailed lithological, geochemical, structural and geophysical mapping of individual intrusions, the treatment of these intrusions as part of the broader intrusive complexes, and analogue and numerical modelling of magma flow within such complexes, along the lines explored by Kerr and Leach (2005) and Li et al. (2009).

References

- Arndt, N.T. (2013) The lithospheric mantle plays no active role in the formation of magmatic ore deposits. *Economic Geology* (in press).
- Begg, G., Hronsky, J.A., Arndt, N.T., Griffin, W.L., O'Reilly, S.Y., Hayward, N. (2011) Lithospheric, cratonic, and geodynamic setting of Ni-Cu-PGE sulfide deposits, *Economic Geology*, 105, 1057-1070
- Kerr, A. and Leitch, A.M. (2005) Self-destructive sulfide segregation systems and the formation of high-grade magmatic ore deposits: *Economic Geology*, 100, 311-332.
- Li, C., Ripley, E.M., and Naldrett, A.J., (2009). A new genetic model for the giant Ni-Cu-PGE sulfide deposits associated with the Siberian flood basalts: *Economic Geology*, 104, 291-301.
- Sobolev S.V., Sobolev A.V., Kuzmin D.V., Krivolutsкая N.A., Petrunin A.G., Arndt N.T., Radko V.A., Vasiliev Yu.R. (2011). Linking mantle plumes, large igneous provinces and environmental catastrophes. *Nature* 477 (7364), 312-316.

Platinum group elements in different types of Ni-laterite profiles from the northern Caribbean: a geochemical comparison

T. Aiglsperger, J.A. Proenza

Departament de Cristal·lografia, Mineralogia i Dipòsits Minerals. Facultat de Geologia, Universitat de Barcelona, C/ Martí i Franquès s/n, E-08028 Barcelona, Spain

J. F. Lewis

Department of Earth and Environmental Sciences, The George Washington University, 20052 Washington D.C., USA

F. Zaccarini, G. Garuti

Department of Applied Geological Sciences and Geophysics, The University of Leoben, P. Tunner Str, 5, A-8700 Leoben, Austria

A. Rojas-Purón

Departamento de Geología del ISMM, Moa, Holguín, Cuba

F. Longo

Falcondo Xstrata Nickel, Box 1343, Santo Domingo, Dominican Republic

A. Chang

Empresa Geominera Camagüey, Carretera Central Este, KM 5.5 Camagüey, Cuba

Abstract. Three different Ni-laterite types from the northern Caribbean have been investigated on their PGE contents and PGE distribution. Relatively high total PGE contents up to 640 ppb have been observed within limonite close to the surface from Mg-silicate type Ni-laterite. These enrichments are believed to be controlled by the presence of chromitites. However, significant enrichment of up to 264 ppb total PGE from a chromitite free Mg-silicate type Ni-laterite and 239 ppb total PGE from a Fe-oxide Ni-laterite show that there might be processes close to the surface which favour the enrichment of these elements. Changing water table, different pH values and biogenic activity could cause re-distribution and local enrichment of PGE.

Keywords. Ni-laterite, PGE, Dominican Republic, Cuba

1 Introduction

The six Platinum Group Elements (PGE) Os, Ir, Ru, Rh, Pt and Pd are referred to strategic metals because of extreme infrequency within Earth's crust and the fact that these elements cannot be substituted for many applications in high end technologies. In 2011 85% of the world mine production of PGE (484t) was accounted by South Africa (59%) and Russia (26%) from only two PGE deposits (Bushveld Complex and Norilsk, respectively) (USGS Minerals Yearbook 2011). The limited life time of these mines together with constantly increasing demand of PGE may cause shortage of these metals in the future. Unconventional PGE deposits (Wilde et al. 2003) like near surface modified ultramafic rocks (e.g., Ni-laterites), sediment hosted Cu deposits (Kupferschiefer) or sediment hosted Ni-Mo-Zn deposits (black shales) could be future PGE suppliers if economic PGE recoveries can be achieved by improved metallurgical methods. Knowledge of PGE concentration mechanisms and determination of present

PGE mineralogy are essential for this purpose.

There is emerging evidence that lateritization of ultramafic rocks can lead to solution, transport and concentration of PGE. This enrichment is intrinsically related to the lateritization process and not only a consequence of residual enrichment of primary PGE mineralization in bedrock. Salpeteur et al. (1995) described Pt and Pd mobility in ferralitic soils from Madagascar and found evidence for neoformation of PGE minerals by the presence of accretionary secondary Pt, Pd oxides which were restricted to the upper oxidized layer. Experimental studies have shown that Pd can be mobilized in Cl-rich solutions at low temperatures (25°C – 28°C) as PdCl_4^{2-} and $\text{PdCl}_3(\text{OH})^{2+}$ at neutral pH values, whereas $\text{Pd}(\text{OH})_2$ is more abundant at pH values >10 (Van Middlesworth and Wood, 1999). Pt can be transported as PtOH^+ , $\text{Pt}(\text{OH})_2$ and PtOH^{3+} in water with high pH and low Cl content, whereas PtCl_4^{2-} is preferred at low pH values (Azaroual et al., 2001). It is important to mention that the presence of organic matter influence the mobility of Pt and Pd in soils as described by Bowles et al. (1995).

In this work we present data of the PGE geochemistry from different Ni-laterite types from the northern Caribbean with the aim to compare their potential as future unconventional PGE deposits.

2 The investigated nickel laterite types

Freyssinet et al. (2005) defined three important nickel laterite types according to their main mineralogical features: (I) Hydrous Mg-silicate, (II) Fe oxide and (III) clay silicate. However, pure end-member types are rare and mixing of all three types in most laterites is common. Dominant features of the laterite profiles in the northern Caribbean examined here are similar allowing a

ready comparison of the profiles to be made.

2.1 Hydrous Mg-silicate type

The Falcondo Ni-laterite deposit is situated in the central part of the Dominican Republic. The parent rock is the Loma Caribe serpentinized peridotite, which mainly consists of lherzolite, clinopyroxene-rich harzburgite and harzburgite containing small masses of dunite (Proenza et al. 2007a). Two laterite profiles have been sampled for this study to verify local variations: Loma Peguera is characterized by meter scaled pods of chromitite (PGE contents up to >2 ppm) within the saprolitic horizon and Loma Caribe (chromitite free).

2.2 Fe oxide type

Located in northeastern Cuba, the Moa Bay district developed from lateritization of serpentinized peridotites (harzburgite and dunite) from the Mayari-Baracoa ophiolite belt (Proenza et al. 1999). Ni and Co enrichment within the profile is bound to goethite (0.3-4.5 wt% and 0.1-1.7 wt%, respectively), maghemite (0.5-8 wt%) and lithophorite (up to 12 wt% and 6 wt%, respectively) (Proenza et al. 2007 b; Roqué-Rosell et al. 2010). The investigated profile can be divided, from bottom to top, into protolith, saprolite (usually <10 m), limonite (up to 50 m) and ferricrust.

2.2 Clay silicate type

The little studied laterite profile San Felipe in central Cuba consists of serpentinized lherzolite, serpentinized harzburgite and dunite (protoliths), which are intruded by gabbros. They are overlain by a major horizon of smectite rich saprolite (~19m) and minor limonite (~1 m) with a thin layer of ferricrust (Gallardo et al. 2010). These authors reported Ni contents up to 2.4% within the saprolite. Nontronite (an Fe-Mg smectite) was found to be the main ore mineral.

3 PGE geochemistry

The samples collected for this study were analyzed at Genalysis Ltd. (Maddington, Western Australia) by ICP-MS after nickel sulfide fire assay collection following the method described by Chan and Finch (2001).

Similarly flat shaped chondrite normalized PGE pattern for Ni-laterites from the hydrous Mg-silicate type show a constant enrichment from parent rock to limonite and display pronounced Ru and Pd positive trends for all weathering products (Fig. 1). However, chondrite normalized PGE pattern for the dunitic parent rock of Loma Caribe are clearly depleted in Pt and Pd relative to the other PGE. Chromitites from Loma Peguera are characterized by a high $(Os+Ir+Ru)/(Rh+Pt+Pd)$ ratio with strong Pd negative trends.

Unfortunately no PGE data are available for the source rock from Moa, whereas only saprolite samples were analysed from San Felipe (Fig. 2). Chondrite normalized PGE pattern reveal rather flat shapes for saprolites from both investigated Ni-laterites, however

Ru and Pd trends are positive. Limonite and ferricrust from Moa are significantly enriched in PGE compared to saprolite. Ferricrust show similar enrichment for the IPGE as limonite but obvious lower enrichment for the PPGE.

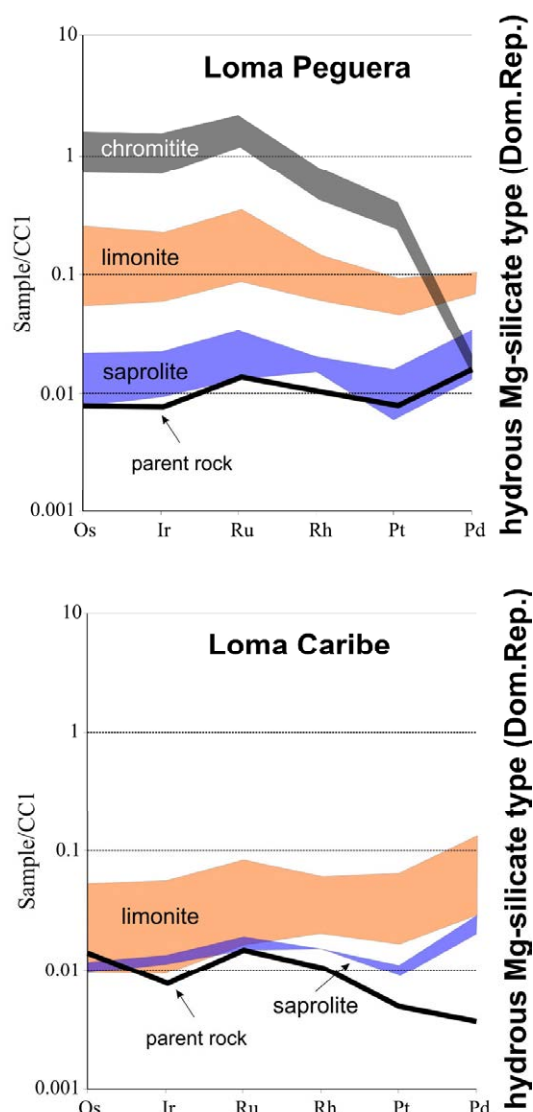


Figure 1. Chondrite normalized PGE pattern of parent rocks and their weathering products from investigated Ni-laterites from Dominican Republic. Normalization was performed using chondrite values from Naldrett and Duke (1980).

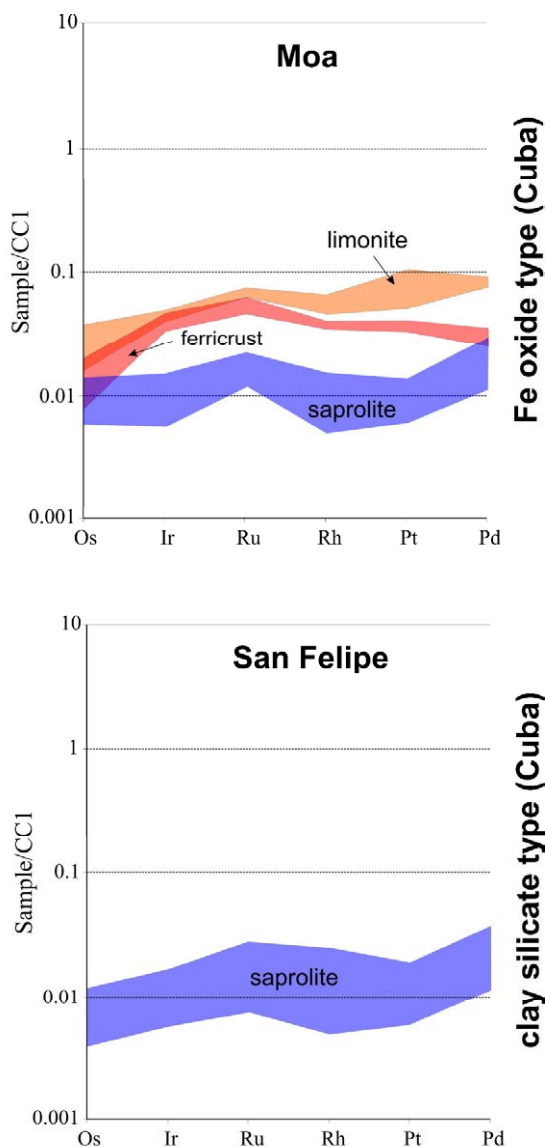


Figure 2. Chondrite normalized PGE pattern of weathering products from investigated Ni-laterites from Cuba. Normalization was performed using chondrite values from Naldrett and Duke (1980).

4 PGE contents

Contents up to 640 ppb total PGE have been observed in the highest limonite levels of the hydrous Mg-silicate type Ni-laterite from Loma Peguera (Table 1). At Loma Caribe a maximum PGE content of 264 ppb (27 ppb Os, 30 ppb Ir, 58 ppb Ru, 12 ppb Rh, 66 ppb Pt, 71 ppb Pd) was measured within limonite close to the surface. Ni-laterites from Moa have maximum contents of 239 ppb (8 ppb Os, 22 ppb Ir, 42 ppb Ru, 13 ppb Rh, 107 ppb Pt, 47 ppb Pd) found within the limonite. The highest total PGE content observed within the saprolite of San Felipe is 78 ppb (6 ppb Os, 9 ppb Ir, 19 ppb Ru, 5 ppb Rh, 19 ppb Pt, 20 ppb Pd).

Excluding the incomplete data from San Felipe a general enrichment trend from saprolite to limonite can be observed (Fig. 3).

Loma Peguera (hydrous Mg-silicate type)

	limonite	saprolite	parent rock
Ir [ppb]	118	12	4
Os [ppb]	129	11	4
Pd [ppb]	37	7	9
Pt [ppb]	91	6	8
Rh [ppb]	29	3	2
Ru [ppb]	236	23	9
ΣPGE [ppb]	640	62	36
Pt/Pd	2,46	0,86	0,89
IPGE [ppb]	483	46	17
PPGE [ppb]	157	16	19
IPGE/PPGE	3,08	2,88	0,89

Table 1. Representative PGE contents and parameters in different horizons of the studied Ni-laterites from Loma Peguera (Dominican Republic)

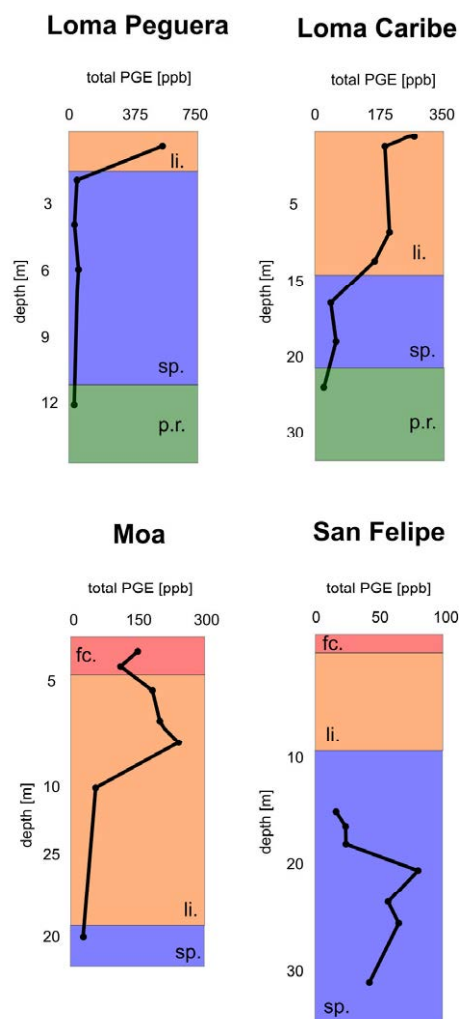


Figure 3. Total PGE distribution within the investigated Ni-laterite profiles. sp. = saprolite; li = limonite; fc. = ferricrust; p.r. = parent rock

5 Final remarks

Limonite close to the surface from Loma Peguera (Mg-silicate type) show the highest enrichment of PGE (up to 640 ppb) among all investigated Ni-laterite types. Previous studies have shown that these enrichments are mainly controlled by the presence of chromitites and therefore residual (Aiglsperger et al. 2011).

However, total PGE contents are also relatively high (up to 264 ppb) within the highest levels of the limonite from Loma Caribe (chromitite free). In addition PPGE behave differently within the ferricrust of Moa (Fe-oxide type) where Pt and Pd are clearly depleted compared with the limonite. According to experimental studies supergene processes can influence the redistribution of some PGE, especially Pt and Pd. These processes (e.g. changing water table, pH, Eh, biogene activity) might have caused local enrichment in some high levels of Ni-laterites.

Using our hydroseparation laboratory in Barcelona we seek to determine the PGE mineralogy of all investigated Ni-laterite types with the aim to find evidence for enrichment factors for PGE in soils developed above ultramafic rocks. These factors could be important for future PGE exploration programs.

Acknowledgements

This research has been financially supported by the Spanish projects CGL2009-10924 and CGL2012-36263 as well as by a PhD grant to TA sponsored by the Ministerio de Educación (Spain). The authors gratefully acknowledge the help and hospitality extended by the staff of Falcondo mine (XSTRATA).

References

- Aiglsperger, T., Proenza, J.A., Labrador, M., Zaccarini, F., Garuti, G., Longo, F. (2011) Geochemistry and mineralogy of PGE in the Falcondo Ni-laterite deposits, Dominican Republic. Proceedings of the 11th SGA Biennial Meeting, 26-29 September 2011, Antofagasta, Chile, 627-629
- Azaroual, M., Romand, B., Freyssinet, P., Disnar, J.R. (2001) Solubility of platinum in aqueous solutions at 25°C and pHs 4 to 10 under oxidizing conditions. *Geochim Cosmochim Acta* 65: 4453-4463
- Bowles, J.F.W. (1995) The developments of platinum group minerals (PGM) in laterites: mineral morphology. *Chronique de la Recherche Minière* 520: 55-63.
- Freyssinet P, Butt CRM, Morris RC, Piantone P (2005) Ore-forming processes related to lateritic weathering: *Econ Geol* 100th Anniversary Volume: 681-722.
- Gallardo T, Chang A, Tauler E, Proenza JA (2010) El Yacimiento de San Felipe (Camagüey, Cuba): un Ejemplo de Lateritas Niquelíferas Tipo Arcilla: *Macla* 13: 87-88
- Hampel W (2012) Discovery of a major unconventional heavy rare earths deposit in Madagascar: *Africa Business Week*: 24 May 2012, Frankfurt am Main: Available at http://www.malekigroup.com/images/AFW2012/Hampel_Wolfgang.pdf. Accessed 21 February 2013
- Naldrett AJ, Duke JM (1980) Platinum metals in magmatic sulfide ores: *Science* 208: 1417-1428.
- Proenza J, Gervilla F, Melgarejo JC, Bodinier JL (1999) Al- and Cr-rich chromitites from the Mayarí-Baracoa Ophiolitic Belt (Eastern Cuba): consequence of interaction between volatile-rich melts and peridotite in suprasubduction mantle: *Econ Geol*

94: 547-566

- Proenza JA, Zaccarini F, Lewis JF, Longo F, Garuti G (2007 a) Chromian spinel composition and the Platinum Group Minerals of the PGE-rich Loma Peguera chromitites, Loma Caribe peridotite, Dominican Republic: *Can Min* 45: 631-648
- Proenza JA, Tauler E, Melgarejo JC, Gali S, Labrador M, Marrero N, Perez-Nelo N, Rojas-Puron AL, Blanco-Moreno JA (2007 b) Mineralogy of oxide and hydrous silicate Ni-laterite profiles in Moa Bay area, northeast Cuba: *Mineral Exploration and Research: Digging Deeper*, 2. Irish Association of Econ Geol: Andrew CJ, et al. (Ed.): 1389-1392
- Roqué-Rosell J, Mosselmans JFW, Proenza, JA, Labrador M, Gali S, Atkinson KD, Quinn PD (2010) Sorption of Ni by "lithiophorite-asbolane" intermediates in Moa Bay lateritic deposits, Eastern Cuba: *Chem Geol* 275: 9-18
- Salpêteur, I., Martel-Jantin, B., Rakotomanana, D. (1995) Pt and Pd mobility in ferralitic soils of the Andriamena area (Madagascar). Evidence of a supergene origin of some Pt and Pd minerals. *Chronique de la Recherche Minière* 520: 27-45
- USGS Minerals Yearbook (2011) Platinum-Group Metals [Advance Release] by Patricia J. Loferski. Oktober 2012. Available at: <http://minerals.usgs.gov/minerals/pubs/commodity/platinum/myb1-2011-plati.pdf>. Accessed 05 February 2013
- Van Middlesworth, J.M., Wood, S.A. (1999) The stability of palladium (II) hydroxide and hydroxy-chloride complexes; an experimental solubility study at 25-85°C and 1 bar. *Geochim Cosmochim Acta*: 63, 1751-1765
- Wilde, A., Edwards, A., Yakubchuk, A. (2003) Unconventional deposits of Pt and Pd: A review with implications for exploration. *SEG newsletter* 52: 1 and 10-18

A new mineralogical method for the determination of metal tenors in Ni-Cu-PGE ores

Jens C. Ø. Andersen, Gavyn K. Rollinson

Camborne School of Mines, University of Exeter, United Kingdom (J.C.Andersen@exeter.ac.uk)

Duncan Pirrie

Helford Geoscience LLP, Penryn, United Kingdom

Abstract. Copper and nickel tenors in sulfide ores can be successfully measured in altered and unaltered rocks using automated mineralogy (by QEMSCAN). However, platinum-group element and cobalt tenors require separate geochemical analysis. The method provides additional mineralogical detail than the traditional geochemical method, and avoids mineralogical restrictions to the original sulfide assemblage. It furthermore allows for the determination of metal tenors in rocks with minor or trace sulfide; and provided the alteration regime is known, the method can also be used to back-calculate the original sulfide composition and metal tenors in altered ores.

Keywords: Ni, Cu, PGE, QEMSCAN

1 Introduction

Metal tenors (defined as the metal content in 100% sulfide), are essential indicators for sulfide fractionation and silicate-sulfide interaction in the formation of Ni-Cu-PGE ores. The Ni- and PGE-tenors are particularly important because of their economic significance.

In this paper, we present a method for the determination of metal tenors in sulfide ores by automated mineralogy using the QEMSCAN system. The system measures the spatial distribution of sulfide minerals directly and removes the need for separate determination of the metal contents in silicate and oxide minerals. The most significant benefit is that the procedure is more widely applicable and provides information on the mineralogical distribution of metals (such as where Ni is carried in pentlandite, millerite, violarite, and heazlewoodite). Significantly the method can be used to reconstruct the original sulfide concentrations and metal tenors in ores that have experienced loss or gain of sulfur or iron during alteration (Cawthorn and Meyer 1993; Maier and Barnes 1996; Andersen 2006; Andersen et al. 2006).

2 Background

Metal tenors are currently estimated from bulk geochemical analyses (S, Ni, and Cu concentrations) under the assumptions that the original sulfide was compositionally similar to an assemblage of pyrrhotite,

pentlandite and chalcopyrite (e.g., Barnes and Lightfoot 2005, Keays and Lightfoot 2004). The Cu, Ni and S, are balanced to form pentlandite and chalcopyrite and remaining S is combined with Fe to form pyrrhotite. Some studies use quantitative XRD by the Rietveld method (Seat et al. 2004, Stone et al. 2004) to better constrain the sulfide mineralogy, while others employ additional techniques to separately determine Ni in the sulfide fraction (Naldrett et al. 2009) or the mafic silicates (e.g., Cawthorn 1999).

The existing method has considerable limitations. Significant Ni, Co and Cu can be included in silicates and oxides, and in mafic-ultramafic hosts, the metals in these minerals can significantly outweigh the metal abundances in the sulfides. Consequently, the accurate determination of metal tenors requires precise knowledge of the modal abundances and metal contents of these minerals (notably olivine, pyroxene, magnetite and ilmenite). As noted by Barnes and Lightfoot (2005), this significantly limits the calculations of metal tenors in mafic-ultramafic hosts that carry small quantities of sulfides. A further restriction is that the method imposes limits on the sulfide compositions that may not truly reflect the natural variability, particularly if primary pyrite, millerite, bornite or magnetite is suspected to have crystallized from a parental sulfide melt. Furthermore, the method cannot be used for rocks where sulfur has been added or lost after the primary sulfide formation.

3 Principles of QEMSCAN analysis

3.1 Instrumentation

The QEMSCAN is a scanning electron microscope with automated beam control, stage movement, and energy-dispersive x-ray acquisition (Gottlieb et al. 2000). The x-ray spectra are assigned into compositional groups (minerals) by comparison to a database, called a species identification protocol (SIP). The spectrum collection (with 1000 x-ray counts per spectrum) and classification takes less than 10 ms allowing for more than 200,000 analyses per hour, including beam and stage movement and other passive measurement time.

3.2 Sample preparation

As with other electron beam techniques, the QEMSCAN requires a polished surface on a sample specimen. If samples are heterogeneous or coarse grained, they must be disaggregated and homogenized before polishing, or larger sample areas must be measured (by the use of multiple sections or blocks). A representative sample is usually prepared by careful grinding, rotary sample splitting, and the use of a filler (graphite flakes) in the mounting resin to prevent differential particle settling while the resin cures. If magnetic minerals are present, the disaggregated sample should be passed through a demagnetizing coil to avoid particle clustering.

3.3 Analysis

The collection of x-ray spectra is carried out with reference to a lower electron backscatter threshold, which is typically defined at the composition of the epoxy-based sample mounting resin. The electron backscattering coefficient is calibrated (on quartz and gold standards) prior to the analysis, and the electron beam calibrated at regular intervals during measurement. Volume and mass conversions are based on specific gravity values for the individual minerals.

The total analysis incorporates a series of analytical points on the sample surface. As a guide, if a total of 1 million points are analyzed, each point will represent 1 ppm by volume.

The QEMSCAN operates in four different analysis modes (Pirrie et al. 2004) of which two have been used in this study. A fieldscan provides analysis of points in a user defined grid (typically at 10 to 100 μm spacing) across a continuous sample surface. A particle mineral analysis (PMA) provides a full characterization of individual particles that are embedded in the epoxy resin and typically at a higher spatial resolution (1 to 20 μm).

3.4 Sources of variability

Variability within the QEMSCAN analysis arises from the following issues:

1) Contamination. Because of the sensitivity of the technique, all particles within the selected region of a sample surface will be measured. While this is not a significant problem for polished rock sections, contamination of particles less than 10 μm can contribute >10 ppm to a particulate sample.

2) Use of non-representative samples. Particle sizes and distributions in samples that are measured must be representative in order to yield accurate quantitative information on mineral abundances. In many cases, this requires disaggregation of the sample material.

3) Limit of detection on X-ray spectra. While the QEMSCAN provides excellent information on the spatial distribution and relative abundances of minerals, the detection of minor constituents within minerals is poor. The typical lower limit of detection is around 3 wt% (Andersen et al. 2009).

4) Misinterpretations. If the data are processed without adequate knowledge of the material, or without the proper attention to detail, misinterpretations are

possible.

5) Boundary effects. Where the electron beam encounters a phase boundary, mixed x-ray signals can be produced. This requires a boundary phase processor that can evaluate boundary spectra on the basis of the spectra of neighboring analytical points.

4 Petrography

Four polished blocks and four grain mounts (disaggregated to less than 250 μm) were prepared from a sample of massive sulfide ore from Pechenga, Russia (Fig. 1) for QEMSCAN analysis. The sample is dominated by pyrrhotite, pentlandite and chalcopyrite with minor magnetite (Table 1). Olivine, clinopyroxene and calcite amount to less than 0.5 wt%, and there are traces of apatite, sphalerite, cobaltite and melonite (all less than 0.02 wt%). The sample has minor pyrite but no voilarite or discrete Ni-sulfides (millerite, heazlewoodite). Pentlandite forms distinct grains up to 1 mm while pyrrhotite and chalcopyrite are intimately mixed within a finer matrix. Magnetite grains up to 100 μm are dispersed evenly throughout the sample and have a closer spatial association with the sulfide (77% of the grain boundary area) than the silicate minerals.

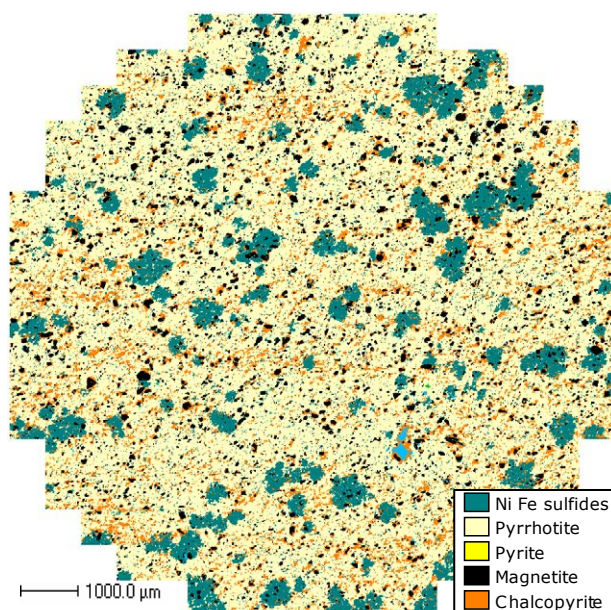


Figure 1. Fieldscan of Pechenga massive sulfide ore showing the distribution of pentlandite (Ni-Fe sulfides), pyrrhotite and chalcopyrite. Minor magnetite and calcite is also present in the sample.

5 Results

5.1 Determination of Ni and Cu tenors

Nickel and Cu tenors are calculated from the metal concentrations of their host sulfide minerals. The investigated sample carries 14.8 wt% pentlandite and 8.2 wt% chalcopyrite in an ore with 87.3 wt% sulfide. No other Ni and Cu bearing sulfides were found, but the

sample carries significant magnetite and pyrite. With 34.2 wt% Ni in pentlandite and 34.6 wt% Cu in chalcopyrite, the Ni tenor is 5.8 wt% and the Cu-tenor 3.3 wt%.

If magnetite is considered part of the original sulfide assemblage (assuming a primary Fe-S-O melt), then the sulfide fraction amounts to 96.3 wt%, which reduces the Ni-tenor to 5.2 wt% and the Cu-tenor to 3.0 wt%.

Mineral	Polished blocks (4 million points)		Grain mounts (1 million points)	
	average	σ	average	σ
Ni Fe sulfides	16.18	1.21	14.79	0.16
Pyrrhotite	63.12	2.49	63.72	0.61
Pyrite	0.01	0.00	0.54	0.04
Magnetite	9.09	0.23	9.05	0.09
Chalcopyrite	11.08	1.70	8.23	0.09
Ni sulfides	<0.01	0.00	<0.01	0.00
Sphalerite	0.02	0.01	0.02	0.00
Calcite	0.24	0.02	0.92	0.04
Olivine	0.20	0.03	2.51	0.04
Clinopyroxene	0.03	0.00	0.19	0.02
Others	0.02	0.00	0.28	0.03
Ni tenor	6.1	0.4	5.79	0.06
Cu tenor	4.2	0.6	3.26	0.03

Table 1. Concentrations of sulfides (in wt%) and calculated Ni- and Cu-tenors (in wt%) for the Pechenga sample.

5.2 Cobalt and platinum-group elements (PGE)

The low abundances limit the determination of Co and PGE-tenors by QEMSCAN alone. This is because of the scarcity and diversity of discrete minerals and the potential for undetected trace concentrations in solid solution in the major sulfide minerals. However, although the determination of Co and PGE tenors requires geochemical analysis, the QEMSCAN analysis provides better constraints on the sulfide abundance and mineralogy. Also, the information from the QEMSCAN analysis can be used to reconstruct the original sulfide assemblage in altered ores and in this way contribute to an understanding of their Co and PGE fractionation.

6 Discussion

6.1 General observations

Although the polished blocks each included more than 50 pentlandite grains, there is significant variability between individual polished blocks. Discrepancies in the abundance of pentlandite, chalcopyrite, pyrite and the associated gangue indicate significant heterogeneity with respect to these minerals. Disaggregation to less than 250 μm provides significantly improved results with fewer analytical points.

6.2 Benefits and limitations of the method

The main benefits are:

1. Nickel and Cu tenors can be estimated without the involvement of other techniques.
2. The method provides detail on the major and trace sulfide minerals in the samples.
3. The method can be directly integrated with mineral compositional data for further refinement of results.
4. The method is independent of the modal abundances and metal contents of associated silicates and oxides and can be used without limitations for rocks that have only minor sulfides.
5. By documentation of the sulfide mineralogy, the method allows for the reconstruction of the original sulfide content and metal tenors in altered ores. This would involve a rebalancing of sulfur against Ni, Cu, and Fe to a primary assemblage of pyrrhotite, pentlandite, and chalcopyrite.
6. Although the method cannot be used to directly determine Co and PGE tenors, it allows for calculations to be made on altered ores, or ores that have trace sulfides in a mafic-ultramafic silicate matrix.

The main limitations are:

1. The method has limited sensitivity to minor components in solid solution. This is significant for Ni in pyrrhotite and pyrite, Co in pentlandite and pyrrhotite, and PGE in sulfides.
2. The measurement of PGE tenors is limited by the scarcity and small grain sizes of platinum-group minerals, and by the lack of information on PGE in solid solution in sulfide minerals.

7 Conclusion

The mineralogical measurement of metal tenors eliminates the need for quantitative determination of the modal concentrations of associated silicate and oxide minerals and their contained metals. The method places no constraints on the primary sulfide mineralogy. It can be applied to altered as well as unaltered ores as long as the nature of the alteration is known. In this respect, the method must be based on petrological observations to ascertain if particular minerals are primary or a product of alteration. The main limitation of the method relates to the poor detection of trace metal concentrations in solid solution. Cobalt and PGE tenors require geochemical analysis.

Acknowledgements

The first author acknowledges financial support through a research agreement with Helford Geoscience LLP. The QEMSCAN is a registered trade mark of FEI Company.

References

- Andersen JCØ (2006) Postmagmatic sulphur loss in the Skaergaard Intrusion: Implications for the formation of the Platinova reef, Lithos, 92: 198-221.
- Andersen JCØ, Thalhammer OAR, Schoenberg R (2006)

- Platinum-group element and Re-Os isotope variations of the high-grade Kilvenjärvi platinum-group element deposit, Portimo layered igneous complex, Finland, *Econ Geol* 101: 159-177.
- Andersen J, Rollinson G, Snook B, Herrington R, Fairhurst R (2009) Use of QEMSCAN for the characterization of Ni-rich and Ni-poor goethite in laterite ores. *Miner Engin* 22: 1119-1129.
- Barnes S-J, Lightfoot PC (2005) Formation of Magmatic Nickel Sulfide Deposits and Processes Affecting Their Copper and Platinum Group Element Contents: *Econ Geol* 100th Anniversary Volume: 179-213.
- Cawthorn RG (1999) Platinum-group mineralization in the Bushveld Complex - a critical reassessment of geochemical models. *South African Journal of Geology* 102: 268-281.
- Cawthorn RG and Meyer FM (1993) Petrochemistry of the Okiep Copper District Basic Intrusive Bodies, Northwestern Cape Province, South Africa: *Econ Geol* 88: 590-605.
- Gottlieb P, Wilkie G, Sutherland D, Ho-Tun E, Suthers S, Perera K, Jenkins B, Spencer S, Butcher A, Rayner J, 2000, Using quantitative electron microscopy for process mineralogy applications: *JOM* April 2000: 24-25.
- Keays RR and Lightfoot PC (2004) Formation of Ni-Cu-Platinum Group Element sulfide mineralization in the Sudbury Impact Melt Sheet: *Mineral Petrol* 82: 217-258.
- Pirrie D, Butcher AR, Power MR, Gottlieb P, Miller GL, 2004, Rapid quantitative mineral and phase analysis using automated scanning electron microscopy (QemSCAN); potential applications in forensic geoscience. In Pye K, Croft DJ (eds.), *Forensic Geoscience, Principles, Techniques and Applications*. Geological Society Special Publ 232: 123-136.
- Maier WD, Barnes S-J (1996) Unusually high concentrations of magnetite at Caraíba and other Cu-sulfide deposits in the Curaçá valley, Bahia, Brazil: *Can Mineral* 34: 717-731.
- Naldrett AJ, Wilson A, Kinnaird J, Chunnett G (2009) PGE Tenor and Metal Ratios within and below the Merensky Reef, Bushveld Complex: Implications for its Genesis. *Journal of Petrology* 50: 625-659.
- Seat Z, Stone WE, Mapleson DB, Daddow BC (2004) Tenor variation within komatiite-associated nickel sulphide deposits: insights from the Wannaway Deposit, Widgiemooltha Dome, Western Australia: *Mineral Petrol* 82: 317-339.
- Stone WE, Heydari M, Seat Z (2004) Nickel tenor variations between Archaean komatiite-associated nickel sulphide deposits, Kambalda ore field, Western Australia: the metamorphic modification model revisited: *Mineral Petrol* 82: 295-316.

The Ioko-Dovyren layered massif (Southern Siberia, Russia): fingerprints of an open magma chamber and compaction of original cumulates conjugated with sulphide percolation process

A.A. Ariskin

Vernadsky Institute, Kosygin Str. 19, Moscow, Russia

L.V. Danyushevsky

Centre for Ore Deposit Research (CODES), University of Tasmania, Private Bag 79, Hobart, 7001 TAS, Australia

A.W. McNeill

Centre for Ore Deposit Research (CODES), University of Tasmania, Private Bag 79, Hobart, 7001 TAS, Australia

G.S. Nikolaev

Vernadsky Institute, Kosygin Str. 19, Moscow, Russia

Yu.A. Kostitsyn

Vernadsky Institute, Kosygin Str. 19, Moscow, Russia

Abstract. The Cu-Ni-PGE fertile Ioko-Dovyren layered massif (Southern Siberia, Russia, $t=728\pm 3.4$ Ma) comprises a lower zone of Pl-Iherzolites overlain by a succession of cumulates ranging from Pl-bearing and adcumulate dunites to troctolite, Ol-gabbro, and Pig-gabbro±quartz gabbro. The rocks display anomalously enriched isotopic compositions, with average $^{87}\text{Sr}/^{86}\text{Sr}(t)=0.71237\pm 0.00134$, $\epsilon_{\text{Nd}}(t)=-14.3\pm 1.1$, which suggest a metasomatised SCLM source consolidated ~2.8 Ga and then reactivated in the Late Riphean. Using the COMAGMAT magma crystallization model, and FeO vs MgO trends for the bulk rock compositions, a range of temperatures (1315-1200°C) and compositions (12-8 wt% MgO, 88-85% Fo in Ol) were calculated for magmas parental to the Dovyren massif. The averaged composition of the Dovyren pluton is ~3 fold depleted in incompatible components with respect to the parental magmas. This indicates the intrusion was solidified as an open magma staging chamber. Thermodynamic modelling using the "sulphide" version of COMAGMAT suggest that the high-Mg parental magma was S-undersaturated, whereas its derivative magmas became S-saturated at $T<1200^\circ\text{C}$. Both mineralogical observations and phase equilibria calculations provide evidence for the compaction of original olivine cumulates conjugated with upward infiltration of intercumulus silicate melt and downward percolation of sulphide liquids.

Keywords. Cumulates, sulphide infiltration, COMAGMAT

1 Geology

The Ioko-Dovyren massif (YDM) is located ~60 km NE of Lake Baikal, and forms a 26 km long ridge, at altitudes up to 2114 m. Geologically, the pluton is a lens-shaped body up to 3.5 km thick (Kislov 1998) which together with associated peridotite sills, diabase dikes, and overlying volcanics (both high-Ti and low-Ti) represents a Riphean (728 ± 3.4 Ma (Ariskin et al 2009, 2013a)) volcanic-plutonic association, formed within a

rifting system (the Olokit trough) at the southern margin of the Siberian craton. A unique feature of the regional geology is the concordance of the igneous rocks with the enclosing carbonate-terrigenous sediments along its strike and dip, which is nearly vertical due to post-intrusive folding. This allows one to sample the entire intrusive complex across the strike, from the lower to the upper contacts.

2 Structure

The modal layering of the central part of the YDM (~3 km thick) was studied in detail. A basal unit of plagioclase Iherzolites (100-150 m thick) is overlain by four zones corresponding to a succession of cumulates, from Pl-bearing and adcumulate dunites (Ol+Chr, 800-900 m), troctolite (Ol+Pl+Chr, ~700 m), Ol-gabbro (Pl+Ol±Cpx±Chr, ~1 km), Pig-gabbro and quartz gabbro (Pl+Cpx±Opx±Pig, ~300m). Despite its age, the YDM has not been metamorphosed significantly, so that most of intrusive rocks are unaltered, preserving both their igneous textures and original mineralogy.

3 Sr-Nd-Pb isotope studies

The isotopic composition of the high Ti-basalts is similar to MORB at the time of emplacement ($0.7028 \leq ^{87}\text{Sr}/^{86}\text{Sr}(t) \leq 0.7048$ and $4.6 \leq \epsilon_{\text{Nd}}(t) \leq 5.8$). These basalts differ from the intrusive rocks and low-Ti basalts, which are geochemically similar, and characterised by anomalously enriched isotopic compositions of Sr, Pb and Nd. The maximum enrichment ($^{87}\text{Sr}/^{86}\text{Sr}(t)=0.71387$ and $\epsilon_{\text{Nd}}(t)=-16.09$) is found in the chilled and lowermost rocks of the layered intrusion, which crystallised from the most primitive high-Mg magmas. Dunites, troctolites and gabbros are less isotopically enriched, which could reflect assimilation of the wall-rocks and/or minor

heterogeneity of the parental melts. Mixing calculations indicate that it is unlikely that the intra-complex variations are due to assimilation of carboniferous sedimentary units at the site of emplacement, as unrealistically large extents of assimilation (40-50%) would be required. These variations are more likely due to mixing with 5-10% of the contemporaneous high-Ti volcanic component.

4 Pre-history of mantle source

Overall, the minor variations in $\epsilon_{Nd}(t)$ among the intrusive and extrusive rocks (-14.3 ± 1.1) are evidence that the entire complex was derived from an isotopically anomalous source. It is suggested that the Dovyren parental melts formed in the Late Riphean from a sub-lithospheric mantle source which was metasomatised ~2 Gy earlier by a mafic component with a low Sm/Nd value. The source then remained isolated from the convecting mantle. Additional support for this hypothesis of an old, re-activated source comes from the trend of Nd isotopic evolution over time which is shared by the Dovyren rocks and the paleo-Proterozoic gabbroids of the Chiny massif, Archaean granites and enderbites of the Baikal region. Geochemical features of the ultramafics and mafic rocks, granulites and granitoids from the southern margin of the Siberian craton suggest that the metasomatised mantle source was formed above a subduction zone which contributed to crustal accretion of the Siberian craton ~ 2.8 Ga (Ariskin et al 2013b).

5 Parental magmas

Parental magma compositions have been evaluated using studies of the chilled zones and underlying ultramafic sills. The most primitive rocks of YDM are at the lower contact and include chilled diabases and picritic rocks containing variable amounts of Ol, and with ophitic textures. The FeO-MgO trend displayed by these high porosity cumulates suggests that they initially contained olivine ~Fo88. The COMAGMAT model calculations indicate the initial temperature of the magma was 1315°C, with the melt containing ~12% MgO. Using this as a starting composition, we simulated the crystallization sequence which corresponds to the mineralogy observed in the YDM cumulates. Estimates of parental magmas for the Ol-gabbroites and Pl-dunites, from ultramafic sills, result in more evolved magma containing Ol~Fo85 at $T \sim 1190^\circ\text{C}$.

6 Fingerprints of an open magma chamber

Both the geochemistry and cumulate structure of the YDM indicate that a significant volume of mafic melt was extracted from the original cumulate pile, followed by its expulsion from the magma staging chamber. The fingerprints of such 'open-system' behavior are recorded in (1) strong depletion in incompatible elements of the bulk YDM composition with respect to the parental magmas, (2) a complementary "over-enrichment" in Ol cumulates and sulfides, (3) insignificant variations of Ol

composition throughout the layered rocks, and (4) the absence of an Upper Border Series and marginal compositional reversal.

7 Fertility vs sulphide percolation

An important feature of the YDM is the presence of massive sulphide ores near the bottom of the intrusion (close to the SW and NE margins), as well as PGE-reefs in anorthosites of the Ol-gabbroite zone (Kislov 1998). Both mineralogical observations and calculations of phase equilibria provide evidence for the compaction of original olivine cumulates combined with downward percolation of sulphides through the porous cumulates, and the probable genetic link of this process with upward migration of intercumulus melts at a post-cumulus stage. Indirectly, this is supported by the basic conclusion on the open-system behavior of the magma chamber (see above).

8 Modelling onset of sulphide saturation in parental magmas

A key aspect of these speculations is the relative timing of the onset of sulphide immiscibility in YDM parental magmas and the original cumulates. To reconstruct the sulphide saturation history, we applied a newly developed sulphide version of COMAGMAT (ver. 5.2, Ariskin et al 2012) to the rocks from the chilled zone of YDM and underlying ultramafic sills, by simulating the course of their crystallization coupled with SCSS calculations. Modeled crystallization trajectories indicate the most primitive parental magmas (1315°C, Fo88), from which the chilled rocks were crystallized, were S-undersaturated. Calculations indicate that the more evolved rocks from the ultramafic sills were S-saturated at their initial conditions (1190°C, Fo85). This correlates with the absence of sulphide ores in the central parts of the pluton and their occurrence in underlying ultramafics and YDM border series containing evolved olivine $\text{Fo} \leq 85$ (the SW and NE margins of the intrusion).

9 Modelling onset of sulphide saturation in original cumulates

Results of the COMAGMAT calculations provide evidence for late sulphide immiscibility occurring in partly crystallized olivine cumulates at lower temperatures. To study this possibility, another set of calculations, demonstrating the effect of the bulk Ni contents in Ol cumulate piles on the post-cumulus evolution of SCSS were carried out. Assuming the Ni and S contents of selected rocks to correspond to their original values, the first calculation involved modelling equilibrium crystallization for an initial mixture of Ol (Fo88) and intercumulus melt (~1320°C), with the starting composition corresponding to a basal Pl-dunite (2315 ppm NiO, 0.030 wt% S). The second set of calculations were done for the initial trapped melt only (517 ppm NiO, 0.067 wt% S), estimated for the primitive Ol orthocumulate.

Table 1. Results of calculations simulating onset of sulphide immiscibility during equilibrium crystallization of Ol-containing and Ol-free magmas starting from the initial temperature of 1320°C

Original Ol-cumulus:	Initial melt only:
1819 ppm Ni, 0.030 wt% S	406 ppm Ni, 0.067 wt% S
Immiscibility before appearance of <i>Pl±Opx</i>	Immiscibility after appearance of <i>Plag</i> and <i>Opx</i>
$T = 1209^{\circ}\text{C}$	$T = 1173^{\circ}\text{C}$
Fo in <i>Ol</i> = 86.3	Fo in <i>Ol</i> = 80.1
Ni in melt = 200 ppm	Ni in melt = 118 ppm
SCSS = 0.078 wt%	SCSS = 0.099 wt%
Ni in sulfide = 17.7 wt%	Ni in sulfide = 12.2 wt%

The major difference between these calculations is the onset of modelled sulphide saturation. In the case of “Ol cumulus pile”, the sulphide liquid appears at 1209°C, slightly earlier than plagioclase and pyroxenes start to crystallize. For the “Ol-free magma”, the Fe-Ni sulphides appear at much lower temperature ($\leq 1173^{\circ}\text{C}$) where the Ol-Pl-Opx-Cpx assemblage is stable. This indicates that the presence of a large amount of Ni-enriched Ol crystals should be considered as a “Ni-buffer” which does not allow the Ni content in the trapped melt to decrease significantly, giving rise to earlier precipitation of sulphides due to the pronounced effect of Ni on sulphide solubility as discussed by Ariskin et al (2010).

10 NiO vs Fo in olivine trends as indicators of sulphide liquid percolation

Li and Naldrett (1999) discussed the genetic significance of the Ni vs Fo variations in Ol from intrusive complexes, in particular the abnormal sub-vertical (sometimes negative) Ni vs Fo trends which are due to Ni and Fe exchange between Ol and coexisting sulphide (Li et al 2003). These trends can be described using the equilibrium constant $K_D = (\text{NiS}/\text{FeS})_{\text{Sul}}/(\text{NiO}/\text{FeO})_{\text{Ol}} >> 1$ (Brenan and Caciagli 2003).

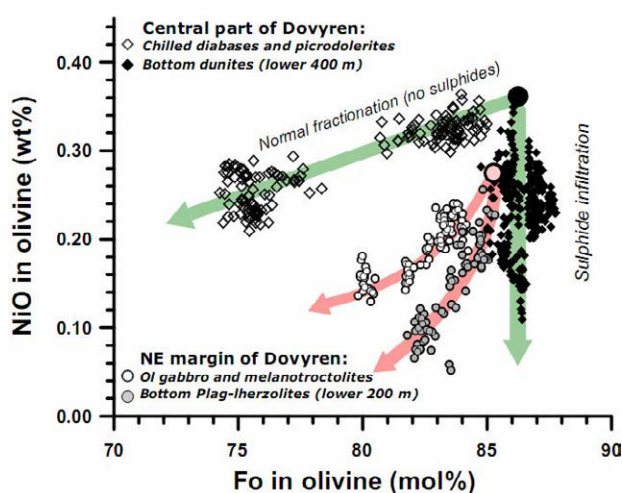


Figure 1. Ni vs Fo in Ol trends observed in the rocks from the central and marginal parts of the Ioko-Dovyren massif

Thus, ‘abnormal’ Ni-Fo trends are the signatures of the olivine-sulphide reactions that could proceed in net-textured ores or in Ol-rich cumulates which experienced infiltration of sulphides. Ol compositions from ultramafic parts of the YDM strongly support the latter conclusion (Figure 1). Olivine from the chilled rocks displays a normal crystallization trend, whereas Ol from overlying dunites demonstrates highly variable NiO, resulting in an ‘abnormal’ vertical “Ni-depleted” trend with a narrow range of Fo contents. Similar (but positive) trends were found in Ol from the rocks composing sections near NE margin of the pluton (Figure 1). These “marginal” trends start from lower Ni and Fo contents, as it is expected from the lower temperature of the magma proposed to be parental for this part of the Ioko-Dovyren massif (see above).

Acknowledgements

This research was supported by AngloAmerican, BHP Billiton and Votorantim Metais through AMIRA project P962, by the Australian Research Council funding to the CODES (Hobart, Australia), and the Russian Foundation for Basic Research (projects 08-05-00194a, 11-05-00268a).

References

- Ariskin AA, Konnikov EG, Danyushevsky LV, Kislov EV et al (2009) The Dovyren Intrusive Complex: problems of petrology and Ni sulfide mineralization. *Geochem Intern* 47: 425–453.
- Ariskin AA, Danyushevsky LV, Bychkov KA, Barmina GS (2010) Modeling sulphide solubility in MORB glasses and Ol cumulate piles: the opposite effect of NiO vs. FeO in the melt. In: *Proc. Intern Platinum Symp 11th* (Sudbury, 21-24 June 2010).
- Ariskin AA, Bychkov KA, Danyushevsky LV, McNeill AW et al (2012) COMAGMAT-5: a new magma crystallization model designed to simulate mafic to ultramafic sulfide-saturated systems. *Proc 12th Intern Ni-Cu-(PGE) symp* (Guiyang, China, June 16-21 2012): 15-18.
- Ariskin AA, Kostitsyn YuA, Konnikov EG, Danyushevsky LV et al (2013a) Geochronology of the Dovyren Intrusive Complex in Neoproterozoic (Northern Transbaikalia, Russia). *Geochem Intern*: in press.
- Ariskin A.A., Danyushevsky LV, Maas R, Kostitsyn YuA et al (2013b) The Dovyren Intrusive Complex (Northern Transbaikalia, Russia): isotope-geochemical signatures of parental magmas contamination and an extreme enrichment of their source. *Geology and Geophysics*: in press.
- Brenan JM (2003) Effects of fS₂, fO₂, temperature, and melt composition on the Fe-Ni exchange between olivine and sulfide liquid: implications for natural olivine-sulfide assemblages. *Geochim Cosmochim Acta* 67:2663–2681.
- Kislov EV (1998) The Yoko-Dovyren Layered Massif. Ulan-Ude: 264 p. (*in Russian*)
- Li C, Naldrett AJ (1999) Geology and petrology of the Voisey’s Bay intrusion: reaction of olivine with sulfide and silicate liquids. *Lithos* 47:1-31.
- Li C, Ripley EM, Naldrett AJ (2003) Compositional variations of olivine and sulfur isotopes in the Noril’sk and Talnakh intrusions: implications for ore forming processes in dynamic magma conduits. *Econ Geol* 98: 69– 86.

Physical processes in magmatic ore formation: fluid dynamics of sulfide liquid droplets in sulfide-silicate emulsions

Stephen J. Barnes, Jesse Robertson, Béilinda Godel

CSIRO Earth Science and Resource Engineering, Australian Resources Research Centre, Kensington, Western Australia

Abstract: The dynamics of ore formation in magmatic sulfide systems are controlled in part by the relative balance of surface tension and inertial forces on transported sulfide liquid droplets. Different domains of behaviour are encountered over a range of magma flow regimes from stagnant to turbulent, and according to droplet size. Sulfide droplets larger than about 1 cm radius are intrinsically unstable in all flow regimes and tend to break up, whereas smaller droplets tend to break up only in either chaotic laminar, or turbulent flows. Droplet coalescence is unlikely during flow within the range of stable droplet sizes. Sulfide liquid pools are likely to be entrained (via ligament formation and fragmentation) as small droplets by silicate magma flowing over them, and this process can lead to cycles of transport and re-deposition. Once segregated, sulfide liquid pools are likely to be highly mobile, and can inject into country rock fractures or by backflow down magmatic conduits under their own hydrostatic head.

Keywords: sulfides, droplets, nickel deposits, magmatic ores

1 Introduction

Fluid dynamic processes controlling the transport and deposition of magmatic sulfide deposits remain some of the least understood aspects of the genesis of this deposit type. There has been a recent vogue for models that attribute the initial segregation and accumulation of sulfide liquid to deep seated processes, occurring in the deep crust well below the eventual level of formation of the actual deposits. For example, models of this type have been invoked for the Voisey's Bay (Lightfoot et al. 2012), Jinchuan (Song et al. 2012) and Noril'sk-Talnakh deposits (Arndt et al. 2003). Similar models have been applied to the chromite deposits of the Bushveld Complex (Eales and Costin 2012).

These models are prompted largely by mass balance considerations: the sulfide deposits are all characterised by a vast excess of sulfide over that which could originally have been dissolved in a body of magma of the dimensions of the host intrusion (Naldrett 1989). Thus, ore formation requires some process of initial segregation of the ore component, followed by mechanical transport to the site of ore deposition. The high density and low viscosity of sulfide liquids can make it difficult to mix these melts with the host silicate magma (Campbell & Turner, 1985) however, raising serious questions about the mechanism by which this may occur.

In this contribution, we consider some of the physical constraints that govern the entrainment, transport and segregation of sulfide liquid/silicate magma emulsions. We consider a number of specific aspects, based largely

on the application of well-established fluid mechanical principals to the behaviour of sulfide liquid droplets: (a) the constraints on upward transport of two-phase mixtures through the crust, (b) processes leading to entrainment and transport of sulfide droplets, and (c) possible deposition mechanisms.

2. Droplet formation, transport and deposition

The average droplet radius of a population of droplets is the critical parameter determining their dynamic behaviour, and this is controlled by two opposing processes: coalescence of droplets causing increasing size and enhancing tendency to settle; and break-up, having the reverse effect (Leshner and Groves 1986). These tendencies are controlled by the interaction of sets of dynamic forces: surface tension, which tends to minimise surface curvature of droplets (which can both help and hinder break-up and coalescence in various circumstances); and inertial, viscous and pressure gradient forces which cause droplets to deform.

2.1 Breakup

Droplet breakup is a crucial process in determining the ability of magma to entrain and transport sulfide liquid, as well as determining the average size of the entrained droplet population. Deforming forces can be due either to buoyancy (in the case of droplet settling), shear forces due to turbulence or to high velocity gradients in the flow (in the case of turbulent or transient laminar magma flow), or surface-tension induced pressure gradients (in the case of capillary breakup of extended droplets). These deforming forces act on the surface of large bodies of sulfide melts, pulling out ligaments of fluid which fragment into droplets, either directly from fluid stresses under conditions of turbulent magma flow, or by capillary relaxation under laminar flow conditions.

Extending studies of gas bubbles in magma flows to the conditions experienced by sulfide droplets suggest that droplets larger than a few centimetres in radius will tend to break up under their own weight (Suckale et al., 2010). Similarly, in turbulent magma flows the inertial stresses imparted by the magma on the sulfide melt allow the formation of very fine populations of droplets. Although it is easier to break up droplets in turbulent conditions, chaotic mixing induced by laminar time-dependent flow may also be enough to remobilise large pools of sulfide by entrainment into droplets without requiring turbulent flow.

2.2 Coalescence

At the other end of the scale of droplet behaviour, droplet coalescence can act to increase the average radius of a population of droplets. However, theoretical and experimental evidence (de Bremond d'Ars et al. 2001), together with the behaviour of basalt lava gas bubbles (which behave in a dynamically similar manner), shows that sulfide droplets should be resistant to buoyancy-driven coalescence within dynamic magma flows at droplet radii less than about 10 mm. This is consistent with the observation that sulfide droplets preserved in rapidly cooled magmatic environments characteristically have spherical geometries. Additionally, droplet coalescence rates between larger, more deformable droplets are slowed in viscous magmas as the time taken to drain the magma between droplets increases. These lines of evidence suggest that droplet coalescence occurs only once droplets have settled out of a dynamic flow.

2.3 Transport & settling

The main constraint on transport of sulfide droplets is the tendency of dense particles to lag behind the flow. This is true for both sulfide droplets and also for solid phases such as olivine which may also be suspended in the magma. Three distinct regimes are potentially important: dilute suspensions of droplets and crystals (<5% particle volume fraction), where particles behave individually with settling velocities determined by droplet size; moderately concentrated suspensions (5 to 30% particle volume fraction), where particle interactions become dominant and can alter settling rates; and strongly concentrated suspensions (>30% particle volume fraction), where there may be so many particles in the magma that they form a touching framework of crystals and bubbles and the bulk material develops a strongly non-Newtonian rheology with particles 'locked into' the microstructure of the suspension.

Calculated settling velocities for the case of an individual sulfide droplet in a crystal free magma with a 10 mm radius are of the order of 0.01 m/s for basaltic magmas, through to 1 m/s for less viscous komatiite magmas (Figure 1). These settling rates are comparable to estimated rates of magma ascent through dykes of typical thickness (Huppert and Sparks 1985). Similarly, the typical droplet sizes of 0.1 to 1 mm seen in many disseminated ore deposits (Godel et al. 2013, Figure 2) would correspond to settling velocities of the order of cm to tens of cm per hour in mafic magmas, implying that vertical transport of small droplets is a plausible scenario in the hottest, crystal-free magmas.

In a uniformly distributed, moderately concentrated

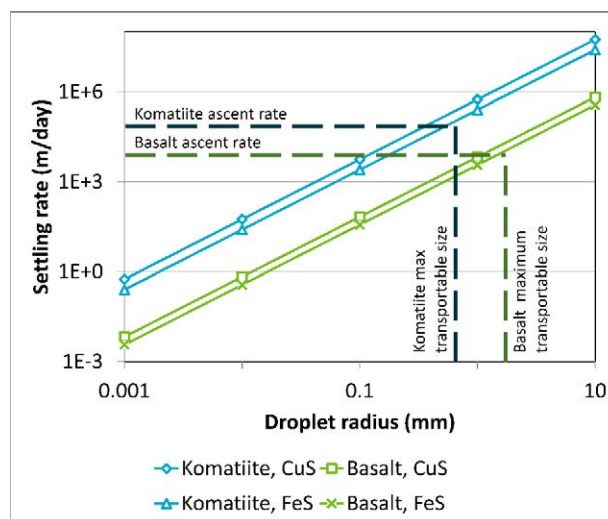


Figure 1: Sulfide droplet settling rates for individual droplets in komatiitic and basaltic host magmas. Sulfide liquid viscosity is 0.02 Pa s; FeS and CuS densities are 4000 and 5000 kg/m³ respectively, silicate liquid viscosities and densities are 1 Pa s and 2800 kg m⁻³ for komatiite and 100 Pa s and 2600 kg m⁻³ for basalt, typical flow rates from Huppert and Sparks (1985).

suspension the increase in particles will tend to hinder settling and favour transport (Bachelor 1972; Manga 1995). However, differences in local concentration of crystals and particles can accelerate settling through the formation of density-driven plumes (Bergantz & Ni 1999).

2.4 Deposition and post-deposition processes

Once sulfide droplets accumulate in sufficiently high proportions, coalescence is governed by the process of film drainage between touching droplets and can take place relatively easily (de Bremond d'Ars et al 2001). However, observations on disseminated ores in slowly cooled cumulate rocks indicate that mm-sized droplets tend to retain their integrity, and show relatively limited degrees of coalescence at proportions of 5% or less (Barnes et al. 2011; Godel et al. 2013). This is a consequence of the tendency of sulfide liquid not to wet silicate phases in the presence of silicate melt (Barnes et al. 2008; Chung and Mungall 2009). Sulfide proportions of several tens of percent over intervals of metres are required before the sulfide liquid column has enough hydrostatic head to force its way through intercumulus porosity of typical igneous cumulates (Chung and Mungall 2009) and generate sulfide rich pools at the base of cumulates. On this basis, formation of massive ores requires initial accumulation of high proportions of sulfide liquid in the absence of substantial crystallisation of silicates.

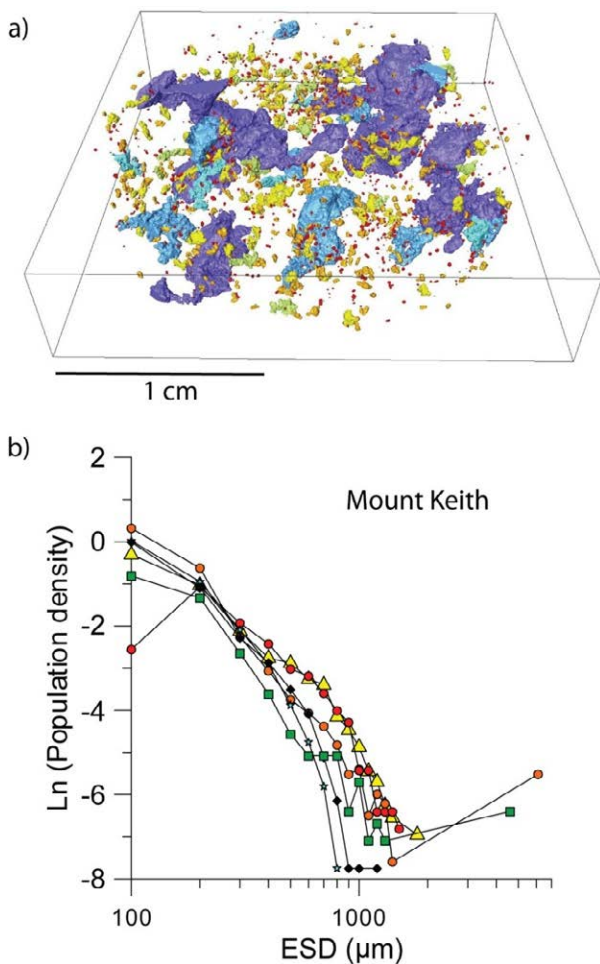


Figure 2. a) MicroCT image of disseminated sulfide droplets in komatiitic dunite, Mt. Keith. Colours indicate range of particle size. Note the irregular coalesced morphologies of large blobs, compared with the relatively spherical morphologies of small droplets. b) Particle size distribution (ESD = equivalent spherical diameter) for sulfide blebs in Mt. Keith komatiite hosted disseminated ores. Each color/symbol combination represents a single sample (Godel et al., in press).

Once formed, the high density and low viscosity of sulfide liquid pools potentially results in extensive lateral and downward migration under their own hydrostatic head. Massive or net-textured sulfide bodies which have a connected vertical extent of more than 10-20 m should have enough hydrostatic pressure at their base to fracture solid rock under typical crustal conditions (Lister & Kerr 1991). The migration of these melts will only be stopped by solidification within the tip of the propagating sulfide dyke as it loses heat to colder country rock.

Similarly, the higher density and lower viscosity of a coalesced sulfide melt may allow it to flow back down dykes after settling and forming a large enough mass in a region of lower strength magma flow (e.g. a region of dyke widening). These backflows will form near dyke walls in regions of high shear strain rates, potentially leading to a cyclic process of local settling and re-entrainment with high mixing efficiencies between silicate and sulfide melts

3 Schematic overview & origin of high R factor sulfide

The dynamic regimes discussed in Section 2 are summarised in Figure 3. As noted above, the two axes (magma flow strength and droplet size) represent the controlling factors in the formation, entrainment, transport and deposition of small sulfide droplets. A position in this diagram represents the local conditions experienced by a population of sulfide droplets in a magma. The locations of the boundaries between dynamic regimes are indicative only, and will depend in detail on a wide range of factors, including all those discussed above. However we can use this diagram in a qualitative sense to examine the cycles of transport and deposition which lead to the formation of a magmatic sulfide deposit.

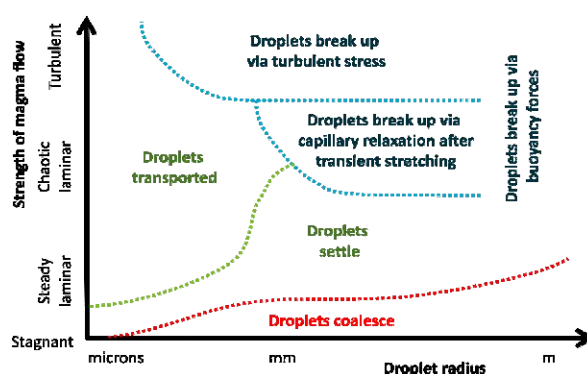


Figure 3. Schematic diagram showing the behaviour of sulfide suspensions. Blue-coloured regimes denote dynamic conditions under which droplet size is reduced, green regimes denote stable droplet sizes, and red regimes denote regions in which sulfide droplet sizes increase.

The regimes in the upper right (blue text) show regions where the dynamic flow of the magma and sulfide will act to reduce the average radius of a population of droplets (as discussed in Section 2.2), by breaking up the larger droplets, thus pushing a population of droplets to the left on the diagram. The regimes on the lower left (green) show dynamic conditions in which a droplet population is transported from regions of high magma flow rate to regions of low magma flow rate and eventually to settle out of the flow altogether (discussed in Section 2.3), thus pushing a droplet population to lower y-axis positions in the diagram. Conversely, an increase in magma flow rate pushes the droplet population to higher positions in the diagram. Finally, once a population has been able to settle, coalescence allows the mean droplet size to grow (discussed in Section 2.4), pushing the droplet populations further to the right on the diagram.

We can envisage the history of the droplets in a deposit as forming a set of cycles through these regimes. Each cycle represents the chance for the sulfide to equilibrate with a new body of magma, and can potentially lead to complex geochemical signals, such as wide variability in PGE contents of sulfide ores or their host rocks.

4. Conclusions

These considerations have several implications for magmatic sulfide ore body formation:

1. The upper limit on size of transportable sulfide droplets is essentially determined by the strong tendency of large droplets to break up; either in turbulent flow regimes, regimes with strong velocity gradients or under their own buoyancy. Hence, the presence of large (>1cm radius sulfide droplets) in cumulate rocks is a potential indicator of proximity to a sulfide-rich orebody or a sulfide-rich crustal source.

2. There appears to be no limit to the extent to which typical stably-sized dispersed sulfide droplets can be transported upward through the crust by potential ore forming magmas, provided the mass concentration of droplets is not high enough to increase the bulk density of the suspension beyond its capability to propagate upward through the crust.

3. Deposition of droplets to form orebodies can be achieved by a variety of mechanisms, but coalescence of droplets to form sulfide pools is likely to take place after deposition, not before. Droplet deposition is likely to be enhanced where density differences due to variation in particle concentrations (both droplets and crystals) can cause buoyancy-driven instabilities and potentially locally rapid accumulation rates.

4. Once formed, large massive sulfide pools can be highly mobile, and are potentially capable of forcing their way into country rock fractures under their own hydrostatic pressure. Backflow of sulfide pools down steep magma conduits is a likely mechanism for emplacement of fracture-hosted massive and breccia massive ores.

5. The evolution of a magmatic sulfide ore system may involve multiple cycles of entrainment, transport, deposition, coalescence and sulfide liquid migration. Such cycles are likely to result in complex geochemical signals in ores and host rocks.

Acknowledgements

This contribution is an output from the CSIRO Minerals Down Under National Research Flagship. Jess Robertson is supported by the CSIRO OCE Postdoctoral Fellowship Scheme. We thank Thomas Poulet and Guy Metcalfe for helpful reviews.

References

- Arndt NT, Czamanske GK, Walker RJ, Chauvel C, Fedorenko VA (2003) Geochemistry and origin of the intrusive hosts of the Noril'sk-Talnakh Cu-Ni-PGE sulfide deposits. *Econ Geol* 98:495-515.
- Barnes SJ, Fiorentini ML, Austin P, Gessner K, Hough R, Squelch A (2008) Three-dimensional morphology of magmatic sulfides sheds light on ore formation and sulfide melt migration. *Geology* 36:655-658.
- Barnes SJ, Osborne GA, Cook D, Barnes L, Maier WD, Godel BM (2011) The Santa Rita Nickel Sulfide Deposit in the Fazenda Mirabela Intrusion, Bahia, Brazil: geology, sulfide geochemistry and genesis. *Econ Geol* 106:1083-1110.
- Batchelor, GK (1972) Sedimentation in a dilute dispersion of spheres. *J Fluid Mech* 52, 245-268.
- Bergantz, GW and Ni, J (1999) A numerical study of sedimentation by dripping instabilities in viscous fluids. *Int J Multiph Flow* 25, 307-320.
- de Bremond d'Ars J, Arndt NT, Hallot E (2001) Analog experimental insights into the formation of magmatic sulfide deposits. *Earth Planet Sci Letts* 186:371-381.
- Campbell, IH, Turner, JS (1985) Turbulent mixing between fluids with different viscosities. *Nature* 313, 39-42.
- Chung H-Y, Mungall JE (2009) Physical constraints on the migration of immiscible fluids through partially molten silicates, with special reference to magmatic sulfide ores. *Earth Planet Sci Letts* 286:14-22.
- Eales HV, Costin G (2012) Crustally contaminated komatiite: primary source of the chromitites and marginal, lower, and critical zone magmas in a staging chamber beneath the Bushveld Complex. *Econ Geol* 107:645.
- Godel B, Barnes SJ, Barnes S-J (2013) Deposition mechanisms of magmatic sulphide liquids: evidence from high-resolution X-ray computed tomography and trace element chemistry of komatiite-hosted disseminated sulphides. *J Petrol*. In press.
- Huppert HE, Sparks RSJ (1985) Komatiites I: Eruption and Flow. *J Petrol* 26:694-725.
- Leshner CM, and Groves DI (1986), Controls on the formation of komatiite-associated nickel-copper sulfide deposits, in Friedrich GH ed, *Geology and Metallogeny of Copper Deposits*: Berlin, Springer Verlag, 63-90.
- Lightfoot PC, Keays RR, Evans-Lamswood D, Wheeler R (2012) S saturation history of Nain plutonic suite mafic intrusions; origin of the Voisey's Bay Ni-Cu-Co sulfide deposit, Labrador, Canada. *Mineral Depos* 47:23.
- Lister JR, Kerr RC (1991) Fluid-mechanical models of crack propagation and their application to magma transport in dykes. *J Geophys Res B* 96:10049-10077.
- Manga M (1996) Waves of bubbles in basaltic magmas and lavas. *J Geophys Res B* 101:17457-17465.
- Naldrett AJ (1989) Ores associated with flood basalts. *Rev Econ Geol* 4:103.
- Suckale J, Hager, B.H., Elkins-Tanton, L.T., Nave, J.-C. (2010) It takes three to tango: 2. Bubble dynamics in basaltic volcanoes and ramifications for modelling normal Strombolian activity. *J Geophys Res* 115:B07410. doi: doi:10.1029/2009JB006917.
- Song XY, Danyushevsky LV, Keays RR, Chen L-M, Wang Y-S (2012) Structural, lithological, and geochemical constraints on the dynamic magma plumbing system of the Jinchuan Ni-Cu sulfide deposit, NW China. *Mineral Depos* 47:277-297.

Cu-Ni-PGE mineralization of felsic dikes along the Grano fault in the Bathtub intrusion (Duluth Complex, Minnesota, USA)

Zsolt Benkó, Aberra Mogessie

Institute of Earth Sciences, Mineralogy and Petrology, Karl-Franzens-University of Graz, 8010 Graz, Austria

Ferenc Molnár

Geological Survey of Finland, 02151 Espoo, Finland

Mark Severson, Steven Hauck

Natural Resources Research Institute, University of Minnesota, Duluth, 55811, Minnesota, USA

Greg B. Arehart

University of Nevada, Reno, 89557 Nevada, USA

Abstract. Occurrence of felsic dikes is extremely common along the N trending Grano fault in the mafic, layered Bathtub Intrusion (BTI) of the Duluth Complex. Based on their geochemical characteristics, the felsic dikes with syenitic-monzonitic composition can be derived from partial melting of granitic rocks that are locally the footwall of the BTI. The dikes with granitic compositions are comparable with rhyolites and icelandites that formed contemporaneously with the emplacement of the BTI in the main magmatic phase of the Keweenawan rift event. The felsic veins are no carriers of precious or base metals but the exsolving fluids during the crystallization may have contributed to metal remobilization and precipitation. Both the felsic dikes and the host troctolite are intensively altered. Chemical composition of the rocks indicates that high temperature and saline fluids interacted with rocks in these alteration zones. These fluids can be connected to local hydrothermal cells developed during emplacement of felsic dikes. Late reductive fluids, produced by serpentinization of troctolite, also resulted in *in situ* modification of base metal mineralogy. We conclude that the Grano fault is not only a feeding channel for the mafic intrusions but a principal pathway for hydrothermal fluids and therefore it forms a zone where the original mineralogy of the magmatic Cu-Ni-PGE ore was modified.

Keywords. Duluth Complex, Bathtub intrusion, Grano fault, felsic veins, hydrothermal alteration, modification of magmatic sulphide ore

1 Introduction

Along the western edge of the South Kawishiwi Intrusion (SKI), the Bathtub Intrusion (BTI) and the Partridge River Intrusion of the Duluth Complex (DC) at least ten Cu-Ni-(PGE) deposits were encountered in the last 60 years (Severson and Hauck 2008).

The BTI, situated between the PRI and the SKI contains one of the largest Cu-Ni-PGE reserves (1 billion tons) among the intrusions of the DC (Severson and Hauck 2008). Location of mineralization in this deposit is largely controlled by early-, and syngenetic footwall structures (Local Boy anticline, Bathtub syncline and Grano fault). Along the faults voluminous

amounts of granitoid and pyroxenite magma intruded into the BTI. The aim of our work was the evaluation of the significance of these late felsic intrusions in modifying of magmatic Cu-Ni-PGE ore dikes. Therefore, we focused our work on the zone of the Grano fault. Detailed geochemical, mineralogical and petrographic investigations have been carried out on the felsic dikes occurring in the B1-262 drill core.

2 Geologic setting

The DC is a part of the aborted Mid-Continental rift system of Keweenawan age (ca. 1.1 Ga). Volcanic and intrusive rocks formed in four magmatic stages (early, dormant, main and late). Volcanic rocks (mainly basalt, subordinately rhyolites and icelandites) formed in each stage, whereas the layered mafic intrusions of the DC intruded between the Archean, Paleoproterozoic basement and volcanic units in the early (1109-1107 Ma) and main (1102-1094 Ma) stages. The economically important layered series (SKI, PRI and BTI) formed subsequently to the emplacement of the anorthositic series, during the main phase of the magmatic activity (Miller and Vervoort 1996).

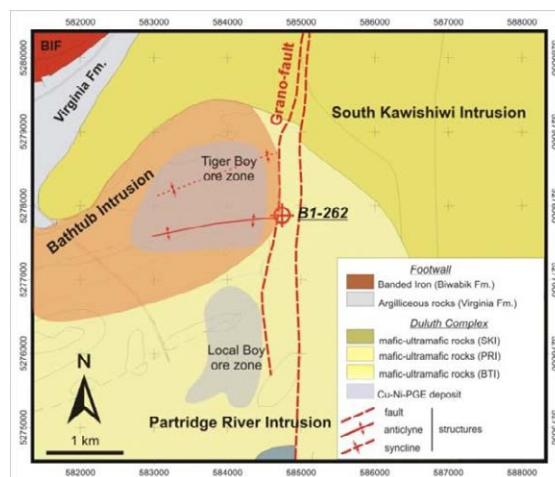


Figure 1. Geologic map of the Bathtub Intrusion

The Bathtub Intrusion is a newly defined intrusion situated between the SKI and PRI (Severson and Hauck 2008; Fig. 1). The hornfelsed and partially molten footwall of the intrusion consists of the Archean (~2.6 Ga) Giant's Range batholith (GRB), the Early Proterozoic Biwabik Iron Formation (BIF) and the argillaceous Virginia Formation. The BTI is divided into two major units. The bottom (350 m) part of the BTI called BT1 unit consists of augite troctolite, gabbro, norite and other ultramafic units with abundant hornfels inclusions near to the intrusion-footwall contact. The magmatic sulphide mineralization is generally coarse grained and disseminated, but close to the contact, local semi-massive pods also occur. The upper BT4 unit (300 m) is composed of troctolite, anorthositic troctolite and augite troctolite. This upper part of BTI is also mineralized, but the mineralization is not as continuous as in the BT1, though the grades are often higher (Severson and Hauck 2008).

The zone of the Grano fault is a north trending, 600 m broad fault system and is considered to be the feeder channel to the BTI (Severson and Hauck 2008). Although felsic dikes and pyroxenite lenses sporadically occur everywhere along the footwall-intrusion contact in the BTI, their number is particularly high along the Grano fault.

3 Results

3.1 Petrography of felsic dikes

Occurrence of felsic dikes in the bottom 300 m section of the B1-262 drill core is highly irregular. The thickness of dikes is highly variable between 5 cm and 3-4 meters. Four different varieties of felsic dikes with sharp contacts to the host troctolite can be distinguished:

Type I: hypidiomorphic granular textured granite-granodiorite with local occurrence of chlorite filled vugs (Fig. 2a).

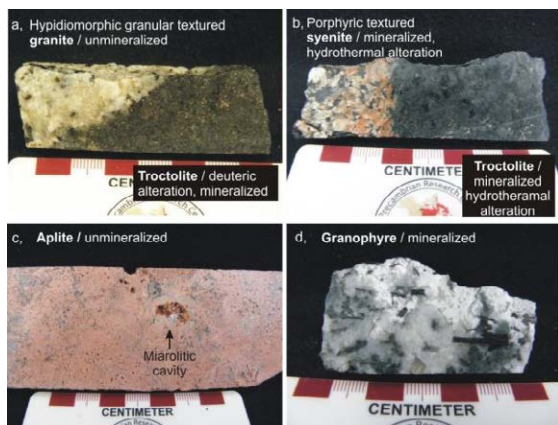


Figure 2. Felsic vein types a) Type I: unmineralized hypidiomorphic granular textured granite b) Type II: mineralized porphyritic textured syenite c) Type III: aplite with BIF inclusions and miarolitic cavities d) Type IV: mineralized granophyre

Type II: porphyritic syenite-monzonite. Vugs and miarolitic cavities between porphyritic feldspar

crystals are common.

Type III: aplite dikes. Hematite-rich xenoliths from the BIF and miarolite-like cavities are abundant. Type II syenite is usually hydrothermally altered and mineralized; whereas no mineralization has been found in the Type III aplite dikes.

Type IV: quartz-K-feldspar bearing mineralized felsic segregates with granophyre texture (Fig. 2d).

3.2 Hydrothermal alterations in the troctolite

Three consecutive phases of deuteric and hydrothermal alteration are distinguished petrographically in the host troctolite and in the felsic dikes.

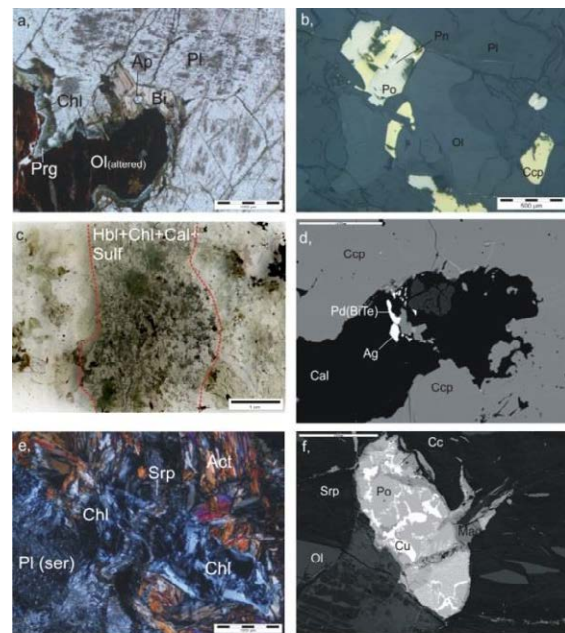


Figure 3. Deuteric alteration of primary mafic minerals in the troctolite: a) olivine (Ol) altered to chlorite (chl) is rimmed by pargasitic amphibole (Prg) and biotite (Bi) intergrown with apatite (Ap). b) Intercumulus granular pyrrhotite (Po) and chalcopyrite (Ccp) between fresh plagioclase (Pl) and olivine (Ol). c) Chloritic (Chl) alteration in troctolite along a vein. d) Chalcopyrite (Ccp), native silver (Ag) and kotulskite in chlorite veins. e) Chlorite (Chl) alteration of troctolite cross-cut by serpentinite (Srp) vein. f) Pyrrhotite (Po) replaced by native copper (Cu) and chalcocite (Cc) along fractures in serpentinitized troctolite.

Deuteric alteration of the troctolite, if present, is confined to the early silicate phases (olivine, pyroxene; Fig. 3a) and can be characterized by a biotite + chlorite + amphibole + apatite assemblage. Main sulphide phases in the fresh and deuteric troctolite are pyrrhotite, chalcopyrite, pentlandite and cubanite (Fig. 3b). The first phase of hydrothermal alteration occurs in fracture related zones with variable thickness (2-10 cm scale). In these zones, primary silicate minerals are completely replaced by amphibole + chlorite + calcite (Fig. 3c). Amphibole has two generations. The euhedral, second generation hornblende is Cl-enriched (0.3 apfu) compared to the first generation of pargasite (0.9 apfu). Space between hornblende crystals is filled by calcite. Chlorite composition is mainly controlled by the host

rock chemistry and chlorite in hydrothermally altered troctolite is Fe-poor (3.5 apfu). The chlorite thermometer of Krandidiotis and McLean (1987), in the hydrothermally altered troctolite gives temperatures around 240–280°C. Cl/(Cl+F) ratio of intercumulus, unzoned apatite in the unaltered troctolite is generally low (below 0.25). In samples with deuteric alteration, apatite is often intergrown with hydrous silicates (eg. biotite) and the Cl/(Cl+F) ratio is slightly increasing (up to 0.36) as a result of the activity of primary magmatic volatiles. In some structurally controlled zones with chlorite + amphibole alteration, bulk apatite indicates a continuous depletion both in F and Cl. The Cl/(Cl+F) ratio is extremely high (>0.8) along fractures in the apatite.

Main sulphide phases associated to amphiboles are chalcopyrite and bornite, whereas galena, selenian galena, sphalerite, kotulskite (PdBiTe), clausthalite (PbSe) and native silver (Ag) occur in trace amounts. The second, fracture related alteration type of troctolite is characterized by serpentine veinlets that intercept all previous alterations (Fig. 3e). In these zones, pyrrhotite and chalcopyrite are replaced by chalcocite + native copper + magnetite along grain boundaries and fractures (Fig. 3e).

3.3 Hydrothermal alterations in the felsic dykes

Even in the less altered Type I dike with almost fresh feldspars and biotite (Fig. 4a) some vugs occur filled by chlorite (Fig. 4b).

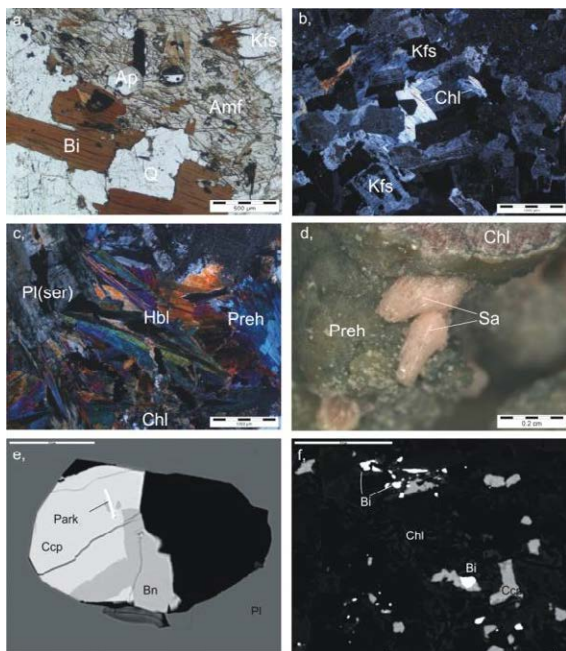


Figure 4. a) Fresh hypidiomorphic textured granite (Type I) (Bi-biotite, Q-quartz, Amf-amphibole, Kfs-K-feldspar). b) Vugs filled by chlorite (Chl) in the hypidiomorphic textured Type I granite. c) First phase hydrothermal alteration in Type II felsic vein with prehnite (Preh), altered plagioclase (Pl), and chlorite (Chl). d) Euhedral overgrown sanidine (Sa) in vugs of chloritized (Chl) Type II veins. e) Granular intergrowth of chalcopyrite (Ccp) and bornite (Bn) in hydrothermally altered Type II dike. f) Native bismuth (Bi) and chalcopyrite (Ccp) in chloritized Type II dike.

Core of amphiboles in Type I dikes is poor both in chlorine (<0.01 apfu) and fluorine (<0.03 apfu) but fluorine increases towards the rim (~0.08 apfu). Apatite is F-rich (Cl/(Cl+F)<0.06) and chemically homogeneous.

The first phase of hydrothermal alteration in Type II dikes is characterized by amphibole + prehnite + chlorite. Feldspars are variously altered to sericite and calcite (Fig. 4c). Amphibole has two generations; Cl-poor (0.4 apfu) hornblende is syntaxially overgrown by Cl-rich (0.6 apfu) edenite. Prehnite is zoned in some samples: from core to rim of individual crystals the Fe³⁺ for Al³⁺ substitution in the octahedral position of the prehnite structure decreases (from 0.7 to 0.17 apfu). Chlorite is Fe-rich (Fe/[Fe+Mg]=0.6). The second phase of hydrothermal alteration resulted in Fe-loss (Fe/[Fe+Mg]=0.4) of chlorite in accordance with Fe-loss in prehnite. Chlorite thermometers give formation temperatures around 248±25°C that is in a good agreement with the occurrence of prehnite that forms below 330°C. In a more advanced stage of the alteration, prehnite and calcite occur along veins and in open spaces between earlier hydrothermal phases. In some vugs, sanidine was also identified (Fig. 4d). No sulphide mineralization can be connected to this late phase of fluid mobilization.

Primary apatite in both Type II and III dikes are Cl-enriched (Cl/(Cl+F)>0.2). A distinct Cl enrichment of rim with respect to core was observed for apatite in the Type II dikes. However, apatite in Type III dikes displays an opposite trend.

Chalcopyrite and bornite are the main sulfide phases associated to the first phase alteration assemblage in the Type II felsic dykes. They are accompanied by froodite (PdBi₂), native bismuth (Bi), native gold (Au), sphalerite, galena, altaite (PbTe), breithauptite (NiSb), greenockite (CdS) and parkerite (Ni₃Bi₂S₂) (Figs. 4d-e).

4 Conclusions

Geochemical similarities to leucosome veins reported in Benkó et al. (2012) from the granitic footwall of the SKI (Fig. 5) and occurrence of BIF inclusions in some Type II dikes suggest that the parent rock could be the partially melted Archean Giant's Range batholith in the footwall of the BTI. However, the bulk geochemical composition of Type I dikes is comparable with silicic volcanic and subvolcanic rocks (rhyolites, icelandites and granophyre bodies) that formed contemporaneously with the mafic rocks of the intrusion in the main magmatic phase of the Keweenawan rift event. Formation of silicic rocks was interpreted to be related to the extensive melting of the crust as a consequence of the intrusion of voluminous mafic magma in the lower crust (Vervoort and Green 1997).

This observation supports the idea that the Grano fault is a deep, crustal scale fault that could be a major channel both for mantle derived mafic rocks and partially molten rocks emerging from the deep continental crust and the proximal contact aureole of the DC. Ore minerals in the felsic dikes are confined to the hydrothermally altered zones. This relationship implies

the felsic dikes were not major carriers of sulphur and precious metals and did not contribute primarily to the mineralization in the intrusion. However, miarolitic cavities filled by chlorite implies that magmatic fluids segregated during the crystallization of the felsic dikes. Elevated Cl/(F+Cl) ratios of apatite and the prevalent occurrence of miarolitic cavities in Type II felsic dikes suggest that these rocks were more fluid saturated in comparison to Type I dikes.

A distinct Cl enrichment of rim with respect to core in apatite in the Type II dikes implies that the segregating magmatic fluids reacted with the primary silicates forming secondary hydrous phases. Apatite in Type III dikes displays an opposite trend, suggesting that Cl-rich volatiles escaped from the crystallizing dikes. Very intense hydrothermal alteration of some Type III dikes and the troctolite around the dikes reinforces this model.

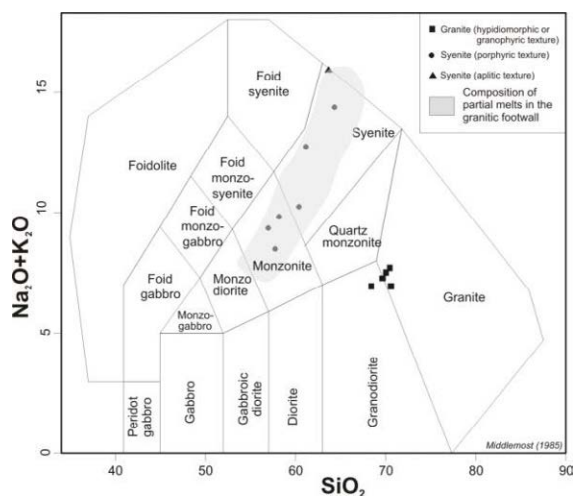


Figure 5. Comparison of bulk rock geochemistry of felsic veins with partial melts of the footwall granites formed during the emplacement of the intrusion and with deep crustal melts that erupted during the main stage of the Keweenaw rift event

Hydrothermal mineral assemblages characterized primarily by chlorite, amphibole, prehnite and calcite alteration and the trace element (F, Cl, Fe) variation of these minerals are similar both in troctolite and in the felsic dikes.

Zonation of hydrothermal minerals may suggest variation in fluid composition, temperature, fO_2 , etc. during the hydrothermal fluid flow. High chlorine activity during fluid flow is suggested based on the Cl-enriched rim of amphibole and the extreme chlorine enrichment of apatite along fissures. This post-crystallization metasomatic phenomenon infers that primary magmatic apatite in magmatic rocks does not necessarily reflect the halogen ratio of the parent magma, since fluids migrating in intrusions under certain conditions are able to change the initial Cl/F ratio. Prehnite forms from near-neutral, alkaline fluids under 220°C (Wheeler et al. 2001). Pd is only mobile below 300°C under acidic and/or highly oxidizing conditions, irrespective of fluid salinity and immobile in association with chlorite, calcite, albite. At higher temperatures transport of Pd is possible under less severe conditions (Wood 2002). Our observations in

agreement with the experimental data prove that Pd and other precious metal bearing minerals are associated with the early hydrothermal amphiboles. The zones characterized by chlorite-prehnite-calcite formed under 300°C and in turn are unmineralized.

Replacement of chalcopyrite by chalcocite and native Cu in the serpentinite alteration zones imply oxidation of the primary mineral assemblage during late fluid flow.

The Grano fault was not only a conduit for magmas, but the extensive hydrothermal alteration in the bottom 300 m of the B1-262 drill core suggest that syngenetic activity of the fault provided a major pathway for hydrothermal fluid flow, as well. However, serpentinization of the mafic and ultramafic rocks in the layered intrusions of the DC is widespread and cannot be connected exclusively to the enhanced permeability and fluid circulation along the Grano fault or to the fluid segregation of the felsic dikes.

Acknowledgements

We acknowledge the financial support from the Austrian Science Fund (FWF-P23157-N21) to Abera Mogessie.

References

- Benkó Z, Mogessie A, Molnár F, Severson M, Hauck S, Lechler P, Arehart G (2012) Contact metamorphism, partial melting and fluid flow in the granitic footwall of the South Kawishiwi Intrusion, Duluth Complex, USA. Geophysical Research Abstracts 14. EGU 2012-6443-1
- Gál B, Molnár F, Benkó Z, Mogessie A, Peterson D, Hauck S A, Severson M J (2012): Halogen-geochemistry of apatite from Cu-Ni-PGE mineralized intrusions of the Duluth Complex: exsolution of Cl-bearing fluids in the waning stages of crystallization. 34th International Geological Congress (IGC): Australia 2012 2286
- Kranidiotis P, MacLean WH (1987) Systematics of chlorite alteration at the Phelps Dodge massive sulfide deposit, Matagami, Quebec. Economic Geology 82: 1898-1911
- Miller JD Jr, Vervoort JD (1996) The latent magmatic stage of the Midcontinent rift: A period of magmatic underplating and melting of the lower crust: Institute on Lake Superior Geology, 42nd Annual Meeting Cable Wis, Proceedings 42, Program and Abstracts 33-35
- Severson MJ, Hauck SA (2008) Finish logging of Duluth Complex drill core and a reinterpretation of the geology at the Mesaba (Babbitt) deposit. Technical Report NRRI/TR-2008/17
- Vervoort JD, Green JC (1997): Origin of evolved magmas in the Midcontinent rift system, northeast Minnesota: Nd-isotope evidence for melting of Archean crust. Canadian Journal of Earth Sciences 34: 521-535
- Wheeler RS, Browne PRL, Rodgers KA (2001) Iron-rich and iron-poor prehnites from the Way Linggo epithermal Au-Ag deposit, southwest Sumatra, and the Heber geothermal field, California. Mineralogical Magazine 65(3): 397-406
- Wood SA (2002) The aqueous geochemistry of the platinum-group elements with applications to ore deposits. In LJ Cabri (ed): The Geology, Geochemistry, Mineralogy and Mineral Beneficiation of Platinum-Group Elements. Can. Inst. Min. Metall. Petrol. Spec. 54: 211-249

Cu-Ni-Au-PGE transport in the partially molten charnockitic footwall of the Spruce Road deposit, South Kawishiwi intrusion, Duluth Complex, Minnesota, USA

Zsolt Benkó, Aberra Mogessie

Institute of Earth Sciences, Mineralogy and Petrology, Karl-Franzens-University of Graz, 8010 Graz, Austria

Ferenc Molnár

Geological Survey of Finland, 02151 Espoo, Finland

Mark Severson, Steven Hauck

Natural Resources Research Institute, University of Minnesota, Duluth, 55811, Minnesota, USA

Greg B. Arehart

University of Nevada, Reno, 89557 Nevada, USA

Abstract. A strong relationship was documented in the charnockitized monzonitic footwall at the Spruce Road deposit (South Kawishiwi Intrusion, SKI) between partial melting processes, mineralogy, texture and the transport mechanism of the sulphide mineralization. In the proximal part of the footwall, dense, Fe-rich mega-sulphide droplets have sunk in the intensively melted diatexite migmatite. The mineral assemblage (pyrrhotite + pentlandite + chalcopyrite) suggests that the source of the sulphide was the basal mineralized zone of the SKI. In the deeper zones with decreasing degree of partial melting, the transport of a Cu-enriched melt was connected to the migration of schlieren neosome veins. In the distal metatexite part of the partially melted footwall, migration of a Cu-rich melt is connected to patch migmatites and partial melt pools, but migration of the melt along microfractures (after solidification of the host rock) was also observed. Involvement of aqueous fluids during retrograde metamorphism resulted in pervasive chloritic and actinolitic alteration of the primary mineral assemblages and the formation of actinolite-chlorite-pumpellyite-calcite-albite veins. The fluid flow locally oxidized pyrrhotite to pyrite. The intergrowth of Chalcopyrite and millerite - with calcite and actinolite suggest local-scale remobilization of base metals from the primary mineral assemblage.

Keywords. Duluth Complex, Archean granite, partial melting, hydrothermal remobilization

1 Introduction

The disseminated Cu-Ni(-PGE) mineralization at the basal contact of the South Kawishiwi- (SKI), Partridge River- (PRI) and Bathtub Intrusions (BTI) of the Mesoproterozoic (ca. 1.1 Ga) Duluth Complex (DC) has been the target of extensive mineral exploration since the 1950s. Recent exploration activities revealed that the second largest cumulative Cu-Ni reserves of the world occur in the lower, up to ca. 100 m thick mineralized zones of the PRI, BTI and SKI (Naldrett 2010).

The charnockitic (e.g. orthopyroxene-bearing granite formed by contact metamorphism) footwall of the SKI locally contains high grade Cu-Ni-Pt-Pd-Au disseminated ore up to a distance of 125 m from the intrusion-footwall contact (Patelke 2003). Peterson

(2010) suggested that formation of this type of ore might be connected to partial melting and dehydration processes generated by the thermal effect of the SKI on the granitic footwall. Molnár et al. (2010) compared sulphur isotopic composition of ores from the footwall and in the SKI and concluded that footwall ores were formed during the early stages of multiple emplacement history of SKI. In order to shed further light on the source and transport of metals in the charnockitic footwall, detailed petrographic and mineralogical, studies were carried out on drill core samples from the WM-002 drill hole (Spruce Road deposit, SKI).

2 Geologic setting

The DC is a part of the aborted Mid-Continental rift system of Keweenaw (ca. 1.1 Ga) age. Magmatic rocks related to the rifting of the Archean and Paleoproterozoic basement formed in four magmatic stages (early, dormant, main and late; Miller and Vervoort 1996). Volcanic rocks formed in each stage, whereas the mafic intrusions of the DC were emplaced during the early (1109-1107 Ma) and main (1102-1094 Ma) stages.

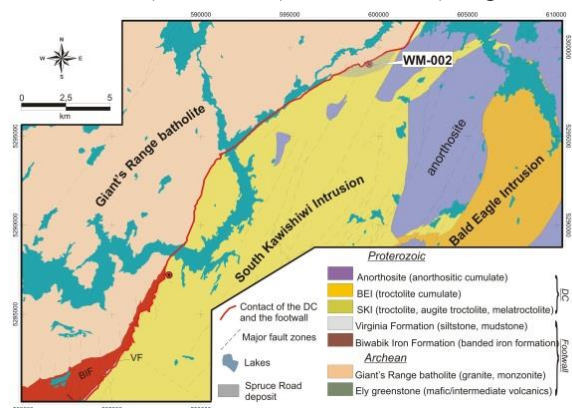


Figure 1. Geologic map of the northern part of the South Kawishiwi Intrusion and the location of the investigated drill hole

The economically important layered series (SKI, PRI and BTI) formed subsequently to the formation of the

anorthositic series, during the main phase of magmatism (Miller and Vervoort 1996).

The Archean (~2.6 Ga) Giant's Range batholith (GRB), the footwall below the SKI at the Spruce Road deposit, consists of granite, granodiorite, monzodiorite and monzonite. These rocks underwent hornblende and pyroxene hornfels facies contact metamorphism due to thermal effect of the SKI (Sims and Viswanathan 1972). Contact metamorphism of the granitic footwall took place between 1.5-2.5 Kbar pressure, calculated based on the cumulative thickness of the overlying intrusive, volcanic and sedimentary rocks (4500-9000 m; Bonnischen 1969).

The sill-like SKI consists of troctolitic, anorthositic olivine-gabbroic and subordinately ultramafic rocks. Models by Peterson (2010) and Molnár et al. (2010) suggested that the emplacement of a metal-laden sulphide-rich melt along the contact of the footwall (Basal Mineralized Zone, BMZ-hereafter) was followed by sulphide-undersaturated magma pulses moving above the early, sulphide-rich magma injection. Mineralization in the BMZ is dominated by a disseminated and fractionated ore with dominance of chalcopyrite and cubanite over pyrrhotite and pentlandite. Along the contact, less-fractionated, semi-massive, small ore pods occur locally. Pyrrhotite and pentlandite are more abundant in this latter ore type than chalcopyrite and cubanite.

3 Results

3.1 Partial melting and deformation of the footwall granite

The mineral composition and texture of the footwall granitoids is highly altered by deformation, partial melting and retrograde metamorphism along the contact with the SKI. The charnockite mainly consists of oligoclase, enstatite, augite and biotite. Accessory minerals are magnetite, apatite, and titanite +/- ilmenite. In a 50 m thick zone under the contact, this rock is slightly foliated in 1-5 m thick discontinuous zones, which are enclosed in less deformed rock units. Oligoclase ($Ab_{0.70-0.87}$) in the undeformed rock is mosaic textured (200-300 μ m) with local occurrence of K-feldspar antiperthite lamellae. Further away from the contact, oligoclase is coarser grained (500-700 μ m) with subhedral or euhedral habits and does not show antiperthite exsolutions. In the deformed zones, feldspars are 1-2 cm anhedral grains with lobate grain boundaries and internal deformation features including deformation twinning, subgrain rotation and internal shear features. Pyroxene (400-600 μ m) up to 300 m from the contact is euhedral or subhedral and occurs between feldspars or form veins without any preferred orientation. Mg/(Mg+Fe) ratio increases both in enstatite (from $En_{0.57}Fs_{0.33}$ to $En_{0.71}Fs_{0.25}$) and augite (from $W_{0.43}En_{0.40}Fs_{0.13}$ to $W_{0.43}En_{0.42}Fs_{0.09}$) towards the distal zones of the drill hole.

Several signs of partial melting were observed in the whole section described above. At incipient melting, a thin film of melt occurs on the rim of the

reactant minerals that crystallized to quartz with cusped grain boundaries (Fig. 2a). Corroded oligoclase has a typical texture characteristic of dry partial melting (Johannes et al. 1994). Parallel to the (001) cleavage plane, plate-like melt drops crystallized to K-feldspar ($Or_{0.92}Ab_{0.08}$) occur (Fig. 2b). With more advanced melting, melt films coalesce and form melt pools up to 1-2 mm size (Fig. 2c). Melt pools are small domains with cusped triangle boundaries between rounded crystals of quartz. With increasing degree of melting in the non-deformed distal part of the footwall oval or round shaped patches of neosome occur that is called patch migmatite (Sawyer 2008). The patches are made of 1-2 mm euhedral biotite. Space between biotite crystals is filled by quartz (Fig. 2d). At the most advanced stage of melting, in the proximal 100 m part of the footwall, schlieren migmatite (veins of melt) dominantly composed of biotite (500-1000 μ m) occurs (Fig. 1e).

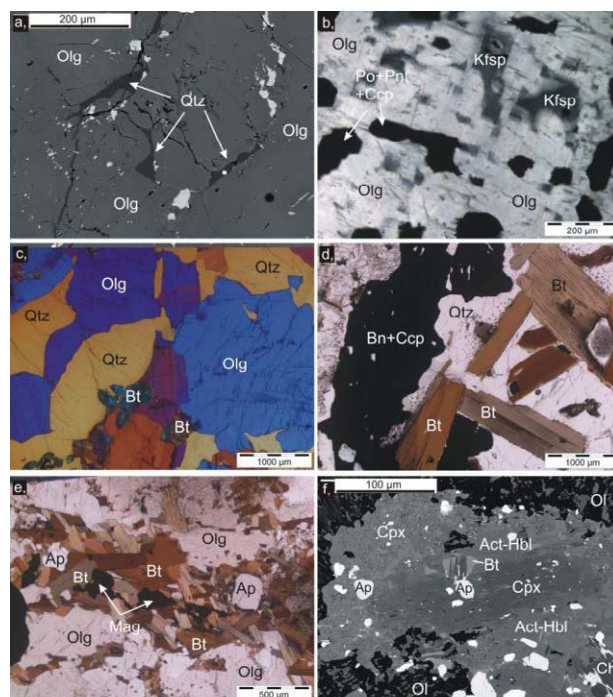


Figure 2. Consecutive stages of partial melting: a) Partial melt films that crystallized to quartz (Qtz) between rounded reactant oligoclase (Olg) crystals. b) Plate-like melt drops crystallized to K-feldspar (Kfsp) in oligoclase (Olg) replaced partially by sulphide melt. c) Partial melt pool that crystallized to quartz (Qtz) between slightly rounded oligoclase (Olg) crystals. (Gypsum plate inserted). d) Patch migmatite: euhedral biotite (Bt) is intergrown with quartz (Qtz). e) Schlieren migmatite: neosome vein composed of biotite, (Bt) andesine, magnetite (Mag) and apatite (Ap). f) Clinopyroxene (Cpx) is rimmed by actinolite (Act) and hornblende (Hbl); towards the rim). Biotite (Bt) is altered to chlorite (Chl).

Schlieren form during the flow of the neosome and are 100-1000 μ m wide and enriched in accessory minerals (e.g. magnetite and apatite). Composition of biotite in the neosome veins varies systematically: towards the intrusion-footwall contact Mg# decreases from 0.75 to 0.60 as does the F (0.17 to 0.02 apfu) and Ti (from 0.3 to 0.1 apfu). Plagioclase in the leucosome is smaller than in the residual rock (50-150 μ m) and more

calicic ($Ab_{0.39}An_{0.6}$). Apatite is abundant in the leucosome veins and is intergrown with biotite. Cl/(Cl+F) ratio in the leucosome veins decreases towards the footwall-intrusion contact from 0.25 to 0.17 whereas apatite in the residual rock is depleted in chlorine ($Cl/(Cl+F)=0.13$).

The primary metamorphic mineral assemblage is retrogressed in cm-m thick zones situated randomly in the footwall. Orthopyroxene is altered to biotite and augite and has a replacement corona consisting of actinolite or hornblende. Biotite replaces orthopyroxene and is partly altered to chlorite along cleavage planes (Fig. 1f). Amphiboles along with chlorite, pumpellyite, prehnite, titanite, quartz, apatite and calcite also form 1-2 cm thick veinlets with an albitic alteration halo. Actinolite is zoned: the rims are enriched in Fe and Cl ($Fe^{2+}/(Mg+Fe^{2+})=0.35$; $X^{Cl}=0.06$) with respect to the core ($Fe^{2+}/(Mg+Fe^{2+})=0.27$; $X^{Cl}=0.03$). The plagioclase component of the perthitic feldspars is pure albite ($Ab_{0.98}An_{0.02}$) in the alteration selvage of these veins. Apatite forms hexagonal elongated crystals intergrown with amphibole and pumpellyite. Calcite was the last phase to crystallize in the open space remaining after the crystallization of the silicates. The composition of veins does not show any variation as a function of distance from the contact.

3.2 Sulphide-platinum group minerals (PGM)-Au-Ag mineralization

In the proximal zones (down to 15 m from the contact), the sulphide mineral assemblage includes granular pyrrhotite with granular or flame like exsolution of pentlandite + chalcopyrite. Sulphide forms rounded interconnected droplets with diameters of up to several cm in the partially molten rock (Fig. 3a). Internally, the droplets show net-texture with rounded subhedral augite and rounded anhedral oligoclase (Fig. 2b). Pyrrhotite displays deformation twinning. Platinum group minerals (PGM) found as inclusions in pyrrhotite and chalcopyrite are sperrylite ($PtAs_2$) and michenerite ($PdBiTe$). In the deeper zones, modal proportion of chalcopyrite increases (visual estimation) and the mineralization is hosted by the biotite-rich schlieren migmatite (Fig. 3c). No difference is detected in biotite composition between the mineralized and unmineralized neosome. The bornite + chalcopyrite + millerite + galena + sphalerite + PGM assemblage occurs 30 m below the intrusion-footwall contact. Ore minerals locally occur in patch migmatite composed of quartz and euhedral biotite (Fig. 3d). Their presence was also observed along fractures in feldspar porphyroblasts. Thickness of veinlets and fractures filled by bornite and chalcopyrite varies from $1\mu m$ to 0.2 mm. Sulphides in the thicker veins are surrounded by a thin biotite selvage (Figs. 3e-f). Micron-size sulphide droplets in feldspars form solid inclusions along fractures. No alteration of the feldspars is detected along these fractures (Fig. 3f). Chalcopyrite and bornite form a symplectitic intergrowth (Fig. 3e). Sphalerite rims chalcopyrite and trace ore mineral phases occur as inclusions in bornite and subordinately in chalcopyrite. Trace minerals in this assemblage are: galena, native gold (Au), native silver (Ag), parkerite

($Ni_3Bi_2S_2$), merenskyite ($PtPdTe_2$), hessite (Ag_2Te), selenian galena ($Pb(S,Se)$). The Pt and Pd content of galena are up to 1.2 wt.%. Galena often occurs in small offshoots around bornite grains (Fig. 3g).

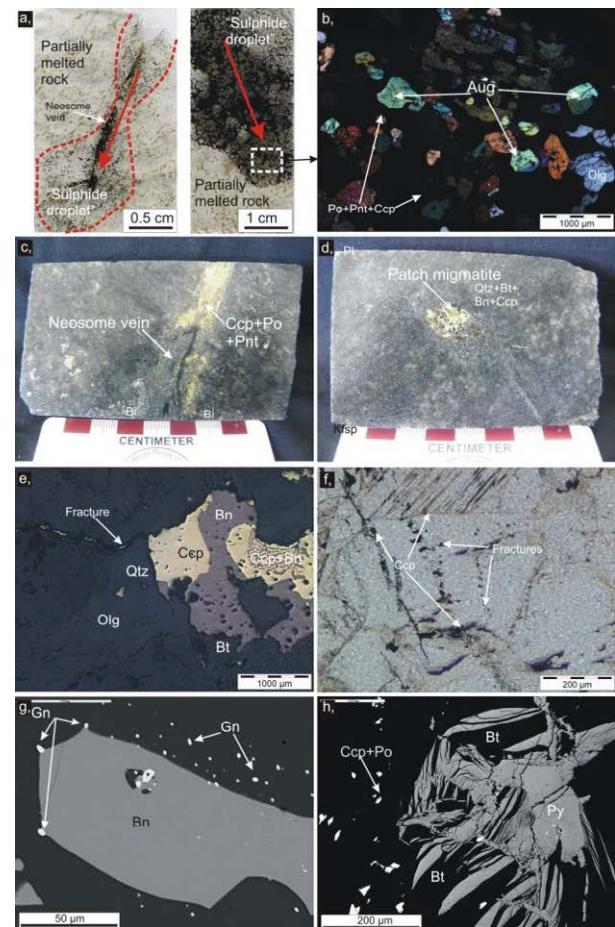


Figure 3. a) Interconnected sulphide droplets. Red arrow indicates the possible direction of migration of the droplet in the partially molten rock b) Net-texture intergrowth of augite (Aug), oligoclase (Olg) with pyrrhotite (Po) + chalcopyrite (Ccp) and pentlandite (Pnt). c) Chalcopyrite (Ccp) + pyrrhotite (Po) vein surrounded by biotite + andesine + apatite neosome. d) Patch migmatite: Quartz (Qtz) + biotite (Bt) partial melt is replaced by bornite (Bn) + chalcopyrite (Ccp) e) Symplectitic intergrowth of bornite (Bn) and chalcopyrite (Ccp) surrounded by biotite (Bt) and quartz (Qtz). f) Chalcopyrite (Ccp) inclusions in microfractures of oligoclase (Olg). g) Galena (Gn) inclusions and dissemination in and around bornite (Bn). h) Pyrite (Py) intergrown with neosome biotite (Bt; central part of Fig. 2a)

Where the primary mineral assemblage is retrogressed, the sulphides are also altered. The rim of the pentlandite has spotty alteration and the pyrrhotite is oxidized to pyrite. In the retrogressed biotite schlieren, pyrite is intergrown with chloritic biotite (Fig. 3h). In the amphibole + chlorite + pumpellyite + calcite veins, chalcopyrite + pyrite + millerite occur intergrown with amphibole.

4 Discussion and conclusions

The occurrence of augite and/or orthopyroxene below to

150 m from the contact defines the lower border of the pyroxene hornfels facies indicating at least 725°C at 2 Kbar pressure at this depth (Naney 1983). The investigated profile can be divided in three major units based on rock texture, mineralization and partial melting features. In the distal ~80 m portion, the occurrence of melt films, melt pools and patch migmatites indicate partial melting under strain-free conditions and formation of a metatexite migmatite with up to 20% partial melting. In the central ~60m part, the common occurrence of schlieren migmatite (neosome veins) suggests intensive melting (melt proportion up to 50%). Biotite is stable up to 850-900°C depending on the water activity (Naney 1983) Therefore; the estimated temperature in this central part of the profile could be between 750-850°C. In the proximal ~15 m of the profile, the degree of partial melting should be as high as 50% but the dynamic recrystallization and local shear features mimic the primary melting features. Absence of prograde biotite in the proximal diatexite suggest temperatures of up to 920°C under water undersaturated conditions at 2 Kbar pressure (Naney 1983). Dynamic recrystallization of the feldspars and biotite-schlieren that crosscut the host rock suggests slow cooling and/or repeated reheating of the footwall in the proximal zones.

The SKI above the investigated profile consists of multiple magma injections (Peterson 2010; Molnár et al. 2010) and each magma pulse could result in partial melting of the granite at some degree.

Sulphide melts can migrate in a partially molten crystal pile in two forms (Chung and Mungall 2009): either as dense sulphide droplets that are smaller than the diameter of the throat between silicates *or* as coalesced mega-droplets with up to several cm diameters move downward because of the pressure gradient in the mega-droplet. Otherwise, capillary forces do not allow migration of a Fe-rich sulphide melt between silicate crystals. In the proximal zones of the investigated drill core, the occurrences of net-textured sulphide-droplets, which have comparable mineralogical composition with the BMZ of the SKI suggest that relatively large Fe-rich sulphide droplets migrated gravitationally from the BMZ. These droplets crystallized into pyrrhotite + chalcopyrite + pentlandite assemblages.

In the central 60m portion, characterized by schlieren migmatite, the increase of modal proportion of chalcopyrite at the expense of pyrrhotite is detected. Substitution of Cu in the Cu-Fe-O-S system considerably lowers the solidus temperature (Naldrett 2010). The decreasing temperature towards the distal zones and the strong connection of sulphide melt to the schlieren veins is in good agreement with the Cu-enriched character of the sulphide melt.

Cu-rich melt may crystallize below 800°C therefore migration of the fractionated Cu-rich sulphide melt in the distal metatexite portion is also possible along fractures (Mungall and Su 2005). However, textural evidence suggests that formation of the chalcopyrite-bornite-rich mineralization is partly connected to the partial melting of the granite.

The amphibole-chlorite-pumpellyite-calcite-albite alteration and veins indicate involvement of aqueous fluids during retrograde metamorphism. The

mineral assemblage proves albite-epidote (300-400°C) and lower, zeolite facies (<300°C) overprint of the primary mineral assemblage. Involvement of fluids resulted in only local scale remobilization of base metals from the primary, partial melting related mineralization.

Acknowledgements

We acknowledge the financial support from the Austrian Science Fund (FWF-P23157-N21) to Aberra Mogessie and the Senior Fellowship support to Ferenc Molnar by the Hungarian-American Enterprise Scholarship Fund.

References

- Bonnichsen B (1969) Metamorphic pyroxenes and amphiboles in the Biwabik Iron-formation, Dunka River area, Minnesota: Mineralog Soc America Spec Paper 2: 217-239
- Chung HY, Mungall EJ (2009) Physical constraints on the migration of immiscible fluids through partially molten silicates, with special reference to magmatic sulfide ores. *Earth and Planetary Science Letters* 286: 14-22
- Johannes W, Koepke J, Behrens H (1994) Partial melting reactions of plagioclases and plagioclase bearing systems. *In: Parsons I (1994): Feldspars and their reactions.* Kluwer Academic Publisher 161-193
- Miller JD Jr, Vervoort JD (1996) The latent magmatic stage of the Midcontinent rift: A period of magmatic underplating and melting of the lower crust: Institute on Lake Superior Geology, 42nd Annual Meeting Cable Wis, Proceedings 42, Program and Abstracts 33-35
- Molnár F, Peterson D, Arehart GB, Poulson S, Hauck SA (2010) Sulfur isotope constraints for a dynamic magmatic sulphide ore deposition model in the sill-like South Kawishiwi Intrusion of the Duluth Complex, Minnesota, USA. *Acta Mineralogica-Petrographica Abstract Series* 6: 228
- Mungall JE, Su S (2005) Interfacial tension between magmatic sulphide and silicate liquidus: Constraints on kinetics of sulphide liquation and sulphide migration through silicate rocks. *Earth and Planetary Science Letters* 234: 135-149
- Naldrett AJ (2010) *Magmatic Sulphide Deposits.* Springer Verlag 3-16
- Naney MT (1983) Phase equilibria of rock forming ferromagnesian silicates in granitic systems. *American Journal of Science* 283: 993-1033
- Patelke R (2003) Exploration drill hole lithology, geologic unit, copper-nickel assay, and location database for the Keweenaw Duluth Complex, Northeastern Minnesota. Technical Report NRRI/TR-2003/21
- Peterson D (2010) Nokomis deposit Duluth Metals in: Guidebook for the Post-symposium field trip. Cu-Ni-PGE deposits in mafic Intrusions of the Lake Superior Region 97-116
- Sawyer EW (2002) Report on thin sections from DDH WM-001, Spruce Road Cu-Ni deposit, South Kawishiwi Intrusion, Duluth Complex. Report of Investigations NRRI/RI-2002/13 1-21
- Sims PK, Viswanathan (1972) Giants Range batholith in: *Geology of Minnesota Centennial Volume* 120-139

Geochemistry of the Sakatti magmatic Cu-Ni-PGE deposit, northern Finland

Will Brownscombe & Richard J. Herrington

LODE, Natural History Museum London, Cromwell Road, London, SW7 5BD, UK

Jamie J. Wilkinson & Andrew J. Berry

LODE, Department of Earth Science and Engineering, Imperial College London, London, SW72 AZ, UK

Jim Coppard & Christian Ihlenfeld

Anglo American Exploration, 20 Carlton House Terrace, London, SW1Y 5AN, UK

Shephanie Klatt & Craig Hartshorne

AA Sakatti Mining OY, 990601 Sodankyla, Finland

Adrian J. Boyce

SUERC, Rankine Avenue, Scottish Enterprise Technology Park, East Kilbride, G75 0QF, UK

Rex N. Taylor

National Oceanography Centre, University of Southampton, Southampton SO14 3ZH, UK

Abstract. The Sakatti deposit comprises disseminated and massive sulphide hosted by an ultramafic cumulate. The cumulate consists of olivine with high Mg (Mg# 0.85-0.91) and high Ni contents (0.3-0.5 wt%). Pt minerals hosted within the sulphide are exclusively tellurides with an unusual array of Pt-Pd-Ni compositions. S isotope compositions are similar to mantle rocks with $\delta^{34}\text{S}$ values clustering around 3‰, whereas the nearby Matarakoski sulphide-bearing sediments show fractionated values. Initial ϵNd values are negative implying the deposit has been contaminated by continental crust. Similarities with the Kevitsa deposit 15 km away suggest that these deposits have a shared genetic history.

Keywords. magmatic-nickel-Finland-Sakatti

1 The Sakatti deposit

The Sakatti deposit is a greenfield discovery in northern Finland that subcrops beneath glacial till and was essentially blind. The deposit consists of both disseminated and massive Cu-Ni sulphide mineralisation, with significant platinum group element (PGE) content, hosted by an olivine cumulate. The cumulate has a conduit-like profile, at least 0.5 km in cross section, surrounded by a volcanic footwall and capped by a breccia.

Sakatti is located in the Central Lapland Greenstone Belt (CLGB), 15 km from the Kevitsa Ni-Cu-PGE deposit that has recently entered production. The stratigraphy of the CLGB, into which both Sakatti and Kevitsa are intruded, contains the substantial Matarakoski sulphide-bearing black schist unit, as well as sedimentary quartzites and mafic-ultramafic volcanics (Lehtonen et al. 2005).

2 Mineral Chemistry

2.1 Silicate mineral chemistry

The olivine cumulate that hosts the Sakatti deposit is

heavily serpentinised. In spite of this, magmatic olivine, pyroxene and amphibole are preserved sporadically throughout the unit. Sampling was designed to target these areas, with moderate success. The chemistry of the primary silicates provides a window through the alteration into the character of the host silicate magma.

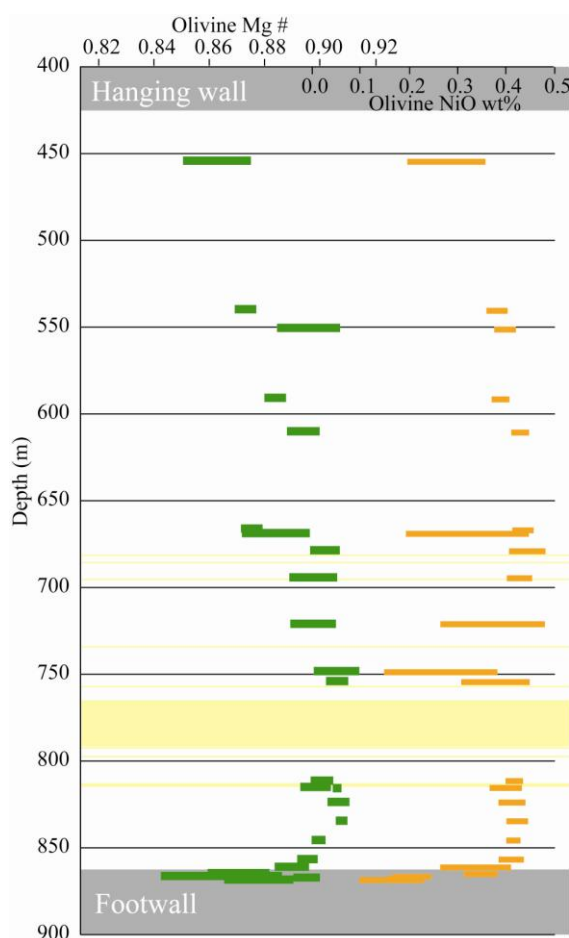


Figure 1. Range of olivine mineral chemistry from the Sakatti deposit plotted against depth down-hole. Mg# is Mg/(Mg+Fe). Data from electron microprobe analysis.

Olivine has a Mg# typically 0.84-0.92 and a Ni content of ~0.4 wt%. Clinopyroxene also consistently contains ~0.1 wt% Ni. Ni content in olivine correlates with Mg# throughout the unit (Fig. 1), although in samples with sulphide mineralisation olivines occasionally show variable Ni within individual crystals.

2.2 Sulphide mineral chemistry

Sulphide at Sakatti comprises a chalcopyrite-pyrrhotite-pentlandite assemblage typical of a magmatic Ni-Cu deposit. Pyrrhotite typically contains ~1 wt% Ni and has sub-mm scale pentlandite flames at crystal boundaries. Pentlandite is also present as discrete grains containing up to 1 wt% Co and is variably altered to millerite and violarite. Chalcopyrite is usually segregated from the pentlandite-pyrrhotite domains.

An unusual alteration style is present where large sub-spherical cobalt-bearing pyrite grains appear to replace the pentlandite-pyrrhotite. Complete pyritisation results in bravoite and pentlandite forming interstitially to the pyrite grains.

2.3 PGE mineral chemistry

PGE are usually important by-products of magmatic Ni deposits, often occurring in discrete phases associated with sulphide. Common phases are sulphides (e.g. braggite), arsenides (e.g. sperrylite), tellurides (e.g. moncheite), bismuthides (e.g. froodite), antimonides (e.g. isomertite) and alloys.

The Sakatti deposit is exceptional as all PGE-bearing mineral phases found to date are tellurides (Fig. 2), with no other PGE semi-metal minerals observed. Over 200 separate PGE telluride grains have been found in 30 samples spread across the Sakatti deposit.

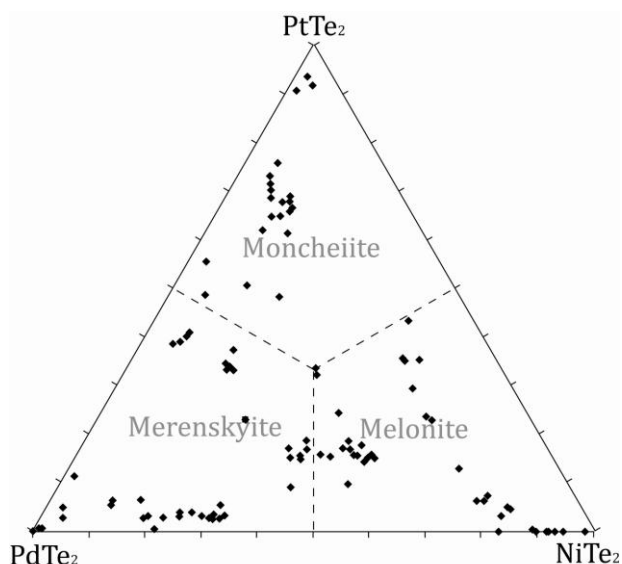


Figure 2. Compositions of (Pt,Pd,Ni) tellurides from the Sakatti deposit. Data from electron microprobe analysis.

There is also a range of composition in these tellurides across the moncheite (PtTe₂) - merenskyite

(PdTe₂) - melonite (NiTe₂) system (Fig. 2). This diverse telluride mineralogy is shared with the Kevitsa deposit (Gervilla and Kojonen 2002). This assemblage is unusual as almost all other known deposits have tellurides falling either on a PtTe₂-PdTe₂ trend or on a PdTe₂-NiTe₂ trend, with Pt and Ni generally being mutually exclusive.

3 Whole rock geochemistry

The application of whole rock geochemistry in cumulate systems must be considered with care. This is because the cumulus and intercumulus phases are unlikely to be in equilibrium and will represent different stages in the evolution of the system. The amount of cumulus relative to intercumulus can therefore dramatically affect whole rock composition without any difference in composition of the coexisting magmatic phases.

At the Sakatti deposit there is also extensive serpentinisation and talc-carbonate alteration, which variably affect whole rock geochemistry. However, REE plots from samples across the deposit are relatively consistent showing a slight LREE enrichment trend and depleted Eu anomaly (Fig. 3).

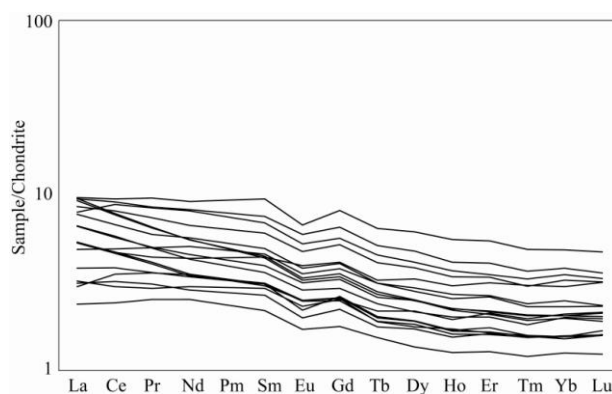


Figure 3. Whole rock REE concentrations normalised to chondrite values from McDonough and Sun (1995).

4 S isotopes

Samples were collected from across the Sakatti deposit and also from nearby sulphide-bearing black schists of the Matarakoski Formation. The schist samples were selected from drillholes within 5 km of the Sakatti deposit to the NW, NE and SE. The samples are graphitic black schist with visible pyrrhotite laminae intercalated with sedimentary laminations. Pyrrhotite from these laminae was separated and analysed. The data are plotted on Figure 4.

Sakatti sulphides from across the deposit display a remarkable S isotopic homogeneity, with a $\delta^{34}\text{S}$ mean of $2.9 \pm 0.8\text{‰}$. In contrast, sulphides in the black schists show a very large S isotopic range from -23.9 to +19.9‰.

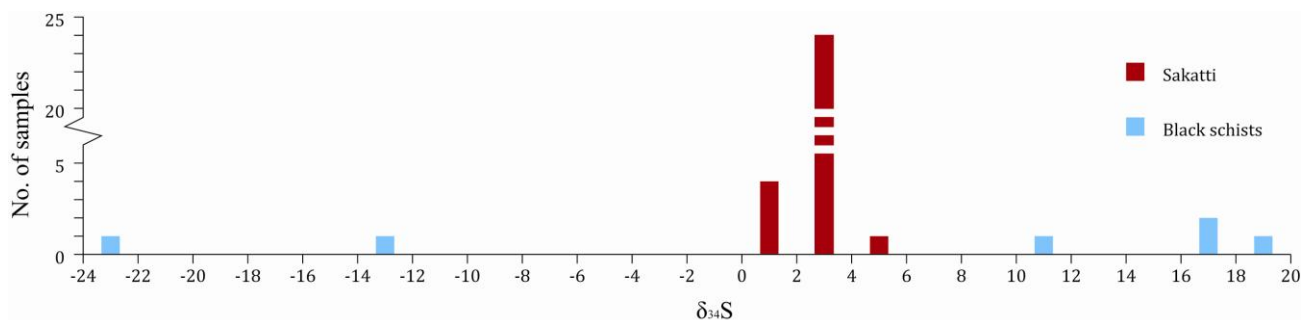


Figure 4. Sulphur isotope data from the Sakatti deposit showing deviation from the V-CDT standard in parts per mil (‰). Note the marked homogeneity of the deposit data (NB break in Y axis), versus the large isotopic range in the background sediments.

4 Nd isotopes

The least serpentinised samples were selected, as determined by thin section study, for Nd isotope analysis. Both whole rock and mineral separates were analysed.

The samples do not provide a valid isochron indicating this system cannot provide a precise age of the Sakatti deposit. However, initial ϵNd_t were calculated from the data and corrected using a geologically estimated range of ages for the deposit (Table 1). This yields a significantly negative ϵNd value.

Depleted mantle ϵNd values across this interval are estimated between +3 and +4 (DePaolo 1981) which differs considerably from these data. Continental crustal material has negative ϵNd values. The deposit has inherited a crustal signature implying that it must have assimilated continental crust.

Depth (m)	ϵNd_t		
	2.2 Ga	2.0 Ga	1.8 Ga
529.08	-2.76	-3.63	-4.50
539.50	-4.32	-5.12	-5.93
666.16	-5.60	-6.27	-6.94
668.20	-4.69	-5.77	-6.85
678.23	-4.62	-5.26	-5.89
744.75	-3.96	-4.61	-5.25
822.20	-2.25	-3.10	-3.94

Table 1. Possible initial ϵNd values for whole rock samples from the Sakatti deposit. The absolute age of the deposit is unknown so the likely range is shown.

6 Discussion

The silicate mineral chemistries provide an insight into the magmatic history of the deposit. The cumulate is remarkably homogeneous with little variation in Mg#. What variation there is shows a general decrease in Mg# from bottom to top, suggesting that the host magma was evolving as the cumulate was being deposited and that the unit is the right way up. Further trace element analysis of olivine is underway to establish if this trend is genuine and if separate pulses of intrusion can be

identified.

The high Ni concentration in the olivine suggests that these olivines did not form from a melt at S saturation and must have crystallised before sulphides formed or been introduced to pre-existing sulphide after they had crystallised. There is variable Ni within a minority of olivine crystals in samples that host abundant sulphide. This is thought to be due to loss of Ni from crystalline olivine by diffusion or late stage olivine growth in an S depleted melt.

There is a decrease in Mg# in the lower 50 m of the unit. While there is abundant textural evidence for melting and assimilation of the mafic footwall into the intercumulus melt, it is unlikely this would affect the cumulus olivine. The decrease in Mg# could be a small marginal reversal at the base of the cumulate, as seen at other mafic-ultramafic intrusions (Latypov 2003).

The unusual telluride chemistry may suggest that the formation of this deposit departs from established models. The fact that this unusual chemistry is shared with Kevitsa deposit implies a shared mode of formation.

Negative ϵNd values indicate that the rock hosting the deposit has been contaminated by crustal material during its history. This is consistent with LREE enrichment. The mineralogy of the deposit is ultramafic, with high Mg olivines, and so crustal contamination must have been limited. The Kevitsa deposit also exhibits significantly negative ϵNd (Hanski and Huhma 2005).

Sulphides analysed throughout the deposit show a remarkable homogeneous $\delta^{34}\text{S}$ around a mean of $2.9 \pm 0.8\text{‰}$. In contrast, the sulphide-rich Matarakoski sediments, which present as an obvious potential source of S contamination, show a distinctly heterogeneous S isotopic range indicating that local incorporation of these sediments is not a realistic mechanism of S saturation.

The $\delta^{34}\text{S}$ value is similar to the main ore at the Kevitsa deposit (Grinenko et al. 2003). The value is consistent with a magmatic S source. This means that the deposit has either formed entirely from mantle-derived S or from assimilation S in Archaean crustal rocks, which have limited S isotope range (Farquhar et al. 2010).

7 Conclusions

The similarity between the Sakatti and Kevitsa deposits, in terms of mineralogy, telluride chemistry, $\delta^{34}\text{S}$ and ϵNd , points towards these two deposits having a shared genetic history. In both deposits, the assimilation of crustal material is implicated in achieving S saturation and thus ore formation. Our S isotope study shows that

assimilation of sedimentary sulphide younger than 2.4 Ga, such as that which occurs in abundance in the Matarakoski schists, is not implicated in the contamination.

Acknowledgements

Thanks are due to Anglo American plc who wholly fund this PhD project. We are also extremely grateful to the Anglo American Exploration Finland team, led by Jim Coppard, who discovered the deposit with Brian Williams and Denis Fitzpatrick. Special thanks are due, but not limited to, Sebastian Stelter, Ryan Preece, Klara Collis and Bo Langbacka.

All SEM and EMPA work was carried out at the Natural History Museum, London, aided throughout by Anton Kearsley and John Spratt. Sample preparation was done by Tony Wighton. S isotope analysis was carried out at the Scottish Universities Environmental Research Centre (SUERC) in Glasgow and was overseen by Alison MacDonald. Nd isotope analysis was undertaken at the University of Southampton, supervised and undertaken by Agnes Michalik and Andy Milton.

References

- DePaolo DJ, (1981) Neodymium isotopes in the Colorado Front Range and crust-mantle evolution in the Proterozoic. *Nature* 291:193-196
- Farquhar J, Nanning W, Canfield DE, and Oduro H, (2010) Connections between sulfur cycle evolution, sulfur isotopes, sediments and base metal sulfide deposits. *Econ Geol* 105:509-533
- Gervilla F, and Kojonen K, (2002) The platinum-group minerals in the upper section of the Keivitsansarvi Ni-Cu-PGE deposit, northern Finland. *Can Mineral* 40:377-394
- Grinenko LN, Hanski E, Grinenko VA, (2003) Formation conditions of the Keivitsa Cu-Ni Deposit, Northern Finland: Evidence from S and C isotopes. *Geochem Int*, 41:154-167
- Hanski E, Huhma H, (2005) Central Lapland greenstone belt. In Lehtinen M, Nurmi P A, Rämö O T (eds) *The Precambrian geology of Finland*, Elsevier, p. 139-193
- Latypov RM, (2003) The origin of marginal compositional reversals in basic-ultrabasic sills and layered intrusions by sortet fractionation. *J Pet* 44:1579-1618
- Lehtonen M, Airo M-L, Eilu P, Hanski E, Kortelainen V, Lanne E, Manninen T, Rastas P, Räsänen J, Virransalo P, (1998) Kittilän vihreäkivialueen geologia. Lapin vulkaniittiprojektin raportti. Summary: The stratigraphy, petrology and geochemistry of the Kittilä greenstone area, northern Finland. A Report of the Lapland Volcanite Project. *Geol. Surv. Finland, Rep. Invest.* 140
- McDonough WF, Sun, SS, (1995) The composition of the Earth. *Chem Geol* 120:223-253

Komatiite-associated Cr and Ni-Cu-(PGE) mineralisation in the Black Thor–Black Label ultramafic intrusive complex, McFaulds Lake greenstone belt, Ontario

Heather JE Carson, C Michael Lesher

Mineral Exploration Research Centre, Dept Earth Sciences, Laurentian University, Sudbury, Ontario P3E 2C6 Canada

Michel G Houlé

Geological Survey of Canada, Québec, Québec G1K 9A9 Canada

Riku T Metsaranta

Ontario Geological Survey, Sudbury, Ontario P3E 6B5 Canada

David A Shinkle

Cliffs Natural Resources, Thunder Bay, Ontario P7B 6M8 Canada

Abstract. The Black Thor - Black Label deposit appears to be one of the largest and best-preserved chromite deposits in the world, and one of an increasing number of deposits recognized to have formed from high-Cr, low-Mg komatiitic magmas. The ores exhibit an exceptionally wide range of textures (disseminated, patchy disseminated, patchy net-textured, net-textured, mottled semi-massive, banded semi-massive, massive, and angular and ameboid magmatic breccia) and are thinly laminated to thickly bedded, with aggregate thicknesses up to 100m. Regardless of texture, individual chromite grains are uniformly 0.1-0.2 mm and euhedral, many massive but some with inclusion-rich cores. The abundance of net-textured chromite, where aggregates of fine-grained chromite form networks to less dense olivine, the presence of extremely fine-scale layering, and the apparent absence of evidence for slumping favour in situ crystallisation, but the inclusion-rich cores appear to require initial mechanical transport and upgrading at high magma:chromite ratios (high R factor).

Keywords: chromite, ultramafic intrusion, komatiite-associated, Ontario

1 Introduction

The Black Thor - Black Label complex is part of the regionally-extensive ‘Ring of Fire’ ultramafic-mafic intrusive suite in the Neoproterozoic McFaulds Lake greenstone belt (Fig. 1) in the Oxford-Stull-LaGrande Domain of the Superior Province (Houlé et al., this volume). The complex is up to 1.5 km thick and >3 km long, and can be subdivided into three main series (Fig. 2): 1) a *lower ultramafic series* of adcumulate-mesocumulate peridotite and dunite containing minor interstitial chromite and locally containing basal and internal disseminated, semi-massive, and massive Ni-Cu-PGE-bearing sulfides, 2) a *middle ultramafic series* of chromite-bearing heteradcumulate-meso-cumulate peridotite and dunite with heteradcumulate-meso-cumulate chromitite, and 3) an *upper ultramafic-mafic series* of mesocumulate-orthocumulate peridotite, pyroxenite, and olivine gabbro with occasional websterite. It is interpreted to represent a transgressive feeder zone and a semi-conformable sill-shaped intrusion (Fig. 3).

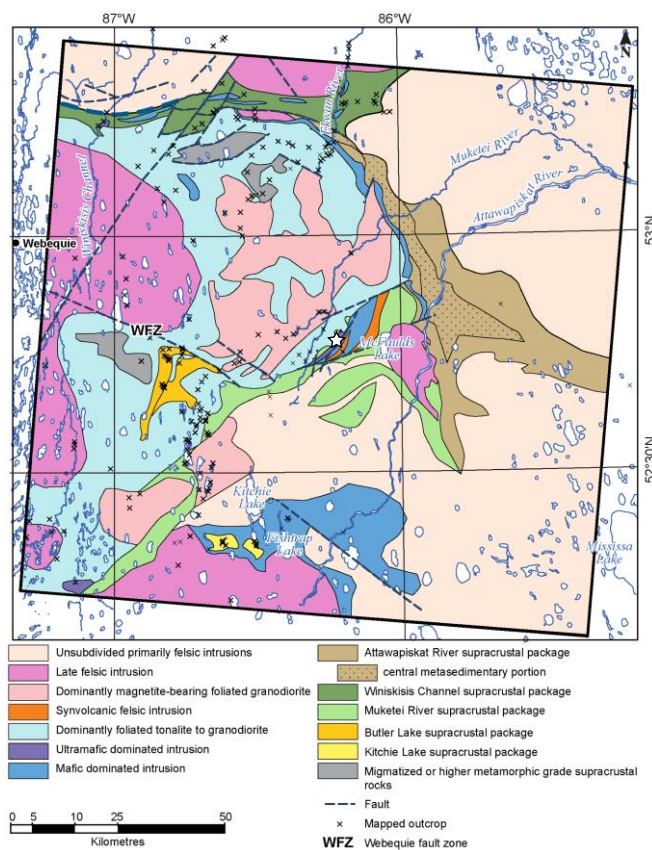


Figure 1. Simplified geology of the McFaulds Lake area (after Metsaranta and Houlé, 2012), showing the location of mafic-ultramafic intrusives (dark blue and purple). The Black Thor – Black Label complex (white star) is located in the centre of the area, ~10 km west of McFaulds Lake.

The complex locally contains inclusions of underlying granitoids and is crosscut by an extensive pyroxenite unit that disrupts Black Label. Multiple gabbroic phases overlie and locally crosscut the intrusion, but the stratigraphic relationships within the uppermost part of complex, particularly with the volcanic rocks, are still unclear at present. Parts of the intrusion are bordered by and/or cut by faults, but most rocks are not penetratively deformed. All rocks have been metamorphosed to lower greenschist facies, but relict igneous olivine and pyroxene are locally preserved.

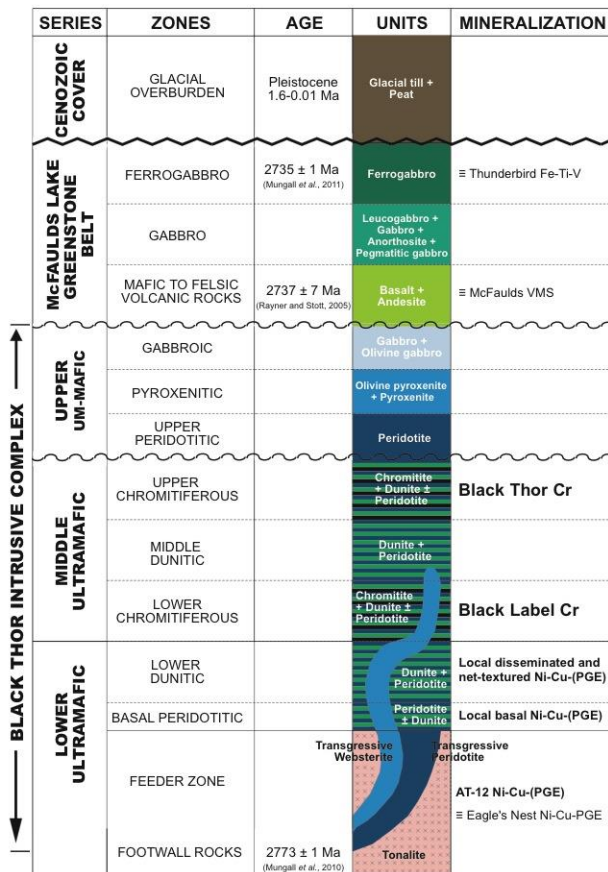


Figure 2. a) Schematic stratigraphic column for the Black Thor – Black Label intrusive complex.

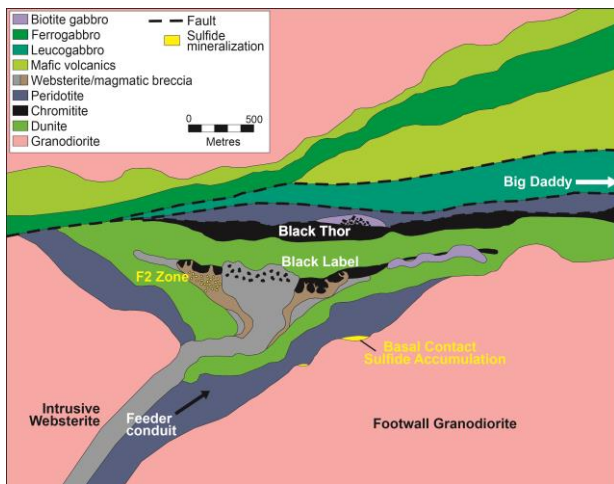


Figure 3. Interpretive section of the Black Thor – Black Label segment of the intrusion.

Mungall et al. (2010) have shown that related intrusive rocks to the SW are derived from a low-Mg komatiitic magma with ~22% MgO, which is also consistent with the mineral phases in the Black Thor – Black Label segment of the system (olivine, chromite, pyroxene, no plagioclase except in the uppermost part). The presence of fine chromite in even the lowermost rocks in the complex indicates that the magma was saturated or close to saturation in chromite at the time of emplacement.

2 Mineralisation

2.1 Chromite

Chromite mineralization occurs in the middle ultramafic series of the complex and includes a lower zone of banded to magmatically brecciated chromite ores (Black Label) and an upper zone of thick-laminated to thick-bedded chromite ores (Black Thor) (Figure 3).

Chromite textures include finely disseminated, patchy disseminated, patchy net-textured, net-textured, semi-massive, and massive (Figure 4, Table 1). Chromite grains, regardless of rock texture, are 0.05-0.15 mm in diameter and euhedral often with no evidence of recrystallisation (Figure 5). The various textural types are complexly interlayered and interbanded, ranging from very thinly laminated (<1mm) to very thickly bedded (>60 cm) (Table 2). The ores in Black Label are magmatically brecciated with angular and amoeboid clasts of chromitite, but no evidence of slumping has been observed in the layered rocks.

Table 1. Chromite textures in the Black Thor – Black Label intrusive complex.

Texture	% Chromite
Finely disseminated	≤15
Patchy disseminated	≤20
Patchy net-textured	20-40
Net-textured	40-60
Semi-massive (incl. banded and mottled)	60-90
Massive	>90

Table 2. Chromite layering in the Black Thor – Black Label intrusive complex.

Bedding	Thickness
Very thick bedded	60 cm
Thick bedded	30 cm
Medium bedded	10 cm
Thin bedded	5 cm
Very thick laminated	3 cm
Thick laminated	3 mm
Thin laminated	1 mm
Very thin laminated	

Adapted from Ingram (1954)

2.2 Sulfides

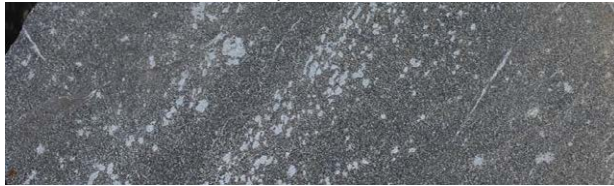
Sulfide mineralisation (pyrrhotite-pentlandite-chalcopyrite ± PGMs (Figure 6) is typically hosted in pyroxenite, exhibits fine disseminated, coarse disseminated (“blebby”), patchy net, and net textures, but it also occurs in some peridotites and in some chromite ores. It is most commonly localized along the lower contact of the intrusion and in associated feeder dykes (Figure 3), but also occurs as fine disseminations throughout the intrusion. Thin veinlets and thin shear zones of chalcopyrite-rich mineralization occur locally.



Disseminated to patchy net-textured, Black Thor



Net-textured – semi-massive, Black Thor



Semi-massive chromitite, Black Thor



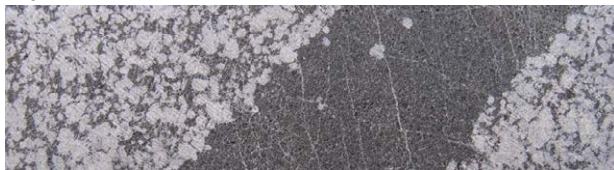
Massive chromitite, Black Thor



Mottled semi-massive, Black Thor



Thin laminated massive – semi-massive – net textured, Black Thor



Thick banded massive – net textured, Black Thor



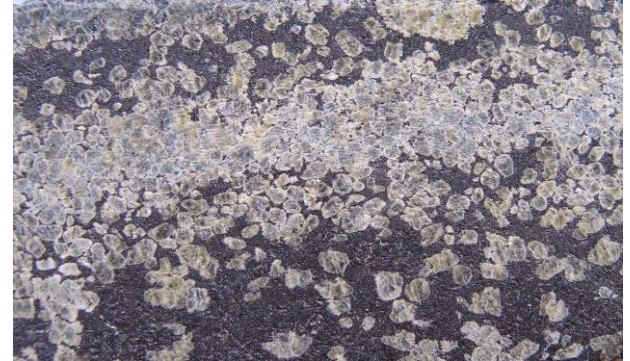
Thick laminated massive – semi-massive, Black Thor



Angular chromite clasts in leucogabbro, Black Thor



Ameboid chromite clast in websterite, Black Label



Olivine and chromite phase layering, Black Thor

Figure 4. Chromite textures in Black Thor and Black Label. All photos are ~5 cm in height (NQ core).

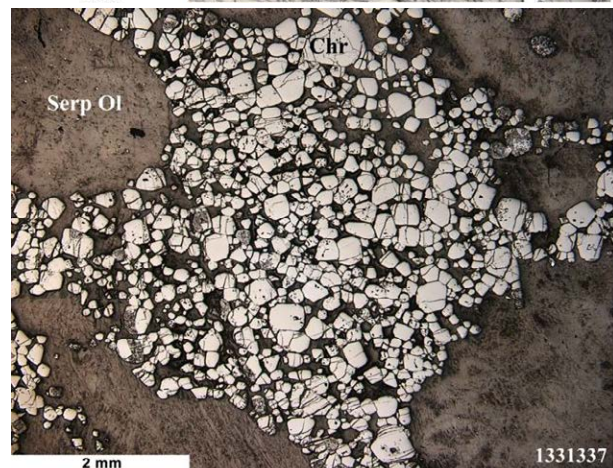
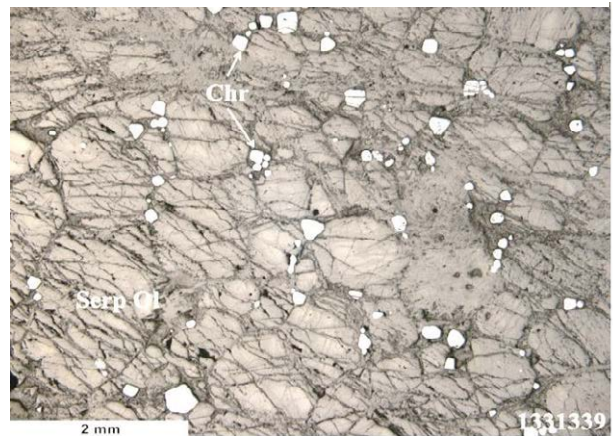
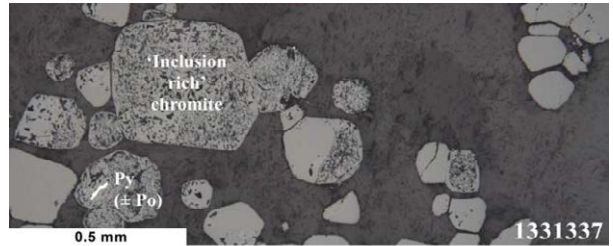


Figure 5. a,b) Disseminated Chr, c) net-textured Chr. Reflected plane polarised light.

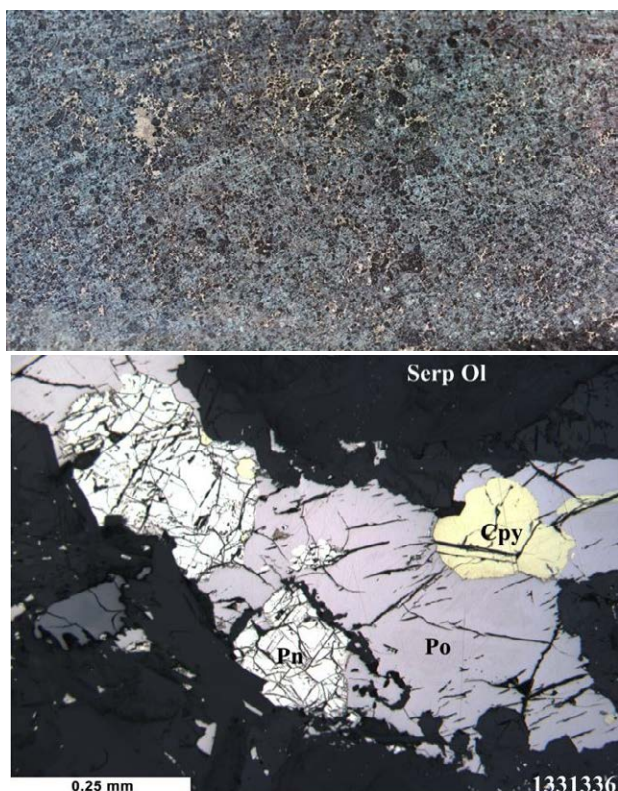


Figure 6 a) Patchy net-textured sulfide (Po-Pn-Cpy). b) Po-Pn-Cpy mineralisation, reflected plane polarised light.

3 Genesis

The overwhelmingly cumulate nature of the chromite ores and olivine-rich host rocks suggests a flow-through magmatic system like other mineralised komatiitic lava channels and feeder sills (e.g., Lesher and Keays, 2002), in which high magma:sulfide and magma:chromite ratios (R factors) control sulfide and chromite compositions.

Several models for the genesis of the deposit are being investigated: 1) physical transportation of slurries of finely-dispersed chromite with or without magmatic slumping (e.g., Mondal and Mathez 2007; Maier et al. 2013), 2) in-situ crystallisation associated with oversaturation of chromite with oxidation (Ulmer 1969), wallrock contamination (Irvine 1975), and/or magma mixing (Irvine 1977), and 3) either of the above with late magmatic diffusional segregation (“ageing”: Boudreau 2010). The uniform grain size of the chromite, the abundance of net-textured chromite, the presence of extremely fine-scale (down to single grain) layering, and the apparent absence of evidence for slumping, all favour in situ crystallisation rather than deposition from a mechanically-transported emulsion or ageing, but the inclusion-rich cores suggest some physical transport. The fine grain size probably reflects homogeneous nucleation accompanying slow diffusion of Cr in a rapidly-crystallizing magma (Hill and Roeder 1974).

Mineralogies (Po-Pn-Ccp ± PGMs) and textures (predominantly disseminated and net-textured) of the sulphides suggest a magmatic origin, but many have been sheared and modified. Some Ccp-rich veins represent residual melts derived by fractional crystallisation of Fe-Ni-IPGE-rich Cu-PPGE-Au-poor MSS.

4 Current Work

Current work is focussed on better defining the magmatic stratigraphy and establishing the geochemical variations. The former will be critical in determining whether individual beds/laminations or packages of beds/laminations can be correlated along and across the intrusion, and to determine how their thicknesses vary laterally, which will be critical in evaluating models involving physical transport, magmatic slumping, and in situ crystallisation. The latter will permit us to better constrain the composition of the parental magma and the chromite and sulphide saturation history of the intrusion.

Acknowledgements

We are very grateful to R Fink, A Mitchell, and R Weston for logistical assistance and helpful discussions, R Kruse for CAD/GIS support, and Cliffs Chromite Ontario, Natural Sciences and Engineering Research Council of Canada, Geological Survey of Canada, and Ontario Geological Survey for financial support.

References

- Alapieti, TT, Huhtelin TA (2005) Early Palaeoproterozoic (2.5-2.4) Tornio – Näränkäväära Layered Intrusion Belt and related chrome and platinum-group element mineralization, Northern Finland. *Geol Surv Fin, Guide 51a, Ch 2: 13 - 31*
- Boudreau A (2010) The evolution of texture and layering in a layered intrusion. *Int Geol Rev 53: 330-352*
- Eales HV (2000) Implications of the Cr budget of the western limb of the Bushveld Complex. *S Afr J Geol 103:141–150*
- Irvine TN (1975) Crystallization sequences in the Muskox intrusion and other layered intrusions—II. Origin of chromitite layers and similar deposits of other magmatic ores. *Geochim Cosmochim Acta 39: 991-1020*
- Hill R, Roeder E (1974) Crystallization of Spinel from basaltic liquid as a function of oxygen fugacity. *J Geol 82: 709-729*
- Irvine TN (1977) Origin of Chromitite layers in the Muskox Intrusion and other Stratiform Intrusions - A new Interpretation *Geology 5: 273-227*
- Lesher CM, Keays RR (2002) Komatiite-associated Ni-Cu-PGE Deposits: Geology, Mineralogy, Geochemistry, and Genesis. *CIM Spec Vol 54: 579-617*
- Maier W, Barnes S-J, Groves DI (2013) The Bushveld Complex, South Africa: formation of Pt–Pd, Cr- and V-rich layers via hydrodynamic sorting of a mobilized cumulate slurry in a large, relatively slowly cooling, subsiding magma chamber. *Min Dep 48(1): 1-56*
- Metsaranta RT, Houlié MG (2012) Progress on the McFaulds Lake (“Ring of Fire”) Region Data Compilation and Bedrock Geology Mapping Project. Ontario Geol Surv Open File Report 6280: 43.1-43.12
- Mondal SK, Mathez EA (2007) Origin of the UG2 chromitite layer, Bushveld Complex. *J Petrol 48: 495-510*
- Mungall JE, Harvey JD, Balch SJ, Azar B, Atkinson J, Hamilton MA (2010) Eagle’s Nest: A Magmatic Ni-Sulfide Deposit in the James Bay Lowlands, Ontario, Canada. *Econ Geol Spec Pub 15: 539-559*
- Mungall JE, Azar B, Hamilton MA (2011) Ni-Cu-PGE-Cr-Fe-Ti-V and VMS mineralization of the Ring of Fire Intrusive Suite, Ontario. GAC-MAC meeting, http://gac.esd.mun.ca/gac_2011
- Rayner N, Stott GM (2005) Discrimination of Archean domains in the Sachigo Subprovince: a progress report on the geochronology. *Ont Geol Surv OF Rept 6172: 10-1 to 10-21*
- Ulmer G C (1969) Experimental investigations of chromite spinels. *Econ Geol Mon 4: 114-131*

Ni-Cu-PGE mineralisation of the Riwaka Complex, Northwest Nelson, New Zealand

A.B. Christie

GNS Science, PO Box 30368, Lower Hutt 5040, New Zealand

R.E. Turnbull

GNS Science, Private Bag 1930, Dunedin 9054, New Zealand

Abstract. The Riwaka Complex is a linear mafic-ultramafic intrusive body, about 45 km long and ranging from 800 m to 8 km wide. It is latest Devonian in age (364 Ma) and is dominated by hornblende-rich mafic and ultramafic units. In the 1970s, exploration for Ni-Cu included 33 shallow (<100 m) diamond drill holes. The highest grade intersections were 2.20% Ni over 1.4 m, 1.42% Cu over 0.6 m. In the late 1980s, drill core from six drill holes were re-assayed for platinum group elements (PGE) with a best grade of 1.044 ppm total PGE over 0.6 m. The mineralisation is disseminated pyrrhotite-chalcopyrite-pentlandite-pyrite-PGE and occurs in gabbro and pyroxenites along the southeastern margin of the complex. New geochemical analyses for a suite of 63 elements were determined for 19 whole-rock samples of drill core. Geochemical trends indicate fractional crystallization of olivine and clinopyroxene from an ultramafic parent magma. Ni-Cr-PGE were deposited following fractional crystallisation and the initial onset of sulphur-saturation. This crystallisation depleted the remaining fractionated and sulphur-saturated melt in Ni-Cr-PGE, resulting in Cu-Fe-S (PGE poor) mineralisation. Sulphur saturation occurred as a result of magma mixing en route to emplacement, and/or contamination with country rocks at the site of emplacement. Possible magma mixing and/or crustal contamination are positive indicators of PGE prospectivity

Keywords. Nickel-copper prospect, platinum group elements, Riwaka Complex, layered mafic intrusion, gabbro, pyroxenite, peridotite, Devonian, petrography, geochemistry

1 Introduction

The Riwaka Complex (late Devonian) is a faulted, linear mafic-ultramafic intrusive body, about 45 km long and up to 8 km wide. Nickel-Cu mineralisation was discovered in 1967 (Gill and Johnston 1970) and sparked exploration programmes, lasting into the late 1970s, by a succession of companies including: MacIntyre Mines, Kennecott Explorations (Australia) Pty Ltd, Western Compass Minerals NL, Mineral Deposits Ltd, Otter Minerals NL and Gold Mines of N.Z. Ltd (Bates 1989). This exploration defined several prospect areas based on anomalous stream sediment, soil and rock geochemistry. Thirty three shallow (<100 m) diamond drill holes were drilled in three of the prospects. Between 1987 and 1989, Sigma Resources reanalysed sections of the Ni-Cu mineralised drill core for PGEs, and also carried out surface exploration. The prospect is currently being explored by Altan Minerals Ltd.

The geology and mineralisation of the Riwaka Complex were described in university MSc theses by Saunders (1997) and Smits (2005).

The Government agency New Zealand Petroleum & Minerals (NZP&M) commissioned GNS Science to undertake a brief study to examine the prospectivity of the Riwaka Complex. This paper reports results of that study, essentially a desktop study including a GIS compilation of previous exploration and research data, and geochemical analyses of 19 samples of the 1960s-1970s drill core that is archived in the NZP&M core library (Christie et al. 2012).

3 Geology

The Riwaka Complex intrudes metamorphosed Takaka terrane sedimentary rocks of Silurian to Devonian age including marble, schist, argillite and siltstone (Fig. 1). The complex is itself intruded along its eastern contact by plutons, dikes and plugs of the early Cretaceous Separation Point Suite.

The Riwaka Complex is made up of a series of ultramafic rocks (Graham Peridotite and Pokororo Pyroxenite) overlain by gabbro (Campbell Gabbro), and an upper unit of massive, non-cumulate diorite (Brooklyn Diorite, dated at 366.7 ± 1.1 Ma by ID-TIMS U-Pb on zircons; Tulloch et al. 2009). The stratigraphically higher gabbro and diorite predominate in the north where the intrusion is widest, whereas the lower ultramafic rocks and gabbro predominate to the south. Lenses of Brooklyn Diorite occur in the gabbroic and ultramafic rocks.

4 Mineralisation

Sulphides are widespread, although their concentrations are greatest in the Campbell Gabbro with locally up to 50% sulphide minerals, with highly variable Ni:Cu concentrations and ratios. The ultramafic rocks of Graham Peridotite and Pokororo Pyroxenite contain 0.5 to 6.0% sulphides, whereas Brooklyn Diorite contains 1 to 5% interstitial sulphides, and is poor in Ni and Cu.

The occurrence of sulphides in Campbell Gabbro ranges from disseminated blebs to abundant, net-textured cumulate sulphides enclosing silicate minerals. The sulphide mineralisation is disseminated in layers up to 5 m thick, within which there are high-grade layers up to 3 m thick. Best grades intersected in drilling were 2.2% Ni over 1.4 m in DDH GV-19, 1.42% Cu over 0.6 m in DDH GV-8, and 0.663 ppm total PGE over 1.8 m (including 1.044 ppm PGE over 0.6 m) in DDH GV-5.

Pyrrhotite is the most abundant sulphide, and is accompanied by subordinate chalcopyrite, cubanite, pentlandite, and linnaeite, and minor pyrite. Abundant magnetite occurs closely associated with some sulphide rich horizons.

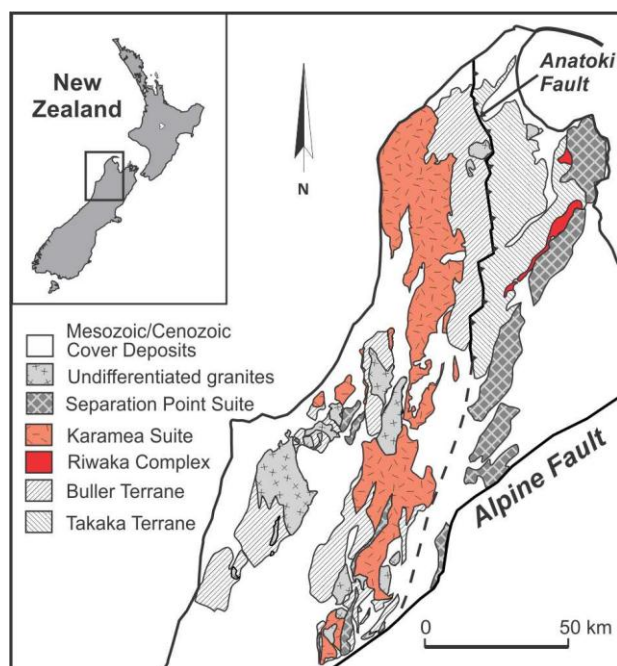


Figure 1. Location of the Riwaka Complex in relation to other major geological units in the Western Province of northwestern South Island, New Zealand.

5 Geochemical analyses and results

Nineteen samples of drill core representative of the various rock types from the mineralised southern portion of the Riwaka Complex, including one sample with ~8% disseminated sulphide, were analysed for a suite of 63 elements in order to identify the processes responsible for ore genesis and the chemical diversification of the magmas, and infer tectonic setting. Therefore, apart from the sample with ~8% disseminated sulphide, the other 18 samples had generally low concentrations of visible sulphides.

The analyses were carried out by Geoscience Laboratories, Ontario Ministry of Northern Development and Mines, Sudbury (www.ontario.ca/geolabs) using ICP-MS, ICP-AES, NiS fire assay and AAS techniques.

The sample with ~8% disseminated sulphide (P80533 GV-19 39.5 ft) returned the highest values for S, Ni and Au, and second highest values for Cu and PGE: 2.0 % S, 4458 ppm Cu, 1614 ppm Ni, 71.1 ppb Au, 61.5 ppb Pt and 56.3 ppb Pd. The other samples had 272 ppm to 1.9 % S, 7 to 6137 ppm Cu, 43 to 1513 ppm Ni, 0.5 to 10.8 ppb Au, 0.32 to 136 ppb Pt, and 0.37 to 89.8 ppb Pd. The highest sample for PGE (P80519, GV-15 135.5-136.5 ft) had 3.32 ppb Ir, 119 ppb Pt, 89.8 ppb Pd, 5.46 ppb Rh, 0.35 ppb Ru, but the lowest concentration of S (272 ppm), and relatively low concentrations of Cu (57 ppm) and Ni (347 ppm). This Pd concentration is slightly higher than Sigma's best value from GV-5, 26.8-27.4 m (i.e. 89.9 ppb versus 71 ppb), but the Pt is much lower (i.e. 119 ppb versus 920 ppb).

6 Petrochemistry

6.1 Major elements and REE

The Riwaka Complex has medium-high-K calc-alkaline to weakly shoshonitic chemistry. This whole-rock chemistry is transitional between a subduction-related and intra-plate setting (Tulloch et al. 2009). MORB-normalised trace element abundance patterns are relatively flat, and show a slight LILE enrichment, negative Nb-anomalies and elevated HFSE relative to mantle; a chemical signature that points towards a subduction setting, and minor crustal contamination in the magma reservoir and/or during magma ascent to the surface. Correlation between crustal contamination indices (La/Sm) and MgO (an indicator of fractional crystallization) indicate that fractionation from an ultramafic parental magma (i.e. Pokokoro Peridotite) can account for most of the observed chemical variation within the Riwaka Complex. Pyroxenite and gabbro with higher La/Sm ratios indicate that they were contaminated with continental crust, or underwent lower degrees of partial melting.

Rare earth element (REE) patterns for the Riwaka Complex have similar slopes to Ocean Island Basalt (OIB) and are enriched ~10-100 times that of C1-chondrite. The lowest REE contents are observed in the primitive peridotite and olivine clinopyroxenite (La ≤ 10 ppm; Lu ≤ 3 ppm), whereas the more silicic gabbro rocks have higher abundances in REE (La ≤ 200 ppm; Lu ≤ 10 ppm). An overall enrichment in REE from peridotite to pyroxenite is consistent with fractional crystallization of both olivine and clinopyroxene. A slight LREE enrichment over HREE occurs, particularly in the more evolved gabbros and is probably the result of pyroxene fractionation or increasing crustal contamination with increasing silica content. The most evolved gabbros also display REE trends similar to average upper continental crust, indicating that contamination with crustal rocks may be responsible for some of their chemical variation. A lack of any significant Eu-anomaly indicates plagioclase fractionation was no more than a minor process.

6.2 PGE, S, Ni, Cr, Cu and Au

The most primitive rocks (peridotite and olivine clinopyroxenite) contain the highest abundances of PGE, Ni and Cr (e.g. Pt = 4-150 ppb; Pd = 4-100 ppb; Ni = 500-900 ppm), and the lowest abundances of S (0.02 – 0.1 wt%). Two gabbro samples (P80524, P80533) with sulphide mineralisation, have similar PGE, Cr and Ni abundances to the more primitive peridotite and clinopyroxenite, however they have much higher S contents (S = ≥ 1 wt%), consistent with a sulphur-saturated magma. Trends of decreasing Mg, PGE, Ni and Cr, coupled with increases in S, on PGE discrimination diagrams, are consistent with simple fractionation of olivine and clinopyroxene from an initially sulphur-undersaturated melt.

Sulphide-rich samples that have low concentrations of Ni and PGE, yet are concentrated in Cu-Fe-S, are likely to have formed following sulphur-saturation of the

melt and earlier crystallization of Ni-PGE-bearing minerals at the initial onset of sulphur-saturation. The Ni-content in the remaining non-mineralised samples is controlled by the crystallization of olivine into which it readily partitions, resulting in Ni depletion in the melt with increasing differentiation.

7 Discussion

On the basis of mineralogy, petrology and field descriptions, the layered Riwaka Complex most likely represents a sulphide-rich Ni-Cu-(PGE) deposit formed within a vertical magma conduit system possibly between a deep staging chamber and a higher level magma chamber. Important examples of these types of deposits include Giant Mascot (British Columbia), Aguablanca (Spain), and Jinbaoshan (China).

Cross-cutting intrusive contacts indicate that the ultramafic peridotite and pyroxenite rocks at Riwaka were emplaced first, followed by gabbro and later diorite intrusion (Smits 2005). A compositional continuum also exists from west to east, with the most primitive peridotite located along the western boundary, and the more evolved gabbro bordering the eastern boundary of the complex.

Major and trace element chemistry and REE trends indicate that fractional crystallization of olivine and clinopyroxene was the main process responsible for producing the range of compositions observed in the peridotite and pyroxenite, and that evolved magmas may have been contaminated with crustal rocks to produce the sulphide-rich gabbro. This is consistent with petrographical observations which show that olivine and clinopyroxene are cumulus minerals and were therefore the first minerals to crystallise within the magmas.

Sulphide mineralisation is almost exclusively restricted to fractionated pyroxenite and gabbro, and was likely controlled by the onset of sulphur-saturation in the melt which occurred as a result of magma mixing en route to emplacement, and/or contamination with country rocks at the site of emplacement.

8 Conclusions

- The Devonian Riwaka Complex consists of a sequence of ultramafic rocks (peridotite and pyroxenite), gabbro and diorite.
- The pyroxenite and gabbro host disseminated pyrrhotite-chalcopyrite-pentlandite-pyrite-PGE mineralisation.
- Exploration drilling has previously demonstrated grades up to 2.20% Ni, 1.42% Cu and 1.044 ppm total PGE.
- New geochemical analyses for a suite of 63 elements were determined for 19 whole-rock samples.
- Geochemical trends indicate fractional crystallization of olivine and clinopyroxene from an ultramafic parent magma similar in composition to the peridotite.
- Ni-Cr-PGE were deposited following fractional

crystallisation and the initial onset of sulphur-saturation, which depleted the remaining fractionated and sulphur-saturated melt in Ni-Cr-PGE, resulting in Cu-Fe-S (PGE poor) mineralisation.

- Sulphur saturation of the melt occurred as a result of magma mixing en route to emplacement, and/or contamination with country rocks at the site of emplacement.
- The Riwaka Complex mineralisation most likely represents a sulphide-rich Ni-Cu-(PGE) deposit formed within a vertical magma conduit system intermediate between a deep staging chamber and a higher level magma chamber.
- Possible magma mixing and/or crustal contamination are positive indicators of PGE prospectivity

Acknowledgements

The Riwaka project work was carried out at GNS Science under a funding contract with the Ministry of Economic Development managed by Rob Robson of NZP&M. Dan Wilmott of Jump NZ assisted with drill core viewing and sampling at the New Zealand Petroleum & Minerals' Core Library at Featherston. Neville Orr prepared the polished thin sections. Christian Timm reviewed the manuscript.

References

- Bates TE (1989) Copper and nickel mineralisation in the Riwaka Complex northwest Nelson. In: Kear D (ed.) Mineral deposits of New Zealand. Australasian Institute of Mining and Metallurgy Monograph 13: 119-123
- Christie AB, Turnbull RE, Lukovic B, Leybourne MS (2012) Mineral potential of the Riwaka Complex, Northwest Nelson, New Zealand. GNS Science Report 2012/26
- Gill KR, Johnston MR (1970) The geology and nickel-copper sulphide mineralisation in the Graham Valley, north-west Nelson. New Zealand Journal of Geology and Geophysics 13: 477-494
- Saunders JK (1997) The petrology, geochemistry and petrogenesis of the Riwaka Complex, South Island, New Zealand. Unpublished MSc thesis, Department of Earth Sciences, Memorial University of Newfoundland
- Smits RG (2005) Geology and petrogenesis of a NiS bearing, arc feeder conduit: the Riwaka Complex, New Zealand. Unpublished MSc thesis, Monash University, Melbourne
- Tulloch AJ, Ramezani J, Kimbrough DL, Faure K., Allibone AH (2009) U-Pb geochronology of Paleozoic plutonism in western New Zealand: implications for S-type granite generation and growth of the east Gondwana margin. Geological Society of America Bulletin 121: 1236-1261

Compositional diversity in chromitites from Eastern Rhodopes (SE Bulgaria): petrogenesis and tectonic implications

Vanessa Colás, Isabel Fanlo

Dpt. Earth Sciences, University of Zaragoza, Pedro Cerbuna 12, 50009 Zaragoza, Spain.

Fernando Gervilla

Dpt. Mineralogy & Petrology & IACT (UGR-CSIC), University of Granada, Fuentenueva s/n, 18002 Granada, Spain

José María González-Jiménez

GEMOC ARC National Key Centre, Dpt. Earth and Planetary Sciences, Macquarie Univ., Sydney, NSW 2109, Australia

Thomas Kerestedjian

Geological Institute, Bulgarian Academy of Sciences, Georgi Bonchev 24, 1113 Sofia, Bulgaria

Abstract. In the Eastern Rhodopes (SE Bulgaria) the low-Al and low-Ti chromite forming chromitite bodies at Yakovitsa and Avren West massifs, and the high-Al and variable Ti chromite forming chromitite bodies at Golyamo Kamenyane (low-Ti) and Chernichevo (high-Ti) occur hosted within a representative ophiolitic mantle sequence formed in a mid-oceanic ridge, which evolved to an island arc/back-arc setting in a supra-subduction zone. Such conclusion is drawn from the diversity of MORB and boninitic affinity of the unaltered chromite cores, deduced from major element distribution in chromite and lithology of the ultramafic massifs.

Keywords. chromitites, major elements, MORB-ZSS affinity, Eastern Rhodopes, Bulgaria

1 Introduction

Chromite is a mineral highly sensitive to alteration under metamorphic and hydrothermal environments (Gervilla et al., 2012). However, even strongly altered grains of chromite may preserve their cores which retain the primary igneous composition. This “unmodified” composition can be used as an indicator for the petrogenesis of the chromitites (e.g. Barnes & Roeder, 2001; Kamenetsky et al., 2001).

Bazilev et al. (1999) use the composition of chromite from different ultramafic massifs scattered in the metamorphic basement of the Rhodope Crystalline Massif in SE Bulgaria (see Georgiev et al. 2006) (Fig.1) to interpret the tectonic setting in which they were formed. However, in their study they did not accurately distinguish the different patterns of alteration in the chromite produced during the metamorphism of the chromitites that recently observed Gervilla et al. (2012).

With the aim to decipher the *true* primary composition of chromite that can be used to constrain the tectonic type of parental melts and the tectonic setting of formation we have re-examined those Eastern Rhodopean chromitites. Through the careful examination of the chemistry of different textural types of chromite we have been able to discriminate between unaltered and modify cores, providing only major (Cr_2O_3 , Al_2O_3 , FeO and MgO) and minor elements (TiO_2) useful for petrogenetic interpretations.

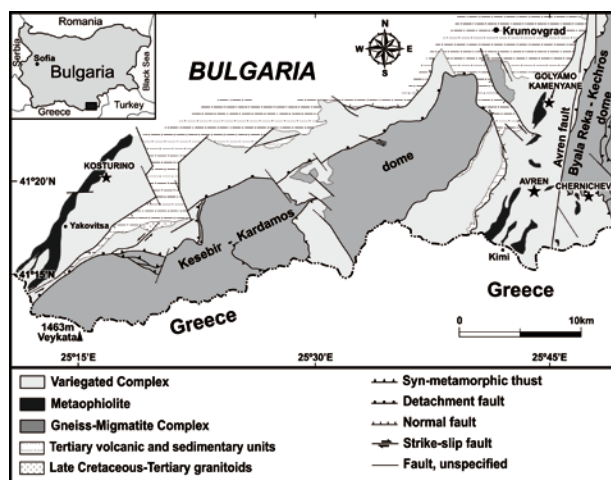


Figure 1: Simplified geological map of the Eastern Rhodope (Bonev, 2006). The metamorphic basement is made up of two tectonostratigraphic complexes, the Gneiss–Migmatite Complex at the bottom and the Variegated Complex at the top, outcropping in two domal structures: the Kesebir–Kardamos Dome and the Byala Reka–Kechros Dome (Georgiev, 2006). The studied Ultramafic Massifs (stars: Yakovitsa, Avren West, Golyamo Kamenyane and Chernichevo) are located in the limbs of the Kesebir–Kardamos Dome, scattered into the Variegated Complex.

2 Geology of the ultramafic massifs

The chromitites that have been re-examined in this study are located in the ultramafic massifs near the villages of Yakovitsa, Avren, Golyamo Kamenyane and Chernichevo in the eastern Rhodope Mountains, south Bulgaria (Fig.1). These ultramafic massifs are suggested to be portions of a dismembered ophiolite affected by poly-phase metamorphism [from UHP/HT eclogite-facies down to amphibolite/greenschist facies; Mposkos & Krohe, 2006; Haydoutov et al., 2004] related to the evolution of a Metamorphic Core Complex (i.e. Rhodope Complex or Rhodope Crystalline Massif). These ultramafic massifs are scattered in upper tectonostratigraphic unit of the core complex (i.e., the Variegated Formation; Kolcheva et al., 2000; Haydoutov et al., 2004) (Fig.1), and mainly consist of serpentinized

Location	Lithology of the Ultramafic Massif	Texture of chromitite	Alteration patterns of chromite	Cr#	Mg#	TiO ₂
Avren West	Meta-harzburgite and meta-dunite	Massive	Partly altered chromite	0.82-0.78	0.54-0.50	0.08-0.02
		Semi-massive	Zoned chromite	0.93-0.84	0.46-0.35	0.09-0.01
		Disseminated				
Yakovitsa	Meta-harzburgite and meta-dunite	Massive	Partly altered chromite	0.83-0.60	0.69-0.40	0.14-0.02
		Semi-massive				
		Disseminated	Zoned chromite	0.73-0.68	0.42-0.39	0.06-0.00
Golyamo Kamenyane	Meta-harzburgite, meta-dunite and meta-gabbros (amphibolite and rodingites)	Massive	Zoned chromite	0.69-0.62	0.57-0.49	0.08-0.01
			Homogeneous chromite	-	-	-
		Semi-massive	Partly altered chromite	0.60-0.52	0.71-0.60	0.13-0.01
			Porous chromite	-	-	-
Chernichevo	Meta-harzburgite, Meta-dunite, meta-gabbros (amphibolite) and pyroxenite dykes	Massive	Partly altered chromite	0.69-0.51	0.58-0.28	1.60-0.37
		Semi-massive				
		Disseminated				

Table 1: Main features of the chromitite samples analysed in this study. Alteration patterns of chromite as defined Gervilla et al. (2012).

harzburgites with variable proportions of dunites and occasionally meta-gabbro sills (rodingites) and/or pyroxenite dykes (Table 1). Meta-harzburgites and meta-dunites often contain variable proportions of tremolite and, to lesser extent, talc. Two of the selected massifs (Golyamo Kamenyane and Chernichevo) also contain meta-gabbros (amphibolites) topping the ultramafic sequence (Table 1). Chromitite bodies of variable size are hosted in the meta-peridotites of the studied ultramafic massifs and were also affected by metamorphism. A body of chromitite from Golyamo Kamenyane is crossed by a sheared zone.

3 Petrology and mineral chemistry of chromitites

The studied chromitites are pods and, to lesser extents tabular or lens-like bodies, of relatively large size in the massif of Golyamo Kamenyane (few hundreds of meters long and tens of meters wide) to small (few tens of meters long and up to few meters wide) in the massifs of Avren West, Chernichevo and Yakovitsa. Chromitite bodies show massive, semi-massive and/or disseminated textures (Table 1) and chromite grains display variable degrees of alteration due to metamorphism. According to the classification of Gervilla et al. (2012) chromite grains exhibit the whole batch of patterns of alteration with *partly altered chromite* (cores surrounded by more reflecting porous zones), *porous chromite* (without defined cores and grains contain pores), *zoned chromite* (homogeneous cores enveloped by highly reflecting rims without pores) and *homogeneous chromite* (grains with mosaic-like, polygonal texture which contain neither cores and pores) (Table 1; Fig.2). Following the ideas of Gervilla and co-workers only partially altered chromites and zoned chromites preserve homogeneous cores that should a priori preserve the primitive igneous composition.

Electron microprobe analyses show that the Cr# [Cr# = Cr/(Cr+Al)] of chromite cores decreases from those of Avren West chromitites (Cr#=0.93-0.78) to those from Yakovitsa (Cr#=0.83-0.60), Golyamo Kamenyane (Cr#=0.69-0.52) and Chernichevo

(Cr#=0.69-0.51) (Table 1; Fig.3.A and B). The Mg# [Mg# = Mg/(Mg+Fe)] is very variable too, ranging from 0.71 to 0.49 at Golyamo Kamenyane, from 0.69 to 0.39 at Yakovitsa, from 0.58 to 0.28 at Chernichevo, and from 0.54 to 0.35 at Avren West (Table 1; Fig.3.A and B). The TiO₂ content of these chromite cores vary from 1.60 to 0.37 wt% at Chernichevo, from 0.14 to 0 wt% at Yakovitsa, from 0.13 to 0.01 wt% at Golyamo Kamenyane and from 0.09 to 0.01 wt% at Avren West (Table 1; Fig.3.C).

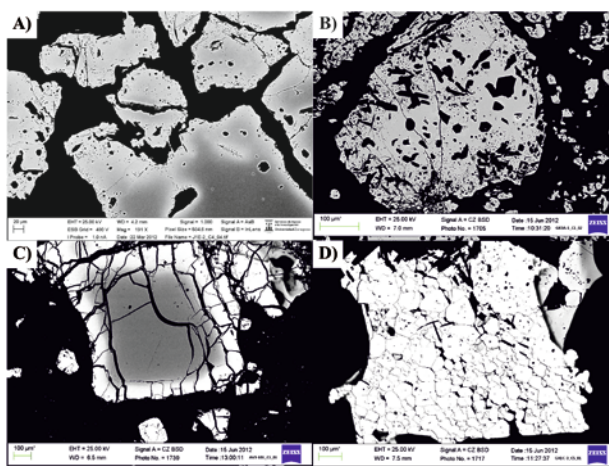


Figure 2: Different alteration patterns of chromite grains from Yakovitsa, Avren West, Golyamo Kamenyane and Chernichevo massifs (back-scattered electron microphotographs). A. Partly altered chromite. B. Porous chromite. C. Zoned chromite. D. Homogeneous chromite.

5 Discussion

Modifications of Mg and Fe contents in chromite cores are more evident in the small bodies with disseminated or semi-massive textures (e.g. Yakovitsa, Avren West and Chernichevo; Fig.3.B), than in those with nearly massive texture independently of their size (e.g. Golyamo Kamenyane, Yakovitsa, Avren West and Chernichevo; Fig.3.A). As well, these variations are higher in chromite grains with zoned texture (e.g. Golyamo Kamenyane, Yakovitsa and Avren West; Fig.3.B) than those with

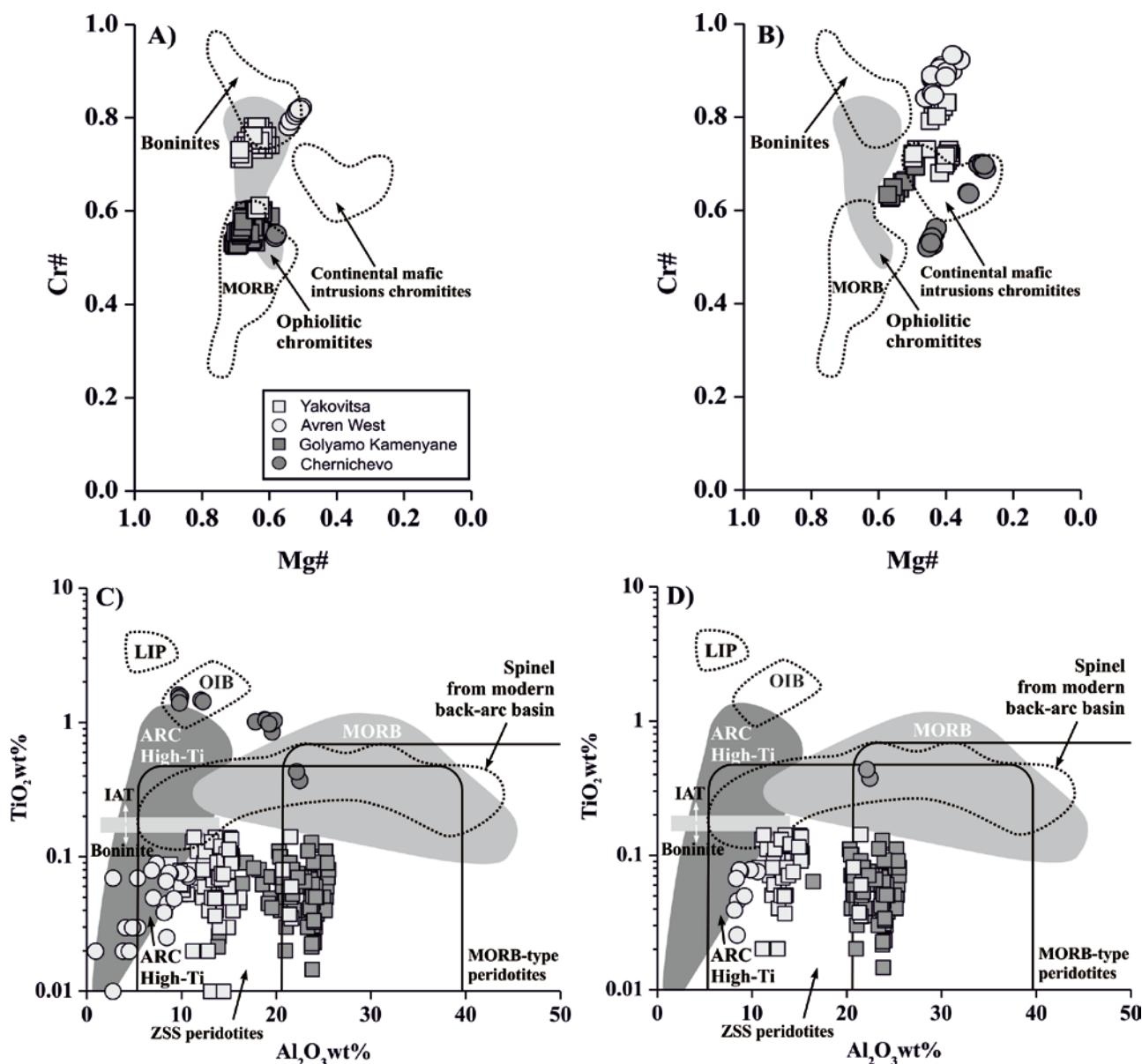


Figure 3: Chemical composition of chromites from Yakovitsa, Avren West, Golyamo Kamenyane and Chernichevo Ultramafic Massifs. A. Mg#[Mg# = Mg/(Mg+Fe²⁺)] and Cr#[Cr# = Cr/(Cr+Al+Fe³⁺)] variations of unaltered cores from partly altered chromites from large chromitite bodies, compared with the composition of chromite crystallized from MORB, boninites and in continental mafic intrusions (Barnes & Roeder, 2001). B. Mg# and Cr# variations of modify cores (zoned chromites and partly altered from small chromitite bodies). C. Al₂O₃ and TiO₂ contents of the studied chromite cores compared with the composition of chromite in modern days tectonic settings (Fields defined by Kamenetsky et al., 2001). D. Al₂O₃ and TiO₂ contents of unaltered cores (partly altered chromites from large chromitite bodies).

partly altered texture (e.g. Golyamo Kamenyane, Yakovitsa, Avren West and Chernichevo; Fig.3.A). However, TiO₂ contents show similar ranges in the whole batch of chromite cores, except those from Chernichevo bodies (Fig.3.C and Fig.3.D).

The Mg and Fe differences between chromite cores from massive chromitites and semi-massive/disseminated chromitites should be related with subsolidus equilibrium between chromite and intergranular olivine. This process promoted Fe²⁺ partitioning to chromite and Mg partitioning to olivine, giving rise to Fe²⁺-rich chromites (Barnes, 2000; Fig.3.B). Intergranular diffusion of Fe²⁺ and Mg becomes more difficult in massive-textured chromitites and therefore chromite tends to preserve its igneous Fe²⁺ and Mg contents. The subsequent reaction between

previous chromite and olivine (according to the alteration path described by Gervilla et al. 2012) implies loss of Al₂O₃ and MgO giving rise to ferrous-chromite rims in partly altered chromites; however this process preserve the previous core composition (Fig.3.A). The addition of magnetite-rich fluids to partly altered chromite would generate zoned chromite with ferrian-chromite rims. Moreover this process could promote further supply of Fe²⁺ to the chromite cores shifting their Mg# towards Fe-rich compositions (Fig.3.B). Alteration of chromite took place during retrograde metamorphism (Gervilla et al. 2012), starting at eclogite-facies conditions (subsolidus equilibrium between chromite and olivine), following at amphibolite-facies conditions (partly altered chromite) and finishing at amphibolite-green schists-facies conditions (zoned chromite).

The scattered distribution of TiO₂ in Fig.3.C would suggest that 1) different bodies of chromitite were formed in different geodynamic environments, 2) this TiO₂ dispersion might be a consequence of its mobilization during the retrogressive metamorphic evolution or 3) it was the result of the overlapping of both effects.

In view of everything previous, it is clear that the composition of some chromite cores were significantly modified in terms of their Mg, Fe²⁺ and Ti contents during retrograde metamorphic pathway. Therefore, we only consider as unaltered and pristine cores those that come from massive chromitite bodies with partly altered chromite grains (Table 1; Fig.3.A and D).

The chemistry of these unaltered cores in Yakovitsa and Avren West is characterized by low Al₂O₃ and TiO₂ content, while those from Golyamo Kamenyane and Chernichevo show high Al₂O₃, but different TiO₂ contents (Fig.3.A and D). This composition is typical from ophiolitic chromitites (Barnes & Roeder, 2001; Fig.3.A), however differences in Al₂O₃ and TiO₂ contents indicate different composition of parental magmas: boninite, suprasubduction-related magmas in Yakovitsa and Avren West, and MORB magmas (probably related with back-arc settings) in Golyamo Kamenyane and Chernichevo (Kamenetsky et al., 2001; Fig.3.A and D).

Haydoutov et al. (2004) consider that meta-orthoamphibolite from the Variegated Complex and from the Gneiss-Migmatite Complex (Eastern Rhodopes) represent compositions between transitional island arc tholeiites and boninites formed in an oceanic island-arc setting developed above supra-subduction zone (SSZ). These rocks could be associated with an ocean crust formed at a mid-ocean ridge and underwent eclogite facies metamorphism, and below with other ocean crust formed in a SSZ setting and underwent later (Variscan?) amphibolite facies metamorphism. However, presence of meta-gabbro sills (rodingites) and/or pyroxenite dykes as well as meta-gabbros (amphibolites) topping the ultramafic sequence at Golyamo Kamenyane and Chernichevo ultramafic massifs (Table 1) indicates that these ultramafic massifs would come from MORB-type peridotites, probably related with back-arc settings. In addition, the latter is supported by high Al₂O₃ contents in unaltered chromite cores from Golyamo Kamenyane and Chernichevo, high TiO₂ contents in unaltered cores from Chernichevo (Fig.3.B and D), as well as flysch nature of meta-sediments from the Variegated Complex (Kozhoukharov, 1987). In the other hand, Bonev (2006) interpreted the origin of massive orthoamphibolites and metagabbro-diorites from the Variegated Complex and amphibolite eclogite from the Gneiss-Migmatite Complex (Eastern Rhodopes) as MORB mantle source, substantially modified in a subduction-zone producing tholeiites in an island arc/back-arc setting. This assumption is related with the supra-subduction back-arc Vardar ocean/island arc system during the Palaeotethys closure and Neotethys widening (Late Permian-Middle Jurassic). However, relatively low TiO₂ contents in unaltered chromite cores from Yakovitsa and Avren West massifs (Fig.3.D.) indicate that these

chromitites could have been formed from boninite mantle source.

This study stresses the importance of understanding how major elements are mobilized during metamorphic alteration of chromitites, in order to select proper unaltered core compositions and avoid errors in petrologic interpretations.

Acknowledgements

This paper is a contribution to the project CGL2010-15171 of the Spanish MINCINN.

References

- Barnes SJ & Roeder PL (2001) The range of spinel compositions in terrestrial mafic and ultramafic rocks. *J. Petrol.* 42: 2279-2302
- Bazilev BA, Zakariadze GS, Zhelyazkova-Panayotova MD, Kolcheva K, Oberhänsli RE & Solov'eva NV (1999) Petrology of ultramafic rocks from the ophiolite association in the crystalline basement of the Rhodope Massif. *Petrologiya.* 7: (2), 192-211
- Bonev N (2006) Cenozoic tectonic evolution of the eastern Rhodope massif (Bulgaria): basement structure and kinematics of syn- to postcollisional extensional deformation. In: Dilek Y, Pavlides S (eds) Post-collisional tectonics and magmatism in the Mediterranean region and Asia. *Geol. Soc. Am. Sp. Pap.* 49: 211-235
- Daieva LA, Haydoutov I & Pristavova S (2007) Geochemical correlation of metabasic rocks from Central and East Rhodopes, Bulgaria. *Geochemistry, Mineralogy, and Petrology.* 45: 109-118
- Georgiev V (2006) Tertiary domes and depressions in the Rhodope massif. *Geosciences 2006, Proceedings:* 106-109
- Gervilla F, Padrón-Navarta JA, Kerestedjian T, Sergeeva I, González-Jiménez JM, Fanlo I (2012) Formation of ferrian chromite in podiform chromitites from the Golyamo Kamenyane serpentinite, Eastern Rhodopes, SE Bulgaria: a two-stage process. *Contr. Min. Petrol.* 164 (4): 643-657
- González-Jiménez J M, Kerestedjian T, Proenza JA, Gervilla F (2009) Metamorphism on chromite ores from the Dobromirski Ultramafic Massif, Rhodope Mountains (SE Bulgaria). *Geol. Acta.* 7: 413-429
- Haydoutov I, Kolcheva K, Dieva LA, Savov I, & Carrigan C (2004) Island arc origin of the variegated formations from the east Rhodope, Bulgaria-implications for the evolution of the Rhodope Massif. *Ophioliti.* 29(2): 145-157
- Kamenetsky VS, Crawford AJ, & Meffre S (2001) Factors controlling chemistry of magmatic spinel: an empirical study of associated olivine, Cr-spinel and melt inclusions from primitive rocks. *J. Petrol.* 42: 665-671
- Kolcheva K, Haydoutov I & Daieva L (2000) Dismembered ultramafic ophiolites from the Avren synform, Eastern Rhodopes. *Geochem Mineral Petrol* 37: 25-38
- Kozhoukharov D (1987) The Rhodopian Supergroup in the Avren Syncline, Eastern Rhodopes. *Geol. Balcanica,* 17 (4), 21-40
- Mposkos E & Krohe A (2006) Pressure-temperature-deformation paths of closely associated ultra-high-pressure (diamond-bearing) crustal and mantle rocks of the Kimi complex: implications for the tectonic history of the Rhodope Mountains, northern Greece. *Canad J Earth Sci.* 43: 1755-1776

The composition of spinels from Mongolia, Poland, Ukraine and Cyprus as an exploration tool for Cr-deposits – preliminary study

Tomasz Ćwiertnia

AGH University of Science and Technology, Faculty of Geology, Geophysics and Environmental Protection, al. A. Mickiewicza 30, 30-059 Krakow, Poland

Adam Piestrzyński

AGH University of Science and Technology, Faculty of Geology, Geophysics and Environmental Protection, al. A. Mickiewicza 30, 30-059 Krakow, Poland

Jadwiga Pieczonka

AGH University of Science and Technology, Faculty of Geology, Geophysics and Environmental Protection, al. A. Mickiewicza 30, 30-059 Krakow, Poland

Władysław Zygo

AGH University of Science and Technology, Faculty of Geology, Geophysics and Environmental Protection, al. A. Mickiewicza 30, 30-059 Krakow, Poland

Abstract. Samples of chromite grains were collected from Bayanlig (Mongolia), Lipowieńki (Ukraine), Tapadła (Poland) and the Troodos ophiolite (Cyprus). EDS analyses were performed on different zones of chromites. The chemical composition of chromite cores, as well as Cr-spinel and magnetite rims in grains are compared. Cr content in chromite and others spinels from barren ophiolites are significantly lower in comparison to those from podiform deposits.

Keywords. Chromite, ophiolite, Cr-spinel, magnetite, Mongolia, Tapadła, Troodos, Lipowieńki.

1 Localization of samples

Samples were collected from the Bayanlig area (Mongolia), Lipowienki (Ukraine), Tapadła (Poland), and the Hadjipavlous mine in the Troodos ophiolite, Cyprus. Selected samples of chromite grains and Cr-spinels were chosen for analyses.

The Bayanlig area is a metamorphic melange of serpentinites, amphibolites, schists, and granitoids. It is possibly an ophiolite structure. Stream sediment samples were collected from a periodic river bed. The area from which the material was collected measures ~6km².

Lipowieńki (Ukraine) may represent an ophiolite structure or a layered intrusion. Total reserves of Ni and Cr are estimated to allow production for the next 40 years. Chromitites occur as lenses (up to 50m long and 26m thick) and as disseminated mineralization in the host rock. The highest content of Cr₂O₃ is 35-48% (Pieczonka et al, 2011).

Samples from Tapadła, Poland, were collected from an old chromite mine, located in the Jordanów-Gogołów massif which consists mainly of serpentinized ultramafic rocks. The ore bodies occur as lenses and nests in serpentinized harzburgites (Delura, 2012).

Samples from Cyprus were collected from the closed Hadjipavlous Cr mine in the Troodos ophiolite.

Most of the chromitites are massif and are enclosed in elongated dunite bodies. No relation between size or

composition of dunites and chromites was found (McElduff, 1991).

2 Chemical composition of chromite-spinel grains

Chromite grains and crystals from Mongolia usually have chromite in the center, surrounded by a zone of Cr-spinel and a Cr-bearing magnetite rim (Fig. 1). Analyses of cores (Fig. 2, no 1,2,9) of chromite grains show an average of 26.72 wt% of Cr (Tab. 1). Towards the rims, a depletion of Cr is observed (from 25.35 wt% to 23.61 wt%, Fig.5). A similar depletion of Al is also observed. The cores contain an average of 18.80 wt% Al, but Al content decreases to 18.00 wt% in the central zone and 1.18 wt% in the rim of the grain (Fig. 5). In contrast, Fe becomes progressively enriched towards the edge of grains (12.47 wt% Fe in core, 20.64 wt% Fe in the middle zone, 48.79 wt% in rim). A depletion of Mg is observed in the same direction (from 9.98 wt% in core to 0.50 wt% Mg in the magnetite rim (Fig.5). A small enrichment in Ti is also observed, from 0.06 wt% of Ti in the chromite core, 0.10 wt% of Ti outside chromite to 0.20 wt% of Ti in magnetite rim.

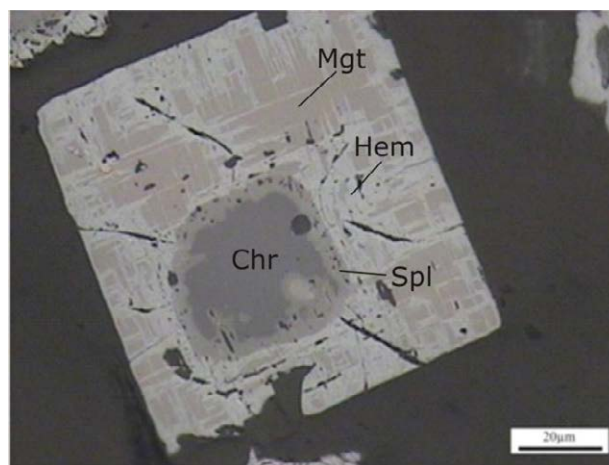


Figure 1. Chromite, hematite, Cr-spinels and Cr-bearing magnetite intergrowth. Reflected light, sample 2M32A1, Bayanlig, Mongolia.

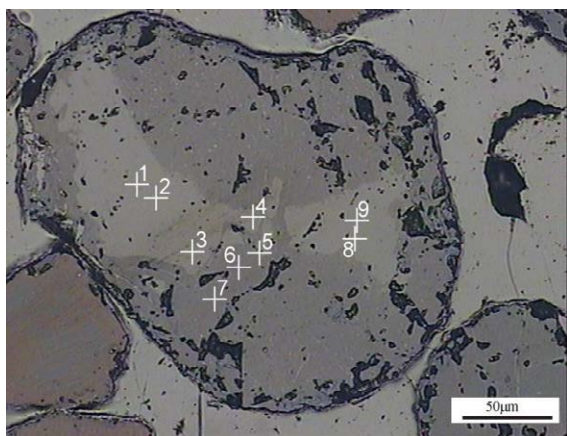


Figure 2. Chromite and Cr-spinel intergrowth with EDS analyses localization points. Area C, K72sz sample, reflected light.

The Ukrainian samples show similar results (Tab. 2), however in sample 413A only Cr-spinels (ferrichromites after Sadłowska, 2011) and Cr-bearing magnetite are observed.

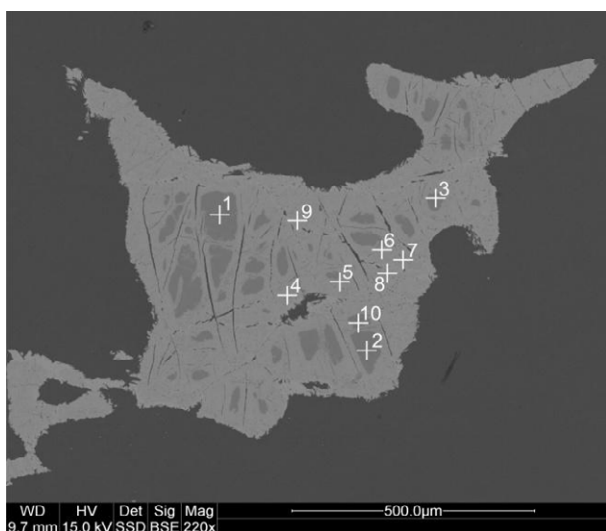


Figure 4. Zoned spinels aggregates. 1-10 EDS analyses. BSE image, Tapadła, Poland.

no	OKα	MgKα	AlKα	SiKα	TiKα
1	31,78	10,06	18,84	0,04	0
2	32,03	9,92	18,67	0,09	0,12
3	30,98	6,61	18,34	0,03	0,10
4	30,51	4,76	17,92	0,11	0,11
5	30,32	4,39	17,74	0,04	0,09
6	25,90	0,43	2,15	0,06	0,18
7	25,57	0,77	0,93	0,21	0,21
8	25,30	0,31	0,45	0,14	0,20
9	31,67	9,95	18,88	0,10	0,06
no	CrKα	MnKα	FeKα		
1	26,68	0	12,61		
2	26,65	0	12,52		
3	25,49	0	18,45		
4	25,55	0	21,05		
5	25,01	0	22,41		
6	23,27	0	48,01		
7	24,41	0	47,90		

8	23,14	0	50,47		
9	26,84	0,23	12,27		

Table 1. EDS analysis of chromite-spinel grains from Mongolia, sample K72sz.

no	OKα	MgKα	AlKα	SiKα	TiKα
1-1	27,01	2,90	6,21	0,09	0,34
1-2	27,88	2,67	6,83	0,05	0,31
1-3	25,92	1,41	3,19	0,06	0,15
2-1	26,72	2,60	6,16	n.d.	0,31
2-2	27,01	2,56	6,02	0,05	0,43
2-3	25,05	1,22	2,57	0,12	0,26
2-4	24,89	1,01	2,41	0,12	0,29
no	CrKα	FeKα	VKα	CaKα	
1-1	24,20	38,92	0,20	0,14	
1-2	26,56	35,47	0,15	0,09	
1-3	15,93	53,04	0,16	0,06	
2-1	26,61	37,33	0,19	0,08	
2-2	25,65	37,91	0,18	0,19	
2-3	13,47	57,07	0,14	0,09	
2-4	14,28	56,65	0,20	0,15	

Table 2. EDS analysis of chromite-spinel grains from Ukraine, 359A sample.

(Fig. 3, Tab. 3). The Cr spinels have 26.18 wt% Cr (Tab.1-3) whereas magnetite replacing spinel has an av. of 11.50 wt% Cr (Fig. 5). A similar zoning is observed in terms of Al content. 7.44 wt% Al occur in chromites and 1.66 wt% in replacement magnetite (Fig.5). Chromites contain 4.34 wt% Mg with a decrease observed in magnetite (1.39 wt%).

Ti content shows a minimal decrease from 0.33 wt% Ti in chromites to 0.35 wt% in magnetite.

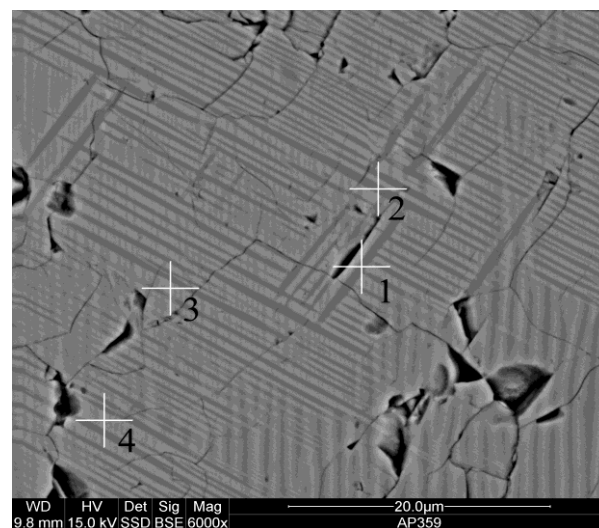


Figure 3. Solid solution structures of chromites. EDS analyses points (1-4). BSE image, Lipowieńki, Ukraine.

no	O Kα	MgKα	AlKα	SiKα	TiKα	V Kα	CrKα
1	30,59	7,85	10,15	0,15	0,24	0,11	26,27
2	25,38	1,66	0,85	0,16	0,23	0,11	9,26
3	26,94	1,66	0,79	0,1	0,23	0,06	9,00
no	MnKα	FeKα	CoKα	ZnKα	NiKα		
1	0,37	23,11	0,22	0,53	0,41		
2	0,25	59,45	0,65	0,56	1,45		

1	0.22	58.95	0.36	0.18	1.51		
---	------	-------	------	------	------	--	--

Table 3. EDS analysis of chromite-spinel grains from Ukraine, sample 413A.

Magnetite replacing chromite is enriched in Fe, similar to the Mongolian samples. An av. 32.78 wt% of Fe in chromites is observed, and an av. 58.03 wt% in magnetite.

The Cr content in chromites from Tapadła is 25.91 wt%, decreasing to 22.65 wt% in Cr-spinels, and 6.41 wt% outside of the spinels (Fig. 5). Mg content of chromite is 6.12 wt% falling to 0.77 wt% in Cr-spinel and 0.23 wt% in magnetite (Fig. 5). An almost total depletion of Al is observed, with 16.39 wt% Al in the core, 0.70 wt% in Cr-spinel and 0.08 wt% in the magnetite.

Chromite cores have 0.15 wt% of Ti, whereas spinel has 0.26 wt% and rims have 0.16 wt% Ti. The content of V shows smaller changes, that is 0.22 wt% in the core of the grains, 0.22 wt% in spinel and 0.13 wt% V in magnetite. Similar to the Ukrainian and Mongolian samples, Fe enrichment is observed towards the rim. An average of 17.04 wt% Fe is observed in the core, 44.38 wt% in Cr-spinels and 64.08 wt% in magnetite. An average of 0.60% Ni is observed in some analyses from the rim.

No magnetite is observed in the samples from Cyprus. Samples from the Hadjipavlou mine show an average of 33.00 wt% Cr in the chromite core. In contrast to samples from Mongolia, Ukraine and Poland, samples from Cyprus show enrichment of Cr outside of the chromite cores. One analysis shows 36.83 wt% Cr (Fig. 5). An enrichment of Fe towards the outside of the grains is also observed, similar to the samples from the other locations. 11.26 wt% Fe is observed in grain cores and 14.30 wt% in the rims (Fig. 5). Magnesium and Al show depletions from core to rim whereas Ti and Co contents remain essentially constant.

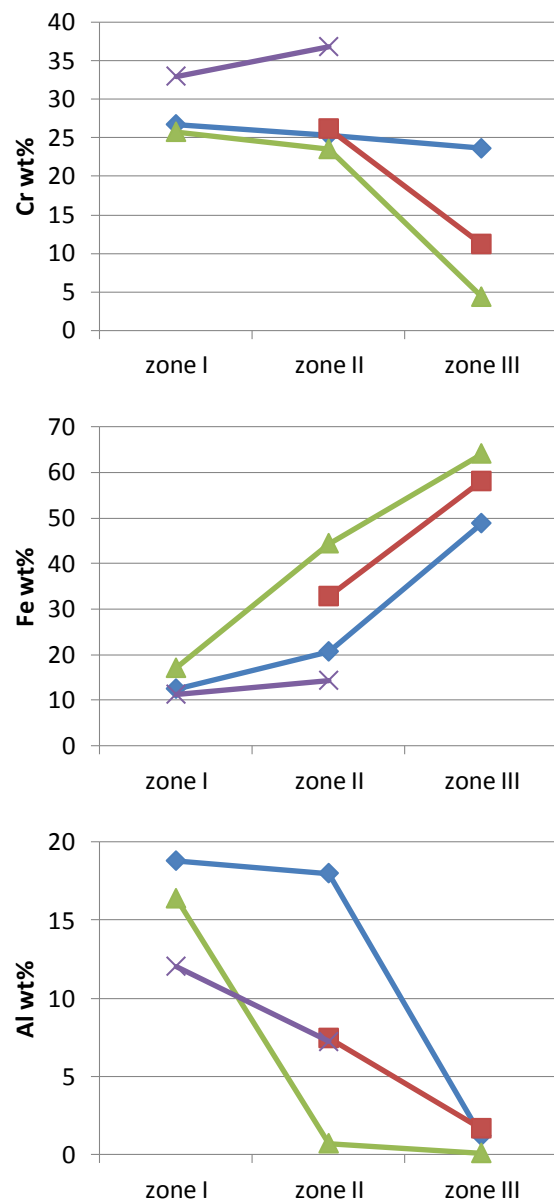
3 Summary of observed trends

Similar depletion of Cr is observed in the Bayanlig and Tapadła samples from the grain cores (Fig. 5) towards Cr-spinel. The Cr depletion from Cr-spinel towards magnetite is greater in Tapadła. In the Bayanlig sample the level of depletion is constant (Fig. 5). The Lipowieńki sample shows depletion of Cr from Cr-spinel towards magnetite (no chromite core is observed). The level of depletion is similar to Tapadła. Only in the samples from Hadjipavlou mine an enrichment of Cr is observed from the chromite core towards the Cr-spinel zone (Fig. 5).

In all the samples an enrichment of Fe is observed from chromite core towards the Cr-spinel zone (Fig. 5). The Cyprus and Lipowieńki samples show moderate Al depletion from chromite core towards Cr spinels (Fig. 5), Bayanlig samples show somewhat stronger depletion and Tapadła samples show a high depletion. All samples show a decrease in Mg from the cores to the rims (Fig. 5).

4 Conclusions

Chemical assays of Cr-spinels show high variability in concentration of basic ions. The concentration of Cr in samples from the economic Troodos chromite deposits are higher than in the other occurrences which comprise sub-economic chromitites in ophiolites (Tapadła), rocks from an ophiolite without chromitites (Bayanlig), and possibly a layered intrusion (Lipowieńki). The data suggest that spinel compositional zoning can be an important tool in the prospection for chromite ores at the very early stage of exploration. Observed zoning in single grains is typical for non-economic concentration of Cr-spinels in ultramafic strata.



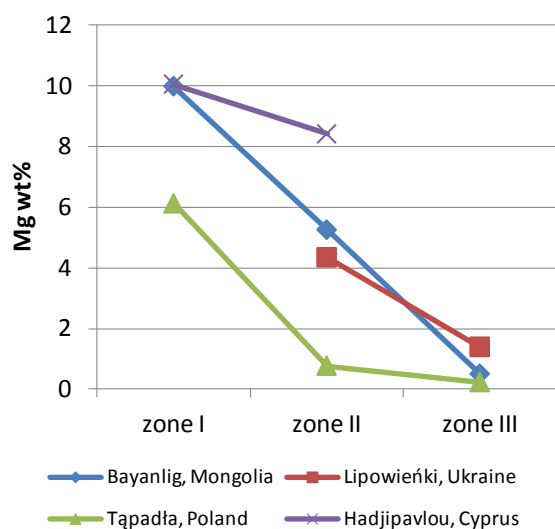


Figure. 5 EDS results for chromite (chromite), Cr-spinel (tr. zone) and rim zone (magnetite). Zone I-chromite core, zone II – Cr-spinel, zone III-magnetite.

Acknowledgements

The work was partially financed by AGH research project B.S. 11.11.140.562

References

- K.Delura, 2012. Chromites from the Sudetic ophiolite: origin and alteration. *Archivum mineralogiae Monography No.4*, Committee of Mineralogical Sciences of the Polish Academy of Sciences.
- J.Krause, G.E.Brugmann, E.V.Pushkarev, 2010. Chemical composition of spinel from Uralian-Alaskan-type Mafic-Ultramafic complexes and its petrogenetic significance. *Contrib Mineral Petrol* 161, p.255-273.
- B.McElduff, E.F.Stumpfl, 1991. The chromite deposits of Troodos complex, Cyprus-evidence for the role of a fluid phase accompanying chromite formation.
- J.Pieczonka, A.Piestrzyński, I.Parańko, 2011. Geology of selected ore deposits, Ukraine. Wydawnictwo AGH, Kraków.
- K.Sadłowska, 2011. Ore mineralization in ultramafics from the Mnich ridge from western part of the Braszowice-Brzeźnica maasif (lower Silesia). *Biuletyn Państwowego Instytutu Geologicznego*, 447, p.99-118.

Geochemistry of different ore-bearing intrusions in the Emeishan large igneous province

Xingxing Du, Jianmin Liu

Institute of Geomechanics, Chinese Academy of Geological Sciences, Beijing, 100081, China

Abstract. The Emeishan large igneous province (ELIP) of China formed during the Permian-Triassic contains world-class magmatic Fe–Ti–V oxide deposits as well as several small magmatic Ni–Cu–PGE sulphide deposits. The host rocks of the ore deposits are all layered mafic-ultramafic intrusive rocks and have a similar age. Generally, a modal of fractional crystallization has been used to explain the formation of the Fe–Ti–V deposits, and a modal of segregation of an immiscible sulfide liquid from silicate magma has been favoured for the Ni–Cu–PGE deposits. However, what actually caused the differences of mineralization in the same tectonic unit remains unknown. Comparison of the previous studies on the geology, petrology and geochemistry of the Fe–Ti–V oxide deposits and the Ni–Cu–PGE sulfide deposits indicates that compositional heterogeneity of the deep mantle and differences in the magmatic evolution may be the main reasons for the differences in the magmatic deposits.

Keywords. Emeishan large igneous province; magmatic deposit; layered intrusion; compositional heterogeneity

1 Introduction

Magmatic sulfide and oxide deposits can be found in different geologic settings, such as large igneous provinces, cratonic rift zones or post-collisional extensional environments in folded belts. The world famous Noril'sk Cu–Ni–PGE sulfide deposits are located in the Siberian large igneous province (SLIP) of Russia. The Emeishan large igneous province (ELIP) of China hosts world-class V–Ti magnetite deposits and several small Cu–Ni–(PGE) sulfide deposits. Both the sulfide deposits and the oxide deposits are hosted in layered mafic-ultramafic intrusions. The occurrence of two kinds of mineralization in the ELIP brings up an important question: what caused the formation of the deposits, and why does the SLIP only contain sulfide ores but no important V–Ti oxide ores?

In the ELIP many layered mafic – ultramafic intrusions are exposed. They can be classified into two types: large mafic layered intrusions that host giant V–Ti magnetite deposits (e.g., Panzhihua, Baima and Hongge), and small sill-like mafic–ultramafic intrusions that host magmatic Cu–Ni–(PGE) sulfide deposits (e.g., Limahe, Jinbaoshan, Zhubu, Yangliuping and Baimazhai). The above intrusions, irrespective whether they host oxide deposits or sulfide deposits, share several features. For instance, they are all located at the western margin of Yangtze craton and related to a rift zone. Their age is similar to that of the Emeishan flood basalts, ~260Ma

(Zhou et al., 2002, 2005, 2008; Fan et al., 2004; Guo et al., 2004; Zhong and Zhu, 2006; He et al., 2007). Because of the uniform tectonic and magmatic background, they are acknowledged as the results of the Emeishan mantle plume. Here we choose several representative intrusions hosting oxide and sulfide deposits in the ELIP to investigate what led to their different mineralization (Song et al., 2003; Wang et al., 2006, 2010; Tao et al., 2007, 2008; Wang, 2008; Zhou et al., 2008; Zhang et al., 2009). The transitional type (e.g., Xinjie) which hosts both V–Ti–Fe deposits and Cu–Ni–PGE sulfide deposits at different stratigraphic levels is not considered in this study.

2 Geochemical characteristics

2.1 Geologic feature

The Permian mafic-ultramafic layered intrusions in the ELIP are exposed along north-south-trending deep faults. The size of the sulfide ore-bearing intrusions is mostly less than 3km², whereas the oxide ore-bearing intrusions are larger (>10km²). The giant magmatic V–Ti–Fe oxide deposits are mainly hosted in layered gabbro complexes, which contain little or no ultramafic rocks. In contrast, the host rocks to the small magmatic Cu–Ni–(PGE) sulfide deposits are both ultramafic and mafic rocks, including peridotites, pyroxenites, gabbros and their transitional rock types. The rock assemblages and the proportion of each rock type in the different sulfide deposits are variable.

2.2 Whole rock chemistry

The layered intrusions with different types of ore deposits display different geochemical features. The host rocks of oxide deposits are relatively rich in Fe, Ti, V and P, while the host rocks of sulfide deposits are rich in Mg, Cr, Ni, Cu and PGE. Total alkali-silica diagrams show that most of the oxide-bearing intrusions from the ELIP are feldspathoiditic-picritic-tephritic, whereas the compositional range of the sulfide-bearing intrusions is from feldspathoiditic-picritic to basaltic (Fig. 1). Additionally, the content of alkaline elements in the oxide-bearing intrusions is higher than in the sulfide-bearing intrusions. It appears that the metallogenesis of the two types of ore deposits is closely related to their different source composition.

All intrusions display variable fractionation between LREE and HREE. Some of the oxide-bearing intrusions have positive Eu anomaly, which reflects the existence of plagioclase in the rocks. By contrast, the sulfide-bearing

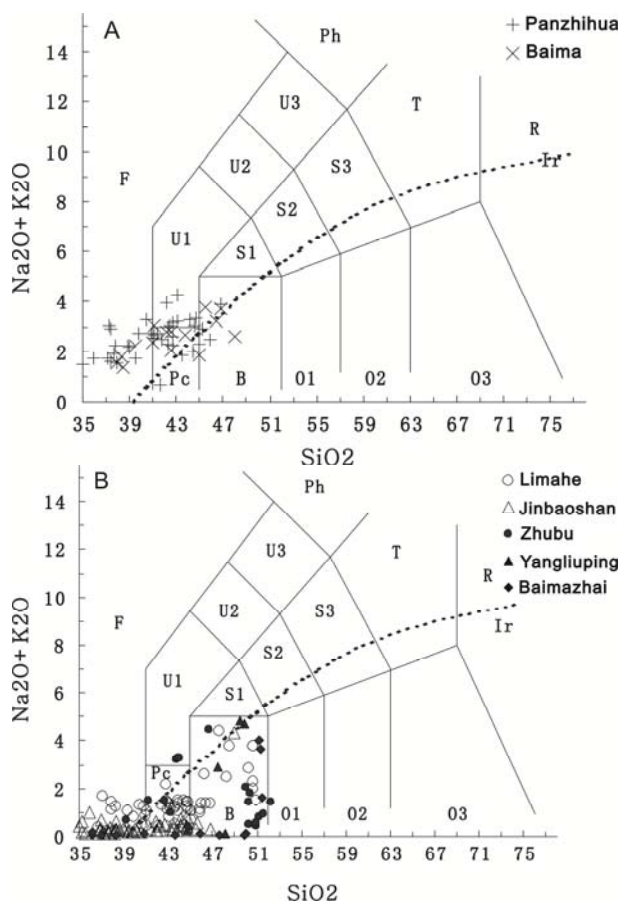


Figure 1. TAS diagrams of the ore-bearing intrusions within ELIP, SW China

A. Panzihua and Baima oxide-bearing intrusions from Zhou et al., 2008; Zhang et al., 2009; B. Limahe, Jinbaoshan, Zhubu, Yangliuping and Baimazhai sulfide-bearing intrusions from Song et al., 2003; Tao et al., 2007, 2008; Wang, 2008; Zhou et al., 2008; Zhang et al., 2009; Wang et al., 2006, 2010

intrusions have no significant Eu anomaly.

The oxide-bearing and sulfide-bearing intrusions have distinctive primitive mantle-normalized trace element patterns. The patterns of the oxide-bearing intrusions are characterized by moderate to strongly positive Ti anomalies and negative Zr and Hf anomalies. The sulfide-bearing intrusions have more regular patterns, but with significant negative Nb and Ta anomalies. The reason of the different trace element patterns between the two types of intrusions could be related to the compositional heterogeneity of the mantle source and crustal contamination.

2.3 Isotope geochemistry

Besides whole rock chemical compositions, the isotopic compositions from the different ore-bearing intrusions are markedly different (Fig. 2). The intrusions hosting oxide deposits have a relatively small range of isotope values, which fall in the field of the Emeishan flood basalts. The intrusions hosting sulfide deposit can be divided into two types: one is distributed in and near the field of the Emeishan flood basalts (Limahe and Jinbaoshan), and the other is distributed away from the field of the Emeishan flood basalts, but close to enriched mantle. The oxide-bearing intrusions have high $\epsilon_{Nd}(t)$

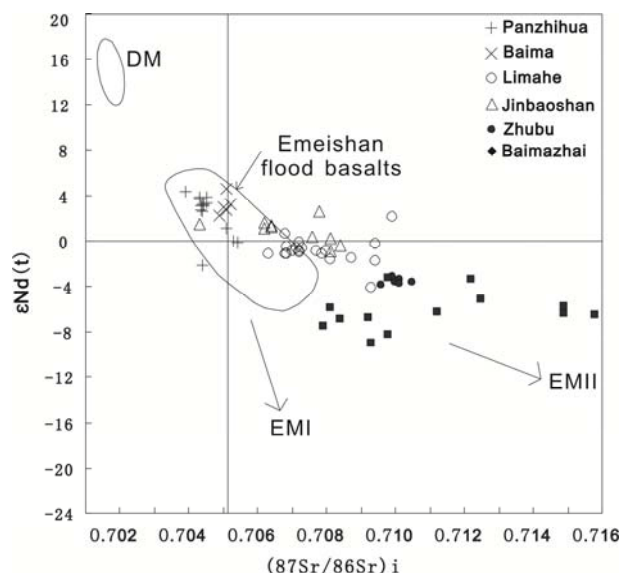


Figure 2. Plots of $\epsilon_{Nd}(T=260 \text{ Ma})$ values versus initial $^{87}\text{Sr}/^{86}\text{Sr}$ ratios of rocks from ore-bearing intrusions within ELIP, SW China

The data in the figure are from the same references as fig. 1. DM (depleted mantle), EMI and EMII fields are from Zindler and Hart (1986). The Emeishan basalt data are from Zhang et al. (2006).

values, whereas the sulfide-bearing intrusions have high initial $^{87}\text{Sr}/^{86}\text{Sr}$ ratios. The information from Sr-Nd isotopes indicates that the magma source of the two types of intrusions may be related to a mantle plume, but it appears that they have evolved along different paths. The sulfide-bearing intrusions have experienced variable degrees of crustal contamination, whereas the oxide-bearing intrusions are less contaminated.

Acknowledgements

We acknowledge the financial support from the Project of Geological Survey of the Geological Survey of China (1212011120183). We are grateful to Wolfgang Maier for his detailed reviews.

References

- Fan WM, Wang YJ, Peng TP (2004) Ar-Ar and U-Pb geochronology of Late Paleozoic basalts in western Guangxi and its constraints on the eruption age of Emeishan basalt magmatism. *Chinese Science Bulletin* 49: 1892–1900 (in Chinese with English abstract)
- Guo F, Fan WM, Wang YJ, Li CW (2004) When did the Emeishan plume activity start? Geochronological evidence from ultramafic–mafic dikes in Southwestern China. *International Geology Review* 46: 226–234
- He B, Xu YG, Huang XL, Luo ZY, Shi YR, Yang QJ, Yu SY (2007) Age and duration of the Emeishan flood volcanism, SW China: geochemistry and SHRIMP zircon U–Pb dating of silicic ignimbrites, post-volcanic. *Earth and Planetary Science Letters* 255: 306–323
- Song XY, Zhou MF, Cao ZM, Sun M, Wang YL (2003) Ni-Cu-(PGE) magmatic sulfide deposits in the Yangliuping area, Permian Emeishan igneous province, SW China. *Mineralium Deposita* 38: 831–843

- Tao Y, Li C, Hu RZ, Ripley EM, Du AD, Zhong H (2007) Petrogenesis of the Pt–Pd mineralized Jinbaoshan ultramafic intrusion in the Permian Emeishan Large Igneous Province, SW China. *Contrib Mineral Petrol* 153: 321–337
- Tao Y, Li C, Song X, Ripley EM (2008) Mineralogical, petrological and geochemical studies of the Limahe mafic-ultramafic intrusion and the associated Ni-Cu sulfide ores, SW China. *Mineralium Deposita* 43: 849–872
- Wang Y (2008) Origin of the Permian Baimazhai magmatic Ni-Cu-(PGE) sulfide deposits, Yunnan: implications for the relationship of crustal contamination and mineralization. *Bulletin of Mineralogy, Petrology and Geochemistry* 27: 332–343 (in Chinese with English abstract)
- Wang CY, Zhou MF, Keays RR (2006) Geochemical constraints on the origin of the Permian Baimazhai mafic-ultramafic intrusion, SW China. *Contrib Mineral Petrol* 152: 309–321
- Wang CY, Zhou MF, Qi L (2010) Origin of extremely PGE-rich mafic magma system: an example from the Jinbaoshan ultramafic sill, Emeishan large igneous province, SW China. *Lithos* 119: 147–161
- Zhang ZC, Mahoney JJ, Mao JW, Wang FS. (2006) Geochemistry of picritic and associated basalt flows of the western Emeishan flood basalt province, China. *Journal of Petrology* 47: 1997–2019
- Zhang ZC, Mao JW, Saunders AD, Ai Y, Li Y, Zhao L (2009) Petrogenetic modelling of three mafic-ultramafic layered intrusions in the Emeishan large igneous province, SW China, based on isotopic and bulk chemical constraints. *Lithos* 113: 369–392
- Zhong H, Zhu WG (2006) Geochronology of layered mafic intrusions from the Pan-Xi area in the Emeishan large igneous province, SW China. *Mineralium Deposita* 41: 599–606
- Zhou MF, Arndt NT, Malpas J, Wang CY, Kennedy AK (2008) Two magma series and associated ore deposit types in the Permian Emeishan large igneous province, SW China. *Lithos* 103: 352–368
- Zhou MF, Malpas J, Song X, Kennedy AK, Robinson PT, Sun M, Leshner CM, Keays RR (2002) A temporal link between the Emeishan large igneous province (SW China) and the end-Guadalupian mass extinction. *Earth and Planetary Science Letters* 196: 113–122
- Zhou MF, Robinson PT, Leshner CM, Keays RR, Zhang CJ, Malpas J (2005) Geochemistry, petrogenesis and metallogenesis of the Panzhihua gabbroic layered intrusion and associated Fe-Ti-V oxide deposit, Sichuan Province, SW China. *Journal of Petrology* 46: 2253–2280
- Zindler A, Hart SR (1986) Chemical dynamics. *Annual Review of Earth and Planetary Science Letters* 14: 493–571

Petrogenesis of massive sulphides from the Lac-des-Iles palladium ore deposits, Western Ontario, Canada

Charley J. Duran, Sarah-Jane Barnes

Sciences de la Terre, Université du Québec, Chicoutimi, Canada G7H 2B1 (charley.duran@hotmail.fr)

John T. Corkery

North American Palladium, 556 Tenth Avenue, Thunder Bay, Ontario, Canada P7B 2R2

Abstract. Previously characterised as a sulphide-poor Pd ore deposit, massive sulphides have recently been discovered in Lac-des-Iles. The massive sulphides occur across the different lithological units and show variable degrees of alteration. The least altered samples comprise a typical magmatic assemblage of pyrrhotite, pentlandite and chalcopyrite. Chalcopyrite-rich samples are found at the edges of the pyrrhotite/pentlandite-rich pods. Base metal and platinum-group element (PGE) compositions indicate that as a whole they represent a frozen sulphide liquid, different from the one that formed the sulphide-poor samples, that was injected along structural features. The altered samples are rich in pyrite and magnetite. Molecular proportions of base metals and S/Se ratios are the same for the altered and unaltered samples indicating that neither S nor Fe has been remobilized from the system. We propose instead that oxidation was responsible for the observed changes in mineralogy. This alteration event appears not to have affected the PGE content.

Keywords. Massive sulphides, structural control, Lac-des-Iles Pd ore deposits

1 Introduction

The Archean Lac-des-Iles (LDI) Complex, western Ontario, is Canada's only primary platinum-group elements (PGE) producer and the world's fourth largest palladium (Pd) producer. In contrast to most PGE ore deposits which occur either as strataform PGE-rich layers within large layered intrusions (e.g. Bushveld and Stillwater) or as PGE-rich Ni-Cu sulphides at the base of mafic intrusions (e.g. Noril'sk and Sudbury), the LDI mineralization occurs as sulphides and platinum-group minerals (PGM) disseminated in a small mafic intrusion of chaotic lithologies (i.e. magmatic breccias and varitextured gabbro-norites). The mineralization is characterized by extreme and variable Pd-enrichment highlighted by unusually high Pd/Pt ratios. Studies by Hinchey et al. (2005), Barnes and Gomwe (2011), and Djon and Barnes (2012), suggest that both PGE collection by a magmatic sulphide liquid followed by Pd-remobilization by later magmas or fluids have contributed in the ore formation. However, the contribution of each process is poorly understood, and relatively little is known about how the Pd-enrichment was achieved.

The LDI complex has been previously characterized as sulphide poor (i.e. < 3%). However massive sulphides have recently been discovered, which raises the question of the processes involved in their formation. Three possible origins may be considered: a)

the sulphides are monosulphide solid solution (MSS) cumulates and the fractionated liquid has migrated away to form the disseminated sulphides; b) the sulphides represent a frozen sulphide liquid; c) the sulphides precipitated from late-magmatic aqueous fluids.

In the current study we document new data on the geology, petrography/mineralogy, and whole rock geochemistry of the newly discovered massive sulphides from the LDI complex in order to consider their origin.

2 Geology of LDI and location of massive sulphides

The LDI Complex consists of three mafic to ultramafic intrusions emplaced into gneissic tonalites and granodiorites, which are in turn intruded by various granitoids. The Mine Block Intrusion is the central intrusion of the complex and is the only one that hosts Pd-deposits (i.e. Roby and Offset zones). The Mine Block Intrusion is concentrically zoned in both composition and texture. Compositions range mainly from leuco- to melano-gabbros and gabbro-norites, including a magnetite-rich gabbro. Magmatic breccias occur in the Roby zone but have not been observed at depth. Varitextured gabbros form a rim around the gabbroic and gabbro-noritic units. Most of the rocks regardless their texture or degree of alteration, have similar compositions (Barnes and Gomwe 2011). The shape of the intrusion suggests an elongation along a SW-NE trend.

The sulphide-rich samples occur as small pods and lenses (8 to 65 cm thick), ranging from densely disseminated (~10% sulphides) to massive sulphides (~90% sulphides). These pods are found in different units and at different stratigraphic levels within the intrusion (Figs. 1 and 2). Despite being present in host rocks that formed at different stages of magma differentiation the sulphide-rich samples have similar textural, petrographical and mineralogical characteristics. The semi-massive sulphides host rounded silicate inclusions and exhibit brecciated textures. All these observations suggest that the sulphides have been injected across the stratigraphy of the intrusion implying that they were in a liquid state. The geological setting thus suggests that the sulphides were emplaced along some structural feature and either represent an immiscible sulphide liquid, or have precipitated from late-magmatic fluids.

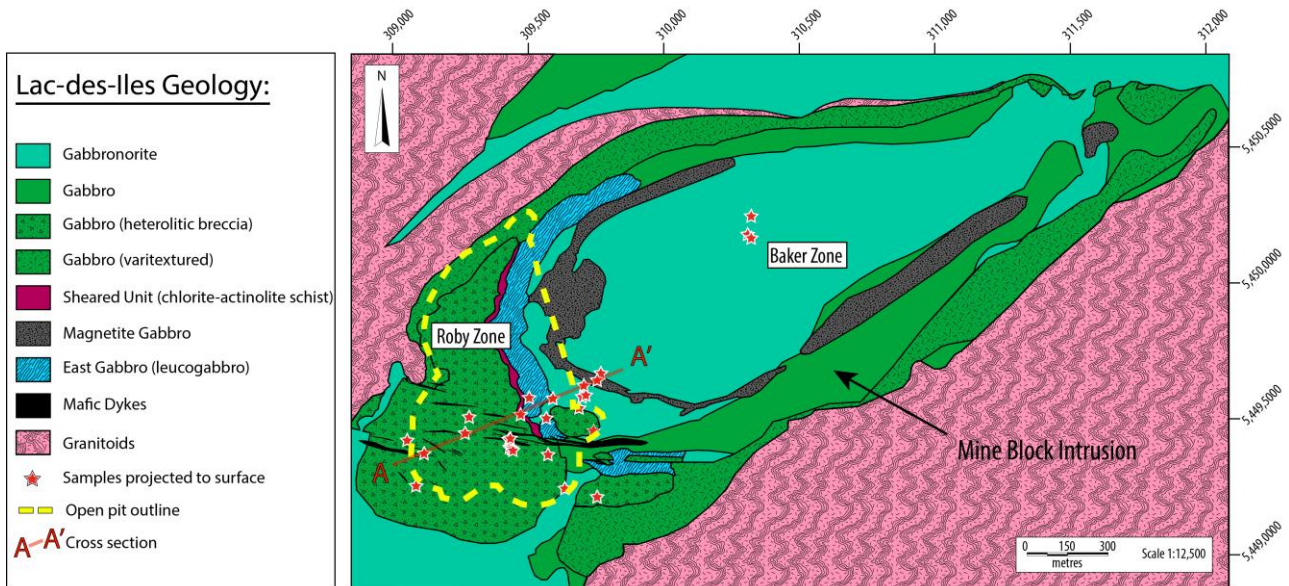


Figure 1. Simplified geological map of the Mine Block Intrusion of the Lac-des-Iles Complex with location of the sulphide-rich samples (Modified from North American Palladium). Note that the samples are projected to surface and form a SW-NE trend. The samples are hosted in the different lithological units.

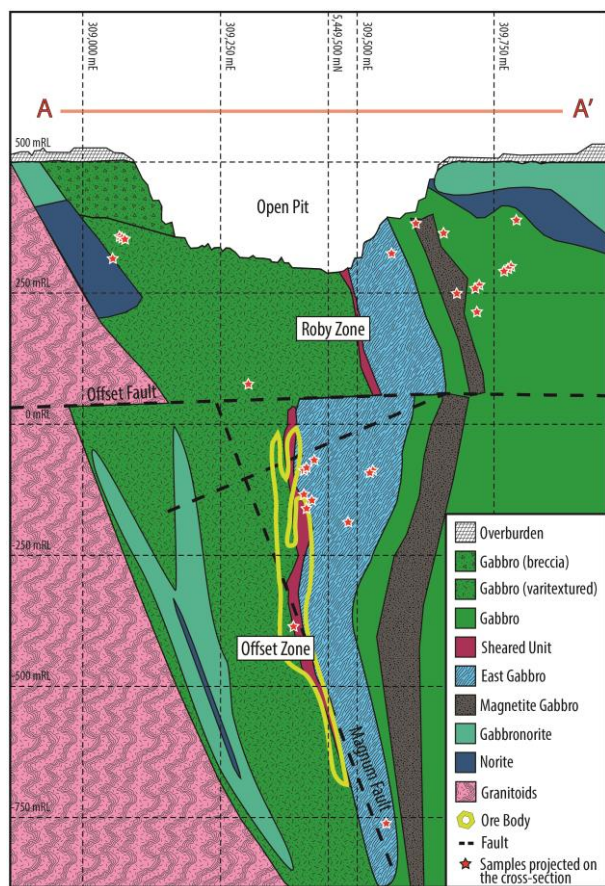


Figure 2. Idealized cross-section of the Mine Block Intrusion of the Lac-des-Iles complex with projected location of samples from drill cores (Modified from North American Palladium). Note that sulphides sampled from the open pit and from Baker zone are not plotted on the cross-section.

3 Petrography

The ore mineral assemblage is mainly composed of pyrrhotite (Po), pentlandite (Pn), pyrite (Py) and magnetite (Mt) with minor amounts of chalcocopyrite (Ccp), ilmenite and discrete PGM up to 100 μm diameter. Most of the PGM are either included in sulphides, or along sulphide-silicate and sulphide-sulphide grain boundaries. Only few of them are included in silicates.

Based on modal proportions, the massive sulphides can be divided into 5 assemblages: i) Po + Pn + minor Py (< 10%) \pm Ccp (Fig. 3a). This assemblage exhibits magmatic textures. Pyrrhotite forms large anhedral crystals surrounded by granular polycrystalline veinlets of Pn. Pentlandite also occurs as exsolution flames in Po; ii) Po + Pn + Py (> 10%) \pm Ccp (Fig. 3b). This assemblage still shows magmatic texture, but the amount of Py present is too high for an igneous assemblage. Pyrite textures vary from subhedral to anhedral individual grains or polycrystalline aggregates. In some rare cases Py occurs as small veins; iii) Py (>50%) + Po + Pn \pm Ccp (Fig. 3c); iv) Mt (>30%) + Py (>10%) + Po + Pn \pm Ccp (Fig. 3d); v) Ccp (>50%) found at the edges of the pods (Fig. 3e). All of the assemblages except v) contains too little Ccp to represent sulphide liquid. Assemblages i) and ii) could represent sulphide cumulates and assemblage v) the fractionated liquid. Assemblages iii) and iv) could be extremely altered sulphide cumulates or they could precipitate from late-magmatic fluids.

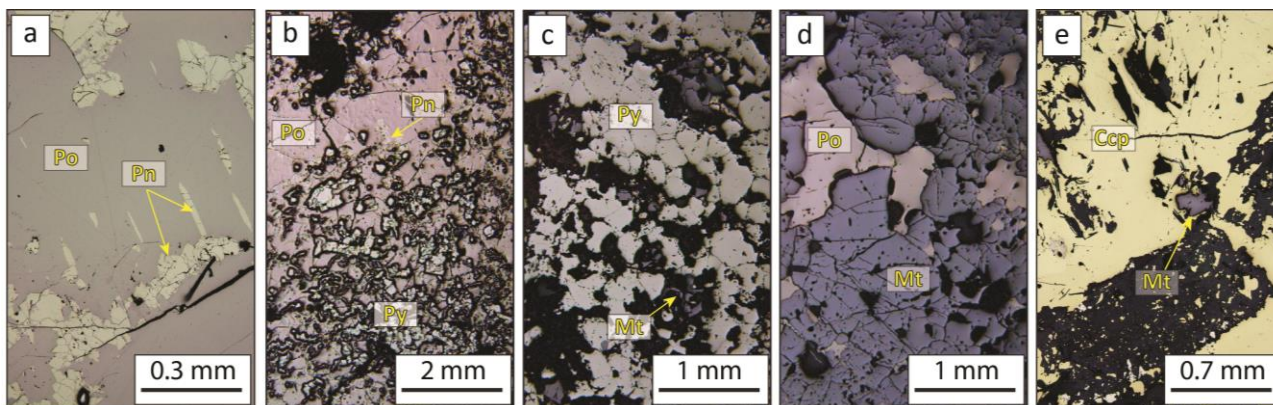


Figure 3. Photomicrographs of the different sulphide assemblages from LDI in reflected light. a) Assemblage i) showing magmatic textures; b) Assemblage ii) where magmatic textures still remain but with considerable amount of Py; c-d) Respectively assemblages iii) and iv) correspond to the most altered samples. Magmatic textures are almost lost and Py and/or Mt are the major phases; e) Assemblage v) where Ccp is the major phase.

4 Geochemistry

4.1 Relationship among the assemblages

Based on the behaviour of relatively immobile elements such as Ir and Rh, we do not think that assemblages iii) and iv) represent hydrothermal deposits. These elements fall on a single trend which includes the disseminated sulphides from the mineralized zones and the sulphide-rich assemblages (Fig. 4).

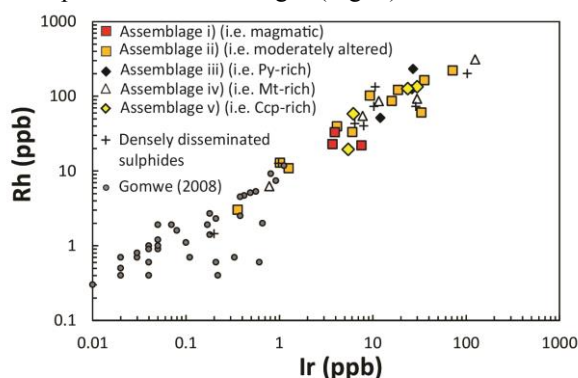


Figure 4. Bivariate plot of whole rock Ir (ppb) versus whole rock Rh (ppb). Values of disseminated sulphides (small circles) from mineralized zones are taken from Gomwe (2008).

Assuming that assemblages ii) to iv) represent altered magmatic sulphides the presence of excess Py and Mt in assemblages ii) to iv) requires either that S has been added or that Fe has been lost from the sulphide assemblage.

In igneous sulphides the molecular proportions of S to Fe + Cu + Ni is approximately 1. Most of the samples including those of assemblage iii) and iv) plot close to the igneous line (Fig. 5). This suggests that for most of the samples, neither S nor Fe has been mobile. The positive correlations between S and Se and S and Ni, combined with S/Se ratios in the mantle range, also suggest that S was not mobile (Fig. 6a,b).

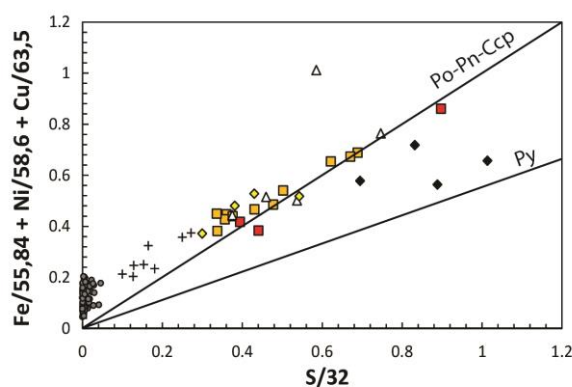


Figure 5. Bivariate plot of molecular proportions of S versus Fe + Ni + Cu. Values of disseminated sulphides (small circles) from mineralized zones are taken from Gomwe (2008).

In order to account for the excess of Py and Mt in assemblages ii) to iv), we suggest that Po was oxidized resulting in the reaction: $Po + O_2 = Py + Mt$. Thus neither Fe nor S was mobile and assemblages i) to iv) represent sulphides which have been partly oxidized during late-magmatic alteration.

On a plot of S versus Cu (Fig. 6c) the samples show a good correlation until approximately 5% S. After that the samples plot on either side of the trend, with the Ccp-rich samples above the trend. This could be because the Ccp-rich samples represent the fractionated liquid complementary to the sulphide cumulate. However this does not appear to be the case because the fractionated liquid should be enriched in Pd and yet the Ccp-rich samples have similar values to the other massive sulphide samples (Fig. 6d). This suggests that the Ccp-rich samples either represent intermediate solid solution cumulates, and the most fractionated liquid has migrated away from the massive sulphide pods. Alternatively Ccp was originally present with Po and Pn in the center of the pods, and has been remobilized to the edges. At present we favour the remobilization because all the massive sulphides have very high Pd/Ir and Pd/Pt ratios (1000-10000; 10-20) which is contrary to the general observation that sulphide cumulates are depleted in Pd.

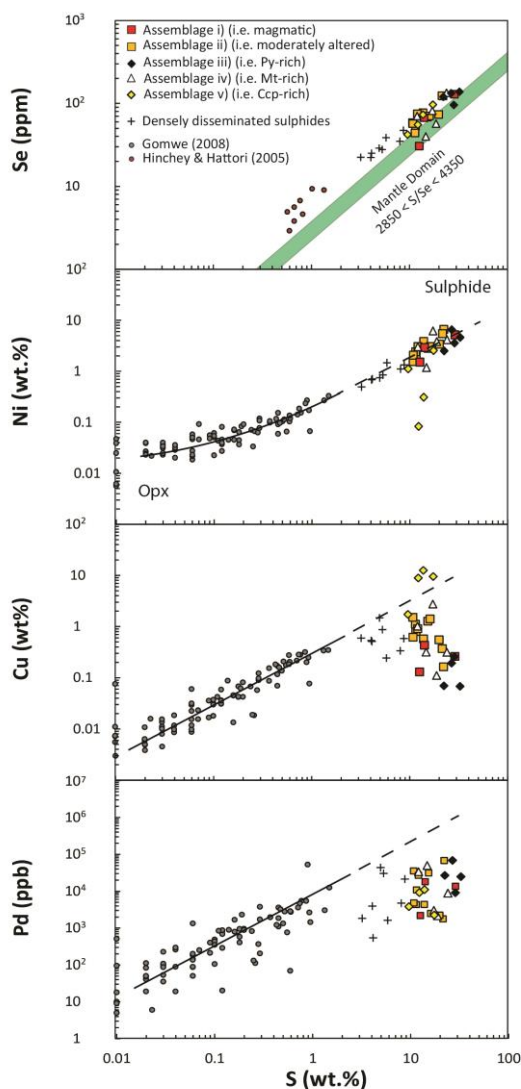


Figure 6. Bivariate plots of whole rock S (wt %) versus whole rock Ni (wt. %), Se (ppm), Cu (wt. %), and Pd (ppb). Values of disseminated sulfides are taken from Gomwe (2008) and Hinchey and Hattori (2005).

4.2 Relationship between massive and disseminated sulphides

If we consider only S, Ni and Se and allow that Cu has been remobilized on the centimeter scale, then it is possible to argue that because the compositions of massive and disseminated sulphides are co-linear, the sulphide component of all the samples represents a sulphide liquid. But when we consider the plot of Pd versus S (Fig. 6d) it is clear that the massive sulphides are depleted in Pd in comparison with the disseminated sulphides. Therefore it cannot be the same liquid.

5 Discussion

Although the position of the sulphides within the complex and their late-magmatic mineralogy could make us think that sulphides might have formed by precipitation from an aqueous fluid circulating through structures within the intrusion, the presence of typical magmatic textures and the geochemical signature of massive sulphides demonstrate their magmatic origin.

Indeed the typical magmatic textures would not have been formed by fluids.

Our model suggests that late in the solidification of the Mine Block intrusion magmatic sulphide liquid was injected from a feeder chamber along structures related to regional crustal movements. Movement along the structures separated the sulphide liquid into pods. The liquid crystallized as Po-Pn-Ccp and PGM.

Deformation or fluid action caused the Ccp to migrate to the edges of the pods and thus forming Ccp-rich and Ccp-poor sulphide assemblages. Oxidation of Po led to the formation of Py and Mt, but does not appear to affect the metal content of the rocks.

6 Conclusions

We propose that: 1) Sulphide liquid accumulated in embayments of a magmatic conduit. 2) This sulphide liquid has been squeezed through dilatencies in consolidated silicate magma and accumulated as massive sulphides across the stratigraphy. 3) The sulphide liquid formed MSS cumulates and a Cu-rich portion. 4) The massive sulphides are not related to the disseminated sulphides as they are poorer in Pd. 5) The primary sulphide assemblage has been altered to Py and Mt by oxidation. 6) This oxidation event did not affect the metal concentrations in the ores; in particular it did not up-grade the Pd because there is no relationship between the sulphide assemblages and the metal contents of the rocks.

Acknowledgements

We are grateful to North American Palladium for funding this project via the Canada Research Chair in Magmatic Ore Deposits Program. We thank the North American Palladium exploration team for technical support in the field and with modelling software. We thank Dany Savard for his assistance with geochemical analyses and Philippe Pagé and Sarah Dare for their constructive comments.

References

- Barnes S-J, Gomwe TS (2011) The Pd-deposits of the Lac-des-Iles Complex, north-western Ontario. Review in Economic Geology 17:351–370
- Djon MLN, Barnes S-J (2012) Changes in sulfide and platinum-group minerals with the degree of alteration in the Roby, Twilight, and High Grade Zones of the Lac des Iles Complex, Ontario, Canada. Mineralium Deposita 47:875–896
- Gomwe TS (2008) The formation of the palladium-rich Roby, Twilight and High-Grade zones of the Lac des Iles complex. Unpublished PhD Thesis, Université du Québec à Chicoutimi, 296 p
- Hinchey JG, Hattori KH, Lavigne MJ (2005) Geology, petrology, and controls on PGE mineralization of the southern Roby and Twilight zones, Lac des Iles mine, Canada. Economic Geology 100:43–61
- Hinchey JG, Hattori KH (2005) Magmatic mineralization and hydrothermal enrichment of the High Grade Zone at the Lac des Iles palladium mine, northern Ontario, Canada. Mineralium Deposita 40:13–23

Estimates of redox conditions and temperatures of closure of the olivine-spinel system in cumulate rocks of the Ioko-Dovyren layered intrusion

I.S. Fomin

Moscow State University, Vorobjevy Gory, 1, Moscow, Russia, Vernadsky Institute, Kosygin Str. 19, Moscow, Russia

G.S. Nikolaev

Vernadsky Institute, Kosygin Str. 19, Moscow, Russia

A.A. Ariskin

Vernadsky Institute, Kosygin Str. 19, Moscow, Russia

Abstract. A new Ol-Sp geothermometer and oxybarometer (Nikolaev et al. 2013) was applied to a set of the Ol-Sp pairs observed in ultramafics of the Ioko-Dovyren massif (the Ioko section). These calculations allowed us to reconstruct f_{O_2} variations through the lower half of the layered intrusion, providing f_{O_2} estimates around QFM (on average QFM+0.3). Systematic deviations of the calculated f_{O_2} towards much reduced conditions (on average QFM-2.5) in the bottom zone of the intrusion were revealed. The location of the “reduction zone” is correlated with accumulation of sulfides in basal feldspathic dunites and lherzolites.

Keywords. Oxygen fugacity, olivine-spinel, thermometry, cumulate

1 Introduction

Estimates of f_{O_2} are of key importance in deciphering conditions of stability of oxide minerals and sulphide solubility in mafic magmas and derivative cumulates. Two main thermo-oxybarometers are commonly used, based on (1) magnetite-ilmenite and (2) olivine-spinel equilibrium (O'Neill and Wall 1987; Ballhaus et al 1991). Often, the Ol-Sp oxybarometers are the only source of information on redox conditions, particularly when applied to mantle xenoliths and cumulate rocks from layered intrusions. The main problem of application of earlier calibrated Ol-Sp f_{O_2} -barometers to mafic-ultramafic complexes is their calibration database including experiments carried out at high-pressures and close to water-saturated conditions. This raises a question on the accuracy of these models at low water contents and relatively low pressures typical of many intrusions. In our recent work we performed a thorough test of the Ballhaus et al (1991) oxybarometer (hereafter referred to as the BBG-model) based on independent data including both 1 atm and high pressure (up to 20 kbar) experiments (Nikolaev et al 2013). Our results indicate that the BBG-model provides realistic values of f_{O_2} at $P > 10$ kbar and $\log f_{O_2} > \text{QFM}-1.8$, however at low pressures it overestimates oxygen fugacity by 1-1.5 log units. To minimize these errors we have calibrated a new Ol-Sp f_{O_2} -barometer allowing for accurate low pressure calculations (Nikolaev et al 2013).

In this paper we present results of the application of this oxybarometer to cumulate rocks from a marginal part of the Ioko-Dovyren massif, Northern Transbaikalia, Russia (Ariskin et al 2009, 2013).

2 Structure of the Ioko section

The mountain Ioko represents the SW edge of the Ioko-Dovyren massif. Due to almost vertical dip the massif was sampled across the strike, from the lower to the upper contact. Contrary to the central part of the intrusion, there are no adcumulate dunites in this section (Ariskin et al 2013). From the base to the top, the succession includes plagioclase lherzolites and plagioclase-dunites (Ol+Chr, ~350 m) followed by troctolites (Ol+Pl+Chr, ~1000 m), Ol gabbro (Pl+Ol±Cpx±Chr, ~700 m), and Ol-free gabbro-norites (Pl+Cpx±Opx±Pig), Figure 1.

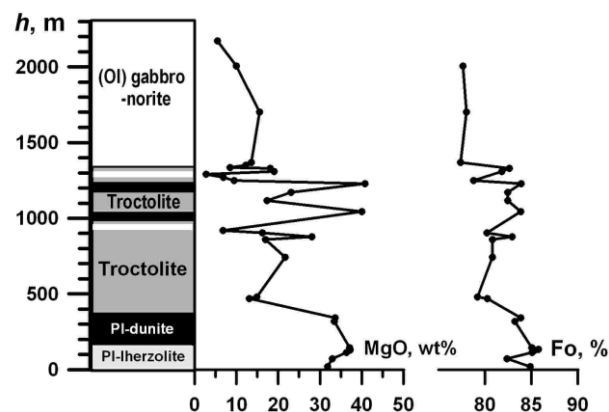


Figure 1. General structure of the Ioko section, showing variation in whole rock MgO content and Fo content in Olivine.

There are two reasons to apply the new Ol-Sp f_{O_2} -barometer to the Ioko cumulates. First, independent estimates argue for a low pressure emplacement? and crystallization of virtually “anhydrous” parental magmas ($P < 1$ kbar, Ariskin et al 2009). Second, the remarkable freshness of the Ol-rich cumulates, allowing for estimates of the original olivine and Cr-spinel compositions (Figure 2).

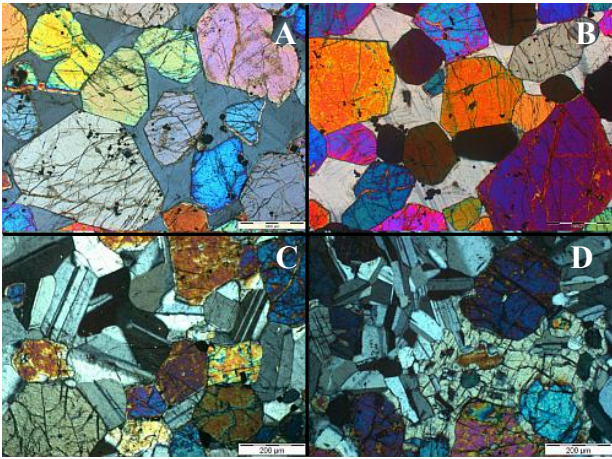


Figure 2. Photomicrographs of Pl-bearing dunites (AB), leuco-troctolite (C), and olivine gabbronorite (D).

3 The effect of sub-solidus re-equilibration

A major problem in the application of the Ol-Sp f_{O_2} -barometers to mineral assemblages is re-equilibration of both Ol and Sp during sub-solidus cooling. This is particularly important for small spinel inclusions in olivine which can easily exchange Fe^{2+} and Mg^{2+} with the hosting mineral. Figure 3A clearly demonstrates this exchange, when naturally observed spinel compositions from the Ioko samples are compared with those obtained in experimental studies at 1 atm pressure.

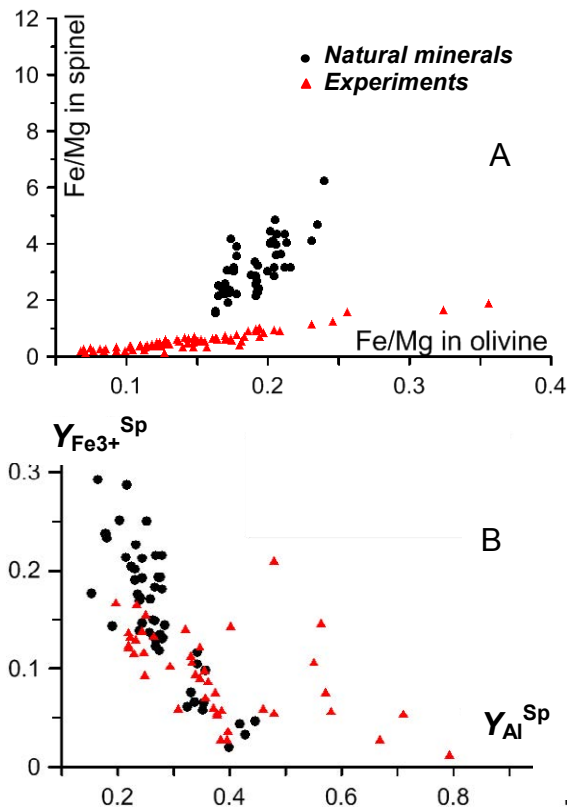


Figure 3. Compositions of Ol-Sp pairs coexisting in the Ioko-Dovyren samples and spinels obtained in 1 atm experiments.

The natural compositions display a much more abrupt trend of $(Fe^{2+}/Mg)_{Sp}$ vs $(Fe^{2+}/Mg)_{Ol}$ than that obtained in the experiments. This is because of the Fe-Mg cation exchange during the post-entrapment cooling within the closed Ol-Sp systems. So Fe^{2+}/Mg ratios in spinel were recalculated according to coexisting olivine. Quantity Note that comparison of the observed and experimental relationship of $Y_{Fe^{3+}}$ vs Y_{Al} in Sp in Figure 3B indicates the absence of an essential re-equilibration of spinels, if R^{3+} -cations are considered. This is an important observation, because the Ol-Sp f_{O_2} -barometer proposed by Nikolaev et al. (2013) includes the ΔQFM value calibrated as a polynomial function of $Fe^{2+}/(Mg+Fe^{2+})$ in Ol, $Fe^{2+}/(Mg+Fe^{2+})$ in Sp, $Fe^{3+}/\Sigma R^{3+}$, and $Al^{3+}/\Sigma R^{3+}$ in spinels, with the $Fe^{3+}/\Sigma R^{3+}$ parameter being the most sensible to the f_{O_2} -variations. Thus, to obtain accurate estimates of redox-conditions controlling the Ol-Sp equilibrium in Ol cumulates, in addition to mineral compositions knowledge of the final (closure) equilibrium temperature for each sample is required.

4 Ol-Sp geothermometry and related f_{O_2} estimates

To approximate the “closure” temperatures, we used an empirical geothermometer calibrated on 52 Ol and Sp experimental compositions obtained in the temperature range 1150-1400°C at 1 atm (40 runs) and 10-20 kbar (12 runs):

$$1000/T(K) = -0.2358 \frac{X_{Mg}^{Sp}}{X_{Fe}^{Ol}} - 0.1458 mg\#(Sp) + 0.1283 Y_{Al}^{Sp} - 0.0040P + 0.7877, \quad (1)$$

where X_{Mg}^{Ol} and X_{Mg}^{Sp} are the molar concentrations of Mg in olivine and spinel, $mg\#(Sp) = X_{Mg}^{Sp} / (X_{Mg}^{Sp} + X_{Fe^{2+}}^{Sp})$, Y_{Al}^{Sp} is $Al/(Al+Fe^{3+}+Cr)$ in spinel (at%), P is the pressure in kbar. Average accuracy of this equation for the used experimental dataset is 14.8K. Experimental data used are from Grove and Bryan (1983); Kohut and Nielsen (2003); Tormey et al. (1987); Murck and Campbell (1986); Thy (1991, 1995); Thy et al. (1991); Ringwood (1976); Gudfinnsson and Presnall (2000).

We applied the geothermometer to a data set of 47 Cr-spinel and host-olivine compositions, from 14 samples representing the lower half of the Ioko section where Sp in Ol is present. Based on the calculated temperatures, f_{O_2} values for each mineral pair were calculated (Figure 4). For comparison, results for the BBG and a modified BBG model (Pushkarev et al. 2004) are also presented. Note that the approach of Ballhaus et al. predicts systematically lower Ol-Sp “closure” temperatures of 600÷800°C than the model of Pushkarev (940÷1125°C) and our model (1205÷1280°C). In general, our model predicts lower f_{O_2} , ranging around QFM+0,5, with several deviations corresponding to $\Delta QFM < -2$.

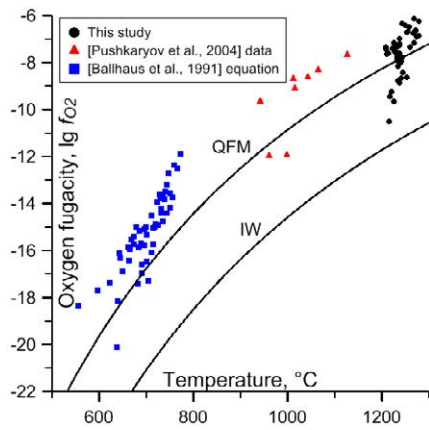


Figure 4. $\log f_{O_2}$ vs “closure” temperatures calculated for the Ioko cumulates, using previous (BBG, Pushkarev et al 2004) and presently proposed geothermo-oxybarometers.

5 Vertical variations of the modelled f_{O_2}

Vertical variations of the average calculated f_{O_2} values through the sampled Ioko section are shown in Figure 5. In addition, changes in the average $Y_{Fe^{3+}}^{Sp}$ for each sample, and bulk S contents in the rocks are given. It is evident that the most “oxidized” samples with the highest $Y_{Fe^{3+}}^{Sp}$ are observed near the bottom of the intrusion. This might be interpreted as a result of wall rock contamination. However, the most intriguing result of these calculations is the fact that the minimum of ΔQFM occurs exactly at the boundary between PI-dunites and PI-lherzolites, 170 m above the lower intrusive contact. This suggests an abrupt reduction of the cumulate system, a model that is supported by the lowest $Y_{Fe^{3+}}^{Sp}$ in spinels. At this stage, both the reason and the main factor of this reduction are unclear.

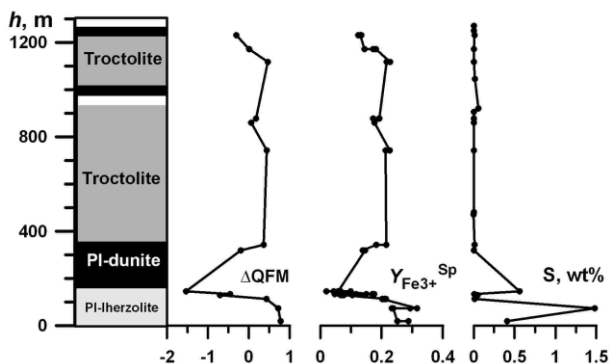


Figure 5. Variations of the calculated ΔQFM values, $Y_{Fe^{3+}}^{Sp}$, and the bulk S content in the rocks through the lower half of the Ioko section.

Another interesting result is that the revealed zone of reduction is correlated with the occurrence of sulfides accumulated near the bottom of the magma chamber, as indicated by the presence of taxitic to net-textured S-enriched PI-dunites and PI-lherzolites, as well as elevated Cu and S contents in the bottom zone. We propose that primary appearance of the immiscible

sulphide liquids could take place at higher levels at late stages of solidification of the troctolite and PI-dunite cumulate piles. Subsequently, these sulfides percolated downward through the porous cumulates (Ariskin et al. 2013), into the reduced zone of the PI-dunites (Fig. 5).

Acknowledgements

This research was supported by the Russian Foundation for Basic Research (project 11-05-00268a).

References

- Ariskin AA, Konnikov EG, Danyushevsky LV, Kislov EV et al (2009) The Dovyren Intrusive Complex: problems of petrology and Ni sulfide mineralization. *Geochem Intern* 47: 425–453.
- Ariskin AA, Danyushevsky LV, McNeill AW et al (2013) The Ioko-Dovyren layered massif (Southern Siberia, Russia): fingerprints of open magma chamber and compaction of original cumulates conjugated with sulphide percolation process: this volume.
- Ballhaus C, Berry RF, Green DH (1991) High pressure experimental calibration of the olivine-orthopyroxene-spinel oxygen geobarometer: implications for the oxidation state of the upper mantle. *Contrib Mineral Petrol* 107: 27–40.
- Grove TL, Bryan WB (1983) Fractionation of pyroxene-phyric MORB at low pressure: an experimental study. *Contrib Mineral Petrol* 84(4): 293–309.
- Gudfinnsson GH, Presnall DC (2000) Melting behaviour of model lherzolite in the system CaO-MgO-Al₂O₃-SiO₂-FeO at 0.7–2.8 Gpa. *J Petrol* 41(8): 1241–1269.
- Kohut EJ, Nielsen RL (2003) Low-pressure phase equilibria of anhydrous anorthite-bearing mafic magmas. *Geochem Geophys Geosyst* 4(7): 1057.
- Murck BW, Campbell IH (1986) The effects of temperature, oxygen fugacity and melt composition on the behaviour of chromium in basic and ultrabasic melts. *Geochim Cosmochim Acta* 50(9): 1871–1887.
- Nikolaev GS, Ariskin AA, Barmina GS, Almeev RR, Fomin IS (2013) Testing and recalibration of the olivine-spinel Ballhaus-Berry-Green's f_{O_2} -geo-barometer. *Geochem Intern*: in press.
- O'Neill HStC, Wall VJ (1987) The olivine-ortho-pyroxene-spinel oxygen geobarometer, the nickel precipitation curve, and the oxygen fugacity of the Earth's upper mantle. *J Petrol* 28:1169–1191.
- Pushkarev EV, Votyakov SL, Chashchukhin IS, Kislov EV (2004) Olivine-chromspinel oxythermobarometry of ultramafic rocks of the Ioko–Dovyren layered massif. *Doklady Earth Sciences* 395: 266–273.
- Ringwood AE (1976) Limits on the bulk composition of the Moon. *Icarus* 28(3): 325–349
- Thy P (1991) High and low pressure phase equilibria of a mildly alkalic lava from the 1965 Surtsey eruption: Experimental results. *Lithos* 26: 223–243
- Thy P (1995) Low-pressure experimental constraints on the evolution of komatiites. *J Petrol* 36(6): 1529–1548
- Thy P, Lofgren GE, Imsland P (1991) Melting relations and the evolution of the Jan Mayen magma system. *J Petrol* 32(2), 303–332
- Tormey DR, Grove TL, Bryan WB (1987) Experimental petrology of normal MORB near the Kane Fracture Zone: 22°–25°N, Mid-Atlantic Ridge. *Contrib Mineral Petrol* 96(2): 121–139.

Olivine cumulates: Centrifuge experiments on the processes and time of formation

Mélanie Forien

*Institut für Geowissenschaften, Universität Frankfurt/Main, Altenhöferalle 1, 60438 Frankfurt/Main, Germany
Now at: Département des Sciences de la Terre, Université du Québec à Chicoutimi, Chicoutimi, G7H 2B1, Canada*

Nick Bagdassarov

Institut für Geowissenschaften, Universität Frankfurt/Main, Altenhöferalle 1, 60438 Frankfurt/Main, Germany

Max W. Schmidt

Institut für Mineralogie und Petrographie, ETH Zurich, Clausiusstrasse 25, 8092 Zürich, Switzerland

Guilio Solferino

Department of Earth Science, St. Francis Xavier University, Antigonish, B2G 2W5, Canada

Abstract. A series of crystal settling experiments in a system composed of 33 vol.% olivine + 67 vol.% basaltic melt was conducted to elucidate the formation mechanisms of gravitational cumulates. Experiments were conducted in a centrifuging piston cylinder at 200-1500 g, 1270-1280°C, and 0.8-1.1 GPa. The mechanical settling of the concentrated olivine suspension occurred at about 1/6 the speed of Stokes settling velocity. The porosity for these orthocumulates (formed by gravitational settling of the crystals) is about 54 vol.%. The time of formation of the olivine orthocumulate was evaluated at 0.1-10 m day⁻¹. A further degree of compaction was achieved mainly due to pressure-dissolution mechanism at olivine grain contacts as shown by a detailed study of fine crystal structure of olivine grains. Olivine reprecipitated in the intragranular space between olivine grains and expelled the residual melt. With the increase of centrifugation up to 400 g over 50 h, we achieved porosities (ϕ) as low as 31 %. The olivine content on the bottom of the gravitational cumulate can be described as $1-\phi \sim \log(\Delta\rho \cdot d \cdot a \cdot t)$, where $\Delta\rho$ is the density difference between crystals and melt, d the crystal layer thickness, a the acceleration, and t the time of centrifuging. The time formation in the case of olivine adcumulates has been calculated to 0.4-2 years.

Keywords. Gravitational cumulates, grain settling, chemical compaction, centrifuge experiments

1 Introduction

Cumulates are produced by precipitation of crystals during fractional crystallization processes in magma chambers or sills. They are formed by accumulation of crystals on the floor of a magma chamber due to density contrast between the silicate minerals and lighter mafic to ultramafic melt. The formation of these cumulates is still actively debated in spite of the numerous investigations over the years from field data (Wager et al. 1960; Holness et al. 2005), analogue experiments (Schwindinger 1999), and numerical modeling (Akatsuka et al. 1999; Hoshida et al. 2006; Tory and Pickard 1977, 1986).

Cumulates are defined according to their texture. For example, orthocumulates are cumulate rocks where the grains are barely in contact and a residual melt fraction has crystallized between them. They are the result of

pure mechanical settling of the grains. Their porosity corresponds to the maximum close packing depending of the grain shapes constituting the cumulate. In general a porosity of ~ 60% is observed in various types of orthocumulates. In contrast, adcumulates are characterized by a smaller melt fraction crystallized between grains; hence their porosity is significantly lower than 60%. Their formation mechanism is still not well understood, but densification of the orthocumulates by a process such as chemical compaction is most likely.

To study compaction, both mechanical and chemical, we have experimentally formed cumulate layers of olivine from a suspension in a basaltic melt using a centrifugal piston cylinder. This allowed us to evaluate the mechanisms and formation time of ortho- and adcumulates (Schmidt et al. 2012).

2 Experimental and analytical techniques

The starting material was a mixture of synthetic simplified MORB glass powder and olivine grains (67 vol.% and 33 vol.%, respectively). The olivine grain size was ca. 1.8 μm . The piston cylinder was first used to obtain chemical equilibration between melt and crystals in static conditions. All experiments were carried out at 1250°C under a pressure of 10 kbar.

A centrifuging piston cylinder was then used to accelerate the separation of melt and crystals by density contrast at the melting temperature of basalt (1270-1280°C) under a pressure between 0.8-1.1 GPa. The experiments were centrifuges for desired amount of time (1-50h) and gravity acceleration (200-1500g, where g is the Earth's gravity).

Finally, the last step is the analytical part of the samples. The samples were cut and back scattered images taken with SEM in order to determine the crystal size distribution. The crystal pile is cut and sliced in several segments perpendicular to the capsule axis in order to calculate the abundance of melt among the olivine cumulates.

3 Results

The crystal size distribution, after 24h in piston cylinder in static conditions, is homogeneous (Fig. 1). The average grain size is ca. 13.1 μm (+/- 2.5) and the melt abundance is 65.9 vol.% (+/- 2.1). In comparison with the starting material (grain size of 1.8 μm and melt abundance of 67 vol.%), the small difference in olivine grain size is explained by the temperature dependence of olivine solubility in our starting basalt melt slightly oversaturated at 1270°C.

After centrifuging, all of the crystals form a single olivine layer at the bottom of the capsule leaving a crystal-free layer of melt at the top of the capsule (Fig. 2). Porosity profiles through the olivine layer are shown in Fig. 3.

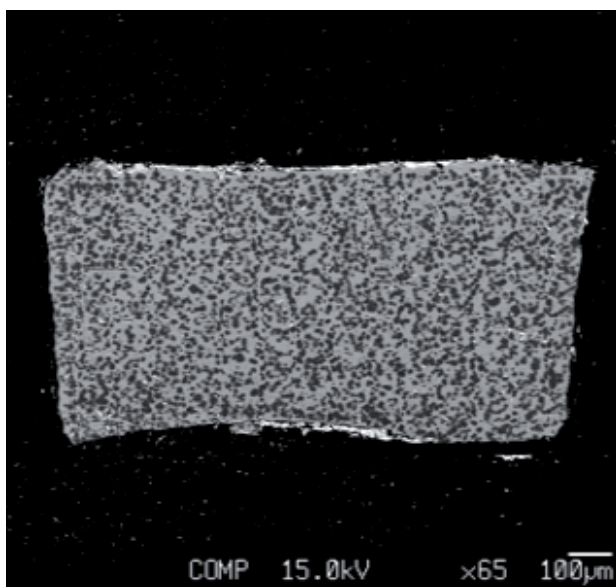


Figure 1. Backscattered electron image of experiment OB-14 (1g, 24h) before centrifuging. The dark phase is olivine grains and light grey is basaltic melt. The black phase is the graphite capsule.

For each experiment, the total force applied to the bottom olivine layer is proportional to:

$$\Delta\rho^{(olivine-basalt)} \cdot h \cdot a \cdot t \quad (1)$$

where $\Delta\rho^{(olivine-basalt)}$ is the density contrast between crystals and melt (in kg/m^3), h the thickness of the olivine layer in the lowermost segment (in m), a the experimental acceleration (in m/s^2), and t time over which the centrifuge acceleration (in s) is applied. Equation (1) is equivalent to $\Delta\rho^{(olivine-basalt)} \cdot h \cdot a \cdot t$ is equivalent to pressure multiplied by time.

The examination of crystal content and crystal distribution within the cumulate layer led to three observations:

1. The average porosity and porosity in any segment of the basal olivine layer increases when the value of $\Delta\rho^{(olivine-basalt)} \cdot h \cdot a \cdot t$ decreases (Fig. 2). In an aggregate of equidimensional spheres, the melt phase is about 37%, and after settling of olivine only (without centrifuging), the melt fraction is about 52%.
2. In each experiment, the melt abundance in the lower 2/3rds of the olivine layer decreases (Fig. 3).

3. On the polished sections, the number of crystals in contact increases with an increasing acceleration (Fig. 5). So, if two crystals touch, then the value of $\Delta\rho^{(olivine-basalt)} \cdot h \cdot a \cdot t$ increases (Fig. 4).

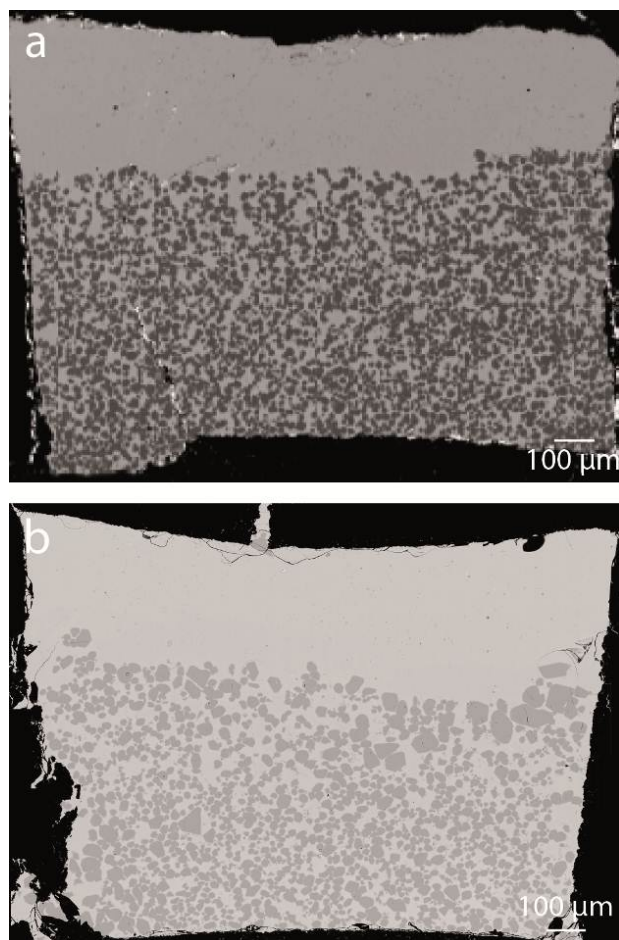


Figure 2. Backscattered electron images of two centrifuged experiments a. ZOB6 (200g, 3h), b. ZOB9 (200g, 1h). As in Figure 1, olivine grains are in dark grey, basaltic melt in light grey and graphite capsule in black.

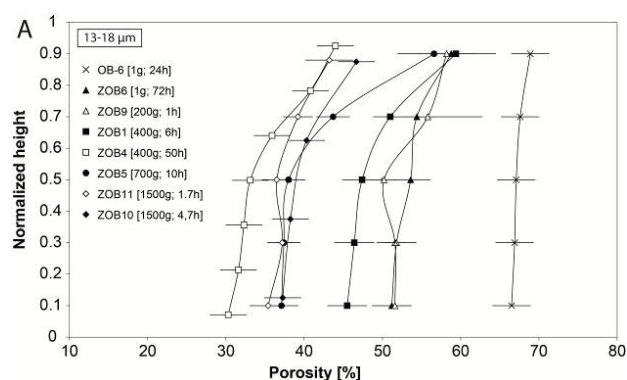


Figure 3. Porosity (vol. %) profiles plotted against the normalized total height of crystal cumulate layers of the experiments.

4 Discussion

Settling velocity of olivine grains in a basaltic melt layer is given by the Stokes' settling velocity (V_s – Stokes 1851):

$$V_s = \frac{1}{18} \frac{d^2 \Delta \rho (n \cdot g)}{\mu} \quad (2)$$

where d is the grain size (13.1 μm), $\Delta \rho$ is the density contrast between solid and liquid (420 kg/m^3), $n \cdot g$ the (vertical) acceleration of the system and μ the calculated liquid viscosity (17 Pa.s - Bottinga et Weill 1972), hence $V_{\text{Stokes}} = 2.31(74) \cdot 10^{-9}$ m/s at 1g. Experimentally, we obtained a settling velocity of $4.17(42) \cdot 10^{-10}$ m/s at 1g. Hence, $V_{\text{suspension}} = 1/7 V_{\text{Stokes}}$ for 33 vol. % of olivine, which is in agreement with the speed of 0.1 Vs observed by Schwindinger (1999) in a suspension of 35 vol. % clay prisms settling in a viscous liquid and where the shape of clay prisms is similar to the olivine grains.

However, in concentrated suspension, the settling velocity becomes slower or faster than the predicted Stoke's velocity. This "hindered" settling velocity $V(\varphi_c)$ is then calculated from the following equation (Tomkins et al. 2005):

$$V(\varphi_c) = V_s \cdot (1 - \varphi_c)^n \quad (3)$$

where φ_c is the crystal fraction and n is the sediment exponent. In the experiments here, the sediment exponent observed is about $n \sim 4.1$

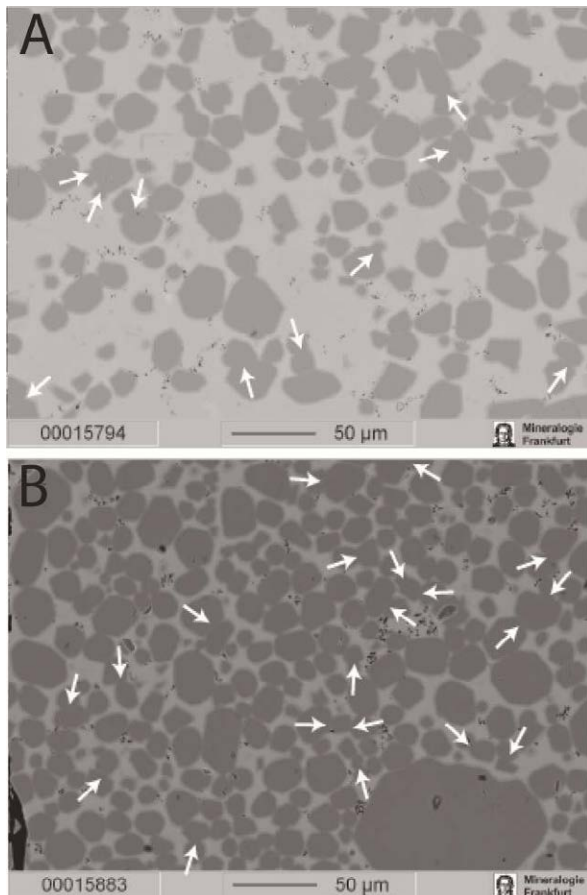


Figure 4. Backscattered electron images (BSE) showing the number of crystal contacts. The BSE images are situated between the middle and the bottom of their respective experiments. A. Experiment ZOB9 (1h; 200g). b. Experiment ZOB11 (1h40; 1500g). White arrows show the contacts where chemical compaction is noticeable.

After the crystals have reached a maximum compaction concentration due to the accelerated piling from above, their locations and porosity in cumulates changed under the influence of solution –

recrystallisation process. The concentration of crystals in a cumulate layer increased much slower than during their sedimentation.

Moreover, thanks to the technology of the focused ion beam (FIB), at the TEM laboratory at GFZ Potsdam, a detailed analysis of the fine structure of olivine (Ol) grain boundaries shows some new evidence of the precipitation – recrystallisation process:

- (1) Presence of Ca (which is characteristic only for MORB-melt) at the interface of two adjacent Ol-grains (Figs. 5a and b) even when the melt phase escaped.
- (2) Presence of some small melt inclusions at the growing or compacting Ol-grains (Fig. 5c).
- (3) New boundary between two Ol-grains is distinct but not fully crystallized indicating that some MORB melt elements (for example, Ca) prevent the recrystallization of Ol in a fully crystalline structure (Figs. 5d to f).

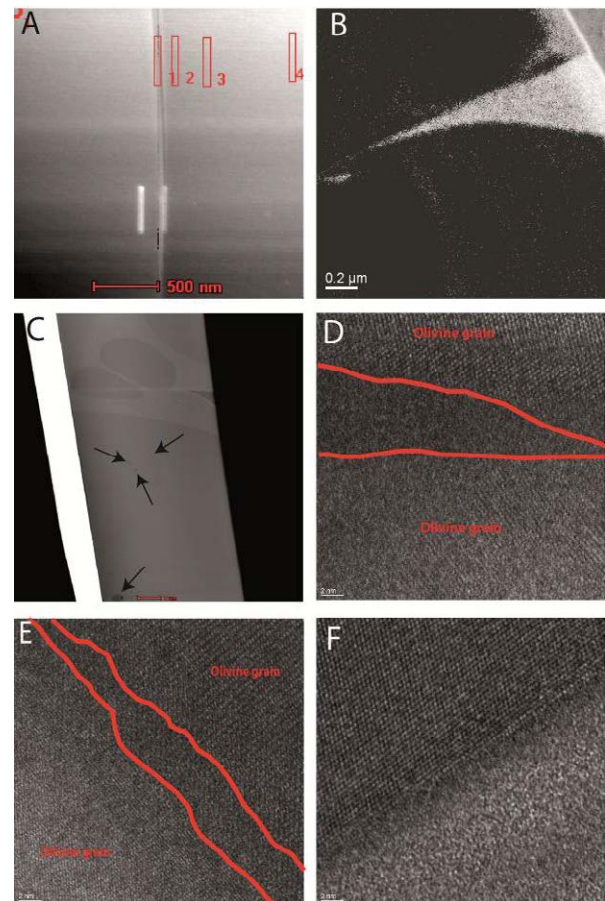


Figure 5. Fine structure of olivine (Ol) grain boundaries. A. Contact of two adjacent Ol-grains with analysis positions in ZOB10 sample. B. Overview of one grain boundary in sample ZOB10. The black arrows indicate the inclusions. C. Calcium map near triple junction between two grains and a melt pocket. White color indicates the calcium distribution. D and E. HREM images showing boundary between two olivines in samples ZOB10 and ZOB11, respectively. F. HREM image showing a boundary between melt (amorphous phase) and one olivine grain (crystallized phase) in sample ZOB10.

In nature, the pressure solution mechanism is proportional to the stresses exerting on crystal contacts. The forces acting on grain contacts are proportional to

the height of the olivine column above the measured section, the density contrast between melt and olivine and the centrifugal acceleration. This lithostatic pressure (P_p) for olivine grains in the basal segment is quantified via:

$$P_p = (1 - \varphi_m) \cdot \Delta\rho^{(olivine-basalt)} \cdot h \cdot a \quad (4)$$

where φ_m is the porosity, $\Delta\rho$ is the density contrast between crystals and melt (in kg/m^3), h the thickness of olivine layer (in m), a the gravity acceleration (in m/s^2).

5 Formation times

From Stoke's settling equation (Eq. 2), the settling time for orthocumulate formation can be calculated as:

$$t_{ortho} = (h \times 0.46 / \varphi_{ci} - h) / V(\varphi_c) \quad (5)$$

where h is the thickness of the uncompacted orthocumulate layer (in m), and $V(\varphi_c)$ the "hindered" stoke's settling (in m/s) calculated from equation (3). Factor 0.46 is the crystal fraction after gravitational settling and φ_{ci} is the initial crystal fraction in melt layer. To produce 1 meter of uncompacted crystal layer of olivine, the times of formation are 242, 39 and 10 hours for a grain size of 2, 5 and 10 mm, respectively. In the case of an initial crystal fraction of $\varphi_{ci} = 0.05$, these formation times become 52, 8.4 and 2.1h.

Resulting from the experiments, an equation describing the time dependence of the chemical compaction at a constant grain size has been used to calculate the meso- and adcumulate formation time. To scale for the grain size, a linear dependence was introduced as appropriate for a dissolution-precipitation process (Boudreau and McBirney 1997; Shimizu 1995; Neijmeijer et al 2009). The compaction time t_{adcum} (in s), that is the time to reduce the porosity from $\varphi_0=0.54$ to φ_m in the basal layer of cumulate, can be calculated as followed:

$$t_{adcum} = \left(\frac{1.803 \times 10^{10}}{100.1487^{\frac{\varphi_m}{\varphi_0}}} - 4.2123 \times 10^6 \right) \times \frac{1}{h_{cum} \cdot g \cdot \Delta\rho^{crystal-melt}} \cdot \frac{d}{d_0}$$

$$= \left(\frac{1.308 \times 10^{14}}{100.1487^{\frac{\varphi_m}{\varphi_0}}} - 3.0561 \times 10^{10} \right) \times \frac{d}{h_{cum} \cdot \Delta\rho^{crystal-melt}} \quad (6)$$

where d is the grain size (in m), d/d_0 is the grain size scaling factor with d_0 is $14.1 \mu\text{m}$ (from experiments), $\Delta\rho$ is the density contrast between crystals and melt (in kg/m^3), and g the Earth's gravity. To produce 1/2 meter of olivine cumulate, the adcumulate formation time with a residual porosity of 0.30 (from orthocumulate layer with an initial porosity of 0.54) are 0.37 - 1.9 years with a grain size of 2 - 10 μm , respectively.

6 Conclusions

From the centrifuging experiments, three conclusions can be highlighted:

- (1) The settling velocity for a dense suspension with an olivine fraction of 0.34 is fast ($1/6 V_{\text{Stokes}}$). For a 5 mm olivine grain size, the velocity will be 22 cm/h.
- (2) The maximum crystal fraction obtained from olivine grains by a pure mechanical process is 0.46 at most.
- (3) The mechanism of chemical compaction through pressure dissolution driven by the cumulate pile gravitational force is a possible mechanism if a linear grain size dependence is introduced as the limit of this process.

Moreover, the solution-precipitation and recrystallization process is a diffusion type mechanism of compaction and has not been addressed experimentally before.

Acknowledgments

We thank Canada Research Chair Magmatic Ore Deposits for the financial support allowing this work to be presented at the SGA conference.

References

- Akatsuka T, Obata M, Yokose H (1999) Formation of layered structure in the Murotomisaki gabbroic complex, especially picrite gabbro, Kochi prefecture, Japan - qualitative evaluation of crystal accumulation. *J. Geol. Soc. Japan* 105: 771-788 (in Japanese with English abstract).
- Bottinga Y, Weill D.F. (1972) The viscosity of magmatic silicate liquids: a model for calculation. *Am. J. Sci.* 272: 438-475
- Boudreau AE, McBirney AR (1997) The Skaergaard layered series. Part III. Non-dynamic layering. *J. Petrol.* 38: 1003-1020.
- Holness MB, Cheadle MJ, McKenzie D (2005) On the Use of Changes in Dihedral Angle to Decode Late-stage Textural Evolution in Cumulates. *J. Petrol.* 46 (8): 1565-1583.
- Hoshida T, Obata M, Akatsuka T (2006) Crystal settling and crystal growth of olivine in magmatic differentiation - the Murotomisaki Gabbroic Complex, Shikoku, Japan. *J. Mineral. Petrol. Sci.* 101: 223-239.
- Neijmeijer A, Elsworth D, Marone C (2009) Significant effect of grain size distribution on compaction rates in granular aggregates. *Earth Planet. Sci. Lett.* 284: 386 - 391
- Schmidt MW, Forien M, Solferino G, Bagdassarov N (2012) Settling and compaction of olivine in basaltic magmas: an experimental study on the time scales of cumulate formation. *Contrib. Mineral. Petrol.* 164 (6): 959-976
- Schwindinger KR (1999) Particle dynamics and aggregation of crystals in a magma chamber with application to Kilauea Iki olivines. *J. Volcanol. Geotherm. Res.* 88: 209-238.
- Shimizu L (1995) Kinetics of pressure solution creep in quartz. *Tectonophysics* 245: 121-134.
- Stokes GG (1851) On the effects of the internal friction on the motion pendulumus. *Camb. Phil. Soc. Trans.* 9 (2): 8-106.
- Tory EM, Pickard DK (1977) A three-parameter Markov model for sedimentation. *Can. J. Chem. Eng.* 55: 655-665.
- Tory EM, Pickard DK (1986) Experimental evidence for a stochastic approach to sedimentation. In: B.M. Moudgil, P. Somasundaran (Ed), *Flocculation, Sedimentation and Consolidation*. AIChE, NY, The Cloister, Sea Island, GA Jan 27-Feb 1, 1985, pp. 297-306.
- Wager LR, Brown GM, Wadsworth WJ (1960) Types of Igneous Cumulates. *J. Petrol.* 1: 73-85.

Reef disturbances of Critical Zone rocks of the eastern Bushveld Complex in the vicinity of the Steelpoort fault, South Africa – petrogenetic implications

C. Gauert, E. Kotzé, J.J. Beukes

Department of Geology, University of the Free State, Nelson-Mandela-Drive, Bloemfontein, R.S.A.

R.J. Giebel

Department of Geology, University of the Free State, Nelson-Mandela-Drive, Bloemfontein, R.S.A.;

Institut für Geologische Wissenschaften, Von-Seckendorff-Platz, Martin-Luther-Universität Halle-Wittenberg, Germany

Abstract. Critical Zone rocks from the MG and UG2 intervals and the Merensky cyclic unit of various sections of the eastern Bushveld complex were investigated in terms of mineralogy and geochemistry. Variations in thickness and texture of sections south and north of the Steelpoort fault zone were compared as well as the density of pegmatoidal pipe development. Approaching the Steelpoort fault from a southerly direction, the density of pegmatoids occurrence increases and the magmatic layering shows more disturbances. In the northern part of the Steelpoort fault zone, pegmatoid density is high but decreases distally to the zone. It is suggested that the post-intrusive fault formed along the position of a magma conduit. Late-stage iron-rich liquids exploited it, intruding the cumulate pile within and in proximity to the fault zone. Increased disturbance of the cumulus pile could have occurred by magma - floor rock interaction due to turbulent flow in the fault's/conduit's vicinity, together with changes in magma pressure, addition of volatiles by floor rock assimilation and degassing. The economic effect caused by the increased volatile situation is, that PGE grade in the vicinity of the fault zone decreases (Two Rivers Platinum Mine) or becomes very erratic (e.g. Rhodium reefs mine). Cumulate thickness variations, as noted in the vertical distance of UG-2 and Merensky reef in the northern sector of the eastern Bushveld with increasing distance from the fault zone, are caused by basement morphology induced compartmentalization. Cumulate facies changes in thickness and composition of UG-2 and MR units within lateral distances of 100s of meters at Two Rivers Platinum mine probably reflect changes in liquid line of descent, intensity of magma convection, pulses of replenishment, contamination and volatile content of the magma.

Keywords. Bushveld Complex, Critical Zone, Steelpoort fault, reef disturbances, PGEs

1 Introduction

Increased mining activities in the past ten years in the eastern Bushveld complex of north-eastern South Africa lately motivated mineralogical and geochemical studies of Critical Zone (CZ) rocks from the Middle group (MG) and Upper group (UG-2) intervals and the Merensky cyclic unit of various intersections. Variations in thickness and texture of sections south and north of the Steelpoort fault were compared as well as the density of pegmatoidal pipe development. MG chromitite layers in the eastern Bushveld at Thorncliffe, Tweefontein (Fig.1) were compared to the western Bushveld complex at Kroondal, revealing an indicated

PGE resource as by-product to chrome in those layers.

The transition from lower to upper Critical Zone is marked by first occurrence of cumulus plagioclase, probably indicating replenishment by lighter more Al- and Fe-rich magma, resulting in higher PGE contents of the LG-6 and -7 as well as MG-2 and -3 chromitites.

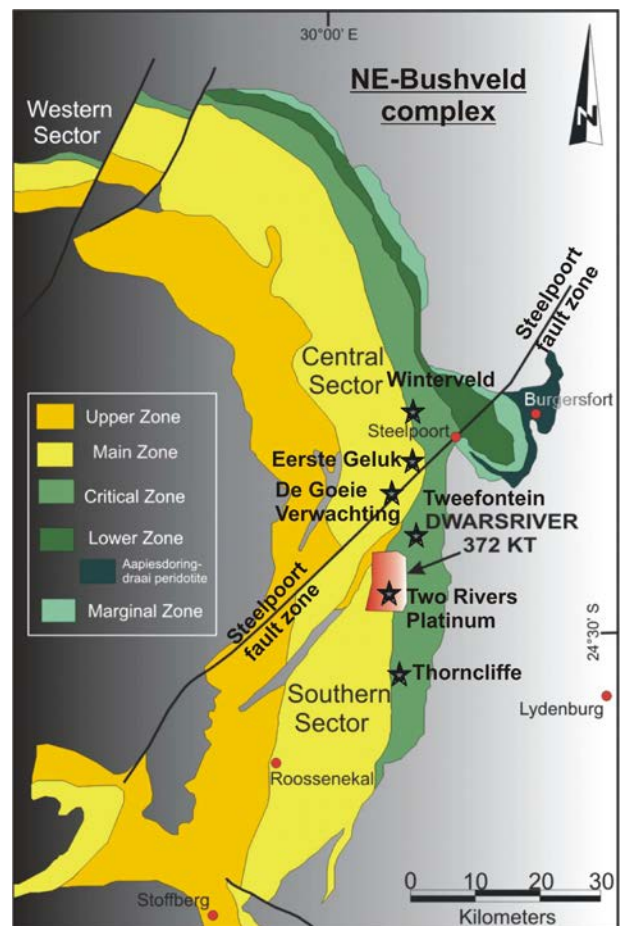


Figure 1. Geological map of the Eastern Bushveld, and prospect or mine drillcore sites of investigation

Studies were extended to the Merensky reef (MR) and UG-2 chromitite layers because of higher PGE contents and accessibility along strike and downdip by company drill cores. This allows for petrological studies of mineralogy in undisturbed and disturbed sections close to the fault.

This paper will discuss the effect of late stage fluids which exsolved during magma emplacement along feeder zones on the igneous layering and the PGE geochemistry during decompression and advanced

crystallization. The hypothesis of the role of highly differentiated iron-rich melts and/or fluids in igneous complexes for the natural concentration of PGE needs to be tested in ultramafic to mafic rocks of the upper CZ south, north of and within the Steelpoort fault zone. Approaching the Steelpoort fault zone from south along the parallel running Dwars River fault (Fig. 2), the density of pegmatoids occurrence increases and the magmatic layering shows more disturbances.

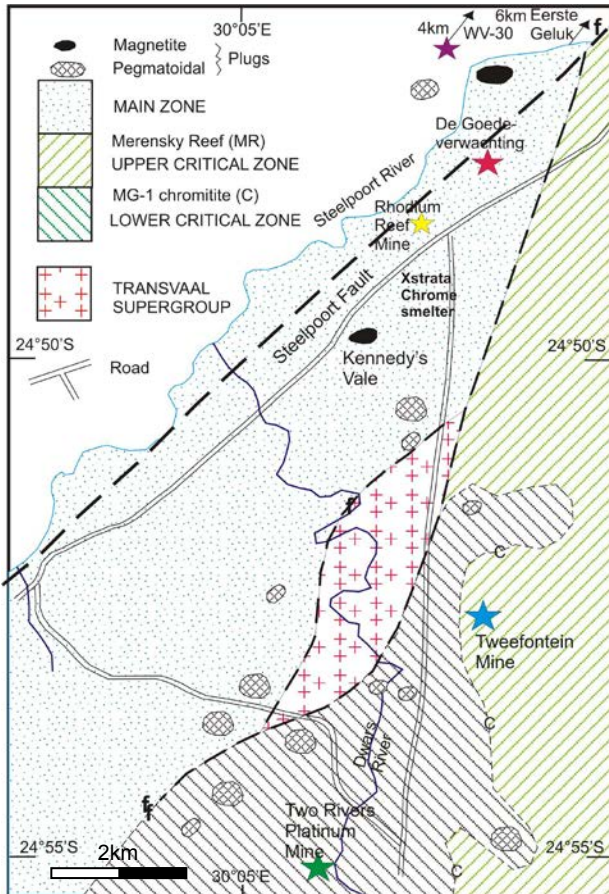


Figure 2. Geological map of the area south of the Steelpoort fault zone between Eastern Chrome, Tweefontein and Two River Platinum Mines.

Immediately north of the Steelpoort fault, pegmatoid density is higher but decreases distally to the fault. It is suggested that the fault acted as a conduit for late-stage iron-rich liquid intruding the cumulate pile especially within and in proximity to the fault zone. Disturbance of the cumulus pile could have occurred by magma - floor rock interaction due to turbulent flow in the fault's or conduit's vicinity, together with changes in magma pressure, addition of volatiles by floor rock assimilation and degassing (Viljoen and Reimold, 1999).

Facies changes in thickness and grade of UG2 and MR units within 100s of meters at Two Rivers Platinum (TRP), could reflect changes in liquid line of descent, intensity of magma convection, pulses of replenishment, contamination and volatile content of the magma.

The cumulate thickness between the UG2 and Merensky Reef decreases with increasing distance from the fault in the northern part of the eastern limb, coinciding with rapid changes in magma chamber bottom morphology. Therefore, compartmentalization of the northern sector, caused by basement up-doming,

influences the thickness of the igneous sequence.

The economic effect caused by the conduit structure is that PGE grade in vicinity of the fault zone decreases (TRP) or becomes very erratic (e.g. defunct Rhodium Reefs Mine, Fig. 2).

2 Petrogenetic processes and disturbance of igneous layering

Within the broad zonation, rocks display abrupt compositional changes, periodic reversals in differentiation trend, repetitive cycles of alternating rock types, layers ranging in thickness from a few cm's to hundred meters.

Lateral persistence of layering on macro scale is remarkable, but important local variations show that conditions were not uniform everywhere at any one time. Layering is thought to be a result of a combination of processes, including the addition of new magma at intervals, convection currents in the magma chamber, chemical contamination by assimilated wall rocks, changes in pressure or the dissolved gas content of the magma (Viljoen and Reimold, 1999).

The role of iron-rich ultramafic pegmatites (IRUPS) in disruption, replacement and redistribution of the PGM deposits is well known (Reid and Basson, 2002; Scoon and Mitchell, 1994). Such studies show the Main Zone (MZ) ultramafic pegmatites are more Mg-rich than the CZ pegmatites.

2.1 MR and UG-2 facies variations

Merensky reef facies variations at TRP are controlled by thickness, rock types and PGE distribution. MR facies types 1 and 3 are generally thicker and show a bi-modal PGE distribution, whereas facies type 2 and 4 are thinner but display a normal PGE distribution. Type 3 and 4 facies occur more distally to the fault zone in the south of the farm Dwars Rivier.

UG-2 facies at TRP are distinguished by the split character of the interlayers: The thickness of the internal pyroxenite and the distribution of the PGE vary, increasing in variability towards the fault zone in the west. Pot-shaped depressions form 'patches' of split reef (Fig.3).

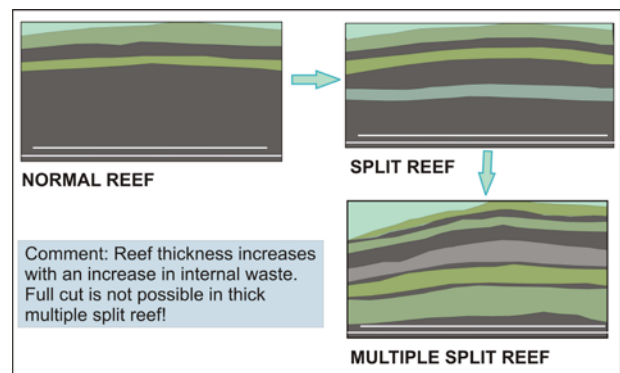


Figure 3. Schematic sketch of normal to split to multiple split reefs at Two Rivers Platinum on the Dwars river (modified after Cowell and Coetzee, 2011)

2.2 Pothole and IRUP frequency

Approaching the Steelpoort fault from south, the density of pothole occurrence and the iron-rich ultramafic pegmatitic rock frequency increases and the magmatic layering shows more disturbances (Fig. 2). Late-stage melts rich in volatiles intruding through the crystal mush could cause such reef disturbances (Reid and Basson, 2002; Scoon and Mitchell, 1994).

2.3 PGE distribution and patterns

The PGE distribution in UG-2 intersections of drillhole intersections on the farm De Goeie Verwachting in the centre of the Steelpoort fault zone (Fig. 2) show a Pd-Pt-Rh-dominated but relatively homogeneous pattern. Patterns are characterised by highly variable Au content and a range of single PGE concentrations of a maximum of one magnitude. Such moderate variance of PGE content could indicate the participation of hydrothermal processes during or shortly after the mineralisation event.

3 Effects of magmatic feeders and fault zones in modifying mineralization

Magmatic feeder channels are areas of dynamic magmatic environments and zones of magma replenishment. Such channels commonly exploiting fault zones are places of enhanced late-magmatic fluids activity. The fluids frequently modify magmatic layering, mineralisation and cause mineral alteration.

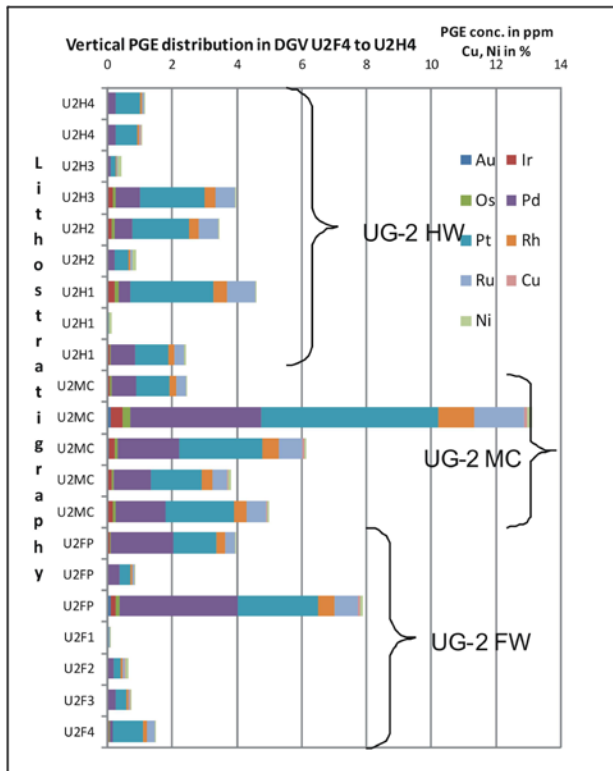


Figure 4. Total PGE abundances of the UG-2 chromitite unit of drill hole samples on the farm De Goeie Verwachting in the Steelpoort fault zone (U2F=foot wall, U2MC=massive chromitite, U2H=hanging wall)

Towards the Steelpoort fault an increase in split-reef development (TRP), and in pothole and increased IRUP development is recognised (Cowell and Coetzee, 2011). The economic implications were of such nature that some mines close to the area operate at variable and marginal grade, whereas in the approximately 5km wide fault zone, mining projects such as the former ‘Rhodium Reefs’ mine in the 1980s were unsuccessful. Under today’s conditions, the mineral resources of such projects appear to be feasible again (Hall and Montpellier, 2010).

3.1 PGE distribution patterns of the layered sequence in the fault zone

The PGE distribution pattern of MR and UG-2 samples from exploration drill holes from south (TRP) and north (Winterveld (WV), Eerste Geluk (EG) ; Fig. 2) of the Steelpoort fault are compared to data from the farm De Goeie Verwachting (DGV) within the fault zone with its discordant geological features (Fig. 2).

Total PGE abundance diagrams from DGV indicate the average values around 3ppm with highest values between 13 and 16 ppm for the main UG-2 chromitite layers (MC), and average values around 2 ppm in the UG-2 hanging and foot walls, respectively. The amount of Rh and Ru is significant. The FW however shows erratic values of total PGEs of up to 8ppm. Solar abundance normalised spiderplots of the MC samples show variation in total PGEs over a magnitude with ‘M’-shaped patterns on the side of Pd to Ru (Fig. 5), and with Pd and Rh dominating Pt in concentration.

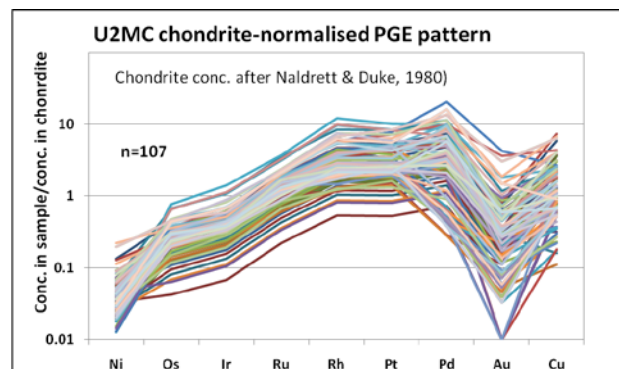


Figure 5. Solar abundance-normalised (Naldrett & Duke, 1980) PGE pattern of UG-2 massive chromitite from the farm De Goeie Verwachting in the Steelpoort fault zone

In a Pt+Pd+Rh versus Ru+Os+Ir variation diagram of samples from the entire DGV UG-2 chromitite interval a large part show ratios similar to the MG chromitite layers 2 and 4 of the NW-Bushveld complex (Teigler, 1990). All PGEs have a positively skewed distribution opposed to a normal distribution for Ni. In a Spearman correlation matrix the PGEs correlate very well with each other, reasonably well (r above +0.5) with Cu and not at all with Ni, indicating their non-occurrence in pentlandite.

3.2 Relationship between PGMs and volatiles

Discussing genetic aspects of these findings in the light of the Kinloch model (1982) the following is of importance: close to the gravity highs of the mafic part

of the Bushveld complex are spatially clustered ultramafic pipes and later alkaline intrusives (Kinloch, 1982). The frequency of reef / layering disturbances in these areas increases, and the sites are centres of volatile activity which plays a role in precious metal mineralization.

Volatile activity in proximity to feeders has profound effects on magmatic structures and the crystallizing ore minerals. Total PGE compositions of the UG-2 interval in the fault zone are modified to distributions which are very similar to each other with high Rh and Ru, and less Pd concentrations.

3.3 Magmatic-hydrothermal PGE mineralization

Based on a regional study by Kinloch (1982), in the UG-2 and MR the mineral form of PGE is influenced by proximity to potential magma feeder channels: Fe-Pt alloys formed at high f_{O_2} and low f_S , and an “arsenic front” occurs with PGE-As further away (Kinloch and Peyerl, 1990; Fig. 6). Finally, the normal magmatic assemblage with sulphides and tellurides occurs further away outside the limits of volatile influence on PGM.

4 Conclusions and future work

A relative increase in ultramafic pegmatite occurrences, reef disturbances, reef splittings, and stratigraphic variations towards the Steelpoort fault zone approaching it from north and south is noted. Similarly an increase in variability and the spread of total PGE abundance with high absolute values proximal to the feeder area is noted.

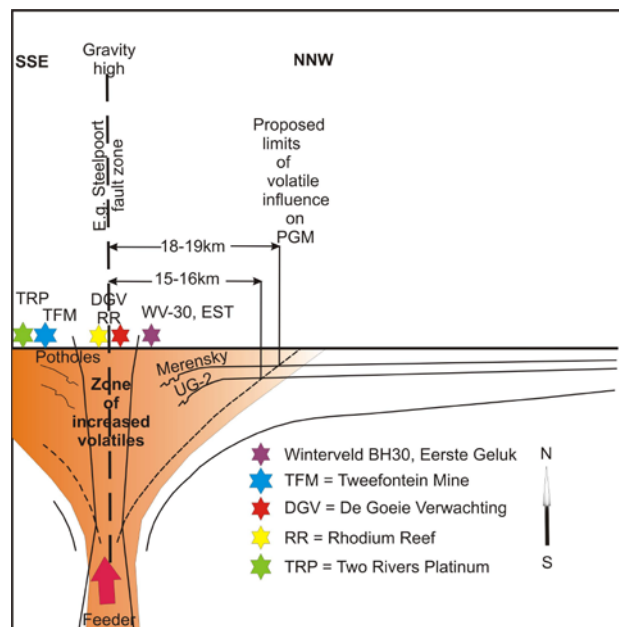


Figure 6. Schematic cross section of typical feeder area along the Steelpoort fault zone showing the limits of volatile influence on the Merensky Reef and the UG-2 layer, modified after Kinloch (1982)

These findings may indicate a zone of increased exsolution volatiles from the ultramafic magma at a late stage (Fig. 3), caused by advanced crystallisation and floor rock - magma interaction.

Such increased volatile activity causes a stronger

alteration of the primary magmatic mineral assemblage but also the formation of late-stage water-rich amphibole and micas confirming thereby the Kinloch and Kinloch & Peyerl (1982, 1990) models.

Further work to substantiate the ‘volatile-influence’ model requires more data from additional locations, and a micro-analytical characterization and quantification of PGMs and PGEs in base metal sulphides as well as isotope (Sr_0 , Pb, Sm-Nd) investigation of various minerals to distinguish and date minerals caused by late stage magmatic hydrothermal fluid event(s).

Acknowledgements

Thanks to NRF/DST – ‘Inkaba yeAfrica’ for funding of projects, and to J. Coetzee of Two Rivers Platinum Mine for making material available and for logistical assistance. J.F. Koekemoer, University of Pretoria, is acknowledged for PGE data, and the Department of Geology at the University of the Free State, South Africa is thanked for the use of analytical facilities.

References

- Cowell M, Coetzee J (2011) Geological and operational overview of the Two Rivers Platinum Mine, ARM-Implats, internal company presentation, 80 slides
- Kinloch ED (1982) Regional trends in the Platinum-Group Mineralogy of the Critical Zone of the Bushveld Complex, South Africa. *Economic Geology* 77: 328-347
- Kinloch ED, Peyerl W (1990) Platinum-Group Minerals in Various Rock Types of the Merensky Reef: Genetic Implications. *Economic Geology* 85: 537-555
- Hall M, Montpellier B (2010) Technical report for the Kennedy’s Vale project. Internal report by MSA Geoservices (Pty) Ltd. on behalf of Eastern Platinum Limited, Johannesburg, 169p
- Naldrett AJ, Duke JM (1980) Platinum Metals in Magmatic Sulfide Ores. *Science* 208 (4451): 1417-1424
- Peyerl W (1982) The Influence of the Driekop Dunitic Pipe on the Platinum-Group Mineralogy of the UG-2 Chromitite in its Vicinity. *Economic Geology* 77: 1432-1438
- Reid DL, Basson IJ (2002) Iron-rich ultramafic pegmatite replacement bodies within the Upper Critical Zone, Rustenburg Layered Suite, Northam Platinum Mine, South Africa. *Mineralogical Magazine* 66(6): 895-914
- Scoon RN, Mitchell AA (1994) Discordant Iron-Rich Ultramafic Pegmatites in the Bushveld Complex and their Relationship to Iron-Rich Intercumulus and Residual Liquids. *Journal of Petrology* 35(4): 881-917
- Teigler B (1990) Platinum Group Element Distribution in the Lower and Middle Group Chromitites in the Western Bushveld Complex Mineralogy and Petrology 42: 165-179
- Viljoen MJ, Reimold WU (1999) An introduction to South Africa’s geological and mining heritage. GSSA and MINTEK, Johannesburg, 193p

Spatial distribution and geochemical characteristics of the talc-carbonate alteration of the Uitkomst Complex, Mpumalanga, South Africa

Christian Günther

Department of Petrology and Economic Geology, Martin-Luther-University, Von-Seckendorff-Platz 3, D-06120, Halle/Saale, Germany

Christoph Gauert

Department of Geology, University of Free State, University Road, RSA-9301 Bloemfontein, South Africa

Abstract. The Uitkomst Complex is an elongated, layered, mineralized, mafic to ultramafic intrusion with a trough- or boat-like form in the Mpumalanga Province, South Africa (Fig. 1) bearing significant amounts of Ni-, Cu- and PGE-ore. The lower three units of complex are intensely saussuritized, amphibolitised, serpentinised, talcified and carbonatised. A talc-carbonate-pyrite-schist frequently occurs in the Chromitiferous Peridotite (PCR) unit. Isolated appearances were also observed in the Lower Pyroxenite (LPxt). The pyrite diminishes the total concentration of the Ni in the ore resulting in local low-grade ore portions in the Nkomati mine. The alteration zones are very widespread and structurally related to the NE-SW trending main faults as well as to the thrusts in the PCR unit. The rocks have high loss on ignitions and high carbonate chlorite indices (Large et al. 2001) near 100. The talc-carbonate-schist was produced by H₂O- and CO₂-rich fluids. These fluids were originated by the assimilation of dolomites by the ultramafic magma. The carbonates degassed and provided the CO₂, which is necessary for the talc-carbonate-alteration. According to modelled pseudosection in the system SiO₂-MgO-CaO-Al₂O₃-H₂O-CO₂ and the composition of the chromites the formation temperature of the alteration paragenesis is estimated to be about 500 °C.

Keywords. talc-carbonate, alteration, Uitkomst complex, Nkomati Nickel, Chromite

1 Introduction

The Nkomati Nickel Mine is the main Ni producer in South Africa, yielding Cu, PGEs, Co and Cr as by-products. During the exploitation of the ore body some problems regarding the flotation of the ore appeared. The pyrite in the talc-carbonate-schist of the Chromitiferous Peridotite as well as in the altered parts of the Lower Pyroxenite Unit lessens the total concentration of the Ni concentrate by preferential flotation of pyrite and dilution resulting in uneconomic ore portions in the Nkomati mine. Information on the distribution and genesis of this talc-carbonate-pyrite schist in the PCR and pyrite-rich portions of the LPXT unit therefore appear to be essential for grade control of the operation. Consequently a geological map was created in open-pit 3 of the benches 20 to 25 in the centre of the complex on the farm Uitkomst.

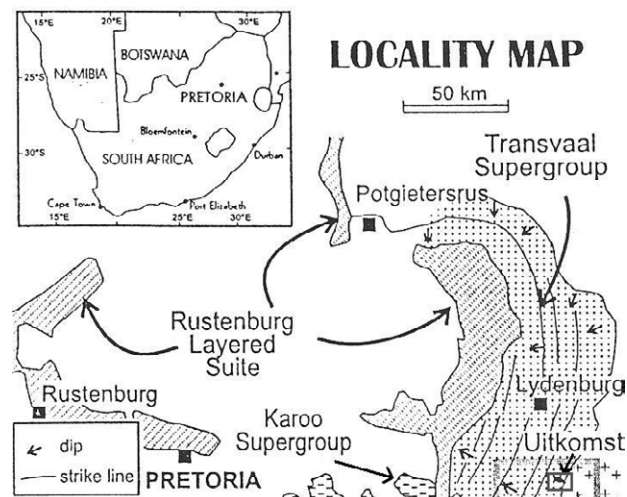


Figure 1. Locality map of the Uitkomst Complex (after Gauert 2001)

2 Geology

The Uitkomst Complex is an elongated, layered, mineralized, mafic to ultramafic intrusion with a trough- or boat-like form and bears significant amounts of Ni-, Cu- and PGE-ore (Kenyon et al. 1986; Gauert et al. 1995). The complex is situated in the eastern Transvaal, South Africa, 35 km east of Machadodorp and 20 km north of Badplaas and outcrops in the farms of Vaalkop, Slaaihoek and Uitkomst for approx. 9 km. The width ranges between 650 and 1600 m. The rock units of the complex are from bottom to top: Basal Gabbro, Lower Pyroxenite (LPXT), Chromitiferous Peridotite (PCR) with a massive chromitite layer on the top, Main Harzburgite (PRD), Upper Pyroxenite, and the Gabbro-norite. Based on geochemical and mineralogical evidence it is suggested that the intrusion is a satellite body of the Bushveld Complex (Gauert et al 1995; Li et al. 2002; Sarkar et al. 2008).

3 Talc-carbonate schist

The talc-carbonate-schist is a soft, fine-grained, and crème-coloured to brownish-grey rock. Macroscopically the minerals talc, calcite, serpentine, tremolite and pyrite could be identified. The talc-carbonate-schist frequently occurs in the PCR unit. Isolated appearances were also observed in the LPXT. The talc-carbonate-schist forms lenses and 'schlieren'.

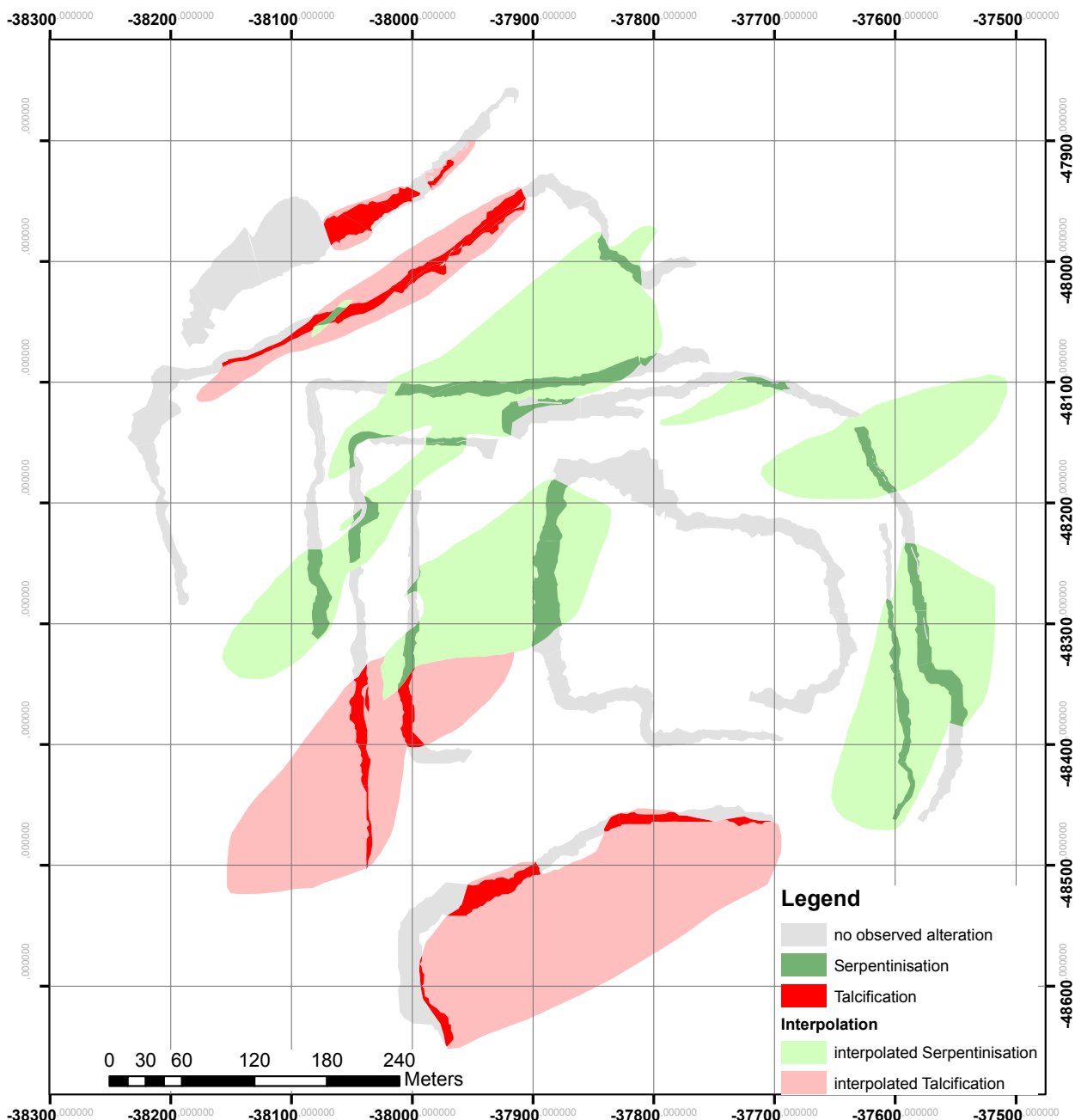


Figure 2. Alteration map of pit 3 in the Nkomati Mine covering benches 19 (north) to 25 (south)

Talc and serpentine are pseudomorphic after olivine or pyroxene. Carbonate occasionally occurs in interstices or in massive appearances. The talc-carbonate-schist is partially oxidised around the pyrite grains, which are idiomorphic and up to 1 cm in size.

4 Mapping

Within the investigated benches, the talcification occurs in the north and south whereas serpentinization is omnipresent (Fig. 2). The alteration zones, which were mapped and illustrated in the map, should be regarded as the minimal spatial distribution of the alteration because investigations of thin sections revealed alteration phenomena in parts of the pit, which were regarded as fresh. Fresh and weakly altered rock specimens were macroscopically very difficult to be differentiated.

The alteration zones have a NE-SW trending tendency, which is parallel to the regional main faults around and in the Uitkomst Complex. The serpentinisation is mainly linked to the LPxt unit whereas the talc-carbonate alteration is related to the PCR unit. The alteration also occurs around big calc-silicate xenoliths. Based on the observations two alteration processes are possible: The first occurred after the degassing event of the dolomite xenoliths. The second took place during the formation of faults and the influx of formation waters from the sedimentary host rocks into the rock units.

The alteration intensity increases with the stratigraphic height up to the Massive Chromitite layer at the top of the PCR unit. The rocks of the overlying Main Peridotite are less altered.

5 Geochemistry

5.1 Whole rock geochemistry

According to XRD investigations the encountered mineral paragenesis of the talc-carbonate-schist comprises a calcite-dolomite-serpentine-chlorite-amphibole-pyrite assemblage, indicative of a low grade retrograde metamorphism.

Serpentine is present in the form of lizardite, which is a typical mineral being formed under greenschist metamorphic conditions (Barnes 2000). Amphiboles are mostly represented by actinolite. The composition of chlorite ranges from chrome-rich species to leuchtenbergite and clinocllore.

Fig. 3 shows an overall positive trend between the CaO-content and the loss of ignition (LOI), implying a large part of the LOI being CO₂ in carbonate. Normal PCR samples plot next to the origin while the talc-carbonate-altered specimens show higher values of CaO as well as of LOI. This can be explained by the occurrence of carbonate minerals like calcite and dolomite in the talc-carbonate specimens, which is an indicator for a higher degree of alteration.

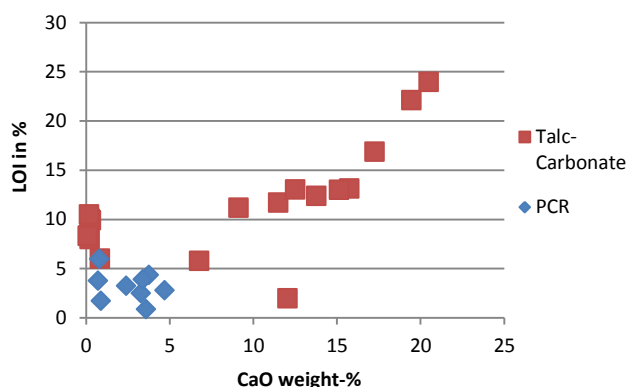


Figure 3. Scatter diagram weight-% CaO vs. LOI

In the alteration box plot after Large et al. (2001) the carbonate-chlorite-pyrite-index (CCPI) versus the alteration index (AI) is depicted. The majority of the studied samples are highly altered (Fig. 4) with CCPI values near 100, which can be explained by the very low concentration of K₂O and Na₂O. The values for the AI vary between 64 and nearly 100. This is due to the high CaO contents in the carbonate dominated specimens. The talc-carbonate specimens plot along the chlorite-carbonate-alteration path. The high values can be assigned to the occurrence of calcite, carbonate, chlorite and pyrite. The PCR samples also show high degrees of alteration at slightly lower CCPI values. Additionally it seems that the PCR specimens follow the chlorite-pyrite-sericite-path in the plot, which is due to the occurrence of pyrite and chlorite as a result of the alteration.

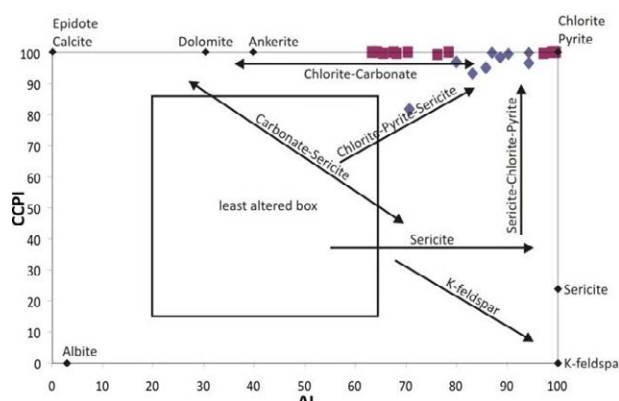


Figure 4. Alteration box plot after Large et al. (2001); blue points are PCR; ruby-coloured points are sheared chromitite

5.2 Mineral chemistry and thermodynamic modelling

In Fig. 5 a Cr-Fe³⁺-Al ternary diagram is depicted. The grey shaded area symbolises the chromite composition under greenschist-facies conditions (Lehbih et al. 2008). It is clearly apparent that the measured chromites plot in or near the border of the field of serpentinised spinels. Consequently, the rocks are weakly metamorphosed. Some of the measurements do not plot in the field of greenschist metamorphism. This could be due to other mobilisation and replacement events or they reflect the original magmatic signature.

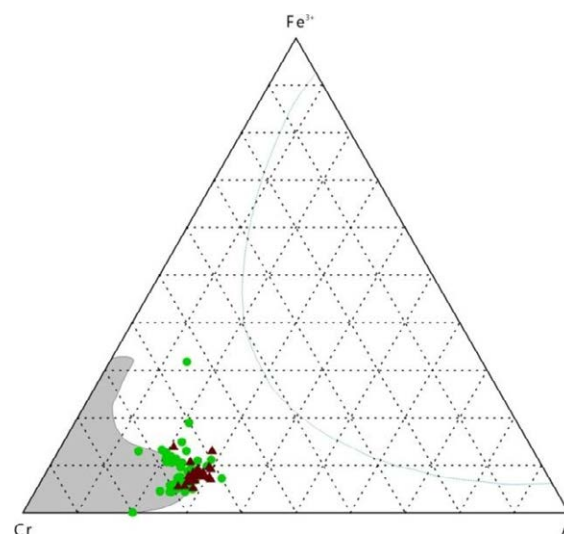


Figure 5. Ternary plot of chromites; green dots are chromites from sheared chromitites, brown triangles are chromitites from the chromitiferous peridotite

The norm plot of Figure 6 shows the ratios of element oxides of an average of sheared chromitite measurements versus the average composition of chromites of the chromitiferous peridotite. It is feasible to assume that the sheared chromite possesses a higher alteration grade than the sample of the PCR.

The trivalent cations show a slight modification. The change in Fe₂O₃ and Cr₂O₃ is nearly negligible whereas Al₂O₃ shows a higher depletion. The decrease in Al content can be explained by the entrapment into chlorite. The divalent cations (Mg, Fe²⁺), represented by their oxides, show a more intense modification in contrast to the trivalent cations. MgO is highly depleted and FeO is

highly enriched. This behaviour was also recognised by Barnes (2000) who explains the depletion of MgO and the enrichment of FeO by the exchange of Mg^{2+} and Fe^{2+} cations with the coexisting silicates such as talc, serpentine and chlorite.

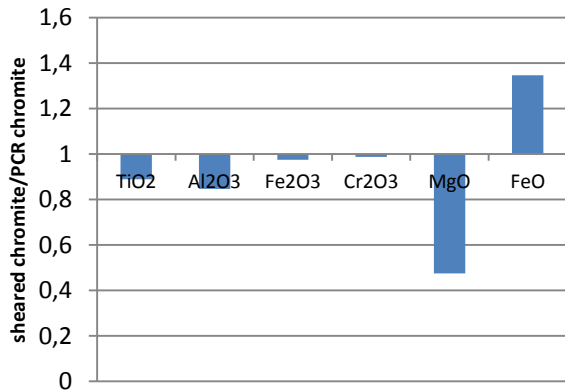


Figure 6. Ratios of the main elements of the measured chromites

Due to the mobilisation of MgO and FeO and the low scatter of the Fe_2O_3 -, Cr_2O_3 -, and Al_2O_3 -values one can conclude that the temperature of the alteration did not exceed 550 °C (Barnes 2000). Otherwise one could recognise a substantial variation of the Fe_2O_3 -, Cr_2O_3 -, and Al_2O_3 -contents. But according to the modelled isobaric pseudosections using *Perple_X* the temperature could not have been significantly lower than 500°C (Fig. 7).

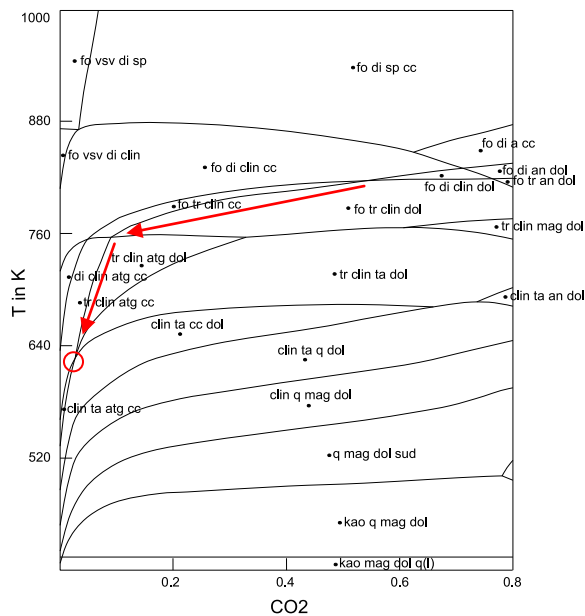


Figure 7. Modelled pseudosections of the talc-carbonate-specimens (with software *Perple_X*); minerals: fo-forsterite, di-diopside, tr-tremolite, clin-clinocllore, ta-talc, cc-calcite, dol-dolomite, atg-antigorite, q-quartz, mag-magnesite, kao-kaolinite, q(l)-quartz in fluid, vsv-vesuvianite, sp-spinel; system: SiO_2 -MgO-CaO- Al_2O_3 -H₂O-CO₂; pressure: 1000 bar

6 Conclusions

The talc-carbonate-schist in portions of the PCR unit

of the Uitkomst complex is a highly altered, secondary rock. The chromitiferous harzburgite precursor rocks are completely replaced by a calcite-dolomite-serpentine-chlorite-amphibole-pyrite assemblage.

It is thought that the fluid, which interacted with the rocks, evolved over time from higher (ca. 750-800 K) to lower (630 K) temperatures and from higher (>0.3) to lower (0.05) CO₂-contents (Fig. 6, red arrow). Convective fluids during and after the emplacement of the cooling magma obtained a relatively high CO₂-content derived from the decarbonisation reactions taking place during degassing and assimilation of the dolomites within the lower part and around the complex. During the cooling process the CO₂-rich deuteric fluid reacted with the ultramafic rocks to generate the talc-carbonate assemblage. The CO₂ was used and the fluid became depleted in CO₂. At the same time the temperatures decreased because of the cooling of the ultramafic intrusion.

According to the modelled pseudosections and the composition of the chromites it is concluded that the formation temperature of the alteration paragenesis was about 500 °C.

Acknowledgements

Nkomati Nickel Mine is thanked for support and organisation of the project, as well as Gregor Borg at MLU Halle-Wittenberg for his support and the initiation of this project. The Dept. of Geology at UFS Bloemfontein is acknowledged for use of analytical facilities.

References

- Barnes SJ (2000) Chromite in Komatiites, II. Modification during Greenschist to Mid-Amphibolite Facies Metamorphism. *J Petrol* 41: 387-409
- Gauert CDK., De Waal SA, Wallmach T (1995) Geology of the ultrabasic to basic Uitkomst complex, eastern Transvaal, South Africa: an overview. *J Afr Earth Sci* 21: 553-570
- Gauert CDK (2001) Sulphide and oxide mineralisation in the Uitkomst Complex, South Africa: origin in a magma conduit. *J Afr Earth Sci* 32: 149-161
- Kenyon AK, Attridge RL, Coetzee GL (1986) The Uitkomst nickel-copper deposit, Eastern Transvaal. In: Anhaeusser C.R.; Maske S. (eds.) *Mineral Deposits of Southern Africa Vol. I & II*, pp 1009-1017
- Large RR, Gemmill JB, Paulick H (2001) The Alteration Box Plot: A Simple Approach to Understanding the Relationship between Alteration Mineralogy and Litho geochemistry Associated with Volcanic-Hosted Massive Sulfide Deposits. *Econ Geol* 96: 957-971
- Lehbih S, Arribas A, Melgarejo JC, Proenza JA, Zaccarini F, Thalhammer O, Garuti G (2008) Chromite Deposits from Western Sahara: Textures, Composition and Platinum Group Minerals. *Rev soc esp mineral* 9: 143-144
- Li C, Ripley EM, Maier WD, Gomwe TES (2002): Olivine and sulfur isotopic compositions of the Uitkomst Ni-Cu sulfide ore-bearing complex, South Africa: evidence for sulfur contamination and multiple magma emplacements. *Chem Geol* 188: 149- 159
- Sarkar A, Ripley EM, Li C, Maier WD (2008) Stable isotope, fluid inclusion, and mineral chemistry constraints on contamination and hydrothermal alteration in the Uitkomst Complex, South Africa. *Chem Geol* 257: 129-138

Geochemistry of ~2.45 Ga mafic dykes in northern Finland: constraints on the origin of PGE mineralization in coeval layered intrusions

Fang-Fang Guo, Wolfgang D Maier
Department of Geosciences, University of Oulu, Finland

Jouni Vuollo
Geological Survey of Finland, Rovaniemi, Finland

Yann Lahaye, Hannu Huhma, Hugh O'Brien
Geological Survey of Finland, Espoo, Finland

Hanna Junttila
Department of Geosciences, University of Oulu, Finland

Abstract. The Karelian craton contains abundant ~2.45 Ga mafic dykes, spatially and temporally related to PGE mineralized ultramafic-mafic layered intrusions. The mafic dykes include siliceous high magnesium basalt (SHMB), gabbro-norite (GBNO), Ti-poor tholeiite (TTH) and Fe-tholeiite (FTH). The SHMB and GBNO have $^{87}\text{Sr}/^{86}\text{Sr}_{(i)}$ ratios (in situ laser ICP-MS analyses on plagioclase) ranging from 0.7028-0.7036, and initial ϵNd (whole rock) ranging from -1.0 to -2.5. These data could indicate moderate degrees (about 10%) of contamination with Archean basement or magma derivation from an enriched mantle source. The TTH show a lower radiogenic Sr isotope composition with an average $^{87}\text{Sr}/^{86}\text{Sr}_{(i)}$ ratio 0.7022, and a higher initial ϵNd ranging from +0.3 to +1.7. These data are broadly consistent with magma derivation from a depleted asthenospheric mantle plume. Most dyke types are undepleted in PGE, with 10-20 ppb Pt and Pd, and mantle-like Cu/Pd ratios in the more primitive members, suggesting sulfide undersaturation both in the source and en route to the surface. Sulfide saturation was achieved in the more evolved magmas, and in many cases the sulfides were entrained by the magma, resulting in high Cu and PGE contents (up to 37 ppb Pd). The data indicate that all 4 magma types represented in the dykes are prospective for PGE mineralization.

Keywords. platinum-group elements, Proterozoic mafic dykes, layered intrusions, mantle source, Northern Finland

1 Introduction

Several ~2.45 Ga layered intrusions occur in the Karelian craton of the North Eastern Fennoscandian Shield (Huhma et al. 1990; Amelin et al. 1996; Hanski et al. 2001; Latypov et al. 2008). Some of these intrusions host important PGE mineralization, such as Penikat and Portimo. The origin of the PGE mineralization is still poorly constrained. The composition of the parental magmas is critical for PGE potential, as only sulphur-undersaturated, PGE-rich magma has the potential to form PGE deposits. Abundant coeval mafic dykes occur in this region (Vuollo and Huhma 2005). The spatial and temporal link between the mafic dykes and the layered intrusions suggests that they may belong to the same magmatic event. In this contribution, we will try to decipher the relationship between the mafic dykes and the layered intrusions, and then constrain the parental

magma composition and the potential of PGE mineralization in these layered intrusions.



Figure 1. Distribution of mafic dykes in the Karelian craton, Finland and Russia.

2 Geological background

The mafic dykes occur throughout the Karelian craton of the northern and eastern Fennoscandian Shield (Fig.1). The Karelian craton is composed of Archean basement and Paleoproterozoic cover rocks. The layered intrusions, including Kemi, Penikat, Portimo, Koillismaa and Olanga (Fig.1), are the most voluminous products of the ~2.45 Ga magmatism. The ~2.45 mafic dykes are spatially closely associated with the layered intrusions. The mafic dykes are sub-divided into 4 groups based on petrology and geochemistry, including SHMB, GBNO, TTH and FTH.

3 Geochemistry and discussion

3.1 Mantle source

The mantle source of the 2.45 Ga magmatism in the Karelian craton remains under debate. Based on Nd isotope data of layered intrusions, Amelin and Semenov (1996) proposed a mantle plume source with small amounts of crustal contamination. This is consistent with Os and Nd isotope data from the 2.45 Ga Koitelainen and Akanvaara intrusions (Hanski et al. 2001). However, the melting of a metasomatically modified lithospheric mantle source cannot be ruled out (Huhma et al. 1990; Amelin and Semenov 1996).

The Ti-poor tholeiites and Fe-tholeiites exhibit no or weak Nb anomalies, positive initial ϵ_{Nd} values (-0.3 to +1.7) and low La/Sm ratios, indicating a depleted asthenospheric mantle source and little crustal contamination of the magma. This model is consistent with relatively low $^{87}\text{Sr}/^{86}\text{Sr}_{(i)}$ ratios (~ 0.7022) (Fig. 2). The SHMB and GBNO dykes have negative initial ϵ_{Nd} values (-1.0 to -2.5), higher $^{87}\text{Sr}/^{86}\text{Sr}_{(i)}$ ratios (0.7028-0.7036) (Fig. 2), and negative Nb anomalies. These features could be explained by either a metasomatized lithospheric mantle source or moderate amounts of crustal contamination.

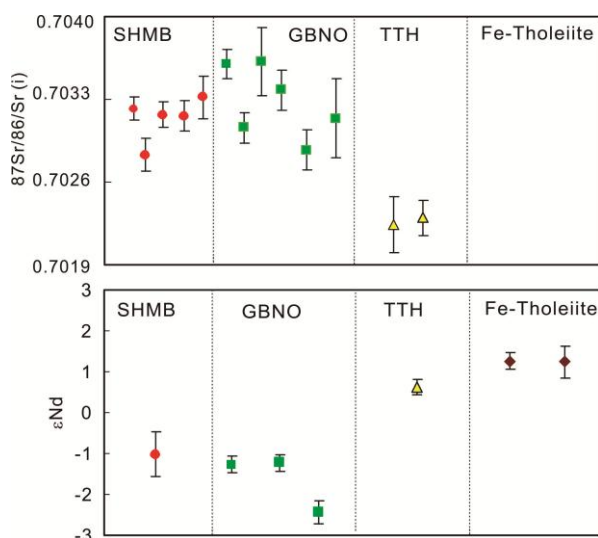


Figure 2. Initial Sr and Nd isotope composition of the mafic dykes.

The olivine from SHMB show relatively high Ni contents (Fig. 3), consistent with a pyroxene-rich (SCLM) mantle source (Sobolev et al. 2007). However, because Pt/Pd ratios of the SHMB and BGNO samples are around unity, there is presently no strong evidence to suggest that the SHMB and GBNO magmas contain a significant SCLM component. Oxygen isotope may provide more constraints on the mantle sources, but at present, we favour a model whereby the bulk of the magmas are derived from asthenospheric mantle, followed by different degrees of interaction with crust.

3.2 Relationship with layered intrusions

The SHMB and GBNO dykes have been correlated with

the lower and upper zones, respectively, of the contemporaneous PGE mineralized layered intrusions in northern Finland (e.g., Penikat, Portimo) based on similarities in major elements composition and mineralogy. The layered intrusions all have very similar initial ϵ_{Nd} values (-1 ~ -2), proposed to represent crustally contaminated plume magma (Amelin and Semenov 1996; Putschel et al. 1997; Hanski et al. 2001; 2012). New Sr isotope data of the dykes resemble those of the Burakovka Complex in south-eastern Karelia, consistent with the dyke magma being parental to the layered intrusions. The tholeiitic dykes have similar initial ϵ_{Nd} ratios to the Tspringa intrusion, suggesting that the tholeiites are parental to the latter, and that they also have formed large layered intrusions.

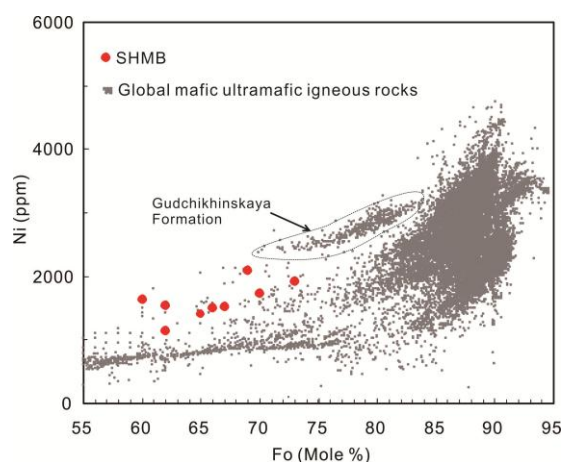


Figure 3. Fo vs. Ni of olivine from the SHMB dykes. Global olivine data is from Sobolev et al. (2007).

3.3 Magma evolution

The An contents of plagioclases from the SHMB dykes (52-67) are slightly higher than those of the GBNO samples (37-63), confirming a more primitive signature of the former. Plagioclases from the TTH and FTH samples have An contents of 47-59 and 46-65, respectively, similar to those of GBNO, indicating similar degrees of differentiation.

The SHMB and GBNO samples have Mg# values of clinopyroxene ranging from 68 to 86, which is similar to that of the Penikat intrusion (75 to 85) (Alapieti and Halkoaho 1995), but lower than that of the Kemi intrusion (86-91) (Alapieti et al. 1989).

3.4 Sulfide saturation

To form PGE-rich sulphide deposits, it is critical that the magma has remained sulphur undersaturated during ascent through the crust. The most primitive SHMB and GBNO samples have PGE undepleted mantle normalized siderophile element patterns (Fig. 4), with high Pd contents (up to 22ppb) and mantle-like Cu/Pd and Cu/Zr ratios (Fig. 5), indicating that the parental magma was sulphur undersaturated during high degree partial melting in the mantle, and remained so en route to the surface. This renders the magmas prospective to form PGE-rich deposits.

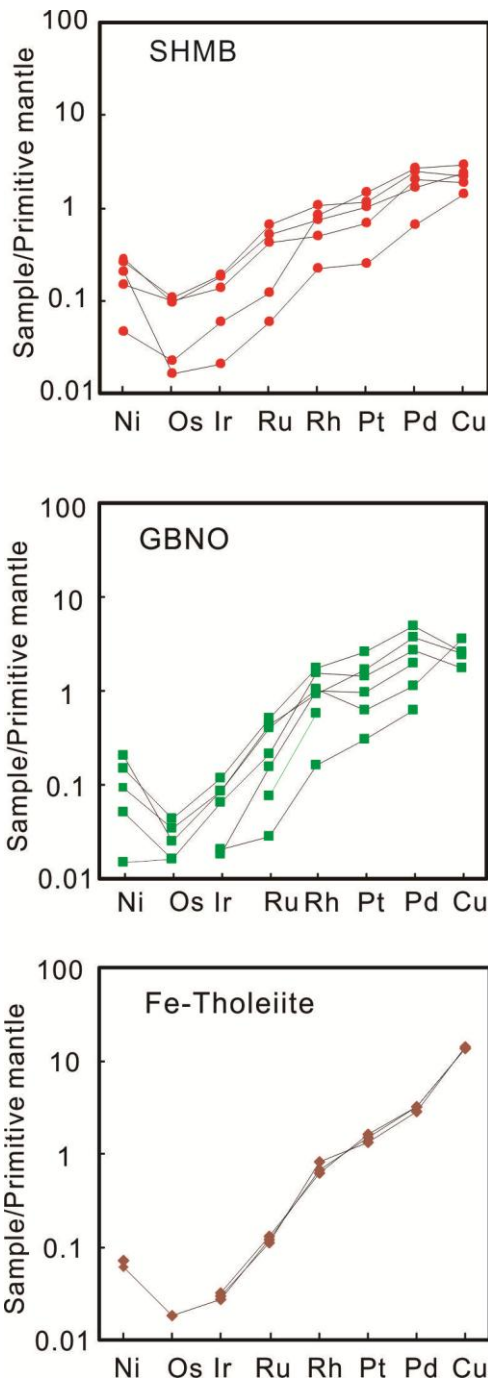


Figure 4. Primitive mantle normalized siderophile element patterns of mafic dykes. Primitive mantle values are from McDonough and Sun (1995).

Another positive indicator are the relatively high Ni contents in olivine from SHMB (Ni=1100-2000 ppm, Fo=60-73) (Fig. 3). However, one SHMB sample and two GBNO samples with lower MgO content (~7%) show very low PGE contents (Pt<0.31 ppb), and there is a decrease of both Cu contents and Cu/Zr ratios in the more evolved magmas with MgO about 5-10% (Fig.5), suggesting sulphide saturation may have occurred in these evolved magmas. This could indicate enhanced PGE reef potential in the relatively differentiated portions of any co-genetic layered intrusion. Notably, PGE reefs occur in the relatively differentiated members of the 2.45 Ga layered suite (e.g., Penikat, Portimo) (Barkov et al. 1999), but are absent in the more primitive,

ultramafic intrusions (e.g., Kemi) (Alapieti et al. 1989).

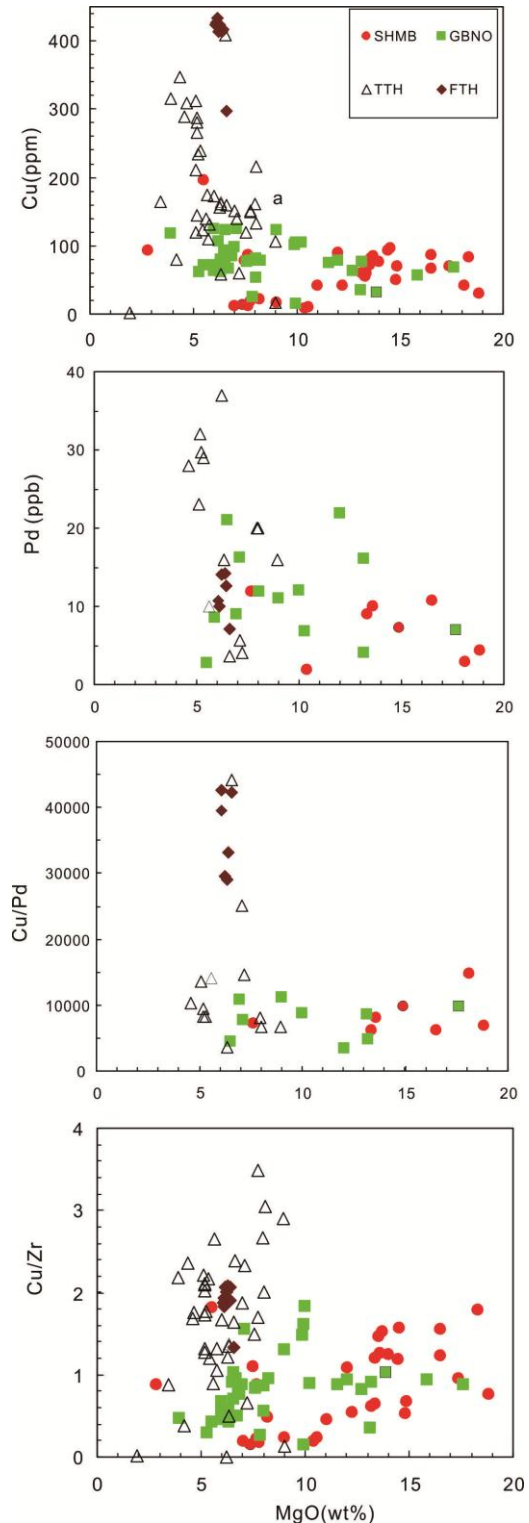


Figure 5. Cu, Pd, Cu/Pd and Cu/Zr vs. MgO of the mafic dykes.

For the Ti-poor tholeiites, the most primitive samples also have mantle-like Cu/Pd ratios (Fig.5), indicating the magmas may not have reached sulphide saturation during the early stage of differentiation. In the more differentiated members of this suite, PGE and Cu contents are highly variable, (2-37 ppb Pd, up to 400 ppm Cu), indicating that sulphide saturation has been reached. Cu/Zr ratios are up to 3.5, suggesting that some of the sulfides were entrained by the magmas.

The Fe-tholeiites have high Cu contents (400 ppm), and Cu/Zr is 2. Pt and Pd contents are around 10 to 14 ppb, and Cu/Pd ranges from 29,000 to 43,000. If the high Cu contents are the result of a Cu rich mantle source and advanced differentiation, then the magma must have equilibrated with small amounts of sulphides to explain the relatively high Cu/Pd.

6 Conclusions

The 2.45 Ga dykes in northern and eastern Finland that are coeval to the PGE mineralized layered intrusions comprise siliceous high-Mg basalt, gabbro-norite, Ti-poor tholeiites and Fe-rich tholeiites. The magmas contain highly variable crustal components, possibly reflecting contamination of asthenospheric mantle-derived magmas. The Ni rich nature of the olivines could suggest magma derivation from a pyroxene-rich (SCLM) mantle source, but unlike in the Bushveld Complex, the magmas do not show high Pt/Pd ratios, a signature that is often interpreted to indicate a SCLM component. Oxygen isotope data may provide further constraints on this question. The primitive members of most magma types are S undersaturated and fertile with regard to PGE, but the more differentiated members have reached S-saturation during advanced differentiation. It appears that in some cases the sulfides segregated, but in several dykes there is evidence that sulfides were entrained, resulting in highly variable metal contents and, in the case of the Ti-poor tholeiites, some of the highest PGE contents recorded in basaltic magmas.

References

- Alapieti TT, Kujanpää J, Lahtinen JJ and Papunen H (1989) The Kemi chromitite deposit, Northern Finland. *Econ Geol* 84: 1057-1077
- Alapieti TT, Halkoaho AA (1995) Cryptic variation of augite in the Penikat layered intrusion, Northern Finland, with reference to megacyclic units and PGE-enriched zones. *Mineral and Petrol* 54: 11-24
- Amelin YV, Semenov VS (1996) Nd and Sr isotopic geochemistry of mafic layered intrusions in the eastern Baltic shield: implications for the evolution of Paleoproterozoic continental mafic magmas. *Contrib Mineral Petrol* 124: 255-272
- Barkov AY, Halkoaho TAA, Roberts AC, Criddle AJ, Martin RF and Papunen H (1999) New Pd-Pb and Pb-V oxides from a bonanza-type PGE-rich nearly BMS-free deposit in the Penikat layered complex, Finland. *Can Mineral* 37: 1507-1524
- Huhma H, Cliff RA, Perttunen V, Sakko M (1990) Sm-Nd and Pb isotopic study of mafic rocks associated with early Proterozoic continental rifting: the Peräpohja schist belt in northern Finland. *Contrib Mineral Petrol* 104: 369-379
- Hanski EJ, Walker RJ, Huhma H and Suominen I (2001) The Os and Nd isotopic systematics of c. 2.44 Ga Akanvaara and Koitelainen mafic layered intrusions in northern Finland. *Precam Res* 109: 73-102
- Hanski EJ (2012) The Evolution of the Paleoproterozoic (2.5-1.9) non-orogenic magmatism in Eastern part of Fennoscandian shield. In: Victor AM, Anthony RP, Anthony EF, Hanski EJ, Aivo L, Lee RK, Harald S (Eds.) *Reading the Archive of Earth's oxygenation*: 179-148
- Latypov RM, Chistyakova SY, Alapieti TT (2008) Fine-grained mafic bodies and preserved portions of magma replenishing layered intrusions: the Nadezhda gabbro-norite body, Lukkulaisvaara intrusion, Fennoscandian Shield, Russia. *Mineral Petrol* 92: 165-209
- McDonough WW, Sun SS (1995) The composition of the Earth. *Chem Geol* 120: 223-53
- Puchtel IS, Haase KM, Hofmann AW, Chauvel C, Kulikov VS, Garbe-Schönberg CD and Nemchin AA (1997) Petrology and geochemistry of crustal contaminated komatiitic basalts from the Vetryny Belt, southeastern Baltic Shield: Evidence for an early Proterozoic mantle plume beneath rifted Archean continental lithosphere. *Geochim Cosmochim Acta* 61: 1205-1222
- Sobolev AV, Hofmann AW, Kuzmin DV, et al. (2007) The amount of recycled crust in sources of mantle-derived melts. *Sci* 316: 412-417
- Vuollo J, Huhma H (2005) Paleoproterozoic mafic dykes in NE Finland. In Lehtinen M, Nurmi PA, Rämö OT (Eds.), *Precambrian Geology of Finland – Key to the Evolution of the Fennoscandian Shield*. Elsevier B.V., Amsterdam: 195-236

Multi-stage emplacement and PGE-enrichment in the River Valley Intrusion, Ontario, Canada: implications for 'contact-type' PGE-Cu-Ni mineralization

David A. Holwell, Emily A. Firth
 Department of Geology, University of Leicester, University Road, Leicester, LE1 7RH, UK

Reid R. Keays
 School of Geosciences, Monash University, Victoria 3800, Australia

Jon Findlay
 Pure Nickel Inc., 95 Wellington Street West, Suite 900, P.O. Box 28, Toronto, Ontario, Canada

Abstract. The River Valley Intrusion (RVI) contains PGE-Cu-Ni sulfide mineralization concentrated in the basal part of the intrusion in unlayered units containing inclusions of gabbro and country rocks in a gabbroic matrix. Identical sulfide assemblages in terms of mineralogy and PGE geochemistry are present in the matrix and all inclusions. Overlying layered units are undepleted of PGE. We propose that crustal contamination triggered early S saturation in a deep conduit and that this was the major ore forming process and PGE enrichment of sulfide and partial crystallisation of the magma occurred at depth. A major pulse of magma then entrained a mixture of fragments of the mineralized and crystallised lower chamber, mineralized footwall rocks and sulfide liquid and emplaced the basal portion of the RVI. This is therefore an example of 'contact-type' mineralization whereby PGE-rich sulfide droplets are generated at depth and are transported in during emplacement, and *in situ* contamination is not a major ore forming process. In such cases, the interpretation of S/Se and Cu/Pd ratios must be used with caution when developing ore genesis and exploration models, as they may not show the expected patterns that would be seen if S saturation was triggered *in situ*.

Keywords. PGE, S saturation, S/Se ratios, River Valley, Platreef

1 Introduction

The River Valley Intrusion (RVI), part of the ~2.48 Ga East Bull Lake Intrusive Suite, Ontario, Canada, is an example of a mafic igneous intrusion with 'contact-type' Ni-Cu-PGE sulfide mineralization along its base. Whilst many 'contact-type' deposits are thought to form from *in situ* contamination by the addition of crustal S during emplacement, there are some intrusions, including the RVI and the Platreef, South Africa, which appear to have a much more complex emplacement history in terms of the number of emplacement stages. The relative timing of S saturation during multi-stage emplacement has profound implications on the interpretation of traditional geochemical relations used in exploration, such as Cu/Pd ratios, and the interpretation of S/Se ratios.

2 Geology of the River Valley Intrusion

The RVI is made up of a basal ~100 m of unlayered, inclusion-bearing units, unconformably overlain by

layered cumulates (Fig. 1). The basal units, which contain the PGE-rich sulfide mineralization contain autoliths of gabbroic rocks and inclusions of footwall gneisses and amphibolites, all within a gabbroic matrix (James et al. 2002). The composition of the matrix and the mafic inclusions is almost identical. The matrix and mafic inclusions can be separated into two distinct textural types: hydrothermally altered greenschist assemblages and unaltered metamorphic amphibolite assemblages.

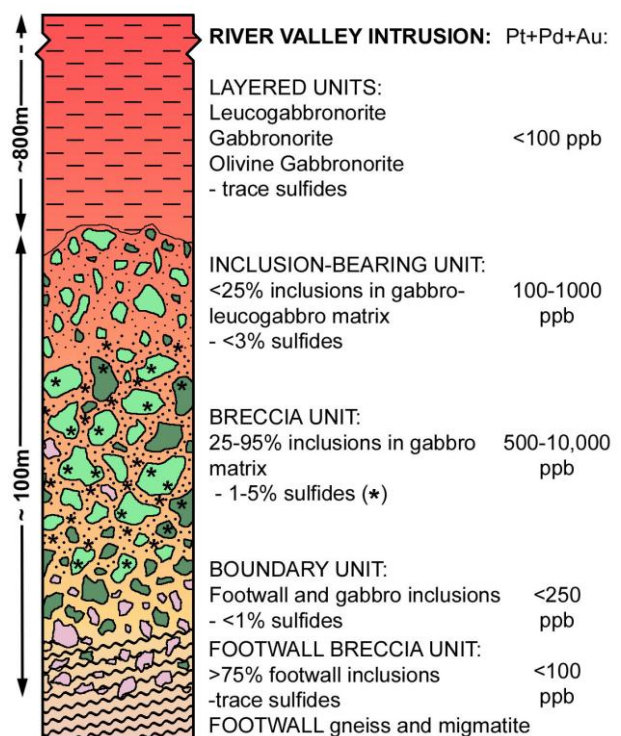


Figure 1. Stratigraphy of the RVI, showing the concentration of mineralization in the inclusion-bearing basal portion, with sulfides present within the matrix and inclusions.

3 PGE mineralization

Platinum-group element-rich magmatic sulfide mineralization occurs throughout both the inclusions and the matrix as blebby and disseminated sulfides and is concentrated within the Breccia Unit where grades range up to 10 ppm Pt+Pd (Fig.1). The sulfides in all rock

types are made up of a typical magmatic assemblage of chalcopyrite-pyrrhotite-pentlandite, and are overprinted by metamorphic amphiboles and micas (Fig. 2).

3.1 Platinum-group mineralogy

The platinum-group mineral (PGM) assemblages vary only between textural host rocks types, and not between inclusions and matrix. Overall, the PGM are dominated by telluride assemblages, mainly of kotulskite (PdTe) with some sperrylite (PtAs₂) in all rock types. However, the hydrothermally altered rocks, compared with those with a metamorphic texture, have fewer tellurides, and an increased number of Sb- and As-bearing PGM such as merrillite I (Pd₁₁(Sb,As)₄). Antimony-bearing PGM are indicative of fluid interaction (e.g. Holwell et al., 2006); however, whilst the PGM may have been recrystallised, they do not appear to not been mobilised significantly away from the base metal sulfides, remaining within less than 1 mm from the altered or overprinted sulfide grains (Fig. 2).

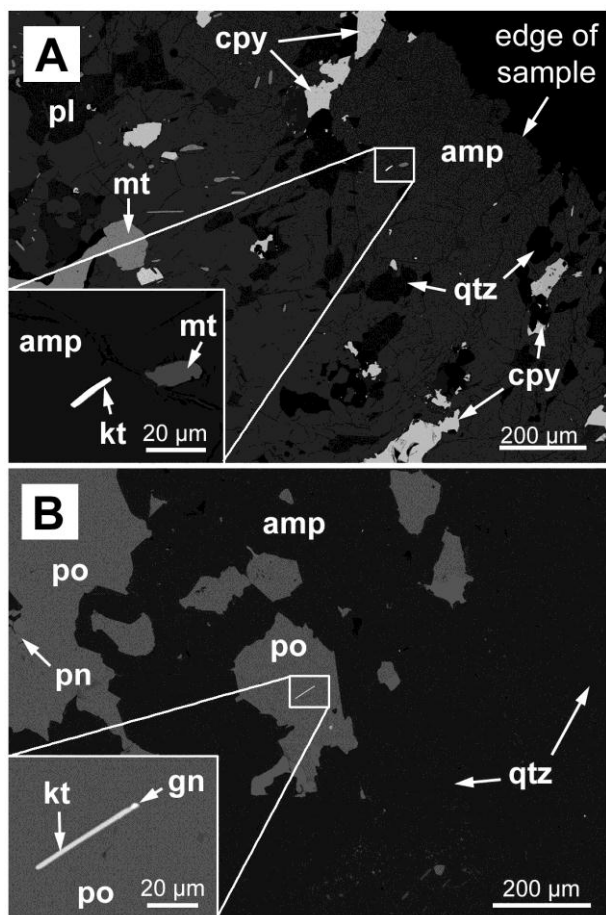


Figure 2. A: Kotulskite (kt) with associated chalcopyrite (cpy), overprinted by metamorphic amphibole (amp). B: inclusions of kotulskite within pyrrhotite (po).

3.2 PGE geochemistry

Precious and base metal geochemistry shows all rock types to have an excellent correlation between all the PGE (Fig. 3A), indicating the presence of a single, well homogenised PGE-rich sulfide liquid. However, Au and

Cu appear to be decoupled from the PGE at low concentrations (<100 ppb Pt; Fig. 3), although correlate well with each other, which is interpreted to be due to minor fluid redistribution which mobilised Au and Pd from the sulfides through interaction around the margins of the sulfide blebs.

There is an excellent correlation between the PGE in all rock types, indicating no difference in PGE distribution between matrix and inclusions, even footwall inclusions. This indicates that the composition of the sulfide liquid present within both the matrix and the inclusions can be considered to be of the same origin.

The overlying Layered Units above the mineralized units are not PGE depleted, indicating the magma that formed these units had not undergone S saturation.

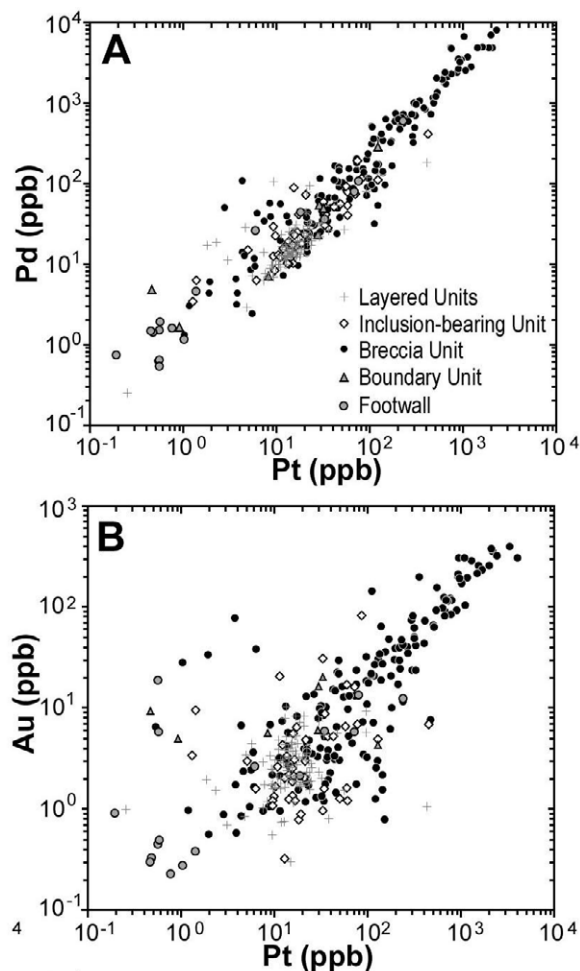


Figure 3. Correlation of: A: Pt with Pd showing a strong relationship in all rocks, and B: Pt with Au, showing a poor relationship at lower concentrations (< 100 ppb Pt).

4 Crustal contamination indicators

Trace element data, including (Th/Yb)PM and (Nb/Th)PM ratios, demonstrate that all River Valley rocks were formed from crustally contaminated magmas induced by interaction with local country rocks in a deeper chamber; although some samples have S/Se ratios indicative of crustal S, most have S/Se ratios lower than the mantle range, indicative of S loss (Fig.

4). We interpret this to be due to the initial sulfide being partially dissolved at depth within the deeper plumbing system. Kerr and Leitch (2005) showed that this may happen in deep magma chambers and conduits as multiple batches of S-undersaturated magmas interact with a sulfide liquid in the lower chamber and result in the upgrading of the tenors of elements with high sulfide/silicate melt partition coefficients. Both Pd and Se will be upgraded by this process and conversely, elements with low partition coefficients such as Fe and S will be resorbed by the magma. Thus, the crustal S/Se signature can become obliterated by this process and the highest tenor sulfides that are produced will actually exhibit the lowest S/Se ratios, as seen in our data (Fig. 4). The broad negative correlation in our data between Pd tenor in the sulfides and S/Se ratios may be indicative of significant dissolution of a low PGE tenor sulfide with an initially crustal S component by the parental magma to the RVI. This process not only masks the crustal signature, but is critical in producing the high metal tenors.

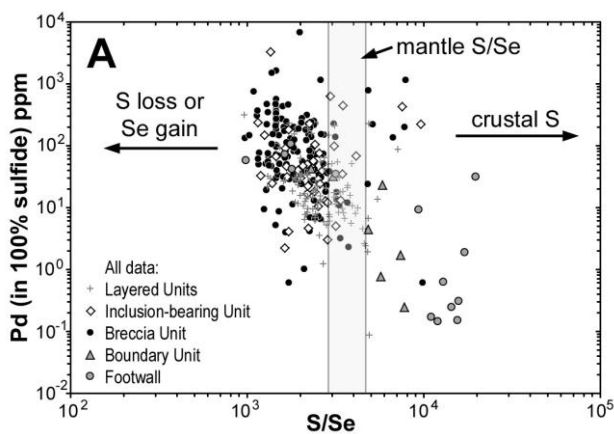


Figure 1. Table and Figure captions use 9pt Helvetica for their titles and 9pt Times New Roman for their text

5 A model for the emplacement of the RVI

Both magmatic and hydrothermal processes have been championed as the major factors involved in PGE mineralization in the RVI. Peck et al. (2001) suggested that the PGE-rich sulfides in the contemporaneous East Bull Lake intrusion were produced by sulfide saturation of a PGE-rich magma prior to emplacement of the East Bull Lake magma and suggested this may be true for all intrusions within the suite, including the RVI. Conversely, Price et al. (2010) suggest on the basis of mineralogical relationships, that hydrothermal activity within the RVI has significantly redistributed PGE and sulfides, post-emplacement.

Our data show a number of characteristic geochemical and mineralogical relationships within the Ni-Cu-PGE mineralization of the RVI. Any genetic model for the mineralization must be able to account for all of the following relationships identified in this study:

1. Restriction of mineralization to the basal units that contain inclusions and the lack of PGE depletion in the overlying cumulates;
2. Identical Pt, Pd, Rh and Ir ratios in the matrix and

inclusions of the mineralized units;

3. The lack of correlation between Pt, Pd, Rh and Ir with Au and Cu at low abundance levels, especially in the Inclusion-bearing Unit;
4. Similarities and variations in the PGM assemblages between rock types
5. The evidence for crustal contamination.

We propose a multi-stage model for the formation of the mineralization in the RVI with a major contamination event at depth with the addition of S from local crustal rocks, inducing sulfide saturation. Sulfide droplets were then enriched in PGE via interaction with a turbulent magma within a conduit system with possible further upgrading of sulfide metal tenors (and reduction of S/Se ratios) via partial dissolution of sulfide. The PGE-enriched sulfide liquid then settled in a staging chamber and partially crystallised before a major pulse of magma entrained sulfide liquid, eroded blocks of pre-crystallised gabbro and footwall rocks and emplaced an inclusion-bearing package as the lower 100m or so of the RVI, forming the main mineralized zone, with mineralization in inclusions and matrix. Later emplacement of main RV magma was from a S-undersaturated, PGE-fertile magma. Finally, minor hydrothermal alteration affected some of the rocks, remobilising Cu and Au on a minor scale, and altering mineralogy in a minor way, possibly during later metamorphism.

6 Implications for 'contact-type' Ni-Cu-PGE deposits

The RVI is thus an example whereby 'contact-type' mineralization is purely a function of the earliest magma intruded containing pre-formed sulfide mineralization and therefore emplacing mineralized rocks at the intrusion margin, rather than *in situ* contamination triggering sulfide saturation. An analogous situation is thought to have occurred in the Platreef, northern Bushveld Complex (Holwell et al., 2007; Ihlenfeld and Keays, 2010), with the major ore forming processes occurring at depth and localised contamination from country rocks during final emplacement acts as an ore-modifying, rather than ore-forming process.

In such cases, processes at depth determine both the generation and subsequent tenor of the mineralization, not localised contamination along the margin of the subsequent intrusion. In particular, dissolution of the sulfide can upgrade metal tenor, but subsequently will reduce S/Se ratios, masking the signature of crustal contamination. In addition, a multi stage emplacement history such as this will not necessarily preserve the characteristic increase in Cu/Pd ratios in the overlying cumulates that is often used in exploration for PGE deposits in mafic intrusions (e.g. Maier et al., 1996). Thus, a full understanding of all the field, geochemical and mineralogical factors is required to construct genetic models for such deposits, and especially in the interpretation of S/Se and Cu/Pd ratios as an indicator of crustal contamination and the presence of PGE mineralization.

This problem is especially prevalent in 'contact-type' deposits such as the RVI and the Platreef. In both these

examples, contamination occurred in a two stage process. In situation where S is added in two, or possibly more, emplacement stages, it becomes critical in terms of developing ore genesis models, that overprinting signatures of later, localised contamination are not mis-interpreted as ore forming processes. However, as stated, if dissolution upgrading has occurred, the earlier signatures may be difficult to trace in bulk rock. Furthermore, metal tenors are likely to differ depending on where sulfide saturation took place. Compared to sulfides formed by in situ contamination, much higher grades would be easier to achieve in sulfides formed at depth that interact with large volumes of magma, and have the ability to partially dissolve.

Therefore, optimal conditions for high grade deposits should involve contamination by crustal S at depth in a staging chamber or conduit inducing sulfide saturation, followed by upgrading of the sulfide liquid this through the interaction of further batches of magma, with partial dissolution of the sulfide. This enriched sulfide may then crystallise in situ within the conduit or be flushed into a higher intrusion as a 'contact-type' deposit

In addition, the RVI shows evidence for syn- or post-magmatic fluid activity. However, this can be considered as only a minor modifier of the magmatic ore deposit. The decoupling of Au and Cu from the PGE at low bulk concentrations in the RVI indicates likely hydrothermal mobilisation of these elements. However, at higher grades (>100 ppb Pt), the sulfides appear to be self-buffering and any fluid affects become insignificant. This is further evidence that post-magmatic hydrothermal activity plays only a minor role in redistributing and recrystallizing PGE

Acknowledgements

Pacific Northwest Capital Corp. are gratefully acknowledged for funding the geochemical analyses used in this study, and for granting permission to publish and present these results.

References

- Holwell DA, McDonald I, Armitage PEB (2006) Platinum-group mineral assemblages in the Platreef at the South Central pit, Sandsloot mine, northern Bushveld Complex, South Africa. *Min Mag* 70:83–101
- Holwell DA, Boyce AJ, McDonald I (2007) Sulfur isotope variations within the Platreef: genetic implications for the origin of sulfide mineralization. *Econ Geol* 102:1091–1110
- Ihlenfeld C, Keays R (2011), Crustal contamination and PGE mineralization in the Platreef, Bushveld Complex, South Africa: evidence for multiple contamination events and transport of magmatic sulfides. *Mineral Dep* 46:813-832
- James RS, Easton RM, Peck DC, Hrominichuk JL (2002) The East Bull Lake intrusive suite: Remnants of a 2.48 Ga large igneous and metallogenic province in the Sudbury area of the Canadian Shield. *Econ Geol* 97:1577–1606
- Kerr A, Leitch AM (2005) Self-destructive sulfide segregation systems and the formation of high-grade magmatic ore deposits: *Econ Geol* 100:311–332
- Maier WD, de Klerk WJ, Teigler B, Mitchell AA (1996) Cu/Pd and Cu/Pt of silicate rocks in the Bushveld Complex: implications for platinum-group element exploration. *Econ Geol* 91:1151-1158.
- Price MM, Samson IM, Fryer BJ, Barrie CT (2010) Platinum

group element mineralization in the River Valley intrusion, Ontario, Canada: characterization and effects of water-rock interaction. In: Jugo P (ed) *Extended Abstracts, 11th Int Plat Symp, Sudbury, Canada. Ontario Geol Surv, Misc Release, Data-269. p. 4*

The Platinova Reef, Skaergaard Intrusion, East Greenland: an example of the formation of low volume, high tenor magmatic PGE-Au mineralization in closed systems

David A. Holwell

Department of Geology, University of Leicester, University Road, Leicester, LE1 7RH, UK

Reid R. Keays

School of Geosciences, Monash University, Victoria 3800, Australia

Abstract. The Skaergaard Intrusion hosts an example of very high tenor, but extremely low volume, stratiform, PGE and Au mineralisation in a zone referred to as the Platinova Reef. We define the reef package, from base upwards, as having a lower subzone, a Pd zone, an Intermediate zone (Pd 0.2-1 ppm), which is capped by a Au zone, overlain by a Cu zone. The mineralised section exhibits high precious metal tenors and there is a very sharp increase in the abundance of low tenor sulfide above the Au zone. Remarkable Cu/Pd vs Pd relationships indicate formation of sulfide from two compositionally distinct magma bodies. We propose a multi-stage model of ore formation, with very late stage S saturation in the magma producing Pd, Au and Cu rich sulfide droplets that sank to the floor, but completely redissolved in an Fe-rich bottom layer. Subsequent S-saturation of this layer then produced high tenor sulfides with metals partitioning into the sulfide liquid according to their $D_{\text{Sul/Sil}}$ values. Sulfides formed in the rest of the chamber were higher volume and low tenor. This demonstrates that sulfide dissolution can take place in closed systems, and that it may be essential in producing PGE-Au mineralization in closed systems.

Keywords. Skaergaard, platinum-group elements, gold, Platinova Reef, sulfide saturation, dissolution upgrading

1 Introduction

The Platinova Reef of the 55Ma Skaergaard Intrusion, east Greenland, exhibits an unusual style of magmatic sulfide precious metal mineralization. This is characterized by: a Pd, Au, Cu-dominant and Ni, Pt-poor nature; offsets in individual metal profiles; anomalously low sulfide contents; a sharp stratigraphic change from high tenor, low volume sulfides to low tenor, higher volume sulfides; and lateral variation in the thickness of the high tenor package. As such, they do not fit easily into either conventional R factor and sulfide settling model for the formation of stratiform magmatic sulfides such as the Merensky Reef of the Bushveld Complex (which would produce more sulfide), or models involving multistage-dissolution upgrading (which requires an open system and more than one batch of magma).

2 Geology of the Skaergaard Intrusion

The 55 Ma gabbroic Skaergaard Intrusion, located in the Kangerlussuaq region of east Greenland, hosts

stratiform Au and PGE mineralization in the upper portions of the magmatic stratigraphy. The Skaergaard Intrusion is believed to have formed by crystallisation of a homogenised batch of tholeiitic magma in a closed system. It consists of three main units: the Layered Series, the Upper Border Series and the Marginal Border Series. From its base upwards, the Layered Series consists of the Hidden Zone, the mafic Lower, Middle and Upper Zones and the Sandwich Horizon, the latter being the most differentiated unit of the intrusion.

The Platinova Reef is located within the Triple Group, a ~100m thick unit at the top of the Middle Zone of the Layered Series. The Triple Group is a series of three macrorhythmic units that takes its name from three prominent leucocratic layers. Upper Zone gabbros, distinguished from the Middle Zone rocks by the presence of cumulus olivine, overlie the Triple Group

3 PGE mineralization: the Platinova Reef

The mineralization is stratiform and made up of a package of mineralised horizons referred to as the Platinova Reef, but is unusual and distinct from many other stratiform PGE reefs in a number of ways. The Platinova Reef is characterised by extremely low sulfide contents ($S < 100$ ppm); a Au- and Pd-dominant mineralogy, and a Pd/Pt ratio of around 10. Other features include: systematic stratigraphic offsets in individual metal peaks and the association of the precious metals with very small (< 0.5 mm) droplets of Cu-rich, Ni-poor sulfides. As such, the Platinova Reef is an example of an extremely high tenor, Au-Pd-rich, and Pt-Ni-poor stratiform deposit, formed in a closed system.

3.1 Precious and base metal geochemistry

We have divided the Platinova Reef into five zones based on the presence of Pd, Au and Cu mineralization (Fig. 1): the lower Subzone, the Pd zone (Pd > 1 ppm), the Intermediate zone (Pd 0.1-1 ppm), the Au zone (Au > 1 ppm) and the upper Cu zone (precious metals < 1 ppm). The mineralization beneath the Cu zone is associated with very low volume (S below detection limit), high tenor sulfides with low Cu/Pd ratios whereas the sulfides in the Cu zone are much lower tenor, higher volume and have high Cu/Pd ratios.

A striking, and consistent feature is the change in

Pd/Au ratio with height. It is highest at the base of the Pd zone and decreases systematically from around 40 to 1 in every single drill hole profile. The Au zone marks the point at which the Pd/Au ratio changes from >1 below, to <1 above (Fig. 1).

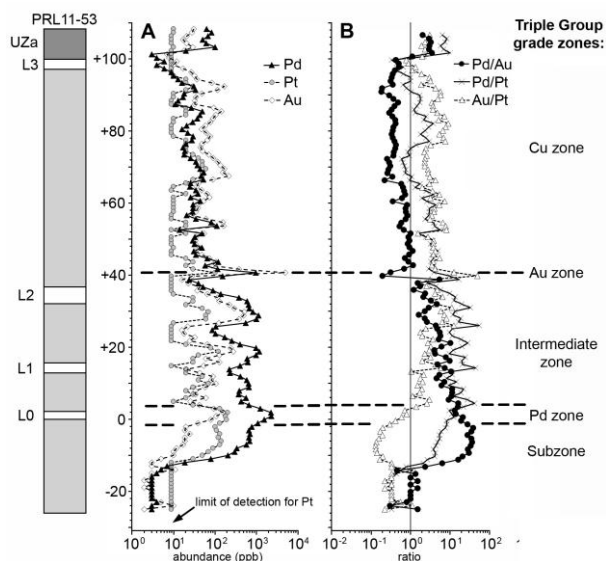


Figure 1. A: Pt, Pd and Au distributions and B: Pt/Pd, Pd/Au and Au/Pt ratios through drillhole PRL11-53. L0, 1, 2 and 3 refer to the leucocratic layers within the Triple Group. UZa = Upper Zone a.

The concentration of Cu increases very slightly in the subzone, but remains low throughout the mineralised zone. There is very little increase in Co and Ni, reflecting the highly evolved nature of the Skaergaard magma, with early fractionation of these elements into oxides and silicates prior to S saturation.

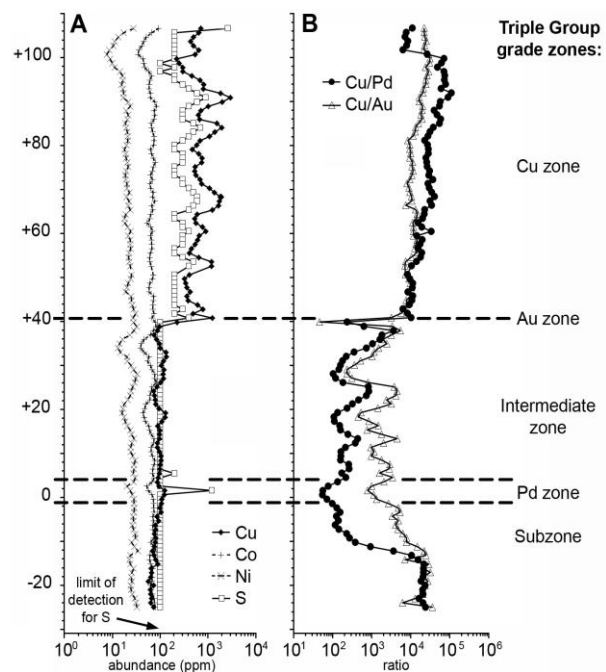


Figure 2. A: Cu, Co, Ni and S distributions and B: Cu/Pd, Cu/Au and Au/Pt ratios through drillhole PRL11-53.

3.2 Apparent R factors

Figure 3 shows the relationship between Cu/Pd ratio and Pd for samples from drill hole PRL11-53, together with tie lines showing the trends for what would be expected from variable percentages of sulfide in the magma at different R factors (c.f. Barnes et al., 1993). The relationship between Pd and Cu/Pd below the Au zone is remarkable, with all samples fitting near-perfectly on a single trend line. The samples from beneath the Subzone plot in the depleted field, but along the same line as all samples from the Subzone up through the Pd zone, Intermediate zone and Au zone, indicating the sulfides in these samples formed from a single magma. All samples from above the Au zone lie in, or close to, the depleted field in a very distinct field on the plot, indicating genesis from a separate magma.

The relationships shown in Figure 3 strongly suggest that the sulfides within the mineralized portion of the Triple Group (from the Subzone through to the Au zone) formed from a PGE-enriched magma under a very high apparent R factor (>100,000) and a maximum amount of sulfide of 0.1%. The variation along the trendline can be interpreted by the amount of sulfide being generated, with the increase in Pd values corresponding to an increase in the amounts of sulfides present. At such high apparent R factors, relative variations in Pd and Cu are very sensitive to changes in tiny amount of sulfide due to the different D_{sul}/s_{il} values. We interpret the Cu/Pd vs Pd trend line defined by samples from the Subzone, the Pd zone and the Intermediate zone to be the product of small variations in sulfide contents through these zones.

In addition, this shows that conversely, the sulfides from above the Au zone were formed from a very different, depleted magma with a much lower apparent R factor. Thus, it appears that two separate generations of sulfide were present, one that separated into an enriched magma, and one that separated into a depleted magma. However, this requires further explanation, given that Skaergaard is a closed, single magma pulse system.

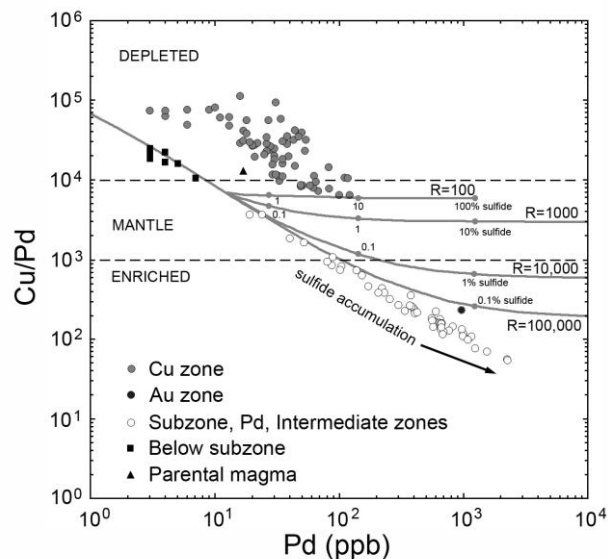


Figure 3. Relationship between Cu/Pd ratio and bulk Pd content through the Triple Group in drill hole PRL11-53.

4 Discussion

There is no current consensus for the formation of the Platinova Reef. Early studies by Bird et al. (1991) and Andersen et al. (1998) invoked a magmatic origin, with the precious metals being concentrated by an immiscible sulfide liquid. Andersen et al. (1998) attribute the differences in precious metal ratios with height to be the result of fractionation of a filter pressed sulfide liquid. Andersen (2006) calculated that there had been a significant amount of post-magmatic S loss from the Skaergaard sulfides and suggested that upward migrating hydrothermal fluids could have caused dissolution and reprecipitation of Pd and Au in a cumulate with several stratiform redox barriers forming the multiple Au- and Pd-dominant reefs. However, Wohlgemuth-Ueberwasser et al. (2012) suggested that this was unlikely and that oxidation of the sulfide produced the low volume, Cu-dominant sulfide assemblage.

It is clear from our data, and that of the previous studies, that the Platinova Reef is a rather unique, stratiform deposit with a number of unusual features. As such, any model that attempts to explain the genesis of the mineralization must explain the following detailed characteristics outlined in this, and previous papers: 1. The very low sulfide content of the mineralized zone; 2. The systematic variations and offsets in PGE and Au concentrations and ratios with height within the Triple Group; 3. The high precious metal tenor of sulfides in the mineralized zones, and the sharp increase in the abundance of low tenor sulfide above the Au zone; 4. The high grade and thin nature of the Au zone and 5. The indication of the formation of sulfides from two compositionally distinct magmas.

5 A model for the formation of the Reefs

The Platinova Reef formed from a magma that had been depleted of the bulk of its Ni and Co (and also some of its Pt) due to fractionation of these elements into earlier forming silicates and oxides, whereas Pd, Pt, Au, Cu and S accumulated in the residual magma. Mineralization was triggered at the top of the Middle Zone following prolonged fractionation of the magma through a multi-stage process of sulfide saturation, metal enrichment, sulfide dissolution and further sulfide saturation, that we believe most completely explains all of the characteristic features of the Reefs. This model can be summarized in the following stages:

Palladium, Au, Cu and S plus some Pt accumulated in the residual magma during crystallization and fractionation of the Skaergaard magma during S-undersaturated conditions.

After ~70% crystallization, the magma along the roof and walls of the chamber became S-saturated due to cooling, causing the separation of a sulfide liquid.

Sulfides settled downwards through the magma, carried by convection currents, scavenging nearly all the Pd, Pt, Au and Cu from the magma.

As the sulfides descended downwards into the hotter regions of the magma chamber, they continued to scavenge Pd, Pt, Au and Cu, but lost S and Fe, and then

Cu, which were resorbed back into the magma. Precious metals were retained in the ever decreasing volume of sulfide due to their much higher $D_{\text{sul/sil}}$ partition coefficients.

In the bottom-most layer of the chamber the temperature was even higher due to the latent heat of crystallization of the crystallizing silicate and oxides: in addition, Fe-rich interstitial melts were present (Holness et al., 2011). As a result, the sulfides were completely dissolved, producing a bottom layer which was very rich in Pd, Pt, and Au, but S-undersaturated.

However, the PGE-rich bottom layer eventually became S-saturated in the vicinity of crystallizing Fe-Ti oxides, the formation of which depleted the silicate melt adjacent to them in FeO and drove it to S-saturation. Tiny droplets of PGE-rich sulfide then formed in these areas of FeO depletion. The sulphides so formed were enriched in metals, in order of the $D_{\text{sul/sil}}$ values of the metals. Hence, the first sulphides to form at the base of the mineralized zone, were Pd- and Pt-rich, but Au-poor whereas later sulphides had less Pd and Pt but more Au, because both Pd and Pt have higher $D_{\text{sul/sil}}$ values than Au. This produced very high tenor sulfides, the progressive decrease in Pd/Au ratio up through the mineralised zone and explains the apparently high R factor of these sulfides.

Sulfides with low precious metal tenors formed throughout the chamber and started to coalesce and settle, aided by convection. As this was happening, the high tenor sulfides at the base became trapped in the crystallising pile forming the Pd and Intermediate zones.

The Au zone formed at the changeover of the *in situ*, low sulfide regime and the dynamic high sulfide regime. With the increase in the amounts of sulfide that were now settling/being swept to the floor, all the Au in the boundary layer was scavenged immediately as the settling sulfide met the floor, forming the Au zone, with all sulfides forming above this being low tenor.

6 Implications for low sulfide, high tenor magmatic PGE-Au deposits

The integrated model we present for the Platinova Reef explains the rare example of the genesis of high tenor, low sulfide PGE reefs, from extremely high apparent R factors following prolonged fractionation of the parental magma. Under normal circumstances, such high R factors may seem unlikely, and such small amounts of sulfide may not be expected to attain such high metal tenors if they do not have the ability (due to size and density) or time to equilibrate with a large amount of magma through settling. This is especially true for an intrusion such as Skaergaard that formed from a single homogenised magma body, preventing the multistage upgrading that took place at Noril'sk, and also experienced no input from external contamination sources that would trigger S saturation.

Our model explains how these high tenors can be attained through effective upgrading of the magma packages into which the sulfide separates. This process is different to the multistage upgrading and multistage-dissolution upgrading discussed and modelled by Kerr and Leitch (2005) as Skaergaard is a closed system.

What we propose that our model for the Skaergaard magma can be described as closed system-dissolution upgrading. This is partly analogous to the multistage-dissolution upgrading, but dissolution occurs within the same magma, in a part of the chamber which differs in composition and temperature such that it is S-undersaturated. This fine balance is almost certainly only possible in cases where S saturation occurs following prolonged fractionation of the magma, rather than in cases where large amounts of contamination trigger a large shift in the S carrying capacity of the magma and the separation of a large amount of sulfide liquid. Furthermore, the late stage timing of S saturation allowed the residual melt to become significantly enriched in Au, Pd, Pt and Cu. Although Kerr and Leitch (2005) state that multistage-dissolution upgrading is more effective at forming enriched ore deposits in open systems, we suggest that a similar process may be able to occur in a closed system such as Skaergaard, and that although the processes may be different dynamically, it can also effectively produce high grade ore deposits. Furthermore, in this case, there is no requirement for the addition of external S through contamination.

Perhaps the most significant implication of the Platinova Reef is that due to its extremely low sulfide content, it is impossible to identify in the field and required a significant amount of serendipity in its discovery (Nielsen et al., 2005). Using conventional exploration criteria for PGE deposits in such magmatic systems, the Skaergaard Intrusion would appear to be unprospective. Thus, for such deposits formed through fractionation, a revised set of criteria for any model should be used. These deposits are most likely to be characterised by low sulfide contents, offsets in metal peaks, be Cu- and Pd(+Pt)-dominant and Ni-poor, and occur in the upper parts of the magmatic stratigraphy. Indicators of contamination and multiple injections of magma are not necessarily essential.

This study also shows how the relative $D_{\text{Sul/sil}}$ values become important in determining metal profiles in such small volume sulfide melts, especially offsets in precious metals such as the PGE and Au. Effectively, our data provide a natural example that confirms the experimentally derived $D_{\text{Sul/sil}}$ values for Pd, Pt, Au and Cu. The offsets of Pd (and Pt) with Au and Cu are not seen in relatively sulfide-rich deposits such as the Platreef (e.g. McDonald and Holwell, 2011), but are observed in the Rincon del Tigre Complex (Prendergast, 2000). Enrichment of the sulfides in all these cases has been suggested to be determined by partitioning behaviour of the individual elements. Our data show an excellent example in which the volume of sulfide available is so small that these effects are magnified over sections of up to 50 m, and manifest as smooth Pd/Au and Cu/Pd profiles up through the section that reflect both these partitioning effects and the amount of sulfide available. In addition, as the magma appears to have been on the boundary of S saturation for some time, the broad correlation between V and Pd also indicates that changes in the fractionation of cumulus phases such as magnetite in such conditions may have an effect on the very sensitive conditions of S saturation and understuration. This role of magnetite fractionation

in triggering S saturation in the Skaergaard magma has also been suggested by Andersen (2006), for the Rincon del Tigre Complex by Prendergast (2000) and for the Stella Intrusion, South Africa, by Maier et al. (2003). Such relationships are not preserved in deposits where sulfide volumes are much greater as the chalcophile elements effectively behave the same in an abundance of sulfide. In addition, in S-poor closed systems, magnetite fractionation may be a key controlling process in determining the position of low-sulfide PGE-reefs.

Acknowledgements

Platina Resources Ltd., and especially Thomas Abraham-James, are gratefully acknowledged for providing the geochemical analyses used in this study, and for granting permission to publish and present these results.

References

- Andersen JCØ, Rasmussen H, Nielsen TFD, Ronsbo JC (1998) The Triple Group and the Platinova gold and palladium reefs in the Skaergaard Intrusion: stratigraphic and petrographic relations. *Econ Geol* 93:488-509
- Andersen JCØ (2006) Postmagmatic sulfur loss in the Skaergaard Intrusion: Implications for the formation of the Platinova Reef. *Lithos* 92:198-221
- Barnes S-J, Couture J-F, Sawyer EW, Bouchaib C (1993) Nickel-Copper occurrences in the Belleterre-Angliers Belt of the Pontiac Subprovince and the use of Cu-Pd ratios in interpreting Platinum-Group Element distributions. *Econ Geol* 88:1402-1418
- Bird DK, Brooks CK, Gannicott RA, Turner PA (1991) A gold-bearing horizon in the Skaergaard Intrusion, east Greenland. *Econ Geol* 86:1083-1092
- Holness MB, Stripp G, Humphreys MCS, Veksler IV, Nielsen TFD, Tegner C (2011) Silicate liquid immiscibility within the crystal mush: late-stage magmatic microstructures in the Skaergaard intrusion, east Greenland. *J Petrol* 52:175-222
- Kerr A, Leitch AM (2005) Self-destructive sulfide segregation systems and the formation of high-grade magmatic ore deposits. *Econ Geol* 100:311-332
- Maier WD, de Klerk WJ, Teigler B, Mitchell AA (1996) Cu/Pd and Cu/Pt of silicate rocks in the Bushveld Complex: implications for platinum-group element exploration. *Econ Geol* 91:1151-1158
- Maier WD, Barnes S-J, Gartz V, Andrews G (2003) Pt-Pd reefs in magnetites of the Stella layered intrusion, South Africa: A world of new exploration opportunities for platinum group elements. *Geology* 31:885-888
- McDonald I, Holwell DA (2011) Geology of the Northern Bushveld Complex and the Setting and Genesis of the Platreef Ni-Cu-PGE Deposit. *Revs in Econ Geol* 17:297-327
- Nielsen TFD, Andersen JCØ, Brooks CK (2005) The Platinova Reef of the Skaergaard Intrusion, in: Mungall JE (ed) Exploration for platinum-group element deposits: *Min Ass Can, Short Course Series* 35:431-456.
- Prendergast MD (2000) Layering and Precious Metals Mineralization in the Rincón del Tigre Complex, Eastern Bolivia. *Econ Geol* 95:113-130.
- Wohlgemuth-Ueberwasser C, Fonseca R, Ballhaus C, Berndt J, (2012) Sulfide oxidation as a process for the formation of copper-rich magmatic sulfides. *Mineral Dep* DOI: 10.1007/s00126-012-0420-9

Temporal and spatial distribution of magmatic Ni-Cu-PGE, Cr, and Fe-Ti-V deposits in the Bird River–Uchi–Oxford–Stull–La Grande–Eastmain superdomain: a new metallotect within the Superior Province

M.G. Houlé

Geological Survey of Canada, GSC-Québec, 490 Couronne Street, Québec, Québec, Canada G1K 9A9

C.M. Lesher

Mineral Exploration Research Centre, Department of Earth Sciences, Laurentian University, 935 Ramsey Lake Road, Sudbury, Ontario, Canada P3E 2C6

R.T. Metsaranta

Ontario Geological Survey, 933 Ramsey Lake Road, Sudbury, Ontario, Canada P3E6B5

J. Goutier

Géologie Québec, Ministère des Ressources naturelles, 70 avenue Québec, Rouyn-Noranda, Québec, Canada J9X 6R1

H.P. Gilbert

Manitoba Geological Survey, 360-1395 Ellice Avenue, Winnipeg, Manitoba, Canada R3G 3P2

V. McNicoll

Geological Survey of Canada, GSC-Ottawa, 601 Booth Street, Ottawa, Ontario, Canada K1A 0E8

Abstract. Cr and Fe-Ti-V mineralization in ultramafic intrusions is known from several areas of the Superior province, but was considered to be of marginal significance until the discovery of world-class Cr deposits and potentially significant Fe-Ti-V mineralization in the McFaulds Lake greenstone belt ("Ring of Fire" area) of northern Ontario. Ni-Cu-(PGE), Cr-PGE, and Fe-Ti-V deposits/occurrences in the northern part of the Superior Province occur predominantly within Neo-archean supracrustal successions along the margins and within the interiors of the Bird River–Uchi–Oxford–Stull–LaGrande–Eastmain domains (BUOGE "superdomain"). This superdomain defines a major Cr-Ni-Cu-PGE-V metallotect that appears to be fundamentally different from other parts of the Superior Province, such as the Abitibi greenstone belt or the apparently relatively unmineralized North Caribou core, Island Lake, and Goudalie domains. Detailed studies of the tectonic, volcanic, and petrogenetic settings of key areas of the BUOGE superdomain are in progress and should provide light on why this metallotect is so different from those in the southern part of the Superior Province.

Keywords: chromite, nickel, Superior Province, Oxford-Stull, LaGrande-Eastmain, Bird River

1 Introduction

The discoveries of world-class Cr deposits, significant Ni-Cu-PGE deposits, and numerous Fe-Ti-V occurrences in the McFaulds Lake (a.k.a. "Ring of Fire") area of northern Ontario have greatly renewed interest in orthomagmatic mineralization associated with mafic-ultramafic intrusions in the Superior Province. Mafic-ultramafic intrusions and ultramafic volcanic rocks are widespread throughout the Superior Province, but their association with significant Ni-Cu-PGE-Cr-V mineralization is not evenly distributed across the craton.

The purpose of this contribution is to identify a new

Cr-Ni-Cu-PGE-V metallotect within the Superior Province based on currently available information and interpretations of the various terrane and domain boundaries within the province.

2 The Superior Province

The Superior Province is one of the largest coherent Archean cratons in the world, with exceptional mineral endowments reflected in the presence of numerous world-class Au, Cu-Zn-(Au) VMS deposits, and significant Ni-Cu-PGE deposits (Poulsen et al. 1992).

Early investigations of the Superior Province recognized a limited number of subprovinces based on general lithological characteristics (e.g., Card and Ciesielski 1986). Subsequently, more detailed lithological and stratigraphic data were used to define the subprovinces as terranes and domains (e.g., Thurston et al. 1991). Since then, however, considerable effort has been devoted by the Manitoba and Ontario Geological Surveys, Géologie-Québec, and the Geological Survey of Canada using high-resolution geochronological, structural, stratigraphic, geochemical, and tectonic data (e.g., Stott et al. 2010) to identify stratigraphically and tectonically-distinct terranes and domains.

The Uchi, Oxford-Stull, La Grande, and Eastmain domains have been correlated across the entire Superior Province (Stott et al. 2010), and the Bird River domain, located across the English River basin from the Uchi, appears to share some geological similarities (Gilbert et al. 2008). Taken together, the geochronological, stratigraphic, structural, tectonic, and metallogenic data suggest that the Bird River–Uchi–Oxford–Stull–La Grande–Eastmain domains form a ~E-W "BUOGE" superdomain across the Superior Province (Fig. 1).

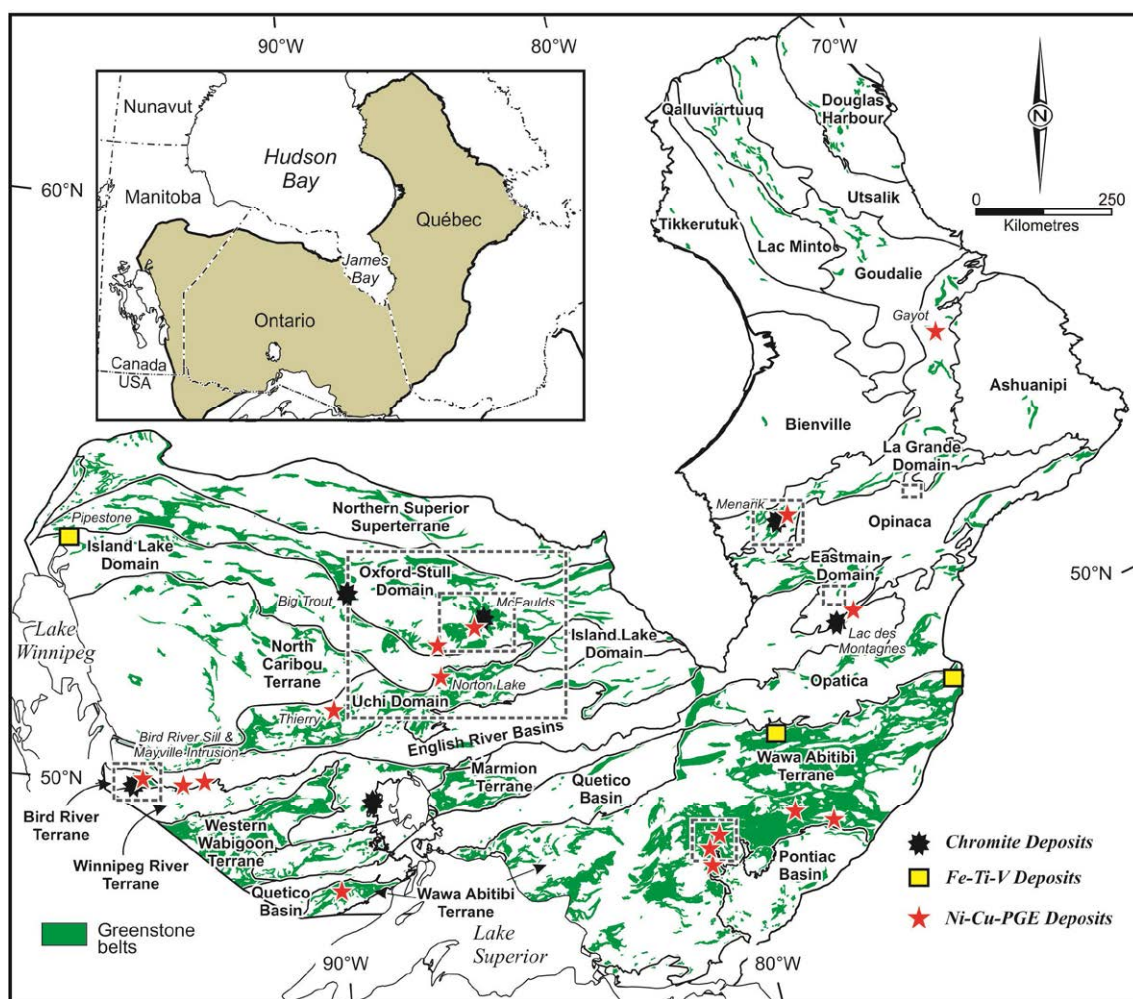


Figure 1. Schematic geological map showing the main Ni-Cu-PGE sulphide and chromite deposits of the Oxford-Stull, LaGrande, and Eastmain domains, and the Bird River and the Abitibi greenstone belts within the Superior Province. Outline boxes indicate the main locations under investigation within the TGI4 high-magnesium ultramafic to mafic systems subproject. Terranes, domains and boundaries are modified from Stott et al. (2010).

3 Komatiites and mafic and ultramafic intrusions in the BUOGE

Komatiites and mafic to ultramafic intrusions occur throughout the entire BUOGE superdomain and range from Meso- to Neoproterozoic. Cr, Ni-Cu-PGE, and Fe-Ti-V mineralization occur preferentially within supracrustal successions along the margins, but also within the interiors of the BUOGE superdomain.

Metallogenic associations within this superdomain provide additional geological constraints for the metallogenic evolution of the Superior Province, for example in the case of Ni-Cu-PGE deposits, which are abundant in the Wawa-Abitibi terrane (Houlé and Lesher 2011) and Bird River domain, but minor in the Uchi, La Grande, and Eastmain domains, and absent in the Island Lake, Wabigoon, and Goudalie domains. Ni-Cu-PGE deposits occur across the BUOGE superdomain and appear to range in age from Neoproterozoic to Mesoproterozoic, with the best examples occurring within the Bird River (e.g., Maskwa – Bird River Sill; Fig. 2A), Uchi (e.g., Norton Lake), Oxford-Stull (e.g., Eagle’s Nest - Ring of Fire Intrusive Complex; Fig. 2B and 2C), Eastmain (e.g., Nisk), and La Grande (e.g., Gayot; Fig. 2D) domains

(Table 1). Cr mineralization is virtually absent in most of the Superior terranes or domains except for domains that potentially belong to the BUOGE superdomain. Similarly to Ni-Cu-PGE deposits, Cr-PGE deposits also occur across the BUOGE superdomain and appear to be mainly Neoproterozoic in age, with the best examples occurring in the Bird River (e.g., Chrome - Bird River Sill; Fig. 3A), Oxford-Stull (e.g., Black Thor and Blackbird - Ring of Fire Intrusive Complex; Fig. 3B and 3C respectively), and La Grande (e.g., Menarik; Fig. 3D) domains (Table 1). In comparison Fe-Ti-V deposits appear to be more spatially restricted and less abundant, and so far have been recognized only within the westernmost parts of the Oxford-Stull domain (e.g., Pipestone). However, other important Fe-Ti-V deposits also occur near the northern margin of the Abitibi terrane in Québec (Bell River and Lac Doré Complexes).

Thus far, only the McFaulds Lake Cr deposits (Black Thor and Black Label deposit, Big Daddy deposit, Blackbird deposit) and McFaulds Lake Ni-Cu-PGE deposits (Noront Eagle’s Nest) appear to be economic, but they demonstrate the potential for much greater amounts of mineralization in the BUOGE (Table 1).

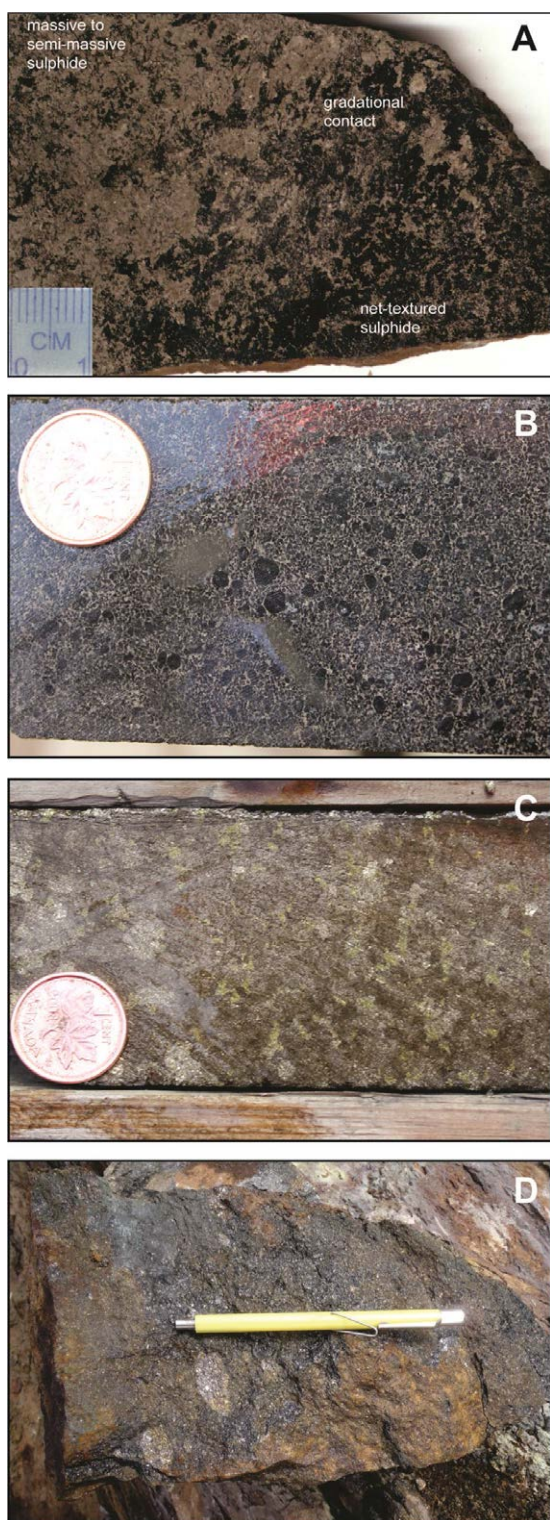


Figure 2. Typical Ni-Cu-PGE mineralization associated with mafic and ultramafic intrusions in the BUOGE superdomain. A) Gradational contact between semi-massive sulphide and net-textured sulphide at the Maskwa deposit, Bird River Sill, Manitoba (after Stansell 2006). B) Net-textured sulphide at Eagle's Nest in the Ring of Fire Intrusive Complex, Ontario. C) Massive sulphide at Eagle's Nest in the Ring of Fire Intrusive Complex, Ontario. D) Peridotite with disseminated sulfides containing cm-scale blebs of massive sulfides from the L occurrence in the Gayot area (courtesy of Mines Virginia).

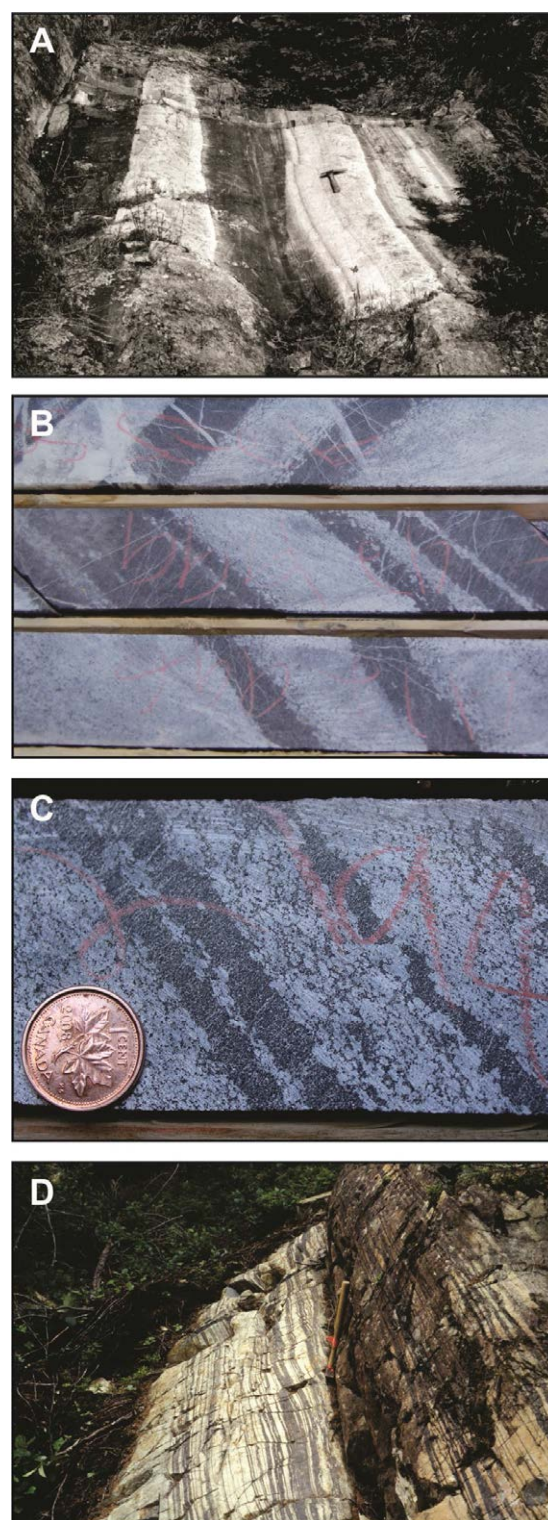


Figure 3. Typical Cr mineralization associated with mafic and ultramafic intrusions in the BUOGE superdomain. A) Layered chromitites in the Bird River Sill, southeast Manitoba (after Williamson 1990). B) Layered chromitites at the Black Thor deposit in the Ring of Fire Intrusive Complex, northern Ontario. C) Layered chromitites at the Blackbird deposit in the Ring of Fire Intrusive Complex, northern Ontario. D) Layered chromitites in the Menarik Igneous Complex, James Bay area, Québec.

4 Concluding Remarks

The BUOGE superdomain defines a major Cr-Ni-Cu-PGE-V metallogenic province that appears to be fundamentally different from the adjacent terrains in terms of magma composition (low-Mg komatiite/high-Mg tholeiite vs. high-Mg komatiite/tholeiite), volcanic-subvolcanic setting (ultramafic intrusions > lava flows vs. ultramafic intrusions < lava flows), and sedimentary environments (oxide-facies iron formation > sulphide-facies iron formation vs. oxide-facies iron formation < sulfide-facies iron formation) from the Ni-Cu-PGE dominated systems in the Abitibi greenstone belt or the apparently relatively unmineralized North Caribou core, Island Lake domain and Goudalie domain.

Detailed studies of the tectonic, volcanic, and petrogenetic settings of key areas of the BUOGE superdomain are in progress and should provide light on why this metallogenic province is so different from those in the southern part of the Superior Province.

Table 1. Ni-Cu-PGE, Cr-PGE, and Fe-Ti-V mineralization in the BUOGE superdomain.

	Ni-Cu-PGE	Cr	Fe-Ti-V
Bird River	<i>Maskwa</i> <i>M2 Mayville</i> <i>Dumbarton</i> Page & Ore Faults	<i>Chrome</i> <i>Page</i> <i>Bird Lake</i> <i>Euclid</i>	
Uchi	<i>Thierry</i> Norton Lake		
Oxford-Stull	<i>Eagle's Nest</i> AT-12	Blackbird Black Thor Big Daddy Black Creek Big Trout	Pipestone Butler Thunderbird <i>Highbank</i>
La Grande	Gayot Menarik	<i>Menarik</i> <i>Nadine</i>	<i>Baie Chapus</i>
Eastmain	Nisk	Lac des Montagnes Lac Fed	

Bold: major, **Bold-Italic:** significant, Plain: minor, *Italic:* Marginal

Acknowledgements

We would like to express our appreciation to numerous colleagues including Greg Stott (formerly Ontario Geological Survey), Tim Corkery (formerly Manitoba Geological Survey), Eric Yang, Scott Anderson, and Paul Kremer (Manitoba Geological Survey), Jean-Yves Labbé, Daniel Bandyayera and Claude Dion (Géologie-Québec) for valuable discussions on the geology of the Superior Province. We also acknowledge the involvement and participation of numerous researchers, students and mining company geologists in the high-magnesium ultramafic to mafic system subproject of the Targeted Geoscience Initiative 4 of the Geological Survey of Canada.

References

- Card KD, Ciesielski A (1986) Subdivisions of the Superior Province of the Canadian Shield. *Geoscience Canada* 13: 5-13.
- Gilbert HP, Davis DW, Duguet M, Kremer PD, Mealin CA, MacDonald J (2008) Geology of the Bird River Belt, southeastern Manitoba (parts of NTS 52L5, 6). Manitoba Science, Technology, Energy and Mines, Manitoba Geological Survey, Geoscientific Map MAP2008-1, scale 1:50 000 (plus notes and appendix).
- Houlé MG, Leshar CM (2011) Komatiite-Associated Ni-Cu-(PGE) Deposits, Abitibi Greenstone Belt, Superior Province, Canada. *Rev Econ Geol* 17:89-121.
- Poulsen KH, Card KD, Franklin JM (1992) Archean tectonic and metallogenic evolution of the superior province of the Canadian shield. *Precambrian Res* 58: 25-54.
- Stansell AE (2006) Sulphide fragments in waste rock at the Maskwa open pit mine, southeastern Manitoba (NTS 52L6 NW): investigations on petrogenesis, potential source rocks and mode of emplacement. B.Sc. thesis, University of Manitoba, Winnipeg, Manitoba: 90 p.
- Stott GM, Corkery MT, Percival JA, Simard M, Goutier J (2010) A revised terrane subdivision of the Superior Province; in Summary of Field Work and Other Activities 2010. *Ont Geol Surv, Open File Report 6260: 20-1 to 20-10.*
- Thurston PC, Osmani IA, Stone D (1991) Northwestern Superior Province: review and terrane analysis, in *Geology of Ontario. Ont Geol Surv, Special Volume 4-Part 1: 81-142.*
- Williamson B (1990) Geology of the Bird River Sill at the Chrome Property, southeast Manitoba. *Geological Survey of Canada, Open File 2067: 44 p.*

Sulfur degassing and nickel sulfide ore forming process in Archean komatiite volcanoes

Carissa Isaac, Marco L. Fiorentini

Centre for Exploration Targeting, ARC Centre of Excellence for Core to Crust Fluid Systems (CCFS), The University of Western Australia

Boswell Wing

Department of Earth and Planetary Sciences, McGill University, Canada

Abstract. Magmatic hydrothermal oceanic vents represent places where metals accumulate in the form of exhalative and sedimentary sulfides associated with submarine felsic volcanoes. These are also loci where life can flourish in the form of a wide range of complex and diversified bacteria colonies. In the Archean Earth, coeval to the emplacement of sulfide-bearing felsic magmas, komatiites locally erupted on the floor of the ocean. These hot and highly turbulent magmas assimilated previously formed volcanogenic exhalative and sedimentary sulfides, leading to the formation of discrete sulfide melts, which concentrated chalcophile and siderophile metals such as nickel, copper and the platinum group elements from the komatiite magma. Multiple sulfur isotope data on sulfides from variably mineralized komatiite units in the Archean north Eastern Goldfields, Western Australia, provide new constraints on these assimilation and ore-forming processes. Although magmatic sulfides from komatiites display very similar $\Delta^{33}\text{S}$ signatures to volcanogenic exhalative and sedimentary sulfides, they have consistently lower $\delta^{34}\text{S}$ values relative to these sources. This lowering of the $\delta^{34}\text{S}$ signature is consistent with degassing of the komatiite-sulfide melt system. At the temperatures and oxygen fugacities relevant to komatiite magmatism, sulfur in the melt exists primarily as ^{34}S -poor sulfide species, whereas sulfur in the co-existing gas would be dominated by ^{34}S -rich SO_2 . Continuous loss of this ^{34}S -enriched gas would lower the $\delta^{34}\text{S}$ values of coexisting sulfide melt, leading to magmatic sulfides with the isotopic compositions measured here. Our results indicate that komatiites from the north Eastern Goldfields of Western Australia, irrespective of their initial sulfur content, degassed upon emplacement at Earth's surface. Understanding the link between geodynamic setting where the komatiites were emplaced and amount and rate of sulfur degassing is key to successful localization of world-class nickel sulfide systems.

Keywords: Komatiite, degassing, multiple sulfur isotopes, nickel sulfides, Archean Earth

1 Introduction

Komatiites are ancient volcanic rocks, mostly over 2.5 billion years old, which formed through high-degree partial melting of the mantle (Arndt et al., 2008; Maier et al., 2009). Upon emplacement, large komatiitic sills and channelized lava flows can thermally erode their substrates, and incorporate sulfur from volcanogenic

exhalative sulfide lenses as well as sulfide-rich sediments that occur close to the volcanic vents (Leshner and Burnham, 2001; Bekker et al., 2009; Fiorentini et al., 2012a). This contamination process locally induces sulfide saturation in komatiite lava flows and channelized sills (Leshner, 1989).

Current models suggest that a magma that attains sulfide saturation develops an immiscible sulfide liquid phase within the silicate magma. Chalcophile elements such as Ni, Cu and the platinum-group elements strongly partition into the immiscible sulfide liquid phase, thus becoming concentrated in the sulfide liquid. The progressive accumulation of immiscible sulfide liquid in volcanological settings such as basal embayments at the bottom of lava channels and/or within magmatic conduits forms metal concentrations of potentially economic interest (Campbell and Naldrett, 1979).

However, results from this study cast a new light on the interpretation of the formation of nickel-sulfide deposits associated with komatiites. The new model that we put forward implies that, upon sulfide saturation, a sulfide liquid coexists at equilibrium with a silicate melt and a sulfur-bearing gas. Under the oxygen fugacity conditions that characterize komatiite magmatism (Canil, 1997), mass-dependent sulfur isotope fractionation occurs among these three phases. Heavy sulfur isotopes are ultimately partitioned into the gas, leaving the sulfide liquid enriched in the lighter sulfur isotopes. This contribution discusses the implications of this new working hypothesis towards the understanding of ore forming processes and the development of targeting tools for komatiite-hosted nickel-sulfide systems.

2 Samples studied

The samples for this study were collected from the Perseverance, Mount Windarra and Olympia nickel-sulfide deposits, respectively in the Archean Agnew-Wiluna, Mount Margaret and Collurabbie greenstone belts of the Eastern Goldfields Superterrane, Yilgarn Craton, Western Australia (Figure 1). We sampled magmatic sulfides hosted in mineralized komatiites and komatiitic basalts as well as sedimentary and hydrothermal exhalative sulfides in adjacent country rocks.

3 Methodology

Sulfur isotope values ($\delta^{33}\text{S}$, $\delta^{34}\text{S}$ and $\delta^{36}\text{S}$) are reported

in the conventional δ notation with respect to VCDT (Vienna-Canon Diablo Troilite) defined as $\delta^xS = 1000 \times [({}^xS/{}^{32}S)_{\text{sample}} / ({}^xS/{}^{32}S)_{\text{VCDT}} - 1]$, where x is 33, 34 and 36, respectively. Most physical and chemical processes fractionate S isotopes according to the mass differences among the isotopes. However, S isotopes of Archean sedimentary and surficial rocks deviate from the mass-dependent fractionation trend, and display so-called ‘mass-independent’ fractionation (e.g. Philippot et al., 2012). $\Delta^{33}S$ and $\Delta^{36}S$ are measures of mass-independent fractionation of the S isotopes, and are defined as $\Delta^{33}S = \delta^{33}S - 1000 \times [(1 + \delta^{34}S/1000)^{0.515} - 1]$ and $\Delta^{36}S = \delta^{36}S - 1000 \times [(1 + \delta^{34}S/1000)^{1.91} - 1]$ (Farquhar and Wing, 2003).

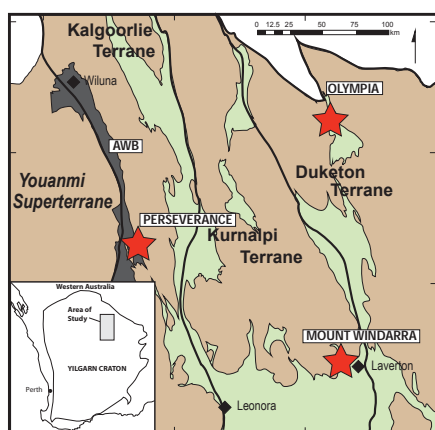


Figure 1. Sampling locations in the Eastern Goldfields Superterrane, Western Australia. Greenstone belts

The S isotopes of sulfide grains from this study were measured in the Stable Isotope Laboratory of the Department of Earth and Planetary Sciences, McGill University. About 2 mg of hand-picked pure sulfide were crushed, and S from the resulting powder was extracted using a Cr-(II) reagent and reacted to Ag_2S . The resulting Ag_2S was fluorinated at 225°C in a Ni bomb under ~20X stoichiometric excess F_2 for more than 9 h. The SF_6 produced was purified cryogenically and chromatographically and analyzed on a Thermo Electron MAT 253 mass spectrometer for multiple sulfur isotope measurements in a dual-inlet mode. Repeated analyses over the entire analytical session returned uncertainties (1σ) on $\delta^{34}S$ and $\Delta^{33}S$ values better than 0.1 and 0.01‰, respectively.

4 Results

Multiple sulfur data from this study indicate that magmatic nickel-sulfides are notably lighter than their country rock sulfur source counterparts. This mass-dependent isotopic difference is most notable in samples from magmatic sulfides hosted in komatiite lava flows and sills analyzed by Bekker et al (2009) in the Agnew-Wiluna Belt (Figure 2), and in samples from komatiite-hosted sulfides from the Perseverance (Figure 3) and Mount Windarra (Figure 4) komatiite systems. The

isotopic shift also occurs, despite being less prominent, in magmatic sulfides associated with the komatiitic basalt sills at Olympia (Figure 5).

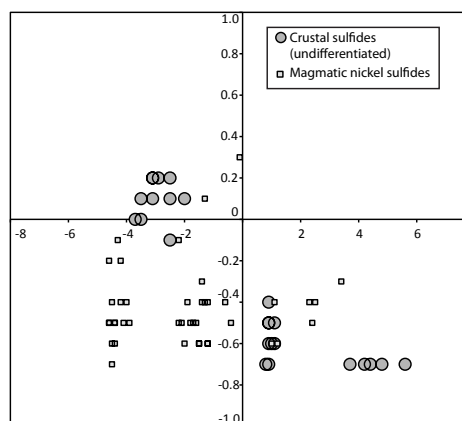


Figure 2. Data from Bekker et al (2009), collected from a number of locations along the Agnew-Wiluna Belt (AWB; cf. Figure 1)

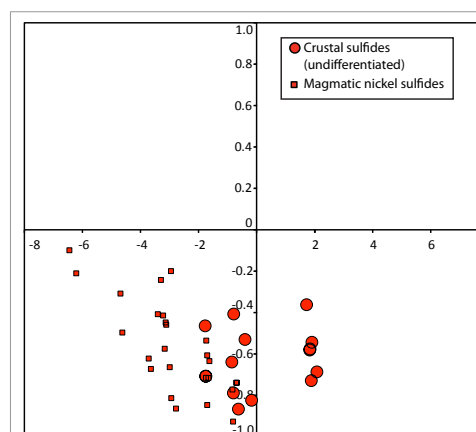


Figure 3. Data from this study from the Perseverance Nickel Deposit along the AWB (cf. Figure 1)

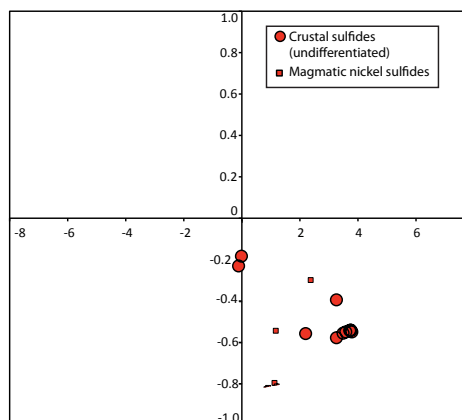


Figure 4. Data from this study from the Mount Windarra Nickel Deposit in the Mount Margaret greenstone belt (cf. Figure 1)

Our modelling shows that the gas coexisting with komatiite lava will be remarkably enriched in heavy isotopes of sulfur. For example, the $\delta^{34}S$ value of such a gas at $\Delta QFM = 0$ and $T=1500^\circ C$ will be ~1 ‰ larger than the $\delta^{34}S$ value of the coexisting silicate melt. Continuous loss of such an isotopically enriched gas will

progressively decrease the $\delta^{34}\text{S}$ value of the silicate melt and, given the minimal S isotope fractionation between sulfide in a silicate melt and a coexisting sulfide liquid (Marini et al., 2011), will similarly decrease the $\delta^{34}\text{S}$ value in the sulfide liquid as well. The $\delta^{34}\text{S}$ differences between sulfur sources and sulfide mineralization identified here (Figures 2-5) imply that ~90-99% of the sulfur in the original sulfide liquid was lost due to degassing.

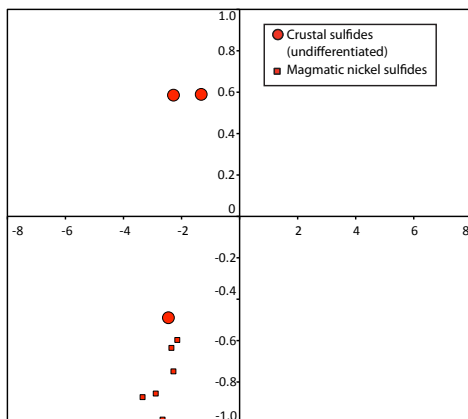


Figure 5. Data from this study from the Olympia Nickel Prospect in the Collurabbie greenstone belt (cf. Figure 1)

5 Discussion

We propose that as the komatiite erupts at surface or in shallow subvolcanic environments, depressurization causes gas to separate from the melt. Although there is much debate about the presence of water in komatiites (Fiorentini et al., 2012b), other gases such as CO_2 and sulfur compounds (chiefly SO_2) occur in otherwise “dry” melts. The formation of SO_2 preferentially takes ^{34}S into the gas phase, which is then lost to the atmosphere, water column or groundwater. Isotopically light sulfur remains in the melt, and imparts a similar isotopic signature to the sulfide liquid and, ultimately, into nickel-sulfide mineralization (Figure 6).

Geological evidence suggests that most komatiite-hosted nickel-sulfide deposits occur in proximal volcanic environments (Leshner, 1989). However, the ore forming process requires not only sulfide saturation but also prolonged partitioning of metals into the sulfide liquid. Current models indicate that the volume ratio between an equilibrating silicate melt and a sulfide liquid (R factor; cf. Campbell and Naldrett, 1979) is the controlling factor on the size and tenor of the resulting nickel-sulfides. In komatiite systems, it has been advocated that high Ni tenors are largely due to the relatively high R factor that characterizes these systems, with large amounts of Ni-rich magma (komatiite) equilibrating with a relatively small crustal sulfur reservoir.

In this study, we argue that degassing plays a crucial role and enables the enhanced partitioning of ore metals (particularly Ni) in a continually decreasing reservoir of sulfide liquid.

This hypothesis has crucial implications for the predictive understanding of the ore-forming process and the localization of different types of komatiite-hosted

mineralized systems. Considering that degassing occurs at various rates according to the thickness of the flow and depth and style of emplacement, it would be possible to predict where more or less degassing has occurred. Accordingly, we argue that this process may play a crucial role not only in controlling the tenor of komatiite-hosted nickel-sulfide deposits, but also ultimately in exerting a first order control on their sizes. While a greater extent of degassing will lead to a greater amount of metals left behind in the sulfide liquid, it will also mean that such a magmatic nickel-sulfide system will be less likely to be preserved, simply because most of the available sulfur is being lost to a gas phase.

6 Conclusive remarks

Barnes and Fiorentini (2012) indicated that the critical factor to form mineralized komatiites requires high magma flux and accessible crustal S sources. At the craton-scale, deep lithospheric structure appears to be the ultimate control on the rate of magma supply between mantle source and crustal emplacement site. These lithospheric structures generally occur at craton margins (Begg et al., 2010), which are also settings where large sulfur reservoirs can form and be easily assimilated upon komatiite eruption and emplacement (Bekker et al., 2009). The work of Fiorentini et al. (2012a) indicated that multiple sulfur isotope data can be utilized in exploration for komatiite-hosted systems at the district to deposit scales.

At the district scale, targeting for komatiite-hosted nickel-sulfides should be based upon a robust understanding of the distribution of country rock sulfides in the stratigraphy. Furthermore, the localization of exhalative sulfides, which are considered to be the primary source of sulfur in known world-class komatiite-hosted nickel-sulfide systems, should be mapped in detail. At the deposit scale, the spatial pattern of mass-independent S isotope values ($\Delta^{33}\text{S}$) in magmatic sulfides and associated host rocks may be utilized as a vector towards high-grade ores of poorly known systems.

Multiple sulfur isotope data on sulfides from variably mineralized komatiite units in the Archean north Eastern Goldfields, Western Australia, provide new constraints on these assimilation and ore-forming processes. Although magmatic sulfides from komatiites display very similar $\Delta^{33}\text{S}$ signatures to volcanogenic exhalative and sedimentary sulfides, they have consistently lower $\delta^{34}\text{S}$ values relative to these sources. This lowering of the $\delta^{34}\text{S}$ signature is consistent with degassing of the komatiite-sulfide melt system. At the temperatures and oxygen fugacities relevant to komatiite magmatism, sulfur in the melt exists primarily as ^{34}S -poor sulfide species, whereas sulfur in the co-existing gas would be dominated by ^{34}S -rich SO_2 . Continuous loss of this ^{34}S -enriched gas would lower the $\delta^{34}\text{S}$ values of coexisting sulfide melt, leading to magmatic sulfides with the isotopic compositions measured here. Our results indicate that komatiites from the north Eastern Goldfields of Western Australia, irrespective of their initial sulfur content, degassed upon emplacement at Earth’s surface. Understanding the link between geodynamic setting where the komatiites were emplaced and amount and rate of sulfur degassing is key

to successful localization of world-class nickel sulfide systems.

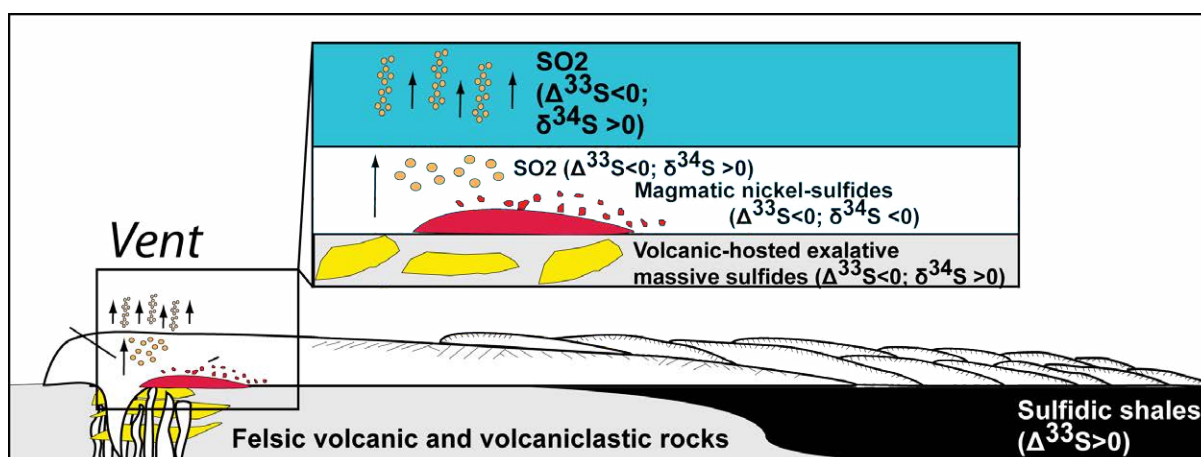


Figure 6. Komatiite-hosted nickel-sulfide systems. The sketch illustrates the isotopic fractionation between a sulfide liquid that coexists at equilibrium with a silicate melt and a sulfur-bearing gas

Acknowledgements

The study was funded by ARC Linkage LP0776780 and Foundation Project “Early evolution of the Earth system and the first life, from multiple sulfur isotopes” within the ARC Centre of Excellence for Core to Crust Fluid Systems. Carissa Isaac is a recipient of a SIRF scholarship from The University of Western Australia.

References

- Arndt, N.T., Barnes, S.J., and Leshner, C.M., 2008, Komatiite: Cambridge, Cambridge University Press, 467 p.
- Barnes, S.J., Fiorentini, M.L., 2012. Komatiite magmas and Ni sulfide deposits: a comparison of variably endowed Archean terranes. *Economic Geology*, 107, 755-780.
- Begg, G.C., Hronsky, J.A.M., Arndt, N.T., Griffin, W.L., O'Reilly, S.Y., and Hayward, N., 2010, Lithospheric, cratonic, and geodynamic setting of Ni-Cu-PGE sulfide deposits: *Economic Geology*, v. 105, p. 1057-1070.
- Campbell, I.H., Naldrett, A.J., 1979. The influence of silicate:sulphide ratios on the geochemistry of magmatic sulphides. *Economic Geology* 74, 503-1505.
- Campbell, I.H., Barnes, S.J., 1984. A model for the geochemistry of the platinum group elements in magmatic sulphide deposits. *Canadian Mineralogist* 22, 151-160.
- Canil, D. (1997). Vanadium partitioning and the oxidation state of Archaean komatiite magmas. *Nature* 389, 842-845.
- Bekker, A., Barley, M.E., Fiorentini, M., Rouxel, O.J., Rumble, D., and Beresford, S.W., 2009, Atmospheric sulfur in Archaean komatiite-hosted nickel deposits: *Science*, v. 326, p. 1086-1089.
- Farquhar, J., and Wing, B.A., 2003, Multiple sulfur isotopes and the evolution of the atmosphere: *Earth and Planetary Science Letters*, v. 213, p. 1-13.
- Fiorentini, M.L., Beresford, S.W., Barley, M.E., Duuring, P., Bekker, A., Rosengren, N., Cas, R., Hronsky, J., 2012a. District to camp controls on the genesis of komatiite-hosted nickel sulfide deposits, Agnew-Wiluna greenstone belt, Western Australia: Insights from the multiple sulfur isotopes. *Economic Geology*, 107, 781-796.
- Fiorentini, M.L., Beresford, S.W., Stone, W.E., Deloule, E., 2012b. Evidence of Water Degassing during emplacement and crystallization of 2.7 Ga komatiites from the Agnew-Wiluna greenstone belt, Western Australia. *Contributions to Mineralogy and petrology*, 164, 143-155.
- Leshner, C.M., 1989, Komatiite-associated nickel sulfide deposits: *Reviews in Economic Geology*, v. 4, p. 45-101.
- Leshner, C.M., and Burnham, O.M., 2001, Multicomponent elemental and isotopic mixing in Ni-Cu-(PGE) ores at Kambalda, Western Australia: *Canadian Mineralogist*, v. 39, p. 421-446.
- Maier, W.D., Barnes, S.J., Campbell, I.H., Fiorentini, M.L., Peltonen, P., Barnes, S.J., Smithies, H., 2009. Mantle magmas reveal progressive mixing of meteoritic veneer into the early Earth's deep mantle. *Nature*, 460, 620-623.
- Philippot, P., van Zuilen, M., Rollion-Bard, C., 2012. Variations in atmospheric sulphur chemistry on early Earth linked to volcanic activity. *Nature Geosci.* 5, 668-674.

The chromite-bearing ultramafic-mafic complexes of the Vizcaíno Peninsula (Baja California Sur, Mexico), re-visited for platinum-group minerals

Luis A. Jiménez-Galindo

Facultad de Ingeniería, Universidad Nacional Autónoma de México. Ciudad Universitaria, 04510 México, D.F., Mexico

José M. González-Jiménez

GEMOC ARC National Key Centre, Department of Earth and Planetary Sciences, Macquarie University, 2129 NSW, Sydney, Australia

Antoni Camprubí, Michelangelo Martini, Elena Centeno-García

Instituto de Geología, Universidad Nacional Autónoma de México. Ciudad Universitaria, 04510 México, D.F., Mexico

Joaquín A. Proenza

Departament de Cristal·lografia, Mineralogia i Dipòsits Minerals, Facultat de Geologia, Universitat de Barcelona, Martí i Franquès s/n, 08028 Barcelona, Spain

William L. Griffin, Suzanne Y. O'Reilly, Norman J. Pearson

GEMOC ARC National Key Centre, Department of Earth and Planetary Sciences, Macquarie University, 2129 NSW, Sydney, Australia

Abstract. The mafic-ultramafic complexes of the Vizcaíno Peninsula, Baja California Sur, northwestern Mexico contain chromitite bodies hosted in dunite-harzburgite. The platinum-group mineralisation in the chromitites is dominated by Ru-, Os-, and Ir-rich minerals. They include members of the laurite-erlichmanite solid solution series, irarsite and Os-Ir alloys associated with Ni-Cu sulfides, all occurring as inclusions in larger chromite crystals or in fractures across them. The fractionation of PGE in the form of PGM is discussed here in terms of a dynamic environment characterized by the turbulent mixing/mingling of batches of melts with distinct PGE compositions, within dunitic channels formed as a result of mantle-melt reactions.

Keywords. Ultramafic-mafic complex, Platinum-group elements, chromitite, Vizcaíno, sulfur saturation

1 Introduction

The ultramafic-mafic complexes of the Vizcaíno Peninsula contain chromitite bodies hosted in highly serpentinised peridotites. Previous works described mineralisation in platinum-group elements (PGE) dominated by IPGE (Ir-group platinum group elements; Os, Ir, Ru). However, the mineralogical expression of such platinum-group mineralisation was scanty. In fact, only a few Os-Ir alloys were described in chromitite bodies of the El Tigre mine (Vatin-Perignon et al., 2000). The limited occurrence of such alloys led the authors to suggest the concentration of the PGE during the formation of chromitites from high-temperature melts with extremely low f_{S_2} .

For this study, we collected chromitite samples from dumps of four localities (corresponding to former workings of the El Tigre mine) to search for platinum-group minerals (PGM).

2 Geological Setting

The Vizcaíno Peninsula is located in the central-NE part of the Baja California Sur state, in northwesternmost Mexico. Several dismembered ultramafic-mafic bodies (*cf.* the Vizcaíno ultramafic-mafic complex) are exposed in a north-south trend along the Pacific coastline, as a result of transtensional displacement of the Pacific plate against the North American one. This complex belongs to the Vizcaíno tectonostratigraphic terrane, and consists of two main geological units: (1) the Vizcaíno Peninsula Ophiolite Complex (VPOC), and (2) the San Andrés-Cedros Volcanoplutonic Complex (Campa and Coney, 1983). The pseudostratigraphy of the VPOC consists of a metamorphic complex (*i.e.*, mélange) of serpentinites overlain by variably serpentinised peridotites (dunite, harzburgite, lherzolite, wherlites and pyroxenite). Chromitite pods, several meters long and up to 10m thick, occur in dunites of the VPOC (Altamirano, 1975). These chromitite bodies (already mined for Cr) are distributed in two main areas of the VPOC: the El Tigre-San Agustín area (north), and minor occurrences in the San Cristóbal area (south).

3 Platinum-group mineralisation

3.1 Distribution of platinum-group elements

Vatin-Perignon et al. (2000) reported relatively high PGE contents in the El Tigre chromitites [370 - 859 ppb]. This particular enrichment in PGE was due to high IPGE contents (Ir-group: Os, Ir, Ru, but Os was not analysed in their work) relative to the PPGEs (Pt-group: Rh, Pt, Pd). These authors reported an enrichment in Ir (up to 556 ppb) relative to Ru (up to 300 ppb) and maximum values of 12 ppb Pt and 11 ppb Pd (Fig. 1).

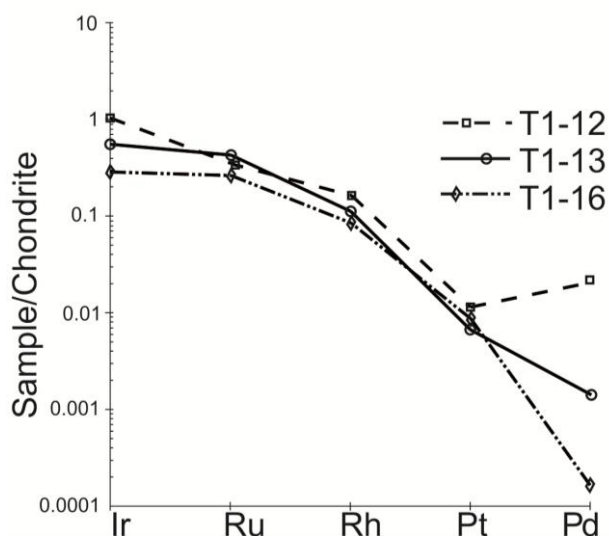


Figure 1. Bulk-rock platinum-group element compositions of the El Tigre chromites, normalised to Chondrite (Naldrett and Duke, 1980). Data from Vatin-Perignon et al. (2000).

3.2. Platinum-group minerals

Vatin-Perignon et al. (2000) reported the existence of inclusions of Os-Ir alloys in the El Tigre chromites. Our detailed study shows that the mineralogy of PGE in the El Tigre chromites is far more complex than that, as it includes, besides Os-Ir alloys, previously unreported sulphides of the laurite (RuS_2)-erlichmanite (OsS_2) solid solution series, irarsite (IrAsS) and base metal sulphides (pentlandite, millerite and chalcocite).

Laurite crystals (ranging in diameter from <1 to $60 \mu\text{m}$) are most frequently found as isolated grains (Fig. 2a), although they may form also composite grains with Os-Ir alloys (Fig. 2b) and/or irarsite.

The PGM are found either wholly encapsulated within larger chromite grains or more commonly in open fractures across chromite grains (Fig. 2c). Most PGM included in chromite are single laurite grains and, to a lesser extent, irarsite (very frequent in altered edges of chromite; Fig. 2d). In this textural position, the Os-Ir alloys always forms polyphase aggregates with laurite \pm irarsite \pm silicates. Interestingly, some laurite crystals host minute inclusions of Ni-Cu sulphides (millerite and chalcocite). Single grains of millerite are also randomly scattered through larger chromite grains.

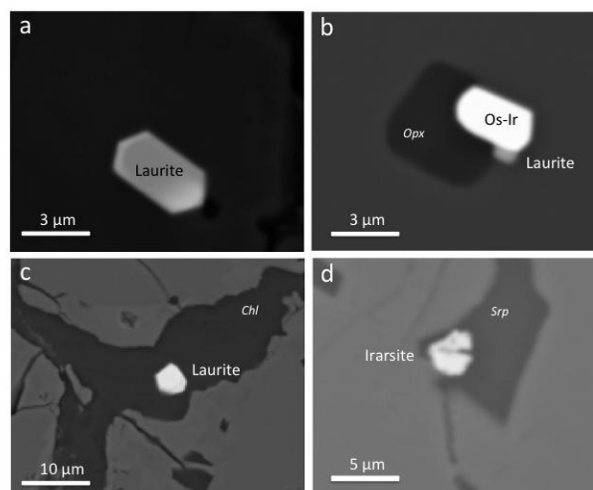


Figure 2. Examples of PGM assemblages in the studied chromites.

4 Discussion

Vatin-Perignon et al. (2000) stated that “Through examinations of cumulative massive chromitite deposits at El Tigre Mine under the scanning electron microscope... we have observed that PGM surrounded by chromite grains and magnesite occur as perfectly euhedral Ru-Os -Ir alloys... characteristics of most ophiolitic chromitites. No laurite-type sulphides (Ru , Os , Ir) S_2 , which are commonly observed in association with Ru-Os -Ir alloys chromitites, have been recognized in these chromitites, indicating an extremely low $f\text{S}_2$ ”. However, we have identified a much more varied platinum-group mineralisation in these chromitites, as minerals of the laurite-erlichmanite series are relatively abundant along with irarsite, and constitute unusually large crystals (up to $\sim 60 \mu\text{m}$ in diameter).

At the pressures and temperatures under which chromitites crystallised in the upper mantle ($\sim 1\text{GPa}$ and $\sim 1200^\circ\text{C}$), the crystallisation of pure laurite (RuS_2) in equilibrium with Os-Ir alloys takes place at $\log f\text{S}_2$ that ranges between -2 and -1.3 , which are much higher values than those expected for mineral associations where Ru-bearing Os-Ir alloys are the sole IPGE-bearing PGMs to have crystallised ($\log f\text{S}_2 > -3$; Brenan and Andrews, 2001; Andrews and Brenan, 2002). The fact that some of the largest laurite crystals contain microinclusions (former droplets) of Ni-Cu sulphides (also scattered through the chromite grains) might indicate a local oversaturation in sulphur in the parental melts of the chromitites. Therefore, there is no role for Os-Ir alloys as the only collectors of the PGEs in the El Tigre chromitites, contrary to the conclusions of Vatin-Perignon et al. (2000). The oversaturation in sulphur enough to produce the immiscible segregation of sulphide droplets, is unexpected in mantle melts from which laurite-bearing chromitites would precipitate (Prichard et al., 2008; González-Jiménez et al., 2012), since such melts are usually S-undersaturated in sulphur in their mantle region (Bockrath et al. 2004). This particular feature in the El Tigre chromitites can be explained considering a model for the precipitation of

chromitites by turbulent mixing/mingling of melts within conduits in the mantle, rather than simple fractional crystallisation and settling as proposed previously by Vatin-Perignon et al. (2000).

An alternative possibility would be that the Ni-Cu sulphides scattered as micro-inclusions within chromite (also found as minute inclusions in laurite) did not precipitate coevally with crystallization of chromite. In such a scenario, these minerals would have already existed in the host peridotites and were incorporated in solid or semi-solid (i.e., partially molten) state to the melts that migrated through the upper mantle, and from which the chromitites would have precipitated later. Then, laurite and chromite, as they nucleated, would have engulfed the preexisting sulphides.

Gonzalez-Jimenez et al. (2012) have recently reported another unusual example of laurite containing inclusions of sulphides, as part of PGM assemblages containing laurite, Os-Ir alloys, Ir sulphoarsenides and abundant base-metal sulphides (pentlandite, millerite, chalcopyrite and chalcocite) as inclusions in chromite. Interestingly, the in-situ analysis of Re-Os isotopes using LA-MC-ICPMS on the later base-metal sulphides yielded older T_{RD} ages than were obtained from the laurite, suggesting the mixing of multiple batches of melts that have sampled different mantle domains. Nevertheless, the chromitites studied by Gonzalez-Jimenez et al. (2012) were located at the edges of chromitite bodies. Therefore, the possibility of pre-existing sulphides cannot be ruled out. The use of the LA-MC-ICPMS technique to further unravel the origin of the El Tigre PGM-bearing chromitites and host rocks will be the main aim of our future work.

Acknowledgements

Financial support was provided by the PAPIIT-UNAM and SEP-CONACYT basic science programs through projects IN110810 and 155662, respectively, and grant 2009-SGR444 of the Catalanian Government. Part of the analytical data were obtained using instrumentation funded by ARC LIEF, and DEST, Systemic Infrastructure Grants, industry partners and Macquarie University.

References

- Altamirano RFJ, Kapadia AH (1975) Exploración minera del yacimiento de cromita "El Tigre", BCS: Consejo de Recursos Minerales.
- Andrews D, Brenan JM (2002) Phase-equilibrium constraints on the magmatic origin of laurite + Ru-Os-Ir alloy: *Can Mineral*, 40: 1705-1716.
- Brenan JM, Andrews D (2001) High temperature stability of laurite and Ru-Os-Ir alloy and their role in PGE fractionation in mafic magmas: *Can Mineral* 39: 341-360.
- Campa MF, Coney PJ (1983) Tectono-stratigraphic terranes and mineral resource distribution in Mexico: *Canadian Journal of Sciences* 20: 1040-1051.
- Moore TE (1986) Petrology and tectonic implications of the Vizcaino Peninsula, Baja California Sur, México: *Geol. Soc. Am Mem* 164: 43-58.
- Prichard HM, Neary CR, Fisher FC, O'Hara MJ (2008) PGE-rich Podiform chromitites in the Al'Ays ophiolite complex, Saudi Arabia: an example of critical mantle melting to extract and concentrate PGE: *Econ Geol* 103: 1507-1529.
- Gonzalez-Jimenez, Fernando Gervilla, William L Griffin, Joaquín A Proenza, Thierry Augé, Suzanne Y O'Reilly, Norman J Pearson (2012) Os-isotope variability within sulfides from podiform chromitites: *Chemical Geology* 291: 224-235.
- Bockrath Conny, Chris Ballhaus, Astrid Holzheid (2004) Fractionation of the Platinum-Group Elements During Mantle Melting: *Science* 305: 1951-1953.
- Vating-Perignon, J Amossé, L Radelli, F Keller, T Castro Leyva (2000) Platinum group element behaviour and thermochemical constraints in the ultrabasic-basic complex of the Vizcaino Peninsula, Baja California Sur, Mexico: *Lithos* 53: 59-80.

Platinum-group-element and -mineral distribution and fine-scale chemical variation of chromite in the UG-2 chromitite, western Bushveld Complex, South Africa

Malte Junge, Thomas Oberthür, Frank Melcher
Federal Institute for Geosciences and Natural Resources, Stilleweg 2, D-30655 Hannover, Germany

Abstract. The UG-2 chromitite of the Bushveld Complex in South Africa contains the world's largest resources of platinum-group elements (PGE). However, only limited work has been conducted on the fine-scale chemical variation of chromite, the distribution of PGE and platinum-group minerals (PGM) within the UG-2. In the present study one drill core covering the sequence of the UG-2 chromitite at the Karee Mine in the Bushveld Complex was studied in detail. Geochemically, Pt correlates well with Pd, but not with Ni, Cu and S, and Pt and Pd show high concentrations at the bottom and in the center of the main UG-2 layer. The mineral chemistry of chromite is characterized by distinct cryptic variation. From bottom to top each sub-layer is defined by an upward decrease of Mg# combined with increases of Cr# and TiO₂. Sulfides (pentlandite, chalcopyrite) interstitial to chromite grains are rare, and associated PGM grains are mainly Pt-Fe alloy, laurite and cooperite/braggite. Platinum and the IPGE are dominantly present as discrete PGM, whereas large proportions of Pd and Rh are hosted in the crystal lattice of pentlandite. Palladium and Rh contents of pentlandite reach maxima of 2.2 wt% Pd and 3 wt% Rh.

Keywords. Bushveld Complex, UG-2 chromitite, PGE, PGE in sulfides

1 Introduction

The Bushveld Complex in South Africa is the largest layered mafic-ultramafic intrusion on Earth with a sub-surface outcrop of circa 60,000 km² and contains the largest resources of platinum-group elements on Earth (Vermaak 1995; Cawthorn 2002; Maier et al. 2013). Scoates and Friedman (2008) dated the emplacement of the Bushveld Complex to an age of 2,054±1.3 Ma. Within the Bushveld Complex, platinum-group element (PGE) mineralization is mainly confined to a layered sequence of mafic-ultramafic rocks referred to as the Rustenburg Layered Suite. The understanding of the formation of chromitite layers hosting elevated concentrations of PGE is still unexplained. The economic PGE-bearing ore bodies are the Merensky Reef, the UG-2 chromitite, and the Platreef.

The UG-2 chromitite is the largest resource of PGE on Earth (Vermaak 1995). It occurs in the Upper Group of the Critical Zone, between 15 to 400 m below the Merensky Reef (Lee 1996). The UG-2 chromitite has a general thickness of about one meter, varying between 0.4 and 2.5 m (Schouwstra et al. 2000). Locally the ore body consists of a number of smaller subsidiary seams which may bifurcate and merge with the main seam (e.g., Davey 1992; Maier and Barnes 2008; Voordouw et al. 2009). The PGE distribution is generally limited to

the UG-2 chromitite seam itself (Hiemstra 1985, 1986; Von Gruenewaldt and Worst 1986; Maier and Barnes 2008; Voordouw et al. 2009).

Vertical textural and compositional variations within the UG-2 were documented by Hiemstra (1985, 1986), Von Gruenewaldt and Worst (1986), Maier and Barnes (2008), and Voordouw et al. (2009). Hiemstra (1985, 1986) performed whole rock analyses on 2-cm segments of the UG-2 from the Western Platinum Mine and noted three distinct cycles of PGE mineralization, starting with high total PGE at the base, in the center and at the top of the UG-2. Each cycle has its own discrete Pt/Pd value. Hiemstra (1986) also proposed that the PGE are predominantly hosted by PGM.

Eales and Reynolds (1986) were the first to analyze chromite grains of the UG-2 by EPMA. These authors identified cryptic variation in one example of the main UG-2 layer, namely increasing Cr/Al ratios from bottom to top. Eales and Reynolds (1986) explained the increasing Cr/Al ratios due to the entry of plagioclase into the crystallization assemblage, with plagioclase failing to appear as a cumulus phase.

Naldrett et al. (2011) studied one drill core of the UG-2 from Waterval in segments of 3 cm and documented a progressive upwards increase in the concentration of vanadium, interpreted to be caused by a changing partition coefficient of V between spinel and magma.

In the present study, one drill core transecting the UG-2 chromitite of the Karee Mine (LONMIN) in the western Bushveld Complex was studied in detail using modern geochemical and mineralogical methods. The work centers on unraveling the fine-scale variation within the UG-2 chromitite regarding the distribution of PGE (whole rock data and concentrations in sulfides), platinum-group minerals (PGM), and the compositional variation of chromite. The study shows that the UG-2 chromitite is composed of a number of chemically distinct chromitite sub-layers. Various geochemical and mineralogical trends are established which provide new insights into the relationship of chromitite and PGE mineralization.

2 Samples and Analytical Methods

Drill core DO-24 from the Karee Mine (LONMIN) is 155 cm long and consists of three separate chromitite layers. The main chromitite seam or layer at the bottom is 106 cm wide and is underlain by an altered, coarse-grained pyroxenite which shows pervasive alteration to anthophyllite-rich rock. The main chromitite layer is

overlain by pyroxenite (5 cm wide), a second chromitite layer (7.5 cm) or “leader seam”, pyroxenite again (12 cm), and finally a third layer of chromitite (10 cm) on top. At the base of the main seam (segments 30 to 32), the chromite grains are annealed to form more compact accumulations.

The drill core was split into segments of 2.5 cm or 5 cm for whole-rock analyses. One or two oriented polished sections each were prepared from these segments and were used for reflected light and scanning electron microscopy (SEM), electron probe microanalysis (EPMA) and laser ablation induced coupled plasma mass spectrometry (LA-ICPMS). Whole rock analyses for major, minor and trace elements were conducted by ACTLABS, Canada, using instrumental neutron activation analysis (INAA) and inductively coupled plasma mass spectrometry (ICP-MS).

Chromite and pentlandite grains were analyzed with a CAMECA SX 100 electron microprobe using the following analytical conditions: for chromite analysis, 20 kV acceleration voltage, 30 nA sample current and 10 s measuring time, electron beam diameter ~1 μm. Detection limits were 75 ppm for Co, 100 ppm for Se, 120 ppm for Rh, 140 ppm for Pd, 160 ppm for Ag and 300 ppm for Pt.

In order to corroborate the EPMA results, the concentrations of the six PGE, Co, Cu and Au in larger pentlandite grains (n = 170) of four polished sections (segments 5, 9, 18 and 26) were analyzed by LA-ICPMS at the University of Erlangen, Germany. Analytical conditions and data corrections performed are identical to those described by Osbahr et al. (2013).

3 Results

3.1 Geochemistry – distribution of Pt, Pd, Au and selected elements within the UG-2

The whole rock data show a distinct covariance between Pt and Pd with two overlapping peaks of Pt and Pd at the bottom and in the central part of the main UG-2 chromitite seam, respectively (Fig. 1). Similar PGE distribution patterns are described for the UG-2 by other authors (e.g., Hiemstra 1985, 1986; Von Gruenewaldt and Worst 1986; Maier and Barnes 2008; Voordouw et al. 2009).

Copper (mostly <50 – 100 ppm) and sulfur contents (mostly <200 ppm) are low. Gold peak values are found coinciding with the top Pt and Pd peaks and on top of the first chromitite layer on top of the sequence. Notably, the latter Au peak concurs with maxima of Cu and S.

Nickel, Zn, Ti, and V (Fig. 1), elements compatible with chromite, illustrate a distinct covariance and have maxima in the massive chromitite at the bottom of the main seam.

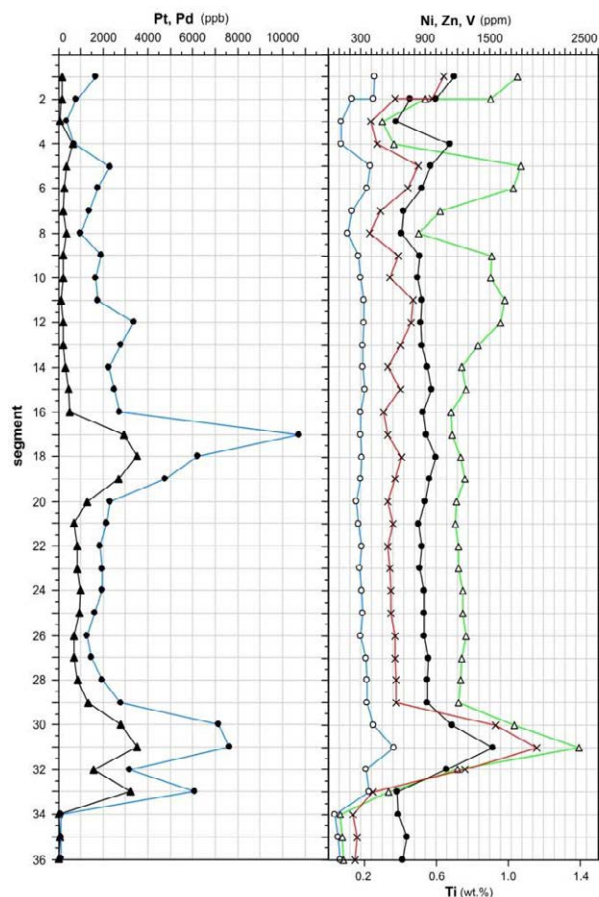


Figure 1. Whole-rock element distribution. Left: Pt (blue/filled circles) and Pd (black/filled triangles) in ppb. Right: Zn (blue/open circles), Ni (black/filled circles), V (green/open triangles) in ppm and Ti (red/crosses) in wt. %.

3.2 Mineralogy – oxides, and chromite chemistry

Chromite grains are generally idiomorphic, optically homogenous, and have grain sizes varying from 0.03 to 0.4 mm. The grains are disseminated or show point contacts within the main seam. At the base of the main seam, the chromite grains are annealed in more compact accumulations often showing triple junctions. Here, the individual chromite grains often show oriented exsolution lamellae of ilmenite. Ubiquitous, individual rutile grains mainly occur in interstices of chromite grains at the base of the main seam.

Altogether, 1290 chromite grains in 32 segments were analyzed by EPMA to investigate the distributions of Mg# (Mg/Mg+Fe) and Cr# (Cr/Cr+Al) in chromite. Between 30 and 50 chromite grains were measured in each polished section. Figure 2 demonstrates the vertical variations in Cr# and Mg# in chromite grains and reveals stepwise (saw-tooth like) cryptic variations upwards, with a basal interval or sub-layer of increasing Mg#, decreasing Cr# and increasing TiO₂ contents, followed by intervals of upward decreasing Mg# combined with increasing Cr# and increasing TiO₂.

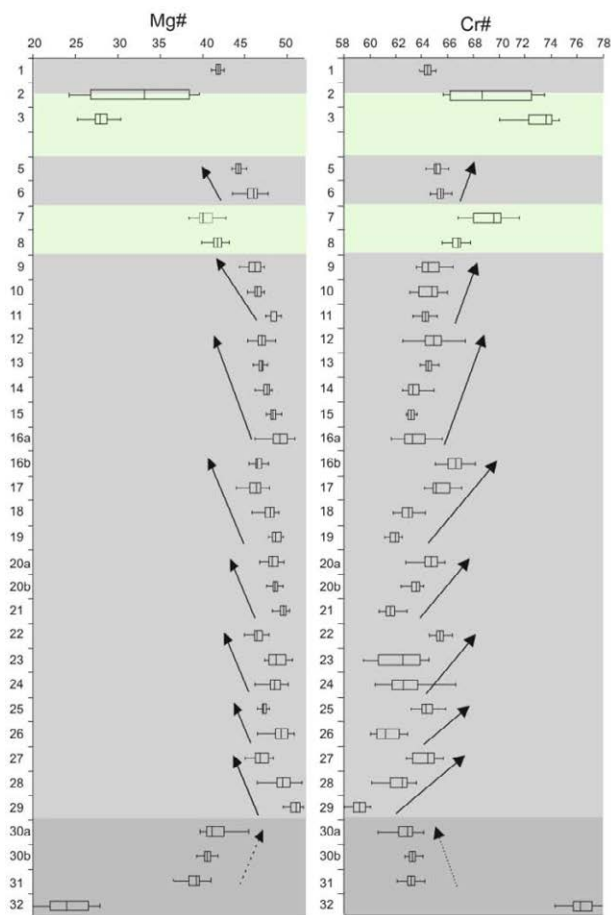


Figure 2. Box-and-whisker plots illustrating the vertical distribution of Mg# and Cr# in chromite within the UG-2 main seam and the overlying pyroxenite and chromitite layers. Chromitites have pale grey background, massive chromitite (segment 30 to 32) have dark grey backgrounds, and pyroxenite layers (segments 2 to 4 and 7 to 8) have green backgrounds. Arrows indicate normal cyclic trends in Mg# and Cr#. Only from segment 30 to 32, at the bottom of the main chromitite seam, is the trend reversed.

3.3 Mineralogy – sulfides, and platinum-group minerals (PGM)

Sulfide grains and grain aggregates of pentlandite, chalcopyrite, rare pyrrhotite and pyrite are found only in the interstices of chromite grains, often associated with silicates. Sulfide grain sizes range from <1 to 50 μm (mostly 10–20 μm).

PGM generally occur in the interstices of chromite grains. The PGM (grain sizes <5 to 20 μm) are locked within, or more commonly, occur at the peripheries of sulfide grains. PGM within chromite are rare and in all cases consisted of laurite grains. Altogether, 356 discrete PGM grains were detected. Major PGM are Pt-Fe alloy grains (30%), often displaying idiomorphic outlines (cubes), laurite $[\text{RuS}_2]$ (29%), cooperite/braggite $[(\text{Pt,Pd,Ni})\text{S}]$ (26%) and rarer zvyagintsevite $[\text{Pd}_3\text{Pb}]$, and potarite $[\text{PdHg}]$. Malanite $[\text{CuPt}_2\text{S}_4]$, irarsite $[\text{IrAsS}]$, platarsite $[\text{PtAsS}]$ and sperrylite $[\text{PtAs}_2]$ are very rare. In general, most of the PGM are Pt-rich or IPGE-rich (laurite), whereas Pd- and Rh-bearing PGM

are rare. This raises the question on the mineralogical siting especially of Pd and Rh in the ores, a matter that will be addressed below.

3.4 PGE in pentlandite - EPMA

The scarcity of Pd- and Rh-bearing PGM led to the assumption that these PGE are present in solid solution within sulfide minerals, especially pentlandite, as published by a number of authors (e.g., Cabri et al. 1984; Cabri 1992; Oberthür et al. 1997; Godel et al. 2007). Concentrations of the PGE in sulfide grains were measured using both EPMA (Pd, Rh and Pt) and LA-ICPMS (all PGE).

Nickel, Fe, Co, S, Se, Pd, Pt and Rh in pentlandite grains were analyzed with EPMA ($n=153$) in polished sections of segments 5, 18 and 31, representing the segments with elevated whole rock PGE contents. Nickel and Fe contents are relatively constant throughout the sequence (median values ranging from 32.51–34.15 wt.% Ni and 31.32–32.92 wt.% Fe). Median Co contents are 0.65, 0.45 and 0.76 wt.% for pentlandite of segments 5, 18 and 31, respectively, whereas Se concentrations decrease from 178 ppm to 114 ppm from bottom to top.

Elevated concentrations of Pd and Rh in pentlandite grains are the rule (hundreds of ppm). Palladium and Rh contents in pentlandite are comparatively low in segment 31, at the base of the main UG-2 seam (median = 1084 ppm Pd and 1520 ppm Rh), and also in segment 5, the first top chromitite layer (median = 456 ppm Pd and 319 ppm Rh). However, median values of 7470 ppm Pd and 2986 ppm Rh (maximum contents 2.2 wt.% Pd and 3 wt.% Rh) were detected in pentlandite of segment 18, which represents the area of the whole rock Pt and Pd peaks, in the centre of the main UG-2 seam (Fig. 1).

3.5 PGE in pentlandite – LA-ICPMS

PGE, Co, Cu and Au contents in sulfide grains ($n=174$) were analyzed with LA-ICPMS in polished sections of segments 5, 9, 18 and 26. With respect to Pd and Rh, the LA-ICPMS work largely confirmed the EPMA results. Maximum Pd and Rh contents (1.75 wt.% Pd and 2.38 wt.% Rh) were found in pentlandite of segment 18 and much lower contents (still in the 100 ppm range) are constantly present in the other segments analyzed. Platinum contents are low and range from <0.2 to 20 ppm, and Au was generally below the detection limit (between 0.1–0.3 ppm). IPGE contents of pentlandite were constantly above the respective detection limit of the method (ca. 0.03 – 0.3 ppm), generally in the lower one digit ppm range. Notably, elevated contents of Ir (up to ca. 100 ppm Ir), unparalleled by Os and Ru contents, were constantly encountered.

It is thought that the PGE in pentlandite largely reflect the capability of pentlandite to host Rh and Pd as well as some Ir in its crystal lattice. In contrast, as Pt is not compatible in pentlandite, this element forms discrete PGM. Ruthenium and Os appear to have undergone a comparable fate like Pt as they are mainly found in laurite.

4 Concluding Remarks

Based on Cr#, Mg# and TiO₂ contents, distinct chromitite sub-layers are distinguishable. It is envisaged that within the main UG-2 seam, eight initially separate sub-layers amalgamated to form the massive chromitite seam. The basal sub-layer presents an exception by showing an extreme enrichment of Fe and Cr and concomitant depletion of Mg and Al of the chromitite grains towards the base. These unusual compositions are linked to the late-magmatic/hydrothermal alteration observed in the bottom part of the core (pegmatoidal pyroxenite showing pervasive anthophyllite alteration).

The PGE are bimodally distributed in the UG-2: Large proportions of Pd and Rh are hosted in pentlandite, whereas Pt and the IPGE are dominantly present in the form of discrete platinum-group minerals (PGM). The distribution patterns of the various PGM suggest that a large proportion of the PGE, primarily concentrated in sulfide at magmatic conditions, was redistributed following the crystallization of sulfides in the subsolidus stage.

The largest numbers of PGM grains were detected in the samples with the most elevated whole rock Pt and Pd contents. In general, the PGM are Pt-rich (Pt-Fe alloy, cooperite/braggite) or IPGE-rich (laurite), whereas Pd- and Rh-bearing PGM are rare. The mineralogical siting especially of the Pt- and IPGE-rich PGM in the ores, within or at the peripheries of sulfide grains, indicates that they originally co-precipitated with sulfide and were later, down-temperature, expelled from the crystal lattice of the annealing sulfides. Platinum is not compatible with any of the sulfides forming and therefore combines with available reaction partners, in our UG-2 case only with S and Fe to form discrete PGM (cooperite/braggite and Pt-Fe alloy). Equally, Ru and Os formed laurite, probably even at magmatic conditions already since it is known that laurite may be a stable phase at magmatic temperatures and may have formed early (Brenan and Andrews 2001).

Acknowledgements

First of all, thanks to LONMIN geologists Jan van der Merwe and Martin Slabbert who supplied us with the core, and to Dennis Hoffmann who assisted us with further geological information. Excellent polished sections were prepared in-house by Peter Rendschmidt, SEM studies were kindly supported by Detlef Klosa, and electron microprobe analyses were ably performed by Jerzy Lodziak and Christian Wöhr. Helene Brätz, University of Erlangen, is thanked for the LA-ICPMS analyses.

References

Barnes S-J., Maier WG (2002) Platinum-group element distributions in the Rustenberg Layered Suite of the Bushveld Complex, South Africa. *In*: Cabri LJ (ed) *The Geology, Geochemistry, Mineralogy and Mineral Beneficiation of Platinum-Group Elements*. Can Inst Mining, Metall. Petrol Spec Vol 54:p.431-458

Brenan JM, Andrews D (2001) High-temperature stability of laurite and Ru-Os-Ir alloy and their role in PGE fractionation

in mafic magmas. *Can Mineral* 39:341-360

Cabri LJ (1992) The distribution of trace precious metals in minerals and mineral products. *Mineral Mag* 56:289-308

Cabri LJ, Blank H, El Goresy A, Laflamme JHG, Nobiling R, Sizgoric MB, Traxel K (1984) Quantitative trace-element analyses of sulfides from Sudbury and Stillwater by Proton Microprobe. *Can Mineral* 22: 521-542

Cawthorn RG (2002) Relationship between PGE and PGM in the Bushveld Complex. *Can Mineral* 40:311-328

Davey SR (1992) Lateral variations within the upper Critical Zone of the Bushveld Complex on the farm Rooikoppies 297 JQ, Marikana, South Africa. *S Afr J Geol* 95:141-149

Eales HV, Reynolds I (1986) Cryptic Variations within Chromitites of the Upper Critical Zone, Northwestern Bushveld Complex. *Econ Geol* 81:1056-1066

Godel B, Barnes SJ, Maier W (2007) Platinum-Group Elements in Sulphide Minerals, Platinum-Group Minerals, and Whole-Rocks of the Merensky Reef (Bushveld Complex, South Africa): Implications for the Formation of the Reef. *J Petrol* 48:1569-1604

Hiemstra SA (1985) The Distribution of Some Platinum-Group Elements in the UG-2 Chromitite Layer of the Bushveld Complex. *Econ Geol* 80:944-957

Hiemstra SA (1986) The Distribution of Chalcophile and Platinum-Group Elements in the UG-2 Chromitite Layer of the Bushveld Complex. *Econ Geol* 81:1080-1086

Lee CA (1996) A Review of Mineralization in the Bushveld Complex and some other Layered Intrusions. *In*: Cawthorn RG (ed) *Layered Intrusions*. Elsevier, Amsterdam, pp 103-145

Maier WD, Barnes S-J (2008) Platinum-group elements in the UG1 and UG2 chromitites, and the Bastard reef, at Impala platinum mine, western Bushveld Complex, South Africa: Evidence for late magmatic cumulate instability and reef constitution. *S Afr J Geol* 111:159-176

Maier WD, Barnes S-J, Groves, D.I. (2013) The Bushveld Complex, South Africa: formation of platinum-palladium, chrome- and vanadium-rich layers via hydrodynamic sorting of a mobilized cumulate slurry in a large, relatively slowly cooling, subsiding magma chamber. *Miner Deposita*, 48:1-56

Naldrett A, Kinnaird J, Wilson A, Yudovskaya M, Chunnett, G. (2011) Genesis of the PGE-enriched Merensky Reef and chromitite seams of the Bushveld Complex: Reviews in *Econ Geol* 17:235-296

Oberthür T, Cabri LJ, Weiser T, McMahon G, Müller P (1997) Pt, Pd and other trace elements in sulfides of the Main Sulfide Zone, Great Dyke, Zimbabwe – a reconnaissance study: *Can Mineral* 35:597-609

Osbahr I, Klemd R, Oberthür T, Brätz H, Schouwstra R (2013) Platinum-group element distribution in base-metal sulfides of the Merensky Reef from the eastern and western Bushveld Complex, South Africa. *Miner Deposita*, DOI 10.1007/s00126-012-0413-8

Scoates JS, Friedman RM (2008) Precise age of the platiniferous Merensky Reef, Bushveld Complex, South Africa, by the U-Pb zircon chemical abrasion in ID-TIMS technique. *Econ Geol* 89:1094-1121

Schouwstra R, Kinloch E, Lee C (2000) A short review of the Bushveld Complex. *Platinum Minerals Rev.* 44:33-39

Vermaak C (1995) *The Platinum-Group Metals - A global perspective*. Mintek, 247 p.

Von Gruenewaldt G, Worst BG (1986) Chromite Deposits at Zwartkop Chrome Mine, Western Bushveld Complex. *In*: Anhaeusser CR, Maske S, (eds) *Mineral Deposits of Southern Africa*. *Geol Soc S Afr*, p. 1217-1227

Voordouw R, Gutzmer J, Beukes NJ (2009) Intrusive origin for Upper Group (UG1, UG2) stratiform chromitite seams in the Dwaars River area, Bushveld Complex, South Africa. *Miner Petrol* 97:75-94

Magma mingling between sulphide-rich and carbonatite magmas to form a multi-commodity metal deposit: reconstruction using QEMSCAN® analysis

Dora Kavecsanski¹, Kathryn R. Moore¹, Gavyn K. Rollinson¹, Frances Wall¹, Paul A.J. Lusty²

¹Camborne School of Mines, College of Mathematics, Engineering and Physical Sciences, University of Exeter, Cornwall Campus, Penryn, Cornwall, TR10 9EZ, UK.

²British Geological Survey, Environmental Science Centre, Nicker Hill, Keyworth, Nottingham, NG12 5GG, UK.

Abstract. The Phalaborwa carbonatite complex has a copper enrichment that is unique amongst carbonatites. QEMSCAN® analysis of bornite ore within the youngest (Transgressive) carbonatite within the complex has revealed rock textures including irregular trails and interfingering channels of sulphide-dominated and carbonate-magnetite-dominated mineral assemblages. The textures are interpreted as evidence for mingling of two magmas, which is further supported by the presence of drop break-up textures and ocelli. Minerals that occur in the reaction zone between the two magmas include chalcopyrite, chalcocite, pyrrhotite, hydrous sheet silicates, graphite, valleriite, spinel, baryte and fluorite. The textural relations between minerals and mineral association data from QEMSCAN® analysis have been used to reconstruct

mineral assemblages and define mineral reactions that represent limited chemical interaction between comparatively reduced sulphide and comparatively oxidised carbonatite magmas that mingled at high temperatures. The copper enrichment at Phalaborwa is thus attributed to a sulphide liquid that did not share the same source as the carbonatite. The results are consistent with previous isotopic studies suggesting that silicate and carbonatite magmas from different mantle sources mixed and further imply a long history of interaction between evolved copper-sulphide magmas, silicate magmas and carbonatites.

Keywords. Phalaborwa, copper sulphide ore, carbonatite, magma mingling

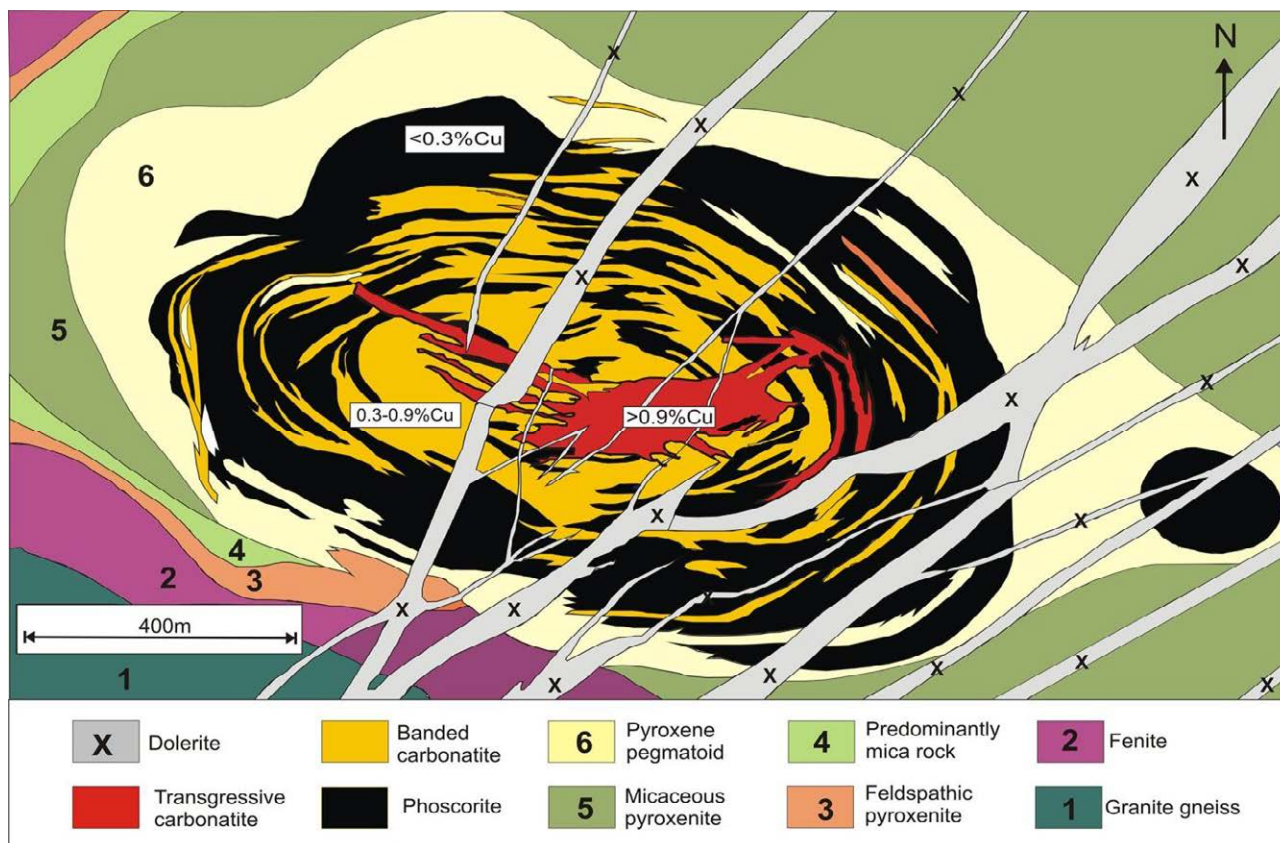


Figure 1. Simplified geological map of Loolekop Hill at the centre of the Phalaborwa Complex indicating prevalent copper grades in phoscorite, banded carbonatite and transgressive carbonatite (after Woolley, 2001; Hanekom et al., 1965).

1 Introduction

The Phalaborwa Igneous Complex (~2060 Ma) intrudes the Kaapvaal craton of South Africa. The oldest intrusions are dominated by pyroxenites: a massive diopside-dominated rock with minor phlogopite and apatite; a younger phlogopite-vermiculite-diopside-apatite rock; and a feldspathic pyroxene at the contact with the Archaean metamorphic granite-gneiss basement, where fenitization occurs in several places. Subsequently, plug-like syenite bodies intruded the outer zones of pyroxenite. Loole Kop, in the centre of the Complex (Figure 1), was formed by successive intrusions that formed a serpentine-magnetite-apatite-phlogopite rock, phoscorite, banded carbonatite, and lastly a transgressive carbonatite (Hanekom et al. 1965; Eriksson, 1989; Woolley, 2001; Wu et al., 2011). The Loole Kop intrusions comprise the Phalaborwa Carbonatite Complex, which is unique amongst carbonatites as a copper deposit with important by-products such as magnetite, sulphuric acid, baddelyite, uranothorianite, gold, silver and platinum group elements (Woolley, 2001). Processes that have been suggested as operating during the formation of the copper-enriched carbonatite complex include the development of hydrothermal mineralisation (Hanekom et al., 1965) magma mixing in silicate magmas (Eriksson, 1989) and fractionation from a copper-rich parent carbonatite (Aldous, 1980). Isotopic studies suggest that the parental magmas are derived from a heterogeneous, metasomatised lithospheric mantle above an ascending asthenospheric mantle plume, that may be associated with the neighbouring Bushveld (~2055 Ma) Complex (Wu et al. 2011).

2 Analytical methods

A sample of the copper ore in the transgressive

carbonatite from the underground mine at Loole Kop has been chemically mapped using QEMSCAN® technology to investigate evidence for magma mixing. The QEMSCAN® is used for the Quantitative Evaluation of Minerals using a Zeiss EVO® 50 scanning electron microscope (SEM). It has four light element X-ray EDS (Energy Dispersive Spectrometer) detectors and an electron backscatter detector that are used in combination to identify minerals. Analysis points return X-ray spectra that are compared with a large database, allowing the assignment of each analysis point to a specific mineral or elemental category (Gottlieb et al. 2000; Pirrie et al. 2004). Each analysis point can achieve up to 200,000 counts per second using digital pulse processors and takes about 10 milliseconds to measure. The false-colour mineral maps produced by QEMSCAN® provide a means to correlate micron-scale mineralogical features with large scale rock textures. It is therefore ideally suited to the investigation of magmatic interactions leading to disequilibrium features in rocks.

3 Magmatic disequilibrium textures

We differentiate between magma mingling, which we define as the heterogeneous mechanical interaction between two magmas with limited chemical exchange, and magma mixing, which implies complete homogenisation between two magmas to produce a single hybrid magma (Moore et al. 2009). Figure 2 shows irregular trails of a sulphide mineral assemblage (dominantly green on the false colour image) through the carbonatite (dominantly blue and black). However, trails of carbonatite through the sulphide assemblage also occur. Irregular interfingering channels along the sharp contact between the two mineral assemblages are associated with carbonate drop break-up textures (Figure 2, areas A and B). This type of texture forms during the mingling of two liquids, depending on

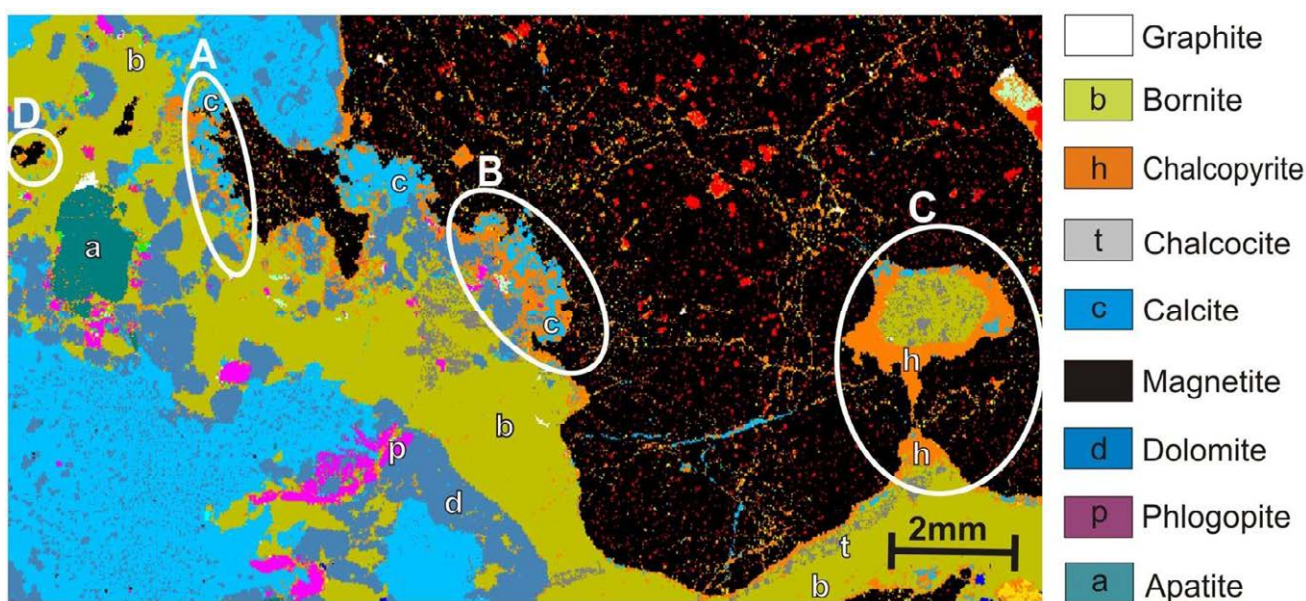


Figure 2. QEMSCAN® image illustrating the relationship between a copper sulphide mineral assemblage and a carbonatite mineral assemblage (transgressive carbonatite, Figure 1). **A-B:** Carbonatite drop break-up texture. **C:** Ocellus within the carbonatite is connected by a necking structure to the main sulphide trail. **D:** Ocellus with a sulphide core and oxide rim within the sulphide trail.

capillary number, viscosity ratio, flow type and the shape of the drop. At first the drop starts to stretch, but if the viscosity number exceeds a critical value the drop breaks up into several drops, with smaller satellite drops between them (DeRoussel et al. 2001). The break-up of carbonate magma trails enables the mechanical incorporation of carbonate minerals into the sulphide trail, such that there entrainment of minerals from one assemblage into the other. A prominent ocellus within the carbonatite is connected by a necking structure to the main sulphide trail (Figure 2 area C). An ocellus with a sulphide core and oxide rim is also observed within the sulphide trail (Figure 2 area D). The observed textural features including the interfingering “liquid”, ocelli, drop break-up and necking globules are typical textures resulting from the mingling of two magmas with contrasting viscosity (DeRoussel et al. 2001). The absence of significant hydrothermal textures supports the interpretation of mingling between sulphide and carbonate magmas with limited chemical exchange.

4 Mineral assemblages

The dominant sulphide phase in the copper ore is bornite, which is accompanied by accessory pyrrhotite, sphalerite, siegenite, acantite and thorite. Chalcopyrite and chalcocite are significant sulphide phases that have a distribution pattern that is closely correlated with the contact between the sulphide and carbonatite assemblages. The chalcopyrite (Figure 2) occurs as a rim around bornite that is in contact with the carbonatite assemblage while the chalcocite exsolves within the bornite close to the contact with the carbonatite assemblage and where fragments of the carbonatite are entrained into the bornite. The carbonatite assemblage is dominated by calcite, magnetite, dolomite and phlogopite. Accessory phases are euhedral and possibly phenocrystic apatite, monazite, celestine, and additional Mg-Fe silicates. The magnetite has a large number of inclusions, a very irregular morphology and is more extensively veined than the rest of the sample. It is possible that the magnetite was a phenocryst phase that underwent dissolution during magma mingling and was later infilled with sulphide phases and spinel.

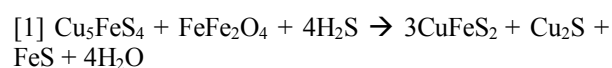
The phenocrysts may also have acted as a point of isolated mingling, such that drop break-up textures are preferentially located along its margins. Dolomite occurs as both a discrete phase and as rod-shaped, sigmoidal or rounded grains that exsolved from high-temperature Mg-rich calcite (Dawson and Hinton, 2003). The subhedral phlogopite is associated with minor vermiculite and talc, particularly close to the contact between the sulphide and carbonatite assemblages. The sample was extracted from a level in the mine below the level of circulation of groundwater, where most vermiculite forms in the Phalaborwa Complex. The alteration phases are thus interpreted to have formed by the addition of high temperature water to phlogopite, rather than the supergene origin prevalent to depths of 50m beneath the surface. The

location of the vermiculite close to the contact between the mineral assemblages raises the question of whether the water for reaction with phlogopite was generated by the interaction of two magmas. Additional mineralogical characteristics that suggest there was some chemical interaction between the two magmas are: (1) graphite (white) overgrowths on apatite; (2) the linear distribution of micron-scale spinel crystals along the contact of bornite with carbonate minerals, as well as infill in magnetite; (3) Valleriite ($\text{Fe}^{2+}, \text{Cu})_4(\text{Mg}, \text{Al})_3\text{S}_4(\text{OH}, \text{O})_6$ and baryte, both of which are also located at the contact between mineral assemblages; and (4) fluorite occurring as a partial rim on calcite.

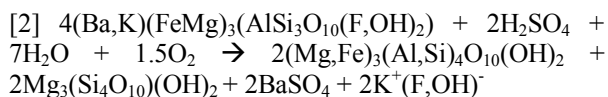
The strength of mineral associations is measured quantitatively during QEMSCAN® analysis and interpreted with reference to disequilibrium textures. Three mineral assemblages are differentiated: (1) A reduced sulphide assemblage dominated by bornite; (2) A relatively oxidized carbonatite mineral assemblage dominated by carbonates and magnetite, with minor silicate minerals and phosphates; and (3) A reaction assemblage that significantly contains reduced carbon (graphite) and hydrated silicate minerals from the carbonatite assemblage, and hydrated and/or oxidised sulphide minerals from the sulphide assemblage.

5 Discussion

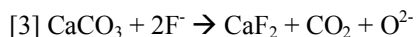
Assemblage 3 shows that oxidation and reduction reactions have occurred, which were accompanied by the evolution of water. The location of significant chalcopyrite and chalcocite, and minor pyrrhotite along the contact between primary magmatic assemblages indicates that these minerals are also involved in magmatic reactions, where volatile species plays a critical role. When a sulphide magma is accompanied by reduced volatiles such as H_2S and is introduced into a magnetite-phyric carbonatite magma, an oxidation reaction [1] may occur.



The equation describes a reaction between magnetite from a carbonatite liquid with bornite and a reduced sulphide species from a sulphide liquid, producing the observed chalcopyrite + chalcocite + pyrrhotite assemblage, where chalcopyrite is more abundant than chalcocite and pyrrhotite. Cobalt, nickel and zinc sulphide minerals are also observed close to the contact with the carbonatite assemblage. In reaction [1], oxidation of the system can readily promote exchange between Fe in pyrrhotite with metals in the magma. Thus, the change in oxidation state of the sulphide magma can generate an enrichment of a diverse assemblage of ore minerals in proximity to the carbonatite magma. The water that is produced as the volatile species in reaction [1] can subsequently react with sulphides and spinel and/or silicates to produce valleriite, or with Ba-rich phlogopite, as in reaction [2], assuming that $K_{\text{mol}} = B_{\text{mol}}$ in phlogopite.



The reaction produces vermiculite, talc, baryte and potassium-fluoride/hydroxide in solution, which may result in fenitizing fluids that escape the reaction area. However, the presence of fluorite adjacent to calcite suggests that potassium preferentially escapes in aqueous solution while fluorine remains in the system, as in reaction [3].



The system may thus become more oxidized and the release of carbon dioxide in the presence of aqueous solutions may result in either immiscible fluids or a carbonic solution with greater potential to transport metal ions, consistent with observed fluid inclusion characteristics (Aldous, 1980).

6 Summary and conclusions

The reactions document the development of a hybrid sulphide-carbonatite magmatic system that did not equilibrate, where the source for the copper enrichment in the late intrusion of transgressive carbonatite is a sulphide magma. Copper enrichment has also been identified in inclusions that represented the earliest carbonatites in the complex (Aldous, 1980). If the copper is derived from sulphide magmas that ultimately has a vary reduced mantle source and is observed in varying concentrations in multiple generations of the carbonatite that has a comparatively oxidised mantle source, then there are two possible explanations. Either the multiple mantle sources are all copper enriched or there has been a long history of magma mingling throughout the generation of the Complex. This latter is in keeping with (1) stable isotope compositions that suggest mixing (Eriksson, 1989) of silicate magma with carbonatite magma, (2) Sr-Nd-Hf isotopic studies (Wu et al. 2011) that indicate multiple mantle terranes in the source region for the Loolo Kop Carbonatite Complex, and (3) the interpretation of bornite-rich ores as high-temperature residual liquids (Ebel and Naldrett, 1996), such that sulphide magmas are available in an open system magma chambers for an extended time interval.

Acknowledgements

D. Kavecsanszki acknowledges the support of a postgraduate fellowship from the College of Engineering, Mathematics and Physical Sciences at the

University of Exeter. The research contributes to the Critical Metals Alliance between the Camborne School of Mines at the University of Exeter and the British Geological Survey. P. Lusty publishes with the permission of the Executive Director, British Geological Survey (NERC)

References

- Aldous R. (1980) Ore genesis in copper bearing carbonatites: a chemical, mineralogical and fluid inclusion study: Unpublished PhD thesis, Imperial College, Univ. London 365p. *In*: Linnen, R.L. and Samson, I.M.(ed)(2004):*Rare-Element Geochemistry and Mineral Deposits, Geological Association of Canada Short Course Notes Volume: 17, 10-11May, 2004: 304-305*
- Baxter S., Feely M. (2002) Magma mixing and mingling textures in granitoides: examples from the Galaway Granite, Connemara, Ireland, *mineralogy and Petrology* 76, 63-74, p:69
- Dawson J B., Hinton R W. (2003) Trace element content and partitioning in calcite, dolomite and apatite in carbonatite, Phalaborwa, South Africa. *Mineralogical Magazine* 67, 921-930
- DeRoussel P., Khakhar D. V., Ottino J. M. (2001) Mixing of viscous immiscible liquids. Part 1: Computational models for strong-weak and Continuous flow systems. *Chemical Engineering Science* 56, 5511-5529. p:5513
- Ebel D S., Naldrett A J. (1996) Fractional crystallization of sulphide ore liquids at high temperature. *Economic Geology* 91, 607-621
- Eriksson S. C. (1989). Phalaborwa: a saga of magmatism, metasomatism and miscibility. *In*: Bell K. (ed) *Carbonatite: genesis and evolution*. Unwin Hyman, London, 221-254
- Gottlieb P., Wilkie G., Sutherland D., Ho-Tun E., Suthers S., Perera K., Jenkins B., Spencer S., Butcher A., Rayner J. (2000) Using quantitative electron microscopy for process mineralogy applications. *JOM*, 24-25
- Hanekom H J., van Staden C.M.v.H., Smit P.J., Pike D.R.(1965) The Geology of the Phalaborwa Igneous Complex. Geological Survey of South Africa, *Memoirs*, 54
- Heaman L.M. (2009) The application of U-Pb geochronology to mafic, ultramafic and alkaline rocks: An evaluation of three mineral standards. *Chemical Geology* 261, 43-52
- Moore K. R., Wall F., Divaev F.K., Savatenkov V.M. (2009) Mingling of carbonatite and silicate magmas under turbulent flow conditions: Evidence from rock textures and mineral chemistry in sub-volcanic carbonatite dykes in Chagatai, Uzbekistan. *Lithos* 110, 65-82
- Pirrie D., Butcher A.R., Power M.R., Gottlieb P., Miller G.L., 2004. Rapid quantitative mineral and phase analysis using automated scanning electron microscopy (QEMSCAN®); potential applications in forensic geoscience. *In*: Pye K., Croft D.J. (Eds.), *Forensic Geoscience, Principles, Techniques and Applications*, vol. 232. Geological Society Special Publication, London, pp. 23-136
- Woolley A.R. (2001) Alkaline Rocks and Carbonatites of the World, Part 3: Africa, The Geological Society of London, p:265
- Wu F.J., Yang Y.H., Li Q.L., Mitchell R.H., Dawson J.B., Brandl G., Yuhara M. (2011) In situ determination of U-Pb ages and Sr-Nd-Hf isotopic constraints on the petrogenesis of the Phalaborwa carbonatite Complex, South Africa, *Lithos* 127, 209-327

Platinum mineralization at Owendale, NSW, Australia: new insights into the genesis of Pt mineralization in Alaskan-type ultramafic complexes

Reid R. Keays

School of Geosciences, Monash University, Melbourne, Victoria, 3800, Australia

Hazel M. Prichard, Peter C. Fisher

School of Earth and Ocean Sciences, Cardiff University, CF10 3AT, United Kingdom

Benjamin A. Sharp

Platina Resources, Varsity Lakes, Queensland, 4227, Australia

Abstract. A total of 639 kg of Pt was recovered from placer deposits in the Fifield region of Australia; it is presumed that this Pt was derived from nearby Alaskan-type intrusive complexes. Detailed studies of primary Pt mineralization in the Owendale intrusion, the probable source of much of the Pt in the Fifield area and a significant target for primary Pt mineralization, has identified three styles of mineralization. These are PGM alloys in pegmatoidal clinopyroxenites, or "P units", disseminated Cu-Pt alloys in serpentinitized dunites/wehrlites, and Pt-Pd-Cu-Au-rich sulfides; the latter two styles of mineralization have identical Pt:Rh:Ir ratios. We suggest that the PGE were originally hosted by PGE-rich sulfides that underwent partial to complete destruction through reaction with high temperature K₂O-rich hydrothermal fluids and serpentinitization of the hosting dunites and wehrlites. The PGE liberated from these sulfides formed a variety of PGM, the most abundant of which are Pt-Fe and Cu-Pt alloys.

Keywords. PGE genesis, Alaskan-type intrusion

1 Introduction

Prior to the discovery of the Bushveld complex, the bulk of the world's Pt production was from secondary placer Pt deposits associated with Alaskan-type intrusions. Very little economic primary Pt has been produced from these intrusions (Johan, 2002). However, an unknown

amount of primary Pt was produced from the Nizhny Tagil complex in the Urals (Augé et al., 2005). The Owendale intrusion hosts significant amounts of primary Pt mineralization in both clinopyroxenites and dunites/wehrlites; this primary mineralization reaches maximum grades around 22 g/t Pt. Platinum mineralization in Alaskan-type intrusions is generally S-poor and dominated by Pt-Fe alloys (Johan, 2002). Unlike the majority of other Alaskan-type intrusions in which much of the primary Pt mineralization is associated with chromite concentrations (Augé et al., 2005), this is not the case at Owendale. However, some of the primary PGE mineralization is associated with Cu sulfides. Although the bulk of the known primary PGE at Owendale occurs as PGM alloys in dunites, wehrlites, and clinopyroxenites, there is strong evidence that the PGE in these alloys were initially hosted by PGE-rich sulfides that were carried into the system in slurries of olivine crystals that solidified to form the dunite and wehrlites observed in the intrusion today.

2 Geology of the Owendale intrusion

The Alaskan-type intrusions in the Fifield region were intruded into Cambro-Ordovician greenschist facies slates and schists and are probably related to spatially associated volcanic rocks that were produced by

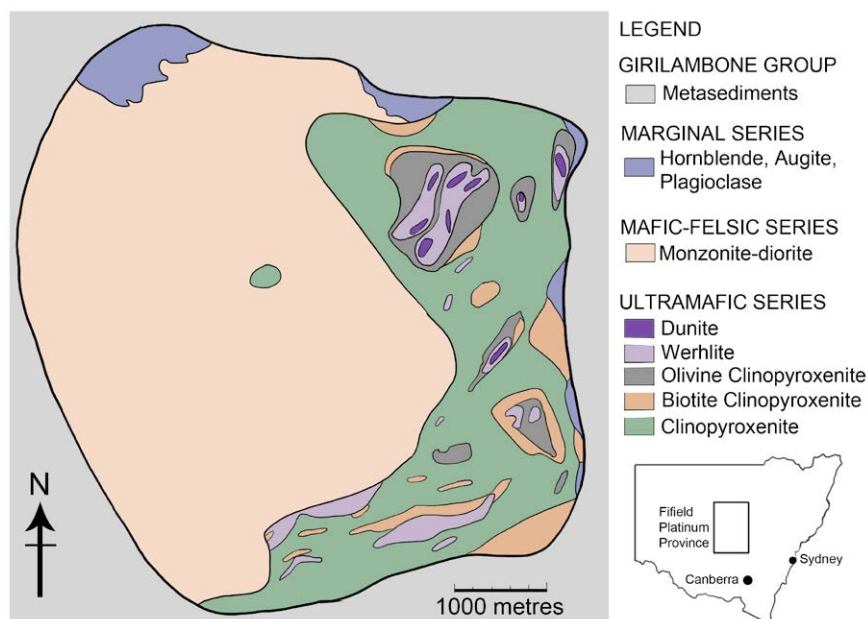


Figure 1. Subsurface geology of the Owendale intrusion (modified from Elliott and Martin, 1991).

shosonitic magmas (Andrew et al. 1995; Crawford et al., 2011). The Owendale Intrusion, which is ~30 km from the village of Fifield, consists of 80% mafic-felsic rocks and 20% ultramafic rocks (Fig. 1). The mafic-felsic rocks comprise diorites and monzonites that are thought to have intruded into the ultramafic rocks, with dunites and wehrlites within the ultramafic rocks cross-cutting the much more abundant olivine clinopyroxenites. Very significant amounts of phlogopite are associated with the dunite/wehrlite bodies; Elliot and Martin (1991) suggested that the phlogopite was produced by the reaction of the ultramafic rocks with K₂O-rich fluids that accompanied the intrusion of the monzonites. Weathering at Owendale has produced a laterite that is up to 60 m thick.

3 PGE mineralization at Owendale

Both placer and residual Pt mineralization associated with deeply lateritized ultramafic rocks are present at Owendale (Elliot and Martin, 1991; Johan et al., 1991). This Pt mineralization was formed by deep weathering of ultramafic rocks that hosted primary Pt mineralization; there are three distinct types of mineralization at Owendale, viz: (1) Pt-rich, Pd-poor, S-poor mineralization in “P units” that are pegmatoidal clinopyroxenites that form irregular lenses and veinlike bodies in olivine pyroxenites and have grades up to 14 g/t Pt over 1.4 m (Elliot and Martin, 1991; Johan et al., 1991); (2) a Cu–S-bearing association with high Pt and moderate Pd and Au concentrations that occurs as irregular veins and segregations of PGE-rich magmatic sulfides in both dunites/wehrlites and clinopyroxenites, as well as in disseminated PGE-rich sulfides over broad zones in the dunites/wehrlites; and (3) a Cu–S–Pd–Au-poor but Pt-rich association with grades up to 24 g/t Pt over 1 m; this style of mineralization is dominated by Cu–Pt and Pt–Fe alloys that are disseminated over broad intervals within partially serpentinized dunites and wehrlites (Brill and Keays, 1990). An important feature of the Pt mineralization within the P units, and the Cu-rich association described above is that they are associated with very large quantities of phlogopite that formed during interaction of high temperature, K₂O-rich fluids with primary magmatic sulfides in the rocks.

4 Platinum Group Minerals (PGM)

Johan et al. (1989) reported that the PGM assemblages associated with the P units are dominated by Pt–Fe alloys together with Os, Pd, Ir and Rh alloys, sulfides, antimonides, and arsenides. The PGM identified in this study are predominantly Cu–Pt and Pt–Fe alloys that may contain Rh, Ir, Ni and Co. They often occur together in composite grains usually in serpentine between grains of olivine (Fig. 2). Cu-rich Cu–Pt alloys have Cu/Pt ratios of approximately 2:1 with higher Pt values in mottled areas of PGM that appear to have lost Cu during alteration. Pt–Fe alloys exhibit a great range of Pt/Fe ratios with Pt varying from 75% to as little as 10%. These alloys are all rounded and irregular and the Cu–Pt

alloys often have a rounded shape veined by Cu-rich veins (Fig. 2). Euhedral irarsite and hollingworthite are associated with the Pt alloys (Fig. 3). PGM may be enclosed by magnetite (Fig. 4). Pd PGMs are rare with only one Pd–Bi (Fig. 5) and one Pd–Sn–Cu alloy located. Virtually all the Cu in the S-poor, but Pt-rich, dunites and wehrlites is hosted by Cu–Pt alloys; e.g., the host rock for sample 2208/659A contains 13.5 ppm Pt but only 22 ppm Cu (cf. Fig. 2).

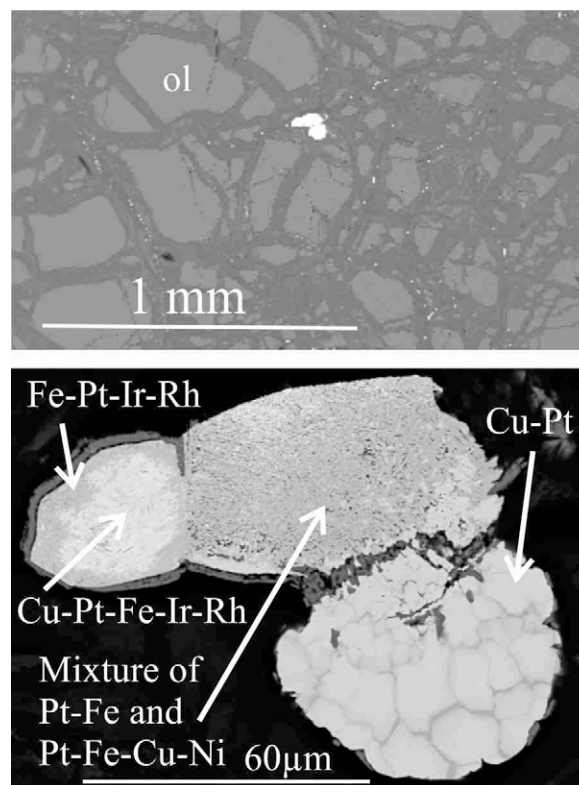


Figure 2. Back scattered electron (BSE) image of a composite grain of PGM alloys in serpentine (dark grey) between olivine (ol) in sample 2208/659A. Note Cu-rich veins in Cu–Pt alloy.

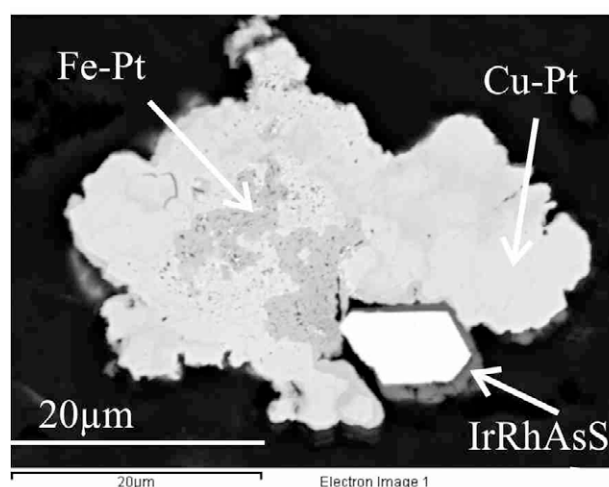


Figure 3. BSE image of a composite grain of PGM alloys with euhedral irarsite.

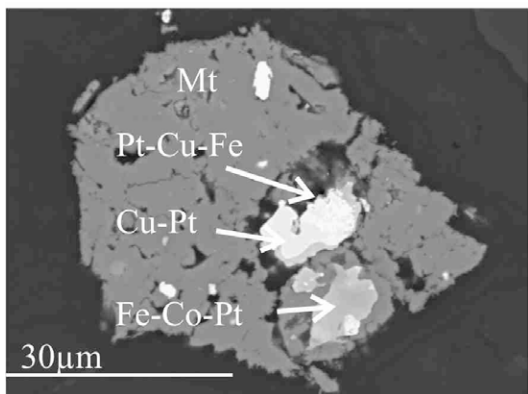


Figure 4. BSE image of PGM alloys enclosed in magnetite.

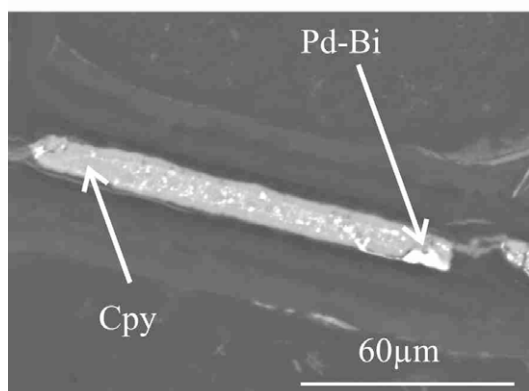
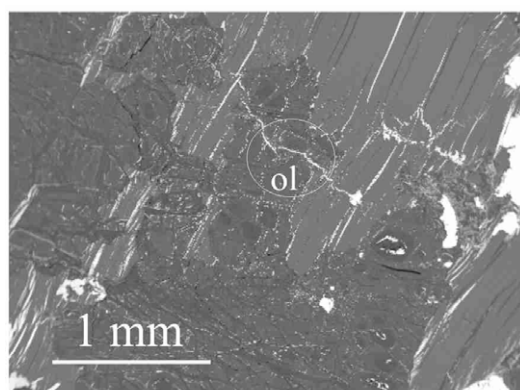


Figure 5. BSE image of Pd-bearing PGM in a chalcopyrite vein in olivine (ol) engulfed by phlogopite (phl).

5 PGE geochemistry

The Cu-S bearing assemblage is associated with elevated Pd and Au concentrations in addition to elevated Pt. Platinum broadly correlates with Cu (Fig. 6) as do Pd and Au. The Pt contents of the Cu-S bearing assemblage are comparable to those of Cu-S-Pd-Au poor assemblages with high Cu concentrations (Fig. 6). Over 70% of the Cu-S-Pd-Au poor samples that have Cu contents of 15 ppm or less still have significant Pt contents (Fig. 6), although the bulk of these samples have Pd concentrations <8 ppb, the effective detection

limit for Pd. Despite the large differences in their Cu, S, Pd, and Au contents, the Cu-S-Pd-Au rich and Cu-S-Pd-Au-poor assemblage have very similar Pt:Rh:Ir ratios, resulting in significant Rh-Pt correlations within overlapping arrays (Fig. 7). The fact that the Rh:Pt array of the laterites overlaps the arrays of the two primary styles of mineralization attests to the immobility of Pt and Rh during lateritization. These data provide strong evidence that the Pt (along with Rh and Ir) in disseminated Cu-Pt and Pt-Fe alloys within serpentinized dunites and wehrlites were initially hosted by PGE-rich sulfides that were co-magmatic with Cu-S-Pd-Pt-Au-rich sulfides present as disseminations, veins and segregations in the dunites/wehrlites and the clinopyroxenites. During serpentinization, all of the S and the majority of the Cu, Pd and Au in the disseminated primary PGE-bearing sulfides within these dunites and wehrlites were driven off, resulting in the formation of Cu-Pt and Pt-Fe alloys. This interpretation is supported by experimental evidence that indicates that Pt-Cu alloys cannot precipitate directly from magmas (James Brennan, pers. comm., 2011), and, as such, the Cu-Pt alloys present at Owendale cannot be primary but must be the product of secondary processes.

Nb/Th and Th/Yb ratios indicate that the parental magmas of the Owendale ultramafic rocks assimilated a significant amount of crustal material; these rocks also host sulfides with S/Se ratios up to 8000, indicating that the magmas that formed these rocks also assimilated crustal S (Keays, 2011).

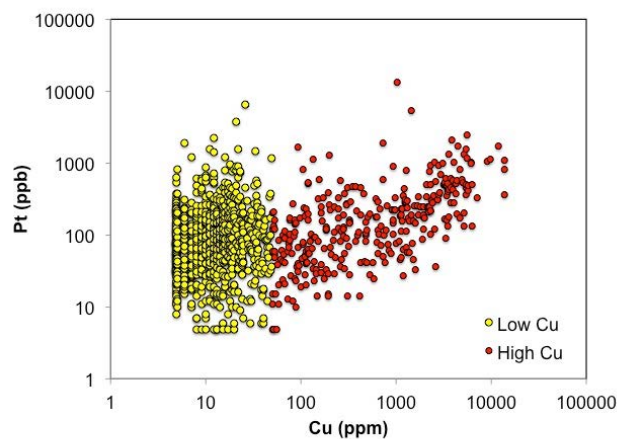


Figure 6. Scattergram of Pt vs Cu for the high Cu and low Cu PGE assemblages. Note the broad Pt-Cu correlation in the high Cu assemblage.

6 Conceptual model

We suggest that the shoshonitic magmas that produced the Owendale ultramafic rocks interacted with crustal rocks in a subchamber somewhere at depth below the Owendale Intrusion. This prompted AFC processes that caused initial crystallization of olivine with subsequent clinopyroxene crystallization within the subchamber, producing a zoned magma chamber. The presence of S

within the crustal rocks assimilated by these magmas caused S-saturation and

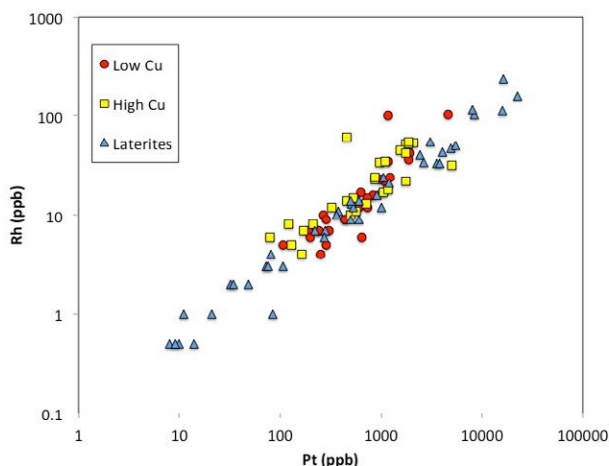


Figure 7. Scattergram of Rh vs Pt for the high and low Cu assemblages as well as for laterites derived from both types of assemblages. Note the overlap in the Rh-Pt arrays for the three types of material.

the segregation of magmatic PGE-rich sulfide droplets that co-precipitated with the olivine. The subchamber was then evacuated, first by extrusion of clinopyroxene-dominated crystal mushes that formed the clinopyroxenite sections of the Owendale intrusion, and then by olivine-dominated crystal mushes that also carried magmatic PGE-rich sulfides. These mushes formed the dunites/wehrlites within the Owendale intrusion, and were probably emplaced as slurries of olivine and PGE-rich sulfides that intruded the earlier-formed pyroxenites. PGE-rich sulfides that lagged behind the olivine slurries were later intruded to form sulfide veins in the ultramafic rocks, with Pt alloys formed from the primary PGE-rich sulfides within the Owendale intrusion either during serpentinization, which generated very strongly reducing conditions, or by the interaction of high temperature K_2O -rich fluids with the magmatic sulfides.

7 Implications

This study has a number of significant implications for our understanding of Alaskan-type ultramafic complexes and the processes that form secondary PGE mineralization. The data presented here indicate that the characteristically low S contents of PGE mineralization and predominance of Pt alloys in Alaskan-type intrusions are likely to be a product of post-magmatic rather than primary processes. This study has demonstrated that the PGE in the Owendale intrusion were carried into the system as PGE-rich magmatic sulfides that were subsequently destroyed either during reaction between these sulfides with K_2O -rich fluids derived from monzonitic magmas that intruded the ultramafics, or during serpentinization of the dunites and wehrlites. If the PGE in the Owendale intrusion were carried into the system in PGE-rich sulfides in olivine-dominated slurries, with some of the PGE-rich sulfides

lagging behind these slurries, then there may be significant quantities of PGE-rich sulfides, possibly at shallow depths, below the Owendale intrusion. If this hypothesis is correct, then other Alaskan-type intrusions also have the potential to be associated with PGE-rich sulfides. Finally, serpentinization of PGE- (and Au-) rich sulfide-bearing ultramafic rocks may provide an important source of Au for Au-forming hydrothermal fluids.

Acknowledgements

Platina Resources is gratefully acknowledged for their support of this project and for granting permission to publish these results.

References

- Andrew AS, Hensen BJ, Dunlop AC and Agnew PD (1995). Oxygen and hydrogen isotope evidence for the origin of platinum-group element mineralization in Alaskan-type intrusions at Fifield, Australia. *Econ Geol* 90: 1831-1840.
- Brill, BA and Keays RR (1990). Fifield Project Report, May 1990, University of Melbourne, unpublished research report prepared for Helix Resources.
- Crawford AJ, Meffre S, Squire RJ, Barron LM, and Falloon TJ (2007). Middle and Late Ordovician magmatic evolution of the Macquarie Arc, Lachlan Orogen, New South Wales." *Aust Jour Earth Sciences* 54(2): 181-214.
- Elliot SJ and Martin AR (1991) The Owendale Alaskan-type intrusive complex and associated PGE mineralization, Fifield belt, New South Wales: 6th International Platinum Symposium, Perth, July 1991. Guidebook for the Pre-Symposium field excursion, p. 12-24
- Johan Z, Ohnenstetter M, Slansky E, Barron LM, and Suppel D (1989). Platinum mineralization in the Alaskan-type intrusive complexes near Fifield, New South Wales, Australia: Part 1, Platinum-group minerals in clinopyroxenites of the Kelvin Grove prospect, Owendale intrusion. *Mineral. Petrol.* 40: 289-309
- Johan Z. (2002). Alaskan-type complexes and their Platinum-group element mineralization. In "The geology, geochemistry, mineralogy and beneficiation of the platinum-group elements", Cabri, L (ed) *Can. Inst. Min. Metall. Petroleum. Spec.* Vol. 54: 669-720
- Keays RR (2011) Platinum mineralization at Owendale/Field. Unpubl. report prepared for Platina Resources

Variation in PGM within two orebodies in the Jinchuan intrusion, Gansu province, NW China

Robert D. Knight, Hazel M. Prichard, Iain McDonald

School of Earth, and Ocean Sciences, Cardiff University, Main Building, Park Place, Cardiff, CF10 3AT, UK

Christina Y. Wang

Key Laboratory of Mineralogy and Metallogeny, Guangzhou Institute of Geochemistry, Chinese Academy of Sciences, Guangzhou 510640, China

Abstract. Platinum-group minerals (PGM) have been examined in samples from orebody #1 and orebody #24 of the Jinchuan Ni-Cu(-PGE) intrusion situated in NW China. There is a significant variation in the types and abundance of PGM identified from each of the two orebodies with more As-bearing PGM observed in the Ni-rich orebody #1 and more Pd-bearing PGM observed in the relatively Cu-rich orebody #24. The PGM observed include irarsite (IrAsS), sperrylite (PtAs₂), froodite (PdBi₂) and michenerite (PdBiTe). Irarsite is commonly located within gersdorffite-cobaltite. Furthermore, scanning electron microscope (SEM) analysis records Rh and Ir in solid solution in the gersdorffite-cobaltite. This highlights the importance of sulpharsenides as PGE collectors. Sperrylite occurs as large infrequent crystals and may be responsible for the widely variable Pt whole rock content noted in previous Jinchuan publications. The variation in the distribution of As-bearing PGM between the orebodies may be related to: i) a difference in the degree of crustal assimilation or in country rock As content during crustal assimilation, ii) the fractionation and separation of monosulphide solid solution (MSS) with early forming As-bearing PGM and the later crystallising Cu-rich Pd-bearing intermediate solid solution (ISS) or iii) the possible generation of orebodies #1 and #24 from different magmas.

Keywords. Jinchuan, platinum, base metal sulphides, sulpharsenides

1 Introduction

The Jinchuan ultramafic intrusion in NW China situated along the northern margin of the fault-bounded Longshoushan Belt is host to the third largest Ni deposit in the world after Noril'sk and Sudbury. The Jinchuan intrusion is approximately 6,000m long, 300m wide, and more than 1,000m thick in its central part. It crosscuts the marbles and gneisses of the Baijiazuizi complex and strikes roughly northwest-southeast, parallel to the regional structural trend.

Debate remains over the affinity of the intrusion, however, it has recently been interpreted as a highly tilted sill (Lehmann et al. 2007) which is cut by a series of northeast trending strike slip faults dividing the intrusion into three sub-chambers; the west, west-central and east sub-chambers hosting orebodies #24, #1 and #2 respectively (Chai and Naldrett 1992; Fig. 1).

Previous studies of Jinchuan ores have identified the following PGM as summarised in Prichard et al. (*in press*): padmaite, sperrylite, irarsite, froodite, michenerite, moncheite, merenskyite and kotulskite. The results presented here are from core samples collected at known depths or stratigraphic positions within the

intrusion from three bore holes from orebody #1 traversing from west to east and from one borehole from the relatively Cu-rich orebody #24.

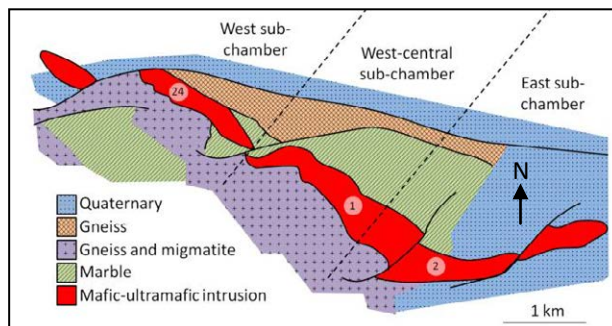


Figure 1. Geological map of the Jinchuan intrusion showing sub-chambers and orebodies. Redrawn after Chai and Naldrett 1992; Lehmann et al. 2007.

2 Samples and ores

The samples selected include the typical lithologies comprising the intrusion; dunite, websterite, lherzolite and plagioclase lherzolite. These samples exhibit different degrees of greenschist facies alteration as well as hosting a variety of sulphide ore types. Olivine is variably altered and may be found rarely as fresh olivine, more commonly as relict olivine enclosed by secondary serpentine and magnetite or completely altered to serpentine. Net-textured sulphide ore is common and is predominantly found in dunite (Fig. 2A). Alternatively, 'patchy' net-textured ore may occur where the interstitial space between olivine crystals is occupied by 'patches' of sulphides and altered silicates in varying proportions (Fig. 2B).

Sulphide mineralisation ranges from disseminated ore (Fig. 2C) to massive ore which may incorporate minor silicate and carbonate material (Fig. 2D). These ores are further complicated by different processes of sulphide remobilisation. Massive sulphide remobilisation may occur, again incorporating both silicate and carbonate material (Fig. 2E). Alternatively, smaller scale remobilisation can involve sulphides being transported by and subsequently crystallising within veins of variable composition (Fig. 2F).

The dominant sulphide phases present are pentlandite, pyrrhotite and chalcopyrite accompanied by minor gersdorffite-cobaltite (NiAsS-CoAsS) and nickeline (NiAs) phases. The sulphides are commonly veined and enveloped by secondary magnetite.

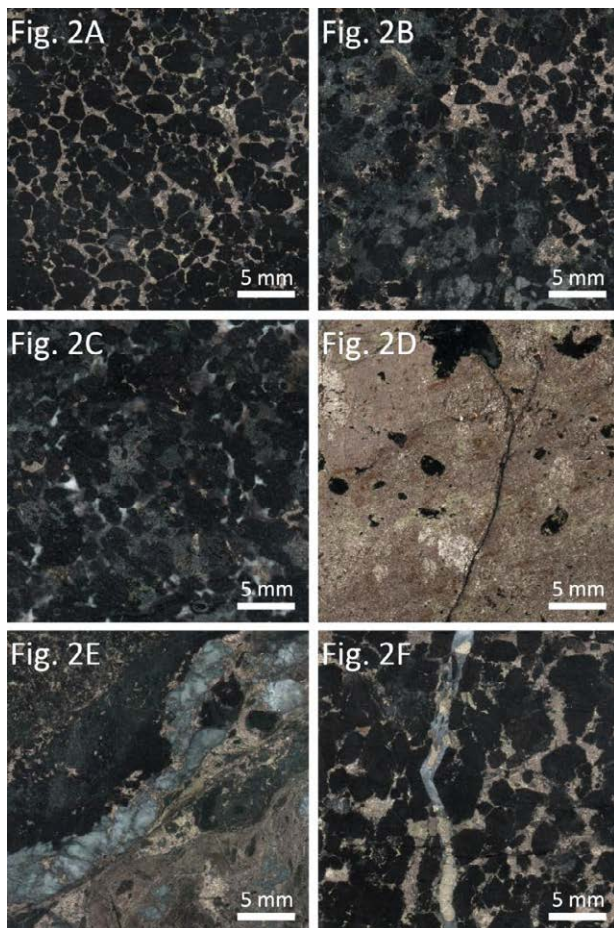


Figure 2. Examples of different sulphide ores sampled. A) Net-textured ore interstitial to olivine. B) 'Patchy' net-textured ore with a variation of interstitial sulphides and altered silicates. C) Disseminated ore. D) Massive ore incorporating minor silicate and carbonate material. E) Massive sulphide remobilisation. F) Small scale sulphide remobilisation in a carbonate vein.

3 Platinum-group minerals

Initial PGM searches of these samples using the SEM has located 86 PGM (and 24 electrum phases) and resulted in the identification of predominantly foolite (PdBi_2), sperrylite (PtAs_2), michenerite (PdBiTe) and irarsite which may include minor constituent Pt and Rh as part of the hollingworthite-irarsite-platarsite solid solution series ($[\text{Ir,Pt,Rh}]\text{-As-S}$). A summary of the PGM identified from the different orebodies with samples categorised into types of sulphide mineralisation is presented in Table 1.

There is a dramatic difference in the platinum-group mineralogy between orebodies #1 and #24. Orebody #1 hosts the majority of the irarsite and all of the sperrylite phases identified in these samples whereas the more Cu-rich orebody #24 hosts a much greater proportion of the Pd-bearing phases (foolite and michenerite). A greater amount of electrum is also observed in orebody #24.

Foolite phases occur as small (typically $1\text{-}4\ \mu\text{m}^2$) anhedral phases associated with either base metal sulphides (BMS) or magnetite which itself is often closely associated with the BMS veining or enveloping the sulphides. Foolite is sometimes associated with

additional phases comprised of variations of Bi, Te, Pb and Se (Fig. 3A).

Sperrylite phases, however, occur as rarer but much larger crystals (from $10\text{-}170\ \mu\text{m}^2$) with subhedral to euhedral forms that are sometimes sheared (Fig. 3B). Sperrylite is identified in sulphide, oxide and silicate phases showing no significant preference for any one host.

Michenerite is present in a variety of crystal forms including anhedral phases similar to foolite as well as more subhedral laths (Fig. 3C) with sizes ranging from $1\text{-}60\ \mu\text{m}^2$ and an average size of $11\ \mu\text{m}^2$. Michenerite is predominantly associated with the BMS and magnetite. On two occasions michenerite is identified in serpentine, however, it retains some association with the BMS as both of the PGM are partially and thinly enveloped by sulphide phases.

Perhaps the most interesting feature of these ores is the overwhelming association of irarsite with gersdorffite-cobaltite phases. Despite the rarity of gersdorffite-cobaltite, particularly in comparison to the other BMS present, irarsite (typically $5\text{-}20\ \mu\text{m}^2$) is consistently identified within small gersdorffite-cobaltite phases (usually $<0.5\ \text{mm}^2$; Fig. 3D). Furthermore, Rh and sometimes Ir are also identified in solid solution in some of these gersdorffite-cobaltite phases under the SEM. In several cases, Rh concentrations are high enough (up to several atomic percent) to produce faint yet visible gradational anhedral patches within the gersdorffite-cobaltite phases.

Alternatively, irarsite may occur outside of the gersdorffite-cobaltite phases and is identified predominantly within silicates but may also be associated with BMS in some cases. Irarsite may be wholly or partially enveloped by hollingworthite (RhAsS ; Fig. 3E).

Electrum and Ag-Te phases also occur in many of the samples studied and vary in abundance depending on the sample type. These phases tend to be more abundant in massive or significantly remobilised ores. Silver telluride phases often accompany PGM whereas electrum occurs as clusters or in patches together (Fig. 3F) within sulphide, oxide and silicate phases.

Other common phases identified include compounds comprised of Bi, Te, Pb and Se in varying concentrations and arrangements. Although these phases are not the focus of this study, they are noted when observed accompanying PGM.

4 Discussion

The crystal forms and associations of the PGM identified here are critical in understanding both the magmatic concentration of PGE and the subsequent remobilisation of PGE during post magmatic hydrothermal alteration.

The awareness of an affinity of PGE with As is fast growing, evidenced by recent literature (e.g., Dare et al. 2010; Godel et al. 2012). The consistent identification of irarsite phases within gersdorffite-cobaltite crystals demonstrates the importance of sulpharsenides as collectors of PGE. Other studies have shown that the

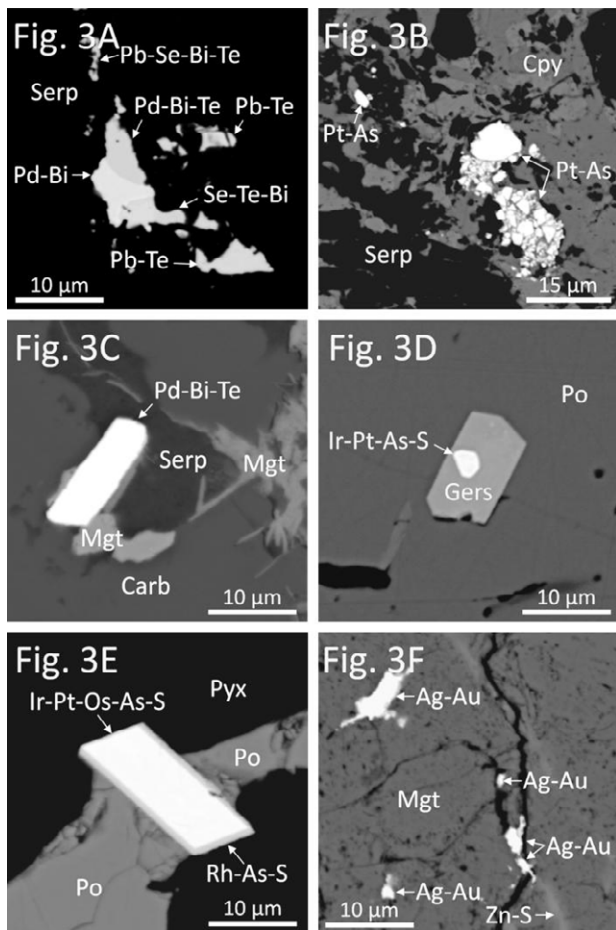


Figure 3. Back-scattered electron (BSE) images of the typical PGM observed. A) Anhedronal froodite (PdBi_2) and michenerite associated with barren semimetal and Pb bearing phases. B) Large sperrylite (PtAs_2) phase which has been sheared and fractured associated with both chalcopyrite (Cpy) and serpentine (Serp). C) Subhedronal michenerite (PdBiTe) associated with magnetite within a mix of serpentine and carbonate (Carb). D) Irarsite (IrAsS) with minor Pt content enclosed within gersdorffite-cobaltite (Gers) which itself is within pyrrhotite (Po). E) Irarsite with minor Pt and Os content partially enveloped by hollingworthite (RhAsS) associated with both pyrrhotite and pyroxene (Pyx). F) Example of a cluster of electrum phases with magnetite, pyrrhotite and a minor zinc sulphide phase (Zn-S).

presence of As in the melt may lead to the early crystallisation of As-bearing PGM. One such example is that of early forming sperrylite becoming trapped in later forming silicates including olivine in an ultramafic complex from western Andriamena, Madagascar (McDonald 2008). At Jinchuan, it appears that both sperrylite and irarsite may have formed relatively early at high temperatures with sperrylite identified within silicates, oxides and BMS and irarsite predominantly found within silicates where not enclosed by gersdorffite-cobaltite.

Jinchuan whole rock data has often shown a large variation in Pt concentrations (e.g., Chai and Naldrett 1992; Song et al. 2006) leading to both positive and negative Pt anomalies which have not yet been satisfactorily explained. This study shows that a Pt nugget effect may be the cause of these erratic Pt concentrations given the presence of large (up to $170 \mu\text{m}^2$) but rare sperrylite phases which show no particular

preference for a mineral host.

Magnetite has been identified in much the same way as that described by Prichard et al. (*in press*) with some PGM, namely froodite, occurring within magnetite selvages on BMS. These PGM may have been formed as PGE and Bi were expelled from the sulphides during post magmatic hydrothermal alteration resulting in simultaneous sulphur loss and magnetite formation.

Electrum and Ag-Te phases are particularly abundant in samples hosting primary and remobilised massive sulphide ores. This association with remobilised ore may reflect the relatively high mobility of Au and Ag against that of the less mobile PGE.

The variation in the distribution of PGM with As-bearing phases predominantly identified in orebody #1 and Pd-bearing phases and electrum more abundant in orebody #24 may be the result of several possible processes. The availability of As from the associated country rocks may vary between the two orebodies with more As-rich material been assimilated by orebody #1 during the emplacement of the Jinchuan intrusion resulting in the crystallisation of more As-bearing PGM.

Conversely the separation in the different PGM types present in the different orebodies may be the result of sulphide liquid fractionation. The early crystallisation of monosulphide solid solution (MSS) from an immiscible sulphide liquid may have been accompanied by early forming As-bearing PGM while leaving Pd to partition into the resulting Cu-rich liquid. This Pd-bearing Cu-rich liquid would have then cooled and crystallised to form intermediate solid solution (ISS) and subsequently a Cu-rich ore (predominantly chalcopyrite) with Pd-bearing PGM. The separation of MSS and ISS in this manner would require sulphide crystallisation to occur in a dynamic environment allowing for the significant movement of the differentiated sulphide crystals and liquids.

A final consideration of the source of these different PGM may be the derivation of orebodies #1 (and #2) from a different magma than that of orebody #24. The question of whether orebody #24 is simply an extension of orebodies #1 and #2 or whether it is a separate intrusion in its own right has been considered previously (e.g., Song et al. 2012). The variation in the PGM types observed in these orebodies may hint at the possibility of the involvement of more than one magma in the formation of the Jinchuan intrusion. Thus the eastern sub-chamber hosting orebody #24 may indeed be an isolated intrusion in its own right having developed separately from the west-central and eastern sub-chambers hosting orebodies #1 and #2 respectively.

Acknowledgements

We would like to thank Professor Mingjie Zhang and Qingyan Tang of Lanzhou University for organising our field trip to Jinchuan and the cooperation and hospitality of Jinchuan Group Ltd. in allowing us to collect the samples required for this study.

Orebody	No. of Samples	Sulphide Ore Description	PdBi ₂	PdBiTe	PtBiTe	PtAs ₂	(IrPtRh)-AsS	AuAg	Other	Total
#1	8	Disseminated	6	1	2	1	-	3	1	
#1	1	Disseminated with BMS stringers	-	-	-	-	1	-	3	
#1	8	Patchy net texture	3	5	-	1	3	5	-	
#1	1	Patchy net texture with BMS stringers	-	-	-	-	1	-	-	
#1	2	Net texture	2	-	-	-	-	3	-	
#1	2	Net texture with BMS stringers	-	-	-	1	1	-	-	
#1	1	Net texture with BMS vein	1	-	-	-	-	-	3	
#1	1	Net texture with shear fabric	-	-	-	-	-	-	-	
#1	1	Net texture with BMS vein (altered)	-	5	-	2	-	2	-	
#1	1	Net texture (altered)	-	-	-	-	1	-	-	
#1	1	Massive and net textured	-	-	-	1	1	1	-	
#1	1	Massive with carbonate	-	-	-	-	3	-	-	
#1	1	Altered/Unknown	-	-	-	-	2	-	1	
Total	29		12	11	2	6	13	14	8	66
#24	1	Disseminated with BMS stringers	-	-	-	-	-	-	-	
#24	1	Patchy net texture	1	-	-	-	-	-	-	
#24	4	Net texture	15	12	1	-	-	-	-	
#24	2	Net textured (altered)	-	2	-	-	1	-	-	
#24	2	Net texture with BMS veins (altered)	-	-	-	-	1	10	-	
Total	10		16	14	1	-	2	10	-	43

Table 1. Summary of the PGM identified divided by orebody number and further categorised by the type of sulphide mineralisation present with the number of samples studied exhibiting each type of mineralisation recognised.

References

Chai G, Naldrett AJ (1992) Characteristics of Ni-Cu-PGE mineralization and genesis of the Jinchuan Deposit, Northwest China. *Econ Geol* 87: 1475-1495

Dare SAS, Barnes S-J, Prichard HM, Fisher PC (2010) The timing and formation of platinum-group minerals from the Creighton Ni-Cu-platinum-group element sulfide rich deposit, Sudbury, Canada: Early crystallization of PGE-rich sulfarsenides. *Econ Geol* 105: 1071-1096

Godel B, González-Álvarez I, Barnes SJ, Barnes S-J, Parker P, Day J (2012) Sulfides and Sulfarsenides from the Rosie Nickel Prospect, Duketon Greenstone Belt, Western Australia. *Econ Geol* 107: 275-294

Lehmann J, Arndt N, Windley B, Zhou M-F, Wang CY, Harris C (2007) Field relationships and geochemical constraints on the emplacement of the Jinchuan intrusion and its Ni-Cu-PGE sulfide deposit, Gansu, China. *Econ Geol* 102: 75-94

McDonald I (2008) Platinum-group element and sulfide mineralogy in ultramafic complexes at western Andriamena, Madagascar. *Trans Inst Min Metall B (Applied Earth Science)* 117: 1-10

Song X-Y, Zhou M-F, Wang CY, Qi L, Zhang C-J (2006) Role of Crustal Contamination in Formation of the Jinchuan Intrusion and Its World-Class Ni-Cu-(PGE) Sulfide Deposit, Northwest China. *Int Geol Rev* 48: 1113-1132

Prichard HM, Knight RD, Fisher PC, McDonald I, Zhou M-F, Wang CY (2013) Distribution of platinum-group elements in magmatic and altered ores in the Jinchuan intrusion, China: an example of selenium remobilization by post magmatic fluids. *Miner Depos* in press

Song X-Y, Danyushevsky LV, Keays RR, Chen LM, Wang Y-S, Tian Y-L, Xiao J-F (2012) Structural, lithological, and geochemical constraints on the dynamic magma plumbing system of the Jinchuan Ni-Cu sulfide deposit, NW Chin. *Miner Depos* 47: 277-297

Dyumtaleysky massif, Taimyr, Russia: a magmatic derivative from a complex mantle source

N.A. Krivolutskaya

V.I. Vernadsky Institute of Geochemistry and Analytical Chemistry RAS, Moscow, Russia

B.I. Gongalskiy

Institute of Ore Deposits RAS, Moscow, Russia

Abstract. The Dyumtaleysky massif in Taimyr has a unique combination of its rock and ore compositions. It is compared here with the similar Chineysky intrusion in the Trans-Baikal region, which also hosts both titanomagnetite and sulfide mineralization. The Dyumtaleysky ores also have common features and is contemporaneous with the Norilsk Intrusive Complex. Although the metal contents and S isotope compositions ($\delta^{34}\text{S} = +10$ to $+12\%$) of the ores in the intrusions are similar, they formed from significantly different magmas. The Dyumtaleysky intrusion crystallized from a primitive mantle-derived magma (with no Ta-Nb and Pb anomalies), whereas the Norilsk intrusions are derived from melts with strong crustal signatures. The features of the Dyumtaleysky massif can be explained by its origin from an unusual sulfide-bearing mantle source that had sulfides through earlier crustal-mantle interaction.

Keywords. Siberian province, layered intrusion, REE, S isotopes

1 Introduction

Relatively few mafic-ultramafic intrusions contain both titanomagnetite and sulfide ore mineralization. The Volkovskaya intrusion in the Urals, the Tsaginsky massif in the Kola Peninsula, and the Chineysky massif in the Northern Transbaikalia are the best known intrusions of this type in Russia.

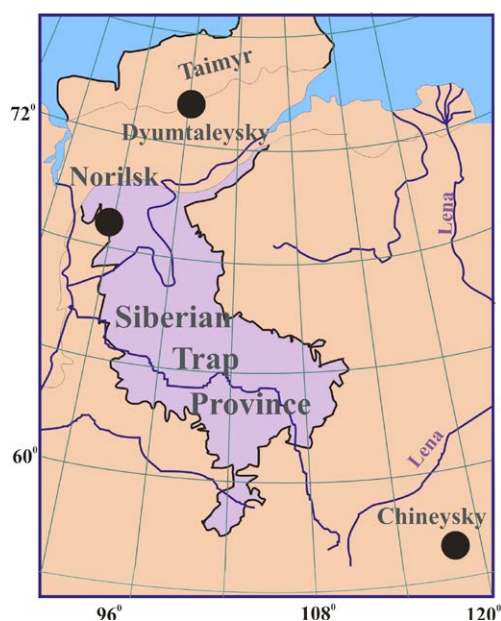


Figure 1. Locations of the studied intrusions in Eastern Siberia.

The Chineysky intrusion is located in the southern part of the Siberian Platform and is of the greatest interest because it hosts the largest V deposit in Russia. The Dyumtaleysky intrusion was discovered by Norilskgeologiya Ltd. in the southern part of the Taimyr Peninsula (Fig. 1) not long ago; it carries mineralization with a composition that is closely similar to that of the Chineysky massif. Because the Dyumtaleysky intrusion is almost completely overlain by Quaternary rocks, its morphology is inferred from geophysical and drilling data. The massif is a tabular body approximately 50 km long and 500-600 m thick, which steeply dips to the north.

2 Stratigraphy and petrography of the Dyumtaleysky massif

The intrusion is composed of two compositionally contrasting zones of similar thickness of about 300 m: (1) an upper zone, which is composed of gabbroic rocks, and (2) an lower zone, which is made up of peridotites (Fig. 2).

Gabbroic rocks have layered textures which are emphasized by uneven distributions of titanomagnetite and are consistent with gravitational magmatic settling, as described by Wager and Brown (1962). The amount of titanomagnetite commonly increases toward a base of a layer. The upper zone is subdivided into four units from A to D downwards: weakly layered rocks (65 m thick), clearly layered rocks (45 m thick), weakly layered rocks (65 m thick), and non-layered rocks (125 m thick). Some of gabbroic rocks are massive, although they are predominantly trachytic in texture in the central parts of the units. The thickness of a cycle within the units varies irregularly with the thinnest B unit being composed of cyclic layers from 1 to 3 m thick. The thickness of the cycles in the A and D units varies 4-12 m. The upper zone of the massif is composed of predominantly titanomagnetite-bearing gabbro, which contains olivine in the C and D units with olivine contents as high as 10 vol. % in the lower part of the D unit. The upper layers of the cycles are commonly composed of leucogabbro. The major minerals are clinopyroxene ($\text{Fs}_{14-18}\text{Wo}_{50-54}\text{En}_{31-33}$), plagioclase (An_{60-75}), olivine (Fo_{59-64} , 0.12 wt.% NiO), titanomagnetite, ilmenite, and spinel, with rare orthopyroxene (Hyp).

The peridotitic lower zone (2) consists of three cyclic units from E to G downwards that are dominated by wehrlite, olivine mesogabbro and pegmatoid gabbro, respectively. The rocks are also characterized by elevated titanomagnetite contents. They show no fine

layering, and their cyclicity reflects compositional variations within a layer and alternation of layers of different compositions. Olivine is richer in Mg and has a higher NiO content (71-80 mol.% Fo, 0.29 wt.% NiO), whereas plagioclase is richer in Ca (up to 85 mol.% An) with respect to olivine and plagioclase in the upper zone.

Iron and titanium oxides are abundant throughout the entire vertical section. Their average content in the upper zone is 10 vol.%, although it reaches 80-90 vol.% near the base of the cycles; they are unevenly distributed in the lower zone, where they account for 1 to 15 vol.% of the rocks.

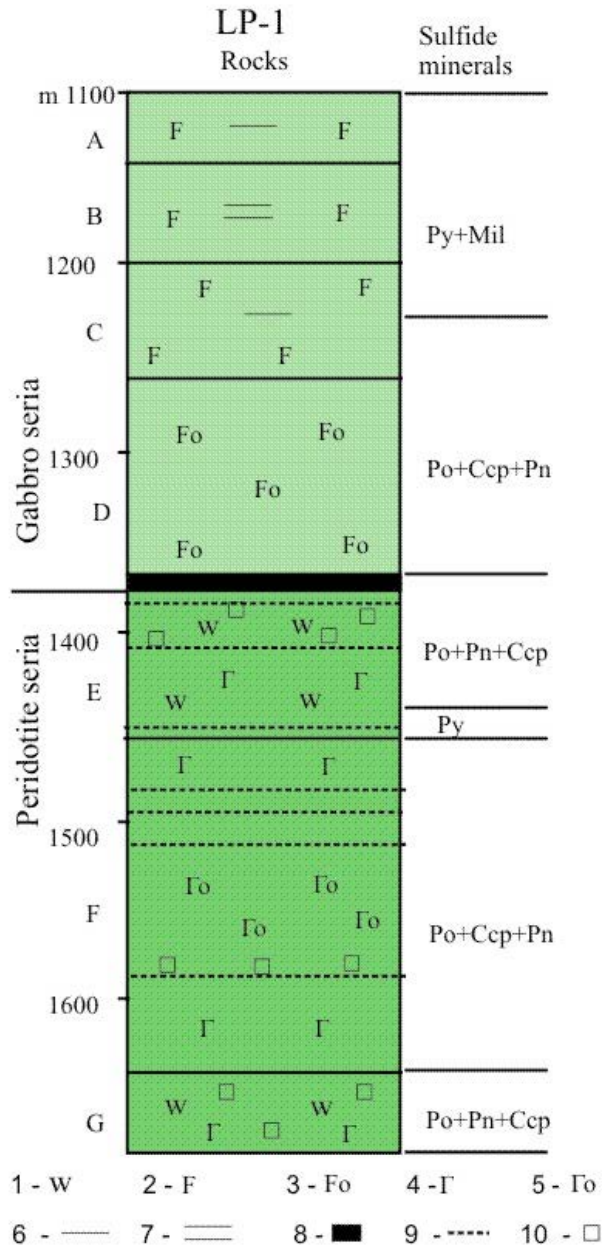


Figure 2. Stratigraphy of the Dyumtaleysky massif in core LP-1. 1 – wehrlite, 2 – ferrogabbro, 3 – olivine ferrogabbro, 4 – gabbro, 5 – olivine gabbro, 6 – weakly-layered rocks, 7 – strongly-layered rocks, 8 – massive titanomagnetite ores, 9 – disseminated titanomagnetite ores, 10 – sulfide ores.

The boundary between two zones is marked by a unit of massive titanomagnetite ore (100% titanomagnetite) and high-grade sulfide mineralization (Fig. 2).

The texture of the titanomagnetite ore gradually changes downwards in the vertical section from fine-grained exsolution texture to coarse-grained equigranular intergrowths between titanomagnetite, ilmenite, and spinel. Magnetite contains up to 1.5 wt.% V₂O₅, 11wt.% TiO₂ and 2.3 wt.% MgO; ilmenite is rich in Mn and Mg up to 5 wt.% MnO and 5.9 wt.% MgO (Komarova et al. 2002).

The lower zone of the massif is similar to the lower parts of other massifs in the southern part of Taimyr (for example, the Luktakhsy massif), but the stratigraphy of the Dyumtaleysky massif differs remarkably from that of the layered intrusions in the Norilsk region.

3 Rock geochemistry

The geochemistry of the Dyumtaleysky rocks is comparable with that of volcanic rocks of the Gudchikhinskaya Formation, which is considered to be products of crystallization of the most primitive magmas in the northern part of the Siberian Flood Basalt Province (Sobolev et al. 2009). The negative Ta-Nb and positive Pb anomalies, which are interpreted as the main indications of crustal origin of volcanic rocks, are absent in the compositions of Gudchikhinsky volcanic rocks and their parental magmas. The steep slope of the right-hand part of the REE pattern and the high Gd/Yb ratio (>2) indicate the presence of garnet in the mantle source (Fig. 3a).

The trace element patterns of intrusive rocks of the Dyumtaleysky massif show the same geochemical features, but the elevated titanomagnetite and plagioclase contents in Dyumtaleysky rocks result to the appearance of the Ti and Sr positive anomalies whereas the Pb high is related to the elevated sulfide content. The different levels of the enrichment in trace element (Fig. 3) reflect the variable proportions of olivine and titanomagnetite in rocks.

The trace element geochemistry suggests that all these rocks were derived from sources of the similar composition, although they are not comagmatic in origin. Isotopic data on picrites of the Gudchikhinsky Formation (Krivolutskaya et al. 2012) and on rocks of the Dyumtaleysky massif (Romanov et al. 2012) confirm their similarity. The variations of ε_{Nd} for Gudchikhinsky rocks are between +1 and +6.6, whereas ε_{Nd} for Dyumtaleysky rocks varies from +2.7 to +4.8. The ⁸⁶Sr/⁸⁷Sr isotope ratio in Gudchikhinsky volcanics varies from 0.7032 to 0.7061, whereas it falls between 0.7044 and 0.7051 in Dyumtaleysky rocks.

In contrast, the geochemistry of the Norilsk intrusions that host the giant reserves of massive Ni-Cu-PGE ores (e.g., Talnakh and Norilsk 1 deposits) is remarkably different. The homogenous ε_{Nd} values (-1 to +2) and high ⁸⁶Sr/⁸⁷Sr ratios (0.7055 to 0.7078) in gabbro-dolerites from the ore-bearing intrusions of the Norilsk Complex indicate that these massifs formed from a source different from that of Dyumtaleysky rocks. This suggestion is confirmed by data from melt

inclusions hosted in olivines from the Talnakh, Kharaelakh, Norilsk 1, and Zelenaya Griva intrusions and clinopyroxene-hosted inclusions from the Southern Maslovsky massif (Maslovsky deposit). Parental magmas for the intrusions hosting major PGE-Cu-Ni deposits had tholeiitic compositions with low TiO₂, elevated MgO contents, and about 0.8 wt.% H₂O.

The trace element distribution in rocks of the Chineysky massif is similar to that in Norilsk intrusive rocks, as the patterns contain clear negative Ta-Nb and positive Pb anomalies, although Chineysky mineralization is close to that of the Dyumtaleysky massif (Fig. 3b).

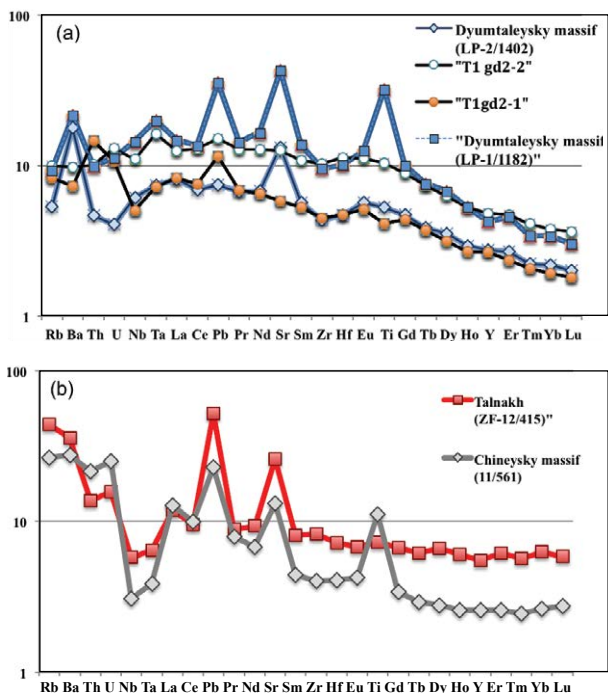


Figure 3. Primitive mantle-normalized trace element patterns of (a) Gudchikhinsky picrites (sample T₁gd₂-1 – 24 wt.% MgO, T₁gd₂-2 – 17 wt.% MgO) and rocks of the Dyumtaleysky massif with the same MgO contents; (2) rocks of the Talnakh massif and the Chineysky intrusions (sample with 18 wt.% FeO) (mantle abundances according to Hofmann (1988)).

4 Sulfide ores

Despite the differences in their parental magma compositions, the sulfide ores of the Dyumtaleysky massif are compositionally similar to the reference intrusions of the Norilsk Complex. Rocks of the Dyumtaleysky massif contain disseminated and stringer-disseminated (up to thin veins) ore mineralization. The Cu and Ni tenors of the ores are similar. The PGE concentrations in the upper part of the vertical section are low (<0.5 ppm PGE), whereas the Pt + Pd contents in the lower zone reach 5 ppm. The compositions of disseminated sulphide assemblages vary in the vertical section: the upper part is dominated by pyrite-millerite assemblages, which downward give way to pyrite-chalcopyrite-pentlandite assemblages (in the lower part of the gabbroic zone), and finally to predominantly pyrrhotite-pentlandite assemblages with minor chalcopyrite. The main horizons of the disseminated

sulfide ores are confined to the contact between the gabbroic and peridotitic zones, as well as to the central and lowest parts of the peridotitic zone.

Major minerals of the sulphide ores are pyrrhotite, chalcopyrite, and pentlandite, and minor minerals include pyrite, millerite, sphalerite, cubanite, violarite, cobaltite. Hauchecornite, niccolite, greigite, sperrylite, froodite are rare, and a few unnamed phases have also been found (Komarova et al 1999). The composition of pentlandite varies significantly through the vertical section: it contains <1 wt.% Co in the lower part of the vertical section, whereas pentlandite is rich in Co up to 7.56 wt.% Co that is analogous to Co-rich pentlandite from disseminated titanomagnetite ores of the Chineysky massif, where it may contain up to 18 wt.% Co. Pyrite contains elevated Ni concentrations (up to 1.2 wt.% Ni) and millerite is rich in Fe (0.6 wt.% Fe).

Although the parental magma of the Dyumtaleysky massif had a chemically primitive composition, the S isotope composition of its sulfides ($\delta^{34}\text{S} = +10$ to $+12$ ‰, n = 9) is similar to that of the Norilsk massifs and deposits. Another interesting feature of Dyumtaleysky rocks is their remarkably light carbon isotope composition ($\delta^{13}\text{C} = +27$ - $+37$ ‰).

5 Discussion

The Dyumtaleysky massif is a mineralized intrusion that was produced by a primitive mantle magma and but contains ores with crustal signatures. This combination can be explained by an unusual geochemical and isotopic composition of the mantle that which have acquired these features due to biogenic factors on the Earth's surface and subsequently were brought to the mantle source in the process of crustal-mantle interaction (for example, subduction). It is highly probable because the Noril'sk deposits were formed in early Mz epoch in contrary to the other magmatic Cu-Ni deposits mostly PR-originated when the mantle compositions was significantly different.

The same process was likely responsible for the isotopic composition of sulfide ore mineralization in the Talnakh and Norilsk deposits. The origin of the significant diversity in the S isotope compositions of Noril'sk ores can be related to heterogeneity of the source. It is well-known that the most primitive magmas in the Eastern part of the Noril'sk region (based on olivine-trapped melt inclusions: Sobolev et al. 2009) have the most heavy S isotope composition (Ripley et al. 2003). The mechanism of this enrichment of magmas in heavy sulfides has been partially explained by subduction of ocean crust and reaction with peridotites (Sobolev et al. 2011).

But at the same time the heavy isotope composition of the sulfides can also result from non-biogenic process. For example, Paleoproterozoic Au-deposits of the Siberian Platform contain sulfides with $\delta^{34}\text{S} = +21$ ‰ (Kryazhev et al., 2003). Additional data are required to more firmly establish the origin of the sulfide.

Acknowledgements

We appreciate geologists of Norilskgeologia Ltd. Yu. Krakovetsky, O. Simonov and N. Kokorin for access to cores of the Dyumtaleysky intrusion. We thank S. Kryazhev, L. Nosik, and D. Zhuravlev for S, C isotope and ICP-MS analyses. This study was financially supported by the Russian Foundation for Basic Research (grant 07-05-01007) and the Program of the President of the Russian Federation "The Leading Russian Scientific Schools" (NS-741.2012.5).

References

- Hofmann AW (1988) Chemical differentiation of the Earth: the relationship between mantle, continental crust, and oceanic crust. *Earth Planet Sci Lett* 90: 297–314
- Komarova MZ, Kozyrev SM, Kokorin NI et al (1999) Layered intrusion of Dyumtaley River: petrology and ore potential. In: *Bowels of Taimyr, Norilsk*, pp. 42-67 (in Russian)
- Krivolutskaya NA, Sobolev AV, Mikhailov VN et al (2012) Parental melt of the Nadezhdinsky Formation: geochemistry, petrology and the connection with Pt-Cu-Ni deposits (Noril'sk area, Russia). *Chem Geol* 302-303: 87-105
- Kryazhev SG, Glukhov AP, Rusinova OV (2003) Isotopic geochemical regime of the Formation of the Sovetskoe Gold-Quartz Deposit. *Prikladnaya geokhimiya (Applied Geochemistry)*, Moscow: IMGRE 4:154–164 (in Russian)
- Romanov AP, Kurbatov II, Malich KN et al (2012) Resources of platinum metals of the Western Taimyr. In: *Platinum of Russia VII, Krasnoyarsk*, pp. 135-160 (in Russian)
- Sobolev AV, Krivolutsкая NA, Kuzmin DV (2009) Petrology of the Parental Melts and Mantle Sources of Siberian Trap Magmatism. *Petrology* 17: 253-287
- Sobolev SV, Sobolev AV, Kuzmin DV, Krivolustkaya NA et al. (2011) Linking mantle plumes, large igneous provinces and environmental catastrophes. *Nature* 477: 312-316
- Wager LR, Brown GM (1967) *Layered igneous rocks*. Oliver and Boyd. Edinburgh

Catastrophic sulfide saturation and genesis of Ni-Cu-PGE mineralization in the Sudbury Igneous Complex

CM Lesher

Mineral Exploration Research Centre, Department of Earth Science, Goodman School of Mines, Laurentian University, Sudbury Ontario P3E 2C6 Canada, mlesher@laurentian.ca

Abstract. Many models for the formation of the Ni-Cu-PGE ores in the 1850 Ma Sudbury Igneous Complex assume that the sulfides exsolved from the melt sheet during slow cooling, that the ore-localizing embayments represent original topographic features, and that the sulfide ores “passively” collected in the embayments. It is more likely, however, that the Ni-Cu-PGE ores in the SIC exsolved almost instantaneously as the superheated melt sheet was catastrophically driven to the liquidus following incorporation of inclusions derived from footwall rocks during crater rebound, injection of footwall dikes, and incorporation of fragmented footwall rocks during the formation of embayments and troughs. This explains the very strong correlation between inclusions, mineralization, and ore-localizing embayments. The equally rapid increase in effective viscosity explains the absence of subsequent settling of semi-massive pods of sulfides in the dikes and coarse disseminated sulfides in Sublayer norite. Lateral variations in chalcophile element enrichment/depletion trends and Pb isotopic contents of norites overlying and away from ore-localizing embayments, and in the S-Os-Pb isotopic compositions and As contents of the various ore zones reflect preservation of these signatures within relatively small (~15 km³) convection cells.

Keywords. Sudbury Igneous Complex, Ni-Cu-PGE, crater rebound, dike emplacement, brecciation, inclusion, ore genesis

1 Introduction

The 1850 Ma Sudbury Igneous Complex (SIC) represents one of the world’s largest accumulations of magmatic Ni-Cu-PGE mineralization (Naldrett 2004). Most models for the genesis of the mineralization involve exsolution of and settling of sulfides during slow cooling of the superheated impact melt sheet (e.g., Keays and Lightfoot 2004; Li and Ripley 2005), generation of breccias and inclusions by crater wall collapse (e.g., Wood and Spray 1998; Scott and Benn 2002), and collection of inclusions and mineralization in topographic features (troughs and terraces) along the floor of the crater (e.g., Morrison 1984). However, such models do not explain the restriction of contact mineralization to footwall embayments, the restriction of inclusion-rich contact Sublayer to embayments, and the paucity of mineralization and inclusions elsewhere along the contact (Coleman 1924). If sulfides had exsolved from the melt sheet and settled, and if the inclusions were produced by crater-wide modification processes, then more of the contact should be covered by Sublayer and more of the contact should be mineralized.

A model that better satisfies all of the observed geological, stratigraphic, geochemical, and isotopic data involves local incorporation of inclusions, catastrophic cooling of the Main Mass, and near instantaneous sulfide segregation.

2 Geologic setting

The Sudbury Igneous Complex comprises the Main Mass and associated quartz-diorite (QD) dikes, and is underlain by the Archean Levack Gneiss Complex on the North Range and East Range and by Huronian mafic volcanic, felsic volcanic, and clastic sedimentary rocks on the South Range, and overlain everywhere by Onaping Formation suevites and fall-back breccias.

The ores in the SIC occur in two primary settings (Naldrett 2004; Farrow and Lightfoot 2005; Ames and Farrow 2007): 1) in embayments along basal contact of the SIC and in underlying footwall rocks (contact-footwall ore systems), and 2) in radiating and concentric QD dikes in the footwall rocks of the SIC (dike-hosted ore systems) that extend (or can be inferred to have extended prior to erosion) from embayments along the contact.

Contact-footwall ore systems are zoned and typically comprise an upper zone of mineralized magmatic breccia (Sublayer), an intermediate zone of mineralized brecciated footwall rocks (footwall breccia), and a lower zone of sulfide veins, veinlets, and disseminations in the footwall rocks (footwall ores). Dike ore systems are zoned from sulfide- and inclusion-free QD margins to sulfide- and inclusion-bearing (IQD) cores (Lightfoot et al. 1997).

The ores are variably fractionated owing to variable degrees of fractional crystallization and accumulation of Fe-Ni-IPGE-rich monosulfide solid solution (MSS) (e.g., Li et al. 1992; Mungall 2007) and Fe-Cu-Zn-rich intermediate solid solution (ISS) (Nelles and Lesher, *accepted*), reaction of sulfide melts with wallrocks (Nelles and Lesher, *accepted*), and segregation of late-stage Cu-PPGE-As-Sb-Bi-Te-rich sulfide melts and/or fluids (e.g., Hanley et al. 2005; Péntek et al. 2013).

3 Geological, stratigraphic, petrological, geochemical, and isotopic constraints

3.1 Geological constraints

- 1) Cross-cutting relationships and inclusions of QD in IQD require two stages of dike emplacement and the symmetry of the zonation requires a single semi-continuous event, not two separate events.

- 2) The close association between embayments, ores, footwall breccias, inclusion-rich contact Sublayer, and mafic norite, requires that they all be co-genetic.
- 3) The restriction of Sublayer and mineralization to embayments and dikes requires that the brecciation and ore-forming processes be local, not a consequence of a crater-wide event like a basin-wide peak-ring or crater-wall collapse.
- 4) The presence of very large, very dense pods of semi-massive to coarse disseminated sulfide in subvertical dikes requires them to have been 'frozen in' and not allowed to completely settle within the dikes.

3.2 Stratigraphic constraints

- 1) Although there are rare discontinuous layers of sulfides in Sublayer and norite, most of the sulfides the Sublayer and Main Mass are disseminated and show no evidence of coalescence or settling.
- 2) Gradational contacts between semi-massive inclusion-rich contact ores, sulfide-rich Sublayer norite, and sulfide-poor norite/gabbro/granophyre require that they formed in that order.
- 3) Norites (including Sublayer) contain cumulus Opx-Plag-(Sul) and a relatively primitive residual liquid, gabbros contain cumulus Plag-Cpx-Ilm-Ap-(Sul) and an intermediate residual liquid, upper K-poor granophyre represents an evolved residual liquid, and lower K-rich granophyre represents the final residual liquid (Dessureau 2003).
- 4) These trends are continuous with no geochemical evidence that the Main Mass separated into upper felsic and lower mafic layers (Golightly 1994, Zieg and Marsh 2005), which would reduce the amount of magma from which the ores might have formed.

3.3 Geochemical and isotopic constraints

- 1) Ni, Cu, and Pb isotope compositions of the norite are different over embayments than outside embayments (Dessureau 2003; Darling et al. 2010; McNamara 2011), requiring them to have behaved as isolated cells (see also Ames et al. 2002).
- 2) S, Os, and Pb isotopes and As contents of Sudbury ores vary significantly from deposit to deposit (Schwarcz 1973; Dickin 1996; Morgan et al. 2002; Ames and Farrow 2007; Darling et al. 2010, McNamara 2011), requiring local incorporation of S and metals, presumably from mineralized Nipissing and East Bull Lake suite mafic-ultramafic intrusions.
- 3) Sulfide/silicate partition coefficients were likely very much higher in the quartz dioritic SIC magma than in most other deposits (Ames et al. 2002).

4 Discussion

4.1 Inclusions in IQD and Sublayer

The presence of inclusion- and sulfide-poor margins on the dikes indicate that entire contact was not once covered with Sublayer and mineralization, which was subsequently sucked into the dikes and embayments during their formation. This, in turn, suggests that the

inclusions in Sublayer and IQD were not generated by a crater-wide process like peak-ring collapse or collapse of large parts of the crater wall. Rather, these features indicate that inclusions and mineralization formed locally via thermomechanical erosion, and together with the evidence for a narrow time interval between intrusion of QD and IQD (Lightfoot et al. 1997), require equally catastrophic processes.

4.2 Mechanics

Rebound of the transient impact crater, accompanied by dilation of footwall rocks, is a likely mechanism to drive the first stage of dike emplacement (and generate the fractures to be exploited later by footwall mineralization). This happens seconds after impact, leaving no time for significant amounts of thermomechanical erosion, crystallization, and/or segregation of sulfides, consistent with the only minor difference between the average compositions of QD and Onaping glasses (Ames et al. 2002).

Readjustments following rebound and the pressure generated by rapid accumulation of the 1.4 km thick Onaping Formation are likely mechanisms to drive the second (main) stage of dike emplacement, in which the throats of the dikes were thermomechanically eroded by the superheated (originally up to 2000°C) impact melt.

Erosion of embayments may not have been quite as catastrophic, but the high temperature of the melt would have actively eroded the footwall rocks, particularly fragmental and fractured rocks. Once generated (see below), very dense, very low-viscosity sulfides would facilitate mechanical erosion, increasing the efficiency of erosion in areas where sulfides accumulated. This, any sulfides melted directly from Nipissing or East Bull Lake suite intrusions would have greatly facilitated erosion.

The key to the uneven distribution of sulfides in the SIC system is that the Main Mass would have rapidly formed numerous ca. 2.5 km diameter convection cells (Ames et al. 2002; Darling et al. 2010a) and that each cell would have behaved as a more-or-less isolated system:

- 1) cells eroding 'rubble' or deeply fragmented areas would have generated embayments like Levack,
- 2) cells exploiting fractures would have generated deep, narrow troughs like Creighton,
- 3) cells eroding the throats of dikes would have created embayment-dike systems like the mouth of the Copper Cliff dike and Whistle embayment at the mouth of the Parkin offset, and
- 4) cells over less erodable contacts would not have generated significant amounts of inclusions or mineralization.

4.3 Thermochemical effects

Assuming vigorous convection, inclusions would have been rapidly mixed into the melt. The effect of adding so many inclusions to the impact melt would have been profound, resulting in catastrophic decreases in temperature and sulfide solubility, and increases in viscosity of the melt (Figs. 1 and 2).

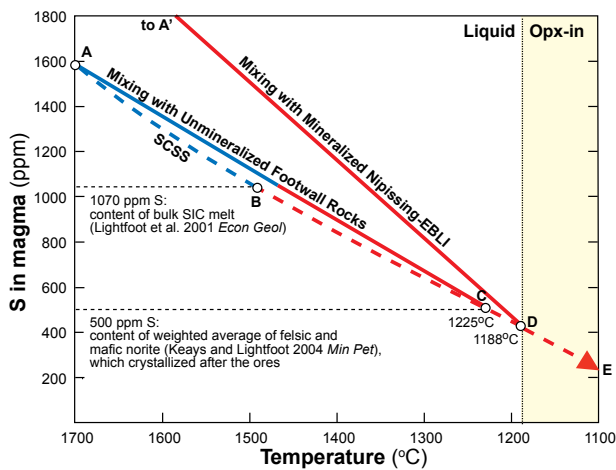


Figure 1. Model sulfide saturation trajectories. Silicate liquidus temperature and sulfide content at sulfide saturation (SCSS) calculated at 1 kbar and $fO_2 = FMQ$ by Li and Ripley (2005) using MELTS and their sulfide solubility model. A-B-C-D-E is the expected trajectory for slow cooling of the Main Mass of the SIC, which results in gradual exsolution of ~570 ppm sulfide as droplets that settle slowly through the Main Mass (see Keays and Lightfoot 2004). A-C-D-E is the trajectory for catastrophic mixing of barren footwall rocks and cooling to near-liquidus temperatures, which produces similar amounts of sulfide, but much more rapidly. A'-D is a trajectory for catastrophic mixing of mineralized footwall rocks, which results in rapid exsolution of greater (potentially much greater) amounts of sulfide, with metal compositions and S-Os-Pb isotopic controlled by the effective magma:sulfide ratio (R factor: see Naldrett 2004).

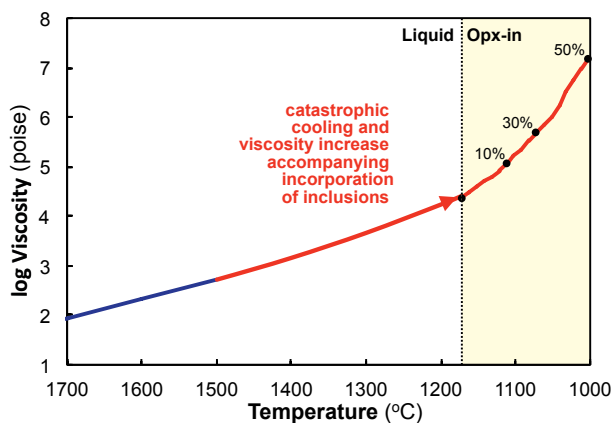


Figure 2. Variation in viscosity of SIC impact melt with temperature. Viscosities of supraliquidus melts calculated using method of Nelson and Carmichael (1979). Temperatures and viscosities of sub-liquidus melts calculated using MELTS (Ghiorso and Sack 1995). Calculated using ASIC2 melt composition of Dessureau (2003).

Mixing melts of footwall rocks into the impact melt would have not significantly changed the sulfide solubility at sulfide saturation (Fig. 1), as the footwall rocks would have had more-or-less the same composition as the melt, but it would have greatly changed the rate at which sulfides were produced and accumulated. Instead of sulfides exsolving slowly and settling slowly through the melt column, they would have segregated almost instantaneously.

The amount of depletion of metals in the melt would depend on $D_{Me}^{Sul/Sil}$, the magma sulfide ratio (R factor), and the amount of metals contributed by local footwall rocks, some of which contained significant amounts of mineralization.

4.4 Ore genesis

The amount of sulfide produced would depend on the volume of magma, the original S content of the magma, amount of inclusions added, the degree of cooling accompanying assimilation of those inclusions, and the solubility of S in the magma, but we can make some estimations. We can assume that the volume of magma was dictated by the size of the convection cells, which from widespread chalcophile element depletion (Keays and Lightfoot, 2004) must have involved the entire Main Mass, not just a lower norite layer or the Sublayer. Assuming that each cell was approximately 2.5 km x 2.5 km x 2.5 km (corresponding to the average thickness of the Main Mass), that the magma density was 2600 kg/m³ (appropriate for an andesite), and that the magma exsolved 570 ppm S (i.e., assuming quantitative extraction), then 6.1×10^{10} kg (61×10^6 tonnes) of sulfide would have been produced, which represents a bulk magma:sulfide ratio of 567, within the range of estimates based on ore tenors (e.g., Keays and Lightfoot 2004). Assuming that the original magma contained 60 ppm each of Ni and Cu, and that $D_{Ni}^{Sul/Sil} = D_{Cu}^{Sul/Sil} = 1500$ (higher than in experiments on basaltic magmas, but appropriate for an intermediate magma with fewer octahedral sites), the sulfide melt would contain 2.8% each of Ni and Cu, and the depleted magma would contain 18 ppm each of Ni and Cu, similar to that required to model whole-rock Ni contents in the Main Mass. Assuming that only 200 ppm S was exsolved, then 1.4×10^9 kg (1.4×10^6 tonnes) of sulfide would have been produced, which represents a bulk magma:sulfide ratio of 1900, the ore tenor would have been 5% each of Ni and Cu, and the depleted magma would have contained 34 ppm each of Ni and Cu.

The rapid increase in viscosity of the silicate melt (Fig. 2) would inhibit settling of sulfides. Those in IQD and Sublayer would be 'frozen' in place, accounting for the absence of evidence for settling and the very fine sulfides that exsolved during the late stages of crystallization of norite, gabbro, and Sublayer.

4.5 Consequences for Main Mass

The observed geochemical element trends in the Main Mass were produced after the melt was driven to the liquidus and began to crystallize, isolating the ores from the melt (and the melt from the ores). Crystallization of the formerly superheated melt, which would have contained few if any crystal nuclei, would have been rapid, explaining the anomalously fine-medium grain size of such a thick igneous unit.

An important implication of the cumulate nature of the norite and gabbro units is that they cannot be directly compared to models of the original melt composition. Together, the segregation of sulfides prior to crystallization of the Main Mass and the cumulate nature

of the norite and gabbro likely explain the apparent mismatch (Keays and Lightfoot 2004) between the compositions of contact and dike-hosted ores (which formed earlier from a metal-rich magma) and the metal depletion in the Main Mass (which formed later from a metal-poor magma).

The upper part of the granophyre is relatively homogeneous and similar in composition to the lowermost parts of the norite (e.g., Naldrett and Hewins 1984; Lightfoot and Zotov 2005), but is enriched in most compatible elements and depleted in most incompatible lithophile elements compared to Onaping glasses (see Ames et al. 2002), suggesting that the upper parts of the melt sheet did not incorporate significant amounts of Onaping Formation.

5 Implications

If the SIC was catastrophically cooled, this has several important implications for the subsequent thermal history of the SIC:

- 1) The Main Mass would have been driven almost instantly to the liquidus, greatly reducing its ability to thermomechanically erode footwall rocks, explaining why Sublayer and IQD are rarely found outside of embayments and dikes, and why the amount of erosion appears to be less than expected.
- 2) The temperature contrast with the underlying rocks would have been significantly less, explaining the relatively thin contact metamorphic aureole and relatively shallow penetration of vein-type footwall ores.
- 3) The temperature contrast with the overlying rocks (Onaping Fm) would have been significantly less, explaining why there is little evidence in the granophyre for a significant Onaping component.

Acknowledgements

I am extremely grateful to Shannon Baird, Marc Constantin, Marcelle Deslauriers, Gilles Dessureau, Rachel Gammel, Steven Gregory, Michelle Huminicki, Taus Joergensen, Joshua Mukwakwami, Edward Nelles, Tom Raskevicius, and Rianne Stout for their contributions to the various pieces of the puzzle, and to Doreen Ames, Balz Kamber, Paul Binney, Bruno Lafrance, Catherine Farrow, Paul Golightly, Reid Keays, Peter Lightfoot, Bill Morris, Jim Mungall, Ed Pattison, Walter Peredery, Doug Tinkham, and many Sudbury exploration and mine geologists for enlightening discussions on Sudbury geology. Logistical and financial support has been provided at various stages by Inco/Vale, Falconbridge/Xstrata, QuadraFNX/ KGHM, Wallbridge, and NSERC.

References

- Ames DE, Farrow CEG (2007) Metallogeny of the Sudbury mining camp, Ontario, GAC-MDD Spec Publ 5: 329–350
- Ames DE, Golightly JP et al. (2002) Vitric compositions in the Onaping Formation and their relationship to the Sudbury Igneous Complex, Sudbury Structure, Econ Geol 97: 1541–1562
- Boast M, Spray JG (2006) Superimposition of a thrust-transfer fault system on a large impact structure, Econ Geol 101: 1583–1594
- Coleman AP (1924) Geology of the Sudbury nickel deposits, Econ Geol 19: 565–576
- Darling JR, Hawkesworth CJ et al. (2010) Isotopic heterogeneity in the Sudbury impact melt sheet, Earth Planet Sci Lett 289: 347–356
- Dessureau (2003) Geochemistry of the Mafic and Felsic Norite in the Whistle Embayment, MSc Laurentian U: 134 pp
- Dicken A et al. (1996) Isotopic evidence for distinct crustal sources of North and South Range ores, Sudbury Igneous Complex, Geochim Cosmochim Acta 60: 1605–1613
- Farrow CEG, Lightfoot PC (2002) Sudbury PGE revisited: Toward an integrated model, CIM Spec Vol 54: 273–297
- Ghiorsso MS, Sack RO (1995) Chemical mass transfer in magmatic processes: IV, Contrib Mineral Petrol 119: 197–212
- Golightly JP (1994) The Sudbury igneous complex as an impact melt; evolution and ore genesis, Ont Geol Surv Spec Vol 5: 105–118
- Grieve RAF (1994) An impact model of the Sudbury structure, Ont Geol Surv Spec Vol 5: 245–270
- Hanley J et al. (2005) Ore metal redistribution by hydrocarbon–brine and hydrocarbon–halide melt phases, North Range footwall of the Sudbury Igneous Complex, Min Dep 40: 237–256
- Keays RR, Lightfoot PC (2004) Formation of Ni–Cu–PGE sulfide mineralization in the Sudbury Impact Melt, Min Pet 82: 217–258
- Li C, Naldrett AJ, et al. (1992) Pt–Pd–Au–Cu-rich stringers at the Strathcona Mine, Sudbury, Econ Geol 87: 1584–1598
- Lightfoot PC, Keays RR et al. (1997) Geochemical relationships in the Sudbury Igneous Complex, Econ Geol 92: 289–307
- Lightfoot PC, Keays RR, Doherty W (2001) Chemical Evolution and Origin of Nickel Sulfide Mineralization in the Sudbury Igneous Complex, Econ Geol 96: 1855–1875
- Lightfoot PC, Zotov AI (2005) Geology and geochemistry of the Sudbury Igneous Complex, Geol Rudn Mest 47: 387–420
- McNamara G (2011) Lead Isotope and Trace Element Variations in the Sudbury Igneous Complex, MSc Laurentian U: 61 pp
- Morgan JW, Walker RJ et al. (2002) ¹⁹⁰Pt–¹⁸⁶Os and ¹⁸⁷Re–¹⁸⁷Os systematics of the Sudbury Igneous Complex, Geochim Cosmochim Acta 66(2): 273–290
- Morrison GG (1984) Morphological Features of the Sudbury Structure, Ont Geol Surv Spec Vol 1: 513–520
- Mungall 2007 Crystallization of magmatic sulfides, Geochim Cosmochim Acta 71: 2809–2819
- Naldrett AJ (2004) Magmatic Sulfide Deposits, Springer, New York: 727 pp
- Naldrett AJ, Hewins R (1984) The Main Mass of the Sudbury Igneous Complex, Ont Geol Surv Spec Publ 1: 236–274
- Nelles and Leshner (accepted) Genesis of Cu–PGE-rich footwall-type mineralization in the Morrison Deposit, Sudbury, Econ Geol
- Nelson SA, Carmichael ISE (1979) Partial molar volumes of oxide components in silicate liquids, Contrib Min Petrol 71: 117–124
- Pentek A, Molnar F et al. (2013) The Significance of Partial Melting Processes in Hydrothermal Low Sulfide Cu–Ni–PGE Mineralization Within the Footwall of the Sudbury Igneous Complex, Econ Geol 108: 59–78
- Prevec SA, Cawthorn RG (2002) Thermal evolution and interaction between impact melt sheet and footwall, J Geophys Res 107, B8, ECV 5: 1–14
- Schwarcz HP (1973) Sulfur isotope analyses of some Sudbury ores, Can J Earth Sci 10: 1444–1459
- Zeig, Marsh (2005) The Sudbury Igneous Complex: Viscous emulsion differentiation of a superheated impact melt sheet, Geol Soc Am Bull 117(11/12): 1427–1450

Platinum-group element contents of kimberlites: constraints on mantle sources

WD Maier

Dept. of Geosciences, Oulu University, Oulu 90014, Finland

I McDonald,

School of Earth and Ocean Sciences, Cardiff University, Cardiff CF10 3AT, Wales

A Le Roex

Dept. of Geological Sciences, University of Cape Town, Rondebosch 7701, South Africa

Abstract. Group I and Group II kimberlites from the Kaapvaal and Karelian cratons have 4–29 ppb Pt+Pd, and high Pt/Pd~1.5. PGE patterns are flat from Ir to Ru, with negative Rh anomalies, and enrichment in Pt, Pd, Au and Cu. Pd/Ir ratios are mostly <10, analogous to komatiites. The patterns are best explained as mixtures between sub-continental lithosphere-derived harzburgite/lherzolite with a melt of MARID or kimberlitic composition. Together with the enrichment of kimberlites in both compatible and incompatible elements their PGE patterns are consistent with derivation of GpI and GpII kimberlites from the SCLM. Apart from kimberlites, Bushveld magmas are almost unique globally in terms of their relative Pt enrichment. This suggests that Bushveld magmas contain an SCLM component. However, as total Pd contents of the Bushveld magmas are in the range of other global basalts, the bulk of the PGE component in the Bushveld magmas is likely asthenosphere-derived.

Keywords. Kimberlite, platinum-group elements, sub-continental lithospheric mantle

1 Introduction

It has been proposed that the SCLM can be relatively PGE rich, and that this would control the PGE prospectivity of cratonic layered intrusions such as the Bushveld Complex (Zhang et al. 2008). In order to test this model, we analysed PGE in kimberlites from the Karelian and Kaapvaal cratons. These rocks are generally believed to be the best candidate for SCLM-derived magmas. Thus, if the SCLM contained any PGE-rich portions, this might be reflected in the kimberlites, as long as the PGE behaved incompatibly during SCLM melting.

2 Results

The analysed Kaapvaal xenoliths comprise GP2 samples from Roberts Victor, Finsch, Swartuggens, Bellsbank and Newlands pipes, and the GP1 samples are from the Kimberley cluster (De Beers, Wesselton, Bultfontein, Big Hole). They have previously been characterized by LeRoex et al., (2003), Becker and LeRoex (2006), and Coe et al. (2008). The Karelian GP2 samples are from the 1.2 Ga Seitäperä intrusion and the Lentiira dike swarm located between the villages of Kuhmo and Lentiira in eastern Finland (O'Brien and Tyni, 1999; O'Brien et al., 2007).

Pt + Pd contents of the GP2 kimberlites vary between 4 and 29 ppb, whereas combined IPGE contents are between 0.5 and 10 ppb (Table 1). Most of the patterns show relatively flat, or slightly increasing slopes from Os to Ru, distinct negative Rh anomalies, a sharp increase from Rh to Pd, flat patterns from Pd to Pt, and increase to Au, and variable slopes from Au to Cu (Fig. 1). The greatest variability is seen in Au and Pd, whereas Ni and Cu contents are relatively constant. With the exception of Finsch, Pd/Ir ratios are 0.5 – 7, in the range of komatiites. The samples from Finsch show fractionated patterns with a progressive increase from Os to Au, and Pd/Ir 23–41, typical of many basalts globally

3 Discussion

The PGE patterns of most kimberlite samples are distinct from both typical basalts and komatiites, which show a progressive increase from IPGE to PPGE, albeit at variable slopes (flatter in komatiites, steeper in basalts). The sloped patterns of the basalts and komatiites are interpreted to result from progressively less compatible behavior from Os and Ir to Pd during melting of convecting mantle. In contrast, the flat IPGE patterns and negative Rh anomalies of the kimberlites resemble those of SCLM-derived mantle xenoliths, whereas the Pt-Pd-Au-Cu enrichment and the broadly positive slopes from Pt to Cu are typical of basalts. Thus, the kimberlite patterns can be interpreted as mixtures between an SCLM component and a partial mantle melt (Fig. 1). For example, a 20% component of average SCLM would result in ~ 0.7 ppb Ir, 0.8 ppb Pt, and 0.3 ppb Pd, accounting for most of the Ir in the analysed kimberlites, but only a fraction of the Pt and Pd. The derivation and nature of the Pt-Pd enriched melt component in the kimberlites is less obvious. However, the high Pt/Pd of the kimberlites is atypical of asthenospheric basalts and komatiites, and more reminiscent of the SCLM. Potential candidates for such SCLM derived melts could be MARIDs that have low IPGE contents, but up to 10 ppb Pt+Pd and Pt/Pd consistently above unity (Maier et al., 2012), or the relatively Pt-rich and IPGE depleted GP2 Finsch kimberlite samples analysed here. The idea that the kimberlites are largely derived from the SCLM is consistent with previous interpretations of Becker and LeRoex (2006).

A surprising feature of our data is the Pt and Pd enrichment of the kimberlites. Most researchers argue that

Sample	Craton	Locality	pipe	Group	Ni	Cu	Os	Ir	Ru	Rh	Pt	Pd	Au
Kai-d2-1A	Karelia			II	618	50	0,62	0,76	1,19	0,20	5,48	2,76	2,57
Kai-d2-1B	Karelia			II	618	50	0,76	0,78	1,12	0,22	4,84	2,81	2,05
16-002-26.95	Karelia			II	1245	62	1,09	1,04	1,87	0,29	8,85	4,70	1,48
16-002 23.83(A)	Karelia			II	1617	68	2,98	2,69	5,50	1,38	15,68	13,76	5,03
16-012 23.83(B)	Karelia			II	1617	68	2,80	2,43	4,72	1,47	13,47	12,59	4,03
RVK2	Kaapvaal	Roberts Victor		II	1349	22	1,38	1,24	2,13	0,62	4,34	3,09	4,20
CCR1	Kaapvaal	Finsch		II	1457	na	0,06	0,13	0,23	0,15	5,19	2,99	1,74
CCR2	Kaapvaal	Finsch		II	1333	na	0,04	0,05	0,14	0,07	4,52	2,19	3,50
N005	Kaapvaal	Swartruggens, Changehouse		II	1557	34	1,43	1,66	3,06	0,57	8,35	0,85	2,23
NC006	Kaapvaal	Swartruggens, Main		II	951	45	0,68	0,76	1,40	0,26	2,15	1,99	2,37
JJG 4676	Kaapvaal	Bellsbank		II	1462	64	1,61	1,56	2,76	0,33	5,61	6,17	3,41
KN2	Kaapvaal	Newlands		II	1682	na	1,43	1,73	2,69	0,41	4,92	11,99	1,65
C14	Kaapvaal	De Beers, Kimberley		I	1467	54	1,68	1,64	2,00	0,32	9,66	5,13	2,35
COL2	Kaapvaal	Big Hole		I	1091	77	1,10	1,04	1,58	0,36	8,61	5,62	1,27
K 119/3	Kaapvaal	Wesselton, sill		I	1398	58	0,77	0,71	1,23	0,17	5,65	0,51	0,66
K 8/10	Kaapvaal	Bultfontein, Kimberley		I	788	95	0,72	0,76	1,11	0,20	12,82	5,31	2,47

Table 1: PGE and Cu-Ni contents of Kaapvaal and Karelian Gpl and GplI kimberlites (normalized to 100% volatile free)

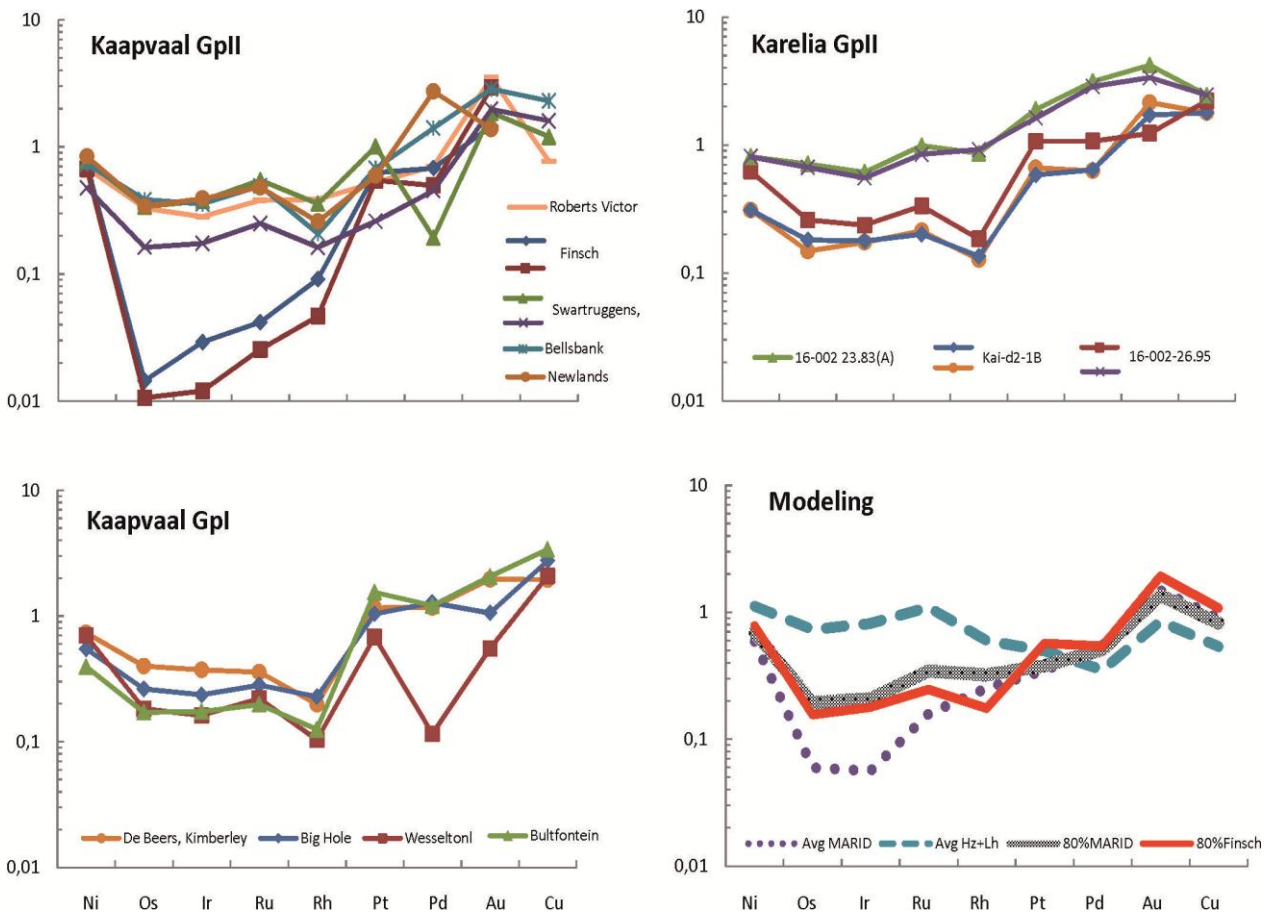


Figure 1. PGE patterns of kimberlites, normalized to primitive mantle (normalization factors from Barnes and Maier, 1999). Data is best modelled by mixing of 20% SCLM and 80% Finsch kimberlite. See text for explanation.

PGE contents in mantle magmas, at least those of asthenospheric derivation, are controlled by the degree of dissolution of mantle sulfide, thereby liberating PGE to the silicate melt. It is normally assumed that ca 20% partial melting is required to dissolve all mantle sulfides. At smaller degrees of partial melting the PGE may be retained in the mantle, as seen, e.g., in the PGE depletion of MORB. As the kimberlites are thought to represent 1-2% partial melting (Becker and LeRoex, 2006), they would be expected to be highly PGE depleted. A possible explanation is that relatively oxidized kimberlite magma had a relatively high S solubility leading to efficient dissolution of mantle sulfide (cf. Mungall et al. 2006). However, being that average (asthenospheric) mantle is believed to contain 28 ppm Cu and 10 ppb Pt+Pd (Barnes and Maier, 1999), this process should have resulted in much higher PGE and Cu contents than observed in the extremely small degree kimberlitic mantle melts; An asthenospheric derivation of the kimberlites is thus inconsistent with their low PGE contents.

In view of the high Pt/Pd ratios in the kimberlites, our preferred explanation for their elevated PGE contents is that metasomatic fluids acted as a flux rendering refractory Pt-alloys and small amounts of metasomatic sulfides in the SCLM fusible or soluble. This interpretation is consistent with the abundant macro- and xenocrysts in the kimberlites, and the unique combination of enrichment in incompatible and volatile elements as well as compatible elements (cf Becker and Le Roex, 2006).

4 Conclusions

- (i) The available data on kimberlites and mantle xenoliths (harzburgites, lherzolites and MARIDs) provide no evidence for PGE enrichment of the SCLM relative to convecting mantle; None of > 100 mantle xenoliths analysed from the Kaapvaal and Karelian cratons has > 20 ppb Pt+Pd, and the Kaapvaal and Karelian kimberlites all have < 30 ppb Pt+Pd. One could argue that PGE have been incompletely extracted from the SCLM by the kimberlites. However, the xenoliths which represent the residues of melting are also PGE poor, inconsistent with this model.
- (ii) The kimberlites show evidence for preferential concentration of Pt relative to Pd during melting of the SCLM. Apart from kimberlites, Bushveld magmas are almost unique globally in terms of their relative Pt enrichment. This is consistent with the suggestion that Bushveld magmas contain an SCLM component (Richardson and Shirey, 2008, Barnes et al., 2010). However, as total Pd contents of the Bushveld magmas are in the range of other global basalts, the bulk of the PGE component in the Bushveld magmas is likely asthenosphere-derived.

Acknowledgments

We are grateful to Hugh O'Brien for providing the samples from Karelia.

References

- Barnes S-J, Maier WD (1999) The fractionation of Ni, Cu and the noble metals in silicate and sulfide melts. In: Dynamic processes in magmatic ore deposits and their application in mineral exploration: R.R. Keays, C.M. Leshner, P.C. Lightfoot, & C.E.G. Farrow (Eds.), Geological Association of Canada, Short Course Notes, 13.
- Barnes S-J, Maier WD, Curl E (2010) Composition of the Marginal Rocks and Sills of the Rustenburg Layered Suite, Bushveld Complex, South Africa: Implications for the Formation of the Platinum-group Element Deposits. *Econ Geol.*, 105, 1481-1511
- Becker M, Le Roex AP (2006) Geochemistry of South African On- and off-craton Group I and Group II kimberlites: petrogenesis and source region evolution. *J Pet* 47, 673-703
- Coe N, Le Roex AP, Gurney J, Pearson DG, Nowell G (2008) Petrogenesis of the Swartuggens and Star Group II kimberlite dyke swarms, South Africa: constraints from whole rock geochemistry. *Con Min Petrol* 156, 627-652.
- Le Roex AP, Bell DR, Davis P (2003) Petrogenesis of Group I kimberlites from Kimberley, South Africa: Evidence from bulk-rock geochemistry. *J Pet*, 44, 2261-2286
- Maier WD, Peltonen P, McDonald I, Barnes SJ, Barnes S-J, Hatton C, Viljoen F (2012) The concentration of platinum-group elements and gold in southern African and Karelian kimberlite-hosted mantle xenoliths: Implications for the noble metal content of the Earth's mantle. *Chemical Geology* 302–303 (2012) 119–135
- McDonald I, De Wit MJ, Smith CB, Bizzi LA, Viljoen KS (1995) The geochemistry of the platinum-group elements in Brazilian and southern African kimberlites. *Geochim. Cosmochim. Acta* 59, 2883-2903.
- Mungall JE, Hanley JJ, Arndt NT, Debecdelievre A (2006) Evidence from meimechites and other low-degree mantle melts for redox controls on mantle-crust fractionation of platinum-group elements. *PNAS* 103, 12695–12700.
- O'Brien HE, Tyni M (1999) Mineralogy and geochemistry of kimberlites and related rocks from Finland. In: Isotopic ages of Lentiira – Kuhmo – Kostomuksha Olivine Lamproite - Group II kimberlites. Gurney, J.J. et al. (eds.) Proceedings of the 7th International Kimberlite Conference, Cape Town, South Africa, pp. 625–636.
- O'Brien H, Phillips D, Spencer R (2007) Isotopic ages of Lentiira – Kuhmo – Kostomuksha olivine lamproite - Group II kimberlites. *Bull Geol Soc Finland*, 79, 203–215
- Richardson SH, Shirey SB (2008) Continental mantle signature of Bushveld magmas and coeval diamonds: *Nature*, v. 453, p. 910–913.
- Zhang M, O'Reilly SY, Wang K-L, Hronsky J, Griffin WL (2008) Flood basalts and metallogeny: The lithospheric mantle connection. *Earth-Science Reviews* 86, 145–174.

Processes affecting the massive sulphide lenses at the Delta deposit, Cape Smith Belt, Canada: implication for the distribution of PGE

Pierre-Jean Misson, Sarah-Jane Barnes, Philippe Pagé
Sciences de la Terre, Université du Québec à Chicoutimi, Chicoutimi G7H 2B1 Canada

Abstract. Two Ni-Cu-PGE massive sulphide lenses associated with komatiitic basalt sills of the Delta deposit (Cape Smith Belt, Canada) have been studied in order to determine the contribution of metamorphism and deformation to the exsolution of platinum-group minerals (PGM) from massive sulphide. Indeed, the post-magmatic processes that affect the deposits are expected to change the primary mineral assemblage and the compositions of the minerals which would result in the redistribution of trace metals such as the PGE. Preliminary results show that (i) the two lenses have been deformed and metamorphosed, but still maintain their magmatic mineral assemblage; (ii) one of the lenses has been injected along a fault far from its parental intrusion; (iii) the incompatible chalcophile elements expected to be associated with chalcopyrite can be found in both chalcopyrite-rich samples and chalcopyrite-poor samples, which are rich in IPGE. This suggests that metamorphism can have an important role for the redistribution of the siderophile and chalcophile elements present in komatiitic massive sulphides.

Keywords. Massive sulphides, platinum-group elements, deformation, metamorphism, Cape Smith Belt

1 Introduction

Many komatiite hosted Ni-Cu-PGE deposits are affected by metamorphism, deformation and possibly the migration of fluids. These post-magmatic processes modify the primary magmatic assemblage of the massive sulphide and consequently the composition of the minerals. This can result in the redistribution of the metals within the massive sulphide lenses. Thus, it is important to understand how the massive sulphides are affected by these post-magmatic processes.

The southern part of the Cape Smith Belt (CSB), northern Quebec, is composed of komatiitic basalts which host Ni-Cu-PGE deposits. The CSB has been metamorphosed at a greenschist to lower amphibolite facies and regionally deformed during the Trans-Hudson orogen (between 1.8-1.7 Ga). We have chosen to study one of these, the Delta deposit, which consists of two massive sulphide lenses associated with a fault zone. These two lenses represent an opportunity to investigate the effects of post-magmatic processes on the massive sulphide lenses.

2 Geological context

The 1.9 Ga Cape Smith Belt, northern Quebec, Canada, corresponds to an oceanic opening in the Archean Superior Province. The belt is divided in two domains,

north and south, composed of rocks showing the transition from an initial continental rift to an ocean basin. The southern domain hosts numerous Ni-Cu-PGE deposits associated with the emplacement of komatiitic basalts into sediments formed during the rift phase. The lavas are thought to have eroded thermo-mechanically into the underlying sediments and assimilated enough sulphur to reach sulphur saturation. This resulted in the formation of multiple massive sulphide lenses at each deposit (Leshner 2007). Sills that represent a part of the feeder conduit of the komatiite lavas intruded the sediment and led to the formation of massive sulphide lenses such as the lenses (D8 and D9) of the Delta deposit. Giovenazzo (1991) reported that the D8 and D9 lenses of the Delta deposit are deformed and metamorphosed.

The D8 lens is overlain by an ultramafic intrusion and underlain by a gabbroic intrusion and could be in situ. In contrast, the D9 lens is overlain by sediments and underlain by a gabbroic intrusion. This location of the D9 lens suggests that it has been displaced along the fault.

3 Sampling and methodology

Twenty samples were selected from drill cores cross cutting the two lenses D8 and D9 of the Delta deposit. The samples were chosen to represent the full stratigraphy of the lenses. Petrographical observations were carried on polished thick sections. Whole rock geochemical analyses were performed at LabMaTer (UQAC) for S, PGE, Ni and Cu. Sulphur was determined by infrared HORIBA EMIA 220V analyser. Copper and Nickel were analysed by Atomic Absorption Spectrometry. Platinum-group elements were analysed by Ni-sulphide fire assay and Te-coprecipitation coupled with ICP-MS. Iron and the other chalcophile elements (Ag, Se, Sb, Cd, Co, As, Zn) were analysed by instrumental neutron activation analysis at the laboratory of the École Polytechnique de Montréal.

4 Preliminary results

4.1 Petrographic observations

Both massive sulphide lenses have a magmatic mineral assemblage composed of 57-83% pyrrhotite, 7-29% pentlandite and 0.2-33% chalcopyrite with accessory magnetite, some rare pyrite and platinum-group minerals (PGM). In both lenses pyrrhotite shows triple junctions (Fig. 1a) and pentlandite can be present as large eyes (1 cm). Chalcopyrite is typically associated

with silicates (Fig. 1b). In some samples, chalcopyrite and silicates are aligned and elongated. Some pentlandite exsolutions are also aligned along the same planes (Fig. 1c). The samples from the lens margins contain more chalcopyrite and silicate inclusions (Fig. 1b).

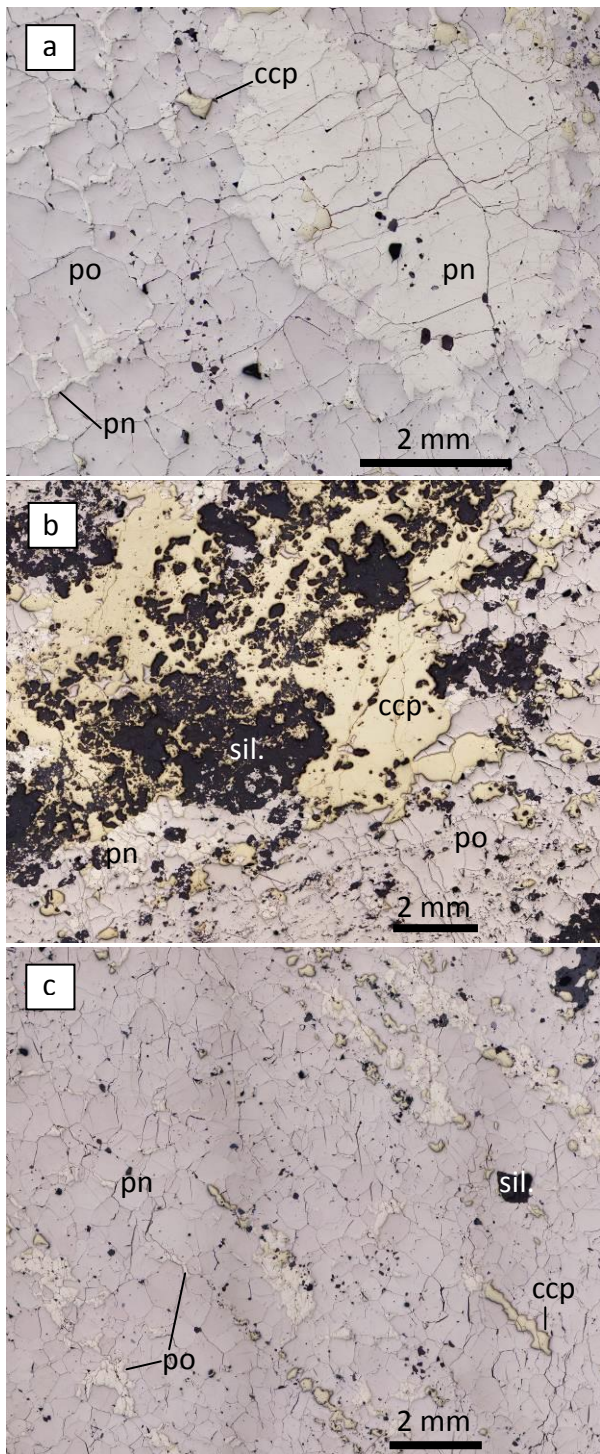


Figure 1. Photomicrographs of the massive sulphides showing: a) the mineral assemblage pyrrhotite (po), pentlandite (pn) and chalcopyrite (ccp). Po has triple junctions, pn is present as large eyes and some pn exsolutions can be observed at po grain boundaries; b) a ccp-rich mineral assemblage at the boundary of the D9 lens. Ccp is associated with an important fraction of silicates (black), po grains still have triple junctions; c) alignment of ccp and silicate within a primary recrystallized assemblage. Ccp grains are elongated along planes and some pn exsolutions follow the same plane.

Giovenazzo (1991) reported the presence of the following PGM: sperrylite (PtAs_2), merenskyite ($[\text{Pd,Pt}][\text{Te,Bi}]_2$), sudburyite ($[\text{Pd,Ni}]\text{Sb}$), testibiopalladinite ($\text{Pd}[\text{Sb,Bi}]\text{Te}$) and kotulskite ($\text{Pd}[\text{Te,Bi}]$).

4.2 Geochemistry

The S/Se ratios of the samples are above the range of the mantle domain, varying from 3550 to 7890. Selenium is an immobile element but S (as Fe) can be very mobile during post-magmatic processes. Considering that the mineral assemblage is magmatic, the only solution to obtain S/Se ratios above the mantle domain is an addition of external S. Thus, the S/Se ratios are in agreement with the hypothesis of S assimilation by the komatiitic basalts proposed by Lesher (2007). Ni usually exceeds Cu (ratio > 1) except for two samples of the D9 lens which are extremely enriched in Cu and have Ni/Cu ratios ~ 0.3. These samples are chalcopyrite-rich with a chalcopyrite fraction varying between 25 and 33%.

The D8 lens shows enrichment in IPGE (Ru, Os, Ir) + Rh and has a relatively flat PGE pattern (Fig. 2a) which is characteristic of monosulfide solid solution (mss). Its IPGE content decreases from the lower gabbroic contact to the upper ultramafic contact suggesting that this lens is a mss cumulate formed from the ultramafic intrusion. The PPGE (Pd, Pt) are enriched at the upper contact. The semi-metals (Sb, As) are enriched in the margins.

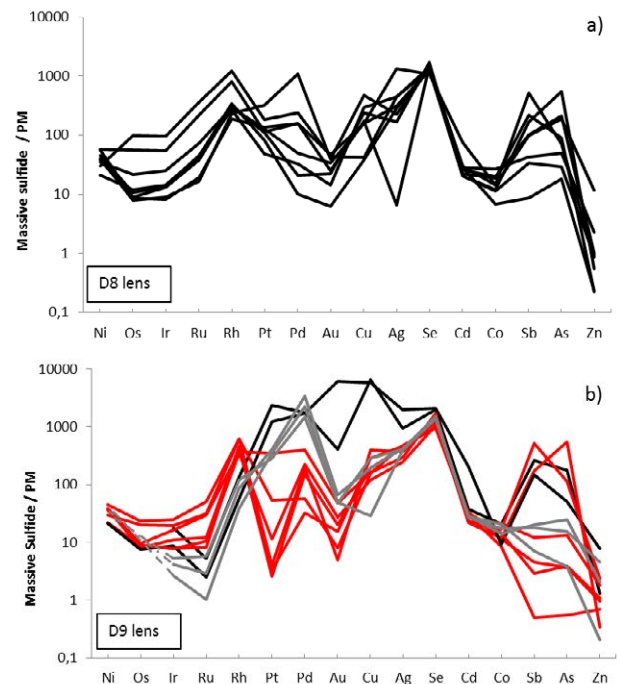


Figure 2. Primitive mantle-normalized chalcophile multi-element diagrams (values for primitive mantle are from Lyubetskaya 2007); elements are ordered according to their degree of compatibility between silicate liquid and sulphide liquid (Barnes personal communication), the elements most compatible with sulphide liquid are on left; a) the D8 lens has a flat PGE pattern characteristic of a mss cumulate; b) the D9 lens contains both mss (red) and more fractionated patterns (black and grey) typical of a more evolved sulphide liquid.

The D9 lens shows more fractionated patterns (Fig. 2) typical of a more evolved sulphide liquid. This lens shows three types of signatures (i) Pt, Au depleted and IPGE-rich samples (Fig. 2b red) which have a mss pattern. These samples are also semi-metal poor except for two samples located at the base of the lens that are the most As- and Sb-rich samples; (ii) the PPGE-rich but semi-metal-poor samples (Fig. 2b grey) which have the lowest IPGE content; (iii) the Cu-rich samples which are also enriched in PPGE (Rh, Pd, Pt) + Au and semi-metal and depleted in IPGE (Fig. 2 black).

The Se, Cd and Co contents show a narrow range of values within both lenses and in agreement with a MSS-sulphide liquid partition coefficient ~1.

5 Discussion

Petrographic study of the lenses reveals that both lenses have been metamorphosed and deformed, but they still have a primary mineral assemblage. Coupled with their location, it appears that the D9 lens is not in contact with its parental intrusion. This suggests that the sulphide liquid was first injected at a liquid state along the fault before being deformed and recrystallized. The D8 lens has a lithological contact with its overlying ultramafic parental intrusion.

Mungall (2007) demonstrates for the Expo Ungava Intrusive Suite of the CSB that intrusive system can assimilate up to 50% of the original mass of magma that leads to the sulphur saturation of the magma. Leshner (2007) shows that the sulphur isotopes of some Cape Smith Belt deposits indicate that sulphur saturation of the parental magma was reached by assimilation of the sediments. The S/Se ratios of the Delta deposit leads to the same conclusion, suggesting that the sills associated with the feeder conduit of the komatiite assimilated material from the sediment formation they intruded. The S/Se ratios also imply that the potential remobilization of mobile elements (such as S) by fluids has not occurred at the Delta deposit.

The distribution of PGE within sulphide minerals is related to the cooling rate of the sulphides. If the cooling rate is fast, the PGE will be mainly in solid solution within the sulphides. Barnes et al. (2006) and Patten et al. (2012) observed that quenched sulphide droplets do not contain PGM and that all the PGE were in solid solution within the sulphides. In contrast, if the cooling rate is slow, more PGE will be exsolved as PGM from the sulphides (Dare 2010). In non-metamorphosed intrusions 40-60% of the PGE are considered to be present in the sulphide minerals (Barnes et al. 2008). It is possible that the metamorphism and the deformation will drive the exsolution of the remaining PGE of the sulphides, resulting in the formation of new mineral phases such as PGM. The same hypothesis can be made for the exsolution of the remaining Ni of the pyrrhotite that will lead to the formation of secondary pentlandite.

6 Conclusions

The massive sulphide lenses of the Delta deposit show evidence of deformation and metamorphism. Our preliminary results suggest that (i) the D8 lens is in

contact with its overlying parental ultramafic intrusion; (ii) the D9 lens was injected at a liquid state along the fault. In addition, the PGE and other chalcophile elements distribution within the lenses shows that (iii) the chalcopyrite-rich samples are enriched in chalcophile elements; (iv) the IPGE-rich samples that contain less than 2% chalcopyrite can have high concentrations of semi-metals. This suggests that the metamorphism possibly led to the formation of PGM in these IPGE-rich samples.

PGM require further study and a precise characterization for each sample in order to determine the contribution of the metamorphism and the deformation to the exsolution of PGM.

Acknowledgements

This research was financed by the NSERC Discovery Grant program and by the Canada Research Chair in Magmatic Ore Deposits Program. We would like to thank Dr Dare for her useful comments, Dany Savard, and Sadia Mehdi from LabMaTer (Chicoutimi) for help in carrying out the analyses.

References

- Barnes S-J, Cox RA, Zientek ML (2006) Platinum-group element, Gold, Silver and Base Metal distribution in compositionally zoned sulfide droplets from the Medvezky Creek Mine, Noril'sk, Russia. *Contrib Mineral Petrol* 152: 187-200
- Barnes S-J, Prichard HM, Cox RA, Fisher PC, Godel B (2008) The location of the chalcophile and siderophile elements in platinum-group element ore deposits (a textural, microbeam and whole rock geochemical study): Implications for the formation of the deposits. *Chem Geol* 248: 295-317
- Dare SAS, Barnes S-J, Prichard HM (2010) The distribution of platinum-group elements (PGE) and other chalcophile elements among sulfides from the Creighton Ni-Cu-PGE sulfide deposit, Sudbury, Canada, and the origin of palladium in pentlandite. *Min Dep* 45: 765-793
- Giovenazzo D (1991) Géologie et caractéristiques géochimiques des minéralisations Ni-Cu-EGP de la région de Delta, Ceinture de Cape Smith, Nouveau-Québec. PhD thesis, Université du Québec à Chicoutimi, 286 pp
- Leshner CM (2007) Ni-Cu-(PGE) deposits in the Raglan area, Cape Smith belt, New Quebec. *Geol Surv Can Spec Pub* 5: 351-386
- Lyubetskaya T, Korenaga J (2007) Chemical composition of Earth's primitive mantle and its variance: 1. Method and results. *J Geoph Res* 112: B03211
- Mungall JE (2007) Crustal contamination of picritic magmas during transport through dykes: the Expo Intrusive Suite, Cape Smith Fold Belt, New Quebec. *J Pet* 48: 1021-1039
- Patten C, Barnes S-J, Mathez EA (2012) Siderophile and chalcophile elements distribution in MORB sulphide droplets: Determination of new sulphide melt-silicate melt partition, coefficients and early sulphide crystallisation history. 12th International Ni-Cu-(PGE) Symposium, Guiyang, China, 18-19 June 2012

Improved in-situ determination of PGE concentration of chromite by LA-ICP-MS: Towards a better understanding

Philippe Pagé, Sarah-Jane Barnes

Canada Research Chair in Magmatic Metallogeny, Université du Québec à Chicoutimi, Chicoutimi, Québec G7H 2B1 Canada

Abstract. The arrival of new LA-ICP-MS equipment at UQAC allowed us to analyse the Os, Ir, Ru and Rh contents of chromite from samples representative of different geological settings including MORB, boninites, komatiites, continental flood basalt picrite, continental-type and oceanic-type chromitites, and chills of the Bushveld Complex. Our new LA-ICP-MS results combined with previous data confirm that chromite could act as the dominant phase in controlling the whole rock budget of Os, Ir, Ru and Rh, but chromite generally share this role with other phases like PGM whose crystallization seems to be influenced by chromite crystallization. Most primitive mantle normalized PGE profiles of chromite show $Ru_N > Rh_N$ with the exception of boninite and arc lavas which tend to show $Ru_N < Rh_N$. The chromite from each different setting has distinctive PGE normalized profiles that can be used to identify parental magma. For example the chromite from the chills of the Bushveld lies between komatiites and picrite rather than boninite.

Keywords. Laser ablation ICP-MS, chromite, PGE, fractionation, partition coefficients.

1 Introduction

Until recently our understanding of the role of chromite in the fractionation of Os, Ir, Ru, Rh, Pt and Pd (PGE) was essentially indirect and based on the correlations between whole rock Cr and whole rock PGE (Pagé et al. 2012, and references therein). The enrichment of Os, Ir and Ru (IPGE) that is commonly observed in all types of chromitites suggests that chromite somehow concentrates these elements. It was still unclear if the trends observed reflect the presence of platinum-group minerals (PGMs) entrapped in chromite during their crystallization and growth (Finnigan et al. 2008), or the presence of PGE in solid solution within the chromite structure. The main difficulty in answering this question arose because it was not possible to carry accurate measurements of the concentration of the IPGE in chromite by in-situ techniques because of the very low concentrations.

The introduction of in-situ analysis of chromite by laser ablation combined with ICP-MS (LA-ICP-MS) has allowed the measurement of Ru content in chromites from Archean komatiitic lavas (Locmelis et al. 2011; Pagé et al. 2012; Méric et al. 2012) and oxidized arc lavas from the Ambae Volcano in the Vanuatu Island Arc in which Os, Ir, Ru and Rh (≤ 82 ppb, ≤ 200 ppb, ≤ 162 ppb, and ≤ 149 ppb, respectively; Fig. 1a) have been reported (Park et al. 2012).

Chromites from plutonic settings are mostly devoid of measurable concentrations of PGE (Park et al. 2012;

Pagé et al. 2012), apart from the chromite from the Jimberlana layered intrusion where concentrations of Ir ≤ 12 ppb have been reported (Park et al. 2012).

There is now a new generation of LA-ICP-MS which has lower detection limits by an order of magnitude (Savard et al. 2012). We present new results on the concentrations of Os, Ir, Ru, and Rh in chromite from samples from various volcanic and plutonic settings. These new results confirm the role of chromite in the fractionation of PGE in partial melting and fractional crystallization. A better understanding of the role of chromite on the fractionation of PGE has multiple implications; it throws light on the mechanisms and the budgets of the transfer and/or the sequestration of PGE between reservoirs (mantle vs. melt vs. cumulate), on the crystallochemistry of chromite, site occupancies, and partition coefficients. The ambivalent nature of the PGE, which turns from a siderophile-dominant behaviour in absence of sulphide to a clear chalcophile-dominant behaviour as the melt reach sulphide saturation, means that the PGE content of chromite can thus be used to track the presence of sulphide mineralization (Locmelis et al. in press; Méric et al. 2012).

2 Analytical procedures and sample set

2.1 Analytical procedures and elements

The major elements Cr_2O_3 , Al_2O_3 , FeO, MgO (Fig. 1), and some minor ones, TiO_2 and V_2O_5 , were analysed with an electron microprobe at Université Laval (details in Pagé and Barnes 2009). The data obtained by EMPA are necessary because Fe is used as the internal standard for the LA-ICP-MS analysis, but also to compare EMPA and LA-ICP-MS which give similar results. The LA-ICP-MS analytical procedures for Mg, Al, Si, S, Ca, Sc, Ti, V, Cr, Mn, Fe, Co, Ni, Zn, Ga, Cu, Ge, As, Y, Mo, Ag, Cd, In, Sn, Sb, W, Re, Au, Pb in chromite are very similar to those for magnetite presented in Dare et al. (2012) and to Pagé et al. (2012) for PGE.

The new results presented here have been obtained with our recent laser ablation system (M-50 resolution Excimer: 193nm from Resonetics) combined with a new ICP-MS (x7700 from Agilent).

2.2 Sample set

Analyses were conducted on chromites from a wide range of samples (Fig. 1) representative of various volcanic settings: MORB, boninites, komatiites, continental flood basalt (CFB picrite) and from various

plutonic settings: mantle podiform chromitites from Thetford Mines Ophiolite (TMO), crustal stratiform chromitites from Stillwater Complex.

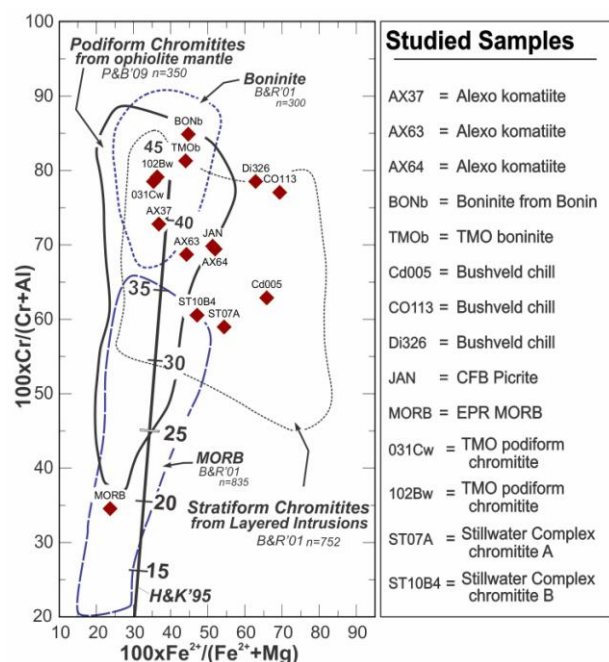


Figure 1. Major element composition of chromite from the studied samples compared to the fields of chromite from podiform chromitites (Pagé and Barnes 2009), from stratiform chromitites, from boninites and from MORB (Barnes and Roeder 2001). They are also compared to a batch melting trend from Hirose and Kawamoto (1995).

3 Results and discussion

3.1 Trace elements and PGE by LA-ICP-MS

A wide range of elements have been analysed by LA-ICP-MS in addition to the major and minor elements and the PGE. Here we focus on Os, Ir, Ru and Rh which have been determined in chromite at concentrations ranging from below detection levels (1-6 ppb) up to ~440 ppb. In certain cases the PGE are clearly present in solid solution in the chromite, and can even be accompanied by PGM, sulphide and silicate inclusions (Fig. 2).

The Os and Ir concentrations (7-69 ppb and 4-46 ppb, respectively) show a strong positive correlation (Fig. 3a), and they also correlate positively with Fe, Ga (*not shown*) and Ni (Fig. 3d), but negatively with Mg. This suggests that Os and Ir behave the same way as Ni, i.e. they prefer the octahedral coordination site, and may be influenced by the proportion of oxidized Fe (Brenan et al. 2012).

The most abundant PGE in chromite is Ru which varies between 20-450 ppb (Fig. 3b) and Rh which ranges from 4-61 ppb (Fig. 3c), they both show a weak positive correlation with Ir. In terms of Ru our samples are forming two distinctive groups: one has low Ru content (20-100 ppb) and the other with higher concentrations ranging from 200-440 ppb (Fig. 3b). Ruthenium shows a stronger positive correlation (*not shown*) with Rh. However, Ru and Rh do not show any correlation with Ni.

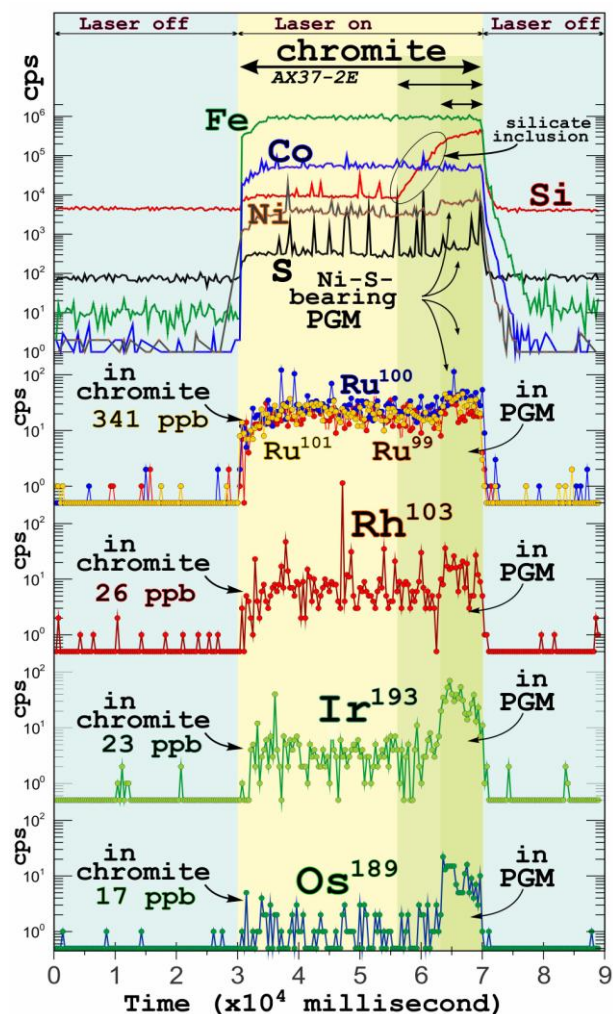


Figure 2. LA-ICP-MS analysis of a chromite from Alexo komatiites showing the profiles for Fe, Co, Si, Ni, S, Ru⁹⁹, Ru¹⁰⁰, Ru¹⁰¹, Rh¹⁰³, Ir¹⁹³ and Os¹⁸⁹ with time. The PGE are both in solid solution in chromite and as PGM inclusions.

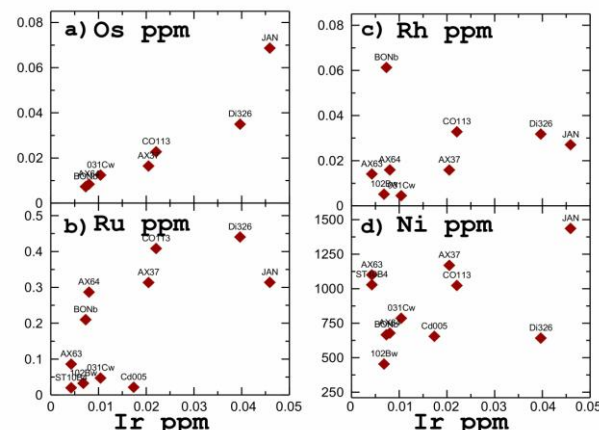


Figure 3. Iridium (ppm) content of chromite against a) Os ppm, b) Ru ppm, c) Rh ppm, and d) Ni ppm.

On the primitive mantle normalized (PM_N) PGE profiles of chromites, we observe a clear enrichment in Ru relative to Os and Ir, which show similar and essentially flat PGE profiles with concentrations from 2x to 20x the primitive mantle values (Figs 4 and 5). On the PM_N PGE profiles of chromite, Ru often defines a positive anomaly with concentrations ranging from 2x

to 90x the primitive mantle values. The lowest concentrations of Ru have been measured in chromite from chromitites in plutonic settings (podiform and stratiform; Fig. 5a) containing abundant PGM such as laurite. The highest concentrations of Ru have been obtained from chromite from volcanic settings, i.e. from the CFB picrite and komatiites, and to a lesser extent from boninites (Fig. 4).

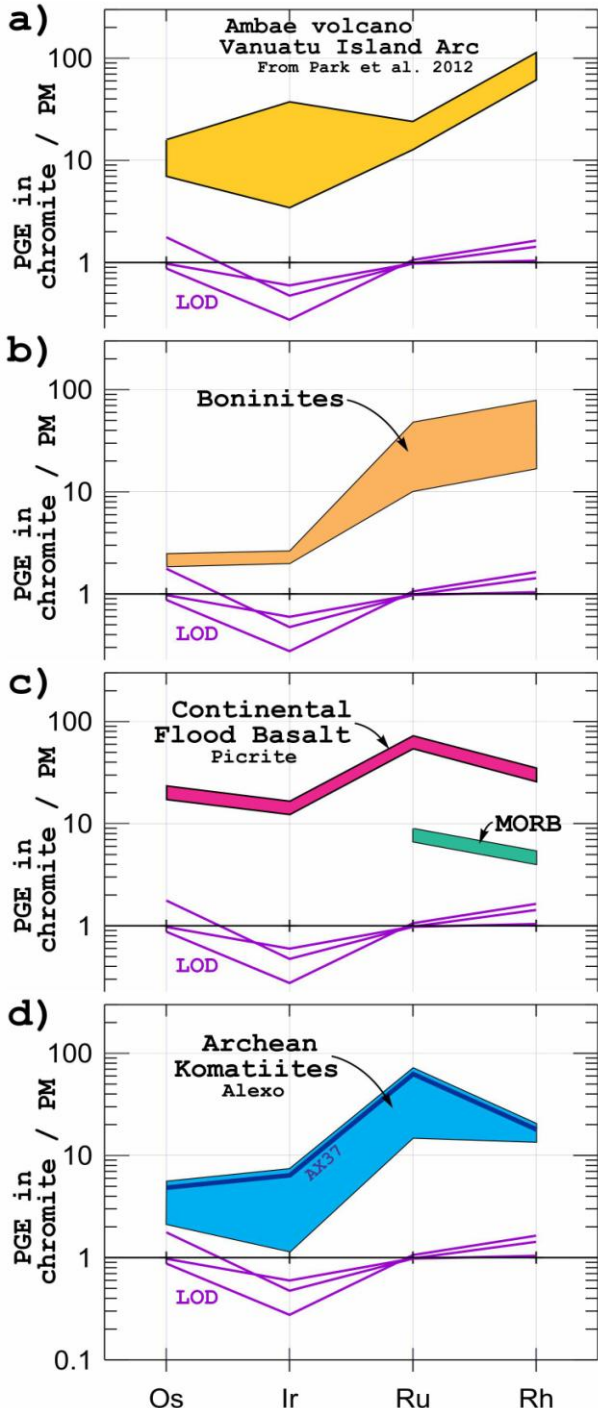


Figure 4. Primitive mantle normalized PGE profiles for chromite from volcanic settings; a) Ambae island arc volcano (data are from Park et al. 2012), b) Boninites, c) Continental flood basalt and a MORB sample, d) Komatiites. Normalizing values (in ppb) are Os=3.4; Ir=3.2; Ru=5.0; Rh=0.9; and are from Lyubetskaya and Korenaga (2007). LOD = Limit of detection.

The high Ru_N/Ir_N ratios correlate with Rh content suggesting that Rh and Ru are preferentially concentrated into chromite relative to Ir (and Os). Most of the PM_N PGE profiles of chromite show $Ru_N > Rh_N$, with the exception of the chromite from boninites and the Ambae volcano which tend to show $Ru_N < Rh_N$ (Fig. 4a, b), a particularity that could characterize oxidized volcanic arc magmas.

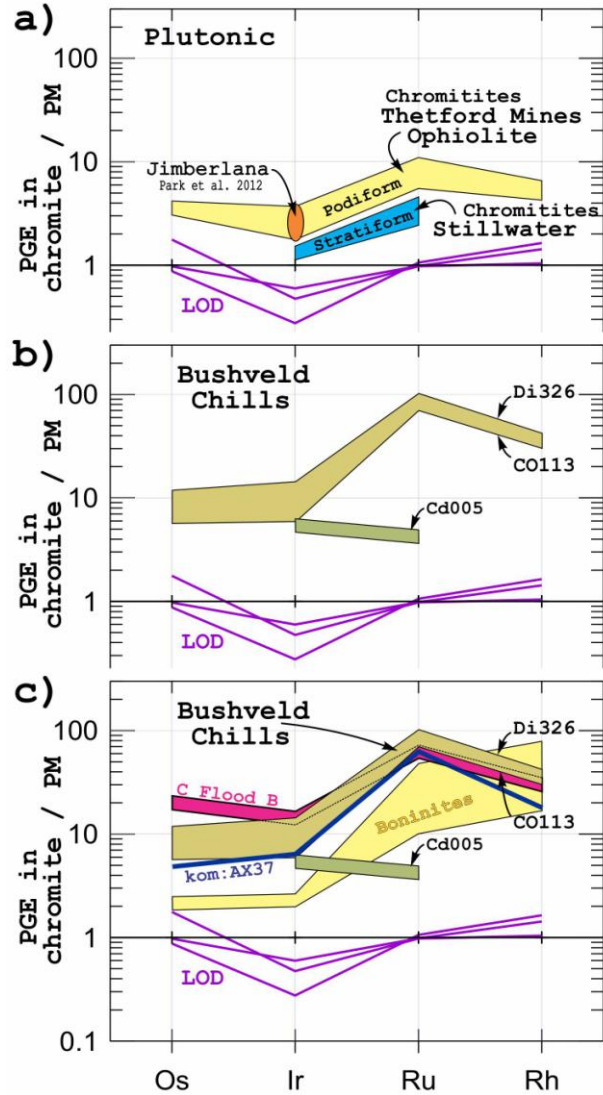


Figure 5. Primitive mantle normalized PGE profiles for chromite from plutonic settings; a) Mantle podiform, crustal stratiform chromitites, b) the chills of the Bushveld Complex, and c) the chills of the Bushveld are compared with chromite from possible parental magmas (continental flood basalt, komatiites and boninites).

On Figure 4, chromites from the various lava samples show distinctive PGE profile that can tentatively be used to identify the nature of the melt from which these chromites have crystallized. In Figure 5c, chromites from the chills of the Bushveld Complex are compared to chromite from potential parental magmas such as continental flood basalt, komatiite and boninite. Chromites from Cd005 sample are clearly different from chromites from the two other samples (Di326 and CO113). When compared with the chromite from the other lava samples, the Bushveld chill chromite most

closely resembles chromite from the continental flood basalt and komatiites, with higher Os and Ir contents, and similar Rh_N/Ru_N of $\sim 0.4-0.5$. There is a clear difference between the chromite from boninite and the chromite from the chills of the Bushveld Complex (Fig. 5c).

3.3 The role of chromite on the PGE budget and $D_{PGE}^{Chr/melt}$

Similarly to Pagé et al. (2012) who evaluated the role of chromite on the whole rock PGE budget, the results from this analysis are summarized in Table 1.

Table 1. Proportion of whole rock PGE accounted for by the chromite from the different lithologies.

Name	Litho	%WR-Os in Chr	%WR-Ir in Chr	%WR-Ru in Chr	%WR-Rh in Chr
AX37	komatiite	18%	25%	$\sim 100\%$	38%
MORB	MORB	<26%	<13%	93%	76%
BONb	boninite	88%	>100%	77%	30%
TMOB	boninite	<5%	<5%	45%	11%
JAN	CFB-picrite	10%	9%	35%	14%

New partition coefficients for Os, Ir, Ru and Rh between chromite and various melts have been calculated (Table 2) following the method of Pagé et al. (2012).

Table 2. Partition coefficients for chromite and various melts.

Name	Litho	$D_{Os}^{Chr/melt}$	$D_{Ir}^{Chr/melt}$	$D_{Ru}^{Chr/melt}$	$D_{Rh}^{Chr/melt}$
AX37	komatiite	9.7	14	60	20
MORB	MORB	<37	<18	129	105
BONb	boninite	183	365	159	61
TMOB	boninite	<14	<13	125	31
JAN	CFB-picrite	40	36	139	56

4 Conclusions

Chromite acts as a sink for the PGE, not only because it can entrap PGM during their crystallization, but also because Os, Ir, Ru and Rh partition into chromite structure. The highest concentration has been measured for Ru reaching ~ 300 ppb in the chromites from continental flood basalt and komatiites, and as high as 440 ppb in the chromite from the Bushveld chills. Chromites from komatiites, flood basalt, podiform chromitites, and from the Bushveld chills show Rh_N/Ru_N of <1 , opposite to chromites from boninites and from Ambae arc lavas ($Rh_N/Ru_N > 1$), which seems to be typical of oxidized arc magmas.

The PGE normalized profiles of chromite can thus be used to characterize the nature of the melt from which the chromite has crystallized. The whole rock data combined with the PGE content of chromites allowed us to present new partition coefficients.

Acknowledgements

This study has been funded by a grant from the Canada Research Chair in Magmatic Ore Deposit. We thank Dany Savard (UQAC) for his assistance with LA-ICP-MS and Sarah Dare for comments on and proof reading this work.

References

- Brenan JM, Finnigan CS, McDonough WF, Homolova V (2012) Experimental constraints on the partitioning of Ru, Rh, Ir, Pt and Pd between chromite and silicate melt: The importance of ferric iron. *Chem Geol* 302: 16-32
- Dare, SAS, Barnes S-J, Beaudoin, G (2012) Variation in trace element content of magnetite crystallized from a fractionating sulfide liquid, Sudbury, Canada: Implications for provenance discrimination. *Geochim Cosmochim Acta* 88: 27-50
- Locmelis M, Fiorentini ML, Barnes SJ, Pearson NJ (in press) Ruthenium variation in chromite from komatiites and komatiitic basalts – a potential mineralogical indicator for nickel-sulfide mineralization. *Econ Geol*
- Locmelis M, Pearson NJ, Barnes SJ, Fiorentini ML (2011) Ruthenium in komatiitic chromite. *Geochim Cosmochim Acta* 75: 3645-3661
- Lyubetskaya T, Korenaga J (2007) Chemical composition of Earth's primitive mantle and its variance: 1. Method and results. *J Geophys Res*: 112, B03211, doi:10.1029/2005JB004223
- Méric J, Pagé P, Barnes S-J, Houllé MG (2012) Geochemistry of chromite from the Alexo komatiite, Dundonald Township: preliminary results from electron microprobe and laser ablation inductively coupled plasma mass spectrometric analyses; in Summary of Field Work and Other Activities 2012, Ontario Geological Survey, Open File Report 6280: 46-1 – 46-12
- Pagé P, Barnes S-J (2009) Trace elements signature of chromites from podiform chromitites of the Thetford Mines Ophiolite, Québec, Canada: products of boninitic melt migration. *Econ Geol* 104: 997-1018
- Pagé P, Barnes S-J, Bédard JH, Zientek ML (2012) In situ determination of Os, Ir, and Ru in chromites formed from komatiite, tholeiite and boninite magmas: Implications for chromite control of Os, Ir and Ru during partial melting and crystal fractionation. *Chem Geol* 302: 3-15
- Park J-W, Campbell IH, Eggins SM (2012) Enrichment of Rh, Ru, Ir and Os in Cr spinels from oxidized magmas: evidence from the Ambae volcano, Vanuatu. *Geochim Cosmochim Acta* 78: 28-50

Structure and dynamics of magmatic Ni-Cu sulphide deposits: theory, analogue modelling and insights from Voisey's Bay (Labrador, Canada)

Benoit M. Saumur, Alexander R. Cruden, David Boutelier
School of Geosciences, Monash University, Clayton, VIC, 3800, Australia

Dawn Evans-Lamswood
Vale Newfoundland and Labrador, St.-John's, Newfoundland and Labrador, Canada

Abstract. The geometry of the Voisey's Bay Intrusion (VBI) is strongly controlled by pre-emplacment ductile and pre-to-syn-emplacment brittle wall-rock structures. Only the final inputs of magma, associated with the feeder dykes of the VBI, contributed massive sulphide mineralisation. Emplacement occurred by a "caldrion subsidence" process in which the roof of a lower chamber collapsed as the floor of an upper chamber subsided; dense sulphides, which were concentrated at the base of the lower chamber, were withdrawn last. Theory and analogue models of entrainment of sulphide liquid by mafic magma during forceful withdrawal suggest that draw-up of sulphide is highly sensitive to flow rates and mafic magma viscosity. Significant draw-up of sulphide can occur at high Reynolds numbers and flow rates (10-1000 m³/s). Finally, because of its high density, low viscosity and low solidus temperature, sulphide can percolate downwards late in the history of the system. This is controlled by a "critical accumulation height", above which sulphide can percolate downwards into anisotropies of given widths. This process was important for the development of mineralisation in the Reid Brook Zone of the VBI, located below a now-eroded magma chamber, where injections of sulphide intrude dominantly in the down-dip directions of host-rock gneiss structures.

Keywords. mafic magma, sulphide liquid, emplacement, withdrawal, entrainment, downward percolation

1 Introduction

Magmatic sulphide deposits represent a significant portion of the worldwide known reserves of Ni, Cu and PGEs, and our knowledge regarding the genesis of Ni, Cu and PGE magmatic sulphide deposits stems from decades of experimental and field-based research (Naldrett 2005) on deposits such as Sudbury (Canada), Norilsk (Russia), Jinchuan (China), Pechenga (Russia) and Voisey's Bay (Canada). However, the controls on the transport, emplacement and concentration mechanisms of sulphide liquids are still debated. Four main factors contribute to their unique behaviour in magmatic systems: (1) their immiscibility with respect to silicate magmas (e.g., Mungall and Su 2005), (2) their high density (4200 to 4500 kg/m³; Dobson et al. 2000; Mungall and Su 2005) compared to mafic magmas and the surrounding crust (3) their low viscosity, on the order of 0.01 Pa s (Dobson et al. 2000), which is 1 to 3 orders of magnitude lower than typical mafic magma, and (4) their low solidus temperatures, which are >150° lower than mafic magmatic systems (Ballhaus et al. 2001). The combination of these factors hinders the withdrawal of sulphide liquids from magmatic staging chambers, acts

against their ascent to higher crustal levels, allows for late emplacement stage mobility of sulphide liquids, and can potentially permit their downward percolation along grain boundaries and fractures within crystallized plutonic rocks and surrounding wall rocks.

In this work we attempt to elucidate the structural and dynamic controls on the emplacement of magmatic sulphide liquids. We present new results from fieldwork at Voisey's Bay, including analysis of data from optical and acoustic televiwer surveys, which provide a better geometric and structural understanding of the system. We also present theory and analogue models on the entrainment of coherent sulphide liquid into ascending mafic magma during withdrawal from a density stratified staging magma chamber. Finally, we discuss the dynamics of sulphide back flow and its importance for intrusion-hosted deposits emplaced in highly anisotropic rocks such as Voisey's Bay.

2 Structure of the Voisey's Bay intrusion

The Mesoproterozoic Voisey's Bay Intrusion (VBI) is a kilometre scale layered mafic intrusion consisting dominantly of troctolite with minor gabbro and norite. It is one of many plutons forming the 20,000 km² Mesoproterozoic Nain batholith in northern Labrador, which coincides with a major Paleoproterozoic suture zone between the Archean Churchill and North Atlantic Cratons (Ryan 1997). The batholith was emplaced during a period of regional transtension (Myers et al. 2008), at mid-crustal depths likely between 9 and 11 km.

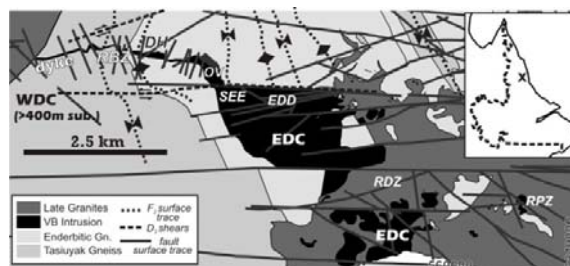


Figure 1. Map of Voisey's Bay, Labrador. Modified from internal Vale Newfoundland and Labrador data. Components of the VBI: EDC: Eastern Deeps Chamber; WDC: Western Deeps Chamber (located over 400 meters in the subsurface). Selected ore bodies: RBZ: Reid Brook Zone, DH: Discovery Hill, OV: Ovoid, SEE: South East Extension, EDD: Eastern Deeps Deposit, RDZ: Red Dog Zone, RPZ: Ryan's Pond Zone.

At first order, the VBI consists of an upper chamber, the Eastern Deeps Chamber (EDC), a lower chamber, the Western Deeps Chamber (WDC), and a complex network of feeder dykes, which emanate from the WDC and intrude the northern base and side of the EDC. In detail, the geometry of the VBI and associated Ni-Cu ore bodies (Fig. 1) are controlled by a complex interplay of internal igneous and pre- to syn-emplacement external tectonic processes. Wall rocks of the Voisey's Bay area were affected by at least three pre-emplacement ductile and two pre- to syn-emplacement brittle deformation events. The locations of mineralisation in the VBI are strongly controlled by pre-emplacement wall rock anisotropies, which acted passively during magma intrusion, and syn-emplacement brittle structures. Noteworthy associations between pre-emplacement wall-rock structure and Voisey's Bay mineralization are (1) the architecture of the Reid Brook Zone, which is controlled by the intersection of an S_1 foliation, D_3 shear zones and late fractures, (2) the coincidence of the South East Extension, Eastern Deeps and Ryan's Pond mineralization with shallow fabrics associated with the hinge zones of deposit scale F_2 folds, and (3) the orientations of dyke margins with respect to fracture and lineament orientations. Changes in conduit thickness and geometry, which locally control the locations of magmatic sulphide mineralisation (Evans-Lamswood et al. 2000), can be explained by thermo-mechanical erosion of dyke walls, locally accentuated where the dyke is deflected by wall-rock anisotropies.

The structure and petrology of the VBI is consistent with an incremental multiphase emplacement history. The Eastern Deeps Chamber (EDC), considered as the upper chamber in the magmatic system, consists of 6 sub-chambers that are partly separated by bodies of wall-rock gneiss. Space for magma accumulation was accommodated by magma underplating and floor subsidence. The upper four sub-chambers of the EDC were fed from the southeast, thin-out towards the northwest, and do not show an obvious geometric link to the (famous) feeder dykes that intrude the northern base of the EDC and carry mineralisation. These sub-chambers consist of a combination of sulphide saturated and undersaturated magmas, suggesting that both were present together during withdrawal from a lower staging chamber. Only the lowermost sub-chamber and its associated feeder dykes, which represent the latest known emplacement event at Voisey's Bay, contain significant massive sulphide mineralization.

Geometric and kinematic relationships suggest that as top-down emplacement of the EDC progressed, more mineralized magma pulses were tapped from the lower chamber. This is consistent with a "cauldron subsidence" emplacement mechanism in which the roof of a lower chamber collapses as the floor of an upper chamber subsides. Dense sulphides concentrated at the base of the lower chamber would have been withdrawn last.

3 Withdrawal and entrainment of sulphide

3.1 Theory

Previous work on intrusion-hosted magmatic sulphide

has shown that sulphide can be carried upwards and laterally as droplets within mafic magma (Leshner and Groves 1986; de Bremond d'Ars et al 2001). This, however, is inconsistent with observations at Voisey's Bay, which suggest that the latest magmatic pluses consisted of coherent sulphide liquid (Evans-Lamswood et al. 2000).

Consider an initial staging chamber in which sulphide liquid has precipitated and settled downwards, resulting in stable density stratification of relatively buoyant and high viscosity mafic magma over dense, lower viscosity sulphide liquid. During upward withdrawal of the mafic magma, upper portions of the chamber will initially be tapped, leaving the mafic / sulphide interface undisturbed. As the height of the mafic magma layer in the lower chamber decreases due to continued withdrawal, the mafic / sulphide interface will be pulled upwards due to an increase in shear stress at the boundary. Eventually, entrainment of sulphide into the conduit will occur once the mafic magma layer reaches a certain thickness d (Fig. 2), known as the critical draw-up height (Blake and Ivey 1986). Such a process cannot be driven by buoyancy because of the high density of the magmas involved; instead it is likely forcefully driven by the foundering of the roof of the chamber, generating high magma flow rates.

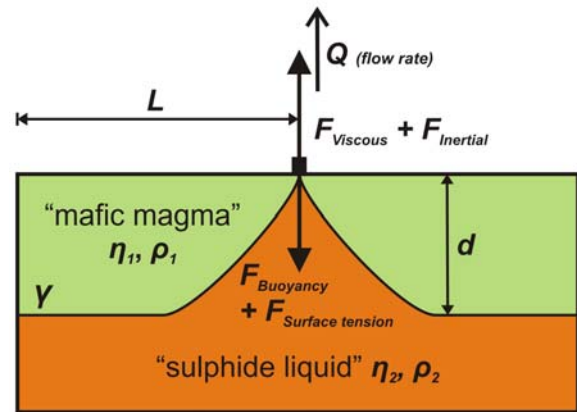


Figure 2. Parameters of withdrawal and entrainment. F are forces, Q is volumetric flow rate, η is kinematic viscosity, ρ is density, d is the critical draw-up height, L is chamber half width.

The fluid dynamics of withdrawal and entrainment have been the subject of several studies scaled to silicic volcanic systems. Blake and Ivey (1986) developed analytical solutions describing the entrainment of mafic magma by felsic magma in a density stratified chamber. The critical draw-up height for strongly depends on whether the system is dominated by inertial forces (turbulent flow) or viscous forces (laminar shear flow). Depending on flow type, d is predicted by the equations (after Blake and Ivey 1986):

$$d_{inertial} = 0.88 \sqrt[5]{Q^2 \rho_2 / g \Delta \rho}$$

$$d_{shear} = 2.42 \sqrt[4]{Q \eta_1 / g \Delta \rho}$$

We can also define a Reynolds number (Re), representing the ratio of inertial and viscous forces, based on the parameters of illustrated in Figure 2,

$$Re \sim \frac{\Delta \rho Q d}{\eta_1 A}$$

in which the characteristic velocity of the system is

expressed as volumetric flow rate Q over the cross sectional area, A , of the vent draining the chamber. Typical values for Q in mafic magma systems are inferred to be much higher than those typical of felsic magma systems, especially when the system is forcefully driven; Q could therefore range between 0.1 and 1000 m³/s. Considering this, along with typical values for the density and viscosity of mafic magma and sulphide liquids, we find that for entrainment via dykes between 1-10 m in width Re -numbers are between 10 and 100,000, which is over 5 orders of magnitude higher than felsic-mafic regimes, and suggests that typical flow regimes are transitional to highly inertial. The equations predict that significant draw-up of sulphide, with d on the order of meters to 10's of meters, can occur at high flow rates (10-1000 m³/s) in highly inertial systems.

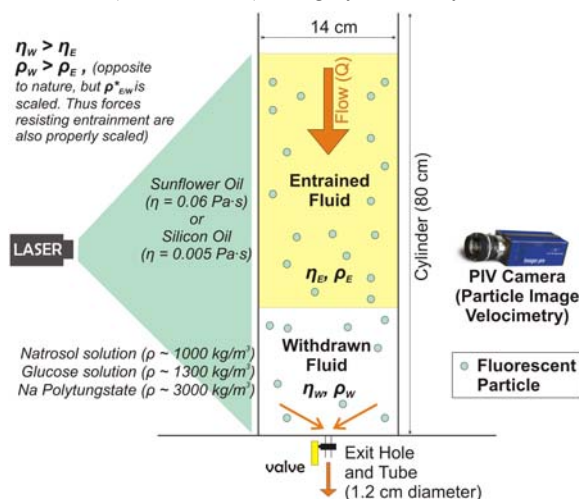


Figure 3. Laboratory Setup: the “Inverted Magma Chamber”. See Figure 2 for explanation of symbols.

The effect of interfacial tension resisting flow can be evaluated using the Weber number (We) which represents the ratio of inertial forces over forces related to surface tension:

$$We = \frac{\Delta\rho Q^2 d}{\gamma A^2},$$

where γ is the coefficient of interfacial tension, evaluated to be ~ 0.6 N/m for sulphide within mafic magma (Mungall and Su 2005). Weber numbers are found to be several orders of magnitude higher than one, indicating that interfacial tension is an insignificant retarding force when draw-up heights are on the order of meters and higher.

3.2 Analogue modelling

Previous numerical and experimental work on magma entrainment in volcanic settings is not scaled to the viscosities, densities and flow rates of sulphide/mafic systems. We describe and present results of analogue experiments scaled to the high Re conditions of immiscible mafic-sulphide systems.

For practical reasons, analogue experiments in this study were performed in an “inverted magma chamber” setup (Fig. 3) with downward-driven flow. In such a setup, the withdrawn liquid is denser than the entrained liquid, which is opposite to the natural prototype, and

downward withdrawal is controlled by gravity. However, in both nature and experiment the density contrast between the fluids stabilizes the interface and retards entrainment. Several different combinations of immiscible liquids were used to achieve a range of viscosity and density ratios.

Experiments were monitored with a particle image velocimetry (PIV) system, which allowed detailed measurements of flow fields and Q , and a high frame rate (60fps) DSLR camera, which allowed precise determination of d (in this case, the “draw-down” height). Experiments were scaled to the natural prototype according to the following scaling laws:

$$\text{length scale: } \lambda = \frac{X_{exp}}{X_{nat}} \sim 1.2 \times 10^{-2}$$

$$\text{time scale: } T = \sqrt{\frac{\lambda}{g}}$$

$$\text{flow rate scale: } Q' = \frac{\lambda^3}{T} \sim 5 \times 10^{-5},$$

where X is length and g the acceleration of gravity. Preliminary results (Fig. 4) allow the evaluation of the roles of Q and η while the density ratio ρ^* between the fluids remains constant. Results presented here were obtained from experiments consisting of sunflower oil ($\eta = 0.063$ Pa s; $\rho = 918$ kg/m³) as the entrained fluid and aqueous solutions of glucose as the lower withdrawn fluid. Concentrations of glucose were varied in order to obtain the desired viscosity ratios with respect to sunflower oil (Fig. 4). Results confirm that d increases with Q , as predicted by analytical solutions (Blake and Ivey 1986). However, our data suggest that the viscosity of the withdrawn layer exerts a strong control on d , which is not predicted for high Re systems. To date, the highest flow rates that we have achieved in the laboratory scale to ~ 20 m³/s in nature, and the associated draw up cone corresponds to a height of ~ 4.8 m.

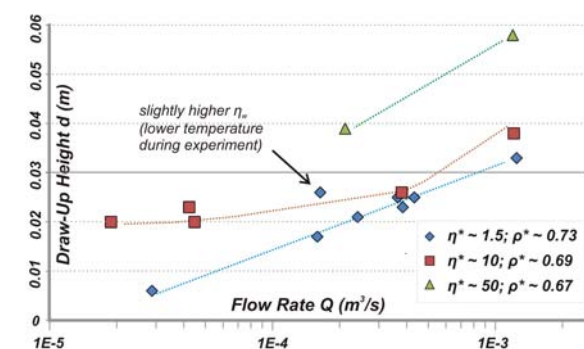


Figure 4. Preliminary results. Relationship between flow rate and draw-up heights measured during experiments.

Theory and preliminary experimental results confirm that a sulphide/mafic interface can be mobilised at high flow rates, thereby forcing sulphide liquid upwards in highly dynamic intrusive systems such as the VBI.

4 Sulphide mobility and backflow

The high density, low viscosity and low solidus temperatures of sulphide liquids contribute to their late- or even post-emplacement mobility, which can occur

along cracks or grain boundaries in the surrounding rocks (Chung and Mungall 2008). The dynamics of sulphide percolation are analogous to the behaviour of dense non-aqueous phase liquids (DNAPL), for which a critical accumulation height (h_d) can be defined to represent the minimum height of dense liquid required to overcome fracture entry pressure (Fig. 5).

$$h_d = \frac{\gamma \cos \phi}{\Delta \rho g w}$$

where
 γ = surface tension
 ϕ = contact angle
 $\Delta \rho$ = $\rho_{\text{sulphide}} - \rho_{\text{crust}}$

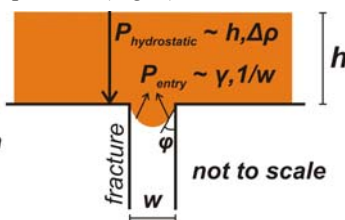


Figure 5. Critical accumulation height for percolation entry into a fracture of width w . The relationship is obtained by balancing hydrostatic and entry pressures. Modified from Kueper and McWhorter (1991).

If we consider that sulphide can flow freely in the absence of mafic magma and is capable of wetting the surrounding rocks ($\phi = 0$), taking γ to be ~ 1 N/m (based on experimentally determined values of interfacial tension of sulphide liquid within mafic magma and the surface tension of pure iron liquid; Mungall and Su 2005; Rusanov and Prokhorov 1996) we find that percolation along grain boundaries ($w \sim 10^{-5}$ m) can occur beneath a sulphide accumulation with a height of at least 7 meters. Furthermore, as percolation progresses h_d increases if the sulphide column remains connected, which implies that narrower anisotropies can be infiltrated as the sulphide front migrates farther downward from its source.

Such a process appears to have been important at Voisey's Bay, most notably in the Reid Brook Zone (RBZ) (Fig. 1), where sulphide liquid forms discrete 1-10 meter wide injections into wall rock gneiss. The RBZ is located structurally below a hypothesised, now-eroded upper chamber with basal accumulations of sulphide (analogous to the EDC or the Ovoid). Downward migration of sulphide liquid was likely promoted by the strongly anisotropic nature of Tasiuyak gneiss, which forms the wall rock of the RBZ. Sulphide injections in the RBZ share similar orientations with shallowly dipping fractures and the strongly developed SE-dipping S_1 foliation in the Tasiuyak gneiss, and tend to be longer and more abundant in the down-dip direction of wall rock anisotropies. Direct intrusion of sulphide liquid into wall rocks would also be favoured during syn-emplacement faulting, which would promoted the migration of mobile sulphide into localised zones of dilation. Such processes are consistent with similar observations from other Ni-Cu sulphide deposits such as Eagle, Michigan (Ripley and Li 2011) and Sudbury's late offset dykes.

Acknowledgements

This work benefited from discussions and critical input from Peter Lightfoot and the many geologists at Vale Newfoundland and Labrador, Ltd. Stefan Vollgger provided analytical assistance and Chris Pierson assisted

with the design of the experimental apparatus. We also acknowledge financial support from a Vale research grant, an NSERC Discovery Grant to ARC, and an NSERC CGS to BMS.

References

- Ballhaus, C., Tredoux, M., Späth, A. (2001) Phase Relations in the Fe-Ni-Cu-PGE-S at Magmatic Temperature and Application to Massive Sulphide Ores of the Sudbury Igneous Complex. *J Petrol*, 42: 1911-1926.
- de Bremond d'Ars, J., Arndt, N.T., Hallot, E. (2001) Analog experimental insights into the formation of magmatic sulphide deposits. *Earth Plan Sci Lett*, 186: 371-381,
- Blake, S., Ivey, G. N. (1986) Magma-mixing and the dynamics of withdrawal from stratified reservoirs. *J Volc and Geotherm Res*, 27:153-178.
- Chung, H.-Y., Mungall, J. E. (2009) Physical constraints on the migration of immiscible fluids through partially molten silicates, with special reference to magmatic sulphide ores. *Earth Plan Sci Lett*, 286: 14-22.
- Dobson, D.P., Crichton, W.A., Vocadlo, L., Jones, A.P., Wang, Y., Uchida, T., Rivers, M., Sutton, S., Brodholt, J.P. (2000) In situ measurement of viscosity of liquids in the Fe-FeS system at high pressures and temperatures. *Am Min*, 85: 1838-1842
- Evans-Lamswood, D.M., Butt, D.P., Jackson, R.S., Lee, D.V., Murrige, M.G. Wheeler, R.I, Wilton, D.H.C. (2000) Physical Controls Associated with the Distribution of Sulphides in the Voisey's Bay Ni-Cu-Co Deposit, Labrador. *Econ Geol*, 95:749-769.
- Kueper, B.H., McWhorter, D.B. (1991) The Behavior of Dense Nonaqueous Phase Liquids in Fractured Clay and Rock, *Ground Water*. 29: 716-728.
- Leshar, C.M., Groves, D.I. (1986) Controls on the Formation of Komatiite-Associated Nickel-Copper Sulphide Deposits. in Friedrich, G.H., et al.: *Geology and Metallogeny of Copper Deposits*, Springer-Verlag Berlin Heidelberg, p. 43-62
- Mungall, J., Su, S. (2005) Interfacial tension between magmatic sulphide and silicate liquids: Constraints on kinetics of sulphide liquation and sulphide migration through silicate rocks. *Earth Plan Sci Lett*, 234:135-149
- Myers, J.S., Voordouw, R.J., Tettelaar, T. A. (2008) Proterozoic anorthosite-granite Nain batholith: structure and intrusion processes in an active lithosphere-scale fault zone, northern Labrador. *Can J Earth Sci*, 45:934
- Naldrett, A.J. (2005) A History of our Understanding of Magmatic Ni-Cu sulphide deposits. *Can Min*, 43:2069-2098.
- Ripley, E.M. and Li, C. (2011) A Review of Conduit-Related Ni-Cu-(PGE) Sulphide Mineralization at the Voisey's Bay Deposit, Labrador and the Eagle Deposit, Northern Michigan, in Li.C. and Ripley E.M. eds., *Magmatic Ni-Cu and PGE Deposits: Geology, Geochemistry and Genesis*, Reviews in Economic Geology, 17:181-198.
- Rusanov, A.I., Prokhorov, V.A. (1996) *Interfacial Tensiometry*, Elsevier Amsterdam, pp.407.
- Ryan B. (1997) The 1997 Howard Street Robinson lecture: The Mesoproterozoic Nain Plutonic Suite in eastern Canada, and the setting of the Voisey's Bay Ni-Cu-Co deposit. *Geosci Can*, 24:173-188.

Petrology of low-sulphide PGE ores of the Norilsk region

Sergey Sluzhenikin, Vadim Distler, Antonina Grigor'eva

Institute of Geology of Ore Deposits, Mineralogy, Petrography, and Geochemistry (IGEM RAS), Staromonetny 35, Moscow 119017 Russia

Abstract. Low-sulphide PGE-bearing horizons in the Norilsk region are localized in a specific zone along upper endocontact of the mafic-ultramafic intrusions, separated from the main Ni-Cu-PGE ores by more than 50m of barren intrusive rocks. The upper endocontact zone is composed of heterogeneously-textured rocks of variable petrographic compositions, most notably leucogabbro and taxitic chromitiferous gabbro. PGE grades average more than 3 ppm, typically range 3-12 ppm, and locally achieve 20-40 ppm and may be up to 60 ppm in individual samples. Most of the bulk PGE content in low-sulphide ores occurs as intermetallics, Fe-Pt alloys, sulphides, and sulpharsenides. Volatile compounds appear to have played an important role in the formation of the low-sulphide PGE horizons.

Keywords. low-sulphide platinum ore, platinum-group minerals, Norilsk, fluid

1 Occurrences of low-sulphide PGE ores in the Norilsk region

The giant Norilsk Ni-Cu-PGE camp is well known for its spectacular endowment of high-sulphide Ni-Cu-(PGE) and PGE-Cu-Ni ores, however, less well known are occurrences of low-sulphide PGE ores, which have been identified in the reserves of economic deposits (e.g., Norilsk I, Talnakh, and Kharaelakh: Sluzhenikin at al. 1994), in the resources of previously non-economic deposits (e.g., Norilsk II, Chernogorsky), and also in intrusions of the Zubovsky leucocratic type (e.g., Zub-Marksheidersky, Pyasino-Vologochansky, Kruglogorsky). This feasibility study of low-sulphide ore reserves was completed in the Zapolyarny Mine.

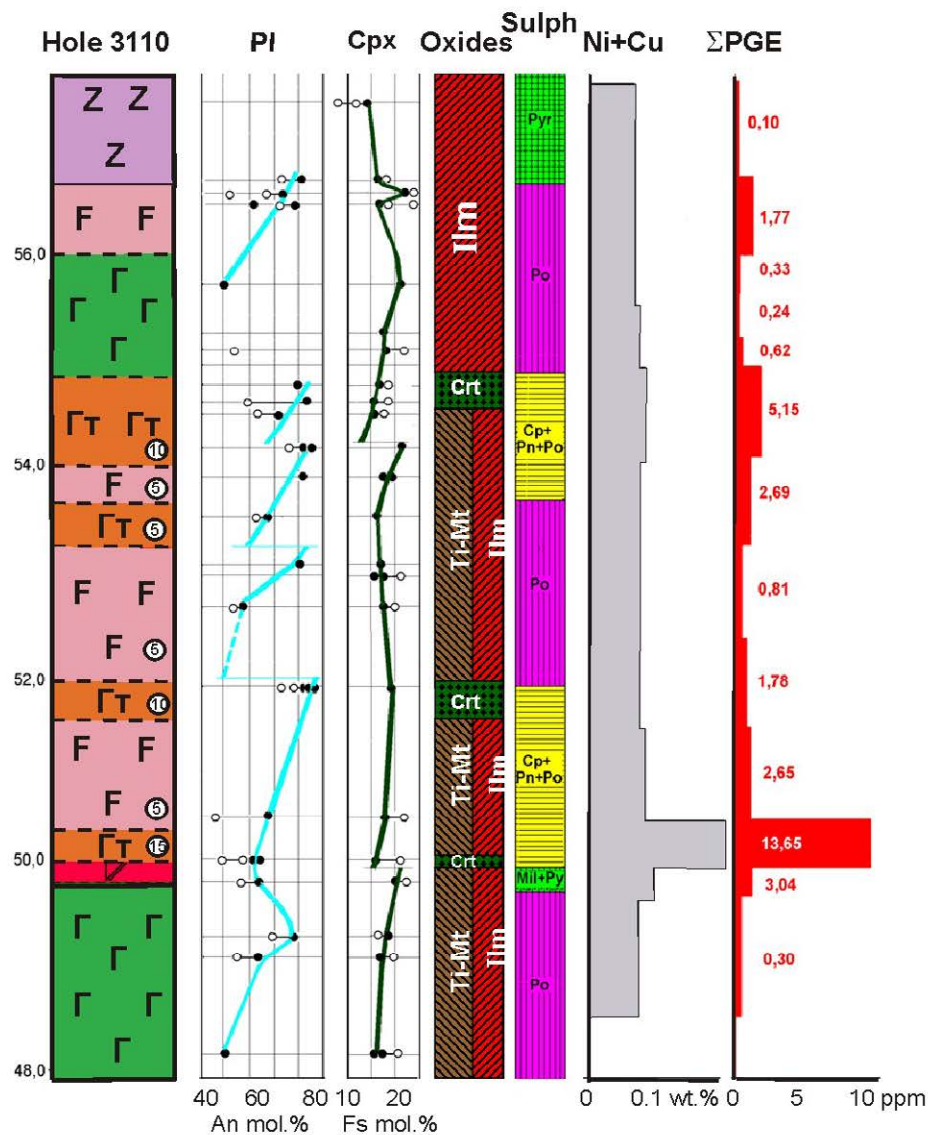
Despite some differences, the occurrences of low-sulphide PGE mineralisation have much in common. The low-sulphide PGE-bearing horizons occur in a distinct location along the upper endocontacts of the intrusions. They are separated from the high-sulphide orebodies by barren rock intervals more than 50m thick. The upper endocontact zone is composed of heterogeneously-textured rocks of variable petrographic compositions, including: irruptive breccia, gabbrodolerite (olivine-free, olivine-bearing, and olivine-rich varieties), gabbrodiorite, leucogabbro and taxitic chromitiferous gabbro. Olivine-rich rocks similar to picritic and troctolitic gabbrodolerite of the lower parts of the intrusions of the Norilsk type are much less abundant in the upper endocontacts. The mineralised host rocks are typically leucogabbro and taxitic chromitiferous gabbro (Fig. 1). Leucogabbroic rocks do not form a continuous horizon at the top of the intrusions, but occur as lenses from a few m to hundreds of m long with variable thickness up to 25m. The leucogabbroic horizon may be in contact with the

country rocks or may be separated from them by marginal gabbrodolerite, gabbrodiorite, and irruptive breccia. Taxitic gabbro forms a few subzones in the limit of the leucogabbroic horizon (Fig. 1), whereas the major taxitic subzone is regularly localized at the bottom of the horizon.

2 Mineral compositions of host rocks

The boundary between leucogabbro and taxitic gabbro is transitional over a few cm. Leucogabbro consists of coarse laths (up to 2 cm) of basic plagioclase An₇₀₋₈₅ between which an aggregate of fine-grained lath-shaped plagioclase An₅₄₋₇₀ is developed. Interstitial augite Fs₁₀₋₁₃Wo₃₉₋₄₄En₇₁₋₇₇ comprises less than 15 vol%. Titaniferous phlogopite ($X_{Mg} = 76-82$ mol%), titanomagnetite, ilmenite, chromite and apatite are secondary and accessory minerals. Leucogabbro is characterized by directive texture with sub-parallel orientation of plagioclase laths. Taxitic gabbro is a heterogeneously-textured rock with uneven distribution of plagioclase and dark-coloured silicates. It is composed of plagioclase (60-70 vol%), augite (20-25 vol%), and olivine (up to 5 vol%).

Orthopyroxene, phlogopite, titanomagnetite, ilmenite, sphene, apatite, and baddeleyite occur as minor secondary phases. Earlier cumulus plagioclase An₇₅₋₈₅ forms coarse tabular zonal crystals 1-20 mm in size, whereas fine-grained prismatic and lath-shaped plagioclase An₅₄₋₆₁ occurs in the intergranular spaces. Clinopyroxene Fs₁₀₋₁₁Wo₄₁₋₄₄En₄₆₋₄₇ forms anhedral grains. Olivine Fo₇₃₋₇₉ is not abundant and occurs as separate grains and in aggregates. Orthopyroxene Fs₂₆Wo₂En₇₀ forms euhedral crystals and reaction rims around olivine. Brown phlogopite has X_{Mg} of about 98 mol%. The wide development of H₂O-, OH-, Cl-, and F-bearing minerals (e.g., prehnite, actinolite, pennine, clinocllore, septechlorites, hydrotalcite, saponite, pumpellyite, analcite, thomsonite, apatite) is typical for these rocks. These minerals replace primary silicates and sulphides as well as fill amygdules up to 15 mm in diameter, which may constitute up to 20-15 vol% of the rock. Actinolite, apatite, chlorites, and saponite contain a significant amount of chlorine (up to 6 wt%). Another typical feature of the taxitic rocks is an elevated amount of Cr-spinels, which may make up to 40 vol% in segregations of a few cm in size. Cr-spinel regularly rims amygdules with water-rich silicates inside and may also intergrow with the silicates. Olivine-rich rocks are commonly located at the bottom of the leucogabbroic horizons.



Z basalt **F** leucogabbro **G** olivine-free gabrodolerite **T** taxitic gabbro **Gabbro** gabbrodiorite **○●** mineral composition: core (open circle) and margin (close circle); oxide mineralization: **Ilm** ilmenite **Ti-Mt** titanomagnetite **Cr** chromite; sulphide mineralization: **Po** pyrrhotite **Cp+Pn+Po** chalcopyrite pentlandite-pyrrhotite **Py** pyrite **Ⓢ** volume proportion (vol.%) of amygdaloid segregations with F⁻, Cl⁻ and OH⁻-bearing minerals

Figure 1. Variations in compositions of rock-forming, oxide, and sulphide minerals and Cu, Ni and PGE contents through the upper contact zone that hosts the low-sulphide PGE horizon in the Noril'sk I intrusion

3 PGE and base metal distribution

The total Cu and Ni content of bulk low-sulphide ore does not exceed 0.20-0.25 wt %. The total PGE contents of the upper endocontact rocks are regularly higher than 0.3 ppm, therefore a range of 0.3-2 ppm can be considered as the background level for barren rocks. The total PGE grade in economic low-sulphide ore at a 3 ppm cut-off grade generally varies between 3-12 ppm, locally achieve 20-40 ppm, and may be up to 60 ppm in individual samples. The PGE abundances recalculated to 100% sulphide are the highest in low-sulphide PGE ore

amongst all ore types in the Norilsk deposits. Σ PGE (ppm)/S (wt%) ratios for low-sulphide mineralisation exceed 5 and reach 40-70, whereas they do not exceed 1.2 in Talnakh disseminated ore and 3.5 in Norilsk disseminated ore. Low-sulphide mineralisation is can be discriminated from disseminated ores of the Norilsk deposits on a plot Σ PGE (ppm) vs Σ Cu+Ni (wt %) (Fig. 2). The Pt/Pd ratio in low-sulphide ores is similar to that in PGE-Cu-Ni ores of the main ore horizons varying from 0.23 to 0.63, with the predominant Pt/Pd values ranging between 0.33 and 0.50.

Types of Intrusions

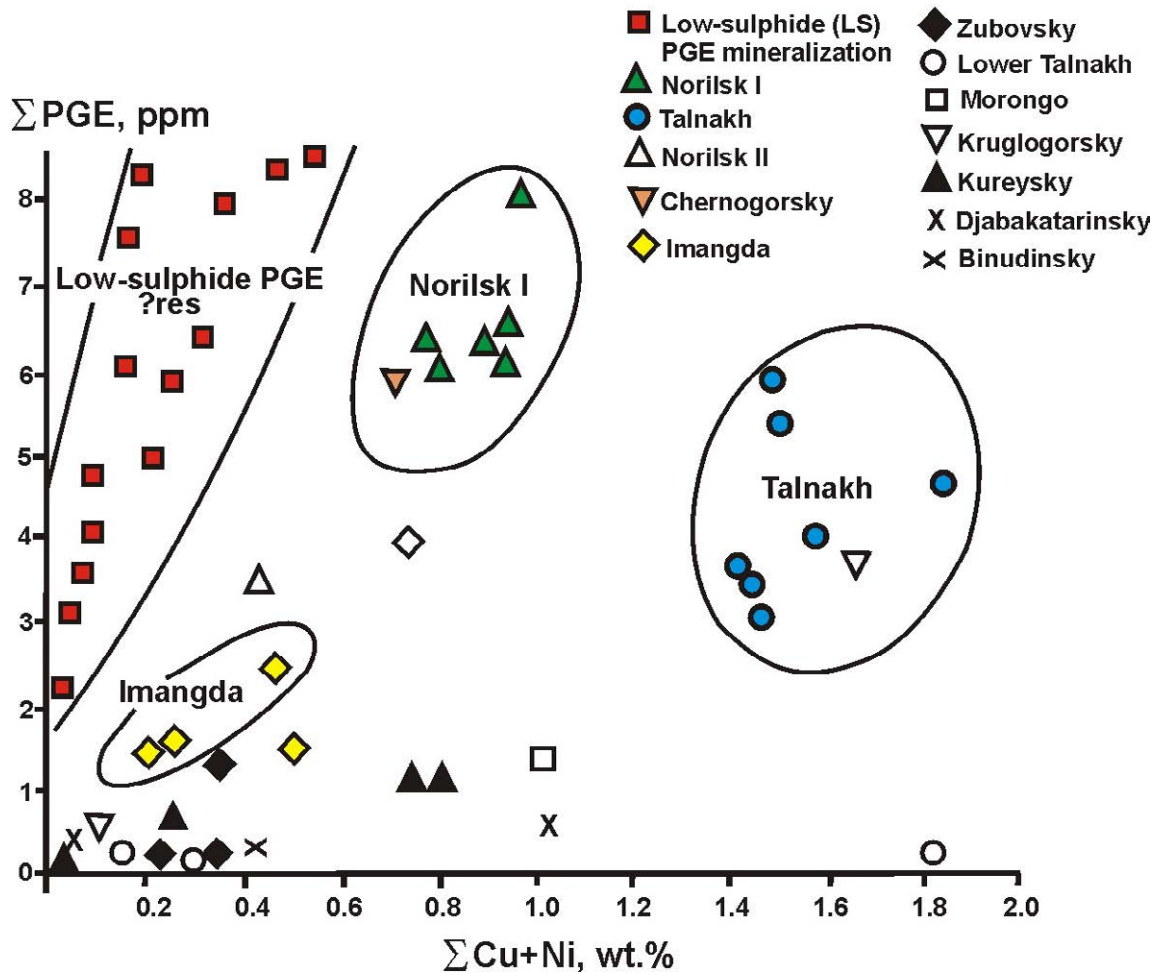


Figure 2. Plot of Σ PGE (ppm) vs Σ Cu+Ni (wt %) for the layered intrusions of the Noril'sk region

The PGE distribution in lateral and vertical sections of the low-sulphide horizon is irregular. The lateral irregularity is related to the uneven distribution of leucogabbroic rocks that host most PGE mineralisation, although elevated PGE grades also occur in irruptive breccia and gabbrodolerite. Some peak PGE grades in the vertical intersection are related to taxitic chromitiferous gabbroic lenses, which contain abundant volatile-rich minerals and productive sulphide assemblages (Fig. 1). PGE grade positively correlates with both the amount of volatile-rich minerals and the amount of Cr-spinel in bulk rock (Fig 1).

The dominant proportion of the PGE bulk content is related to discrete intermetallides, Fe-Pt alloys, sulphides, and sulpharsenides. The grain sizes of platinum-group minerals ranges 3-90 microns, but is predominantly 5-40 microns. Most platinum group minerals (90% of those observed) occur among H₂O-, Cl- and F-bearing minerals that replace sulphides.

4 Conclusions

The formation of the rock assemblage of the Upper Gabbroic Series is considered to be a consequence of differentiation of fluid-saturated melt in the intrusive magmatic chamber. Leucogabbroic evolved melts are enormously important for the development of low-

sulphide mineralisation, as they accumulate volatile compounds that decrease melting temperature. Preferential fractionation of trace elements, including noble metals and possibly chromium into fluid and their further transport as volatile compounds results to their concentration in leucogabbroic and taxitic horizons enriched regularly with all these components.

Acknowledgements

The study is partially supported by RFBR, grant 11-05-00014.

References

- Sluzhenikin SF, Distler VV, Dyuzhikov OA, Kravtsov VF, Kunilov VE, Laputina IP, Turovtsev DM (1994) Low sulphide platinum mineralization in the Noril'sk differentiated intrusive bodies. *Geol Ore Deposits* 36: 171-195
- Pokrovskiy BG, Sluzhenikin SF, Krivolutsкая NA (2005) Interaction conditions of Noril'sk trap intrusions with their host-pocks: isotopic (O, H, and C) evidence. *Petrology* 13: 49-72

The emplacement and relative timing of PGE mineralisation within the northern Bushveld Complex

Jennifer Smith, David Holwell

The Department of Geology, University of Leicester, University Road, Leicester LE1 7RH, UK

Adrian J. Boyce

Scottish Universities Environmental Research Centre, Rankine Avenue, East Kilbride, G75 0QF, UK

Iain McDonald

School of Earth and Ocean Sciences, Cardiff University, Park Place, Cardiff, CF10 3YE, UK

Abstract. The northern limb of the Bushveld Complex is currently a highly active area for both platinum-group element (PGE) exploration and research. Although the relationship of the Platreef with the rest of the Bushveld Complex is still debated, it is generally accepted that sulphur saturation occurred prior to emplacement at depth in a staging chamber. Therefore sulphides were not developed in situ but transported into the Platreef. The ultimate source of the mainstage of sulphides within the Platreef is equivocal (mantle or crustal), however, there is strong evidence from S isotopes of local ore modification, post emplacement. To the south of the Ysterberg-Planknek Fault, the PGE-bearing GNPA member is developed instead of the Platreef. In the first detailed S isotopic study on the GNPA member, it is clear that contamination by crustal S has been widespread with no evidence of a local footwall control. The timing of contamination relative to ore-genesis is complicated by the presence of mantle-like signatures associated with a limited number of the most primary sulphide phases. Thus, the isotopic data suggests a minor but early magmatic S source which was overridden by a strong, widespread crustal component which is evident throughout most of the GNPA member.

Keywords. Bushveld Complex, GNPA member, Platreef, sulphur saturation, contamination, sulphur isotopes, S/Se ratios

1 Introduction

The northern limb of the Bushveld Complex is host to the Platreef, the world's third largest PGE deposit. Platreef mineralisation is associated with a 10–400m thick package of pyroxenitic units, located at the base of the magmatic succession. From the town of Mokopane northward, the Platreef progressively transgresses through the Palaeoproterozoic Transvaal Supergroup (Sharman-Harris et al. 2005; van der Merwe 2008) to rest on Archaean basement in the far north (Fig. 1).

The genesis of Platreef mineralisation is ascribed to primary orthomagmatic processes involving: (i) separation of a sulphide liquid; (ii) enrichment and upgrading of the sulphide melt through repeated interaction with large volumes of magma in a staging chamber; and (iii) entrainment and transport of the PGE enriched sulphides into the Platreef (Lee 1996; McDonald and Holwell 2007; Holwell et al. 2007). Although it is agreed S saturation occurred prior to emplacement, the source of S responsible is less clear. Holwell et al. (2007) suggested a purely magmatic

origin with the addition of crustal S acting only as a local ore-modifying process. A more recent study however has proposed that early, widespread contamination by crustal S at depth was essential in ore-formation (Ihlenfeld and Keays 2011).

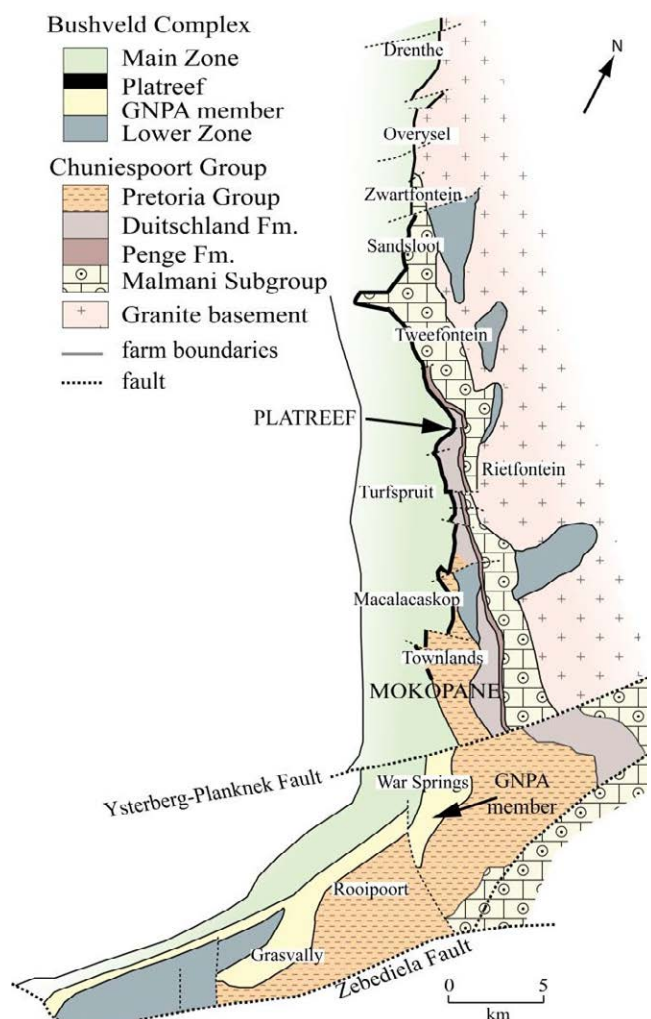


Figure 1. Geological map of the northern limb of the Bushveld Complex

To the south of the Ysterberg-Planknet Fault, the PGE-bearing Grasvally Norite-Pyroxenite-Anorthosite (GNPA) member is developed instead of the Platreef. The GNPA member comprises a 400–800m thick layered package of mafic cumulates dominated by gabbronorite, norite, anorthosite and pyroxenite. Two laterally continuous PGE-rich chromitites are also

developed towards the base of the succession.

At present it remains unclear whether the GNPA member represents a facies of the Platreef (von Gruenewaldt et al. 1989; van der Merwe 2008) or a completely distinct ore-body. This paper elucidates the genesis of the GNPA mineralisation, by demonstrating the significant role crustal S played in ore-formation. We also discuss the relative timing of contamination and S saturation in comparison to those ideas described for the Platreef (Holwell et al. 2007; McDonald and Holwell 2007; Ihlenfeld and Keays 2011).

2 Sulphur saturation

2.1 Inducing S saturation

Sulphur saturation and the development of an immiscible sulphide liquid is a fundamental process for concentrating economic volumes of PGE, Ni and Cu within a magmatic system. The assimilation of crustal S is considered by many as being essential in inducing S saturation (Leshner and Groves 1986), and thus is believed to be the most practical mechanism for producing the extraordinary quantities of sulphide required to form giant magmatic ore deposits such as the Bushveld Complex (e.g., Li et al. 2002).

However, in low-S systems like the Bushveld, sulphur saturation can also be achieved through a number of other mechanisms, these include; contamination by silica through assimilation of felsic rocks; increasing the f_{O_2} through assimilation of oxygen bearing rocks, both contamination processes lower FeO content and thus the S-carrying capacity of the magma; low pressure fractionation; and mixing of compositional distinct undersaturated magmas (see review by Maier 2005).

2.2 Application of S isotopes – The Platreef

Sulphur isotopes ($\delta^{34}S$) provide an opportunity to assess the role externally derived S plays in the development of PGE-bearing sulphides. Mantle derived S is dominated by $\delta^{34}S$ around $0 \pm 2\%$ (Omhoto and Rye, 1979), thus if the isotopic composition of country rock S is distinct from that of the mantle then a quantitative estimate of S assimilation can be determined.

If sulphide saturation is driven solely by contamination by external S, then a crustal S component should be evident (e.g., Noril'sk) in all sulphides (early and late forming). Within the Platreef, Holwell et al. (2007) found that the earliest formed sulphides exhibit values consistent with mantle S. Secondary sulphides were found to have a wider isotopic range of $\delta^{34}S$ -2 to +11%. From this data it was concluded that the addition of crustal S was not critical to primary ore genesis, with the higher values attributed to local contamination of S acting only to modify pre-existing sulphides.

Mantle S dominance has however been recently challenged by Ihlenfeld and Keays (2011). They argue from geochemical data, for an early, pre-emplacement contamination event, proposing mantle-like isotopic signatures were attained during ascent of the magma through isotope exchange.

3 GNPA mineralisation

3.1 Style and nature of mineralisation

Platinum-group element mineralisation within the GNPA member is also thought to result from primary orthomagmatic processes. The initial style of base-metal sulphide (BMS) and PGE mineralisation is consistent with fractionation of a sulphide liquid (Holwell and McDonald 2010) and is characterised by the primary sulphide assemblage pyrrhotite-chalcocopyrite-pentlandite (Fig. 2a) with magmatic Pt-As and Pd-Bi-Te dominated platinum-group mineral assemblage. Low temperature alteration has altered much of the primary mineralogy developing pyrite dominated assemblages (Smith et al. 2011; Fig. 2b) with associated Sb-bearing PGM. This alteration has also resulted in the preferential remobilisation of Pd and Au.

The GNPA member, like the Platreef, is irregularly mineralised and is also a Pd-dominant deposit, with Pt/Pd ratios typically <1 . PGE grades are generally lower than the Platreef and highly variable ranging from 1-4 ppm. The mineralised horizons cannot be correlated with confidence along strike or down dip.

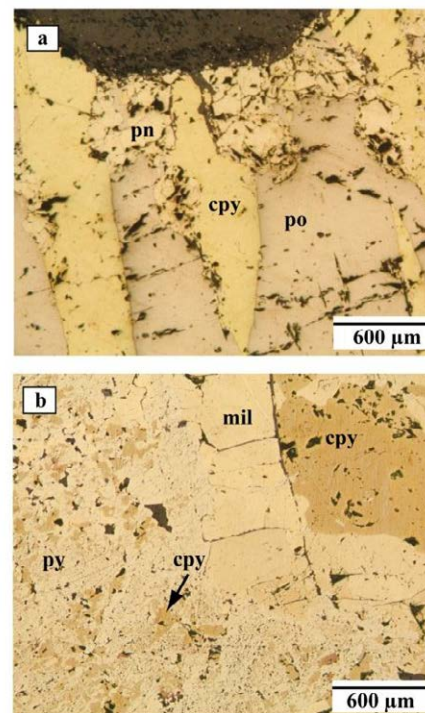


Figure 2. a) primary sulphide, dominated by pyrrhotite (po) with chalcocopyrite (cpy) exsolution flames and pentlandite (pn) around the margins and b) secondary sulphide with pyrite (py) and millerite (mil) replacing primary phases

3.2 Sulphur isotopes

We have performed the most detailed and comprehensive S isotope study on the GNPA member, with over 110 analyses from Warsprings, Rooipoort and Grasvally (Fig. 1). The dominance of signatures distinctly greater than those typical of the local mantle S, inferred from the Klipspringer kimberlite ($\delta^{34}S$ -1.8‰ to +2.4‰; Fig. 3;

Westerlund et al. 2004), indicates that the GNPA member has been extensively contaminated. A crustal S component is evident in both the early (pyrrhotite, chalcopyrite and pentlandite) and late (pyrite and millerite) forming sulphide phases with values reaching up to $\delta^{34}\text{S} +6\text{‰}$ (Fig. 3). It should also be noted even where the GNPA member is directly underlain by Lower Zone cumulates, all the primary sulphides analysed exhibit slightly heavier signatures than the mantle range. There is no indication isotopic values systematically increase with depth where pyrite-bearing quartzites form the footwall.

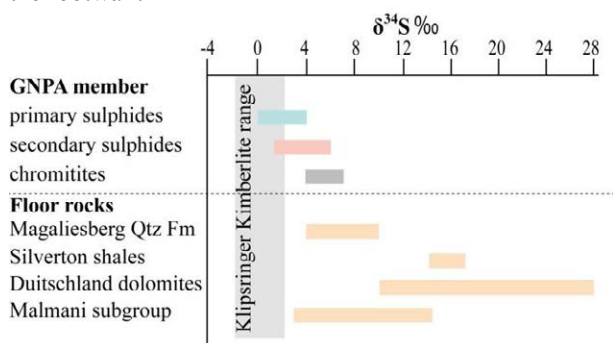


Figure 3. Range in S isotope values for sulphides within the GNPA member and footwall lithologies. Values of the mantle beneath the Bushveld are provided by the Klipspringer kimberlite.

Although the GNPA member has a strong contaminated signature, values consistent with mantle S ($\delta^{34}\text{S} 0 \pm 2\text{‰}$) were identified within a small number of primary and secondary sulphide analyses (<15 in total). Within a single sulphide bleb both crustal and magmatic signatures are occasionally preserved (Fig. 4) with the latter generally associated with relicts of the primary assemblage (mainly pyrrhotite and chalcopyrite). The distribution/preservation of mantle signatures is completely random within the GNPA member, with no evidence of a local footwall control over their distribution.

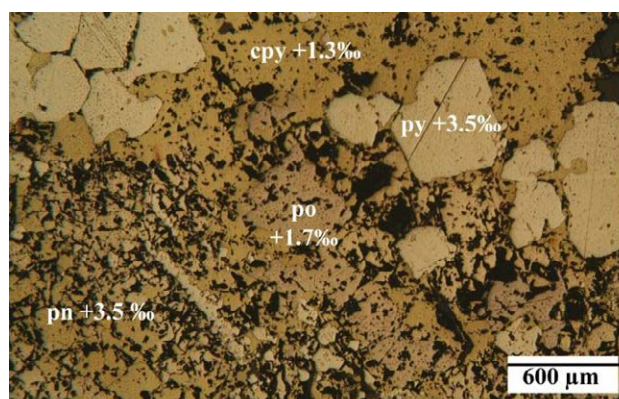


Figure 4. Relicts of primary chalcopyrite (cpy) and pyrrhotite (po) which retain mantle S signatures. Later overprinting pyrite (py) and pentlandite (pn) exhibit crustal S values.

The chromitites are interesting in that their sulphides consistently appear 1-2‰ heavier than the rest of the GNPA member, being characterised by $\delta^{34}\text{S} +4$ to $+7\text{‰}$ (Fig. 3). This is a wide-scale feature of the GNPA member, identified on Grasvally, Rooipoort and

Warsprings.

Although not present in abundance, sulphides have also been found to occur within the Magaliesberg Quartzite Formation which underlies part of the GNPA member. This study has shown that isotopically they are distinct from mantle S, ranging from $\delta^{34}\text{S} +4$ to $+10\text{‰}$. Sulphides interpreted to have migrated into the floor rocks, exhibit values consistent with those contaminated within the GNPA member varying between $\delta^{34}\text{S} +3$ to $+5\text{‰}$.

In addition to S isotopes, the role of crustal contamination in the formation of magmatic sulphides can also be independently assessed using S/Se ratios (Eckstrand and Hulbert 1987). Using laser-ablation-ICP-MS we have also quantified the Se content of the individual sulphide grains and therefore, for the first time, we are able to directly compare S/Se ratios with S isotopic signatures on a mineralogical scale. In general, the most primary phases reveal S/Se ratios within the mantle range (2000–4000; Eckstrand and Hulbert 1987) with higher values indicative of contamination associated with later pyrite, which broadly correlate with the S isotope signatures. In detail, however, this correlation is rather more complicated with composite primary sulphide grains showing both mantle and contaminated S/Se ratios. Furthermore, our study has also revealed that low S/Se values do not always correspond to those isotopic signatures consistent with mantle S. This highlights that the application of just one of these proxies in assessing crustal contamination and the subsequent interpretations of such data should be treated with caution.

4 Discussion

Sulphur isotopic data are consistent with the addition of crustal S into the GNPA magmatic system. Determining the timing of contamination relative to ore genesis is however complicated by the complex nature of the isotopic results. Thus it is only when the isotope data is combined with other techniques such as S/Se ratios (which are currently being determined for the GNPA member) that we are able to fully comprehend the role crustal S played within the magmatic system.

When considering only the S isotopic data, the key findings of this study are; (i) the presence of mantle S signatures in association with relicts of primary sulphides; (ii) strong crustal S component within both primary and secondary sulphides; and (iii) the extensive nature of contamination. It is important that any future ore genesis model for the GNPA member accounts for all of these interesting features.

Although we are yet to fully constrain whether mineralisation within the GNPA member was generated in a similar manner to that proposed for the Platreef (staging chamber model; Lee 1996; McDonald and Holwell 2007; Holwell et al. 2007) the S isotope data is rather comparable to that documented for parts of the Platreef by Holwell et al. (2007). From the results presented here it is clear that within the GNPA member there was an early magmatic S source, from which the first sulphides (those with mantle signatures) formed. Although it is currently unclear whether contamination

occurred at depth prior to emplacement or in situ, it is thought that the magmatic source was overwhelmed by a genetically important crustal component which is seen to dominate sulphides throughout the GNPA member. As all our results exhibit positive $\delta^{34}\text{S}$, the underlying sediments of the Palaeoproterozoic Transvaal Supergroup represent a likely source of crustal S as they too are dominated by positive $\delta^{34}\text{S}$ (Fig. 3).

Acknowledgements

We thank Caledonia Mining Corporation, in particular Trevor Pearton, for access to the drillcore. Jennifer Smith's PhD is funded by NERC (NE/1528426/1).

References

- Eckstrand OR, Hulbert LJ (1987) Selenium and the source of sulfur in magmatic nickel and platinum deposits. *Geol Assoc Canada/Mineral Assoc Canada: Program with Abstracts* 12:40
- Ihlenfeld C and Keays RR (2011) Crustal contamination and PGE mineralisation in the Platreef, Bushveld Complex, South Africa: evidence for multiple contamination events and transport of magmatic sulphides. *Min Dep* 47:1011-1026
- Lee CA (1996) A review of mineralisation in the Bushveld Complex and some other layered intrusions. In: Cawthorn G (ed) *Layered Intrusions*, Elsevier, pp103-146
- Leshner CM and Groves DG (1986) Controls on the formation of komatiite-associated nickel-copper sulphide deposits. In: Friedrich GH, et al. (eds) *Geology and Metallogeny of Copper Deposits*. Proc. 25th Int. Geol. Congr., Moscow, Springer, Berlin (1986), pp 43–62
- Li C, Ripley EM, Maier WD, Gomwe TES (2002) Olivine and S isotopic compositions of the Uitkomst Ni-Cu sulfide ore-bearing complex, South Africa: Evidence for S contamination and multiple magma emplacements. *Chemical Geology* 188: 149–159
- Holwell DA, Boyce AJ and McDonald I (2007) Sulfur isotope variations within the Platreef Ni-Cu-PGE deposit: Genetic Implications for the origin of sulfide mineralisation. *Econ Geol* 102:1091–1110
- Holwell DA and McDonald I (2010) A Review of the Behaviour of Platinum Group Elements within Natural Magmatic Sulfide Ore Systems. *Platinum Metals Rev* 54: 26-36
- Maier WD (2005) Platinum-group element (PGE) deposits and occurrences: Mineralisation styles, genetic concepts and exploration criteria. *Journ Afr Earth Sci* 41: 165-191
- McDonald I and Holwell DA (2007) Did Lower Zone magma conduits store PGE-rich sulphides that were later supplied to the Platreef?, *South Afr Journ Geol* 110:611-616
- Ohmoto H, Rye RO (1979) Isotopes of sulfur and carbon. In: BarnesHL (ed) *Geochemistry of hydrothermal ore deposits*, 2nd ed: London, Wiley and Sons, pp 509–567
- Sharman-Harris, et al., (2005) A new look at sulfide mineralisation of the northern limb, Bushveld Complex: A stable isotope study. *Appl Earth Sci (Trans Inst Min Metall B)* 114: B252–B263
- Smith JW, Holwell DA and McDonald I (2011) The mineralogy and petrology of platinum–group element-bearing sulphide mineralisation within the Grasvally–Norite–Pyroxenite–Anorthosite (GNPA) member, south of Mokopane, northern Bushveld Complex, South Africa. *Appl Earth Sci (Trans Inst Min Metall B)* 120: B158–B174
- Van der Merwe MJ (2008) The geology and structure of the Rustenburg Layered Suite in the Potgietersrus/Mokopane area of the Bushveld Complex, South Africa. *Min Dep* 43: 405-419
- Von Gruenewaldt G, Hulbert LJ and Naldrett AJ (1989) Contrasting platinum group element concentration patterns in cumulates of the Bushveld Complex. *Min Dep* 24: 219-229
- Westerlund KJ, Gurney JJ, Carlson RW, Shirey SB, Hauri EH, Richardson SH (2004) A metasomatic origin for late Archean eclogitic diamonds: Implications from internal morphology of diamonds and Re-Os and S isotope characteristics of their sulfide inclusions from the Late Jurassic Klipspringer kimberlites. *South African Journal of Geology* 107:119–130

(sulfate) to S^{2-} (sulfide) is an 8 electron exchange, and if this is to be driven by conversion of Fe^{2+} to Fe^{3+} (one electron), 8 moles of Fe need to be converted for every mole of S. Magnetite crystallisation is a somewhat inefficient reductant of sulfate, because of this 8/1 mole ratio. However, despite its inefficiency, crystallisation of moderately abundant magnetite is still effective in causing sulfate reduction to sulfide because the proportion of S dissolved in the melt is typically significantly lower than 1 %, whereas the proportion of magnetite crystallised can be significantly higher.

2.2 Graphite-induced saturation

We studied the Opirarukaomappu Gabbroic Complex (OGC) in the Hidaka metamorphic belt, Hokkaido, Japan. This region preserves a tilted arc cross section and the OGC represents a deep crustal magma mixing zone where arc basalt magma intruded into the base of the arc, mixing with tonalitic magmas derived from adjacent granulite facies metamorphic rocks. Some of the migmatitic metasedimentary rocks contain significant amounts of graphite, as do some of the tonalities, gabbros and massive sulfide bodies within the gabbro; the C isotope signature of graphite in these intrusive rocks matches that in the graphitic migmatites (Tomkins et al., 2012).

We performed redox budget modelling (see Evans, 2006; 2012) to evaluate the reducing effect of adding graphite to oxidised arc basalt. This method is essentially a mass balance-based approach that takes into account the number of moles of reductants and oxidants in a model system. In the case of adding graphite to a relatively oxidised environment, reduction proceeds as C is oxidised to CO_2 , which is a 4 electron exchange (at magmatic conditions in the deep crust the graphite buffer is significantly more reduced than FMQ; Fig. 1). Using the redox budget approach we found that relatively little graphite would be needed to reduce even highly oxidised basalts with a high proportion of dissolved sulfate (Figs. 2 and 3). Moderately oxidised magmas with lower

mixing involving felsic melt containing 1% graphite, and the second with felsic melt containing 0.5% graphite. The basalt end-member (basalt x) contains 1% S and has fO_2 at FMQ+2. For comparison, the saturation curve for MORB basalt is shown in grey (basalt z). From Tomkins et al. (2012).

sulfate are easier to reduce to the point of sulfide saturation. The observation of graphite in gabbros and semi-massive sulfide accumulations indicates that these magmas were reduced to the graphite buffer, whereas the tectonic setting implies that the basaltic magma was likely initially relatively oxidised.

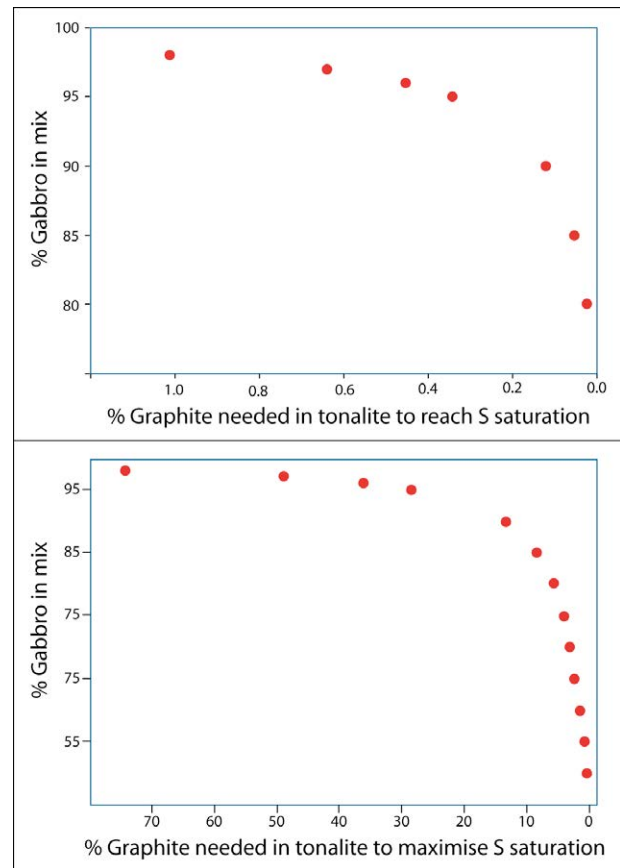


Figure 3. The proportion of graphite needed in tonalite mixing with gabbro (at FMQ+2 containing 1% S as sulfate), to bring on sulfide saturation (top diagram), and to maximise sulfide saturation (bottom diagram).

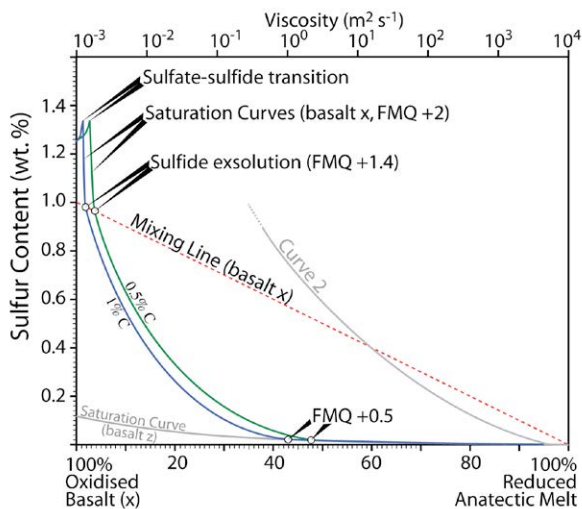


Figure 2. The effect of mixing graphite-bearing crustal felsic melt with oxidised basaltic melt on the solubility of sulfur in the mixture. Two sulfur saturation curves are shown, one for

Because very little graphite is needed to bring on sulfide saturation, this can be achieved with only minor assimilation of graphitic rocks, or mixing with graphitic magma, and so the magma can still be gabbroic and of low viscosity when sulfide exsolves, allowing gravitational separation. Furthermore, this information also implies that highly supersaturated magma could conceivably be developed suddenly and at relatively large scales. Highly supersaturated magmas tend to exsolve numerous small globules of sulfide, rather than sparse large globules, and the combination of high surface area and abundance would tend to extract metals efficiently from the magma. The downside of this high number density of sulfide globules is that a lower R factor results, because individual globules compete with each other in diffusive sequestration of metals (Mungall

2002). Although, in a turbulent, or migrating magmatic system, small sulfide droplets are likely to interact with a larger volume of silicate magma, and may thereby still develop relatively high R.

3 New Concepts in Magmatic Sulfide Formation from Arc Magmas

3.1 Other triggers of RISS?

The question of whether there are other factors that can trigger RISS requires consideration of, (1) the possible reducing contaminants that could be introduced to an arc basalt, or (2) whether there are oxidised minerals, other than magnetite, that could crystallise from arc basalt.

Dehydration melting of biotite in metasedimentary and metavolcanic rocks (which generates voluminous felsic magmas) generates minor ilmenite as part of the melting reaction because biotite typically contains > 4% TiO₂. Stoichiometric ilmenite (FeTiO₃) contains iron only as Fe²⁺, although there is solid solution with magnetite, so it can contain some Fe³⁺. Small crystals of peritectic phases like ilmenite can be incorporated in felsic magmas escaping from their migmatitic source regions (Tomkins et al. 2009; Clemens & Stevens 2012). Addition of ilmenite from this source via assimilation or magma mixing would cause some reduction of an oxidised arc basalt. However, given the minor quantities generated by biotite melting and the even lower proportion incorporated into escaping felsic melts, ilmenite is unlikely to cause sufficient reduction at a large scale.

Because of its abundance, Fe is one of the most effective reductants available in the crust. Magmas generated by partial melting of the crust can contain a significant proportion of Fe, particularly those generated by the hotter stages of dehydration melting. Some of these crustal magmas are generated in the presence of graphite and so the Fe³⁺/ΣFe of any escaping magma is low. Similarly, magmas generated in equilibrium with ilmenite are expected to be reduced. When these reduced and relatively Fe-rich crustal magmas interact with oxidised arc basalt equilibration of the Fe³⁺/Fe²⁺ will drive reduction of the basalt. Redox budget modelling suggests that if the Fe contents of the arc basalt and crustal magma are similar, magma mixing can drive RISS via this mechanism, particularly where mixing involves significant proportions of crustal magma.

Adding crust derived sulfide to arc basalt has the combined effect of increasing the proportion of sulfur and reducing the oxidation state. Sulfide can be carried from a crustal source region in anatectic magmas (Tomkins & Mavrogenes 2002; Tomkins et al. 2009).

Crystallisation of anhydrite from the magma would drive the oxidation state of the melt towards sulfide saturation. However, anhydrite crystallisation is unlikely to occur early in the fractionation history of a basaltic magma, and is thus insignificant to formation of magmatic sulfide systems. It may, however, play a role in porphyry Cu deposit genesis.

3.2 On the metal content of RISS-related sulfides

Fractionation of oxidised basaltic magma leads to enrichment of sulfur well beyond that possible in reduced systems, and coincident removal of Ni in olivine. So, if sulfide saturation occurs after Ni-removal, high Cu/Ni ores could potentially form. Jenner et al. (2010) recognised this point, suggesting that bornite-like sulfide would evolve from the Pual Ridge magmas. A significant difference between magnetite-induced and graphite-induced reduction is that graphite can be added to the system at any point in the fractionation, so if reduction happens before olivine fractionation sulfides can be Ni-rich, whereas reduction after olivine fractionation would produce high Cu/Ni ores. The massive to disseminated sulfides in the OGC are relatively low in Ni and somewhat enriched in Cu, but are dominated by pyrrhotite.

The OGC sulfides also contain appreciable proportions of cobaltite, and the As needed to form this mineral would come from the carbonaceous shales that sourced the tonalite because these sediments contain 1-4 orders of magnitude more As than the mantle (cf. McDonough and Sun 1995; Lee et al. 1998). Development of high-As sulfide liquids is important because As-rich sulfosalt melt can exsolve from sulfide and partition PGE, allowing focussed accumulation of these elements (Tomkins, 2010).

3.3 Issues with ore formation after saturation

The problem with all forms of RISS is that the process tends to inhibit the possibility of gravitational sulfide separation. Magnetite crystallisation occurs after some fractionation, so the magma will be more viscous and the sulfide droplets will have a suspension of crystals to navigate during settling. Graphite contamination requires assimilation or magma mixing both of which cool the magma and increase its viscosity. Furthermore, to form a large mineral deposit sulfide must accumulate from a large volume of magma (Ripley & Li, 2013), so RISS has to be effective across the required volume. To be effective as an agent of ore formation RISS has to occur across a large volume at a stage of magma evolution that allows separation of sulfide, and this would be most likely where minimal contamination is required to bring on sulfide saturation, or where only minor magnetite crystallisation is required.

3.4 Implications for temporal distribution of deposits

Evans and Tomkins (2011) showed that Archean and Proterozoic subduction is unlikely to have led to generation of oxidised arc basalts. This is because in the modern Earth much of the oxidising potential of subducting slabs is inherited from sea floor metasomatism by sulfate-bearing sea water; the deep oceans contained little sulfate prior to ~ 550 Ma (see Scott et al. 2008; Planavsky et al. 2011; Farquhar et al. 2010; Tomkins 2013). Slab derived sulfate is likely to be responsible for much of the oxidation of the mantle

wedge (Evans and Tomkins, 2011). If it is correct that Precambrian arc basalts were not oxidised, and it should be noted that this is not yet firmly established (see Malmann & O'Neill, 2009; Evans et al. 2012), then ore deposits that form through RISS would not be found in rocks older than ~ 550 Ma. More work is needed on establishing the oxidation state of Precambrian arc basalts.

4 Summary – an idealised scenario

By way of summarising our findings we envisage an idealised situation for forming an arc-hosted magmatic sulfide deposit as follows. In the Phanerozoic, a large volume of oxidised basalt (perhaps ~ FMQ+2) intrudes into the lower crust of a continental arc, inputting a large amount of heat into the crust and starting to crystallise olivine. This heat input causes widespread high temperature dehydration melting of surrounding graphitic sulfidic metasedimentary rocks, generating a felsic magma that equilibrates with graphite ensuring a low $Fe^{3+}/\Sigma Fe$, but potentially still elevated Fe content. This crustal magma escapes its source region taking with it graphite, ilmenite and iron sulfide. The basaltic magma fractionates but does not quite reach the point of magnetite crystallisation, leaving behind olivine and Ni, becoming enriched in S (up to 1.5%), Cu and PGE. These two magmas mix, perhaps in a mid-crustal magma chamber, at a high proportion of basaltic to crust-derived magma (> 90% basalt). The graphite, ilmenite, sulfide and low $Fe^{3+}/\Sigma Fe$ in the contaminating crustal magma drive rapid reduction and a high degree of sulfide saturation throughout the mixture. Numerous small sulfide droplets exsolve and efficiently scavenge Cu and PGE, and these are then carried upward along narrow conduits in a fresh surge of magma migration triggered by the mixing event, promoting a high R factor. Sulfides then accumulate in slow flow domains in the mid to upper crust allowing formation of PGE rich, high Cu/Ni ores. Erosion of the arc to a level of isostatic equilibrium brings the mid to upper crustal mineral deposits into a position where they are exposed at the surface.

Acknowledgements

We thank in Ryo Anma and Hiroyuki Kamiyama for assistance during the planning and execution stages of fieldwork in Japan, and subsequently with various enquiries. Ian Nichols and Louise Edwards are thanked for editing and helpful comments regarding the igneous petrology. Katy Evans is gratefully acknowledged for discussion on redox budget modeling.

References

Carroll MR, Rutherford MJ (1985) Sulfide and sulfate saturation in hydrous silicate melts. *J Geophys Res* 90:C601–C612
 Carroll MR, Rutherford MJ (1987) The stability of igneous anhydrite: experimental results and implications for S behavior in the 1982 El Chichón trachyandesite and other evolved magmas. *J Pet* 28:781–801
 Evans KA (2006) Redox decoupling and redox budgets: Conceptual tools for the study of earth systems. *Geology* 34:489–492

Evans KA (2012) The redox budget of subduction zones. *Earth Sci Rev* 113:11–32
 Evans, K. A., Elburg, M. A. & Kamenetsky, V. S., 2012. The oxidation state of sub-arc mantle. *Geology* 40, 783–786
 Evans KA, Tomkins A, (2011) The relationship between subduction zone redox budget and arc magma fertility. *Earth Planet Sci Lett* 308:401–409
 Farquhar J, Wu N, Canfield DE, Oduro H (2010) Connections between sulfur cycle evolution, sulfur isotopes, sediments, and base metal sulfide deposits. *Econ Geol* 105:509–533
 Jenner FE, O'Neill HSC, Arculus RJ, Mavrogenes JA (2010) The magnetite crisis in the evolution of arc-related magmas and the initial concentration of Au, Ag and Cu. *J Pet* 51:2445–2464.
 Jugo PJ, Luth RW, Richards JP (2005) An experimental study of the sulfur content in basaltic melts saturated with immiscible sulfide or sulfate liquids at 1300°C and 1.0 GPa. *J. Pet* 46:783–798
 Jugo PJ, Wilke M, Botcharnikov RE (2010) Sulfur K-edge XANES analysis of natural and synthetic basaltic glasses: Implications for S speciation and S content as function of oxygen fugacity. *Geochim Cosmochim Acta* 74:5926–5938
 Keays RR, Lightfoot PC (2010) Crustal sulfur is required to form magmatic Ni-Cu sulfide deposits: Evidence from chalcophile element signatures of Siberian and Deccan Trap basalt. *Min Deposita* 45:241–257
 Lee J-S, Chon H-T, Kim J-S, Kyoung-Woong Kim K-W, Moon H-S (1998) Enrichment of potentially toxic elements in areas underlain by black shales and slates in Korea. *Env Geochem Health* 20:135–147
 Malmann, G., and O'Neill, H.S.C., 2009, The crystal/ melt partitioning of V during mantle melting as a function of oxygen fugacity compared with some other elements (Al, P, Ca, Sc, Ti, Cr, Fe, Ga, Y, Zr and Nb): *Journal of Petrology*, v. 50, p. 1765–1794
 McDonough WF, Sun S-s (1995) The composition of the Earth. *Chem Geol* 120:223–253
 Mungall JE (2002) Kinetic controls on the partitioning of trace elements between silicate and sulfide liquids. *J Pet* 43:749–768
 Planavsky NJ, McGoldrick P, Scott C, Li C, Reinhard CT, Kelly AE, Chu X, Bekker A, Love GD, Lyons TW (2011) Widespread iron-rich conditions in the mid-Proterozoic ocean. *Nature* 477:448–451
 Ripley EM, Li C (2013) Sulfide saturation in mafic magmas: Is external sulfur required for magmatic Ni-Cu-(PGE) ore genesis? *Econ Geol* 108:45–58
 Scott C, Lyons TW, Bekker A, Shen Y, Poulton SW, Chu X, Anbar AD (2008) Tracing the stepwise oxygenation of the Proterozoic ocean. *Nature* 452:456–459
 Tomkins AG, (2010) Wetting facilitates late-stage segregation of precious metal-enriched sulfosalt melt in magmatic sulfide systems. *Geology* 38:951–954
 Tomkins AG (2013) A biogeochemical influence on the secular distribution of orogenic gold. *Econ Geol* 108:192–196
 Tomkins AG, Mavrogenes JA (2002) Mobilization of gold as a polymetallic melt during pelite anatexis at the Challenger gold deposit, South Australia: A metamorphosed Archean deposit. *Econ Geol* 97:1249–1271
 Tomkins AG, Rebryna KC, Weinberg RF, Schaefer BF (2012) Magmatic sulfide formation by reduction of oxidised arc basalt. *J. Pet.* 53:1537–1567
 Tomkins AG, Weinberg RF, McFarlane CRM (2009) Preferential magma extraction from K- and metal-enriched source regions in the crust. *Min Deposita* 44:171–181
 Clemens JD, Stevens G (2012) What controls chemical variation in granitic magmas? *Lithos* 134–135: 317–329

Geology and stratigraphy of the Black Thor and Black Label chromite deposits, James Bay Lowlands, Ontario, Canada

Ryan J. Weston

Cliffs Natural Resources Inc., 200 - 1159 Alloy Drive, Thunder Bay, Ontario, Canada, P7B 6M8

David A. Shinkle

Cliffs Natural Resources Inc., 200 - 1159 Alloy Drive, Thunder Bay, Ontario, Canada, P7B 6M8

Abstract. The Black Thor and Black Label Chromite Deposits are situated within the Neoproterozoic McFaulds Lake greenstone belt at the contact between a granodiorite pluton and metavolcanic rocks. The deposits occur within a steeply dipping, over-turned layered ultramafic sill up to 1.5 km thick by over 3 km long, which is part of a regional volcanic-intrusive complex known as the 'Ring of Fire' ultramafic-mafic intrusive suite. The sill consists of cyclically layered dunite to peridotite progressing upward to olivine-pyroxenite, feldspathic pyroxenite, and gabbro. Cumulus chromite occurs throughout much of the stratigraphy but is most abundant in two principal horizons: Black Label and Black Thor. The sill is largely overlain by, and is in fault contact with, an altered leucogabbro of uncertain relationship to the ultramafic sequence.

Black Thor represents ~95% of the chromite mineral resource and occurs as a continuous thickly-bedded chromitite horizon at the transition from olivine-dominant to pyroxene-dominant lithologies. Mineralization in the Black Label horizon is located stratigraphically below Black Thor and occurs as discontinuous layers of semi-massive to massive chromitite within peridotite and dunite that are disrupted and brecciated by a late websterite intrusion. This intrusion is interpreted to represent the final stage of ultramafic magmatism within the sill.

Keywords. Black Thor, Black Label, chromite, Ring of Fire, McFaulds Lake

1 Introduction

The Black Thor and Black Label Chromite Deposits were discovered in 2008 and 2009, respectively, by Freewest Resources Inc. while exploring for magmatic Ni-Cu-PGE mineralization following the 2007 discovery of the Eagle's Nest Ni-Cu-PGE Deposit located 8 km to the southwest. The current estimate of chromite mineralized material at Black Thor is >100Mt at ~31% Cr₂O₃ to a depth of approximately 400 m below surface. Recent deep drilling continues to intersect wide zones of high-grade (>20% Cr₂O₃) mineralization at Black Thor to depths of greater than 650 m below surface, indicating the deposit remains open at depth, and making this one of the most significant chromite discoveries in recent time.

These deposits are located within the remote James Bay Lowlands of Northern Ontario, Canada. They lie within a northeast striking, steeply dipping ultramafic sill located at the contact between a foliated granodiorite pluton, dated at 2773 Ma (Mungall et al. 2010), and mafic metavolcanic rocks of the Muketei River Supracrustal Package (Metasaranta and Houlié 2012) with age dates ranging between 2737-2770 Ma

(Rayner and Stott 2005; Mungall et al. 2011). Several other chromite-mineralized ultramafic intrusions (e.g. Big Daddy, Blackbird) of presumably similar age occur along strike to the southwest at, or in close proximity to the granodiorite-metavolcanic contact.

While no age date has been acquired for the ultramafic sill, a potentially co-eval ferrogabbro sill was dated at 2734 Ma by Mungall et al. (2010), suggesting an association with the younger volcanic sequences of the Muketei River Supracrustal Package.

2 Property geology and stratigraphy

The ultramafic sill hosting the Black Thor and Black Label Chromite Deposits is a funnel-shaped intrusion up to 1.5 km thick by greater than 3 km in strike (Figure 1). Based on the overall cumulate stratigraphy, a pronounced feeder conduit to the north, and the general regional trend, the intrusion is interpreted to be younging to the southeast with a near-vertical to slightly overturned dip to the northwest. Regional greenschist metamorphism has converted olivine-rich lithologies to an assemblage of serpentine-talc-magnetite, and pyroxene-rich lithologies to an assemblage of chlorite-talc-tremolite/actinolite. Despite the degree of metamorphism, however, orthomagmatic textures remain well preserved throughout most of the stratigraphy.

The intrusion is composed of olivine and pyroxene-dominant lithologies including dunite, lherzolite, olivine-pyroxenite, and websterite. Feldspar-bearing lithologies clearly associated with the ultramafic sill are poorly represented, and consist of feldspathic pyroxenite to gabbro preserved in the southwest portion of the property only.

Crude modal layering within the sill is evident in airborne magnetic surveys, with olivine-dominant lithologies occurring as pronounced magnetic highs (due to magnetite formation during serpentinization) and pyroxene-rich lithologies occurring as magnetic lows. Finer scale layering is observed in drill core, with cumulate modal layering of olivine, chromite and pyroxene-rich layers defining several fractionation cycles.

The intrusion is separated into three principal stratigraphic divisions, illustrated in Figures 1 and 2, based on the large-scale appearance of chromite and presence (or absence) of olivine.

1. *Lower Ultramafic sequence:* Estimated to average approximately 400 m in thickness, but up to 900 m thick, this sequence forms the base of the funnel-shaped intrusion and is dominated by dunite and lherzolite

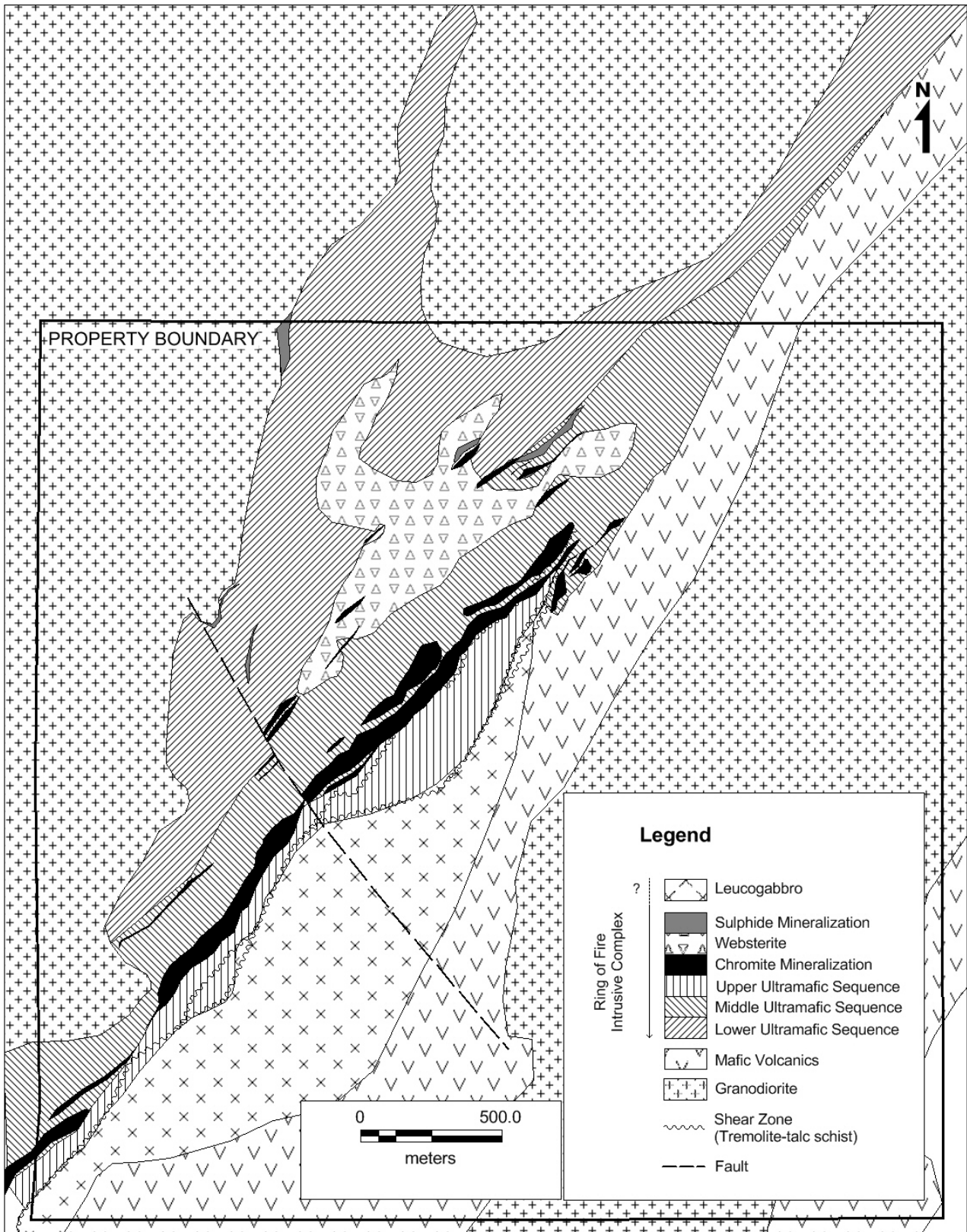


Figure 1. Simplified geology map of the Black Thor and Black Label deposit

lithologies that are largely barren of chromite mineralization. The upper contact is defined as the onset of large-scale chromite mineralization associated with the Black Label Chromite Deposit. Basal phases of this sequence locally host magmatic Ni-Cu-PGE sulphides. The sequence is cross-cut by a sizeable late-stage websterite body described in greater detail below.

2. Middle Ultramafic sequence: Estimated to average approximately 200 m in thickness, this sequence is dominated by dunite and lherzolite lithologies with chromite as an accessory to minor cumulate mineral phase. The upper contact is defined as the onset of thick chromitite layers associated with the Black Thor

Chromite Deposit. The late-stage websterite body forms a sill largely along the base of this sequence.

3. *Upper Ultramafic sequence*: Estimated to be 50 m to 200 m in thickness, however, sheared upper and lower contacts preclude an accurate estimate of the original thickness. This sequence is dominated by lherzolite progressing upward to olivine pyroxenite and feldspathic pyroxenite to gabbro along the southwest margin of the intrusion. The late websterite body is absent from this sequence.

Confined to the lower and middle ultramafic sequences, the late-stage websterite body occurs as a funnel-shaped intrusion approximately 1500 m long by up to 700 m wide. It displays a remarkably similar form to its host sill with an inferred feeder conduit to the north, and flat sill-like upper contact preferentially along the Black Label horizon. Geophysically the websterite is manifest as a magnetic low, but gravity high (due to negligible pore-space). This unit is easily distinguished from other ultramafic lithologies by its coarser grain size, general lack of olivine, lighter colour (due to general lack of serpentine minerals) and weak magnetic susceptibility. Along its margins and within thin apophyses, the websterite is present as a magmatic breccia with oblate xenoliths of dunite/lherzolite and chromitite within a mixed matrix suggesting intimate co-mingling with a semi-crystalline host sill. Invariably, these magmatic breccia zones host disseminated sulphides which often contain significant Ni-Cu-PGE values.

3 Chromite mineralization

Chromite mineralization associated with the Black Thor horizon is present as thick (40 to 80 m) intervals of fine-grained, heavily disseminated to semi-massive to massive chromitite layers continuous along strike for 2.3 km with discontinuous mineralization occurring over a strike length greater than 3 km. The Black Thor horizon can be subdivided into three main domains along its strike. The southwest and northeast domains consist of two prominent chromitite layers separated by weakly mineralized dunite/lherzolite, while the central domain consists of multiple thinner chromitite horizons separated by dunite/lherzolite. Within the northeast domain, chromitite horizons appear to be structurally repeated along longitudinal faults roughly parallel to the stratigraphy.

Chromite mineralization associated with the Black Label horizon consists of thin (5 to 40 m) discontinuous layers of fine-grained, heavily disseminated to semi-massive and massive chromitite which can be traced intermittently along strike for 2.3 km. Where proximal to the late-stage websterite body, mineralization occurs within chromitite-bearing magmatic breccias and partly dismembered semi-massive to massive chromitite. Although largely absent from the centre of the late-stage websterite body, individual chromitite horizons present along its margins appear to be traceable across its length suggesting minimal vertical displacement of the Black Label horizon.

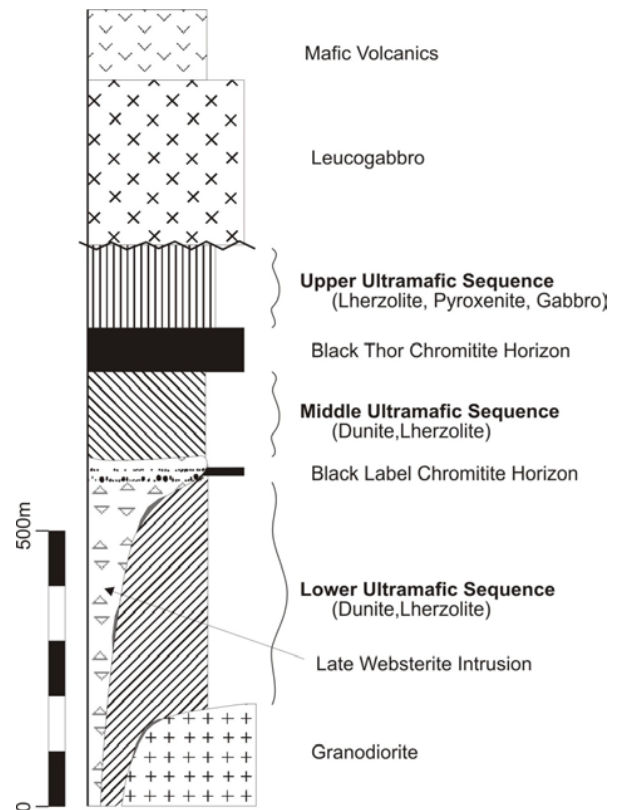


Figure 2. Simplified stratigraphic column of the Black Thor and Black Label deposits

References

- Metsaranta R, Houlé MG (2012) Project Unit 10-004: Progress on the McFaulds Lake ("Ring of Fire") Region Data Compilation and Bedrock Mapping Project, Ontario Geological Survey Open File Report 6280: 43-1 to 43-12
- Mungall JE, Azar B, Hamilton MA (2011) Ni-Cu-Cr-Fe-Ti-V and VMS Mineralization of the Ring of Fire Intrusive Suite, Ontario, GAC Abstract
- Mungall JE, Harvey JD, Balch SJ, Azar B, Atkinson J, Hamilton MA (2010) Eagle's Nest: A Magmatic Ni-Sulfide Deposit in the James Bay Lowlands, Ontario, Canada, Economic Geology Special Publication 15, v2: 539-557
- Rayner N, Stott GM (2005) Project Unit 03-011, Discrimination of Archean Domains in the Sachigo Subprovince: A Progress Report on the Geochronology, Ontario Geological Survey Open File Report 6172: 10-1 to 10-21

The structure of sulfide droplets zone in the “Rudniy” mafic intrusion (Tsagaan-Shuvuut ridge, NW Mongolia)

Andrey Vishnevskiy, Maria Cherdantseva, Andrey Izokh

V S Sobolev Institute of Geology and Mineralogy SB RAS, Novosibirsk, Russia, vishnevsky@igm.nsc.ru
Novosibirsk State University, Novosibirsk, Russia

Abstract. Sulfide droplets are known to occur in some Cu-Ni-PGE deposits. In this paper we present the results of a study of sulfide droplets zone with large amount of PGE mineral grains, which have recently been found in NW Mongolia. Based on the study of the structure and texture of this zone, we have identified two horizons of sulfide droplets, Upper and Lower, which differ from each other in terms of droplet size, shape, and PGE-telluride content. Sulfide droplets are surrounded by narrow metasomatic rims containing no olivine and spinels, but there are minerals containing OH, F, and especially Cl. A common mineral in these rims and within the sulfides is ilmenite, which forms skeletal crystals and with pyrrhotite partially replaces cumulus titanomagnetite. Crystallization of such droplets can be considered as a quasi-closed system. Their study is important for understanding the distribution of the major, PGE, and other trace elements during crystallization and subsolidus transformation of natural sulfide melts.

Keywords. Sulfide droplets, Cu-Ni-PGE ores, Mongolia, fluids

1 Introduction

It is well known that the supersaturation of magmatic melt by sulfur causes silicate-sulfide immiscibility. As a result, a sulfide melt is formed, the amount and composition of which depends on abundances of sulfur, chalcophile elements, and siderophile elements. This melt can form small inclusions in silicate minerals, fill spaces between them, and form massive ore bodies due to migration and segregation of separate portions of the melt. An intermediate variant between massive and disseminated ores is the formation of sulfide droplets with sizes ranging 0.5 - 5 cm. These droplets are known in some large and small deposits of magmatic Cu-Ni ores (e.g., Barnes et al. 2006; Prichard et al. 2004).

As the temperature of the sulfide melt decreases, it crystallizes cumulate MSS and the Cu-enriched residual liquid crystallizes ISS. PGE and other trace elements are distributed between the two phases according to the effective partition coefficients. With further decrease of temperature, MSS exsolves pyrrhotite and pentlandite in lower parts of droplets, and chalcopyrite and cubanite exsolve from ISS, forming intergrowths in the upper parts of droplets. PGE and trace elements are mobile during these subsolidus transformations and also can form individual minerals (Osbaehr et al. 2013).

Isolated sulfide droplets crystallize later than the silicate matrix, inhibiting the large-scale transfer of matter. Therefore, the study of sulfide droplets can give us unique information about the crystallization of multicomponent natural sulfide melts under close to closed-system conditions. In this paper we present the

results of a study of sulfide droplets zone with a large number of grains of PGE minerals, which have recently been found in NW Mongolia.

2 Geological setting

Sulfide droplets were found in a small mafic body in the eastern part of the Tsagaan-Shuvuut ridge, which is located on the border of Tuva (Russia) and Uvs Aimag (Mongolia). The outcrop area of this intrusion is approximately 250 metres x 70 meters (Fig. 1).

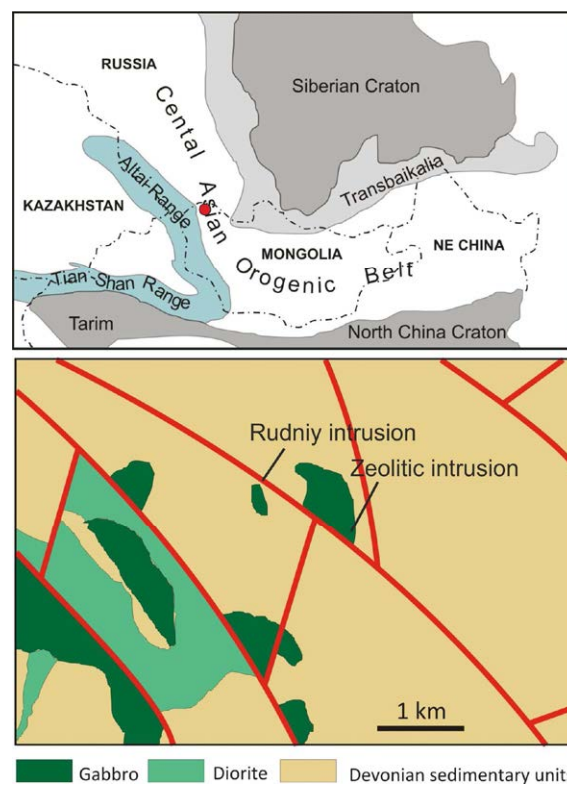


Figure 1. Geological scheme of the study area. Diorite and gabbroic intrusions of Torgalyg complex located in the sedimentary rocks of Early and Middle Devonian terrigenous formations.

It is located on a steep slope of the ridge (~30 degrees) and elongated in the meridional direction. Two intrusive units are distinguished in the structure of the intrusion. The western part of the body is composed of leucocratic gabbro containing MgO 8-9 wt.%. In contact with sedimentary rocks are aphanic dolerites, which gradually change from to fine-grained and coarse-grained. The width of this unit in the outcrop is about 40 meters. The eastern part of the body more melanocratic and it exhibits a clear differentiation of all major and trace elements. The most magnesian rocks are observed in the western part of this unit, and contain

more than 20 wt.% MgO, and have higher concentrations of Cr and Ni. Closer to the eastern contact of this unit, Mg# drops accompanying by increases in the contents of K, Ti and Al. Thus, in the structure of the intrusion are two units: a western unit consisting of dolerite and leucogabbro, and an eastern unit composed of melanocratic olivine gabbro and olivine gabbro, however, contact between them in the rocky outcrop was not observed.

Ar-Ar data for biotite from the eastern unit suggest an age of 348 Ma, corresponding approximately to the Devonian-Carboniferous boundary. In Devonian time, the area was characterized by an extensional geodynamic setting, the formation of large basins, rift-type magmatism, and the accumulation of thick sequences of terrigenous sediments. Gabbroic and dioritic bodies that are located in Tsagaan-Shivuut ridge belong to Torgalyg intrusive complex, intruded the terrigenous sedimentary rocks of south-western part of Tuvian trough.

3 Ore zone

Sulfide droplets were found in the high-Mg part of eastern unit, 20 meters above the slope of the sampling line. They are elongated parallel to the interpreted contact between western and eastern units. Olivine gabbro with sulfide droplets can be traced over a distance of about 10 meters and a width of about 20 centimeters. Based on the study of the structure and texture of this zone, we have identified two horizons of sulfide droplets – an Upper horizon and a Lower horizon. The width of the Lower horizon ranges from 3 to 7 cm and the width of the Upper horizon ranges from 10 to 15 cm (Fig. 2).

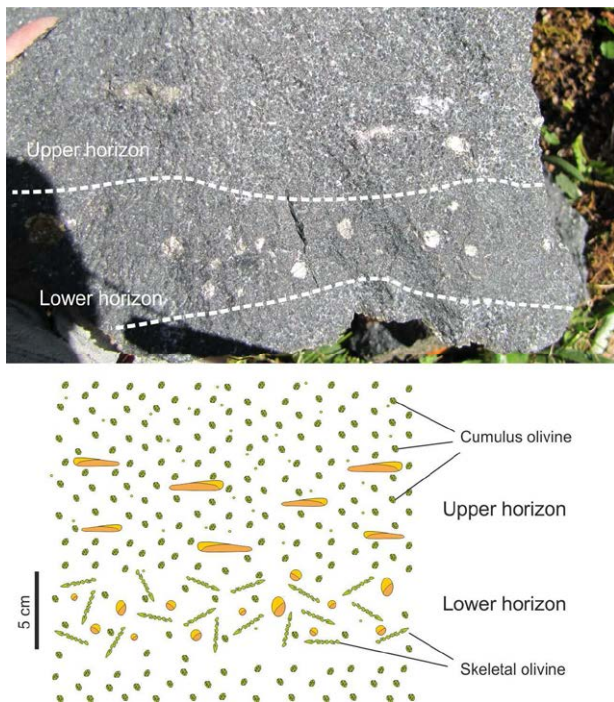


Figure 2. Photo and sketch showing structure of the ore zone.

Sulfide droplets from the both horizons have a fundamentally similar classic structure: the lower part of the droplets is dominated by pyrrhotite, the middle part by pentlandite, and the upper part by chalcopyrite and cubanite (Fig. 3). However, the horizons differ from each other in terms of droplets size and shape, types of olivine crystals, and PGE mineralization.

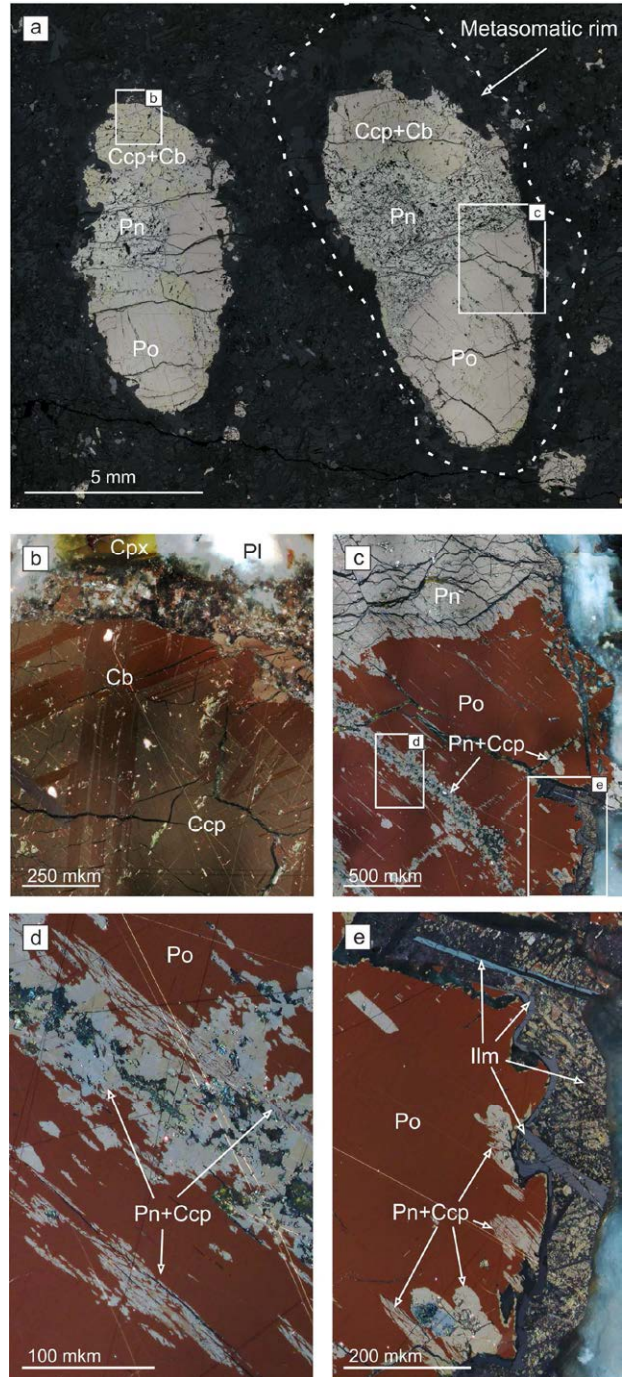


Figure 3. Typical structure of vertically elongated droplets from the Lower horizon. a - general view of the droplets and metasomatic rims around them, b - cubanite lamellae in chalcopyrite, c, d - chalcopyrite-pentlandite lamellae and veins in pyrrhotite, e - chalcopyrite-pentlandite lamellae and ilmenite rims. Reflected light.

3.1 Upper horizon

Sulfide droplets in the this horizon are predominantly flattened or elongated, rarely irregular. The droplet size is typically 15-20 mm in the long axis, in rare cases, up to 40 mm. The distance between individual droplets is usually 5-7 cm. Flattening of droplets is parallel to elongation of the sulfide zone.

3.2 Lower horizon

Sulfide droplets in this horizon are round (isometric) or vertically elongated (Fig. 2 and 3). The droplet size is usually 3-15 mm in the long axis, and their concentration is significantly higher than in the Upper horizon. The distance between the droplets is usually 1-3 cm. The silicate matrix of the Lower horizon macroscopically looks darker due to elevated amounts of olivine, ilmenite, and chromspinel.

4 Sample preparation and techniques

Samples of sulfide droplets from both horizons chosen for study were sawn, mounted in epoxy resin, and polished. Sixteen sections from the Upper horizon and 23 sections from the Lower horizon were studied. The samples were studied in reflected light using a Carl Zeiss Axiolab 40 Pol compound polarizing microscope. The study of minerals was carried out using a scanning microscope Tescan Mira 3 with high resolution Oxford X-Max 80 EDS. Thin sections from both horizons were prepared to study the silicate matrix.

5 Petrography of ore zone and droplets structure

The rock that hosts droplets of the Upper horizon is a typical olivine gabbro with an equigranular structure. The main minerals are olivine FO_{81-85} (30-35%), clinopyroxene (15-30%), plagioclase An_{64-75} (20-40%). Less common are hornblende, biotite, apatite, Cr-spinel, magnetite, ilmenite, and secondary minerals (serpentine and chlorite).

The mineralogical composition of olivine gabbro from the Lower horizon is generally similar to that in the Upper horizon, however, there are significant differences in the structure of rock and minerals. First, this horizon has an elevated content of olivine (up to 70%) and Cr-spinel. Second, about half of the olivine and Cr-spinel crystals have a skeletal structure. Spinel forms skeletal crystals of isometric shape up to 300-400 mm in diameter. Skeletal olivine crystals are strongly elongated, with lengths of 20-30 mm and width not exceeding 2 mm (Fig. 4, a). The spatial arrangement of these crystals varies, but most are oriented approximately orthogonal to the droplet layer. In some parts of the Lower horizon skeletal olivines arranged parallel to each other, forming a harrisite-like structure (Fig. 4, b). These structures are described in some ultrabasic intrusions and are evidence of very rapid crystallization, for which strong supersaturation is necessary (e.g., O'Driscoll et al. 2007).

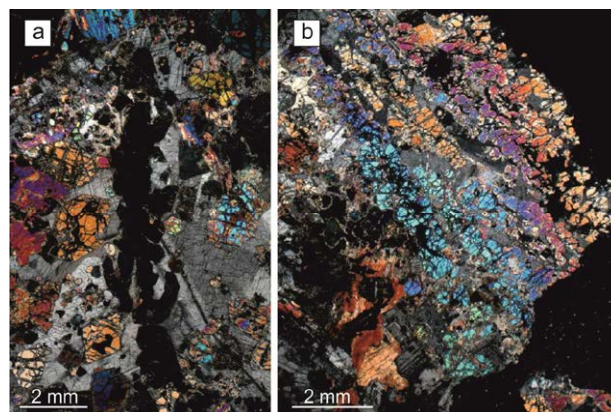


Figure 4. Thin sections from the Lower horizon. a – single skeletal olivine crystal, b – harrisite-like structure. Crossed nicols.

5.1 Metasomatic rims

All droplets have rims of silicate minerals, a significant portion of which are minerals that contain large amounts of volatile components – OH, Cl, and F. The widths of the rims depends on their spatial position and size of the droplet. The most extensive rims (up to 7-8 mm) are observed above the tops of large droplets from the Lower horizon. The rims are devoid of olivine and contain almost no Cr-spinel (excluding the outer part of the rims), with most of them consisting of augite, plagioclase (An_{10-25}), and hornblende, with minor fluorapatite, ilmenite, chlorite, and biotite. Hornblende is close in composition to potassic chlorohastingsite, and contains up to 30 wt.% FeO and 5-6 wt.% Cl.

Thus, it is clear that every single droplet of sulfide melt carried dissolved chloride fluid, or, at least, was associated with such a fluid. During the crystallization of MSS and ISS this fluid separated from the sulfide melt and metasomatized enclosing silicates. Based on numerous studies of natural and experimental systems, we know that at the temperatures when sulfide melts beginning to crystallize, silicates, which make up the gabbro, are already almost completely crystallized (e.g., Naldrett 2004). Thus, the scale of interaction and mass transfer during the formation of reaction rims is limited to few millimeters. Consequently, the crystallization of sulfide droplets can be considered as quasi-closed system crystallization of natural sulfide melt. A detailed study of the structure and composition of such droplets will allow us to interpret the migration of PGE and trace elements during crystallization and subsolidus transformations.

5.2 Inclusions in droplets

Two main types of inclusions are observed in the outer zones of droplets.

The first type is elongated skeletal crystals of ilmenite, up to 10 mm in length and up to 0.2-0.3 mm in width (Fig. 5, a) Most of these ilmenites form discontinuous intermediate rims between sulfides and silicates, however, in some cases the cross-cut sulfide

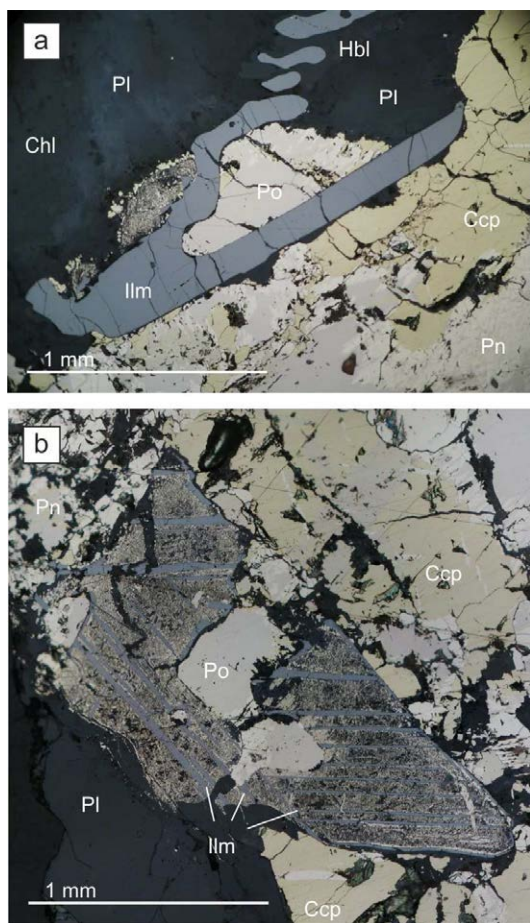


Figure 5. Inclusions in sulfide droplets. a – ilmenite skeletal crystal, b – pyrrhotite and ilmenite after titanomagnetite

droplets. It is important to note that the ilmenite is not found outside of sulfide droplets and metasomatic rims around them, which means a lower oxygen activity during their formation.

The second type of inclusions are grains of titanomagnetite partially replaced by pyrrhotite. They have a reticulated structure formed by the preserved lamellae of ilmenite (Fig. 5, b). Such pseudomorphs enclosed within sulfide droplets indicate early crystallization of magnetite from sulfide melt and a subsequent change in redox conditions, which occurred after the crystallization of the main silicate minerals.

And finally rare type of inclusions are euhedral apatite grains enclosed in sulfides.

Acknowledgements

The work was supported by the Ministry of Education and Science of the Russian Federation (Grant # 14.B37.21.0879) and RFBR grants 13-05-01132, 13-05-00951 and 12-05-00435.

References

- Barnes S-J, Cox RA, Zientek ML (2006) Platinum-group element, Gold, Silver and Base Metal distribution in compositionally zoned sulfide droplets from the Medvezky Creek Mine, Norilsk, Russia. *Contrib Mineral Petrol*, 152: 187-200
- Naldrett AJ (2004) *Magmatic sulfide deposits. Geology, geochemistry and exploration.* Berlin Heidelberg: Springer-Verlag
- O'Driscoll B, Donaldson CH, Troll VR, Jerram DA, Emeleus CH (2007) An Origin for Harrisitic and Granular Olivine in the Rum Layered Suite, NW Scotland: a Crystal Size Distribution Study *J Petrol* 48: 253-270
- Osbaer I, Klemd R, Oberthür T, Brätz H, Schouwstra R (2013) Platinum-group element distribution in base-metal sulfides of the Merensky Reef from the eastern and western Bushveld Complex, South Africa. *Miner Deposita* 48: 211-232
- Prichard HM, Hutchinson D, Fisher PC (2004) Petrology and Crystallization History of Multiphase Sulfide Droplets in a Mafic Dike from Uruguay: Implications for the Origin of Cu-Ni-PGE Sulfide Deposits. *Econ Geol* 99: 365-376

Strontium isotope disequilibrium of plagioclase in the upper critical zone of the Bushveld complex: evidence for mixing of crystal slurries

Shenghong Yang, Wolfgang Maier
Department of Geosciences, University of Oulu, Finland

Yann Lahaye, Hugh O'Brien
Geological Survey of Finland, Espoo, Finland

Abstract. We report the first in-situ Sr isotope data for plagioclase of the Bushveld Complex. We found disequilibrium Sr isotopic compositions on several scales, (i) between cores and rims of plagioclase grains in the Merensky pyroxenite, the Bastard anorthosite, and the UG1 unit and its noritic footwall, (ii) between cores of different cumulus plagioclase grains within thin sections of anorthosite and pyroxenite of the Merensky Unit, the footwall anorthosite of the Merensky reef, and the footwall norite of the UG1 chromitite. The data indicate co-accumulation of cumulus plagioclase grains that had crystallized from different magmas, followed by late stage overgrowth of the cumulus grains in a residual liquid derived from a different level of the compacting cumulate pile. We propose that the rocks formed through slumping of semi-consolidated crystal slurries at the top of the Critical Zone during subsidence of the centre of the intrusion. Slumping led to sorting of crystals based on density differences, resulting in a layered interval of pyroxenites, norites and anorthosites.

Keywords. Bushveld Complex, Merensky Reef, Plagioclase, In-situ strontium isotopes

1 Introduction

The origin of PGE reefs in layered intrusions remains under debate. In the case of the Bushveld Complex, it has been suggested that mixing of two compositionally contrasting magmas triggered sulfide saturation and the formation of the PGE reefs (Campbell et al. 1983; Naldrett et al. 2009). One of the key observations that led to the development of this model was the Sr isotopic variation in the cumulate sequence. Over the years, several workers have studied the whole rock Sr isotopic variations through the Complex (Kruger and Marsh 1982; Eales et al. 1990; Teigler 1990; Kruger 1994). Detailed studies have shown isotopic disequilibrium in the rocks of the Lower Critical Zone, based on replicate whole rock and mineral separate analyses of the same sample (Eales et al. 1990). Prevec et al. (2005) found different initial Nd isotope ratios of orthopyroxene and plagioclase separates from the same sample, and proposed Nd isotopic disequilibrium between orthopyroxene and plagioclase due to magma replenishment. Seabrook et al. (2005) found that plagioclase separates in the Merensky and Bastard units generally have a Main Zone Sr isotopic character, whereas orthopyroxene separates have a Critical Zone affinity. These results suggest that important petrogenetic information is lost during whole rock isotope analyses in cumulate rocks. In the present study, we show that the in-situ Sr isotope analytical method using Laser ablation multi-collector

inductively coupled plasma mass spectrometry (LA-MC-ICP-MS) (Ramosa et al. 2004, 2005) broadly reproduces the general trend of whole rock isotopic variation, but in addition provides further constraints on the scale of isotope disequilibrium, and thus the formation of the Merensky reef.

2 Sample locations and descriptions

Most samples in this study are from the Union Section in the western Bushveld Complex, described in detail by de Klerk (1992) and Eales et al. (1990). One sample (EK 22.299.1) is from the Amandelbult section. We analysed samples from the Bastard, Merensky, Merensky footwall, UG1 and UG1 footwall units, including norites, orthopyroxenites and anorthosites.

3 Analytical method

In situ Sr isotope analyses of plagioclase were performed using a Nu Plasma HR multi-collector inductively coupled plasma mass spectrometry (MC-ICP-MS) and a Photon Machine Analyte G2 laser microprobe at the Geological Survey of Finland in Espoo. During the laser ablation the data were collected in static mode (^{84}Sr -Kr, ^{85}Rb , ^{86}Sr -Kr, ^{87}Rb -Sr, ^{88}Sr). Measured isotope ratios were corrected for instrument fractionation using an exponential law and a $^{86}\text{Sr}/^{88}\text{Sr}$ value of 0.1194. The isobaric interference of ^{87}Rb on ^{87}Sr was monitored and corrected using the ^{85}Rb ion signal and a value of 0.38571 for the $^{87}\text{Rb}/^{85}\text{Rb}$ ratio. The isobaric interference of ^{86}Kr on ^{86}Sr was corrected using a 30s background measurement preceding every ablation. The $^{85}\text{Rb}/^{86}\text{Sr}$ ratio was used for age correction. Major element composition of plagioclase was analysed using electron microprobe at the University of Oulu.

4 Analytical results

The in-situ Sr isotope analytical method using LA-MC-ICP-MS broadly reproduces the trend of whole rock isotopic variation in the Bushveld UCZ (Fig.1). Disequilibrium Sr isotopic compositions were observed on several scales, (i) between cores and rims of plagioclase grains, in the Merensky pyroxenite, Bastard anorthosite, the UG1 unit and its noritic footwall, and (ii) between cores of cumulus plagioclase grains within single thin sections of anorthosite and pyroxenite of the Merensky Unit, the footwall anorthosite of the Merensky reef, and the footwall norite of the UG1 chromitite.

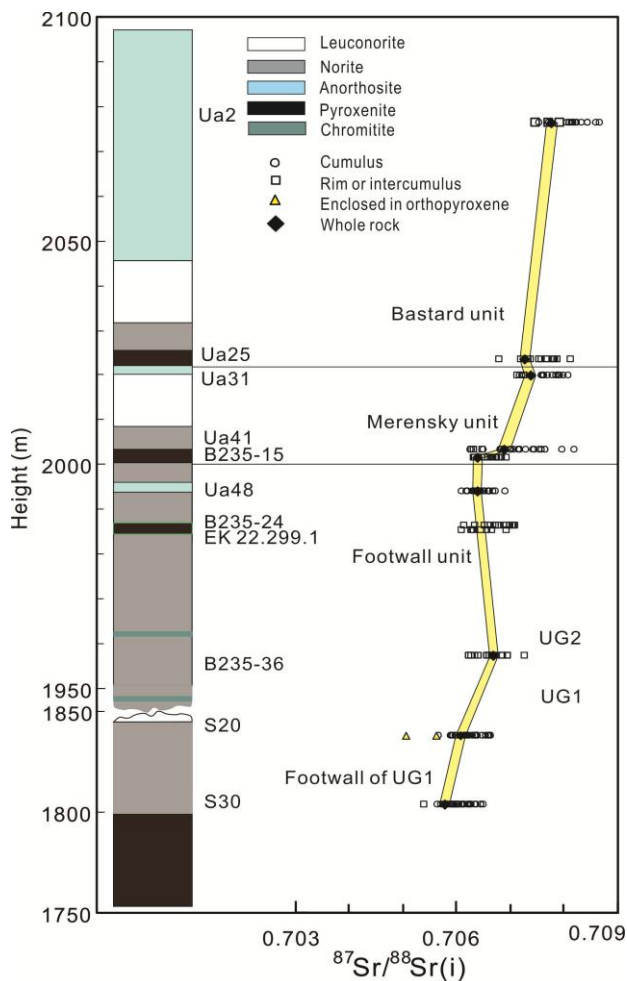


Figure 1. Plots of Sr_i ratios of plagioclase grains and whole rock versus stratigraphic height for samples from Union Section, western Bushveld Complex.

5 Discussion

5.1 Disequilibrium between rims and cores of cumulus plagioclase

In several of our samples, Sr isotopes between the core and rim domains of plagioclase grains show strong disequilibrium. For example, in the footwall pyroxenite of the UG1 chromitite (sample S30), core domains of intercumulus plagioclase have a Sr_i ratio of ~ 0.7065 with An around 75 mole%, but the rims have much a lower Sr_i ratio of 0.7058 and a lower An of ~ 71 mole% (Fig. 2). Similar disequilibrium occurs in cumulus plagioclase grains of the Bastard anorthosite (sample UA2) (Fig. 2) and the Merensky anorthosite (sample UA31). The variation could be explained by upward percolation of residual liquids of LZ or LCZ derivation, intervals that have significantly lower Sr_i ratio than the Upper Critical Zone (UCZ) and MZ. An alternative explanation could be that plagioclase grains of UCZ signature were suspended in a new influx of B1 magma resulting in the relatively non-radiogenic overgrowths. A systematic core-to-rim decrease of Sr_i ratio in plagioclase has also been documented in the E1 Chichon Volcano, Mexico (Tepley III et al. 1999). It was proposed that the initial magma assimilated high- Sr_i ratio crust resulting in crystallization of plagioclase

cores with relatively radiogenic Sr_i ratio, but subsequent magma recharge events lowered the Sr_i ratio of the magma resulting in relatively less radiogenic rims (Tepley III et al. 1999).

In contrast, in an orthopyroxenite of the UG1 unit (B235-36), the cores of plagioclase grains show higher An content but lower Sr_i ratio than the rim (Fig. 2). Relatively radiogenic plagioclase rims in the Upper Critical Zone were also reported by Chutas et al. (2012) using progressive leaching methods. They argued that the disequilibrium was due to late-stage infiltration of a relatively radiogenic component. During the compaction of the cumulates, some residual melt could have been expelled upward. However, the LZ and LCZ cumulate rocks generally have lower Sr_i ratio than the upper part, and thus could not produce the more radiogenic rims in sample B235-36. Instead, dense residual liquids from anorthosite layers in stratigraphically higher levels of the cumulate pile could locally percolate down. Alternatively, relatively non-radiogenic LZ and LCZ plagioclases could have remained suspended in the residual magma and acquired their radiogenic cores when the chamber was replenished with B2/B3 magma (Eales 1990).

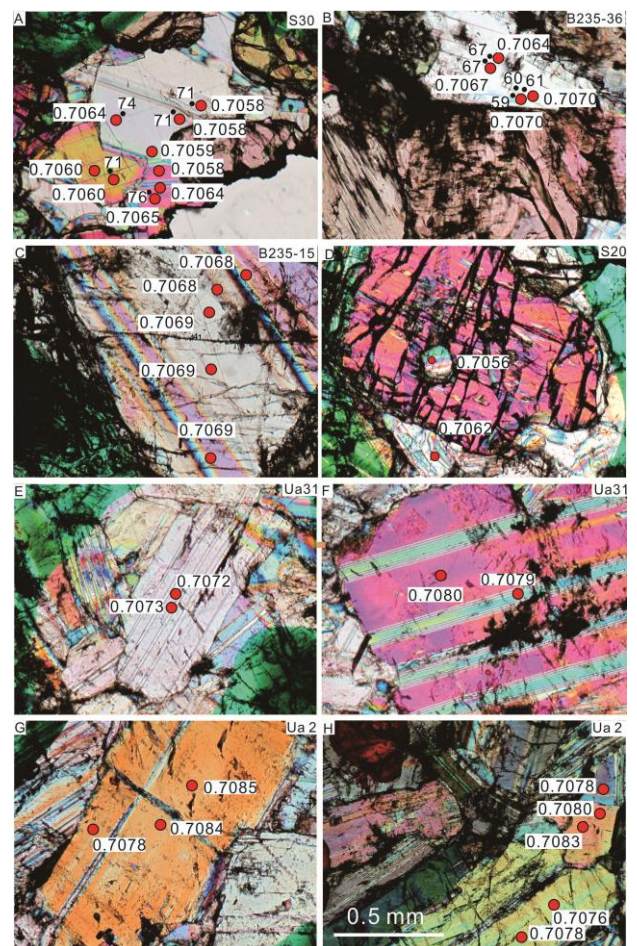


Figure 2. Photomicrographs of Merensky pyroxenite from drill core. A. Pyroxenite of the UG1 footwall; B. Pyroxenite from the UG1 unit; C. Merensky pyroxenite. D. Norite of the UG1 footwall; E-F. Anorthosite from the Merensky unit; G-H. Anorthosite from the Bastard unit. Black circle and numbers with 2 digitals indicate the spot of microprobe and anorthite content, the red circle and numbers with 4 digitals indicate the spot of laser and Sr_i ratio.

A trend of increasing Sr_i ratio from cores to rims of plagioclase grains was also reported in the Rum intrusion (Tepley III and Davidson 2003). The authors suggested that plagioclase crystals may have crystallized from liquids that underwent progressively larger degrees of in-situ contamination. This model assumes that the rate of crystallization of plagioclase was slower than the rate of crustal contamination. However, the Bushveld Complex is a much larger magma system than Rum, and the rate of change in magma composition due to putative in-situ wall rock contamination would very likely have been much slower than in smaller intrusions, having little effect on the magma composition.

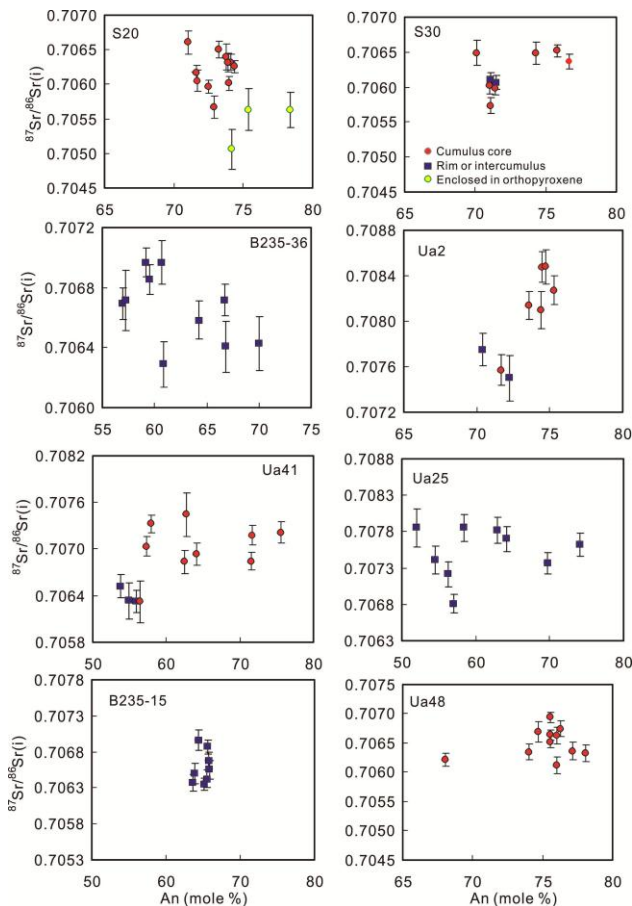


Figure 3. Plot of Sr_i ratios vs. anorthite contents of plagioclases in single thin sections from the Union Section, Western Bushveld Complex.

5.2 Disequilibrium between cumulus plagioclase grains within individual samples

The sample from the base of the Merensky pyroxenite (B235-15) exhibit Sr_i ratios ranging from 0.7064-0.7069 (Fig. 1), consistent with derivation from Critical Zone magma. However, in another pyroxenite (UA41) located 2m above the Merensky base, Sr_i ratio of plagioclase grains varies from 0.7065 to 0.7074, overlapping with the composition of both the Critical and Main Zones (Fig. 1). Similar variation of Sr_i ratio also occurs in the Merensky anorthosite (UA31) (Fig. 2), Bastard anorthosite (UA2) (Fig. 2), Merensky footwall anorthosite (UA48) and the footwall norite and pyroxenite of the UG1 chromitite (S20 and S30). The heterogeneity of Sr_i ratio between cores of different

grains may potentially be explained by re-equilibrium of crystallized plagioclase with a melt which has distinct composition. However, the diffusion of Sr in plagioclase is relatively slow, and isotopic re-equilibration of plagioclase cores is thus considered unlikely (Tepley III and Davidson 2003). Therefore, the highly heterogeneous Sr_i isotope ratios in cumulus plagioclase cores indicate that these grains crystallized from magmas with different compositions. In addition, some of these samples are plagioclase adcumulates with very low fractions of intercumulus liquid, and thus there should have been little opportunity for cumulus plagioclase to interact with interstitial melt. In a footwall orthopyroxenite of the UG1 chromitite (S20), plagioclase inclusions in orthopyroxene have a lower radiogenic Sr_i ratio, but higher An content than the other grains (Figs. 2 and 3). The variation in Sr_i of plagioclases in these samples is considered to be of primary origin. Similar Sr isotope disequilibrium between pyroxene and plagioclase, and between plagioclase grains of different texture occur in the UCZ, and it has been suggested that these plagioclase grains could not have crystallized from a single magma (Eales et al. 1990). The authors suggested that the anorthosite layers formed by a process of gravitational fractionation whereby pyroxenes settled preferentially and plagioclase remained suspended in the magma before settling to form anorthosite layers.

Past studies have proposed that the LZ and LCZ are derived from magnesium basaltic Bushveld 1 (B1) magma (Barnes et al. 2010; Godel et al. 2011) and the Main Zone from tholeiitic B2/B3 magmas (Maier and Barnes 1998; Barnes et al. 2010). The observed variation in our data could potentially be explained by a model whereby plagioclase crystallizing from relatively non-radiogenic B1 magma remained suspended in the residual magma. When the magma chamber was replenished with relatively radiogenic B2/B3 magma, additional new plagioclase grains with higher Sr_i crystallized. The Sr_i composition of some plagioclases lie between the Sr_i composition of the two magmas, suggesting that these magmas may be the result of mixing between the two silicate melts. The compositionally contrasting grains then settled to form the UCZ cumulates (Seabrook et al. 2005).

An alternative model has been proposed by Maier et al. (2013). The authors suggested that the UCZ cumulate layers form through density sorting of crystals when semi-consolidated noritic crystal slurries slump to the centre of subsiding magma chambers. In intervals where compositionally contrasting magmas occur this would result in cumulates with mixed populations of crystals of similar density but distinct compositions.

5.3 Implication for the origin of the reefs

It has long been proposed that the sulfide mineralization in the Merensky reef was caused by magma mixing (Naldrett et al. 2009; Wilson and Chunnnett 2006). Seabrook et al. (2005) favoured mixing of crystals instead of magmas, and all the above studies argued that the reefs formed when sulfide liquid settled through resident magma to be concentrated on top of the

cumulate pile. Maier et al. (2013) have argued that the sulfide contents of Bushveld magmas were too low to trigger sulfide saturation in response to magma mixing. They presented evidence consistent with movement of crystal slurries driven by magma chamber subsidence. This process was particularly efficient in the UCZ because of enhanced subsidence related to the very significant Main Zone magma replenishment event. Sorting led to layers that are either enriched in pyroxene, chromite and sulfide (forming pyroxenites and melanorites, including the Merensky Reef), or in plagioclase (forming anorthosites). Individual layers may contain crystals derived from both UCZ and MZ magmas, resulting in the observed isotopic disequilibrium of plagioclase cores. Isotopically distinct overgrowths on cumulus plagioclase grains may be the result of downward or upward percolation of residual liquids.

6 Conclusions

The in situ Sr isotope analytical method using LA-MC-ICP-MS reproduces the trend of whole rock isotopic variation in the Bushveld UCZ extremely well. In situ Sr isotopic data on plagioclase grains record variable compositions of plagioclase cores in individual samples of the UCZ. The data suggest that plagioclase grains from both Main Zone and Critical Zone magmas have contributed to the Merensky and Bastard units. This is interpreted to result from mineral sorting of slumping crystal mushes resulting in mixing of crystals. Disequilibrium of Sr isotopes between core and rim domains of plagioclase grains indicates overgrowth of plagioclase in silicate melts with different compositions. The new data are consistent with a model whereby the UCZ cumulate layers, including the PGE reefs, form through density sorting of crystals when semi-consolidated noritic crystal slurries slump to the centre of subsiding magma chambers.

References

- Campbell IH, Naldrett AJ, Barnes SJ (1983) A model for the origin of the platinum-rich sulfide horizons in the Bushveld and Stillwater Complexes. *J Petrol* 24: 133–165
- Chutas NI, Bates E, Prevec SA, Coleman DS, Boudreau AE (2012) Sr and Pb isotopic disequilibrium between coexisting plagioclase and orthopyroxene in the Bushveld Complex, South Africa: microdrilling and progressive leaching evidence for sub-liquidus contamination within a crystal mush. *Contrib Mineral Petrol* 163: 653–668
- de Klerk WJ (1992) Petrogenesis of the Upper Critical Zone of the Western Bushveld Complex with emphasis on the UG1 footwall and Bastard Units. Ph.D. thesis, Rhodes University, Grahamstown: 294 pp
- Eales HV, de Klerk WJ, Teigler B (1990) Evidence for magma mixing processes within the Critical and Lower Zones of the northwestern Bushveld Complex, South Africa. *Chem Geol* 88: 261–278
- Kruger FJ (1994) The Sr-isotopic stratigraphy of the western Bushveld Complex. *S Afr J Geol* 97: 393–398
- Maier WD, Barnes S-J, Groves DI (2013) The Bushveld Complex, South Africa: Formation of platinum-palladium, chrome and vanadium-rich layers via hydrodynamic sorting of a mobilized cumulate slurry in a large, relatively slowly cooling, subsiding magma chamber. *Mineral Depos* 48: 1–56
- Müller W, Shelley M, Miller P, Broude S (2009) Initial performance metrics of a new custom-designed ArF excimer LA-ICPMS system coupled to a two-volume laser-ablation cell. *Journal of Analytical Atomic Spectrometry* 24: 209–214
- Naldrett AJ, Wilson A, Kinnaird J, Chunnett G (2009) PGE tenor and metal ratios within and below the Merensky Reef, Bushveld Complex: Implications for its genesis. *J Petrol* 50: 625–659
- Nebel O, Scherer EE, Mezger K (2011) Evaluation of the ^{87}Rb decay constant by age comparison against the U–Pb system. *Earth Planet Sci Lett* 301: 1–8
- Prevec SA, Ashwal LD, Mkaza MS (2005) Mineral disequilibrium in the Merensky Reef, western Bushveld Complex, South Africa: new Sm–Nd isotope evidence. *Contrib Mineral Petrol* 149: 306–315
- Rankenburg K, Lassiter JC, Brey G (2004) Origin of megacrysts in volcanic rocks of the Cameroon volcanic chain – constraints on magma genesis and crustal contamination. *Contrib Mineral Petrol* 147: 129–144
- Ramosa FC, Wolff JA, Tollstrupa DL (2004) Measuring $^{87}\text{Sr}/^{86}\text{Sr}$ variations in minerals and groundmass from basalts using LA-MC-ICPMS. *Chem Geol* 211: 135–158
- Ramosa FC, Wolff JA, Tollstrupa DL (2005) Sr isotope disequilibrium in Columbia River flood basalts: Evidence for rapid shallow-level open-system processes. *Geol* 33: 457–460
- Rankenburg K, Lassiter JC, Brey G (2004) Origin of megacrysts in volcanic rocks of the Cameroon volcanic chain - constraints on magma genesis and crustal contamination. *Contrib Mineral Petrol* 147: 129–144
- Scoates JS, Friedman RM (2008) Precise age of the platinumiferous Merensky reef, Bushveld Complex, South Africa, by the U–Pb zircon chemical abrasion ID-TIMS technique. *Econ Geol* 103: 465–471
- Seabrook CL, Cawthorn RG, Kruger FJ (2005) The Merensky Reef, Bushveld Complex: mixing of minerals not mixing of magmas. *Econ Geol* 100: 1191–1206
- Teigler B (1990) Mineralogy, petrology and geochemistry of the Lower and Lower Critical Zones, northwestern Bushveld Complex. Ph.D. thesis, Rhodes University, Grahamstown
- Tepley III FJ, Davidson JP, Clynne MA (1999) Magmatic Interactions as Recorded in Plagioclase Phenocrysts of Chaos Crags, Lassen Volcanic Center, California. *J Petrol* 40: 787–806
- Tepley III FJ, Davidson JP (2003) Mineral-scale Sr-isotope constraints on magma evolution and chamber dynamics in the Rum layered intrusion, Scotland. *Contrib Mineral Petrol* 145: 621–648
- Wilson AH, Chunnett G (2006) Trace Element and Platinum Group Element Distributions and the Genesis of the Merensky Reef, Western Bushveld Complex, South Africa. *J Petrol* 47: 2369–2403

Origin of Bushveld magmas via new constraints from Pb-Hf zircon systematics

Marina Yudovskaya

EGRI, University of the Witwatersrand, Pvt Bag 3, Wits 2050, South Africa
Institute of Geology of Ore deposits, Petrography, Mineralogy and Geochemistry, Moscow 119017, Russia

Judith Kinnaird

EGRI, University of the Witwatersrand, Pvt Bag 3, Wits 2050, South Africa

Elena Belousova, Norman Pearson

GEMOC ARC National Key Centre, Department of Earth and Planetary Sciences, Macquarie University, NSW, 2109, Australia

Jan Kramers

Department of Geology, University of Johannesburg, P.O. Box 524, Auckland Park 2006, South Africa

Dmitry Kuzmin

Max Planck Institute (MPI) for Chemistry, Post Office Box 3060, 55020 Mainz, Germany

Abstract. Trace element and combined U-Pb and Lu-Hf isotope data on zircon from different stratigraphic zones and suites of the Bushveld Complex show that zircon from the ultramafic rocks has distinct geochemistry and the most non-radiogenic Hf isotope composition whereas acid rocks of the Complex may form at “mixing” between new juvenile and old crustal end-members. The data may indicate anomalous Archaean SCLM under the Kaapvaal craton with a non-radiogenic Hf isotopic signature that is distinct from both the depleted mantle source and the Archaean continental crust.

Keywords. Bushveld Complex, zircon, Lu-Hf isotope systematics, Kaapvaal craton

1 Introduction

The mantle affinity of Bushveld parental magma is assumed based on the earth's highest Cr and PGE reserves in the Bushveld Complex that can not be provided by any of other accessible reservoirs. It is consistent with high-Mg low-Ti compositions of the most primitive cumulates and inferred chemical composition of their parental melt (Wilson 2012; Eales and Costin 2012) as well as supported by their relatively low initial $^{87}\text{Sr}/^{86}\text{Sr}$ (~0.703 - 0.705) and a low $^{187}\text{Os}/^{188}\text{Os}$ (~0.122) which is just slightly higher than contemporary mantle (Harmer and Sharpe 1985; Schoenberg et al. 1999). On the other hand, high silica content, crustal Nd initial isotope compositions, elevated $\delta^{18}\text{O}$ values of rocks and minerals and enrichment in some incompatible elements indicate that either the mantle source had to be contaminated with a crustal component during melt ascending or the Archaean subcontinental lithospheric mantle (SCLM) beneath the Kaapvaal craton has had a unique composition different from the modern MORB mantle. The Lu-Hf systematics of zircon are known to be hardly affected by metamorphic events unless modified by melting or significant resorption. If coupled with the U-Pb systematics, they allow distinguishing between mantle

and crustal signatures and calculating the Hf model age of melt derivation. A combined U-Pb and Lu-Hf isotope study was carried out on zircon from different stratigraphic zones and suites of the Complex including ultramafic and chromititic horizons as well as acid rocks of the roof to test a hypothesis on local or deep-crustal contamination.

2 Sampling and analytical techniques

The Bushveld Complex comprises the Rooiberg volcanic suite that acts as both a roof and a floor for the Rustenburg layered ultramafic-mafic suite (RLS) overlain by the Lebowa Granite and Rashedoop Granophyre Suites. The volcanic andesite-rhyolitic Rooiberg Group represents the earliest phase of Bushveld-related magmatism. Chemical similarity and both gradational and intrusive contacts between rhyolite and granophyre support the view that while the Stavoren granophyre was emplaced as a magmatic sheet-like body beneath the Rooiberg volcanic cover, another type of granophyre with spherulitic texture was formed by recrystallisation of Rooiberg rhyolite (Walraven 1987). Different types of Bushveld Granites form sheet-like bodies overlying the mafic layered rocks but also occur as sills and dykes which crosscut both mafic-ultramafic rocks and the earlier granite.

Fresh samples of rhyolite and granophyre were collected in road-cuts in the Rooiberg and Groblersdal areas following mapping and sampling as described in Walraven (1987). The samples of young Bushveld granite were collected in the Mogolokwena Central open pit where granite forms granophyric veins cross-cutting the Platreef sequence. The samples of chromitite came from the Platreef and the Rustenburg section of the western limb; ultramafic rocks are represented by PGE-mineralised feldspathic pyroxenite from the Merensky Reef on Rustenburg and the Platreef on Vaalkop and Sandsloot as well as by Lower Zone pyroxenite from the northern limb on Sandsloot.

Electron microprobe and LA-ICPMS data on zircon compositions were obtained at the Max Plank Institute for Chemistry. The coupled Lu-Hf and U-Pb isotope analyses were carried out using a LA sampling with MC-ICPMS determination at Macquarie University.

3 Mineral compositions of rocks

Chromitite, pyroxenite, feldspathic pyroxenite and harzburgite contain different proportions of cumulus olivine, orthopyroxene and chromite with intercumulus plagioclase, clinopyroxene, amphiboles and phlogopite. The intercumulus assemblage includes base metal sulphides, platinum-group minerals, rutile, quartz, apatite, sphene and thorite. Baddeleyite is found as inclusions in chromite, discrete coarse euhedral grains and as relics replaced by later zircon. Two varieties of zircon grains 10-500 μm in size were found in the heavy separates and polished sections: partially metamict cathodoluminescent-dark zircon grains and cores in the complex zircon grains, and more abundant pinkish coloured transparent euhedral grains or overgrowths on the older cores.

Rhyolite in our set is partially recrystallised and has a spherulitic fine-grained texture. Feldspars and quartz are major minerals; hornblende, hematite, chlorite and muscovite are minor. A long list of accessory minerals includes rutile, fluorite, pyrite, sphalerite, arsenopyrite, sphene, galena, REE-carbonates, thorite and monazite. One variety of zircon mostly forms pinkish transparent grains 20-100 μm in size, another variety forms rare

red-coloured coarser crystals up to 200 μm in size.

Granophyre is compositionally similar to recrystallised rhyolite but has coarser-grained granophyric and granoblastic textures with perthitic feldspar intergrowths. The major minerals are the same as in rhyolite – quartz and feldspars. The minor and accessory ones are phlogopite, hornblende, hematite, fluorite, sphene, anatase, orthite and arsenopyrite. A most abundant zircon variety comprises pinkish fine transparent grains 10-70 μm in size with numerous mineral inclusions; two other varieties comprise red- and brown-coloured crystals and fragments which are partially metamict.

Two types of granite were sampled from the cross-cutting veins: albitic microgranite and granophyric granite. Albitite reveals pseudogranophyric texture with recrystallised albite intergrown with quartz. Minor and accessory minerals are represented by micas, Ca-plagioclase, chlorite, ilmenite, pyrite, chalcopyrite, sphene, monazite, anatase and orthopyroxene. The granophyric granite contains the most diverse accessory minerals that include abundant blue sphene, amphiboles, apatite, pyrite, galena, chalcopyrite, molybdenite, pentlandite, thorite, thorianite, pyrochlore, pyrite, Nb-titanate, calcite and uraninite. Four different zircon varieties could be distinguished based on the colour and morphology: most abundant pinkish transparent crystals, whitish partially metamict rounded grains, dark-yellow coarser crystals and partially metamict grey to black crystals with finest inclusions of galena and other opaque minerals.

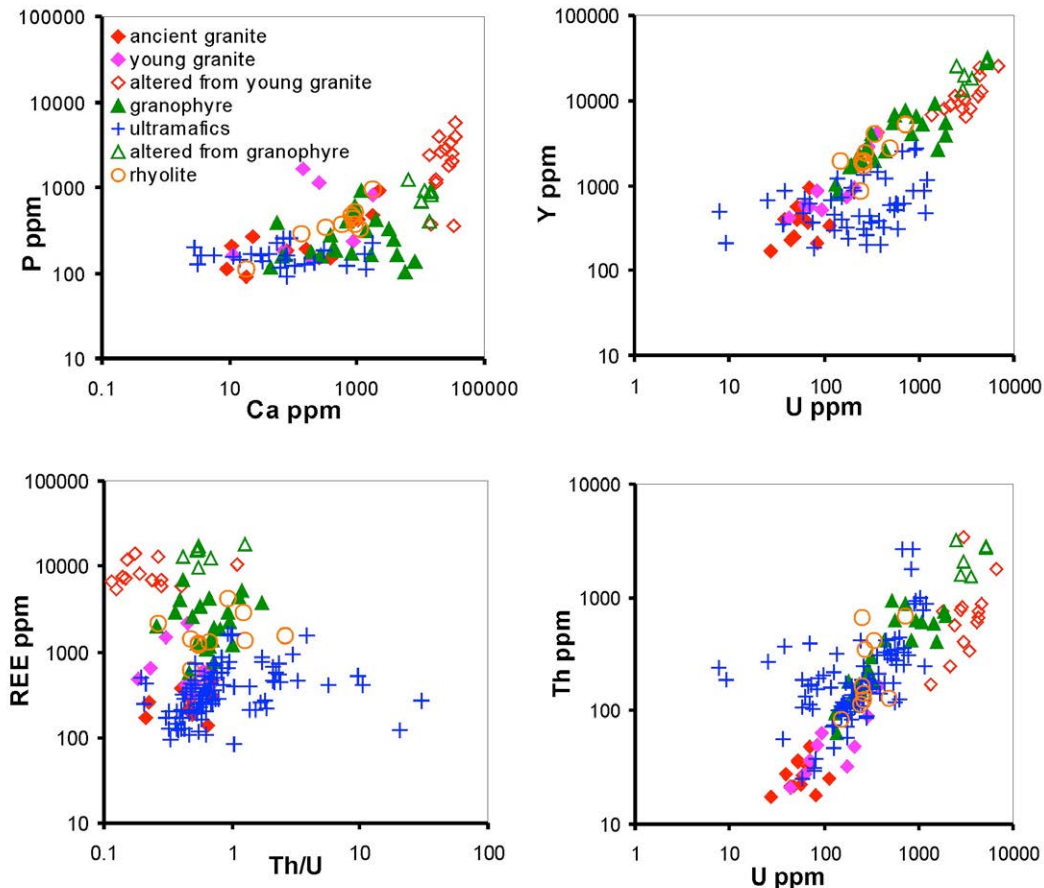


Figure 1. Trace element abundances in zircon from the different rocks of the Bushveld Complex.

The mineral compositions of acid roof rocks reflect the elevated content of incompatible elements such as F, Cl and As. The sulphide mineralisation in cross-cutting granitic veins was mobilised from the host Platreef mineralised magmatic horizons whereas fluorite-rich mineralisation in rhyolite and granophyre is developed at the post-magmatic hydrothermal stage.

4 U-Pb isotope data

The U-Pb zircon age determinations for rhyolite and granophyre yield indistinguishable ages within error - 2056.4 ± 3.6 Ma and 2053.6 ± 6.1 Ma, correspondingly, that is within error of the accepted Bushveld age (Scoates and Friedman 2008) and is also within error of a concordia age of 2056.2 ± 4.4 Ma for ultramafic rocks and chromitites. The young granitic-granophyric veins cross-cutting the Platreef sequence contain at least two zircon populations: an old population with apparent concordant U-Pb ages of 2870-2930 Ma and young zircons, which mainly discordant U-Pb data lie on a discordia with an upper intercept at 2027 ± 55 Ma.

5 Trace element geochemistry of zircon

Zircons from the cross-cutting granitic veins (old and young populations) are similar to zircon from ultramafic rocks in terms of total REE, Y, P and Hf contents (Fig. 1). However, ultramafic zircons show a wider range of Th and U contents from enriched to extremely depleted in Th and U. Both Th-U-poor and Th-U-rich zircons from mineralised ultramafic rocks and chromitites have an elevated Th/U ratio with highest values (up to 30) occurring in the Merensky Reef and Platreef zircon cores. Generally, the zircon cores in ultramafic rocks are enriched in REE, Y, Th and U and are characterised by distinctly flatter REE patterns in contrast to those of the

rims and transparent homogenous crystals.

Geochemistry of zircon from granophyre and rhyolite appeared to be very similar although granophyre contains abundant red- and brown-coloured altered zircons, which show discordant U-Pb values and are highly enriched in all trace elements. Altered or re-equilibrated zircons (grey-black variety) with highly discordant U-Pb ages are also common in the young granitic veins and are also characterised by the higher trace element abundances.

6 U-Pb and Lu-Hf isotope systematics of zircon

Coupled U-Pb and Lu-Hf systematics in zircon are widely used to establish an age and a source of magmatic intrusions. The $^{176}\text{Hf}/^{177}\text{Hf}$ ratios at the time of zircon crystallisation, which is determined in terms of an apparent U-Pb isotope age, can yield information on crustal or mantle origin of the parent magma. The Hf model age show us the time when parental melts was derived from the Chondritic Uniform Reservoir ($T_{\text{Hf CHUR}}$) or from the depleted mantle ($T_{\text{Hf DM}}$). It is known that very few zircons worldwide lie on the depleted mantle line and have their Hf model age similar to the U-Pb crystallisation age that was generally explained by a new crust formation event approximately 2.7 Ga ago in the Archaean. The Hf isotope ratios are also commonly expressed as ϵ_{Hf} , which is the deviation of the $^{176}\text{Hf}/^{177}\text{Hf}$ ratio of the sample from the contemporaneous ratio of the Chondritic Uniform Reservoir (CHUR), multiplied by 10^4 . Therefore, mantle-derived magmas should have positive ϵ_{Hf} in between CHUR and DM lines whereas crustal magmas should have negative values of ϵ_{Hf} and non-radiogenic Hf isotope composition.

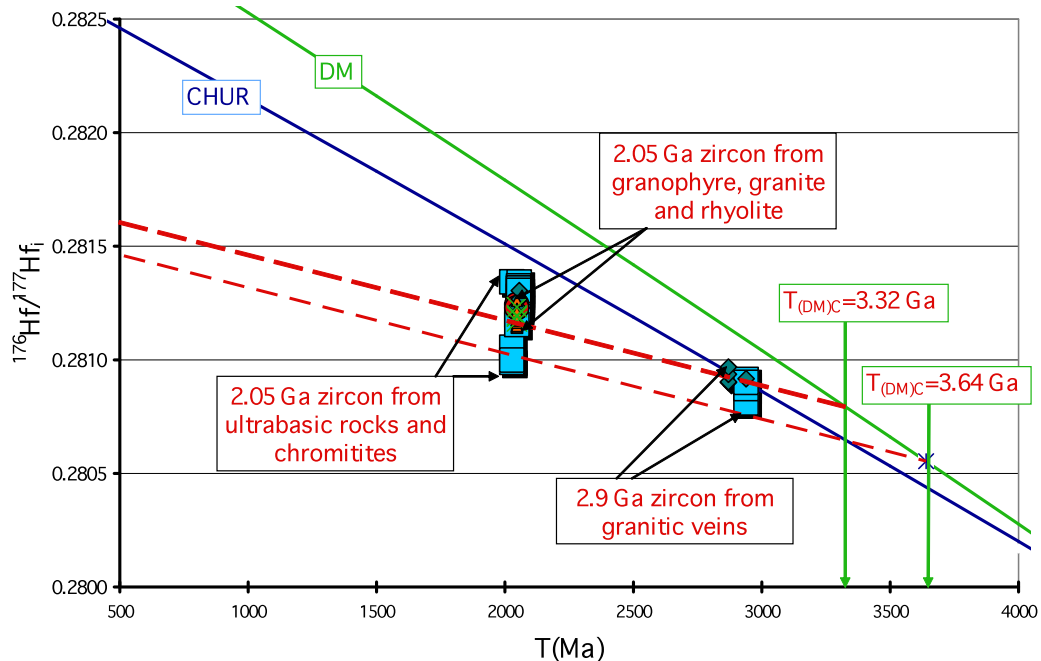


Figure 2. Graphical representation of the Hf isotope composition in zircon from the Bushveld Complex. The Hf isotope evolution of the depleted mantle (DM) and chondritic uniform reservoir (CHUR) is shown. T(Ma) indicates an apparent U-Pb isotope zircon age. Red lines show hypothetical crustal evolution line with $^{176}\text{Lu}/^{177}\text{Hf}=0.015$ for old and young zircon populations.

Zircons from the ultramafic rocks have the most non-radiogenic Hf isotope composition, which range in ϵ_{Hf} from -12 to -7.7 (Fig. 3). Their $T_{\text{Hf DM}}$ crustal model ages range from 3090 to 3300 Ma, which is 1050-1250 Ma older than their emplacement ages (Fig. 2). Zircons from the rhyolite and granophyre have similar but more radiogenic Hf isotope composition, which range in ϵ_{Hf} from -4.6 to -8.2. The ancient zircon population from granitic veins has the highest ϵ_{Hf} values ranging from -2.9 to +0.9 and their $T_{\text{Hf DM}}$ crustal model ages range from 3300 to 3600 Ma, which is 400-700 Ma older than their crystallization ages (Fig. 2).

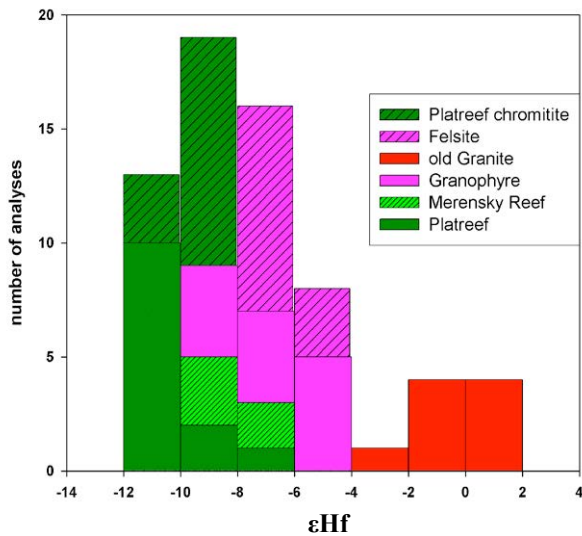


Figure 3. Histogram of Hf isotope composition in zircon from ultramafic rocks and acid roof rocks of the Bushveld Complex.

7 Conclusions

Younger cross-cutting granitic veins formed mainly by remobilisation and partial remelting of Archaean granite-gneisses caused by high heat flow from ultramafic intrusions. Some inherited zircon grains retained undisturbed U-Pb isotope systematics in this process. The geochemistry of zircons from ultramafic rocks has much in common with that of zircon from granitic veins whereas zircon from the roof rocks (rhyolite and granophyre) has a distinct geochemical signature.

The Lu-Hf data suggest that zircon in the ultramafic sequence did grow not from mantle-derived but from crustally-derived magma whereas acid rocks of the Complex may have formed from “mixing” between new juvenile and old crustal end-members. The ages of old zircon population are in agreement with data of Zeh (2009), who showed that a part of the Kaapvaal Craton was formed between 2.75 and 2.95 Ga (according to the zircon U-Pb emplacement ages) in an accretionary margin with extensive assimilation of older crust. Alternatively, our data could be interpreted as an indication on an anomalous Archaean SCLM under the Kaapvaal craton with a non-radiogenic Hf isotopic signature that is distinct from both the depleted mantle source and from the Archaean continental crust (Griffin et al. 2000).

Acknowledgements

Authors thank IvanPlats and AngloPlatinum for the access to the cores and support in all aspects. The study is partially supported by NRF of South Africa through THRIP and RFBR through grant 11-05-00014.

References

- Eales HV, Costin G (2012) Crustally contaminated komatiite: primary source of the chromitites and Marginal, Lower, and Critical Zone magmas in a staging chamber beneath the Bushveld Complex. *Econ Geol* 107: 645–665
- Griffin WL, Pearson NJ, Belousova E, Jackson SE, van Acherbergh E, O’Reilly S.Y., Shee SR (2000) The Hf isotope composition of cratonic mantle: LAM-MC-ICPMS analysis of zircon megacrysts in kimberlites. *Geochim Cosmochim Acta* 64: 133–147
- Harmer RE, Sharpe MR (1985) Field relations and Sr isotope systematics of the marginal rock of the Eastern Bushveld Complex. *Econ Geol* 80: 813-837
- Schoenberg R, Kruger FJ, Nögler TF, Meisel T, Kramers JD (1999) PGE enrichment in chromitite layers and the Merensky reef of the western Bushveld complex; a Re–Os and Rb–Sr isotope study. *Earth Planet Sci Lett* 172: 49-64
- Scotates JS, Friedman RM (2008) Precise age of the platiniferous Merensky Reef, Bushveld Complex, South Africa, by the U-Pb zircon chemical abrasion ID-TIMS technique. *Econ Geol* 103: 465-471
- Walraven F (1987) Textural, Geochemical and genetic aspects of the granophyric rocks of the Bushveld Complex. *Mem Geol Surv S Afr* 72
- Wilson AHA (2012) A chill sequence to the Bushveld Complex: insight into the first stage of emplacement and implications for the parental magmas. *J Petrol* 53: 1123-1168
- Zeh A, Gerdes A, Barton JM (2009) Archean accretion and crustal evolution of the Kalahari Craton - the zircon age and Hf isotope record of granitic rocks from Barberton/Swaziland to the Francistown Arc. *J Petrol* 50: 933–966

S3.7:

Orogenic gold deposits

Convenors:

Pasi Eilu, Richard Goldfarb & Iain Pitcairn

KEYNOTE SPEAKER

The orogenic gold mineral system

T. Campbell McCuaig

Centre for Exploration Targeting and Australian Research Council Centre of Excellence for Core to Crust Fluid Systems, School of Earth and Environment, The University of Western Australia, Perth, Australia.

Jon M.A. Hronsky

Western Mining Services and Centre for Exploration Targeting, School of Earth and Environment, The University of Western Australia, Perth, Australia.

Abstract. Mineral systems-based analysis of orogenic gold, as opposed to the traditional deposit-centric approach to understanding this mineralisation style, is dramatically changing our understanding of processes that lead to the formation of world-class deposits and how we explore for them.

The past decade of research at the deposit scale has delivered several advances in understanding orogenic gold deposits, including recognition of multiple fluids and multiple pulses of gold mineralisation in single deposits under a wide range of structural controls. We now realise these systems form very rapidly, as geological 'lightning bolts' in a longer maelstrom of deformation, fluid flow, and hydrothermal alteration that is largely barren. These new data pose a serious challenge to the widely accepted metamorphic model for orogenic gold deposits.

Fundamental advances at the larger scale have increased our understanding of the role of inherited architecture in controlling the location and geometry of large orogenic gold deposits from craton/lithosphere to deposit scale, and of aspects of terrane fertility, whereby some areas of the Earth's lithosphere are inherently enriched in Au and more amenable to the formation of large gold systems. These advances have led to the recognition that orogenic gold forms in a very consistent tectonic setting – inverted retro-arc peri-cratonic rift zones, during their inversion phase, particularly during the termination of long-lived accretionary orogens that are associated with supercontinent formation.

Parallel to these advances in understanding gold deposits has been a breakthrough in understanding how mass and energy transfer organises itself in the lithosphere as self-organised critical systems (SOCS). Application of SOCS thinking moves us from a deformation and chemistry-centric to an architecture and fluid physics-centric paradigm for these deposits.

All of this information is encompassed in a systems approach to understanding orogenic gold deposits from fluid source to fluid sink. This approach recognises a hierarchy of processes that control the formation of world class deposits including terrane fertility, transient geodynamic events that trigger mineralisation, favourable architecture, and depositional process.

Keywords. orogenic gold, mineral systems.

1 A need for better predictive models

Although major advances have been made in understanding orogenic gold deposits over the past several decades through an ever-increasing volume of research, the predictive power of our current mineral deposit models for world-class orogenic gold resources remains limited. It is postulated here that a fundamentally different way of organising our understanding of ore-forming processes in a mineral

systems context has the potential to lead to better 'mappable' targeting elements for orogenic gold, as well as other deposit types, and hence greater predictive power.

2 A decade of deposit-scale advances

The past decade of research at the deposit scale has heralded several advances in understanding orogenic gold deposits. The key advances at this scale include the recognition that multiple ore fluids are involved in deposit genesis (Neumayr et al. 2008) and the recognition of multiple timings of gold mineralisation within single deposits or camps (Robert et al. 2005, and references therein).

The recognition of multiple fluids involved in gold deposition/mobilisation in single deposits has been revealed through detailed studies of specific deposits and camps, particularly in the Eastern Goldfields terrane of the Archaean Yilgarn craton of Western Australia. In the Yilgarn, the presence of at least two distinct ore fluids has been identified at several of the largest deposits on the basis of mineralogical; stable, radiogenic, and noble gas isotopic analysis; and whole rock chemistry: a reduced acid fluid (As and muscovite-pyrrhotite-pyrite association) and an oxidised fluid (Bi-Mo and phengite-magnetite-hematite-pyrite association: c.f. Neumayr et al. 2008). Mantle and deep crustal source components are identified in these fluids from radiogenic isotopes and noble gas analyses of mineral phases and fluid inclusions, respectively (Cleverley et al. 2009; Kendrick et al. 2011). Debate ensues on the genesis of these fluids, and their relative timing. Although it has been suggested they were broadly coeval (c.f. Kendrick et al. 2011), more detailed studies indicate these fluid events are likely to be sequential in nature (Miller et al. 2010; Duggan 2010). There is good evidence for a fairly direct relationship between the oxidised fluid and spatially associated magmatic intrusions (Miller et al. 2010a), whereas the source of the reduced fluid is more uncertain. Nevertheless, both fluids have been shown to introduce gold into the terrane (Miller et al. 2010a, b) and the alteration footprint of these fluids can be mapped by widely available spectral and portable XRF technologies. Detailed studies of alteration assemblages, in combination with experimental petrology, have shown that at least some high-temperature deposits, particularly those at mid-amphibolite to granulite facies, have been metamorphosed, and in some cases partially melted (Phillips and Powell 2009; Tomkins and Grundy 2009).

High precision geochronology has recognised multiple pulses of gold mineralisation in individual terranes (cf. Robert et al. 2005). Moreover, we now

realise the speed of these orogenic systems, forming as geological ‘lightning bolts’ in a longer maelstrom of deformation, fluid flow, and hydrothermal alteration that is largely barren. For example, it has long been recognised that the Juneau gold belt deposits of the northern Cordillera form within analytical error of ^{40}Ar - ^{39}Ar (mica) systematics at 56-55 Ma (Goldfarb et al. 2005). Recent dating of Carlin deposits shows that almost 100 Moz of Au was introduced in 40,000 to as little as 12,000 years (Hickey and Dipple, 2011). Studies of gold flux in active hydrothermal systems have shown that the largest Au deposits could be formed in as little as 50,000 years (Simmons and Brown 2008).

Another key advance is the recognition that the mineralising processes are often occurring multiple times in the same rock mass. Large et al. (2007) have shown potential early enrichment of Au in sedimentary basins hosting major gold deposits. Several studies have shown that giant gold deposits often show multiple periods of hydrothermal alteration and ore formation (Robert et al. 2005 and references therein) under a wide range of kinematics (Miller et al. 2010a,b). In concert, these new data have re-invigorated intrusion-related models and pose a serious challenge to the more widely accepted metamorphic fluid model (cf. Phillips and Powell 2009) for orogenic gold deposits. This realisation of multiple ore-forming events in highly endowed terranes dramatically changes the question of genesis from “why is the gold deposited in this specific depositional site in this deformation event” to “why did this volume of rock get struck by lightning so many times?” The exploration question concomitantly changes to “how can I predict where there are more mineralisation lightning rods at depth?” To answer this question requires us to think on a scale much larger than the deposits themselves, where the traditional focus of our research has been.

3 Appreciation of larger scale processes

A series of advances in understanding the genesis of giant orogenic gold deposits has come from stepping away from the deposits and understanding the larger scale context in which the deposits are located. The key advances in this space are: (1) understanding the control of whole lithospheric architecture and long-lived, vertically-accretive structures; (2) the recognition of the consistent regional-scale tectonic setting in which these deposits occur; (3) the recognition of the transient geodynamic events that trigger gold deposition; (4) self-organising critical systems (SOCS) and their control on mineral systems; and (5) the realisation that some areas of the Earth’s lithosphere are preferentially enriched in gold, and thus more fertile for the formation of giant gold deposits.

There has been a long-recognised association of major orogenic deposits with large-scale structures (O’Driscoll 1986; ‘first order’ structures: c.f. Goldfarb et al. 2005; Robert et al. 2005). These structures are now recognised to be long-lived structures, generally rooted in the mantle lithosphere and at the margins of old mantle lithospheric blocks. They are vertically-accretive structures, continually propagating upwards over new crust deposited or obducted over the top of them. They

often have a subtle expression at surface, but a strong expression in isotopic or geophysical datasets that image to great depth (Hronsky et al. 2012; Mole 2012). This inherited architecture plays a role in controlling the location and geometry of large orogenic gold deposits from craton/lithosphere to district scale (McCuaig et al. 2010; Miller et al. 2010b)

Multiple regional-scale targeting studies, covering a wide diversity of orogenic gold provinces throughout geological time, have led to the recognition that orogenic gold forms in a very consistent tectonic setting, which is in inverted retro-arc and/or peri-continental rifts. Furthermore, peaks of orogenic gold formation correlate strongly with final collisional orogeny that terminates a long-lived accretionary orogen, explaining the long-observed relationship between orogenic gold and supercontinent assembly (Goldfarb et al. 2005; Kerrich et al. 2005). The events leading to assembly of “intermediate supercontinents”, such as the Pan African part of Gondwana, are as prospective as those that produce the final assembly of supercontinents.

The importance of transient geodynamic controls has been recognised as increasingly high-precision geochronology shows the short timescales of ore-forming events. These transient geodynamic events involve stress switches, during which the system passes through a neutral stress state (R. Tosdal, oral commun., 2009), permeability-creating active deformation is limited, and therefore the upper crust itself forms a barrier to ascending fluids and magmas. Under these conditions, the system goes to criticality and self-organises (cf. Bak 1996), with gold deposits and associated high-grade oreshoots forming in the transient exit conduits above the barrier (Figure 1, Hronsky 2011). Such processes can explain, for example, the occurrence of gold deposits in preferred rock volumes adjacent to, but not within, the largest high strain structures. Application of SOCS has the potential to dramatically change how we understand and explore for gold from terrane to oreshoot scales, in that it moves us from a deformation and chemistry-centric to a fluid physics and architecture-centric paradigm for these deposits.

Seminal work by Loucks and others (Loucks 2012) in Neogene arcs and porphyry Cu-Au systems has demonstrated that Au acts as an incompatible element during mantle-melting, and that Au is therefore likely preferentially enriched in the mantle lithosphere below giant gold systems (Hronsky et al. 2012). Moreover, a review of North and South American Cordilleran terranes shows distinct regions that host large gold systems of a range of ages and deposit types (Sillitoe 2008), again supporting the notion of a preferentially enriched lithosphere. This enrichment may come from small-volume alkaline melts stalling in the mantle lithosphere, for example in areas of flat subduction (Hronsky et al. 2012), although we are just beginning to understand these source processes. This is clearly an area for further research that will impact heavily on terrane selection.

4 A mineral systems approach

All of the advances outlined above are encompassed in a systems approach to understanding orogenic gold deposits from fluid source to fluid sink (Figure 1). This approach recognises that there is a scaled hierarchy of processes that control gold systems. The approach of McCuaig et al. (2010) has been applied to produce an integrated synthesis of the orogenic gold mineral system. The critical elements of terrane fertility, favourable architecture, transient geodynamics, and depositional process provide a framework for recognising constituent elements at relevant scales (Table 1).

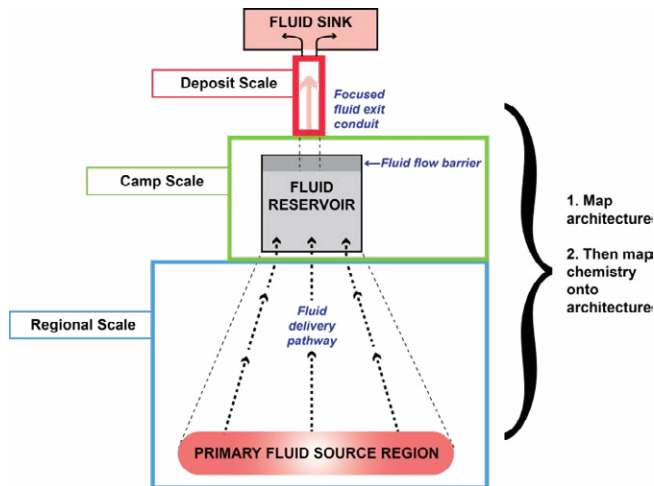


Figure 1, Consideration of the orogenic gold system from fluid source to fluid sink. Key to this formulation is the concept of a threshold barrier, or fluid flow barrier, the transient breaching of which forms ore deposits. Different processes operate at different scales.

Some of the key paradigm shifts that arise from the mineral systems approach include: (1) a move from structure and chemistry-driven research to fluid physics and 4D architecture-driven research in understanding mineral systems; (2) an understanding that deposit-scale chemical processes of ore deposition are a final consequence of, rather than a driver of, the mineral system, and (3) a recognition of the connections between differing 'styles' of gold deposits (e.g., Hronsky et al. 2012), which has very important regional targeting implications. For example, we predict that the intrusion-related gold, Au-rich VMS, and orogenic gold deposit types will occur in similar tectonic settings, although forming at different times.

The recognition of processes operating at nested scales is critical, as the required understanding to make exploration decisions at the small scale has little importance on the larger scale, and vice-versa. This scale dependence must be recognised in targeting criteria (McCuaig et al. 2010).

Key research directions include understanding mantle contributions to systems; determining the precise, high-resolution geodynamic context of ore formation events, particularly where multiple events occur; the rate of formation and genesis of high-grade ore shoots; more innovative ways to map 4D architecture at a range of

scales; and mapping of geochemistry onto this architecture to hunt the fluid conduits in 3D, and *then* find the ore.

Acknowledgements

TCM gratefully acknowledges funding for this work through ARC Linkage Projects LP110100667 and LP0776780. This is contribution 305 from the ARC Centre of Excellence for Core to Crust Fluid Systems (<http://www.cafs.mq.edu.au>).

References

- Bak P (1996) How nature works: the science of self-organized criticality. Copernicus, Springer-Verlag, New York, 212 p.
- Cleverley JS, Hough R, Ryan C, Maas R, Blake K, Nugus M (2009) Gold Precipitation: The Big Picture from Microchemical Processes. In: Williams PJ et al (eds) Smart Science for Exploration and Mining: Proceedings of the 10th Biennial SGA Meeting of The Society for Geology Applied to Mineral Deposits, Townsville Australia, p. 213-215.
- Duggan B (2010) The evolving footprint: a spatial and temporal study of alteration footprints on gold bearing structures in the Greater reverege Area, St. Ives, Western Australia. MSc Thesis, The University of Western Australia.
- Goldfarb RJ, Baker T, Dube B, Groves DI, Hart CJR, Gosselin P (2005) Distribution, character, and genesis of gold deposits in metamorphic terranes: In: Hedenquist JW, Thompson JFH, Goldfarb RJ, and Richards JP (eds) Econ Geol 100th Anniversary Volume. Society of Economic Geologists, Littleton, Colorado, p. 407-450.
- Hickey K A, Dipple G M (2011) The brevity of hydrothermal fluid flow revealed by thermal haloes around giant Au-deposits. GSA Annual Meeting, Minneapolis.
- Hronsky JMA, (2011) Self-organized critical systems and ore formation: The key to spatial targeting? Society of Economic Geology Newsletter 84: 14-16.
- Hronsky JMA, Groves DI, Loucks RR, Begg GC (2012) A unified model for gold mineralisation in accretionary orogens and implications for regional scale targeting methods. Min Dep 47: 339-358.
- Kendrick MA, Honda M, Walshe J, Petersen K (2011) Fluid sources and the role of abiogenic-CH₄ in Archean gold mineralization: Constraints from noble gases and halogens Precam Res 189: 313 – 327.
- Kerrick R, Goldfarb RJ, Richards J (2005) Metallogenic Provinces in an evolving geodynamic framework. In: Hedenquist JW, Thompson JFH, Goldfarb RJ, and Richards JP (eds) Econ Geol 100th Anniversary Volume. Society of Economic Geologists, Littleton, Colorado, p. 1097-1136.
- Large RR, Maslennikov VV, Robert F, Danyushevsky LV, Scott RJ, Chang Z-S (2007) Multi-stage sedimentary and metamorphic origin of pyrite and gold in the giant Sukhoi Log deposit, Lena Goldfield, Russia. Econ Geol 102: 1023-1267.
- Loucks R (2012) Chemical Characteristics, Geodynamic Settings, and Petrogenesis of Gold-Ore-Forming Arc Magmas. Centre for Exploration Targeting Newsletter, June 2012, p. 1, 4-12.
- McCuaig TC, Beresford S, Hronsky J (2010) Translating the mineral systems approach into an effective exploration targeting system. Ore Geol Rev 38: 128-138.
- Miller JM, McCuaig TC, Duggan B, Adams G (2010a) Camp-scale controls on world-class gold systems in the Yilgarn craton. In: Tyler IM, Knox-Robinson CM (eds) Fifth International Archean Symposium Abstracts. Geological Survey of Western Australia Record 2010/18: 316-319.
- Miller J, Blewett R, Tunjic J, Connors K (2010b) The role of early formed structures on the development of the world class St Ives Goldfield, Yilgarn, WA. Precam Res 183: 292-315.
- Mole D (2012) Evaluating the lithospheric architecture of the Archean Yilgarn craton in space and time: implications for

komatiite volcanism and earth evolution. PhD Thesis, The University of Western Australia.

Neumayr P, Walshe J, Hagemann S, Petersen K, Roache A, Frikken P, Horn L, Halley S (2008) Oxidized and reduced mineral assemblages in greenstone belt rocks of the St. Ives gold camp, Western Australia: vectors to high-grade ore bodies in Archaean gold deposits. *Min Dep* 43: 363–371.

O'Driscoll EST (1986) Observations of the lineament–ore relation. *Phil Trans Roy Soc Lond A317*: 195–218.

Phillips GN, Powell R (2009) Formation of gold deposits: Review and evaluation of the continuum model. *Earth Sci Rev* 94: 1–21.

Robert F, Poulsen KH, Cassidy KF, Hodgson CJ (2005) Gold metallogeny of the Superior and Yilgarn Craton. In: Hendequist JW, Thompson JFH, Goldfarb RJ, Richards JP (eds) *Econ Geol*

100th Anniversary Volume. Society of Economic Geologists, Littleton, Colorado, p. 1001–1033.

Sillitoe RH (2008) Major gold deposits and belts of the North and South American Cordillera: distribution, tectonomagmatic settings and metallogenic considerations. *Econ Geol* 103: 663–688.

Simmons SF, Brown KL (2008) Precious metals in modern hydrothermal solutions and implications for the formation of epithermal ore deposits. *Society of Economic Geologists Newsletter* 72: 1, 9–12.

Tomkins AG, Grundy C (2009) Upper temperature limits of orogenic gold deposit formation: constraints from the granulite-hosted Griffin's Find Deposit, Yilgarn Craton. *Econ Geol* 104: 669–68

		CRITICAL ELEMENTS			
		FERTILITY	FAVOURABLE GEODYNAMICS	FAVOURABLE ARCHITECTURE	DEPOSITIONAL PROCESS
SCALE	ORE-SHOOT	NA at this scale	NA at this scale	Localised dilatant zone in host structure	2nd order - pressure drops; 3rd order - favourable substrate (chemical rx)
	DEPOSIT			Pipe-like rock volume more favourable for fracturing by fluid-exit pulse (either local structural complexity or pipe of more competent rock)	
	CAMP	Period of low active tectonic strain, e.g. stress switch causing transient neutral stress state causing fluid system to self-organise. Areas of greatest uplift favoured (provides stress switch and high rates of energy and mass transfer)	Major heterogeneity (e.g. cross-structure intersection) along trend of inverted rift-axial (or rift-marginal) fault with associated physical seal (e.g. an informal culmination or unconformity)	1st order - upper 10 km of crust AT THE TIME OF MINERALISING EVENT where fluid pressure (+T, X) gradients are greatest	
	PROVINCE	Discrete Au-enriched upper Lithospheric domain; particularly near its margins. Potentially mantle lithosphere enriched by small volume partial melts prior to termination of orogeny	Terminal phase of syn-ore orogenic event (e.g. the transition to incipient extension associated with the termination of collision and locus of subduction retreating oceanward).		Inverted retroarc rift; preferably developed at a continental margin, or margin of deep mantle lithosphere root. Long lived 'vertically-accretive' structure
	CONTINENTAL	Currently unclear but the occurrence of the Western US Gold Superprovince suggests that some control at this scale exists.	A major collisional orogenic event within the history of an evolving accretional orogen; the major collision that actually terminates a long-lived (>200Ma) accretionary orogen is most prospective and usually associated with a peak of super-continent formation		Major "O'Driscoll-type" sub-continental scale lineament (representing long-lived zone of transverse dislocation within accretionary orogen). Long lived 'vertically-accretive' structure

Table 1. Critical and constituent processes in the formation of orogenic gold deposits. The scale dependence of processes needs to be translated into scale dependant targeting elements that can be mapped either directly or by proxy in existing or obtainable geoscience datasets at that scale.

The boron isotope composition of tourmaline from the Val-d'Or orogenic gold deposits, Québec, Canada

Georges Beaudoin

Département de géologie et de génie géologique, Université Laval, Québec (QC) Canada

Claire Rollion-Bard, Gaston Giuliani

CRPG, UMR 7358, CNRS-UL, GET, UMR 5563 CNRS-IRD-CNES Toulouse, Vandoeuvre, France

Abstract. Tourmaline from the Val-d'Or orogenic gold vein field is dravitic, plotting in the alkali field with a sodic, low calcium, composition. The boron isotope composition of tourmaline ranges from -16.7 to -8.3 ‰. Higher $\delta^{11}\text{B}$ in tourmaline is related to higher Ti and $\text{Mg}/(\text{Mg}+\text{Fe})$. Tourmaline fibers display a circa 2 ‰ increase in $\delta^{11}\text{B}$ over a growth length of less than 1 cm. The range in $\delta^{11}\text{B}$ values cannot be explained by boiling in veins or by a range of equilibrium temperatures. The variance in tourmaline $\delta^{11}\text{B}$ values (-16.4 ‰ to -10.7 ‰) in one large deposit (Sigma) is almost as large as that for the vein field. The boron isotope composition in the Val-d'Or vein field tourmaline is determined by various mixtures of locally derived boron from metamorphic devolatilization of the crustal sequence. This contrasts with tourmaline $\delta^{18}\text{O}$ values that are homogeneous at the deposit scale in the Val-d'Or orogenic gold vein field (Beaudoin and Pitre 2005).

Keywords Boron, isotope, gold, vein, metamorphic, fluid, orogenic

1 Introduction

The Val-d'Or (Québec, Canada) vein field is a classical example of orogenic gold deposits hosted in Archean rocks. The Val-d'Or vein field contains a large number of early quartz-carbonate (QC) and later quartz-tourmaline-carbonate (QTC) gold-bearing veins within a consistent structural setting. The veins formed during two successive hydrothermal events.

The stable isotope composition of vein minerals (C, O and S) from the QC and QTC veins from the Val-d'Or vein field was studied by Beaudoin and Pitre (2005), who concluded that the veins formed by water-rock reaction and mixing between evolved Archean seawater trapped in the volcanic rocks porosity and a deep-seated metamorphic fluid. Beaudoin et al. (2006) used numerical modelling to show that the regional pattern of fluid $\delta^{18}\text{O}$ values calculated from vein quartz, resulted from drainage of the hydrothermal fluids along the Cadillac-Larder Lake crustal shear zone. Beaudoin and Chiaradia (2010) showed that quartz and tourmaline are in oxygen isotope equilibrium at approximately 350°C, and that the temperature-independent Sr isotope composition covaries with $\delta^{18}\text{O}$ values of tourmaline.

In this study, we document the in-situ boron isotope composition of tourmaline from QTC veins to gain a better understanding of deposition processes and hydrothermal fluid sources for gold mineralization.

2 Analytical method

Tourmaline chemistry was measured using the 5 wavelength dispersive spectrometer CAMECA SX-100 by electron probe micro-analysis (EPMA) at Université Laval, Québec, Canada. Analytical conditions were 15 kV at 20 nA, and calibration using a set of natural and artificial standards.

The boron isotope composition of tourmaline was measured using the CAMECA IMS 1270 secondary ion mass spectrometer at the CRPG, Nancy, France. A primary beam of $^{16}\text{O}^-$ ions with an intensity of ≈ 5 nA was focused to a spot of about 20 μm . A mass resolution of 3,000 was used for the analyses. Boron isotopes were measured in monocollection mode using the central Faraday cup. The typical intensities are about 2×10^7 cps on $^{11}\text{B}^+$. The typical internal error was ± 0.2 ‰. The reference material was a tourmaline (Tourm812, $\delta^{11}\text{B} = -13.3$ ‰) and the external error based on the repeated measurements of this tourmaline was between 0.1 and 0.4 ‰ (1s). Lithium concentrations are low such that no matrix effect correction is needed.

3 Composition of gold vein tourmaline

3.1 Major elements

The major element composition was measured on 124 tourmaline grains from 25 samples from 15 deposits, representative of the Val-d'Or vein field. Nine samples are from various parts of the Sigma deposit. Tourmaline

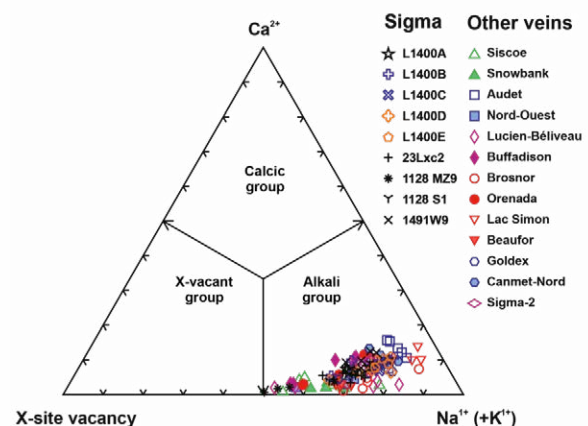


Figure 1. X-site vacancy-Ca-Na(+K) ternary diagram for Val-d'Or orogenic gold vein tourmaline.

is dravitic, with a few samples plotting at the boundary with schorlitic tourmaline. Figure 1 shows that tourmaline is alkali, forming a trend from Ca-poor, higher X-site vacancy tourmaline, towards higher Ca, dominantly sodic tourmaline.

3.2 Boron isotope composition

The $\delta^{11}\text{B}$ values of 176 spot analyses from 17 samples from nine gold deposits distributed across the Val-d'Or orogenic gold vein field range from -16.7 ‰ to -8.3 ‰, with a normal distribution (Fig. 2). The Sigma deposit was studied in greatest detail. Eight samples, including five documenting successive increments of opening of a single extensional vein, yield a range of $\delta^{11}\text{B}$ values (-16.4 to -10.7 ‰) almost as large as that for the whole vein field. Sigma samples from levels 11 (343 m depth) to 32 (975 m depth) display no systematic change in $\delta^{11}\text{B}$ values with depth.

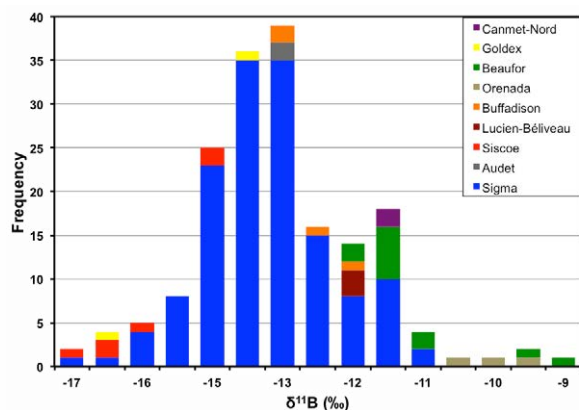


Figure 2. Histogram of $\delta^{11}\text{B}$ values for vein tourmaline from the Val-d'Or orogenic gold vein field.

The boron isotope composition is almost independent of the chemical composition of tourmaline. Only weak covariation shows that tourmaline with higher $\delta^{11}\text{B}$ values has lower Ti and $\text{Mg}/(\text{Mg}+\text{Fe})$.

In several samples, cm-long arrays of narrow tourmaline fibers, intergrown with quartz during extension and vein opening, were analyzed along the growth direction. The data, plotted along a profile, does not track the $\delta^{11}\text{B}$ values in one single fiber, but instead “bulk” tourmaline in the direction of the vein opening, and younger vein filling. Figure 3 shows that $\delta^{11}\text{B}$ increases from low values (~ -16 ‰) to higher values (~ -13.5 ‰) after 5 mm, then drops to ~ -15.5 ‰ to rise again to values near -13 ‰ after more than 1 cm of tourmaline fiber growth.

4 Discussion

Tourmaline ^{11}B - ^{18}O isotopologues plot in a broad array in Figure 4. The array is at high angle to the equilibrium composition of tourmaline precipitated from a fluid with a $\delta^{11}\text{B}$ of -9 ‰ and a $\delta^{18}\text{O}$ of 4 ‰ (Beaudoin and Pitre 2005) at temperatures ranging from 100 to 500 °C (Fig. 4). Tourmaline B-O isotopologues, therefore, cannot be explained by precipitation along a temperature gradient.

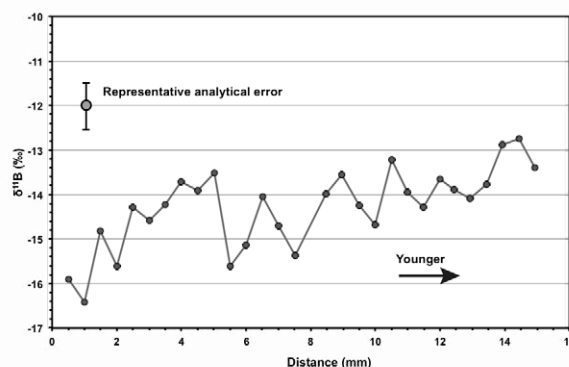


Figure 3. Profile of $\delta^{11}\text{B}$ along an array of growth fibers in an extensional vein (L1426Wa, Sigma deposit).

Using the B isotope fractionation of Meyer et al. (2008), the 2 ‰ increase in $\delta^{11}\text{B}_{\text{H}_2\text{O}}$ values during the approximate 1 cm length of tourmaline fiber growth would require a temperature change from 200 to 350 °C. Although this temperature range is similar to the range of fluid inclusion homogenization or decrepitation temperatures measured in the same sample by Boullier and Robert (1992) and Robert et al. (1995), there is no indication in the fluid inclusion studies for a systematic temperature gradient on a cm-scale. Such a high, cyclic, temperature range is also inconsistent with the interpreted mid-crustal depth of formation of the Sigma QTC veins (Boullier and Robert 1992; Robert et al. 1995).

Precipitation of tourmaline by evaporation of boric acid yields a $\Delta^{11}\text{B}_{\text{v-l}} \sim 0.5$ ‰ (Palmer et al. 1992). The gradual increase in $\delta^{11}\text{B}$ documented along fiber arrays (Fig. 3) indicates that tourmaline cannot precipitate as a consequence of liquid to vapour phase separation because the isotope effect is too small for the 2 ‰ increase in $\delta^{11}\text{B}$ values, but more importantly, because the liquid becomes depleted in ^{11}B during boiling, contrary to the increase in $\delta^{11}\text{B}$ values documented in Figure 3.

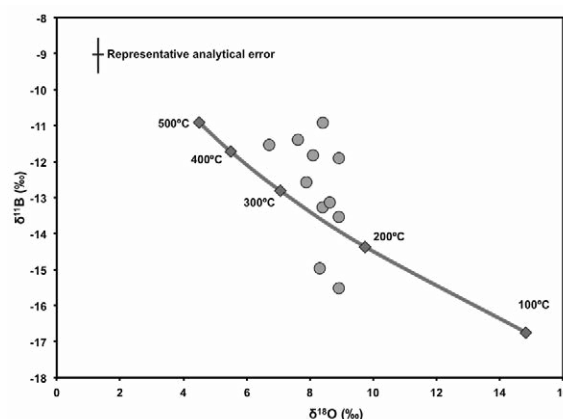


Figure 4. Tourmaline B-O isotopologue composition compared to the equilibrium composition of tourmaline with a fluid with $\delta^{11}\text{B}$ of -9 ‰ and $\delta^{18}\text{O}$ of 4 ‰ at different temperatures, using Meyer et al. (2008) and Blamart (1991). The $\delta^{11}\text{B}$ value is the sample average composition from SIMS in-situ analyses, whereas the $\delta^{18}\text{O}$ value is the bulk mineral concentrate composition (Beaudoin and Chiaradia 2010).

The range of tourmaline $\delta^{11}\text{B}$ values from -16.7 ‰ to -8.3 ‰ yields calculated $\delta^{11}\text{B}_{\text{H}_2\text{O}}$ values from -5.1 ‰ to -13.5 ‰, at 350 °C, using Meyer et al. (2008). The range in $\delta^{11}\text{B}_{\text{H}_2\text{O}}$ values could have been derived from metamorphic devolatilization of average continental crust (van Hinsberg et al. 2011). It is important to take into consideration the regional distribution of tourmaline $\delta^{11}\text{B}$ values. The fact that almost all the boron isotope variance is displayed within one large vein deposit, such as Sigma, indicates that local sources of boron contributed in various proportions to yield the tourmaline compositions. The large $\delta^{11}\text{B}$ variance in one deposit contrasts with the $\delta^{18}\text{O}$ values of quartz, which have been shown to display a low variance at the deposit scale (Beaudoin and Pitre 2005). In addition to this local variance in boron sources, the average $\delta^{11}\text{B}$ values for each deposit displays regional change from lower values (~ -15 ‰) in the western part of the vein field, to higher average values (~ -10 ‰) in the eastern part.

The boron isotope composition of tourmaline from orogenic gold veins in Val-d'Or is similar to those reported for tourmaline from other gold deposits. Garda et al. (2009) reported $\delta^{11}\text{B}$ values ranging from -15 to -8 ‰ for tourmaline associated with gold mineralization in the Serra do Itaberaba Group in Brazil. The range of boron isotope compositions was attributed to various contributions of low $\delta^{11}\text{B}$ from metamorphism of the continental crust and higher $\delta^{11}\text{B}$ from metamorphism of volcano-sedimentary rocks altered by seawater. At the Hira Buddini orogenic gold deposit, India, Krienitz et al. (2008) report that tourmaline displays a bimodal distribution of $\delta^{11}\text{B}$ values with modes at -2 ‰ and 6 ‰, which is interpreted to indicate mixing between two distinct hydrothermal fluids, a low $\delta^{11}\text{B}$ (+1 ‰) fluid released by metamorphism of mafic volcanic rocks, and a higher $\delta^{11}\text{B}$ (+10 ‰) fluid derived from degassing of I-type intrusions. A similar metamorphic fluid interpretation is proposed for the Big Bell orogenic gold deposit, Australia, based on $\delta^{11}\text{B}$ values ranging from -21.9 ‰ to -21.4 ‰ (Jiang et al. (2002).

5 Conclusions

The range in tourmaline $\delta^{11}\text{B}$ values (8.4 ‰) is too large to result from either a temperature gradient or from liquid-vapour phase separation. The increase in $\delta^{11}\text{B}$ values, of ~2 ‰ over ~1 cm, along the growth of tourmaline fibers in extensional veins is also incompatible with both processes. The large variance of $\delta^{11}\text{B}$ values at the scale of a deposit, and the regional change in average $\delta^{11}\text{B}$ values, both are interpreted to result from mixing of various boron sources from the local crustal rocks. The local source for boron is in contrast to the low variance of $\delta^{18}\text{O}$ values in tourmaline and quartz at the deposit-scale, indicating that boron and oxygen source reservoirs are decoupled in the hydrothermal fluids. This reflects a local and heterogeneous source for boron in contrast to the deep-seated metamorphic fluid source inferred for the high $\delta^{18}\text{O}$ hydrothermal fluid component (Beaudoin and Pitre

2005, Beaudoin et al. 2006).

Acknowledgements

François Robert and Paolo Garofalo are thanked for some of the Sigma deposit samples. This research is funded by a Discovery Grant to GB from the Natural Science and Engineering Research Council of Canada.

References

- Beaudoin G, Pitre D (2005) Stable isotope geochemistry of the Archean Val-d'Or (Canada) orogenic gold vein field. *Mineralium Deposita* 40: 59-75.
- Beaudoin G, Therrien R, Savard C (2006) 3D numerical modelling of fluid flow in the Val-d'Or orogenic gold district: major crustal shear zones drain fluids from overpressured vein fields. *Mineralium Deposita* 41: 82 - 98.
- Beaudoin G, Chiaradia M (2010) Tourmaline Sr-O isotopes: evidence for fluid mixing in the Val-d'Or orogenic gold vein field. *Acta Mineralogical-Petrographica* 6: 250.
- Blamart D (1991) Les concentrations tungstifères et stannifères: caractérisation isotopique (H-O) des fluides minéralisateurs, sur l'exemple du gisement Sn-W de Walmes (Maroc central). Détermination de quelques fractionnements isotopiques (H-O) entre minéraux et eaux Institut National Polytechnique de Lorraine, pp 1667.
- Boullier A-M, Robert F (1992) Paleoseismic events recorded in Archean gold-quartz vein networks, Val d'Or, Abitibi, Quebec, Canada. *Journal of Structural Geology* 14: 161-179.
- Garda GM, Trumbull RB, Beljavskis P, Wiedenbeck M (2009) Boron isotope composition of tourmalinite and vein tourmalines associated with gold mineralization, Serra do Itaberaba Group, central Ribeira Belt, SE Brazil. *Chemical Geology* 264: 207-220.
- Jiang S-Y, Palmer MR, Yeats CJ (2002) Chemical and boron isotopic compositions of tourmaline from the Archean Big Bell and Mount Gibson gold deposits, Murchison Province, Yilgarn Craton, Western Australia. *Chemical Geology* 188: 229-247.
- Krienitz M, Trumbull R, Hellmann A, Kolb J, Meyer F, Wiedenbeck M (2008) Hydrothermal gold mineralization at the Hira Buddini gold mine, India: constraints on fluid evolution and fluid sources from boron isotopic compositions of tourmaline. *Mineralium Deposita* 43: 421-434.
- Meyer C, Wunder B, Meixner A, Romer R, Heinrich W (2008) Boron-isotope fractionation between tourmaline and fluid: an experimental re-investigation. *Contributions to Mineralogy and Petrology* 156: 259-267.
- Palmer MR, London D, Morgan Vi GB, Babb HA (1992) Experimental determination of fractionation of $^{11}\text{B}/^{10}\text{B}$ between tourmaline and aqueous vapor: A temperature- and pressure-dependent isotopic system. *Chemical Geology: Isotope Geoscience section* 101: 123-129.
- Robert F, Boullier A-M, Firdaus K (1995) Gold-quartz veins in metamorphic terranes and their bearing on the role of fluids in faulting. *Journal of Geophysical Research* 100: 12861-12879.
- van Hinsberg VJ, Henry DJ, Marschall HR (2011) Tourmaline: An ideal indicator of its host environment. *Canadian Mineralogist* 49: 1-16.

Various alteration stages in the Nalunaq gold deposit, south Greenland

Robin-Marie Bell, Jochen Kolb

De Nationale Geologiske Undersøgelser for Danmark og Grønland - GEUS

Abstract. The Nalunaq gold deposit is located on the Nanortalik Peninsula, South Greenland and is characterized by narrow quartz veins and exceptionally high gold grades of up to 5240 g/t. Field observations and petrographic analyses have identified and constrained separate alteration stages that pre- and post-date the gold-bearing quartz veins. Regional metamorphism of the host rocks to amphibolite facies predates all alteration stages. Bands of discoloured host rock are an early feature, whose nature remains unresolved; either primary or alteration. An early hydrothermal alteration stage is characterized by garnet and epidote (GE alteration) and low gold grades. Next followed a clinopyroxene alteration stage that overprints the GE alteration. Gold is located within the Main Quartz Vein (MV), which cross cuts the earlier alteration assemblages. Simultaneously to the formation of the MV, barren quartz-calcite veins formed in a cross-hatched pattern, suggesting a compressional environment during quartz-gold vein formation. Later hematite alteration may have caused gold remobilization, resulting in high gold grades. The detailed description of the alteration stages within Nalunaq gold deposit could aid the discovery of further sites of significant gold grade within the both Nalunaq area and throughout South Greenland.

Keywords: Gold, Alteration, South Greenland, Multiple Stages, Palaeoproterozoic

1 Introduction

The Nanortalik Peninsula in South Greenland has long been recognized as a gold province and contains the Nalunaq gold deposit, which has been mined since the early 2000's (Schlatter and Olsen 2011). Although the area has been studied extensively, the origin and formation of the Nalunaq gold deposit remains unknown. Previous studies have not differentiated between separate alteration assemblages within the Nalunaq gold deposit, terming all alteration 'calc-silicate alteration' (Kaltoft 2000 et al., Porritt 2000, Schlatter and Olsen 2012). As a result, attempts to study the Nalunaq gold deposit using whole-rock and fluid inclusion analysis have so far been inconclusive.

A minimum of four separate alteration stages have been identified by this study and the order of these stages, as well as their exact relation to each other is not thoroughly understood.

A combination of field observations and microscope work will be undertaken to better constrain the petrography and relative order of alteration stages as well as their relationship to each other.

1.2 Nalunaq Mine

The Nalunaq mine is currently owned by Angel Mining Corp, who purchased the site from Crew Gold Corp in

2004. Crew Gold completed over 19,000 m of tunneling, producing 308,000 oz of gold in total (www.angelmining.com). Since then, Angel Mining Corp has continued to develop the project, extending the tunnels and building an underground processing plant, the world's first, in order to manufacture all gold bars on site. Since their first gold pour in 2011, Angel Mining Corp has produced 9,877 oz of gold (Angel Mining 2012). In total, over 9.8 t of gold have been produced. The mine is currently reaching the end of its economic life, with production expected to cease within the next 6-18 months.

2 Regional Geology

The southern tip of Greenland is affected by the Palaeoproterozoic Ketilidian Orogeny, which developed as result of a northward subducting oceanic plate propagating under the North Atlantic Craton (Garde et al. 2002). This orogen has been divided into four zones from north to south; the Border Zone, the Julianehåb Batholith, the Psammite Zone and the Pelite Zone (Garde et al. 2002). The Nalunaq gold deposit is situated within the Psammite Zone, close to the contact with the Julianehåb Batholith (Fig. 1).

The Nalunaq gold deposit is located within the Nanortalik Nappe of the Psammite zone, a sequence of overthrust meta-basalts and meta-dolerites, which have since been largely eroded with the exception of three klippen, Lake 410, Nalunaq and Ippatit (Fig. 1; Petersen and Pedersen 1995; Petersen et al. 1997). The Nanortalik Nappe overthrusts a sequence of meta-arkoses and metapelites which are thought to represent detritus eroded from the Julianehåb Batholith (Garde et al. 2002).

The meta-basalts and meta-dolerites have been metamorphosed to amphibolite facies grades (Porritt 2000). Both the area surrounding the Nalunaq gold deposit and the Nanortalik Nappe have been intruded by several later generations of granitic intrusions (Petersen and Pedersen 1995).

The Nanortalik Peninsula is an area of elevated gold, with visible gold recorded at Ippatit and Lake 410 (Fig 1; Petersen et al. 1997).

2.1 Structure of the Main Vein

The Nalunaq gold deposit comprises a series of laterally extensive quartz veins, which are exposed for c. 2 km on the surface of Nalunaq Mountain (Kaltoft et al 2000). Only one of these, Main Quartz Vein (MV), has significant mineable gold grades of 25.5 g/t (Grammatikopoulous et al. 2004), however visible gold has occasionally been identified in two other veins; the hanging wall and footwall veins. These veins are situated approximately 10 m above and below the MV respectively, occupying shear zones.

The MV varies in width between 0.5-2 m (Schlatter and Olsen 2011) and has a strike of 47° and an average

dip of 36°, however it has a observed dip variation of between 22° and 55° (Kaltoft et al 2000; Grammatikopoulos et al. 2004).

The quartz veins commonly form a pinch and swell structure (Porritt 2000) and there is no simple association between the width of the quartz veins and gold grade (Grammatikopoulos et al. 2004).

The veins are formed of a series of quartz lenses with fragments of host rock commonly observed incorporated into the vein. Quartz veins containing host rock fragments are more likely to host high gold grades (Christensen 2011, 2012 pers comms.).

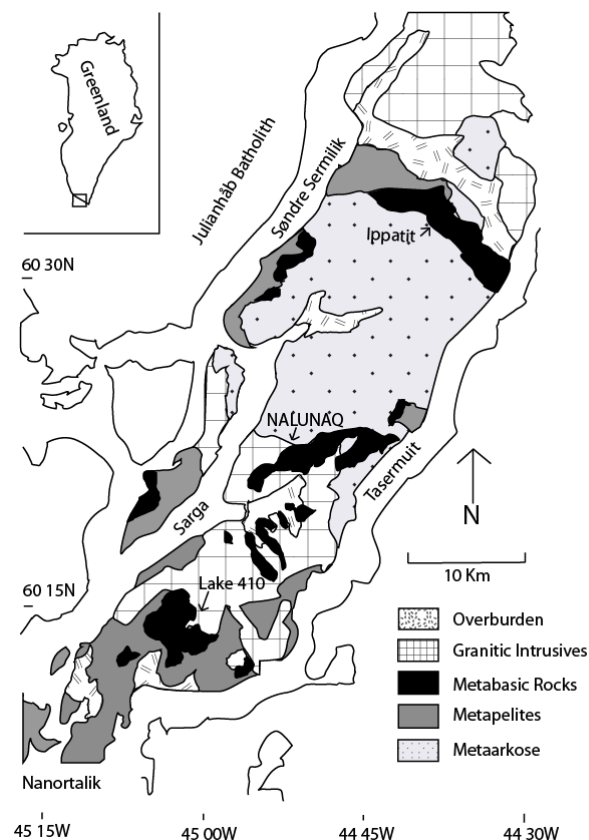


Fig. 1: Geological map of the Nanortalik Peninsula. The two areas of significant gold mineralization (Lake 410 and Ippatit) have also been marked (adapted from Kaltoft et al. 2000 and Petersen and Pedersen 1995).

3 Wall Rocks

The quartz-gold veins are hosted by coarse-grained meta-dolerites and fine-grained meta-basalts, which have undergone metamorphism to amphibolite facies. This metamorphism pre-dates all hydrothermal alteration within Nalunaq gold deposit (Porritt, 2000; Schlatter and Olsen, 2011). These rocks generally contain hornblende, plagioclase and minor quartz and are often black in colour, but can be dark grey or green due variable mineralogy. The majority of host rock observed hosting the MV is fine-grained.

Additional lithologies are observed in outcrop at the surface of Nalunaq Mountain. These include fine- to medium-grained meta-volcaniclastic rocks (Fig 2a) and meta-basalts with ellipsoidal bleached areas (Fig 2b).

These structures have been previously interpreted as pillow structures (Petersen, 1993).

A discordant cross-cut fabric indicates that metamorphism of the host rocks predates the permeation of the alteration stages (Schlatter and Olsen 2011).

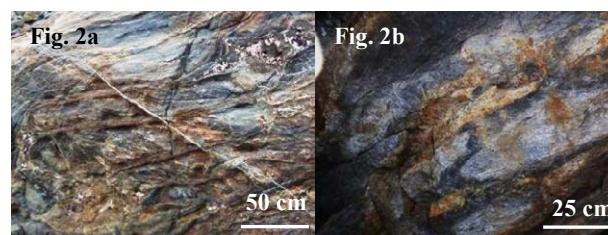


Fig. 2a: Photograph of meta-volcaniclastic rocks located on the southern face of the Nalunaq Mountain. **Fig 2b:** Photograph of potential pillow basalts (southern face of Nalunaq Mountain.)

4 Alteration Stages

A new classification for alteration stages is proposed from field observations and hand sample analysis.

4.1 Splayed discolouration of host rocks

Pale grey or green vein-like bands of discoloured host rock can be observed, usually situated 1-2 m from MV within the host rock. These bands can often be seen forming a discordant set, with one band running parallel to the MV, and another set at c. 80° to the MV. These discordant bands are more prevalent further from the MV whereas closer to the MV, the bands mostly run parallel (Fig. 4). These bands have undergone intense deformation, with some bands displaying isoclinal folding, placing them early in the alteration history. The primary component is a translucent to transparent mineral with a brown/greenish colour, probably an amphibole. Occasional small bands of pyrrhotite are also observed. The bands appear to have a replacement texture, and the grain size of the alteration is variable.

4.2 Garnet-epidote alteration

Garnet-epidote (GE) alteration has affected the Nalunaq gold deposit (Fig. 3a). This alteration is bright green in colour and often features clusters of 0.25-1 cm garnets. Large (up to 1 cm) crystals of pyrite and chalcopyrite are also present. The texture of this alteration varies from replacement to strong veining in lower mine areas. This alteration is not observed on all levels, and is more prevalent at the peripheries of the deposit.

4.3 Clinopyroxene alteration

This stage can be identified by 0.25-5 cm pockets of 0.25-2 mm biotite and feldspar crystals, and a green coloured clinopyroxene-quartz granular halo 2-30 cm in width (Fig 3b). With the exception of the biotite - feldspar pockets, the grain size is fine and comparable with the host rock. Arsenopyrite and pyrrhotite are associated with this alteration. This alteration assemblage overprints the GE alteration (Fig 4).

Identification of the clinopyroxene comes from both hand samples and previous company reports.

4.4 Quartz and calcite veins

The MV can be primarily identified as a 0.25-2 m wide vein of mainly quartz (>90%) with transparent to translucent quartz grains and host rock slivers incorporated within it. This stage hosts the bulk of gold within Nalunaq gold deposit. On the eastern face of the Nalunaq Mountain, a later pegmatite intrudes, and the Nalunaq gold deposit is not observed again. Towards the west the vein thins, and the gold grades become lower.

The MV both cross cuts, and is cross cut by a set of barren quartz/calcite veins (Fig. 4). These veins form a network of extension veins adjacent to the MV in a cross hatched pattern parallel to the plane of MV formation. They are 99-100% calcite-quartz. Both these veins (Fig. 3d) and the MV and have no apparent associated alteration zone.

4.5 Hematite Alteration

A final stage of alteration post-dating the formation of the MV is observed in some areas. This stage is classified by the presence of hematite and an orange/brown rust-like staining of the quartz within the MV (Fig. 3c). One of the major diagnostic features used by the geologists at the Nalunaq Mine is a rusty coloured staining of the quartz veins and alteration zones. Areas with this type of alteration often correlate with high gold grades.

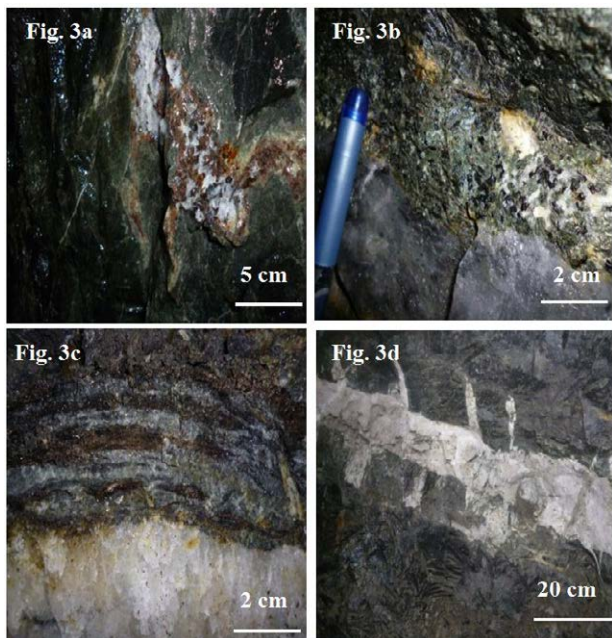


Fig. 3a Garnet-epidote alteration. **Fig. 3b** Clinopyroxene alteration. **Fig. 3c** An extremely high gold grade area, with Clinopyroxene alteration: rich in biotite and pyrrhotite. Orange staining of the quartz grains may indicate later hematite alteration. **Fig. 3d** Barren calcite-quartz extension veins, indicating extension in multiple directions.

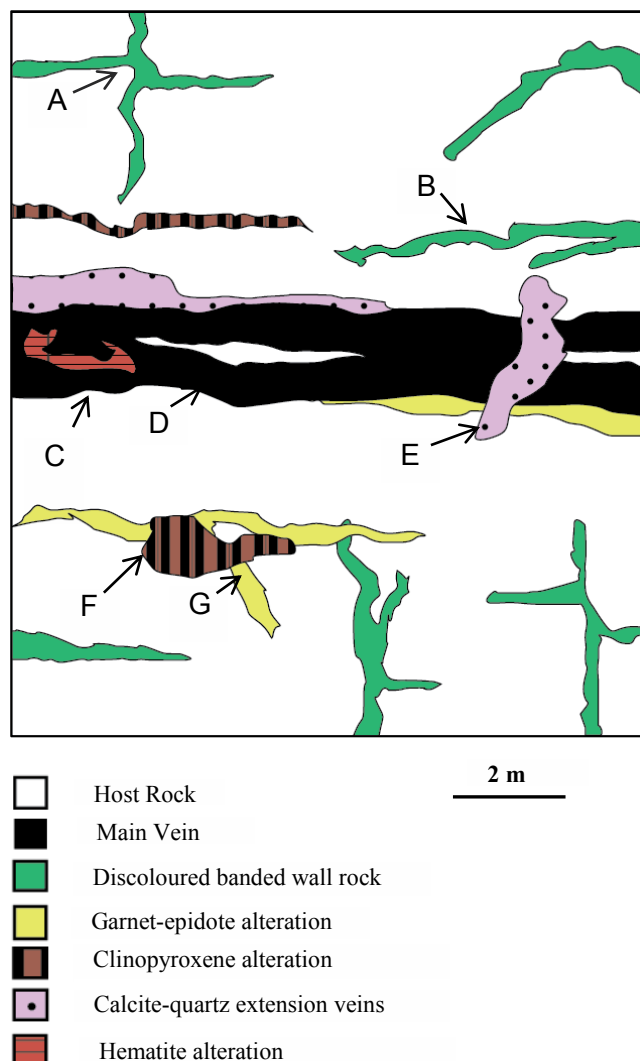


Fig. 4: Schematic diagram of the alteration features observed with the Nalunaq gold deposit. **A.** Disjointed bands of discoloured wall rock. **B.** These bands are often transposed parallel to the MV nearer to the MV-host rock contact. **C.** Hematite alteration. This can often be observed by staining of the quartz. **D.** The MV. This often incorporates fragments of the host rock. **E.** The barren quartz/calcite veins observed both overprinting and being overprinted by the MV. **F.** Clinopyroxene alteration is observed both as circular blebs and sheared sections running parallel to the MV. It can be observed overprinting the GE alteration. **G.** GE alteration can be observed both in disjointed bands within the host rock and horizontal bands close to the MV.

5 Discussions and Conclusions

There has been extensive post-metamorphic alteration of the Nalunaq Mountain. This alteration includes the hydrothermal fluid sequence that resulted in the gold bearing quartz veins. Multiple overprinting alteration events have produced complex mineralogy and textures. This paper demonstrates that mineralization within this deposit cannot be treated as a single event, rather a series of distinct alteration stages.

5.1 Non- Gold Mineralized Alteration

Observations of the structures in the Nalunaq gold deposit have found no relation between variations of clinopyroxene alteration, the discoloured banding and the gold grade within the deposit. The presence or absence of barren calcite-quartz veins also appears to have no effect.

The discoloured bands are a point of contention. They clearly predate all other alteration within Nalunaq gold deposit, and although classified in this paper as an alteration stage, they have also been theorized as either a metamorphic feature, or as primary compositional banding of the host rock, however the observation of discordant sets of veins makes the latter interpretation unlikely.

The clinopyroxene alteration commonly forms replacement textures and due to the fine grain size of the host rock, identification of minerals is difficult. Thin sections will have to be cut to better constrain the mineralogy of this stage.

5.2 Gold mineralization within the MV

Gold is primarily observed on the surface of slivers of host rock that have been incorporated into the MV. This pattern is not repeated at the host rock/MV boundary. The increase in surface area on the slivers of rock could account for this discrepancy. The geochemistry or mineralogy of the host rock slivers may make them a site for preferential gold deposition by destabilization of the gold complex in the ore fluid.

The highly complex overprinting by different alteration assemblages means that it is difficult to accurately determine the presence of an alteration halo specifically related to the MV.

5.3 Alteration associated with gold

There is an apparent relationship between the presence of GE alteration and low gold grades. If the precipitation of gold is chemically controlled, it could be that the GE alteration assemblage represents an unfavorable environment for gold deposition. Alternatively, as the mineralized quartz veins are thinner, and less developed further away from the center of the MV deposit, low gold grades could be explained by unfavorable rheology, structural setting or later remobilization.

The later hematite alteration shows strong replacement textures. It is thought that this replacement is the result of infiltration of surface-derived meteoric waters causing the breakdown of sulphides. This later alteration may have caused gold remobilization into high ore shoots.

6 Concluding Remarks

The Nalunaq gold deposit formed in a complex, multistage alteration system. Each alteration stage can be characterized by separate mineral assemblages and location within the deposit. By segregating these stages it may be possible to constrain an environment for preferential gold precipitation and remobilization as well

as other investigations, such as determining a source for the alteration.

A comprehensive model of gold deposition and factors controlling grade will aid future exploration in identifying comparable deposits in South Greenland.

Further research will be based on a selection of chemical and petrographic techniques in order to thoroughly constrain Nalunaq gold deposit's mineralogy. This information will be combined with age dating, stable isotope geochemistry and used to construct a 4D map of the mineralizing system for the Nalunaq gold deposit and surrounding area.

Acknowledgements

The author would like to thank the staff of Angel Mining Corp, in particular Kurt Christensen for offering his advice and experiences and Nigel Handley for accommodating us on site and aiding with the practical side of the investigations.

References

- Garde AA, Hamilton MA, Chadwick B, Grocott J, and McCaffrey KJW (2002) The Ketilidian orogen of South Greenland: geochronology, tectonics, magmatism, and fore-arc accretion during Palaeoproterozoic oblique convergence. *Can. J. Earth Sci.* 39(5):765-793.
- Grammatikopoulos T, Porritt L, Petersen JS, Christensen K (2004) Mineralogical Characterization of Gold-bearing rocks from the Nalunaq gold deposit, Greenland. *Appl. Earth Sci. (Trans. Inst. Min. Metall. B)* 113:197-203
- Kaltoft K, Schlatter DM, Kludt L (2000) Geology and genesis of Nalunaq Palaeoproterozoic shear zone-hosted gold deposit, South Greenland. *Appl. Earth Sci.*, 109 (Sect. B):23-33.
- Petersen JS (1993) Nalunaq Project 1993: Results of geological investigations on gold mineralization in the Nalunaq area, Nanortalik Peninsula, SW Greenland. Nunaoil, internal report, (Unpublished) pp. 49
- Petersen JS, Pedersen JL (1995) Geological setting Proterozoic gold mineralization in the Nanortalik Peninsula, South Greenland. In: Ihlen M., Pedersen M. and Stendal H. (ed.) *Gold mineralization in the Nordic Countries and Greenland: Extended abstracts and field trip guide*, pp. 69-73
- Petersen JS, Kaltoft K, Schlatter DM (1997) The Nanortalik gold district in South Greenland. In: Papunen, H (ed.) *Mineral deposits: research and exploration. Where do they meet?* Balkema, Rotterdam, pp. 285-288.
- Porritt L, (2000) Alteration surrounding the Main Vein of the Nalunaq gold deposit, South Greenland, M.Sc. thesis, University of Exeter.
- Schlatter DM, Olsen S (2011) The Nalunaq gold mine: a reference sample and compilation and interpretation of geochemical data. *GEUS Rapport* 2011, 31, pp. 79
- Stendal H, Frei R (2000) Gold occurrences and lead isotopes in Ketilidian Mobile Belt, South Greenland. *Appl. Earth Sci.*, 109:6-13.

World-class Mesozoic orogenic gold deposits, Jiaodong Peninsula, eastern China: constraints on timing, structural controls, and mineralization styles

Hong-Rui Fan, Fang-Fang Hu, Kui-Feng Yang, Xiao-Chun Li, Ting-Guang Lan

Key Laboratory of Mineral Resources, Institute of Geology and Geophysics, Chinese Academy of Sciences, Beijing 100029, China

Abstract. The world-class gold camps and deposits in the Jiaodong Peninsula demonstrate a number of common features as well as great diversity in a number of geological characteristics compared with orogenic gold deposits. The diversity of the deposits reflects the complex interplay of physical and chemical processes at a depositional trap. The gold mineralization event coincided with tectonic reactivation of the North China Craton, as marked by asthenosphere upwelling, voluminous igneous rocks, and high crustal heat flow, which may have provided sufficient heat energy and fluid input required for the formation of the gold deposits.

Keywords. orogenic gold deposit, genesis, Jiaodong Peninsula, eastern China

1 Gold deposits in the Jiaodong Peninsula

The Jiaodong Peninsula is currently the most important gold province in China, with a total gold ore reserve of >1300 tons (Li et al., 2007). Seven world-class gold deposits (> 100 t gold), eight large gold deposits (20 to 100 t gold) and more than one hundred middle to small gold deposits (< 20 t gold) have been discovered in the peninsula during the past three decades, accounting for about 25% of China's gold reserves (Fan et al., 2003). It is located along the southeastern margin of the North China Craton, which is the largest and oldest (3.8–2.5 Ga) craton in China (Zhai and Santosh, 2011). Mesozoic granitoids, occupying >50 percent of the northwestern part of the Jiaodong Peninsula, intrude Precambrian basement rocks that have undergone amphibolite to granulite facies metamorphism. The majority of gold resources (>95%) are hosted by these granitoids, making the Jiaodong gold province one of the largest granitoid-hosted gold provinces recognized in the world (Qiu et al., 2002).

The Jiaodong Peninsula occupies the easternmost edge of the Eastern Block of the North China Craton and is geologically divided into the southeastern Ludong terrane and the northwestern Jiaobei terrane by the Mishan fault. The Ludong terrane petrostructurally belongs to the northern margin of the South China Block, which records a subduction history associated with a Triassic collisional event (Zheng et al., 2009).

The Jiaobei terrane petrostructurally belongs to the North China Craton. Almost all gold deposits are hosted in the Jiaobei terrane (Zhai et al., 2004), and more than 80% of the gold reserves are concentrated in the Zhaoyuan-Laizhou gold belt. The Precambrian basement in the Jiaobei terrane is principally defined by the Archean Jiaodong Group and the Paleoproterozoic

Fenzishan and Jingshan Groups (Tam et al., 2011). Mesozoic magmatic rocks are widely exposed in the Jiaobei terrane and two main periods of magmatism are recognized, Jurassic and Early Cretaceous. The Jurassic magmatic activity is represented by the crustally-derived Linglong, Luanjiahe, and Kunyushan granitoids, emplaced at 160–155 Ma (Wang et al., 1998; Yang et al., 2012). In the Early Cretaceous, extensive magmatism took place through strong crust-mantle interaction, including formation of widespread granitoids (130–113 Ma), mafic to felsic volcanic rocks in the Jiaolai Basin (130–110 Ma), and numerous mafic dikes (124–122 Ma) (Goss et al., 2010; Yang et al., 2012). The Mesozoic granitoids are hosts for most gold deposits.

Gold deposits in the peninsula can be divided into three mineralized belts from west to east, which include Zhaoyuan-Laizhou, Penglai-Qixia, and Muping-Rushan. Each belt is separated by Jurassic to Cretaceous volcanic-sedimentary basin. Gold deposits have been classified as the Linglong-type and the Jiaojia-type, both of which are essentially fault controlled. The Linglong-type mineralization is characterized by massive auriferous quartz veins hosted in subsidiary second- or third-order faults cutting Mesozoic granitoids, whereas the Jiaojia-type mineralization consists of disseminated- and stockwork-style ores located in regional faults, which are enveloped by broad alteration halos.

Recent investigations have shown that deposit mineralogy, hydrothermal fluid compositions, and stable isotope compositions. Ore-forming P-T conditions of the Jiaodong gold deposits are similar to those of typical orogenic gold deposits (Goldfarb et al., 2001; Qiu et al., 2002).

2 Diversity in structural controls and mineralization styles

Linglong-type gold deposits in the Jiaodong Peninsula are represented by those in the Linglong, Jiuqu, Denggezhuang, and Jinqingding camps. This mineralization occurs as single or multiple, relatively continuous quartz veins that are as long as several hundred meters to more than one kilometer in strike, ranges from a few centimeters to a few meters in width, and extends for at least a few hundred meters down-dip. In the Linglong gold camp, more than 100 auriferous quartz veins are hosted in the second- or third-order faults. The lodes are locally zoned from a central massive sulfide zone, as thick as 1 m and consisting of pyrite and minor chalcopyrite, galena, and sphalerite, to marginal zones of quartz-pyrite veins. The quartz veins

are translucent to milky and gray and appearing to fill pre-existing faults, as they are commonly bounded by fault gouge or thin zones of quartz-sericite schist. The veins may contain fragments of the wallrocks and also rarely cut the foliation of the bounding schist or the fault gouge, suggesting that at least some of the hosting faults were formed prior to the quartz veins. Most of the quartz veins, and particularly zones of massive sulfide minerals within the veins, have been fractured, brecciated, or boudinaged. The veins occur as lenticular discrete bodies bounded by the fault gouge, although, in rare cases, undeformed comb-textured quartz veins are present. Wallrock alteration adjacent to the quartz veins commonly includes silicification, sericitization, sulfidation, and potassic alteration. Intensity of wallrock alteration in the different camps or even between individual quartz veins is variable.

Jiaojia-type gold deposits are represented by the Sanshandao, Jiaojia, Xincheng, and Yinge Zhuang camps. These disseminated- and stockwork-style deposits occur along the second-order regional faults that are gently dipping, and are surrounded by broad alteration halos. The faults commonly outcrop as cataclastic deformation zones that are a few hundred meters wide and, although sometimes described as shear zones, they show few or no ductile features in areas of extensive wallrock alteration and the late brittle deformation. In the fault zones that host the Jiaojia-type mineralization, a main straight and smooth fault plane is most developed, and gold ore bodies are mainly located in the footwall of the main fault plane. Outward from the main fault plane, the following alteration zones are well common within the granitoid-hosted Jiaojia-type deposits: (1) a fault gouge zone that may be as much as 50-cm-thick, consisting of gray, white, or black clay materials (commonly >80%) with variably-sized, round fragments of wallrock granitoids. Economic gold mineralization is rarely present, although locally gold-rich fragments are observed; (2) a pyrite-sericite zone may be as thick as several meters to locally >10 m. It comprises quartz, sericite, and disseminated pyrite, with lesser calcite, and is the product of extensive wallrock alteration; (3) an additional pyrite-sericite may be as thick as 50 m and characterized by disseminated pyrite and pyrite-quartz stockworks. It is composed of silicification, sericitization, and pyritic granitoid; and (4) an outer reddish alteration zone that extends for as much as several hundred meters, and is characterized by K-feldspar and sericite in cataclastically deformed granitoid. Thin quartz veins with pyrite are present in the reddish rock and economic gold ores are locally present where there is a high density of pyrite-quartz stockworks.

3 Timing constraints of gold mineralization

In recent years, detailed dating of gold mineralization in the Jiaodong Peninsula has been done using Ar-Ar methodology on sericite, muscovite, K-feldspar, and quartz, Rb-Sr method on pyrite, and high-precision SHRIMP on hydrothermal zircon (Hu et al., 2004; Li et al., 2003, 2008; Yang and Zhou, 2001; Zhang et al., 2003). Ages of different deposits by different methods

are similar. Large-scale gold metallogeny in the Jiaodong Peninsula occurred in the period of 120 ± 10 Ma. Gold deposition happened during a short period, and formed in the same tectonic-geological setting and from the same type of ore fluid. Although different mineralization and alteration stages can be defined, these stages are the results of the same broad metallogenic event.

4 Suggested ore genesis

Low-moderate salinity, mixed aqueous-carbonic hydrothermal fluids capable of carrying Au, Ag and several other metals, but with limited capacity to transport base metals, are generally invoked for gold deposits in the Jiaodong Peninsula (Fan et al., 2003). Given that similar hydrothermal fluids are present in the most orogenic gold deposits, variations in alteration mineralogy and zonation, results from fluid-wallrock interaction, in chemically different host rocks, and the prevailing temperature-pressure conditions.

Characteristics of mineralization, alteration, and ore fluids suggest that the gold deposits in the Jiaodong Peninsula share many features of orogenic gold deposits hosted in Precambrian cratons worldwide (Groves et al., 1998; Goldfarb et al., 2001, 2007). These deposits formed mostly in the time intervals of 2.8 to 2.55 and 2.1 to 1.8 Ga in compressional to transpressional tectonic regimes, and were coupled with metamorphism during craton stabilization. However, regional metamorphism in the eastern North China Craton took place in the Late Archean to early Paleoproterozoic (Zhai and Santosh, 2011; Zhao et al., 2005), billions of years prior to the Early Cretaceous gold mineralization. Thus, a regional metamorphic fluid component during craton stabilization is regarded as unlikely for the gold mineralization in the Jiaodong Peninsula.

Previous studies on stable isotopes of the gold deposits showed that oxygen isotope ratios for auriferous quartz samples ranged from 9.7 to 13.7‰, with the calculated ore-fluid $\delta^{18}\text{O}$ values being 6.6 to 10.9‰, and the hydrogen isotopes measured for inclusion fluids extracted from auriferous quartz ranged from -81 to -48‰ (Fan et al., 2003; Mao et al., 2008). These data plot within or adjacent to the magmatic water region in the plot of δD vs. $\delta^{18}\text{O}$, suggesting that a magmatic fluid might have formed the deposits. Nevertheless, the ore fluids may also contain some meteoric waters, as some δD values are lighter than typical values of primary magmatic waters. Furthermore, a typical exsolved magmatic fluid is characterized by high temperatures and relatively high salinity (Audétat et al., 2008), so an external, largely meteoric fluid is needed to mix with the magmatic fluid to produce the moderate-temperature and low salinity ore-forming fluids as suggested by fluid inclusions in the gold deposits. This lends additional support for the involvement of meteoric water in the ore-forming system.

It is possible that during fluid generation and migration, Sr and Nd entered the ore fluids, and during large scale and intense fluid-rock interactions, the isotopic signature of the fluids was recorded in the newly formed hydrothermal minerals. Zhou et al. (2003) analyzed Sr-Nd isotopic composition of ores (pyrite),

granites, intermediate-basic dikes, and basement metamorphic rocks in the Jiaodong Peninsula. Liu et al. (2003) measured Sr-Nd isotopic composition of carbonate minerals from the Jiaojia and Jinqingding gold deposits. Li et al. (2013) also measured Sr-Nd isotopic composition of hydrothermal minerals, including secondary K-feldspar, sericite and pyrite from alteration and mineralized zones. The results show that Sr-Nd isotopic composition of ores are close to that of mantle rocks or mafic dikes in the peninsula, and also have some similarities to Precambrian basement rocks and Mesozoic granites. The gold and related minerals were therefore derived from a mixed source, and mantle components were involved in ore-forming processes (Li et al., 2013; Zhou et al. 2003).

One of the most important observations on the North China Craton resulting from various studies in the last few decades is that the lithosphere at the base of this craton was considerably modified during the Phanerozoic, where the cold and thick cratonic lithosphere (~200 km) present in the Paleozoic was replaced by a hot and thin "oceanic" one (<80 km) (Griffin et al., 1998). During this process, the stability of the coupled lithospheric mantle and crust was affected, leading to lithospheric mantle thinning and being refertilized as well as to the crust active (Zhai, 2008; Li et al., 2013). In Early Cretaceous, mafic to felsic magmatism was wide spread in the eastern North China Craton, and it has been commonly interpreted as crust-mantle interaction (Zhang et al., 2013). The presence of metamorphic core complexes (Liu et al., 2005), formation of NE-striking half-graben basins (Ren et al., 2002), and reactivation of large-scale strike-slip faults (Tan-Lu fault) (Zhu et al., 2001) indicate an extensional geodynamic setting. It is conceivable that voluminous magmas from different sources, induced by asthenosphere upwelling and crustal reactivation, could have provided the heat and fluids for the large-scale gold mineralization. In addition, asthenospheric upwelling and strong crust-mantle interaction within a thinned lithosphere led to a high geothermal gradient, which could have induced voluminous meteoric fluid flow important to the ore-forming process. Extensional structures were formed in the upper crust, providing flow channels and sites for gold precipitation.

Acknowledgements

Special thanks are due to the management and staff of Shandong Gold Group Co. Ltd. for their hospitality during the fieldwork. Dr. Richard Goldfarb is thanked for his constructive and valuable comments which greatly contributed to the improvements of the manuscript. This study was financially supported by the Natural Science Foundation of China (41173056) and 100 Talents Programme of Chinese Academy of Sciences.

References

Audétat A, Pettke T, Heinrich CA, Bodnar RJ (2008) The composition of magmatic-hydrothermal fluids in barren and mineralized intrusions. *Econ Geol* 103: 877-908

- Fan HR, Zhai MG, Xie YH, Yang JH (2003) Ore-forming fluids associated with granite-hosted gold mineralization at the Sanshandao deposit, Jiaodong gold province, China. *Miner Deposita* 38: 739-750
- Goldfarb RJ, Groves DI, Gardoll S (2001) Orogenic gold and geologic time: a global synthesis. *Ore Geol Rev* 18: 1-75
- Goldfarb RJ, Hart C, Davis G, Groves DI (2007) East Asian gold: Deciphering the anomaly of Phanerozoic gold in Precambrian cratons. *Econ Geol* 102: 341-345
- Goss SC, Wilde, SA, Wu FY, Yang JH (2010) The age, isotopic signature and significance of the youngest Mesozoic granitoids in the Jiaodong Terrane, Shandong Province, North China Craton. *Lithos* 120: 309-326
- Griffin WL, Zhang AD, O'Reilly SY, Ryan CG (1998) Phanerozoic evolution of the lithosphere beneath the Sino-Korean Craton. In: Flower MFJ, Chung SL, Lo CH, Lee TY (Eds.) *Mantle Dynamics and Plate Interactions in East Asia*. Geodynamic Series. American Geophysical Union, Washington DC, pp 107-126
- Groves DI, Goldfarb RJ, Gebre-Mariam M, Hagemann SG, Robert F (1998) Orogenic gold deposits: A proposed classification in the context of their crustal distribution and relationship to other gold deposit types. *Ore Geol Rev* 13: 7-27
- Hu FF, Fan HR, Yang JH, Wan YS, Liu DY, Zhai MG, Jin CW (2004) Mineralizing age of the Rushan lode gold deposit in the Jiaodong Peninsula: SHRIMP U-Pb dating on hydrothermal zircon. *Chinese Sci Bull* 49: 1629-1636
- Li QL, Chen FK, Yang JH, Fan HR (2008) Single grain pyrite Rb-Sr dating of the Linglong gold deposit, eastern China. *Ore Geol Rev* 42: 263-271
- Li JW, Vasconcelos PM, Zhang J, Zhou MF, Zhang XJ, Yang FH (2003) $^{40}\text{Ar}/^{39}\text{Ar}$ constraints on a temporal link between gold mineralization, magmatism, and continental margin transtension in the Jiaodong gold province, Eastern China. *J Geology* 111: 741-751
- Li SX, Liu CC, An YH, Wang WC, Huang TL, Yang CH (2007) *Ore Deposit Geology of the Jiaodong Gold Province*. Geology Press, Beijing (in Chinese)
- Li XC, Fan HR, Santosh M, Hu FF, Yang KF, Lan TG (2013) Hydrothermal alteration associated with Mesozoic granite-hosted gold mineralization at the Sanshandao deposit, Jiaodong gold province, China. *Ore Geol Rev* doi: 10.1016/j.oregeorev.2013.01.020
- Liu JL, Davis GA, Lin Z, Wu FY (2005) The Liaonan metamorphic core complex, Southeastern Liaoning Province, North China: a likely contributor to Cretaceous rotation of Eastern Liaoning, Korea and contiguous areas. *Tectonophysics* 407: 65-80
- Liu JM, Ye J, Xu JH, Sun JG, Shen K (2003) C-O and Sr-Nd isotope geochemistry of carbonate minerals from gold deposits in East Shandong, China. *Acta Petrol Sin* 19: 775-784 (in Chinese with English abstract)
- Mao JW, Wang YT, Li HM, Pirajno F, Zhang CQ, Wang RT (2008) The relationship of mantle-derived fluids to gold metallogenesis in the Jiaodong Peninsula: Evidence from D-O-C-S isotope systematics. *Ore Geol Rev* 33: 361-381
- Qiu YM, Groves DI, McNaughton NJ, Wang LG, Zhou TH (2002) Nature, age, and tectonic setting of granitoid-hosted, orogenic gold deposits of the Jiaodong Peninsula, eastern North China craton, China. *Miner Deposita* 37: 283-305
- Ren J, Tamaki K, Li S, Zhang J (2002) Late Mesozoic and Cenozoic rifting and its dynamic setting in eastern China and adjacent areas. *Tectonophysics* 344: 175-205
- Tam PK, Zhao GC, Liu F, Zhou X, Sun M, Li SZ (2011) Timing of metamorphism in the Paleoproterozoic Jiao-Liao-Ji Belt: New SHRIMP U-Pb zircon dating of granulites, gneisses and marbles of the Jiaobei massif in the North China Craton. *Gondwana Res* 19: 150-162
- Wang LG, Qiu YM, McNaughton NJ, Groves DI, Luo ZK, Huang JZ (1998) Constraints on crustal evolution and gold metallogeny in the northwestern Jiaodong Peninsula, China, from SHRIMP U-Pb zircon studies of granitoids. *Ore Geol Rev* 13: 275-291
- Yang JH, Zhou XH (2001) Rb-Sr, Sm-Nb, and Pb isotope

- systematics of pyrite: Implications for the age and genesis of lode gold deposits. *Geology* 29: 711-714
- Yang KF, Fan HR, Santosh M, Hu FF, Wilde SA, Lan TG, Lu LN, Liu YS (2012) Reactivation of the Archean lower crust: implications for zircon geochronology, elemental and Sr-Nd-Hf isotopic geochemistry of late Mesozoic granitoids from northwestern Jiaodong Terrane, the North China Craton. *Lithos* 146-147: 112-127
- Zhai MG (2008) Lower crust and lithospheric mantle beneath the North China Craton before the Mesozoic lithospheric disruption. *Acta Petrol Sin* 24: 2185-2204 (in Chinese with English abstract)
- Zhai MG, Fan HR, Yang JH, Miao LC (2004) Large-scale cluster of gold deposits in east Shandong: Anorogenic metallogenesis. *Earth Sci Frontiers* 11: 85-98 (in Chinese with English abstract)
- Zhai MG, Santosh M (2011) The Early Precambrian odyssey of the North China Craton: A synoptic overview. *Gondwana Res* 20: 6-25
- Zhang HF, Zhu RX, Santosh M, Ying JF, Su BX, Hu Y (2013) Episodic widespread magma underplating beneath the North China Craton in the Phanerozoic: Implications for craton destruction. *Gondwana Res* 23: 95-107
- Zhang XO, Cawood PA, Wilde SA, Liu RQ, Song HL, Li W, Snee LW (2003) Geology and timing of mineralization at the Cangshang gold deposit, north-western Jiaodong Peninsula, China. *Miner Deposita* 38: 141-153
- Zhao GC, Sun M, Wilde SA, Li SZ (2005) Late Archean to Paleoproterozoic evolution of the North China Craton: Key issues revisited. *Precambrian Res* 136: 177-202
- Zheng YF, Chen RX, Zhao ZF (2009) Chemical geodynamics of continental subduction-zone metamorphism: insights from studies of the Chinese Continental Scientific Drilling (CCSD) core samples. *Tectonophysics* 475: 327-358
- Zhou XH, Yang JH, Zhang LC (2003) Metallogenesis of superlarge gold deposits in Jiaodong region and deep processes of subcontinental lithosphere beneath North China Craton in Mesozoic. *Sci China Earth Sci* 46(supp.): 14-25
- Zhu G, Song CZ, Wang DX, Liu GS, Xu JW (2001) Studies on $^{40}\text{Ar}/^{39}\text{Ar}$ thermochronology of strike-slip time of the Tan-Lu fault zone and their tectonic implications, *Sci China Earth Sci* 44: 1002-1009

Mesozoic quartz-vein hosted Au (Ag-Pb-Zn-Cu) mineralisation at Mineral de Talca, Coastal Range, Chile: the role of felsic intrusives

Emily A. Firth, David A. Holwell

Department of Geology, University of Leicester, University Road, Leicester, LE1 7RH, UK

Matthew P. Rovardi

Kinross Gold Corporation, Cerro Colorado 5240, Torre del Parque 2, Piso 18, Santiago, Chile

Nick H. S. Oliver

Holcombe Coughlin Oliver, PO Box 3533, Hermit Park, QLD 4812, Australia

Adrian J. Boyce

Scottish Universities Environmental Research Centre, Rankine Avenue, Scottish Enterprise Technology Park, East Kilbride, G75 0QF, UK

James K. Mortensen

Earth, Ocean and Atmospheric Sciences, University of British Columbia, Vancouver, BC, V6T 1Z4, Canada

Abstract. Mineral de Talca is a rare occurrence of Mesozoic vein-hosted gold mineralisation situated within the Coastal Range of Northern Chile. Although displaying many characteristics of orogenic gold deposits, significant amounts of base metal sulphides associated with the gold, and their proximity to felsic granitoid intrusions, raise the possibility of an intrusion-related gold classification. Initial mineralogical work reveals three distinct styles of mineralisation; (1) nuggety gold in quartz, (2) gold in quartz with Pb-Zn-Cu-Ag-Cd sulphides and (3) gold with arsenopyrite in pyrite in sulphidised wall rock. Vein sulphides and the host rock meta-sediments show a heavy S isotopic signature, interpreted to represent incorporation of crustal S into the mineralising system. Mantle S isotope signatures in the granitoids suggest no genetic link in terms of S source to the mineralisation, and Pb isotopes in vein galena and granite feldspars are distinct, implying the granites were not a source of metals. However, the granitoids are still regarded as key to the emplacement of the mineralisation by providing a structural competency contrast that has focused the mineralisation at areas of dilational jog along the Metalera Fault to form WNW-trending veins. As such, the mineralisation is classed as orogenic style, and the identification of the key mineralogical, isotopic and structural features have implications for exploration and the development of similar deposits along the Coastal Range.

Keywords. Orogenic gold, Intrusion-related gold, Base metal sulphides, Chile, S isotopes

1 Introduction

Orogenic and intrusion-related gold deposits are sub classifications of epigenetic gold deposits in metamorphic terranes. Orogenic gold deposits define deposits that have a genetic affiliation of mineralisation to metamorphic processes of late stage compressional to transpressional regimes of an accreting orogeny (Groves et al. 2003). Intrusion-related gold deposits are those which have a genetic affiliation with intermediate to felsic magmas (Thompson et al. 1999), more distal from

active convergent plate margins than orogenic gold deposits (Groves et al. 2003).

Orosur Mining's Mineral de Talca project, situated 375 km north of Santiago in the IV Region of northern Chile, is a shear-zone associated, quartz-vein hosted gold deposit that has been mined artisanally for over a century (Orosur Mining, 2012). Gold-bearing quartz veins, occasionally with significant Cu-Pb-Zn sulphides, are focused along regional and local shear zones associated with the uplift of the coastal cordillera. They are hosted in late Proterozoic-Jurassic metasediments, meta-volcanics and granitic intrusions. Until now, no academic work has been undertaken on Mineral de Talca, and whilst it shares many of the characteristics of classic orogenic gold style deposits, the presence of the granitic intrusions in the area, and a high base metal content, raise the possibility of an intrusion-related classification.

2 Geology

2.1 Regional Geological Setting

The geology of Chile is characterised by a W-E cross section of a Coastal Range, Central Valley, and the Andean Cordillera. Discontinuous outcrops of metamorphic rock complexes occur along the Coastal Range, and are composed of ultrabasic and basaltic rocks, meta-sandstones and meta-cherts which host evidence of a prolonged history of deformation and metamorphism in the Late Palaeozoic through to Early Mesozoic (Moreno & Gibbons, 2007).

Pre-Cenozoic magmatism in the IV Region can be broadly categorized into three main events. These began with subduction along the western margin of Gondwana during the Carboniferous to Early Permian. During the Late Permian to Early Jurassic extensive plutonic activity developed during a period of halted subduction associated with extensional tectonics and large-scale crustal partial melting, producing only minor volumes of

mantle-derived rocks (Moreno & Gibbons, 2007). From the Middle Jurassic to the Early Cretaceous, subduction-related magmatism with bimodal volcanism and calc-alkaline plutonic activity occurred with progressively more mantle material involved (Moreno & Gibbons, 2007).

Mesozoic orogenic gold deposits in such settings are widely known in western North America and other areas around the circum Pacific (Goldfarb et al., 2000), but there are no published accounts of such occurrences in Chile.

2.2 Deposit Geology

Gold-bearing quartz veins, occasionally with significant Cu-Pb-Zn sulphides, are focused along NNW-trending regional and local shear zones, and secondary dilational veins running NW-SE off the main shears. The gold veins on the property are hosted in Paleozoic rocks such as quartzite, gneisses and meta-basalts of Devonian-Carboniferous age, and inter-fingering marine and continental sediments of Upper Carboniferous to Permian age. Granite, microgranite, microgranodiorite and gabbro intrusions are locally intruded into these meta-sedimentary rocks (Orosur Mining, 2012) (Figure 1). All are cut by the mineralised faults.

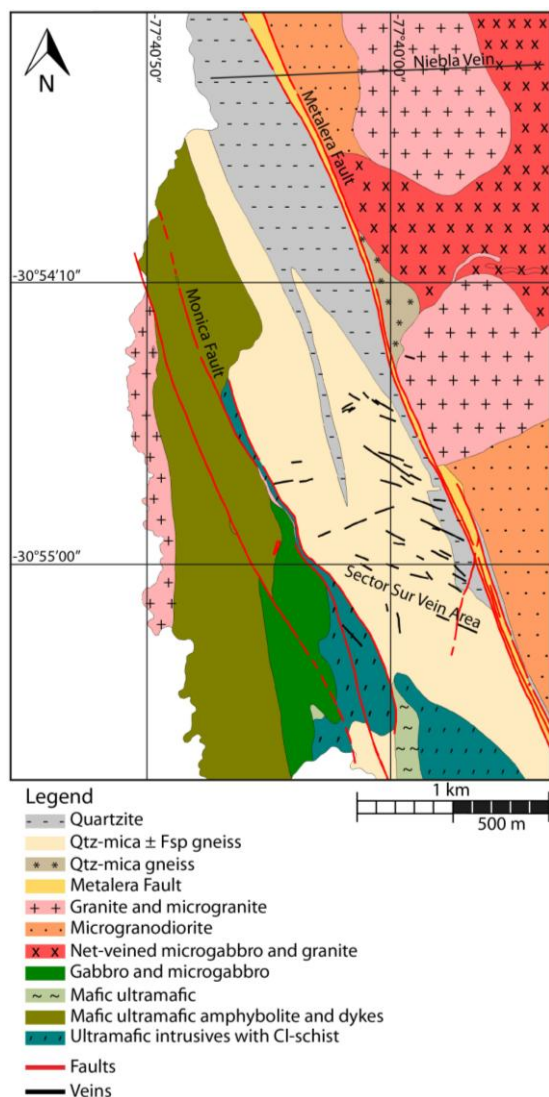


Figure 1. Geological map of Mineral de Talca.

3 Classification of Veins Type

Mineralogical and petrological work has been completed on samples of the quartz veins and has identified two vein types; sulphide-poor quartz veins and Cu-Zn-Pb bearing quartz veins.

The sulphide-poor quartz veins contain small amounts of pyrite, galena and minor chalcopyrite, making up less than 1% of the total rock. The Cu-Zn-Pb bearing quartz veins are more abundant in a variety of sulphide minerals (up to 5% of total rock) and sulphides are also coarser compared to the sulphide-poor quartz veins, up to 2 mm diameter. Pyrite and galena are observed with an increased amount of chalcopyrite and sphalerite, plus minor amounts of the Cd sulphide; greenockite. Both vein types are 1-2 m wide, and extend for variable distances, typically a few hundred metres.

3.1 Secondary Enrichment Zone

There is a large amount of sulphide alteration in the Cu-Zn-Pb bearing quartz veins, constituting a secondary enrichment zone close to the surface extending down to around 150 m depth. Covellite and bornite replacing chalcopyrite around the rims are common. Low temperature alteration in these rocks is characterized by fibrous intergrowths of acicular crystals of Pb-sulphate minerals and colloform banding of Fe-silicates. A variety of unusual silver minerals were also found in the Cu-Zn-Pb bearing quartz veins, including stromeyerite (AgCuS) and acanthite (Ag_2S). It is not yet known how this secondary alteration zone affects gold mineralisation.

4 Gold Mineralogy

Precious metal (Au and Ag) mineralogy has been characterised by composition, size and association. On this basis, three distinct styles of gold mineralisation have been identified (Table 1).

Table 1. Classification of gold mineralisation styles.

Composition of Au grains (wt.% Au)	Morphology of Au grains	Association	Host Rock
Type 1 Min: 89.0 Max: 89.6 Average: 89.3	Well formed, rounded grains	Inclusions within quartz	Sulphide-poor quartz veins
Type 2 Min: 89.0 Max: 89.6 Average: 89.3	Well formed, rounded grains	Base metal sulphides (+ Ag minerals)	Cu-Zn-Pb bearing quartz veins
Type 3 Min: 89.0 Max: 89.6 Average: 89.3	Irregular grains	Inclusions in pyrite with arsenopyrite	Host rock of veins

Type 1 gold mineralisation is observed as rounded gold grains as inclusions within quartz in the sulphide-poor vein material. Commonly the gold is concentrated into large nuggets of gold, around 3 cm in diameter.

Type 2 gold mineralisation is observed in the Cu-Zn-Pb bearing vein material as disseminated grains amongst base metal sulphides and silver minerals, preferentially

occurring with the finer crystals (< 1 mm diameter).

Type 3 gold mineralisation is observed as irregular grains of gold with close association to arsenopyrite as inclusions within pyrite. This mineralisation type is observed as alteration of the wall rock.

Samples of gold mineralisation styles have been imaged by High Resolution X-ray Computed Tomography to assess the textural relationships between minerals. Figure 2 shows a scan of Type 3 gold mineralisation.

On-going fluid inclusion studies are being undertaken to correlate fluid characteristics with these mineralogical associations.

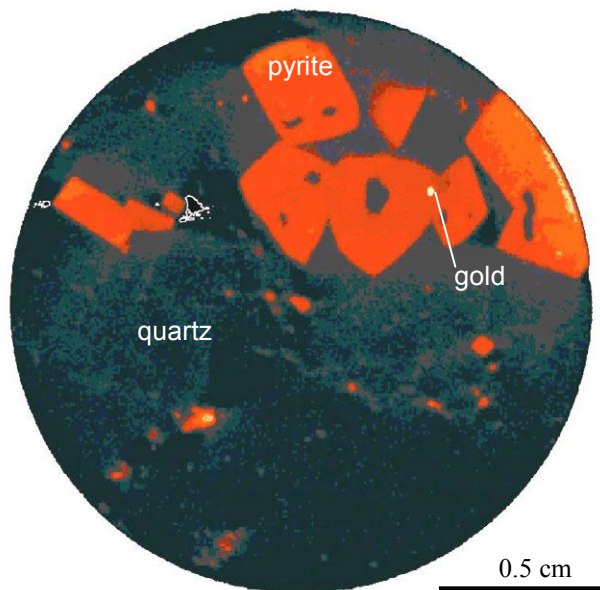


Figure 2. CT scan image of Type 3 gold mineralisation. The image shows a vertical slice through the sample clearly displaying the cubic shape of the pyrite with inclusions of high density minerals (including some gold with arsenopyrite). The white lines define the boundaries of the sample.

5 Geochemical Association

Geochemical data was collected in October 2011 through grab samples along river valleys. Base metal values were up to 1297 ppm Pb, 369 ppm Zn and 7531 ppm Cu. Gold abundances exceeded the upper limit of detection at 10 ppm Au.

A geochemical appraisal was produced by Holcombe Coughlin Oliver consultants, in which alteration depletion and metal enrichment indices applied to the dataset in map form were shown to reveal several WNW- to W-trending zones that intersect the Metalera Fault at a high angle. Though the orientation is similar to that of the Sector Sur vein trends, the spatial pattern is more complex.

The E-W trending anomalous patches in the geochemistry correspond to weak bends in the Metalera Fault. It is theorised that the shape of the fault and the anomalous zones have been influenced by underlying structures in the basement metamorphic rocks. However, as the gold postdates the ductile deformation history and the zones are at a high angle to the foliation, these shapes may simply be a function of perturbation of the Metalera

Fault and vein system as it ruptures through the foliated metamorphic rocks. Another explanation may be that it is the result of the Metalera Fault bending around the massive structurally competent granitoid pluton.

In addition, geochemical maps were produced in Micromine to show the spatial distribution of arsenic (As) and gold (Au), which clearly reflects the relationships shown in the mineralogical data. Type 3 Au mineralisation is associated with both Au and As, whereas Type 1 and 2 have high Au and low As. These associations can be located on a large scale of 1000s metres.

6 Sulphur Isotopes

Sulphur isotope signatures of sulphides within the veins, host rock meta-sediments and the granitoid rocks were analysed to assess the source of S in the mineralised veins. In particular, this was to test the role of the granitoids in the mineralising process in the context of an intrusion-related vs orogenic model.

The great majority of sulphides in vein material have $\delta^{34}\text{S}$ which are not consistent with a direct magmatic input around $0 \pm 2\%$. Instead $\delta^{34}\text{S}$ from all vein types is typically enriched in ^{34}S , ranging from +2.1 to +7.5‰ (Figure 3). Limited data from host rock meta-sediments also show an enrichment in ^{34}S , and offer themselves as a realistic source for the gold-associated sulphides. An exception may be the S signature of Type 3 which overlaps the mantle value, but it is only 1 value. The local granitoids have a $\delta^{34}\text{S}$ signature consistent with a mantle source.

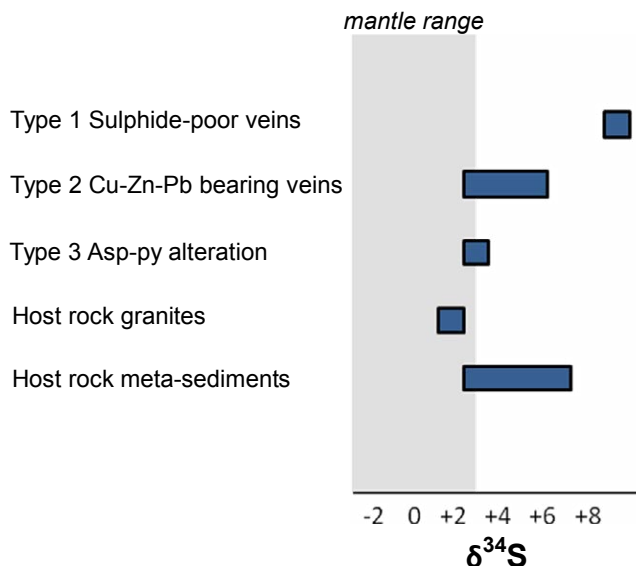


Figure 3. Summary of S isotope data for sulphides in the different mineralisation styles and host lithologies observed at Mineral de Talca.

7 U-Pb Geochronology and Pb Isotopes

Samples of granite and granodiorite from east of the Metalera Fault were dated using laser ablation ICP-MS U-Pb methods on zircon. The granite sample yielded a U-Pb zircon age of 219.6 ± 1.0 Ma, whereas the granodiorite sample contained mainly xenocrystic

zircons that range in age from 260-1065 Ma. A single zircon grain recovered from the granodiorite sample gave an age of 221.3 Ma, suggesting that this phase is likely similar in age to the granite.

Pb isotopic analyses of galena from the Cu-Zn-Pb bearing quartz veins show a tight cluster of compositions somewhat less radiogenic than typical model upper crustal growth curves. Igneous feldspars from the two dated intrusions show similar but consistently more radiogenic Pb isotope compositions than the vein galenas. Therefore it is unlikely that the metals within the veins were derived directly from the granites. The tight clustering of galena Pb signatures is consistent with a large and robust hydrothermal system that has leached and homogenized Pb from several metal reservoirs of different compositions, or that the metals were derived from a large but isotopically homogeneous reservoir. This is more consistent with an orogenic source rather than an intrusion-related source from the adjacent granites.

8 Discussion

The Metalera Fault is the main structure that has introduced gold into the system at Mineral de Talca. Results of structural mapping indicate that early normal movement as a strike slip fault juxtaposed younger intrusives against the metamorphic rocks from depth. Left-lateral strike slip reactivation, with ≥ 2 km displacement, was caused by the σ_1 orientation to NW ($\approx 30^\circ$ from Metalera strike). Later rotation of this stress field to σ_1 orientation of 305° caused the initial lock-up of the Metalera Fault.

The Metalera Fault and Sector Sur veins are consistent with being a coupled tensile vein array, and the dilational WNW-trending veins were the main focus of the mineral rich fluids. The majority of mineralisation is concentrated at a dilational jog along the Metalera Fault.

Several phases of mineralisation have been identified: (1) classic orogenic-style gold mineralisation (with gold associated with pyrite and arsenopyrite wall rock alteration along quartz veins); (2) a gold phase associated with base metal sulphides and (3) nugget style gold mineralisation. Changes in the stress field (strength and orientation) would have given rise to slight reactivation of the Metalera Fault and may go some way to explain the multiple phases of mineralisation. A later stage supergene enrichment process has also altered these phases.

The close association of the granitoid intrusions to the mineralisation led to the consideration that they may be fundamental to the genesis of the mineralisation. However, S isotopes showed that the S in the granite did not contribute significantly to the vein sulphides. Pb isotopes of igneous feldspars and vein galenas showed a difference in composition which again indicate that the metals in the veins are not directly linked to the tested intrusions. However, there is still some ambiguity. It is possible the metals may be derived from a different set of intrusions, and the type clustering of Pb isotope values is more indicative of intrusion-related gold mineralisation. Irrespective of this argument, the

positioning of the mineralisation may have been caused by the competency boundary of the meta-sediments to the west, and the granite to the east of the fault. In this way, the granites may have influenced the focus of gold emplacement, by controlling the position of dilational jogs through differences in shape and competency.

A temporal context for the mineralisation can be achieved as the U-Pb isotopes constrain the age of the granite to 219.6 ± 1.0 Ma, and the mineralisation along the Metalera Fault crosscuts this. The intrusives can be considered to be part of the extensional tectonic regime of the Triassic-Jurassic plutonic event defined by Parada et al. (1999), and it is likely that the orogenic gold mineralisation took place in the subsequent onset of compressional tectonics in the mid Jurassic.

The genetic model for Mineral de Talca therefore is one of a classic orogenic gold setting, with granitoids providing lithological competency contrasts to focus deformation and fluid flow, rather than necessarily providing metals and S. This genetic model places significant constraints on exploration models for the area. The work completed at Mineral de Talca has implications on exploration and development of similar deposits and terranes along the coast, as the timing and setting fits within the context of the multiple Mesozoic-Tertiary orogenic gold provinces located around the Circum-Pacific, for which there is little account in Chile.

Acknowledgements

Thanks go to Orosur Mining who have provided samples and data to facilitate this study and funded the analytical work through a research grant to DAH. We also acknowledge discussions with David Groves and Rich Goldfarb. Richard Siddle is acknowledged for his advice on Micromine processing.

References

- Goldfarb RJ, Groves DI, Gardoll S (2000) Orogenic gold and geological time: a global synthesis. *Ore Geol Rev* 18:1-75
- Groves DI, Goldfarb RJ, Robert F, Hart CJR (2003) Gold Deposits in Metamorphic Belts: Overview of Current Understanding, Outstanding Problems, Future Research, and Exploration Significance. *Econ Geol* 98:1-29.
- Moreno T, Gibbons W (eds) (2007) *The Geology of Chile*. The Geological Society, London, 414
- Orosur Mining. 2012. Talca Project: http://www.orosur.ca/exploration_chile/talca/
- Parada MA, Levi B, Nystrom JO (1999) Geochemistry of the Triassic to Jurassic plutonism of Central Chile (31° - 34° S): geochemical and Sr-Nd isotopic evidence, and tectonic implications. *Lithos* 46:505-521
- Thompson JHF, Sillitoe RH, Baker T, Lang JR, Mortensen JK (1999) Intrusion-related gold deposits associated with tungsten-tin provinces. *Miner Deposita* 34:323-334

Multistage mineralization of the giant Obuasi gold deposit, Ghana

Denis Fougerouse, Steven Micklethwaite, John Miller, T. Campbell McCuaig

Centre for Exploration Targeting, University of Western Australia, School of Earth and Environment, Crawley, Western Australia 6009, Australia

Stanislav Ulrich

AngloGold Ashanti Ltd, Brownfields Exploration Technical Hub, Continental Africa Region, 44 St George Terrace, Perth, Western Australia 6000, Australia

Abstract. Debate surrounds many of the world's largest gold deposits as to whether they benefited from multiple episodes of mineralization. The giant Obuasi gold deposit in western Africa is hosted in metasediments affected by a complex deformation history, with at least three structural stages. We used a combination of underground and field mapping, 3D visualization of drill core data, and microstructural studies to investigate the controls on gold mineralization. The majority of the resource is contained between graphite-rich shears, in two distinct styles. These include gold-bearing disseminated arsenopyrite in sedimentary rocks and visible gold within microfractures in quartz veins as much as 4-m-thick. Microstructural observations demonstrate that the arsenopyrite-hosted ore formed coevally with the second stage of cleavage development. In contrast, the underground/field mapping and the 3D visualization of drill core data indicate that the visible gold ore formed coevally with the latest stage of folding and cleavage development. Our results confirm that the Obuasi gold deposit formed during at least two different structural stages. This may indicate that gold was locally remobilized from arsenopyrite into late-stage microfractures, or it may be due to two overprinting and unrelated mineralizing events.

Keywords. Ghana, gold, multistage, Birimian, Ashanti

1 Introduction

The giant Obuasi gold deposit (also named the Ashanti mine) is the largest deposit in western Africa, with more than 60 Moz of gold. The deposit extends for 8 km along strike and is 1.6-km-deep, with active exploration continuing below this depth. The deposit is located at the contact between the Kumasi volcanosedimentary basin and the Ashanti greenstone belt. It contains more than 20 individual ore shoots within a corridor between graphite-rich fault planes belonging to the Ashanti fault.

There are two distinct gold mineralization styles;

1. sub-microscopic gold contained within arsenopyrite and, less commonly, in pyrite,
2. visible gold contained within micro-fractures, hosted in quartz veins as much as 4-m-thick, which border the graphite-rich fault rock.

Two competing models have been invoked to explain mineralisation at Obuasi. Oberthür et al. (1994) argued that the sulfide ores predate the quartz veins ores, but did not distinguish whether there were two distinct mineralization events or two different styles that overlapped in time. Conversely, Allibone et al. (2002) concluded mineralization occurred at a late stage during

sinistral reactivation of the Obuasi shear zone during NW-SE to N-S shortening. The present study re-examines the timing of mineralization at Obuasi and tests between these two existing models, using new data made available due to development of the mine.

2 Geological setting

The Paleoproterozoic Birimian belts in Ghana consist of volcanosedimentary basins and volcanic greenstone belts (Fig. 1), intruded by several generations of granitoids (Junner 1935; Leube and Hirdes 1986; Leube et al. 1990). The Birimian belts were formed during the Eburnean orogeny between 2200 and 2088 Ma (Bonhomme 1962; Abouchami et al. 1990; Allibone et al. 2002). The volcanic belts are older than 2186 Ma based upon U/Pb zircon ages obtained from intruded granitoids (Boher et al. 1992; Hirdes et al. 1992; Oberthür et al. 1998), but the sedimentary rocks of the basins are younger than 2130 Ma based upon U/Pb on detrital zircons (Davis et al. 1994; Oberthür et al. 1998). The conglomeratic Tarkwaian rocks are the product of inversion and erosion of the previously formed volcanosedimentary basins. The eroded rocks were then

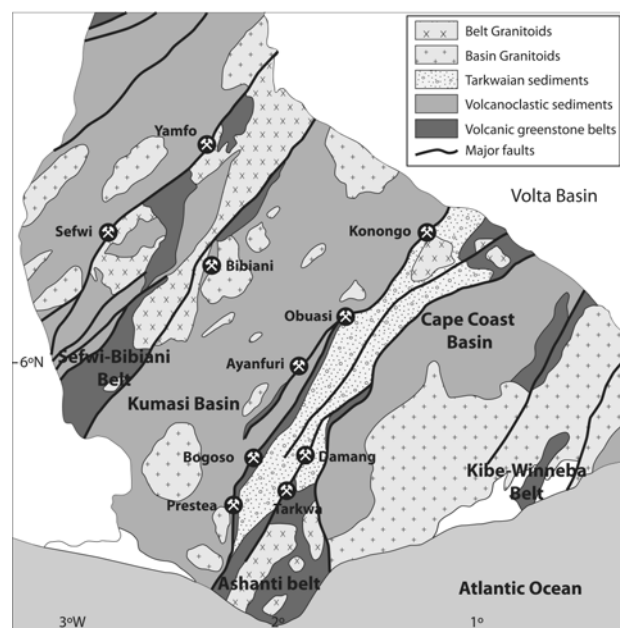


Figure 1. Geological map of Northern Ghana geology and locations of major gold deposits (modified from Allibone et al., 2002).

deposited as conglomerates over the greenstone belts (Allibone et al. 2002). Gold mineralization is thought to be temporally associated with the post-metamorphic peak of the Eburnean orogeny, at ca, 2100 Ma (Milesi et al. 1989).

The Obuasi gold deposit is hosted in the Kumasi volcano-sedimentary basin, within turbiditic and volcanoclastic sedimentary rock. All gold mineralization at Obuasi is either spatially associated with or hosted within the Ashanti fault (Blenkinsop et al. 1994; Oberthür et al. 1994; Allibone et al. 2002).

A complex structural sequence has been recognized at Obuasi, and two slightly different schemes have been previously proposed to explain this (Blenkinsop et al. 1994; Allibone et al. 2002). There is an early cleavage (S1) that is only weakly developed and has an acute angle with respect to the bedding (S0). The second and most dominant cleavage (S2) strikes northeast and dips steeply to the northwest. The F2 fold axes gently plunge to the northeast. Peak metamorphic conditions occurred at $400\pm 50^\circ\text{C}$ and 2 kbar (Schwartz et al. 1992) during the development of this S2 cleavage. Finally, late cleavage (S3) and associated fold axial planes strike east-northeast, with gentle to steep dips to the north-northwest. The F3 folds deform previous structures. The fold amplitudes are centimeter to tens of meter in scale, with axes plunging at 20 to 50° to the northeast.

It has been proposed that the northeast-striking graphitic faults hosting the mineralization may have nucleated along early S1 cleavage (Allibone et al. 2002). The second and main S2 cleavage is the results of a NW-SE compression (D2) that transposed S0 into S2 cleavage. This fabric is S1 in the structural sequence defined by Blenkinsop et al., (1994). The late S3 cleavage is interpreted to be the product of a NNW-SSE to N-S shortening. This fabric is referred to as S2 and S4 by Blenkinsop et al. (1994) and Allibone et al. (2002), respectively.

3 Ore types and geometry

3.1 Disseminated sulfide ores

Greater than 50% of the gold production in Obuasi is derived from gold-bearing sulfides which are disseminated in metasedimentary rock (Milési et al. 1991). The textures, timing, geological setting, and chemistry of this ore have been previously examined by Leube et al. (1990) and Oberthür et al. (1994). The ore mineralogy comprises arsenopyrite, pyrite, pyrrhotite, marcasite, chalcopyrite, and rare micrograins of native gold (Oberthür et al. 1994). The ore mineral are dominated by arsenopyrite (60-95%). Several generations of arsenopyrite exist, with zonation present in the bigger crystals. Within the arsenopyrite, gold is heterogeneously distributed as gold-rich rims and gold-poor cores (Oberthür et al. 1994). Gold is also locked in the crystal lattice of sulfides, as micronuggets close to arsenopyrite or in microfractures cutting arsenopyrites.

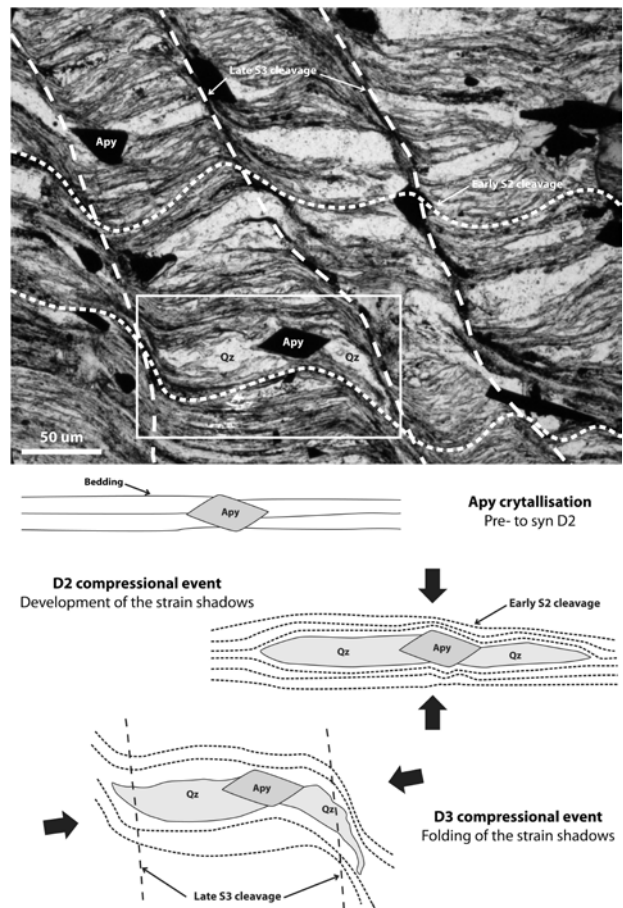


Figure 2. Optical microphotograph, and interpreted sketches; Quartz strain fringes developed along S2 and folded along S3; sample DF038, Obuasi underground (L21 XC343).

Strain shadows are present in association with a large proportion of the gold-bearing arsenopyrite and pyrite. The strain shadows are developed along the S2 cleavage and are microfolded by the S3 crenulation cleavage (Fig. 2).

However, some arsenopyrites do not display any strain shadows, indicating that there may be multiple generations of arsenopyrite nucleation and growth. Allibone et al. (2002) present possible evidence for needles of arsenopyrite overprinting the latest cleavage (S3 this study).

3.2 Quartz vein ores

The highest grade ores at Obuasi are contained within thick quartz veins, as much as 4-m-wide. These ores are characterized by visible gold in microfractures cutting through, but contained entirely within the quartz veins. The quartz veins usually dip to the west and are very close to the graphitic shears. Several quartz veins may be present in the same ore zone. The veins comprise quartz, minor ankerite, and host rock fragments. The quartz can have a smoky, milky, or glassy appearance, but only the first two categories are associated with elevated gold grades. Within the microfractures, gold is accompanied by muscovite, graphite, galena, chalcopyrite, sphalerite, bournonite, boulangerite, and austrobitine (Oberthür et al. 1994).

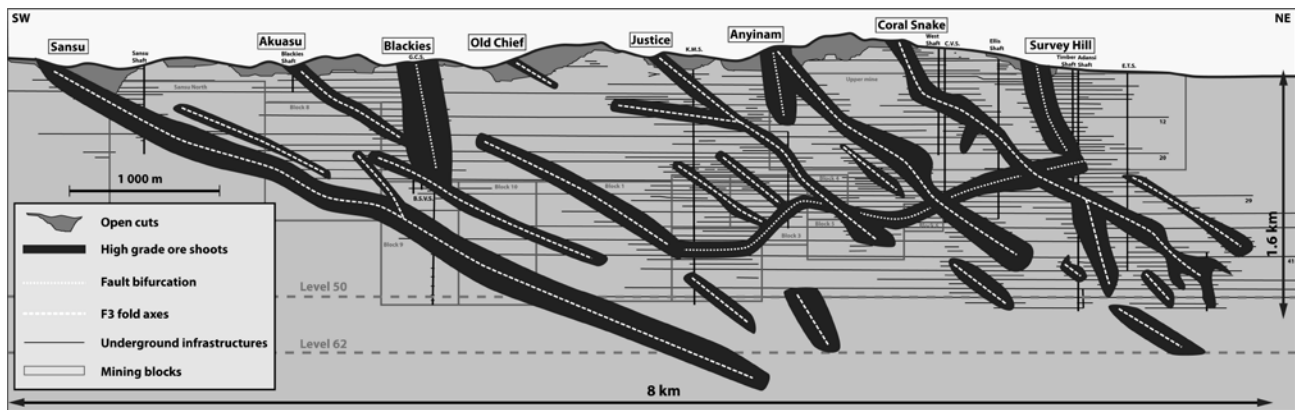


Figure 3. Projected long-section of high-grade ore shoots, underground infrastructures, and surface mining. Steep and horizontal ore shoots coincide with the intersection of fault splays. In contrast, moderately plunging ore shoots are associated with both folding of the Ashanti fault system (F3) and/or the intersection of S3 cleavage (modified from Allibone et al. (2002)).

3.3 Deposit-scale geometry

At the kilometer-scale, in long-section, both ore types are associated with two distinct geometric styles, which can be related to at least two separate structural controls (Fig. 3). The first style of ore shoot is steeply dipping to the northwest, or subhorizontal in long-section, and this corresponds to branch-lines derived from fault splays (Walsh et al. 1999). The second style plunges moderately ($30\text{--}50^\circ$) to the northwest, corresponding to F3 folding of the Ashanti fault and the intersection line between the Ashanti fault and S3 cleavage (Blenkinsop et al. 1994).

4 Discussion

Recent studies compiling craton-scale observations have highlighted how several stages of mineralization can be identified in the larger gold deposits of well-endowed greenstone terrains, such as in the Superior and Yilgarn cratons (Robert et al. 2005).

At the Obuasi deposit, two models exist for the timing of gold mineralization (Oberthür et al. 1994; Allibone et al. 2002). The first model states that the sulfide ore predates the quartz vein ore based on evidence from ore mineralogy and textures (Oberthür et al. 1994). Oberthür et al. (1994) argued that the two ore styles may have formed progressively during transition from a regime dominated by ductile deformation processes and pervasive fluid flow to a brittle regime. The second model is that a late sinistral reactivation of the fault system controls the gold mineralization. This model is based upon the field mapping of dilatational jogs matching the ore shoot position, as well as vein asymmetries showing sinistral motion during their formation (Allibone et al. 2002).

Relative to the structural sequence defined in this study, we find that the gold-bearing arsenopyrite grains formed pre- to syn-D2, based on the geometry and deformation of their strain shadows (Fig. 2). This constitutes an early stage of mineralization within the Obuasi system.

In contrast, the geometry of the ore shoots, containing high grade ore and visible gold mineralization, are parallel with F3 folding of the Ashanti fault and/or the intersection of the fault with the S3 cleavage. This geometric relationship implies microfracturing of quartz veins and precipitation of visible gold occurred during D3. In addition, the vein style ore is associated with a different mineral assemblage relative to the disseminated ore.

In summary, the results of this study indicate the Paleoproterozoic Birimian terranes of western Africa host large deposits, which underwent multiple episodes of gold deposition. The giant Obuasi gold deposit has been subjected to at least two episodes of mineralization. It is not yet clear whether the vein ores are the product of remobilization of gold from the disseminated ores, or whether the two ore types are genetically unrelated, but spatially overlapping. Research is ongoing to constrain the timing and origin of the different mineralization episodes observed at the Obuasi gold deposit.

Acknowledgements

This study forms part of a Ph.D. project at the Centre for Exploration Targeting, University of Western Australia. AngloGold Ashanti is gratefully acknowledged for site access and financial support. The authors would like to thank the Obuasi team for sharing their experience and knowledge. McCuaig and Miller acknowledge receipt of a large ARC linkage LP110100667.

References

- Abouchami W, Boher M, Michard A, Albarede F (1990) A Major 2.1 Ga Event of Mafic Magmatism in West Africa: An Early Stage of Crustal Accretion. *J Geophys Res* 95 (B11):17605-17629. doi:10.1029/JB095iB11p17605
- Allibone AH, McCuaig TC, Harris D, Etheridge M, Munroe S, Byrne D, Amanor J, Gyapong W (2002) Structural Controls on Gold Mineralization at the Ashanti Gold

- Deposit, Obuasi, Ghana. Society of Economic Geologists Special Publication 9:29
- Blenkinsop T, Schmidt Mumm A, Kumi R, Sangmor S (1994) Structural geology of the Ashanti gold mine. *Geologisches Jahrbuch D* 100:131-153
- Boher M, Abouchami W, Michard A, Albarede F, Arndt NT (1992) Crustal Growth in West Africa at 2.1 Ga. *J Geophys Res* 97 (B1):345-369. doi:10.1029/91jb01640
- Bonhomme M (1962) Contribution à l'étude géochronologique de la plate-forme de l'Ouest africain. *Géologie et Minéralogie*, vol. 5.62
- Davis DW, Hirdes W, Schaltegger U, Nunoo EA (1994) U/Pb age constraints on deposition and provenance of Birimian and gold-bearing Tarkwaian sediments in Ghana, West Africa. *Precambrian Research* 67 (1-2):89-107. doi:10.1016/0301-9268(94)90006-x
- Hirdes W, Davis DW, Eisenlohr BN (1992) Reassessment of Proterozoic granitoid ages in Ghana on the basis of U/Pb zircon and monazite dating. *Precambrian Research* 56 (1-2):89-96. doi:10.1016/0301-9268(92)90085-3
- Junner N (1935) Gold in the gold coast. *Gold Coast Geol Surv Mem* 4:67
- Leube A, Hirdes W (1986) The Birimian Supergroup of Ghana: Depositional environment, structural development, and conceptual model of an early Proterozoic suite. *Rep Arch BGR Hannover* 99 (529):260
- Leube A, Hirdes W, Mauer R, Kesse GO (1990) The early Proterozoic Birimian Supergroup of Ghana and some aspects of its associated gold mineralization. *Precambrian Research* 46 (1-2):139-165. doi:10.1016/0301-9268(90)90070-7
- Milesi J, Feybesse J, Ledru P, Dommangeat A, Ouedraogo M, Marcoux E, Prost A, Vinchon C, Sylvain J, Johan V (1989) West African gold deposits in their Lower Proterozoic lithostructural setting. *Chron rech min* 497:3-98
- Milési JP, Ledru P, Ankrah P, Johan V, Marcoux E, Vinchon C (1991) The metallogenic relationship between Birimian and Tarkwaian gold deposits in Ghana. *Mineral Deposita* 26 (3):228-238. doi:10.1007/bf00209263
- Oberthür T, Vetter U, Davis DW, Amanor JA (1998) Age constraints on gold mineralization and Paleoproterozoic crustal evolution in the Ashanti belt of southern Ghana. *Precambrian Research* 89 (3-4):129-143. doi:10.1016/s0301-9268(97)00075-2
- Oberthür T, Vetter U, Schmidt Mumm A, Weiser T, Amanor J, Gyapong W, Kumi R, Blenkinsop T (1994) The Ashanti gold mine at Obuasi, Ghana: Mineralogical, geochemical, stable isotope and fluid inclusion studies on the metallogenesis of the deposit. *Geologisches Jahrbuch D* 100:31-129
- Robert F, Poulsen KH, Cassidy KF, Hodgson CJ (2005) Gold metallogeny of the Superior and Yilgarn cratons. *Economic Geology* 100th Anniversary Volume:1001-1034
- Schwartz MO, Oberthuer T, Amanor J, Gyapong WA (1992) Fluid inclusion re-equilibration and P-T-X constraints on fluid evolution in the Ashanti gold deposit, Ghana. *European Journal of Mineralogy* 4 (5):1017-1033
- Walsh JJ, Watterson J, Bailey WR, Childs C (1999) Fault relays, bends and branch-lines. *Journal of Structural Geology* 21 (8-9):1019-1026. doi:[http://dx.doi.org/10.1016/S0191-8141\(99\)00026-7](http://dx.doi.org/10.1016/S0191-8141(99)00026-7)

Fluid inclusion and oxygen isotope constraints on gold mineralisation in the Senoufo Greenstone Belt, Côte d'Ivoire

Lynnette Greyling, Chris Harris

Department of Geological Sciences, University of Cape Town, Rondebosch, 7701, South Africa

Paul Harbidge

Randgold Resources, 3rd Floor, Unity Chambers, 28 Halkett Street, St Helier, Jersey, JE2 4WJ, United Kingdom

Abstract. The Birimian greenstone belts of the West African Craton host numerous orogenic gold deposits and occurrences. Mineralisation is related to the Eburnean Orogeny, during which compressional deformation and transcurrent faulting mobilised fluids along regional shear zones and focused these fluids into structural traps. Fluid inclusion and stable isotope data for northern Côte d'Ivoire indicate that ore formation at the Tongon deposit is related to CO₂-bearing, low-salinity, aqueous NaCl-MgCl₂ fluids. Aqueous-carbonic CO₂ and CH₄-rich inclusions are also present. Quartz from silicified ore zones had high $\delta_{18}\text{O}$ values (12.8 to 17.8 ‰) that are consistent with the fluids being generated by dehydration reactions in metasedimentary country rocks.

Keywords. Birimian, greenstone, orogenic gold, fluid inclusions, oxygen isotopes

1 Introduction

Gold mineralisation is hosted in the Birimian Senoufo Greenstone Belt of northern Côte d'Ivoire on the southern part of the West African Craton in the Baoulé-Mossi Palaeoproterozoic domain (Bessoles, 1977), and is mined at the Tongon deposit in the centre of the belt (Figure 1). This deposit is located within a zone of dilation adjacent to an inferred sinistral shear structure that can be followed for ~ 130 km using remote sensing. The Birimian belts are northeast-trending, steeply-dipping metavolcanic rocks and metasedimentary rocks that were deformed during the Eburnean Orogeny at ca. 2.2 – 2.0 Ga (Bonhomme, 1962), and gold mineralisation is broadly related to this event of compressive deformation and transcurrent shearing (Allibone et al. 2002, Feybesse et al. 2006, Milési et al. 1992, and references therein).

The estimated resource at Tongon is 98 t Au at an average grade of 2.67 g/t. The two orebodies at the deposit are currently developed from open pits. Mineralisation is hosted in intermediate and mafic volcanic rocks with multiple lenticular shears, striking to the southwest and with moderate to steep dips to the northwest, and in a continuous east-west trending mineralised zone with hangingwall and footwall graphitic carbonaceous shales and near-vertical dips to the north.

In both orebodies, high gold grades coincide with siliceous shears that crosscut and exploit inferred lithological contacts. Gold mineralisation occurs in andesitic tuffs, andesites, and volcanoclastic rocks

composed of andesite clasts and fragments cemented by tuff and argillaceous sediments. As is the case for many orogenic gold deposits, primary depositional textural features of the host rock are widely overprinted by carbonate alteration (e.g. Reed 1997, Robb 2005). This is presumed to result from the interaction of metamorphic CO₂-rich ore fluids with the wallrock (Reed 1997) at temperatures between 150 to >475 °C (Groves et al 1998). The typical Tongon alteration assemblage includes sericite, biotite, chlorite, and Mg-Ca (-Fe) carbonates (classification by Reed 1997), with brittle-ductile deformation and silicification associated with brecciation. Arsenopyrite occurs as the dominant ore sulphide, with minor pyrite and pyrrhotite in the more weakly mineralised units.

Anomalous (>0.2 g/t Au) gold mineralisation occurs intermittently along the strike-length of the greenstone belt. It is envisaged that, similar to the distribution of the majority of gold deposits in metamorphic terranes located off deep-crustal fault zones (Goldfarb et al. 2005), gold mineralisation at Tongon was localised at the intersection of a regional shear zone with second and/or third order structures.

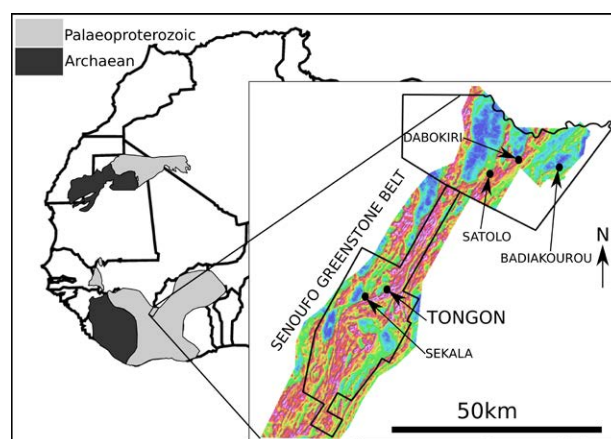


Figure 1. Location of the study area in the Palaeoproterozoic Baoulé-Mossi domain of the West African Craton. The inset shows the location of the Tongon deposit in the Senoufo Greenstone Belt on the electromagnetic conductivity image and outlines of the Diaouala (northern) and Nielle exploration permits (WA Craton outline after Boher et al. 1992).

2 Sample selection

Arsenopyrite is the dominant gold-bearing sulphide, which occurs as acicular disseminations and coarse

aggregates in biotite-chlorite-carbonate-sericite altered intermediate metavolcanic rock units at Tongon (Figure 2). Minor gold mineralisation also occurs with hydrothermal pyrite, which is distinct from earlier syngenetic pyrite that occurs in discrete laminations in carbonaceous shale units predominantly, but not exclusively, in the Northern Zone (NZ) orebody. Fine-grained silica alteration is often observed with disseminated pyrrhotite.

Subsequent to formation of the early alteration and deposition of disseminated gold, the host units were silicified and sulphides were either remobilised or added. The silicified units generally contain high gold grades (≥ 3 g/t Au) and diamond drill core of these units were sampled for fluid inclusion and stable isotope study.

In addition to the mineralised Tongon samples, quartz vein outcrop and subcrop from exploration pits and trenches were sampled along the strike length of the belt (e.g. Figure 2d). The presence of kinematic indicators may be used to reconstruct the deformational history of such samples in an attempt to compare such samples with those collected at Tongon.

3 Fluid characteristics

3.1 Fluid inclusions

Fluid inclusion microthermometry of gold-bearing (2.76 to 5.50 g/t Au) quartz samples from siliceous ore zones of the NZ at the Tongon deposit indicates the presence of at least four different fluids trapped during early mineralisation as primary isolated fluid inclusions, and two fluids trapped during later fluid pulses in secondary trails of inclusions. The early fluids consist of CO₂-rich carbonic solutions, aqueous NaCl-MgCl₂ solutions with low salinities between 1.4 to 6.3 wt.% eNaCl, and CH₄-rich carbonic solutions. In addition, there was evidence for a mixed aqueous-carbonic fluid from a single inclusion, in which T_mCO₂ is measured at -123 °C and T_hCO₂ at -87.2 °C, thus indicating a second CH₄-bearing fluid. Salinity was estimated from T_mice measurements in the late aqueous secondary inclusions and ranged from 4.2 to 7.0 wt.% eNaCl. Final homogenisation was to the liquid phase at 172 ± 10°C. Final homogenisation (T_{htot}) of secondary aqueous-carbonic inclusions was to the vapour phase at temperatures between 284 and 338 °C.

Less detailed fluid inclusion data collected from the Southern Zone (SZ) orebody at Tongon indicate the presence of a mixed aqueous-carbonic fluid, in which T_mCO₂ was measured between -67.5 and -57.9 °C indicating CO₂-rich fluids with varying CH₄, N₂, and possibly H₂S contents.

The presence of low-salinity aqueous fluids and CO₂-rich fluids is in good agreement with fluids documented from other orogenic gold deposits (Groves et al. 1998, Goldfarb et al. 2001). The H₂O-CO₂ rich fluids observed in the fluid inclusions may be derived from devolatilisation reactions involved in the production of metamorphic water at temperatures above 300 °C during prograde metamorphism (Stevens et al., 1997). These reactions occur at temperatures that correspond with

minimum trapping temperatures of aqueous-carbonic inclusions (T_{htotal}(V)=284 – 338 °C). Aqueous fluid circulation occurred at temperatures between 230 and 245°C (corrected from T_{htotal}(L)=172-181°C using pressures of 1.05 to 1.35 kbar from Coulibaly et al. 2008). These aqueous fluids are present as secondary trails and may be indicative of subsequent meteoric fluids. However, additional microthermometry is required to establish the possible link with gold mineralization.

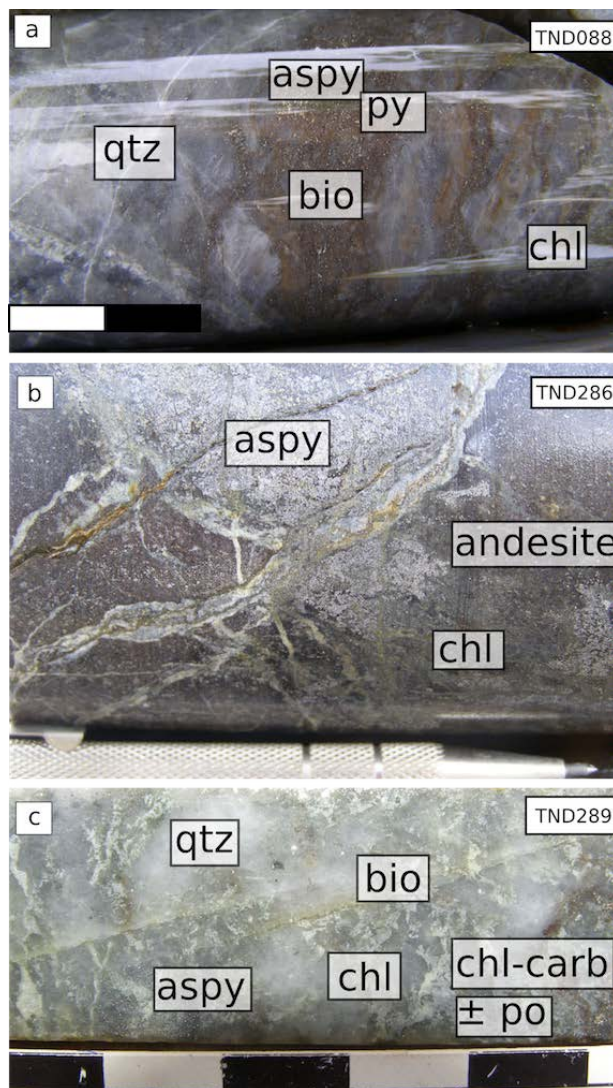


Figure 2. Tongon mineralised samples (a-c) showing disseminated sulphides and silicified units. Scale bars units in images (a) and (c) are in centimetres.

3.2 Oxygen isotopes

Oxygen isotope data were obtained by both conventional and laser fluorination methods at the University of Cape Town. The $\delta_{18}\text{O}$ values of auriferous quartz from the two Tongon orebodies are between 12.8 and 15.9 ‰ (NZ), and 14.8 and 17.7 ‰ (SZ), respectively. Using the equation for oxygen fractionation between quartz and water of Zhang et al. (1989), the fluid $\delta_{18}\text{O}$ value is estimated to have ranged from 6.0 to 9.1 ‰ assuming a temperature of 316°C (mean for T_{htotal}=284-338°C obtained from fluid inclusions) for the NZ, and 8.6 to

11.7 ‰ for SZ. To the west of Tongon, quartz veins from the Sekala area have similar high $\delta_{18}\text{O}$ values of 16.9 – 17.0 ‰ (and $\delta_{18}\text{O}$ of the fluid between 10.1 and 10.2 ‰ at 316°C), These $\delta_{18}\text{O}$ values of the fluids are in agreement the 5 to 10 ‰ of those typically associated with orogenic gold deposits (Goldfarb et al. 2001).

The $\delta_{18}\text{O}$ values of quartz veins from exploration targets generally decrease in the Senoufo Belt to the northeast of the Tongon deposit, and are between 10.0 and 14.1 ‰ at Dabokiri ($\delta_{18}\text{O}$ of the fluid is between 3.2 and 7.3 ‰ for 316°C), 10.6 and 13.6 ‰ at Badiakourou ($\delta_{18}\text{O}$ of the fluid is between 8.4 and 11.4 ‰ for a temperature of 550°C of broad amphibolite facies metamorphism of the host rocks), and 12.7 and 13.7 ‰ at Satolo (with corresponding $\delta_{18}\text{O}$ of the fluid is between 8.5 and 9.5 ‰ at a temperature of 316°C), The $\delta_{18}\text{O}$ values of the quartz and silicified ore zones generally increase with increasing gold grades (Figure 2), and the preliminary fluid $\delta_{18}\text{O}$ values should be checked with homogenization temperatures from microthermometry. Moreover, if pressure is assumed at ± 1 kbar for gold quartz mineralization in the south (Coulibaly et al. 2008), the isochores of $T=172\pm 10^\circ\text{C}$ aqueous inclusions would intersect a temperature of around 230°C. The estimates of fluid $\delta_{18}\text{O}$ value depend on temperature; for example, if the trapping temperature was 100°C higher than T_h , (i.e. 416°C), the $\delta_{18}\text{O}$ value of the fluid would be about about 2.5 ‰ higher.

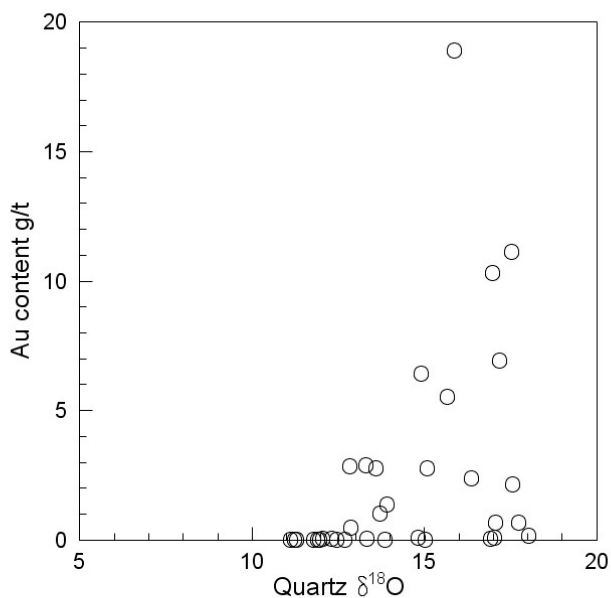


Figure 2. Oxygen isotopes vs gold grade for selected samples of the Senoufo Belt.

There are several possible explanations for the range in quartz $\delta_{18}\text{O}$ values, which relate to changing fluid $\delta_{18}\text{O}$ value and/or temperature. Firstly, the higher $\delta_{18}\text{O}$ of quartz values might be related to lower temperatures in a fluid-buffered system, where fluid $\delta_{18}\text{O}$ value is relatively constant. Secondly, high $\delta_{18}\text{O}$ values might be due to greater exchange between those fluids and rocks such as carbonates or shales, leading to significant variation in fluid $\delta_{18}\text{O}$ value at relatively constant temperature. Thirdly, the lower $\delta_{18}\text{O}$ values may be due

to mixing with surface water having much lower $\delta_{18}\text{O}$ value. The association of Au with quartz of high $\delta_{18}\text{O}$ value suggests that either of the first two mechanisms, or a combination, might be responsible for Au deposition. Mixing of Au-rich metamorphic fluid with surface waters is not, therefore, a viable mechanism for Au precipitation.

4 Conclusions

Fluid immiscibility may be one possible ore genesis model for the Tongon gold deposit due to the presence of low-salinity NaCl-MgCl₂ aqueous- and CO₂-rich fluid inclusions. These fluid compositions are similar to those documented from other orogenic deposits (Goldfarb et al. 2001 and references therein). The presence of an additional CH₄-rich fluid may be explained as being locally derived from metamorphosed and sheared carbonaceous shales. Moreover, mixing at minimum temperatures between 284 and 338 °C of a fluid sourced from or circulated through carbonaceous shales would raise the $\delta_{18}\text{O}$ of the fluid, and is implicated in not only the NZ with strong carbonaceous shale hangingwall and footwall controls, but also in the SZ orebody due to high $\delta_{18}\text{O}$ values. Although relatively low temperatures are documented from homogenisation temperatures of fluid inclusions, the inclusions are secondary and the influence of a meteoric fluid is ruled out by high $\delta_{18}\text{O}$ values.

Acknowledgements

This work is funded by Randgold Resources and UCT through a post-doctoral fellowship to LNG. Fayrooza Rawoot is thanked for help with the stable isotope measurements, David Wilson for preparation of the double polished wafers, John Lanham for help with the mass spectrometer, and Dioumacor Senghor and the CI Exploration team for facilitating access to the area.

References

- Allibone AH, McCuaig TC, Harris D, Etheridge M, Munroe S, Byrne D, Amanor J, Gyapong W (2002) Structural controls on gold mineralization at the Ashanti Deposit, Obuasi, Ghana. SEG Spec Pub 9:65-93
- Bessoles B (1977) Géologie de l'Afrique. Le craton Ouest-Africain. Mémoires BRGM, Paris, pp 88
- Boher M, Abouchami W, Michard A, Albaredo F, Arndt NT (1992) Crustal growth in West Africa at 2.1 Ga. J Geoph Res 97:345-369.
- Bonhomme M (1962) Contribution a l'étude géochronologique de la plate-forme de l'Ouest africain. These. Ann. Fac. Sci. Univ. Clermont-Ferrand, Fr. Géol. Minéral 5, p.62.
- Coulibaly Y, Boiron MC, Cathelineau M, Kouamelan AN (2008). Fluid immiscibility and gold deposition in the Birimian quartz veins of the Angovia deposit (Yaouré, Ivory Coast). JAES 50:234-254
- Goldfarb RJ, Groves DI, Gardoll S (2001) Orogenic gold and geologic time: a global synthesis. Ore Geol Rev 18:1-75
- Groves DI, Goldfarb RJ, Gebre-Mariam M, Hagemann SG, Robert F (1998) Orogenic gold deposits: A proposed classification in the context of their crustal distribution and relationship to other gold deposit types. Ore Geol Rev 13:7-27
- Feybesse JL, Billa M, Guerrot C, Duguey E, Lescuyer JL, Milesi JP, Bouchot V (2006) The paleoproterozoic Ghanaian

province: Geodynamic model and ore controls, including stress modelling. *Pre Res* 149:149-196

Milési JP, Ledru P, Feybess JL, Dommangeat A, Marcoux E (1992) Early Proterozoic ore deposits and tectonics of the Birimian orogenic belt, West Africa. *Pre Res* 58:305-344

Reed MH (1997) Hydrothermal alteration and its relationship to ore fluid composition. In: Barnes HL (ed) *Geochemistry of hydrothermal ore deposits*, 3rd ed, pp 303-365

Robb LJ (2005) *Introduction to ore-forming processes*. Blackwell

Publishing 373pp

Stevens G, Boer R, Gibson RL (1997) Metamorphism, fluid flow and gold remobilization in the Witwatersrand Basin: towards a unifying model. *SAJG* 100:363-375

Zhang L, Liu J, Zhou H, Chen Z (1989) Oxygen isotope fractionation in the quartz-water-salt system. *Econ Geol* 84:1643-1650

Gold systems in the Lower Crustal Section (“bottom”) of Greenstone Belts

Steffen G. Hagemann

Centre for Exploration Targeting, University of Western Australia, M006, 35 Stirling Hwy, Crawley, WA 6009, Australia

Kevin F. Cassidy

Bare Rock Geological Services Pty Ltd, Fremantle, WA 6160, Australia

Walter Witt

The Walter Witt Experience, 122 Edward Street, Bedford, WA 6052 Australia

Abstract. Three main groups of gold systems are located at the lower crustal sections (>8km depth) of Archean greenstone belts and hosted in lower amphibolite to granulite facies supracrustal and granitic rocks: (1) orogenic-hypozonal gold systems where single or two stage gold mineralisation was introduced either at different crustal levels during the tectono-metamorphic history of the host terrain or under isobaric cooling; (2) intrusion-related related gold systems where mineralisation is post-peak metamorphism and related to either proximal- or distal-derived magmatic fluids; (3) metamorphosed, gold systems where mineralisation was introduced prior to peak metamorphism.

The careful differentiation between these main groups of gold systems is of importance in the mineral system analyses (i.e., genetic models) of gold systems. It is also significant in exploration because each of these groups is characterized by diverse structural, hydrothermal alteration and geochemical footprints, and thus potentially requires different exploration methods.

Keywords. Orogenic gold systems, hypozonal, intrusion-related, metamorphosed

1 Introduction

Gold systems preserved in the “basal” (bottom) parts, i.e., high temperature and pressure end of the crustal spectrum, of greenstone belts are not well defined, partly because of similar geological characteristics of traditional orogenic and intrusion-related systems but also because of difficulty in determining the relative timing of mineralisation with respect to single or multiple metamorphic events and/or a paucity of robust geochronological data to support cross-cutting relationships. Currently there appear to be three gold systems represented: the first group are hypozonal gold deposits that represent an open system where external hydrothermal fluids infiltrated syn-deformational structures (e.g., Renco deposit in Zimbabwe, New Concert deposit in South Africa, Three Mile Hill, Norseman and Southern Cross gold deposits, the latter three in Western Australia). In the second group the system was open and there is distinct evidence of syn-intrusion gold mineralisation, influx of hydrothermal magmatic fluids, and mineralisation in both intrusions and surrounding supracrustal wallrocks. The former would represent endoskarns (e.g., stage 2 mineralisation in the Chalice deposit in Western Australia), the latter exoskarn (e.g., Big Bell in Western Australia) gold

systems. The third group represent gold deposits that were metamorphosed in a closed system without external fluids or melts (e.g., Challenger deposit in South Australia, Griffin’s Find in Western Australia and Hemlo in Ontario, Canada).

2 Orogenic hypozonal gold systems

Hypozonal orogenic gold deposits were formed at greenstone belt crustal levels of >8 km depth (i.e., >3 kbars and 500°C, assuming lithostatic pressure conditions). They are hosted in lower to upper amphibolite facies supracrustal and granite rocks where single or two stage gold mineralisation was introduced either at different crustal levels during the tectono-metamorphic history of the host terrain (e.g., Renco: Kolb et al. 2000) or under isobaric cooling (e.g., Coolgardie: Knight et al. 2000). In the Yilgarn craton these deposits have been described in detail by Witt (1991, 1993, 2001), Groves et al. (1992), Neumayr et al. (1993), Hagemann et al. (1998), Knight et al. (2000). Much of the recent research on hypozonal gold mineralisation is from Archean gold systems in southern Africa and India.

Kolb et al. (2000) showed that at the Renco deposit in Zimbabwe, deformation and mineralisation occurred at temperatures of 600 to 700°C and that mineralisation is located in mineralized shear zones that correspond to the regional-scale retrogression of high-grade metamorphic rocks (granulite facies) wall-rocks during the late-Archean thrusting of the Northern Marginal Zone onto low- to medium grade (greenschist facies) terrains of the Zimbabwe craton. As such, the Renco gold deposit represents an orogenic gold deposit that formed during the retrograde amphibolite facies hydration of granulites in a mid-crustal (hypozonal) environment, likely sourced from metamorphic fluids generated from dehydration of subcreted greenstone belt rocks of the Zimbabwe craton.

At the Hutti mine in the Dhawar craton, India, Kolb et al. (2005) demonstrated that auriferous shear zones, located within amphibolites and meta-rhyolites that were metamorphosed to amphibolites facies assemblages, were emplaced under retrograde upper greenschist to lower amphibolite facies conditions. Subsequent reactivation of the reefs at lower greenschist facies conditions resulted in formation of the main gold-

bearing laminated quartz veins within the reefs. Gold mineralisation is interpreted to have been introduced either during isobaric cooling or at different crustal levels during the tectono-metamorphic history of the eastern Dhawar craton.

Otto et al. (2007) showed for the New Consort gold mine at Barberton, South Africa, that two stages of gold mineralisation comprise an early high temperature and pressure loellingite, pyrrhotite and calc silicate alteration mineralisation event localised in upper amphibolites facies rocks of the Onverwacht Group, and a second, main-stage mineralisation characterized by arsenopyrite-pyrrhotite in the upper portion of the mine to arsenopyrite-pyrrhotite-chalcopyrite-loellingite in the deeper parts in rocks of the Fig Tree Group. Textural and cross-cutting relationships indicate mineralisation was synchronous with upper-greenschist syn-peak metamorphism of the Fig Tree Group but post-peak metamorphism of the upper amphibolite facies rocks of the Onverwacht Group.

3 Intrusion-related gold system

Specific types of deep intrusion-related gold systems have been proposed to represent distinct Archean gold systems (e.g., Robert 2001) including skarns (Mueller 2009), which are different to traditional orogenic gold systems. Some researchers have attempted to include these magmatic-related gold systems in Archean granite-greenstone belts within the traditional orogenic gold system framework (e.g., Groves et al. 2003).

At the middle to upper amphibolite facies mafic to ultramafic rock-hosted Chalice deposit in Western Australia Stage 2 gold mineralisation is localised in a monzogranite dyke. It contains disseminated gold in equilibrium with igneous quartz and feldspar and is associated with quartz-gold, quartz-diopside-gold, actinolite-gold and molybdenite-tellurobismuthite-gold veins (Bucci et al. 2002; 2004). Based on geochronology of this stage of gold mineralisation, the monzogranite dyke and spatially associated gneissic monzogranite pluton as well as the gold equilibrium mineralogy and textures, Bucci et al. (2004) interpret stage 2 gold mineralisation as magmatic in origin.

At the Big Bell deposit in Western Australia, Mueller et al. (1996) demonstrated with detailed geochronology analyses that the main gold event (gold-sulfide-scheelite mineralisation) occurred about 80 m.y. after the peak of amphibolite facies contact metamorphism. However, Mueller et al. (1996) also state that no intrusion with ages similar to that of the main gold mineralisation event (concordant U-Pb almandine age of 2662 ± 5 Ma from a low-grade cummingtonite-hornblende contact skarn) have been identified in the Big Bell mine area. The interpretation of Mueller et al. (1996) is at variance with Wilkins (1993) who interprets gold mineralisation at Big Bell as post-peak metamorphism under significantly retrograde conditions.

The origin of gold mineralisation in several amphibolite facies mafic and ultramafic rock hosted gold deposits near Southern Cross in Western Australia is also hotly debated. For example, pyrrhotite-rich

hedenbergite-actinolite and almandine-hornblende ore bodies at the Nevorvia gold deposit have been classified, on the basis of their alteration assemblages and spatial association with granites, as gold-rich skarns by Mueller (1997) and Mueller et al. (2004). The Nevorvia orebodies are cut by pegmatite dikes and are underlain by a 500-m-thick pluton of peraluminous two-mica granite, with a concordant zircon U-Pb age of 2634 ± 4 Ma. Mueller and McNaughton (2000) also dated gold skarn mineralisation from the Corinthian gold deposit at 2620 ± 6 Ma and amphibolite facies contact metamorphism at 2772 ± 5 Ma. They interpret these ages as evidence that skarn mineralisation formed 150 m.y. after contact metamorphism, thus significantly post-peak metamorphism. In contrast, Witt et al. (2003) describe banded iron-formation hosted gold deposits at Marvel Loch and Yilgarn Star in which quartz-clinopyroxene-pyrrhotite veins cut folded mesobanding and a foliation formed at mid to upper amphibolite facies. These shear-zone hosted deposits comprise quartz-diopside-calcite-pyrrhotite veins that are boudinaged and folded within an amphibolite facies shear fabric. Witt et al. (2003) and other authors, such as Bloem et al. (1994), Dalstra et al. (1997), Hagemann et al. (1998), Ridley et al. (2000) use these relationships to propose that gold mineralisation at various deposits in the Southern Cross area formed concurrently with late syn-peak metamorphism, and thus represent hypozonal orogenic gold systems.

4 Metamorphosed (orogenic) gold system

At the Neoproterozoic Challenger gold deposit in South Australia, Tomkins and Mavrogenes (2002) provide experimental and textural evidence, including the occurrence of invisible gold in loellingite but not in adjacent arsenopyrite, and the presence of spherical gold sulfide inclusions in peak metamorphic garnet and other silicates, for a pre-peak metamorphic gold mineralisation event. During peak granulite facies metamorphism ($\sim 7.5 \pm 1.5$ kbars and at least 800°C) a gold-rich polymetallic melt was mobilized into leucosomes synchronously with silicate melt. Visible gold is restricted to migmatitic leucosomes and, to a lesser extent, melanosomes. Large inclusions of gold coexist with arsenopyrite, pyrrhotite, and bismuth and are hosted in silicate minerals such as garnet and at grain boundaries. The Challenger deposit represents the first well-characterized metamorphosed Archean gold deposit hosted in granulite facies rocks with leucosome-hosted gold in migmatites.

Lin (2001) demonstrated through detailed surface and underground mapping and compilation of data from three gold mines in the Hemlo area, Ontario, Canada that hydrothermal alteration and gold mineralisation occurred prior to peak amphibolite facies metamorphism. This conclusion is supported by microscopic observations that show the altered and mineralized rocks have typical metamorphic textures (Burk et al. 1986; Lin 2001). Tomkins et al. (2004) show that the ore mineral assemblage at Hemlo underwent partial melting during middle-amphibolite facies metamorphism ($600\text{--}650^\circ\text{C}$, 6–7 kbars), primarily through breakdown of stibnite and

arsenopyrite in a high-*f*S₂ environment. Concurrent deformation led to segregation of the resulting Sb- and As-rich sulfosalt melt. Interaction between this melt and a range of unmelted sulfides led to further melting and incorporation of other elements into the melt. The gold-bearing melt was mobilized from compressional high-strain sites into dilational domains such as boudin necks and extensional fractures developed in competent lithologies. Ore minerals that did not melt significantly (pyrite, pyrrhotite, molybdenite and sphalerite) were not extensively mobilized and largely remained within high-strain compressional domains. The segregation of melt from residue thus resulted in the observed heterogeneous distribution of ore minerals within the deposit. Heiligmann et al. (2008) also recognized that Hemlo represents a metamorphosed gold deposit with original orogenic gold mineralisation T-P conditions of 400-500°C and 3-5 kbars. They consider the very high *f*S₂ and high activity of potassium during alteration and mineralisation responsible for the: (1) occurrence of pyrite and muscovite-microcline in the ore zone, and (2) simultaneous decrease, and eventually absence, of garnet-staurolite and kyanite from the unaltered metasedimentary rocks to the ore zone.

Tomkins and Grundy (2009) demonstrated via textural work that gold textures in some parts of the Griffin's Find deposit, Western Australia are consistent with both solid-state prograde and retrograde metamorphic reactions, whereas in other parts are consistent with the development of a gold-rich polymetallic melt. At the high temperature and pressure of peak metamorphism (700-750°C, < 5.5 kbars) at Griffin's Find, the influx of typical orogenic gold fluids would have been precluded. The presence of gold and sulphides in textural equilibrium with peak metamorphic minerals, particular cordierite, suggests that extensive external fluids could not have been introduced substantially post-peak metamorphism either as these silicates would have been retrogressed to hydrous phases. Gold mineralisation, therefore, is interpreted to have been introduced prior to granulite facies metamorphism and subsequently been metamorphosed. Hagemann and Gilg (2011) demonstrate for Griffin's Find that oxygen and hydrogen isotopic values of hydrothermal diopside, quartz and fluid inclusions, respectively suggest an ¹⁸O-enrichment when compared to values for other Archean orogenic gold deposits in the Yilgarn craton. They conclude that the ¹⁸O-enrichment of the ore fluid can be related to the local abundance of metasedimentary rocks (cf. Sheppard 1986) and additionally implies no major involvement of ¹⁸O-depleted surface waters during gold mineralisation. This further suggests a meso- to hypozonal origin for the pre-metamorphic mineralisation at Griffin's Find.

5. Conclusions

There is on-going academic discussion concerning Archean gold systems, particularly orogenic gold systems, which are interpreted to have formed and subsequently preserved at deeper crustal levels within high grade metamorphic terranes (with lower

amphibolite to granulite facies metamorphic assemblages). Although this dispute has led some workers to question the origin of orogenic gold deposits in general (e.g., Phillips and Powell, 2009), detailed system analysis of orogenic gold systems, particularly in the Yilgarn craton of Western Australia (e.g., Hagemann and Cassidy 2000; Cassidy et al. 2005; Barnicoat 2008; Czarnota et al. 2011), demonstrates that such deposits are the consequence of larger Archean orogenic systems, with some deposits likely to have been metamorphosed during late stages of the orogeny, particularly in the deeper crustal parts of some terranes or where terranes have been subsequently caught up in deformation and metamorphism linked to a later orogeny.

We propose that gold systems hosted in a variety of metamorphic rocks at the lower crustal section ("bottom") of greenstone belts belong to three groups: (1) single or multiple stage gold mineralisation within lower to upper amphibolite facies supracrustal and granite rocks that was introduced either at different crustal levels during the tectono-metamorphic history of the host terrain (e.g., Rencó: Kolb et al. 2000) or under isobaric cooling (e.g., Coolgardie: Knight et al. 2000), (2) middle to upper amphibolite facies rocks that may have been mineralized by intrusion-related gold systems close to the peak of metamorphism (e.g., Chalice stage 2 mineralisation: Bucci et al. 2002, 2004 and Big Bell: Mueller et al. 1996); the origin of these systems is currently ardently debated with Au skarn versus hypozonal orogenic models proposed, (3) middle amphibolite (e.g., Hemlo: Tomkins et al. 2004) to granulite facies rocks (e.g., Challenger: Tomkins and Mavrogenes, 2002; Griffin's Find: Tomkins and Grundy, 2009) where gold mineralisation was introduced prior to peak metamorphism and then subsequently metamorphosed.

Exploration in high grade metamorphic terranes, i.e., the basal part of the greenstone belts needs to carefully differentiate these groups of gold systems as each show different geological characteristics which may result in different structural, hydrothermal alteration and geochemistry footprints.

Acknowledgements

SGH and WW thanks staff, postdoctoral fellows and students of the Centre for Exploration Targeting and Geological Survey of Western Australia (particularly Michael Doublier) for many stimulating discussions about gold mineralisation and deposits.

References

- Barnicoat A.C. (2008) The pmd*CRCs Mineral Systems approach, *in*: Korsch, R.J., and Barnicoat, A.C., eds., *New Perspective: The Foundations and Future of Australian Exploration: Abstracts for the June 2008 pmd*CRC Conference*, Perth, Geoscience Australia, Record 2008/08:1-6
- Bloem EJM, Dalstra HJ, Groves DI, Ridley JR (1994) Metamorphic and structural setting and amphibolite-hosted gold deposits near southern Cross, Southern Cross Province, Yilgarn Block: *Ore Geol Rev* 9:183-208
- Bucci LA, Hagemann SG, Groves DI, Standing JG (2002) The Archean Chalice gold deposits: a record of complex, multi-stage, high-temperature hydrothermal activity and gold

- mineralization associated with granitic rocks: *Ore Geol Rev* 19:23-67
- Bucci L, McNaughton NJ, Fletcher IR, Groves DI, Kositsin N, Stein HJ, Hagemann SG (2004) Timing and duration of high-temperature gold mineralization and spatially associated granitoid magmatism at Chalice, Yilgarn Craton, Western Australia: *Econ Geol* 99:1123-1144
- Burk R, Hodgson CJ, Quartermain RA (1986) The geological setting of the Teck-Corona Au-Mo-Ba deposit, Hemlo, Ontario, Canada. In Mac-Donald AJ (ed.), *Gold'86: Willowdale, Ontario, Konsult international:311-326*
- Cassidy KF, Champion DC, Huston DL (2005) Crustal evolution constraints on the metallogeny of the Archean Yilgarn craton. In Moa J, Bierlein FP, (eds.), *Mineral deposits research: Meeting the global challenge: Berlin, Springer-Verlag:901-904.*
- Czarnota K, Champion DC, Cassidy KF, Goscombe B, Blewett RS, Henson PA, Groenewald PB (2010) Late Archean geodynamic processes: How the Eastern Goldfields Superterrane evolved in time and space. *Precamb Res* 183, 2:175-201
- Dalstra H, Bloem EJM, Ridley JR (1997) Gold in amphibolite facies terrains and its relationship to metamorphism, exemplified by syn-peak metamorphic gold in the Transvaal deposit, Yilgarn Block, Western Australia. *Chron Rech Min* 529:3-24
- Groves DI and 11 others (1992) Sub-greenschist to granulite-hosted Archean lode-gold deposits of the Yilgarn craton: A depositional continuum from deep-sourced hydrothermal fluids in crustal-scale plumbing systems. In Glover JE, Ho SE (eds) *The Archean: Terranes, processes and metallogeny*. Geology Department (Key Centre) and University Extension, UWA, Publication 22:325-337
- Groves DI, Goldfarb RJ, Robert F, Hart CJR (2003) Gold Deposits in Metamorphic Belts: Overview of Current Understanding, Outstanding Problems, Future Research, and Exploration Significance. *Econ Geol* 98:1-29
- Hagemann SG, Stern P, Brown PE, Ridley JR, Fournelle J (1998) Petrology, chemistry and timing of electrum in the Archean hypozonal Transvaal lode-gold deposit, Western Australia. *Econ Geol* 93:271-291
- Hagemann SG, Cassidy KF (2000) Archean orogenic lode gold deposits. *Rev Econ Geol* 13:9-68
- Hagemann SG, Gilg HA (2011) Oxygen and hydrogen isotope study of the Achaean granulite-hosted Griffin's Find gold deposit, Western Australia. In Fernando et al. (eds.) *Proceedings of the 11th Biennial Meeting of the Society for Geology Applied to Mineral Deposits, SGA, Antofagasta, Chile, 26-29th September 2011:557-559*
- Heiligmann M, Williams-Jones AE, Clark JR (2008) The role of sulfate-sulfide-oxide-silicate equilibria in the metamorphism of hydrothermal alteration at the Hemlo gold deposit, Ontario. *Econ Geol* 103:335-351
- Knight JT, Ridley JR, Groves DI (2000) The Archean amphibolite facies Coolgardie Goldfield, Yilgarn craton, Western Australia: Nature, controls, and gold field-scale patterns of hydrothermal wall-rock alteration. *Econ Geol* 95:49-83
- Kolb J, Kisters AFM, Hoernes S, Meyer FM (2000) The origin of fluids and nature of fluid-rock interaction in auriferous mylonites of the Renco mine, southern Zimbabwe. *Miner Dep* 35:109-125
- Kolb J, Rogers A, Meyer MF (2005) Relative timing of deformation and two-stage gold mineralization at the Hutti Mine, Dharwar craton, India. *Miner Dep* 40:156-174
- Lin S (2001) Stratigraphic and structural setting of the Hemlo gold deposit, Ontario, Canada. *Econ Geol* 96:477-507
- Mueller AG, Campbell IH, Schiotte L, Sevigny JH, Layer PW (1996) Constraints on the age of granitoid emplacement, metamorphism, gold mineralization, and subsequent cooling of the Archean greenstone terrane at Big Bell, Western Australia. *Econ Geol* 91:896-915
- Mueller AG (1997) The Nevoria gold skarn deposit in Archean iron-formation, Southern Cross greenstone belt, Western Australia; Part I, Tectonic setting, petrography, and classification. *Econ Geol* 92:181-209
- Mueller AG, Nemchin AA, Frei R (2004) The Nevoria gold skarn deposit, Southern Cross greenstone belt, Western Australia: II. Pressure-temperature-time path and relationship to post orogenic granites. *Econ Geol* 99:453-478
- Mueller AG (2009) Oxidised gold deposits and Cu-Au skarns in the Eastern Goldfields Superterrane, Western Australia: Structural setting and space-time relations to I-type intrusions. In Williams PJ et al (eds.) *Smart Science for Exploration and Mining: Proceedings of the 10th Biennial SGA Meeting of The Society for Geology Applied to Mineral Deposits Townsville, Australia, August 2009, 2:954-956*
- Mueller AG, McNaughton NJ (2000) U-Pb ages constraining batholith emplacement, contact metamorphism, and the formation of gold and W-Mo skarns in the Southern Cross Area, Yilgarn Craton, Western Australia. *Econ Geol* 95:1231-1257
- Neumayr P, Cabri LJ, Groves DI, Mikucki EJ, Jackmann JA (1993) The mineralogical distribution of gold and relative timing of gold mineralization in two Archean settings of high metamorphic grade in Australia. *Can Mineral* 31:711-725
- Otto A, Dziggel A, Kisters AFM, Meyer FM (2007) The New Consort gold mine, Barberton greenstone belt, South Africa: orogenic gold mineralization in a condensed metamorphic profile. *Miner Dep* 42:715-735
- Ridley JR, Groves DI, Knight JT (2000) Gold deposits in amphibolite and granulite facies terranes of the Archean Yilgarn craton, Western Australia: Evidence and implications of synmetamorphic mineralization. *Rev Econ Geol* 11:265-290
- Robert F (2001) Disseminated syenite-associated gold deposits in the Abitibi greenstone belt, Canada. *Miner Dep* 36:503-516
- Sheppard SMF (1986) Characterisation and isotopic variations in natural waters. *Rev Mineral* 16:165-180
- Phillips GN, Powell R (2009) Formation of gold deposits: Review and evaluation of the continuum model. *Earth Sci Rev* 94:1-21
- Tomkins AG, Mavrogenes JA (2002) Mobilization of gold as a polymetallic melt during pelite anatexis at the Challenger deposit, South Australia. A metamorphosed Archean gold deposit: *Econ Geol* 97:1249-1271
- Tomkins AG, Pattison DRM, Zaleski E (2004) The Hemlo gold deposit, Ontario: An example of melting and mobilization of a precious metal-sulfosalt assemblage during amphibolite facies metamorphism and deformation. *Econ Geol* 99:1063-1084
- Tomkins AG, Grundy C (2009) Upper temperature limits of orogenic gold deposit formation: Constraints from the granulite-hosted Griffin's Find deposit, Yilgarn craton. *Econ Geol* 104:669-685
- Wilkins C (1993) A post - peak metamorphic, post - deformational origin for the Archaean Big Bell gold deposit, Western Australia. *Ore Geol Rev* 7:439-483
- Witt WK (1991) Regional metamorphic controls on alteration associated with gold mineralization in the Eastern Goldfields Province, Western Australia: implications for the timing and origin of Archean lode-gold deposits. *Geology* 19:982-985
- Witt WK (1993) Gold mineralisation in the Menzies-Kambalda region, Eastern Goldfields, Western Australia. Western Australia Geological Survey, Report 39:165pp
- Witt WK, Drabble M, Bodycoat FM (2001) Yilgarn star gold deposit, southern Cross greenstone belt, western Australia: geological setting and characteristics of an amphibolite-facies orogenic gold deposit: Western Australia Geological Survey Record 2001/17: 45-62

Gold and associated mineralisation in the Tyndrum area, Scotland: orogenic or intrusion-related?

Nyree J. Hill, Gawen R.T. Jenkin

Department of Geology, University of Leicester, Leicester, LE1 7RH, UK

Christopher J.S. Sangster

Scotgold Resources Ltd, Upper Tyndrum Railway Station, Tyndrum, Scotland, FK20 8RY

Abstract. The Dalradian metamorphic belt of Scotland and Northern Ireland hosts a number of gold deposits including the Cavanacaw, Curraghinalt and Cononish deposits. Whilst the Cavanacaw and Curraghinalt deposits are relatively well understood, the conditions and formation mechanisms for ore deposition at the Cononish deposit are poorly understood with the deposit being previously been classified as both intrusion-related and as orogenic gold, here we discuss this issue. The structural setting, metal associations and Au:Ag ratios all indicate mineralisation may be intrusion-related. Field mapping and petrography have constrained relative time relationships that indicate gold mineralisation occurred significantly post-peak metamorphism. The presence of large post-metamorphic granites north of the Tyndrum area provides a potential source of metals and hydrothermal fluids. The timing of mineralisation is crucial to understanding of the evolution of the hydrothermal system. This study supports the growing body of evidence that mineralisation at Cononish and in the wider Tyndrum area is intrusion-related.

Keywords. Orogenic gold, Dalradian, Caledonides

1 Introduction

Tyndrum is within the Neoproterozoic-Cambrian metasedimentary Dalradian supergroup (Fig. 1) which forms the Scottish and Irish portion of the Caledonide orogenic belt. A number of gold deposits have been identified in the region with Cavanacaw currently in production.

The Cononish deposit, near Tyndrum in the Scottish Highlands, is a gold-bearing quartz vein which will become Scotland's first modern gold mine when it goes into production in early-2014. Cononish hosts a resource, reported in accordance with the JORC 2004 code, of 169,200 oz Au and 631,300 oz Ag in the Measured, Indicated and Inferred categories.

Regional exploration work in the Tyndrum area has identified a wider variety of mineralisation types and igneous activity than previously noted. Cononish-style gold mineralised veins have been mapped across the study area (Fig. 2). In addition, mineralised breccia bodies occur at Beinn Udlaigh and molybdenite mineralisation in Glen Orchy (Fig. 2).

This study aims to clarify the nature of mineralisation at both Cononish and in the regional showings. Gold mineralisation in the Caledonides has been described as orogenic (Goldfarb et al., 2005); whereas previous work concluded Cononish was intrusion-related (Curtis et al., 1993). Clarifying the nature of mineralisation is crucial in order to streamline exploration and therefore improve cost effectiveness and to extend current understanding of the evolution of the Scottish Dalradian.

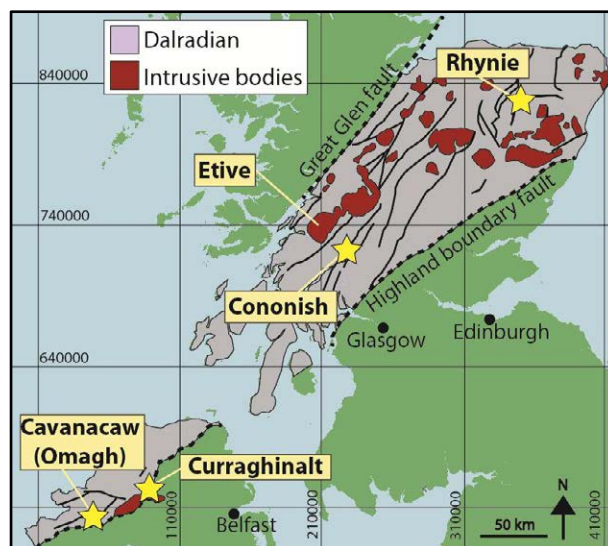


Figure 1. Regional extent of the Dalradian terrane in Scotland and Northern Ireland, showing main gold occurrences (stars) and major intrusive bodies.

2 Orogenic or Intrusion-related?

2.1 Tectonic and structural setting

The Dalradian sedimentary sequence underwent intense deformation during closure of the Iapetus Ocean between 480-465 Ma (Oliver 2001). The metamorphic grade throughout the belt is highly varied, reaching garnet grade, lower amphibolite facies in the Tyndrum area (Tanner 2012; Harte 1988). The Dalradian terrane is bounded by the Great Glen and Highland Boundary faults; both crustal scale structures (Fig. 1). Mineralisation in the Tyndrum area is highly structurally controlled by the Tyndrum fault to the south (Fig. 2) and Ericht-Laidon fault to the north; both sub-parallel to the major NE-SW structural trend of the Dalradian suite.

Cononish is a <6 m wide steeply-dipping quartz vein running sub-parallel to the NE-trending Tyndrum Fault (Fig. 2). The vein cuts lower to middle Dalradian psammities and pelites with some calcareous units. Many of the newly identified gold veins observed in the area also trend sub-parallel to the Tyndrum fault. Explosion breccia bodies at Beinn Udlaigh are interpreted to have formed in space created by movement of the Tyndrum and Ericht Laidon faults as a shear couple (Tanner 2012). Molybdenite bearing veins are hosted in brittle NNE trending fractures, which cross cut metamorphic foliation of host psammities. Groves et al. (1998) suggest orogenic gold deposits form in lower order structures near large-scale faults in metamorphic rocks. Therefore, gold mineralisation in the Tyndrum area could be interpreted to be orogenic as mineralisation is hosted in

metamorphic rocks in lower order structures sub-parallel to the Tyndrum fault. However, in intrusion-related gold systems large-scale faults have been observed to be reactivated during- and post-intrusion emplacement (Lang and Baker, 2001 and references therein).

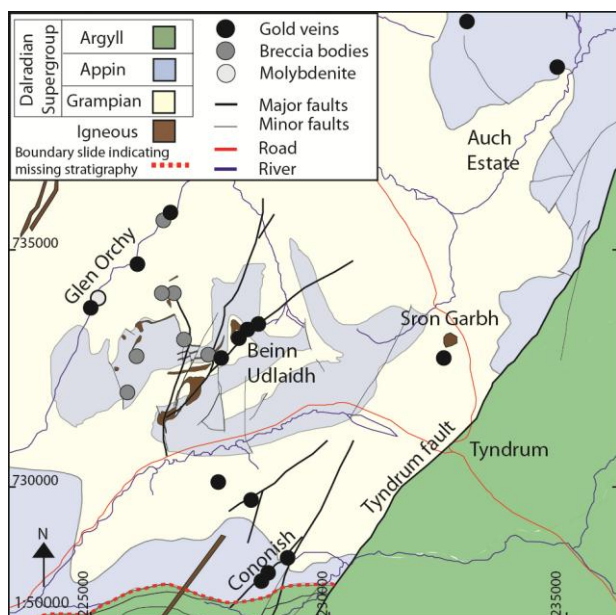


Figure 2. Study area showing generalised geology and location of newly identified mineralised veins and breccia bodies relative to Cononish.

2.2 Mineralisation style

Mineralisation in the Tyndrum area is complex with four main mineralising events (Fig. 3):

- Early molybdenite associated with K-feldspar alteration of host rock and minor pyrite (Fig. 4A).
- Gold 1; as electrum associated with early galena hosted as inclusions in pyrite (Fig. 4B).
- Gold 2; as electrum, in fractures within pyrite, with late void-filling galena and sphalerite with some hessite (AgTe_2) (Fig. 4C&D)
- Pb-Zn mineralisation thought to be Carboniferous cross-cuts earlier mineralisation.

Early K-feldspar alteration with molybdenite, as observed in Glen Orchy, occurs in many intrusion-related gold deposits (Lang and Baker, 2001). Intrusion-related gold is more commonly associated with sericite alteration (Lang and Baker, 2001), as seen in the Tyndrum area (Fig. 4C).

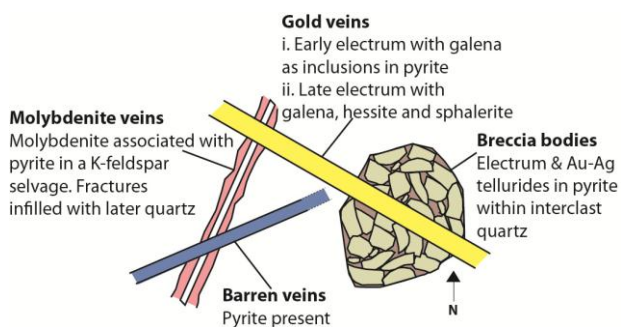


Figure 3. Schematic of cross cutting relationships in Glen Orchy area.

Both orogenic and intrusion-related gold deposits are associated with similar metal associations; anomalous As, Bi, Sb, Te and W (Groves et al., 2003). Gold mineralisation in the Tyndrum area exhibits strongly enriched Te (1000x crustal average) but much lower enrichments of As, Bi, Sb or W (all <100x crustal average). Anomalously high Pb-Zn (up to 2% and 1% respectively) is associated with the gold 2 mineralising event. High Pb-Zn is often found distally in intrusion-related deposits (Groves et al., 2003) but not associated with orogenic gold. The Au:Ag ratio observed at Cononish and in other gold showings indicates silver is anomalously high in the Tyndrum area and is not characteristic of orogenic gold (Fig. 5).

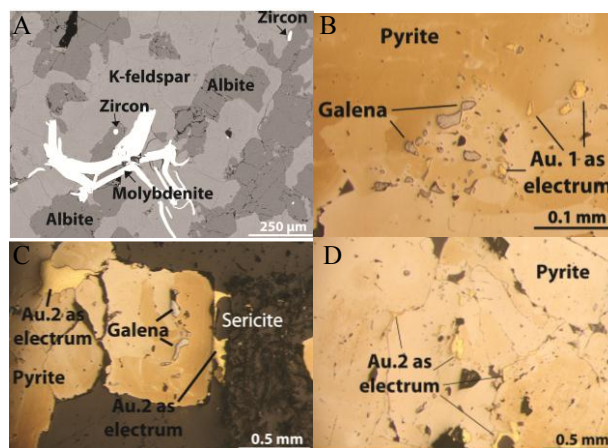


Figure 4. Petrography images of molybdenite and gold mineralisation. A, molybdenite with distinct K-feldspar alteration. B, gold 1 as inclusions in pyrite. C&D, gold 2 with late void filling galena. A – SEM image. B-D – reflected light.

2.3 Relationship to intrusions

There are widespread granite and gabbro batholiths of varying age across the Dalradian (Fig. 1). When considering mineralisation in the Tyndrum area, the Caledonian granites emplaced between 435 – 395 Ma (Lowry et al., 2005) are significant. There is no surface exposure of any Caledonian granite within 10 km of mineralisation in the Tyndrum area. However, a negative gravity anomaly extending south-eastwards from the Etive complex towards Tyndrum is interpreted to represent a blind granite pluton. The Etive complex (Fig. 1) also has recorded molybdenite mineralisation (Porter and Selby, 2010).

This study has identified widespread lamprophyric intrusions across the field area. Within the lowest stratigraphic units lamprophyric sills, up to 2 m in thickness, are abundant. Lamprophyre has been identified at Beinn Udlaigh from drill core and a hornblende body is observed at Sron Garbh (Fig. 2). No clear relationship between gold and lamprophyric rocks is observed. Breccia pipes, however, contain clasts of lamprophyre indicating a relative timing relationship. Lamprophyric intrusions to the SW, interpreted to be comparable to lamprophyres in the Tyndrum area, are dated 422 - 429 Ma (Rogers and Dunning, 1991).

The spatial association with batholiths and lamprophyre dykes at Cononish and in the surrounding area does not preclude the mineralisation from being

orogenic gold in style as these deposits are commonly spatially associated with continental margin batholiths and lamprophyre dykes (Groves et al., 2003). However, the relative timing of metamorphism, mineralisation and magmatism suggests an orogenic origin is unlikely. Orogenic gold deposits commonly form relatively soon after peak metamorphism (Bierlein et al., 2004).

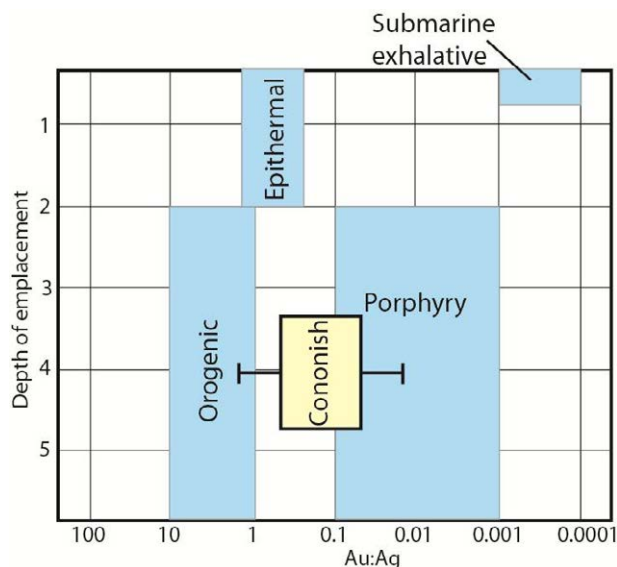


Figure 5. Average bulk Au:Ag ratios and depth of emplacement. All data from Groves et al. (1998) and references therein. Cononish data ($n=175$) is from this study; box represents 1 sigma standard deviation and whiskers, maximum variation.

In the Tyndrum area, peak metamorphism occurred at ~ 473 - 465 Ma (Baxter et al., 2002). Cross-cutting relationships indicate gold is younger than molybdenite mineralisation, which cross cuts the metamorphic foliation. Mineralisation at Cononish has been tentatively dated at ≥ 410 Ma (K-Ar and Ar/Ar dating of hydrothermal K-feldspar; Treagus et al. 1999). New dating suggests the age is very close to this (Rice et al. 2013) indicating mineralisation occurred significantly post-peak metamorphism and overlaps with Caledonian granite emplacement.

3 Conclusion

While the orogenic gold model (Groves et al. 1998) fits for some gold deposits in the Caledonides, we suggest it does not fit mineralisation in the Tyndrum area. Based on the assumption gold mineralisation is all part of the same system and of comparable age to Cononish; mineralisation occurs significantly post-regional metamorphism. This work supports the hypothesis of a late magmatic-related origin advocated by Curtis et al. (1993), Tanner (2012) and Rice et al. (2013); the Tyndrum gold veins and in this case wider mineralisation is an intrusion-driven mineralising system, most likely related to Caledonian granites. Work is ongoing to further constrain age relationships of these mineralising events.

Acknowledgements

NJH is CASE funded by Natural Environment Research Council (NERC) studentship #RP14G0129 in conjunction with Scotgold Resources Ltd. Scotgold are acknowledged for their continuing support and for access to company information.

References

- Baxter EF, Ague JJ, DePaolo DJ (2002) Prograde temperature-time evolution in the Barrovian-type locality constrained by Sm/Nd garnet ages from Glen Clova, Scotland. *J. Geol. Soc. Lond.* 159:71-82.
- Bierlein FP, Christie AB, Smith PK (2004) A comparison of orogenic gold mineralisation in central Victoria (AUS), western South Island (NZ) and Nova Scotia (CAN): implication for variations in the endowment of Palaeozoic metamorphic terrains. *Ore Geol. Rev.* 25: 125-168.
- Curtis SF, Patrick RAD, Jenkin GRT, Fallick AE, Boyce AJ, Treagus JE (1993) Fluid Inclusion and stable isotope study of fault related mineralisation in Tyndrum area, Scotland. *Trans Inst Min Metall (section B: Appl Earth Sci)* 102: 39-47.
- Goldfarb RJ, Baker T, Dube B, Groves DI, Hart CJR, Gosselin P (2005) Distribution, character and genesis of gold deposits in metamorphic terranes. In: Hedenquist JW, Thompson JFH, Goldfarb RJ, Richards JP. (eds) *Econ. Geol. 100th Anniversary volume 1905-2005*, 407-450.
- Groves DI, Goldfarb RJ, Gebre-Mariam M, Hagemann SG, Robert F (1998) Orogenic gold deposits: A proposed classification in the context of their crustal distribution and relationship to other gold deposit types. *Ore Geol. Rev.* 13: 7-27.
- Groves DI, Goldfarb RJ, Robert F, Hart CJR (2003) Gold deposits in metamorphic belts: Overview of current understanding, outstanding problems, future research and exploration significance. *Econ. Geol.* 98: 1-29.
- Harte B (1988) Lower Palaeozoic metamorphism in the Moine-Dalradian belt of the British Isles. In: Harris AL & Fettes DJ (eds) *The Caledonian-Appalachian Orogen*. Geological Society, London, Special Publications, 38: 123-134.
- Lang JR, Baker T (2001) Intrusion-related gold systems: the present level of understanding. *Min. Dep.* 36: 477-489.
- Lowry D, Boyce AJ, Fallick AE, Stephens WE and Grassineau NV. (2005) Terrace and basement discrimination in northern Britain using sulfur isotopes and mineralogy of ore deposits. In: McDonald, I., Boyce, A.J., Butler, I.B., Herrington, R.J. & Polya, D.A. (eds) *Deposits and Earth Evolution*. Geological Society, London, Special Publications, 248: 133-151.
- Oliver GJH (2001) Reconstruction of the Grampian episode in Scotland: its place in the Caledonian Orogeny. *Tectonophysics* 332: 23-49.
- Porter SJ, Selby D (2010) Rhenium-Osmium (Re-Os) molybdenite systematics and geochronology of the Cruachan granite skarn mineralisation, Etive complex: implications for emplacement chronology. *Scottish J. Geol.* 46: 17-21.
- Rice CM, Mark DF, Selby D, Hill NJ (2013) Dating vein-hosted gold deposits in the Caledonides of N. Britain. Mineral Deposit Studies Groups meeting abstracts. *Applied Earth Science (Trans. Inst. Min. Metall. B)*. *In press*
- Rogers G, Dunning GR (1991) Geochronology of appinitic and related granitic magmatism in the W Highlands of Scotland: constraints on the timing of transcurrent fault movement. *J Geol Soc, Lond* 148: 17-27.
- Tanner PWG (2012) The giant quartz-breccia veins of the Tyndrum-Dalmally area, Grampian Highland, Scotland: their geometry, origin and relationship to the Cononish gold-silver deposit. *Earth Env. Sci. Trans. Royal Soc. Edin.* 103:1-26.
- Treagus JE, Patrick RAD, Curtis SF (1999) Movement and mineralisation in the Tyndrum Fault Zone, Scotland and its regional significance. *J Geol Soc, Lond* 156: 591-604.

Mineralogical characteristics of a metasedimentary hosted Hosko gold deposit from the Archaean Hattu Schist Belt, eastern Finland

Asko Käpyaho, Ferenc Molnár
Geological Survey of Finland, P.O. Box 96, FI-02151 Espoo, Finland

Grigorios Sakellaris
Endomines Oy, Pampalo Mine, Pampalontie 11 FI-82967 Hattu, Finland

Abstract. The late Archaean Hattu schist belt and the associated plutonic rocks in Eastern Finland host several orogenic gold occurrences and deposits. In the Hosko deposit, the ore veins are hosted by a turbiditic metasedimentary unit, which is extensively tourmalinised and sericitised along the veins. The subvertical quartz-feldspar-tourmaline veins are concordant to the layering and schistosity of the rocks. The selvage of the veins is brecciated and contains subangular fragments of the host rock, whereas some parts of the veins show complex ductile deformation features. These zones also contain boudins of early stage veining. Free gold is present in the quartz-feldspar infillings and as inclusions in arsenopyrite. The gold often is associated to Bi-Te minerals. Occasionally, the gold-bearing veins and veinlets also have minor amount of scheelite. On the basis of the field observations and mineralogical observations it is concluded that the deposit show similarities with the turbidite-hosted gold deposits described elsewhere.

Keywords: Gold, sedimentary, tourmaline, telluride, orogenic gold

1 Introduction

The Late Archaean ca. 2.75 Ga Hattu schist belt, located in eastern Finland, is a predominantly N-S trending greenstone belt and it is known to host several orogenic gold deposits (Eilu et al., 2012; Fig 1). The linear array of deposits and showings is often referred to as the Karelian Gold Line (Fig 1). The northernmost of the currently known deposits is the metasedimentary rock hosted Hosko deposit, which was discovered by the Geological Survey of Finland during a mineral exploration project in the late 1980's. In 1996, Endomines acquired claim rights and conducted further exploration at the Hosko prospect. The deposit is entirely covered by several meter thick till but it has been drilled in several phases since 1992. On the basis of current data, the mineralised zone is approx. 600 metres long, 2-15 metres wide and it is at least 100 m deep (Endomines, 2013). Currently, the deposit is estimated to have ca 1 Mt @ 2.8 g/t Au (measured+indicated+inferred; Endomines, 2013). In this abstract we summarise results from a mineralogical study with the aim to characterise the gold and associated minerals from the samples collected in the outcrop and drillcores.

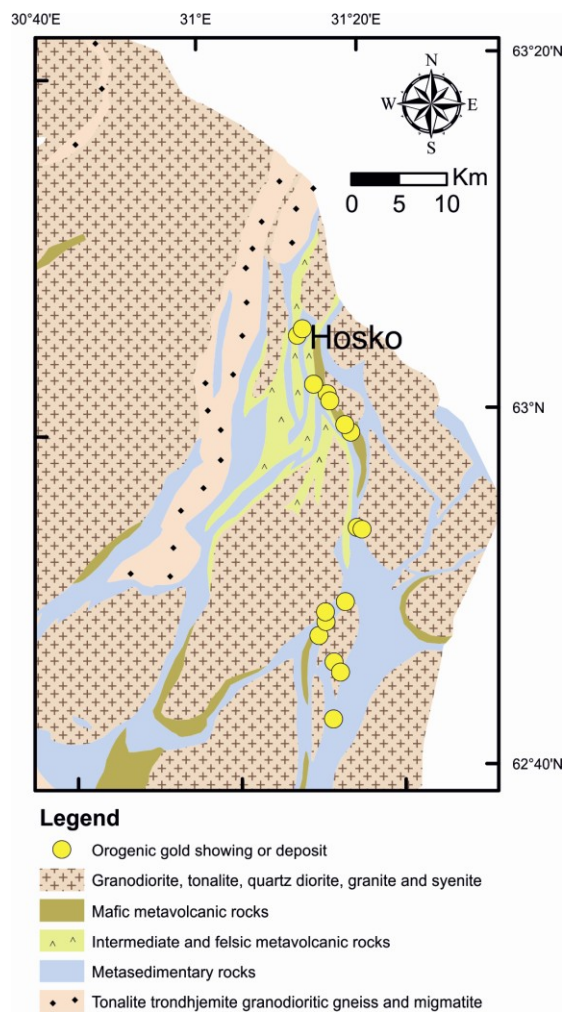


Figure 1. Bedrock map after Korsmann et al., (1997) showing the known gold showings or deposits classified as orogenic in origin (Eilu et al., 2012) and forming Karelian gold line.

2 Geological background of the Archaean Hattu Schist belt

The Hattu schist belt is composed of abundant metasedimentary rocks including mica schists, volcanoclastic schists, conglomerates and banded iron formations. These rocks are intercalated with metavolcanic rocks that include metabasalts locally showing pillow lava structures, metakomatiites and andesitic pyroclastic rocks (Fig 1). Felsic porphyry dikes locally intrude the metasedimentary-metavolcanic sequence. Zircon U-Pb ages from a greywacke sample

together with crosscutting relationships place sedimentation at ca 2.75 Ga, which is somewhat coeval with the volcanic rocks from the belt (Huhma et al., 2012). Also, the adjacent plutonic rocks surrounding the Hattu schist belt have fairly similar reported ages. A U-Pb concordia age of 2741 ± 9 Ma from the Kuittila pluton (Heilimo et al., 2011), earlier dated by U-Pb TIMS at 2745 ± 10 Ma by Vaasjoki et al., 1993, is among the oldest crystallisation ages known from the area. However, zircon xenocrysts with an age of ca. 3.3 Ga are also known from some of the plutonic rocks (Sorjonen-Ward and Claoué-Long, 1993). Monazite and titanate U-Pb ages with ca. 2.7 Ga have been related to metamorphism and this is considered to post-date at least some of the mineralisation events at the Hattu schist belt (Vaasjoki et al., 1993). A Paleoproterozoic tectonothermal event at around 1.9-1.8 Ga is evidenced by K-Ar ages of biotite and hornblende (Kontinen et al., 1992), and this event is also considered to have significance in terms of gold mineralisation (Poutiainen and Partamies 2003).

3 Description of the Hosko deposit

The host rock for the Hosko gold deposit is a fine-grained and equi-granular metapelitic schist that is mainly composed by plagioclase, quartz, muscovite, biotite and ilmenite as main minerals. Primary sedimentary features such as layering and lamination are well preserved in places. Garnet porphyroblasts are locally present and occurrence of sillimanite is also reported by Mustajärvi (1999). In the studied outcrop, a leucocratic 20 cm thick muscovite-garnet pegmatite vein that is concordant with bedding is also observed.

The gold is associated predominantly with the stratabound medium- to fine-grained quartz±feldspar vein units generally having N-S orientation (Fig 2). The veins units are typically bedding-parallel and they often contain sub-angular to plastically deformed and folded pieces of the tourmaline-bearing host rock. In some instances, angular fragments of fine-grained tourmaline rocks are also present in the veins units. The contacts to the hosting metasedimentary rocks are often sharp.

The vein system together with the fine-grained tourmalinised host rock form structurally complex units. Where the ductile deformation is the most advanced the internal structure of the vein-complexes resembles schollen migmatite. The most intensive ductile deformation seems sometimes to have concentrated in the central parts of the vein complexes. Formation of the veins has taken place in several stages as some veinlets seems to crosscut each other (Fig 3). Some of the veins are boudinaged (Fig 4a). Fine-grained and thin tourmaline bands that are parallel to sedimentary layering are also observed within metasedimentary host rock. Their thickness varies from few mm up to few cm.

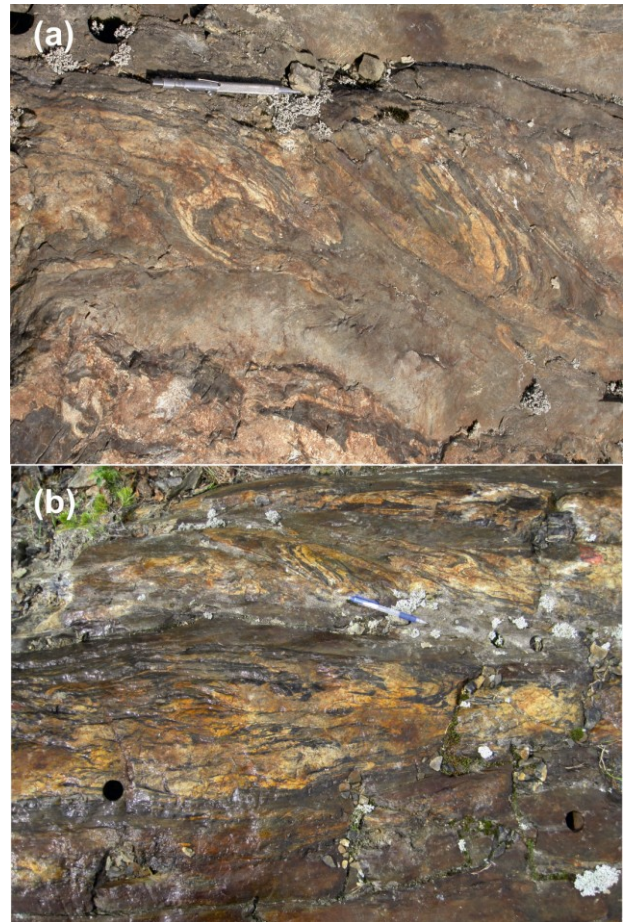


Figure 2. (a) Folded and intensely deformed quartz-feldspar vein unit with several generations of veins hosted by a metapelitic schist from the the Hosko deposit. (b) The darkest material within the leucocratic vein material consists mostly on fine-grained tourmaline.

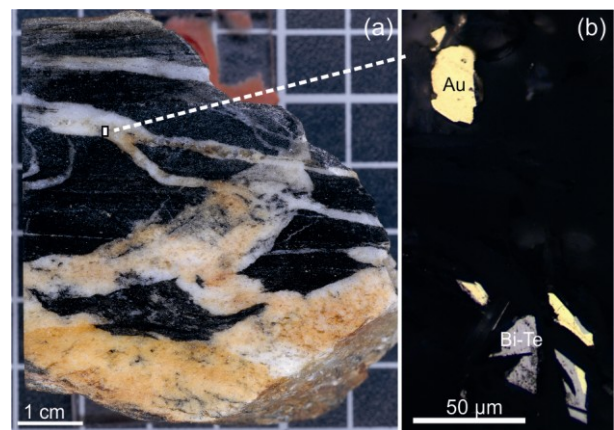


Figure 3. (a) A gold-bearing sample showing leucocratic quartz-feldspar veins crosscutting extensively tourmalinised host rock from the Hosko deposit. (b) Plane polarised microscope image shows the gold grains (yellow) also occur together with tellurobismuthite (grey grains) in the cross-cutting late veinlet. Site of the photo is indicated by white square.

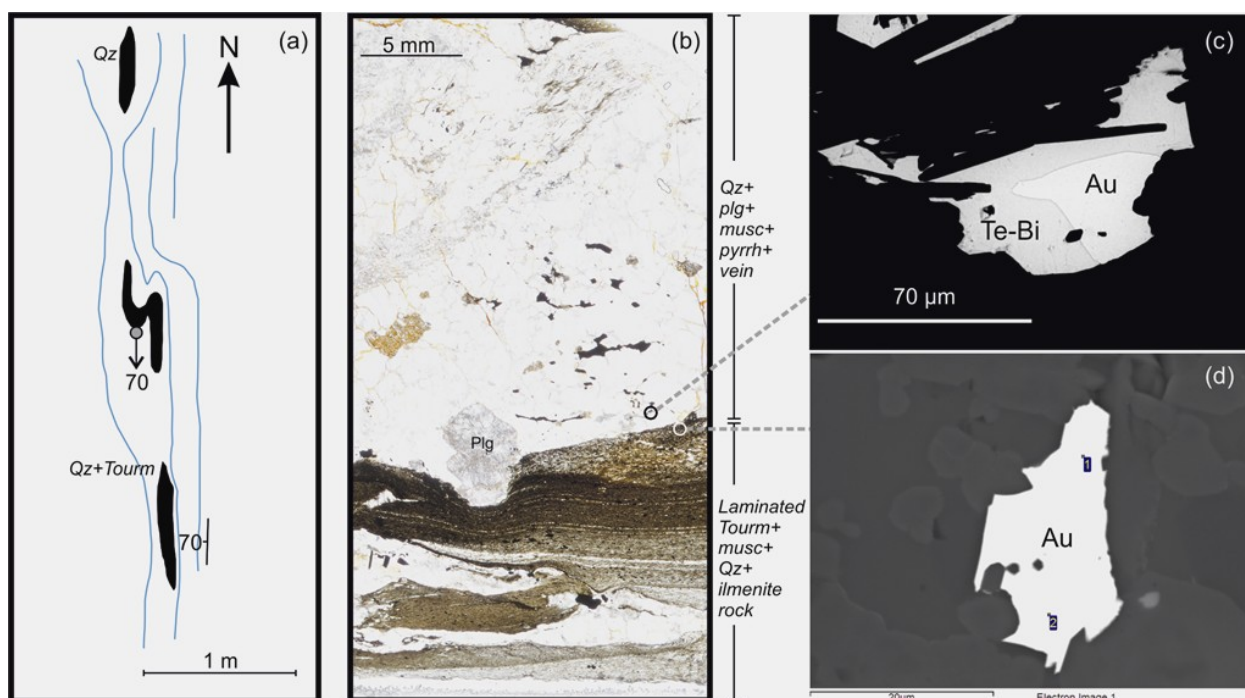


Figure 4. (a) A detailed map showing boudinaged and folded quartz- and tourmaline-bearing vein within a greywacke from the studied outcrop from the Hosko deposit. (b) A gold-bearing thin section showing a quartz dominated vein with a sharp contact to layered and pervasively tourmalinised fine grained rock unit. The specimen contains gold grains both in the (c) quartz vein and (d) within the tourmalinised rock.

Locally, the tourmalinised gold bearing units reveal internal structures resembling sedimentary layering and rhythmic lamination (Fig 4b). At microscopic scale, the lamination is caused by proportional variation of very fine-grained quartz+feldspar dominating laminas and tourmaline-rich laminas. Often quartz-feldspar veins seem to crosscut these laminar features (Fig 4b).

The gold grains are typically observed in the veins or in the tourmalinised wall rock next to veins (Fig 4 c and d). The veins also contain variable amounts of sulphides; typically anhedral pyrrhotite that is locally associated with anhedral chalcopyrite. The pyrrhotite is partially replaced by euhedral arsenopyrite. Some parts of the veins are dominated by euhedral arsenopyrite that contains gold inclusions. In some instances the gold and telluride inclusions occur next to small vugs of arsenopyrite.

The gold grains often are paired with euhedral tellurobismuthite or located close to them (Figs 3b and 4c). Gold together with Te-Bi minerals can be seen both in quartz-feldspar veins (and their tourmalinised host rock) and as inclusions within arsenopyrite. Some of veins or thin veinlets contain minor amount of scheelite grains, which are often located along the contact zones.

4 Preliminary insight to mineralisation genesis

Occurrences of gold grains are restricted to the quartz-feldspar veins that are hosted by the extensively tourmalinised fine-grained metasedimentary units. The tourmalinisation is also the dominant alteration surrounding the veins, but sericite is also present in the host rocks. Therefore, it is proposed that the hydrothermal event causing the quartz-feldspar veins in Hosko deposit is related to same hydrothermal event causing tourmalinisation and sericitisation of the host rock.

The layered and laminar texture of the fine-grained tourmalinised rocks associated with gold-bearing vein units closely resembles those of the unmineralised sedimentary rocks. In this study it is considered that such a small scale features are a result of tourmalinisation of the laminar host-rock. This tourmalinisation event is interpreted to be closely related to the hydrothermal event that produced the gold-bearing quartz feldspar veins.

The relationship between the ductile deformation and generation of the auriferous quartz-feldspar veins is not straightforward. Some of the veins are boudinaged and therefore clearly predating the intensive ductile deformation. The complex internal structures within the veins sometimes give, however, an impression that ductile deformation may have been taking place simultaneously with the vein generation. Some of the

garnets in the host rocks show "snow ball" structures indicative of synmetamorphic deformation.

Based on field observations and microscopic observations the sedimentary host rock underwent a hydrothermal event that caused tourmaline alteration in the host rock and emplacement of emplacement of banding parallel or crosscutting Au-Bi-Te-As-(W) bearing quartz±feldspar -vein units. These mineralised rocks were then deformed and metamorphosed.

Sedimentary rock hosted gold-bearing veins with above mentioned metallogeny together with associated tourmaline alteration of the host rock resembles to some of the deposits classified as "turbidite hosted gold deposits" (e.g. Boyle, 1986). It is therefore proposed that Hosko deposit is an Archaean example of those deposits. The zircons separated from the host rock from the Hosko deposit are currently on the way to U-Pb SIMS study and they are expected to set new age new constraints to gold bearing veins in near future.

Acknowledgements

Iain Pitcairn is warmly thanked for comments and suggestions that improved this abstract.

References

- Boyle, R.W. (1986) Gold deposits in turbidite sequences: Their geology, geochemistry and history of the theories of their origin, in Keppie, J.D., Boyle, R.W., Haynes, S.J., (Eds.), *Turbidite-hosted Gold Deposits*, Geological Association of Canada, Special Paper 32, pages 1-14.
- Endomines (2013) <http://www.endomines.com/hosko.php> (web page 5th of Jan, 2013)
- Eilu, P., Ahtola, T., Äikäs, O., Halkoaho, T., Heikura, P., Hulkki, H., Iljina, M., Juopperi, H., Karinen, T., Kärkkäinen, N., Konnunaho, J., Kontinen, A., Kontoniemi, O., Korhikoski, E., Korsakova, M., Kuivasaari, T., Kyläkoski, M., Makkonen, H., Niiränen, T., Nikander, J., Nykänen, V., Perdahl, J.-A., Pohjolainen, E., Räsänen, J., Sorjonen-Ward, P., Tiainen, M., Tontti, M., Torppa, A. & Västi, K. (2012) Metallogenic areas in Finland. Geological Survey of Finland, Special Paper 53, 207–342.
- Heilimo, E., Halla, J. & Huhma, H. (2011) Single-grain zircon U-Pb age constraints of the western and eastern sanukitoid zones in the Finnish part of the Karelian Province. *Lithos* 121, 87–99
- Huhma, H., Mänttari, I., Peltonen, P., Kontinen, A., Halkoaho, T., Hanski, E., Hokkanen, T., Hölttä, P., Juopperi, H., Konnunaho, J., Layahe, Y., Luukkonen, E., Pietikäinen, K., Pulkkinen, A., Sorjonen-Ward, P., Vaasjoki, M. & Whitehouse, M. (2012) The age of the Archaean greenstone belts in Finland. Geological Survey of Finland, Special Paper 54, 74–175.
- Kontinen, A., Paavola, J., Lukkarinen, H., 1992. K-Ar ages of hornblende and biotite from Late Archaean rocks of eastern Finland - interpretation and discussion of tectonic implications. *Geological Survey of Finland Bulletin*, vol. 365 pp.
- Poutiainen, M. Partamies, S (2003) Fluid evolution of the late Archaean Rämepuro gold deposit in the Ilomantsi greenstone belt in eastern Finland
- Mustajärvi, J. (1999) Ilomantsin Hoskon kultamineralisaation ja sen rakennegeologinen kontrolli. Unpublished MSc thesis. Department of Geology, University of Helsinki. 33 p. (in Finnish).
- Sorjonen-Ward, P. & Claoué-Long, J. 1993. Preliminary note on ion probe results for zircons from the Silvevaara granodiorite, Ilomantsi, eastern Finland. In: Autio, S. (ed.) *Geological Survey of Finland, Current Research 1991–1992*. Geological Survey of Finland, Special Paper 18, 25–29.
- Vaasjoki, M., Sorjonen-Ward, P. & Lavikainen, S. 1993. U-Pb age

determinations and sulfide Pb-Pb characteristics from the late Archaean Hattu schist belt, Ilomantsi, eastern Finland. In: Nurmi, P. & Sorjonen-Ward, P. (eds.) *Geological development, gold mineralization and exploration methods in the late Archaean Hattu schist belt, Ilomantsi, eastern Finland*. Geological Survey of Finland. Special Paper 17, 103–131.

Hypozonal orogenic gold deposits: are they a myth?

Jochen Kolb

Department of Petrology and Economic Geology, Geological Survey of Denmark and Greenland, ØsterVoldgade 10, 1350 Copenhagen K, Denmark, jkol@geus.dk

Annika Dziggel, F. Michael Meyer

Institute of Mineralogy and Economic Geology, RWTH Aachen University, Wüllnerstrasse 2, 52062 Aachen, Germany

Abstract. In recent years, the existence of hypozonal orogenic gold deposits has been questioned, mainly because of the evidence for recrystallization and partial melting in some deposits formed at high-T metamorphic grades. We present four examples of hypozonal gold deposits that contradict the generalization of this hypothesis. Our main arguments are: (1) the hypozonal alteration assemblages replace high-T metamorphic mineral assemblages; (2) no leucosomes are developed in the ore; (3) gold is hosted in young structures; (4) the alteration minerals define young structures and lack static recrystallization fabrics. Some hypozonal deposits formed in collisional orogens or significantly after accretion and are, thus, situated in different settings compared to the mesozonal counterparts. Exploration for these deposits should focus on such terranes, where the geothermal gradient was inverted or increased during the structural evolution.

Keywords. Hydrothermal Alteration, Metamorphism, Continuum, Gold

1 Introduction

Orogenic gold deposits are characterized by their structurally controlled deposit location and their similar alteration (Si, K, Rb, Ba, Li, Cs, Tl, S, H₂O, CO₂ enrichment) and ore (Au-Ag ± As, Sb, Te, W, Mo, Bi) chemistries (e.g.; McCuaig and Kerrich, 1998). They are characterized by different hydrothermal alteration assemblages that reflect different PT conditions of formation. This observation led to the classification into different groups (epizonal, mesozonal and hypozonal), in which the high-temperature group was named hypozonal (Gebre-Mariam et al., 1995). A clear definition of this group is, however, lacking and different PT-depth parameters are discussed, with a lower limit at 475-550°C, 3 kbar and depth > 10-12 km, and an upper limit of < 700-740°C and 5-6 kbar (Gebre-Mariam et al., 1995; McCuaig and Kerrich, 1998; Phillips and Powell, 2009; Ridley et al., 2000). The comparison between PT conditions of mineralization and alteration and regional pressure-temperature-deformation (PTD) paths shows that the gold mineralization formed syn- to late-peak metamorphism and late in the structural evolution of the host terrane (Ridley et al., 2000). A problem in establishing relative timing of metamorphism and hydrothermal alteration is the textural equilibrium between alteration and metamorphic mineral assemblages generally observed in the hypozonal deposits.

In addition, “hypozonal” mineral assemblages in deposits such as Griffins Find, Challenger and Hemlo

have recently been shown to having formed by metamorphic recrystallization of pre-existing hydrothermal alteration assemblages (e.g.; Tomkins and Grundy, 2009). The typical maximum temperature for the formation of orogenic gold deposits was defined at ≤ 600-650°C, which is in conflict with the upper T limit given above, and used to restrict orogenic gold deposits to the epizonal and mesozonal temperature range (Tomkins and Grundy, 2009).

In this paper, we summarize data from four gold deposits studied by the authors in order to provide constraints on the PT limit of hypozonal gold mineralization, to give evidence for the peak- or postpeak-metamorphic nature, and to discuss the tectonometamorphic terrane evolution.

2 Lode gold mineralization at temperatures > 475°C

2.1 Hypozonal orogenic gold deposits

Hypozonal orogenic gold deposits are hosted in ductile shear zone systems in a variety of rock types ranging from (ultra)mafic meta-volcanic, meta-sedimentary to granitic (McCuaig and Kerrich, 1998; Ridley et al., 2000). The shear zones are commonly located at lithological contacts, and the orebodies form lenticular structures within the shear zones, or are hosted in fold hinges and disseminated or as stockwork in competent lithologies (Ridley et al., 2000). Commonly, the gold deposits are spatially associated with felsic intrusions. The hydrothermal alteration assemblages are grouped into: (1) an amphibole class (+ biotite, plagioclase, quartz); (2) a diopside class (+ biotite, amphibole, quartz, garnet); and a microcline-muscovite-andalusite class (+ quartz) (McCuaig and Kerrich, 1998; Ridley et al., 2000). Quartz veins commonly have mono- or biminerally, < 1 cm thick selvages of a characteristic alteration mineral. Typical ore assemblages in textural equilibrium with alteration minerals are (1) pyrrhotite, (2) pyrrhotite-arsenopyrite±pyrite, (3) pyrrhotite-arsenopyrite-löllingite, and (4) pyrrhotite-pyrite-chalcopyrite (Ridley et al., 2000).

Sulfur and Te are significantly enriched in hypozonal deposits, whereas CO₂ and Au/S ratios are lower than in mesozonal deposits. Commonly, the alteration halos are enriched in K or Ca and depleted in Na (McCuaig and Kerrich, 1998; Ridley et al., 2000). The general geochemical signal of the deposits is, however, not significantly different from the typical mesozonal ores.

2.2 Prepeak-metamorphic gold deposits

This group of gold deposits was first defined by Hamilton and Hodgson (1986); and Phillips (1985). In general, pre-peak metamorphic gold deposits share a lot of characteristics with those described above, but show (1) evidence for desulfidation and decarbonation, (2) leucosomes associated with the ores, (3) deformed quartz veins and orebodies and (4) granoblastic quartz fabrics in the veins (Phillips and Powell, 2009). Well-rounded to subspherical inclusions of various sulfides and gold in textural equilibrium in the ores are interpreted to reflect a crystallized polymetallic sulfide melt or the recrystallization of an earlier-formed sulfide-gold ore assemblage (Tomkins and Grundy, 2009). The commonly observed composite grains of pyrrhotite-arsenopyrite-löllingite-gold indicate a complex metamorphic history of prograde and later retrograde reactions at approximately 700°C (Tomkins and Grundy, 2009). Unusual host rock compositions that are Fe-deficient and K-, Al- and Mg-rich with cordierite-sillimanite-garnet assemblages may indicate prograde metamorphism of hydrothermally altered rocks, where Fe-bearing sulfides sequestered the Fe from the silicate assemblage (Tomkins and Grundy, 2009). However, the idea developed by Tomkins and Grundy (2009) and Phillips and Powell (2009) that all hypozonal orogenic gold deposits represent prepeak-metamorphic gold deposits contradicts many observations of mineral fabrics, textures and the regional geological evolution of host terranes.

3 Examples of hypozonal orogenic gold deposits

3.1 New Consort (South Africa)

The New Consort gold mine is situated at the northern margin of the Palaeo- to Mesoarchean Barberton Greenstone Belt, South Africa. The mine is located in the immediate hanging wall of an exhumed gneiss dome, where it is hosted by narrow shear zones at, or close to the contact, between the mafic to ultramafic metavolcanic rocks of the Onverwacht Group and metasedimentary rocks of the Fig Tree Group (Otto et al., 2007). The Onverwacht Group rocks in the footwall mainly record conditions of 600-700°C and 5 ± 1 kbar, followed by isothermal decompression to ca. 500-650°C and 1-3 kbar (Dziggel et al., 2006). Locally, peak conditions of 600-700°C and 6-8 kbar have been observed (Otto et al., 2007).

The main stage of gold mineralization is associated with quartz veins and semi-massive sulfide lenses within discrete mylonitic shear zones (Otto et al., 2007). The shear zones have been intruded by syn-kinematic pegmatite dykes. A clinopyroxene-hornblende-pyrrhotite-löllingite ± garnet, K-feldspar, quartz, biotite, calcite alteration assemblage defines an early high-T (645-715°C) mineralization that is restricted to the Onverwacht Group. A second stage of alteration, with the assemblage muscovite-K-feldspar-quartz ± plagioclase, hornblende, biotite, tourmaline, calcite,

titanite, yields temperatures between 520°C and 600°C with temperatures increasing with structural depth. The main stage of gold mineralization has been dated at ca. 3040-3030 Ma (Dziggel et al., 2010). It was broadly syn-peak metamorphic with respect to the Fig Tree Group, but postdates the metamorphic peak in the structurally underlying Onverwacht Group by up to 200 m. y. The mineralizing fluids, thus, must have been derived from an external source.

The greenstone belt may have formed in a contractional continental back-arc setting at ca. 3100 Ma, which then was in changing extensional and compressional settings during metamorphism and mineralization along with accretionary tectonics in the periphery (Dziggel et al., 2007).

3.2 Renco (Zimbabwe)

The Renco gold mine is situated in the granulite facies Limpopo Belt approximately 5 km south of the contact with the Zimbabwe Craton, the North Limpopo Thrust Zone (NLTZ; Blenkinsop and Frei, 1996). The host rock enderbite was emplaced into a Neoproterozoic granulite basement (Blenkinsop and Frei, 1996). Peak metamorphic conditions in the enderbite are estimated at 730-750°C and 6-7.8 kbar (Kolb and Meyer, 2002). Retrogression occurred at 600-680°C and 4-6.5 kbar and in the greenschist facies (Rollinson, 1989).

The gold mineralization is disseminated in mylonites and breccias, and hosted in a complex, higher-order shear zone system in the hanging wall of the NLTZ (Kolb et al., 2000). Also syn-kinematic pegmatites are gold mineralized. The garnet-biotite-K-feldspar-quartz-pyrrhotite-chalcopyrite ± siderite, amphibole alteration assemblage replaced the peak metamorphic assemblage in the auriferous shear zones. The PT conditions were estimated at 610-710°C and approx. 4 kbar (Kolb et al., 2000). P-T conditions of gold mineralization overlap with regional conditions of retrogression and also show local retrogression in the greenschist facies.

Hydrothermal fluids (H₂O-NaCl-CO₂-CH₄-N₂) were externally derived as indicated by their enriched oxygen ($\delta^{18}\text{O} = 9\text{‰}$) and strontium isotope signature compared to the wall rock, possibly by devolatilization of metasedimentary rocks (Blenkinsop and Frei, 1996; Kolb et al., 2000).

The host rock enderbite intruded into lower crust at 2571 ± 5 Ma, which was at granulite facies grades from ca. 2720 Ma. Exhumation and shearing in the amphibolite facies on top of the Zimbabwe Craton occurred in a collisional orogen ca. 40 m.y. after intrusion. Late-tectonic granites postdate gold mineralization (Blenkinsop, 2004).

3.3 Hutti and Hira Buddini (India)

The Hutti and Hira Buddini gold mines are situated in the Neoproterozoic Hutti-Maski Greenstone Belt in amphibolites and narrow felsic metavolcanic units that record peak metamorphic conditions of 660 ± 40°C and 4 ± 1 kbar. Retrogression occurred at 530 ± 20/-30°C and 3 kbar and in the greenschist facies (Rogers et al., 2007).

The gold mineralization is disseminated or in quartz veins, which are hosted in NNW- and ENE-trending shear zones (Krienitz et al., 2008; Rogers et al., 2013). The biotite-plagioclase-calcite-pyrite-arsenopyrite \pm K-feldspar, actinolite, tourmaline alteration assemblage replaced the peak metamorphic assemblage in the auriferous shear zones. Pseudosection modelling indicates P-T conditions of 460-510 °C and 3 kbar, whereas conditions of 510-590°C are estimated from fluid inclusions and mineral fabrics (Kolb and Meyer, 2008; Krienitz et al., 2008). P-T conditions of gold mineralization overlap with regional conditions of retrogression.

Hydrothermal fluids (H₂O-NaCl-CO₂-CH₄) were derived from metamorphic devolatilization as indicated by oxygen and hydrogen isotope signatures ($\delta^{18}\text{O} = 7.5\text{-}10.1\text{‰}$; $\delta\text{D} = -23$ to -29‰). Boron isotopes in tourmaline of $\delta^{11}\text{B}$ between -3‰ and $+6\text{‰}$ indicate both metamorphic and juvenile magmatic ore fluid sources and local mixing in the deposits (Krienitz et al., 2008; Rogers et al., 2013).

The greenstone belt probably formed in an island-arc setting at ca. 2590 Ma and was subsequently metamorphosed to amphibolite facies grades caused by crustal thickening in an accretionary setting. Retrograde shearing in a NW-SE compression setting and contemporaneous I-type intrusions at ca. 2545 Ma indicate terrane exhumation in a still active subduction setting contemporaneous with hypozonal orogenic gold mineralization. Subsequent exhumation and the intrusion of post-tectonic granitoids caused a second stage of mesozonal orogenic gold mineralization ca. 10 m.y. after the hypozonal event (Rogers et al., 2013).

3.4 Navachab (Namibia)

The Navachab gold mine is situated in the Southern Central Zone of the Pan-African Damara Orogen, Namibia. Peak metamorphic conditions vary between approx. 550°C and 2 kbar and approx. 750°C and 5 kbar (Dziggel et al., 2009).

The gold mineralization is disseminated in breccias and sheeted quartz veins on the steep limb of an anticlinal dome structure, which is developed on top of a blind NW-vergent thrust (Wulff et al., 2010). The garnet-biotite-clinopyroxene-quartz-pyrrhotite-chalcopyrite-sphalerite-arsenopyrite \pm K-feldspar, actinolite alteration assemblage replaced the peak metamorphic assemblage in the wall rocks (Wulff et al., 2010). The PT conditions were estimated at $550 \pm 50^\circ\text{C}$ and approx. 2 kbar (Dziggel et al., 2009). P-T conditions of gold mineralization overlap with regional peak metamorphic conditions.

Hydrothermal fluids (H₂O-NaCl-CaCl₂-CO₂) have a metamorphic stable isotope signature ($\delta^{18}\text{O} = 12\text{-}14\text{‰}$; $\delta\text{D} = -40$ to -60‰) and were derived from metapelites at deeper levels that underwent prograde metamorphism (Wulff et al., 2010).

The Southern Central Zone is a typical low-P, high-T arc-like terrane, and forms the core of the Damara Orogen (Dziggel et al., 2009). Peak metamorphism was reached at ca. 550 Ma during tectonic collision, which was followed by post-collisional re-heating and related

late- to post tectonic granite emplacement 25-80 m.y. after the metamorphic peak.

4 Discussion

The critical factor for gold mineralization in high-metamorphic terranes is the relative timing of hydrothermal alteration and peak metamorphism. High water activity during hypozonal hydrothermal alteration will cause anatexis of felsic wall rocks at approx. 650-700°C and mafic wall rocks at approx. 800-850°C, which will limit the effect of hydrothermal mineralization to below these temperatures. This was taken as the main argument to state that synpeak-metamorphic mineralization in high-grade terranes is unlikely and that prepeak-metamorphic mineralization under mesozonal conditions was the norm (Phillips and Powell, 2009; Tomkins and Grundy, 2009).

The four examples shown here demonstrate clear evidence for synpeak-metamorphic to retrograde hypozonal hydrothermal gold mineralization:

- Alteration assemblages replaced peak-metamorphic mineral assemblages
- Orebodies are hosted in retrograde structures; alteration minerals are in textural equilibrium with gold and define the fabrics
- Host rocks are younger than metamorphic peak (Renco)
- Syn-metamorphic and -tectonic pegmatites crosscut the orebody but are also gold mineralized in places

Renco and New Consort record the highest PT conditions for gold mineralization of $\leq 715^\circ\text{C}$, which is below the host rocks wet solidus (enderbite: 700°C; amphibolite: 800-850°C). In both mines, pegmatites are widespread, and those at Renco are also mineralized. However, the high-T alteration assemblages show no evidence of partial melting, indicating alteration at conditions below the solidus. Hypozonal hydrothermal alteration is, therefore, likely restricted to temperatures $< 650\text{-}850^\circ\text{C}$, depending on host rock composition.

The PT evolution of the host terrane largely defines the tectonic scenario of hypozonal gold mineralization but also shows possible fluid sources at depth. For syn- to postpeak-metamorphic gold deposits, the model of deep-later metamorphism was developed, where the metamorphic peak is reached later at depth either due to crustal thickening or heating from below and denudation at the surface, possibly expelling fluids during prograde metamorphism (Stüwe, 1998). Such a setting is supported by the granites and pegmatites that were emplaced syn-peak or retrograde, which could be derived from prograde anatexis at depth. In several hypozonal deposits the isotopic fluid signature indicates an external fluid source or the involvement of a magmatic fluid. These deposits show a terrane evolution characterized by tectonics that invert the metamorphic gradient by thrust imbrication (Renco) or generate a steep metamorphic gradient by extensional shearing (New Consort). The shearing is an effective mechanism to create major pathways for different types of externally derived fluids. Juxtaposition of units with

different metamorphic histories is also efficient in causing prograde metamorphic dehydration in buried lower metamorphic units. This means that auriferous fluids may form by metamorphic devolatilization at considerably lower temperatures (e.g.; greenschist-amphibolite facies transition) than the hypozonal conditions of gold mineralization. Such a dynamic setting is regarded critical for the formation of hypozonal gold deposits, where fluids are derived from prograde metamorphism and contemporaneous magmatism in an evolving orogen.

The geodynamic setting of the terranes hosting the hypozonal deposits varies. Hutti is situated between the accretionary wedge and an arc in the central transpression zone of an accretionary orogen, whereas Renco and Navachab are situated in major shear zones or dome structures of the foreland and the center of a collision orogen. New Consort is situated in an extensional setting that followed accretionary orogeny.

Contemporaneous I-type granite emplacement and hypozonal gold mineralization at Hutti suggest a still active oceanic subduction régime, whereas Renco, New Consort and Navachab likely formed later in the syn-collisional stage of their orogens. Hutti belongs to the amphibole-class deposits that formed in a setting similar to mesozonal gold ores but may represent a deeper equivalent. Renco, Navachab and New Consort formed in a different setting, which is important for the exploration of this type of hypozonal gold deposits. The geodynamic setting appears not to be the critical factor for hypozonal orogenic gold mineralization. The more important factors are the regional PTD evolution, the presence of suitable host and source rocks, as well as pathways for the mineralizing fluids.

Acknowledgements

The authors would like to thank the Deutsche Forschungsgemeinschaft for financing.

References

- Blenkinsop, T.G., 2004. Orebody geometry in lode gold deposits from Zimbabwe: implications for fluid flow, deformation and mineralization. *Journal of Structural Geology*, 26: 1293-1301.
- Blenkinsop, T.G. and Frei, R., 1996. Archean and Proterozoic mineralization and tectonics at the Renco mine (Northern Marginal Zone, Limpopo Belt, Zimbabwe). *Economic Geology*, 91: 1225-1238.
- Dziggel, A., Knipfer, S., Kisters, A.F.M. and Meyer, F.M., 2006. P-T and structural evolution during exhumation of high-T, medium-P basement rocks in the Barberton Mountain Land, South Africa. *Journal of Metamorphic Geology*, 24: 535-551.
- Dziggel, A., Otto, A., Kisters, A.F.M. and Meyer, F.M., 2007. Tectono-metamorphic controls on Archean gold mineralization in the Barberton greenstone belt, South Africa: an example from the New Consort gold mine. In: M.J. van Kranendonk, R.H. Smithies and V. Bennet (Editors), *Earth's oldest Rocks. Developments in Precambrian Geology*. Elsevier, Amsterdam.
- Dziggel, A., Poujol, M., Otto, A., Kisters, A.F.M., Trieloff, M., Schwarz, W. and Meyer, F.M., 2010. New U-Pb and $^{40}\text{Ar}/^{39}\text{Ar}$ ages from the northern part of the Barberton greenstone belt, South Africa: implications for the formation of Mesoarchean gold deposits. *Precambrian Research*, 179: 206-220.
- Dziggel, A., Wulff, K., Kolb, J., Meyer, F.M. and Lahaye, Y., 2009. Significance of oscillatory and bell-shaped growth zoning in hydrothermal garnet: evidence from the Navachab gold deposit, Namibia. *Chemical Geology*, 262: 278-292.
- Gebre-Mariam, M., Hagemann, S.G. and Groves, D.I., 1995. A classification scheme for epigenetic Archean lode-gold deposits. *Mineralium Deposita*, 30: 408-410.
- Hamilton, J.V. and Hodgson, C.J., 1986. Mineralization and structure of the Kolar gold field, India. In: A.J. Macdonald (Editor), *Proceedings of the Gold '86 Symposium, An International Symposium on the Geology of Gold*, Toronto, pp. 270-283.
- Kolb, J., Kisters, A.F.M., Hoernes, S. and Meyer, F.M., 2000. The origin of fluids and nature of fluid-rock interaction in auriferous mylonites of the Renco Mine, southern Zimbabwe. *Mineralium Deposita*, 35(1): 109-125.
- Kolb, J. and Meyer, F.M., 2002. Fluid inclusion record of the hypozonal orogenic Renco gold deposit (Zimbabwe) during the retrograde P-T evolution. *Contributions to Mineralogy and Petrology*, 143: 495-509.
- Kolb, J. and Meyer, F.M., 2008. Balanced mineral reactions for alteration zones developed in auriferous shear zones of the Hutti Mine, Dharwar craton, India. *Zeitschrift der Deutschen Gesellschaft für Geowissenschaften (ZDGG)*, 159(2): 331-348.
- Krienitz, M.-S., Trumbull, R.B., Hellmann, A., Kolb, J., Meyer, F.M. and Wiedenbeck, M., 2008. Hydrothermal gold mineralization at the Hira Buddini gold mine, India: constraints on fluid evolution and fluid sources from boron isotopic compositions of tourmaline. *Mineralium Deposita*, 43: 421-434.
- McCuaig, T.C. and Kerrich, R., 1998. P-T-t deformation fluid characteristics of lode-gold deposits: evidence from alteration systematics. *Ore Geology Reviews*, 12: 381-453.
- Otto, A., Dziggel, A., Kisters, A.F.M. and Meyer, F.M., 2007. The New Consort gold mine, Barberton greenstone belt, South Africa: Orogenic gold mineralization in a condensed metamorphic profile. *Mineralium Deposita*.
- Phillips, G.N., 1985. Interpretation of Big Bell/Hemlo-type gold deposits: Precursors, metamorphism, melting, and genetic constraints. *Geological Society of South Africa Transactions*, 88: 159-173.
- Phillips, G.N. and Powell, R., 2009. Formation of gold deposits: Review and evaluation of the continuum model. *Earth-Science Reviews*, 94: 1-21.
- Ridley, J.R., Groves, D.I. and Knight, J.T., 2000. Gold deposits in amphibolite and granulite facies terranes of the Archean Yilgarn craton, Western Australia: Evidence and implications of synmetamorphic mineralization. *Reviews in Economic Geology*, 11: 265-290.
- Rogers, A.J., Kolb, J., Meyer, F.M. and Armstrong, R.A., 2007. Tectono-magmatic evolution of the Hutti-Maski Greenstone Belt, India: Constrained using geochemical and geochronological data. *Journal of Asian Earth Sciences*, 31(1): 55-70.
- Rogers, A.J., Kolb, J., Meyer, F.M. and Vennemann, T.W., 2013. Two stages of gold mineralization at Hutti mine, India. *Mineralium Deposita*, 48: 99-114.
- Rollinson, H.R., 1989. Garnet-orthopyroxene thermobarometry of granulites from the north marginal zone of the Limpopo Belt, Zimbabwe. In: J.S. Daly, R.A. Cliff and B.W.D. Yardley (Editors), *Evolution of metamorphic belts*. Geological Society of London Special Publication, pp. 331-335.
- Stüwe, K., 1998. Tectonic constraints on the timing relationships of metamorphism, fluid production and gold-bearing quartz vein emplacement. *Ore Geology Reviews*, 13(1-5): 219-228.
- Tomkins, A.G. and Grundy, C., 2009. Upper Temperature Limits of Orogenic Gold Deposit Formation: Constraints from the Granulite-Hosted Griffin's Find Deposit, Yilgarn Craton. *Economic Geology*, 104(5): 669-685.
- Wulff, K., Dziggel, A., Kolb, J., Vennemann, T.W., Böttcher, M.E. and Meyer, F.M., 2010. Origin of mineralizing fluids of the sediment-hosted Navachab gold mine, Namibia: constraints from stable (O, H, C, S) isotopes. *Economic Geology*, 105: 285-302.

The Velkua gold prospect in the high metamorphic grade area of south-western Finland

Niilo Kärkkäinen, Asko Käpyaho, Raimo Lahtinen, Tuomo Törmänen
Geological Survey of Finland

Abstract. The Velkua Au prospect is situated in the high metamorphic grade Paleoproterozoic Svecofennian (1.9-1.8 Ga) bedrock of Southwestern Finland. Gold is enriched in an amphibolite formation surrounded by migmatitic mica gneiss (cordierite-garnet-K-feldspar) and coarse grained granites. Regional metamorphism corresponds to upper amphibolite or granulite facies. Gold occurs as native grains associated with silicate minerals and as inclusions and composite grains with sulphides. Larger gold grains are locally zoned, the core being an Ag-Au alloy and the border pure gold. No retrograde features are observed in silicate mineralogy of the host rock.

Keywords

Gold, mineral occurrence, zoned gold grain, Svecofennian, Finland

1 Introduction

The Velkua Au occurrence in the Turku archipelago is situated in the high metamorphic grade Paleoproterozoic Svecofennian bedrock of Southwestern Finland (Fig. 1). Gold is hosted by an amphibolite formation with intercalations of felsic and intermediate gneisses surrounded by migmatitic greywackes. The whole sequence is metamorphosed at upper amphibolite to granulite facies metamorphic conditions. Only minor historical iron ore pits and occurrences of Fe sulphides are previously known in the district. This paper introduces some mineralogical features of the Velkua Au prospect, which is under active exploration by the Geological Survey of Finland (GTK) (Kärkkäinen et al. 2012a).

The first observation of gold occurred in 2006 from a sulphide-rich outcrop during follow-up study of a nationwide lithogeochemical mapping by GTK. Two end-member styles of mineralization have been identified. Higher grade mineralization, up to 24 ppm Au per 1 m section, comprises native gold associated with silicate minerals. In lower grade (0.2–2 ppm Au) zones gold is closely associated with sulphides. Larger gold grains are locally zoned so that the more voluminous core is Ag-Au alloy that is irregularly rimmed by pure gold.

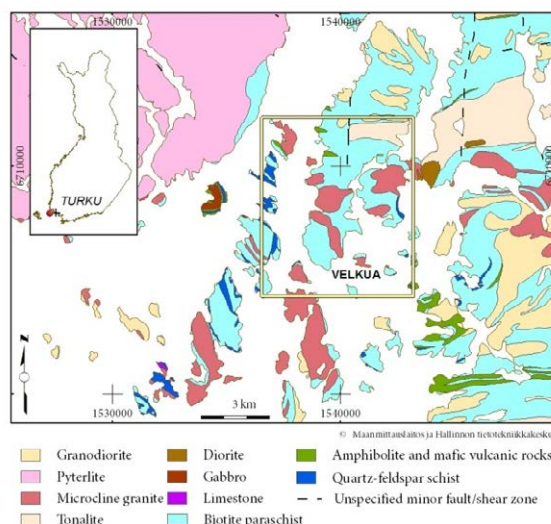


Figure 1. Location of the Velkua area. Bedrock map of Finland is based on DigiKP200 of GTK.

2 The Velkua prospect

2.1 Local geology

The major host rocks of the Velkua Au prospect are amphibolites that are mainly massive, but locally banded, plagioclase porphyric, or containing some leucosome material. There are 1–20-m-thick interlayers of quartz-plagioclase or biotite-plagioclase gneisses and clinopyroxene-bearing gneiss. A network of granite pegmatites intrudes the amphibolites formation.

The amphibolite formation, which can be up to 100 m in thickness, is surrounded by strongly metamorphosed and partly melted metagreywacke with sub-conformable and irregular leucosome veins, bands and lenses. Younger leucosome and pegmatite veins cut the rock in the direction of second phase schistosity. Pelitic layers comprise large garnet aggregates and cordierite porphyroblasts.

The orientation of layering and predominant schistosity is NW-SE and the dip is about 60° SW and is cut by almost east-west-striking second schistosity, in which direction minor pegmatite veins and apophyses intrude. The amphibolite unit is also gently folded.

2.2 Mineralization

Mineralized amphibolite is characterized by narrow quartz and quartz-feldspar veins and small lenses (Fig. 2). There are several parallel 0.5 to 8 m thick zones with disseminated sulphides, and locally scheelite, tourmaline and apatite. The ore minerals in Au-mineralized rocks are pyrrhotite, arsenopyrite, löllingite, ilmenite, chalcopyrite, ilmenomagnetite, native gold, native bismuth and ullmannite. Biotite-plagioclase gneiss interlayers also contain arsenopyrite. Scheelite is observed as individual grains and thin stripes most commonly associated with clinopyroxene. Tourmaline and biotite are most abundant in arsenopyrite-enriched zones.

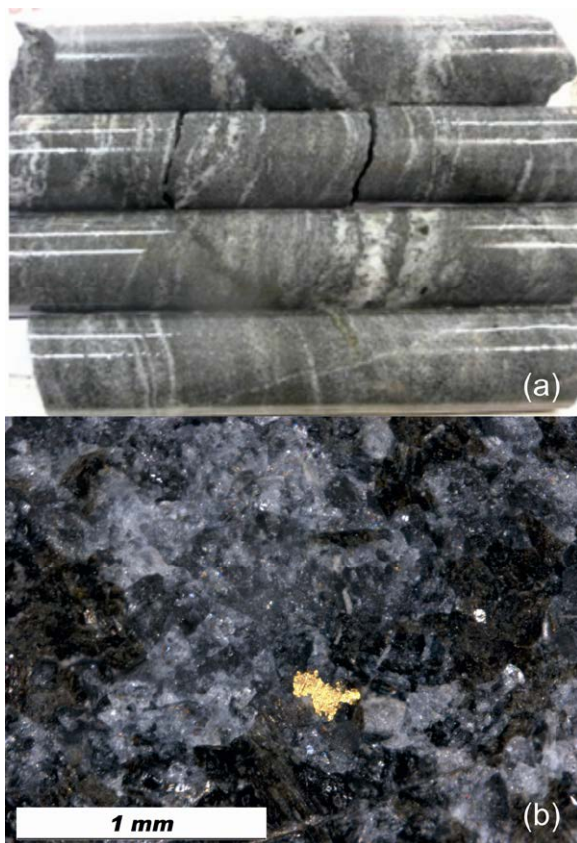


Figure 2. (a) Au-mineralized quartz banded amphibolite from Velkua (24.2 ppm Au, R301 35.25–36.25 m). There are only small amounts of sulphides (arsenopyrite and pyrrhotite) in this section. Light bands are leucosomes and quartz veins. (b) Visible gold grains in this section are associated within in quartz veinlets (figure taken from sawed surface at R301 35.80 m).

Chemical analyses from drill cores indicate elevated gold contents (>100 ppb Au) in a drilling sections up to 30 m long. Clearly Au mineralized rocks (>0.5 ppm) occur in three, 1 to 9 m wide, zones that are separated by barren rock or rock with only slightly elevated Au contents (>20 ppb). The best drill section is 8 m with 5.3 ppm Au including 24.2 ppm at 1 m. Parallel 1 - 4 m sections contain lower grade ore with 0.5 - 2 ppm Au and

between 0.2 and 1.3% As. Gold correlates with arsenic only when the Au values are relatively low.

The rock hosting highest Au grades is similar in appearance to barren rocks (Fig. 2). Characteristic features for both mineralized and barren rocks are thin quartz veins, clusters of quartz and feldspar-quartz veins, patches of coarse-grained clinopyroxene in quartz-feldspar veinlets, biotitization and tourmaline.

2.3 Gold

Gold occurs as discrete grains with silicates and arsenopyrite. The grain size typically varies from 10 µm to 200 µm. Arsenopyrite and löllingite occur locally in small composite grains with gold in silicates. Commonly coarse-grained As sulphides host gold inclusions or in some cases make up a core for enveloping arsenopyrite, or make up a group of minute inclusions within arsenopyrite. Native bismuth is a typical trace mineral with gold.

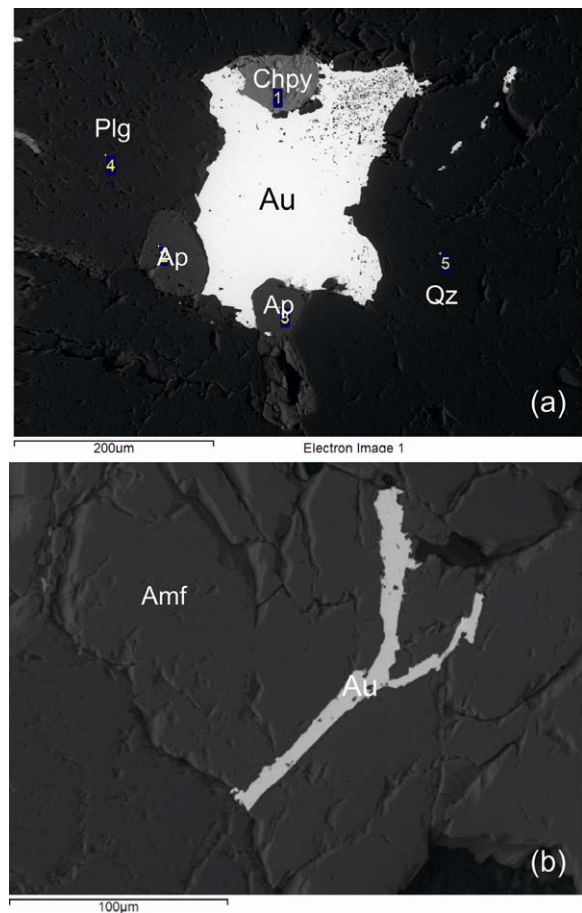


Figure 3. (a) Back scatter electron image on gold grain that is associated with chalcopyrite (Chpy) and apatite (Ap) grains in quartz-plagioclase dominating gneiss sample R308 90.60. (b) Gold is also observed to within the amphibole (Amf) from the same sample.

Gold occurs as inclusions in quartz, plagioclase and hornblende in the high-grade ores (Figs. 3 and 4). The composition and texture of the metamorphosed host rock of the high-grade ore does not differ from the surrounding equigranular barren amphibolite. The gold grains inside silicate minerals commonly are small with a typical grain size of 10–30 μm , but in some instances larger grains can be seen (Figs 2b and 3a).

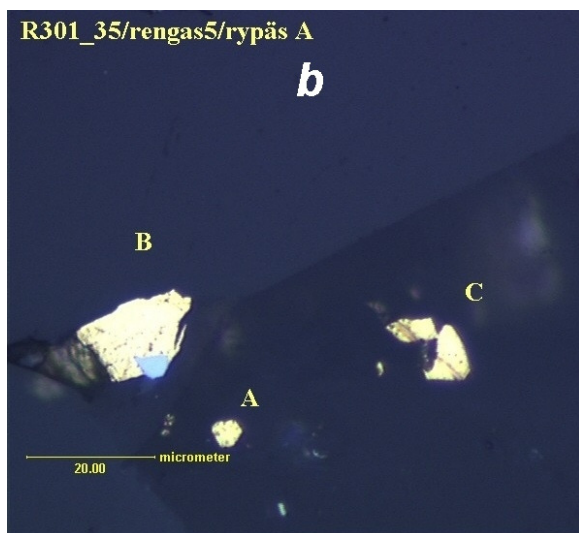
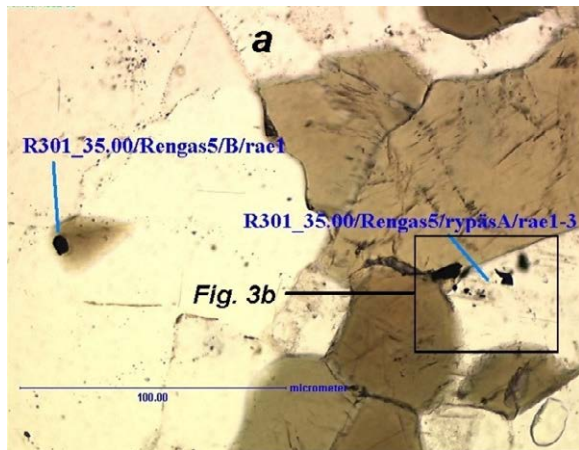


Figure 4. Gold inclusions in silicates of the Velkua Au-enriched amphibolite. Gold is in transmitted light (a) as the opaque mineral, and in the blow-up (b) reflected light. The composition of gold is in all grains (A-C) 94 % Au and 6 % Ag. (Drill hole R301 depth 61.00 m).

According to microprobe analyses the composition of gold averages 93% Au and 7% Ag (Kärkkäinen et al. 2012). Small gold inclusions in arsenopyrite and discrete large (zoned) Au-grains may contain more Ag. Some larger gold grains of the low-grade arsenopyrite-dominated ore type are zoned. Major part of the grain is lighter-coloured Ag-Au-alloy, which is covered by a rim or patches of deep yellow pure gold (Fig. 5).

Gold occurs at Velkua also as a swarm of small inclusions or sub-euhedral large inclusions in arsenopyrite in the low-grade mineralization. Arsenopyrite is usually rather coarse grained and

euhedral and commonly has several clear zones or irregular patches of löllingite in the core (Fig. 6). Native bismuth and rarely ullmannite were observed with gold and arsenopyrite.



Figure 5. A zoned gold grain composed mainly of lighter Ag-Au alloy (point 1: 81.4 % Au, 18.5 % Ag) and partially rimmed by darker pure gold (99.4 % Au, 0.6 % Ag). The grain is separated from a crushed bulk rock sample from the discovery outcrop. Analysis from Kärkkäinen et al. (2012) appendix 1, sample JA-29Aconc./gr B/p1 and p2.

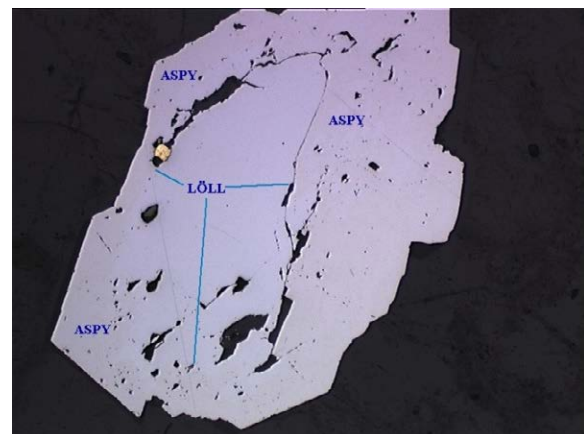


Figure 6. Gold grain (94% Au and 6% Ag) in the contact of löllingite (core) and arsenopyrite (outer zone).

3 Discussion and conclusions

The bedrock in the Velkua area is metamorphosed to upper amphibolite or lower granulite facies conditions that also caused partial melting of the rocks. The silicate minerals of the host rock of the Velkua Au prospect do not show any features of retrograde alteration. As gold is observed within metamorphic silicate minerals it appears likely that gold mineralization took place before the regional metamorphism. However, south-eastern Finland has gone through two periods of regional metamorphism, 1.88–1.87 Ga and 1.83–1.80 Ga (Korsman et al. 1999, Väisänen et al. 2002, Mouri et al. 2005, Skyttä et al. 2006, Skyttä and Mänttari 2008, Pajunen et al. 2008, Lahtinen et al. 2005). It is assumed that at least the supracrustal host rocks at Velkua have been affected by both metamorphic events (Kärkkäinen

et al. 2012a). Based on our observations, it can be said that gold is older than the last metamorphic event 1.83–1.81 Ga (Kärkkäinen et al. 2012a).

An interesting observation is the zoning of gold in the large gold grains of the Velkua occurrence. Zoned gold grains are usually observed in soil, where zoning is connected to weathering, but endogenic origin of zoning of some of placer gold is also presumed (Chapman et al. 2002, 2006). At Velkua the surface weathering is unlikely caused the zoning. The outcrop sample contains fresh unaltered arsenopyrite and pyrrhotite, and zoned grains have also observed in drillcore samples. Zoning of the gold grains could be explained as resulting from at least two hydrothermal stages. Similar zoning of gold grains has observed elsewhere in Southwestern Finland, at least in the Paimio area east of Turku (Grönholm et al. 2012) and in the Kullaa area (Kärkkäinen et al. 2012b).

Ongoing studies at Velkua include an estimate of the economic potential, the dimensions and grade of the prospect. In addition, future U-Pb geochronological analysis of the host rock will be carried out constrain the age of mineralisation.

The Velkua Au occurrence is a metamorphosed Au deposit. More research is needed to fully understand the genesis of the mineralization including the relationship to metamorphism and the mineralogy of the deposit. Understanding the primary processes that caused enrichment in gold and also the significance of the amphibolites formation, which is common in this part of the Turku-Åland archipelago, are the key importance for regional exploration in the area.

References

- Chapman, R., Leake, B., Styles, M., 2002. Microchemical characterization of alluvial gold grains as an exploration tool. *Gold bulletin* 35 (2), 53-65.
- Chapman, R. J., Mortensen J.K., 2006. Application of microchemical characterization of placer gold grains to exploration for epithermal gold mineralization in regions of poor exposure. *Journal of Geochemical Exploration* 91, 1-26.
- Grönholm, S., Kärkkäinen, N., Rosenberg, P. & Airo, M.-L. 2012. Gold at Korvenala, Paimio and Kultaanummi, Halikko (Salo), in the high-grade metamorphic terrain of SW-Finland. Geological Survey of Finland, Special Paper 52, 101–114.
- Kärkkäinen, N., Lahtinen, R., Pakkanen, L., 2012a. Discovery and mineralogy of gold occurrence at Velkua, Southwestern Finland. In: *Gold in Southern Finland : results of GTK studies 1998-2011*. Geological Survey of Finland. Special Paper 52. Espoo: Geological Survey of Finland, 115-130.
- Kärkkäinen, N., Lehto, T., Pakkanen, L. & Rosenberg, P., 2012b. Exploration and the mineralogy of gold in the Kullaa area, southwestern Finland. Geological Survey of Finland, Special Paper 52, 131–148.
- Korsman, K., Korja, T., Pajunen, M., Virransalo, P. & GGT/SVEKA Working Group 1999. The GGT/SVEKA Transect: structure and evolution of the continental crust in the Palaeoproterozoic Svecofennian orogeny in Finland. *International Geology Review* 41, 287–333.
- Lahtinen, R., Korja, A., Nironen, M., 2005. Paleoproterozoic tectonic evolution. In: Lehtinen, M., Nurmi, P.A., Rämö, O.T., (Eds.), *Precambrian Geology of Finland – Key to the Evolution of Svecofennian Shield*. Elsevier Science, B.V., Amsterdam, 481-532.
- Mouri, H., Väisänen, M., Huhma, H., Korsman, K., 2005. Sm-Nd garnet and U-Pb monazite dating of high-grade metamorphism and crustal melting in the West Uusimaa area, southern Finland. *GFF* 127, 123-128.
- Pajunen, M., Airo, M.-L., Elminen, T., Mänttari, I., Niemelä, R., Vaarma, M., Wasenius, P., Wennerström, M., 2008. Tectonic evolution of the Svecofennian crust in southern Finland. In: *Tectonic evolution of the Svecofennian crust in southern Finland - a basis for characterizing bedrock technical properties*. Geological Survey of Finland, Special Paper 47, 15–160.
- Skyttä, P., Mänttari, I., 2008. Structural setting of late Svecofennian granites and pegmatites in Uusimaa Belt, SW Finland : age constraints and implications for crustal evolution. *Precambrian Research* 164, 86–109.
- Skyttä, P., Väisänen, M., Mänttari, I., 2006. Preservation of Palaeoproterozoic early Svecofennian structures in the Orijärvi area, SW Finland - evidence for polyphase strain partitioning. *Precambrian Research* 150, 153–172.
- Väisänen, M., Mänttari, I., Hölttä, P., 2002. Svecofennian magmatic and metamorphic evolution in southwestern Finland as revealed by U-Pb zircon SIMS geochronology. *Precambrian Research* 116 (1-2), 111-127.

Structural controls on orogenic gold mineralisation along the Dugbe Shear Zone, eastern Liberia

R.G. Langdon, J.C.Ø. Andersen & R.K. Shail
Camborne School of Mines, University of Exeter, UK

D.A. Pelham
Hummingbird Resources plc, London, UK

Abstract. Intensive exploration along the Dugbe Shear Zone in Eastern Liberia by Hummingbird Resources plc resulted in the discovery of a gold resource in excess of 3.81 Moz. The three closely spaced deposits that make up the project are believed to lie in an unexplored extension of the highly prospective Birimian terrane. Geological mapping and sampling were carried out with the aim of understanding the structural controls on mineralisation and to compare the deformation sequence with the Birimian of West Africa. Field observations are consistent with the polyphase tectonic model proposed for the Birimian. Progressive D1-D2 collisional tectonics gave way to a D3 transcurrent dominated regime. Mineralisation primarily occurred late in the orogenic sequence with ore bodies variably distributed in F2 and F3 antiform hinge and limbs at F2-F3 domal fold intersections. The Dugbe Shear Zone controlled fluid flow and deposit distribution on a regional scale with gold mineralisation occurring in lower-order, proximal, antiform structures. This structural setting is common to orogenic gold deposits worldwide.

Keywords. Orogenic Gold, Liberia, Birimian

1 Introduction

The Palaeoproterozoic Birimian terrane of West Africa is one of the fastest growing areas for discovery, development, and production of gold. Published work has indicated that the eastern third of Liberia forms the south western extremity of the Birimian province (Hurley et al. 1971; Behrendt and Wotorson 1974). Until recently prolonged periods of civil war have hindered exploration of this highly prospective region.

Hummingbird Resources plc, founded in 2005, was a first mover in Eastern Liberia. Intensive exploration along the Dugbe Shear Zone led to the discovery of three closely sited gold deposits with a total resource of over 3.81 Moz.

Ongoing fieldwork has focussed on establishing the deformation sequence in the Dugbe-1 Project area and comparing this with the regional evolution of the Birimian terrane in order to better understand the structural controls on gold mineralisation.

2 Geological Setting

2.1 Regional

Geochronological studies have highlighted three age provinces in the Precambrian basement rocks of Liberia.

The Archean Leo-Man Shield (a segment of the West African Craton) is overlain by Birimian aged metasedimentary, metavolcanic, and plutonic rocks in the south east of the country, relating to a period of crustal accretion during the Eburnean orogeny around 2.0 Ga. A Pan-African province has been described along the coast (Fig. 1A) (Hurley et al. 1971; Hedge et al. 1975). Behrendt and Wotorson (1974) identified a pronounced break in the structural grain in aeromagnetic data that approximates the proposed Archean-Birimian age province boundary. The exact surface trace of the contact is unclear due to limited age dates, mixed aeromagnetic signal, and low resolution geological mapping. Additional complexity is likely the result of interfolding of the two age provinces at the contact.

Four major NE-trending shear zones have been identified in the Liberian Birimian terrane. These are broad mylonitic zones, with contrasting rock types and aeromagnetic patterns either side of the shear zones (Tysdal and Thorman 1983). Elsewhere in West Africa, similar Birimian crustal-scale structures have been prime locales for gold deposits; for example the Ghanaian Ashanti Belt (Feybesse et al. 2006). As such, Hummingbird Resources' plc initial land package and subsequent exploration programme focussed on these structures.

2.2 Study Area

Intensive exploration initially using geochemical methods and observations of artisanal mining led to the discovery of the Dugbe F (1.76 Moz), Tuzon (2.05 Moz), and Sackor (uncalculated resource) deposits proximal to the Dugbe Shear Zone. The three deposits are within a 2.6 km radius of each other and make up the Dugbe-1 Project (Fig. 1B).

Small-scale geological mapping of the Dugbe-1 Project formed a key component of this study in understanding the local geology. Previous work at a regional 1:250 000 scale lacked the resolution necessary to decipher both the geological history and controls on mineralisation (Tysdal 1977). LiDAR topography, satellite imagery, and Liberian outcrop hunters were employed to identify outcrop exposures in the dense jungle terrain allowing construction of detailed geologic maps and sections.

Fieldwork identified a number of lithological units spatially associated with mineralised rock. These include quartz-biotite gneisses containing varying proportions of orthopyroxene and garnet displaying macro and microscopic evidence for migmatitisation.

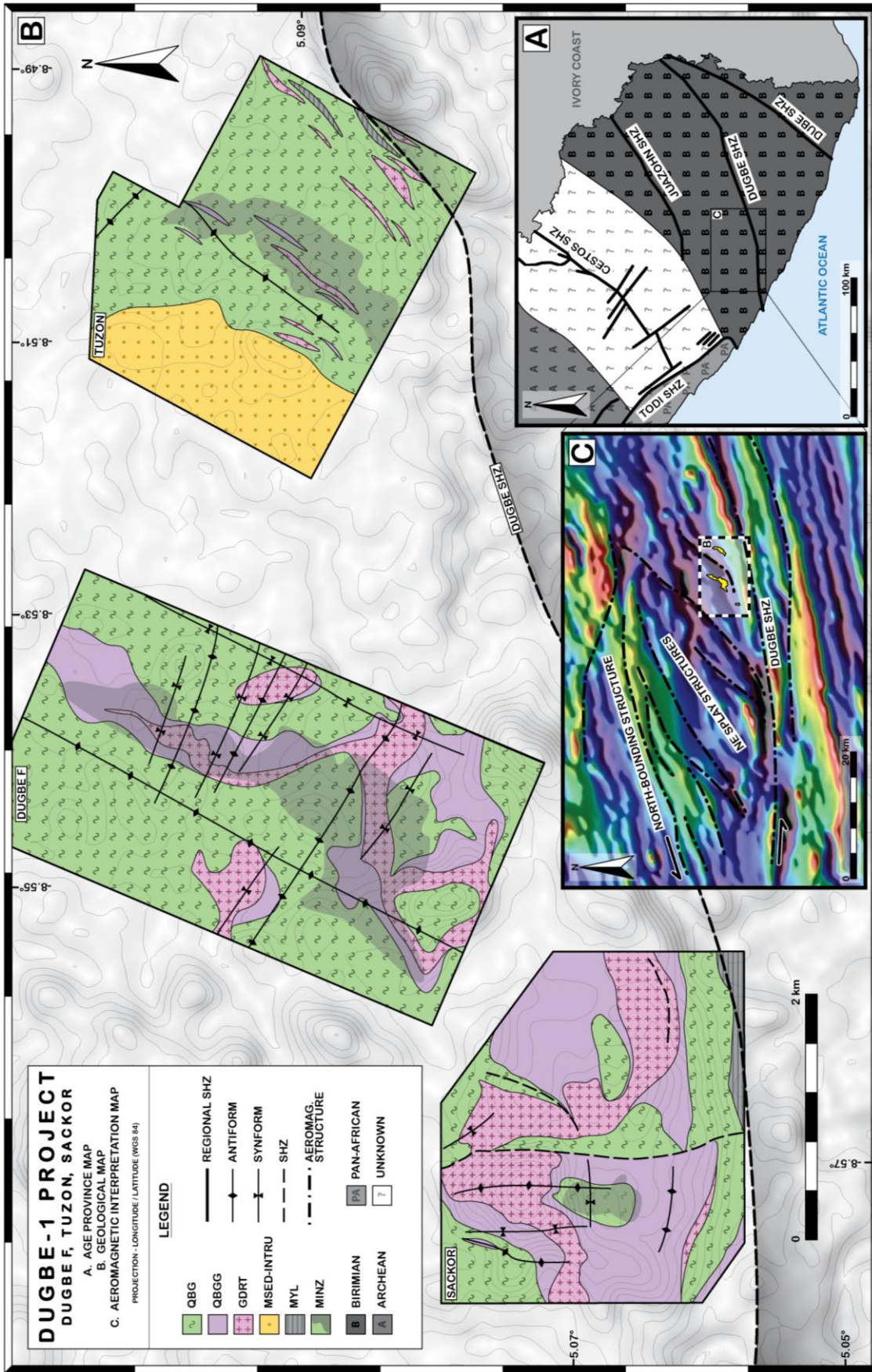


Figure 1. (A) Basement age province map of Central and Eastern Liberia with regional shear zones (SHZ), (after Tysdal and Thorman 1983). (B) Geological map of the Dugbe-1 deposits, (Dugbe F map after Mihalyuk and Logan 2011, unpublished work; Hummingbird Resources plc, personal communication). QBG - quartz-biotite-(± orthopyroxene) gneiss; QBGG - quartz-biotite-garnet gneiss, GDRT - granodiorite; MSED-INTRU - undifferentiated metasediments and intrusives; MYL - mylonite; MINZ - drill intercept of mineralised rock at depth (grey shaded domains); SHZ - shear zone. (C) Total magnetic intensity, regional, aeromagnetic (AEROMAG) map with geologic structural interpretation including the Dugbe Shear Zone (SHZ), (after Kolf 2012).

Sill shaped granodiorites commonly intrude the gneiss alongside cross-cutting and foliation parallel pegmatites. Mylonitic outcrops are linked with the surface trace of the Dugbe Shear Zone.

Structural observations are consistent with a polyphase tectonic model, similar to that proposed for the Birimian of Ghana and Burkina Faso (Milési et al. 1992; Feybesse et al. 2006; Baratoux et al. 2011). Initially collisional tectonism (D1) dominated during crustal accretion at the onset of the Eburnean orogeny (Feybesse and Milési 1994). Birimian rocks were placed in thrust contact with underlying Archean age rocks. Syn-tectonic melting occurred as a result of crustal thickening, forming migmatic structures aligned with S1, a penetrative foliation sub-parallel to parallel to original lithological contacts and primary bedding. Granodiorite sills were emplaced early during this phase of deformation. This is characterised by foliated sill margins, foliation parallel transitional contacts with quartz-biotite gneiss units, and subsequent folding. Continued progressive deformation of S1 resulted in both small- and large-scale tight NNE- to NW-trending folds (F2) across the Dugbe-1 area. A transition in tectonic style to a transcurrent regime defines the D3 event. Movement was primarily accommodated along shear zones that localised along major pre-existing structures. The crustal scale nature of the Dugbe Shear Zone is confirmed by Baratoux et al. (2011) who report it's along strike continuation into Burkina Faso. D3 sinistral motion along the Dugbe Shear Zone is characterised by near vertical mylonitic fabrics (S3), a distinct laterally continuous change in topography, shear zone parallel large scale ESE- to NE-trending orientated open folds (F3), and NE-trending orientated en echelon splay structures visible in aeromagnetic data (Kolf 2012). These splay structures are possibly linked to a strike-slip duplex at a left-stepping bend in the Dugbe Shear Zone (Fig. 1C). Their activation may have rotated earlier fold generations. In addition F2 folds were refolded about late F3 folds forming a dome and basement like arrangement. A number of poorly exposed N-trending shear zones have been tentatively attributed to a D4 event. Late brittle structures related to uplift (D5) are of minimal extent and are primarily observed as joint sets and laterally impersistent brittle faults.

3 Dugbe-1 Project Mineralisation

Foliation parallel disseminated gold is the dominant ore type across the Dugbe-1 deposits. Locally polyminerale mm-scale sulphide stringers with gold are observed. Gold bearing quartz veinlets are rarely observed. The paragenesis (in decreasing order of abundance) comprises: pyrrhotite, chalcopyrite, arsenopyrite, löllingite, pyrite, sphalerite, free gold, cobaltite-gersdorffite, and tetradyrite. Graphite is commonly present in the ore zones. Lithologically, gold and associated sulphides are primarily hosted in mafic-rich zones within the quartz-biotite-gneiss. Garnet-bearing gneissic units tend to have low gold grades, whilst interspaced granodiorite sills and pegmatites are barren.

The structural controls on mineralisation and ore body

distribution show some variation between the Dugbe-1 deposits and are discussed individually below:

3.1 Dugbe F

The 1.76 Moz Dugbe F deposit is formed of a single tabular shaped ore body that crops out at surface and gently dips to the ESE. The ore body is up to 40 m thick, unconstrained at depth, and has been traced along strike for 2.5 km with an average grade of 1.3 g/t. It is mainly hosted in quartz-biotite-orthopyroxene gneiss in the ESE limb of an F2 antiform underlying a granodiorite sill and quartz-biotite-garnet gneiss unit. At the intersection with an F3 generation fold there is a deflection in orientation of the ore body to a SSW dip direction (Fig. 1B). The gold zone appears to be gently undulating about two orthogonal fold axes (Mihalynuk and Logan 2011, unpublished work). The ore body is distal to the Dugbe Shear Zone compared to the other deposits sitting 1.5 to 3.0 km from the structure.

3.2 Tuzon

The 2.05 Moz Tuzon deposit is primarily comprised of up to 8 vertically stacked lensoid ore bodies that dip gently to the SE and in places crop out at surface. The largest lenses are 40 m thick, unconstrained down dip, and continue along strike for 2 km with an average grade of 1.2 g/t. Gold is mainly hosted in quartz-biotite gneiss with variable proportions of orthopyroxene. Barren granodiorite sills and pegmatites are distributed throughout the vertical section containing ore bodies. The lensoid ore bodies are seated in the hinge and SE limb of a F3 antiform. Additional minor stacked ore bodies are found in the SW limb of a F2 antiform north of the intersection with the gold hosting F3 antiform (Fig. 1B). Some of the highest grades coincide with the F2-F3 fold intersection at depth. The ore bodies lie within 400 m of mylonitic outcrops associated with the Dugbe Shear Zone.

3.3 Sackor

The total resource for the Sackor deposit is currently unconstrained. Initial observations show a series of vertically stacked ore bodies with similar grades to Dugbe F and Tuzon that outcrop at surface. The ore bodies are within the quartz-biotite gneiss containing variable amounts of orthopyroxene. An envelope of barren quartz-biotite-garnet gneiss surrounds the mineralised rock package with the whole sequence capped by a granodiorite sill. The ore bodies are situated in the domal culmination of an F2-F3 fold intersection and follow the shallow dip of the structure (Fig. 1B). Current estimates are that the deposit is less than 1 km from the Dugbe Shear Zone.

4 Discussion and Conclusions

A number of structural similarities between the Dugbe-1 deposits provide evidence for multi-scale structural controls on mineralisation. All three deposits are

proximal to the first order Dugbe Shear Zone with ore bodies sited in lower order antiformal structures. This structural setting is common in Palaeoproterozoic greenstone terranes worldwide (Goldfarb et al. 2005).

At a deposit scale, mineralised rock is concentrated around F2-F3 domal fold interference structures. Tabular to lensoid ore bodies are variably developed in hinge and limb zones of both generations of folds. High grades commonly occur at the fold intersection, with deposits pinching out distal to the culmination. Numerous authors suggest that antiforms and in particularly domal culminations are zones of maximum permeability due to favourable low mean stress in the hinge and limbs compared to the surrounding stress field (Ridley 1993; Groves et al. 2000; Feybesse et al. 2006;). Thus, they act as structural traps where fluid preferentially accumulates leading to the development of ore bodies. On this basis it is proposed that fluids were focussed along foliation planes within the gneissic units into F2-F3 fold culminations to form disseminated ore bodies. Overlying weakly- to non-foliated granodiorite sills at Dugbe F and Sackor likely acted as semi-impermeable cap rocks, focussing fluid flow.

At a regional scale the Dugbe Shear Zone provided the major control on deposit distribution. It acted as a conduit for large volume auriferous fluid flow needed to form gold lodes and spatially controlled the location of deposit scale structural traps. The left bend in the Dugbe Shear Zone seen in topographic and aeromagnetic data is thought to be important in focusing fluid flow.

If sinistral motion along the Dugbe Shear Zone is assumed, as is common elsewhere in the Birimian (Milési et al. 1992; Feybesse et al. 2006), then preliminary aeromagnetic interpretation suggests that regional NE-trending splay structures bisecting the Dugbe-1 area may be related to a dilatational strike-slip duplex (Kolf 2012).

Gold mineralisation appears to be emplaced late in the orogenic cycle at the end of the D3 deformation event. F2 and F3 folds variably host ore bodies at their intersection, suggesting formation of the structures pre-mineralisation. Moreover, D4 structures are barren and there is no evidence for mineralisation associated with late brittle deformation. Petrographic observations support late kinematic mineralisation; ore zone minerals and associated alteration products appear undeformed and unmetamorphosed. It is clear that the transition from collisional (D2) to transcurrent (D3) dominated deformation had a strong influence on fluid flow at a regional scale.

Vertically stacked ore bodies at Tuzon and Sackor contrast to the single tabular ore body at Dugbe F. The reason for this is not yet fully understood, but it is hypothesised that proximity to the Dugbe Shear Zone is a controlling factor.

The structural controls on mineralisation discussed above show an affinity with other major Birimian gold deposits in West Africa. This supports the theory of an extension of the Birimian terrane in Eastern Liberia (Feybesse et al. 2006). It is also clear that the Dugbe-1 deposits display structural characteristics typical of orogenic gold deposits. Regional structures provide the main control on deposit distribution with mineralised

rock occurring in lower order structures late in the orogenic sequence (Groves et al. 1998; Groves et al. 2000).

Acknowledgements

Hummingbird Resources plc are gratefully acknowledged for financing and facilitating this study. The geological and logistical team in Liberia are thanked for insightful discussions and valuable support in the field. G. Rollinson, S. Uren, and S. Pendray are acknowledged for assisting with lab work and sample preparation.

References

- Baratoux L, Metelka V, Naba, Jessell MW, Grégoire M, Ganne J (2011) Juvenile Paleoproterozoic crust evolution during the Eburnean orogeny. *Precamb Res* 191:18-45
- Behrendt JC, Woterson CS (1974) Geological Surveys of Liberia with Tectonic and Geologic Interpretations. US Geol Surv Prof Pap 810, p 33
- Feybesse JL, Milési JP (1994) The Archean/Proterozoic contact zone in West Africa: a mountain belt of décollement thrusting and folding on a continental margin related to 2.1 Ga convergence of Archean cratons? *Precamb Res* 69:199-227
- Feybesse JL, Billa M, Guerrot C, Duguey E, Lescuyer JL, Milesi JP, Bouchot V (2006) The paleoproterozoic Ghanaian province: Geodynamic model and ore controls, including regional stress modelling. *Precamb Res* 149:149-196
- Goldfarb RJ, Baker T, Dubé, Groves DI, Hart CJ, Gosselin P (2005) Distribution, Character, and Genesis of Gold Deposits in Metamorphic Terranes. *Soc Econ Geol* 100th Anniv Vol pp. 407-450
- Groves DI, Goldfarb RJ, Gebre-Mariam M, Hagemann SG, Robert F (1998) Orogenic gold deposits: A proposed classification in the context of their crustal distribution and relationship to other gold deposit types. *Ore Geol Rev* 13:7-27
- Groves DI, Goldfarb RJ, Knox-Robinson CM, Ojala J, Gardoll S, Yun GY, Holyland P (2000) Late-kinematic timing of orogenic gold deposits and significance for computer-based exploration techniques with emphasis on the Yilgarn Block, Western Australia. *Ore Geol Rev* 17:1-38
- Hedge CE, Marvin RF, Naeser CW (1975) Age Province in the Basement Rocks of Liberia. *J Res US Geol Surv* 3:425-429
- Hurley PM, Leo GW, White H, Fairbairn HW (1971) Liberian Age Province (about 2,700 m.y.) and Adjacent Provinces in Liberia and Sierra Leone. *Geol Soc Am Bull* 82:3483-3490
- Kolff L (2012) Proven Iron Ore District in Liberia, Mines and Money London, 3 Dec 2012. Tawana Resources NL, http://www.tawana.com.au/index.php?option=com_investorcentre&view=files&id=4&Itemid=13. Accessed 2 February 2013
- Milési JP, Ledru P, Feybesse JL, Dommanget A, Marocux E (1992) Early Proterozoic ore deposits and tectonics of the Birimian orogenic belt, West Africa. *Precamb Res* 58:305-344
- Ridley J (1993) The relations between mean rock stress and fluid flow in the crust: With reference to vein- and lode-style deposits. *Ore Geol Rev* 8:23-37
- Tysdal RG (1977) Geologic Map of the Juazohn Quadrangle, Liberia. US Geol Surv Map I-779-D
- Tysdal RG, Thorman CH (1983) Geological Map of Liberia. US Geol Surv Map I-1480

Structural framework and evolution of the world class Siguiri orogenic gold district (Guinea, West Africa)

Erwann Lebrun, John Miller, Nicolas Thébaud, T. Campbell McCuaig

Centre for Exploration Targeting, Robert Street Building, M006, The University of Western Australia, 35 Stirling Highway, Crawley, WA, 6009, Australia

Stanislav Ulrich

AngloGold Ashanti Ltd - Brownfields Exploration Technical Hub - Continental Africa Region, 44 St George Terrace, Perth, WA, 6000, Australia

Abstract. With over 17 deposits, the Siguiri gold district is the only world-class district in the Siguiri Basin (Guinea), one of the largest volcano-sedimentary basins of Paleoproterozoic age in West Africa. Hosted in a turbidite sequence, the Siguiri deposits underwent at least three main deformation events: D1s is characterised by a weak N-S compression developing locally minor thrust faults; D2s is associated with an E-W compression and develops N-S thrusts and NE-trending dextral shear zones, it is responsible for the bulk of the deformation in the Siguiri Basin; and D3s, a NW-SE compression event that refolds earlier structures and is linked to a NE- to NNE-trending cleavage. Mineralisation appears to be mainly localised along the D2s N-S and NE-SW cross-structures. It is associated with localised stockworks of gold-bearing quartz veins displaying a prominent SE-dipping population. NE-SW shear zones are in places associated with gold-bearing pyrite and localised carbonatisation of the host rocks. This study documents for the first time the lithology, structural and mineralogical characteristics of this major deposit and integrates the observations made at the deposit scale within the broader West African Craton architecture.

Keywords: Siguiri, tectonics, orogenic gold, West Africa

1 Introduction and regional setting

The world class Siguiri gold district represents one of the major gold sources in the West African Craton. With estimated resources and reserves in excess of 7 Moz in Dec 2011, the Siguiri deposits have produced over 250,000 oz/year since its acquisition by AngloGold Ashanti in 2004. While such a large system was mined thousands of years ago by the Mali Empire (Watts 2010, unpublished), it has received to date little to no attention from the scientific community.

The West African Craton can be subdivided into two domains: the Archean Kenema-Man domain, and the Proterozoic Baoule-Mossi domain. The Kenema-Man domain was formed during two main orogenic events: the Leonian, from 3000 to 2900 Ma, and the Liberian, from 2900 to 2600 Ma (Milési et al. 1989; Egal et al. 2002; Thiéblemont et al. 2004). The Baoule-Mossi domain was accreted against this Archean domain during the Eburnean orogeny between 2200 and 2000 Ma (Egal et al. 2002; Thiéblemont et al. 2004).

The Siguiri gold district sits in the north of the Siguiri Basin, which is located amidst a mobile Paleoproterozoic greenstone belt spreading across Guinea, Mali and extending close to the Cote d'Ivoire

border. The Basin consists of lower Birimian volcanic rocks and sediments of volcanoclastic origin intruded by late Eburnean intrusions (Abouchami et al. 1990; Paranhos 2008, unpublished). The Birimian sediments represent the bulk of the Basin lithostratigraphy and are interpreted to be derived from Paleoproterozoic granitoids emplaced during the earliest stage of the Birimian collision between the Leo-Man-Ghana Craton and the Taoudeni Subcraton (Milési et al. 1989; Begg et al. 2009; Feybesse and Milési 1994).

2 Mine geology

2.1 Host rocks

The Siguiri gold district is hosted in a thick volcano-sedimentary sequence metamorphosed to sub-greenschist facies.

The sediments display repetition of massive to slightly graded greywacke beds, fining upward to alternating siltstone and claystone beds (upper parallel laminations of the Bouma sequence; Bouma 1962). Sedimentary facies indicate a decrease in flow velocity (waning turbidity currents; Mulder and Alexander 2001): rip-up (mud) clasts, characteristic of high-energy flow conditions, and asymmetric ripple marks found at the surface of exposed siltstone beds, indicate lower flow regime. Additional sedimentary facies include localised conglomerate deposits, interpreted as the product of marine debris flow events. Bed thicknesses of up to 6 m of coarse sandstone-size greywacke suggest a channelized depositional environment. Together, the sedimentary facies and facies associations are indicative of a turbidite depositional environment which possibly formed as a thick sequence of proximal, channel-fill deposits.

The turbidite sequence is intruded by the late Eburnean Malea monzogranite to the north and multiple granodiorite dykes of the same age (Fig. 2).

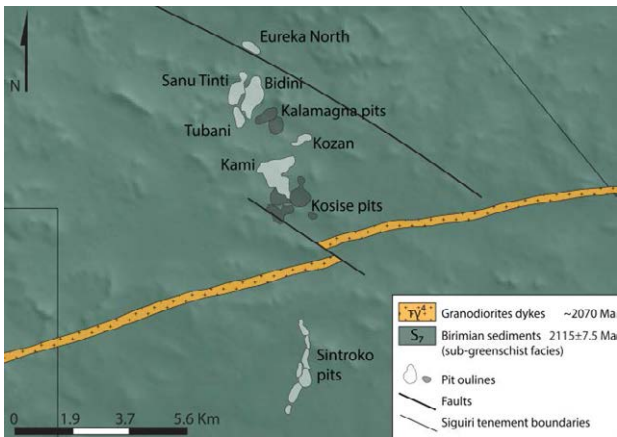


Figure 2. Simplified geological map of the Siguiri gold district, in the central part of the AngloGold Ashanti owned Siguiri tenement (Fig. 3). Modified from Egal et al. (1999).

2.2 Structural evolution

Gentle upright folds are ubiquitous in the Kami deposit (central part of the Siguiri Gold District) and two prominent fold axis orientations were observed: a weak ENE-WSW to ESE-WNW (F1s, s = local Siguiri event history), and a main N-S to NNW-SSE (F2s). F1s closed recumbent folds occur in the Eureka North deposit in the northernmost part of the Siguiri gold district, with fold axes gently plunging to the W-NW. Although no clear axial planar cleavage (S1s) was observed, ESE-WNW thrusts axial planar to the F1s folds were observed in the Kalamagna PB1 pit in the northern part of Siguiri gold district. F2s fold axes strike NNE-SSW to NNW-SSE with variable dip angles (Fig. 3).

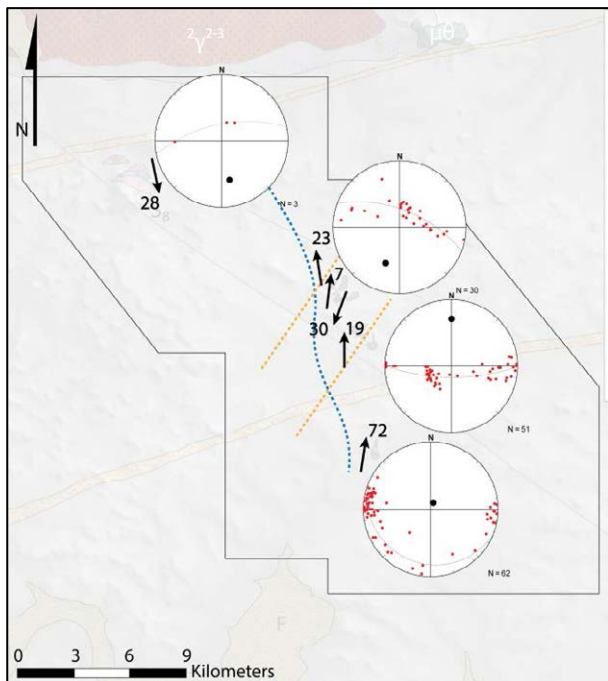


Figure 3. Bedding orientation readings taken in the Siguiri tenement. The curved blue dashed line represents the second compressional event fold axis trajectory which was refolded by the third compressional event (NNE-striking orange dashed lines). Arrows represent measured and calculated fold axes, as displayed in the stereonets (bedding poles in red, fold axes in black and ac planes (cylindrical best fit) represented as dashed grey lines). Equal angle/Wulff stereonets.

The fold typology displays variable geometries including: upright isoclinal horizontal and vertical-sinistral folds in the Sintroko deposit to the south, gentle upright to open slightly-inclined N-plunging W-verging folds occur in the Kosise deposit in the centre, whereas open to isoclinal gently-inclined W- to NW-verging folds occur in the Bidini deposit to the north of the Siguiri gold district.

N-S oriented thrusts and dextral NNE- to ENE-trending sub-vertical shear zones occur throughout the Siguiri gold district. There are also bedding-parallel and en-echelon quartz-carbonate veins (V2As) around the N-S to NNW-SSE fold hinges indicative of flexural slip during folding (Fig. 4).

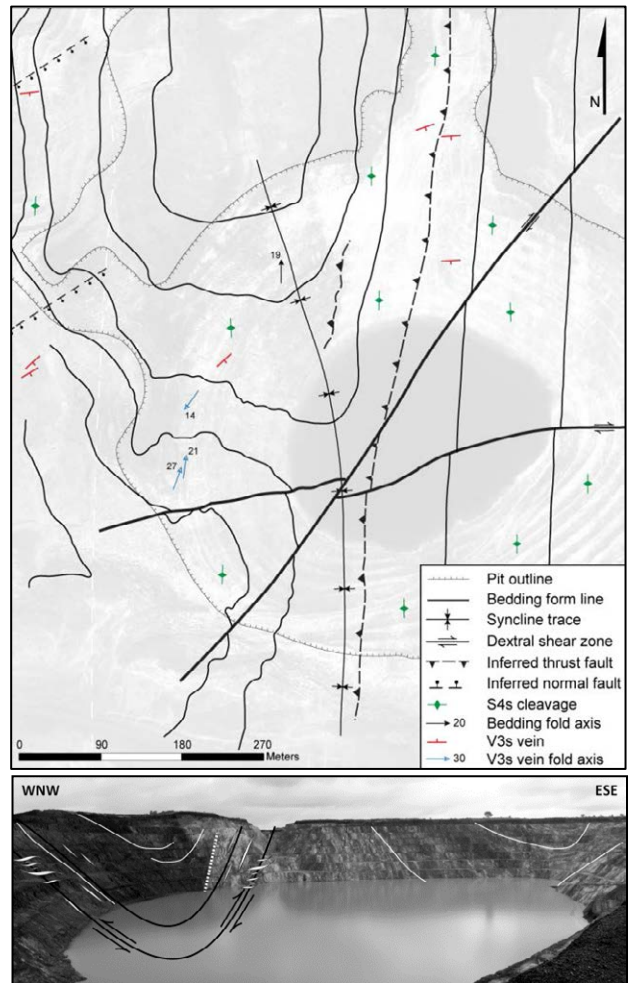


Figure 4. Structural form-line map and idealised cross-section of Kosise pit.

A set of quartz-carbonate veins (V2Bs) cuts across the early fold generation and early veins (V2As). V2Bs have arsenopyrite and minor pyrite along their selvages and represent the main structural feature linked to gold in the Siguiri gold deposit (Fig. 4). These veins strike to the ENE-WSW and dip steeply to the SSE. Local conjugate vein sets have been used to reconstruct the paleo-orientation of the principal stresses at the time of veining and point toward a stress field where sigma 1 and 2 are very close, switching from a NNW-SSE extensional to transtensional setting (sigma 1 and 2 girdles in Fig. 5).

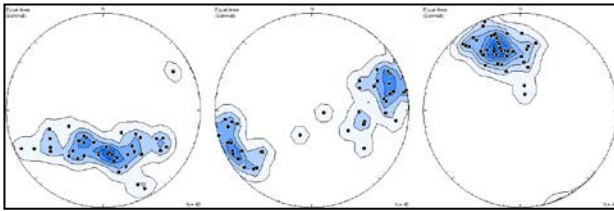


Figure 5. From left to right: Calculated orientation of sigma 1, 2 and 3 respectively, based on conjugate mined vein sets. The girdle of sigma 1 and 2 orientations is consistent with an emplacement in a setting where sigma 1 nearly equals sigma 2. Equal area/Schmidt stereonets.

Overprinting all other structural elements (e.g. V2Bs veins in Fig. 6), is a penetrative sub-vertical NE-SW to NNE-SSW planar fabric that is well developed throughout the Siguiri Basin and adjacent Malea monzogranite. This late planar fabric appears to be axial planar to large scale open folds (F3s) that refold early F1s and F2s fold generations (Fig. 3).

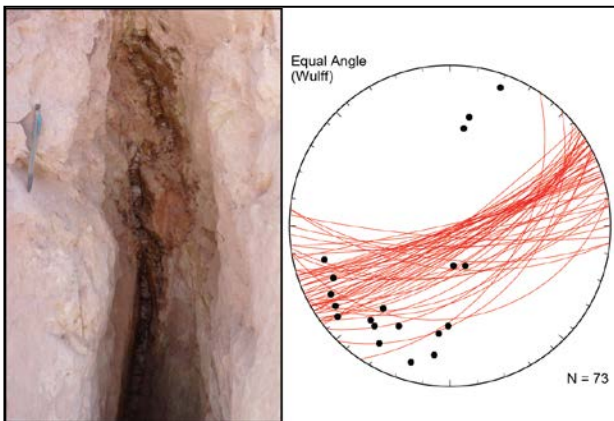


Figure 6. Mined vein folded by a NW-SE compressional event. The stereonet shows the orientation of these mined veins in red and their measured fold axis in black.

2.3 Mineralisation

Mineralisation in the Siguiri gold mine is locally associated with compressional or extensional to transtensional structures. The N-S thrusts and dextral NNE- to ENE-trending sub-vertical shear zones are associated with carbonate alteration and represent a large component of the primary ore shoots and highest grades in the Siguiri gold district. Gold assemblages include ankerite, gold-rich pyrite and albite developed as brecciated veins and alteration halos around the aforementioned cross-structures.

However, since the processing plant in operation is not sulphide capable, all gold produced at Siguiri is associated with the late oxidised V2Bs veins. The mineralogy of these veins includes a quartz-ankerite mineral assemblage with arsenopyrite and minor pyrite along their selvages. These veins are mined by local villagers, and the V2Bs veins represent the main host for free gold (but gold also appears to be present in the sulphide crystal lattice). Free gold in the veins is usually located within the quartz or at the contact with quartz and ankerite.

Minor native gold concentrations are also extracted from small Phanerozoic paleochannels (placer-like

deposit) and from hydromorphic reconcentration in and below the mottled zone of the lateritic profile. Local villagers have recently found individual nuggets of up to several tens of kilograms in weight.

3 Discussion and synthesis

Crosscutting relationships documented in the field show that the Siguiri Basin has undergone a protracted deformation history. The local structural elements encountered in the field have been chronologically regrouped under the deformation event scheme below.

Cryptic F1s folds with fold axes gently plunging to the W-NW, together with ESE-WNW thrusts, are interpreted to have developed during an early N-S compression (termed D1s). At the regional scale, a similar compression direction, associated with ESE-WNW thrusts have been described along the north-eastern border of the Archean Kenema-Man domain by Milési et al. (1989) and defined as the first Eburnean tectonic event, D1.

D2s represents a major tectonic event affecting the Siguiri Basin sediments, and is responsible for the bulk of the deformation observed in the Siguiri gold district. Based on F2s folds orientations, we suggest that D2s was associated with E-W compression under a brittle-ductile regime. Bedding parallel and en-echelon vein set orientations that developed during flexural slip along the fold limbs are consistent with an E-W compression. We infer that as plastic deformation eventually failed to accommodate further folding, the rocks start to break, developing N-S oriented thrusts. As the stress tensor gets isotropic and switches progressively from an E-W compressional setting to a NNW-SSE extensional to transtensional setting, dextral NE-SW shear zones form and localise fluid flow. F2s folds and ductile-brittle structures have been related to the second Eburnean tectono-metamorphic phase, D2, as described by Milési et al. (1989). Precipitation of gold-rich pyrite in veins and brecciated horizons along these thrusts and shear zones is associated with localised ankeritisation and broad albitisation of the host rock, which is symptomatic of orogenic gold deposits.

Cutting through the F2s folds are the mineralised arsenopyrite bearing veins (V2Bs), mainly ENE-trending. These developed as stockwork-like structures in association with the N-S and NE-SW cross-structures, in a NNW-SSE extensional to transtensional setting during a late stage of D2s. The V2Bs veins are the main source of gold produced at Siguiri.

V2Bs arsenopyrite-bearing veins are commonly folded into gently dipping folds with fold axes oriented NNE-SSW. This folding episode represents the last deformation event recorded in the Siguiri Basin. A penetrative S3s cleavage is axial planar to this last folding episode and overprints all other structural elements, as well as the pre- to syn-tectonic Malea monzogranite to the north of the mine. The S3s cleavage is interpreted to have developed during a NW-SE compression termed D3s. This event was responsible for the refolding of F2s folds, creating interference fold patterns and rotating D2s fold axes (Ramsay and Huber

1987). This last phase of deformation has also been recognised in the rest of the West African Craton (D3 in Milési et al. 1989).

4 Conclusion

Preliminary conclusions derived from this study of the Siguiri gold deposit suggest that:

- 1) The turbidite sequence of volcano-sedimentary origin hosting the deposit was deposited in a proximal channel-fill environment;
- 2) The protracted and polyphase deformation recorded in the Siguiri gold deposit can be divided in three distinct local deformation stages (D1s to D3s) all attributed to the Eburnean orogeny;
- 3) Within the deformation evolution presented, gold mineralisation appears to have been taken place during a late stage of D2s;
- 4) D2s is responsible for the bulk of the deformation observed at Siguiri mines and is interpreted to have developed in response to an E-W oriented compression event widely recognised in the West African Craton.
- 5) D2s mineralisation developed as high-grade gold-rich pyrite and ankerite brecciated veins along N- to ENE-trending cross-structures. These structures control the location of stockwork areas in a local NNW-SSE directed extensional to transtensional setting. Stockwork-associated mineralisation consists of auriferous quartz-carbonate-arsenopyrite-(pyrite) veins and represents the main host for the gold produced at Siguiri.

Acknowledgements

This project is funded by AngloGold Ashanti Limited. Shawn Kitt, Katharina Wulff, Eddie Connell, Craig Duvel and Lourens Erasmus are acknowledged for

providing site access, support and inspiring discussions. Prof. Julien Bourget is also acknowledged for his precious help regarding sedimentology. Thanks also to everyone I could not mention here above.

References

- Abouchami W, Boher M, Michard A, Albarede F (1990) A Major 2.1 Ga Event of Mafic Magmatism in West Africa - an Early Stage of Crustal Accretion. *J Geophys Res-Solid* 95:17605-17629
- Begg GC, Griffin WL, Natapov LM, O'Reilly SY, Grand SP, O'Neill CJ, Hronsky JMA, Djomani YP, Swain CJ, Deen T, Bowden P (2009) The lithospheric architecture of Africa: Seismic tomography, mantle petrology, and tectonic evolution. *Geosphere* 5:23-50
- Bouma AH (1962) Sedimentology of some Flysch deposits: A graphic approach to facies interpretation. pp 168
- Egal E, Lahondere D, Costea AC, Diabate B, Diallo A, Diallo AB, Diallo S, Gaye F, Iliescu D, Minthe D (1999) Carte geologique de la Guinee a 1/200 000 ; Feuille Siguiri. BRGM
- Egal E, Thiéblemont D, Lahondère D, Guerrot C, Costea CA, Iliescu D, Delor C, Goujou J, Lafon J, Tegye M, Diaby S, Kolie P (2002) Late Eburnean granitization and tectonics along the western and northwestern margin of the Archean Kénéma-Man domain (Guinea, West African Craton). *Precam Res* 117:57-84
- Feybesse J-L, Milési J-P (1994) The Archean/Proterozoic contact zone in West Africa: a mountain belt of décollement thrusting and folding on a continental margin related to 2.1 Ga convergence of Archean cratons? *Precam Res* 69:199-227
- Milési JP, Feybesse JL, Ledru P, Dommanget A, Ouedraogo MF, Marcoux E, Prost A, Vinchon C, Sylvain JP, Johan V, Teguey M, Calvez JY, Lagny P (1989) Les minéralisations aurifères de l'Afrique de l'Ouest. Leurs relations avec l'évolution lithostructurale au Protérozoïque inférieur. *Chronique de la recherche minière* 497:3-98
- Mulder T, Alexander J (2001) The physical character of subaqueous sedimentary density flows and their deposits. *Sedimentology* 48:269-299
- Ramsay JG, Huber MI (1987) The techniques of modern structural geology: Vol.2: Folds and fractures. Academic Press, London.
- Thiéblemont D, Goujou JC, Egal E, Cocherie A, Delor C, Lafon JM, Fanning CM (2004) Archean evolution of the Leo Rise and its Eburnean reworking. *J Afr Earth Sci* 39:97-104

Deep crustal-scale controls of orogenic gold mineral systems – Hodgkinson metallogenic zone, north Queensland, Australia

Vladimir Lisitsin, Paul Donchak, Matthew Greenwood
Geological Survey of Queensland

Abstract. The bulk of significant orogenic gold deposits in the late Paleozoic Hodgkinson Province in north Queensland occur in a narrow belt (<20 km wide), discordant to most of the surface geological structures. This metallogenic zone lies along the inferred edge of the Proterozoic Etheridge Province underlying the south-western Hodgkinson Province in the middle crust. The position of this deep crustal feature is indicated by a recent deep seismic survey and marked by a change from I- and A-type Carboniferous to Permian magmatism and the sub-greenschist facies regional metamorphic grade in the south-western Hodgkinson Province to the S-type Permian magmatism and the greenschist facies in the rest of the province. The geometry and architecture of the Paleo-Proterozoic continental margin affected both the initial development of the Hodgkinson Province and the subsequent structural and thermal history of its south-western part. The combination of these factors resulted in the formation of a discrete orogenic gold metallogenic zone within a much larger geological province. Similar deep crustal metallogenic zone-scale controls probably operated in central Victoria (the Selwyn Block) and in the Charters Towers region.

Keywords: orogenic gold; metallogenic zone; Queensland

1 Introduction

Research into exploration targeting of orogenic gold mineral systems has largely focused on geological controls that operate at two very distinct scales: metallogenic provinces ($>n * 10,000 \text{ km}^2$), on the one hand, and deposits ($<n * 10 \text{ km}^2$), on the other. As a result, the importance of broad regional factors in defining the scale of gold endowment of a province and the role of more local geological features (faults, folds, rock composition) in the localisation of individual gold deposits and ore fields are relatively well understood. However, the nature and even existence of the geological controls operating at the intermediate scales often remain enigmatic, especially when they are not obvious in traditional geological datasets. These controls may lead to major heterogeneities of the spatial distribution of gold deposits within some provinces, often expressed as discrete linear trends or zones of mineralisation.

This paper discusses such metallogenic zone-scale controls in the Hodgkinson Province of north Queensland (Australia) and considers broader implications of the inferred spatial and genetic relationships between mineralised zones and regional geological features for exploration targeting in this region and other orogenic gold provinces.

2 Regional Geological Background

2.1 Geological setting

The Hodgkinson Province is part of the Paleozoic Mossman Orogen, formed along the convergent Pacific margin of the Australian Craton in the Silurian to Carboniferous (Henderson et al. 2013). It is separated from the Paleo- to Mesoproterozoic Etheridge province by the Palmerville Fault. At the current erosional level, it is dominated by regionally deformed Devonian turbidites, with minor basalts, cherts and limestones, intruded by late to post-tectonic Carboniferous to Permian granites and locally covered by Permian to Quaternary sedimentary and volcanic rocks. The total area of the province is more than 40,000 km² (including later magmatic rocks and cover), with >20,000 km² of exposed Siluro-Devonian volcano-sedimentary rocks.

Interpretation of the recent deep seismic data (Korsch et al. 2012) indicates that the Hodgkinson Province represents only a relatively thin top portion of the crust (<12 km thick in the south-west), completely underlain by sub-horizontal sections of older continental crust: the Neoproterozoic to Ordovician Thompson Orogen, an inferred Mesoproterozoic section and the sub-surface extension of the Etheridge Province along the south-western margin. The Palmerville Fault moderately dips to the north-east and bifurcates and shallows at depth, defining the sub-horizontal bases of the Hodgkinson (at <12 km) and underlying Thompson (at <20 km) provinces. All the other identified major faults in the province are listric and sole onto the base of the Hodgkinson Province.

The tectonic setting of the province in the Silurian and Devonian remains controversial. Suggested models include a back-arc basin and a forearc accretionary prism (Henderson et al. 2013). The back-arc model suggests that the province was originally formed on the attenuated continental crust of the Thompson Orogen and the Australian Craton. In contrast, the accretionary prism model suggests that the province originally formed in an oceanic forearc environment, on the oceanic crust which was subsequently consumed by subduction. In this model, the Hodgkinson Province was removed from its original oceanic crust substrate and obducted over the older continental crust before the late Carboniferous. Both models suggest that the current deep crustal architecture was in place before the final stages of the first orogenic event which affected the province at ~360 Ma (Henderson et al. 2013).

The regional metamorphic grades range from the prehnite–pumpellyite facies in the western and south-

western Hodgkinson Province (along the Palmerville Fault) up to the greenschist facies in the rest of the province (Bain and Draper 1997; Garrad and Bultitude 1999; Henderson et al. 2013). Widespread intrusive and extrusive magmatism (mostly of a felsic to intermediate composition) affected the region in the late Carboniferous and Permian.

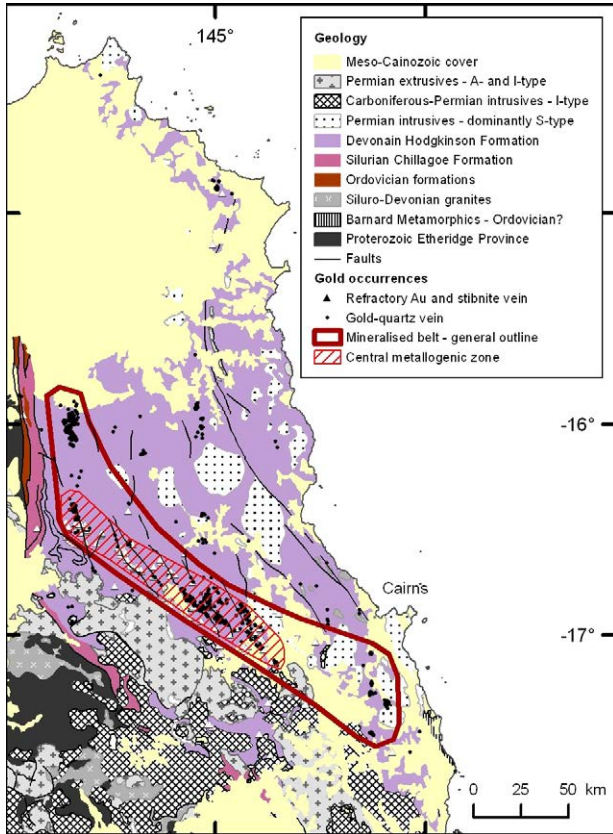


Figure 1. Regional geology and orogenic gold mineralisation in the Hodgkinson Province

2.2 Orogenic gold mineralisation

Three distinct styles of orogenic gold deposits are present in the region. Most of the historically mined deposits are characterised by free gold (0.01 mm to >1 mm) in quartz veins, with minor pyrite and arsenopyrite (Peters et al. 1990; Garrad and Bultitude 1999). Deposits of this style jointly account for more than 11 t of gold bullion production.

The second major deposit style is characterised by the prevalence of refractory, or ultra-fine (usually <10 µm), gold in sulphide grains (arsenopyrite and pyrite), which occur in thin veins and stockworks or disseminated in host turbidites. Total identified endowment includes 5 t of gold production from oxidised ores and 19 t of gold contained in remaining primary sulphidic ores. Typical gold grades of the refractory gold deposits range between 1.5 g/t and 10 g/t, mostly averaging less than 5 g/t.

The third deposit style is represented by quartz-stibnite±gold veins. They were of a limited historic significance as a source of gold, producing mostly stibnite concentrate.

The geochronology of gold mineralisation in the

region remains relatively poorly understood. In relative timing, it is generally accepted that quartz-stibnite veins post-date the main phase of gold-quartz vein mineralisation (Peters et al. 1990). Vos et al. (2007) indicated that quartz-stibnite veins also post-date the refractory gold mineralisation. The relative timing of the gold-quartz vein and refractory gold mineralisation is uncertain. The absolute geochronology remains poorly constrained as Carboniferous, with reported ages of ~340 Ma (Vos et al. 2007) and ~300 Ma (Morrison 1988), pre-dating the bulk of the felsic magmatism in the area.

3 Metallogenic and Spatial Statistical Analysis

3.1 Spatial distribution of gold deposits

Orogenic and associated alluvial gold deposits are widely distributed throughout the province (Fig. 1). However, the bulk of primary deposits of all three mineralisation styles, including all eight known primary ore fields with >1 t of contained gold, occur in a relatively narrow belt in the south-west and west of the province. Its particularly well mineralised central part (~130 km long and <20 km wide, Fig. 1) contains ~95% of the total endowment of the refractory gold and quartz-stibnite±gold deposits identified to date in the 20,000 km² of exposed Siluro-Devonian volcano-sedimentary rocks of the Hodgkinson Province. This metallogenic zone, which closely corresponds to the historic Hodgkinson Goldfield, trends at a low angle to most of the surface geological structures and its likely geological controls have not been previously identified.

3.2 Deep crustal heterogeneity in the south-western Hodgkinson Province

A major deep crustal discontinuity can be inferred in the south-western Hodgkinson Province on the basis of properties of Carboniferous to Permian felsic magmatic rocks, supported by a trend in regional metamorphic grades.

Granite geochemistry and geochronology has long been used to infer the composition of the deep crust and regional geological evolution. In particular, boundaries between domains characterised by dominant I-type or S-type magmatism have been interpreted to represent major geological boundaries in the deep crust (Chappell et al. 1988), which often do not correspond to any distinct geological structures at the surface.

The south-western part of the Hodgkinson Province experienced intrusive I-type magmatism in the late Carboniferous (~320-300 Ma), followed by extensive shallow intrusive and extrusive I- and A-type magmatism in the early to middle Permian (~290-275 Ma) – similar to the adjacent Etheridge Province (the Herberton and Tate Igneous subprovinces, Champion and Bultitude 2013a). In contrast, the rest of the Hodgkinson Province (the Daintree Igneous Subprovince) was only affected by the middle to late Permian (~280-260 Ma) predominantly S-type intrusive magmatism, which strongly distinguishes that area from

the rest of the Kennedy Igneous Association of north Queensland (Champion and Bultitude 2013a). Geochemical evidence suggests that crustal source rocks of the granites of the Daintree Subprovince were distinctly different from those of the Herberton and Tate subprovinces (Champion and Chappell 1992; Champion and Bultitude 2013b). In particular, granites of the Daintree Subprovince are characterised by more isotopically 'juvenile' signature ($\epsilon\text{Nd}(t) = -2.3 - -6.7$, depleted mantle model age $T_{2\text{DM}} = 1.0 - 1.5$ Ga) compared to more isotopically 'evolved' Carboniferous I-type granites in the south-western Hodgkinson Province ($\epsilon\text{Nd}(t) = -7 - -9.7$, $T_{2\text{DM}} = 1.6 - 1.8$ Ga) and the Etheridge Province, with $\epsilon\text{Nd}(t) = -8.8 - -12.5$, $T_{2\text{DM}} = 1.6 - 2.0$ Ga (Champion and Bultitude 2013a, b), as illustrated on Figure 2.

The boundary between the Daintree and Herberton igneous subprovinces, as defined by Champion and Bultitude (2013a), is almost identical to the regional metamorphic zone boundary between the sub-greenschist facies in the western and south-western Hodgkinson Province and the greenschist facies in the rest of the province as defined by Bain and Draper (1997) (Fig. 2). This close spatial association suggests that both boundaries may be related to the same regional geological phenomenon. However, they do not apparently correspond to any recognised surface geological feature.

The spatial patterns of the granite geochemistry and regional metamorphism are consistent with the deep seismic interpretation indicating that the Proterozoic Etheridge Province underlies the south-western Hodgkinson Province in the middle crust (Fig. 6b in Korsch et al. 2012; Henderson et al. 2013). The igneous subprovince and metamorphic zone boundaries probably represent the eastern extent of the geological 'zone of influence' of this older subsurface crustal block.

3.3 Regional controls of the orogenic gold mineralisation in the Hodgkinson Province

On the province, or metallogenic belt, scale, the total gold endowment of the Hodgkinson Province is probably controlled by its nature as part of an orogen completely underlain by thick older continental crust. This broad crustal architecture limited the volume of hydrous Siluro-Devonian volcano-sedimentary rocks in the middle crust – the most likely source of auriferous fluids for the orogenic gold mineral systems in the province, thus limiting its ultimate gold endowment. A lack of any deep crustal-scale faults also limited a possibility of a direct focused material or energy input from the mantle or lower crust. The broad spatial heterogeneity of the volume of the inferred source rocks within the province, thinning to <5 km towards the province margins as suggested by gravity modelling, is likely to be a reason for the absence of any significant gold mineralisation within ~20 km from the margins. However, the province-scale considerations fail to adequately account for the prominent clustering of orogenic gold mineralisation in the south-west.

The Hodgkinson metallogenic zone in the south-west displays a close spatial association with the inferred sub-

surface boundary of the Etheridge crust. More than 85% of all primary gold occurrences recorded in the province, including all 8 ore fields with >1 t contained gold and all identified refractory gold deposits, lie within 16 km from the approximate position of the boundary, indicating the strongest recognised metallogenic zone-scale control on gold mineralisation within the province.

Proximity to and geometry of major faults also appear to be relatively strong mineralisation controls. However, while segments of some major faults host significant mineralisation within the metallogenic zone, they remain barren or only poorly mineralised outside the zone, sometimes for >100 km. They can only be considered as more local ore field-scale controls within the province.

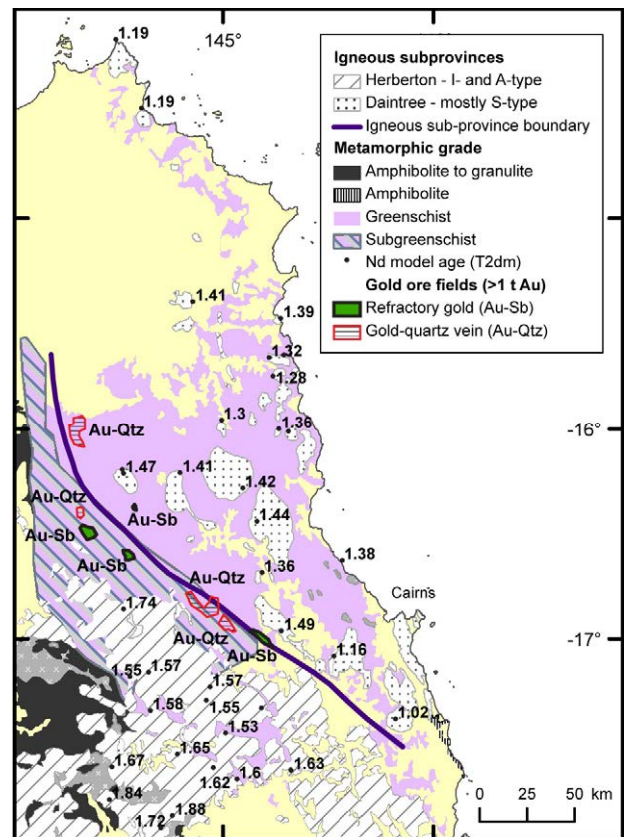


Figure 2. Regional metamorphic grades, igneous geochemistry and significant orogenic gold ore fields in the Hodgkinson Province

4 Discussion

Results of the broad metallogenic analysis suggest that crustal-scale geological features, with only subtle expressions in traditional geological datasets, act as strong metallogenic zone-scale controls on the orogenic gold mineral systems in the Hodgkinson Province. The exact mechanism by which the margin of the Paleo-Proterozoic crustal block in the middle crust affected the mineral systems remains unclear. The margin probably represents an even more fundamental lithospheric-scale heterogeneity of the Paleo-Proterozoic continental margin, which affected the initial development of all the younger orogens (including the Hodgkinson Province)

and focused the subsequent Permo-Carboniferous tectonic, magmatic and thermal events. A combination of all these factors contributed to the formation of a discrete orogenic gold metallogenic zone within a much larger metallogenic province.

Similar deep crustal heterogeneities probably acted as major metallogenic controls in other orogenic gold provinces. One likely analogue is the inferred western edge of the Selwyn Block in central Victoria, Australia. The Selwyn Block of the Proterozoic (?) continental crust underlies the eastern half of the Western Lachlan Orogen (Cayley et al. 2011). Its inferred western margin, oblique to the surface regional geological structures, is marked by a transition from greenschist facies rocks intruded by Early Devonian I-type granites to its west to sub-greenschist facies rocks intruded by Late Devonian S- and I-type granites to the east. This deep crustal margin closely corresponds to a mineralised trend defined by several of the largest ore fields in the region (Wilson et al., 2009; Lisitsin and Rawling 2011; Hronsky et al. 2012).

Metallogenic zone-scale controls related to deep crustal geological features are also probable in the Charters Towers region in north Queensland, Australia. A regional E-W trending structural zone has been considered a major control of the Devonian Charters Towers goldfield (>200 t Au) (Hutton et al. 1994; Kreuzer et al. 2007). It is likely to represent a crustal-scale fault identified in the middle to lower crust by deep seismic data (Korsch et al. 2012). There are also subtle indications of an approximately N-S trending deep crustal boundary in the vicinity of Charters Towers and the Permian Mt Leyshon intrusion-related gold deposit. Granites to the west are geochemically similar to the granites of the Proterozoic Etheridge Province. They are characterised by $\epsilon\text{Nd}(t) < -9$ and $T_{2\text{DM}} > 1.8$ Ga indicating a significant contribution of isotopically evolved crust. In contrast, the granites to the east are geochemically different, with much more 'juvenile' isotopic signatures, mostly with $\epsilon\text{Nd}(t) > -2$ and $T_{2\text{DM}} < 1.2$ Ga (Hutton 2011; Henderson et al. 2013; Champion and Bultitude 2013a). This may indicate that the Paleo-Proterozoic crust underlying the western Charters Towers province (Hutton, 2011) extends as far east as Charters Towers and Mount Leyshon. The geological and metallogenic significance of this inferred deep crustal discontinuity requires further investigation.

Regional to local geological features traditionally represented on geological maps and investigated by most deposit-scale studies (faults, folds, lithological and stratigraphic units) are typical mineralisation controls on the deposit to ore field scale. However, they often inadequately discriminate between metallogenic zones and poorly mineralised parts of provinces at larger scales.

Crustal-scale geological elements, which are not limited to major faults, often act as critical controls on orogenic gold mineral systems. Boundaries of older continental blocks extending under younger orogens in the deep crust can control the distribution of orogenic gold deposits, sometimes defining distinct richly endowed metallogenic zones. Positions of such deep crustal boundaries in some cases can only be inferred on

the basis of subtle indirect evidence, such as significant changes of magmatism, metamorphism and geophysical fields with no apparent relationships to the surface geology.

References

- Bain JHC and Draper JJ (Compilers) (1997) Atlas of North Queensland Geology 1:3 Million Scale. AGSO, Dep of Primary Industry and Energy and Geol Surv of Qld.
- Cayley RA, Korsch RJ, Moore DH et al (2011) Crustal architecture of central Victoria: results from the 2006 deep crustal reflection seismic survey. *Aust J Earth Sci* 58:113-156
- Champion DC, Bultitude RJ (2013a) Kennedy Igneous Association. In: Jell PA (Ed), *Geology of Queensland*. Geol Surv of Qld, Brisbane:473-514
- Champion DC, Bultitude RJ (2013b) The geochemical and Sr-Nd isotopic characteristics of Paleozoic fractionated S-types granites of north Queensland: Implications for S-type granite petrogenesis. *Lithos* 162-163:37-56
- Champion DC, Chappell BW (1992) Petrogenesis of felsic I-type granites: an example from northern Queensland. *Transactions of the Royal Soc of Edinburgh: Earth Sci* 83:115-126
- Chappell BW, White AJR, Hine R (1988) Granite provinces and basement terranes in the Lachlan Fold Belt, southeastern Australia. *Aust J Earth Sci* 35:505-521
- Garrad PD, Bultitude RJ (1999) Geology, mining history and mineralisation assessment of the Hodgkinson and Kennedy Provinces, Cairns Region, North Queensland. *Qld Minerals and Energy Review Series*. Dep of Mines and Energy, Qld. 305 p
- Henderson RA, Donchak PJT, Withnall IW (2013) Chapter 4: Mossman Orogen. In: Jell PA (Ed), *Geology of Queensland*. Geol Surv of Qld, Brisbane:231-314
- Hronsky JMA, Groves DI, Louks RR, Begg GC (2012) A unified model for gold mineralisation in accretionary orogens and implications for regional-scale exploration targeting methods. *Miner Deposita* 47:339-358
- Hutton LJ, Rienks IP, Tenison Woods KL, Hartley JS, Crouch SBS (1994) Geology of the Ravenswood Batholith, north Queensland. *Qld Geol Record* 1994/4, Geol Surv of Qld, Brisbane
- Hutton LJ (2011) Petrogenesis of Palaeozoic granites – northeastern Australia. VDM Verlag Dr Müller, Saarbrücken
- Korsch RJ, Huston DL, Henderson RA et al (2012) Crustal architecture and geodynamics of North Queensland, Australia: Insights from deep seismic reflection profiling. *Tectonophysics* 572-573:76-99
- Kreuzer OP, Blenkinsop TG, Morrison RJ, Peters SG (2007) Ore controls in the Charters Towers goldfield, NE Australia: Constraints from geological, geophysical and numerical analyses. *Ore Geol Rev* 32:37-80
- Lisitsin V, Rawling T (2011) Regional prospectivity analysis of orogenic gold mineral systems in central Victoria, Australia. In: *Proceedings of the 11th biennial SGA meeting of the Society for Geology Applied to Mineral Deposits*
- Morrison GW (1988) Palaeozoic gold deposits of northeast Queensland. In: Morrison GW (Ed), *Epithermal and porphyry style gold deposits in north Queensland*. James Cook University of N Qld Econ Geol Res Unit Contrib 29:11-21
- Peters SG, Golding SD, Dowling K (1990) Melange- and sediment-hosted gold-quartz veins, Hodgkinson Goldfield, Queensland, Australia. *Econ Geol* 85:312-327
- Vos IMA, Bierlein FP, Phillips D (2007) The Palaeozoic tectono-metallogenic evolution of the northern Tasman Fold Belt System, Australia: interplay of subduction rollback and accretion. *Ore Geol Rev* 30:277-296
- Wilson CJL, McKnight SW, Dugdale AL et al (2009) Illite crystallinity and the b-spacing values of white micas and their implications for gold mineralisation in the Lachlan Orogen. *Aust J Earth Sci* 56:1143-1164

Depth variation characteristics at the Carruagem orebody, Archean BIF-hosted Lamego gold deposit, Quadrilátero Ferrífero, Brazil

L. M. Lobato, B. S. Martins, C. A. Rosière, R. C. Figueiredo e Silva, A. M. Victória.

Departamento de Geologia, Universidade Federal de Minas Gerais, Av. Antônio Carlos 6627, Pampulha, 31270-901, Belo Horizonte, Minas Gerais, Brazil

L. H. A. Lemos, F. L. S. P. Villanova, L. F. S. Amaral.

AngloGold Ashanti Córrego do Sítio Mineração S/A, Mina do Lamego, Sabará, Minas Gerais

Abstract. The Lamego orogenic gold deposit is exploited underground by AngloGold Ashanti Córrego do Sítio Mineração S/A, and is located in Sabará, Minas Gerais, Brazil. It is hosted in the Archean Rio das Velhas greenstone belt, Quadrilátero Ferrífero region. Underground geological and structural mapping at a scale of 1:100 was undertaken in levels 1, 2, and 5.1 of the Carruagem orebody. From bottom to top, the rock sequence is metabasalt, banded iron formation (BIF that is interfingered with metachert), carbonaceous and sericitic phyllite, and zones of silicification with smoky and milky quartz occupying spaces indiscriminately along the top of the whole sequence down to the contact with the carbonaceous phyllite. Progressive ductile deformation events D_1 - D_2 are followed by a D_3 ductile-brittle event. With increasing depth, there are striking lithological and structural variations. Whereas the BIF thickens, the silicification zones tend to be narrower and more constricted. The structural variations are represented by the increase in the abundance of folds in the BIF and smoothing in the dip of the structure.

Keywords: Rio das Velhas Greenstone Belt, Lamego deposit, Quadrilátero Ferrífero, orogenic gold, structural control, pinch-and-swell

1 Introduction

In the Quadrilátero Ferrífero (QF) region, Minas Gerais, Brazil, gold mineralization is mainly hosted in the Rio das Velhas metavolcano-sedimentary greenstone belt rocks. It has an estimated production of ~30 Moz of gold (Goldfarb et al., 2001). The QF ($20^{\circ}15'$ and $43^{\circ}30'$) covers an area of approx. 7000 km² in the southern of the São Francisco Craton (Almeida, 1967; Dorr, 1969; Almeida and Hasui, 1984). Proterozoic cover includes the Minas and Espinhaço Supergroups (Fig. 1).

The Lamego deposit is located near the town of Sabará (Fig. 1), and is one of the Rio das Velhas greenstone belt gold deposits (Sales, 1998, Martins et al., 2011).

2 Geology of the Lamego gold deposit

From bottom to top, the concordant lithostratigraphic sequence at Lamego is metabasalt, banded iron formation (BIF) that is interfingered with metachert, and carbonaceous and sericitic phyllites. Zones of silicification, characterized by smoky and milky quartz, occupy spaces in open fractures and vugs indiscriminately along the whole sequence down to the

contact with the carbonaceous phyllite. They constitute irregular masses that invade these rocks, locally exhibiting brecciated and pinch-and-swell structures.

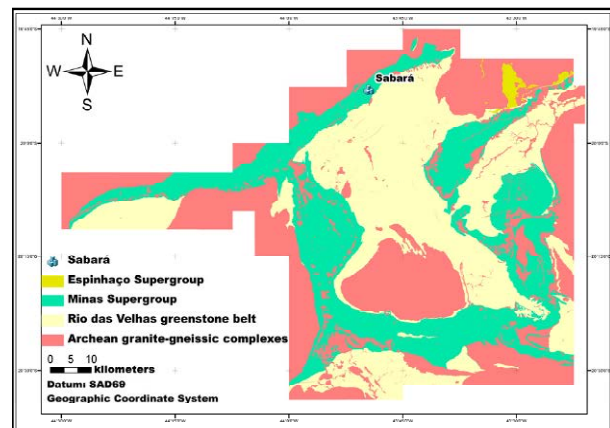


Figure 1: Simplified geological map of the QF region showing the location of the town of Sabará, where the Lamego gold deposit is located (modified after Baltazar et al., 2005).

The structure at Lamego can be characterized as a type-2 Ramsay (1967) interference pattern (Fig. 2). The thick hinge zone corresponds to the Cabeça de Pedra orebody (120/25 plunge, Fig. 2), the Arco da Velha orebody (105/25 plunge) is the normal flank, the Queimada orebody (102/29 plunge) represents the inverted flanks, and the Carruagem orebody (95/22 plunge) represents the intersection of the normal and inverted flanks. Carruagem is related to the existence of an oblique-ramp transpressive zone. On the other hand, the structures at the Queimada orebody are related to a frontal ramp, whereas the Cabeça de Pedra orebody would be the fold closure. The main structure at Lamego encompasses a penetrative S_2 foliation.

2.1 Petrography of the mineralization

The Lamego mineralization is mainly hosted by a replacement-style, sulfide-rich BIF. There is transition between pyrite (arsenian) to arsenopyrite, and this is the principal stage of gold precipitation (Fig. 3 a, b).

Silicification resulted in three quartz generations, which are macroscopically and petrographically distinct. They are all present in mineralized BIF: (i) deformed, coarse-grained smoky quartz that is rich in fluid inclusions, and occurs as irregular masses, both concordant and discordant, within the mineralized zones;

(ii) fine-grained, granoblastic, white and milky quartz, formed from recrystallization of smoky quartz, and (iii) milky quartz, particularly in fault zones cutting across the former two generations (Fig. 3c).

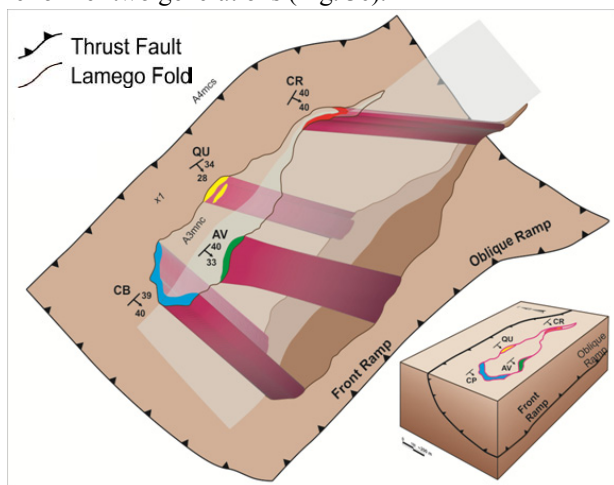


Figure 2: Sketch of the Lamego mine with the respective orebodies (Martins, 2011): QM – Queimada, AV – Arco da Velha, CB – Cabeça de Pedra, and CR – Carruagem.

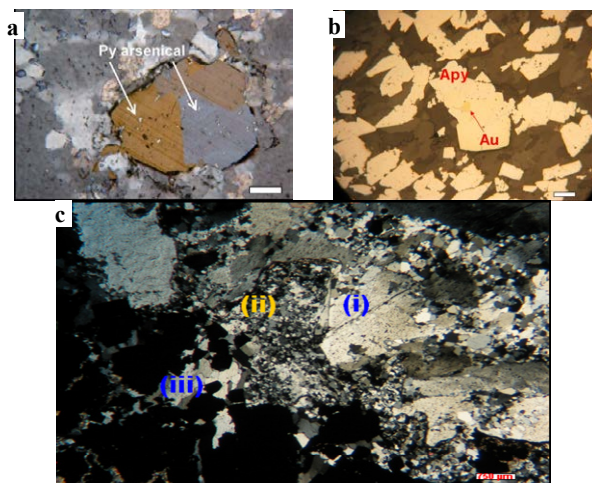


Figure 3: Petrography of the mineralized zones: (a) transition between pyrite (arsenian) to arsenopyrite (reflected light, uncrossed nicols; scale bar 200 μ m), (b) gold associated with arsenopyrite (transmitted light, crossed nicols; scale bar 400 μ m), (c) three generations of quartz.

2.2 Geological maps of the Carruagem orebody

The Carruagem orebody is located in the NE of the Lamego fold. It carries the highest gold grades at Lamego, and contains 62% of the reserves. From levels 1 to 5.1, mineralization is predominantly associated with smoky quartz. From levels 5.1 to 8, the BIF thickens, and the amount of gold increases proportionately.

The underground lithological and structural mapping at a 1:100 scale of the Carruagem orebody, on levels 1, 2, and 5.1, shows significant geological variations with depth, as is summarized below. Level 1: (a) depth of 200 m (800 m altitude) with respect to surface; (b) a NE-SW orientation; (c) BIF with a thickness of as much as 10 m totaling 15.331,22 m²; (d) plan length of 440 m; (e) predominance of silicification zones in the NE part of the map; (f) predominance of BIF in the NW part of the map; (g) metabasalts in the center of the map; and (h)

fault zones between metabasalts and carbonaceous phyllites (Fig. 4).

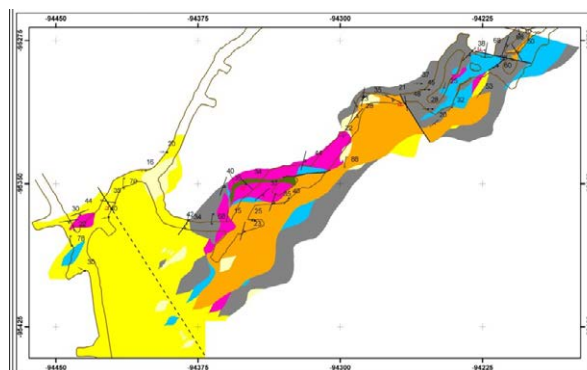


Figure 4: Geological map of the Carruagem orebody level 1. Orange: metabasalt; pink: BIF(±metachert); blue: smoky quartz zones; cream to off white: milky quartz; gray: carbonaceous phyllite; yellow: sericite phyllite.

Level 2: (a) depth of 250 m (750 m altitude) with respect to surface; (b) a NE-SW orientation; (c) BIF with a thickness of as much as 12 m totaling 27.264,84 m²; (d) plan length of 470 m; (e) predominance of silicification zones in the NE part of the map with some BIF; (f) predominance of BIF in the center of the map; (g) metabasalts in the SW and SE part of the map; and (h) fault zones between metabasalts and carbonaceous phyllite (Fig. 5).

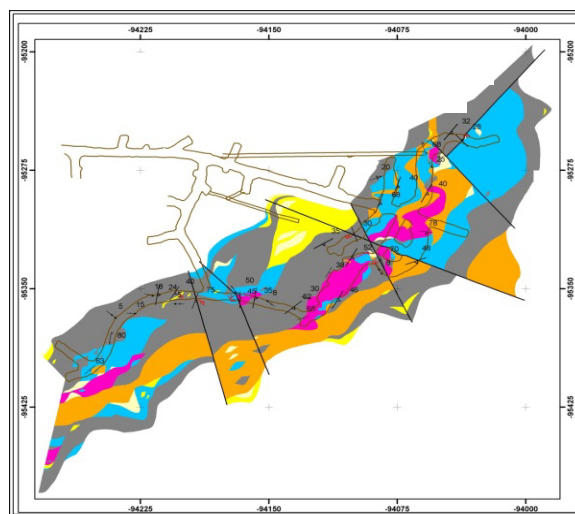


Figure 5: Geological map of the Carruagem orebody, level 2. Legend according to Figure 4.

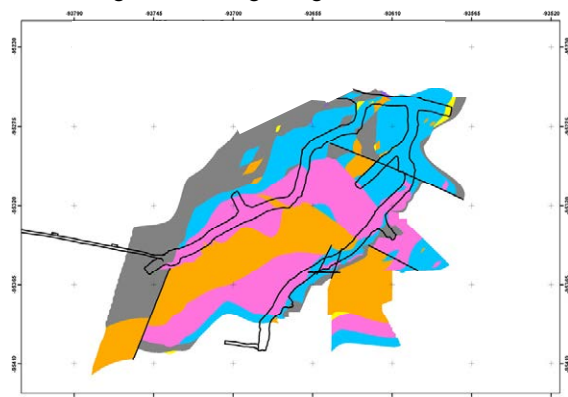


Figure 6: Geological map of the Carruagem orebody, level 5.1. Legend according to Figure 4.

Level 5.1: (a) depth of 420 m from the surface (580 m altitude); (b) NE-SW orientation; (c) BIF with a thickness of as much as 10 m totaling 5.219,78 m², (d) plan length of 240 m; (e) silicification zones in the NE part of the map; (f) predominance of BIF in the SE and SW; (g) metabasalts in the SW; and (h) fault zone between metabasalts, carbonaceous phyllite, and BIF (Fig. 6).

2.3 Primary structures (S₀)

The planar structures (S₀) at Lamego are the compositional and gradational banding.

For all mapped levels, the trend of S₀ dips mainly to the SE. At the Carruagem orebody, on levels 1 and 2, S₀ concentrates in the SE (Figs. 7 a, b), with a modal orientation of 138/38. However, on level 5.1, there is a great circle dispersion with an 134/35 axis orientation (Fig. 7 c).

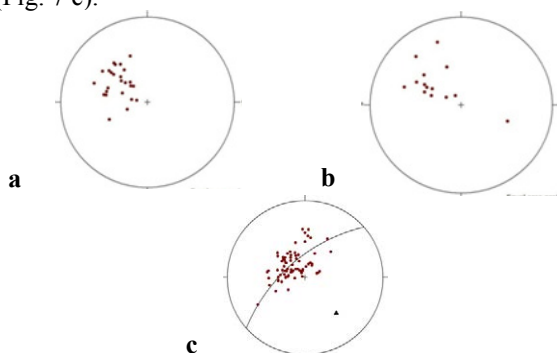


Figure 7: Stereographic projections of bedding (S₀) for the Carruagem orebody (a) level 1; (b) level 2; (c) level 5.1.

2.4 Foliation S₁₋₂, lineation L₁₋₂ and folds F₂

The S₁₋₂ foliation is parallel or sub-parallel to the bedding planes (S₀). These structures are mainly present in the carbonaceous phyllite and the hydrothermally altered metabasalts.

The L₁₋₂ lineation is parallel to the: (i) F₂ fold axes, (ii) Lm₁₋₂ mineral lineation, mainly quartz and carbonate, (iii) Le₁₋₂ mineral stretching lineation, and (iv) striations.

Figure 8 shows the variation for the foliation on levels 1, 2, and 5.1 at the Carruagem orebody. It varies from the SE to the SW, with axes 164/28, 160/32, and 195/18, respectively, for levels 1, 2, and 5.1 (Figs. 8 a, b, c). Lineations for levels 1 and 2 are dispersed from ESE to SSE, with an orientation of 135/38 (Figs. 8 a, b), whereas for level 5.1 they concentrate in the SE quarter (Figs. 8 c).

Folds are not always well visualized for levels 1 and 2, and are better defined by the bedding plane S₀ and the S₁₋₂ foliation. Where present, they are always associated with phyllites and metavolcanic rocks, and rarely with BIF. However, folds are readily seen in BIF on level 5.1.

For levels 1 and 2, the attitudes of the fold axes are concentrated in the SE, plunging close to 25°, parallel to sub-parallel to the mineral lineation L₁₋₂. For level 5.1, fold axes are concentrated in the SE, dipping about 18° (Fig. 8d).

2.5 Crenulation cleavage (S₃), lineations (L₃), and folds (F₃)

Other structures in the Lamego deposit are the (i) S₃ crenulation cleavage, (ii) L₃ mineral lineation, distributed on the N-S planes that coincide with the S₃ crenulation cleavage, and (iii) F₃ folds, which are open and best identified in the carbonaceous phyllite.

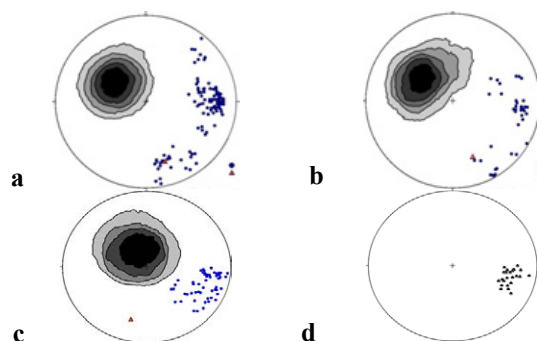


Figure 8: Stereographic projections of the S₁₋₂ foliation and L₁₋₂ lineation, Carruagem orebody. (a) level 1; (b) level 2; (c) level 5.1. The stereographic projection of the fold axes for level 5.1 is shown in (d) for comparison.

For all three levels, the L₃ pole figure depicts a N-S girdle coincident with the S₃ foliation plane (Fig. 9 d). Orientations are 115/87, 115/85, and 093/89, respectively, for levels 1, 2, and 5.1 (Figs. 9 a, b, c).

The F₃ fold axes plunge consistently to the south, dipping on average at about 10° (Fig. 9 d). The axial planes are N-S and coincident with the S₃ crenulation cleavage (Fig. 9 e).

2.6 Faults and shear zones

Shear zones are mapped in all schistose layers and lithological contacts on centimeter to meter scale, with the development of S-C structures that indicate shearing towards the NW. Faults are restricted to the carbonaceous phyllite and dip 30° to 90°, with a consistent NW sense of reverse slip.

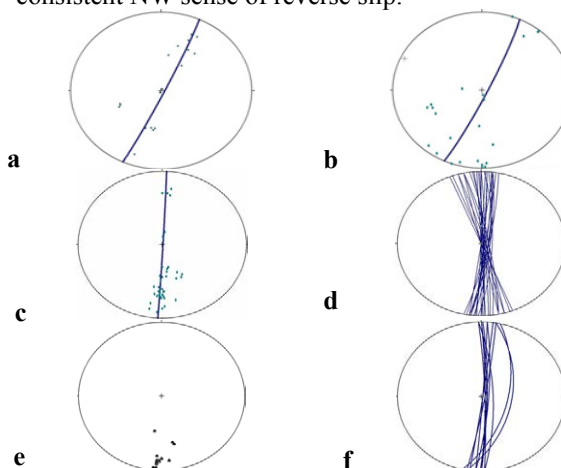


Figure 9: Stereographic projections of the L₃ lineations, Carruagem orebody. (a) level 1, (b) level 2, (c) level 5.1. (d) Stereographic projection of the S₃ crenulation; (e) Stereographic projection of the F₃ fold axes; (f) Axial planes of the F₃ folds.

In general, pole figures of the fault planes typically comprise SW-dipping girdles that are perpendicular to the fold axes (Figs. 10 a, b, c). Such fault plane distribution is similar to that of foliation S₁₋₂. This is not

the case for Carruagem level 1, where the planes are not distributed in a great circle. As for level 2, a large number of faults has a direction to NE, dipping SW, whereas for level 5.1 faults are concentrated in the SE.

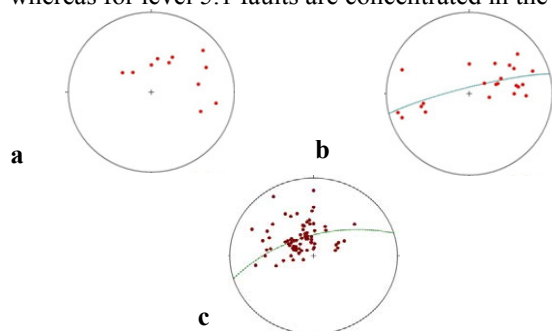


Figure 10: Stereographic projections of faults and shear zones for Carruagem orebody: (a) level 1, (b) level 2 and (c) level 5.1.

3 Conclusions

The lithological mapping of the Carruagem orebody allows for some important conclusions regarding a series of geological depth variations that exist in the BIF-hosted Lamego gold deposit.

There is a large volume of hydrothermal silicification, smoky and milky quartz, and lesser amounts of BIF in levels 1 and 2, compared to level 5.1. In contrast, BIF is relatively more abundant and thicker, and strongly folded and sheared in level 5.1.

Three deformation events affected the rocks at Lamego. The D_1 - D_2 , deformation event is progressive, ductile, and formed folds, lineation, and shear zones. These are overprinted by faults and folds developed during the ductile-brittle D_3 . The folds developed during D_1 - D_2 and D_3 are observed in all levels, but are best exposed in level 5.1.

The F_2 fold axes plunge (Fig. 8d) to the same quadrant of the lineation L_2 (Fig. 8 a, b, c). In level 5.1 (Fig. 8d), these axes behave similarly to the lineation L_2 , but are constrained in quadrant SE with a modal of 98/25.

One of the most striking depth variations in the Carruagem orebody is probably related to the existence of an oblique-ramp transpressive zone. In addition to the increased presence of folds, with depth it is deduced that the structure is becoming shallower, as can be observed in the stereographic projections represented on Figures 7, to 10.

The orientation of the L_3 lineation is variable in the different levels. For levels 1 and 2, L_3 shows similar girdle distributions with orientation 115/87 and 115/85, respectively. For level 5.1, the modal value is similar to that of the S_3 crenulation (093/89).

The pole figures of faults depict a girdle (great circle) that indicates a $h0l$ orientation for these structures, with intersection parallel to the folds axis.

Other findings from our results are: (i) all mapped faults have a right-lateral and thrust slip; (ii) mineral lineations are poorly represented in the ore zones; (iii) pinch-and-swell structures are well preserved from the centimeter to the decameter scales; (iv) shear zones are best developed on level 5.1; and (v) gold is associated with arsenian pyrite, similar to what is reported for the world-class, nearby BIF-hosted Cuiabá gold deposit

(Lobato et al., 2001).

Acknowledgements

This research is the result of the on-going Ph.D. thesis by the second author at the Federal University of Minas Gerais-UFMG, which is fully financed by Brazil's National Council of Technological and Scientific Development-CNPq, Vale and AngloGold Ashanti Córrego do Sítio Mineração S/A-AGA. The student's scholarship is granted by CNPq. The authors also thank AGA for their logistic support. Special thanks are due to Rodrigo Martins who has maintained his commitment to our research group throughout, and other colleagues at the Lamego site. We acknowledge the support of UFMG, CAPES, FAPEMIG and FUNDEP. LML and CAR are recipient of CNPq bursaries.

References

- Almeida FFM (1984) Origem e evolução da plataforma brasileira: Departamento Nacional da Produção Mineral. Divisão Geologia Mineral, Boletim, Rio de Janeiro 241, p 36
- Almeida FFM, Hasui Y (1984) O Pré-Cambriano do Brasil. Edgar Blücher Ltda, São Paulo
- Baltazar OF, Baars FJ, Lobato LM, Reis LB, Achtschin AB, Berni GV, Silveira VD (2005) Mapa Geológico com nota explicativa em Escala 1:50.000. In: Lobato LM, Baltazar OF, Reis LB, Achtschin AB, Baars FJ, Timbó MA, Mendonça BRV, Berni GV, Ferreira DV, Projeto Geologia do Quadrilátero Ferrífero – Integração e Correção Cartográfica em SIG. CODEMIG, Belo Horizonte
- Dorr JVN (1969) Physiographic, stratigraphic and structural development of the Quadrilátero Ferrífero, Minas Gerais, Brazil. United States Geological Survey, Professional Paper 641-A, p 115
- Goldfarb R (2001) Orogenic gold and geologic time: a global synthesis. *Ore Geo Rev* 18: 1-75
- Lobato LM, Ribeiro-Rodrigues LC, Vieira FWR (2001) Brazil's premier gold province: Part II. Geology and genesis of gold deposits in the Archean Rio das Velhas greenstone belt, Quadrilátero Ferrífero. *Mineral Deposita* 36: 249-277
- Martins BS (2011) Controle da Mineralização Aurífera de Lamego, Sabará, Quadrilátero Ferrífero, MG. Unpublished MSc dissertation, Universidade Federal de Minas Gerais, Brazil, p 330
- Martins BS, Rosière CA, Lobato LM, Figueiredo e Silva RC, Baars FJ, Tschiedel MW, Oliveira H, Penha UC (2011) Mineralization Control of the Lamego Gold Deposit, Sabará, Quadrilátero Ferrífero, Minas Gerais, Brazil. 11th Biennial Meeting SGA 2011, Let's Talk Ore Deposits, Antofagasta, Chile, pp 583-585
- Ramsay JG (1967) Folding and fracturing of rocks. McGraw-Hill Book Co, New York.
- Sales M (1998) The geological setting of the Lamego banded iron-formation-hosted gold deposit, Quadrilátero Ferrífero District, Minas Gerais-Brazil. Unpublished MS. thesis, Queen's University, Canada, p 182

Zircon multi-isotopic mapping in Wabigoon Subprovince, western Superior Craton: implications for lithospheric architecture and controls on orogenic gold mineral systems

Yong-jun Lu, T. Campbell McCuaig

Centre for Exploration Targeting, Australian Research Council Centre of Excellence for Core to Crust Fluid Systems (CCFS), School of Earth and Environment, The University of Western Australia, Crawley, WA 6009, Australia

Pete Hollings

Department of Geology, Lakehead University, 955 Oliver Road, Thunder Bay, ON P7B 5E1, Canada

Kirsty Ketchum

SRK Consulting (Canada) Inc. Suite 202 - 5204 50th Avenue, Yellowknife, NT, X1A 1E2, Canada

Robert Kerrich

Department of Geological Sciences, University of Saskatchewan, Saskatoon, SK, Canada S7N 5E2

Mark Smyk

Ontario Geological Survey, 435 James St. South, Thunder Bay, ON P7E 6S7, Canada

John Cliff

Centre for Microscopy, Characterization and Analysis, The University of Western Australia, 35 Stirling Highway, Crawley, Western Australia 6009

Leon Bagas

Centre for Exploration Targeting, Australian Research Council Centre of Excellence for Core to Crust Fluid Systems (CCFS), School of Earth and Environment, The University of Western Australia, Crawley, WA 6009, Australia

Abstract. There is pronounced spatial correlation between trans-lithospheric boundaries and the location of large mineral systems globally. A study undertaken in the Wabigoon Subprovince in western Superior Craton of Canada is testing the hypothesis that deep lithospheric boundaries specifically control the distribution of orogenic gold deposits. Zircon Hf-O isotopes indicate that supracrustal recycling and juvenile crustal growth in the Wabigoon subprovince occurred at ca. 2.7 Ga in the orogenic phase. By contrast, proceeding 3.2-2.9 Ga felsic magmatism represents reworking of old crust without a supracrustal input. There are thus fundamental differences in crustal evolution pre- and post-2.7 Ga in the Wabigoon subprovince and the gold mineralization was coeval with the post-2.7 Ga magmatism. Zircon isotopic mapping images lithospheric boundaries which were unrecognized previously. The newly defined lithospheric boundaries show strong spatial correlation with orogenic gold deposits, indicating that lithospheric boundaries are important in controlling the location of the deposits.

Keywords. Zircon, SHRIMP U-Pb, Hf-O isotopes, Wabigoon Subprovince, western Superior Craton, orogenic gold deposit

1 Introduction

Recent studies in the Yilgarn Craton of Western Australia demonstrate that multi-isotopic maps are a powerful tool for mapping crustal growth and imaging lithospheric blocks of different age that are interpreted as paleocraton margins. Such maps are based on *in-situ*

zircon U-Pb and Lu-Hf analyses that are combined with whole-rock Sm-Nd data. As the lithospheric boundaries sometimes cannot be seen in modern seismic images, the isotopic mapping is instead a form of paleogeophysics for imaging paleocraton margins.

It has been shown that there is a strong spatial correlation between lithospheric boundaries and the concentration of a variety of mineral deposit types (e.g. Champion and Cassidy 2007; McCuaig et al. 2010; Begg et al. 2010; Mole et al. 2012). The interpretation is that these isotopic boundaries mark lithosphere-scale structures that control magma and fluid flux, and thus the location of large mineral systems through time. However, the only available case studies in Archean terranes are from the Abitibi belt (Calvert and Ludden 1999; Kerrich and Ludden 2000) and the Yilgarn Craton, and the latter is only focused in the center of the craton. Therefore, it is critical to test this hypothesis in other parts of the world.

A comparative study has been started in the Wabigoon Subprovince (WS) in the western part of the Superior Craton of Canada to complement the existing results obtained from the Yilgarn Craton. The gold deposits in WS are orogenic type with gold occurring mainly in quartz-carbonate veins in shear zones. These gold deposits formed late in the evolution of the host terranes, typically at approximately 2.7 Ga (Percival et al. 2006; Smyk and Franklin 2007).

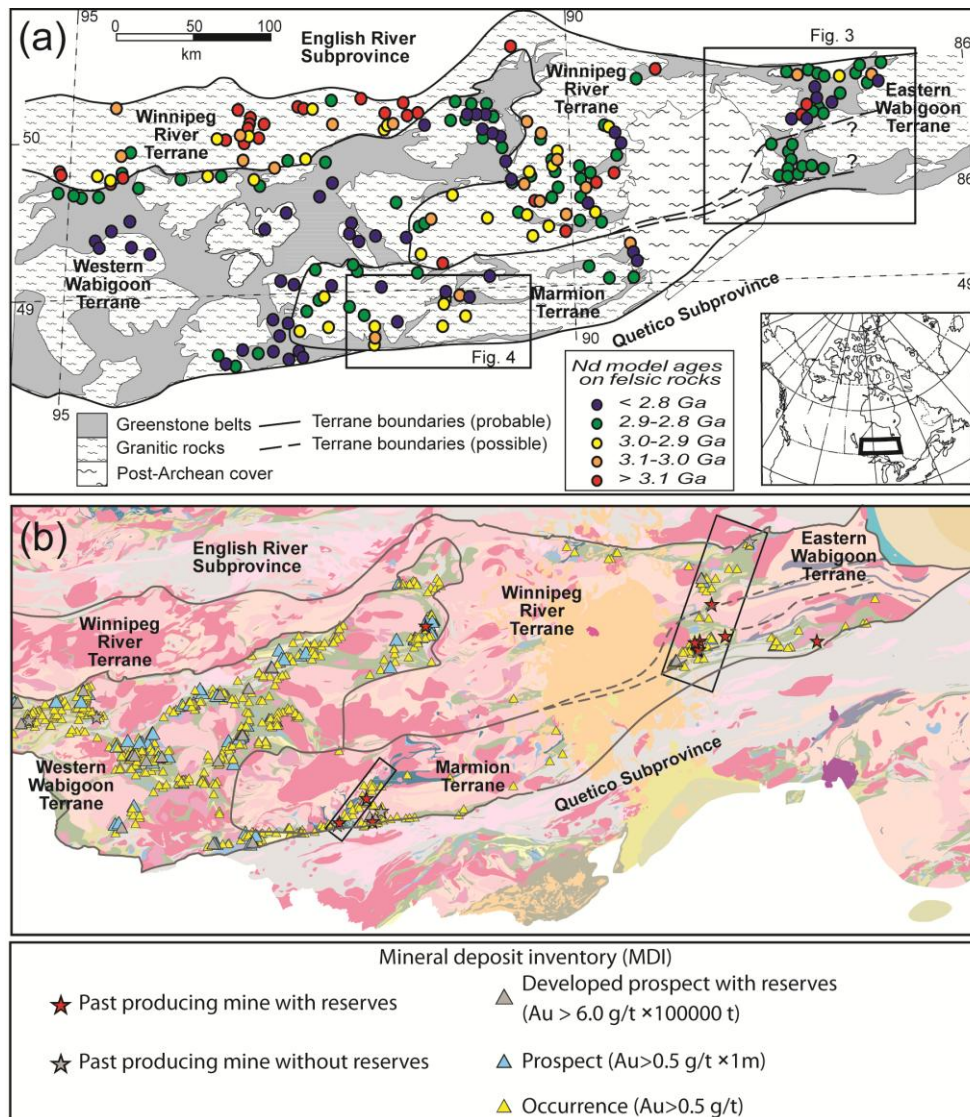


Figure 1. (a) Simplified geological map of the Wabigoon Subprovince, western Superior Craton, Canada. The inset shows the location of the study area. The subprovince has been divided into the Winnipeg River, Marmion, Western Wabigoon, and Eastern Wabigoon terranes based on whole-rock Nd isotope data (Tomlinson et al., 2004); (b) the location of gold mineralization. Two rectangles highlight the two gold camps in the eastern Wabigoon and Marmion terranes, respectively. The terrane boundaries in (b) are the same as in (a).

2 Method

Zircon grains were embedded in epoxy resin, polished to one-half their thickness, and coated with gold, then imaged by cathodoluminescence (CL) prior to SHRIMP (U-Th)-Pb dating at the John de Laeter Centre for Mass Spectrometry, Curtin University. After SHRIMP dating, O isotope analyses were conducted close to the SHRIMP pit within a domain of uniform CL texture on the same zircon by Cameca IMS 1280 ion microprobe at the Centre for Microscopy, Characterisation and Analysis, The University of Western Australia. Finally, the Hf isotope ratios were acquired with the New Wave/Merchantek UP-213 laser-ablation microprobe attached to a Nu Plasma multicollector ICP-MS at GEMOC (Macquarie University), typically by directly ablating the pit generated by the preceding O analysis.

3 Results and discussion

3.1 Crustal growth and evolution

The WS can be subdivided into four terranes based on the whole-rock Sm-Nd isotopic data (Fig. 1a; Tomlinson et al. 2004). Importantly, these isotopically defined boundaries are not readily imaged in seismic transects (Musacchio et al. 2004), and are interpreted to represent steep boundaries in the deepest crust and mantle lithosphere, i.e. in the source regions of the magmas responsible for the intrusions within the WS.

Zircon oxygen and hafnium isotopic data from samples collected in the WS are presented in Figure 2. Samples from felsic plutons (tonalite, granodiorite, monzogranite, and monzonite) and volcanic rocks (rhyolite and dacite) in the Eastern Wabigoon, Winnipeg River, and Marmion terranes show a similar temporal evolution of $\delta^{18}\text{O}$ values (Fig. 2a). In the period between 3252 and 2716 Ma, both felsic plutons and volcanic rocks have mantle-like $\delta^{18}\text{O}$ values of 5.3-5.9‰. From 2715 to 2682 Ma, the $\delta^{18}\text{O}$ values rise to 6.1-7.3‰ (Fig. 2a). These oxygen data suggest that supracrustal recycling in the WS became important after ca. 2715 Ma, which was coincident with the central Superior

Orogeny at 2.71-2.70 Ga, when the juvenile Western Wabigoon terrane accreted to the Winnipeg River terrane (Percival et al. 2006).

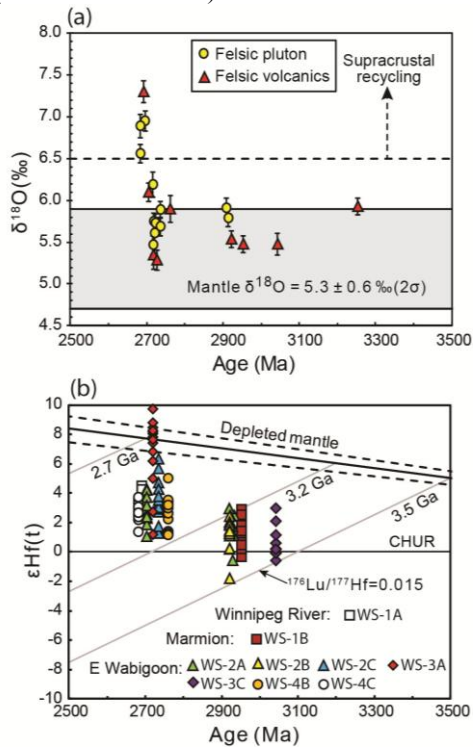


Figure 2. (a) Zircon $\delta^{18}\text{O}$ values vs age (Ma). The grey field in (a) highlights the range of $\delta^{18}\text{O}$ values of mantle zircon (Valley et al., 1998); (b) zircon $\epsilon_{\text{Hf}}(t)$ vs age (Ma). The three gray lines represent the average continental crust derived from the depleted mantle at 3.5, 3.2, and 2.7 Ga. It is noted that the samples from the Eastern Wabigoon, Winnipeg River, and Marmion terranes show similar trends in (a) as the $\delta^{18}\text{O}$ values increased at ca. 2.7 Ga.

The zircon Hf isotopes show that the 3042-2921 Ma felsic magmas in the Eastern Wabigoon and Marmion terranes were derived by reworking the 3.5-3.2 Ga crust without obvious juvenile mantle input (Fig. 2b). By contrast, felsic magmatism at 2760-2704 Ma in the Winnipeg River and Eastern Wabigoon terranes clearly involved more juvenile mantle input, as evidenced by the zircon $\epsilon_{\text{Hf}}(t)$ values close to or within a depleted mantle evolution trend (Fig. 2b).

The combination of the above zircon Hf and O isotope data suggests that supracrustal recycling and juvenile crustal growth in the WS occurred at ca. 2.7 Ga, whereas the proceeding 3.2-2.9 Ga felsic magmatism represents reworking of the crust without a supracrustal input. The zircon Hf-O difference between the 3.2-2.9 Ga and ca. 2.7 Ga magmatic events in the WS may reflect a fundamental difference in crustal evolution pre- and post-2.7 Ga. Importantly, the orogenic gold deposits in the WS were coeval with the ca. 2.7 Ga magmatism, suggesting there might be a genetic relationship between orogenic gold mineralization and juvenile crustal growth and supracrustal recycling. However, more data across the whole subprovince are necessary to confirm these trends.

3.2 Lithospheric architecture and mineral systems

The orogenic gold deposits in WS are shown in Figure 1b. It is noted that gold mineralization occurred pervasively within the WS, which is demonstrated by numerous gold occurrences and prospects. However, the most economic gold mineralization, i.e. defined by the gold mines, clusters mainly in the Eastern Wabigoon and Marmion terranes (Fig. 1b).

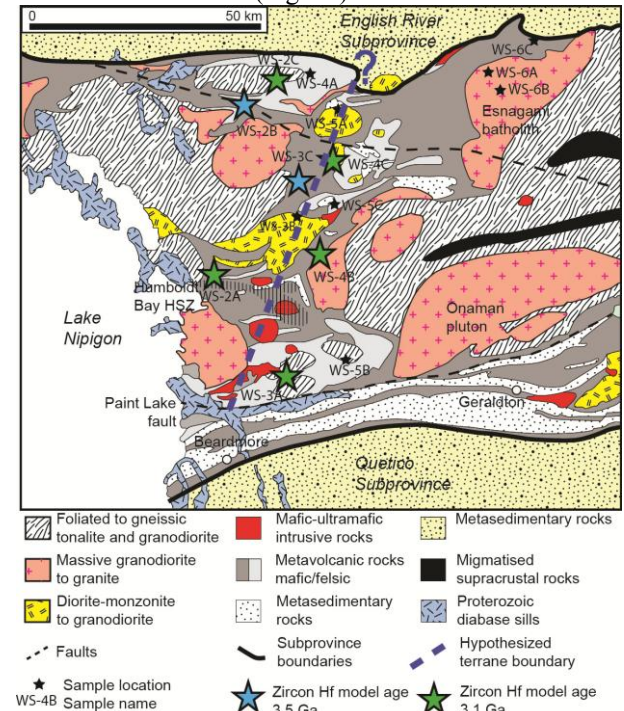


Figure 3. Geology of the eastern part of the Wabigoon Subprovince. The analyzed zircon samples are shown by blue and green stars. The thick blue dashed line marks the proposed terrane boundary, which separates the western part with older zircon Hf model ages from the eastern part with younger zircon Hf model ages. Note the distribution of the mafic-ultramafic intrusive rocks along the postulated boundary. The map is modified after Tomlinson et al. (2004).

In eastern WS, the assumed terrane boundaries based on Nd isotopes trend eastward, whereas the gold deposits form a zone trending NE (Fig. 1b). This discrepancy suggests that the terrane boundary may in fact trend NE (Fig. 3). Zircon Hf isotopic analyses show that samples collected west of this suggested NE-striking boundary have older Hf model ages (3.5 Ga) than those from east of the boundary (3.1 Ga), indicating that the area in the west has an older basement than the east (Fig. 3). This confirms the presence of the Winnipeg River terrane (Fig. 1a) in eastern WS, as proposed by Tomlinson et al. (2004) based on Nd model ages. The spatial distribution in zircon Hf model ages, however, suggests that the boundary in eastern WS trends NE, which is consistent with the spatial arrangement of Au deposits in the region. Moreover, mafic-ultramafic intrusive rocks are distributed along the postulated boundary, supporting the idea that this boundary was a possible lithospheric structure.

In southern WS, the gold deposits are located along the boundary between the Marmion terrane and the Quetico Subprovince, as well as along a NE-trending zone within the Marmion terrane (Fig. 1b). The NE-

trending mineralization in the Marmion terrane is coincident with a NE-striking structure and the Finlayson greenstone belt (Fig. 4). Importantly, there is a contrasting difference in magnetic anomalies on both sides of this structure within the Marmion terrane,

which indicates a major change in batholith character across this boundary. The Hammond Reef deposit with 10 M oz of Au is close to this structure, highlighting the potential importance of this inferred terrane boundary (Fig. 4).

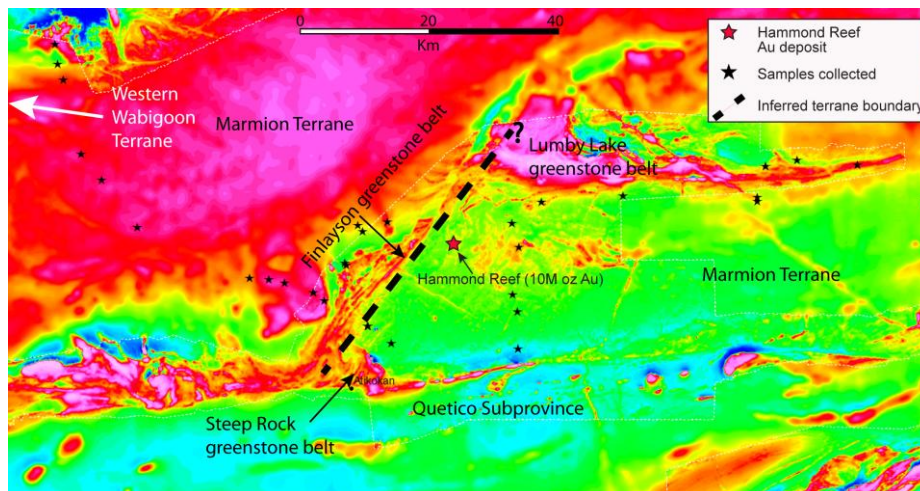


Figure 4. Residual total field magnetic image of the Atikokan area. Warm and cold colors represent positive and negative anomalies, respectively. The magnetic character shows a marked change in the Marmion terrane across the NE-trending Finlayson greenstone belt, which can be inferred as a terrane boundary. The Hammond Reef deposit with 10 Moz Au is located proximal to the inferred terrane boundary. However, it is noted that this magnetic image is probably only showing features down to about 20 km depth, and therefore it didn't image deep lithosphere, as opposed to the isotope data. The boundary between the Marmion and Western Wabigoon terranes is west of this map area, as indicated by the white arrow. The map is modified after Beakhouse et al. (2011).

4 Summary

Zircon Hf-O isotopes indicate that the supracrustal recycling and juvenile crustal growth in the WS mainly occurred at ca. 2.7 Ga in the orogenic phase. By contrast, the proceeding 3.2-2.9 Ga felsic magmatism mainly represents reworking of old crust without supracrustal input. This difference may suggest there was a significant change in the crustal evolution at ca. 2.7 Ga in the WS. The orogenic gold mineralization was coeval with the ca. 2.7 Ga magmatism, which suggests a possible genetic relation between gold mineralization and juvenile crustal growth and supracrustal recycling. Zircon isotopic mapping images lithospheric boundaries that were previously unrecognized. The newly defined lithospheric boundaries show strong spatial correlation with orogenic gold deposits, supporting the concept that lithospheric boundaries are important in controlling the location of orogenic gold deposits.

Acknowledgements

This project is funded by the ARC Centre for Excellence for Core to Crust Fluid Systems (CCFS). CMCA (UWA) and GEMOC (Macquarie) are thanked for O-Hf analysis. Gerry White, Robert Cundari, Mark Puumala, and Shannon Zurevinski are thanked for field assistance. Shannon Zurevinski also compiled the mineralization data in WS, which is greatly appreciated.

References

Beakhouse GP, Webb JL, Rainsford DRB, Stone D, Josey SD

- (2011) Western Wabigoon GIS synthesis-2011; Ontario Geol Sur, Miscellaneous Release-Data 280.
- Begg GC, Hronsky JAM, Arndt NT, Griffin WL, O'Reilly SY, Hayward N (2010) Lithospheric, Cratonic, and Geodynamic Setting of Ni-Cu-PGE Sulfide Deposits. *Econ Geol* 105:1057-1070.
- Calvert AJ, Ludden JN (1999) Archean continental assembly in the southeastern Superior Province of Canada. *Tectonics* 18: doi: 10.1029/1999TC900006. issn: 0278-7407.
- Champion DC, Cassidy KF (2007) An overview of the Yilgarn Craton and its crustal evolution. *Kalgoorlie 2007 abstract Volume*, pp 8-13.
- Kerrich R, Ludden J (2000) The role of fluids during formation and evolution of the southern Superior Province lithosphere: an overview. *Canadian J Earth Sci* 37: 135-164
- Kerrich R, Goldfarb RJ, Richards JP (2005) Metallogenic provinces in an evolving geodynamic framework. *Econ. Geol.* 100th Anniversary Vol: 1097-1136
- Mole DR (2012) Evaluating the lithospheric architecture of the Archean Yilgarn Craton in space and time: Implications for Komatiite volcanism and Earth evolution: unpublished PhD thesis at the University of Western Australia, 768pp.
- Musacchio G, White DJ, Asudeh I, Thomson CJ (2004) Lithospheric structure and composition of the Archean western Superior Province from seismic refraction/wide-angle reflection and gravity modelling. *J Geophys Res* 109: B03304, doi:10.1029/2003JB002427.
- Percival JA, Sanborn-Barrie M, Skulski T, Stott GM, Helmstaedt H, White DJ (2006) Tectonic evolution of the western Superior Province from NATMAP and Lithoprobe studies. *Canadian J Earth Sci*, 43: 1085-1117.
- Tomlinson KY, Stott GM, Percival JA, Stone D (2004) Basement terrane correlations and crustal recycling in the western Superior Province. *Precamb Res* 132: 245-274.
- Smyk MC, Franklin JM (2007) A synopsis of mineral deposits in the Archean and Proterozoic rocks of the Lake Nipigon Region, Thunder Bay District, Ontario. *Can. J. Earth Sci.* 44: 1041-1053.
- Valley JW, Kinny PD, Schulze DJ, Spicuzza MJ (1998) Zircon megacrysts from kimberlite: oxygen isotope variability among mantle melts: *Contrib Min Pet* 133: 1-11

Structural setting and mineralisation of the carbonate-hosted Sadiola gold deposit, Mali, West Africa.

Quentin Masurel, John Miller, Nicolas Thebaud, T.C. McCuaig
*Centre for Exploration Targeting, Robert Street Building, M006, The University of Western Australia,
35 Stirling Highway, Crawley, WA, 6009*

Stanislav Ulrich
AngloGold Ashanti Australia Limited, Continental Africa Region, 44 St. Georges Terrace, Perth, WA, 6000

Abstract. Gold mineralisation at Sadiola gold mine is hosted within Palaeoproterozoic Birimian volcano-sedimentary rocks in southwest Mali. Detailed field-based investigation suggests that mineralisation was coeval with a regional NW-SE compression event (D2) temporally associated with the late stages of the Eburnean tectono-magmatic history. Gold endowment is hosted within the N-S oriented Sadiola Fracture Zone, and in a smaller extent the D2 NE-trending high-angle faults and thrusts. Mineralisation appears coincident with a zone of lower amphibolite facies contact metamorphism associated with the emplacement of syn- to late-D2 porphyritic felsic dykes. Ore-related potassic hydrothermal alteration overprints the latter contact-metamorphic assemblage. The ore displays a positive correlation with Au-Sb-As-Fe-S based on petrographic observations. Gold occurs as three main forms: (1) native free gold, (2) aurostibite, and (3) as rare blebs in disseminated arsenopyrite and tetrahedrite.

Keywords: gold, Birimian, Sadiola, structures

1 Introduction

The West African Craton hosts a number of world-class deposits related to a long-lived period of episodic crustal accretion and deformation referred to as the Eburnean orogeny (c. 2.2–2.0 Ga) (Abouchami et al. 1990; Liégeois et al. 1991; Taylor et al. 1992; Hirdes et al. 2002; Pawlig et al. 2006; Gueye et al. 2007). The 10 Moz Sadiola gold mine is located 420 km northwest of Bamako, in the Kédougou-Kénieba Inlier, a window of deformed Birimian volcano-sedimentary rocks along the Mali-Senegal border.

Despite the Sadiola deposit having a long history of production and study, current interpretations about its genesis remain controversial. Based on a recent field and petrographic investigation this paper summarizes the geology, structural framework and ore-related alteration of the Sadiola gold deposit in an attempt to clarify its genesis.

Our results show that the Sadiola deposit is (1) hosted in metalimestones and metagreywackes, (2) structurally-controlled, (3) developed in proximity to altered diorite and porphyritic felsic dykes and (4) associated with a strong enrichment in antimony. All these observations combined make the Sadiola deposit remarkably different when compared to other classical Paleoproterozoic orogenic gold deposits.

2 Deposit geology

2.2 Lithostratigraphy

Based on pit mapping of the Sadiola opencast (Fig. 1), the lithostratigraphy consists of a metalimestones unit unconformably overlain by a younger sequence of metagreywackes. Well-preserved way-up indicators such as fining upwards sequences and rare cross-bedding in greywackes indicate a younging direction to the east. The east wall of the pit consists of an approximately 250 m thick package of bedded impure metalimestones (or “marly limestone”) and massive metalimestones. The bedded impure metalimestone is the dominant sedimentary facies and is characterised by abundant thin (0.2-2 cm) argillaceous-silty interbeds. The massive facies is a fine-grained calcitic marble, and has a grey, blocky appearance. On the west walls of the pit, a turbiditic package is dominated by dark grey, fine to medium-grained, massive metagreywacke with discrete decimetre scale beds. The turbidite sequences include minor metasandstone and metapelitic interbeds, especially observed close to contact with the carbonate unit.

The metasedimentary rocks have been intruded by three different generations of intrusives (Fig. 1). The first and oldest intrusive consists of a diorite sill-swarm emplaced at the contact between the metalimestones and metagreywackes. The second generation of intrusions cross-cuts all lithologies and consists of NNE-trending quartz-feldspar porphyritic felsic dykes (5% quartz and 5% feldspar phenocrysts set in a quartz-rich aphanitic groundmass) generally up to 1.5 m thick. The third generation corresponds to late and discrete NE-trending diorite dykes.

2.2 Metamorphism

Two metamorphic facies were recognised at the Sadiola main pit. Mineral assemblages of interest identified in host rocks consist of chlorite-muscovite-quartz-biotite in greywackes and uralitised pyroxenes replaced by actinolitic-hornblende in diorite. These observations are consistent with greenschist facies regional metamorphism. The metalimestones locally display porphyroblastic tremolite-actinolite, scapolite, minor diopside and accessory garnet and magnetite. This mineral assemblage is consistent with lower amphibolite facies and is interpreted to represent hornblende-hornfels conditions in the contact aureole of the diorite sills.

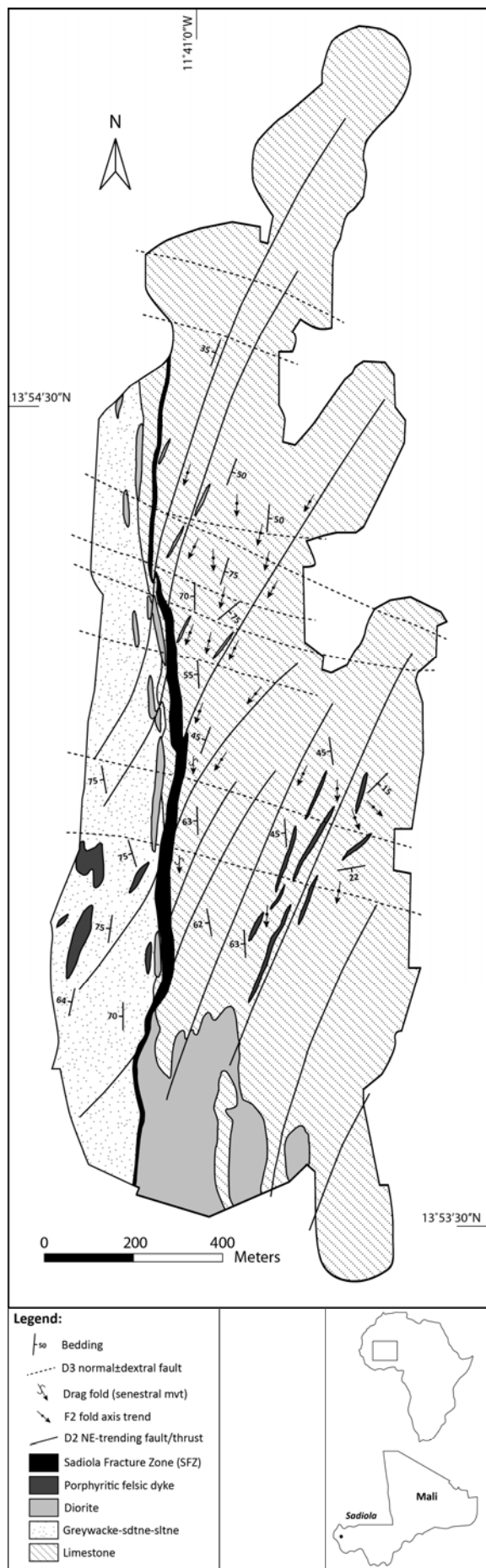


Figure 1. Simplified geological map and interpreted structures of the Sadiola main pit, Mali, West Africa.

Numerous Kfeldspar-quartz-(biotite) veins (termed the inner aureole), silicification within the Sadiola Fracture Zone, the local development of porphyroblasts and an epidote-chlorite-albite assemblage (termed the outer aureole) have also been observed in the opencast and in core. These observations can be related to contact metasomatism during emplacement of the unmetamorphosed porphyritic felsic dykes.

2.3 Structural framework

Field investigation of the Sadiola opencut has recognised many different structures (Fig. 1), which are presented herein in order of overprinting relationships:

The earliest structural element consists of low-angle thrusts with associated sheath-folds in carbonate units with a sub-horizontal NNW-trending lineation. However, due to the rare occurrence of these structures, the overall understanding of this structural component remains poorly understood. These have not been assigned a deformation number in the following section.

The turbidite sequences are dipping steeply to the west, whereas the metalimestones in the easternmost part of the pit dip gently to ESE. The contact between the metagreywackes and metalimestones is faulted and referred to by local geologists as the Sadiola Fracture Zone. The Sadiola Fracture Zone strikes N-S and dips moderately to steeply to the west. It ranges in thickness from 10 to over 50 m, and consists of an anastomosing network of brittle fracture and ductile shear. The associated pinch and swell geometry extends both along strike and down the dip. Kinematic indicators along the Sadiola Fracture Zone display evidence for a late sinistral movement. However stratigraphic duplication at the district scale may be indicative for early reverse kinematics prior to its sinistral reactivation. Parallel to the Sadiola Fracture Zone and axial planar to a large-scale N-S oriented Sadiola monocline, a steep NNW-trending and west-dipping planar fabric (S1) is visible in the central part of the pit. The N-S oriented diorite sill emplaced parallel to bedding is boudinaged within S1.

A second NE-trending planar fabric (S2), which is moderately to steeply dipping to the east, is visible in the eastern walls of the pit. This fabric appears to be associated with small-scale refolding (F2) of the Sadiola monocline. F2 folds consist of disharmonic folds with asymmetric to recumbent geometries. Field measurements show that F2 fold axes plunge gently to the SSW and have a vergence towards the WNW. A number of thin-skinned, NE-trending and east-dipping high-angle reverse faults and thrusts are associated with the F2 folds. NE-trending high angle faults have kinematic indicators that exhibit a late sinistral movement possibly associated with the late reactivation of the Sadiola Fracture Zone. F2 folds and the NE-trending faults are intruded by felsic porphyritic dykes. However, these dykes appear to be locally folded by F2 suggesting a syn to late emplacement age.

A late overprinting normal movement (eastern block down) has been observed on some earlier thrusts and high-angle reverse/sinistral faults. Chlorite, calcite and minor pyrite define the infill on dilatation features.

The late generation of NE-trending diorite dykes intruding into the metalimestones exhibit no foliation but a well-defined amphibole-phyric texture.

A late generation of WNW-trending sub-vertical brittle faults cuts across all earlier structures. These faults range from 10 cm to over 10 m wide and contain fault gouge and clasts of host rocks. Kinematic indicators suggest an oblique normal/dextral movement.

2.4 Deposit geometry

Sadiola ore body has been mined over a 2 km strike length along the Sadiola Fracture Zone. The bulk of the ore is hosted by sheared metalimestone and sheared metadiorite within the Sadiola Fracture Zone, as well as in the deformed footwall metalimestones. The hangingwall metagreywackes are only mineralised in direct proximity to the Sadiola Fracture Zone, which has focused the greatest amount of dilation and permeability. The NE-trending high-angle faults become sparsely mineralised with low grades as distance increases away from the major discontinuity.

2.5 Mineralisation

The gangue assemblage consists of biotite-phlogopite + calcite + quartz ± tremolite-actinolite ± tourmaline ± sericite ± chlorite ± Kfeldspar ± titanite with accessory rutile, apatite and fluorite. Opaque minerals include arsenopyrite, pyrite, pyrrhotite, minor chalcopyrite, and a wide range of accessory minerals including stibnite, tetrahedrite, berthierite, native antimony, marcasite, sphalerite, molybdenite, galena, scheelite, malodonite, tetradymite, cobaltite and gersdorffite. Gold occurs as three main forms, by order of decreasing appearance: (1) native gold (generally ~5-25 µm), (2) Aurostibite, and (3) rare blebs (~1-10 µm) in disseminated arsenopyrite porphyroblasts and tetrahedrite. Based on petrographic observations, Au mineralisation seems to display a positive correlation with Sb, As, Fe and S.

3 Discussion

3.1 Integration with regional tectonics

Field observations show that the Sadiola deposit has been affected by at least two phases of folding. Based on our results, the following event sequence is proposed:

Little is known about the structure and kinematics of the earliest phase corresponding to low-angle thrust. N-S transport direction is inferred from the sheath-folds geometry and this set of structures may have formed during initial phase of low-angle thrusting under ductile conditions. This was also recognised by Van Der Merwe in 2002 and Miller in 2011 in their unpublished reports to AngloGold Ltd.

The NNW-trending S1 fabric and greenschist facies metamorphism are associated with the formation of the Sadiola monocline. The stratigraphic duplication at the district scale, together with the attitude of the Sadiola monocline boudinage of the diorite sill and the geometry of the Sadiola Fracture Zone all have been correlated

with a phase of E-W compression (D1). This deformation stage can be correlated at the regional scale with E-W compression described in western Burkina Faso (D1 in Baratoux et al. 2011).

The second major deformation event that can be derived from field observations is associated with smaller-scale refolding of the Sadiola monocline and formation of the NE-trending high angle reverse faults and thrusts. The attitude of the F2 folds, fault geometries and kinematic indicators are consistent with a NW-SE oriented compression (D2a). Quartz-feldspar porphyritic felsic dykes were emplaced during this phase and contact-metamorphosed adjacent host rocks to lower amphibolite facies. Late sinistral reactivation recorded on the Sadiola Fracture Zone and the NE-trending high-angle faults is coeval with potassic alteration and the main stage of mineralisation. This late phase of deformation (D2b) is interpreted to have either developed during a progressive deformation event (D2) or alternatively as a later deformation increment. At the regional scale, the D2 deformation event may be related to a period of NW-SE oriented transcurrent tectonics with sinistral strike-slip faults (D2 in Milési et al. 1992; D2 in Baratoux et al. 2011). These correlations suggest that analogous to most gold deposits in the Western African Craton, the deformation events D1 and D2 as documented at Sadiola may represent the principal imprint of the Eburnean orogeny (Milési et al. 1992; Feybesse et al. 2006).

The latest deformation event recognised at Sadiola, and correlated with the formation of WNW-trending sub-vertical normal-dextral brittle faults, has been termed D3. Based on kinematic observation this phase of deformation is inferred to be associated with post-Eburnean NE-SW extension.

3.2 Mineralisation style and relative timing

The main mineralisation event is suggested to have been taken place during the late stage of the Eburnean tectono-magmatic history, which correspond to D2b NW-SE compression at Sadiola. It is however not excluded that minor pulses occurred during D2a as some mineralised thrusts and high-angle reverse faults have been observed in core (Fig. 2). The main ore-forming stage is interpreted to result from the linkage of the Sadiola Fracture Zone and the sinistral NE-trending high-angle faults. That critical link between the NE-trending structures, the Sadiola Fracture Zone and mineralisation was first been suggested by Hanssen (1998), and later by Van Der Merwe (2002), and Cameron (2011) in their unpublished reports to AngloGold Ltd. The current interpretation is based on field mapping and core logging combined with Leapfrog modelling of the grade distribution.

The diagnostic hydrothermal alteration assemblage biotite + calcite + pyrrhotite suggests that fluids circulated at a temperature typical of upper greenschist to lower amphibolite facies (Eilu et al. 1999). Mineralisation is possibly linked to re-establishment of hydrothermal circulation in the area coeval with emplacement of the porphyritic felsic dykes as no direct

link between the latter dykes and the ore has yet been established.

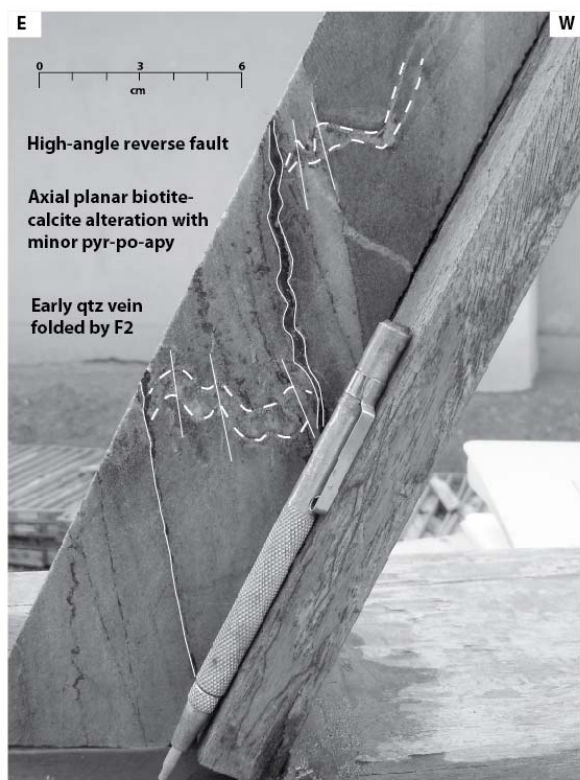


Figure 2. Oriented core photograph illustrating minor ductile gold mineralisation during D2a at Sadiola.

4 Concluding remarks

Most important features related to the Sadiola deposit are summarized hereafter:

- (1) The bulk of the mineralisation is hosted in impure metalimestones.
- (2) Mineralisation is structurally-controlled and has been emplaced during the late stages of the Eburnean tectono-magmatic history.
- (3) The major phase of gold mineralisation is correlated with D2b NW-SE compression at Sadiola.
- (4) Host structures to mineralisation are the Sadiola Fracture Zone, which has focused the greatest amount of dilation and permeability, and in a lesser extent the NE-trending high-angle faults and thrusts.
- (5) Mineralising fluids are suggested to have circulated at a temperature typical of upper greenschist to lower amphibolite facies.
- (6) Based on petrographic observations, Au seems to display a positive correlation with Sb, As, Fe and S.

The relationship between mineralisation and the late porphyritic felsic dykes remains poorly understood. These represent late high-level intrusive units and could be associated with magmatic-hydrothermal mineralising fluids. Further work will be needed to fully understand the complex connection between magma generation and metal endowment, the absolute timing of magmatism, and hydrothermal alteration.

Acknowledgements

This study forms part of a Ph.D. project started in February 2012 at the Centre for Exploration Targeting, UWA. SEMOS, a joint venture between AngloGold Ashanti, IAMGold and the Malian government, is gratefully acknowledged for its financial support. The authors would like to thank the Sadiola exploration staff for their enthusiasm for the study and their constructive discussions.

References

- Abouchami W, Boher M, Michard A, Albarède F (1990) A major 2.1 Ga old event of mafic magmatism in West Africa: an early stage of crustal accretion. *J Geophys Res* 95:17605-17629
- Baratoux L, Metelka V, Naba S, Jesell MW, Grégoire M, Ganne J (2011) A juvenile Paleoproterozoic crust evolution during the Eburnean orogeny (c. 2.2-2.0 Ga), western Burkina Faso. *Precamb Res* 191:18-45
- Eilu PK, Mathison CI, Groves D, Allardycy WJ (1999) Atlas of alteration assemblages, styles and zoning in orogenic lode-gold deposits in a variety of host rocks and metamorphic settings. Centre for Strategic Mineral Deposits, the University of Western Australia. Publication No 30
- Feybesse JL, Billa M, Guerrot C, Duguey E, Lescuyer JL, Milési JP, Bouchot V (2006) The Paleoproterozoic Ghanaian province: geodynamic model and ore controls, including regional stress modelling. *Precamb Res* 149:149-196
- Gueye M, Siegesmund S, Wemmer K, Pawlig S, Drobe M, Nolte N (2007) New evidence of an early Birimian evolution in the West African Craton: an example from the Kedougou-Keniéba Inlier, southeast Senegal. *S Afr J Geol* 110:511-534
- Hirdes W, Davis DW (2002) U-Pb geochronology of Paleoproterozoic rocks in the southern part of the Kedougou-Kéniéba Inlier, Senegal, West Africa: evidence for diachronous accretionary development of the Eburnean province. *Precamb Res* 118:83-99
- Liégeois JP, Claessens W, Camara D, Klerx J (1991) Short-lived Eburnean orogeny in southern Mali: geology, tectonics, U-Pb and Rb-Sr geochronology. *Precamb Res* 50:111-136
- Milési JP, Ledru P, Feybesse JL, Dommanget A, Marcoux E. (1992) Early Proterozoic ore deposits and tectonics of the Birimian orogenic belt, West Africa. *Precamb Res* 58:305-344
- Pawlig S, Gueye M, Klischies R, Schwarz S, Wemmer K, Siegesmund S (2006) Geochemical and Sr-Nd isotopic data on the Birimian of the Kedougou-Kéniéba Inlier (Eastern Senegal): implications on the Palaeoproterozoic evolution of the West African Craton. *S Afr J Geol* 109:411-427
- Taylor PN, Moorbath S, Leube A, Hirdes W (1992) Early Proterozoic crustal evolution in the Birimian of Ghana: constraints from geochronology and isotope geology. *Precamb Res* 56:97-111

The amphibolite facies Lindsays deposit, Coolgardie Goldfield, Yilgarn Craton, Western Australia: a type example of the crustal continuum model?

John Miller

Centre for Exploration Targeting, School of Earth and Environment, The University of Western Australia, Perth, Australia

Garry Adams

Focus Minerals Limited 44 St Georges Terrace, Perth WA 6000

Abstract. In the Crustal Continuum Model syn-metamorphic orogenic gold deposits can form from prehnite–pumpellyite to granulite facies conditions. The validity of this model has recently been questioned for metamorphic conditions outside of greenschist facies. The Lindsays deposit in the Coolgardie Goldfield in the Yilgarn craton of western Australia is one of the type examples of the Continuum model. It has been inferred to be a relatively deeper-level member of the continuum. We present detailed kinematic analyses of the fault vein arrays associated with gold mineralisation (integrated with the alteration assemblages). The Lindsays dolerite-hosted deposit has fault-vein array geometries almost structurally identical to what is observed in dolerite-hosted deposits in greenschist facies systems. The field relationships indicate the veins associated with gold mineralization developed at high temperature with quartz, arsenopyrite, pyrrhotite, scheelite, plagioclase, biotite, calcite and calcic amphibole. Evidence for a later high-T overprint at amphibolite facies is not present. The field relations are compatible with the application of the Crustal Continuum Model for this deposit.

Keywords: Crustal Continuum model, orogenic gold, Yilgarn Craton, structure

1 Introduction

The Crustal Continuum Model was developed as a unifying theory for orogenic gold deposits in the 1990's (Groves et al. 1992; Groves 1993). This model postulates that gold deposits could form from prehnite–pumpellyite to granulite facies conditions and over a vertical interval of up to 25 km in the crust. A series of papers (Phillips and Powell 2009; Tomkins and Grundy 2009) have questioned the validity of the Crustal Continuum Model proposed by Groves et al. (1992, 2003). Phillips and Powell (2009) argued that higher metamorphic grade deposits reflect gold formation at greenschist facies conditions followed by metamorphism of the deposit to higher metamorphic grade. This has implications for targeting gold systems as it implies targeting for gold deposits within amphibolite-facies or higher metamorphic grade belts must always take into account the overprinting of the primary mineral assemblages and structures associated with gold mineralization by a high temperature event.

The Lindsays deposit in the amphibolite facies Coolgardie Goldfield of Western Australia (Fig. 1) is one of the type examples of the Crustal Continuum Model, and has been inferred to be a relatively deeper-level member of the continuum (Knight et al. 1993). This contribution presents structural mapping of these gold lodes integrated with the observation of associated

mineral assemblages. It assesses the outcrop scale field relationships for the timing of the gold mineralization with respect to evidence for syn-peak lode development against post lode metamorphism and deformation.

2 Scientific background

Phillips and Powell (2009) and Tomkins and Grundy (2009) presented different critiques of the continuum model, and both addressed the granulite-hosted Griffin's Find deposit in the Yilgarn. They used petrographic observations combined with thermodynamic modeling of the mineral assemblages to argue the continuum model should not be applied to granulite facies rocks. Tomkins and Grundy (2009) produced new estimates on the peak metamorphism at Griffin's Find at 820°C to 870°C and at least 550 MPa. Tomkins and Grundy (2009) argued that the difficulty of transmitting hydrothermal fluids through rocks above 600°C to 650°C without causing partial melting, means that this temperature range should be regarded as an upper limit for the formation of orogenic gold deposits. In contrast, Phillips and Powell (2009) argued that the metamorphic range for gold deposit formation was considerably more restricted, and was likely to be mostly within the greenschist facies, and not sub-greenschist or amphibolite facies. Phillips and Powell (2009) assessed a large range of factors with respect to the Crustal Continuum Model for several gold deposits (e.g. the variance of mineral assemblages, the thermal evolution and fluid timing during metamorphism). They argued that higher metamorphic grade deposits reflect gold formation at greenschist facies conditions followed by metamorphism of the deposit to higher metamorphic grade. The argument presented by Phillips and Powell (2009) follows the "deeper later" and "deeper earlier" model of Powell et al. (1991) where the peak of metamorphism can be diachronous in the greenstone pile. In this model the Yilgarn high-temperature gold systems are examples of 'deeper earlier' systems where fluids are released and then rise into the overlying pile (producing gold deposits) before the overlying section has reached its metamorphic peak. Phillips and Powell (2009) also argued that the type deposit examples in sub-greenschist domains (e.g. Wiluna) appear to be incorrectly ascribed.

3 Geology

The Coolgardie Gold Field lies within the Norseman-Wiluna greenstone belt within the Eastern Goldfields

Province of the Yilgarn Craton. This belt is dominated by ca. 2.7 Ga volcanosedimentary assemblages consisting of predominantly mafic and ultramafic lavas and intrusive rocks, which have been metamorphosed to grades ranging from upper greenschist facies to lower amphibolite facies.

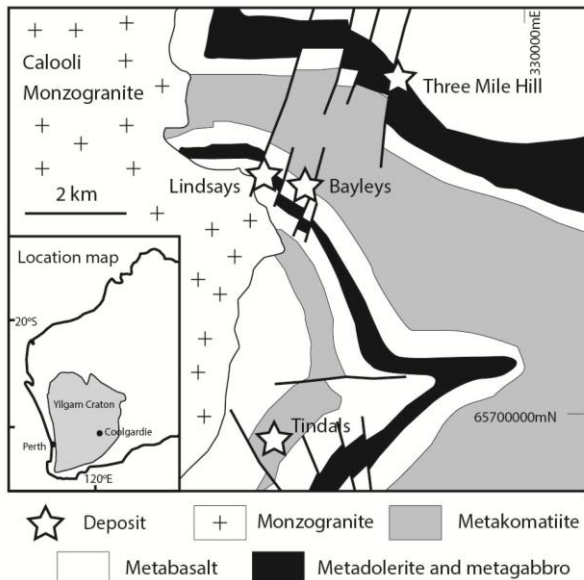


Figure 1. Location and geological map of the Coolgardie Goldfield (modified from Knight et al. 1993).

A range of mineralisation styles are present in the Coolgardie Goldfield, with deposits hosted by dolerite, basalt, sediments and diorite dykes. Previous studies have highlighted that the deposits show evidence for equilibrium textural relationships between gold, sulphides, and high-temperature silicate gangue (Knight et al. 2000). The presence of garnet is mainly controlled by the Mg number of the host mafic rocks and the deposits have been divided into; 1) garnet-absent with amphibole-plagioclase-biotite-calcite and; 2) garnet-present with garnet-hornblende-plagioclase-calcite alteration assemblages (Knight et al. 2000).

Knight et al. (2000) inferred that the Calooli monzogranite had some genetic control on the hydrothermal alteration at Coolgardie. In contrast, Standing (2000) argued the deposits have no convincing evidence for lateral fluid flow under the genetic influence of the Calooli Pluton.

Multiple structural models have been proposed for the Coolgardie region. However, for the basalt- and dolerite-hosted Lindsays and Kings Cross gold deposits the gold-related kinematics defined by Standing (2001) are identical to those described by Knight et al. (1993). Gold mineralisation was related by both authors to an event associated with WNW-ESE shortening (commonly termed D3, e.g. Standing 2001).

The Lindsays deposit is a basalt and dolerite hosted deposit on the northeast flank of the Calooli monzogranite (Fig. 1). Gold is associated with quartz, arsenopyrite, pyrrhotite, scheelite, plagioclase, biotite, calcite and calcic amphibole. Knight et al. (2000) produced estimates of 510° to $520^{\circ}\text{C} \pm 50^{\circ}$ for the gold-related alteration at the Lindsays deposit. The dominant mineralized structures within the Lindsays deposit are NNW-, N- and NNE-trending and dip steeply to the east

(Fig. 2 and 3). These shears are brittle-ductile structures associated with tension vein arrays.

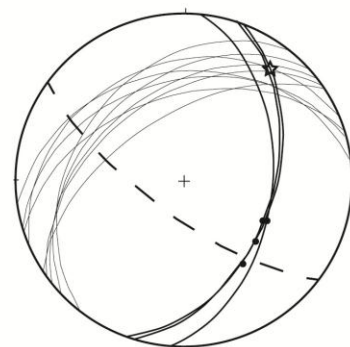
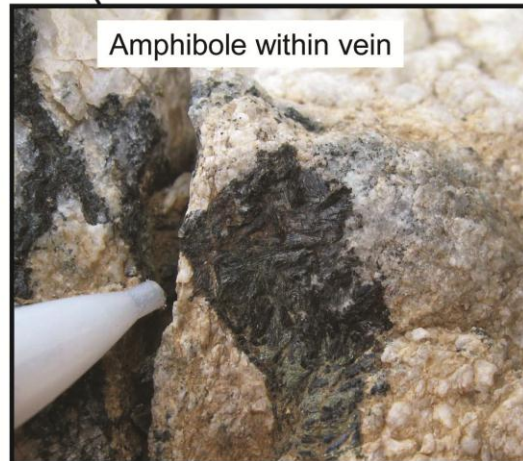
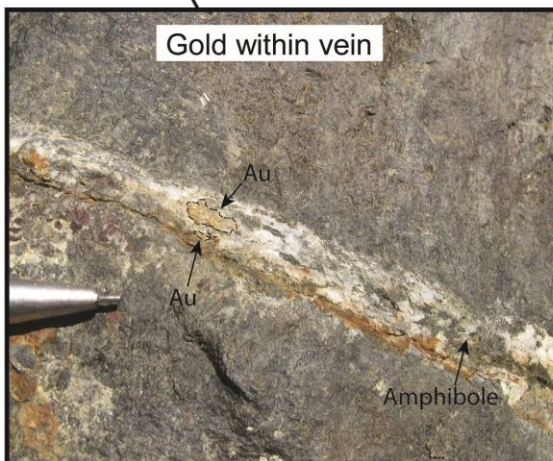
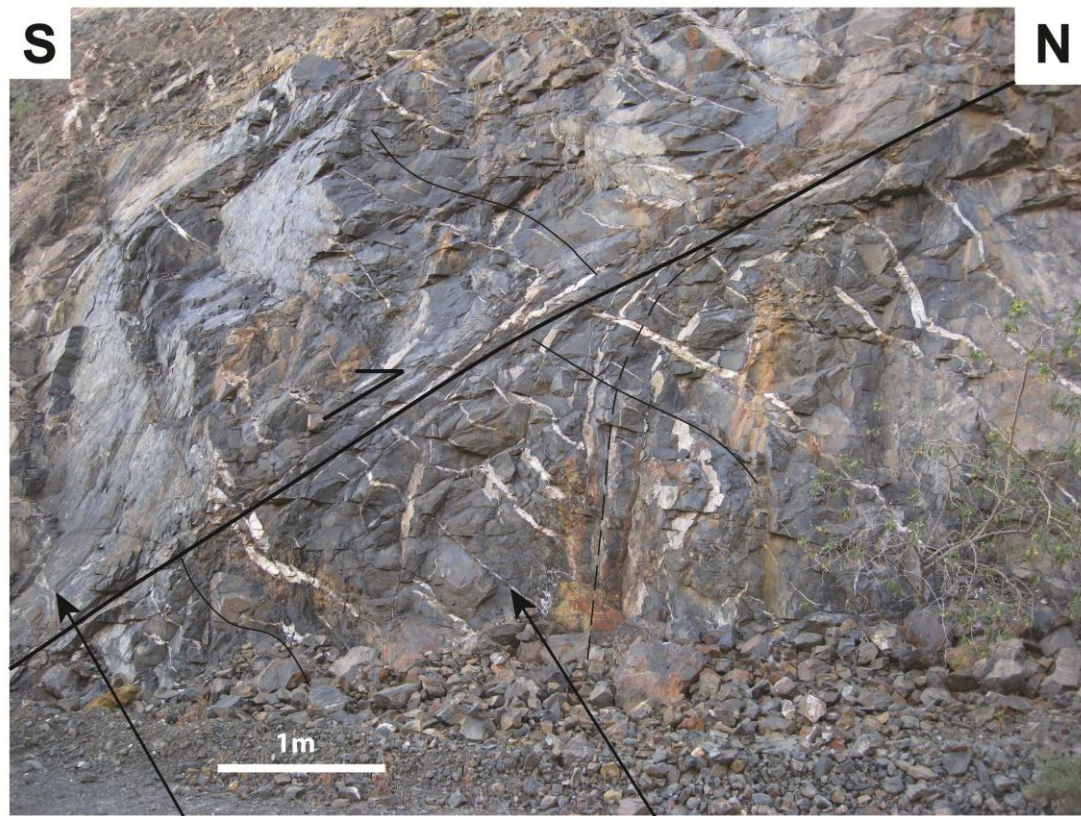
Our kinematic analysis of the ductile shear zones (Fig. 2 and 3), and associated vein arrays, consistently gives a sinistral-reverse movement sense. Fault drag of earlier layer parallel veins is prominent (Fig. 2). The slip direction implies NW-SE shortening associated with gold mineralization, which agrees with the syn-gold kinematics presented by Knight et al. (1993) for the deposit. The tension vein arrays have a consistent dip (Fig. 2 and 3), are gold-bearing, and have the assemblage quartz-amphibole-plagioclase-calcite-biotite-scheelite. The associated ductile shears have strong amphibole and plagioclase mineral lineations.

The extension veins and lineations have structural relationships consistent with having formed coevally. This is highlighted by the intersection of the M-plane calculated from the amphibole-bearing vein arrays matching the mineral lineation defined by amphibole (Fig. 2). This indicates that the stretching direction marked by the mineral lineation is the same as that defined by the vein arrays. Evidence for a later high-T overprint, or gold linked to lower retrograde greenschist-facies deformation, is not present at the Lindsays deposit.

4 Discussion and conclusions

One of the most striking observations is that the Lindsays dolerite-hosted deposit has fault-vein array geometries almost structurally identical to what is observed in the dolerite-hosted deposits in greenschist facies systems in the Yilgarn. These veins occur adjacent to shears with strong mineral lineations and the extension direction recorded by the vein arrays matches the lineation (Fig. 2). This is exactly the same structural and mineralogical relationships documented by Nguyen et al. (1998) for fault-vein arrays at the Revenge deposit within the St Ives gold system. Such consistent relationships between faults, vein arrays and mineral lineations are normally interpreted to mean these formed synchronously with the formation of the gold lodes. The only difference between the field relationships at Coolgardie (Fig. 2), and the fault-vein systems at St Ives (Nguyen et al. 1998), is that the lineations and vein arrays are defined or infilled by higher temperature assemblages (Knight et al. 2000). The Lindsays deposit has more ductile shearing of the wall rock adjacent to the lodes compared to Revenge e.g. Fault drag in Fig. 2.

Phillips and Powell (2009) and Tomkins and Grundy (2009) demonstrate that some gold camps belts will contain metamorphosed deposits, and that there are serious problems with applying the Crustal Continuum Model to rocks metamorphosed to granulite facies (i.e. Griffin's Find) and to upper amphibolite facies. With respect to the conclusions of Phillips and Powell (2009), we argue the field relationships are compatible with lode development at amphibolite facies and there is no evidence for a later metamorphic overprint. This is compatible with the application of the Crustal Continuum Model as argued by Knight et al. (1993).



Thick lines = Shears
Thin lines = Veins
Points = amphibole lineation
Dashed lines = M plane (vein related)
Star = incremental stretch

Figure 2. Gold-bearing fault-vein arrays from the Lindsays Deposit, Coolgardie. Dashed line highlights early veins affected by fault drag consistent with reverse movement. Solid lines annotate veins associated with fault. The mineralized structures have the assemblage amphibole-plagioclase-biotite-calcite. The veins and lineations have relationships consistent with having formed coevally (the intersection of the M-plane calculated from the amphibole-bearing vein arrays matches the mineral lineation defined by amphibole).

The formation of gold deposits in any region needs to be carefully matched with the structural, metamorphic and tectonic evolution of a region. Targeting for gold deposits within amphibolite-facies or higher metamorphic grade belts must take into account the potential for overprinting of the primary mineral assemblages and structures associated with gold mineralization by a later high temperature event. The potential for gold associated with retrograde overprinting of amphibolite facies terranes also needs to be considered. However, in some terranes amphibolite facies grade rocks will contain high-temperature syn-metamorphic deposits, such as the Lindsays deposit at Coolgardie. The Lindsays deposit remains a well constrained type example of the Crustal Continuum Model as argued by Knight et al. (1993).

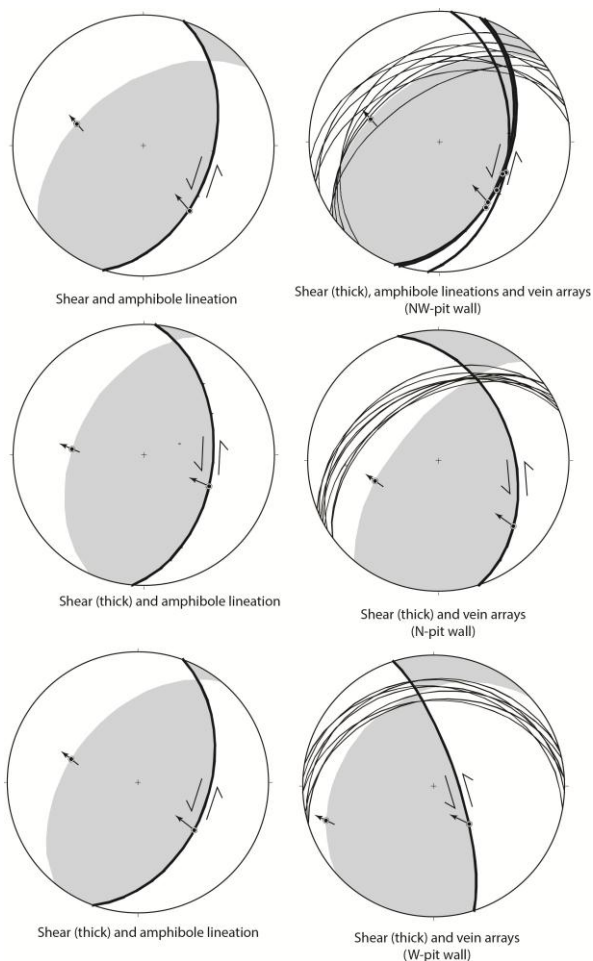


Figure 3. Kinematic analyses of D3 mineralized faults from the Lindsays deposit.

Acknowledgements

We thank the geologists at Focus Minerals Limited for field support and research input.

References

- Abouchami W, Boher M (1990) A Major 2.1 Ga Event of Mafic Magmatism in West Africa: An Early stage of Crustal Accretion. *J Geophys Res* 9:17605-17629
- Boher M, Abouchami W, Michard A, Albarede F, Arndt N (1992) Crustal Growth in West Africa at 2.1 Ga. *J Geophys Res*

- 97:345-369
- Groves DI (1993) The crustal continuum model for late-Archaean lode-gold deposits of the Yilgarn Block, Western Australia. *Min Dep* 28:366-374
- Groves DI (2009) Predictive vs Forensic Mineral Deposit Geology: Viewing Giant Deposits at Appropriate Scale. In: Williams PJ et al. Proceedings of the 10th Biennial SGA Meeting of The Society for Geology Applied to Mineral Deposits Townsville Australia, Smart Science for Exploration and Mining, 17th - 20th August 2009, pp 2-4
- Groves DI, Barley ME, Barnicoat AC, Cassidy KF, Fare RJ, Hagemann SG, Ho SE, Hronsky JMA, Mikuck, EJ, Mueller AG, McNaughton NJ, Perring CS, Ridley JR, Vearncombe JR (1992) Sub-greenschist to granulite-hosted Archaean lode-gold deposits of the Yilgarn Craton: a depositional continuum from deep-sourced hydrothermal fluids in crustalscale plumbing systems. *Geol Dept (Key Centre) and Univ Extension, Univ West Aust Publ* 22, 325-337
- Groves DI, Goldfarb RJ, Robert F, Hart CJR (2003) Gold deposits in metamorphic belts: Overview of current understanding, outstanding problems, future research, and exploration significance. *Econ Geol* 98:1-29
- Knight JT, Groves DI, Ridley JR (1993) The Coolgardie Goldfield, Western Australia: district-scale controls on an Archaean gold camp in an amphibolite facies terrane. *Min Dep* 28:436-456
- Knight JT, Ridley JR, Groves DI (2000) The Archaean Amphibolite Facies Coolgardie Goldfield, Yilgarn Craton, Western Australia: Nature, Controls, and Gold Field-Scale Patterns of Hydrothermal Wall-Rock Alteration. *Econ Geol* 95:49-84
- Neumayr P, Walshe J, Hagemann S, Petersen K, Roache A, Frikken P, Horn L, Halley S (2008) Oxidized and reduced mineral assemblages in greenstone belt rocks of the St. Ives gold camp, Western Australia: vectors to high-grade ore bodies in Archaean gold deposits? *Min Dep* 43:363-371
- Nguyen PT, Cox SF, Harris LB, Powell CM (1998) Fault-valve behaviour in optimally oriented shear zones: An example at the Revenge gold mine, Kambalda, Western Australia. *J Struct Geol* 20:1625-1640
- Phillips GN, Powell R (2009) Formation of gold deposits: Review and evaluation of the continuum model. *Earth Sci Rev* 94:1-21
- Powell R, Will TM, Phillips GN (1991) Metamorphism in Archaean greenstone belts: calculated fluid compositions and implications for gold mineralization. *J Met Geol* 9:141-150
- Standing J (2000) Structural geology and controls on gold mineralisation at the Empress Gold Deposit, Tindals Mine Camp, Coolgardie, Western Australia. Unpublished report prepared by Fluid Focus Pty Ltd on behalf of MPI Mines Ltd, pp. 18
- Standing J (2001) New insights into the structural and stratigraphic setting of the Coolgardie district: implications for gold exploration. Unpublished report prepared by Fluid Focus Pty Ltd on behalf of MPI Mines Ltd, pp. 74
- Tomkins AG Grundy C (2009) Upper temperature limits of orogenic gold deposit formation: constraints from the granulite-hosted Griffin's Find Deposit, Yilgarn Craton *Econ Geol* 104:669-686

Signatures of overprinting mineralisation processes in the orogenic gold deposit of the Pampalo mine, Hattu schist belt, eastern Finland

Ferenc Molnár, Hugh O'Brien, Yann Lahaye, Asko Käpyaho
Geological Survey of Finland

Grigorios Sakellaris
Endomines Oy.

Abstract: The paper presents results of detailed mineralogical, textural, and geochemical studies carried out on an Archean orogenic gold deposit in eastern Finland. Observations on the mineralogy of ore and hydrothermally altered rocks together with the results of lead- and sulphur isotope LA MC-ICPMS spot analyses and fluid inclusion studies suggest that overprinting hydrothermal processes, mostly in relation to the Paleoproterozoic Svecofennian orogeny modified the primary ore.

Keywords: orogenic gold, wall rock alteration, ore mineralogy, lead isotopes, sulphur isotopes, fluid inclusions, overprint

1. Regional geology, metallogeny, mining

The Hattu schist belt (HSB) is one of the Archean greenstone belts in the Karelian Province of the Baltic Shield (Fig. 1). The extension of the N-S oriented belt in Eastern Finland is approx. 50 km in length with max. 20 km width and it continues as the Kostamushka greenstone belt in Russian Karelia. The HSB consists of felsic volcanic and epiclastic units of around 2.75 Ga age with local intercalations of mafic and ultramafic volcanic rocks. These units are aligned between TTG and leucogranite intrusions of similar ages (2.75-2.73 Ga; Sorjonen-Ward and Korsakova, 2012) thus these granitoids do not represent the basement of the greenstone belt.

Lower amphibolite facies metamorphism at 4-6 kbars

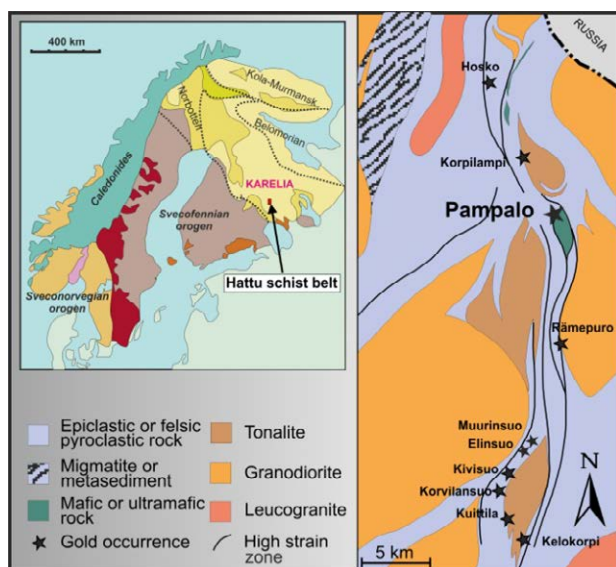


Figure 1: location and regional geology of the HSB.

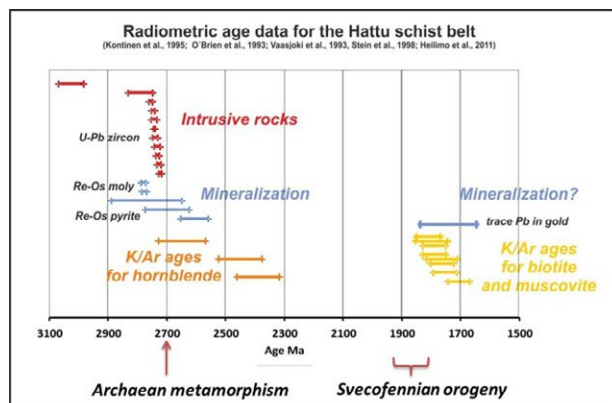


Figure 2: radiometric ages for intrusions, mineralisation and tectonothermal events in the Hattu schist belt.

pressures and at 500-600°C temperatures affected rocks of HSB at ca. 2.74-2.63 Ga (O'Brien et al., 1993). Emplacement of NW-trending gabbroic dikes took place from 2.3 to 2.0 Ga in relation to the Paleoproterozoic rifting of the Archean craton. At ca. 1.85 and 1.7 Ga, tectonothermal processes affected the Karelian Province due to overthrust of the up to 5-6 km thick east-verging Svecofennian nappe complex. This process re-set K-Ar and Rb/Sr ages of biotite and muscovite in the Archean basement, however, amphibole remained largely intact in the region of the HSB (Kontinen et al., 1992; O'Brien et al., 1993; Fig. 2). The nappe complex was completely eroded away during the Neoproterozoic exhumation of the Archean basement.

In the HSB, several orogenic gold deposits along N-S and NE-SW trending shear zones, that cross-cut folded epiclastic and volcanogenic units were discovered by the Geological Survey of Finland during mineral exploration projects between 1986 and 1992 (Nurmi et al., 1993; Fig.1). Occurrences of banded iron formations and intrusion related Mo-W-Au stockwork mineralization along the contact zones of the tonalite pluton at Kuittila have also been recognised in the HSB. The Outokumpu Mining Ltd. produced 1784 kg gold from the Pampalo mine between 1996 and 1999 (Sorjonen-Ward and Korsakova, 2012). The Endomines Oy. purchased mining and exploration licences for the whole HSB in 2006 and re-started gold production in 2011. The Pampalo mine has yielded 1482.4 kg gold since then. The currently known cumulative ore resource of gold deposits in the HSB is 4.8208 Mt and the Pampalo mine has 1.6488 Mt resource with 4.3 g/t Au grade (Sorjonen-Ward and Korsakova, 2012). The general characteristics of gold deposits in the HSB are largely comparable with

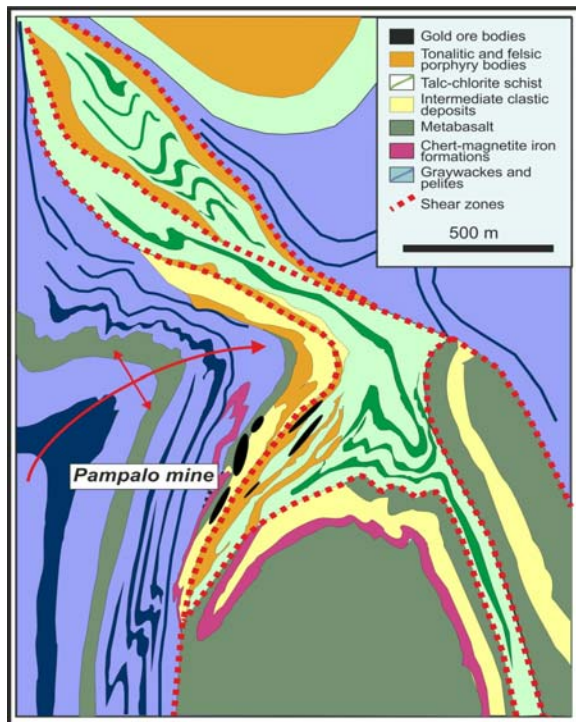


Figure 3: geology in the surroundings of the Pampalo mine (after Nurmi et al., 1993).

orogenic gold systems formed on several Archean cratons at around 2.7 Ga, however, it appears that their formation took place under peak metamorphic conditions (Sorjonen-Ward, 1993). An interesting additional peculiarity of the region is the possible metallogenic role of the overprinting Svecofennian orogeny, especially in the light of the 1725 ± 120 Ma trace lead isotope model age for gold from the Pampalo Mine reported in Vaasjoki et al. (1993). In order to investigate this question we carried out detailed micro-textural, mineralogical and geochemical studies on ore and host rock specimens and analysed metal distributions along drillcore and mine profiles. We also investigated the micro-textural constraints of the ore and alteration mineral assemblages on lead isotope compositions of minerals (e.g. galena, altaite, hydrothermal K-feldspar) by using LA MC-ICPMS technique. Fluid inclusion studies were carried out in texturally and isotopically well characterised mineral assemblages.

2. Results

2.1 Host rocks and structures

The major gold ore bodies at the Pampalo Mine are located along a NNE-SSW oriented shear zone that cut the subvertical-vertical western limb of a synform (Fig.3). The extension of orebodies towards the depth are following the plunge of the synform and thus they occur as irregular-ellipsoid ore shoots with up to 10-15 m in horizontal diameter and with 40-60° dip to NNE. The extension of mineralisation is known to about 500 m down from the surface and is open towards the depth. The ore hosting synform is superimposed on the eastern limb of a northeasterly plunging large antiform structure. Current results of mine exploration revealed that the complex fold structure is also cut by an E-W

oriented, northerly dipping mylonitic fault zone in the northern part of the deposit and that cross-cutting structure is also mineralised. Local gold enrichments also occur along NW-SE oriented subvertical faults that cut across the southern zones of the synform.

The footwall of the mineralisation consists of metagreywacke with some pelitic and magnetite-chert iron formation (BIF), which is overlain by a tholeiitic metabasalt (greenstone) forming the immediate footwall to the mineralized meta-andesitic tuff unit. This unit is also termed as mafic schist due to the very intense biotite enrichment along the cross cutting shear planes. The volcanoclastic unit is overlain by a talc-chlorite schist, which is a metamorphosed komatiitic volcanic unit. The mafic schist and the talc-chlorite schist host blocks of a felsic porphyry rock with dacitic composition. These felsic units appear to be deformed dikes (boudins) in some mine profiles. The talc-chlorite schist also hosts to blocks of porphyritic tonalite. In some outcrops the tonalite and felsic porphyritic units are in contact and suggest intrusion of tonalite into felsic porphyry.

There are no well developed veins in the Pampalo deposit. Gold mineralisation appears in the form of disseminations and oriented/unoriented sets of thin carbonate(-feldspar-quartz) veinlets.

2.2. Alteration geochemistry and mineralogy

Concentration of gold is generally confined to the mafic schist and the felsic porphyry units in the Pampalo mine. In the mineralised felsic porphyry rock, the most profound geochemical signature of hydrothermal alteration is the enrichment of Na_2O (up to 8-10 wt% (Fig.4). Results of mass transfer calculations suggest that the sodium enrichment is associated with depletion of other oxides, especially SiO_2 and K_2O (Rasilainen, 1994). The strong Na_2O enrichment in the felsic porphyry units is due to albitisation of rock forming plagioclase and crystallisation of fine grained albite in the groundmass. The metasomatic albite porphyroclasts are strongly deformed and corroded by the fine grained groundmass in the shear zones. In addition to albitisation, the felsic porphyry units locally also contain tourmaline-biotite stockwork and pyrite dissemination. The mineralised mafic schist locally also contain Na_2O enriched zones, however, occurrences of alteration zones with up to 10-12 wt% K_2O content are more common, especially along the contacts to the footwall and hanging wall mafic and ultramafic metavolcanics (Fig. 4). Strong K-metasomatic alteration is usually also associated with local enrichment of gold. Results of geochemical profiling along mine sections also show K_2O enrichment of mafic schist along the contact to the enclosed felsic dike units and in some felsic dikes, too. The potassium enrichment overprints albitisation because albite porphyroclasts are replaced by K-feldspar. It is also remarkable that carbonate-adularia- quartz veins are also present in the potassium rich zones of the mafic schist. The hydrothermal K-feldspar replacing albite or occurring in veins is not deformed. The mafic schist locally also contains small knots of quartz-tourmaline-muscovite alteration. The strongly sheared zones are

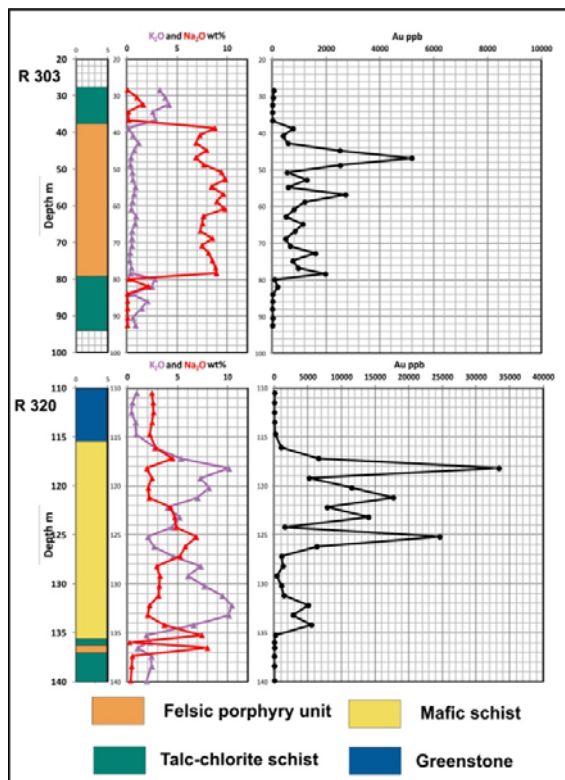


Figure 4: representative example of N_2O , K_2O and Au distributions in two drillholes.

enriched in biotite which forms elongated seams in the shear planes. Coarse grained skarn with up to 10 cm large actinolite and finer grained biotite (\pm tourmaline \pm iron rich hornblende \pm quartz, calcite) is present along the contacts of the talc-chlorite schist with felsic and tonalitic porphyry units and mafic schist. Formation of skarn also overprinted albitisation. The banded iron formation in the footwall is characterised by replacement of magnetite by pyrrhotite in some zones. Sulphurisation appears to overprint the garnet-biotite metamorphic assemblage in this unit.

2.3. Ore geochemistry and mineralogy

In the mineralized mafic schist and felsic porphyry units, concentrations of gold are usually well correlated with the Ag, Bi, Te contents of ore. Accordingly, the most common Au-bearing minerals are native gold with up to 29 % silver, calaverite and petzite with associated hessite, altaite, tellurobismuthite, tsumoite, rucklidgeite, frobergite and less commonly monbrayite, native bismuth and an unknown AuSbTe phase (Kojonen et al., 1993). These minerals form round inclusions in pyrite, overgrowths on surfaces of pyrite crystals and disseminations in the fine grained quartz-feldspar groundmass of host rocks. Our observations also suggest that Bi-tellurides and especially a late generation of altaite replace Au-bearing minerals. Ore mineralogy suggests to relatively low temperature crystallisation conditions due to the fairly low melting temperatures of some mineral associations (e.g. gold-calaverite-petzite – 304°C, calaverite-altaite-gold – 402°C, calaverite-altaite– 426°C; Affifi et al., 1988) and that is in contrast with formation of the ore deposit under peak metamorphic conditions (500-600°C). Local occurrence

of calcite-fluorite-chlorite veins cutting the schistosity of mineralised mafic schist was also observed in the Pampalo mine. Disseminations of molybdenite, galena and magnetite occur along these late veins.

2.4. Lead and sulphur isotopes

The application of the LA MC-ICPMS technique allowed us to complete more than 150 analyses in polished thin sections. Spot analyses (30-150 μm^2 LA raster areas) were carried out according to the textural and paragenetical settings of galena, altaite, chalcopyrite, pyrite and adularia grains. The least radiogenic Pb-isotope ratios for galena and altaite were obtained from inclusions of pyrite and chalcopyrite and from galena disseminated in the groundmass of the host rocks. Calculated model ages for these minerals are around 2.7 Ga ($\mu=9.4$, $\kappa=3.8$, S&K two stage growth model). However, most of galena grains, especially those ones which occur as overgrowths on pyrite crystals, as well as the euhedral undeformed adularia crystals from veins provided more radiogenic lead isotope ratios. Distribution of the least radiogenic lead isotope ratios from these samples outline a trend (Fig. 5a) which corresponds to mixing of less radiogenic lead from the

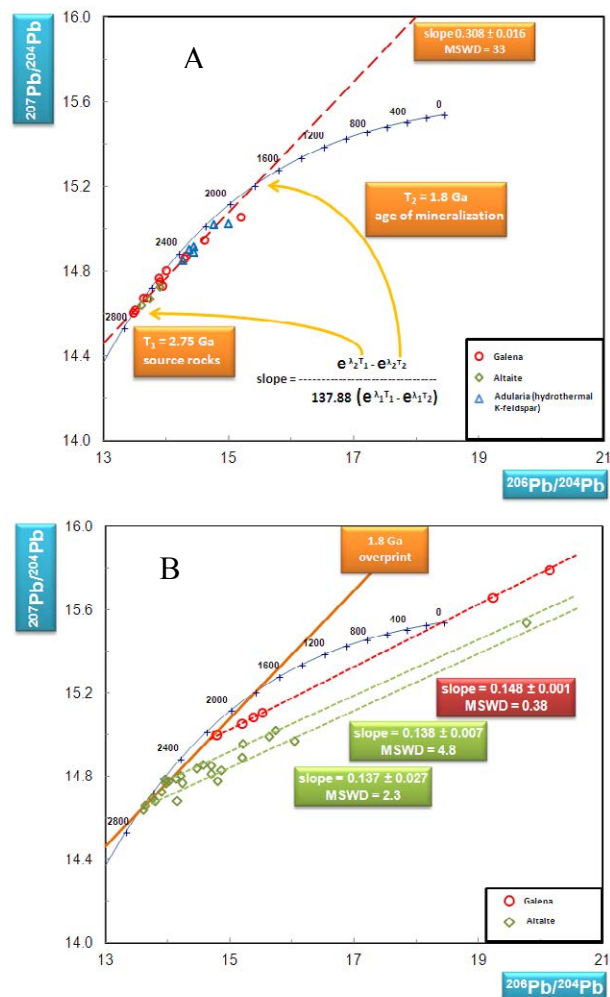


Figure 5: lead isotopic ratios measured in galena, altaite and adularia crystals from the Pampalo deposit. A – the co-linear array of the least radiogenic data from each sample. B – lead isotopic composition of galena associated to late stage fluorite bearing veins and late stage altaite. S&K growth curve, $\mu=9.4$

Archean mineralisation with more radiogenic lead released by the host rocks at the time of the Svecofennian tectonothermal processes (e.g. around 1.8 Ga). Data for galena and adularia along this trend show very small variation within samples but large variations between samples. Isotopic heterogeneity was not observed in profiles across large galena grains. Preliminary results of sulphur isotope data from pyrite and chalcopyrite associated to galena from the above described trend show shift of $\delta^{34}\text{S}$ values from around 0‰ to around -10 ‰ suggesting mixing of sulphur from two reservoirs.

Galena associated with the late calcite-fluorite-chlorite veining provided the most radiogenic lead isotopic ratios with high variation among different grains. A regression line for these data points (Fig. 5b) suggests to the occurrence of another mixing process between the lead from the ore with already modified lead isotopic composition at cca. 1.8 Ga and more radiogenic lead sourced from an unknown reservoir. Data for altaite replacing galena and Au-minerals also show similar trend, suggesting that those late stage fluids also caused local re-distribution of metals.

2.5. Fluid inclusions

Fluorite from the late stage veins contains primary and secondary aqueous fluid inclusions. Increase of homogenisation temperatures and salinities from the time of primary inclusions' entrapment to the formation of secondary ones (Fig. 6), as well as the very saline nature of secondary fluid inclusions with still relatively low homogenization temperatures together with the very radiogenic lead isotopic compositions of galena grains associated to the fluorite bearing veins permit the hypothesis that the late stage fluid circulation interacted with the gold mineralization during the evolution of a post-Svecofennian sedimentary basin. Adularia with lead isotopic ratios sitting along the 2.75-1.8 Ga mixing line on Fig. 5 hosts to primary aqueous-carbonic fluid inclusions. These inclusions contain relatively low density carbonic fluid phase with almost pure CO_2 and intermediate salinity aqueous phase. They homogenized into the aqueous phase at around 300°C (Fig.6). The overall characteristics of these fluid inclusions are comparable with those aqueous-carbonic fluid inclusions which were described as ore forming fluids in the

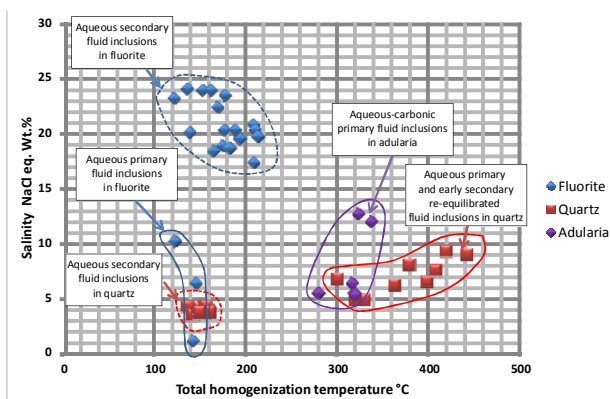


Figure 6: fluid inclusion data for quartz, adularia and fluorite from the Pampalo mine

Rämepuro deposit (Fig.1) by Poutiainen and Partamies (2003). The latter authors also suggested Svecofennian origin of these fluids. Most of primary aqueous fluid inclusions are surrounded by re-equilibration induced fractures in quartz from mineralised zones. Due to re-equilibration, their salinities are anomalously increased parallel with the decrease of their bulk densities: this is expressed by increased homogenisation temperatures in re-equilibrated fluid inclusions with relatively high salinities (see field of re-equilibrated fluid inclusions on Fig. 6). Quartz also entrapped secondary aqueous fluid inclusions at the time of late stage fluid circulation and formation of fluorite bearing veins.

3. Conclusions

Results of our studies suggest that the orogenic gold deposit exploited in the Pampalo mine has been formed by multiple hydrothermal processes. The most important stage of ore formation took place during the Archean evolution of the HSB, however, fluid-rock interaction and mobilisation of metals also occurred during the Paleoproterozoic Svecofennian orogeny. We also found evidences of local reworking of ore by post-Svecofennian fluid flow events. Modification of Archean or Proterozoic ores by processes related to a younger orogeny is not an uncommon phenomenon on the Baltic Shield (Vaasjoki, 1981; Romer and Wright, 1993). The practical importance of recognition of these processes is that conduits of the overprinting fluid flow systems may be places of re-deposition of ore and thus may represent new targets for mineral exploration.

4. References

- Afifi AM, Kelly WC, Essene EJ (1988) Phase relations among tellurides, sulphides, and oxides: I. Thermochmeical data and calculated equilibria. *Economic Geology* 83:377-394
- Kontinen A, Paavola J, Lukkarinen H (1992) K-Ar ages of hornblende and biotite from late Archean rocks of eastern Finland – interpretation and discussion of tectonic implications. *Geol Surv Finland Bull* 365 pp 31.
- Nurmi PA, Sorjonen-Ward P., Damsten M (1993) Geological setting, characteristics and exploration history of mesothermal gold occurrences in the late Archean Hattu schist belt, Ilomantsi, eastern Finland. *Geol Surv Finland Spec Paper* 17: 193-232
- O'Brien HE, Huhma H, Sorjonen-Ward P (1993) Petrogenesis of the late Archean Hattu schist belt, Ilomantsi, eastern Finland. *Geol Surv Finland Spec Paper* 17: 133-146
- Poutiainen M, Partamies S (2003) Fluid evolution of the late Archean Rämepuro deposit in the Ilomantsi greenstone belt in eastern Finland. *Miner Deposita* 38:196-207
- Romer RL and Wright JE (1993) Lead mobilization during reactivation of the western Baltic Shield. *Geochim Cosmochim Acta* 57: 2555-2570
- Sorjonen-Ward P (1993) An overview of structural evolution and lithic units within and intruding the late Archean Hattu schist belt, Ilomantsi, eastern Finland. *Geol Surv Finland Spec Paper* 17: 193-232
- Sorjonen-Ward P, Korsakova M (2012) Ilomantsi Au, Mo. *Geol Surv Finland Spec. Paper* 53: 255-260
- Vaasjoki M (1981) The lead isotopic composition of some Finnish galenas. *Geol Surv Finland Bull* 294:1-66.
- Vaasjoki M, Sorjonen-Ward P, Lavikainen S (1993): U-Pb age determinations and sulfide Pb-Pb characteristics from the late Archean Hattu schist belt, Ilomantsi, Eastern Finland. *Geol Surv Finland Spec Paper* 17: 103-132.

Mineralization style and geochronology of the Sekisovka gold deposit, eastern Kazakhstan

Evgeniy Naumov

*Institute of Geology and Mineralogy SB RAS, prosp. Koptyuga, 3, Novosibirsk, Russia, 630090, naumovevg@gmail.com
Novosibirsk State University, 2 Pirogova st, Novosibirsk, Russia, 630090*

Arkady Mizerny

East Kazakhstan State Technical University, Ust-Kamenogorsk, Kazakhstan

Reimar Seltmann

Natural History Museum, Earth Sciences Department, CERCAMS, Cromwell Road, London SW7 5BD, United Kingdom

Konstantin Kovalev, Andrey Izokh

Institute of Geology and Mineralogy SB RAS, Novosibirsk, Russia

Abstract. Oxidized and primary stockwork-type ores characterize the Sekisovka Au-Ag deposit, eastern Kazakhstan. Primary ores occur as hydrothermally altered breccia bodies localized within a multiphase granitoid massif. Mineralization is represented by two main types: disseminated and stockwork networks. Both types of mineralization occur in the cement of explosive-hydrothermal breccias. The major ores minerals are pyrite, chalcopyrite, sphalerite, pyrrotite, galena, and tetrahedrite. Less common are altaite, hessite, argentite, native gold, petzite, sylvanite, calaverite, and krennerite. To determine the age of the ore-hosting Sekisovka granite massif, we analyzed zircon (U-Pb, SHRIMP-II) from a typical biotite plagiogranite, which yielded an age of 368.4 ± 4.2 Ma. An age of crystallization of a leucogranite-porphry dike with abundant pyrite at Sekisovka is 304.5 ± 2.6 Ma. A similar age was previously determined for small intrusions of plagiogranite and diorite of the Kunush complex elsewhere in eastern Kazakhstan. To determine age of mineralization, we applied the $^{40}\text{Ar}/^{39}\text{Ar}$ method to sericite from gold-bearing quartz veinlets. A plateau age of 306.6 ± 3.8 Ma overlaps the Late Carboniferous magmatism.

Keywords. Gold deposits, Kazakhstan, geochronology, granitoid-hosted, breccia

1 Introduction

The Sekisovka deposit is located in the Rudny Altai in eastern Kazakhstan, 40 km south of the Ust-Kamenogorsk administrative center. The deposit is localized within the multiphase, Sekisovka plagiogranite massif which referred to collision-related Zmeinigorsk granitoid complex. Sekisovka massif was emplaced at the intersection of four regional faults (Figs. 1, 2). The massif is composed of rocks of four intrusive phases: gabbro, granodiorite, plagiogranite, and numerous dikes. The dikes are represented by fine-grained diorites, lamprophyres, granite porphyries, and quartz-albite porphyries, and they are localized along the discontinuous regional fault systems. The intrusions of the complex are calc-alkaline, island-arc, I-type granites or granitoids of “mixed crust-mantle” origin (Kuibuda et al., 2008). The Sekisovka massif was emplaced into a Middle to Late Devonian differentiated basalt-dacite-

rhyolite siliceous-terrogenous formation. This sequence includes quartz-albite porphyry, felsite, plagiogranite porphyry, and pegmatite dikes, as well as explosive breccia bodies with hydrothermally altered fragments of intrusive rocks of varied composition and quartz-calcite-pyrite cement (Rafailovich 2009). Most of the gold is concentrated in mineralized cement of the breccias.

2 Characteristics of the orebodies

Oxidized and primary stockwork-type ores are recovered at the Sekisovka deposit. According to a 2011 company report, total resources (JORC), with a cut-off grade of 0.5 g/t for the open pit and 3.0 g/t for the underground, are 1.93 Moz Au and 2.67 Moz Ag.

Gold is irregularly distributed in elongated zones (“streams”) and in rounded clots (“nests”). Oxidized ores, extending to a depth of 40-60 m, are hosted by brecciated ironstone. Clasts of intrusive rocks are weathered, kaolinitized and sericitized, and cemented by a porous, coarsely-streaky, spotted quartz-goethite-hydrogoethite aggregate containing abundant limonite pseudomorphs over pyrite. Primary ores are represented by explosive hydrothermal breccias, which are composed of fragments of igneous rocks cemented by finely ground material of either similar composition or cut by quartz-carbonate veinlets containing pyrite, sphalerite, and galena. In addition to the gold-rich breccias, subeconomic gold concentrations characterize quartz-sericite-albite-pyrite altered granitoids and propylitically altered gabbros. All the known orebodies at the deposit are localized within the altered explosive-hydrothermal breccias, which have a pipe-like, elongate shape, with sizes ranging from 40 x 100 m to 120 x 500 m. The breccias are traceable to a depth of more than 950 m. Variable clast sizes, from fine to macrofragments, are present in all the breccia types. The 1st and 2nd types are generally characterized by a more intense degree of hydrothermal alteration. The size of the clasts range from 0.1 m to 2 m, with most ≤ 0.5 m, although large blocks of country rock are found locally. The periphery zones of the breccias are subjected to hydrothermal alteration.

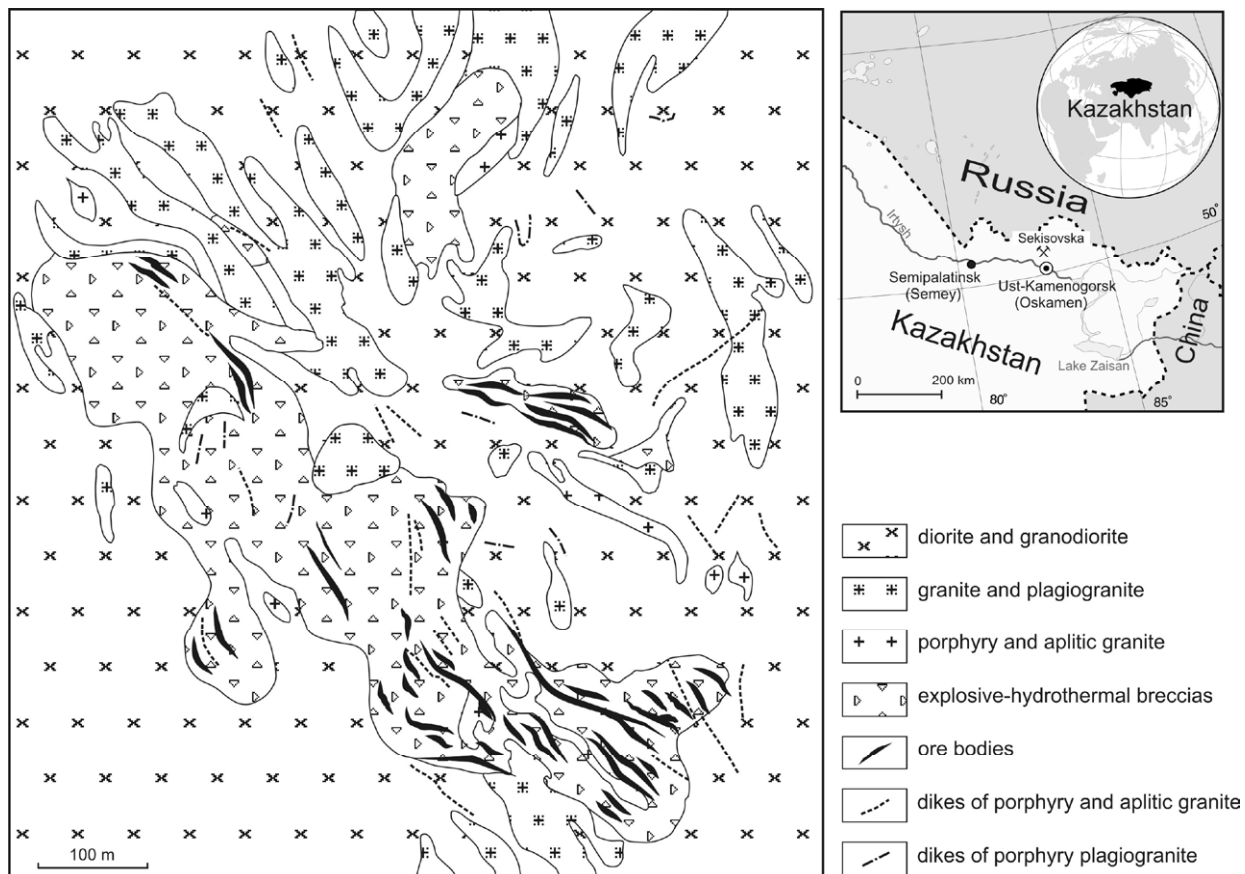


Figure 1. Geographic location and geological sketch map of the Sekisovka deposit (after Rafailovich 2009)

The thickness of alteration zones ranges from 1 to 5 cm and is visually observed as a bleaching of breccia margins. Breccias are cemented by ground hydrothermally altered rocks of quartz-sericite-chlorite composition with impregnations of sulfides, mainly pyrite, but also rarely with inclusions of rock debris. The quartz-carbonate-sulfide stockwork network is widespread in the cement of the breccias. Gangue minerals are mostly present in the form of irregularly shaped clots varying in size from a few mm to 20-30 cm, and with an irregular distribution. Sulfide content in breccia cement is variable and reaches a maximum abundance of 15%. Gold mineralization is spatially and genetically associated with sulfides in the stockworks. However, a direct correlation between the volume of sulfides and gold is not established. The orebodies are distinguished on the basis of chemical analysis, as gold is distributed extremely unevenly. The highest gold concentrations occur at the contacts between various types of breccias, as well as along the contacts of breccias with diorites and dikes of acid composition. Four mineralized zones are distinguished in the breccias, each of which includes a number of distinct orebodies. The auriferous zones are: (1) central zone divided into the northeast (orebodies 3 and 6) and southwest (orebodies 1, 5, and 8) subzones; (2) the northern zone (orebody 2); (3) the western zone (orebody 11); and (4) the southwestern zone (orebody 10). The orebodies strike between 280° and 350°, except for orebody 2 that has an E-W to NW trend. The orebodies generally dip 60-85° to the northeast, whereas orebody 2 dips steeply from 80-85°

3 Ore mineralogy

Mineralization at the deposit is localized in explosive-hydrothermal breccias and is represented by disseminated and stockwork style ores. Both types of mineralization occur in the cement of explosive-hydrothermal breccias.

The primary ore minerals are pyrite, rutile, chalcopryite, sphalerite, pyrrotite, galena, and tetrahedrite. Less common are altaite, hessite, argentite, native gold, petzite, sylvanite, calaverite, and krennerite. Pyrite represents more than 90% of all ore minerals. It is present in an early alteration stage, and subsequent, early and late gold-bearing stockwork stages.

The major ore elements are gold and silver. The anomalous base metals, tellurium, and bismuth are subeconomic. Elements of environmental concern, particularly arsenic and antimony, are at background levels. Contents of alumina and silica are 12-15 % and 50-60%, respectively.

The disseminated mineralization is associated with the process of beresitization (quartz-sericite-albite-pyrite assemblage) that accompanied the formation of explosive-hydrothermal breccias and is unevenly distributed in the breccia cement. Little of the overall gold resource is contained in this mineralization. The concentration of sulfide minerals ranges from 1 to 10% of the cement volume. The main hypogene minerals are pyrite (as much as 90%), rutile (as much as 1.5%), and lesser titanomagnetite and ilmenite that are accessory minerals of initial breccia-forming rocks.

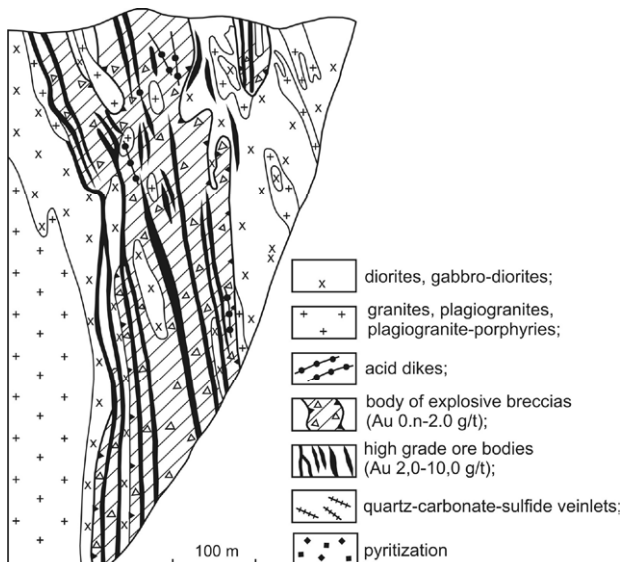


Figure 2. Geological cross-section of Sekisovka deposit (after Rafailovich 2009)

Less common are pyrrhotite, chalcopyrite, sphalerite, and extremely rare native gold. The stockwork networks are superimposed on the zones of brecciation in the breccia. The primary mineral assemblage of the first veinlet event is chalcopyrite-sphalerite-pyrite-quartz, whereas a gold-telluride-sulfide-quartz association, containing the majority of the gold resource at the deposit, is related to the later veinlet-forming event.

Gold is spatially and genetically related to sulfides and gangue minerals such as quartz and carbonate. The chalcopyrite-sphalerite-pyrite-quartz mineral assemblage makes up more than 90% of the stockwork mineralization. The most abundant mineral is pyrite, which is unevenly distributed in the veinlets and clots, locally making up large almost monomineralic pyrite veinlets 3-5 cm in thickness. Occasionally, pyrite forms rare, almost microscopic inclusions in quartz. Tabular and cubic crystals are typical. Thin veinlets of sphalerite, chalcopyrite, and rarely galena and native gold, which is a few microns in size, rarely occur along fractures in this pyrite. The sphalerite contains as much as 25% chalcopyrite inclusions.

The gold-telluride-sulfide-quartz veinlet assemblage commonly occurs in the form of small stockworks and thin discontinuous veinlets confined to breccias near the later felsic dikes. These veinlets and stockworks are characterized by a zonal structure. Sulfides and tellurides usually representing complex aggregates are located in the central part of the veinlets. Gray quartz is developed at the periphery and partially in the center and vein selvages are composed of white and gray-white quartz. The distribution of sulfides and tellurides is extremely irregular. The composition of the ore mineralization is complex, with pyrite, sphalerite, chalcopyrite, galena, tennantite, pyrrhotite, altaite, petzite, hessite, sylvanite, calaverite, krennerite, argentite, and native gold. Pyrite does not form large massive segregations. It has diverse crystal morphology, and contains a large amount of small inclusions of gold, a variety of tellurides, and sulfides that sharply distinguish it from pyrite of the earlier mineral event.

Sphalerite commonly contains chalcopyrite exsolution features. Chalcopyrite and sphalerite are commonly intergrown with galena, silver-rich tetrahedrite, native gold, and a variety of tellurides.

3 Geochronological data on magmatic rocks and ore mineralization

Geochronological studies (U-Pb method on zircons, SHRIMP-II, done at the Karpinskiy VSEGEI, Saint-Petersburg, Russia) indicated ages of 377.7 ± 6.1 Ma for plagiogranites and 371.5 ± 2.2 Ma for leucogranites of the Zmeinogorsk complex (Kuibuda et al. 2008). The Late Devonian ages indicate that formation of the Zmeinogorsk complex occurred along the active continental margin of the Kazakhstan microcontinent, with melt contributions from both metabasites of the Rudny Altai oceanic basement and sedimentary rocks of the upper crust.

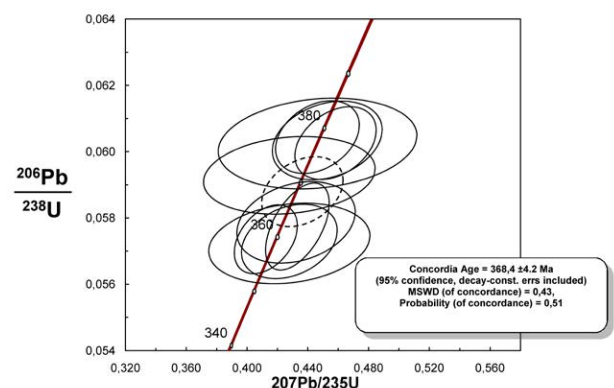


Figure 3. Concordia Age (367 ± 4.2 Ma) zircons from Sekisovka granite massif.

To determine the age of the adjacent Sekisovka granite pluton, the body that hosts the gold deposit, we separated zircons from a biotite plagiogranite sample SKS-02. Ten spots were analyzed in seven zircon grains. The spots were located in both inner and outer parts of the grains. All ten analyses, after correction for common lead, plot on concordia as a relatively tight cluster and yield a $^{206}\text{Pb}/^{238}\text{U}$ concordia age (Fig. 3) of 368.4 ± 4.2 Ma (MSWD=0.42), which is a good estimate of crystallization age of sample SKS-02, and is a similar age to those of the intrusions of the adjacent Zmeinogorsk complex.

A similar technique (SHRIMP II) was used to determine the age of crystallization of a plagiogranite-porphphyry dike at the deposit, which was highly altered and contained abundant pyrite (sample SKS-05). The SHRIMP dating (by 10 points in 10 grains) yielded a much younger age of age of 304.5 ± 2.6 Ma (MSWD=0.00069) (Fig. 4). A similar age had earlier been established for small intrusions of plagiogranite and diorite of the Kunush complex (306.7 ± 8.7 and 299 ± 2.3 Ma; U-Pb SHRIMP, Vladimirov et al. 2008), which is located elsewhere in eastern Kazakhstan.

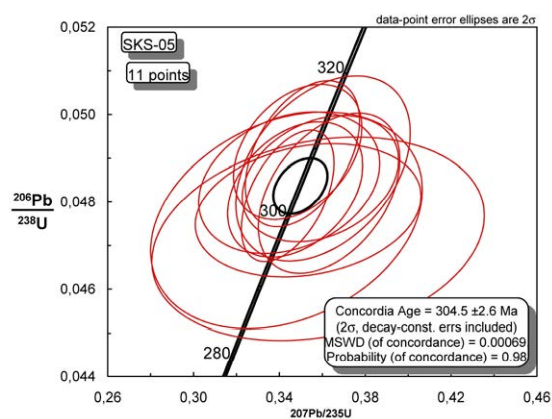


Figure 4. Concordia Age (304.5 ± 2.6 Ma) zircons from acid dyke, Sekisovka deposit.

In addition, we applied the $^{40}\text{Ar}/^{39}\text{Ar}$ method to determine the age of sericite from ore veins of the Serkisovskoe deposit. Analyses were done in the analytical center of the IGM SB RAS, Novosibirsk, Russia. The obtained plateau age of 306.6 ± 3.8 Ma (Fig. 5) overlaps the younger late Carboniferous magmatism.

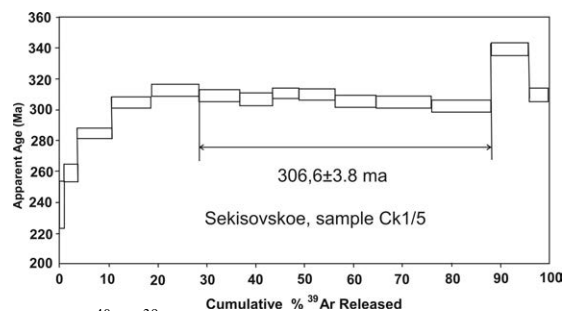


Figure 5. $^{40}\text{Ar}/^{39}\text{Ar}$ step-heated spectrum for sericite sample yielded a 306.6 ± 3.8 Ma plateau age

4 Conclusions

The observed mineralogical assemblages allow us to classify mineralization at the Sekisovka deposit as the gold-telluride type. It is presently the only recognized Te-rich economic Au-Ag deposit in eastern Kazakhstan. The age of mineralization determined on sericite from the main ore stage at the Sekisovka deposit is coeval with intrusion of small bodies of felsic composition. A similar age (304.9 ± 4.2 Ma, U-Pb SHRIMP) was obtained for plagiogranite porphyries that are present at the Zherek gold deposit in the Semipalatinsk goldfield also in eastern Kazakhstan (Kovalev et al. 2009). However, the Zherek gold mineralization differs from that of the Sekisovka deposit in that gold forms microinclusions in arsenopyrite and a late stibnite stage at Zherek (Kovalev et al. 2011). The age of ores from the gold-arsenopyrite type deposits in eastern Kazakhstan, as well as in northeastern Kazakhstan (e.g., Suzdal, Bolshevik, Bakyrchik, Balazhal, Baturinskoye) (Naumov et al. 2011), all determined by Ar-Ar dating of hydrothermal sericite, are all 280 ± 5 Ma. Some large and giant gold deposits in central Asia can also be attributed to the same age: Muruntau (175 Moz Au, 287.5 ± 1.7 Ma), Kumtor (19 Moz Au, 288-284 Ma) (Mao et al. 2004), and deposits of the Chinese Altai (Saerbulake) (Mao et al. 2003).

A similar gold-telluride analogue to the Sekosovka deposit is the Novolushnikovo deposit in the Tom-Kolyvan zone, which is part of the Ob-Zaisan fold belt (Naumov et al, 2011) that also hosts the Sekisovka deposit. The age of the Novolushnikovo gold-telluride deposit is 299.8 ± 2.7 Ma ($^{40}\text{Ar}/^{39}\text{Ar}$). It formed subsequent to porphyry Cu-Mo mineralization in the cupola of the Novolushnikovo plagiogranite massif.

The geochronological data indicate two main ages of formation of productive gold mineralization within the Ob-Zaisan fold belt. An age of 305 ± 5 Ma, characterizes gold-telluride type deposits. The major gold-bearing mineral is pyrite, anomalous arsenic is absent, and silver-, tellurium-, and bismuth-bearing minerals are present. An age of 280 ± 5 Ma is when gold-arsenopyrite type deposits formed, which are characterized by widespread, high-grade gold ores and overprinting late stibnite mineralization.

Acknowledgements

Authors are grateful to management and geologists of Hambleton Mining. The work was supported by grants RFBR 13-05-00998 and IGCP-592 sponsored by IUGS-UNESCO.

References

- Kovalev KR, Kalinin YuA, Naumov EA, Kolesnikova MK, Korolyuk VN (2011) Gold-bearing arsenopyrite in Eastern Kazakhstan gold-sulfide deposits. *Russ Geol Geophys* 52:178–192. DOI: 10.1016/j.rgg.2010.12.014. ISSN: 1068-7971
- Kovalev KR, Kalinin YuA, Naumov EA, Pirajno F, Borisenko AS (2009) A mineralogical study of the Suzdal sediment-hosted gold deposit, Kazakhstan: implications for ore genesis. *Ore Geol Rev* 35:186-206. DOI: 10.1016/j.oregeorev.2008.11.007
- Kuybida ML, Kruk NN, Paderin IP (2008) Plagiogranite magmatism of Ore Altay region, Russia. *Granites and Earth Evolution: geodynamic position, petrogenesis and ore content of granitoid batholiths. First International Geological Conference.* 26-29 August 2008 Ulan-Ude, Russia
- Mao J, Goldfarb R, Seltmann R, Wang D, Xiao WJ and Hart C (Eds) (2003) Tectonic evolution and metallogeny of the Chinese Altai and Tianshan. *International Association on the Genesis of Ore Deposits (IAGOD), Guidebook Series 10, CERCAMS NHM, London*
- Mao J, Konopelko D, Seltmann R, et al (2004) Postcollisional age of the Kumtor gold deposit and timing of hercynian events in the Tien Shan, Kyrgyzstan. *Econ Geol* 99(8): 1771-1780
- Naumov E, Borisenko A, Kovalev K, Kalinin Y, Fedoseev G, Seltmann R (2011) Gold deposits of Western Siberia and Eastern Kazakhstan: types and ages of mineralization, correlation with magmatic events. In: Barra F et al (eds) *Let's Talk Ore Deposits, Proceedings of the 11th Biennial SGA Meeting of The Society for Geology Applied to Mineral Deposits, Antofagasta, Chile, 26-29th September*, pp 82-84
- Rafailovich MS (2009) Gold mineral resources of Kazakhstan: geology, metallogeny, prognostic evaluation. Complex, Almaty (in Russian)
- Vladimirov AG, Kruk NN, Khromykh SV, et al (2008) Permian magmatism and lithospheric deformation in the Altai caused by crustal and mantle thermal processes: *Russ Geol Geophys* v.49(7): 468-479

Gold-bismuth mineralisation in the orogenic gold occurrences of the Kuhmo greenstone belt (Finland)

Konstantin Novoselov

Institute of Mineralogy UB RAS, Miass, Russia

Elena Belogub

Institute of Mineralogy UB RAS, Miass, Russia

Olga Ermolina

Institute of Mineralogy UB RAS, Miass, Russia

Alexandr Mikhailov

Mineral Exploration Network (Finland), Cardiff, UK

Abstract. There is a strong association of gold with bismuth in the gold occurrences of the Kuhmo greenstone belt. It reflects relatively low-temperature conditions in reduced environments. Textural relations between ore minerals suggest that arsenopyrite was formed earlier than the gold and bismuth minerals. Mineralogical features associated with the gold can be explained using the Liquid Bismuth Collector Model.

Keywords. Kuhmo greenstone belt, orogenic gold, Finland, Archaean

1 Introduction

Komatiite-hosted Ni, VMS, and orogenic gold are the most common metallogenic components in Archaean greenstone belts. Canadian shield, Western Australia and other Archaean areas have well-known examples of orogenic gold deposits.

Gold mineralisation in the Fennoscandian shield is not very extensively investigated and the ore mineralogy is studied in detail for only a few deposits or deposit camps (Kojonen 2006). We have investigated the ore mineralogy of selected gold occurrences in the central and southern part of the Kuhmo greenstone belt. This work was based on drill core of known, previously drilled occurrences. Ore mineral assemblages were investigated using polished sections and heavy mineral concentrates at the Institute of Mineralogy UB RAS using optical microscopy and SEM with EDA REMMA-202M (analyst V. Kotlyarov).

2 Geological background

The Finnish part of the Fennoscandian shield comprises three major domains. There are the Archaean cratonic nucleus (Karelian domain) and the Paleoproterozoic mobile belts of Kola-Lapland and Svecofennia.

The Archaean bedrock can be subdivided into TTG-type complexes, and a few major supracrustal belts: Oijärvi, Kuhmo-Suomussalmi and Ilomantsi. The Kuhmo-Suomussalmi volcano-sedimentary complex (Kuhmo, Suomussalmi and Tipasjärvi greenstone belts combined) was probably formed in an intra-plate, oceanic environment (Lahtinen et al. 2011). Its central

part (the Kuhmo greenstone belt) has a symmetrical syncline structure with a submeridional trend. The most voluminous rocks are mafic volcanic rocks (Papunen et al. 2009). Several phases of the Archaean TTG granitoids have intruded the greenstone belt.

A number of drilling-indicated gold occurrences have been identified in the Kuhmo greenstone belt (e.g., Piilola, Jousijärvi, Mujesuo, Hetteilä, Aittoranta). On the basis of mineral assemblages in the gold occurrences and their host and adjacent rocks, the degree of regional metamorphism is from upper-greenschist to lower-amphibolites facies. Certain features of selected occurrences are summarised below, mostly based on Eilu and Pankka (2009) and references therein. Also original observations were obtained during core revision in the Loppi Drill Core Depot.

The Jousijärvi occurrence is hosted by biotite and muscovite-biotite schists with pyrrhotite dissemination. Deposit structure is a steeply-dipping monocline. Gold content is up to 3.6 ppm for 2.6 m of drill core and it shows a linear positive correlation with As. The As content is up to 1300 ppm in the gold-mineralised schist.

Gold mineralisation at Piilola is hosted by mica schist near its contact with a granite gneiss. Gold grades are variable and up to 17.3 ppm (0.5 m of drill core). Mineralised zones are associated with sulphide dissemination. There is a positive correlation between Au and As in the mineralised rocks.

Talc-carbonate, chlorite-tremolite, actinolite, and actinolite-chlorite schists, alteration products of mafic and ultramafic rocks, host ore and form the immediate wall rocks at Mujesuo. Gold contents are up to 9 ppm per metre, and the high grades occur in both quartz veins and the altered rocks around the veins.

The Hetteilä occurrence is hosted by garnet-amphibole-magnetite-pyrrhotite rocks and banded amphibolites near a NNW-trending shear zone. Gold contents are up to 1.6 ppm per metre of drill core.

The Aittoranta occurrence is located in the eastern margin of a N-trending shear zone. It is hosted by mafic volcanic rocks with quartz-tourmaline-arsenopyrite veins and zones of tourmalinisation. No gold grades are reported from Aittoranta.

3 Ore mineral assemblages

Sulphide mineralisation in the host and wall rocks of the investigated occurrences is predominantly disseminated. Most of the sulphides are fine-grained. Pyrrhotite breccia is known from Piilola and Jousijärvi. The sulphides also form impregnation structures and irregular spots in the quartz and quartz-feldspar veins.

The main ore minerals are, in a decreasing order of abundance, pyrrhotite, arsenopyrite, and pyrite. Only in a few locations, arsenopyrite forms visible grain aggregates. Chalcopyrite and pentlandite commonly occur as intergrowths together. The abundance of magnetite is a specific feature of the Hetteilä occurrence.

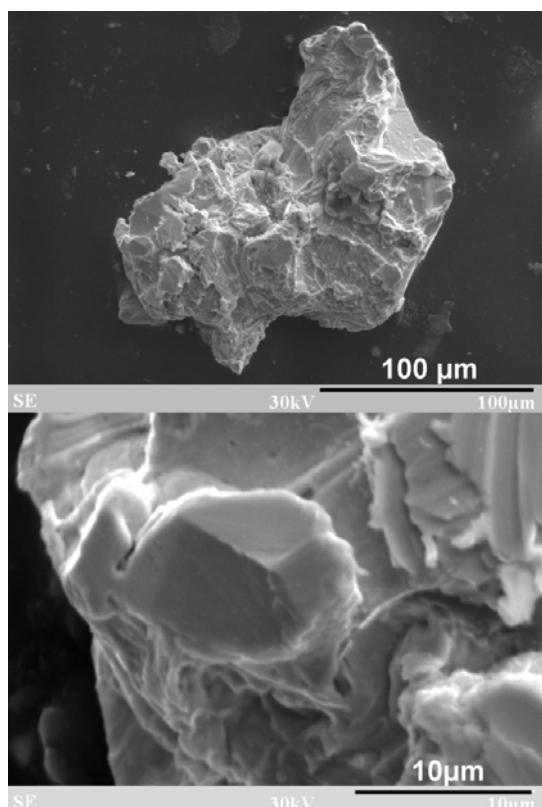


Figure 1. Shape of the gold particles from the Jousijärvi occurrence. Xenomorphic grains with rare rhombic dodecahedron boundaries. BSE Image.

Native gold has been observed at Piilola, Jousijärvi, Mujesuo, and Hetteilä, and is predominantly associated with arsenopyrite. Bismuth minerals have been detected in the ore at Piilola, Hetteilä, Mujesuo, and Jousijärvi. Native gold forms inclusions in arsenopyrite and silicate minerals. Inclusions in chalcopyrite or pyrrhotite are rare (e.g. Mujesuo). Native gold has also been observed as inclusions in magnetite at Hetteilä. Gold particles extracted from heavy mineral concentrates have lumpy, isometric to elongated shape (Fig.1). In places, gold have fragments of rhombic dodecahedron boundaries. Size of gold grains varies from 0.09 to 0.3 mm. In general, the fineness of gold is high. The Au content in the native gold increases in the following order: Jousijärvi, Mujesuo, Piilola, Hetteilä (Fig. 2). One analysis with Au

at only 43.85 wt.% was obtained from Hetteilä. Copper content in the native gold usually is no more 0.01 apfu.

Arsenopyrite from the gold-bearing mineral associations is usually non-stoichiometric. The As:S ratio varies from 0.88 to 1.27. Arsenopyrite from Jousijärvi contains, in places, Co and Ni.

Bismuth minerals, where present, occur in contact with native gold, and intergrowths of the native gold and bismuth have been detected in some occurrences. The bismuth minerals detected include native bismuth, maldonite, and a bismuth telluride. Native bismuth was observed as anhedral inclusions up to 50 µm in diameter within arsenopyrite and magnetite. Frequently, it forms intergrowths with native gold (Fig. 3). Maldonite forms xenomorphic inclusions within arsenopyrite. As a rule, maldonite occurs in association with native bismuth, and contains Ag (up to 0.8 wt.%) and Cu (up to 0.25 wt.%). One very small inclusion of bismuth telluride was found in magnetite from Hetteilä, and only a qualitative composition was obtained from this grain.

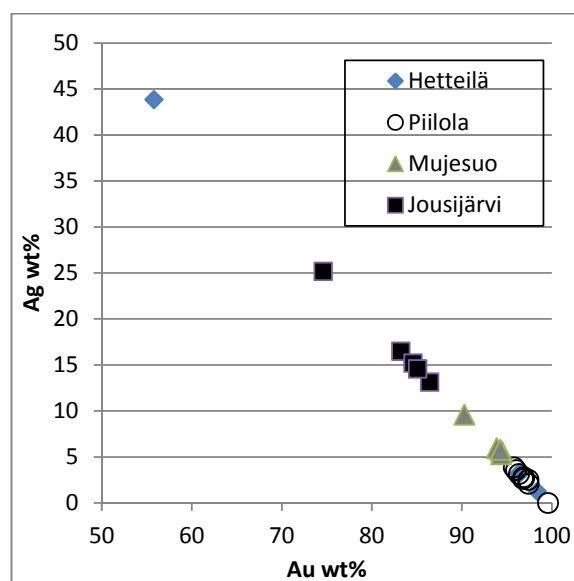


Figure 2. Composition of the native gold from different occurrences of the Kuhmo greenstone belt.

4 Application of LBC model to mineralisation

Natural Bi compounds are recognised as the petrogenetic indicators for gold deposits. Moreover, the presence of Bi in a hydrothermal system may lead to gold concentration with Bi. Bismuth has a melting temperature of only 271 °C. In a hydrothermal solution with temperature more than 271 °C, bismuth may form a separated liquid. In the concordance with a theory known as Liquid Bismuth Collector Model (LBCM) (Douglas et al. 2000), bismuth melt can scavenge gold from undersaturated hydrothermal fluids. Further gold transportation and deposition occurs in bismuth droplets. Liquid Bi can incorporate 17 at.% Au and will crystallise as native Bi and maldonite at 241°C (Okamoto and Masaalski 1983). These are the reasons for gold enrichment in Bi-bearing mineral assemblages relative

to the hydrothermal sulphide assemblage in a mineral deposit. Also, gold may be mobilised into an anatectic melt during metamorphism at upper-greenschist facies and higher PT conditions (Tomkins et al. 2007).

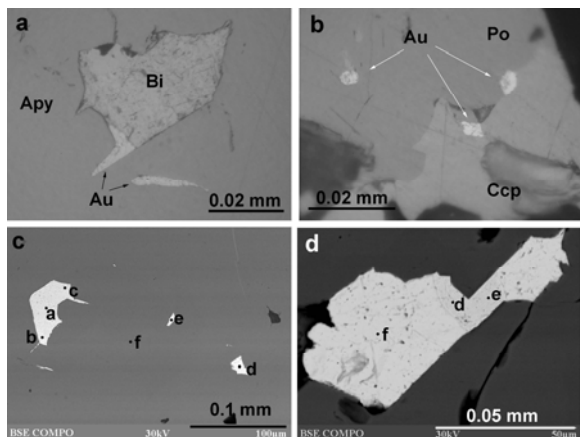


Figure 3. Gold and bismuth mineralisation from the different occurrences of the Kuhmo greenstone belt: a. Native gold (Au) and bismuth (Bi) in arsenopyrite (Apy), Jousijärvi, RL; b. Gold (Au) impregnations among pyrrhotite (Po) and chalcopyrite (Ccp), Mujesuo, RL; c. bismuth (point d), gold (a, b, c), and maldonite (e) in arsenopyrite (f), Piilola, BSE image; d. gold (points d, e) and bismuth (f) in arsenopyrite, Piilola, BSE image.

The Au-Bi mineral association occurs usually as inclusions and intergrowths with arsenopyrite. Textural relationships evidence late-stage formation of gold-bearing mineral assemblages, after the formation of arsenopyrite. For the Kuhmo belt occurrences, estimation of arsenopyrite crystallisation temperature has been carried out on the basis of As content in arsenopyrite grains, according to the method by Kretschmar and Scott (1976). Arsenopyrite from Piilola and Jousijärvi occurrences suggests a temperature range of about 450–550 °C and confirms the results of a fluid inclusion study for Aittoranta (Poutiainen and Partamies 2003). Temperature estimation for quartz from quartz-tourmaline-arsenopyrite veins is 450–500 °C and the pressure 2.5–3.5 kbar.

From the data above, we may suggest the minimum temperature of mobilisation and transportation of gold and bismuth being about 270–300 °C. The dominance of pyrrhotite in the ore mineral assemblage, the scarcity of Te-Bi minerals and the previous thermodynamic estimations (Ciobanu et al. 2006) indicate that deposition of gold in the Kuhmo belt occurred under reduction conditions. These conditions correspond with the estimated regional metamorphic grade.

5 Summary

In conclusion, the association of gold with bismuth in the gold occurrences of the Kuhmo greenstone belt has been established. It reflects low-temperature conditions in reduced environments. Textural relations between ore minerals indicate that arsenopyrite was formed earlier than gold-bismuth minerals.

Acknowledgements

Analytical investigations were supported by Urals Branch of Russian Academy of Science. We are especially grateful to the company “Mineral exploration network (Finland)”.

References

- Ciobanu CL, Cook NJ, Damian F, Damian G (2006) Gold scavenged by bismuth melts: an example from alpine shear-remobilizates in the Highis Massif, Romania. *Mineral Petrol* 87:351–384.
- Douglas N, Mavrogenes J, Hack A, England R (2000) The liquid bismuth collector model: an alternative gold deposition mechanism. 15th Austr Geol Conv:135.
- Eilu P, Pankka H (2009) FINGOLD – A public database on gold deposits in Finland. Version 1.0. Geol Surv Finland Digital Data Prod 4
- Kojonen K (2006) Au-Ag telluride-selenide deposits in Finland Au-Ag-Te-Se deposits (Proceedings of the 2006 Field Workshop). Geol Surv Finland:85–92.
- Kretschmar U, Scott SD (1976) Phase relations involving arsenopyrite in the system Fe-As-S and their application. *Can Mineral* 14:364–386.
- Lahtinen R., Holttä P, Kontinen A, Niiranen T, Nironen M, Saalman K, Sorjonen-Ward P (2011) Tectonic and metallogenic evolution of the Fennoscandian shield: key questions within emphasis on Finland. *Geol Surv Finland Spec Pap* 49:23–33.
- Okamoto K, Masaalski TB (1983) Au-Bi. Binary alloy phase diagrams. Vol. I. ASM Intl:238–240.
- Papunen H, Halkoaho T, Luukkonen E (2009) Archaean evolution of the Tipasjarvi-Kuhmo-Suomussalmi greenstone complex, Finland. *Geol Surv Finland Bull* 403.
- Poutiainen M, Partamies S (2003) Fluid inclusion characteristics of auriferous quartz veins in Archean and Paleoproterozoic greenstone belts of eastern and southern Finland. *Econ Geol* 98:1355–1369.
- Tomkins A, Pattison D, Frost R (2007) On the initiation of metamorphic sulfide anatexis. *J Petrol* 48:511–535.

Age constraints on host rocks for gold mineralisation in the Ashanti Belt, Ghana

Luis A. Parra, Marco L. Fiorentini, John Miller, and T. Campbell McCuaig.

Centre for Exploration Targeting, ARC Centre of Excellence for Core to Crust Fluid Systems, School of Earth and Environment, The University of Western Australia., Perth, Australia.

Yan Bourassa

Golden Star Resources LTD., 10901 W.Toller Drive, Suite 300, Littleton, CO, United States.

Stéphane Perrouty

Université de Toulouse, UPS (SVT-OMP), GET, 14 av. Edouard Belin, F-31400 Toulouse, France

Abstract. The Ashanti Belt region, Ghana possesses one of the richest gold endowments of the West African Craton, hosting several multi-million ounce deposits. One of these deposits is Wassa along with the Benso satellite deposits, located in the southern section of the Belt. Wassa is hosted in a series of interlayered mafic flows and volcanoclastic beds with greywackes, detrital magnetite units, mafic intrusives and plagioclase rich porphyritic intrusive rocks; while the Benso is hosted within a mafic intrusive complex and sheared mafic volcanic flows. The ages of the Wassa porphyry host rock and the Benso G-zone sample were determined using U-Pb SHRIMP dating methods, respective dating of 2192.7 ± 4.6 Ma and 2159.5 ± 7.5 Ma. These intrusions are considerably older than the previously reported gold hosted intrusions from that region (ca. 2103 Ma, Oberthür et al. 1998). As a result, this new data confirms the presence of older stratigraphy in the southern Ashanti Belt. These results, in combination with recent structural studies that interpret the Wassa mineralisation to be of pre-Eburnean origin strongly support the possibility of significant gold mineralisation occurring during the Eoeburnean orogeny ca. 2190-2140 Ma and brings a new understanding of gold mineral systems in the Ashanti Belt.

Keywords. Ghana, Benso-Wassa, gold, U-Pb SHRIMP.

1 Geology

The Birimian Terrane of the West Africa Craton which extends over large portions of Burkina Faso, Ghana, Mali, Ivory Coast, and Guinea, mainly comprises relatively narrow sedimentary basins and linear or/and arcuate volcanic belts (Leube et al. 1990; Dampare et al. 2008). The terrane resulted from an accretion event at ca. 2200-2100 Ma, when there is evidence of eruption of tholeiitic basalts and rhyolites within the Baoule Mossi Domain (Bonhomme 1964; Abouchami and Boher 1991; Boher et al. 1992; Taylor et al. 1992; Dampare et al. 2008).

The Birimian formation is subdivided into three major units: (1) The Upper Birimian, dominated by detrital and volcanoclastic rocks of mostly mafic to felsic affinity that include turbidites, shales, and carbonates interbedded with calc-alkaline volcanics; (2) the Lower Birimian, which consists of a series of volcanics represented by dolerites, gabbros, and tholeiitic basalts; locally interlayered with sediments and carbonates; and (3) narrow late sedimentary basins known as the Tarkwaian. The formations have been intruded by

granitoids, which appear to range from pre-kinematic to syn-kinematic to post-tectonic (Abouchami and Boher 1990; Boher et al. 1992).

The geology of Ghana is dominated by the Paleoproterozoic Birimian rocks. In the southwest, these units form a series of NE-trending greenstone belts, one of which is the Ashanti Belt. The belts are separated by sedimentary basins (Bonhomme, 1962; Perrouty et al. 2012).

Wassa, a multi-million ounce deposit, is positioned within the southern section of the Ashanti Belt in Ghana, 35 km east of Bogoso. It lies in the eastern limb of the Tarkwa syncline and is enclosed by the Cape Coast granites to the east and the Tarkwaian sediments to the west (Golden Star Resources LTD. 2012).

The Wassa deposit is polydeformed and hosted in a series of mafic flows, volcanoclastic beds, greywacke intercalated with layers of detrital magnetite units, and intruded by diorites and plagioclase rich felsic porphyry intrusive bodies (Golden Star Resources LTD. 2012).

The Benso deposit consists of four ore bodies that range between 50k and 100k ounces each. It is located southwest from the Wassa deposit also within the Ashanti Belt. It is hosted within a series of mafic to intermediate intrusive rocks which are intercalated with sheared mafic volcanic flows and intruded by plagioclase porphyry rocks (Golden Star Resources LTD. 2012).

2 Samples and Analytical methods

Samples included: (1) Unmineralised porphyry intrusion representative of the Wassa southeast zone host rock obtained from diamond drill core ID number JM012; (2) unmineralised granodiorite from the Benso G-zone, collected from diamond drill core ID JM020 (Fig. 1). Even though the samples do not contain gold, they are representative of the main host rock type for both deposits.

Samples were crushed and processed to obtain zircon concentrates. Zircon grains were handpicked, mounted in epoxy (mount GH1) and polished with diamond film polishing mats. All mounted grains were imaged by backscattered electron and cathodoluminescence methods using a JEOL 6400 at the Centre for Microscopy, Characterisation and Analysis (CMCA), which is located at the University of Western Australia (UWA). The imaging process was intended to determine internal

textures and select grains that were not extremely cracked or that showed strong metamict damage.

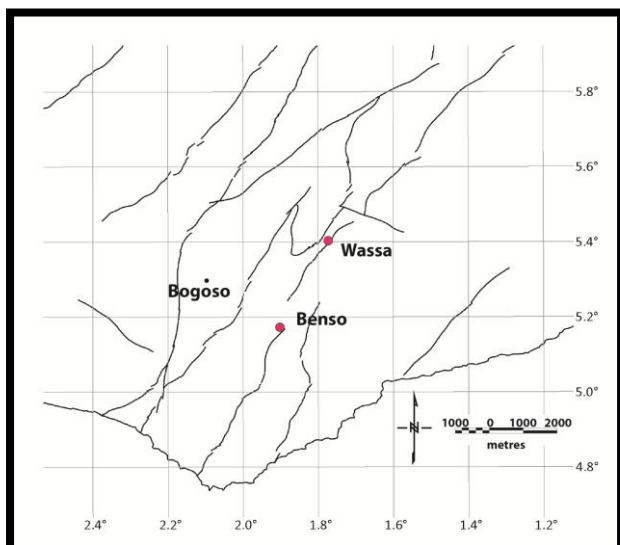


Figure 1. Simplified map of SW Ghana showing the approximate location of the town of Bogoso and the Wassa and Benso deposits.

Mount GH1 was analysed using Sensitivity High Resolution Ion Microprobe (SHRIMP) at the John de Laeter Centre for Isotope Research of Curtin University, Perth, Western Australia. Eleven analyses of the standard BR266 were performed during the session, with an external spot-to-spot uncertainty of 0.85% (1σ) and $^{238}\text{U}/^{206}\text{Pb}$ calibration uncertainty of 0.29% (1σ). The calibration uncertainties were included in the error of the $^{238}\text{U}/^{206}\text{Pb}$ ratios. For unknown analysis limit values were established as follows: (1) common Pb < 1.0%; (2) U < 100 ppm; and (3) $^{232}\text{Th}/^{238}\text{U}$ ratio > 0.15.

3 Results

Sample JM012: Analyses were concordant to up to 33% discordant. All discordant analyses were kept because they formed a well-constrain discordia with the concordant groups. Three age groups were clearly identified: (1) Two analyses, JM012-12 and JM012-9, with ages of 2141 ± 9 Ma and 2152 ± 11 Ma, were discarded as crystallisation age due to Pb loss; (2) main population comprised of 22 analyses, with a weighted mean age of 2190 ± 4.4 Ma, MSWD of 1.4; intercept age of 2192.7 ± 4.6 Ma, MSWD 1.3 and lower intercept at 64 ± 65 Ma (Fig. 2); and (3) two analyses JM012-4.1 (core) and JM012-14 with ages of 2211 ± 8 and 2223 ± 8 Ma, respectively. The age of 2192.7 ± 4.6 Ma is interpreted as the magmatic crystallisation age.

Sample JM020: Analyses were concordant to up to 15% discordant. Three age groups were clearly identified: (1) Two analyses, JM020-20.1 and JM020-16, with ages of 2128 ± 10 Ma and 2136 ± 7 Ma respectively, discarded as crystallisation age due to Pb loss; (2) main population comprised of 19 analyses, with a weighted mean age of 2158.2 ± 3.4 Ma, MSWD of 1.2; intercept age of 2159.5 ± 7.5 Ma, MSWD 1.3 and lower intercept at 76 ± 350 Ma (Fig. 3); and (3) two analyses

JM020-8.1 (core) and JM020-14 with ages of 2238 ± 7 Ma and 2242 ± 8 Ma, respectively. The age of 2159.5 ± 7.5 Ma is interpreted as the magmatic crystallisation age.

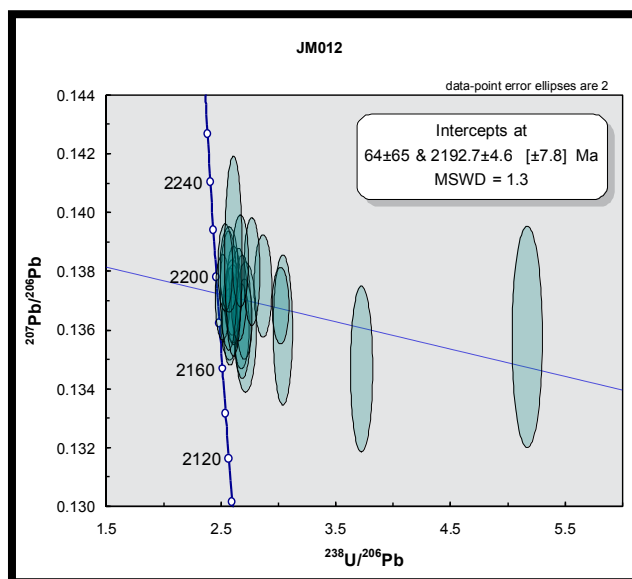


Figure 2. Tera-Wasserburg plot of sample JM012 showing intercept crystallisation age.

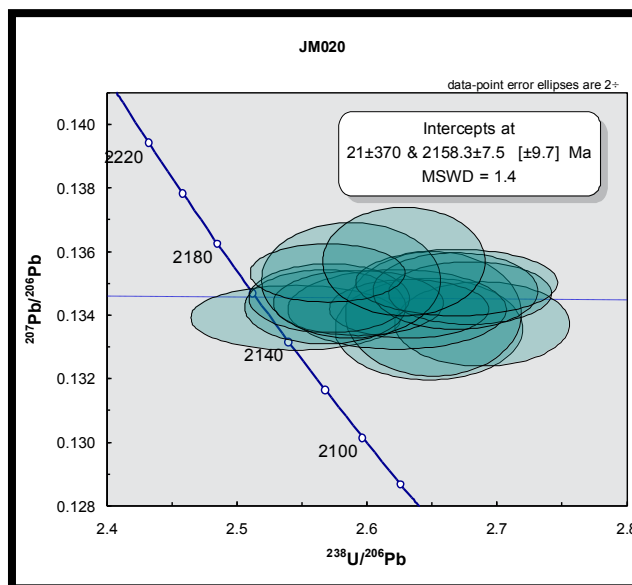


Figure 3. Tera-Wasserburg plot of sample JM020 showing intercept crystallisation age.

4 Discussion

Oberthür et al. (1998) presented data showing that the age of crystallisation of the gold bearing granitoid intrusions near the Anyankyerim, Nhyiaso, Yaomensakrom and Ayanfuri deposits northeast from Wassa along the western flank of the Ashanti Belt was ca. 2105 ± 2 Ma. They suggested that in the case of Anyankyerim the three zircons that yield an age between 2142 and 2159 Ma were the result of detrital zircons incorporated into the granitoid melt. The other localities mentioned in Oberthür et al. (1998) yielded a crystallisation age between ca. 2103 and 2111 Ma.

The Wassa sample has an interpreted crystallisation

age of 2192.7 ± 4.6 Ma which is older than any age obtained by Oberthür et al. (1998). Even if the two younger analyses, (discarded due to Pb loss) are interpreted as the crystallisation age they remain older than the ages reported by Oberthür et al. (1998). A similar situation occurs with Benso JM020 granodiorite sample, where the interpreted crystallisation age of 2159.5 ± 7.5 Ma and even the analyses discarded due to Pb-loss (ca. 2128-2136 Ma) are older than the intrusion ages reported by Oberthür et al. (1998). The new data indicates there are granitoid intrusions that are mineralised with much older ages than previously reported. These intrusions are older than the Birimian sediments that host the world class Obuasi deposit (Perrouty et al. 2012).

Perrouty et al. (2012) defined the Eoeburnean phase as magmatism-deformational events that occurred between 2187 and 2158 Ma. They suggested that mineralisation may have occurred in this period, which potentially could be part of the source for the Tarkwaian paleoplacer deposits in Ghana. The 2193 Ma age of the Wassa porphyry that intrudes the Wassa host rocks indicates that this polydeformed deposit has a host stratigraphy that would have been affected by the Eoeburnean deformation phase (in contrast to the Obuasi and Anyankirim deposits that have host rocks younger than this deformation phase). The Wassa deposit has host rocks that could have a phase of gold with an age compatible with an early gold source. An absolute age on the Wassa mineralisation has not yet been constrained. But structural evidences on the gold bearing quartz veins indicate a complex deformation history, suggesting an Eoeburnean timing. Additionally Perrouty et al (2012) demonstrate that the mineralisation is affected by a folding event that predates the Tarkwaian.

5 Conclusion

This study shows the occurrence of gold mineralised intrusions from the Wassa and Benso deposits that are older than other mineralised intrusions previously documented for the southwest Ashanti Belt region in Ghana. The interpreted crystallisation ages of the mineralised intrusions from the Wassa and Benso deposits are respectively: 2192.7 ± 4.6 Ma and 2158.3 ± 7.5 Ma and confirm the interpreted older age of this portion of the Ashanti Belt as interpreted by Perrouty et al (2012). It is possible that the rocks that are the host for the Wassa deposit could have been mineralised during the Eoeburnean phase ca. 2187-2158 Ma and that they are a potential source to the Tarkwa paleoplacer deposits.

Acknowledgements

We thank Golden Star Resources LTD. for providing the samples required for the present work. We acknowledge the facilities, and scientific and technical assistance of the Australian Microscopy & Microanalysis Research Facility at the Centre for Microscopy, Characterisation & Analysis of UWA, a facility funded by the University, State and Commonwealth Governments. We thank the staff and facilities of the John De Laeter Centre for

Isotope Research, hosted at Curtin University. We wish to gratefully acknowledge AMIRA International and the industry sponsors, including AusAid and the ARC Linkage Project LP110100667, for their support of the WAXI project (P934A). We are also appreciative of the contribution of the various Geological Surveys and Departments of Mines in West Africa as sponsors in kind of WAXI. Finally, we wish to recognize our WAXI research colleagues from the various Institutions from around the world.

References

- Abouchami W, Boher M (1990) A Major 2.1 Ga Event of Mafic Magmatism in West Africa: An Early stage of Crustal Accretion. *J Geophys Res* 9:17605-17629
- Boher M, Abouchami W, Michard A, Albarede F, Arndt N (1992) Crustal Growth in West Africa at 2.1 Ga. *J Geophys Res* 97:345-369
- Bonhomme M, (1962) Contribution à l'étude géochronologique de la plate-forme de l'Ouest Africain. *Ann. Fac. Sci. Univ. Clermont-Ferrand Géol. Minéral* 5:62
- Dampare SB, Shibata T, Asiedu DK, Osae S, Banoeng-Yakubo B (2008) Geochemistry of Paleoproterozoic metavolcanic rocks from the southern Ashanti volcanic belt, Ghana: petrogenetic and tectonic setting implications. *Precamb Res* 162:403-423
- Golden Star Resources LTD (2012) Wassa Drill results, Plans and Sections. <http://www.gsr.com/Operations/Wassa.asp>. Accessed 22 January 2013
- Leube A, Hirdes W, Mauer R, Kesse GO (1990) The early Proterozoic Birimian supergroup of Ghana and some aspects of its associated gold mineralization. *Precamb Res* 46:139-165
- Oberthür T, Vetter U, Davis DW, Amanor JA (1998) Age constraints on gold mineralization and Paleoproterozoic crustal evolution in the Ashanti belt of southern Ghana. *Precamb Res* 89:129-143
- Perrouty S, Laurent A, Jessell MW, Baratoux L, and Bourassa Y (2012) Revised Eburnean geodynamic evolution of the gold-rich southern Ashanti Belt, Ghana, with new field and geophysical evidence of pre-Tarkwaian deformations. *Precamb Res* 204-205:12-39
- Taylor PM, Moorbath S, Leube A, Hirdes W (1992) Early Proterozoic crustal evolution in the Birimian of Ghana: constraints from geochronology and isotope geochemistry. *Precamb Res* 56:97-111

The importance of black shales in the origin of the Amantaytau orogenic gold deposit in Uzbekistan: evidence from pyrite chemistry and sulfur isotope data

Jan Pašava, Anna Vymazalová, Petr Dobeš
Czech Geological Survey, Geologická 6, 152 00 Prague 5, Czech Republic

Hartwig Frimmel
Institute of Geography and Geology, University of Würzburg, Am Hubland, D-97074 Würzburg, Germany

Alexandr V. Jukov, Rustam I. Koneev
National University of Uzbekistan, Vuzgorodok, 700174 Tashkent, Uzbekistan

Abstract: The local host rock, Late Ordovician – Early Silurian carbonaceous shales, have likely been an important source of Au, As, Ni, and S in the formation of the shear zone-hosted Amantaytau orogenic gold deposit. Syn-depositional pyrite in these shales contain, elevated Au, As, and Ni concentrations of, on average, 0.34, 1658, and 1971 ppm, respectively. The $\delta^{34}\text{S}$ values for pyrite (–0.13 to +7.30 ‰ CDT) from barren and mineralized samples are consistent with marine sulfate being the principal source of the ore sulfur. Assuming a formation temperature of between 300 and 400 °C for the main stage of mineralization, as indicated by the alteration mineral assemblage, the calculated $\delta^{18}\text{O}_{\text{fluid}}$ is between 9.5 and 13.4 ‰ V-SMOW, which points at a metamorphic origin for the ore fluid.

Keywords. Amantaytau, black shale, orogenic gold, sedimentary Au source, sulfur isotopes, pyrite chemistry

1 Introduction

The Altaid orogenic collage, which formed in response to a series of Paleozoic accretionary events and subsequent Alpine-Himalayan deformational overprint, is host to a great variety and number of gold deposits. Most deposits are located in the Tien Shan, the world's second largest gold province (Yakubchuk et al. 2002). Three tectonic zones are distinguished within the Tien Shan: (1) the northern zone, which consists of an early Paleozoic arc and its Precambrian basement, (2) the middle zone, consisting of a late Paleozoic arc, and (3) the southern zone, a complex fold-and-thrust belt with Late Palaeozoic accretionary wedge and fore-arc complexes thrust southwards onto Palaeozoic passive margin successions and Precambrian basement. Only the latter two zones are well endowed with gold. Most of the gold deposits in the middle Tien Shan are arc-related, whereas those in the southern Tien Shan are predominantly shear zone-hosted, with the most famous example of the latter type being the giant Muruntau deposit in western Uzbekistan (Yakubchuk et al. 2002). There is little doubt that many of the major sediment-hosted and structurally controlled gold deposits in this Hercynian fold-and-thrust belt of Kyrgyzstan and western Uzbekistan formed in middle to late

Carboniferous and Early Permian times during the convergence and eventual suturing of the Kazakhstan and Karakim-Tarim continental masses (e.g., Zonenshain et al. 1990, Yakubchuk et al. 2002). They are, therefore, typically classified as orogenic-type gold deposits. The various orogenic-type gold deposits in the southern Tien Shan display different mineralization styles that have been interpreted as reflecting different depths of formation (Yakubchuk et al. 2002). The fact that the orogenic-type gold deposits in the southern Tien Shan are hosted predominantly by metamorphosed black shales, mainly of early Paleozoic age (e.g., Muruntau, Amantaytau, Daugystau, and Vysokovoltnoe), but also of Carboniferous age (e.g., Kokpatas), raises the question as to the possible role of pre-enrichment of Au and other metals in these shales in the genesis of these deposits.

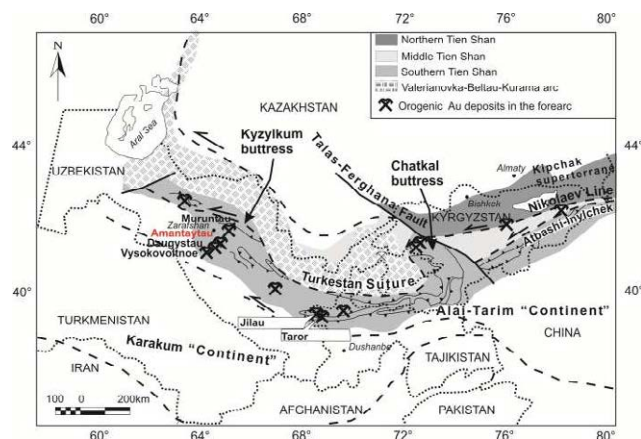


Figure 1. Location of the Amantaytau deposit (adapted from Yakubchuk 2005).

Previously Kotov and Poritskaya (1990) and Kotov et al. (1993) have suggested a two-stage metallogenic evolution, with syn-tectonic hydrothermal remobilization of Au from the black shales into their current position. In this study, we provide new geochemical, mineral chemical, and S isotope data for the Amantaytau deposit (Fig. 1), showing the importance of pre-concentration of Au, As, S, and other elements during the deposition of black shales for the much later formation of this type of

orogenic gold deposit.

2 Material and methods

Twelve samples of about 2 kg each, representing barren (AMT-39, 40, 41, 49, 50), low-grade Au (AMT 42, 44 and 48), and high-grade Au samples (AMT43, 45, 46 and 47) were taken at level 140 of the Amantaytau Northern deposit. The details on material and methods are described in Pasava et al. (2013).

3 Results

The $\delta^{34}\text{S}$ values of synsedimentary to early diagenetic pyrite from barren black shale range widely from -0.1 to $+7.3$ ‰. In the low- and high-grade Au mineralized samples the $\delta^{34}\text{S}$ values of hydrothermal pyrite are between $+2.6$ and $+5.5$ ‰.

Altogether a total of 56 LA-ICPMS spot analyses were obtained, which are regarded as representative of the actual pyrite chemistry and are not, or only minimally, affected by micro-inclusions. These data were collected on pyrite grains of different morphology (anhedral, subhedral, and euhedral grains including cubes, skeletal grains, and framboids) within barren, low-grade Au, and high-grade Au samples.

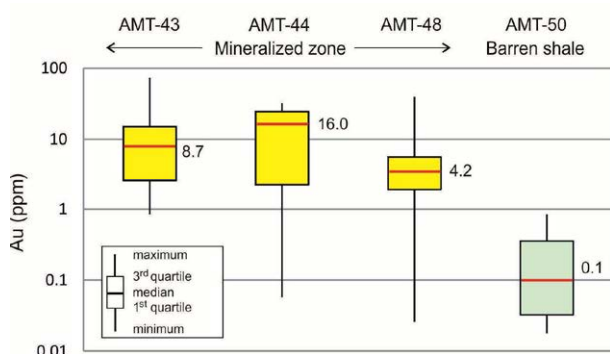


Figure 2. Au concentrations in pyrite from barren and mineralized zone at the Amantaytau deposit.

Systematic differences in the pyrite chemistry exist between the barren host rock reference sample (AMT-50) and the Au-mineralized samples (AMT-43, 44, 48), irrespective of the degree of mineralization, but little differences were noted between different textural types of pyrite within a given sample. Pyrite in the mineralized samples shows a marked enrichment by one to two orders of magnitude in As, Cu, and Au, and to a minor extent in Sb. The sample average As concentration in the pyrite from the barren host rock is 1083 ppm compared with average values of 11583, 16331, and 5257 ppm in the mineralized samples. Average Cu concentration in pyrite from the barren sample is 7 ppm as opposed to 55, 99, and 111 ppm in the mineralized samples. Similarly, the average Au content in the pyrite from the barren host rock is 0.23 ppm, which is significantly lower than in the pyrite from the mineralized samples in which it reaches

values of as much as 14.3 ppm (Fig. 2).

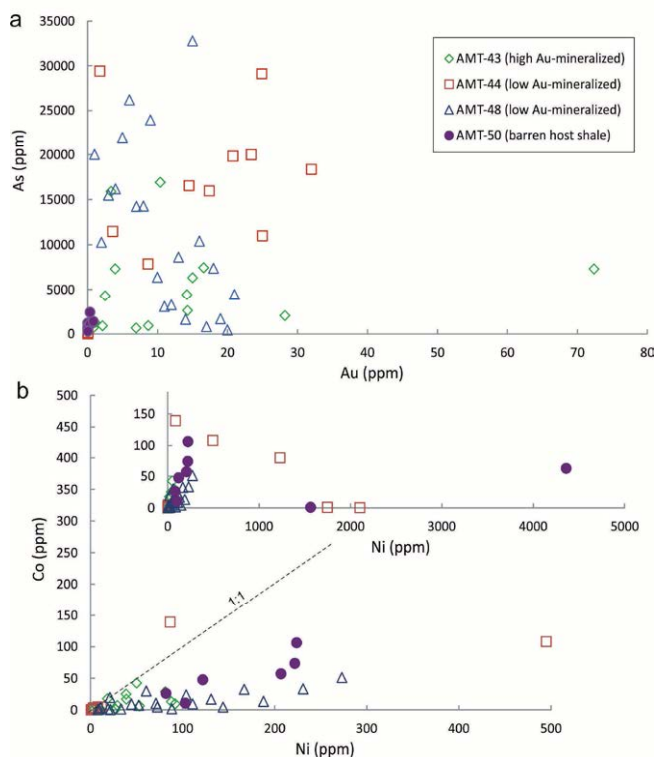


Figure 3. (a) Plot of Au vs. As in pyrite from barren, low Au- and high-grade Au mineralized samples of the Amantaytau deposit. (b) Plot of Ni vs. Co in pyrite from barren, low Au- and high-grade Au-mineralized samples of the Amantaytau deposit.

The high Au contents in some pyrite grains are unlikely to be an artifact of minute gold inclusions as is evident from multiple spot analyses of the same pyrite grain, e.g. the central part (72.4 ppm Au) and rim (28.2 ppm Au) in a large euhedral pyrite grain in the highly mineralized sample (AMT-43). Whereas both As and Au contents are comparatively low in the pyrite from the barren host rock, the extent of enrichment of these two elements in the pyrite from the mineralized zone shows no correlation at all, with some pyrite grains being strongly enriched in Au with little As and vice versa (Fig. 3a). In contrast, the pyrite in the mineralized samples is markedly depleted in Bi (from 4.9 ppm in the barren host rock to average values between 0.15 and 0.94 ppm), slightly depleted in Ni (from 861 ppm in the barren host rock to average values between 38 and 475 ppm) and Co (from 48 to average values between 11 and 31 ppm). The variation in the average Pb concentration is minimal.

Of particular interest is the Co/Ni ratio, as it is a useful discriminator between different genetic types of pyrite (see discussion below). With a single exception, all pyrite analyses yielded Co/Ni ratios that are much lower than unity (Fig. 3b), with no significant differences between pyrite in barren host rock and in mineralized samples. Pyrite in the strongly mineralized sample (AMT-43) is particularly poor in Co and Ni, whereas a few pyrite grains from a weakly mineralized sample (AMT-48) and the barren host rock yielded Ni

concentrations of a few thousand ppm (Fig. 3b).

4 Discussion

Whereas the mineralizing fluid, analogous to Muruntau, was likely derived from metamorphic devolatilization reactions, possibly combined with some input from the mantle as documented by He isotope data for Muruntau (Graupner et al. 2006), the question of the source of the various ore components remains to be answered. Goldfarb et al. (1997) and Chang et al. (2008) have shown a remarkable parallelism between the S isotopic composition of pyrite in many sediment-hosted gold deposits and that of coeval seawater sulfate through geologic time. Our $\delta^{34}\text{S}$ data for the Amantaytau pyrite are consistent with S derivation from marine sulfate. This would suggest that sulfidation took place very early in the diagenetic evolution when seawater was still available as the principal fluid, similarly as suggested by Large et al. (2009) for various sedimentary rock hosted orogenic gold deposits.

Vymazalová et al. (2009) reported PGE values from host rocks and Au-mineralized samples of various orogenic gold deposits in Uzbekistan, including Amantaytau. They found that barren black shale has almost identical Pt and Pd values as Au-ore samples (3.93 ppb and 3.81 ppb Pt and 0.83 and 0.92 ppb Pd, respectively) and concluded that the PGE in the Au-mineralized samples were derived from the black shale host rock. A similar scenario can be also suggested for both the pyrite and the gold.

High Ni contents in the host rock pyrite from Amantaytau are typical of sedimentary to early diagenetic pyrite, as is its low Co/Ni ratio. Hydrothermal pyrite is typically characterized by Co/Ni >1, whereas the dominance of Ni in early diagenetic pyrite (Co/Ni <0.2) is a characteristic feature of carbonaceous shales and other organic-rich deposits (e.g., Raiswell and Plant 1980; Large et al. 2007, 2009). Degradation of organic matter and subsequent release of Ni from organometallic complexes into the surrounding pore waters invariably leads to Ni-enrichment in early diagenetic pyrite (Tribouillard et al. 2006). Interestingly, the pyrite in the mineralized zone, though clearly a product of hydrothermal fluid flow, also has a low Co/Ni ratio. Although it is somewhat higher than in the barren host rock, it is below 1.0 and thus lower than expected for hydrothermal pyrite (Fig. 3b). It may be deduced from this observation that the syngenetic/diagenetic pyrite was generally poor in Co and/or the overall reducing environment hindered Co mobility during devolatilization of the pyrite.

Both As and Cu, which occur in much greater concentrations in the hydrothermal pyrite from the mineralized zone, must have been either transported by the ore fluid from an external source or derived from a more local leaching of the country rock. The latter is more likely, considering the preferential incorporation of these elements into organic-rich deposits (e.g. Coveney 2000). The same applies also to Au. Due to its lower solubility, it might not have been scavenged as effectively by the percolating metamorphic fluid as As or

Cu. Nevertheless, an order of magnitude difference in the Au concentration in pyrite from the mineralized zone compared to the barren host shale is noted (Fig. 3), clearly showing that the overall high Au grade of the ore zone is reflected by the pyrite chemistry. Evidence of metamorphic conversion of diagenetic pyrite to pyrrhotite being the critical reaction to release As and Au into the ore fluid as suggested by Goldfarb and Leach (1989) and Large et al. (2011) could not be found in this study. The absence of pyrrhotite in the immediate surroundings of the ore body does not preclude, however, the possibility of pyrrhotite being present at deeper levels and/or nearer the inferred pluton at depth, where either regional or contact metamorphic grades would be somewhat higher.

Although the average Au content in the pyrite from the barren host rock is much lower than in the mineralized zone, it is with nevertheless more than 200 ppb higher than in many other diagenetic pyrites within carbonaceous shales from other parts of the world, for which Large et al. (2011) give a mean value of 600 ppb. Thus the question arises as to the significance of pre-concentration of Au in pyrite in the host shale 200 m.y. prior to the formation of the ore deposit. Black shales are generally enriched in numerous metals, including Au, for reasons discussed by Coveney (2000). For example, average Au and As contents in about 9000 black shale samples (Yudovich and Ketris 1994) are 7 ppb Au and 30 ppm As, which is markedly higher than average crustal values of 1.8 ppb Au and 1.4 ppm As. In comparison, the barren black shales surrounding Amantaytau are characterized by 38 ppb Au and 166 ppm As, and thus strongly enriched relative to other black shales. Our data are consistent with the results of Shayakubov (1998) who reported average regional background Au content of 49 ppb in sedimentary rocks of the central Kyzylkum area in the southern Tien Shan and also with the results of Barchudarov and Shashorin (1985) and Shashorin (1991) who reported average Au contents of 58 ppb, 118 ppb, and 46 ppb for barren rocks of the so-called Green, Varied, and Gray parts of the Besopan Formation, respectively.

In summary, the local host rocks surrounding the Amantaytau deposit are clearly enriched in Au, which is regarded as a syngenetic to diagenetic feature, similarly as reported from the neighboring Muruntau gold deposit (Badalov 1978, 1980), and other orogenic-type Au deposits (Large et al. 2009).

4 Conclusions

Amantaytau is a typical shear-zone hosted gold deposit within a monotonous flyschoid carbonaceous sequence of the Middle Ordovician Early Silurian Besopan Formation. There are no indications of magmatic activity exposed at the present surface, but a geophysically indicated granitic pluton is suggested at a depth of 3-4 km. Our data show, however that the local host rock acted as an important source of Au, As, Ni, and S that are present in the epigenetic ore deposit.

The $\delta^{34}\text{S}$ values in pyrite from barren country rock shale and high-grade Au ore zones are consistent with

seawater sulfate being the principal source of sulfur in both, which implies that the sulfur in the ores was originally very early in the sedimentary basin history.

Laser ablation ICP-MS study of the chemistry of different morphological types of pyrite from barren, low-grade Au and high-grade Au samples revealed a strong enrichment of pyrite in the mineralized zone in As, Cu, Ni, and Au. However, even pyrite from the barren host black shale is enriched in these elements relative to other black shale deposits elsewhere in the world.

Acknowledgements

This is a contribution to the project INGO II (LG 13006) from the Ministry of Education, Youth and Sports of the Czech Republic and grant 323000 from the Czech Geological Survey to J. Pašava. HEF thanks H. Bratz for her assistance with the LA-ICPMS analyses. We thank R. Goldfarb for stimulating review that helped to improve the MS.

References

- Badalov ST (1978) Metodology of the study of different forms of gold associated with organic matter in rocks and ores (in Russian). Tashkent, Zapiski of the Uzbek Division, All-Russian Mineralogical Society 31:79-80
- Badalov ST (1980) Research principles of classification of ore-forming processes (on the example of gold). Tashkent, Zapiski of the Uzbek Division, All-Russian Mineralogical Society 33:72-94
- Barchudarov VA, Shashorin JN (1985) Gold potential of lithological complexes in the Central Kyzalkum area (in Russian). Tashkent, Zapiski of the Uzbek Division, All-Russian Mineralogical Society 38:105-107
- Chang Z, Large RR, Maslennikov V (2008) Sulfur isotopes in sediment-hosted orogenic gold deposits: evidence for an early timing and a seawater sulfur source. *Geology* 36:971-974
- Coveney RM (2000) Metalliferous shales and the role of organic matter, with examples from China, Poland, and the United States. *Reviews in Economic Geology*, 9: 251-280
- Goldfarb RJ, Leach DL, Rose SC, Landis GP (1989) Fluid inclusion geochemistry of gold-bearing quartz veins of the Juneau Gold Belt, southeastern Alaska—Implications for ore genesis: *Econ Geol*, Monograph 6: 363-375.
- Goldfarb RJ, Miller LD, Leach DL, Snee LW (1997) Gold deposits in metamorphic rocks in Alaska. In: Goldfarb RJ, Miller LD (eds) *Mineral Deposits of Alaska*. *Econ Geol* Monograph 9: 151–190.
- Graupner T, Niedermann S, Kempe U, Klemd R, Bechtel A (2006) Origin of ore fluids in the Muruntau gold system: Constraints from noble gas, carbon isotope and halogen data. *Geochim Cosmochim Acta* 70: 5356-5370
- Kotov NV, Poritskaya LG (1990) Generalized genetic model of gold accumulation in gold sulfide metasomatic ore formation in blackschist series (central Kyzylkumy), *Soviet Geology and Geophysics* 31(11): 46-53
- Kotov NV, Zverev YuN, Poritskaya LG (1993) Zoloto-chernoslantsevoe rudoobrazovanie (Tsentral'nye Kyzylkumy) (Gold ore formation in black shales of the central Kyzyl Kum), St. Petersburg: Nevskii Kur'er, 112 p.
- Large RR, Bull SW, Maslennikov VV (2011) A Carbonaceous Sedimentary Source-Rock Model for Carlin-Type and Orogenic Gold Deposits. *Econ Geol* 106:331-358
- Large RR, Danyushevsky L, Hollit C, Maslennikov V (2009) Gold and trace element zonation in pyrite using a laser imaging technique: Implications for the timing of gold in orogenic and Carlin-style sediment-hosted deposits: *Econ Geol* 104(5): 635-668
- Large RR, Maslennikov VV, Robert F, Danyushevsky LV, Chang Z (2007) Multistage sedimentary and metamorphic origin of pyrite and gold in the giant Sukhoi Log deposit, Lena gold province, Russia. *Econ Geol* 102:1233-1267
- Pašava J, Frimmel HF, Vymazalová A, Dobeš P, Jukov AV, Koneev RI (2013): A two-stage evolution model for the Amantaytau orogenic-type gold deposit in Uzbekistan. *Min Deposita*, doi:10.1007/s00126-013-0461-8
- Raiswell R, Plant J (1980) The incorporation of trace elements into pyrite during diagenesis of black shales, Yorkshire, England. *Econ Geol* 75, 684-699
- Shashorin JN (1991) Geochemistry of gold in the process of formation of endogenous halos and natural concentrations (on example of Central Kyzylkum region). Extended abstract of Ph.D. Thesis (15 p), Tashkent
- Shayakubov TS (1998) Au-deposit Muruntau. FAN Acadamia of Sciences of Uzbekistan, Tashkent. pp 539
- Tribovillard N, Algeo TJ, Lyons T, Riboulleau A (2006) Trace metals as paleoredox and paleoproductivity proxies: An update. *Chem Geol* 232: 12-32
- Vymazalová A, Pašava J, Koneev RI, Jukov AV, Khalmatov RA, Mun Y (2009) Geochemistry of Platinum Group Elements in Gold Deposits in Uzbekistan. In Williams PJ (ed) *Smart Science for Exploration and Mining*. Proceedings of the 10th Biennial SGA Meeting, Townsville, vol 2: 1003-1005
- Yakubchuk A, Cole A, Seltmann R, Shatov V (2002) Tectonic setting, characteristics, and regional exploration criteria for gold mineralization in the Altaid orogenic collage: The Tien Shan Province as a key example In: Goldfarb RJ, Nielson RL (eds) *Integrated Methods for Discovery: Global Exploration in the Twenty-First Century*. Society of Economic Geologists, Littleton, Spec. Publ. No. 9: 177-202.
- Yakubchuk A, Shatov, VV, Kirwin D, Edwards A, Tomurtogoo O, Badarch G, Buryak VA (2005) Gold base metal metallogeny of the central Asian orogenic supercollage In: Hedenquist JW, Thompson JFH, Goldfarb RJ, Richards JP (eds) *Economic Geology One hundredth anniversary volume*. Society of Economic Geologists, Littleton, Colorado 1035-1068
- Yudovich YE, Ketris MP (1994) Trace elements in black shales. Nauka Publisher, Ekaterinburg p 303 (in Russian)
- Zonenshain LP, Kuzmin MI, Natapov LM (1990) *Geology of the USSR: A plate tectonic synthesis*. American Geophysical Union Geodynamics Series Monograph 21, p. 242

Reaction mechanisms and gold mineralisation

Mark A. Pearce, James S. Cleverley, Robert M. Hough

CSIRO Earth Sciences and Resource Engineering, 26 Dick Perry Avenue, Kensington, WA 6151, Australia

Abstract

Fluid-rock reaction is a key factor in the formation of economic gold deposits. Reactions associated with gold mineralisation have been examined in a sample from the Junction deposit, Western Australia. Detailed x-ray mapping and electron back-scatter diffraction techniques have been applied to identify the reactions taking place and reaction products that are formed. A pre-mineralisation assemblage containing biotite and calcite is altered to dolomite-siderite-chlorite-muscovite during gold mineralisation. Gold occurs along reaction interfaces between biotite and muscovite-chlorite and fills porosity in both the carbonates and the micas. Reaction of biotite to chlorite occurs by diffusion of reactants along cleavages, and to muscovite by nucleation of new grains. Calcite is replaced by siderite and dolomite by solution-precipitation and new carbonate grows at the expense of biotite by nucleation of adjacent calcite grains.

The relationship of the reactions to the causative mechanism for gold mineralisation is still unclear. However, creation of porosity and redox effects are both possible factors which are still being explored. The processes observed in this rock operate relatively quickly compared to diffusional processes. This is compatible with gold mineralisation being a rapid process that occurs on timescales which are reconcilable with brittle failure and fluid flow through the crust.

Keywords: Gold, reaction mechanism, replacement

1 Introduction

Gold deposits are often formed at sites of intense brittle deformation and quartz veining. The deformation allows gold-bearing fluid to access the rocks and causes deposition by changing the pressure or chemical environment of the fluid (e.g. Cox et al. 1987). However, in many orogenic gold deposits the gold is not explicitly associated with quartz veins but rather, resides in the wall rock. The minerals surrounding the gold grains are undergoing chemical reactions caused by the ingress of fluid, presumably the gold-bearing fluid, into the rock.

Deposition by reactions is most likely a slow process compared to the sudden catastrophic failure of the rock by fracturing and the subsequent influx of fluid. In order to understand better the mineralising system and how the timescales of reactions and fluid flow couple it is necessary to understand the individual processes operating. Fracturing, crystal plasticity, and fluid mediated solution-precipitation all allow fluids to access minerals more easily but have different microstructural expressions. In addition they all operate at different rates at any given temperature because the processes that control them are usually temperature dependant.

In this contribution we document the reaction microstructures spatially associated with gold mineralisation from the Junction deposit in the Yilgarn of Western Australia. These microstructures allow reaction mechanisms to be determined, leading to a complete model of controls on orogenic gold deposition.

2 Geological Setting & Sample Description

The Junction deposit is located in the southern Yilgarn craton, Western Australia. Mineralisation is hosted in the Junction dolerite. This Fe-rich sill intrudes the lowermost Black Flag beds and is temporally and lithologically equivalent to the Condenser dolerite and Golden Mile dolerite, which hosts the giant Golden Mile gold deposit. The Junction deposit is 3km east of the Boulder-Lefroy fault and mineralisation is likely associated with deformation resulting from movement on this shear zone.

The Junction dolerite has four subdivisions defined on the basis of both petrographic and compositional variation resulting from igneous differentiation. Units 3 and 4 are enriched in iron oxide with respect to the bulk composition and host the highest grade mineralisation, generally >2g/t but commonly >20g/t in the most enriched parts of the deposit. The mineralisation post dates uppermost greenschist facies metamorphism and is synchronous with retrogression at lower greenschist facies. The alteration associated with veining introduces carbonate and sulphide into the mineral assemblage.

The sample studied in this work (sample 150 of Polito et al. 2001) grades at 3.25g/t and comes from a drill core, which was subsequently mined out. The sample comprises quartz-albite-biotite-chlorite-calcite-ilmenite with secondary chlorite and muscovite after biotite, siderite after calcite, and anatase after ilmenite (Figure 1). It includes part of a quartz vein, which is fractured and infilled with carbonate, and wall rock, which hosts the gold.

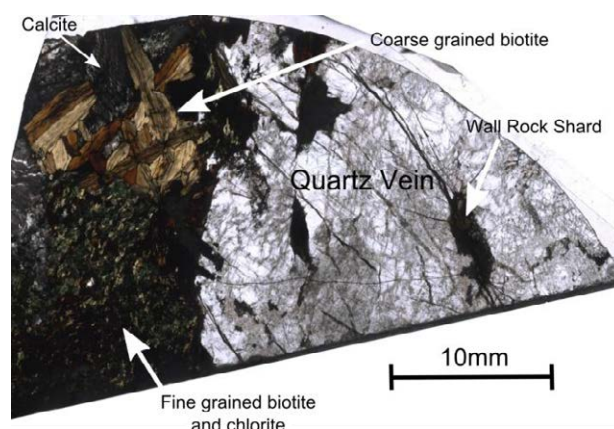


Figure 1. Plane polarised light image of the sample examined in this study showing the quartz vein and wall rock containing the different microstructural domains.

The wall rock microstructures are heterogeneous on the scale of the thin section and include several subdomains:

- (1) Large biotite and carbonate grains
- (2) Finer grained biotite and chlorite grains with a dolomite matrix
- (3) Albite 'breccia' with a quartz and dolomite matrix

3 Methods

The sample was prepared as a 200 µm thick polished section. A final chemical-mechanical polish was applied prior to the application of a thin (~5nm) carbon coat. Studies were made of the gold and surrounding reaction zones using scanning electron microscopy (SEM). The sample was imaged using back-scattered electrons (BSE) to show variations in mineral composition. Energy dispersive x-ray (EDX) maps were made to map the variation in chemistry around the gold bearing areas. EDX measurements were coupled with electron back-scatter diffraction (EBSD) which records the orientation of the crystal lattice at a given point. Mapping changes in the crystal lattice, or relationships between adjacent grains gives information about deformation mechanisms (e.g. crystal plasticity) and crystallographic controls on chemical reactions.

All analyses were performed on a Zeiss Ultra Field Emission Gun SEM at the Australian Resources Research Centre, Western Australia. Imaging and EDX maps were conducted with a beam current of 2.9 nA at either 10 keV or 20 keV (depending on the require resolution) with the sample perpendicular to the electron beam. EBSD maps were recorded with the specimen tilted at 70° and with a beam current of 12.9 nA at 20 keV.

4 Results

4.1 Chemical Maps of Phases Associated with Visible Gold

Free gold is visible in the sample associated with muscovite selvages along biotite grain boundaries (Figure 2) and where chlorite is present as new grains. Chloritisation is visible along the biotite cleavages and as distinct grains adjacent to the muscovite. Also present are small quartz grains and Mg-Fe carbonate 'veins' which grow along the biotite cleavages. In addition, small rutile grains are present in muscovite. This is consistent with the muscovite being a reaction product from the biotite because Ti is less soluble in muscovite than biotite.

Gold is also found associated with carbonate reactions, mainly calcite reacting to siderite and dolomite (Figure 3). Both of these reactions are enhanced by the presence of twin boundaries in the calcite grains which act as conduits for the reactants. The siderite is mainly present along boundaries between calcite and biotite. There are large pores created adjacent to the dolomite grain bordering the gold. In addition, smaller pores are created along the calcite twins. On the right hand side of the map, biotite is being replaced by carbonate.

Closer examination of the relationship between the gold and the dolomite (Figure 4) reveals that the dolomite is chemically zoned with variable iron content. Growth zones are arranged in a radial pattern from the gold grain into what is now porosity. In addition, the adjacent biotite grain is reacting to chlorite. Reaction is

limited where the biotite is protected by the gold, although the gold itself appears to be penetrating the biotite cleavage giving it a 'frilly' appearance.

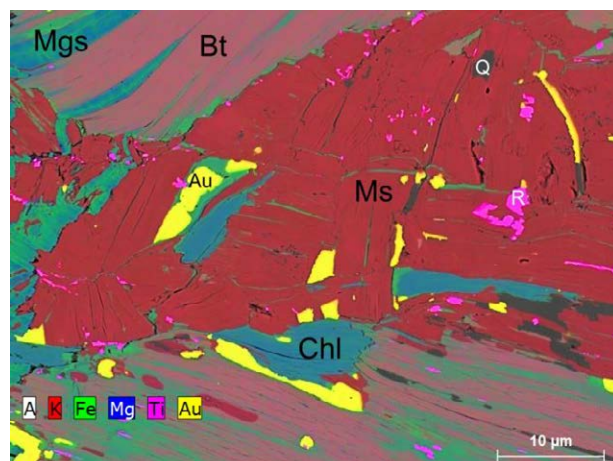


Figure 2. EDX map showing gold (Au) mineralisation associated with biotite (Bt) reacting to muscovite (Ms) and chlorite (Chl). Also present as veins are magnesite (Mgs) and rutile (R) which is exolved from the biotite.

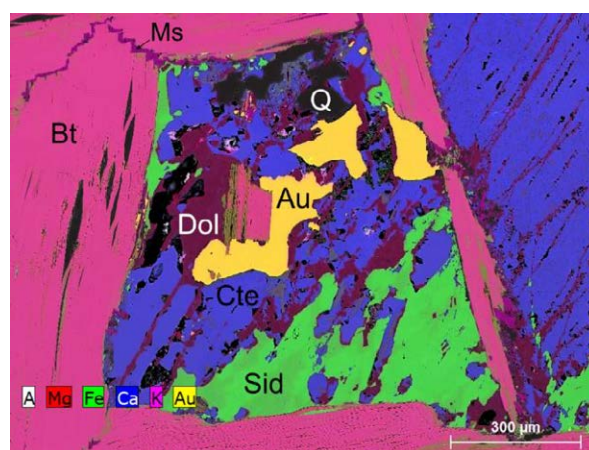


Figure 3. EDX map of calcite (Cte) reacting to dolomite (Dol) and siderite (Sid) associated with mineralisation of large gold (Au) grains. Also note the reaction of biotite (Bt) to muscovite (Ms) adjacent to the carbonates and the presence of quartz (Q).

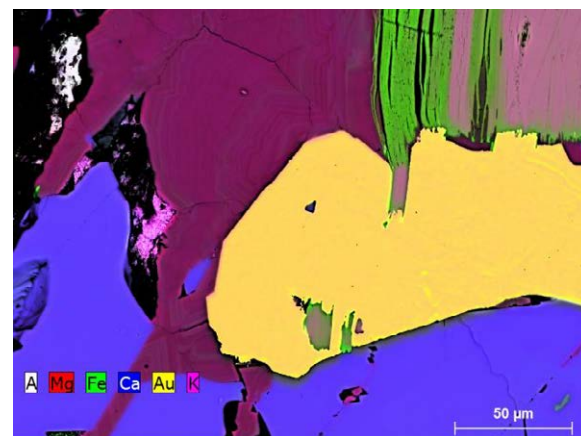


Figure 4. Detailed EDX map of dolomite growth zoning adjacent to gold grain. Dolomite is replacing calcite and biotite is reacting to chlorite.

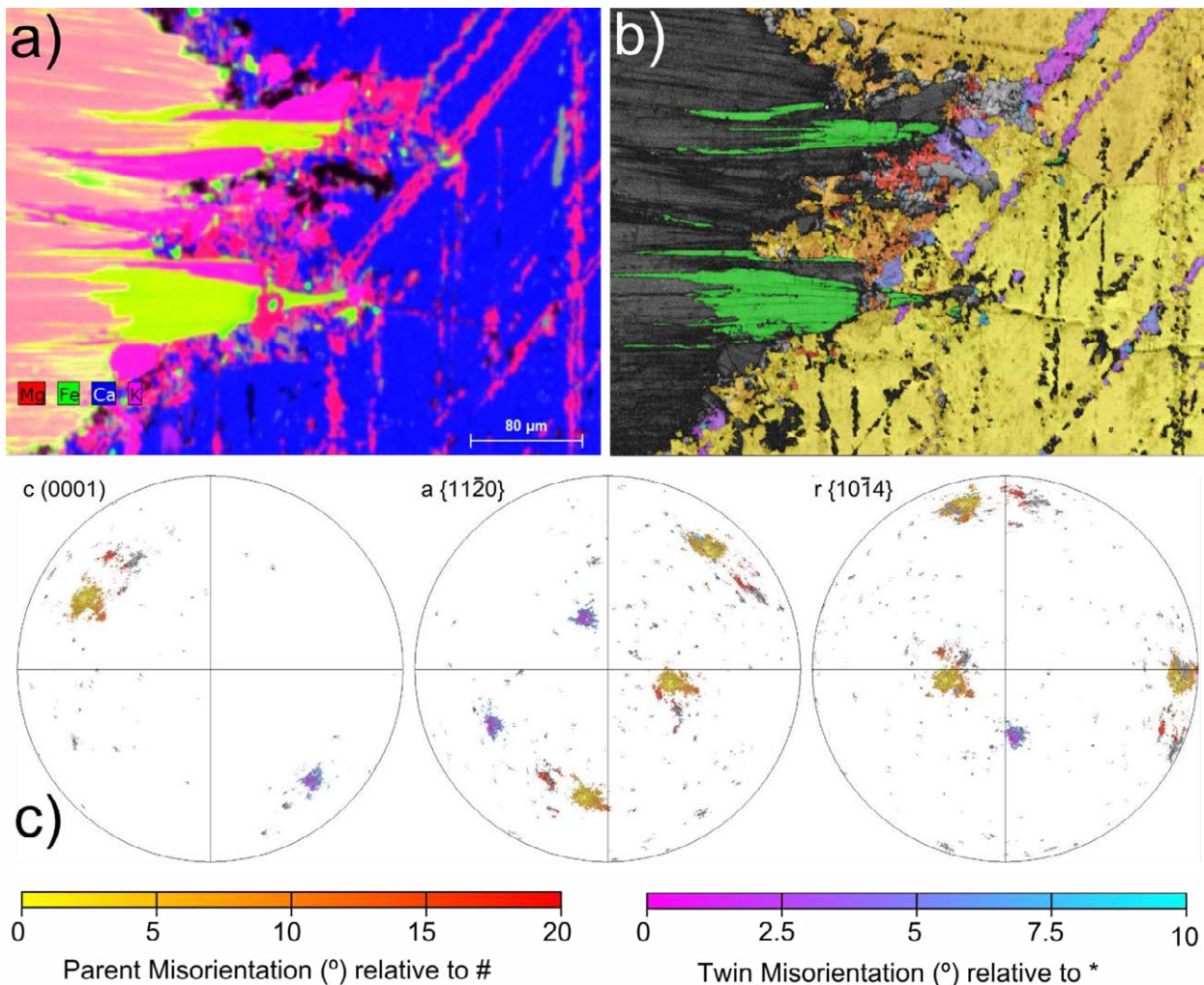


Figure 5. Chemistry and crystallographic orientation of carbonate replacing biotite. a) EDX map showing the interface between a large, twinned calcite grain and a biotite grain. The reaction interface has small grains of dolomite and calcite growing along it on the carbonate side and muscovite and chlorite replacing the biotite. Porosity is in black. b) Crystallographic orientation coloured relative to the main calcite grain (yellow shades) and twin (purples). Dolomite and calcite are coloured the same and the dolomite calcite mixture has broadly the same orientation (within 20°) as the large calcite grain as seen on the stereograms (c). Chlorite is coloured green. Muscovite and biotite are not indexed.

4.2 Relationships between Crystallography and Chemistry

EBS data are difficult to accurately obtain for phyllosilicates but the orientation of the basal planes gives a good indication of crystallographic orientation. Biotite is reacting to chlorite by gradual chloritisation along the cleavage planes (Figure 2). This process involves replacement of the K ion with brucite ($Mg(OH)_2$) molecules leaving the silicate framework undisturbed. Diffusion is along the basal plane which is relatively fast compared to diffusion rates in most silicates (Cherniak and Dimanov 2010). In some cases, chlorite has formed new grains with distinct boundaries (Figure 2). However, the basal plane is still sub-parallel to the grain that is replacing. In these cases the chlorite is more magnesian than that formed by ion exchange with the biotite (Figure 2).

The majority of the muscovite has formed as new grains. These are not in the same orientations as the biotites they are replacing and form a mosaic of grains (Figure 5a). There are some small patches where the biotite has been ‘muscovitised’ in situ but

these are less common.

Where micas are being replaced by carbonate (right-hand side of Figure 3), EBSD shows that the newly grown grains are in a similar orientation to the adjacent large calcite grain (Figure 5b, c). They are growing in both parent and twin orientations. As well as replacing the biotite, dolomite is replacing calcite along the twins and is also cross-cutting the chlorite produced by breakdown of biotite (Figure 5a)

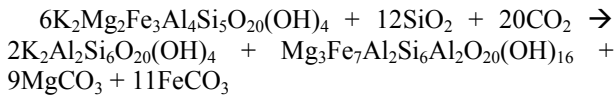
5 Reactions Associated with Gold Mineralisation

Gold has been located within the zone containing the large biotite and carbonate grains and at the edge of the quartz vein. The chemical maps and crystallographic data presented above show that two different reactions are occurring adjacent to the gold mineralisation in the sample from the Junction deposit. There are as follows:

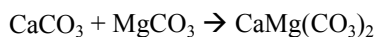
- 1) Calcite \rightarrow Siderite + Dolomite
- 2) Biotite \rightarrow Muscovite + Chlorite + Calcite + Dolomite

In addition to these reactions, ilmenite is being replaced by TiO₂ phases and the porosity created by loss of iron is being filled by dolomite.

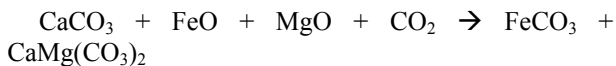
These two reactions are not independent of each other as the iron and magnesium needed to balance reaction (1) is likely supplied by the breakdown of biotite (2) resulting in the following reaction:



Where calcite is adjacent to the biotite that is breaking down, the MgCO₃ is incorporated into dolomite via the following reaction:



Siderite replaces calcite by a dissolution-precipitation mechanism (Putnis 2009) leading to topotactic replacement of calcite by siderite (similar to the relationship observed in Figure 5). This releases calcium which can also be used to precipitate dolomite:



The FeO and MgO for this reaction are both released from biotite. Where biotite breaks down in the absence of calcite (Figure 2) the carbonate products are precipitated as magnesite and siderite.

Since solution precipitation reactions do not require long range grain boundary diffusion (and any diffusion is through a fluid therefore is fast) or lattice diffusion, they occur relatively rapidly when compared to most solid state reactions (Putnis 2009). In addition, they are more kinetically favourable because many examples of these reactions use topotactic nucleation which reduces the activation energy for nucleation and allows the reactions to proceed.

There is a spatial link between the reaction microstructures and the gold mineralisation. From the reactions outlined above, a CO₂-rich fluid is likely to be the reaction trigger. The causative link between the observed reactions and the gold mineralisation is uncertain. Release of iron from the biotite may destabilise gold-bearing bisulphide complexes (Ridley et al. 1996), although the lack of sulphides associated with gold mineralisation in this sample suggest that this is not important here. Alternatively, the reactions that remove CO₂ from the fluid may be the cause of the gold deposition (Phillips and Evans 2004). Fluid inclusion studies have identified methane-rich inclusions in the quartz vein part of the sample. Changes in the oxidation state of the fluid could be a cause of gold deposition but this is the subject of ongoing work.

Another effect of the reactions documented here is the reduction in solid volume which leads to increased porosity and permeability allowing further fluid-rock interaction. The porosity created provides space for gold deposition (Figure 3). Gold is also found along reacting mica cleavages (Figure 2) and along reaction interfaces

(e.g. chlorite – biotite in Figure 2) which provide defects where the gold can nucleate in addition to any chemical driving force derived from the reaction.

The creation of porosity and permeability by reactions, which also precipitate gold, may be a key factor in the formation of gold deposits. Brittle failure under high fluid pressures to form veins such as those adjacent to the wall rock studied here allows fluids into the rock but does not lead to much fluid-rock interaction. By creating permeability, the vein evolves rapidly from a conduit to a reservoir, from which the fluid can enter the rock, promoting reaction. Solution-precipitation reactions have been shown to operate at laboratory timescales. The whole sequence of fluid flow through shear zones and veins, and reaction to produce gold deposits has the potential to operate on vary short timescales possible even within the earthquake cycle.

6 Conclusions

Gold mineralisation is associated with breakdown of biotite to muscovite and replacement of calcite by siderite and later growth of dolomite. The breakdown of biotite by the addition of CO₂ to the rock triggers the release of iron to form siderite. This occurs as the replacement of calcite by siderite by a dissolution precipitation mechanism which is more efficient than nucleation of many new siderite grains. The calcium removed from the calcite forms dolomite. The cause of the gold mineralisation during this episode is threefold:

- 1) Gold is present in a fluid
- 2) Iron is available for reaction due to addition of CO₂. The exact nature of the interaction is unclear but is the subject of ongoing work.
- 3) Porosity is created by mica-carbonate reactions both enhancing permeability and providing space for gold deposition.

Rapid reactions such as those observed here suggest that gold mineralisation occurs rapidly even when associated with wall-rock reaction.

References

- Cherniak D j., Dimanov A (2010) Diffusion in Pyroxene, Mica and Amphibole. *Reviews in Mineralogy and Geochemistry* 72: 641–690. doi:10.2138/rmg.2010.72.14
- Cox SF, Etheridge MA, Wall VJ (1987) The role of fluids in syntectonic mass transport, and the localization of metamorphic vein-type ore deposits. *Ore Geology Reviews* 2: 65–86
- Phillips GN, Evans KA (2004) Role of CO₂ in the formation of gold deposits. *Nature* 429: 860–863
- Polito PA, Bone Y, Clarke JDA, Mernagh TP (2001) Compositional zoning of fluid inclusions in the Archaean Junction gold deposit, Western Australia: a process of fluid – wall-rock interaction? *Australian Journal of Earth Sciences* 48: 833–855. doi:10.1046/j.1440-0952.2001.00903.x
- Putnis A (2009) Mineral Replacement Reactions. *Reviews in Mineralogy and Geochemistry* 70: 87–124. doi:10.2138/rmg.2009.70.3
- Ridley J, Mikucki EJ, Groves DI (1996) Archean lode-gold deposits: fluid flow and chemical evolution in vertically extensive hydrothermal systems. *Ore Geology Reviews* 10: 279–293

Genesis of Archean batholith-hosted gold veins at the Lac Herbin deposit, Val-d'Or, Canada: mineralogical and fluid inclusion constraints

Hervé Rezeau, Robert Moritz,
Earth and environmental sciences, University of Geneva, Switzerland

Georges Beaudoin
Department of geology and geological engineering, University of Laval, Québec, Canada

Abstract. The Val-d'Or area, Abitibi greenstone belt, Canada, underwent regional greenschist to amphibolite metamorphism and gold-bearing veins in the area post-date metamorphism. The Lac Herbin deposit consists of a network of parallel steep reverse faults within the synvolcanic Bourlamaque granodiorite batholith. There are two related quartz-tourmaline-carbonate vein sets in the faults, which consist of subvertical veins associated with subhorizontal veins between shear zones.

The paragenetic sequence is characterized by a main ore stage of carbonate, tourmaline, pyrite, and quartz. Pyrite contains inclusions of gold, chalcopyrite, tellurides, pyrrhotite, and cubanite. Most of the gold and chalcopyrite associated with Ca-Fe-Mg-Mn carbonates was precipitated late in fractures in deformed pyrite, with local pyrrhotite, sphalerite, cobaltite, galena, and tellurides.

Fluid inclusion petrography and microthermometry outlines three unrelated and time independent hydrothermal fluids: (1) aqueous-carbonic inclusions arranged in three-dimensional intragranular clusters in quartz crystals and interpreted as the ore-forming fluid; (2) high-temperature aqueous liquid-vapor inclusions observed in healed fractures and post-dating the aqueous-carbonic inclusions and unrelated to the mineralizing event; and (3) low-temperature brines and low-temperature aqueous inclusions in fractures, formed late in the hydrothermal history of the district.

Keywords : Canada, Val-d'Or, orogenic gold, mineralogy, fluid inclusion

Introduction

The Val d'Or mining district, located in the south-eastern part of the Abitibi greenstone belt within the Superior province of Canada, constitutes a typical example of an auriferous vein field of orogenic gold deposits. The deposits are hosted by secondary shear zones adjacent to a regional deep-crustal Cadillac-Larder-Lake fault (Robert, 1990). Previous studies indicate mafic volcanism at 2705 Ma, synvolcanic felsic intrusion at 2700 Ma (i.e. Bourlamaque batholith), emplacement of late felsic intrusions at 2645-2611 Ma, and regional greenschist to amphibolite metamorphism at 2690-2675 Ma. However, the timing of ore formation and the source of the ore-forming fluid, the number of gold mineralizing events, and the main mechanism of gold precipitation are still debated.

The Lac Herbin deposit is located within the synvolcanic Bourlamaque batholith. This fluid inclusion

study is the first one of a batholith-hosted auriferous vein system in the Val-d'Or mining district and could provide a new understanding of the mineralizing fluids in this world-class mining district.

Careful microscopy allowed us to determine the paragenetic sequence of ore-related events and to select fluid inclusion assemblages (FIA). We also focused studies on telluride mineralogy and trace elements in pyrite by microprobe analyses. The fluid inclusion study combined detailed petrography and cathodoluminescence of inclusions hosted in quartz. Finally, microthermometry and Raman spectroscopy were used to characterize fluid composition, and pressure and temperature conditions.

1 Structural geology and vein textures

1.1 Structural geology

The Lac Herbin deposit consists of a network of parallel high-angle reverse faults, ranging from <1 m to 3.5 m in width. Gold quartz veins in the faults are interpreted to have formed dominantly under a compressional regime, and extensional veins are associated with many subvertical veins hosted by shear structures. Based on dip and strike orientation, we can distinguish three types of structures (Fig.1) : (1) main mineralized structures (S1, S3, HW, HW2, BZ and LH), (2) subsidiary mineralized structures (S2 and WE), and (3) a barren post-mineralization structure (FF).

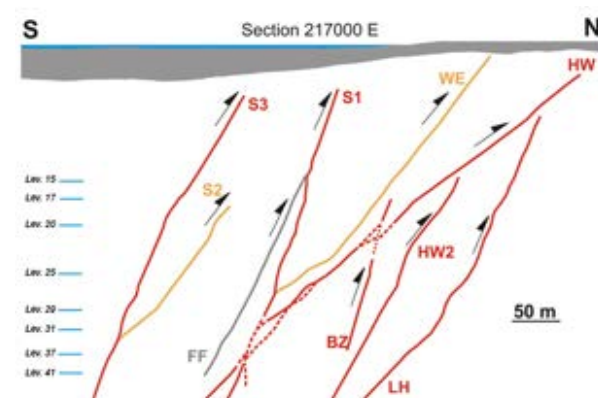


Figure 1. Cross-section showing the main (red) and the secondary (yellow) mineralized structures, and the post-mineralization structure (grey). From Lemarchand (2011).

1.2 Vein textures

Subvertical veins are by far the most abundant ones and are the main targets for ore extraction at the Lac Herbin deposit. Subvertical veins commonly consist of a banded texture with tourmaline ribbons, quartz, carbonates, and sulfides, resulting from incremental reopening of existing veins (Fig.2a).

According to the fault-valve model of Sibson et al. (1988), extensional veins are interpreted as contemporaneous with subvertical veins. Their typical open-space filling texture is characterized by euhedral or radiating crystal aggregates of hydrothermal minerals, such as tourmaline, carbonates, and sulfides, attached to the vein walls (Fig.2b).

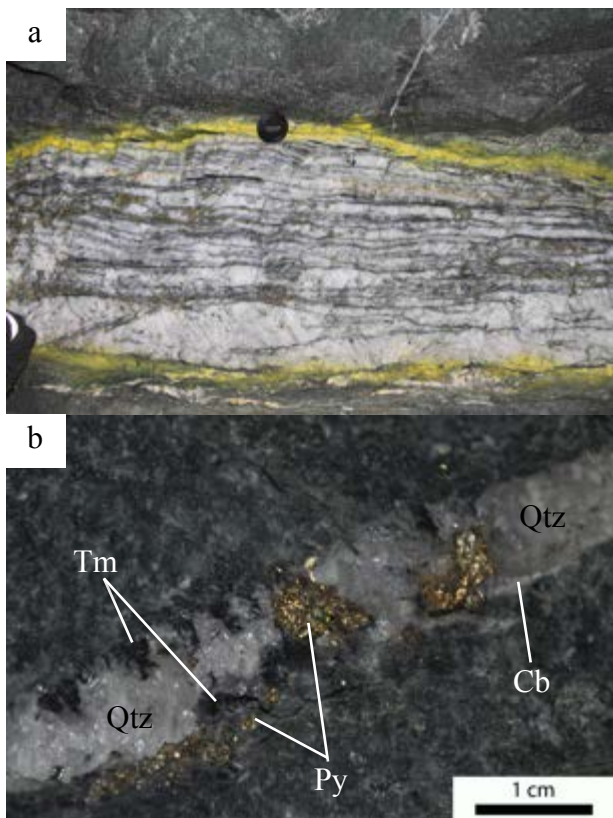


Figure 2. a) Fault-fill vein with typical banded textures (i.e. parallel tourmaline ribbons). b) Extensional vein with typical open-space filling texture. *Cb* : carbonate, *Qtz* : quartz, *Py* : pyrite, *Tm* : tourmaline.

2 Paragenetic sequence

Although mineral ratios change from one vein to another, the textural relationships and relative timing among minerals remain constant throughout the mine. The paragenetic sequence proposed at the Lac Herbin deposit is the same for both subvertical and subhorizontal veins (Fig.3). Moreover, the paragenetic sequence is very similar to the one described by Robert and Brown (1986) at the Sigma deposit, except for the timing of the fracturing event.

The main vein filling is characterized by the deposition of white mica and the first generation of carbonate, systematically precipitated along the wall

rock of the veins. This generation of carbonate contains growth zones and it is roughly contemporaneous with tourmaline precipitated at the margin of the veins. Tourmaline occurs within and surrounds pyrite crystals. The latter contain inclusions of gold, pyrrhotite, chalcopyrite, cubanite, and tellurides, as well as trace element enrichments such as Co, Ni, and As. Quartz precipitated continuously with pyrite and tourmaline. The late fracture filling is characterized by the precipitation of the second generation of carbonate associated with most of the gold and chalcopyrite, with local sphalerite, pyrrhotite, cobaltite, galena, and tellurides. Their relationship with chlorite is not clear, and therefore we interpret chlorite to be coeval or post-dating the second generation of carbonate and ore minerals. Chlorite is spatially associated with oxides (i.e. ilmenite and rutile). No telluride minerals are associated with pyrrhotite, cobaltite, sphalerite, and galena in the mineral assemblages of the late fracture filling. This observation is in agreement with the different conditions characterizing the stability fields of pyrrhotite and tellurides, reflecting the limited solubility of tellurium in reduced ore fluids at sulfur fugacities above the pyrrhotite-pyrite buffer (Afifi et al., 1988).

The two mineralization styles are interpreted in terms of an early main vein filling followed by a late fracture filling. It is reasonable to explain the main vein filling stage by the successive mineral deposition during incremental reopening events. Each vein reopening fractures minerals (i.e. pyrite, tourmaline, and quartz) precipitated during previous events. These late fracturing events resulted in precipitation of ore minerals that include most of the gold and chalcopyrite, and the local pyrrhotite, sphalerite, cobaltite, galena, and tellurides. Finally, the mineralization styles in both stages are similar and likely related to the same ore-forming fluid. However, the timing between these two mineralizing events cannot be constrained by this study.

MINERALS	MAIN VEIN FILLING	LATE FRACTURE FILLING
Carbonates	—	—
Tourmaline	—	—
Pyrite	—	—
Ilmenite / Rutile	—	—
Pyrrhotite	—	—
Cobaltite	—	—
Chalcopyrite	—	—
Cubanite	—	—
Sphalerite	—	—
Galena	—	—
Chlorite	—	—
White mica	—	—
Quartz	—	—
Gold / Electrum	—	—
Tellurobismuthite	—	—
Tetradymite	—	—
Tsumoite	—	—
Rucklidgeite	—	—
Hessite	—	—
Volynskite	—	—
Petzite	—	—
Stützite	—	—
Calaverite	—	—
Melonite	—	—
Parkerite	—	—
Buchornite	—	—

Figure 3. Paragenetic sequence at the Lac Herbin deposit.

3 Fluid inclusion study

3.1 Fluid inclusion types and distribution

Rare aqueous-carbonic fluid inclusions (type 1) were observed with constant or variable liquid/vapor ratios in the same FIA. They have been subdivided into three subtypes based on the volume of the CO₂ phase at room temperature: subtype 1a with 10-25 CO₂ vol. %, subtype 1b with 70-90 CO₂ vol. %, and subtype 1a/b with 40-50 CO₂ vol. % (Figs.4a-b). Type 1 inclusions are randomly distributed forming three dimensional clusters interpreted as intra-granular in quartz crystals. They represent the earliest fluid inclusion generation at the Lac Herbin deposit. Neither cathodoluminescence imaging, nor petrography of these fluid inclusions revealed any evidence that may allow us to classify them as primary inclusions.

High-temperature, two-phase aqueous fluid inclusions (type 2), with a vapor phase occupying 15 to 30 vol. % of the inclusion at the room temperature, are more abundant than type 1 fluid inclusions. They are distributed in trails along healed fractures (Fig.4c) and crosscut quartz grain boundaries, and therefore they are interpreted as secondary inclusions relative to the host crystal. Even if there are no crosscutting relationships with type 1 inclusions, we consider type 2 inclusions as post-dating type 1 inclusions because of their occurrence along healed fractures crosscutting grain boundaries.

Abundant low-temperature, two-phase aqueous fluid inclusions (type 3) with (subtype 3a) or without a daughter mineral (subtype 3b) generally occur together (Fig.4d) and in trails along healed fractures. As they crosscut quartz grain boundaries, they can be interpreted as secondary inclusions relative to the host crystal and they post-date type 1 and 2 inclusions. Moreover, there is a positive spatial correlation between fracture abundance and low temperature aqueous fluid inclusion abundance.

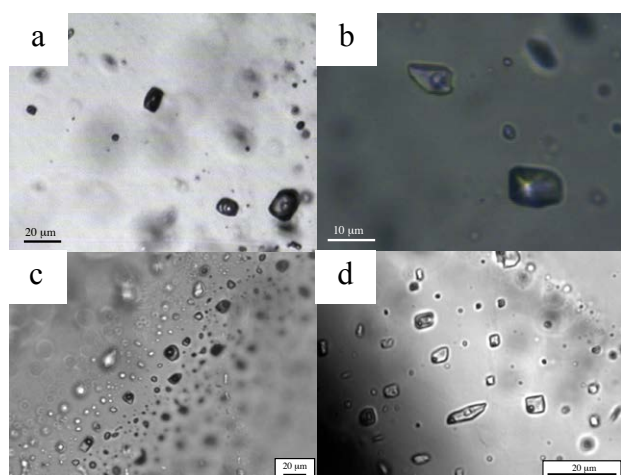


Figure 4. a) Subtype 1b FIA. b) Subtypes 1a and 1b inclusions. c) Type 2 FIA. d) Subtypes 3a and 3b FIA.

3.2 Fluid inclusion characterization and interpretation

Three unrelated and time independent hydrothermal

fluids have been defined at the Lac Herbin deposit:

(1) the low-salinity (<10% NaCl eq.; Fig.5) aqueous-carbonic fluid (CO₂-H₂O-NaCl) is similar to that described in deposits hosted by volcanic rocks of the Val d'Or district (Robert and Kelly, 1987; Robert et al., 1995; Boullier et al., 1998; Neumayr and Hagemann, 2002; Olivo and Williams-Jones, 2002; Olivo et al., 2006; Neumayr et al., 2007), in terms of homogenization temperatures (250°-350°C to the liquid phase) and CO₂ volume percent. Raman spectroscopy analyses did not detect CH₄ and N₂ dissolved in CO₂ of the gaseous phase. The pure CO₂ composition of the aqueous-carbonic fluid inclusions at the Lac Herbin deposit is the main difference for these batholith-hosted ores compared to those described in deposits hosted by volcanic rocks.

Microthermometric measurements revealed that the CO₂ and total homogenization temperatures are constant in a given FIA containing only subtype 1a inclusions, whereas they are highly variable in FIAs composed of subtypes 1a, 1a/b, and 1b inclusions. It is important to note that subtype 1b inclusions systematically decrepitated before total homogenization.

The combined petrographic observations and microthermometric measurements are interpreted in terms of post-entrapment modification rather than fluid immiscibility. This is in contrast to observations by Robert and Kelly (1987), Robert et al. (1995), Boullier et al. (1998), and Neumayr and Hagemann (2002). It also differs from the fluid mixing proposed by Olivo and Williams-Jones, (2002) and Olivo et al. (2006). Nevertheless similar to these previous studies, the previous studies, the H₂O-CO₂ fluid is the most likely ore-forming fluid. The subtype 1a is considered to be the closest in composition to the initial mineralizing fluid, rather than subtypes 1a/b and 1b inclusions, which have suffered reequilibration (Fig.6).

(2) the moderate-salinity (20% NaCl eq.; Fig.5) high-temperature aqueous fluid (H₂O-NaCl-CaCl₂) has higher homogenization temperatures (400°-450°C to the liquid phase) and salinity than the type 1 aqueous-carbonic fluid. Moreover, Raman spectroscopy analyses indicated no detectable CO₂ in the vapor phase. Therefore, this fluid cannot correspond to one end-member resulting from fluid immiscibility of a parent H₂O-CO₂ fluid. This contrasts with respect to the scenario suggested by Robert and Kelly (1987), Robert et al. (1995), and Boullier et al. (1998) for the other deposits of the Val d'Or district.

The absence of type 2 fluid inclusions in some deposits of the Val-d'Or district, such as those along the Cadillac tectonic zone, as well as their occurrence in barren veins in other deposits (i.e. Donalda and Sigma deposits), indicates that the high-temperature, saline fluid is not related to and post-dates the gold mineralizing event. Finally, the introduction of the high-temperature type 2 H₂O-NaCl-CaCl₂ fluid could explain the heating of the entire host rock environment, resulting in post-entrapment modification of type 1 inclusions (Fig.6).

(3) high-salinity (30% NaCl eq.; Fig.5) low-temperature aqueous fluid inclusions (H₂O-NaCl-CaCl₂) were systematically described in all previous studies of

the Val-d'Or district. The low homogenization temperatures (50°-130°C to the liquid phase) and the association of liquid-vapor and salt-saturated liquid-vapor inclusions are similar characteristics to the Ca-Na-Cl-rich ground water and brines described by Kerrich and Kamineni (1988) in the Superior province. Type 3 inclusions may represent the infiltration of aqueous and saline fluids at the Canadian Shield scale and they are interpreted as a late and different fluid, unrelated to the mineralizing event (Fig.6).

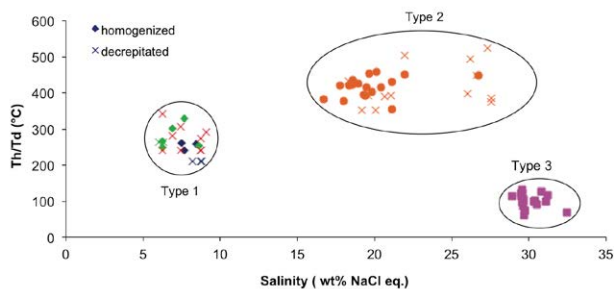


Figure 5. Final homogenization temperatures (Th) and decrepitation temperatures (Td) versus salinity.

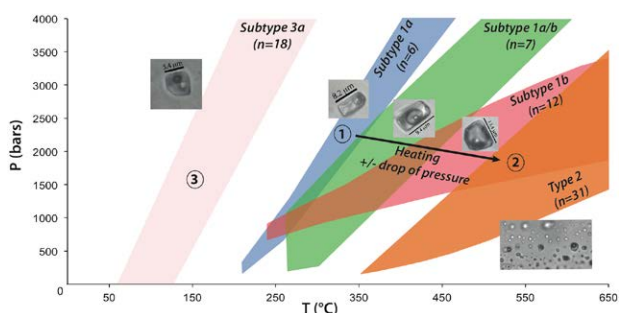


Figure 6. Isochores of the different fluid inclusion types recognized in this study and their relative timing interpretation. Post-entrapment modification of type 1 inclusions, is attributed to heating of the direct host environment, followed by trapping of type 2 inclusions. Type 3 inclusions were trapped during cooling and exhumation.

Acknowledgements

This study has been supported by the Augustin Lombard foundation (SPHN), by the Swiss Academy of Sciences (Sc. Nat) and by the Natural Sciences and Engineering Research Council of Canada (NSERC). We also acknowledge QMX Gold Corporation for their great collaboration, and we gratefully acknowledge Jérémy Lemarchand for providing his understanding about the regional and the structural geology during fieldwork.

References

Afifi AM, Kelly WC, and Essene EJ (1988) Phase relations among tellurides, sulfides, and oxides: Pt.I, Thermochemical data and calculated equilibria. *Econ Geol* 83:377- 394.

Boullier AM, Firdaus K, and Robert F (1998) On the significance of aqueous fluid inclusions in gold-bearing quartz vein deposits from the southeastern Abitibi Subprovince (Quebec, Canada). *Econ Geol* 93:216-223.

Kerrich R, Kamineni D (1988) Characteristics and chronology of fracture—fluid infiltration in the Archean, Eye Dashwa Lakes pluton, Superior Province: evidence from H, C, O-isotopes and fluid inclusions. *Contrib to Mineral and Petrol* 99:430-445.

Lemarchand J, Tremblay A, Ruffet G and Gobeil C (2011) Minéralisations filoniennes aurifères du pluton de Bourlamaque (Val d'Or, Abitibi) : caractérisation structurale et apport de la datation $^{40}\text{Ar}/^{39}\text{Ar}$. Ecole Thématique du CNRS, 7-9 February 2011, Orléans, poster.

Neumayr P, Hagemann SG (2002) Hydrothermal fluid evolution within the Cadillac Tectonic Zone, Abitibi Greenstone Belt, Canada: Relationship to auriferous fluids in adjacent second- and third- order shear zones. *Econ Geol* 97:1203-1225.

Neumayr P, Hagemann S, Banks D, Yardley BWD, Couture JF, Landis G, and Rye R (2007) Fluid chemistry and evolution of hydrothermal fluids in an Archean transcrustal fault zone network: the case of the Cadillac Tectonic Zone, Abitibi greenstone belt, Canada. *Can J Earth Sci* 44 :745-773.

Olivo GR, Williams-Jones AE (2002) Genesis of the auriferous C quartz-tourmaline vein of the Siscoe mine, Val d'Or district, Abitibi subprovince, Canada: structural, mineralogical and fluid inclusion constraints. *Econ Geol* 97:929-947.

Olivo GR, Chang F, and Kyser TK (2006) Formation of the auriferous and barren North Dipper Veins in the Sigma Mine, Val d'Or, Canada: constraints from structural, mineralogical, fluid inclusion, and isotopic data. *Econ Geol* 101:607-631.

Robert F (1990) Structural setting and control of gold-quartz veins of the Val d'Or area, southeastern Abitibi subprovince: Gold and Base-Metal Mineralization in the Abitibi Subprovince, Canada, with Emphasis on the Quebec Segment. University of Western Australia, Short Course Notes 24:167-210.

Robert F, Brown AC (1986) Archean gold-bearing quartz veins at the Sigma Mine, Abitibi greenstone belt, Quebec; Part II, Vein paragenesis and hydrothermal alteration. *Econ Geol* 81:593-616.

Robert F, Kelly WC (1987) Ore-forming fluids in Archean gold-bearing quartz veins at the Sigma Mine, Abitibi greenstone belt, Quebec, Canada. *Econ Geol* 82:1464- 1482.

Robert F, Boullier AM, and Firdaus K (1995) Gold-quartz veins in metamorphic terranes and their bearing on the role of fluids in faulting. *J Geophysical Res* 100:12861-12812.

Sibson RH, Robert F, and Poulsen KH (1988) High-angle reverse faults, fluid-pressure cycling, and mesothermal gold-quartz deposits. *Geology* 16:551-555.

Geological setting of the Telfer gold-copper deposit and surrounding areas, Paterson orogen, Western Australia

C. Schindler, S.G. Hagemann

Centre for Exploration Targeting, University of Western Australia, Crawley, WA 6009, Australia

Abstract. The Telfer Au-Cu deposit is one of the largest Au-Cu deposits in Australia (resources of 660 t Au and 1220 kt Cu). It is surrounded by several Neoproterozoic granitoids. A major tungsten-skarn is located at the contact of the O'Callaghans granite and the overlying calcareous metasedimentary rocks. The Telfer gold-copper deposit contains multiple generations of mineralised (chalcopyrite-pyrite-gold) veins defining several discrete ore bodies: (1) reef type chalcopyrite-gold mineralisation, (2) localised chalcopyrite-pyrite-gold vein stockworks, and (3) discordant pyrite-chalcopyrite-gold veins crosscutting stratigraphy. All veins are hosted by metasedimentary rocks. Preliminary fluid inclusion studies of the different vein sets reveal a mixture of hypersaline (35 to 50 wt% NaCl equiv.) and carbonaceous and aqueous medium saline (10 to 26 wt% NaCl equiv.) fluids. Such copper enrichment and high salinity fluid inclusions are not characteristic for orogenic gold systems.

Keywords: Telfer, gold, copper, granite, Paterson orogen, Western Australia

1 Introduction

The Telfer region, including the world class Telfer Au-Cu deposit (resources of 660 t Au and 1220 kt Cu, Newcrest Mining Annual report, 2012) and the large O'Callaghans tungsten-skarn (resources of 78 Mt @ 0.33% WO₃, Newcrest Mining Annual report, 2012), is situated in the Paterson orogen, Western Australia, about 1300 km north northeast of Perth. There are several distinct Neoproterozoic monzogranitic intrusions in the Telfer region (e.g. Mount Crofton, Minyari, Wilki, and O'Callaghans, Fig. 1, Schindler et al. 2012a) which may have played an important role in the mineralisation process of the deposit.

This study provides an overview of the geological setting of the Telfer deposit and summarises the results of recent investigations on fluid inclusions trapped in mineralised veins from several Telfer ore bodies (Schindler et al. 2012c), and geochemistry data of some of the surrounding granitoids (Schindler et al. 2012a) including the O'Callaghans style W mineralisation (Schindler et al. 2012b).

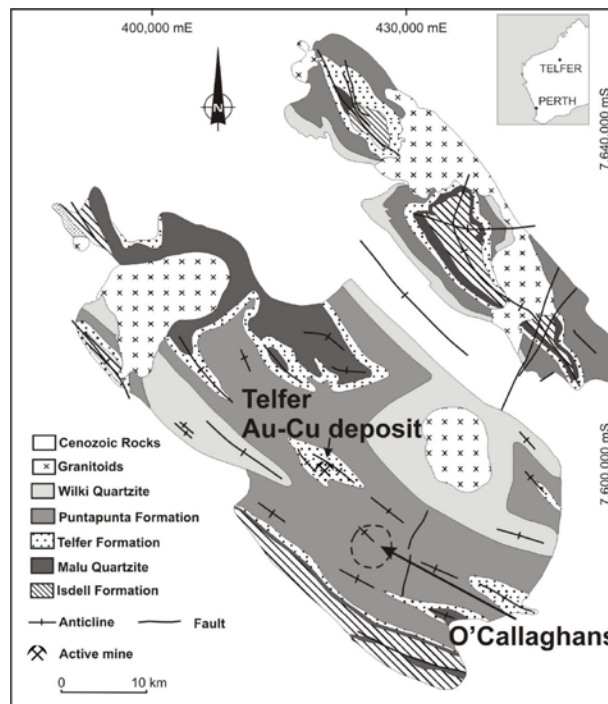


Figure 1: Location and regional geology of the Telfer area; (modified after Goellnicht et al. 1989)

2 Geological Setting, Petrography and Geochemistry of Telfer Granites

The Mount Crofton granite (MTC) is a fine- to coarse-grained biotite monzogranite, with accessory titanite, hornblende, magnetite, apatite, zircon and rutile. The Minyari granite (MIN) is a fine- to medium-grained biotite monzogranite with accessory hornblende, apatite, zircon and rutile. Both igneous bodies locally contain mafic enclaves, and are largely undeformed. The Wilki granite (WIL) consists of a medium- to coarse-grained, red biotite monzogranite with accessory magnetite, zircon, and apatite (Goellnicht 1992; Schindler et al. 2012a).

The O'Callaghans granite (OCG) is not exposed, but its upper surface is comprehensively defined by drill holes at depths between 300 and 400 m. The OCG is a medium-grained biotite monzogranite with accessory zircon and apatite. The upper parts of the OCG are locally strongly foliated and exhibit coarse alkali-feldspar phenocrysts (up to 2 cm). The entire granitoid stock is covered by 300-400 m of calcareous metasedimentary rocks of the Neoproterozoic Puntapunta Formation. A tungsten-skarn is observed at the contact of the O'Callaghans granite with the metasedimentary rocks. The main ore minerals are scheelite and wolframite. Some non-economic quartz-pyrite-molybdenite-scheelite veins crosscut into the

granite (Schindler et al. 2012a).

The Telfer granitoids are high in SiO₂ (dominantly >71 wt.%), K₂O (average 4.4-4.9 wt%), Rb, relatively high in Na₂O (generally >3.2 wt%), U and Th, and low in MgO, CaO, TiO₂ and P₂O₅ (Goellnicht et al. 1991). All Telfer granites share features of typical I-type granites after Chappell and White (1974) (e.g. mol Al₂O₃/(Na₂O + K₂O + CaO) < 1.1, relatively high Na₂O, normally >3.2%) and can be classified as I-type granites (Goellnicht et al. 1991).

Interpretation of trace element ratios (e.g. Rb/Sr) suggest an increasing degree of fractionation from the OCG, WIL and MIN to MTC (Goellnicht et al. 1991). This is in contrast to Pb isotope data defined by Goellnicht et al. (1991), who suggest heterogeneous source for the different Telfer granites, rather than fractionation of the granites from the same source. These isotope analyses, combined with Rb/Sr analyses provided by Trendall (1974), imply direct mantle derivation or a short crustal residence time for the MTC (Goellnicht et al. 1991). For the other granites, only Pb isotope data is available to date, and a firm definition of the magma source is therefore not possible.

3 Telfer Gold-Copper Mineralisation

Telfer represents one of Australia's largest Au-Cu deposits, with total contained resources at the time of discovery in 1972 comprising approximately 930 t of gold and 1450 kt of copper. Ore bodies are hosted in Neoproterozoic metasedimentary rocks of the Lamil Group and consist of several different mineralised vein types: (1) reef type chalcopyrite-gold mineralisation (sub-parallel to bedding, concordant with lithological boundaries, and forming laterally extensive quartz-pyrite-chalcopyrite-bornite-chalcocite-gold or carbonate-pyrite-chalcopyrite-bornite-chalcocite-gold lodes), (2) localised dolomite-quartz-chalcopyrite-pyrite-gold vein stockworks, and (3) laterally extensive discordant carbonate-quartz-pyrite-chalcopyrite-gold veins (Schindler et al. 2012c).

Preliminary microthermometry results revealed that all mineralised veins show three different types of fluid inclusions: (1) three phase aqueous (L+V+S) inclusions with one or two solids, (2) three phase aqueous-carbonic (L_{aq}+L_{carbonic}+V_{carbonic}) inclusions, and (3) two phase aqueous (L+V) inclusions.

These inclusion types are trapped in different fluid inclusion assemblages (FIAs) using the criteria from Goldstein and Reynolds (1994): (1) three phase aqueous-carbonic (L_{aq}+L_{carbonic}+V_{carbonic}) liquid rich inclusions, (2) three phase aqueous-carbonic (L_{aq}+L_{carbonic}+V_{carbonic}) vapour and liquid rich inclusions, (3) three phase aqueous (L+V+S) liquid rich inclusions, (4) two phase aqueous (L+V) liquid rich inclusions, and (5) two phase aqueous (L+V) liquid and vapour rich inclusions (Schindler et al. 2012c).

Three phase aqueous inclusions have salinities from 35 to 50 wt% NaCl equiv., two phase aqueous and three phase aqueous-carbonic inclusions have salinities of up to 26 wt% NaCl equiv. (Goellnicht et al. 1989).

4 Discussion and Outlook

The four major granite bodies surrounding the world class Telfer Au-Cu deposit share many geological features, e.g. all are SiO₂ rich, highly fractionated, and I-type monzogranites (Goellnicht et al. 1991).

Fluid inclusion studies on samples from the Telfer Au-Cu deposit show broad similarities to orogenic Au and porphyry Cu±Au deposits, but with a number of important differences that argue against a direct association with either. Hypersaline inclusions are typical for porphyry deposits (Ulrich et al. 1999), but significant CO₂-CH₄ contents comparable to those found at Telfer (Goellnicht et al. 1989) are not reported in porphyries, and are more typical of orogenic lode gold deposits (Ridley and Diamond 2000) and intrusion related gold deposits (Lang and Baker 2001). Both the high salinity of some CO₂-CH₄ bearing inclusions and abundance of Cu (1220 kt Cu, Newcrest Mining Annual report, 2012) at Telfer, however, are atypical of orogenic and intrusion related gold systems.

The distance of Au-Cu mineralisation to potentially related intrusions (10–40 km), and the absence of concentric alteration zones (Rowins et al. 1998) are also significant arguments against a classic porphyry Cu±Au association (see Sillitoe 2010; Lowell and Guilbert 1970).

Acknowledgements

This abstract is part of a PhD project of CS funded by a scholarship for international research fees (SIRF), a university international stipend (UIS) and Newcrest Mining Ltd. The authors thank Newcrest Mining Ltd. for access to the areas described in this abstract and for financial support of this project.

References

- Chappell B, White AJR (1974) Two contrasting granite types. *Pac Geol* 8:173-174
- Goellnicht NM, Groves DI, McNaughton NJ, Dimo G (1989) An epigenetic origin for the Telfer gold deposit, Western Australia. In: Keays RR, Ramsay WRH, Groves DI (eds) *Econ Geol Mono.* 6:151-167
- Goellnicht NM, Groves DI, McNaughton NJ (1991) Proterozoic fractionated granitoids of the mineralized Telfer area, Paterson Province, Western Australia. *Precambrian Res* 51:375-391
- Goellnicht NM (1992) Late proterozoic fractionated granitoids and their role in the genesis of gold and base-metal mineralisation in the Telfer district, Western Australia. University of Western Australia, Perth, pp 132
- Goldstein RH, Reynolds TJ (1994) Systematics of fluid inclusions in diagenetic minerals. *SEPM Short Course* 31:199
- Lang J, Baker T (2001) Intrusion-related gold systems: the present level of understanding. *Miner Deposita* 36:477-489
- Lowell JD, Guilbert JM (1970) Lateral and vertical alteration-mineralization zoning in porphyry ore deposits. *Econ Geol* 65:373-408
- Ridley JR, Diamond LW (2000) Fluid chemistry of orogenic lode-gold deposits and implications for genetic models. In: Hagemann S, Brown PE (eds) *Gold in 2000*, *Rev Econ Geol.* 13:141-162
- Rowins SM, Groves DI, McNaughton NJ (1998) Neoproterozoic telfer-style Au (Cu) deposits. *AGSO J Aust Geol Geoph* 17:217-223
- Schindler C, Hagemann SG, Batt G, Maxlow J (2012a) Mineralogy

- and geochemistry of Neoproterozoic granites in the Telfer region, Paterson Orogen, Western Australia 34th International Geological Congress. Brisbane
- Schindler C, Hagemann SG, Batt G, Maxlow J (2012b) The geological setting and petrography of the O'Callaghans granite and W skarn mineralization in the Telfer area, Paterson Orogen, Western Australia Society of Economic Geologists 2012 Conference. Lima, Peru
- Schindler C, Hagemann SG, Maxlow J (2012c) Preliminary results from fluid inclusion petrography and microthermometry on quartz and calcite from different types of orebodies at the Telfer Au-Cu deposit, Paterson Orogen, Western Australia In: Mernagh TP, Hagemann SG, Kamenetsky VS (eds) 4th Biennial Conference on Asian Current Research on Fluid Inclusions ACROFI IV. Brisbane
- Sillitoe RH (2010) Porphyry Copper Systems. *Econ Geol* 105:3-41
- Trendall AF (1974) The age of a granite near Mount Crofton, Paterson Range Sheet. Western Australia Geological Survey, Annual Report 1974:92-96
- Ulrich T, Gunther D, Heinrich CA (1999) Gold concentrations of magmatic brines and the metal budget of porphyry copper deposits. *Nature* 399:676-679

Geological, petrographical and geochemical characteristics of the granitoid hosted Amphibolite Ridge gold occurrence in south Greenland

Denis Martin Schlatter
Helvetica Exploration Services GmbH

Alfons Berger
Institut für Geologie, Universität Bern

Ole Christiansen
NunaMinerals A/S, Nuuk

Abstract. South Greenland is a recognized gold province that hosts Greenland's first gold mine, Nalunaq. Because Nalunaq consists of an auriferous quartz-vein hosted in altered metavolcanic rocks these rocks were traditionally regarded as being most favourable for gold exploration and only limited gold exploration was carried out in other settings. Here we present recent results from exploration work that targeted granitic rocks at Amphibolite Ridge (AR) about 25 km north of Nalunaq. Diamond drilling has intersected large portions of gold mineralized granitic rocks together with auriferous quartz-veins associated with shear zones. The hydrothermal alteration fluids have added gold to the granitoids, and the presence of bismuth-rich tellurides implies that the fluids responsible for the introduction of gold were also enriched in Bi and Te. The granitic rocks were subjected to Kfs (K-feldspar), sericite and carbonate hydrothermal alteration together with silicification. Surface mapping of the AR has revealed that the gold mineralization occurs near the contact of granitoids and quartz-diorites. Because all these are typical features of intrusion-related gold systems (IRGS), we suggest that the granitoid hosted AR gold mineralization is a member of the IRGS class. Future gold exploration in South and in South-east Greenland should target K and Si-altered granitic rocks containing quartz-veins associated with shear zones near contacts of rocks with contrasting competence.

Keywords. Intrusion-related gold systems, granitic rocks, Niaqornaarsuk peninsula, South Greenland

1 Introduction

South Greenland is recognized as a gold province of early Paleoproterozoic age (Steenfelt 2000) and hosts Nalunaq, Greenland's first producing gold mine. Nalunaq is a shear hosted high-grade gold deposit with abundant visible gold (VG) in quartz (Kaltoft et al. 2000, Schlatter and Olsen 2011). The quartz-vein is hosted in hydrothermally altered metavolcanic rocks and is associated with a shear zone. The hydrothermal alteration is characterized by addition of gold together with Si and K (Schlatter and Kolb 2011). Renewed exploration activities in South Greenland have regionally targeted not only metavolcanic rocks but also granitoids that showed similar K and Si hydrothermal alteration than seen from Nalunaq. Here we present the results of the first drill program of six holes totalling 1193 metres together with preliminary geological,

geochemical and petrological data. The drill program has targeted for the first time granitic rocks belonging to the Julianehåb Batholite Zone that occur on the AR on the Niaqornaarsuk peninsula (Fig. 1) just 25 km north of the existing Nalunaq mine.

2 Regional geology

The Ketilidian orogen evolved between 1850 Ma and 1725 Ma during northward subduction of an oceanic plate under the southern margin of the Archaean North Atlantic craton. The orogen is divided into four geological domains (Chadwick and Garde 1996): (1) the Ketilidian Border Zone, (2) the Julianehåb Batholith Zone, (3) the Psammite Zone and (4) the Pelite Zone (Fig. 1). AR is located in the Julianehåb Batholith Zone and is made up of granites, granodiorites, diorites and gabbros metamorphosed to greenschist facies.

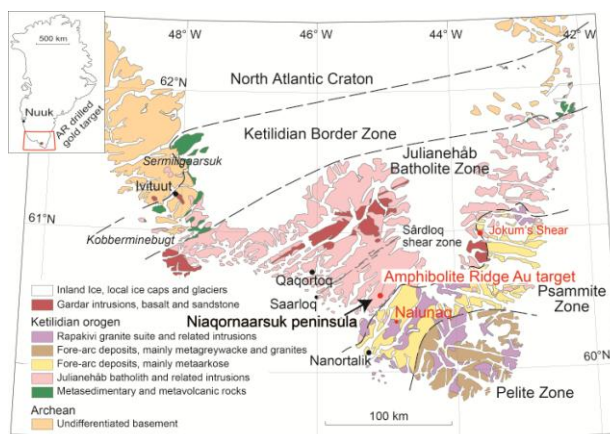


Figure 1. Schematic geological map of the Ketilidian Orogen, South Greenland (modified after Chadwick and Garde 1996) showing the Amphibolite Ridge gold target which is located on the Niaqornaarsuk peninsula about 25 km north of the existing Nalunaq gold mine.

2.1 Geological setting of the AR gold occurrence and drill results

The gold mineralized zone of the AR gold target is at least 79 m wide and comprises two narrow shear zones associated with auriferous quartz-veins containing VG (Fig. 2). Both vein systems are hosted in hydrothermally

altered and gold mineralized Kfs-rich granitoid rocks. The gold mineralized zone also comprises enclaves of mafic rocks at the contact of the auriferous quartz-veins. These mafic rocks crop out on the eastern flank of the AR and are best described as Kfs and pyroxene-rich alkali lamproites. Drill hole VAG-12-02 intersected a wide gold mineralized zone (Fig. 2, table 1) and the end of the drill hole is still mineralised.

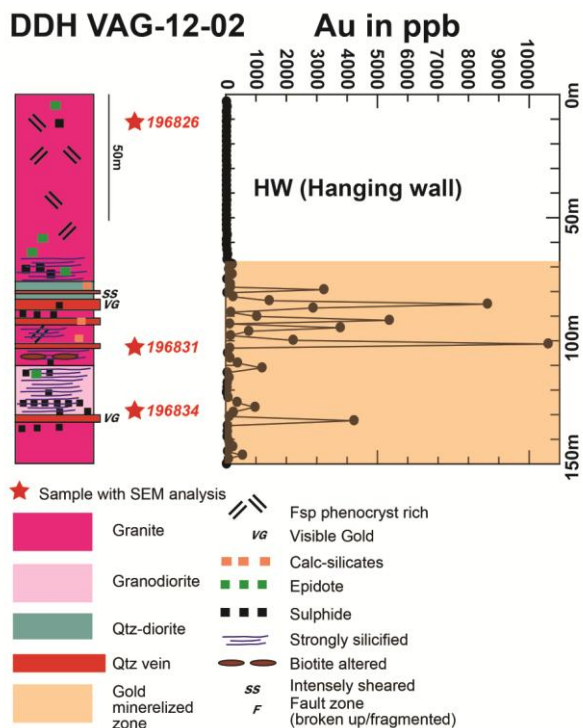


Figure 2. Simplified geological log of the diamond drill hole VAG-12-02 that intersected at the AR gold mineralized granitoid rocks and two narrow quartz-veins with VG.

Drill core samples, based on an average two-metre intersections, were analysed for gold using fire assay methods at Actlabs in Nuuk. A selection of these samples were check assayed at a second, independent laboratory (SGS Toronto). The results of these check assays showed an acceptable level of repeatability.

Hole ID	From (m)	To (m)	Interval (m)	Gold (g/t)
VAG-12-01	70.00	78.00	8.00	0.76
including	72.30	74.00	1.70	2.74
VAG-12-02	68.00	147.00	79.00	0.96
including	78.70	133.40	54.70	1.33
including	78.70	102.00	23.30	2.47
VAG-12-03	62.00	76.00	14.00	0.57
including	62.00	64.00	2.00	2.74
VAG-12-04	294.55	304.00	9.45	0.40
including	295.20	298.50	3.30	0.94
VAG-12-06	28.00	66.00	38.00	0.18
including	54.00	56.00	2.00	0.99

Table 1. Summary of the drill program 2012 at AR.

Other drill holes of the AR together with excellent surface exposure reveals that the footwall (FW) and the hanging wall (HW) are made up of granitic rocks. A few hundred metres south of drill hole VAG-12-02 a rigid 200 m wide diorite body occurs and it is interpreted that the granitoids have intruded into the diorite.

2.2 Hydrothermal alteration and introduction of gold

The granitic rocks are variable altered and alteration as identified from hand lens inspection of drill cores and surface rock outcrops includes silicification, quartz veining and hydrobrecciation as well as precipitation of Kfs, pyrite and pyrrhotite (occurring in both patches and stockwork like fine stringers), calc-silicate, biotite and epidote. The alteration pattern is complex with narrow zones of strongly altered rocks and wider zones of less altered rocks.

3 Lithochemistry and pathfinder elements for gold

The lithochemical study is based on 42 surface samples and 39 drill core samples that were analysed for major and trace elements at Actlabs in Ancaster. The classification of the rocks as identified in the field are largely confirmed by geochemical assessments (Fig. 3). The rocks from AR plot into the fields of granodiorite, granite, adamellite, tonalite, quartz-diorite, monzogabbro and monzonite (Fig. 3). The rock classification based on major elements (Fig. 3) confirmed most of the rock names given in the field, and lithochemistry also helped to verify and to refine the rock classification.

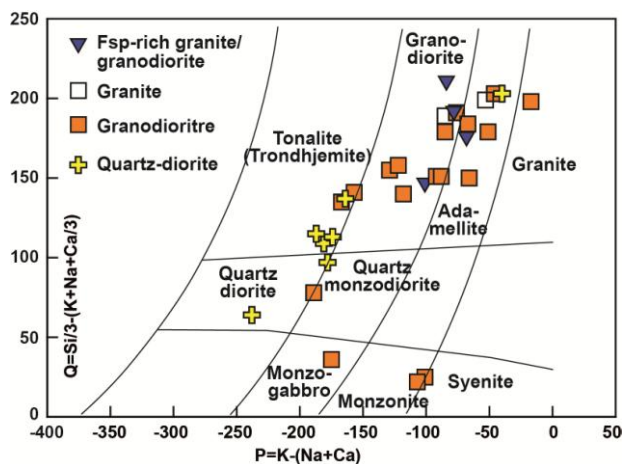


Figure 3. Least to weakly hydrothermally altered felsic igneous plutonic rocks from AR classified by applying the diagram of Debon and LeFort (1982). In the diagram 32 least to weakly altered samples from drill core and 27 samples from surface rocks are plotted.

Preliminary geochemical results based on 594 drill core and 275 surface samples show that the hydrothermally altered granitoids are elevated in gold and in bismuth with a weak correlation between these elements for drill core samples (Fig. 4). Correlation

between Bi and Au has been reported from orogenic gold deposits (e.g. Eilu and Groves 2001) and from IRGS (Hart 2007). Other elements that are elevated in the gold zone at AR are silver (up to 6 ppm), gallium (up to 20 ppm), tungsten (up to 22 ppm) and barium (up to 2000 ppm) whereas the base metals copper, zinc and lead are only slightly elevated. Arsenic contents of the samples from the AR gold mineralized zone are low (less than 25 ppm for all samples) which is in strong contrast to the nearby Nalunaq gold mine where the FW and HW are strongly arsenic enriched (Schlatter and Kolb 2011).

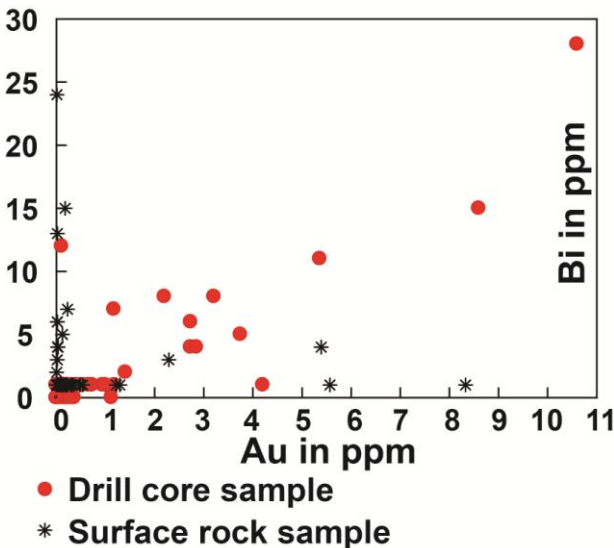


Figure 4. Drill core samples from the AR region show a weak correlation between Au and Bi (Spearman rank coefficient of correlation $r' = 0.56$) whereas surface samples show no correlation between Au and Bi.

4 Petrography

The petrographic study is based on 18 polished thin sections from drill core samples and 11 polished thin sections from surface rocks. Here we present preliminary petrographic results from the scanning electron microscope (SEM) and observations from the optical microscope for samples 196826, 196831 and 196834. Drill core sample 196826 is from the weakly to moderately altered HW of the AR gold mineralization and the two other drill core samples are taken from the gold mineralized zone intersected by drill hole VAG-12-02 (Fig. 2). The granite from the HW (sample 196826) comprises Kfs, plagioclase, quartz, biotite, sericite and chlorite. The back-scattered electron (BSE) image reveals that feldspars are moderately sericite and chlorite altered which we regard as distal alteration (Fig. 5). The sericite-rich patches (Fig. 5) also contain in some places calcite. The strongly altered granite (sample 196831) that occurs in the gold mineralized zone comprises quartz, plagioclase, relict amphibole and chalcopryrite. Optical microscope observations (Fig. 6) reveals that the rock is strongly sericite altered and SEM work shows that the rock contain fluorite and bismuth-rich tellurides. In sample 196834, albite is strongly sericite and chlorite altered (Fig. 2) and quartz is

delicately rimmed by Kfs which appear to be an important characteristic of the proximal hydrothermal alteration at the AR. In the same sample Au and Ag-rich sulphosalts hosted in quartz were identified together with monazite, allanite and barium-rich Kfs (Fig. 7). This mineral assemblage is characteristic of proximal alteration at the AR gold mineralization.

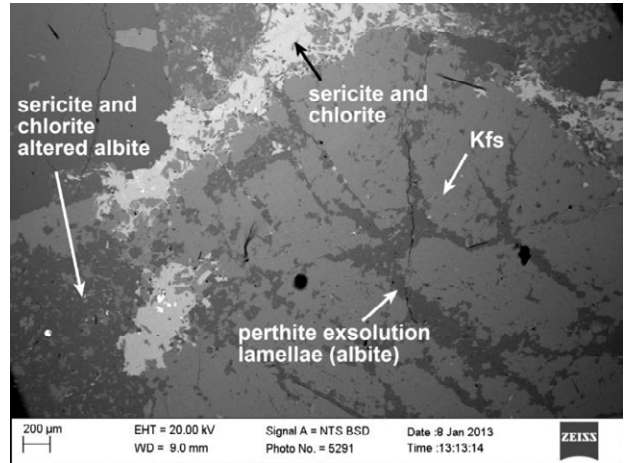


Figure 5. Sample 196826 is weakly to moderately altered granite from DDH VAG-12-02. The BSE image shows that the feldspars are hydrothermally altered. The large Kfs contains perthite exsolution lamellae that can also be identified from the optical microscope.

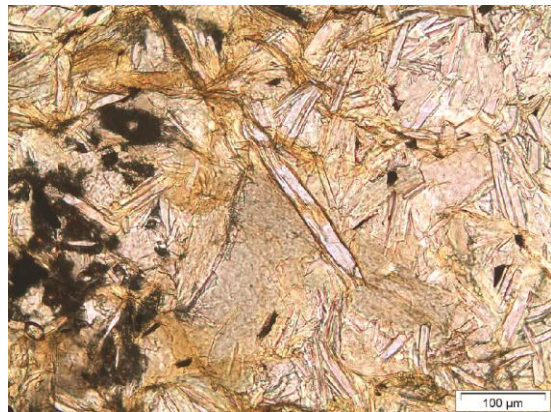


Figure 6. Sample 196831 is strongly altered granite from DDH VAG-12-02. The photomicrograph taken under plane-polarized light shows abundant fine grained muscovite (sericite).

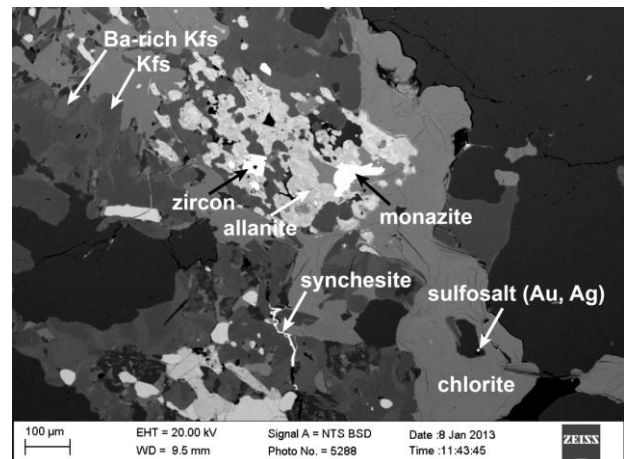


Figure 7. Sample 196834 from DDH VAG-12-02 is strongly altered granodiorite containing Au and Ag rich sulphosalt. The BSE image reveals that the alteration minerals are Kfs, chlorite, monazite and allanite.

5 Discussion and conclusions

The characteristics of the AR mineralization are elevated W, Bi and Te in the alteration zones, sericite, chlorite, biotite, epidote, sulphide and carbonate altered rocks, presence of shear zones with Qtz and VG, and the typical granite-granodiorite host rock. At the AR a large quartz-diorite body that was likely intruded by granitic rocks at relatively shallow crustal level possibly represents a favourable contact trap for the gold. The gold zone intersected at the AR (table 1) shows that large portions of the granitic rocks are mineralized in strong contrast to Nalunaq where the gold is hosted by a narrow, gold-rich quartz-vein (Schlatter and Kolb 2011). In South and South-east Greenland, several gold occurrences and showings are located near the southern margin of the Julianehåb Batholith Zone within the granites and metavolcanic rocks (Stendal and Frei 2000). Recent exploration by NunaMinerals A/S in a locality known as Jokum's Shear in South-east Greenland (Fig. 1) yielded several samples of strongly silicified and sulphidized intrusive plutonic rocks with more than 1 g/t gold including one rock chip sample yielding 9.3 g/t gold over a width of 3.1 metres as well as one composite sample with 3.7 g/t gold over a width of two metres. Several characteristics are recognized at the AR gold occurrence that are typical for IRGS such as widespread gold mineralization of granitoid rocks, granitoid rocks in FW and HW, elevated Bi in the gold zone as well as proximal sericite, Kfs and carbonate alteration. The setting of quartz-diorite intruded by granitic rocks at the AR possibly represents a roof zone as defined by Hart (2007) from work that he carried out in the Tintina Gold Province in Yukon and Alaska. The presence of different deposit styles in South Greenland (narrow gold-rich quartz-vein at Nalunaq, wide gold mineralized granitic rocks at AR) within the same district is as well a typical characteristic of IRGS (Hart 2007)

The results of this preliminary investigation suggest that additional gold resources are to be found in South and South-east Greenland in altered granitic rocks of the southern margin of the Julianehåb Batholite (Fig. 1). Future mineral exploration should drill-delineate the newly discovered AR mineralization and regional exploration should target silicified and Kfs- altered granitic rocks that are elevated in gold and bismuth. Contacts between hydrothermally altered granitic rocks and quartz-diorites or any other contact between altered granite and rocks with a competence and/or a chemical contrast seems to be a favourable locus of gold mineralizations in South and South-east Greenland.

Acknowledgements

This study has been funded by NunaMinerals A/S, Nuuk Greenland. Jochen Kolb, Joshua Hughes and Lauren Bibby are thanked for interesting discussions and comments that have helped us to better interpret the new data presented in this study. Finally Iain Pitcairn is thanked for his detailed review which has substantially improved this extended abstract.

References

- Chadwick B, Garde AA (1996) Palaeoproterozoic oblique plate convergence in South Greenland: a reappraisal of the Ketilidian Orogen. In: Brewer TS (ed) Precambrian crustal evolution in the North Atlantic region. *Geol Soc Spec Publ* 112:179-196
- Debon F, Le Fort P (1982) A chemical-mineralogical classification of common plutonic rocks and associations. *Transactions of the Royal Society of Edinburgh: Earth Sciences* 73:135-149
- Eilu P, Groves DI (2001): Primary alteration and geochemical dispersion haloes of Archaean orogenic gold deposits in the Yilgarn Craton: the pre-weathering scenario. *Geochemistry: Exploration, Environment, Analysis* 1:183-200
- Groves DI, Goldfarb RJ, Robert F, Hart CJR (2003) Gold deposits in metamorphic belts: Overview of current understanding, outstanding problems, future research, and exploration significance. *Econ Geol* 98:1-29
- Hart CJR (2007) Reduced intrusion-related gold systems. In: Goodfellow WD (ed) *Mineral deposits of Canada: A Synthesis of Major Deposit Types, District Metallogeny, the Evolution of Geological Provinces and Exploration Methods*: Geological Association of Canada, Mineral Deposits Division, Special Publication No.5: 95-112
- Kaltoft K, Schlatter DM, Kludt L (2000) Geology and genesis of Nalunaq Palaeoproterozoic shear zone-hosted gold deposit, South Greenland. *Appl Earth Sci* 109:B23-B33
- Schlatter DM, Kolb J (2011): Host rock composition and hydrothermal alteration as tools for exploration in the Nanortalik gold district. Conference proceedings, "Let's talk ore deposits." 11th Biennial SGA Meeting, Antofagasta, Chile, pp 544-546
- Schlatter DM, Olsen SD (2011) The Nalunaq gold mine: a reference sample collection and compilation and interpretation of geochemical data. *GEUS Rapport* 2011/31, 77 p
- Stendal H, Frei R (2000) Gold occurrences and lead isotopes in Ketilidian Mobile Belt, South Greenland. *Appl Earth Sci* 109 (Section B):B6-B13
- Steenfelt A (2000) Geochemical signatures of gold provinces in South Greenland. *Appl Earth Sci* 109 (Section B):B14-B22

Svartliden gold mine: shear zone and BIF-hosted orogenic gold deposit, Gold Line, northern Sweden

Katerina Schlöglova, Chris Gordon, Roman Hanes & Henrik Ask
Dragon Mining Sweden AB, Pauträsk 100, 923 98 Storuman, Sweden

Curt Broman

Department of Geology & Geochemistry, Stockholm University, 106 91, Stockholm, Sweden

Abstract The Svartliden gold deposit is found within a metamorphosed volcano-sedimentary sequence within the Bothnian Basin and has been recognized as an orogenic, lode-style gold deposit with strong stratigraphic and structural controls on mineralization. The entire volcano-sedimentary sequence and mineralization have been overprinted by several episodes of deformation including a first episode of tight folding, followed by intense shearing which has divided the geology into discontinuous shear lenses, a second episode of gentle folding, and late-stage brittle deformation. The ore zone is situated at the contact between amphibolite, banded-iron formation (BIF), and meta-sediments. The ore zone is associated with a quartz mylonite which is interpreted to have been created by a fault/shear zone and which served as the main conduit for hydrothermal fluid flow. The BIF acted as a chemical trap for low-salinity, deep-sourced As-Au-bearing fluids. Ore bodies contain massive calc-silicate and silica-rich mineral assemblages and are mineralized with löllingite-arsenopyrite-pyrrhotite. Gold is present in the form of electrum with 18–32 % silver and occurs at the löllingite-arsenopyrite interface. The main phase of hydrothermal alteration and ore formation is considered to be pre- to syn-metamorphic and the peak metamorphic conditions reached lower to mid-amphibolite facies.

Keywords Gold Line, orogenic lode-gold, banded-iron formation, amphibolite facies metamorphism

1 Introduction

The Svartliden gold deposit is located in the Storuman-Lycksele area, ca. 50 km southwest from the well-known Skellefte District in northern Sweden. The NW-SE trending anomalous gold belt known as the “Gold Line” is situated in supracrustal rocks of Paleoproterozoic age and hosts a number of gold deposits and occurrences, e.g. Knaften, Fäboliden, Svartliden, Stortjärnhobben, Barsele, and Blaiken (Bark 2008). The Svartliden gold deposit is the only deposit in production in this region, operating since 2005 by open-cut and underground mining methods. By September 2012, the mine had produced 307,286 ounces of gold from 2.38 million tonnes of ore grading 4.42 g/t gold.

2 Regional geology

The prominent Skellefte District hosts a large number of Au-rich massive sulfide deposits, a few low-grade porphyry Cu deposits and a number of gold deposits. It is considered to be a relic of a Palaeoproterozoic volcanic arc which was formed at the margin of an Archaean continental landmass to the north and a

sedimentary basin to the south (Allen et al. 1996). In the Early Proterozoic, the Archaean craton rifted with the final break-up at ca. 1.95 Ga, generating a large oceanic basin to the south referred to as the Bothnian Basin (Nironen 1997). The Bothnian Basin mainly consists of a sequence of meta-greywackes and meta-pelites, with a thickness (> 10 km) suggesting formation at a shallow continental margin (Lundqvist 1987), as well as mafic meta-volcanic rocks (Kathol & Weihed 2005). The supracrustal rocks were intruded by S-type granites of the Skellefte-Härnö and Revsund calc-alkaline suite, and to a lesser extent by gabbros, during the Svecofennian orogeny (1.9 to 1.77 Ga; Claesson & Lundqvist 1995).

The geology of the Storuman-Lycksele ore province is dominated by sedimentary and mafic volcanic rocks of the Bothnian Supergroup metamorphosed to conditions of lower to mid-amphibolite facies, with abundant Svecofennian granitic plutons (Kathol & Weihed 2005).

3 Geology of the Svartliden deposit

3.1 Geological setting and tectonic evolution

The Svartliden gold deposit is hosted by two major rock types: meta-volcanics and meta-sediments (Fig. 1). The sequence is dominated by meta-sedimentary rocks, which bound and split the meta-volcanics into separate northern and southern units. The meta-sedimentary rocks mostly consist of biotite-rich schists. The northern boundary with the meta-volcanics is marked by a graphite and sulfide-bearing schist. The mineralization occurs at the contact between the northern amphibolite and the middle sediment package and is related to beds and lenses of banded iron formation. The entire Svartliden sequence was intruded by numerous granites dikes and sills of the Skellefte-Härnö suite (Andersson 2012) at 1800 ± 8 Ma (Persson 2011).

The Svartliden deposit has a complex deformational history with several episodes occurring after mineralization and subsequently deforming the ore body. The earliest structure observed in the sequence is likely related to a quartz mylonite, typically located adjacent to the ore zone, generally between the BIF and the amphibolite. While not mineralized, its proximity to mineralization is significant and discussed in the following sections.

Based on thickness changes, observed parasitic folds and the geometry of the ore body, the sequence appears to be tightly folded, with an axial plane roughly parallel to strike, and has created the appearance of multiple lodes. While folds often create fluid traps as observed in

the Victoria Gold Fields and elsewhere (Narayanaswami et al. 1960, Schaubs & Wilson 2002, and others), the folding at Svartliden appears to occur post-mineralization based on observed parasitic folds of the ore body as well as the geometry of the lodes which lack prominent saddle reefs.

The most significant deformational event occurred post-folding in the form of intense and widespread shearing that affected the entire sequence. This deformation complicated the geology by creating an echelon shear lenses that are observed from hand specimen to regional scale in most lithologies. The effect is more pronounced in the mineralized zone where rheological contrasts and previous deformation associated with the quartz mylonite are localized. The result is a lack of continuity in the ore body as well as stratigraphy since the shear lenses act as boudins on a local and regional scale. Sulfides are often remobilized along the shear planes that bound those lenses present near the ore zone resulting in locally elevated gold values.

Post-shearing, the deposit was folded once again, albeit rather gently and creating a gentle synform with a fold axis perpendicular to strike. Lastly, brittle faulting cuts the stratigraphy with the greatest offset occurring in the middle of the deposit along a primarily left-lateral strike-slip fault.

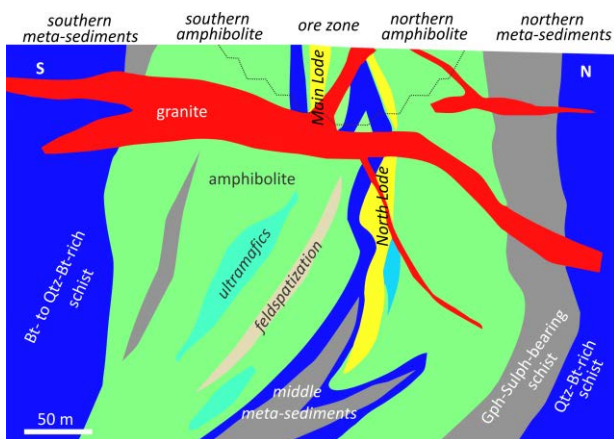


Figure 1 Idealized vertical profile of the Svartliden deposit.

3.2 Petrography of host rocks and their alteration styles

The meta-sedimentary units dominantly consist of biotite-rich schist with variable content of quartz (quartz-rich layers) and rarely andalusite and chlorite alteration. The graphite-sulfide-bearing schists, located on the boundary with the northern meta-volcanic unit, are very fine-grained, dark grey to black rocks which shows elevated magnetic susceptibility (10^{-3} to 10^{-2} SI) as a result of the presence of variable amounts of pyrrhotite(-pyrite) veins and veinlets.

Meta-volcanic rocks of the Svartliden deposit are dominated by amphibolites stratigraphically divided into northern and southern units which differ in extent, thickness and alteration styles. The amphibolites consist of calcic amphiboles, plagioclase, biotite, and accessory titanite and ilmenite. Fine-grained amphibolites are in places hydrothermally recrystallized and are locally

intercalated by coarse-grained plagioclase-rich sills and dikes. The southern amphibolite unit also hosts metamorphosed dark green to grey ultramafics which consist of clinopyroxene, basic plagioclase, serpentinized olivine and fine- to coarse-grained magnetite.

Several different alteration styles are hosted by the amphibolite. The most notable style is potassic alteration. Biotitization appears as large recrystallized biotite grains or fine-grained biotite completely replacing amphiboles and is also observed as distinct biotite-rich bands. The southern amphibolite hosts a distinct zone (up to 30m wide) of strong K-rich alteration, pink to reddish in color, with mineral associations of plagioclase (up to 70 vol. %), biotite, clinopyroxene, titanite, hematite, and pyrrhotite (rarely up to 20 vol. %). Calc-silicate alteration of amphibolite appears in the form of distinct veins, hosting diopside-hornblende-garnet-quartz \pm wollastonite mineral associations. Those veins often reveal zoning with garnet in the central portion and diopside and eventually quartz at the edges. This alteration style is also observed in the sediments adjacent to the mineralization. Pervasive calc-silicate alteration is present in the ore zone (Fig 2).

The granite dikes and sills are light grey, two-mica leucogranites with variable textures from equigranular to pegmatitic with large K-feldspar phenocrysts, plagioclase, quartz, biotite, occasionally garnet, and are rarely pyrrhotite mineralized.

3.3 Whole rock geochemistry

The concentration of major and trace elements including rare earth elements (REE) was analyzed by ICP-MS or ICP-AES by ALS Chemex laboratories.

The meta-sedimentary precursors are classified as greywackes or locally Fe-rich shales (Herron 1988) deposited in a turbidite system in a continental island arc tectonic setting, according to Bhatia & Crook 1986.

All amphibolites (46–52 wt. % SiO_2) are characterized by low alkali concentration trends (1.7–2.8 wt. % $\text{Na}_2\text{O}+\text{K}_2\text{O}$) corresponding to tholeiitic basalts (Le Bas et al. 1986). This is confirmed by their Co–Th ratios (Hastie et al. 2007). The bulk REE contents are generally very low ($\Sigma\text{REE}<60$ ppm) and they exhibit a nearly flat REE pattern with slightly depleted LREE ($\text{La}_N/\text{Lu}_N=0.5\text{--}2.5$; normalized by the CI-type chondrite after McDonough & Sun, 1995). The immobile elements Ti, Zr, Y, Mn, and P confirm that the amphibolite precursors originated at the ocean floor or an immature island arc setting (Mullen et al. 1983).

The ultramafic rocks are recognized as picrites (16–19 wt. % MgO , and up to 0.7 wt. % $\text{Na}_2\text{O}+\text{K}_2\text{O}$; Kerr & Arndt 2001; and 0.22–0.31 $[\text{Al}_2\text{O}_3]$ vs. 0.035–0.064 $[\text{TiO}_2]$ according to Hanski et al. 2001).

Granites intruding the Svartliden deposit are hydrothermally altered, peraluminous S-type granites (Andersson 2012), and they appear to be syn-collisional orogenic products (Bachellor & Bowden 1985).

3.4 Gold mineralization and the BIF

Gold mineralization is located along the contact between the meta-sediments (hanging wall) and the northern amphibolite (foot wall). Two mineralization forms are distinguished within the lode (ore zone), based on mode and texture of alteration and ore assemblages. First, a quartz- or diopside-dominated arsenopyrite- and pyrrhotite-rich ore typically present south of the banded-iron formation ore (Fig 1).

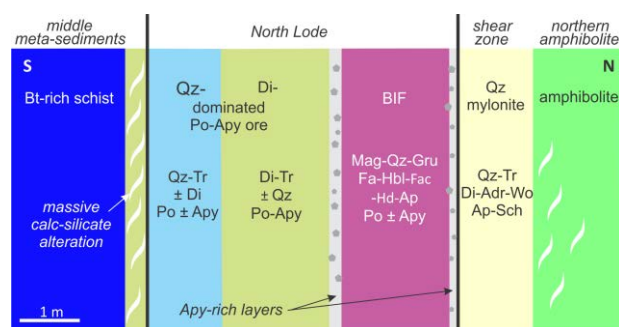


Figure 2 Idealized profile of the ore zone.

Diopside-dominated Apy-Po ore typically contains light green, strong calc-silicate alteration and weak to moderate silicification. It consists mostly of coarse-grained diopside, amphibole, quartz, and gold-bearing pyrrhotite-arsenopyrite-löllingite associations. Sulfides form massive aggregates, bands or veins with fluidal texture. The quartz-rich ore type is dominated by bluish, pervasive silicification with traces of calc-silicate alteration present mostly in the form of diopside-amphibole patches or veins with disseminated pyrrhotite and subordinate amounts of arsenopyrite. Both ore types usually form lodes that range from decimeters to several m's in thickness, but in places the ore zone can appear up to 40 m wide as a result of structural thickening (folding and shearing). At the contact between the ore types, a thin layer (up to 30 cm) of massive arsenopyrite in a silicified matrix occurs. Gold-bearing arsenopyrite is also disseminated in the adjacent southern amphibolite, but not in economic quantities.

The banded-iron formation is variably deformed and preserved along the strike of ~ 1 km and is usually present as a few decimeters to several meters wide, boudinaged lenses. The least altered BIF samples preserve primary micro-banding of quartz and magnetite, and meso-bands intercalated with grunerite. Additional phases are fayalite, fluoro-apatite, hedenbergite, hornblende, ferro-actinolite, chlorite, and pyrrhotite-arsenopyrite-löllingite with minor chalcopyrite, ilmenite and pyrite. The Svartliden BIF is described as Algoma type (Sciuba, 2013).

The ore zone is bounded towards the foot wall by a barren quartz mylonite with a quartz-diopside-tremolite-wollastonite-andradite assemblage.

Gold is present as electrum grains enclosed in arsenopyrite-löllingite aggregates or in gangue minerals. Electrum composition reveals two generations of formation: when the majority of gold is associated with an arsenopyrite-löllingite association, one can expect 68–71 wt. % Au, whereas single electrum grains associated with quartz or silicates usually contain a

higher gold content (74–82 wt. %; Eklund 2007).

3.5 Fluid inclusion study

Fluid inclusions from representative drill core samples and hand specimens from the Svartliden ore zone were studied by microthermometry and Raman microspectrometry (Broman 2010).

Primary aqueous fluid inclusions were found in diopside, actinolite, andradite, quartz and apatite in the ore zone and adjacent quartz mylonites, whereas quartz veins intersecting the ore zone preserve secondary aqueous-, methane- and nitrogen-bearing fluid inclusions. The primary aqueous inclusions consist of a low to moderately saline fluid with 2.4–8.5 wt. % NaCl eq. The homogenization temperature, uncorrected for pressure, is $300 \pm 50^\circ\text{C}$ for inclusions found in calc-silicate minerals and apatite. Secondary inclusions trapped in quartz reveal salinities lower than 7 wt. % NaCl eq. and a homogenization temperature of 155–233°C.

3.6 Geothermobarometry

A geothermometric study of graphite crystallinity on samples from ore zone was conducted (Broman 2010, and references therein). The peak metamorphic temperature that has affected the Svartliden area, estimated from the graphite geothermometer, is 600°C for the andradite-diopside assemblage in quartz mylonite and around 550°C for the ore-related assemblage. Pressure-temperature (P - T) conditions of 554–604°C and 3.5–6.4 kbar were calculated to have affected the amphibolites based on a Grt-Bt-Pl-Qz mineral equilibrium (Berglund 2010, and references therein). The peak P - T conditions for the least altered BIF sample show a temperature range of 540–600°C which were predicted by thermodynamic modeling using the method of P - T Pseudosection (Sciuba, personal communication). Paleo-pressure, linked to the formation of mineralization, was estimated by Broman (2010) using an isochore for a homogenization temperature of ca. 300°C obtained from primary fluid inclusions from the ore zone.

4 Discussion: metamorphic evolution and ore formation

Metamorphic conditions that affected the Svartliden deposit span 540–600°C at estimated pressures of 3–6 kbar. Lower to mid amphibolite facies metamorphic conditions are supported by the presence of the hydrothermal alteration assemblage quartz-diopside-andradite \pm wollastonite (Eilu et al. 1999) which is in agreement with regional metamorphic grades of supracrustal lithologies within the Bothian Basin (550–700°C at 3–5 kbar; Lundquist 1990).

The quartz mylonite contains very low concentrations of immobile and incompatible elements, suggesting that the original rock prior to deformation was directly precipitated from aqueous fluids, perhaps in an open extensional structure by localized fluid flow rather than by host-rock emplacement, whereas the ore formation mechanisms have to be further examined. The

timing of the mylonitisation relative to ore formation is most likely to be post-mineralization. This steeply dipping fault/shear zone is likely a second order structure splaying off the regional crustal scale “Gold Line” shear zone which acted as a conduit for deeply sourced, low salinity, metamorphic devolatilization fluids. The quartz mylonite is located in a stratigraphic interval of large rheological contrast between the BIF/meta-sediments and an amphibolite body and likely acted as a local conduit for hydrothermal fluid flow. In this scenario the banded-iron formation was a geochemical barrier, whose sulfidation lead to the precipitation of sulfides from aqueous fluid in iron-rich lithologies, thus destabilizing the ligands and resulting in gold precipitation. The sediments would have served as a suitable mechanical trap for mineralizing fluids. Löllingite-gold intergrowths are most likely relics of high-temperature (> 540°C) prograde transformation of gold-bearing arsenopyrite to pyrrhotite-löllingite-Au assemblage (Tomkins & Mavrogenes 2001). A possible origin for the sulfur and arsenic could be the presence of sulfidic-graphitic sediments (Tomkins et al. 2006) in the Bothnian Supergroup. High-grade metamorphism resulted in partial melting of sedimentary precursors and emplacement of syn- to early post-peak metamorphic S-type granite. The granite dikes seem to have intruded along pre-existing structures, in many cases along the same structure as the mineralization. There is strong evidence that this event remobilized gold mineralization based on timing and lithologic relationships between the mineralization and the granite dikes.

5 Conclusions

The Svartliden gold deposit is situated in a volcano-sedimentary sequence of the Paleoproterozoic Bothnian Basin and has undergone regional metamorphic and deformational overprint in lower to mid amphibolite facies during the Svecokarelian orogeny. The deposit is interpreted to be a BIF-hosted orogenic, lode-style gold deposit. The desulfidation of aqueous fluids and precipitation of auriferous mineralization occurred along an Fe-rich geochemical barrier facilitated by local structural complexities.

Acknowledgements

Dragon Mining Ltd. is acknowledged for funding the fluid inclusion study, radiometric dating and numerous theses and projects in this area. The authors also appreciate valuable inputs from David Dolejs.

References

- Allen RL, Lundström I, Ripa M, Simeonov A & Christofferson H (1996) Setting of Zn-Cu-Au-Ag massive sulfide deposits in the evolution and facies architecture of a 1.9 Ga marine volcanic arc, Skellefte district, Sweden. *Econ Geol* 91 (6):1022–1053.
- Andersson J (2012) The Svartliden Granite. Petrography, whole rock chemistry and stable isotope composition. Master thesis, Luleå University of Technology, pp 87.
- Bark G (2008) On the origin of the Fäboliden orogenic gold deposit, northern Sweden. Doctoral thesis, Luleå University of Technology, ISSN 1402-1544.
- Berglund A (2010) The Svartliden Gold Deposit – Ductile Deformation and Metamorphic Conditions. Master thesis, Uppsala University, ISSN 1650-6553.
- Bhatia MR & Crook KAW (1986) Trace element characteristic of greywackes and tectonic discrimination of sedimentary basins. *Contrib Min Petrol* 92:181–193.
- Broman C (2010) Fluid inclusion study of the shear zone hosted gold deposit at Svartliden, northern Sweden. An internal unpublished report of Dragon Mining Sweden AB.
- Claesson S & Lundqvist T (1995) Origins and ages of Proterozoic granitoids in the Bothnian Basin, central Sweden; isotopic and geochemical constraints. *Lithos* 36:115–140.
- Eilu PK, Mathinson CI, Groves DI & Allardyce WJ (1999) Atlas of alteration assemblages, styles and zoning in orogenic lode-gold deposits in a variety of host rock and metamorphic settings. The University of Western Australia 30, pp 50.
- Eklund D (2007) Mineralogy of the hypozonal Svartliden gold deposit, northern Sweden, with emphasis on the composition and paragenetic relations of electrum. Undergraduate thesis, Uppsala University, ISSN 1650-6553.
- Hanski E, Huhma H, Rastas P & Kamenetsky VS (2001) The Paleoproterozoic Komatiite-Picrite Association of Finnish Lapland. *J Petrol* 42 (5):855–876.
- Hastie AR, Kerr AC, Pearce JA & Mitchell SF (2007) Classification of altered volcanic island arc rocks using immobile trace elements: development of the Th Co discrimination diagram. *J Petrol* 48:2341–2357.
- Herron MM (1988) Geochemical classification of terrigenous sands and shales from core or log data. *J Sediment Petrol* 58:820–829.
- Kathol B & Wehred P (2005) Description of regional geological and geophysical maps of the Skellefte District and surrounding areas. Geological Survey of Sweden Ba57, ISSN 0373-2657.
- Kerr AC & Arndt NT (2001) A Note on the IUGS Reclassification of the High-Mg and Picritic volcanic rocks. *J Petrol* 42 (11):2169–2171.
- Le Bas MJ, Le Maitre RW, Streckeisen A & Zanettin B (1986) A chemical classification of volcanic rocks based on the total alkali-silica diagram. *J Petrol* 27:745–750.
- Lundqvist T (1987) Early Svecofennian stratigraphy of southern and central Norrland, Sweden, and the possible existence of an Archaean basement west of the Svecokarelidides. *Precambrian Res* 35:343–352.
- McDonough WF & Sun SS (1995) The composition of the Earth. *Chem Geol* 120:223–253.
- Mullen ED (1983) MnO/TiO₂/P₂O₅: a minor element discriminant for basaltic rocks of oceanic environments and its implications for petrogenesis. *Earth Planet Sc Lett* 62:53–62.
- Narayanaswami S, Ziauddin M & Ramachandra AV (1960) Structural control and localization of gold-bearing lodes, Kolar Gold Field, India. *Economic Geology* 55:1429–1459.
- Nironen M (1997) The Svecofennian Orogen: a tectonic model. *Precambrian Res* 86:21–44.
- Persson PO (2011) Dateringsresultat av granit från Svartliden, Naturhistoriska Riksmuseet, Unpublished internal report of Dragon Mining Sweden AB (in Swedish).
- Sciuba M (2013) Mineralogy and geochemistry of the banded iron-formation in Svartliden mine, Gold Line, Northern Sweden. Master thesis, Luleå University of Technology, pp 121.
- Schaubs PM & Wilson JL (2002) The relative controls of folding and faulting in controlling gold mineralization along the Deborah Anticline, Bendigo, Victoria, Australia. *Economic Geology* 97:351–370.
- Tomkins AG & Mavrogenes JA (2001) Redistribution of Gold within Arsenopyrite and Löllingite during Pro- and Retrograde Metamorphism: Application to Timing of Mineralization. *Econ Geol* 96:525–534.
- Tomkins AG, Frost BR & Pattison DRM (2006) Arsenopyrite melting during metamorphism of sulphide ore deposits. *Can Mineral* 44:1045–1062.

Fluid inclusion studies, and sulfur and oxygen isotope signatures at the Carvoaria Velha orogenic gold deposit, Quadrilátero Ferrífero, Brazil

Rosaline C Figueiredo e Silva, Yuri Ribeiro, Lydia M Lobato

Universidade Federal de Minas Gerais, CPMTIC-IGC-UFGM, 31270-901, Belo Horizonte, MG, Brazil

Steffen Hagemann, John Cliff

University of Western Australia, School of Earth and Environment, Centre of Exploration Targeting, M006, Crawley WA 6009, Australia

Abstract. The Córrego do Sítio lineament is a 16-km-long, NE-trending ductile shear zone, which controls 14 gold deposits, including Carvoaria Velha. The mineralization is hosted in Archean rocks of the Rio das Velhas greenstone belt, represented by carbonaceous phyllites and metagraywackes-metaturbidites, metamorphosed to greenschist facies. The main gold mineralization styles at the Carvoaria Velha deposit are quartz-carbonate-sulfide±sulfosalt veins of varied distribution, classified as: (V1) quartz-ankerite-pyrite-berthierite-gold veins, which are parallel to the main regional foliation; (V2) quartz-ankerite-pyrite veins, which are developed along crenulation cleavage, are extensional, and only locally contain gold; (V3) quartz-ankerite veins, which fill late fractures, mostly lacking sulfides and sulfosalts; and (V4) local extensional quartz-calcite veins hosted by metamorphosed mafic dikes and sills, with no preferential orientation. The most common ore minerals in all vein types are arsenopyrite, pyrite, berthierite, and pyrrhotite. Microthermometric data from fluid inclusions indicate the hydrothermal fluid evolved from (i) an early fluid, trapped in smoky quartz, with ~8.5 eq. wt% NaCl salinity, and a minimum trapping temperature of $280\pm 17^\circ\text{C}$, to (ii) a late fluid trapped in recrystallized quartz with ~4.6 eq. wt% NaCl salinity, and a minimum trapping temperature of $315\pm 33^\circ\text{C}$. Isotopic values of $\delta^{18}\text{O}_{\text{fluid}}$, $\Delta^{33}\text{S}$, and $\delta^{34}\text{S}$ suggest that the hydrothermal fluid responsible for the gold mineralization at the Carvoaria Velha deposit had a metamorphic origin, and interacted with metasedimentary rocks during its ascension. The addition of CH_4 during fluid-rock reactions may have caused a decrease in the f_{O_2} of the fluid, which as a consequence, destabilized gold-bearing sulfur complexes liberating S^{2-} for the formation of the Fe sulfides and sulfosalts, and resulting in gold precipitation.

Keywords. Orogenic gold, Quadrilátero Ferrífero, fluid inclusions, stable isotopes, Brazil

1 Introduction

The Quadrilátero Ferrífero (QF) region represents an important Brazilian metallogenic province located at the southern border of the São Francisco Craton. The 16-km-long, NE-trending Córrego do Sítio regional lineament is located in the northeastern part of the QF, near the town of Santa Bárbara, and is the location of 14 gold deposits and two prospects (Lima, 2012).

The Córrego do Sítio lineament was defined in 1981, and is comprised of a succession of metamorphosed, carbonaceous, turbiditic graywacke-siltstone-shale and slates of the Nova Lima Group, Rio

das Velhas Greenstone Belt. These rocks host lode-gold mineralization in and adjacent to quartz-carbonate-sulfide veins (Lima, 2012), with Cachorro Bravo, Laranjeiras, and Carvoaria Velha representing the main ore deposits. They are presently exploited by AngloGold Ashanti Brasil Mineração. This study focuses on the Carvoaria Velha deposit, encompassing petrographic analyses, in addition to fluid inclusion, oxygen isotope, and sulfur isotope studies in order to understand and characterize the hydrothermal fluids involved in the formation of the gold deposit.

2 Materials and Methods

Different mineralized and barren quartz-carbonate vein types from drill core FCS 926 were collected, and detailed petrographic mapping of fluid inclusion assemblages and types conducted. Fluid inclusion microthermometric studies used a fully automated Linkam THMSG600 heating and freezing stage with a TMS 93 temperature controller, and calculations of physico-chemical parameters used the MacFlinCor program. Raman spectroscopy was used to identify gases and fluids contained within the fluid inclusions-FIs that were obtained on a Jobin Yvon/Horiba LABRAM-HR 800 spectrographer equipped with a He-Ne laser (632.8 nm). In-situ oxygen and sulfur isotope ratios were determined using a Cameca IMS 1280 multi-collector ion microprobe located at the Centre for Microscopy, Characterisation and Analysis (CMCA), University of Western Australia.

3 Vein Classification

In all lithologies at the Carvoaria Velha deposit, 10-mm- to 6-m-thick veins are composed mainly of quartz and carbonate, which may contain ore minerals such as sulfides and sulfosalts.

The studied veins are classified, based on their structure and mineralogy, as types V1, V2, and V3, hosted in metasedimentary rocks, and V4, hosted in metamorphosed mafic dikes and sills (Ribeiro, 2013). The V1 type veins consist of quartz-ankerite-pyrite-berthierite-gold and are <6-m-thick. They are present as irregular lenses, which may be folded, boudinaged, and locally form pinch-and-swell structures (Fig. 1). They are typically discontinuous, parallel to the main regional foliation, sheared, and may contain gold. The V2 extensional veins comprise quartz-ankerite-pyrite,

are <3 m in width, develop along crenulation cleavage, and are typically barren. The V3 quartz-ankerite veinlets, <20-cm-wide, form continuous lenses, fill fractures, are locally brecciated, and are characterized by saccharoidal texture. They lack sulfides and sulfosalts. Quartz-calcite V4 veinlets, <15-cm-wide, are restricted to metamorphosed dikes and sills (Lima, 2012), appear as breccia or in lenticular form, and have no preferred orientation.

Microscopically, quartz (65-80% of total volume) and carbonates (5-20% of total volume) are the most abundant minerals in all veins. Two types of quartz include coarse-grained, smoky quartz (Qtz I), showing evidence of deformation, such as subgrain formation and undulose extinction, and granoblastic, fine-grained quartz (Qtz II), with straight extinction, rarely undulose, and a product of Qtz I recrystallization. Carbonates also form two groups comprising stained and twinned, coarse-grained crystals (Carb I), and fine-grained clear crystal aggregates (Carb II). Sulfides and sulfosalts are disseminated within all four vein types, forming fine to medium-grained aggregates, and constituting as much as 8% of the vein's total volume. The most abundant sulfides and sulfosalts are pyrite, chalcopyrite, arsenopyrite, pyrrotite, and berthierite. Stibnite, galena, boulangerite, ullmannite, tetraedrite, argentopentlandite, and cobaltite are rare and restricted to V1; these may overgrow the most abundant sulfides and sulfosalts, and are only identified via microprobe analyses.

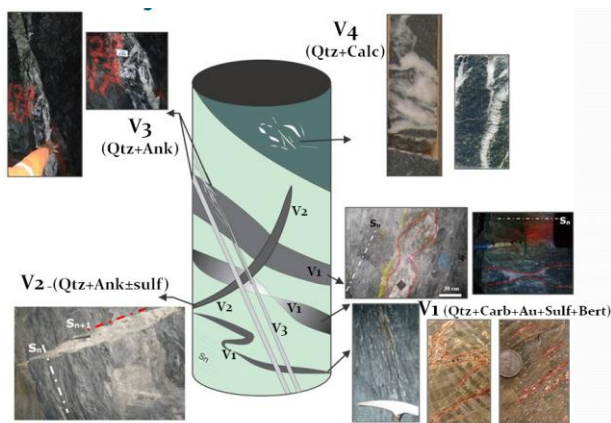


Figure 1. Schematic diagram illustrating different vein types at the Carvoaria Velha deposit, and photographs of examples from core and hand samples (Ribeiro (2013)). Veins types hosted in the metasedimentary rocks are: V1 – quartz-ankerite-sulfide-sulfosalt-gold, along main foliation; V2 – quartz-ankerite-pyrite, developed along crenulation cleavage; V3 – quartz-ankerite, tabular lenses filling fractures, locally brecciated; V4 veins restricted to metamorphosed mafic dikes and sills – quartz-calcite, brecciated and lenticular.

4 Geochemical studies

4.1 Fluid inclusions

The two main types of FI are type 1 pseudosecondary and secondary aqueous-carbonic $H_2O-CO_2\pm CH_4-NaCl$ inclusions, and type 2 pseudosecondary aqueous $H_2O\pm NaCl$ inclusions (Ribeiro, 2013). Type 1 inclusions occur in barren or mineralized quartz veins that are

hosted in metasedimentary rocks. Type 2 inclusions are restricted to veins hosted in the mafic dikes and sills. Type 1 can be divided into three fluid inclusion assemblages (FIA): Type 1a are pseudosecondary inclusions restricted to Qtz I, prismatic in shape (5 to 20 μm), and with constant liquid/gas ratio of $\sim 9:1$; Type 1b pseudosecondary inclusions are restricted to Qtz II, rounded and irregularly shaped (5 to 30 μm), and with liquid/gas ratios of 9:1; and type 1c are secondary, two-phase inclusions, form continuous trails throughout crystal edges, are oval and irregular in shape (4 to 40 μm), and have less variable liquid/gas ratios between 7:3 and 9:1. It is possible to observe necking down due to typical deformation of recrystallized quartz.

Type 1 inclusions show low temperatures of initial melting, between -48 and -36 $^{\circ}C$, with an average of $-43^{\circ}C$, indicating the presence of other cation complexes, such as Fe^{2+} and Mg^{2+} , in addition to Na^+ (Borisenko, 1977 in Goldstein and Reynolds, 1994). Clathrate melting temperatures range from 2 to $9^{\circ}C$, with an average of $4.6^{\circ}C$ for type 1a FIA, $6.6^{\circ}C$ for type 1b FIA, and $6.0^{\circ}C$ for type 1c FIA. Values of CO_2 melting temperature range from $-65.3^{\circ}C$ to $-57.0^{\circ}C$, suggesting the presence of other volatile species in addition to CO_2 , as is also indicated by Raman microscopy. Type 2 inclusions have initial melting temperatures from -55 to $-45^{\circ}C$, again indicating the presence of other cation complexes in addition to Na^+ . Final ice melting temperatures are lower than those of type 1, ranging from -17.0 to $-7.8^{\circ}C$.

All type 1 inclusions show an increase of size in the carbonic vapor phase at temperatures above $250^{\circ}C$, but the majority decrepitate before total homogenization, with decrepitation temperatures between 260 and $340^{\circ}C$, and averages for type 1a, 1b, and 1c FIA of $283^{\circ}C$, $315^{\circ}C$, and $285^{\circ}C$, respectively (Figs. 2A-C). Only a few type 1b FIA exhibited total homogenization to vapor, with a temperature range of 420 to $460^{\circ}C$. Type 2 inclusions show homogenization into the liquid at temperatures between 174 and $215^{\circ}C$ (Fig. 2D).

Type 1 inclusions have variable salinities, with averages of 8.2 eq. wt% NaCl for type 1a FIA, 3.7 eq. wt% NaCl for type 1b FIA, and 4.6 eq. wt% NaCl for type 1c FIA (Figs. 2A-C). Type 2 FIA are the most saline, with values higher than 11.5 eq. wt% NaCl, and an average of 14.9 eq. wt% NaCl (Fig. 2D). Type 1 inclusions are H_2O -rich containing between 89 to 98 mol% H_2O . The carbonic phase in FIA types 1a, 1b, and 1c, when considering that CO_2 is the predominant phase, has a similar average value of 3.1 mol% for the three FIA, reaching maximum values of 6.0, 7.4, and 6.1 mol%, respectively. Concentrations of CH_4 are more variable, with type 1a containing <1.8 mol%, type 1b <3.2 mol%, and type 1c <2.3 mol%.

4.2 Oxygen and sulfur isotopes

Samples for oxygen isotopes analyses were selected from V1, V2, V3, and V4 vein types. A total of 105 *in-situ* measurements were performed on Qtz I and Qtz II crystals. Measured values of $\delta^{18}O$ are presented in Table 1 and Fig. 3. The calculated fluid values are similar for V1, V2, and V3 vein types (Fig. 3). In the case of V4

vein type, hosted in the mafic dikes and sills, values are lower (Fig. 3).

$\geq 315 \pm 33^\circ\text{C}$), and containing some 1b type FIA reaching $\sim 450^\circ\text{C}$ (Fig. 2B).

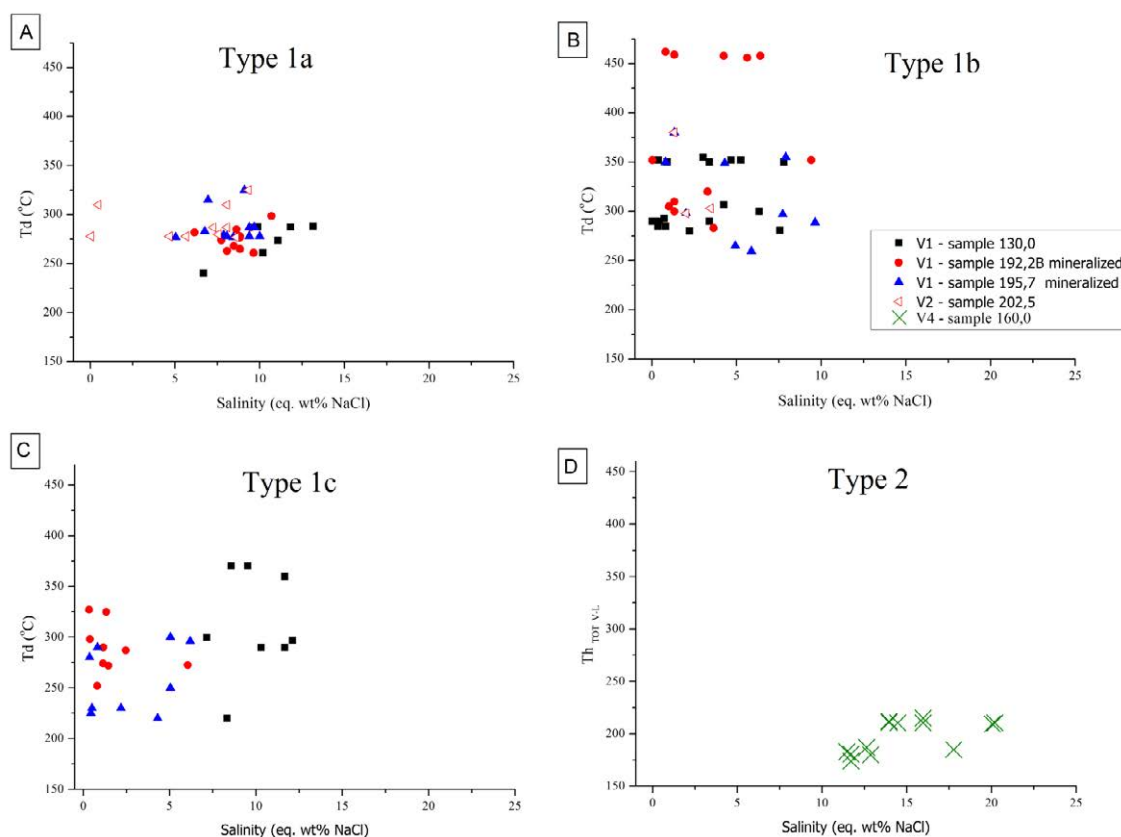


Figure 2. Diagram showing salinity versus decrepitation temperature (Td) for inclusions A) type 1a; B) type 1b; C) type 1c; and salinity versus temperature of total homogenization (Thtot L-V) for D) type 2 inclusions.

Table 1. Oxygen isotope values for quartz from different vein types, and sulfur isotope values of chalcopyrite, pyrite, and pyrrhotite from the Carvoaria Velha deposit veins, as obtained using ionprobe SIMS 1280.

In-situ analyses of sulfur isotopic composition ($\delta^{34}\text{S}$) were performed on eight sampled V1 and V4 veins, and on sulfides from along the margins of V2 and V3 veins. A total of 71 measurements were made on of pyrite, chalcopyrite, and pyrrhotite (Table 1 and Fig. 4) crystals. Mass independent $\Delta^{33}\text{S}$ for sulfides were calculated using equation of Farquar et al. (2002) (Fig. 4).

5 Discussions and Conclusions

5.1 Fluid inclusions

The fluid inclusion results suggest that the Carvoaria Velha gold deposit was deposited from aqueous-carbonic, low- to medium-salinity (<8.5 wt% NaCl) mineralizing fluids, at a minimum temperature of $280 \pm 17^\circ\text{C}$, which is typical of metamorphic fluids suggested to form orogenic gold deposits (e.g., Groves et al., 1998). The hydrothermal fluid data are interpreted to reflect at least two paragenetic stages. First, an early fluid stage, represented by pseudosecondary type 1a FIA was trapped in smoky quartz Qtz I (~ 8.5 eq. wt% NaCl; $\text{CO}_2:\text{CH}_4$ of 5.4; $T_{\text{trap}} \geq 280 \pm 17^\circ\text{C}$). A late-stage fluid, represented by pseudosecondary type 1b FIA was trapped in recrystallized quartz Qtz II, and by secondary type 1c FIA along trails crossing both Qtz I and Qtz II crystals (~ 4.6 eq. wt% NaCl; $\text{CO}_2:\text{CH}_4$ of 4.9; T_{trap}

Vein type	Sample	$\delta^{18}\text{O}$ (‰ SMOW)			Sulfide	mass independent: $^{33}\text{S}/^{32}\text{S}$		
		max	min	average		max	min	average
V1	84.40	+18.0	+15.9	+16.9	Py	+3.9	+3.5	+3.7
	95.00	+16.2	+15.6	+15.9	Py	+5.1	–	–
		–	–	–	Cpy	+3.6	–	–
	130.80	+16.1	+15.5	+15.8	–	–	–	–
	192.20B	+16.2	+15.7	+16.0	–	–	–	–
195.70	+17.3	+16.6	+17.0	Py	+4.7	+4.4	+4.6	
V2	202.50	–	–	–	Py	+4.0	+3.3	+3.6
	202.50	–	–	–	Po	+2.0	+0.7	+1.5
	202.50	+16.9	+15.6	+16.2	Cpy	+3.7	+3.2	+3.4
V3	139.50	+16.4	+14.5	+15.7	Py	+6.5	+2.7	+5.7
	169.63	+19.6	+14.5	+15.8	–	–	–	–
V4	150.00	+15.9	+14.5	+15.1	Py	+1.0	+0.7	+0.9

It is suggested that type 1 inclusions represent the mineralizing fluid trapped in V1 veins during a first deformational event. The presence of CH_4 in type 1 inclusions from V1 and V2 veins may reflect fluid interaction with Córrego do Sítio and Santa Quitéria carbonaceous metasedimentary wallrocks.

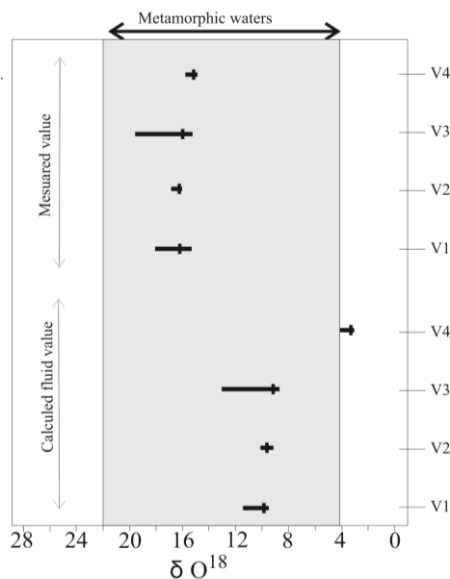


Figure 3. Diagram showing $\delta^{18}\text{O}_{\text{qtz}}$ and $\delta^{18}\text{O}_{\text{fluid}}$ for V1, V2, V3, and V4 vein types; $\delta^{18}\text{O}_{\text{fluid}}$ calculated according to equations of Matsuhisa et al. (1979) for quartz formed from 196 to 318°C.

5.2 Oxygen and sulfur isotopes

The $\delta^{18}\text{O}_{\text{fluid}}$ values calculated for V1, V2, and V3 vein quartz coincide with those typically found in orogenic gold deposits worldwide, in the +4 to +15‰ range (Ridley and Diamond, 2000), indicating a mineralizing fluid of metamorphic origin (Taylor, 1974). The V4 vein quartz exhibits the lightest values of ~+2‰ (Fig. 3), and these are slightly lighter than the range for magmatic fluids (4.0-8.0 per mil; Taylor, 1974), suggesting the possible involvement of meteoric waters, with fluid flow restricted to mafic dike and sill margins. The dike margins may have acted as pathways for the circulation of surface waters, and therefore diluted values of any magmatic waters to slightly lighter isotopic signatures.

The $\delta^{34}\text{S}$ values for sulfides have a significant range between -2.9 to +6.1‰, and this large range of values overlaps a number of common sulfur reservoirs, including mantle-derived magmatic rocks (Hoefs, 2007), making it difficult to constrain the original composition of the sulfur source. According to Farquhar et al. (2002), this relatively wide range of $\delta^{34}\text{S}$ may be related to recycling of sedimentary materials. In the case of pyrite from V4 veins hosted in the mafic dikes and sills, isotopic values display relatively light values of +0.9‰, indicating a magmatic contribution (Fig. 3). However, as pointed out for $\delta^{18}\text{O}_{\text{fluid}}$ data, an interaction of meteoric waters must be considered.

Results of mass independent $\Delta^{33}\text{S}$ for sulfides from the V1 veins hosted in metasedimentary rocks vary from +0.3 to +3.5‰ (Fig. 4). The positive $\Delta^{33}\text{S}$ values suggest sedimentary sulfur that was probably incorporated from the crust (Farquhar et al., 2002). On the other hand, sulfides from V4 veins, with $\Delta^{33}\text{S}$ in the range of 0.3 to 0.5‰, indicate sulfur with a mantle derivation (Fig. 4) (Farquhar et al., 2002). The incorporation of $\Delta^{33}\text{S}$ in sulfides from mineralized V1 veins further suggests that

the hydrothermal fluid responsible for gold mineralization at the Carvoaria Velha deposit had interacted with the host metasedimentary rock sequences during its ascent.

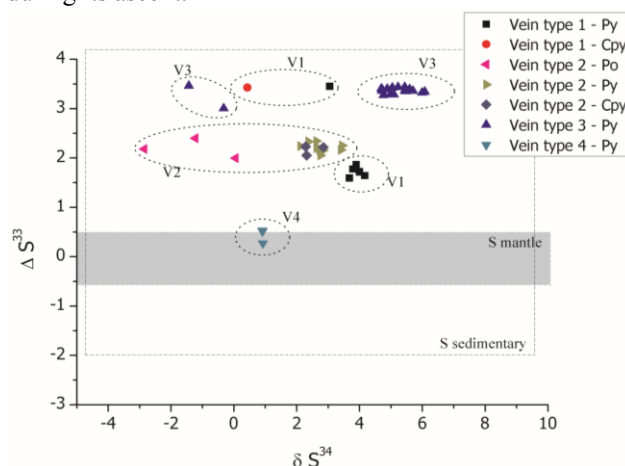


Figure 4. Plot of $\delta^{34}\text{S}$ vs. $\Delta^{33}\text{S}$ data. $\Delta^{33}\text{S}$ values are calculated used $\Delta^{33}\text{S} = \delta^{33}\text{S} - 1000 \times [(1 + \delta^{34}\text{S}/1000)0.515 - 1]$ (Farquhar et al., 2002).

Acknowledgements

This research is the result of the M.Sc. by Y. Ribeiro at UFMG, which was fully financed by CNPq, Vale, and FAPEMIG. The student's scholarship was granted by CAPES. We wish to thank Anglogold Ashanti for providing logistical and technical support. Thanks are also due to UFMG and UWA for technical assistance, and geologists LC Lima and MA Sequetto.

References

- Goldstein RH, Reynolds TJ (1994) Systematics of fluid inclusions in diagenetic minerals. SEPM Short Course 31, Tulsa, 199 pp.
- Groves DI, Goldfarb RJ, Gebre-Mariam M, Hagemann SG, Robert, F (1998) Orogenic gold deposits: a proposed classification in the context of their crustal distribution and relationship to other gold deposit types. *Ore Geol. Rev.* 13:7-27
- Farquhar J, Wing BA, McKeegan KD, Harris JW, Cartigny P, and Thiemens MH (2002) Mass-independent sulfur of inclusions in diamond and sulfur recycling on early Earth. *Science* 298: 2369-2372
- Hoefs J (2007) Stable isotope geochemistry, (5th edition): New York, Springer-Verlag, 244p.
- Lima LC (2012) Depósito lode Au-As-Sb Laranjeiras, em metaturbitos do Grupo Nova Lima, Quadrilátero Ferrífero, Minas Gerais. MSc thesis, Instituto Geociências, Universidade Federal de Minas Gerais. Belo Horizonte, Brasil, 306 p.
- Matsuhisa Y, Goldsmith JR, and Clayton RN (1979) Oxygen isotopic fractionation in the system quartz-albite-anorthite-water. *Geochim Cosmochim Acta* 43(7):1131-1140
- Ribeiro Y (2013) Estudo de inclusões fluidas e isótopos de oxigênio e enxofre em veios de quartzo-carbonato-sulfetos do depósito Carvoaria Velha, lineamento aurífero Córrego do Sítio, QF, MG, Brasil. Msc Thesis, UFMG, 103p.
- Ridley JR, Diamond LW (2000) Chapter 4 - Fluid Chemistry of Orogenic Lode Gold Deposits and Implications for Genetic Models, *SEG Reviews* 13:141-162
- Taylor HP, Jr (1974) The application of oxygen and hydrogen isotope studies to problems of hydrothermal alteration and ore deposition. *Econ Geol* 69: 843-883

The orogenic and not so orogenic gold deposits of the Agnew Gold Camp (Yilgarn Craton, Western Australia)

Nicolas Thébaud, John Miller, Campbell McCuaig

Centre for Exploration Targeting, Robert Street Building, M006, The University of Western Australia, 35 Stirling Hwy, Crawley, WA, 6009, Australia

Louise Fisher, Iris Sonntag

2 CSIRO Australian Resources Research Center 26 Dick Perry Ave., Kensington 6151 Western Australia

Abstract. Archean gold deposits are commonly considered to be orogenic. However, as for Phanerozoic examples, orogenic deposits often form in close proximity to and coeval with intrusion-related gold systems. In the Agnew Gold Camp (Yilgarn Craton, Western Australia), a recent field investigation delineated the structural framework and mineral paragenesis associated with mineralisation in four individual deposits, namely the Songvang, Crusader, Waroonga and New Holland–Genesis deposits. Results from this study indicate that mineralisation in the Agnew Gold Camp was structurally controlled by the formation of the Lawlers Antiform during regional E–W contraction. Structural and paragenetic relationships, combined with geochronological data compilation, indicate that mineralisation has developed during a two-stage process involving contrasting fluid sources. The initial event is related to the onset of folding and presents the characteristics of magmatic intrusion-related mineralisation. The second mineralisation event is more akin to typical Archean orogenic-like gold mineralisation, and has developed at a late stage of the Lawlers Antiform formation. The spatial and temporal cohabitation of intrusion-related and orogenic-style deposits, such as the one preserved in the Agnew Gold Camp, holds significant implications for the understanding of Archean gold mineral systems and for the delineation of future exploration strategies.

Keywords. Yilgarn Craton, orogenic gold, protracted mineralisation, Agnew Gold Camp

1 Introduction

The Agnew Gold Camp sits in the southwest corner of the Agnew–Wiluna belt in the Eastern Goldfields Superterrane (Fig. 1), and consists of a moderately tightly folded greenstone belt bound to the west by the Waroonga Shear Zone. This shear zone is a 2 km wide, dextral strike-slip zone of intense ductile deformation separating the greenstones from a granite-gneiss terrane (Platt et al. 1978). Multiple structural models have been proposed for the Agnew Gold Camp (Platt 1978; Beardsmore 2002; Blewett and Czarnota 2007; Duuring et al. 2012) and there is currently some variation in the deformation numbers applied to the deformation event sequence proposed. Regionally, the most widely used nomenclature is the D1 to D4 event history proposed by Swager (1997). However, recent structural studies have proposed up to 12 local deformation events (Duuring et al. 2012). Regardless of the structural scheme proposed, the bulk of the Agnew Gold Camp architecture appears to be related to a regional E–W contraction (D2 after

Swager 1997). The resulting folding event led to the formation of the Lawlers Antiform plunging 50–60° to the north in the core of the Agnew Gold Camp. The Lawlers Antiform is interpreted to have developed during a progressive deformation event leading to reverse shearing, flexural slip on fold limbs and the development of shear zones axial planar to the fold hinges (Platt et al. 1978). On the western limb of the Lawlers Antiform, the contact with the metasediments of the Scotty Creek formation is faulted along the NNE-trending Emu Shear Zone, which hosts or is close to the majority of existing high-grade Au deposits (Aoukar and Whelan 1990). These include from north to south, the New Holland–Genesis, the Waroonga, the Redeemer, the Crusader and the Songvang deposits. Mineralisation in each of these deposits is associated with vastly different alteration styles including magnetite-rich quartz and sulphide-poor Au mineralisation at Crusader, a gold and silver-rich system with biotite-fluorite-amphibole-chalcocopyrite at Songvang and quartz-arsenopyrite-pyrite-biotite-amphibole in the New Holland–Genesis, Waroonga and Redeemer deposits. Determining whether such a variety in alteration reflects the onset of a single mineralisation event, or alternatively is caused by distinct stages of gold mineralisation occurring at different times, is critical to understanding the Agnew Gold Camp mineral system.

This paper presents the results of a field based structural investigation of each individual deposit with the overall objective of defining a revised camp-scale structural framework to the mineralisation. The results of this study suggest that the wide variety of mineralisation expressed in the Agnew Gold Camp reflects in part different mineralisation events that punctuated the progressive formation of the Lawlers Antiform. Structural and mineralogical observations, together with newly acquired U–Pb SHRIMP geochronological constraints, suggest that mineralisation developed during two distinct periods at c. 2662 Ma and c. 2630–2640 Ma.

2 Regional geology

The lower lithostratigraphic unit exposed at the base of the supracrustal sequence comprises a ~5 km thick package of tholeiitic basalt, high-Mg basalt, gabbro, komatiite, differentiated gabbro–pyroxenite–peridotite sills, and minor interflow sedimentary units (Platt et al. 1978). Stratigraphically, this lower section has been subdivided from bottom to top into the Lawlers Basalt, the Agnew Komatiite, the Redeemer Basalt and the Vivien Dolerite (Squire et al. 2010). One interflow

sediment unit located above the Agnew Komatiitic unit, but below the Vivien Dolerite, returned a maximum deposition age of 2692 ± 3 Ma (Dunphy et al. 2003) suggesting that the lower package is akin to the typical Kalgoorlie stratigraphic sequence (Squire et al. 2010).

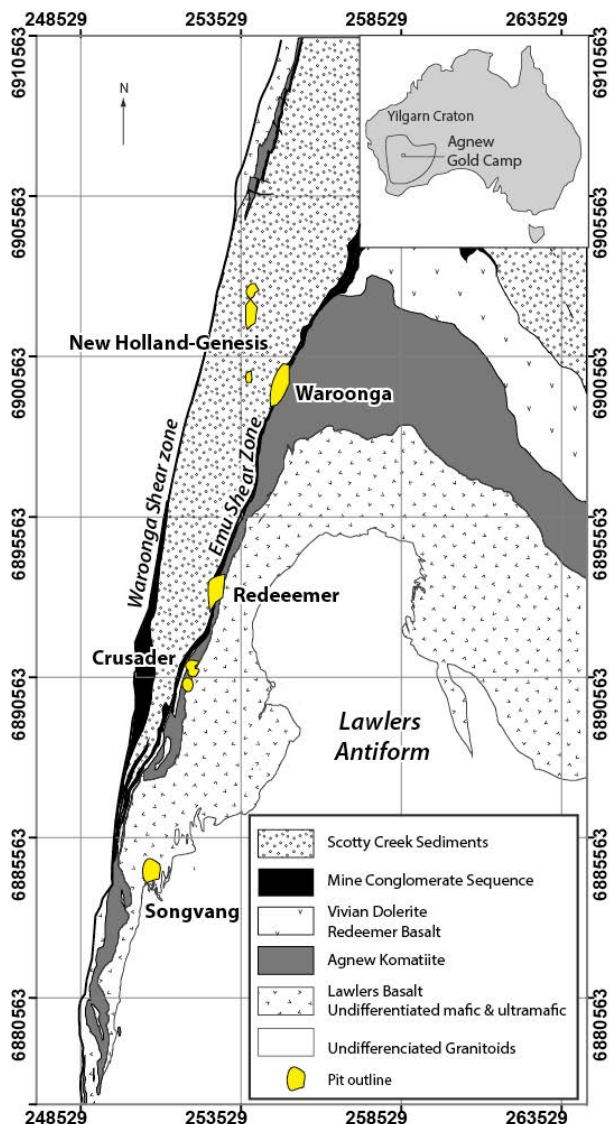


Figure 1. Simplified geological map of the Agnew gold camp.

The dominantly mafic-ultramafic rock sequence is unconformably overlain by the Scotty Creek sedimentary formation (Squire et al. 2010). At the base of the Scotty Creek formation, a polymictic conglomerate, locally termed the Mine Conglomerate Sequence, is composed of rounded pebbles of komatiite, basalt, and tonalite. Higher up the sequence, the basal conglomerate grades into cross-bedded quartzo-feldspathic sandstone. Coarse beds from the Scotty Creek sequence near the New Holland-Genesis deposit host detrital zircons that provided a maximum depositional age for the sandstone of 2664 ± 5 Ma, with an inherited zircon population ages of 2.70 to 2.69 Ga and 2.82 to 2.81 Ga (SHRIMP U-Pb on zircon (Dunphy et al. 2003). Granitoids, including the 2680 ± 17 Ma “Lawlers tonalite” (SHRIMP U-Pb on zircon, Thébaud unpublished 2012), intrude the hinge of the Lawlers antiform. Later, ca. 2665 ± 4 Ma, monzogranite and leucogranite suites intrude the Lawlers

tonalite (SHRIMP U-Pb on zircon, Champion unpublished 2003). The Waroonga gneiss, separated from the Scotty Creek Sediments by the Waroonga Shear Zone, is mainly tonalitic in composition and is intruded by titanite-biotite granodiorite dated at 2655 ± 4 Ma (SHRIMP U-Pb on zircon; Fletcher et al. 2001).

3 Structural framework to the mineralisation

In the following section, structural observations from four of the key deposits from the Agnew Gold Camp are summarised.

3.1 Songvang

Songvang is the southernmost deposit of the Agnew Gold Camp. It is located at the contact between a granitic to tonalitic pluton and the basaltic supracrustal cover (Fig. 1). Structural observations indicate that two main shear zones that are both localised on, and partially crosscutting, the margins of the tonalitic intrusion locally control the mineralisation. The larger structure is well exposed along the western wall whereas the second and less prominent structure lies on the eastern side of the Songvang pit. Both shear zones converge, the western shear zone dips steeply to the east, and the eastern shear zone dips $30\text{--}40^\circ$ to the west. Sub-horizontal stretching lineations indicate strike-slip movement, however, locally preserved reverse movement may suggest a prolonged reactivation history. Cryptic kinematic indicators on the eastern shear zone indicate dextral shearing associated to ENE-WSW shortening. The Songvang gold deposit sits within the strongly sheared mafic and tonalitic rocks and is associated with enrichment in Ag, Cu, W, As, Sn and Bi (Fisher et al. 2011). The ore-related mineral assemblage consists of biotite + quartz + chlorite + actinolite + carbonate + titanite + fluorite + pyrite and chalcopyrite as sulphide phases. The gold-related alteration assemblage displays a strong preferential orientation suggesting that mineralisation developed early to syn-shearing. U-Pb dating of hydrothermal titanites returned an age of 2662 ± 7 Ma (Thébaud unpublished 2012).

3.2 Crusader

The Crusader Complex is found at the contact between the Lawlers Basalt and Agnew Ultramafics (Fig. 1). The stratigraphic contact between the mafic and ultramafic unit is variably dipping from 70° W to steeply E. The main planar fabric is well preserved in the mafic unit and strikes N-S, dipping 80° to the W. A strong mineral lineation defined by elongated amphiboles in the mafic unit plunges shallowly ($\sim 25^\circ$) to the north. Ore shoots form narrow oblique pipe-like bodies parallel to the shallow north plunge of parasitic folds, the mineral lineation and to the stratigraphic-axial planar cleavage intersection (McCuaig et al. 2003 unpublished). Mineralisation is interpreted to have occurred during the onset of the Lawlers Antiform formation with parasitic folding, developed within local ENE-WSW shortening, controlling the lode geometry. Au mineralisation has an

unusual amphibole-magnetite-epidote-dominated hydrothermal alteration assemblage, and is variably associated with scheelite, Bi-tellurides and minor chalcopyrite. A set of late- to post-mineralisation shear zones transects the foliation and the stratigraphic contact. Steeply dipping to the east, these shear zones are associated with coarse decussate amphibole that obliterates the structural fabric making it difficult to establish the kinematics. However, local pull-apart quartz veins and locally preserved S-C fabrics are consistent with oblique normal-sinistral sense of shearing linked to NW-SE shortening.

3.3 Waroonga

The Waroonga deposit lies directly to the west of the old Agnew town-site on the western limb of the Lawlers Antiform. Mineralised rocks at Waroonga occur as distinct ore shoots termed the Main lode, the Kim Lode and the Rajah Lode which are located at or near the contact between the Scotty Creek Sediments and the Mine Conglomerate Sequence that dip $\sim 60^\circ$ to the WNW. Examination of the lodes shows that two distinct phases of mineralisation occurred. Early quartz lodes formed at the intersection of the sandstone-conglomerate stratigraphic contact and north trending discrete sinistral-normal shear zones creating the northerly plunge ($\sim 50^\circ$ N) of the Kim and Main Lode. This stage of mineralisation is characterised by variably deformed laminated quartz veins and breccia with a link to NW-SE shortening. Late mineralisation clearly overprints the early quartz lodes and comprises relatively undeformed flat tension veins locally forming en-echelon vein sets. Shallowly dipping easterly and westerly conjugated mineralised vein sets imply reverse-dextral sense of shearing within a local ENE-WSW shortening event at the time of mineralisation. Both early and late mineralisation stages at Waroonga are characterised by quartz + calcite + actinolite + biotite with arsenopyrite >> chalcopyrite + galena as sulphide phases and associated with enrichment in Ag, As, W, Sn and Bi. This alteration assemblage similarity suggests that both mineralisation stages were intimately related. The obliteration of all early fabrics by the alteration mineral assemblage suggests that mineralisation developed syn- to late-deformation.

3.4 New Holland-Genesis

The New Holland-Genesis deposit is hosted by the Scotty Creek Sediments located directly west of the Waroonga deposit (Fig. 1). The deposit lies within a coarse sandstone unit that has a sharp contact with a fine-grained siltstone on the eastern footwall. The mineralised coarse sandstone fines gradually upward into the fine-grained hanging wall sediments (Beardsmore 2002). Similar to the Waroonga deposit, detailed mapping of the pit and underground faces suggests two phases of mineralisation. The first phase is associated with a N-trending sinistral normal shear zone related to NW-SE shortening. Boudinage of these early-mineralised veins suggest an early to syn-deformation emplacement. The second, and main mineralisation

event is characterised by well-developed conjugate sets of en-echelon veins and conjugated thrusts related to ENE-WSW shortening. The coarser sandstone lenses within the stratigraphy package exerted a strong rheological control on vein development and kinematic analysis on thrusts and vein sets points to dextral-reverse movement. The rather undeformed nature of the veins and thrust suggests a late emplacement compared to the earlier mineralisation event. However, similar to Waroonga, both mineralisation stages display a unique alteration mineral assemblage which consists of quartz + calcite + actinolite + biotite + albite with arsenopyrite >> chalcopyrite + galena as sulphide phases.

4 Discussion

Gold mineralisation developed in the Agnew Gold Camp during the main folding event leading to the formation of the Lawlers antiform (D4 and D5 in Blewett et al. 2010 and D2 and D3 in Swager 1997). The compilation of the data collected suggests that mineralisation took place during two distinct events. The early relative timing and ductile character of the mineralisation in the Songvang and Crusader deposits suggests their development at an early stage of the folding of the belt. Songvang has developed along a conjugate set of N-trending shear zones accommodating the folding, whereas Crusader formed in response to the intersection between the axial planar cleavage and the flexural slip of the mafic-ultramafic contact. Atypical mineral assemblages documented at both Songvang and Crusader have been proposed to represent possible felsic intrusive-related hydrothermal mineralisation, rather than typical "orogenic-style" Au mineralisation and recent $\delta^{18}\text{O}$ and $\delta^{13}\text{C}$ data acquired on Songvang suggest a magmatic fluid origin (Fisher et al. 2011). At Songvang, U-Pb dating of hydrothermal titanites returned an age of 2662 ± 7 Ma, coeval with the emplacement of monzogranite and leucogranite plutons at c. 2665 provide evidence for coeval mineralisation and magmatism.

In contrast to this initial stage of mineralisation, both Waroonga and New Holland-Genesis systems appear to have developed during a second mineralisation event. This second mineralisation event is interpreted to have formed at a later stage of the Lawlers Antiform formation and presents characteristics typical to vein-hosted orogenic lode-gold deposits, as defined by Groves et al. (1998). Detailed structural observations indicate that this second mineralisation event developed via a two-stage deformation process with distinct kinematics. However, the homogeneous alteration mineral assemblage documented suggests a homogeneous fluid source throughout, which may suggest a close temporal association. Stage one of this second mineralisation event is characterised by the development of oblique sinistral shearing axial planar to the main fold geometry compatible with NW-SE local compression. The intersection of the faults with the stratigraphy provided the required permeability for mineralising fluids. This stage was followed by a rotation of the local stress field or "stress switch" to ENE-WSW contraction, which generated en-echelon vein sets and oblique reverse

thrusts, observed in the New Holland–Genesis and Waroonga systems. Geochronological constraints from the nearby Redeemer deposit, which presents some structural similarity to the Waroonga system, returned an age of 2636 ± 8 Ma (Re–Os Molybdenite Colgan writ. comm. 2002).

5 Conclusion

Mineralisation in the Agnew Gold Camp appears to have taken place during two distinct events closely related to the late-tectonic evolution of the Yilgarn Craton. The initial event presents the characteristics of magmatic intrusion-related mineralisation whereas the second event is akin to orogenic-like gold mineralisation. The temporal overlap between gold mineralization and the emplacement granitoids has been widely recognised in Archean terrane (i.e. Robert et al. 2005). Given the evidence for multiple gold mineralizing events such as in the Agnew Gold Camp, it is apparent that, for most of the Yilgarn Craton, no single mineralisation event can explain the formation of all gold deposits.

Although it may be virtually impossible to separate orogenic and magmatic processes because they overlap in space and time, the recognition and detailed characterisation of the various mineralisation styles as encountered in the Agnew Gold Camp provides further evidences for the progressive formation of gold deposits. This progressive mineralisation history implies the superimposition of distinctive processes during the late geodynamic evolution of the terrane. The early development of intrusion-related deposits at mid-crustal level stresses the importance of magmatism during the onset of the regional contraction and prior to the widespread development of syn- to late-orogenic gold deposits. The understanding of these processes, and documentation of the associated architecture, is not only fundamental for the overall understanding gold formation in Archean terrane but also for the delineation of future exploration strategies.

Acknowledgements

Financial support for this study was provided by Goldfields Agnew Mine, and the authors would like to acknowledge Ian Pegg, Peter Johansen, Steve Woods, Janet Tunjic, Marco Licht for their ongoing assistance and input to this study. The authors would like to

acknowledge Barrick Gold and specifically Susan Murray for providing site to the New Holland–Genesis mine.

References

- Aoukar N, Whelan P (1990) Emu Gold Deposit, Agnew In: Hughes FE (ed) *Geology of the Mineral Deposits of Australia & Papua New Guinea*. AusIMM Monograph, Melbourne, pp 323–329
- Beardsmore T (2002) *The Geology, Tectonic Evolution and gold mineralisation of the Lawlers region: a Synopsis of present knowledge*. pp 291
- Blewett RS, Squire R, Miller JM, Henson PA, Champion DC (2010) Architecture and geodynamic evolution of the St Ives Goldfield, eastern Yilgarn Craton, Western Australia. *Precam Res* 183:275–291
- Dunphy JM, Fletcher IR, Cassidy KF, Champion DC (2003) *Compilation of SHRIMP U–Pb geochronology data, Yilgarn Craton, Western Australia, 2001–2002* Geoscience Australia Record. pp 139
- Duuring P, Bleeker W, Beresford SW, Fiorentini ML, Rosengren NM (2012) Structural evolution of the Agnew–Wiluna greenstone belt, Eastern Yilgarn Craton an implication for komatiite-hosted Ni sulphide exploration. *Aust J Earth Sci* 59:765–791
- Fisher L, Sonntag I, Barnes SJ, Cleverley J, Hough R (2011) *Integrated 3D Geochemistry and Ore Characterisation at the Agnew Gold Mine*. CSIRO, Perth
- Fletcher I, Dunphy J, Cassidy K, Champion C (2001) *Compilation of SHRIMP U–Pb geochronology data, Yilgarn Craton, Western Australia*. 2000–01
- Groves DI, Goldfarb RJ, Gebremariam M, Hagemann SG, Robert F (1998) *Orogenic Gold Deposits – a Proposed Classification In the Context Of Their Crustal Distribution and Relationship to Other Gold Deposit Types*. *Ore Geol Rev* 13:7–27
- Platt JP, Allchurch PD, Rutland RWR (1978) *Archaean tectonics in the Agnew supracrustal belt, Western Australia*. *Precam Res* 7:3–30
- Robert F, Poulsen K, Cassidy K, Hodgson C (2005) *Gold Metallogeny of the Superior and Yilgarn Cratons*. *Econ Geol 100th Anniversary Volume*:1001–1033
- Squire RJ, Allen CM, Cas RAF, Campbell IH, Blewett RS, Nemchin AA (2010) Two cycles of voluminous pyroclastic volcanism and sedimentation related to episodic granite emplacement during the late Archean: Eastern Yilgarn Craton, Western Australia. *Precam Res* 183:251–274
- Swager CP (1997) *Tectono-Stratigraphy Of Late Archean Greenstone Terranes In The Southern Eastern Goldfields, Western Australia*. *Precam Res* 83:11–42

A model for the Shuangwang hydrothermal breccia gold deposit, Taibai County, Shaanxi Province, China

Wang Jianping, Liu Jiajun, Qi Kaijing, Liu Zhenjiang, Wang Kexing, Liu Bizheng, Zeng Xiangtao, Wang Huan
State Key Laboratory of Geological Processes and Mineral Resources, China University of Geosciences, Beijing, China

Abstract: The Shuangwang gold deposit is a large gold deposit in the Fenxian-Taibai fore-arc basin and its reserves are more than 70t. The gold deposit is characterized by its ferrodolomite-cemented hydrothermal breccia ores. All orebodies occur in a NW-trending breccia belt, which is conformable with the regional Devonian Xinghongpu Formation. Four specific hydrothermal systems have been identified through detailed field investigations. Combining this with geochemical study, a three-step ore-forming model is suggested. The Devonian Xinghongpu sedimentary rocks have a high background in gold and can serve as the source for gold mineralization. Linear folds and faults formed during Triassic orogenic processes, and provided the subsequent pathways for ore-forming fluids and traps for gold ores. Post-orogenic magmatic hydrothermal activity and metamorphic events both were important for ore formation. High-pressure conditions during ore-fluid migration led to hydrofracturing and formation of breccia-style ores.

Key words: Shuangwang gold deposit, hydrothermal breccia, ore-forming model, Shaanxi

1 Introduction

The western Qinling belt is emerging as one of the most important gold regions in China. Almost all gold deposits in the belt can be classified into two distinct genetic types: orogenic gold lodes hosted in middle to late Paleozoic (mainly Devonian) clastic metasedimentary rocks and Carlin-like deposits hosted in unmetamorphosed to weakly metamorphosed, mainly Middle to Late Triassic clastic and carbonate rocks (Mao et al. 2002). The Shuangwang gold deposit, hosted in a hydrothermal breccia, is one of the larger gold deposits (>70t) in the belt. A great deal of research has been carried out since its discovery in 1976 (Shi et al. 1989, Zhang et al. 2004, Zeng et al. 2005), but its genesis is still controversial. Li et al. (1989) classified it as a Carlin-type gold deposit, whereas Zhang et al. (2004), Mao et al. (2002), and Zhou et al. (2002) argue that it is an orogenic gold deposit formed in a collisional environment. We provide geological and geochemical evidence that this is a unique style of orogenic gold deposit and put forward a three-step ore-forming model for the Shuangwang breccia-type gold deposit.

2 Geological setting

The Shuangwang gold deposit is situated in the northern part of the central segment of the Qinling orogenic belt, which represents the area of the complex closing of an ocean basin between the North China and Yangtze blocks. After long-term subduction, accretion, and collision, the Qinling orogenic belt underwent intracontinental orogenesis during the late Indosinian (Triassic) epoch

(Zhang et al., 1996; Mao et al., 2002). The deposit is hosted in a NW-trending belt of hydrothermal breccias, which is about 11.5-km-long and hosted by Devonian strata of the Fengxian-Taibai basin that was defined as a fore-arc basin by Zhang et al. (2009). Large numbers of SEDEX type Pb-Zn deposits, including the Bafangshan, Yindongliang, and Shoubanya deposits, are present in Devonian strata. Many Carlin-type gold deposits, such as the Baguamiao (80 t Au, 30 km to the northwest) gold deposit, also are located in this area (Li et al., 1998).

The Devonian strata are composed of weakly metamorphosed clastic-carbonate rocks of neritic facies, which include the Lower Devonian Wanjialing, Middle Devonian Gudaoling, and Upper Devonian Xinghongpu and Jiuliping Formations. The gold-bearing breccia belt lies in sodic-clastic sedimentary rocks of the Xinghongpu formation. The Xinghongpu Formation occurs along the NE limb of the Yingdonggou anticline, which is a secondary fold of the Xiba regional anticline.

The main structures formed during orogeny, including the Xiba anticline and deep-crustal faults, all trend NW. The Shuangwang deposit lies between the Shangxian-Danfeng and Fengxian-Shangyang faults. The main ore-hosting breccia belt is confined by the NWW-trending Wanjialing and Xiushiya faults. Sinistral post-ore NNE-trending faults cut the ore-bearing breccia belt such that the eastern section of the belt is offset about 600 m to the north.

Plutons of the Xiba batholith, dominated by quartz monzodiorite and monzogranite, intruded the axis of the Xiba anticline (Wang et al. 2011). The age of the intrusions is ca. 218-215 Ma. Also a small granite porphyry occurs in the western section of the breccia belt. Detailed underground investigations show that many lamprophyre dikes are emplaced into the breccia belt. The dikes are undeformed and this indicates that they are the products of post-ore magmatism in an extensional environment.

3 Ore deposit geology

The ore-hosting breccia belt, stratabound within the Xinghongpu Formation, is about several tens to hundreds of meters wide. The breccia belt is not continuous at the surface and is divided into the No. I through V breccia bodies from west to east. In addition, the Xiaomiaogou and Miaogounao breccia bodies outcrop north of the main breccia belt. Although there is gold mineralization along the entire breccia belt, no economic orebodies have been found in the No. I and V breccia bodies. Orebodies KT2 and KT6 are located in the No. II breccia body, KT5 in the No. III breccia body, and KT7, KT9, and KT8 in the No. IV breccia body.

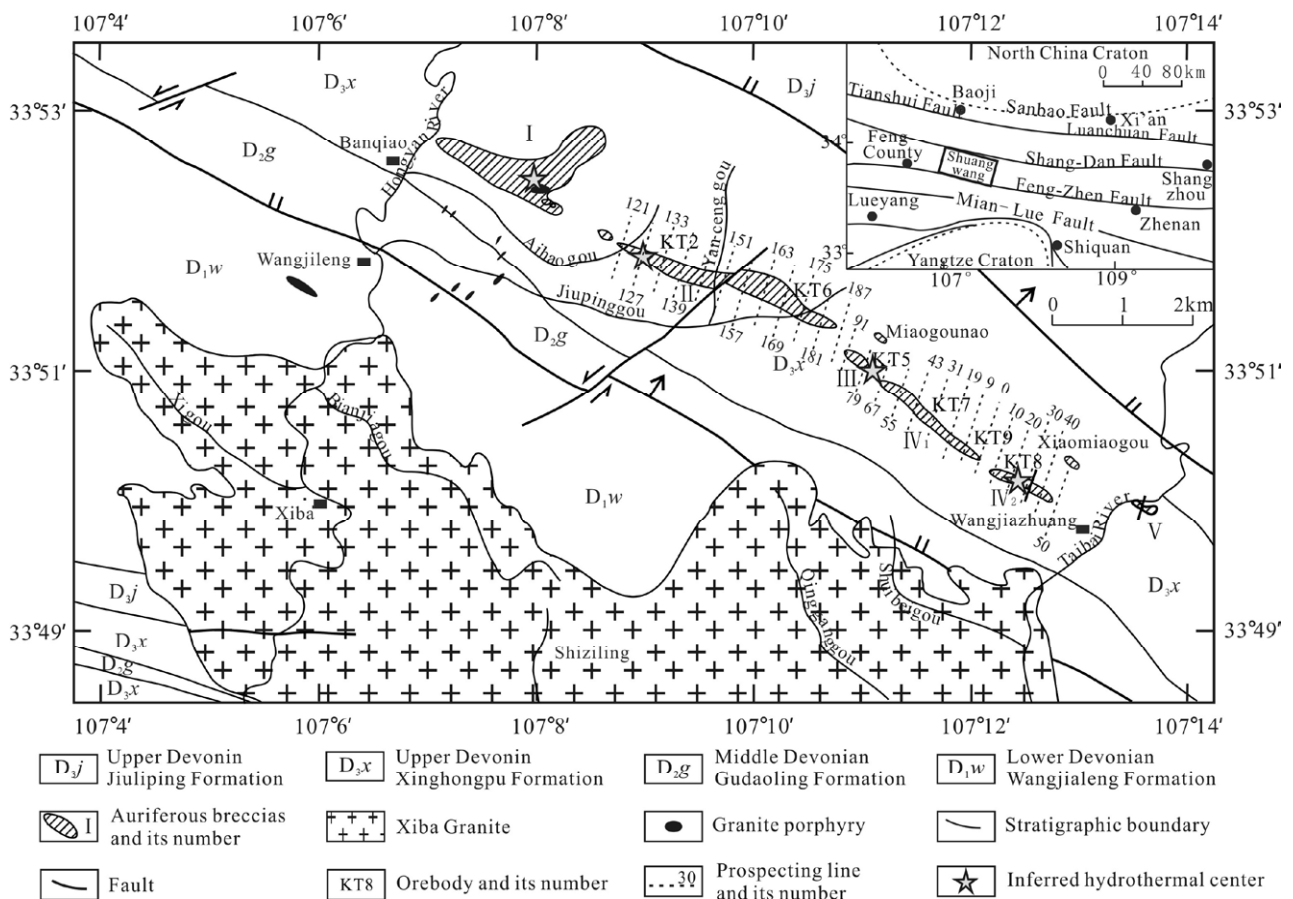


Figure 1 Geological sketch map of the Shuangwang gold deposit (Modified from Shi et al, 1989)

Generally gold mineralization is most extensive in shallower levels of the breccias and in eastern part of the belt. The largest orebody is the KT8 in the No. IV breccia body. It typically dips to the NNE at about 78°-85°, although the dip becomes as low as 38°-55° in the shallow parts of orebody to the west of prospecting line 32. The KT8 orebody is about 650-m-long, has an average thickness of about 30 m, and extends for more than 400 m in depth. Average grade of orebody KT8 is 3.08 g/t Au.

The ores of the Shuangwang gold deposit are typified by their breccia form. Detailed field investigation, microscopic observation, and structural analysis indicate that the gold-bearing breccias are hydrothermal breccias. The breccias contain angular fragments of country rock that show little sign of transport. Some fragments can be pieced together. Composition of the fragments is mainly albitized slate and siltstone, as well as partial silty sericitic slate. Fragments vary from several centimeters to tens of meters in length, with the larger breccias typically at shallower levels (Shi et al. 1989). Cements are composed of ferrodolomite (about 25%), albite (5%-7%), calcite (5%-15%), quartz (3%-5%), and pyrite (3%-6%) (Zhang et al., 2004).

Gold occurs in native form mainly in the pyrite and ferrodolomite cement of the breccias. The abundance of cement minerals varies from east to west in the breccia belt. In orebodies KT8, KT9, and KT7, ferrodolomite and pyrite are dominant. Pyrite increases and ferrodolomite decreases in the breccia belt in the western segment, particularly in orebodies KT6 and KT2. Local pyrite-cemented breccias are present in KT2. The amount

of calcite and gypsum increase in KT6 and KT2, but mineralization is not as well developed as that in orebodies KT8, KT9, and KT7, which are mainly cemented by ferrodolomite.

Past research indicates that the site of the most intense hydrothermal activity is located between KT8 and KT9 (No. 24 prospecting line in KT8, Shi et al. 1989), where shattered breccias are found. The breccias are very fine and resemble Quaternary unconsolidated accumulations. Detailed field investigations show that there may be three other areas of intense hydrothermal activity in the gold-bearing breccia belt (Fig. 1). Highly fractured rock occurring as powdered material characterizes the No. I breccia body, where the granite porphyry was emplaced. Similar features are also found along the No. 124 prospecting line in KT2. Collapse breccias are found along the No. 73 and 75 prospecting line in KT5. Coarse wallrock fragments mixed with finer ones are located in a pipe suggestive of extreme hydrofracturing. Sulfide minerals are complex in this pipe. Euhedral galena, sphalerite, and hematite occur in the cavities between fragments (Fig. 2).

It is recognized that the Shuangwang breccia bodies resulted from abnormally high-pressure fluids (Shi et al. 1989). Our investigation substantiates that supercritical gold-bearing fluids, perhaps driven by local magmatism, were focused into four main locations during the hydrothermal activity. When fluid pressure exceeded confining pressure, hydrofracturing resulted and the breccia belt was formed. Fluid inclusion studies show that the breccias formed at depths of about 3-6 km and the hydrothermal event was much shallower in the west

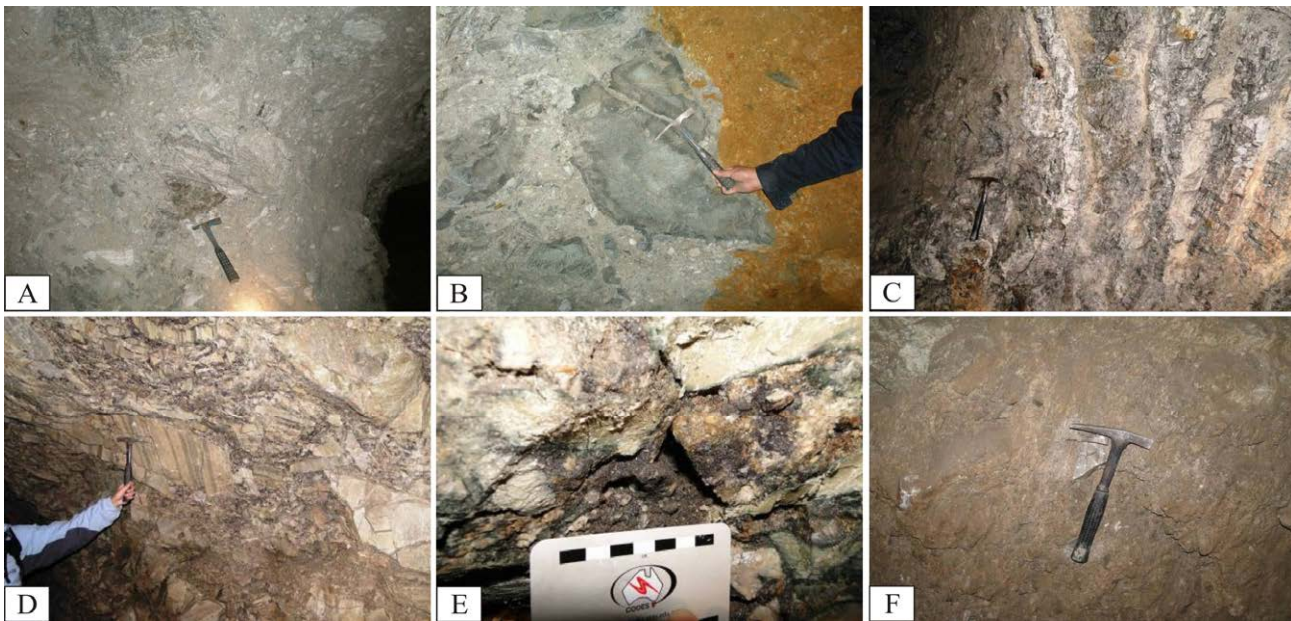


Figure 2 Areas of most intense hydrothermal activity in the Shuangwang gold-bearing breccias belt
 A-loose and broken breccia in No. I breccia body; B-fragments of granitic rock in No. I breccia body; C-loose and broken breccia in line 129 of KT2; D-“collapse breccias” in line 75 of KT5; E-hydrothermal center in line 75 of KT5, where hematite indicates oxidation of the ore; F-loose and broken breccia in line 24 of KT8

section than in the east section (Liu et al, 2011). Hydrofracturing brecciated the sedimentary rocks and large amounts of gold-bearing fluids migrated upward. The brecciation took place at deeper levels in the east and the higher pressure environment, with greater pressure fluctuation, may be one reason why gold mineralization is better in the east section.

According to general features of different orebodies, crosscutting of ore veins, replacement relationships, and paragenesis of ore and gangue minerals, gold mineralization in the Shuangwang gold deposit may be divided into four stages.

There was an early stage of replacement mineralization before the brecciation, which is characterized by a ferrodolomite-quartz-albite assemblage. A major feature of stage I is alteration of calcareous siltstone and silty sericitic slate to yellowish albitized slate and black fine siliceous ferrodolomite metasomatite. A small amount of pyrite was deposited and gold mineralization is very weak.

Stage II exhibits a quartz-albite-pyrite-ferrodolomite assemblage. This is the main gold mineralization stage and is characterized by infilling of euhedral ferrodolomite in open space created during brecciation. Large amounts of gold-bearing pyrite are disseminated in ferrodolomite. Most gold deposited during this stage was the result of the sudden pressure decrease.

Stage III is dominated by a pyrite-calcite-quartz assemblage. As the ore-forming fluids evolved, calcite and quartz replaced ferrodolomite. Pyrite, quartz and calcite are present as irregular veins and pods. Superimposition of the stage III hydrothermal assemblage on the stage II minerals caused local formation of high-grade ores.

Stage IV shows a final fluorite-dickite-gypsum assemblage. This stage is influenced by meteoric water influx and is the product of low temperature

hydrothermal activity. Stage IV is well developed in the western section of the belt. No sulfides or gold are deposited during this event.

4 Geochemical features

Systematic fluid inclusion study of hydrothermal minerals from the KT8, KT7, KT9, KT5, KT6, and KT2 orebodies shows that the ore-forming fluids for the Shuangwang gold deposit had diverse characteristics (Liu et al. 2011). The range of homogenization temperatures of inclusions in Stages I, II, and III are 300 to 463 °C, 220 to 340 °C, and 100 to 279 °C, respectively. The characteristics of the main ore-forming stage II fluid are low to moderate salinity (2.1%-22.7% NaCl eqv), high CO₂, as well as detectable N₂ and CH₄. The fluid pressure decreased gradually in the breccia belt from east to west. Observations of fluid inclusions in Stage II ores indicate that ore-forming fluids of the Shuangwang gold deposit underwent fluid unmixing at pressures from 100 to 170 MPa. Fluid immiscibility caused by decreasing fluid pressure is the most important reason for gold deposition. Grains of pyrite, ankerite, halite, and arsenopyrite were detected in some fluid inclusions (Xie et al. 2000).

Hydrogen and oxygen isotope composition of different stages of hydrothermal quartz, albite, calcite, and ferrodolomite are variable (Wang et al. 2013). Analyses show that the stage I fluid was of metamorphic origin. Stage II, the main gold event, formed from a fluid with magmatic and metamorphic components. Stage III fluids were mainly of magmatic origin, with a minor meteoric component. During stage IV, meteoric water was dominant.

The $\delta^{13}\text{C}_{\text{PDB}}$ and $\delta^{18}\text{O}_{\text{smow}}$ values of calcite from stage III range from -6.72‰ to $+0.51\text{‰}$ and 6.30‰ to

17.96‰, whereas ferrodolomite values range from -14.4‰ to +0.68‰, 12.81‰ to 20.21‰, respectively. These data indicate that carbon was derived mainly from a deep magmatic source and also partly from the dissolution of carbonate strata.

The $\delta^{34}\text{S}$ values of pyrite from the Xiba batholith vary from 3.8‰ to 6.1‰, in agreement with magmatic values. The $\delta^{34}\text{S}$ values of pyrite from ore-hosting sedimentary rocks show a wide range from -6.6‰ to 14.9‰, with an average of 6.4‰. The $\delta^{34}\text{S}$ values of pyrites from stage II breccias have great variation, from 2.6‰ to 26.4‰, with an average of 10.5‰. These data suggest that sulfur is of a mixed origin, with contributions from both host sedimentary rocks and magmatic rocks.

5 The three-step ore-forming model

In Early Devonian, EW-striking extensional rifting along the northern margin of the Yangtze Craton led to the formation of the ancient Mianlue Ocean. Early Devonian sedimentary rocks were deposited at that time. During Middle and Late Devonian, strong extension occurred mainly in the northern part of the Qinling orogenic belt and formed the nearly 1100-km-long Mianxian-Lixian-Fengzheng-Shangyang string of basins. The Feng-tai basin, hosting the Shuangwang gold deposit, is one of these basins. Rocks of the Middle and Late Devonian Gudaoling, Xinghongpu, and Jiuliping Formations were deposited successively. Gold-bearing muddy, silty clastic sedimentary rocks of the Xinghongpu Formation compose the primary ore-source strata.

From Early Triassic to Late Triassic, the Yangtze Craton subducted under the Qinling terranes to the north. The Indosinian movement in Late Triassic sutured the Yangtze and the North China Cratons, closing the two basins and leading to widespread deformation. Magmatism and metamorphism were ongoing during the orogenic process. Northwest- to W-trending linear folds and faults formed under strong N-S convergence. These structures provided pathways for later ore-forming fluids.

The late Indosinian marked the transition between collision orogeny and post-orogenic extension. The Shuangwang gold deposit formed during this transition. During this time, the Shangxian-Danfeng and the Fengxian-Shangyang deep-crustal faults were reactivated. Lower crust and upper mantle melts formed syntectonic granitoids. The Xiba batholith intruded along the axis of the Xiba regional anticline. Large volumes of exsolved magmatic fluid mixed with metamorphic fluids to form the ore-bearing fluids. The fluids accumulated in extensional fractures along the axis of regional fold and at different levels. They reacted with the country rocks

to form early stage replacement mineralization. When fluid pressure increased to a critical level, hydrofracturing occurred and hydrothermal breccias formed. Sudden pressure decreases caused immiscibility in the fluid and large amounts of gold were deposited with pyrite and ferrodolomite, which filled the extensional space of breccias as cements.

Acknowledgements

This study was funded by the National Basic Research Program of China (No.2012CB416600), National Nature Science Foundation (No. 41272106, 41030423), and a special program on mineral resources survey from CAGS (No.1212011220923).

References

- Li ZP, Peters SG (1998) Comparative geology and geochemistry of sedimentary-rock-hosted (Carlin-Type) gold deposits in the People's Republic of China and in Nevada, USA. USGS Open-File Report 98-466.
- Liu BZ, Wang JP, Wang KX et al. (2011) Characteristics and geological significance of fluid inclusions in the Shuangwang gold deposit, Shaanxi province. *Geosciences*, 25(6):1088-1098.
- Mao JW, Qiu YM, Goldfarb RJ, et al. (2002) Geology, distribution, and classification of gold deposits in the western Qinling belt, central China. *Miner Deposita*, 37(3/4): 352-377.
- Shi ZL, Liu JX, Fan SC et al. (1989) Geological characteristics and genesis of Shuangwang gold deposit, Shaanxi Province. Xi'an: Science and Technology Publishing House of Shaanxi: 1-98.
- Wang H, Wang JP, Liu JJ et al. (2011) Mineralogy of the Xiba granitoid pluton in the southern Qinling Orogenic Belt and its implications for Petrogenesis. *Geosciences*, 25(3):489-502
- Wang KX, Wang JP, Liu JJ et al. (2012) Geology and stable isotope geochemistry of the Shuangwang gold deposit in Taibai County, Shaanxi Province. *Geology in China*, 39(5):1359-1374.
- Wang ZQ, Yan QR, Yan Z, et al. (2009) New division of the main tectonic units of the Qinling Orogenic Belt, Central China. *Acta Geologica Sinica*, 83(11): 1527-1546.
- Xie YL, Xu JH, He ZL et al. (2000) Discovery and genesis significance of daughter minerals of pyrite and ferrodolomite etc. in fluid inclusions in Taibai gold deposit (i.e. Shuangwang gold deposit). *Mineral Deposits*, 19(1):54-60.
- Zhang ZH, Mao JW and Li XF (2004) Geology, geochemistry and metallogenic mechanism of Shuangwang breccia type gold deposit. *Mineral Deposits* 23(2):241-252
- Zeng QS, Wang JC and Chen GH (2005) Formation of gold-bearing hydrofracturing breccia bodies in tectonic lenses: a case study on Shuangwang gold deposit, Shaanxi, China. *Geotectonica et Metallogenia*, 29(2):93-106.
- Zhang GW, Meng R, Yu Z et al. (1996) Orogenic process and dynamic characteristics of Qinling orogenic belt. *Sci China (Ser D)* 26:193-200.
- Zhou T, Goldfarb RJ, Phillips GN (2002) Tectonics and distribution of gold deposits in China – an overview. *Miner Deposita* 37: 249-282.

Structure of the Mick Adam gold deposit: Yilgarn Craton, Western Australia

James Warren

Phoenix Gold Ltd., 73 Dugan St, Kalgoorlie, Western Australia 6430

Nicolas Thébaud

Centre for Exploration Targeting, Robert Street Building, M006, The University of Western Australia, 35 Stirling Hwy, Crawley, WA, 6009, Australia.

Steven Micklethwaite

Centre for Exploration Targeting, Robert Street Building, M006, The University of Western Australia, 35 Stirling Hwy, Crawley, WA, 6009, Australia.

Abstract. The influence of granitoids on gold mineralisation in the Yilgarn Craton has been hotly contested. They have been invoked as sources of metals and heat, or locations of local stress heterogeneity for subsequent deformation and mineralisation. The Mick Adam gold deposit is hosted in the thin, tail-like extension of a tonalite pluton (Kintore Tonalite) located on the Kunanalling Shear Zone in the Kalgoorlie Terrane of the Yilgarn Craton, Western Australia. The deposit and shear zone are contained within a mafic-ultramafic sequence. Preliminary data on the geometric relationship between gold bearing, southwest dipping quartz extension veins and shearing along the tonalite-basalt contact indicates that mineralisation occurred during normal dip-slip shear on the tonalite-basalt contact. The field data is consistent with either a period of extension in the regional deformation sequence, or local dilation resulting from strain heterogeneities due to the rheology and shape of the Kintore tonalite.

Keywords granitoid hosted gold, lode gold, stress rotation, Yilgarn Craton

1 Introduction

Research in the Yilgarn and Pilbara Cratons has highlighted the importance of granitoid domes as a heat engine and possible fluid source for mineralised Archean lode gold systems (Henson et al. 2007; Mickucki 1998; Neumayr et al. 2008; Ridley and Diamond 2000; Thebaud et al. 2006). Alternatively, when emplaced prior to mineralisation, granitoid plutons provide a competency contrast with the country rock, enabling localisation of strain and potential permeability enhancement (Duuring et al. 2007). The shape and orientation of granitoid plutons within greenstone sequences in a far-field stress regime can induce local changes in the orientation of the stress field (Thebaud et al. 2010). Typical examples of such processes include many Archean granitoid-hosted, lode gold deposits such as the Tarmoola (Duuring et al. 2006) and Granny Smith (Ojala et al. 1993) deposits in Western Australia.

Situated on the Kunanalling Shear Zone in the Yilgarn Craton, Western Australia, the Kintore Tonalite has a current resource of ~1.18 Moz Au at 1.6 g/t defined within the top 100 m from surface. The Mick Adam deposit is the largest of the deposits hosted within the Kintore Tonalite, with a current resource of ~0.6 Moz Au. This paper examines the structural setting of the

Mick Adam deposit and discusses the role of the Kintore pluton for mineralisation.

2 Geological Setting

The Mick Adam deposit is 40 km northwest of the town of Kalgoorlie in the Archean Yilgarn Craton of Western Australia (Fig. 1). The deposit lies within the Kalgoorlie Terrane of the Eastern Goldfields Superterrane, which is host to numerous world class gold deposits including the >60 Moz Golden Mile Deposit. The Kalgoorlie Terrane is further subdivided into a series of structurally bound domains with locally distinct volcanic facies relationships (Swager 1997). Lithology of the Kalgoorlie Terrane consists of meta-volcanic, sedimentary and granitic rocks which were deposited between ~2.72-2.68 Ga on sialic crust (Swager 1997). Multiple structural histories have been proposed for the evolution of the Eastern Goldfields Superterrane and there is currently some variation in the deformation numbers applied to the various structural elements as summarised in Table 1. The majority of mineralisation is typically interpreted to have occurred late in the evolution of the craton, associated with a regional E-W contraction (D3 after Swager 1997) event termed the Kalgoorlie Orogen (Weinberg et al. 2003).

The Mick Adam deposit is located on the Kunanalling Shear Zone, which is a domain bounding fault, separating the Coolgardie domain in the west from the Depot Domain in the east (Cassidy et al. 2006) (Fig. 1). Hosted within the Kunanalling Shear Zone, a tonalitic pluton referred to as the Kintore Tonalite, intruded into folded and foliated northwest striking meta- mafic and ultramafic rocks. The Kintore Tonalite has been dated at 2696 ± 4 Ma (Fletcher et al. 2001) and thins towards the south in the region of the Mick Adam Deposit. The Kunanalling Shear Zone strikes predominantly northwest, dips steeply east and has previously been interpreted to bend around the flank of the eastern margin of the Kintore Tonalite. The Kunanalling Shear Zone is in turn cross-cut by late north to northeast striking faults (Fig. 1).

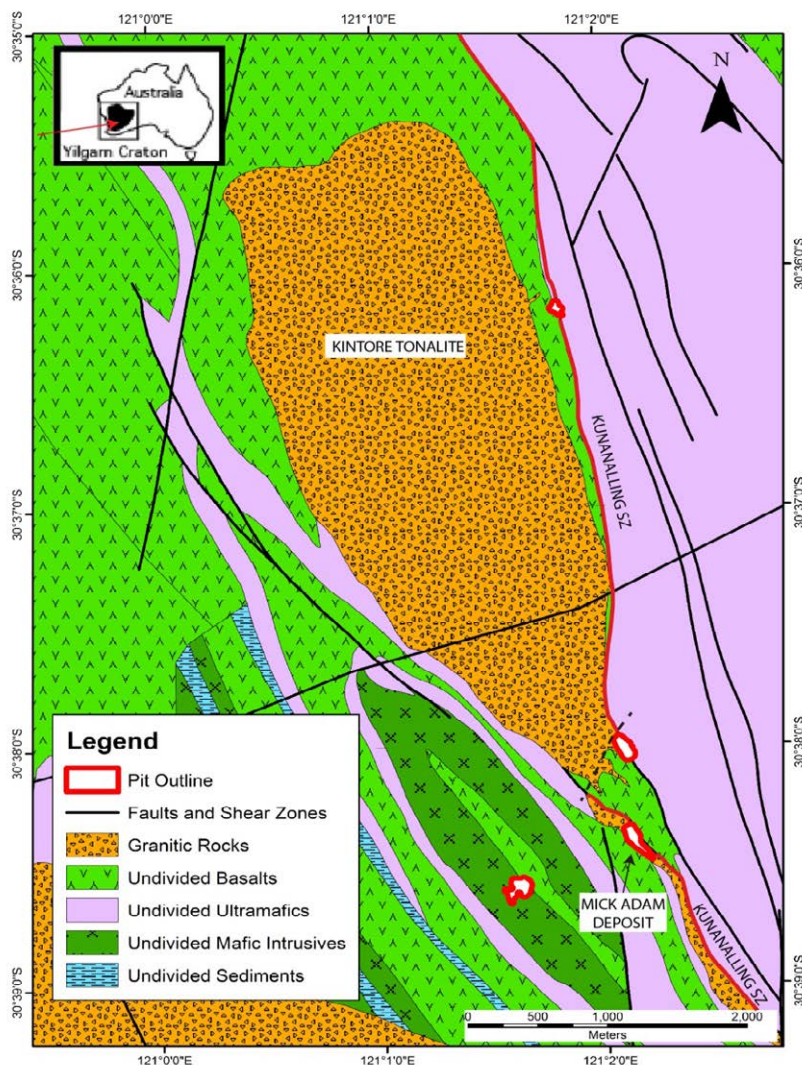


Figure 1. Geological map of the Kintore Tonalite region showing the location of the Mick Adam deposit within the Yilgarn Craton of Western Australia.

Deformation Event		Structural History						
		Mueller 1988	Swager 1997	Nguyen 1997	Weinberg et al. 2003	Blewett 2004	Miller 2006	Blewett & Czarnota 2010
Proterozoic Contraction								
Minor Extension	Collapse		Collapse			late De		D6
Dextral strike-slip		D3	D4	D4	D4	D4	D4	D5
Sinistral tranpression	NW-SE local compression	D2	D3	D3	D3	D3	D3	D4b
	Late basin upright folding	D1	D2	D2	D2	D2b	D2	D4a
Extensional doming	Stage 2 Late Basins		DE	DE3	D2e	D2e		D3b
	Stage 1 Late Basins						D1	D3a
Upright folding and reverse faulting			D1		D1	D2a		D2
Extension with intermittent compression			DE	DE1-2	D1e	De		D1

Table 1. Compilation of the deformation histories proposed for the Eastern Goldfields Superterrane by various authors.

3 Analysis of the Mick Adam Deposit

3.1 Methods

The geometric relationship between faults and connected veining can be used to interpret kinematics of the fault (e.g. Miller and Wilson 2002). The Mick Adam pit was mapped using this approach to determine structural

controls on mineralisation within the deposit. Preliminary orientation data was collected from the sheared basalt-tonalite contact, and a series of southwest dipping, quartz extension veins located within the tonalite (Fig. 2). Mineralisation in the Mick Adam deposit is closely related to these veins, which are up to 30 cm thick and dip on average 68° to 225° (Fig. 3).

They have a gangue mineralogy of quartz±biotite, and display pure opening mode textures. They display variable amounts of silica-sericite-biotite alteration with gold typically occurring within the veins and in the wall-rock alteration. These veins remain relatively undeformed.

3.2 Results

Hosted at the contact between a tonalite and basalt, Mick Adam is a structurally controlled deposit. The major fault observed in the Mick Adam pit is the sheared contact of the Kintore Tonalite with the basalt (Fig. 2). The contact dips 66° to 050°, has ubiquitous quartz

veining, is strongly foliated and is associated with intense biotite alteration within the basalt and tonalite proximal to the margin. The planar fabric (S_1), defined by biotite alignment is dipping 60° to 045° and carries a mineral lineation (L_1) plunging 67° to 016°. Whilst the basalts display a strong foliation throughout the pit, the foliation within the tonalite dies out rapidly. Similarly, biotite alteration associated with the sheared tonalite-basalt contact only extends approximately 5 m into the tonalite. Results presented in Figure 3 indicate the mineralised extension veins developed during normal movement on the east dipping Kintore Tonalite contact. The vein-derived transport direction is consistent with the observed mineral lineations.

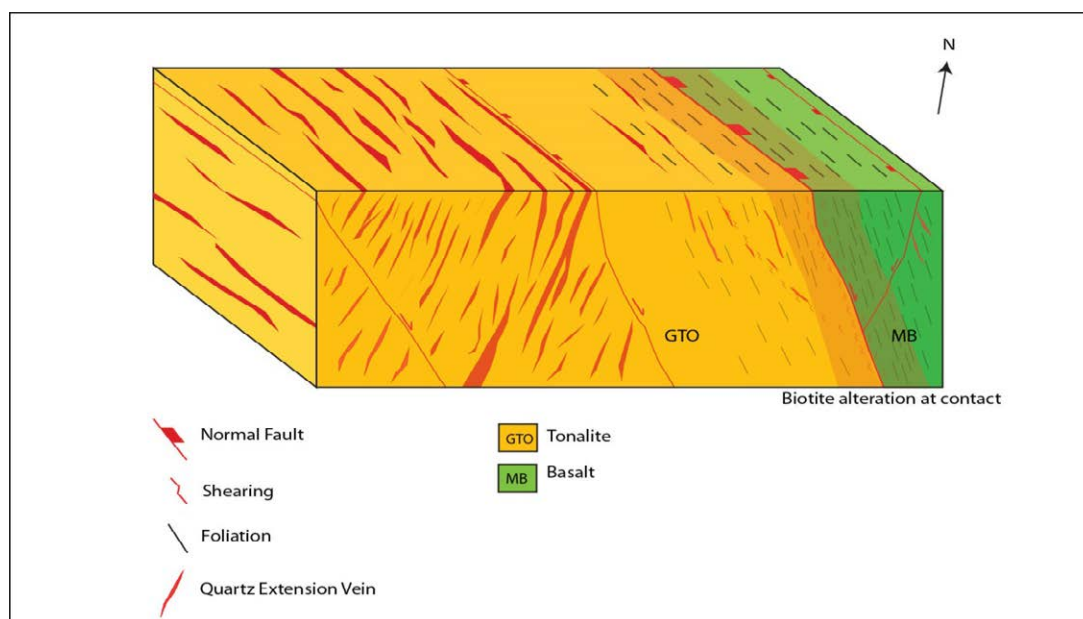


Figure 2. Block diagram illustrating the fault-vein relationships observed in the Mick Adam pit.

4 Discussion

The occurrence of mineralised extension veins in the Kintore Tonalite demonstrates that mineralisation postdates crystallisation of the intrusion. Together with the absence of widespread veining in the basaltic country rock it is suggested that the tonalite acted as a competent host that aided the development of the extensional veins at the time of mineralisation. The preliminary field data collected for this paper suggests a model of mineralisation coeval with local NW-SE extension.

Weinberg and van der Borgh (2008) argue that the mineralisation of the Kintore Tonalite occurred during one of two successive regional extensional deformation events, bracketing a major period of shortening termed the Kalgoorlie Orogen (Weinberg et al. 2003; or D_2 - D_4 after Swager 1997).

The model of Weinberg and van der Borgh (2008) does not easily explain why mineralisation is not distributed throughout the entire Kintore tonalite. An alternative but preliminary model, is

that the Mick Adam deposit formed during localised extension and veining, due to stress-strain heterogeneities imposed by the shape of the Kintore Tonalite during the transpressive deformation of the Kalgoorlie Orogen. Similar controls on mineralisation have been interpreted for the Tarmoola (Duuring et al. 2001) and Granny Smith (Ojala et al. 1993) gold deposits. Granitoid margins become important conduits for fluid flow, because rheological contrasts between competent granitoid and ductile country rock result in the localisation of strain along the granitoid margins, enhancing permeability and fluid flow (Duuring et al. 2001). Ongoing research, combining field mapping and structural geophysics is directed toward distinguishing between the two models.

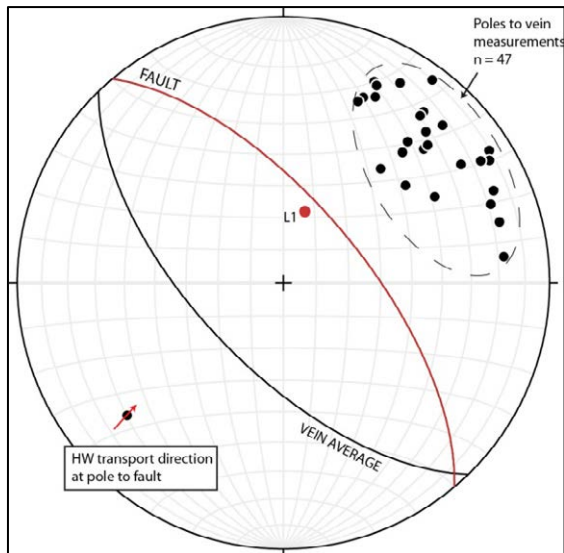


Figure 3. Stereographic projection showing the relationship between the tonalite-basalt contact fault, the southwest dipping quartz veins (calculated average) and measured lineations. The arrow indicates the interpreted hangingwall transport direction.

Conclusion

Extension related to normal dip-slip shear movement of the Kintore Tonalite-basalt contact is a critical factor controlling granitoid hosted mineralisation at the Neoproterozoic Mick Adam gold deposit, West Australia.

Field data is consistent with mineralisation during a period of extension within the regional deformation sequence of the Eastern Goldfields Superterrane. Alternatively, extension occurred during local dilation, resulting from strain heterogeneities arising from the rheology and shape of the Kintore tonalite.

Acknowledgements

Phoenix Gold Ltd. is gratefully acknowledged for providing outstanding financial and logistical support for this PhD project.

References

Blewett RS, Cassidy KF, Champion DC, Henson PA, Goleby BS, Jones L, Groenewald PB (2004) The Wangkathaa Orogeny: an example of episodic regional 'D2' in the late Archaean Eastern Goldfields Province, Western Australia. *Precam Res* 130:139-159

Blewett RS, Czarnota K, Henson PA (2010) Structural-event framework for the eastern Yilgarn Craton, Western Australia, and its implications for orogenic gold. *Precam Res* 183: 203-229

Cassidy KF, Champion DC, Krapez B, Barley ME, Brown SJA, Blewett RS, Groenewald BP, Tyler IM (2006) A Revised Geological Framework for the Yilgarn Craton, Western Australia. *West Austr Geol Surv Record* 2006/8, p 8

Duuring P, Cassidy KF, Hagemann SG (2007) Granitoid-associated orogenic, intrusion-related, and porphyry style metal deposits in the Archaean Yilgarn Craton, Western Australia. *Ore Geol Rev* 32

Fletcher IR, Dunphy JM, Cassidy KF, Champion DC (2001) Compilation of SHRIMP U-Pb geochronological data, Yilgarn Craton, Western Australia, 2000-2001. *Geoscience Australia Record* 2001/47

Henson P, Blewett R, Champion D, Goleby B, Czarnota K (2007) How does 3D architecture of the Yilgarn Craton control hydrothermal fluid focussing. In: Berlein F, Knox-Robinson C (eds) *Kalgoorlie '07*, vol., Kalgoorlie, pp 57-61

Mikucki EJ (1998) Hydrothermal transport and depositional processes in Archaean lode-gold systems: A review. *Ore Geol Rev* 13:307-321

Miller JM (2006) Linking structure and alteration in Laverton with specific reference to Sunrise Dam and Wallaby. *Predictive Mineral Discovery Cooperative Research Centre, Extended Abstracts from the April 2006 Conference, Perth. Geoscience Australia Record* 2006/07: 62-67

Miller JM, Wilson CJL (2002) The Magdala lode gold system, Stawell, southeastern Australia; structural style and relationship to gold mineralization across the western Lachlan fold belt. *Econ Geol* 97:325-349

Mueller AG, Harris LB, Lungan A (1988) Structural controls of greenstone-hosted gold mineralisation by transcurrent shearing: a new interpretation of the Kalgoorlie mining district, Western Australia. *Ore Geol Rev* 3:359-387

Neumayr P, Walshe J, Hagemann S, Petersen K, Roache A, Frikken P, Horn L, Halley S (2008) Oxidized and reduced mineral assemblages in greenstone belt rocks of the St. Ives gold camp, Western Australia: vectors to high-grade ore bodies in Archaean gold deposits? *Miner Deposita* 43:363-371

Nguyen PT, Donaldson JS, Ellery SG (1998) Revenge Gold Deposit, Kambalda. *Australasian Inst Mining Metall Monogr* 22: 233-238

Ojala VJ, Ridley JR, Groves DI, Hall GC (1993) The Granny Smith gold deposit: the role of heterogeneous stress distribution at an irregular granitoid contact in a greenschist facies terrane. *Miner Deposita* 28:409-419

Ridley J, Diamond LW (2000) Fluid Chemistry of Orogenic Lode Gold Deposits and Implications for Genetic Models. In: Hagemann SG, Brown PE (eds) *Rev Econ Geol* 13: 141-162

Swager CP (1997) Tectono-stratigraphy of late Archaean greenstone terranes in the southern Eastern Goldfields, Western Australia. *Precam Res* 83:11-42

Thebaud N, Duclaux G, Gessner K, Doublier M (2010) 3-D thermal mechanical models of Archaean Dome and Keel Formation: Insights from Southern Cross district. In: *IAS 2010, Fifth International Archaean Symposium, Perth, Australia*, p 5

Thébaud N, Philippot P, Rey P, Cauzid J (2006) Composition and origin of fluids associated with lode gold deposits in a mid-Archaean greenstone belt (Warrawoona Syncline, Pilbara, WA) using Synchrotron radiation X-Ray Fluorescence. *Contr Mineral Petrol* 152:485-503

Weinberg RF, Moresi L, Borgh Pvd (2003) Timing of deformation in the Norseman-Wiluna Belt, Yilgarn Craton, Western Australia. *Precam Res* 120:219-239

Weinberg RF, van der Borgh P (2008) Extension and gold mineralization in the Archaean Kalgoorlie Terrane, Yilgarn Craton. *Precam Res* 161:77-88

Ore genesis study of the shear zone-hosted Tianjingshan gold deposit, Anhui Province, China

Yuling Xie, Yancen Jiang, Yanwen Tang
University of Science and Technology Beijing, Beijing 100083, China

Simon C Dominy
Snowden Mining Industry Consultants Pty Ltd, Ballarat, Victoria, Australia;
WA School of Mines, Curtin University, Perth, WA, Australia

Aiguo Wang
Nanjing Institute of Geology and Mineral Resource, Chinese Academy of Geoscience, Nanjing 210016, China

Abstract. Field studies, petrography, microscopy, and SEM/EDS analysis of ore and wallrocks were undertaken from the Tianjingshan gold deposit, Anhui province, China. Gold mineralization occurs in quartz veins, with only minor gold hosted in altered wallrocks. Mineralization is closely related to sericitization, Fe-bearing carbonization, chloritization, and sulfidation. It occurs later than formation of main quartz veins and regional metamorphism. Mineralization relates to brittle deformation of the quartz veins. Petrographic, microthermometric, and LRM results of quartz-hosted fluid inclusions show that the ore-forming fluid was a water-rich, CO₂-bearing fluid with a moderate to high temperature (286–380°C) and low salinity (3.0–5.1 wt% NaCl eq). Analyses of fluid inclusions by LA-ICP-MS in quartz show elevated amounts of Pb, Zn, Cu, Bi, Mo, and Sb in the fluid and H-O isotope results indicate a dominant magmatic fluid origin. During flow of the magmatic fluid along a reactivated fault zone, decreasing temperature and pressure resulted in the unmixing of water and CO₂. The degassing of CO₂ shifted the fluid pH and resulted in the precipitation of gold, sulfide minerals, sericite, and Fe-bearing carbonate minerals.

Keywords. Tianjingshan gold deposit, shear zone, brittle deformation, fluid inclusion, gold

1 Geology background

The Tianjingshan gold deposit, with 316 kg of gold resources (332 Geological Brigade of Anhui Bureau of Geology and Mineral Resource, 2003), is located in Xiuning county, Anhui province, China. It lies in the eastern segment of the Qingzhou-Hangzhou metallogenic belt (Yang and Mei, 1997). Tectonically, it is situated along the suture between the Yangtze and South China blocks (Fig. 1a).

The region is underlain by Proterozoic metamorphic rocks, the Neoproterozoic Jinningian granite, and limited outcrops of the Jurassic Hongqin Formation conglomerate, sandstone, and pelitic siltstone. The metamorphic rocks include the Neoproterozoic Jingtan Formation volcanic and volcanoclastic rocks, and the Mesoproterozoic Niuwu Formation flysch (Fig. 1b). In addition to the Jinningian granite, other minor intrusive rocks include Yanshanian (Jurassic-Cretaceous) granite, monzonitic granite, granodiorite, quartz monzonite porphyry, granite porphyry, and diabase dikes. The Yanshanian intrusions are genetically related to gold mineralization (Li, 1989). Structure in the area is

dominated by NE- and NW- trending faults. The NE fault set is the largest and shows multi-stage activity. The NE-trending faults control the distribution of the metallogenic belt and the shear zone within the metamorphic rocks. The gold deposits are located along the NE-trending Huangmao-Wuchen-Tunxi shear zone (Wu and Zhang, 2010), which is about 25-km-long and locally several kilometres wide (Geological Survey of Anhui Province, 2005).

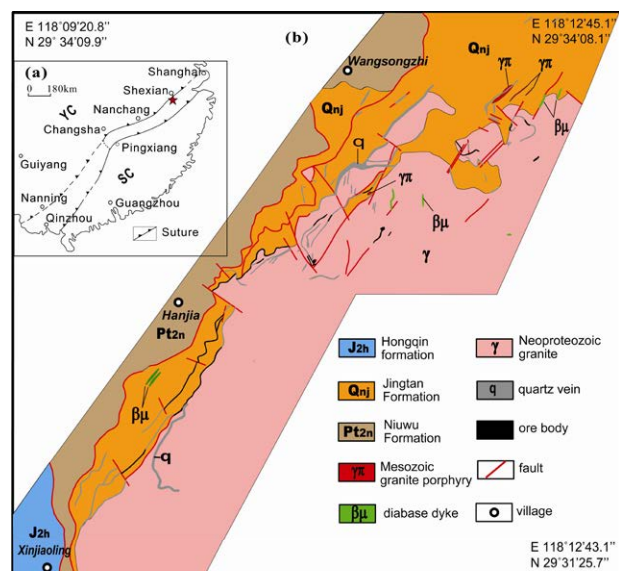


Figure.1 Simplified map of Qingzhou-Hangzhou metallogenic belt (a) (after Yang and Mei, 1997) and geological map of Tianjingshan area (b) (after Geological Survey of Anhui Province, 2005)

YC-Yangtze block; SC-South China block; Red star-location of the Tianjingshan gold deposit

2 Mineralization and alteration

Quartz veins are well-developed in the deposits (Fig 2a) and include composite veins and stockworks. Gold mineralization occurs mainly in quartz veins (Fig 2b), with minor amounts in altered wallrock. Field observations, petrographic, and SEM/EDS (Scanning Electron Microscopy and Energy Dispersive Spectrometer) results indicate that the dominant alteration styles are silicification, sericitization, Fe-carbonization, chloritization, and sulfidation. Alteration mineral assemblages comprise quartz, sericite, ankerite, manganosiderite, chlorite, pyrite, chalcopyrite,

sphalerite, galena, and arsenopyrite. Silicification was an early event, with most resulting quartz veins being parallel to the schistosity. Sericitization and Fe-bearing carbonization occur as in-fillings or as cements in brecciated quartz (Fig 3a, b), which displays a brittle deformation character. Gold occurs as native gold, together with sericite and Fe-bearing carbonate, in the fractures in quartz (Fig 4).

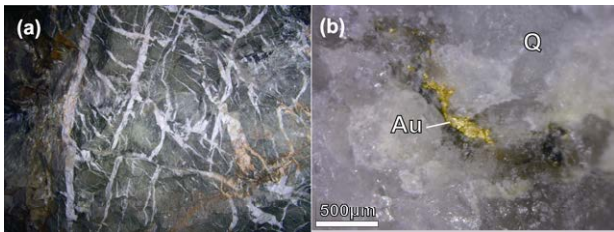


Figure 2 Photos of (a) the underground vein system and (b) gold in quartz from Tianjingshan gold deposit

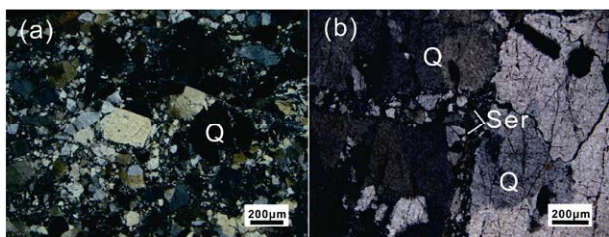


Figure.3 Photomicrographs of the mineralized quartz veins (a)-quartz with cataclastic texture (transmitted light, cross polarized); (b)-cataclastic texture and sericitization in the fractures of quartz (transmitted light, cross polarized); Q-quartz; Ser-sericite

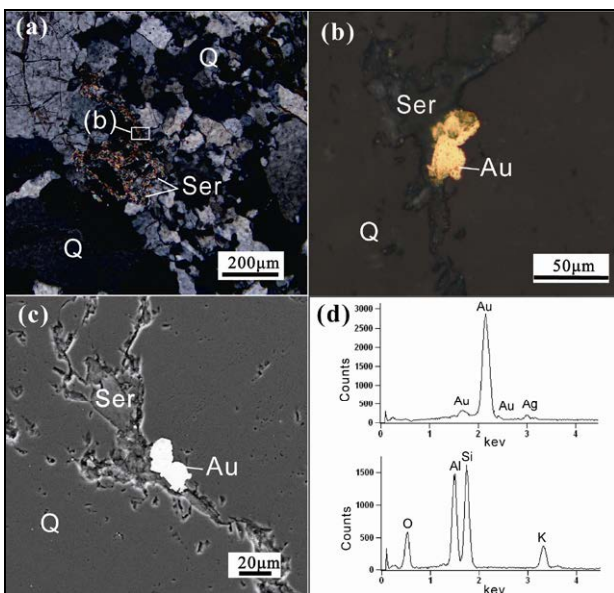


Figure.4 The micrograph and energy spectra of native gold in the Tianjingshan gold deposit (a)-sericitization and brecciated quartz (transmitted light, cross polarized); (b)-native gold and sericite in quartz fracture (reflected light, for frame in Fig4a); (c) BSE image of native gold and sericite in quartz fracture; (d) X-ray energy spectra of native gold and sericite

Cathodoluminescence (CL) imaging of mineralized quartz shows cataclastic textures and the growth zones crosscut

by sericite and other styles of alteration (Fig 5). At least two stages of hydrothermal activity post-date quartz vein formation and can be recognized based on CL analysis. This is consistent with the fluid inclusion assemblages in quartz (see below).

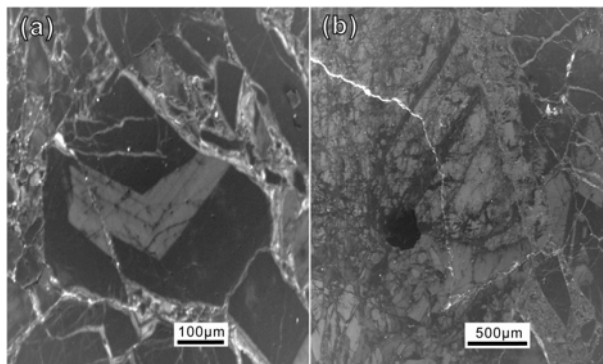


Figure.5 Cathodoluminescence image of a quartz vein in the Tianjingshan gold deposit (a)-the growth zoning in fragmented quartz breccia; (b) fragmented quartz and the later fluid alteration fingerprint (bright white line)

3 Fluid inclusion results

Petrographic results indicate that almost all the fluid inclusions in vein quartz show secondary inclusion characteristics. At room temperature, there are two fluid inclusion assemblages that can be recognized: (1) Aqueous-carbonic inclusion comprising water and vapor CO₂ (AC type) and comprising vapor or vapor and liquid CO₂ types (C type); and (2) aqueous and vapor type inclusions (AV type). The AC fluid inclusions have varied vapor volume percentages ranging from 20 vol. % to more than 80 vol. %. The AV fluid inclusions have lower vapor volume percentages (5-10 vol. %) than the AC type and crosscut the AC-C inclusion assemblages, showing a late formation relationship. The CO₂-rich, aqueous-carbonic inclusion assemblages appear to be coeval with sericitization, Fe-bearing carbonization, and gold mineralization. Coexistence of the AC and C types and the varied vapor volume percentages, indicate fluid unmixing between CO₂ and water during ore-fluid evolution. Petrographic, microthermometric, and LRM (Laser Raman Microspectrometry) results show that the AC fluid inclusions have a low salinity (3.0-5.1 wt% NaCl eq), moderate to high temperature (286-380°C), and CO₂-rich character.

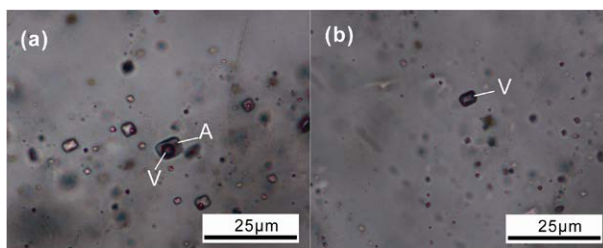


Figure.6 Photomicrographs of fluid inclusions in quartz from Tianjingshan gold deposit (a) CO₂-bearing aqueous fluid inclusions; (b)-CO₂-rich vapor fluid inclusions; A-aqueous phase; V-vapor phase

Due to decrepitation during laser ablation, LA-ICP-MS analyses of AC inclusions were not successful, although the ICP-MS spectrum still provided useful information (Fig. 7). Analyses showed enrichments of Pb, Zn, Cu, Bi, Mo, and Sb in the inclusions, with slightly anomalous Ag. Isotope analyses for inclusion waters show that the δD_{H_2O} varied from -67.3 to -57.4 per mil and the $\delta^{18}O_{H_2O}$ varied from 2.01 to 7.31 per mil, implying a dominantly magmatic origin with meteoric water contamination.

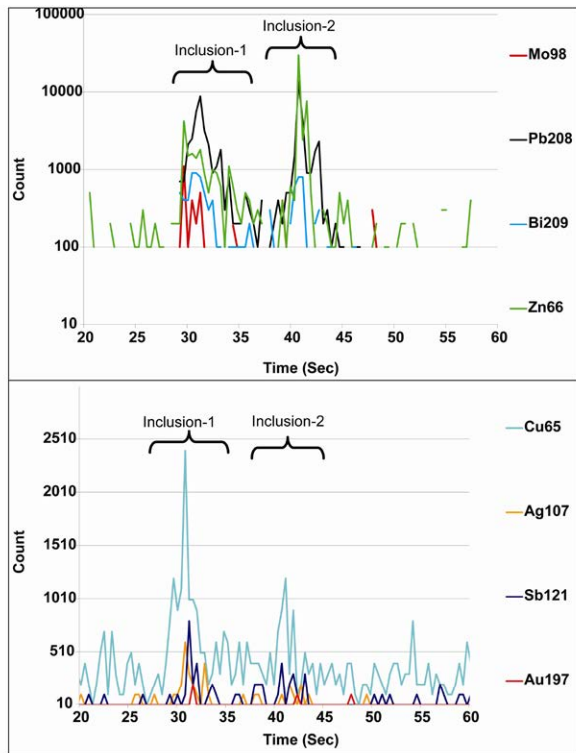


Figure.7 The spectra images of gas and liquid phases fluid inclusion from quartz by LA-ICP-MS in Tianjingshan Au deposit (a)-Mo, Pb, Zn, Bi spectra images; (b) Cu, Sb, Ag, Au spectra images

4 Discussion and conclusion

The Tianjingshan deposit is situated in Huangmao-Wuchen-Tunxi shear zone, which cuts Proterozoic metamorphic rocks and granite, and displays a similar mineralization and alteration style to typical orogenic gold deposits. In this case, gold mineralization is later than shear zone formation and regional metamorphism. The spatial relationship between the local Mesozoic felsic intrusions and gold mineralization, the alteration assemblages, and the H-O isotope composition of ore-forming fluid, imply a genetic link between gold mineralization and Yanshanian magmatism.

Petrographic results show that the quartz veins underwent a period of brittle deformation resulting in a fragmented texture. Gold mineralization occurs as infillings, together with sericite and Fe-bearing carbonate, which indicates that gold mineralization post-dates regional metamorphism, shear deformation, and dominant silicification.

Subduction of the Pacific plate below the South China craton during the Mesozoic period, caused regional uplift and reactivation of the Huangmao-Wuchen-Tunxi shear

zone. Additionally, the Yanshanian magmatism took place during this period. The reactivated shear zone permitted both magma and fluid migration. The Yanshanian intermediate to felsic intrusions are well-developed in this area, including quartz monzonite and granite porphyries, and show a shallow emplacement character. The exsolution of magmatic fluids resulted in formation of the gold-bearing ore-forming fluids. The ore fluids migrated along the reactivated fault, resulting in a decrease in their temperature and pressure. Along with the decrease of T and P, fluid immiscibility occurred. The degassing of CO₂ caused a change in fluid pH and triggered the precipitation of gold and sulfides, as well as sericite and Fe-carbonate minerals.

Acknowledgements

This study was supported by the China National Key Technology R&D Program (No. 2011BAB04B02). Many thanks go to Xinyu Zeng and the 332 Geological Brigade, Anhui Bureau of Geology and Mineral Resource for their help in the field work.

References

- Geological Survey of Anhui Province (2005). The gold and multi-metal resource evaluation report of Xiuning-Shexian area (in Chinese)
- Li Z, Yang W, Wang Y and Xiong L (1989). Relation between magmatism and gold mineralization in South Anhui Province. *Contributions to Geology and Mineral Resources*, 4(2): 42-53
- Wu J and Zhang J (2010). Study Prospecting potential and breakthrough direction of the Tianjingshan Gold Deposit based on comparing with the metallogenic characteristics of the Tianjingshan Gold Deposit and the Jinshan Gold Deposit. *Mineral Deposits*, 29(sup): 1003-1004 (in Chinese).
- Xu Y, Wu X, Lou F (2008). Division and correlation of the Middle Proterozoic strata in Jiangnan Old Land. *Resources Survey & Environment*, 29(1): 1-11 (in Chinese with English abstract).
- Yang M and Mei Y (1997). Characteristics of geology and metallization in the Qinzhou-Hangzhou Paleoplate Junction. *Geology and Mineral Resources of South China*, (3): 52-59 (in Chinese with English abstract).
- 332 Geological Brigade of the Anhui Bureau of Geology and Mineral Resource (2003). Exploration report for Tianjingshan segment of Tianjingshan gold deposit in Shandou of Xiuning county, Anhui province (in Chinese).

Structural evolution and settings of orogenic gold and intrusion-related gold deposits in the central part of the Bohemian Massif, Czech Republic

Jiří Zachariáš

Institute of Geochemistry, Mineralogy and Mineral Resources, Faculty of Science, Charles University in Prague, Albertov 6, Prague 2, Czech Republic

Abstract. Orogenic gold and intrusion-related gold deposits in the central part of the Bohemian Massif formed under similar tectonic conditions, in local extension settings within a regional tectonic zone along the boundary between two crustal blocks. Older age (347-341 Ma) and greater depths (15-11 km) characterize the intrusion-related gold deposits with respect to the group of orogenic-gold deposits (340-337 Ma and 9-7.5 km). Formation of both types of gold deposits occurred during the uplift of the tectonic block with the Central Bohemian Plutonic Complex.

Keywords. Gold deposits, Bohemian Massif, extension, age

1 Introduction

The Bohemian Massif hosts numerous ore deposits (Au, Ag-Pb-Zn, U, Sn-W) related to Variscan (Hercynian) metallogeny. Among them, the gold deposits have remarkable potential for future mining; about 200-300 t of gold is available in the present reserves. One-half of them corresponds to orogenic gold and the other to intrusion-related gold deposits.

Gold deposits in the central part of the Bohemian Massif mostly occur within an approx. 100 km long and 30 km wide zone along the SE boundary between the low-grade Teplá-Barrandian (TB) and the high-grade Moldanubian (MLD) blocks/units. The Variscan tectonic evolution of the Bohemian Massif dates back to 380 Ma at the start of the SE-oriented subduction of the Saxothuringian plate beneath the present-day Teplá-Barrandian and Moldanubian units. This process led to the NW-SE oriented transpression of the TB, more or less coeval with a formation of a volcanic arc – the present-day Central Bohemian Plutonic Complex (CBPC; c. 355-335 Ma, mostly I and I/S granites, minor S-types). Several large-scale tectonic zones can be distinguished along and within the CBPC and the nearby units (TB, MLD). For example Dörr and Zulauf (2010) suggest “elevator tectonics” along ductile to semi-ductile steep shear zones situated at the TB and MLD terrane boundaries, which led to sinking of the cold TB (orogenic plateau) into the partly molten MLD stratum and to extrusion of the MLD block at c. 345-335 Ma. Other authors, however, documented wrench-like tectonics for the same zone (Rajlich et al. 1988; Pitra et al. 1999).

A common feature of all gold deposits in the above-described zone is a variable but generally low sulfide content (< 5 vol. % of pyrite, arsenopyrite, pyrrhotite) and quartz-dominated gangue (e.g. Morávek and Pouba

1987, 1990; Morávek et al. 1992). They were traditionally classified as orogenic gold deposits, except the Petrůvkova Hora and the Mokrsko deposits, which more closely match the intrusion-related type of gold deposits (Zachariáš et al. 2001, Boiron et al. 1999, respectively). Formation of most of gold deposits in the central part of the Bohemian Massif occurred from 345 to 338 Ma (coevally with magmatic activity of the CBPC). Only the electrum-bearing (Au-Ag) deposits located inside the MLD unit to the SE of the CBPC are probably younger (c. 290-300 Ma).

2 Intrusion-related gold deposits

The **Petrůvkova hora deposit (PHD)** is spatially related to a composite intrusive stock (c. 348-346 Ma) that intruded the Cambrian sediments of the TB close to the CBPC. Five types of quartz veins (Q1-Q5) were distinguished here (Zachariáš et al. 2001), all of which are younger than the youngest intrusive phase of the composite stock (i.e. the granodiorite with associated aplite dikes). Molybdenite from Q1 and Q2 veins was dated to 344.4±2.8 Ma by the Re-Os method (op cit). The Au-quartz veins (Q2 and Q4) form of a swarm of parallel, irregularly-spaced, steep veins that trend NW-SE. They are also parallel to the swarm of dikes of granodiorite porphyries that represent the pre-granodiorite intrusive phase. This indicates long-lived persistence of the NE-SW (EEN-WWS) oriented subhorizontal extension in the study area. The tectonic regime temporally switched to E-W oriented extension during formation of late aplites and early quartz veins (Q1). Late quartz veins (Q5) that are much younger than Q1-Q4 formed under WSW-ENE oriented compression.

The **Mokrsko-West deposit (MWD)** is hosted mainly by the Sázava tonalite (354±4 Ma; U-Pb zircon; Janoušek et al. 2004) of the CBPC. The near-by Mokrsko-East and Čelina deposits are hosted by metabasalts and metarhyolites of the Neoproterozoic Jílové belt (TB). Quartz veins at all these three deposits are steeply inclined and uniformly trend E-W. Most of them represent mode-I (tension) fractures. They form either an approx. 300 m wide zone of sheeted veinlets (<1-5 mm thick, uniformly spaced, the MWD), or swarm of parallel irregularly-spaced veins (up to 30 cm thick; Mokrsko-East and Čelina deposits). Their formation, as well as the formation of some post-ore faults, is compatible with the N-S oriented extension. Formation of quartz veins was preceded by intrusion of steeply dipping granodiorite porphyries, also trending E-W. The extension stage was preceded by two

compression phases (NE-SW and NW-SE oriented). Molybdenite from quartz veins at MWD was dated to 342.9 ± 1.4 Ma (Re-Os; Zachariáš and Stein 2001), which is also the age of the extension stage.

2 Orogenic gold deposits

The **Jílové deposit (JD)** is located in the northern part of the Neoproterozoic Jílové belt (TB). Three basic types of gold ores were mined here (e.g., Morávek 1971): 1. Veins related to reverse fault zones (strike NNE-SSW, dip $30\text{--}50^\circ$ SE; 4–7 km long). Individual veins are up to 2 m wide and accompanied by subhorizontal tension gashes; 2. Irregular to ladder-like quartz stockworks spatially related to WNW- and NNE-trending dikes (microdiorite, porphyry, and lamprophyre); and 3. Irregularly-shaped quartz stockworks grading into low-grade impregnation zones. The relative age of the individual ore types is difficult to determine. Type 1 ore zones locally displace some of the WNW-trending dikes and quartz veins/stockworks. The prominent feature of whole Jílové belt is subvertical NNE-trending cleavage with marked subhorizontal stretching lineation. The formation was broadly coeval with the intrusion of the Sázava tonalite (354 ± 4 Ma; U-Pb zircon; Janoušek et al. 2004). Formation of steeply inclined magmatic dikes, tension joints and quartz veins/stockworks, all trending WNW–ESE, occurred under identically oriented subhorizontal extension. The tectonic activity on the NNE-trending fault zones that host type 1 ores records two stress phases: an older strike-slip regime and a younger compressional phase (NW-SE oriented). The later phase was dated to 339.0 ± 1.5 Ma (Zacharias et al. in press).

The **Krásná Hora deposit (KHD)** represents a rare type of Au-Sb mineralization, whose origin is still unresolved (single Au-Sb mineralization event or two superimposed events, where the Au-phase is older). The ore zones are related to E-W trending steep tectonic zones, mostly in the Těchnice-type porphyric granodiorite of the CBPC. The formation of the mylonitic zones as well as of Au-quartz veins was preceded by the formation of the E-trending dikes (minette and lesser granodiorite porphyry). The age of the swarm of minettes at Krásná Hora is unknown. A single dike of minette located in the TB unit, about 30 km to the W from the KHD, was dated to 338 ± 0.5 Ma (Žák et al. 1997).

The **Libčice deposit (LD)** is located at the NW periphery of the CBPC in the rocks of the TB unit. Mineralization is represented by a single quartz vein, up to 2 m thick, which thermally recrystallized during the intrusion of the peripheral granite of the CBPC (Hrstka et al. 2011). Weakly inclined (about 30° S) dikes of aplite crosscut the Au-mineralized quartz vein, the peripheral granite and also the N-S trending dikes of kersantite. The N-trending steep quartz veins (up to several cm thick only) are only weakly mineralized or even barren and probably postdate the aplite. The regional stress field therefore should evolve from N-S to E-W subhorizontally oriented extension (both probably under strike-slip regime), with a temporal switch to a compression phase, during which a weakly inclined dike

of aplite intruded.

The **Bělčice deposit (BD)** is hosted within the endocontact of the Blatná granodiorite (346 ± 2 Ma; SIMS U-Pb zircon, Janoušek et al. 2010) of the CBPC, close to the border with the MLD unit. The ore and gangue minerals are younger than the granodiorite host by approx. 8 Ma, as revealed by dating of hydrothermal molybdenite (338.5 ± 1.3 Ma Re-Os; Zachariáš and Stein 2001). The quartz veins are highly irregular in a horizontal cross-section (adit level); however, on a vertical section they resemble an irregular enechelon array of tension fractures, pointing to subvertical orientation of the extension stress axis during vein formation.

3 Age relationships between the gold-bearing events and the magmatic and metamorphic processes

Two major intervals of gold deposition in the metallogenic zone along the northwestern margin of the CBPC were identified: 1) the 347 to 341 Ma gold-mineralization interval overlaps with the intrusive activity of the Blatná high-K suite of the CBPC. The associated gold deposits (Mokrsko and Petrůvkova hora) exhibit strong affiliation to the group of intrusion-related gold deposits; and 2) the 340 to 337 Ma gold-mineralization interval, which is coeval with the ultrapotassic magmatism in the CBPC and in the MLD areas and which is also coeval with the approx. 340 Ma peak-metamorphic event in the MLD unit (e.g. Kröner et al. 2000). Gold deposits (Jílové, Bělčice, Libčice deposits) formed during this interval resemble more or less “classical” orogenic gold-type deposits; however, they are relatively rich in Bi-Te accessory phases. The Au-Sb type of gold mineralization (Krásná Hora deposit) because of the age of the mineralization, most probably also belongs to the latter group.

4 Depth of gold deposits formation

Fluid inclusion studies (e.g. Zachariáš et al. 1997, 2001; Hrstka et al. 2011) revealed the upper limit of the quartz gangue formation at about 300–400 MPa, corresponding to a depth of about 11–15 km, for the Mokrsko and Petrůvkova hora intrusion-related gold deposits and about 200–250 MPa (i.e. depth of 7.5–9 km) for the orogenic gold deposits (Bělčice, Jílové, Libčice). The conditions of Au deposition are difficult to define precisely, but the most frequent interval is 230 to 130 MPa; conversion to a depth interval is however problematic due to uncertainty in the hydrostatic or lithostatic pressure load.

5 Relation of gold deposits to large-scale crustal structures

Three large-scale deep crustal tectonic zones run parallel (i.e. NW-SE) to the boundary between the TB and MLD units and to the strike of the CBPC: one is situated along the NW-margin of the CBPC, another one is situated approximately in the middle of the CBPC and the last

one rims the CBPC at its SE-margin. The SE zone represents a ductile detachment zone dipping moderately to the NW, along which the CBPC subsided and the MLD block was uplifted. The NW zone, based on geophysical data (seismic, gravity), is steeply inclined and allowed about 6 km uplift of the CBPC relative to the TB. Numerous kinematic indicators at outcrops, however, point to subhorizontal movements in this zone. The wrench-like tectonics therefore probably overprinted the older tectonic signature. Gold deposits (irrespective of genetic type) are mostly located in between the northwestern and the central tectonic zones, and are lacking in the area between the central and the southeastern tectonic zones.

6 Summary

The spatial distribution of gold deposits in the central part of the Bohemian Massif, structural analysis of the individual deposits and the available geochronological data point to the formation of gold-bearing quartz veins in the study area exclusively in local extensional settings with NE-SW to N-S -oriented subhorizontal extension. The gold mineralization on a regional scale is coeval with the main to late stages of magmatic activity of the CBPC. On a deposit scale, gold ores and related gangue, however, usually postdate local intrusive rocks of the CBPC. Deposits with marked affinity to the group of intrusion-related gold deposits seem to follow the high-K calc-alkaline magmatism within the CBPC. Fluid inclusion data indicate that early-to-main quartz gangue formation occurred at depths of 11-15 km below the paleosurface for the intrusion-related gold-deposits and at depths of 7.5-9 km for the orogenic gold-deposits. This is in accordance with the slight delay of the formation of the latter group (340-337 Ma), relative to the former group (347-341 Ma). This also documents the formation of orogenic gold deposits during the uplift of the CBPC block.

Acknowledgements

This research benefited from the support of the Czech Science Foundation, from research support from the Ministry of Education to the Faculty of Science, Charles University (MSM0021620855) and from the UNESCO-IGCP project No. 540 "Fluid inclusions in orogenic Au deposits".

References

- Boiron MC, Barakat A, Cathelineau M, Banks DA, Durisova J, Moravek P (2001) Geometry and P-V-T-X conditions of microfissural ore fluid migration: the Mokrsko gold deposit (Bohemia). *Chem Geol* 173:207–225
- Dörr W, Zulauf G (2010) Elevator tectonics and orogenic collapse of a Tibetan-style plateau in the European Variscides: the role of the Bohemian shear zone. *Int J Earth Sci* 99:299–325
- Hrstka T, Dubessy J, Zachariáš J (2011) Bicarbonate-rich fluid inclusions and hydrogen diffusion in quartz from the Libčice orogenic gold deposit, Bohemian Massif. *Chem Geol* 281:317–332
- Janoušek V, Braithwaite CJR, Bowes DR, Gerdes A (2004) Magma-mixing in the genesis of Hercynian calc-alkaline granitoids: an integrated petrographic and geochemical study of the Sazava intrusion, Central Bohemian Pluton, Czech Republic. *Lithos* 78:67–99
- Janoušek V, Wiegand BA, Žák J (2010) Dating the onset of Variscan crustal exhumation in the core of the Bohemian Massif: new U–Pb single zircon ages from the high-K calc-alkaline granodiorites of the Blatná suite, Central Bohemian Plutonic Complex. *J Geol Soc London* 167:347–360
- Morávek P (1971) Ore-deposits structure and mineralization of the Jílové gold-mining district (in Czech with extensive English summary). *Sborník geologických Věd, řada LG* 13:1–170
- Morávek P, Pouba Z (1987) Precambrian and Phanerozoic history of gold mineralization in the Bohemian Massif. *Econ Geol* 82:2098–2114
- Morávek P, Pouba Z (1990) L'or dans la metallogenie du massif de Bohême. *Miner Depos* 25 (Suppl):S90–S98
- Morávek P, Pouba Z, Janatka J, Malec J, Novák F, Litochleb J, Váňa T, Veselý J, Vaněček M, Kalenda Z, Aichler J, Hauk J, Skácel J, Punčochář M, Mrázek I, Tásler R, Klominský J, Duda J, Ďurišová J, Sztacho P, Pudilová M, Soukup B, Šponar P, Doškář Z, Květoň P (1992) Gold in the Bohemian Massif. Czech Geological Survey, Prague, 245 p. (in Czech with extensive English summary)
- Pitra P, Burg JP, Guiraud M (1999) Late Variscan strike-slip tectonics between the Teplá-Barrandian and Moldanubian terranes (Czech Bohemian Massif): petrostructural evidence. *J Geol Soc London* 156:103–120
- Rajlich P, Schulmann K, Synek J (1988) Strain analysis of conglomerates in the Central Bohemian shear zone. *Krystalinikum* 19:119–134
- Zachariáš J, Žák K, Pudilová M, Snee LW (in press) Multiple fluid sources/pathways and severe thermal gradients during formation of the Jílové orogenic gold deposit, Bohemian Massif, Czech Republic. *Ore Geol Rev*
- Zachariáš J, Stein H (2001) Re-Os ages of Variscan hydrothermal gold mineralisations, Central Bohemian metallogenic zone, Czech Republic, in Piestrzyński, A., et al. eds., *Mineral Deposits at the Beginning of the 21st Century: Swets & Zeitlinger Publishers Lisse*, p. 851–854
- Zachariáš J, Pudilová M, Žák K, Morávek P, Litochleb J, Váňa T, Pertold Z (1997) P-T conditions, fluid inclusions and O, C, S isotope characteristics of gold-bearing mineralizations within the Central Bohemian Metallogenic Zone. *Acta Universitatis Carolinae – Geologica* 41:167–178
- Zachariáš J, Pertold Z, Pudilová M, Žák K, Pertoldová J, Stein H, Markey R (2001) Geology and genesis of variscan porphyry-style gold mineralization, Petrackova hora deposit, Bohemian Massif, Czech Republic. *Miner Depos* 36:517–541
- Žák K, Vlašímský P, Snee LW (1997) $^{40}\text{Ar}/^{39}\text{Ar}$ cooling ages of selected rocks of the Příbram ore region and the question of timing of sulfidic hydrothermal mineralization. *Zprávy o geologických výzkumech v roce 1997 (Research in Geosciences in 1997)* 172–173

Re–Os age dating of the Hadamengou Au deposit, Inner Mongolia, China and its geological significance

Wei-Bo Zhang

China University of Geosciences, Beijing 100083, China

Wan-Rong Hou

No.2 Gold Geological Party of CAPG, Huhhot 010010, China

Feng-Jun Nie

Institute of Mineral Resources, 26 Baiwanzhuang Road, Beijing 100037, China

Abstract. The Hadamengou deposit, located in western Inner Mongolia, China, is one of the largest Au deposits in northern China. The deposit is hosted by Archean metamorphosed volcano-sedimentary sequences of the Wulashan Group in the southern margin of Wulashan anticlinorium of Yinshan uplift and it is surrounded by a number of middle to late Paleozoic granitoid dikes and a batholith. The Au mineralization occurs in quartz-K feldspar and quartz veins related to these intrusions. Isotopic dating on molybdenite separates from the veins yields a Re–Os isochron age of 386.6 ± 6.1 Ma, which shows the main metallogenic epoch is Early Devonian, although later hydrothermal activity is probably superimposed on the early stage. The deposit formed during Devonian intracontinental extensional tectonics after arc-continent collision.

Keywords. Hadamengou, gold deposit, Re–Os, Inner Mongolia, northern North China Craton

1 Introduction

The Hadamengou gold deposit is located 20 km northwest of Baotou City, Inner Mongolia, China, at longitude $109^{\circ}33'15''\text{E}$ and latitude $40^{\circ}41'45''\text{N}$ (Fig.1). The deposit was discovered in 1986, the proven total reserves are 127t Au, with an average grade of 4.13 g/t. The deposit is located at the intersection of the westernmost part of the northern margin of the North China Craton uplift (Inner Mongolian axis) and the Ordos depression. Numerous gold occurrences are scattered within the mainly Precambrian outcropping rocks of the region. The Hadamengou gold deposit is the most important of these in the northwestern North China Craton, and the associated hydrothermal activity is considered to be significant in helping to understand the complex tectonic evolution history of the craton margin. Therefore, both Chinese and foreign geologists have conducted a number of geochronological studies of the magmatic rocks and gold deposits in the region. Over the past ten years, major alteration and gangue minerals related to the gold mineralization were dated by Ar–Ar, K–Ar, SHRIMP U–Pb, Rb–Sr and other methods, with resulting ages spanning range of 311–386 Ma (table1). In the present study, we conclude that the molybdenite Re–Os method directly provides the best estimate of the mineralization age, being more accurate than the previous ages obtained by other methods. Field observations show that the molybdenite is hosted in fractures in the auriferous quartz veins and gold-bearing

potassically altered rocks, and polished section studies indicate the molybdenite is coeval with gold and pyrite. Therefore, dating of the molybdenum provides the age of gold mineralization. In this study, we carried out Re–Os dating investigations on molybdenite from the Hadamengou Au deposit to clearly constrain the timing of mineralization.

2 Geological Setting

The Hadamengou gold deposit and surrounding district comprises mainly Archean metamorphic sequences of the Jining and Wulashan Groups and Proterozoic volcano-sedimentary rocks of the Sertengshan and Chaertai Groups. Paleozoic marine sedimentary rocks and Mesozoic subaerial volcano-sedimentary rocks are also present (Nie et al., 1994). The Wulashan Group high-grade metamorphic rocks are the most important host rocks of the Hadamengou gold deposit. The Huhhot–Baotou and Linhe–Jining deep-crustal faults control the distribution of the magmatic rocks and gold deposits (Fig.1). Post-metamorphic Precambrian and Phanerozoic plutons, stocks, and dikes, composed of diabase, quartz diorite, granodiorite, diorite porphyry, aplite, pegmatite, biotite, granite, and syenite, are reported from the district (Nie et al., 1994; Hart et al., 2002). The largest intrusions in the area include the late Paleozoic Dahuabei granitoid batholith (200 km^2) and Paleozoic Shadegai granitoid batholith. The Dahuabei batholith outcrops about 10 km west of the Hadamengou orebodies and consists of a medium- to coarse-grained, alkali-feldspar biotite granite that is texturally zoned with a coarser-grained center (Gan et al., 1994; Hart et al., 2002). More than 90 percent of the gold-bearing quartz–K feldspar and quartz veins are distributed in garnet–biotite–plagioclase gneiss, hornblende–plagioclase gneiss, and amphibolite of the Wulashan Group. Locally, gold-bearing quartz veins are also hosted by granulite, leptyte, and magnetite-bearing quartzite.

The gold-bearing veins groups can be divided into seven main orebodies, namely the No.1, No.13, No.24, No.49, No.59, No.113, and No.313 vein groups. There are a number of distinct gold veins within each group. Most veins range in length from 50 to 2200 m, and in width from 0.6 to 9.5 m. Commonly, the Au mineralization occurs in single irregular veins, stratabound layers, or lenses, which are controlled by

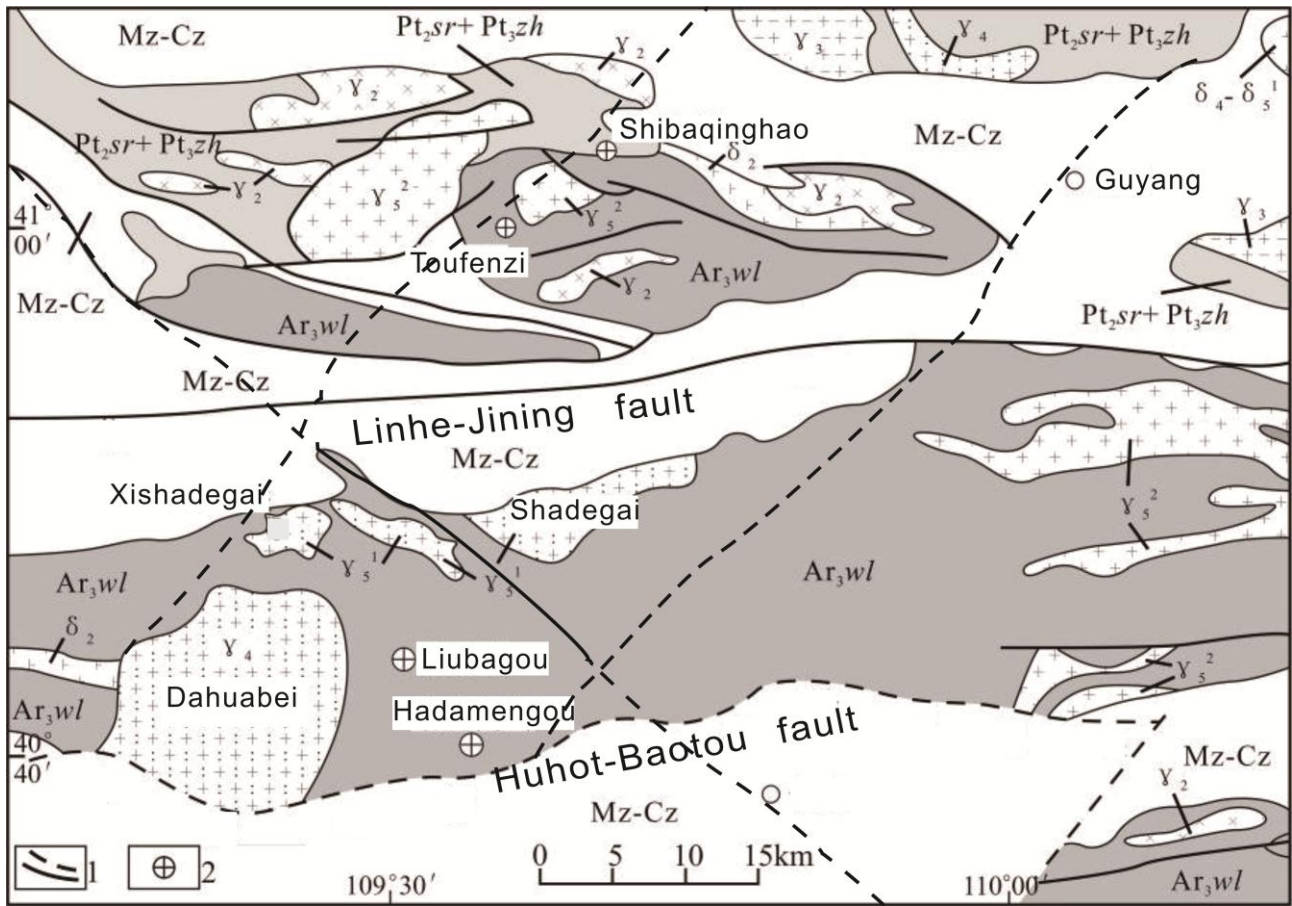


Figure 1. Simplified Geological Map of the Hadamengou region showing the location of the Hadamengou Au deposit and the intrusions in this area (modified after the Gold Headquarters of the CPAF,1995).

1–Fault and inferred fault; 2–Gold deposit; Mz-Cz–Jurassic-Cretaceous sedimentary and volcanic rocks; Pt_{2sr}+Pt_{3zh}–Middle Proterozoic greenschist of the Sertengshan Group and Late Proterozoic metamorphosed volcano-sedimentary rock of the Chaertai Group metamorphic rocks; Ar_{3wl}–Archean gneiss, marble, amphibolite and migmatite of the Wulashan Group; γ_5^2 –Yanshanian granitoid intrusion; γ_4 - γ_5^1 –Hercynian-Indosinian granitoid intrusion; γ_3 –Caledonian granitoid intrusion; γ_2 –Proterozoic granitoid intrusion; δ_4 - δ_5^1 –Hercynian-Indosinian diorite intrusion; δ_2 - Proterozoic diorite intrusion.

Table 1. Geochronology of Dahuabei intrusion, gold-bearing potassium altered rocks and gold ores of the Hadamengou mineralized district, Inner Mongolia

Sample detail	Dated minerals/rocks	Dating method	Age (Ma)	Data sources
Potassic altered rock in Piedmont Potassic Alteration Zone	K-feldspar	K-Ar	311.5±6.1	Gold Headquarters of the CPAF,1995
Potassic altered rock in Piedmont Potassic Alteration Zone	Sericite	Ar-Ar	323+3	Nie et al.,2005
Vein selvage with potassically-altered wall rock #113 Auriferous quartz vein	Fuchsite molybdenum	Ar-Ar Re-Os	351.8±0.8 386.6±6.1	C.J.R.Hart, 2002 This paper
Monzogranite in Dahuabei granitoid batholith	zircon	SHRIMP U-Pb	353±7	Miao et al.,2001
Monzogranite in Dahuabei granitoid batholith	whole rock	Rb-Sr	322±22	Nie et al.,1994

Table 2. Re-Os isotopic analyses of molybdenite separate from the Hadamengou Au deposit, Inner Mongolia

No. samples	Weight (g)	Re(μg/g)		Re ¹⁸⁷ (μg/g)		Os ¹⁸⁷ (ng/g)		Model age(Ma)	
		Measured	2σ	Measured	2σ	Measured	2σ	Measured	2σ
H11311	0.02014	9.353	0.076	5.878	0.048	37.77	0.35	384.4	5.6
H11348	0.04786	10.90	0.09	6.853	0.058	44.59	0.42	389.3	5.8
WLS-1	0.04867	7.473	0.061	4.697	0.038	30.25	0.25	385.3	5.5
WLS-4	0.08035	4.201	0.033	2.640	0.021	17.07	0.15	386.7	5.5

Decay constant: $\lambda(^{187}\text{Re}) = 1.666 \times 10^{-11}/\text{year}$. The uncertainty in each individual age determination was about 1.02% including the uncertainty of the decay constant of ¹⁸⁷Re, uncertainty in isotope ratio measurement, and spike calibration.

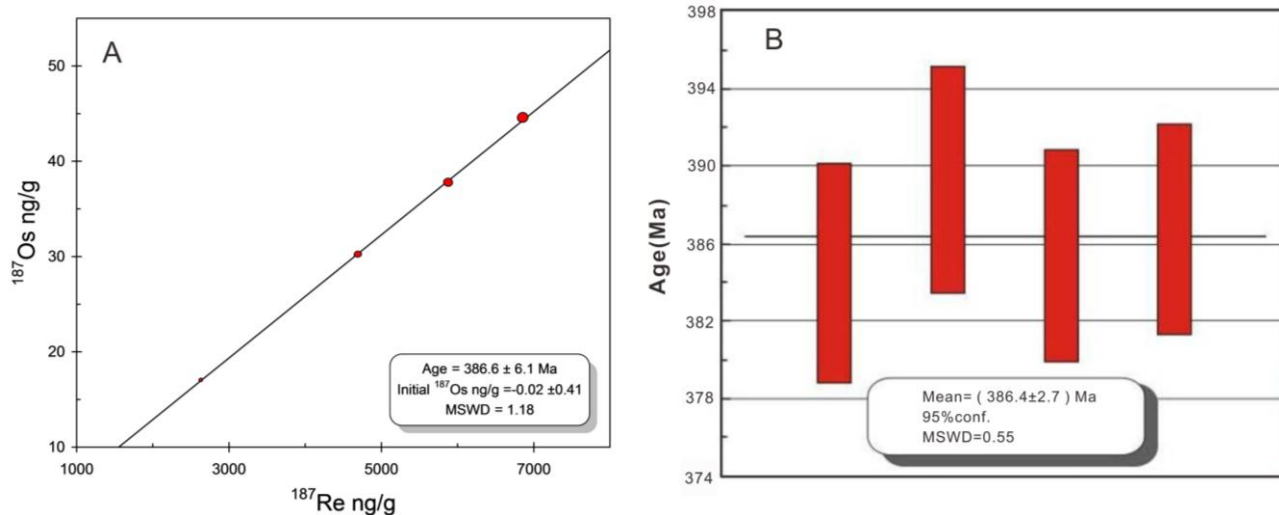


Figure 2. Re-Os isotopic isochron diagram (A) and weighted mean model age diagram (B) of molybdenite separates from the Hadamengou Au deposit, Inner Mongolia

E-W- and NE-SW-trending structures. In addition to veining, ore styles may include stockwork, breccia, and disseminated to replacement type mineralization. Metallic minerals are mainly pyrite, with lesser galena, molybdenite, chalcopyrite, sphalerite, magnetite, and hematite. Gangue minerals are quartz, K-feldspar, and plagioclase. Wallrock alteration includes K-feldspar, silicification, sericitization, chloritization, and carbonatization. The deposit can be divided into quartz-K-feldspar, K-feldspar-quartz-pyrite, quartz-sulfide, and quartz-calcite paragenetic stages.

3 Sampling and analytical methods

Based on field, petrographic, and mineralogical studies, we selected four molybdenite samples from the quartz-sulfide stage of the No.113 gold veins of Hadamengou gold deposit for dating. Sample H11311 was collected from an elevation of 1305 m and sample WLS-1 was collected from an elevation of 1185 m, with gold-bearing quartz veins with molybdenite at both locations. Samples H11348 and WLS-4 are K-feldspar altered gold-bearing gneiss containing molybdenite.

The Re-Os isotopic analyses were performed at the National Research Center of Geoanalysis, Chinese Academy of Geosciences. The details of the chemical procedures have been described by Du et al. (1995, 2001), Shirey et al. (1995) and Markey et al. (1998).

4 Results

Results of molybdenite Re-Os dating are listed in Table 2. The concentrations of Re and ^{187}Os range from 4.201 to 10.90 ppm and 17.07 to 44.59 ppb, respectively. The four samples give a Re-Os model age of 384.4 ± 5.6 Ma to 389.0 ± 5.8 Ma and a weighted mean age of 386.4 ± 2.7 Ma (Fig.2). The data, processed using the ISOPLOT/Ex program (Ludwig, 2004), yielded an isochron age of 386.6 ± 6.1 Ma, with $\text{MSWD}=1.18$, and an initial ^{187}Os of

0.02 ± 0.41 ppb (Fig. 2). The nearly identical model age and isochron age suggest that the analytical results are reliable.

5 Mineralization age and its geological significance

The Gold Headquarters of the CPAF (1995) first reported the mineralization as middle Hercynian. Nie et al. (2005), however, reported Ar-Ar ages for sericite from potassically altered rock, with average age of 323 ± 3 Ma, suggesting some mineralization in the area also took place in the Hercynian. Hart et al. (2002) reported Ar-Ar ages for fuchsite from a vein selvage within potassically-altered wallrock of 351.8 ± 0.8 Ma, which is identical to the SHRIMP ages of the Dahuabei granite (353 ± 7 Ma, Miao et al., 2001), and thus the intrusion may have provided at least the heat for the mineralization. Our new study yielded ages of molybdenites from of 386.6 ± 6.1 Ma (early Hercynian), the oldest dates yet on mineralization. These age data cumulatively record a complex gold metallogenic history, with different periods of hydrothermal activity and gold deposition at the Hadamengou gold deposit.

The Hadamengou gold deposit is located in the northwestern North China Craton, where the opening and closure of an ocean basin is documented during early Paleozoic (Caledonian) orogenesis and inevitably impacted the adjacent margin of the craton (Shao, 1991). The 386 Ma Hadamengou gold deposit formed subsequent to the Caledonian orogenesis. It is a product of magmatic-hydrothermal activity during middle Paleozoic extension (Zhang et al., 2010). In Early Devonian, the extension led to reactivation of the Kaiyuan-Chongli-Guyang regional fault that served as the conduit for magmas and magmatic hydrothermal fluid flow. These magmas formed the alkaline igneous complexes and the fluids of the Hadamengou gold deposit.

6 Conclusions

Four molybdenite samples yielded an isochron age of 386.6 ± 6.1 Ma (2σ), with an initial ^{187}Os of 0.02 ± 0.41 ppb ($\text{MSWD}=1.18$), and model ages for individual analyses range from 384.4 ± 5.6 Ma to 389.0 ± 5.8 Ma. These data provide important information about the geological evolution and mineralization of this region. Combined with data from alkaline igneous complexes in this region, the formation of the Hadamengou Au deposit during Early Devonian time was closely related to the magmatic-hydrothermal events during post-Caledonian regional extension.

Acknowledgements

We wish to thank Wei Li, Zhenning Pan and Jun Xie at Inner Mongolia Bao Tou Xinda Gold Mining Industry Co., Ltd. for cooperation with the field work. We are grateful to convenor Dr. Richard Goldfarb for his incisive and constructive comments on the manuscript. Finally, this project was financially supported by a grant (No.41030421) to FJN from National Natural Science Foundation of China (NSFC), and is a part of one of the State Basic Scientific Research Projects (No.2013CB429805) from the Ministry of Science and Technology, China.

References

- Du AD, He HL, Yin NW (1995) A study of the rhenium–osmium geochronometry of molybdenites. *Acta Geological Sinica* (8) 171–181.
- Du AD, Wang SX, Sun D, Zhao D, Liu D (2001) Precise Re–Os dating of molybdenite using Carius tube, NTIMS and ICPMS. In: Piestrzynski (Ed.), *Mineral Deposits at the 21st Century*: 405–407.
- Gan SF, Qiu YM, Yang HY, Van Reenen DD (1994) The Hadamengou mine: A typical gold deposit in the Archean granulite facies terrane of the North China craton. *International Geology Review* 36(9): 850–866.
- Gold Headquarters of the CPAF(1995) *Geology of Hadamengou pegmatitic gold deposit in Inner Mongolia*. Seismological Press(Beijing):89–108.
- Hart CJ, Goldfarb RJ, Qiu YM, Snee L, Miller LD, Miller ML (2002) Gold deposits of the northern margin of the North China craton: Multiple late Paleozoic–Mesozoic mineralizing events. *Mineralium Deposita* 37(3): 326–351.
- Ludwig KR (2004) *Isoplot/Ex, Version 3.0: a Geochronological Toolkit for Microsoft Excel*. Berkeley Geochronology Center, Berkeley, CA
- Markey R, Stein H, Morgan J (1998) Highly precise Re–Os dating for molybdenite using alkaline fusion and NTIMS. *Talanta* 45: 935–946.
- Miao LC, QiuYM, Guan K, McNaughton N, Qiu YS, Luo ZK, Groves DI (2001) A chronological study of SHRIMP U–Pb of zircon from the Dahuabei intrusion in the Wulashan area, Inner Mongolia. *Geological Review* 47(2): 169–174.
- Nie FJ, Bjorlykke A (1994) Lead and sulfur isotope studies of the Wulashan quartz–K feldspar and quartz vein gold deposit, southwestern Inner Mongolia, People's Republic of China. *Economic Geology* 89: 1289–1305.
- Nie FJ, Jiang SH, Liu Y, Hu P (2005) Re-discussions on the time limitation of gold mineralization occurring within the Hadamengou deposit, south-central Inner Mongolia autonomous region. *Acta Petrologica Sinica* 21(6): 1719–1728.
- Shao JA (1991) The crust revolution in the middle part of the northern margin of the Sino-Korean plate. Peking University Press. Beijing: 1–130.
- Shirey SB, Walker RJ (1995) Carius tube digestion for low-bank rhenium–osmium analysis. *Analysis Chemical* 67: 2136–2141.
- Zhang XH, Zhang HF, Jiang N, Zhai MG, Zhang YB (2010) Early Devonian alkaline intrusive complex from the northern North China craton: a petrological monitor of post-collisional tectonics. *Journal of the Geological Society, London*(167): 717–730.

S 3.8

Hydrothermal ore-forming processes

Convenors:

Thomas Wagner & Kalin Kouzmanov

Ag-Hg vein deposits hosted by Triassic dolostones from the Mina de la Guerra Antigua, Villahermosa del Río (Castelló, Spain)

Albert Acedo, Marina Galindos, Miriam Pastor, Ricard Segura, Sandra Amores, Joan Carles Melgarejo
Departament de Cristal·lografia, Mineralogia i Dipòsits Minerals, Universitat de Barcelona, Barcelona, Catalonia, Spain

Abstract. Cu-As-Ag-Hg veins hosted in lower Triassic limestones were mined in the vicinity of Villahermosa del Río town, Castelló, Spain. Zoned tennantite is the main primary ore, accompanied by minor amounts of enargite, galena and pyrite. Tennantite is locally enriched in Sb, Hg and Ag. The origin of sulphur is stated to be the framboidal pyrite associated with the hosting dolomitized organic-rich limestones. Tetrahedrite has been replaced during supergene processes by complex arsenates and carbonates assemblages along with native silver and several chlorides and sulphochlorides of Ag and Hg. Triassic evaporites could have been the source of Cl.

Keywords. vein, tetrahedrite, mercury, weathering

1 Introduction

MVT deposits have been extensively mined in Western Europe, and contain large reserves for Pb-Zn in this region. Most MVT deposits in Europe have been traditionally associated to Mesozoic extensional tectonics related with the break-up of Pangea. However, connection with Alpine tectonism cannot be ruled out (Muechez and Heijlen, 2003; Muechez et al., 2005).

The Iberian Ranges in Spain contain many Mesozoic limestones-hosted Pb-Zn MVT deposits, as well as several barite veins, locally enriched in Sb-Hg as in the Espadà ridge case (Tritlla & Cardellach, 1991, 1993). Grandia et al. (2000) reported an age of 62.6 ± 0.7 Ma for one of the Pb-Zn deposits from the Maestrat Basin, N of the Castelló province, indicating thus this deposits precipitated during rift or post-rift stages in Early Tertiary times.

A striking mineralogical anomaly in this general scenario occurs near the Villahermosa del Río town, N of the Castelló province. Tennantite veins were mined during 19th century in the Minas de la Guerra Antigua and Amorosa (San Rafael claim) along deep trenches and galleries. Although the nature of the extracted ores is not known, they are traditionally said to have been mined for copper. Cinnabar is also reported in the association (Cócera et al., 2010), suggesting similarities with the mineral associations described in the Ba-Sb-Hg veins of the close Espadà ridge.

The aim of this contribution is to provide data on the geology and petrography of the Villahermosa deposits, in order to constrain the origin of these deposits.

2 Geology

The Iberian Chain in the Iberian Peninsula is a large mountain system of about 600 km long that extends

roughly NE-SW from the Basque Country to the Mediterranean Sea. The Iberian Chain is an intraplate range that resulted from the Paleogene (Late Eocene-Early Oligocene) inversion of the NW-SE trending Iberian Rift Basin (Salas and Casas, 1993). The Iberian Rift developed between the Late Permian and the Late Cretaceous in two major stages of rifting, followed by two stages of post-rift thermal subsidence (Salas et al., 2001). Rifting created successive sedimentary basins and sub-basins. The Penyalgosa sub-basin, which encloses the study area, is located in the south-eastern margin of Maestrat basin. Its structure is characterized by a system of NE-SW trending listric fault system recording two periods of rifting (Climent-Doménech et al., 2006): a) Triassic-early Jurassic; b) late Jurassic-early Cretaceous.

The Triassic sequence in the study area is not complete, and in the proximities of Villahermosa del Río the outcrops are limited by tectonic contacts (Canerot & Gautier, 1966; Fig. 1).

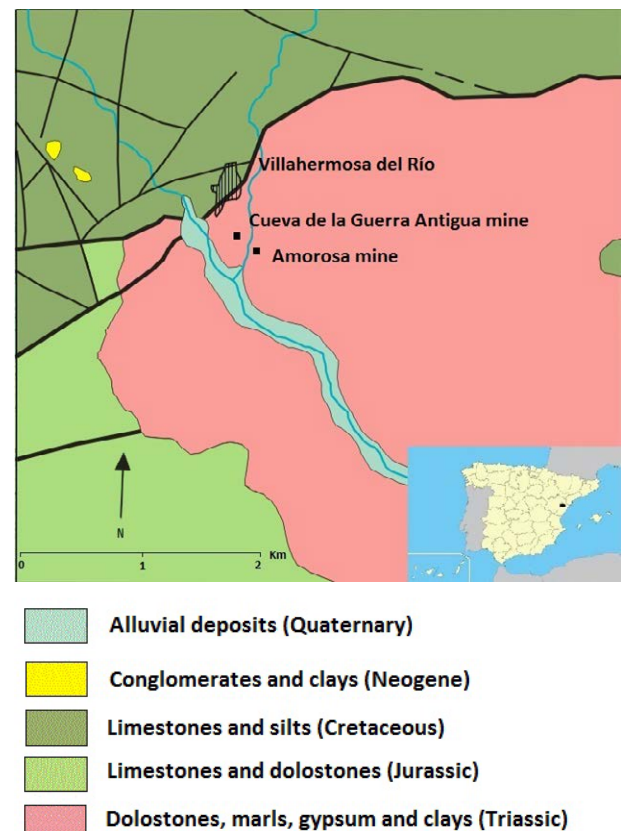


Figure 1. Geological map of the study area (adapted from IGME, 1979, slightly modified).



Figure 2. Aspect of the veins in the Cueva de la Guerra Antigua mine.

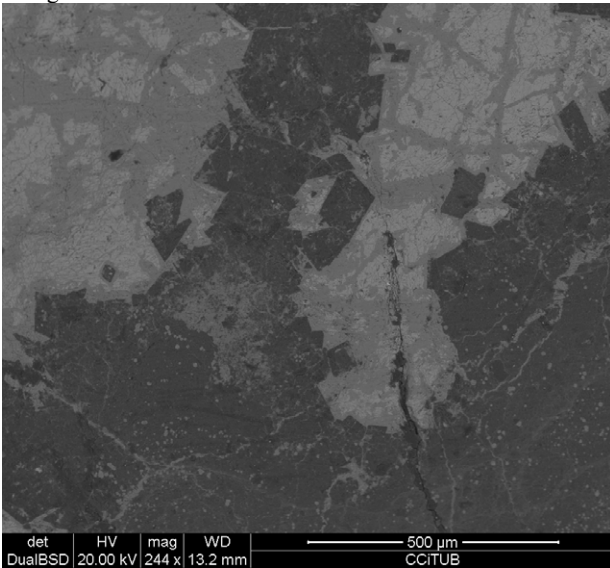


Figure 3. Baroque dolomite at the contact of the tennantite vein (brighter, veined by secondary arsenates) with the host rock; note the abundance of framboidal pyrite. SEM image, BSE mode.

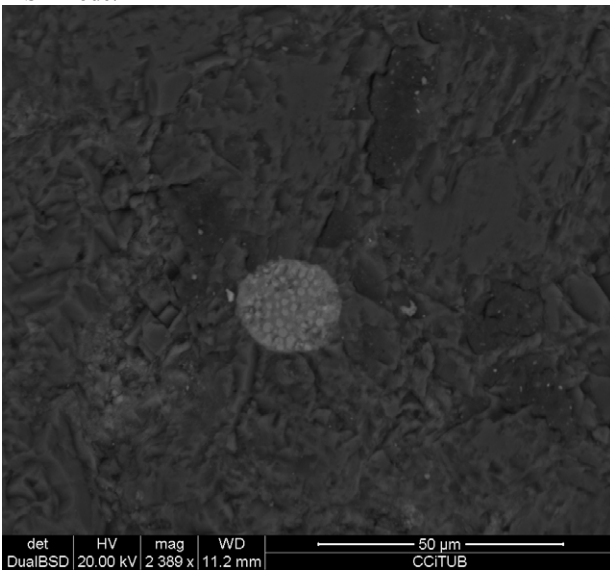


Figure 4. Detail of pyrite framboids. SEM image, BSE mode.

The outcropping Triassic succession is more than 200 m thick (IGME, 1979). It comprises up to 100 m of clays and marls interbedded with gypsum beds in Middle Muschelkalk facies, nearly 50 m of dolostones

of the Upper Muschelkalk facies and other evaporite-bearing series interbedded with marls, clays and dolostones (Keuper facies, more than 50 m thick). The Cretaceous series consist of more than 1300 m of carbonate facies, ranging from Early Barremian to Alban in age (Climent-Doménech et al., 2006).

The compression during the Paleogene produced the reactivation of Mesozoic fractures and the activation of strike-slip faults trending approximately NE-SW.

3 Structure of the deposit

The deposit is hosted in dolostones of the Upper Muschelkalk facies. Mineralization could be described partially as stratabound. The veins are discontinuous and no more than 2 cm thick. Most of these veins and veinlets are gently dipping to the SW (15-20°) and sub-parallel to the bedding. In addition, some veins fill sub-vertical joints (Fig. 2). The contact with the hosting dolostones is irregular and clearly replacive. Corroded fragments of the host dolomites as inclusions within the veins are observed.

The galleries were mined following the veins on both sides of a large open joint, which is related with the activity of strike-slip sub-vertical NW-SW trending faults. Mineralization is absent along these faults or the joint, which only contain carstic calcite infilling.

The mineral reserves are small, less than 1,000 t (Grandia et al., 2003).

4 Mineralogy and textures

The hosting marls and limestones are dolomitized. Millimetric euhedral saddle dolomite crystals occur at the contact of the veins with the host rocks (Fig. 3). Framboidal pyrite is remarkably abundant in the host rocks (Fig. 4).

The main ore minerals in these veins are members of the tetrahedrite-tennantite series. Vein infilling is almost complete; drusy porosity is rare. Tetrahedrite grains are generally anhedral, although scarce euhedral tetrahedral crystals can be observed within geodic porosity. All the analysed compositions clearly lie into the tennantite domain (Ochando et al., 1997). However, the crystals show an oscillatory zoning generally due to slight variations in the Sb and As content (Fig. 5). Although Hg and Ag content are generally below detection limit of the microprobe, the concentration on these metals is remarkable in some analysed Sb-rich tennantite crystals. Thus, compositions into the argentotennantite domain are raised. The content of other elements such as Bi, Co, Te, Pb and Se are below the detection limits.

Enargite has been observed only in some areas of the Amorosa mine. It occurs as scarce subhedral prismatic crystals less than 1 cm in length. This phase generally shows alteration to supergene minerals.

Galena and sphalerite are rare in these deposits and only some anhedral grains occur as minute inclusions of few microns in size into tetrahedrite crystals.

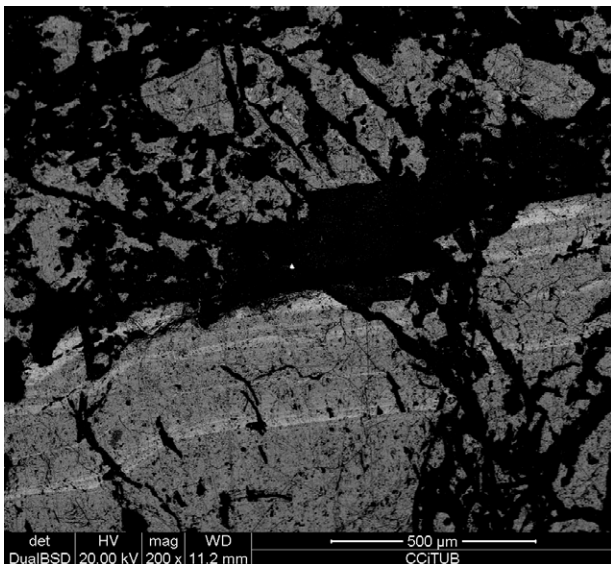


Figure 5. Zoned tennantite crystals, with brighter bands enriched in Sb. Note the occurrence of a small native silver grain (bright) outstanding in the dark matrix of secondary arsenates. SEM image, BSE mode.

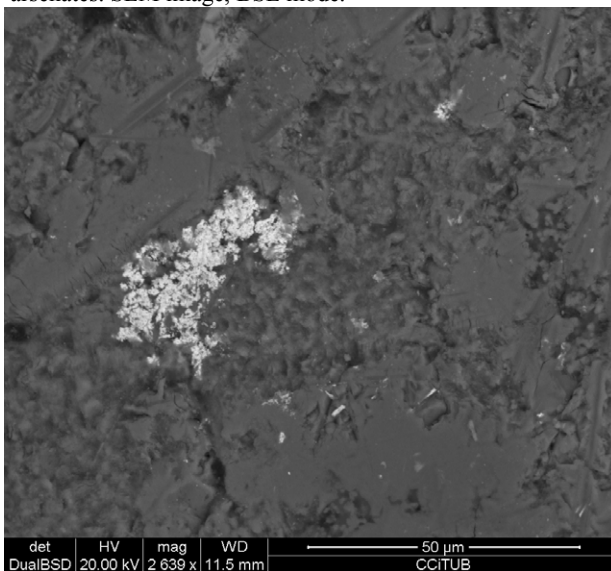


Figure 6. Cinnabar aggregates (brighter) associated with supergene conicalcrite $\text{CaCu}(\text{AsO}_4)(\text{OH})$ (dark). Note iltisite needles in the same association. SEM image, BSE mode.

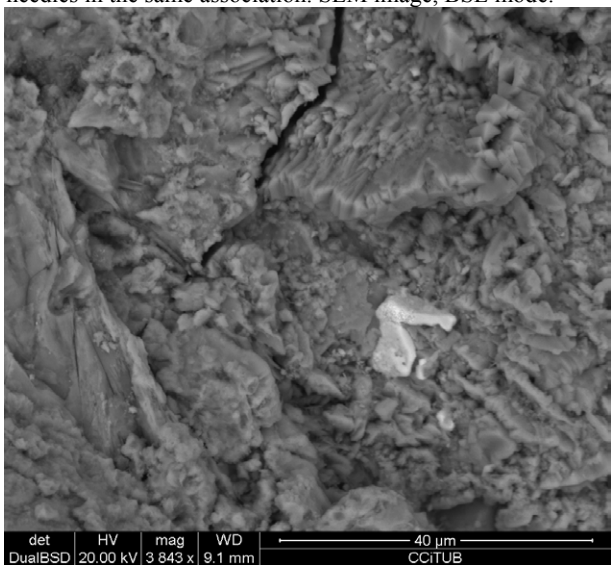


Figure 7. Chlorargyrite crystals (brighter) overgrowing atacamite prismatic crystals. SEM image, BSE mode.

Chalcopyrite is also scarce and has been detected only in some late irregular veinlets probably replacing tennantite. These veinlets are less than 1 mm in thickness and do not pass to the host rock.

Primary ores have been strongly altered to a supergene association comprising copper arsenates, sulphates, carbonates and chlorides (Cócera et al., 2010). In addition, study on polished sections reveals the occurrence of a complex paragenesis of Hg- and Ag-minerals, including halide minerals. All these phases and the above mentioned supergene minerals are observed to form intergrowths.

Cinnabar, which is common in the deposit, is the dominant Hg-bearing mineral. It is found as discrete anhedral grains, less than 5 μm in diameter, or in irregular powder-like aggregates (Fig. 6). Iltisite ($\text{HgAgS}(\text{Cl},\text{Br})$) is often observed to form euhedral crystal needle-shaped less than 5 μm in length (Fig. 6).

Chlorargyrite (AgCl) occurs as subhedral crystals (Fig. 7) in association with other chlorides such as atacamite ($\text{Cu}_2(\text{OH})_3\text{Cl}$) or bismoclite ($(\text{BiO})\text{Cl}$). Native silver is usual, generally as anhedral grains.

5 Stable isotopes

A total of 9 $\delta^{34}\text{S}$ analyses were obtained on tetrahedrite, returning values in a narrow range between -5.2 ‰ to -6.4 ‰. These values are similar to those obtained in the contiguous Mas de la Mina-Cedraman Pb-Zn MVT deposits (Grandia et al. 2003).

6 Discussion and conclusions

A distinctive aspect of the Villahermosa del Río ores is the absence of minerals that are common in the other deposits of the area, in particular barite, galena and sphalerite. However, Hg-rich tetrahedrite is also detected as veins hosted in Muschelkalk carbonates in the Betxí-Eslida area in the nearby Espadà ridge (Tritlla & Cardellach, 1997). These veins are also associated with NE-SW trending faults. In this case, two muscovite samples from the carbonate-hosted mercury veins gave two K/Ar ages of $85 \pm 3 \text{ Ma}$ (2σ) and $84 \pm 4 \text{ Ma}$ (2σ), constraining the hydrothermal event to the Santonian (Tritlla & Solé, 1999). In the case of Villahermosa del Río deposits, the distribution of the vein surfaces would not be compatible with a compression related to the NE-SW strike-slip faults. It seems to be rather connected with detachment movements along the stratification surfaces. In any case, the mineralization should be related with the compressive stages.

The deposition of mercury minerals is typical of low-T conditions; these conditions, in fact, would help to explain the lack of other elements (Hazen et al., 2012). However, the source of mercury remains uncertain. A mantle origin for Hg is often proposed for many deposits (i.e., Higuera et al., 2013). Alkaline intraplate volcanism is present in the Iberian domain (Orti & Vaquer 1980), but no evidences of mineralization were found in connection to these volcanic rocks. Black

shales could be source for mercury too, but they are not known in the Mesozoic series. Enrichments in Hg have been found in Silurian black shales in the Catalan Coastal Ranges (Canet et al., 2003), being these pre-concentrates remobilized during the Mesozoic towards barite-polymetallic veins (Parviainen et al., 2008).

The hosting dolostone could be interpreted as the source for sulphur since they are enriched in biogenic pyrite. The negative $\delta^{34}\text{S}$ values would be in good agreement with this statement.

Finally, the development of powder-like cinnabar, along with Hg-chlorides and sulphochlorides, is a common feature in the Iberian Ranges. It is commonly attributed to alteration of Hg-rich tennantite-tetrahedrite. Tritlla & Cardellach (2003) proposed that cinnabar and related sulphochlorides could be produced by oxidation of the primary sulphides during a late hydrothermal episode. However, at least in the case of Villahermosa del Río, the cinnabar and sulphochlorides association with silver and typical supergene minerals suggests that these minerals were produced by supergene enrichment during weathering processes. The fact that Ag is abundant enough to be considered as potential mining objective in these deposits must be emphasized.

Thick evaporite deposits occur either in the middle Muschelkalk or in the Keuper facies. The evaporitic series located close to the deposits could be proposed as the source for halogens such as Cl and Br. Ag- and Hg-chlorides are strongly insoluble (Hazen et al., 2012) and can easily precipitate when descending meteoric fluids leaching evaporite beds intercept the weathering Hg- and Ag-rich tennantites.

Acknowledgements

Samples were analyzed in the Centres Científics i Tecnològics of the University of Barcelona. Funding was provided by the Consolidated Research Group Grant SGR 444 of the Generalitat de Catalunya.

References

- Canérot J, Gautier F (1966) Sur le Crétacé inférieur du massif de la Peñagolosa et ses relations avec le Trias de Villahermosa del Río (prov. de Castellón, Espagne). *C.R. Soc. Géol. Fr.* 10:393-395.
- Canet C, Alfonso P, Melgarejo JC, Jorge S (2003). PGE-bearing minerals in Silurian sedex deposits in the Poblet area, southwestern Catalonia, Spain. *Can. Mineral.*, 41: 581-595.
- Climent-Doménech H, Bover T, Caja MA (2006) Evolución sedimentaria y estructural del Cretácico inferior en el sector Benicàssim-Orpesa, Cadena Ibérica oriental. *Geogaceta* 41:47-50.
- Cócera H, Menor-Salván C, Muñoz-Alvarado R (2010) Mineralogía de la concesión San Rafael, Villahermosa del Río, Castellón, España. *Acopios* 6:1-51.
- Grandia F, Asmerom Y, Getty S, Cardellach E, Canals A (2000) U-Pb dating of MVT ore-stage calcite: implications for fluid flow in a Mesozoic extensional basin from Iberian Peninsula. *J. Geochem. Explor* 69-70: 377-380.
- Grandia F, Cardellach E, Canals A, Banks DA (2003) Geochemistry of the Fluids Related to Epigenetic Carbonate-Hosted Zn-Pb Deposits in the Maestrat Basin, Eastern Spain: Fluid Inclusion and Isotope (Cl, C, O, S, Sr) Evidence. *Econ. Geol.* 98:933-954.
- Hazen RM, Golden J, Downs RT, Hystad G, Grew ES, Azzolini D, Sverjensky DA (2012) Mercury (Hg) mineral evolution: A mineralogical record of supercontinent assembly, changing ocean geochemistry, and the emerging terrestrial biosphere. *Am. Mineral.* 97:1013-1042.
- Higuera P, Oyarzun R, Lillo J, Morata D (2013) Intraplate mafic magmatism, degasification, and deposition of mercury: The giant Almadén mercury deposit (Spain) revisited. *Ore Geol. Rev.* 51: 93-102.
- IGME (1979): Mapa geológico de España 1:50.000. Hoja 592, Villahermosa del Río. Madrid, Servicio de Publicaciones, Ministerio de Industria y Energía.
- Muchez Ph, Heijlen W (2003) Origin and migration of fluids during the evolution of sedimentary basins and the origin of Zn-Pb deposits in Western and Central Europe. *J. Geochem. Explor.* 78-79: 149-152.
- Muchez Ph, Heijlen W, Banks D, Blundell D, Boni M, Grandia F (2005) Extensional tectonics and the timing and formation of basin-hosted deposits in Europe. *Ore Geol. Rev.* 27: 241-267.
- Ochando LE, Casanova, JM; Esteve V, Reventós, MM, Bastida J (1997) Nota sobre la presencia de sulfoarseniuros de cobre en mineralizaciones filonianas del Muschelkalk de Villahermosa del Río (Castellón). *Bol. Soc. Española Mineral.* 20A:72.
- Ortí E, Vaquer R (1980) Volcanismo jurásico del sector valenciano de la Cordillera Ibérica. Distribución y trama estructural. *Acta Geologica Hispanica* 15:127-130.
- Parviainen A, Gervilla F, Melgarejo JC, Johanson B (2008) Low-temperature, platinum-group elements-bearing Ni arsenide assemblage from the Atrevida mine (Catalonian Coastal Ranges, NE Spain). *Neues Jahr. Mineral., Abh.* 185: 33-49.
- Salas R, Casas A (1993) Mesozoic extensional tectonics, stratigraphy and crustal evolution during the Alpine cycle of the eastern Iberian basin. *Tectonophysics* 228:33-55.
- Salas J, Guimerà J, Mas R, Martín-Closas A, Meléndez A, Alonso A (2001) Evolution of the Mesozoic central Iberian Rift System and its Cainozoic inversion (Iberian chain). In: Ziegler, P.A., Cavazza, W., Robertson, A.H.F., Crasquin-Soleau, S. (Eds.), *Peri-Tethyan Memoir 6: Peri-Tethyan Rift/Wrench Basins and Passive Margins. Mém. Mus. Natn. Hist. Nat.* 186, (Paris): 145-185.
- Tritlla J, Cardellach E (1991) Primeros datos sobre mineralizaciones de cinabrio en los materiales del Buntsandstein del área de Xovar (Sierra de Espadán, Castellón). *Bol. Soc. Española Mineral.* 14:95-96.
- Tritlla J, Cardellach E (1993) Origin of the carbonate-hosted mercury veins from the Espadán Mountains (Iberian Ranges, Eastern Spain): Evidence from fluid inclusions and stable isotopes". *Current Research in Geology Applied to Ore Deposits*, Vol. 1, pp. 265-268.
- Tritlla J, Solé J (1999) A new dated Cretaceous hydrothermal event in the Iberian Ranges (E of Spain) and its significance within the Mesozoic thermic scenario in the Iberian Peninsula. *Ore Geol. Rev.* 15: 243-259.
- Tritlla J, Cardellach E (1997) Fluid inclusions in pre-ore minerals from the carbonate-hosted mercury deposits in the Espadán Ranges (eastern Spain). *Chem. Geol.* 137: 91-106.
- Tritlla J, Cardellach E (2003) Ba-Hg deposits in the Espadán ranges (Iberian Chain, Eastern Spain): an example of Cretaceous fluid circulation and Alpine overprinting. *J. Geochem. Explor.* 78-79: 579-584.

Hydrothermal ree rich minerals in granites from Lagoa Real uranium province Ba-Brazil

Lucas Eustáquio Dias Amorim, Monica Elizetti Freitas, Francisco Javier Rios
 CNEN/CDTN/SETEM, P.O.Box 941, Belo Horizonte, Brazil

Evando Carele de Matos
 INB - Industrias Nucleares do Brasil, Caetité, Bahia, Brazil

Abstract. REE minerals have already been identified in granites from Lagoa Real Uranium Province, the main uranium deposit in Brazil. This contribution will provide information about the textures and chemistry of REE minerals, and present observations about the hydrothermal/pos-magmatic REE genesis in the Lagoa Real region.

Keywords. Lagoa Real, REE Minerals, Mineral Chemistry.

1 Introduction

Brazil has the fifth largest uranium reserve in the world. The Lagoa Real Uranium Province (PULR), located in central-southern Bahia state, is actually the most important and best known area it comprises 30% of Brazil's total reserves, being the only region in exploration in Latin America.

The PULR main litology includes Archean/Paleoproterozoic basement rocks (granites, migmatites and gneissic rocks) and the Paleoproterozoic Lagoa Real granites-gneissic complex, which is composed of rocks of the 1.7 Ga St. Timoteo granite (mainly sienogranites, charnockites and diorites) and gneissic rocks.

Lagoa Real uranium deposits are tabular to lensoid orebodies known as albititos. They are emplaced in granitic to gneissic rocks. These orebodies occur in ductile shear zones and consist mainly of albite-oligoclase rich rocks (over 60% by volume). Pyroxene (aegirine-augite), amphibole, biotite, garnet, magnetite/hematite, and Ca-carbonate are the other essential minerals. Uraninite is the primary U mineral which is associated to pyroxene-, amphibole-, garnet-, hematite-albitites (Fuzikawa *et. al* 1988; Maruejol 1989; Lobato & Fyfe, 1990, Cruz 2004).

Studies carried out to date indicate that albitites are not all the same type neither are they all mineralized. The ore formation must be associated to U remobilization and probably came from a source rock which may have been these granites.

Although, St. Timóteo granites are one of the main lithologies found in the PULR, only few studies have been developed in these rocks. Many authors have considered the granites as the protolith of the gneissic rocks and that they were related, by metassomatic and/or hydrothermal processes, to uranium ore bodies named albitites (Fuzikawa *et. al* 1988; Maruejol 1989; Lobato & Fyfe, 1990, Cruz 2004).

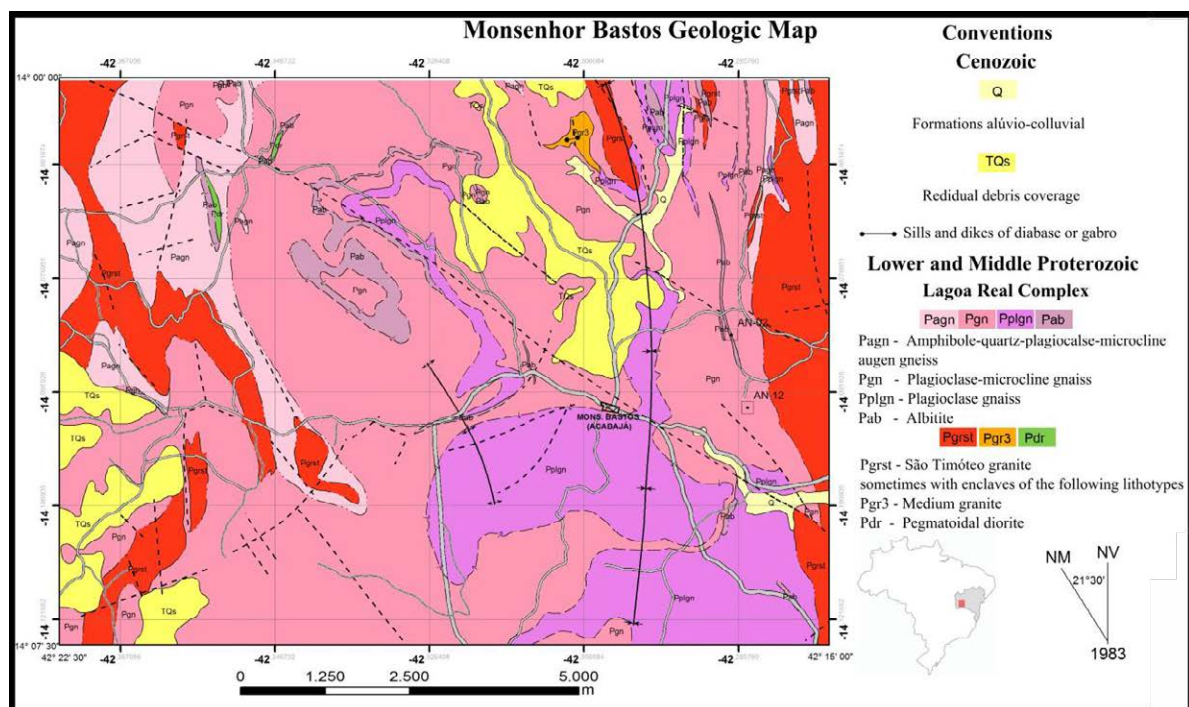


Figure 1. Map of Lagoa Real Uranium Province, Monsenhor Bastos sector (Amorim, 2012)

Previous studies developed in gneissic and albitites rocks have identified Nb and Ta minerals and also REE-rich minerals without, however, addressing their scope and mineral chemistry. In this work REE-rich minerals, mainly Ce and La ones, with F and CO₃ are identified in the southwest PULR granites in the Monsenhor Bastos Sector (FIG 1), and verified the processes involved with the formation of these mineral and its possible association with the U mineralization, though the studies of mineral chemistry and texture.

2 Textures of REE Minerals

The REE minerals appear associated with structures formed by sequential layers, which do not seem to follow any order. They occur in a complex simplectitic intergrown association of fluorcarbonates, silic-carbonates (these minerals shall be referred generically as parisite), associated together with allanite, titanite, ilmenite, zircon and thorite. Unlike, what is common in granites, they are not euhedral and have circular shapes with variation to the center. This texture is similar to that found in the amphiboles observed in these same rocks, which draws attention to the complexity and type of occurrence, as described by Amorim (2012).

The REE minerals, in general, have round shapes, irregular edges, constituting an agglomeration of concentric minerals. These agglomerates can be found within the phenocrysts feldspars, always associated with fractures (FIG2B). When they occur in the rock matrix, they can be formed in the interstices of recrystallized quartz crystals, usually joining and preserving inside these quartz. The best evidence of this is shown in texture on the image of secondary electrons (FIG 2A) that still preserves the contacts of the quartz crystals. Some have titanite partially or completely filling the internal portion.

The agglomerates can still be found, associated with clusters of mafic minerals, mainly with amphibole and biotite. Most of these have allanite on the edges, differentiating towards the center.

The allanite may show irregular concentric or patchwork zoning, which can be observed by electron microscopy by varying the grayscale images of backscattered electrons (FIG 3). However, in most samples, the edge of this mineral has homogeneous appearance. In some clusters the allanite is associated with ilmenite and forming a thin intergrowth in the middle or central portions of association. Different grains of ilmenite and allanite are evidenced by the embossed images of secondary electrons (FIG 3).

The REE fluorcarbonates usually occur in the inner portions of these clusters, associated with small crystals of thorite and zircon. They can show massive aspect, they are homogeneous and form irregular areas in the nucleus or irregular blades intergrown with silic-carbonates and silicates (FIG 4). Due to their very small dimensions and very similar chemical compositions, the fluorcarbonates and silic-carbonates cannot be separated in detail, even in electronic images.

In some portions of the blades, the REE fluorcarbonates and silic-carbonates can be observed in the outer sectors of the agglomerates, percolating

fractures and the crystal interstices of the matrix, and connecting these agglomerates (FIG 2A and B).

These images show in detail the different portions of these mineral associations, where the minerals are richer in F and CO₃ (fluorcarbonates and silic-carbonates) which are porous, containing microcavities of vermicular form, rounded or polygonal, particularly when present in the core structure (FIG 4).

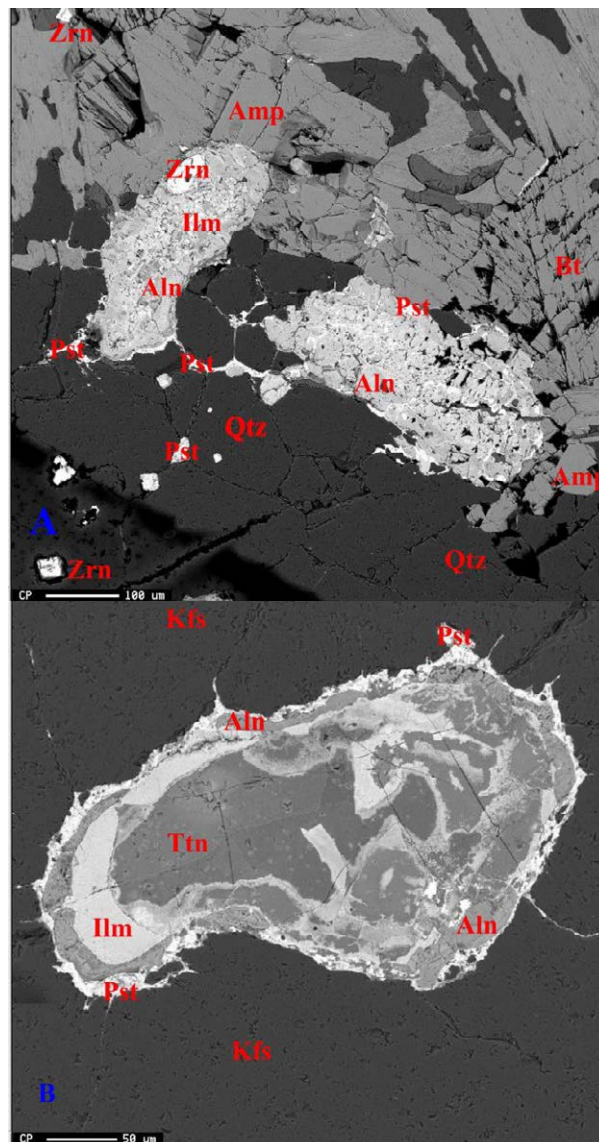


Figure 2. A: REE minerals with quartz, amphibole and biotite. This image shows the highest concentration of rare earths carbonates, the lighter portion, and the edges of minerals and percolating fractures, along a small cloud of zircon, which may have formed together. **B:** Association of REE minerals included in K-feldspar. Fractures permeate the quartz matrix and connect the association of REE minerals. Inside the structure, allanite, titanite and ilmenite are identified. Abbreviations, Amp: Amphibole, Bt: Biotite, Ilm: Ilmenite, Aln: Allanite, Zrn: Zircon, Pst: Parisite, Qtz: Quartz, Kfs: K-feldspar, Ttn: Titanite

3 Mineral Chemistry

The allanite has a great thickness variation in the structure of complex mineral association. Its composition is also varied, sometimes being noticeable a

zonation. The mineral found in the sample is a Ce-allanite (ferriallanite) with up to 8-0 wt % of La_2O_3 , 4 to 0.16 wt % of Nd_2O_3 , 2-0 wt % of ThO_2 and 3-0.2 wt % of F. Its composition differs from the ideal formula by the presence of Fe^{3+} in the M site, deficiency of divalent cations, and the presence of F.

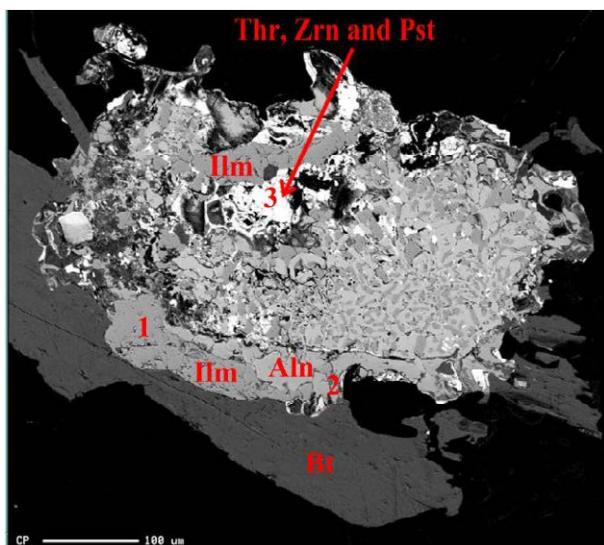


Figure 3. - Ilmenite and allanite intergrown BSE image. 1 - Biotite in contact with ilmenite; 2 - ilmenite in contact with allanite; 3 - This portion comprising thorite, zircon and REE carbonate. At the core, it is evident an ilmenite and allanite intergrowth. Abbreviations, Bt: Biotite, IIm: Ilmenite, Aln: Allanite, Thr: Thorite, Zrn: Zircon, Pst: Parisite.

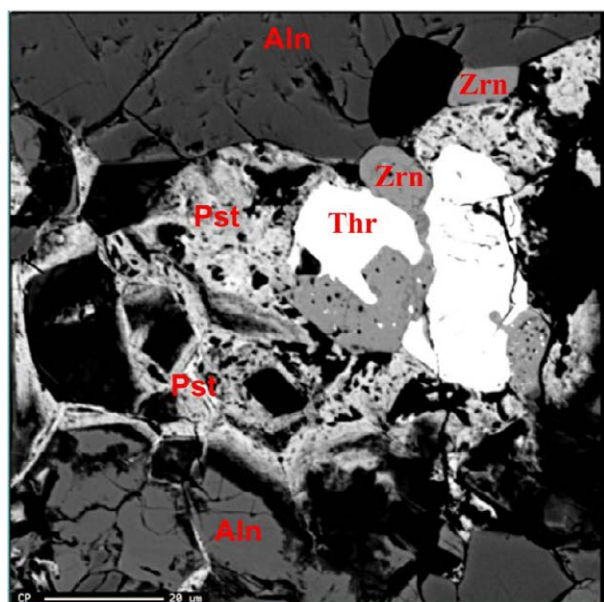


Figure 4. REE minerals core structure BSE image. Thorite associated to zircon with REE fluor-carbonates. Around the zircon, REE carbonates are replacing another mineral of medium atomic weight. Around this structure there is ilmenite intergrown with allanite. Inclusions of thorite are observed in zircon. Abbreviations, Aln: Allanite, Thr: Thorite, Zrn: Zircon, Pst: Parisite

The titanite does not always appear in the REE-rich minerals association. When found, it has the characteristic common to mineral association: the presence of F (2.45 to 0.24 wt%), and high

concentrations of REE (15.16-3.86 wt% Ce_2O_3 , 5.47-0.54 wt% La_2O_3 , 4.73-1.06 wt% Nd_2O_3), besides ThO_2 (10.62-2.81 wt%).

Ilmenite is found at the interface with other minerals. It has, as distinctive features, the presence of Nb_2O_3 and MnO (1.88-0.84 wt% e 2.89-1.12 wt%, respectively). UO_2 was locally measured (up 0.13wt%).

REE Carbonates possess greater chemical variation and are more enriched in F, CO_3 , LREE, Nb, Th and U. The silic-carbonate has 13.49-2.22wt% of CaO, 7.28-0.55wt% of Th_2O , 23.41-7.67wt% of La_2O_3 , 29.89-16.36wt% of Ce_2O_3 , 12.52-5.65wt% of Nd_2O_3 , and up to 0.59 wt% of UO_2 . However, as the dimensions of these minerals are not micrometric, X-ray diffraction study was conducted. The designation of kainosite is generic to exemplify the silic-carbonates which may be more complex, or analyses that may result from a mixture of mineral finely interleaved.

Meng et al (2002) explain that the fluorine-series mineral carbonates are often affected by stacking faults, mixed in chemical composition, syntactic intergrowth, polytypism and twinning during crystallization with other mineral phases. Thus, it becomes difficult to obtain fine crystallographic and chemical data on these minerals in situ. Chemical analyzes by electron microprobe did not provide conclusive results, thus, the actual proportion of elements could not be measured in all analyses.

The parisite has variable composition and displays however similar characteristics to those of kainosite (35.37-16.23wt% of Ce_2O_3 , up to 24.52wt% of ThO_2 , 21.88-7.12wt% of La_2O_3 , 11.08-5.81wt% of Nd_2O_3 , and 0.37wt% of UO_2). Thorite was identified together with these minerals.

Whole rock analyses show that the average REE is 700 ppm, with only 40% Ce. Maruejol (1989) presented REE concentrations between 120-4000 ppm for the gneiss and 300-800 ppm for the albitites rocks. These data demonstrate that the REE concentration in these rocks is much higher than that found in granite, in which it is also large. Thus it is possible to assume that the REE may be following the U, and that the event responsible for the transport of these elements is the same.

4 Discussion

The chemical and textural studies showed that the PULR granites, despite being considered the best preserved rocks in the province, were affected by a post magmatic/hydrothermal event, characterized by a fluid rich in F and CO_3 (Amorim, 2012). Agreeing with Monecke et al. (2011) REE-Cl complexes show preferential partitioning in the liquid phase, whereas REE-F complexes partitioned in the CO_2 -bearing vapor phase. Such solutions may be related to the presence of more evolved granites that have not yet been mapped. Large concentrations of REE, Nb, Ta, U and Th can be mobilized and transported by F and Cl rich fluids (Keppler, Wyllie, 1991). In this way, it is possible that the fluid responsible for the formation of silic-carbonates and fluor-carbonates in PULR may also be related to the U mobilization and subsequent U mineralization. The fluoro-carbonates are usually reported to hydrothermal

environments, mainly related to carbonatites (Smith et al. 2000, Yang & Le Bas 2004), but this type of minerals in granitic systems is not common.

The allanite and ilmenite intergrowth (FIG 3), suggests that ilmenite is formed by exsolution. Initially allanite was formed in high temperature and pressure and this condition promoted the enrichment in Fe and Ti. After the decrease of temperature and pressure thereafter, large concentrations of Ti and Fe became incompatible with the structure of allanite and this caused the exsolution of these elements and the formation of ilmenite.

The complex arrangement of clusters of earth minerals suggests that allanite was the first to crystallize. After its precipitation the fluid was still rich in REE and Th, leading to formation of more complex mineral composition rich in REE. The remaining volatiles stayed in the crystals interstices and were responsible for the formation of pores.

The fractures that cut the REE-rich mineral association extends towards to parisite and kinosite places, or may be filled by them, suggesting that these minerals may have been the last to form.

Figure 2A shows rounded REE mineral agglomerates formed in the interstices of quartz crystals and then joined together forming a single structure. As quartz was already recrystallized, this texture proves that the formation of these minerals is late or occurred after the deformation / metamorphism (related to gneissification process), showing, once again, that it is a late post-magmatic / hydrothermal event unrelated to the original formation of igneous granite.

There is evidence of changes generated by fluids circulating on the studied granites. In a recent work, Amorim, 2012, described the occurrence of amphibole that has F and Cl in its composition. These data suggest that the same type of fluid can be responsible for the formation of both the amphibole, as well as parisite, kinosite, allanite, titanite, and a second generation zircon.

5 Conclusions

This work characterizes the occurrence of complex minerals of REE, Th, Ti and U in PULR granites, showing that such association is not restricted principally to the gneisses and albitites, as first supposed. The post-magmatic / hydrothermal event responsible for their formation did not affect only the granites, but also the other rock and U-mineralized bodies in the region. Under the economic point of view, the presence of REE-rich minerals is important, because it may represent a byproduct in the exploration and beneficiation of the U.

Finally, the textures shown in this work are not frequently reported in literature, so it is important to expand their study and their significance. Future studies can clarify the characteristics of the processes related to the REE mineral formation.

Acknowledgements

Financial support and infrastructure for this study was provided by CNEN/CDTN, CAPES, FAPEMIG (project CAG PPM00666-11 and PEE-00083-13), and CNPq (project 307546/2011-0). The authors express special thanks to Sônia P. Prates (CDTN Researcher) for help reviewing the text.

References

- Amorim LED (2012) O granito São Timóteo no perfil Monsenhor Bastos, província uranífera de Lagoa Real: mineralogia, geoquímica e fluidos. Master dissertation, Centro de Desenvolvimento da Tecnologia Nuclear
- Fuzikawa, K., Alves, J. V., Maruêjol, P., Cuney, M., Kostolany, C., Poty, B. 1988. The Lagoa Real uranium province, Bahia state, Brazil: Some petrographic aspects and fluid inclusion studies. *Geoch. Brasil.*, **2**: 109-118.
- Cruz SCP (2004) A interação entre o Aulacógeno do Paramirim e o Orógeno Araçuaí-Oeste Congo. PhD dissertation, Universidade Federal de Ouro Preto
- Keppler H., Wyllie P.J.(1991) "Partitioning of Cu, Sn, Mo, W, U, and Th between melt and aqueous fluid in the systems haplogranite-H₂O-HCl and haplogranite-H₂O-HF" *Contributions to Mineralogy and Petrology*, **Vol.109**, pp.139-150.
- Lobato, L. & Fyfe, W. 1990. Metamorphism and mineralization at Lagoa Real, Bahia, Brasil. *Econ. Geol.*, **5**: 968- 989.
- Maruêjol P (1989) Métasomatose alcaline et minéralisation uraníferes: les albitites du gisement de Lagoa Real (Bahia,Brésil) et exemples complémentaires de Xihuashan (SEChine), Zheltorechensk (Ukraine) e Chuling Khola (Népal central). PhD dissertation, Centre du Recherche sur laGeologie de l'uranium.
- Meng Dawei , Wu Xiu ling, Han Yuji ng & Meng Xin (2002): Polytypism and microstructures of the mixed-layer member B2S, CaCe₃(CO₃)₄F₃ in the bastnäsite-(Ce) – synchysite-(Ce) series. *Earth Planet. Sci. Lett.* **203**, 817-828.
- Monecke, T., Kempe, U., Trinkler, M., Thomas, R., Dulski, P., Wagner, T. (2011) Unusual rare earth element fractionation in a tin-bearing magmatic-hydrothermal system. *Geology*, **39**, 295-298.
- Smith , M.P., Hender son, P. & Campbe ll, L.S. (2000): Fractionation of the REE during hydrothermal processes: constraints from the Bayan Obo Fe-REE-Nb deposit, Inner Mongolia, China. *Geochim. Cosmochim. Acta* **64**, 3141-3160.
- Yang, Xuemi ng & Le Bas, M.J. (2004): Chemical compositions of carbonate minerals from Bayan Obo, Inner Mongolia, China: implications for petrogenesis. *Lithos* **72**, 97-116.

Two types of non-conventional PGE mineralizations near Poblet, Catalonia (Spain): a possible metallogenic heritage?

Carlos Arbiol-González, Núria Conesa, Àngels Canals, Joaquín A. Proenza, Joan Carles Melgarejo
Departament de Cristal·lografia, Mineralogia i Dipòsits Minerals, Facultat de Geologia, Universitat de Barcelona

Esteve Cardellach
Departament de Geologia, Universitat Autònoma de Barcelona

Abstract. The Silurian series of the Prades Mountains (SW Catalonia, Spain) host stratiform massive sulphide beds containing Cu-Pb-Zn-As-Ni-Co-Bi-Te-Se-Au-Ag-PGE concentrations. PGE occur as discrete minerals or included within the structure of some arsenides. The Atrevida vein (Upper Triassic-Lower Jurassic age) crosscuts the Silurian massive sulphide beds becoming enriched in Ni-Co-PGE. Mineral associations in both environments and sulphur isotopes of sulphides suggest the existence of a metallogenic heritage, between both environments.

Keywords. Heritage, PGE, Ni, Co, arsenides, S isotopes

1 Introduction

The PGE have been traditionally related to mafic or ultramafic magmatism. However, in the last years the existence of unconventional types of PGE deposits has been widely documented (i.e., Jowitt & Keays 2011).

In the Prades Mountains (Catalonia, Spain) two types of PGE occurrences have been identified: stratiform PGE-bearing sulphides within the Silurian series and Ni-Co-PGE minerals in veins of Mesozoic age. The aim of this contribution is to provide evidence of heritage between the two different types of PGE occurrences from mineralogical and S isotope data.

2 Geological Setting

The study area is located near the Poblet Monastery in Vimbodí, at the N border of the Prades Mountains, SW of the Catalanian Coastal Ranges (CCR), NE Spain (Fig. 1). In this area, the CCR are made up of a metamorphosed basement of Paleozoic age, unconformably overlain by a sedimentary sequence of Triassic age (Germanic facies; Melgarejo 1992).

The Paleozoic series commence with quartzites interbedded with black shales of Upper Ordovician to Early Silurian age, achieving more than 100m in thickness. The upper part (up to 30 m thick) is composed of a stratiform sulphide-rich unit. These materials vertically grade into a sequence of black shales (Ludlowian-Wenlockian), unconformably overlain by more than 2000 m of turbiditic units (Visean-Namurian).

The Paleozoic series are affected by the Hercynian orogeny producing NW-SE trending folds, and thrusts following the Ordovician and Silurian black shales

levels. Deformation produced a regional very low grade metamorphism.

A suite of Late Hercynian I-type granitoids ranging in composition from quartzdiorites to leucogranites intruded the series, producing contact metamorphic aureoles (Melgarejo 1992).

The Paleozoic series are unconformably overlain by sediments of Triassic age, and begin with a 50 to 100m thick red-bed sequence (conglomerates, sandstones and lutites of the Buntsandstein facies). This unit is followed by carbonates (lower Muschelkalk facies) with more than 50 m in thickness, by a regressive sequence of red lutites, clays and gypsum (Middle Muschelkalk facies, up to 100 m) and a transgressive sequence of limestones and dolostones (Upper Muschelkalk facies). The Keuper facies consists of more than 200 m of lutites interbedded with clays and gypsum units. The deposit of all these facies was controlled by syn-sedimentary NNW-SSE trending normal faults.

The compressive stage during the Paleogene (Alpine orogeny) affected the materials previously mentioned producing NW-SE trending faults which were reactivated as normal during the Neogene.

3 PGE styles of the mineralizations

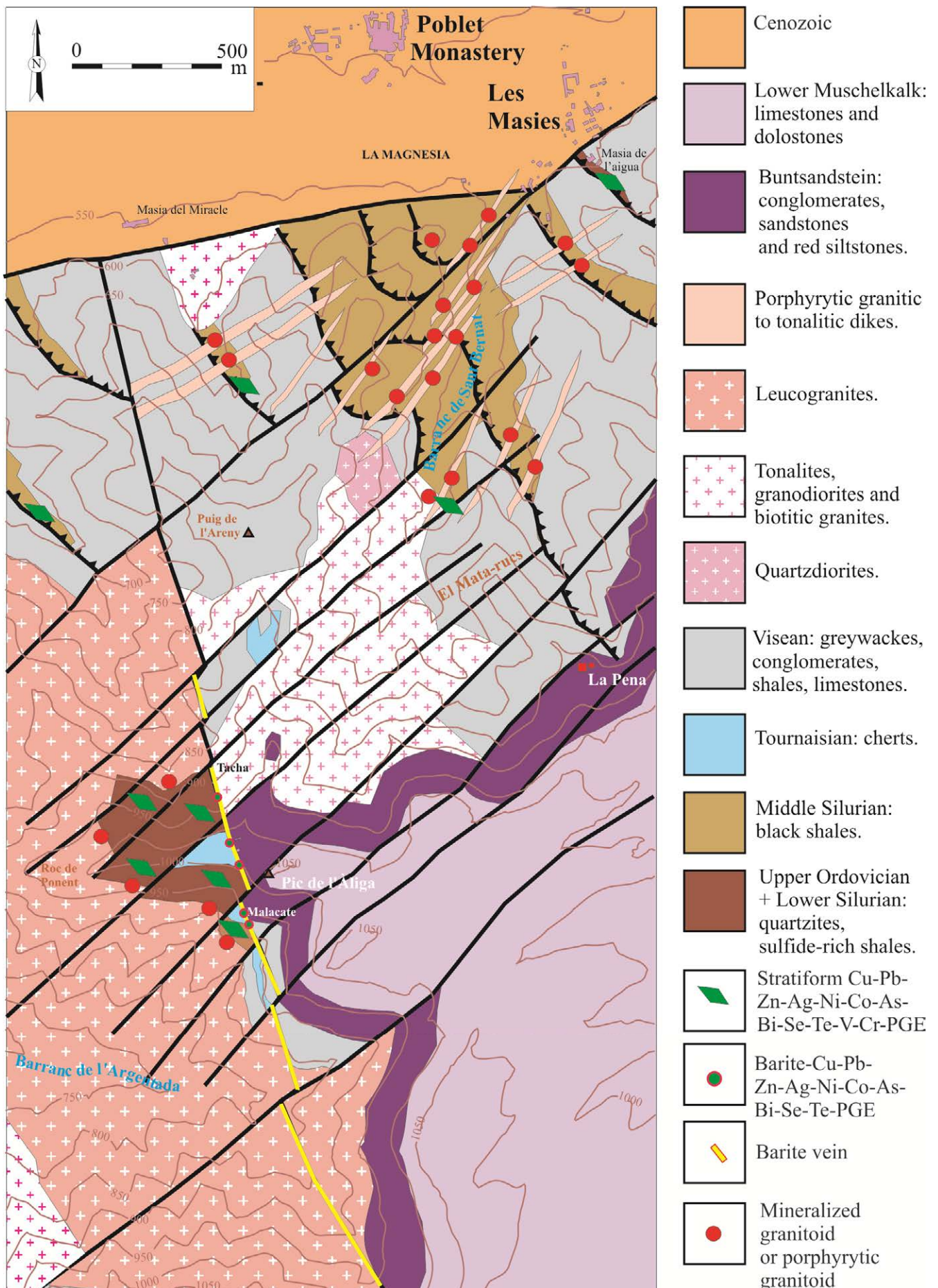
PGE concentrations were identified as two types of deposits in the Prades Mountains, near the Poblet monastery, SW Catalonia, Spain: stratiform massive sulphides and veins.

3.1 PGE-bearing stratiform mineralization

These PGE occurrences are found within stratiform massive sulphides in the lower Silurian series. These deposits were mined, probably for Au, during the Roman times. The mineralized unit consists of sulphide beds (up to 1m thick), interbedded with anorthite-rich beds, calcosilicate beds, quartzites and black shales (Canet et al., 2003a). Mineralization ranges from massive to disseminated.

Textural observations allowed distinguishing 4 stages of mineralization (Fig. 2): a) synsedimentary, b) regional metamorphism, c) contact metamorphism and d) late veinlets and replacements.

Primary bedded ores are fine-grained. The dominant sulphide is pyrrhotite accompanied by minor chalcocopyrite, sphalerite and löllingite and trace amounts of molybdenite and tungstenite, suggesting a deposition



	Sedimentary-exhalative	Regional metamorphism	Contact metamorphism	Late hydrothermal
	Llandoveryan	Westphalian	Permian	Alpine
Armenite				—
Chlorite				—
Barite				—
K-Feldspar				—
Acanthite				—
Pyrite				—
Stibiopalladinite			—	
Pd arsenide ?			—	
Gold			—	
Petzite			—	
Native bismuth			—	
Bitellurides			—	
Allanite-(Ce)			—	
Wolframite			—	
Hessite			—	
Clausthalite			—	
Arsenopyrite			—	
Goldmanite			—	
Chromite			—	
Coulsonite			—	
Cordierite			—	
Andalusite			—	
Hedenbergite			—	
Biotite		—	—	
Muscovite		—	—	
Amphiboles		—	—	
Xenotime-(Y)			—	
Monazite-(Ce)			—	
Titanite			—	
Uraninite			—	
Rutile		—	—	
Ilmenite		—	—	
Quartz	—	—	—	—
Sperrylite	—			
Sphalerite	—			
Galena	—			
Scheelite	—			
Löllingite	—			
Tungstenite	—			
Molybdenite	—			
Chalcopyrite	—			
Pyrrhotite	—			
Apatite	—			
Anorthite	—			

Figure 2. Mineral sequence in the stratiform deposit. Note the existence of episodes of mineralization separated in time. Adapted from Canet et al. (2003b).

under low sulphur activity. High concentrations of other redox-sensitive elements in these rocks, as V and Cr (Canet et al., 2003c), the occurrence of tungstenite (WS₂), uraninite, rare V³⁺ and Cr³⁺ oxides (vuorelainenite, coulsonite, crichtonite, eskolaite) as well as other U- and Th-bearing minerals indicate a deposition under reducing conditions.

Low-grade regional metamorphism produced minor changes in the ores, only observed as limited flattening of the crystals. Contact metamorphism produced annealing of grains and development of metamorphic minerals. The high V and Cr contents of this unit resulted in the development of goldmanite (V-Cr garnet), V-rich amphibole and V-rich biotite. Late metamorphic processes include replacement of löllingite by selenides (clausthalite, aguilarite) and tellurides (altaite, hessite).

Late hydrothermal processes comprise introduction of low-T, Ba-rich alkaline fluids which replace anorthite by K-feldspar and armenite (Fig. 2), and the V-silicates by chlorite. These minerals are accompanied by barite and S-rich sulphides as pyrite and acanthite.

PGE occur as: a) solid-solution within Ni-Co rich löllingite, and b) sperrylite, stibiopalladinite, native palladium and a palladium arsenide, associated with

electrum, native gold, and Au-Ag tellurides. Most of the discrete PGM are found as small grains (1-20 µm in size) displayed along the replacive contact between PGE-bearing löllingite and PGE-free arsenopyrite, suggesting that PGE were removed during the sulphidation of löllingite (Canet et al., 2003b).

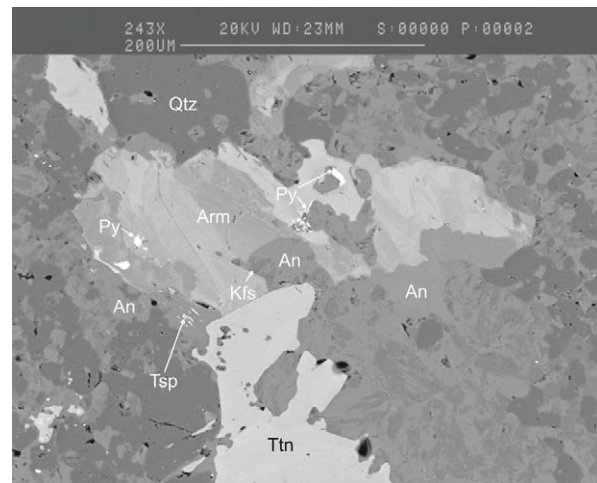


Figure 3. Replacement of the metamorphic minerals (anorthite, An; titanite, Ttn; quartz, Qtz) in the stratiform mineralization by metasomatism of S, Ba- and K- producing armenite (Arm), thioespinels (Tsp), microcline (Kfs) and pyrite (py). SEM image, BSE mode.

3.2 PGE in the Atrevida vein deposit

The second type of PGE mineralization is found in the Atrevida barite vein. It extends more than 3 km in a NNW-SSE direction, crosscutting metasediments of Silurian and Carboniferous age, a late Hercynian granite and Buntsandstein facies. Atrevida, a 1–6 m thick and 200 m of known depth, is one of the largest veins in NE Spain and was mined during the 20th century for barite.

Vein filling largely consists of banded and brecciated barite, locally cemented by a complex polymetallic assemblage of F-Pb-Zn-Cu-Co-Ni-As-Bi-Ag-Se-Sb-Te-U ores (Melgarejo & Ayora, 1985a). Massive Ni arsenide and sulpharsenide assemblages, up to 1 m in width, occur only where the vein crosscuts the sulphide-bearing metasediments of Silurian age. They consist of Ni-Co arsenides and sulphides, along with galena, sphalerite, chalcopyrite, marcassite, hessite, silver sulphosalts, native silver and fluorite (Melgarejo & Ayora, 1985b). Most of these minerals display rosettes, spherules, colloform and botryoidal textures. Ni arsenides and sulpharsenides contain trace PGE (Parviainen et al., 2008). Palladium (up to 157 ppm) is the most abundant PGE, and occurs in solid-solution in all the studied phases, having the highest values in rammelsbergite and Ni-skutterudite. Pt occurs in nickeline (54–1338 ppm Pt) and in gersdorffite (29–360 ppm Pt).

4 Fluid inclusion and S isotope data

According to Canals et al. (1992), fluid inclusion and mineral equilibria data show that the Atrevida vein was deposited at low temperatures (Th=80-110°C). The vein formed by mixing of two fluids: a) a cold, oxidized and

sulphate-rich water originated from the dissolution of evaporites of the Keuper facies (Upper Triassic) and b) a hotter, ascending fluid carrying Ba, F, metals and reduced sulphur. Sulphur isotopes on barite and sulphides show highly variable values indicating that sulphates and sulphides precipitated from different S-sources. Sulphides (galena and sphalerite) have $\delta^{34}\text{S}$ values between -9 and -12‰.

In the stratiform beds, $\delta^{34}\text{S}$ of pyrrhotite decreases along the sequence (from -7.6‰ at the base to -19.9‰ at the top). Based on these isotope data, Alfonso et al. (2002) suggested that the sulphur source in the massive sulphides was largely derived from a biogenic seawater sulphate reduction (BSR).

The similar $\delta^{34}\text{S}$ values of sulphides in Atrevida vein points to a hydrothermal fluid that leached sulphur and metals from the basement rocks, namely Silurian black shales enriched in Ni-Co and PGE. Therefore, Ni-Co-PGE mineralogy of the Atrevida vein represents a possible heritage of pre-existing PGE concentrations within the Paleozoic rocks. This is consistent with Pb and Sr isotope data (Canals & Cardellach 1997) as they concluded that in Atrevida vein metals derived from leaching of late Hercynian basement granites, although contributions from metasedimentary rocks could not be ruled out. The new findings on Ni-Co-PGE occurrences in the enclosing rocks as well in the Atrevida vein, support this idea.

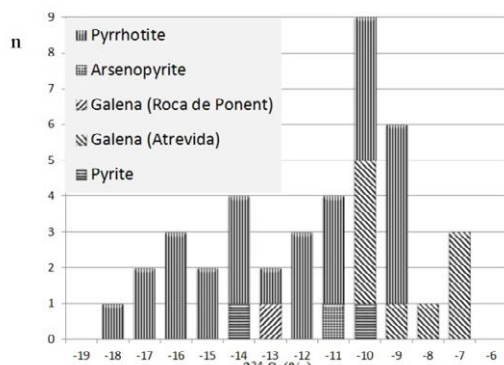


Figure 4. Comparison of $\delta^{34}\text{S}$ isotope values of sulphides from Atrevida vein and from hosting stratiform sulphides.

5 Discussion and conclusions

The presence of numerous sulphide occurrences (massive or disseminated) within the Paleozoic basement of the CCR, may act as sulphur and metal source for later mineralization processes. Granites and porphyritic dikes are enriched in sulphides and arsenides where they cut these series (Arbiol-González et al. 2012).

The development of armenite and K-feldspar as replacement products of anorthite indicates the existence of a Ba metasomatism associated with low temperature K alteration. In addition, the development of high-sulphidation minerals in this late event contrasts with the syn-sedimentary conditions favouring the development of pyrrhotite, and might be similar to the conditions that produced extensive development of marcassite, pyrite and thiospinels in the Atrevida vein. Therefore, these late stages of mineralization in the

stratiform deposit can be produced by interaction with the Atrevida-vein forming fluids.

Sulphur isotope values are very similar when comparing the stratiform sulphide mineralization and sulphides from the Ni-Co mineralization cementing the barite breccia in Atrevida vein. The negative $\delta^{34}\text{S}$ values of sulphides in Atrevida vein can be explained by leaching of biogenic sulphur from the stratiform mineralization. A similar mineralogy and the presence of PGE in both deposits would be consistent with this hypothesis.

Therefore, the enrichment of PGE in the Atrevida vein can be considered as a case of heritage and suggests that PGE can easily be mobilized in a diversity of environments.

Acknowledgements

Funding was provided by the Consolidated Research Group Grant SGR 444 of the Generalitat de Catalunya.

References

- Alfonso P, Canet C, Melgarejo JC, Fallick AE (2002) Sulphur isotope composition of Silurian shale-hosted PGE-Ag-Au-Zn-Cu mineralizations of the Prades Mountains (Catalonia, Spain). *Miner Deposita* 37: 198-212.
- Arbiol-González C, Arias-Pacheco D, Artiaga-Torres D, Palma-López T, Proenza JA, Enrique-Gisbert P, Melgarejo JC (2012): Reconcentración de Metales por Diques de Pórfidos: el Ejemplo de Poblet (Cataluña). *Macla* 16: 250-251.
- Canals A, Cardellach E, Rey DM., Ayora C (1992) Origin of the Atrevida vein (Catalonian Coastal Ranges, Spain): mineralogic, fluid inclusion and stable isotope study. *Econ Geol* 87: 142-153.
- Canals A, Cardellach E (1997) Ore lead and sulphur isotope pattern from the low-temperature veins of the Catalonian Coastal Ranges (NE Spain). *Miner Deposita* 32: 243-249.
- Canet C, Alfonso P, Melgarejo JC, Jorge S (2003) V-rich minerals in contact-metamorphosed Silurian sedex deposits in the Poblet area, southwestern Catalonia, Spain. *Can Mineral* 41: 561-580.
- Canet C, Alfonso P, Melgarejo JC, Jorge S (2003b) PGE-bearing minerals in Silurian sedex deposits in the Poblet area, southwestern Catalonia, Spain. *Can Mineral* 41: 581-595.
- Canet C, Alfonso P, Melgarejo J.C, Belyatsky BV (2004) Geochemical evidences of the sedimentary-exhalative origin of the shale-hosted PGE-Ag-Au-Zn-Cu deposits of the Prades Mountains (Catalonia, Spain): trace-element abundances and Sm-Nd isotopes. *J Geochem Exploration* 82: 17-33.
- Jowitt SM, Keays RR (2011) Shale-hosted Ni-(Cu-PGE) mineralisation: a global perspective. *Appl Earth Sci* 120: 187-197.
- Melgarejo JC (1992) Estudio geológico y metalogenético del Paleozoico del Sur de las Cordilleras Costeras Catalanas. *Mem Inst Tecnol Geominero España* 103, p 605.
- Melgarejo JC, Ayora C (1985a) La Mina Atrevida (Ba, F, Pb, Zn, As, Ni, Ag), Cadenas Costeras Catalanas: Un ejemplo de filón triásico de zócalo-cobertera. *Rev Inv Geol* 40: 87-102.
- Melgarejo JC, Ayora C (1985b) Mineralogía, paragénesis y condiciones de deposición del filón Atrevida (Ba, F, Pb, Zn, As, Ni, Co, Ag), Cadenas Costeras Catalanas. *Rev Inv Geol* 41: 47-65.
- Parviainen A, Gervilla F, Melgarejo JC, Johanson B (2008) Low-temperature, platinum-group elements-bearing Ni arsenide assemblage from the Atrevida mine (Catalonian Coastal Ranges, NE Spain). *Neues Jahr Mineral Abh* 185: 33-49.

The Huanuni Sn-W-Pb-Zn-Ag vein deposits, Bolivia: structure and mineralogy

Laia Arqués Farré, Andreu Cacho Amorós, David Artiaga Torres, Belén Torres Cueva, Lisard Torró i Abat
Joan Carles Melgarejo i Draper
Departament de Cristal·lografia, Mineralogia, Dipòsits Minerals, Universitat de Barcelona

Ramiro Condori, Néstor Guevara
Empresa Minera Huanuni, COMIBOL, Bolivia

Oswaldo Arce
Colegio de Geólogos de Bolivia, Edificio Señor de la Exaltación. Av. Hernando Siles entre calles 1 y 2, La Paz

Abstract. The Huanuni worldclass deposit is probably the biggest Sn mine in the world. Sn-, Pb- and Zn- veins are exploited in the district. In a central domain, connected with a porphyritic intrusion, cassiterite is the dominant ore, as in the Veta Grande vein. The distal areas are enriched in Zn-Pb ores, as in the veins Bonanza or La Suerte.

Keywords. Vein, Sn, Zn, In, Huanuni deposit

1 Introduction

The Huanuni deposit is located in the Pantaleón Dalence province, SW Bolivia, 275 km SSE of La Paz and 45 km SE of Oruro, capital city of the department of Oruro, in the central portion of the Bolivian Andes.

The Huanuni deposit is currently the most important Sn mine in Bolivia. It was discovered in 1745 and at the present moment it employs around 4600 miners. The production is expected to be increased by 2014 in order to produce 3000 t of Sn per day.

Despite the importance of the mine, there is no available recent information on the mineralogy. Hence, the aim of this contribution is to provide data on the mineral chemistry on the main ores from the deposit. For this reason, sampling of the most important veins of Sn and Zn was performed.

2 Geology

The Huanuni district is located in the Central Ranges of the Eastern Cordillera (Fig. 1). The Eastern Cordillera is made up of Ordovician to Cretaceous sedimentary sequences, comprising thick black shales, siltstones, limestones, sandstones, slates, and quartzites. The Andean orogeny produced regional faults and fold systems trending NNW-SSE, accompanied locally by thrusting (McQuarrie & DeCelles 2001). The ensemble has been affected only by very low grade regional metamorphism.

Intrusions of Miocene acid stocks and domes are found in the central part of the Eastern Cordillera, and are partly covered by ignimbrite fluxes of upper Miocene age.

To the East of the mining area, an ensemble of porphyritic dikes, trending approximately N-S, crops out along more than 1,5 km.

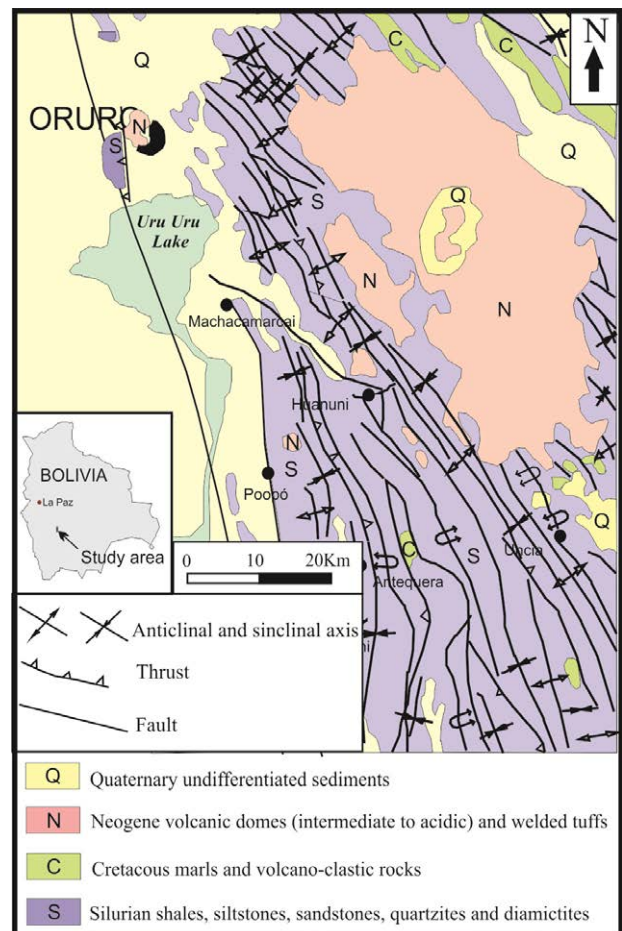


Figure 1. Geological map of the Huanuni area. After GEOTECMIN (2001).

3 Structure of the deposit

The Huanuni deposit is hosted by Silurian quartzites and quartz-rich sandstones of the lower member of the Llallagua Formation (Ahfeld & Schneider-Scherbina 1964). The highest ore concentrations are located in fractures, joints and veins.

The Sn deposit has a polymetallic mineralization with W, Pb, Ag and Zn, that shows a lateral zoning with the high-temperature minerals like cassiterite in the central part of the deposit, at Cerro Pozokoni, and decreases to moderate-temperature minerals such as

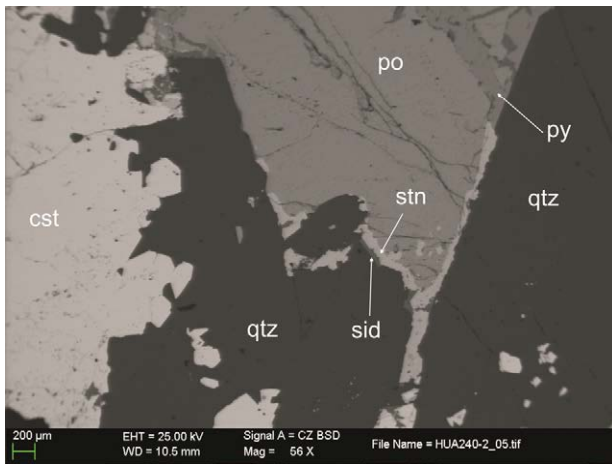


Figure 2. Example of sequences in the vein infilling. Cassiterite (cst) forms euhedral crystals covered by dark quartz, which is rimmed by stannite (stn) and siderite (sid). Pyrrhotite (po) overgrows the above minerals and is on its turn overgrown by pyrite (py). Veta Grande, level 240. SEM image, BSE mode.

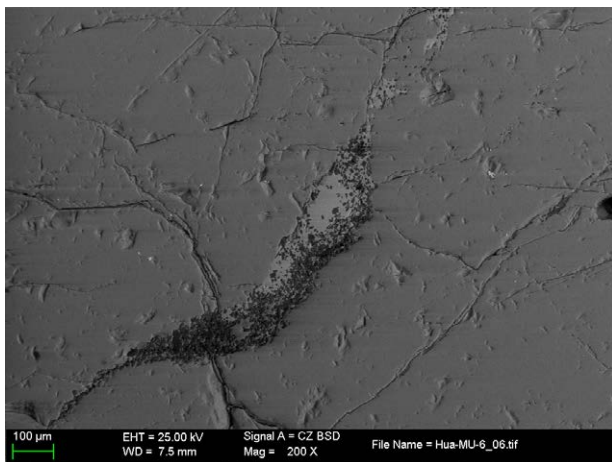


Figure 3. Pyrite crystals veined by an assemblage of euhedral schorl crystals (dark) and stannite. SEM image, BSE mode.

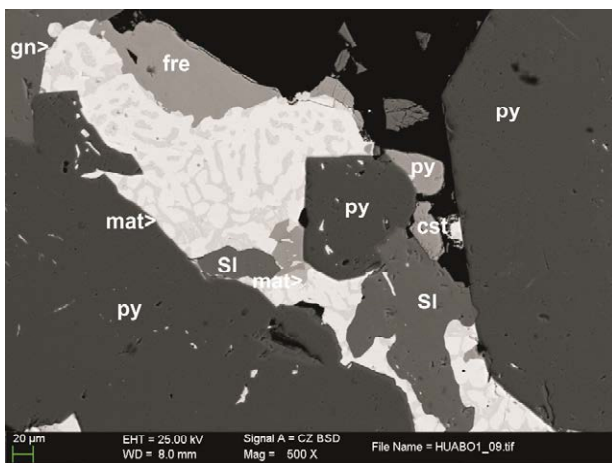


Figure 4. Succession of silver sulphosalts and other minerals filling porosity between pyrite crystals (py). Note symplectites among galena (gn) and matildite (mat). The association has sphalerite (sl), cassiterite (cst), freibergite (fre). Bonanza mine, SEM image, BSE mode.

galena or sphalerite in the peripheral sectors of the deposit. The Sn-mineralized zone comprises an area of 1500 km length (SE direction) and 1200 m wide. The most important Sn-bearing vein, the so-called Veta Grande, reaches up to 0,5 m in width.

The peripheral area of the district is enriched in Zn, and some mines are currently operating for extraction of sphalerite. These veins have a width of 10-70 cm (Suerte mine) and 25 cm (Bonanza mine). However, these veins contain also Sn and Ag minerals.

4 Mineralogy and textures

Vertically, the Sn mineralization in Veta Grande changes from pyrite-pyrrhotite-cassiterite on top, downward to pyrite-pyrrhotite-cassiterite-chalcopyrite and sphalerite and finally to pyrite-pyrrhotite-marcasite; arsenopyrite is found at depth (Ahfeld & Schneider-Scherbina 1964). Stannite tends to form after cassiterite. Tin ores are massive and often display geodic infilling. The grain size is in the order of millimetres to centimetres.

Vein infilling in Veta Grande is observed to record sequences of minerals, generally without replacements among them (Fig. 2).

Ore minerals may be accompanied by quartz or siderite; in some cases members of the tourmaline group may also appear (Fig. 3), thus indicating a high activity of boron in the hydrothermal fluids.

Similar textures can be encountered in Bonanza and Suerte. However, these veins may be enriched in Ag minerals and the mineral sequence becomes complex (Figs. 4 and 5). Silver may be distributed in galena_{s,s}, or as discrete phases such as freibergite, matildite, cervelleite and others.

5 Mineral chemistry

In order to study the chemical compositions, in particular the tenors of rare elements, samples were analyzed with electron microprobe.

5.1 Cassiterite

Tantalum concentration is in general very low, but a sample from the 240 level returned values up to 0,3 wt%. Taking into account the large volume of cassiterite in the deposit, a more comprehensive study of a larger number of samples from this deposit is planned. Indium is not present in the studied samples, and the tenors of Ti and Nb are close to the detection limit of the microprobe. Iron is also low, and hence crystals from this locality are very pure and close to the stoichiometric ideal composition. Samples from other galleries in the mine and from La Suerte vein are also very pure and devoided of rare elements.

5.2 Stannite

Stannite is described in many deposits worldwide as a In-bearing mineral. Unfortunately, in the case of Huanuni this mineral do not contains indium. However, analysed stannite often return significant concentrations of silver, up to 0,3 wt%.

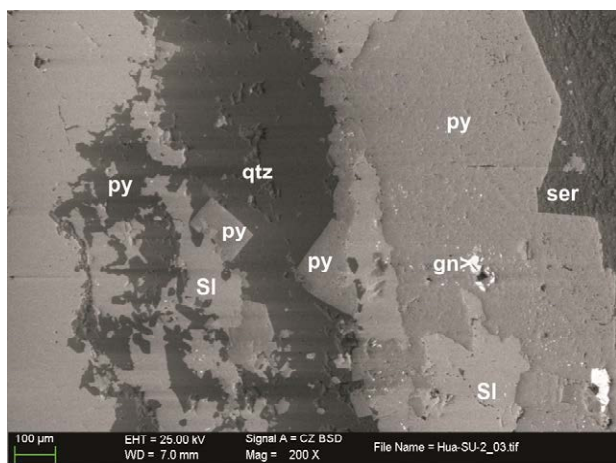


Figure 5. Symmetric filling of a veinlet in sericitized host rocks. Note a typical passive sequence. Suerte mine, SEM image, mode BSE.

5.3 Sphalerite

Sphalerite is generally marmatite, and is black because of its high Fe content - systematically close to 10 wt %. However, a late botryoidal generation of sphalerite occurs as filling porosity. This sphalerite is almost transparent and Fe-poor. In contrast, it is strongly enriched in Cd (up to 5,33 wt%). Indium content is very low in all analysed samples, commonly below detection limit.

5.4 Arsenopyrite

Arsenopyrite is slightly enriched in Co (up to 0,2 wt%). Values for Ni and Sb are close to detection limit.

6 Discussion and conclusions

Samples from all the localities return interesting tenors of Ag and Sn minerals.

Galleries are hosted by thick sequences of black shales and therefore the possibility of finding Au and PGE enrichments in arsenopyrite cannot be discarded.

Despite the tenors of Ta in cassiterite are low when compared with those found in cassiterite from evolved pegmatites, it must be taken into account that Huanuni is one of the largest mines of Sn in the world and the production of Sn is very large. Hence, it should be convenient to analyze with more detail the distribution of Ta in the cassiterite of the Huanuni deposit. In particular, the veins located close to the porphyritic intrusive are suggested to be those of higher potential for this metal.

Acknowledgements

The Corporación Minera de Bolivia (COMIBOL) allowed us to visit the mines and publish the results. Samples were analyzed in the Centres Científics i Tecnològics of the University of Barcelona. Dr. X. Llovet helped with the microprobe calibration. Funding was provided by the Consolidated Research Group Grant SGR 444 of the Generalitat de Catalunya and the AECID grant A3/042750/11.

References

- Ahfeld F, Schneider-Scherbina A (1964) Los yacimientos minerales y de hidrocarburos de Bolivia. Departamento Nacional de geología del ministerio de minas y petróleo, La Paz, Bolivia. Boletín N° 5 (Especial): 167-171.
- Arce OR (2009) Metalliferous ore deposits of Bolivia. La Paz, Bolivia, SPC Impresores SA.
- GEOTECMIN (2001) Mapa geológico de Bolivia 1:1000.000. La Paz, Bolivia.
- McQuarrie N, DeCelles PG (2001) Geometry and structural evolution of the central Andean backthrust belt, Bolivia. *Tectonics* 20: 669 – 692.
- Müller B, Frischknecht R, Seward TM (2001) A fluid inclusion reconnaissance study of the Huanuni tin deposit (Bolivia), using LA-ICP-MS micro-analysis. *Mineral Deposita* 36: 680-688.
- Sugaki A, Shimada N, Ueno H, Kano S (2003) K-Ar Ages of Tin-Polymetallic Mineralization in the Oruro Mining District, Central Bolivian Tin Belt. *Resource Geol.* 53: 273–282.
- Turneure, F.S. (1971) The Bolivian tin-silver province. *Econ Geol* 66: 215–225.

The Viloco Sn-W-Mo-As deposits, Bolivia: geology and mineralogy

David Artiaga, Belén Torres, Lisard Torró, Esperança Tauler, Joan Carles Melgarejo

Departament de Cristal·lografia, Mineralogia i Dipòsits Minerals, Universitat de Barcelona, c/Martí I Franquès s/n 08028 Barcelona, Catalonia, Spain

Oswaldo R. Arce

Colegio de geólogos de Bolivia, C/ Federico Suazo 1673, Edificio SERGEOTECMIN

Abstract. The Viloco vein field is hosted in black shales around a granitic intrusion. The paragenesis in these veins depend on their position with respect to the granites, with a domain of W-As-Bi-Cu in the intrusives or in their vicinity, an intermediate domain with Sn (cassiterite) and a distal enriched in Zn (sphalerite) and stannite domain. The order of deposition according to the mineral sequence built in this work for each domain is also similar to that of the regional zoning. The highest tenors of In in the mineral sequence are found in stannite of the distal domain.

Keywords. Vein, Sn, hydrothermal alteration, mineral sequence, granite, zoning, Viloco deposit

1 Introduction

The Viloco mining town is located in the Loayza province, in La Paz department in Bolivia, 80 km SE of the capital. Mines are found in the Tres Cruces Range, at the Cordillera Real, a part of the Eastern Cordillera of the Andes. Most of the mines are found at altitudes largely exceeding 4500 m. The mining district is enclosed into the Bolivian tin belt (Ahlfeld 1967; Turneure 1971). The mines were discovered at the end of the 19th century. They were formerly known as “Araca mines”. Currently, some tens of galleries are in activity in an area that covers around 30 km². The mines are operated by small mining cooperatives that occupy more than 250 miners.

In addition to their Sn-W production, the mines are worldwide famous among mineral collectors because of their big and beautiful caramel-coloured cassiterite crystals, used in jewelry as gems. In spite of the significance of these deposits, only few old and uncompleted data are published on them (i.e., Ahlfeld & Schneider-Scherbina 1964; Kelly & Turneure 1970). The aim of this contribution is to supply data on the structure, mineral chemistry and paragenesis of the deposits.

2 Geology

The Cordillera Real is mainly made up of Paleozoic metasedimentary rocks intruded by granitic rocks. The Quimza Cruz batolite, which is related to the Viloco deposits, crops out to the SW of this range (Condarco 1976).

The Paleozoic sedimentary series were deposited in submarine environments and may reach up to 10,000 m in thickness (McQuarrie et al. 2001). The series begins with black shales with minor quartzites interbedded of

the Amutara Fm. (upper Ordovician). These strata pass vertically to the shales of the Uncía and Catavi Fms. (Silurian). The top of the series comprises the Vila Vila Fm lower Devonian shales.

The Paleozoic sedimentary rocks were regionally metamorphosed under low-grade conditions, producing slate, phyllite and minor quartzite (Martinez 1980). Andean deformation took place between the upper Oligocene and the Miocene (Heuschmidt et al. 2000) and produced folding and thrusting steeply dipping to the W along faults trending approximately NNW-SSE (Gillis et al. 2006). At the N of the Viloco town, the Amutara Fm. is folded in the Viloco syncline. Late fractures as faults and joints trend in several directions, being the NE-SW the dominant.

The Quimza Cruz intrusion is composed of two units (McBride et al. 1983; Kennan et al. 1995) the Mina Argentina (Mina Caracoles) body that consists of cordierite-bearing granodiorite and monzogranite, and the Mina Viloco porphyritic two-mica monzogranite with K-feldspar megacrysts. The respective ages, obtained by U-Pb in zircon, are late Oligocene with 26.2 ± 0.2 Ma and 25.4 ± 0.2 Ma (Gillis et al. 2006).

The Quimza Cruz granodioritic batholith was shallowly emplaced (Mlynarczyk & Williams-Jones 2005) after the bulk of upper crustal shortening in the Eastern Cordillera (Lamb and Hoke 1997) and produced a wide aureola of contact metamorphism on the black shales of the Amutara Fm., with an extensive development of hornfelses on the eastern side of the Viloco syncline.

3 Structure of the deposits

Vein deposits are mainly located in the vicinity of the granitic intrusives, hosted by the metamorphosed black shales of the Amutara formation. However, veins inside porphyritic granite dikes or hosted by granitic rocks were also found. Veins are nearly vertical and most of them have a direction roughly trending N 40° E and N 60°E (Fig. 1). They are grouped in sets, and the spacing among two veins is generally of a few meters. The vertical and longitudinal continuity of the veins can achieve several hundreds meters, and their width ranges from some mm to 50 cm.

Metal zoning is developed around the granite. Quartz veins inside the granite or in its vicinity are mainly rich in As-W-Bi-Cu. Tin predominates in veins found 500-2000 m far of the contact. Zn-(Pb) predominates in distal positions (Fig. 1).

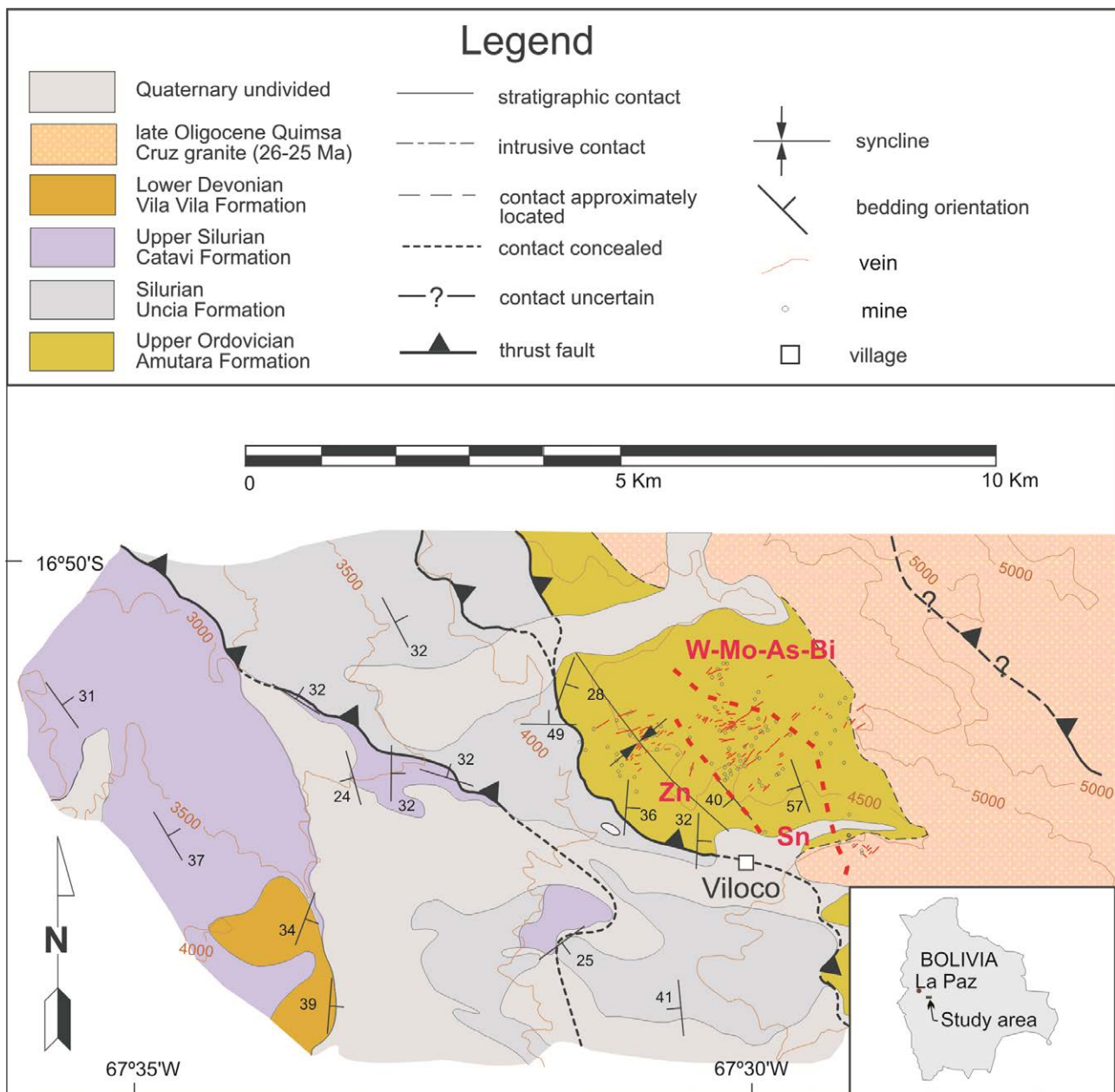


Figure 1. Zoning of the Viloco district and distribution of the mineralized veins and mines. Geological map after Gillis et al. (2006)

4 Mineralogy and textures

Most of the veins have drusy infill, with typical comb textures and euhedral crystals lining cavities. Cockade textures are also present in some brecciated domains. Grain sizes of the minerals typically range from 1 mm to 5 cm, with the exception of the trace minerals which present micrometric crystal sizes.

The hydrothermal alteration of the hosting schists consists largely of tourmalinization and silicification, accompanied locally by kaolinization and chloritization. Potassic and sericitic alterations have been observed in veins hosted in granitic rocks too.

The mineral sequence is quite similar in all domains of the district (Fig. 2). The differences are mainly related to the relative proportion of the minerals.

The mineral sequence starts with the precipitation of tourmaline, quartz, Sn-rich rutile, monazite, zircon, Fe-

rich chlorite and cassiterite, with löllingite and ferberite (Fig. 3).

A second sulphidation stage produced the replacement of löllingite by arsenopyrite, which is accompanied by sphalerite, chalcopyrite, stannite, native bismuth, bismuthinite and other trace minerals (Fig. 4). Chalcopyrite contains sphalerite stars, interpreted as exsolutions.

Ferberite is the dominant or unique ore mineral in the proximal domain; in some cases it is accompanied by minor amounts of scheelite. The mines situated at the northern side of the field concentrate wolframite and lesser amounts of arsenopyrite. Cassiterite would be the unique ore mineral phase in some parts of the Sn domain (as in the case of Veta Principal), and sphalerite would be the dominant or unique ore mineral at the distal parts of the district.

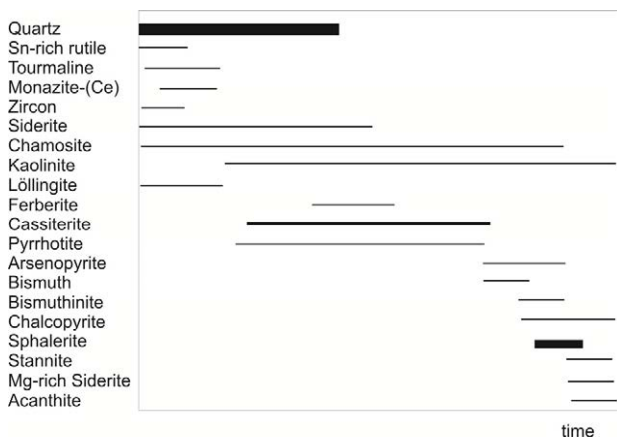


Figure 2. General sequence of crystallization in the veins of the Viloco district.

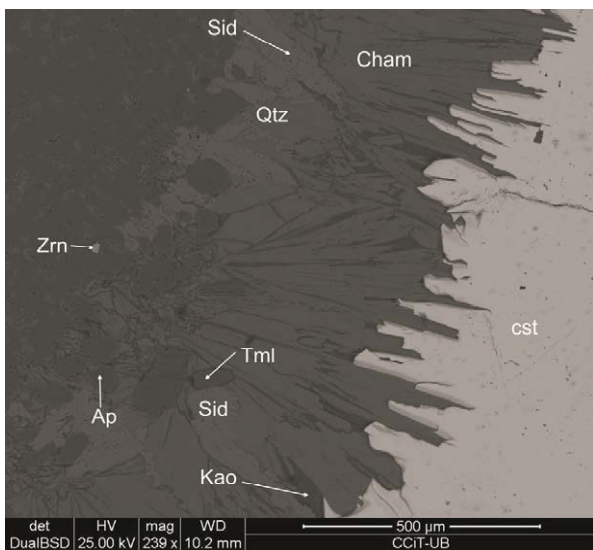


Figure 3. Detail of the contact of a typical vein and the host rock in the Sn domain. Zrn, zircon; Qtz, quartz; Sid, siderite; cham, chamosite; Ap, apatite; Tml, tourmaline; Kao, kaolinite; cst, cassiterite. SEM image, BSE mode.

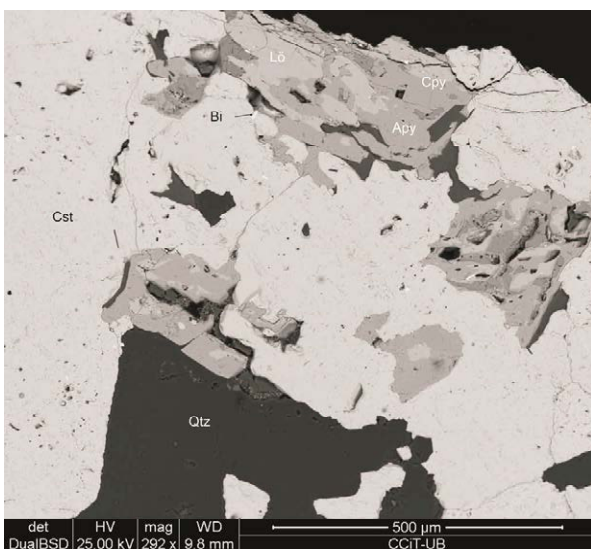


Figure 4. Detail of the second stage of mineralization. Quartz (qtz), cassiterite (cst) and subhedral löllingite (llo) are replaced by a second assemblage of arsenopyrite (apy) and chalcopyrite (cpy). SEM image, BSE mode.

In contrast, some of the mines located to the E of the Viloco town and hosted in granite have a remarkably different mineral sequence than that above. The sequence begins with the development of tabular hematite crystals, which are partly replaced by cassiterite, scheelite, löllingite and pyrite. The ensemble is largely replaced by magnetite and siderite; hematite is pseudomorphosed by magnetite (mushketovite variety). Finally, the above mineral assemblage is in turn replaced by another sulphide-rich stage, which includes abundant pyrrhotite, stannite, chalcopyrite, Fe-rich pyrrhotite, native bismuth and other minority minerals phases.

5 Mineral Chemistry of the ores

Samples from different veins were analyzed with electron microprobe. Some of the minerals from Viloco mines have a remarkably variable composition depending on their position with respect to the intrusive, within proximal or distal facies.

5.1 Stannite

Stannite has the higher proportions of In in the deposit, and contain up to 2,04 wt% In (0,08 apfu) in some stannite grains of the distal mines. In has a negative correlation with Sn, suggesting that In substitutes Sn in the structure of stannite. The proportion of Zn does not exceed 0,4 apfu, thus indicating variable ratios in the kesterite-stannite series.

5.2 Cassiterite

Cassiterite is almost pure, and the degree of substitutions of Sn by Nb, Ti, Ta and Fe is very low. TiO₂ contents does not exceed 0,8 wt%. However, the 0,2 wt% Ta contents on cassiterites locally found would be similar to those reported in deposits in apical granite intrusions, as in Brasil (Costi et al. 2000), thus opening an interesting line for Ta exploration.

5.3 Sphalerite

Sphalerite is moderately Fe-rich, accordingly with the dark colour of the mineral; the average content is about 11-12 wt% Fe. The In content is about 0.2 wt% in average. These concentrations are not very high when compared with other localities described in the literature (i.e., up to 6,7 wt% In in sphalerite, Cook et al. 2009) but can be considered an interesting byproduct of Zn mining. Other elements such as Ga, Ge, Sn, Cu, Hg or Mn are below the detection limit of the electronic microprobe.

5.4 Arsenides

Löllingite is enriched in Co and Ni. Thus, it achieves concentrations up to 4,57 wt% Co. The arsenopyrite crystals that replaced löllingite are poor in these elements. These relations are similar to those found in Pd-rich löllingites in Catalonia (Canet et al. 2003).

6 Discussion and conclusions

The Viloco deposits constitute an example of zoned peribatolitic Sn-W district. The zonal distribution of ores suggests that hidden deposits could be found in the parental granites.

Sn-(W) vein deposits have been recently recognized as important In suppliers (Ishihara et al. 2009). In the Viloco deposit, In is concentrated in the stannite formed during the late stages by replacement of cassiterite. A similar enrichment process has been described in the Mt Pleasant tin deposit in Canada (Boorman & Abbott 1967). Although the In contents in sphalerite are lower, sphalerite is much more abundant in these deposits and could host the main portion of the reserves of this element.

On the other hand, the deposits are hosted by thick series of black shales that could be a possible preconcentration for many other elements, including Au and PGE. Gold enrichment has been described in similar environments (i.e. Lerouge et al. 2007). It should be noted that the löllingite structure may concentrate precious elements (i.e. Canet et al. 2003). The occurrence of large amounts of Co-rich arsenides in the veins suggests that these black shales were a good trap for redox-sensitive elements. Hence, a survey on arsenopyrite and löllingite should not be discarded.

Acknowledgements

The association of mining cooperatives in Bolivia (FENCOMIN) allowed us to visit the mines and publish the results. Samples were analyzed in the Centres Científics i Tecnològics of the University of Barcelona. Dr. X. Llovet helped on the microprobe calibration. Funding was provided by the Consolidated Research Group Grant SGR 444 of the Generalitat de Catalunya and the AECID grant A3/042750/11.

References

- Ahlfeld F, Schneider-Scherbina AI (1964) Los yacimientos minerales y de hidrocarburos de Bolivia. *Bol Dept Nac Geol, La Paz* 5: 388 p.
- Ahlfeld F (1967) Metallogenetic epochs and provinces of Bolivia. *Miner Deposita* 2: 291–311.
- Boorman RS, Abbott D (1967) Indium in co-existing minerals from the Mount Pleasant tin deposit. *Can Mineral* 9: 166–179.
- Canet C, Alfonso P, Melgarejo JC, Jorge S (2003) PGE-bearing minerals in Silurian sedex deposits in the Poblet area, southwestern Catalonia, Spain. *Can Mineral* 41: 581–595.
- Condarco J (1976) Estudio geológico minero del yacimiento de Viloco. Unpubl. Bsc thesis Geologicl Enginery - Universidad Mayor de San Andrés, Departamento de Geociencias, 67 pp.
- Cook NJ, Ciobanu CL, Pring A, Skinner W, Shimizu M, Danyushevsky L, Saini-Eidukat B, Melcher F (2009) Trace and minor elements in sphalerite: A LA-ICPMS study. *Geochim Cosmochim Acta* 73(16): 4761–4791.
- Costi HT, Horbe AMC, Borges RMK, Dall'Agnol R, Rossi A, Sighnolfi G (2000) Mineral chemistry of cassiterites from pitinga province, Amazonian craton, Brasil. *Rev Bras Geoc* 30: 775–782.

- Gillis RJ, Horton BK, Grove M (2006) Thermochronology, geochronology, and upper crustal structure of the Cordillera Real: Implications for Cenozoic exhumation of the central Andean plateau. *Tectonics*, 25, TC6007, doi: 10.1029/2005TC001887.
- Ishihara S, Hoshino K, Murakami H, Endo Y (2006) Resource evaluation and some genetic aspects of indium in the Japanese ore deposits. *Res Geol* 56: 347–364.
- Kelly WC, Turneure FS (1970) Mineralogy, paragenesis and geothermometry of the tin and tungsten deposits of the eastern Andes, Bolivia. *Econ Geol* 65: 609–680.
- Kennan L, Lamb S, Rundle C (1995) K-Ar dates from the Altiplano and Cordillera Oriental of Bolivia: implications for Cenozoic stratigraphy and tectonics. *J S Am Earth Sci*, 8: 163–186.
- Heuschmidt B, Miranda Angles V, Bellot-La Torre J, Claire-Zapata J, Casas-Saavedra A (2000) Sinopsis de la metalogenia en Bolivia. *Bol. Serv. Nac. Geol Min*, 19: 56 pp.
- Lamb L, Hoke L (1997): Origin of the high plateau in the central Andes, Bolivia, South America, *Tectonics*, 16: 623 – 649.
- Lerouge C, Deschamps Y, Piantone P, Gilles Ch, Breton J (2007) Metal-carrier accessory minerals associated with W ± Sn mineralization, La Chataigneraie tungsten ore district, Massif Central, France. *Can Mineral*, 45(4): 875–889.
- Martínez C (1980) Structure et évolution de la chaîne hercynienne et de la chaîne andine dans le nord de la Cordillère des Andes de Bolivie, *Trav. Doc. ORSTOM*, 119: 352 pp.
- McBride SL, Robertson RCR, Clark AH, Farrar E (1983) Magmatic and metallogenetic episodes in the Northern Tin Belt, Cordillera Real, Bolivia. *Geol. Rundsch.* 72: 685–713.
- McQuarrie N, DeCelles PG (2001) Geometry and structural evolution of the central Andean backthrust belt, Bolivia. *Tectonics*, 20: 669 – 692.
- Mlynarczyk MSJ, Williams-Jones AE (2005) The role of collisional tectonics in the metallogeny of the Central Andean tin belt. *Earth Planet Sc Lett*, 240: 656–667.
- Turneure F S (1971): The Bolivian tin-silver province, *Econ Geol*, 66: 215–225.

Formation conditions of Hg-silver deposition at the Imiter deposit (Anti-Atlas, Morocco)

A.S.Borisenko, A.A. Borovikov, G.G. Pavlova, Yu.A. Kalinin, P.A. Nevolko, L.V. Gushchina
Institute of Geology and Mineralogy SB RAS, Novosibirsk, Russia

V.I. Lebedev
Tuva Institute for Exploration of Natural Resources SB RAS, Kyzyl, Tuva

L. Maacha
MANAGEM company group ONA, Morocco

A.V. Kostin
Institute of Geology of Diamond and Noble Metals SB RAS, Yakutsk, Russia

Abstract. New data about the ages of the mercury-silver (Ag-Hg) mineralization and Mesozoic magmatism at the Imiter deposit and around (Anti-Atlas, Morocco) have been obtained. According to the $^{40}\text{Ar}/^{39}\text{Ar}$ dating, age of the Ag-Hg mineralization is about 254.7 \pm 3.2 Ma. $^{40}\text{Ar}/^{39}\text{Ar}$ dating of two biotite and potassium feldspar samples from microsyenite dikes indicates 204.5 \pm 2.5 and 199.5 \pm 2.4 Ma (both of Triassic age). The age of Ag-Hg mineralization and magmatic rocks coincides with stage of development of Early Mesozoic rifting and magmatism in the Anti-Atlas. Fluid inclusion study in minerals of silver ores from the Imiter deposit shows that quartz-silver veins were formed at the temperature from 220 to 114 $^{\circ}\text{C}$ from hydrothermal fluid, which consists of concentrated (26 wt%) chloride solution and $\text{N}_2\text{-CH}_4$ gas phase. Dolomite-polysulfide veins deposited at temperatures <250 $^{\circ}\text{C}$ from the solution with concentration from 15 to 5 wt% containing CO_2 gas phase.

Keywords. Ag-Hg deposits of Morocco and Russia; Imiter deposit in Morocco, Anti-Atlas; $^{40}\text{Ar}/^{39}\text{Ar}$ dating; fluid inclusions study; $\text{CH}_4\text{-CO}_2\text{-N}_2$ gas phase.

1 INTRODUCTION

Mercury-containing silver and Ag-Hg intermetallics occur in the primary and oxidized ores of various types of ore deposits: Ni-Co-Ag-Bi-U, mercury, polymetallic, Ag-Sb and Ag-Hg. However, in economically important quantities they are present only in the ores of Ni-Co-Ag-Bi-U and Ag-Hg deposits. The mercury-silver (Hg-Ag) deposits represent a specific type of silver mineralization, which differs from the other by predominant Hg-silver as the main ore mineral and presence of the other silver sulfides and sulfosalts. There are several ore districts with Hg-Ag mineralization such as Anti-Atlas in Morocco, Verkhoyansk in Yakutia, Altai-Sayan in Russia, etc. The largest of them is Anti-Atlas, where three Hg-Ag deposits are known: Imiter, Igoudran, Zgounder and several occurrences including Bou-Azzer cobalt deposit ore field (Levrèsse, 2001; Essaraj et al., 1998, 2005). The most economically important is the Imiter deposit mined since the 8th century BC and to the present day.

2 Geology of the Imiter deposit and the age of Hg-Ag mineralization

The ore fields of the Imiter and Igoudran deposits are composed by Middle Neoproterozoic terrigenous rocks (sandstones, aleurolites and black shale), which cut by Neoproterozoic intrusions of gabbro, diorite and granodiorite. They are unconformably overlain by Late Neoproterozoic (NP₃) effusive rocks: andesite, rhyolites, and ignimbrites. Dykes and stocks of andesite, dolerite, rhyolite and granite porphyry (NP₃) are also known. Deposits of different types (Mo-greisen, Au-Ag, Ag-polymetallic, Co-As and barite veins) preceded Ag mineralization. Neoproterozoic rocks which overlain by platform sediments of the Cambrian age are cut by dolerite, monzonite and high-K-microsyenite dykes. Their geological age is indicated as post-Ordovician. The age of microsyenite obtained on biotite and K-feldspar samples using $^{40}\text{Ar}/^{39}\text{Ar}$ method in Analytical Centre of the Institute of Geology and Mineralogy SB RAS (Novosibirsk, Russia) is about 204.5 \pm 2.5 and 199.5 \pm 2.4 Ma (Fig. 1).

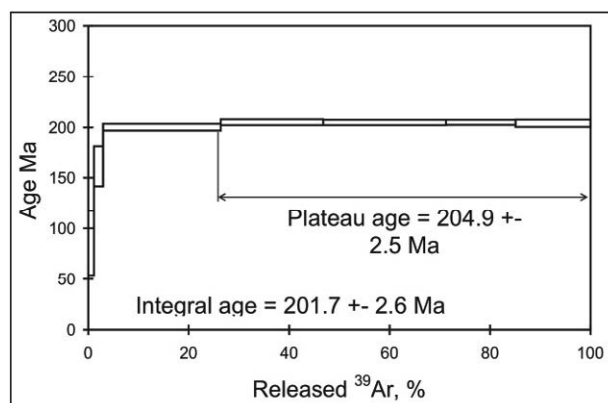


Figure 1. $^{40}\text{Ar}/^{39}\text{Ar}$ age of biotite and K-feldspar from microsyenite dyke, Imiter deposit.

Industrial Hg-Ag mineralization of the Imiter and Igoudran deposits was studied by many authors (Baroudi et al., 1999; Levrèsse, 2001; Cheilletz et al., 2002; Levrèsse et al., 2004; Gasquet et al., 2005; Tuduri et al., 2006). The ores are localized in black shales as quartz-

carbonate veins and vein zones with pink dolomite, Hg-silver, sulfosalts of Ag, Cu, and Pb, imiterite (Ag_2HgS_2), galena, sphalerite and arsenopyrite. Two main mineral associations are distinguished: dolomite-polysulfide (pink dolomite, galena and sphalerite, chalcopyrite, sulfosalts of Ag, Cu, Pb, including freibergite with Ag contents from 25.5 to 42.5 wt% and Hg contents about 0.2 wt%, acanthite, etc.) and quartz-silver (sugar-like grey quartz, adularia, Hg-silver and arsenopyrite). The last mineral association represents the main ore stage. Native silver occurs as impregnations in the sugar-quartz veins with different quantities of quartz, rich silver-bearing veins (up to 0.5 m), thin veinlets and disseminations in black shale. Mercury contents in native silver range from 1 to 36 wt%, sometimes with Sb impurity (up to 2 wt%). Hg-Ag Zgounder deposit situated in the west Anti-Atlas is similar to Imiter by ore composition and conditions of their localization. In the ore field of the Co-Ni-As Bou-Azzer deposit Hg-Ag mineralization was found as independent zone with native silver in altered quartz diorite. Hg-silver is associated with quartz, adularia, albite and spatially separated from the cobalt mineralization. The age of this mineral assemblage is 218 Ma (Levresse, 2001; Essaraj et al., 2005). Silver mineralization of the Imiter deposit attributed to the Late Neoproterozoic stage of magmatism and mineralization, and was linked with rhyolite dykes (Levresse, 2001, 2004, etc.). To determine the age of Ag-Hg mineralization at the Imiter deposit we performed the $^{40}\text{Ar}/^{39}\text{Ar}$ dating of adularia from a vein of grey quartz (drill hole SFG 289, depth 56.5 m). These veins are composed of fine-grained grey quartz with Hg-silver impregnation. Small rhombic adularia crystals occur along the selvages of vein (Fig. 2). According to the $^{40}\text{Ar}/^{39}\text{Ar}$ dating the age is about 254.7 ± 3.2 Ma (Fig. 3). This age is close to the age of Triassic microsyenite dykes, dolerite dykes of the Bou-Azzer deposit (Lebedev, 1998), dolerite dykes of the Haute Moulouya, Foug Zguid and Ighrem dykes (210-200 Ma) (Feichtner et al., 1992; Sebai et al., 1991; Silva et al., 2006; Palencia-Ortas et al., 2011), and both magmatic and ore events correspond to the initial stage of the Early Mesozoic rifting development in Anti-Atlas.

3 Fluid inclusion study

Fluid inclusion study in quartz from silver ores (grey quartz and quartz from dolomite-polysulfide veins), and from different types of ores of earlier hydrothermal mineralization have been performed to determine the physico-chemical conditions of Ag-ores deposition at the Imiter deposit. Grey quartz contains primary gas and 2-phase fluid inclusions located in the growth zones (Fig. 4 a, b). There are two-phase inclusions containing trapped native Ag, indicating the capture of these inclusions during simultaneous crystallization of Ag and quartz (Fig. 4 c, d). Gas phase composition of the two-phase inclusions in grey quartz is characterized by the absence of CO_2 with a variable ratios of nitrogen and methane according to the Raman spectroscopy data (N_2 from 88.6 to 0.0, and CH_4 from 100.0 to 11.4 mol %) (Fig. 5). Homogenization of fluid inclusions occurred at the 220 -

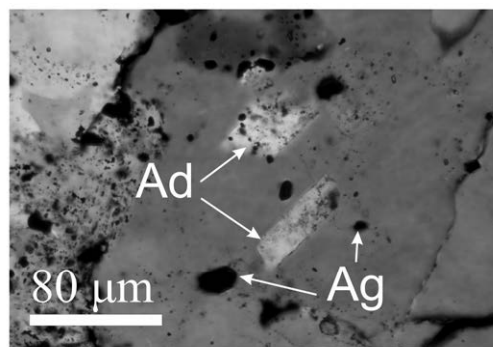


Figure 2. Adularia crystals 30-70 μm size (Ad) and native silver (Ag) in the grey quartz veinlet. Imiter deposit, drill hole SFG 289, depth 56.5 m.

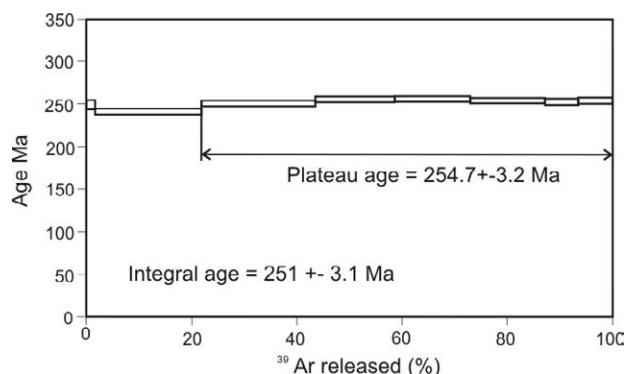


Figure 3. Results of $^{40}\text{Ar}/^{39}\text{Ar}$ dating of adularia from the veinlet of grey quartz.

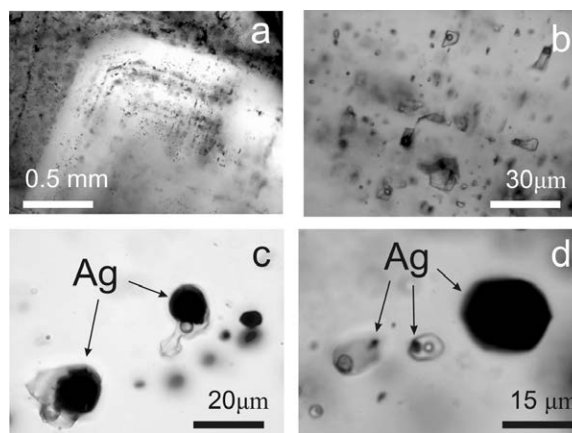


Figure 4. Primary gas and 2-phase inclusions in grey quartz (a, b) and inclusions containing trapped native Ag phase (c, d).

114°C, that indicates low temperatures of the grey quartz formation. The concentration of salts ($\text{NaCl} + \text{CaCl}_2$) in the inclusion solutions ranges from 26 to 7 wt% accordingly to the cryometry data. In fluid inclusions with highly concentrated solutions $\text{Ca}/(\text{Ca} + \text{Na})$ ratio ranges from 0.4 to 0.5. Similar homogenization temperatures (230-90°C), solution concentrations (30-22 wt%) and gas phase composition of fluid inclusions in quartz were determined in quartz of the late veins with Hg-silver and adularia crystals from the Bou-Azzer and Zgounder deposits (Essaraj et al., 2005). At the same time, these parameters of quartz-Ag-Hg mineral assemblage are very different from the other types of hydrothermal mineralization in the ore fields of these deposits.

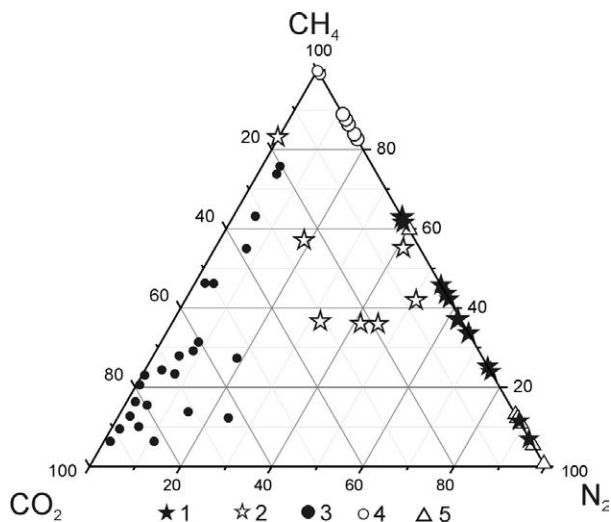
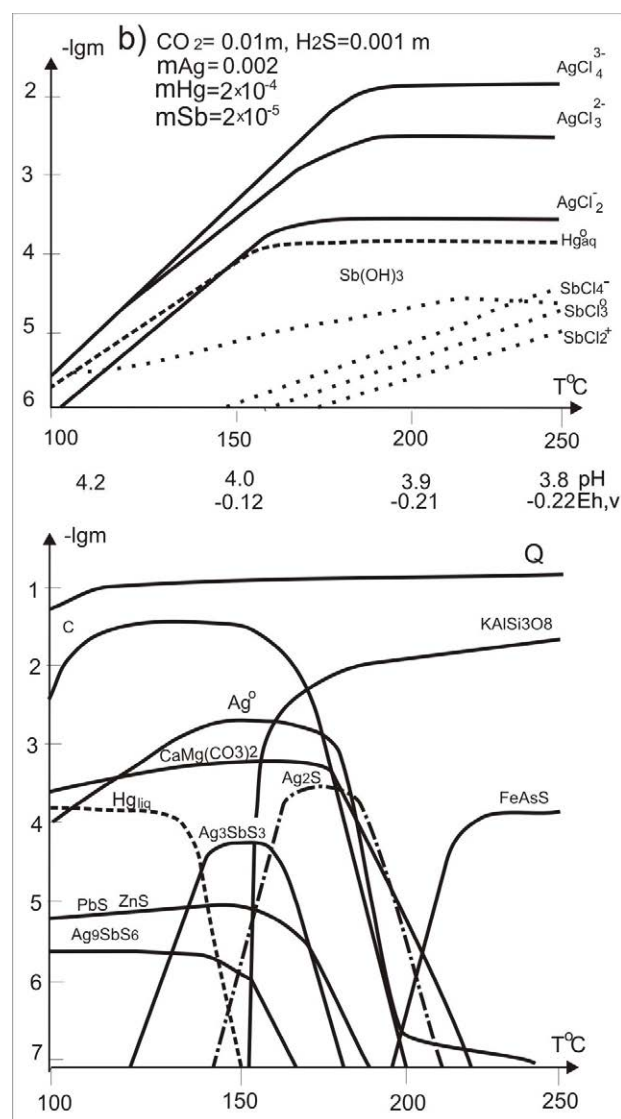
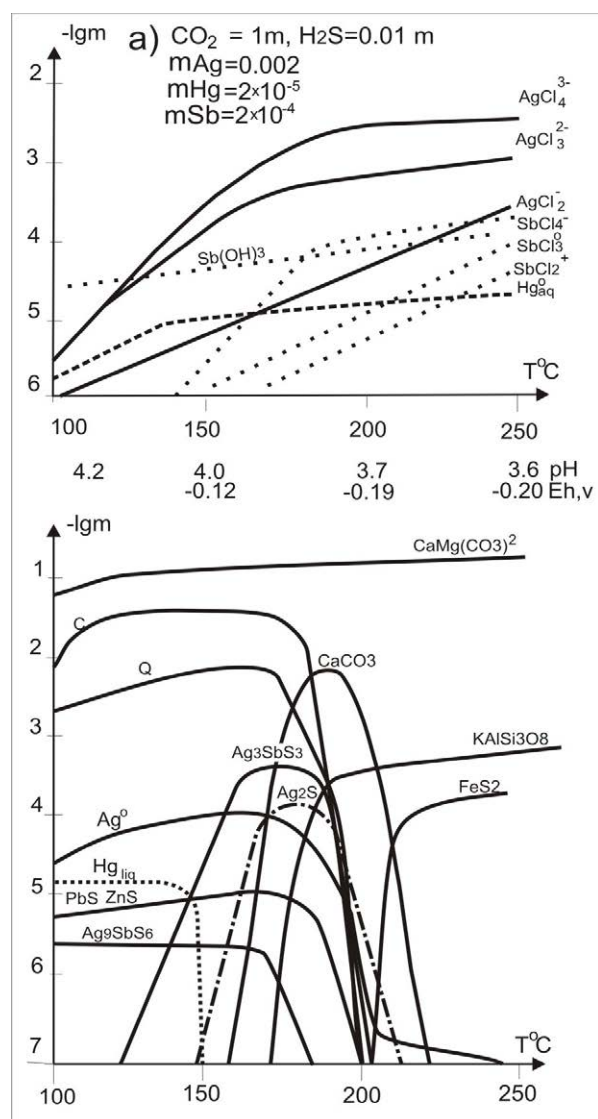


Figure 5. Composition of gas phase of fluid inclusions in quartz from Hg-Ag and earlier other types of mineralization. Imiter deposit: 1 – grey quartz and 2 – quartz of dolomite-polysulfide stage by authors data; 3 – quartz of earlier veins from (Baroudi et al., 1999); Bou-Azzer deposit: 4 - data from (Essarraj et al., 2005); 5 – (Lebedev, 1998).

Quartz from dolomite-polysulfide veins contains gas and two-phase primary fluid inclusions, which are located in the growth zones. In the composition of the gas phase N_2 (44.3-5.6 mol %), CH_4 (90-55.7 mol %) and CO_2 (56.5-2.5 mol %) are present (Fig. 5). Homogenization temperature of inclusions $<250^\circ C$, the concentration of solutions ranges from 15 to 5 wt%. Thus, grey quartz and quartz of dolomite-polysulfide Ag stages differ in composition of gas phase of fluid inclusions. Inclusions in grey quartz are characterized by N_2 - CH_4 composition and gas phase of higher density than the inclusions in quartz from other types of hydrothermal mineralization. With the depth N_2 portion decreases and methane portion increases up to 100% at the 1150 m horizon (SFG 289-56.5 m sample). The grey quartz vein formation was due to degassing and partial CO_2 and H_2S removal from hydrothermal fluid accordingly to the thermodynamic modeling data (Fig. 6).

Figure 6. Concentration of Ag, Hg, Sb chemical species in 4.6 m chloride solutions with different CO_2 and H_2S contents (a, b), and amounts of mineral phases precipitated during cooling of the solutions and pressure decrease from 50 to 20 MPa.



These events led to the local redox-potential decrease and pH increase that together with other factors (lowering of temperature), resulted in massive deposition of Hg-silver instead of Ag and Hg sulfides.

The predominant chemical specie in weakly acidic chloride solutions is Hg_{aq}^0 , and Hg-silver deposition occurs at the overlap of mercury and silver stability fields at low temperatures <150°C (Obolensky et al., 2006). Due to the lack or very low CO₂ content in the hydrothermal fluid, no carbonates were deposited. Hydrothermal solutions during the dolomite-polysulfide Ag stage forming were more acidic in the result of CO₂ and H₂S presence in the fluid that resulted in the formation of carbonate mineral association with sulfides Ag, Hg, Pb, Cu, Zn, and Fe.

The other large ore district with Hg-silver mineralization is the Verkhoiansk province in Yakutia, where three silver ore districts have been found (Kostin et al., 2011). Three types of silver mineralization are distinguished by mineral composition and main ore minerals: galena, pyrargyrite, fahlore and native silver, which forms a row of zonation: Ag-Pb → Ag-Sb → Ag-Hg. Minor ore minerals are sphalerite, acantite, lenaite, boulangerite, jamesonite, diaphorite, stephanite, imiterite, cinnabar and stibnite. Gangue minerals are mainly quartz and siderite. Native Hg-silver occurs as veinlets, films, plates, breccia cement and aggregates up to 5 kg. Mercury contents in native silver range from 11 to 34 wt%, Sb from 14.5 to 15.7 wt%. Hydrothermal silver mineralization is known also in the Altai-Sayan region of southern Siberia, where native Ag aggregates were found with weight up to 30 kg.

Acknowledgements

The authors are grateful to the mine management of the Imiter mine for access to underground workings and drill core. The work is supported by RFBR grant 11-05-12058-OFI-M-2011 and Presidium of RAS grant 27.2.

References

- Baroudi Z, Beraouz H, Rahimi A, Saquaque A., Chouhidi M (1999) Mineralisations polymetalliques argentiferes d'Imiter Jbel Saghro, Anti-Atlas, Maroc: mineralogie, evolution des fluides mineralisateurs et mecanismes de depots. *Chron Rech Min* 536-537: 91-111
- Cheilletz A, Levresse G, Gasquet D, Azizi-Samir MR, Zyadi R, Archibald DA, Farrar E (2002) The giant Imiter silver deposit: Neoproterozoic epithermal mineralization in the Anti-Atlas, Morocco. *Miner Deposita* 37: 772-781
- Essaraj S, Boiron MC, Cathelineau M, Banks D, El Boukhari A, Chouhaidi MY (1998) Brines associated to Ag deposition in the Zgounder silver deposit (Anti-Atlas, Morocco). *Eur. J. Mineral* 10: 1215-1226
- Essaraj S, Boiron MC, Cathelineau M, Banks DA, Banharref M (2005) Penetration of surface-evaporated brines into the Proterozoic basement and deposition of Co and Ag at Bou Azzer (Morocco): Evidence from fluid inclusions. *J. African Earth Sciences* 41: 25-39
- Fiechtner L., Friedrichsen H, Hammerschmidt K (1992) Geochemistry and geochronology of Early Mesozoic tholeiites from Central Morocco. *Geologische Rundschau* 81/1: 45-62
- Gasquet D, Levresse G, Cheilletz A, Azizi-Samir MR, Mouttaqi A (2005) Contribution to a geodynamic reconstruction of the

- Anti-Atlas (Morocco) during Pan-African times with the emphasis on inversion tectonics and metallogenic activity at the Precambrian-Cambrian transition. *Precambrian Research* 140: 157-182
- Lebedev VI (1998) Ore-magmatic systems of typical arsenide-cobalt deposits. SB RAS Press. Novosibirsk [in Russian]
- Levresse G (2001) Contribution a l'etablissement d'un modele genetique des gisements d'Imiter (Ag-Hg), Bou Madine (Pb-Zn-Cu-Ag-Au), Bou Azzer (Co, Ni, As, Au, Ag) dans l'Anti-Atlas marocain. Institut National Polytechnique de Lorraine. 218 p
- Levresse G, Cheilletz A, Gasquet D, Reisberg L, Deloule E, Marty B, Kyser K (2004) Osmium, sulphur, and helium isotopic results from the giant Neoproterozoic epithermal Imiter silver deposit, Morocco: evidence for a mantle source: *Chemical Geology* 207(1-2) : 59-79
- Kostin AV, Okunev AE, Denisov GV, Osipov LV (2011) Peculiarities of silver mineralization of the Nizhneimkansky and Allara-Sakhsky ore clusters (Eastern Yakutia). *Otechestvennaya geologia* 5: 3-11 [in Russian]
- Obolensky AA, Gushchina LV, Borisenko AS (2006) Physicochemical models for ore formation processes at mercury deposits. *Russian Geology and Geophysics* 47(12): 1344-1359
- Palencia-Ortas A., Ruiz-Martinez VC, Villalain JJ, Osete ML, Vegas R, Touil A, Hafid A, McIntosh G, van Hinsbergen DJJ., Torsvik TH (2011) A new 200 Ma paleomagnetic pole for Africa and paleo-secular variation scatter from Central Atlantic Magmatic Province (CAMP) intrusives in Morocco (Ighrem and Fom Zguide dykes). *Geophysical Journal International* 185: 1220-1234
- Sebai, A., Feraud, G., Bertrand, H., Hanes, J. (1991) ⁴⁰Ar/³⁹Ar dating and geochemistry of tholeiitic magmatism related to the early opening of the Central Atlantic rift. *Earth and Planetary Science Letters* 104: 455-472
- Silva PF, Henry B, Marques F O, Madureira P, Miranda JM (2006) Paleomagnetic study of the Great Fom Zguid dyke (Southern Morocco): a positive contact test related to metasomatic processes. *Geophysical Research Letters* 33(21): L21301
- Tuduri J, Chauvet A, Ennaciri A, Barbanson L (2006) Model of formation of the Imiter silver deposit (eastern Anti-Atlas, Morocco). *New structural and mineralogical constraints. Comptes Rendus Geosciences* 338 (4): 253-261

Proterozoic metallogeny in the NW border of Botswana

Sergi Cardona, Lisard Torró, Marc Campeny, Eloi Andreu, Joan Carles Melgarejo, Joaquín A. Proenza

Dpt. Cristal·lografia, Mineralogia i Dipòsits Minerals, Universitat de Barcelona. C/ Martí i Franquès s/n 08028 Barcelona, Catalonia, Spain

Mike C.J. De Witt, James M. Bruchs

Tsodilo Resources Limited. Canada Trust Tower. BCE Place. 161 Bay Street, P.O. Box 508 Toronto, ON M5J 2S1 (Canada)

John F. Lewis

Department of Earth and Environmental Sciences, George Washington University, Washington, DC 20052, USA

Abstract. A drilling program in NW Botswana based on anomalies detected by geophysical prospecting allowed discovering the structure of the Proterozoic basement and several styles of mineralizations. A riftogenic Proterozoic basin trending NW-SE was filled with sedimentary series, mainly black shales and conglomerates in the depocenter and conglomerates, quartzites and limestones at the margins. Opening of the basin resulted in mantle rising and basaltic vulcanism. SEDEX-type Cu-Pb-Zn-Ni-Co-Ag sulphide deposits accumulated in black shales. During a compressive stage, tectonic inversion produced reactivation of the above mentioned normal faults as inverse and the emplacement of ophiolitic sequences. Movement of basal hydrothermal fluids during this stage produced the remobilization of sulphides along with As-Au-Bi-Mo-REE-Th-U. These filled the Pb-Zn-Ni-Co-Ag-As-Au-Bi-Mo-REE-Th-U veins in the sheared zones and developed IOCG deposits replacing the margins of the basin. The ensemble suffered folding and regional metamorphism in amphibolite facies. Post-tectonic granites also have vein polymetallic mineralization that could correspond to an Intrusion-Related Gold Deposits model; they produce skarns on the hosting limestones. The studied skarns are poor in metals, but the context can be favourable for Au-bearing skarns.

Keywords. Botswana, IOCG, magnetite, skarn, shear, ophiolite, rift, tectonic inversion, heritage, SEDEX, IRGD.

1 Introduction

Many areas in Botswana are covered by large extensions of alluvial sediments associated with the Okavango delta. Therefore, no much information was available about the geology of the Precambrian basement of the area. During exploration for hidden kimberlites, Tsodilo Resources Ltd found huge geophysical anomalies extending tens of kilometres. Drilling on these areas allowed establishing the geology of the basement and opened an interesting window to the exploration of an unsuspected area. The aim of this work is to give a first draw of the metallogenetic events registered in the area.

2 Geographic and geological setting

The Tsodilo Hills are located at the NW of Botswana, 200 km NW far of the Maun City (Fig. 1), close to the Okavango delta. Most of the area is covered by recent sediments (e.g. Kalahari formation, thick soils, calcretes and alluvial materials of the Okavango River).

Therefore, information on the underlying formations can only be achieved by applying geophysical methods and diamantine drilling. New data obtained by Tsodilo Company suggest that the area has an Archaean gneissic basement unconformably overlain by series of neoproterozoic rocks affected by the PanAfrican orogeny. Thrusting caused by that event can be observed to be roughly parallel to the Okavango River, approximately NNW-SSE.

These thrusts seem to define an undescribed Upper Proterozoic sedimentary basin with an elongate shape, oriented approximately NNW-SSE. This basin is roughly parallel to the Okavango River.

The Okavango River currently forms a delta in an endorheic basin close to the Maun city. This endorheic basin is recent in age, and is controlled by extensional faults roughly NW-SE. Lacustrine sediments and evaporites are currently being deposited in it.

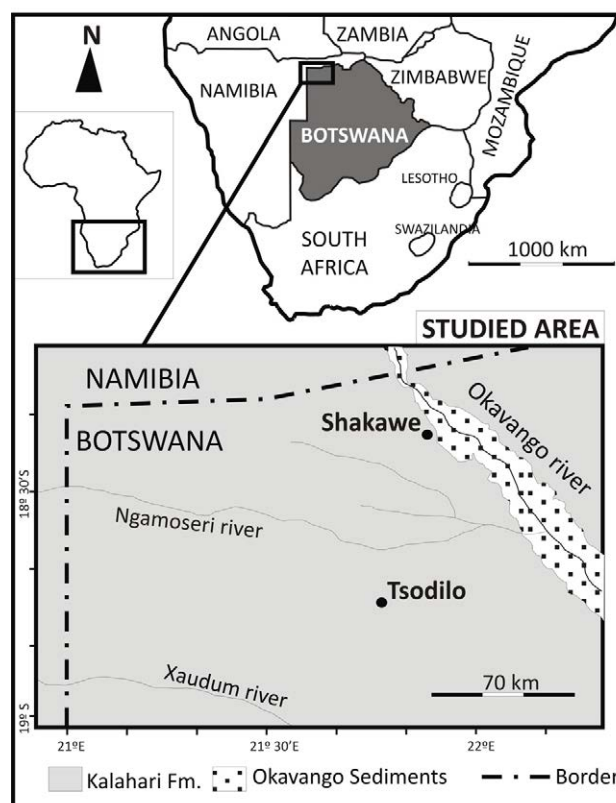


Figure 1. Overview of the study area.

3 Metallogenic domains

A total of 16 cores were sampled to study the mineralogy and textures of the ores, by using transmitted-reflected light microscopy, SEM-EDS and EMP. 12 of them were taken along profiles approximately perpendicular to the regional structure marked by the NNW-SSE thrusting. Based on the cores from the recent diamantine drilling program together with the regional structure and the geophysical data, some tectonostratigraphic domains are identified. The features of these NNW-SSE striking domains are summarized below.

3.1 Western Ultramafic Domain

The Western Ultramafic Domain is characterized by the occurrence of peridotitic rocks overthrusting schistose series. These ultramafic rocks are serpentinized and represent ophiolitic sequences. Contacts between this unit and the Western Conglomerate Domain have been produced along regional faults since an intense gauge and more extensive hydrothermal alteration exist. Hydrothermal alteration occurs mainly in form of serpentinization accompanied by talcification close to the faults.

3.2 Western Conglomerate Domain

The Western Conglomerate Domain is characterized by the existence of thick series of conglomerates and olistostromes of Archaean gneisses setting into metapelitic series. The gneissic olistostromes reach a maximum thickness of more than 200 m. The lateral extent may be one kilometre or more. The detrital series are essentially black metapelites, but some quartzitic units may be interbedded. When these are more developed, it is common to find a conglomeratic unit, characterized by matrix support and with only few heterometric clasts of rounded granites or limestones.

Epigenetic magnetite mineralization is observed in the matrix of the conglomerates, normally in highly silicified areas. Magnetite is clearly premetamorphic. Some olistostromes can be interpreted as basement gneisses overthrusting the black schists, but the association with poorly classified conglomerates suggests that they are synsedimentary. In any case, the contacts with the schists are tectonic.

Some post-tectonic granitic stocks are found intruding all the above indicated materials.

3.3 Central Domain

The Central Domain is characterized by the extensive development of black schists. These schists tend to be more aluminous than those interbedded with the quartzites in the conglomerate units. These series of black schists could represent the deposition of pelagic sediments or distal turbidites in a euxinic basin. Scarce amphibolitic beds can represent the metamorphic equivalents of basic tuffs. SEDEX mineralizations (*sensu* Goodfellow et al., 1995; Sangster & Hillary, 1998) are common and consist of mm-thick bands of pyrrhotite and chalcocopyrite interbedded with black shales.

Sulphide mineralizations in veins along thrust planes are common. They are associated with hydrothermal alterations typically produced by hypersaline fluids (development of scapolite, tremolite-actinolite, Cl-rich apatite, albite...) and show a complex paragenesis with Pb-Zn-Ni-Co-Ag-As-Au-Bi-Mo-REE-Th-U (Fig. 2). These ores can be produced by leaching of metals from the black schists and are affected by metamorphism.

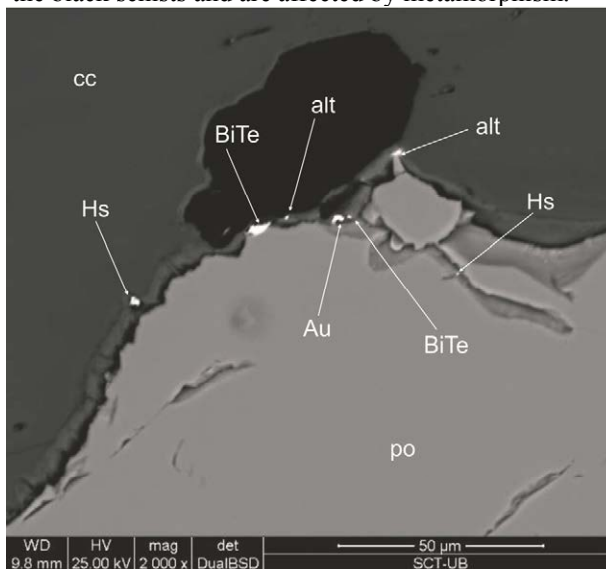


Figure 2. Detail of the veins associated with shear bands in the Central domain. Au, gold; BiTe, bismuth tellurides; alt, altaite; hs, hessite; po, pyrrhotite; cc, calcite. SEM image, BSE mode.

3.4 Eastern Conglomerate Domain

The more remarkable feature of this domain is the development of thick conglomerates and quartzite. Conglomerates are slightly mineralized in epigenetic magnetite whereas quartzites are strongly mineralized. Magnetite replaces these rocks commonly along with albite and ankerite. Chalcocopyrite, sphalerite and galena are also observed, as well as scarce and minute REE, U and Th minerals. All these mineralizations are affected by metamorphism (Fig. 3).

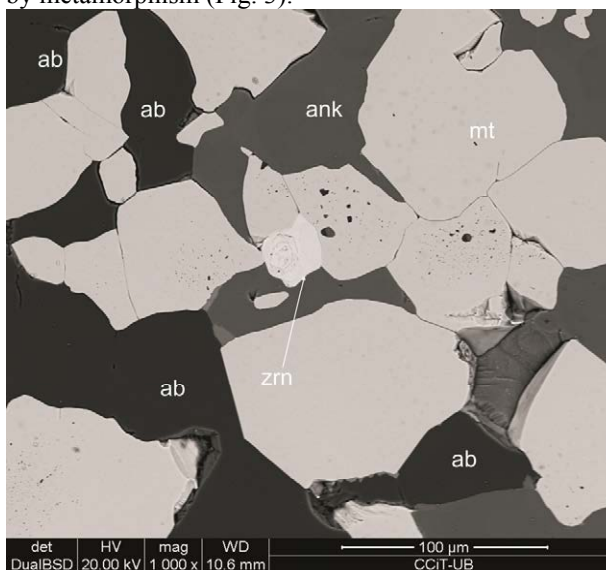


Figure 3. Metamorphosed assemblage of magnetite (mt), albite (ab), ankerite (ank) and zircon (zrn) in the epigenetic magnetite deposits. Note the granoblastic textures. SEM image, BSE mode.

Amphibolites are also widely spread in this unit. However, some of them, mineralized in magnetite, should be considered not true amphibolites but rocks affected by strong sodic-calcic alteration.

Some post-tectonic granitic intrusives are also present. They are mineralized close to the contact with the host rocks. The mineralization is found in millimetric to centimetric veinlets following joints in the granite. The type of mineralization and the strong alterations are typical of high-temperature alterations (potassic alteration, tourmalinization and minor sericitization).

3.5 Eastern Domain

Thick piles of massive limestones predominate in this domain. Most of these limestones have been replaced by skarn mineralization close to the contact with some post-tectonic granitic intrusions. The granites form small dikes in the host rock, probably as a mechanism of cauldron subsidence. These intrusives lack mineralization.

The endoskarn and the exoskarn units are well represented as prograde and retrograde episodes. Amphibolites are also present in these units. Sulphide mineralization has been found replacing the limestones, and quartzites have been found replaced by magnetite.

4 Basin Evolution

The area has an Archaean gneissic basement unconformably overlain by sedimentary series of probable PanAfrican age. The Proterozoic series have strong lateral and vertical changes of facies and thicknesses. Sedimentary domains can be established on the basis of the dominant lithotypes in the stratigraphic profiles. In some areas, carbonate platform facies dominate, whereas other domains are made up of sequences of black shales and quartzites with minor metabasites and conglomerates. Sedimentary domains are limited by NNE-SSW trending thrusts. This type of geometrical relationships between tectonics and stratigraphy can be explained by PanAfrican tectonic inversion affecting an earlier Proterozoic riftogenic basin. This evolution can be divided in the following stages:

4.1 Stage 1. Rifting

In a first stage, riftogenic, several Upper Proterozoic sedimentary basins of first or second order were formed due to the activity of synsedimentary extensional listric faults. The activity of these listric faults could favour the development of large olistostrome bodies of the basement and conglomerates sedimented as mud flows. These conglomerates include fragments of the basement and intraclasts and, in many cases, carbonatic components.

The depocenter of these upper Proterozoic sedimentary basins would contain materials formed in distal positions, enriched in fine sediments, as shales and clays. The organogenous character of these polymictic materials suggests that these basins could be

closed and, in consequence, poorly oxygenated. This circumstance could produce the extensive development of black shales and favour the growth of disseminated pyrite.

The existence of SEDEX deposits is also in good agreement with this type of geology. The existence of limestones in some domains suggests that these rocks were produced in some sedimentary highs, where only scarce or none detrital material arrived. Unfortunately, the high grade metamorphism undergone by these sediments obliterated or erased the existence of paleontological record.

Finally, the occurrence of mantle rocks of ophiolitic origin would suggest that the basin evolved enough during the riftogenic process, and oceanic lithosphere was produced. Unfortunately, we do not have chemical data to establish the type of lithosphere involved in these processes, in order to distinguish the environment of formation (back arc basin, MORB, etc). Volcanism associated with the rifting processes is also registered, and the metabasites can be interpreted as product of the metamorphism of basic volcanic rocks. However, some of them could be produced by the metamorphism of marls or tuffaceous sediments.

4.2 Stage 2. Tectonic inversion

During a stage of compression the above existing listric faults would be reactivated as low-angle thrusts (tectonic inversion). This hypothesis would explain why the lithostratigraphic domains are delimited by regional thrusts.

Thrusting favoured the movement of hydrothermal fluids, probably hypersaline fluids of basin origin, as evidenced by the alteration paragenesis replacing all of the previous rocks (carbonates, conglomerates, schists). These fluids could produce veins associated with thrusting and the magnetite deposits. Therefore, these magnetite deposits are not related with the granite intrusions, which would be post-tectonic. Thus, these magnetite deposits are clearly epigenetic and replace the carbonates, conglomerates and probably siliciclastic sediments. It is not clear if some of the quartzites associated with the magnetite bodies are actually the result of silicification of preexisting rocks.

The ensemble was affected by regional metamorphism in the upper part of the amphibolite facies (development of cordierite and andalusite), and a main stage of foliation was produced. Metamorphism is contemporaneous with shearing, as evidenced by textural relations of the metamorphic poikiloblasts. The magnetite bodies have been metamorphosed and sheared, as indicated by the relationships of magnetite and the metamorphic poikiloblasts.

4.3 Stage 3. Post tectonic magmatism

Intrusives in the area are post-tectonic and consist of granitic rocks ranging from diorite to leucogranite, with minor subvolcanic diabase dikes. The granite intrusions seem to be intruded in the mesozone, and produced the development of skarns when are found intruding limestones.

5 Link between Sulphide Veins and IOCG

Both the sulphide mineralizations in veins associated with shear bands and the magnetite deposits have some common points:

- a) All these mineralizations are epigenetic, in veins or replacing other lithologies.
- b) The hydrothermal fluids are hypersaline, as indicated by albitizations and sodic-calcic alterations found in both types of deposits.
- c) Both types of mineralizations have the same REE-Th-U accessory minerals, which produces a distinct geochemical anomaly. These characteristics suggest that both types of deposits were formed by similar fluids. This aspect is of especial importance. Assuming that the fluids producing magnetite deposits and shear deposits are probably similar, gold could be present in the magnetite deposits.

However, other aspects of the mineral assemblages establish significative differences between the two deposit types:

- d) Pyrite replaces carbonates without significative silicification.
- e) Magnetite has never been found in association with pyrrhotite.
- f) When found in contact, magnetite replaces pyrite, but the contacts pyrite-magnetite have been re-equilibrated and annealed during metamorphism.
- g) Magnetite is clearly pre-dating the metamorphic climax, because it is included into the metamorphic poikiloblastic minerals, whereas pyrrhotite may be contemporaneous.

Therefore, all these characteristics suggest that the next order could be established for the formation of the epigenetic deposits:

- 1) Pyrite replaces carbonates or other favourable lithologies
- 2) Quartz+magnetite (in some cases, with albite, chalcopyrite, galena and sphalerite) replace the above association.
- 3) The above assemblages are reequilibrated and annealed during the metamorphic climax
- 4) Pyrrhotite mineralization in veinlets is produced in shears affecting the depocenter of the basin.

Most of the mineral deposits from the Tsodilo area can be envisaged as forming part of the dynamics of a tectonically controlled sedimentary basin that suffered tectonic inversion after a period of rifting. This rifting developed enough to create oceanic lithosphere; the resulting ophiolites were uplifted during the compressive stage. The rifting episode is potentially interesting as producer of SEDEX type deposits. The basin is euxinic and tectonically very active, as indicated by the occurrence of important vertical and lateral changes of facies. However, up to the present moment the discovered SEDEX can only represent a distal position and are not economically interesting.

The compressive stage produced the remobilization of the preexisting normal faults as thrusts. Basinal hydrothermal fluids were remobilized along these faults. The interaction with these fluids produced hydrothermal alteration of the host rocks, including sodic-calcic, potassic, scapolitization and tourmalinization. Magnetite

bodies, associated to an important silicification and albitization, replaced marbles, carbonate cement and infilled porosity in detrital rocks. Replacement was produced in the margins of the basin, in the vicinity of the thrusts. Magnetite is accompanied by REE, and Cu-Pb-Zn-Ni-Co-Ag-As-Au-Bi-Mo-REE-Th-U association. The REE content is mainly in silicates of difficult extraction. This type of deposit fits with the IOCG model (Sillitoe 1993, 2003, Williams et al. 2005, Groves et al. 2010), and the occurrence of U and REE is well documented worldwide (Oreskes & Einaudi 1990, Hitzman & Walenta 2005). In the depocenter of the basin, the basinal fluids produced the deposition of sulphide mineralizations with Cu-Pb-Zn-Ni-Co-Ag-As-Au-Bi-Mo-REE-Th-U along the thrusts. These deposits have a lower potential than the IOCG.

Post tectonic granites have also polymetallic mineralized veins that could correspond to the Intrusion-Related Gold Deposits model (McLeod et al. 2008, Mair et al. 2011); they produced skarns on the hosting limestones. The studied skarns are poor in metals, but the context can be favourable for gold-bearing skarns.

Acknowledgements

Samples were analyzed in the Centres Científics i Tecnològics of the University of Barcelona. Funding was provided by the Consolidated Research Group Grant SGR 444 of the Generalitat de Catalunya.

References

- Goodfellow WD, Lydon JW, Turner RJW (1995) Geology and genesis of stratiform sediment-hosted (SEDEX) zinc-lead-silver sulfide deposits. *Geol. Assoc. Canada Spec. Paper* 40: 201-251.
- Groves DI, Bierlein FP, Meinert LD, Hitzman MW (2010) Iron oxide Copper-Gold (IOCG) Deposits through Earth History: Implications for Origin, Lithospheric Setting, and Distinction from Other Epigenetic Iron Oxide Deposits. *Econ. Geol.* 105: 641-654.
- Hitzman MW, Valenta RK (2005) Uranium in iron oxide-copper-gold (IOCG) systems. *Econ Geol* 100: 1657- 1661.
- Mair JL, Farmer GL, Groves DI, Hart CJR, Goldfarb RJ (2011) Petrogenesis of postcollisional magmatism at Scheelite Dome, Yukon, Canada: evidence for a lithospheric mantle source for magmas associated with intrusion - related gold systems. *Econ Geol* 106: 451-480.
- McLeod MJ, Hoy D, Thorne KG (2008) History, tectonic setting, and models for intrusion-related gold deposits in southwestern New Brunswick, Canada: examples from the Clarence stream area. *Explor Mining Geol* 17: 1-12.
- Oreskes N, Einaudi MT (1990): Origin of rare-earth element-enriched hematite breccias at the Olympic Dam Cu- U-Au-Ag deposit, Roxby Downs, South Australia: *Econ Geol* 85: 1-28.
- Sangster DF, Hillary EM (1998) SEDEX lead-zinc deposits-proposed sub-types and their characteristics. *Explor Mining Geol* 7: 341-357.
- Sillitoe RH (1993) Intrusion - related gold deposits. *Gold Metallog. Explor.* 165-209.
- Sillitoe RH (2003) Iron oxide copper-gold deposits: an Andean view: *Miner Deposita* 38: 787-812.
- Williams P, Barton MD, Johnson DA, Fontboté LI, De Haller A, Mark G, Oliver NHS, Marschik R (2005) Iron Oxide Copper-Gold Deposits: Geology, Space-Time Distribution, and Possible Modes of Origin. *Econ Geol* 100th An Vol: 371-405.

REEY characteristics in hydrothermal gangue carbonates within the sediment-hosted Nkana-Mindola Cu-Co deposit (Zambia) and in two polymetallic vein-type deposits (Kipushi and Dikulushi, Democratic Republic of Congo)

David Debruyne, Philippe Muchez

Geodynamics and Geofluids Research Group, KU Leuven, Celestijnenlaan 200E, B-3001 Leuven, Belgium

Lieve Balcaen, Frank Vanhaecke

Department of Analytical Chemistry, Ghent University, Krijgslaan 281-S12, B-9000 Ghent, Belgium

Abstract. The Central African Copperbelt is a world-class metallogenic province characterized by sediment-hosted stratiform Cu-Co ore deposits and polymetallic vein-type deposits. This project investigates the rare earth element and yttrium (REEY) compositions of the hydrothermal gangue carbonates associated with these mineralizations. In the Nkana-Mindola Cu-Co deposit, layer-parallel to irregular veins display variable REEY patterns, which can be explained by interaction with different sources and varying amounts of remobilization. The uniform REEY composition in the late massive mineralizations at Nkana-Mindola likely reflects similar sources and physicochemical conditions. Their heavy rare earth element (HREE) enrichment is inherited from their sources or generated during precipitation of a light rare earth element (LREE)-selective mineral phase. In the vein-type Kipushi deposit, Fe- and REEY-poor dolomites display upward-convex REEY-patterns while REEY- and Fe-rich dolomites show square-root shaped patterns with prominent negative Eu-anomalies. Both cement phases are closely associated with the main mineralization phase, and likely reflect interaction with different sources at distinct physicochemical conditions. This bimodality is absent at the polymetallic Dikulushi deposit, where the REEY in the Cu-Ag phase are likely remobilized from the earlier Cu-Pb-Zn-Fe phase.

REE, hydrothermal, fluid-rock interaction

1 Introduction

The Neoproterozoic Central African Copperbelt, located at the border between Zambia and the Democratic Republic of Congo (DRC), is the world's richest sediment-hosted Cu-Co province. It contains about 200 Mt of copper (Cailteux et al. 2005) and over 8 Mt of cobalt (Misra 2000) in stratabound deposits alongside other metals (e.g., Pb, Zn) in vein-type deposits. The latter are generally thought to be leached from the continental basement rocks by multiple pulses of hot, saline fluids migrating upward through the Precambrian basement along permeable, fractured zones (Selley et al. 2005; Heijlen et al. 2008). With regard to the sediment-hosted Cu-Co deposits, most recent papers propose a multiphase mineralization (Selley et al. 2005; Cailteux et al. 2005; Dewaele et al., 2006; El Desouky et al. 2009; Muchez et al. 2010). The Cu-Co mineralizing fluids are thought to leach their metals from the basement or the overlying siliciclastics, after which interaction with either reducing sediment layers rich in organic matter or

hydrocarbon reservoirs resulted in metal-sulfide precipitation (Annels 1989; Selley et al. 2005; Muchez et al. 2008).

This project seeks more insight into the nature and evolution of the fluids responsible for the mineralizations, by comparing the REEY composition of hydrothermal gangue carbonates in both the Nkana-Mindola Cu-Co deposit (Zambia) and in two polymetallic vein-type deposits at Kipushi and Dikulushi (DRC).

2 Geological context

2.1 The Central African Copperbelt

The Copperbelt deposits are hosted by the Katanga Supergroup, a Neoproterozoic sedimentary sequence mainly deposited between < 880 Ma and ca. 573 Ma (Armstrong et al. 2005; Master et al. 2005). The Katanga basin that contains this supergroup is generally considered to be part of a failed intracontinental rift (e.g., Clemmey 1974; Porada and Berhorst 2000). The Roan Group forms the base of the Katanga Supergroup and hosts the majority of mineralizations. It consists of siliciclastic and carbonate sequences which record the transition from a continental rift basin to a Red Sea-type proto-ocean with predominantly dolomitic shales in the Upper Roan and the overlying Nguba Group (Clemmey 1974). Convergence between the Congo and Kalahari cratons during the Lufilian Orogeny between 590 and 530 Ma (Rainaud et al. 2005) resulted in closing of this basin, folding and predominantly northward displacement of nappes, generating the Lufilian Fold-and-Thrust Belt currently present as a northward convex arcuate belt measuring 150 by 700 km. The Zambian Nkana-Mindola mine is located near the southeastern edge of this arcuate belt, while the Congolese Kipushi and Dikulushi deposits are located roughly 125 km northward of Nkana-Mindola and in the Lufilian foreland, about 250 km north of the Lufilian arc, respectively.

2.2 Nkana-Mindola deposit (Cu-Co)

At Nkana-Mindola, mineralization occurs in layer-parallel veins (LPV), which record supra-lithostatic pressures at the onset of basin inversion during the

Lufilian orogeny near peak metamorphic conditions at ca. 450 °C and 0.2 GPa (Brems et al. 2009; Muchez et al. 2010). At this stage, fluid migration is thought to be dominantly lateral, originating from the deeper parts of the Katanga sedimentary basin, although a vertical component of fluid flow originating from the basement is also possible. Isotopic evidence indicates that irregular veins reflect remobilization during the Lufilian deformation of earlier formed mineralization in layer-parallel veins (Brems et al. 2009; Muchez et al. 2010). Relatively undeformed massive veins crosscut all earlier mineralizations and likely represent a new fluid input originating from the basement (Muchez et al. 2010).

2.3 Kipushi deposit (Cu-Pb-Zn-Fe)

The vein-type Cu-Pb-Zn-Fe mineralization at Kipushi in the southeastern part of the Copperbelt is mainly hosted by carbonate and to a lesser extent by siliciclastic rocks, which underwent regional metamorphism at low-grade greenschist conditions (Heijlen et al. 2008). This post-orogenic mineralization was dated at 451 Ma (Schneider et al. 2007) and occurred when a metalliferous brine came in contact with a reducing hydrocarbon reservoir, as indicated by the occurrence of relict organic matter and a sulfur isotopic composition indicative for thermochemical sulfate reduction. The main Zn-Cu-(Ge, Pb) sulfide mineralization phase precipitated from a high temperature - high salinity fluid (290-380°C; 30-43 eq. wt% NaCl), while a late mineralization phase occurred at lower temperature and moderate to high salinity (<80-170°C; 23-31 eq. wt% NaCl; Heijlen et al. 2008).

2.4 Dikulushi deposit (Cu-Pb-Zn-Fe + Cu-Ag)

The Cu-Pb-Zn-Fe mineralization at Dikulushi originated from a moderately saline - medium temperature fluid (20-25 eq. wt% NaCl; 100-200°C). A second Cu-Ag mineralization phase likely represents a remobilization of the first phase, whereby mineralization results from mixing of a moderately saline fluid (>19 wt% NaCl eq.) with a low salinity fluid (3 wt% NaCl eq.) in thermal equilibrium with their host rocks at ca. 65 °C (Haest et al. 2009).

3 Results

3.1 Nkana-Mindola deposit (Cu-Co)

Figure 1 reveals that the layer-parallel and irregular veins at Nkana South generally have lower La/Lu ratios compared to their counterparts at Nkana Central and display either relatively flat HREE transects or enrichments towards the HREE. Significant Eu-anomalies are absent in REE-poor LPV, whereas the REE-rich veins display negative Eu-anomalies.

The nodule and layer-parallel veins at Mindola and Nkana-Central are relatively REE-poor and show upward-convex UCC-normalized REE patterns with pronounced positive Eu-anomalies. However, the LPV patterns at Nkana-Central show negative Ce-anomalies and lower La/Lu ratios compared to the Mindola nodule.

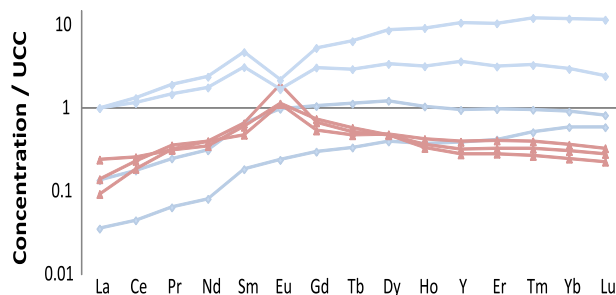


Figure 1. Upper Continental Crust (UCC)-normalized REEY patterns of 6M HCl leachates from nodules and layer-parallel veins at Mindola and Nkana Central (triangles), layer-parallel and irregular veins at Nkana South (diamonds). Analyzed with ICP-MS; UCC composition from Rudnick and Gao (2003).

The massive veins displayed in Figure 2 are generally characterized by low La/Lu ratios, negative Eu-anomalies and a distinct HREE enrichment. Compared to layer-parallel and irregular veins, their REEY-patterns show less variability and their REE-content is generally higher (Σ REE 43-75 ppm), except when compared to the REE-richest LPV (Σ REE ~150 ppm). Two REE-poor massive veins (Σ REE ~25 ppm) show positive Eu-anomalies and lack the HREE enrichment found in all other massive veins.

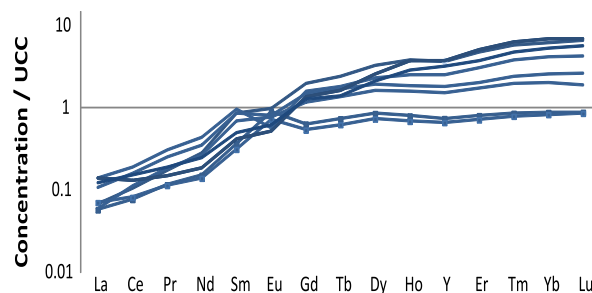


Figure 2. Upper Continental Crust (UCC)-normalized REEY patterns in the massive vein carbonates at Nkana (squares or unbroken lines). Analyzed with ICP-MS; UCC composition from Rudnick and Gao (2003).

3.2 Kipushi deposit (Cu-Pb-Zn-Fe)

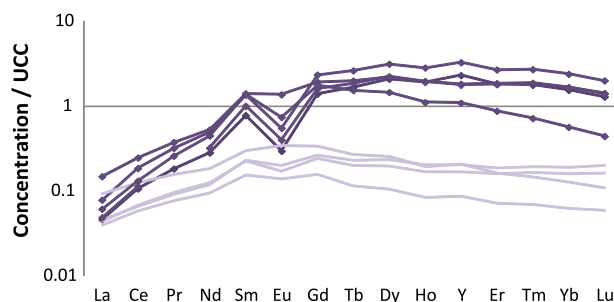


Figure 3. Upper Continental Crust (UCC)-normalized REEY patterns of the Kipushi carbonates. The Fe-poor and Fe-rich dolomite cements are represented by unbroken lines and diamonds respectively. Analyzed with ICP-MS; UCC composition from Rudnick and Gao (2003).

As shown in Figure 3, the gangue dolomites at Kipushi exhibit bimodal REEY patterns: on one hand, Fe-poor dolomite cement displays upward-convex REEY-patterns with relatively low REE contents (avg. Σ REE 15 ppm) and small negative Eu-anomalies. In contrast, the Fe-rich dolomite phase shows square root-like REEY-patterns with a total REE content between 46 and 150 ppm.

75 ppm, generally associated with pronounced negative Eu anomalies.

3.3 Dikulushi deposit (Cu-Pb-Zn-Fe + Cu-Ag)

Figure 4 shows that the dolomite and especially the calcite associated with the Cu-Pb-Zn-Fe mineralization are characterized by extremely high REEY-concentrations, with Σ REE between 94 and 757 ppm. The calcite associated with the Cu-Ag mineralization displays REEY patterns similar to the preceding calcite cement, yet contains less REE (Σ REE 41-74 ppm).

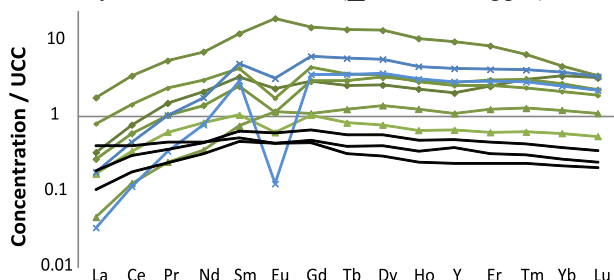


Figure 4. Upper Continental Crust (UCC)-normalized REEY patterns in calcite (diamonds) and dolomite (crosses) associated with the Cu-Pb-Zn-Fe mineralization phase at Dikulushi. The triangles represent the calcite cement associated with the Cu-Ag phase while the unbroken lines correspond to 6M HCl leachates of the Gombela dolomite hosting the mineralization. Analyzed with ICP-MS; UCC composition from Rudnick and Gao (2003).

4 Discussion

4.1 Nkana-Mindola deposit (Cu-Co)

At Nkana South, the REE-rich layer-parallel vein (LPV) signatures shown in Figure 1 are similar to the ones of the REE-poor LPV. This suggests that their higher REE concentrations relate to fluids with higher REE/(Ca+Mg) ratios or less prominent kinetic effects during crystallization, rather than to a difference in source composition. The presence of negative Eu-anomalies in the REE-rich veins can probably be explained by preferential loss of fluid-mobile divalent Eu during subsequent fluid pulses and remobilization.

In contrast, the LPV and the nodule at Nkana Central and Mindola display positive Eu-anomalies. The latter are typical for hydrothermal carbonates and are commonly explained by less efficient sorption and differences in complexation behavior between thermochemically reduced Eu^{2+} and the trivalent REE (e.g., Allwood et al. 2010). The negative Ce-anomalies in the LPV at Central could indicate interaction with their host rocks under oxidizing conditions or inheritance from a marine fluid (cf. Fernández-Nieto et al. 2003). The higher La/Lu ratio in the Mindola nodule compared to the LPV likely relates to its high hydrothermal muscovite content and suggests some extent of equilibration between its parent fluid and the clay-rich dolomitic siltstone host.

Most massive veins in Figure 2 display similar REEY patterns characterized by low La/Lu ratios, an increasing HREE trend and negative Eu anomalies. These similarities suggest near-identical sources and

physicochemical conditions for these mineralizations. Two REE-poor massive veins with flat HREE transects and positive Eu-anomalies possibly belong to a different mineralization phase.

Those hosted by the ore shale and the footwall sandstone display similar REEY patterns, indicating that interaction with their host rocks did not affect their REEY signature significantly. Moreover, the similar REEY composition in massive veins at Nkana South and Mindola, about 14 km apart, indicates that their REEY characteristics are representative for a relatively large area, unlike the patterns in the layer-parallel veins. Precipitation of one or more LREE-selective mineral phases prior to mineralization could explain their LREE-depleted REEY signature and would also result in a relative increase in HREE. The HREE-enrichment in the massive veins could also be inherited from their sources, for instance the HREE-enriched anorogenic granites in the basement below the Zambian Copperbelt (cf. Katongo et al. 2004). Preferential complexation of HREE in the mineralizing brine seems unlikely since Cl^- and F^- preferentially complexate the LREE (Migdisov et al. 2009) and these are probably important ligands in Cl-rich hydrothermal brines (Kučera et al. 2009).

4.2 Kipushi deposit (Cu-Pb-Zn-Fe)

The two REEY pattern types in Figure 3 correspond to the Fe-poor and Fe-rich dolomite cements respectively. Although both dolomite phases are probably closely associated with the main high temperature - high salinity mineralization phase (Chabu 1995; Heijnen et al. 2008), physicochemical conditions in both hydrothermal fluids are not necessarily similar. For instance, the difference in Fe-content probably relates to a different oxidation potential in the hydrothermal brines. At oxidizing conditions, Fe is mostly trivalent and therefore immobile in hydrothermal fluids (e.g., Fernández-Nieto et al. 2003). Because changes in the oxidation potential most likely do not influence the mobility of normally trivalent REE at hydrothermal conditions (e.g., Wood et al. 1990; Haas et al. 1995), the two distinct REEY patterns in the fluids are interpreted to reflect interaction with different sources at distinct physicochemical conditions.

4.3 Dikulushi deposit (Cu-Pb-Zn-Fe + Cu-Ag)

The carbonates associated with the Cu-Pb-Zn-Fe phase are extremely REEY-rich, indicating mineralizing fluids with high REE/[Ca (+Mg)] ratios, likely related to physicochemical conditions favorable for REE mobilization. The variable Eu-anomalies in the calcite likely reflects variable redox conditions during mineralization and remobilization. Surprisingly, the distinct geochemistry of the two mineralization phases (Cu-Pb-Zn-Fe and Cu-Ag) is not reflected in the REEY patterns. The latter supports the hypothesis from Haest et al. (2009), who interpreted the Cu-Ag mineralization phase as a remobilization of the earlier Cu-Pb-Zn-Fe phase. In this scenario, the lower REEY-concentrations likely reflect less efficient REE mobilization at the lower salinities and temperatures resulting from this mixing.

Acknowledgements

We are grateful to dr. Elvira Vassilieva, dr. Stijn Dewaele, dr. Hamdy El Desouky and drs. Jorik Van Wilderode for stimulating discussions on the geochemical analysis, REE geochemistry and metallogenesis of the Copperbelt deposits. David Debruyne and Lieve Balcaen are respectively Research Assistant and Senior Research Assistant of the Fund for Scientific Research – Flanders (FWO-Vlaanderen). This research is also financially supported by the research grant G.A078.11 from FWO-Vlaanderen (Belgium).

References

- Allwood AC, Kamber BS, Walter MR, Burch IW, Kanik I, (2010) Trace elements record depositional history of an Early Archean stromatolitic carbonate platform. *Chem Geol* 270:148-163.
- Annels AE, (1989) Ore genesis in the Zambian Copperbelt with particular reference to the northern sector of the Chambishi basin. *Geol Ass Can Spec Pap* 36:27-452.
- Armstrong RA, Master S, Robb LJ (2005) Geochronology of the Nchanga Granite, and constraints on the maximum age of the Katanga Supergroup, Zambian Copperbelt. *J Afr Earth Sci* 42: 32-40.
- Brems D, Muchez P, Sikazwe O, Mukumba W (2009) Metallogenesis of the Nkana copper-cobalt South Orebody, Zambia. *J Afr Earth Sci* 55:185-96.
- Cailteux JLH, Kampunzu ABH, Lerouge C, Kaputo AK, Milesi JP, (2005) Genesis of sediment-hosted stratiform copper-cobalt deposits, central African Copperbelt. *J Afr Earth Sci* 42:134-158.
- Chabu, M. (1995) The geochemistry of phlogopite and chlorite from the Kipushi Zn-Pb-Cu deposit, Shaba, Zaïre. *Can Mineral* 33:547-558.
- Clemmey H (1974) Sedimentary geology of a late Precambrian copper deposit at Kitwe, Zambia. In: Bartholomé P (éd), Gisements stratiformes et provinces cuprifères Centenaire de la Société Géologique de Belgique, Liège, pp 255-265
- Dewaele S, Muchez P, Vets J, Fernandez-Alonzo M, Tack L (2006) Multiphase origin of the Cu-Co ore deposits in the western part of the Lufilian fold-and-thrust belt, Katanga (Democratic Republic of Congo). *J Afr Earth* 46:455-469.
- El Desouky HA, Muchez P, Cailteux J (2009) Two Cu-Co sulfide phases and contrasting fluid systems in the Katanga Copperbelt, Democratic Republic of Congo. *Ore Geol Rev* 36:315-332.
- Fernández-Nieto C, Torres-Ruiz J, Pérez IS, González IF, López JMG (2003) Genesis of Mg-Fe Carbonates from the Sierra Menera Magnesite-Siderite Deposits, Northeast Spain: Evidence from Fluid Inclusions, Trace Elements, Rare Earth Elements, and Stable Isotope Data. *Econ Geol* 98:1413-26.
- Haas JR, Shock EL, Sassani DC (1995) Rare earth elements in hydrothermal systems: Estimates of standard partial molal thermodynamic properties of aqueous complexes of the rare earth elements at high pressures and temperatures. *Geochim Cosmochim Acta* 59:4329-50.
- Haest M, Muchez P, Dewaele S, Boyce AJ, Von Quadt A, Schneider J (2009) Petrographic, fluid inclusion and isotopic study of the Dikulushi Cu-Ag deposit, Katanga (D.R.C.); implications for exploration. *Miner Deposita*. 44:505-22.
- Heijlen W, Banks DA, Muchez P, Stensgard BM, Yardley BWD (2008) The Nature of Mineralizing Fluids of the Kipushi Zn-Cu Deposit, Katanga, Democratic Republic of Congo: Quantitative Fluid Inclusion Analysis using Laser Ablation ICP-MS and Bulk Crush-Leach Methods. *Econ Geol* 103:1459-1482.
- Katongo C, Koller F, Kloetzli U, Koeberl C, Tembo F, De Waele B (2004) Petrography, geochemistry, and geochronology of granitoid rocks in the Neoproterozoic-Paleozoic Lufilian-Zambezi belt, Zambia: Implications for tectonic setting and regional correlation. *J Afr Earth Sci* 40:219-44.
- Kučera J, Cempírek J, Dolníček Z, Muchez P, Prochaska W (2009) Rare earth elements and yttrium geochemistry of dolomite from post-Variscan vein-type mineralization of the Nizký Jeseník and Upper Silesian Basins, Czech Republic. *J Geochem Explor* 103:69-79.
- Master S, Rainaud C, Armstrong RA, Phillips D, Robb LJ (2005) Provenance ages of the Neoproterozoic Katanga Supergroup (Central African Copperbelt), with implications for basin evolution. *J Afr Earth Sci* 42:41-60.
- Migdisov AA, Williams-Jones AE, Wagner T (2009) An experimental study of the solubility and speciation of the Rare Earth Elements (III) in fluoride- and chloride-bearing aqueous solutions at temperatures up to 300 °C. *Geochim Cosmochim Acta*, 73: 7087-7109.
- Misra KC (2000) Understanding mineral deposits, Kluwer Academic, Dordrecht
- Muchez P, Vanderhaeghen P, Desouky H, Schneider J, Boyce A, Dewaele S (2008) Anhydrite pseudomorphs and the origin of stratiform Cu-Co ores in the Katangan Copperbelt (Democratic Republic of Congo). *Miner Deposita* 43:575-89.
- Muchez P, Brems D, Clara E, De Cleyn A, Lammens L, Boyce A, De Muynck D, Mukumba W, Sikazwe O, (2010) Evolution of Cu-Co mineralizing fluids at Nkana Mine, Central African Copperbelt, Zambia. *J Afr Earth Sci* 58:457-474.
- Porada H, Berhorst V (2000) Towards a new understanding of the Neoproterozoic-early palaeozoic Lufilian and northern Zambezi belts in Zambia and the Democratic Republic of Congo. *J Afr Earth Sci* 30:727-771.
- Rainaud C, Master S, Armstrong R, Robb L (2005) Geochronology and nature of the Palaeoproterozoic basement in the Central African Copperbelt (Zambia and the Democratic Republic of Congo), with regional implications. *J Afr Earth Sci* 42:1-31.
- Roberts S, Palmer MR, Cooper MJ, Buchaus P, Sargent D (2009) REE and Sr isotope characteristics of carbonate within the Cu-Co mineralized sedimentary sequence of the Nchanga Mine, Zambian Copperbelt. *Miner Deposita* 44:881-891.
- Rudnick, RL, Gao, S (2003) The composition of the Continental Crust In: Holland HD, Turekian KK (eds), *Treatise on geochemistry*, Elsevier-Pergamon, Oxford, pp 1-64
- Schneider J, Melcher F, Brauns M (2007) Concordant ages for the giant Kipushi base metal deposit (DR Congo) from direct Rb-Sr and Re-Os dating of sulfides. *Miner Deposita*. 42:791-7.
- Selley D, Broughton D, Scott R, Hitzman M, Bull S, Large R, McGoldrick P, Croaker M, Pollington N, Barra F (2005) A New Look at the Geology of the Zambian Copperbelt. *Soc Econ Geol 100th Anniversary Volume*:965-1000.
- Wood SA (1990) The aqueous geochemistry of the rare-earth elements and yttrium: 1. Review of available low-temperature data for inorganic complexes and the inorganic REE speciation of natural waters. *Chem Geol* 82:159-86.

Understanding gold mineralisation: linking chemical and structural changes

Angela Halfpenny, Louise Fisher, Robert Hough, James Cleverley
CSIRO, Earth Science and Resource Engineering, ARRC, 26 Dick Perry Avenue, Kensington, Perth, WA, 6151

Abstract. Recent advances and developments in micro-analytical facilities now allow co-located structural and chemical data to be collected at micron resolution. Co-located data can be used to identify the dominant fluid pathways and elucidate the defining characteristics of areas rich in native gold. We used a combination of optical and scanning electron microscope based imaging, electron backscatter diffraction, energy and wavelength dispersive spectroscopy and X-ray fluorescence performed at the Australian Synchrotron to identify the fluid pathways. The fluids utilise pre-existing weaknesses to move through the country rock and then travel along grain boundaries to penetrate into and across veins. The gold mineralising fluids cause Fe enrichment in the surrounding carbonate phases. The gold external shape is controlled by the space it is growing into. High concentrations of gold occur in the cross-cutting, interaction zones of two or more veins. This interaction is essential for the formation of high gold grade. This work highlights the importance of developing a clear vein paragenesis to identify the cross-cutting relationships which control gold mineralisation.

Keywords. gold microstructure, electron backscatter diffraction, X-ray fluorescence microscopy, Australian Synchrotron, Maia-384 detector

1 Introduction

Structural observations, at all scales, are an important component in the study of ore genesis. The quantification of geological microstructures is an extremely powerful tool for understanding the crystallisation and deformation history of a rock. Due to advances in specimen preparation and micro-analytical techniques, it is now possible to collect co-located structural (crystallographic) and chemical composition measurements at micron resolution.

In recent years, the application of electron backscatter diffraction (EBSD) to mineral texture analysis has become a standard geological tool (Farla et al. 2011; Halfpenny et al. 2006; Halfpenny et al. 2004; Halfpenny et al. 2012; Martin et al. 2011; Prior et al. 2004). EBSD is a surface technique that uses backscattered electrons to generate Kikuchi diffraction patterns (otherwise known as electron backscatter patterns). These are imaged on a phosphor screen, recorded by a CCD camera and indexed against a database of minerals using specialised software to identify the phase and its crystallographic orientation (Prior et al. 2009). Mapping using EBSD provides information on variations in orientation within mineral grains, across grain boundaries and the phase distribution of minerals in a sample (Prior et al. 1999). EBSD can be used to analyse the interaction between ore and gangue mineral phases, providing quantitative analysis of the

internal microstructure which permits a greater understanding of the mineralisation processes in economic deposits.

Linking crystallographic information with data on chemical variations provides a new methodology for identifying the localised fluid pathways that transported metal enriched fluids to the site of mineralisation. The chemical variations can also be used to identify variations that were formed during growth versus post mineralisation modification. In this paper we present a number of crystallographic and chemical data sets. We show that gold mineralisation is concentrated by the focussing of iron-rich fluids at the intersection of two carbonate veins.

2 Geological Setting

All samples were collected from AngloGold Ashanti's Sunrise Dam gold mine which is characterised as an Achaean lode gold deposit and is located in the Eastern Yilgarn Craton, Western Australia. The deposit is situated within the structurally complex Laverton Domain which is characterised by tight folding and thrusting (Newton et al. 1998) and is part of the Kurnalpi Terrane. The Kurnalpi Terrane is bounded by the NNW-trending Ockerburry (west) and Hootanui (east) fault systems (Blewett et al. 2010). The deposit consists of complexly deformed and altered package of shallowly NW-dipping units.

Samples were chosen for this study due to the presence of large accumulations of native gold. The samples consist of: (1) weak breccias – that contain randomly orientated wall rock clasts mainly cemented by carbonate, with some quartz. Visible gold and pyrite are located in the matrix between the wall rock clasts, (2) discrete veins - that are typically centimetres thick and are dominated by carbonate, visible gold and with minor amounts of quartz.

3 Methodologies

3.1 Sample preparation

All collected rock samples were cut to produce thin section billets (5 x 2.5 x 1cm, rock blocks). A standard 30µm, polished thin section was prepared off the top of each thin section billet. The thin sections were used to identify the modal mineralogy, classify the dominant textures and recognize the location(s) of native gold. 25mm diameter round blocks were cut, from the billets, at the locations showing the highest concentration of native gold. All samples were prepared at the CSIRO facilities in Kensington, Perth, Western Australia.

A standard preparation polish is acceptable for optical and scanning electron microscope (SEM) based imaging and the collection of chemical spectra but EBSD requires a higher standard of polish. To produce a suitable surface for EBSD the samples were polished using colloidal silica for between 3-5 hours on a Buehler Vibromat 1 to prepare the hard phases, such as quartz (Halfpenny 2010) and subsequently prepared using broad ion beam polishing (BIBP) to prepare the softer gold (Halfpenny et al. accepted).

3.2 Optical imaging

After initial preparation the entirety of each sample was imaged using plane polarised, cross-polarised and reflected light on an automated stage Zeiss Axio optical microscope at 2.5x magnification. These optical images were then used to identify areas of interest in the sample for higher magnification imaging using optical microscopy and SEM imaging.

3.3 SEM imaging

The samples were first imaged using backscattered electrons (BSE) in a Philips XL40 controlled pressure SEM. The SEM was operated at a chamber pressure of 0.5 mBar (no conductive carbon coating was required) and an accelerating voltage of 30 kV. Images were collected using a Robinson backscattered electron detector. Then the samples were carbon coated and imaged using both secondary electrons (SE) and backscattered electrons (BSE) in a Zeiss Ultraplus field emission gun (FEG) SEM, operated at a chamber pressure of 2×10^{-6} mbar and an accelerating voltage of 20 kV.

3.4 Electron backscatter diffraction

EBSD, full crystallographic orientation data were obtained from automatically indexed Kikuchi diffraction patterns collected on a Zeiss Ultraplus FEG SEM at the CSIRO facilities, Kensington, WA. The SEM was operated using an accelerating voltage of 20 kV, a 120 μm aperture, in high current mode which produced a beam current of 12.1 nA. The EBSD data were collected using the Bruker Quantax Espirit 1.9 software, using an EBSP resolution of 200x150 pixels, a 10-1 5ms exposure time and a step size in-between measurements which ranged from 0.5-2 μm (determined by the size of the smallest grain of interest). If the pattern quality was poor then the software was unable to find the correct crystallographic solution and the point was not indexed. Non-indexed points are common in areas of poor surface quality, on grain boundaries, cracks and where the surface is contaminated.

3.5 Energy dispersive spectra

Energy dispersive x-ray spectra (EDS) were collected at the CSIRO facilities, Kensington, WA, on both a Philips XL40 variable pressure SEM fitted with an EDAX brand EDS detector and a Zeiss Ultraplus FEG SEM fitted with a Bruker EDS detector. EDS were collected as both

single spot analyses and area maps.

3.6 Wavelength dispersive spectra

Wavelength dispersive x-ray spectra (WDS) were collected on a Cameca SX50 electron microprobe at the CSIRO facilities, Kensington, WA. The microprobe was operated using a 15 kV accelerating voltage and a 30 nA beam current. Some samples were also analysed using the Jeol 830F microprobe at the University of Western Australia, operated using a 15 kV accelerating voltage and a 50 nA beam current. WDS were collected as both single spot analyses and area maps.

3.7 X-ray fluorescence microscopy

X-ray fluorescence (XRF) microscopy was performed at the Australian Synchrotron using the KB mirror microprobe and the Maia-384 element silicon array detector with 18.5 kV beam energy, energy resolution 300-400 eV, 4 μm step size and a dwell of 1.9 msec/pixel (Ryan et al. 2010a; Ryan et al. 2010b).

4 Results

A number of samples have been analysed but data shall be presented on only thin section WSZA in this abstract. Sample WSZA contains two coarse-grained carbonate dominated veins that cross-cut the strongly sheared country rock (Fig. 1). The native gold penetrates from the vein margins across the full width of the vein mainly following the easiest pathway, along the carbonate grain boundaries. However, there are occasions when the gold network cross-cuts a single, carbonate crystal (Fig.2). The gold network appears to begin to enter the vein where pyrite dominated zones contact the boundary between the carbonate vein and the country rock. The majority of the gold is concentrated in the interaction zone between the two carbonate veins (Fig. 1).

From the XRF based trace element analysis, two trends of chemical variations can be identified. The first is the variation in Fe and Sr concentrations in the carbonate crystals (Fig. 2 – variations between dark and light blue). The second is a Fe rich overprint which spatially coincides with the gold mineralisation (Fig. 2 – lighter green areas easily identified around the gold network).

To examine the relationships between phase, the pattern of elemental enrichment and crystallography EDS and EBSD were performed. The EDS map for selected area (white box Figure 2) of WSZA shows the Fe enrichment (Fig. 3 – pink network). Comparing Figure 3 and Figure 4, the majority of the Fe enrichment is located on the grain boundaries (Fig. 4 – black lines represent grain boundaries). However, there are areas where the Fe enrichment cross-cuts a carbonate grain and does not correspond to a grain boundary (Fig. 3 and Fig. 4).

The Fe enrichment appears to be grain size dependant, with smaller grains exhibiting a higher (brighter pink) concentration than larger grains (compare the carbonate grains to the left of the gold grains in Figure 3 and Figure 4, with the ones below).

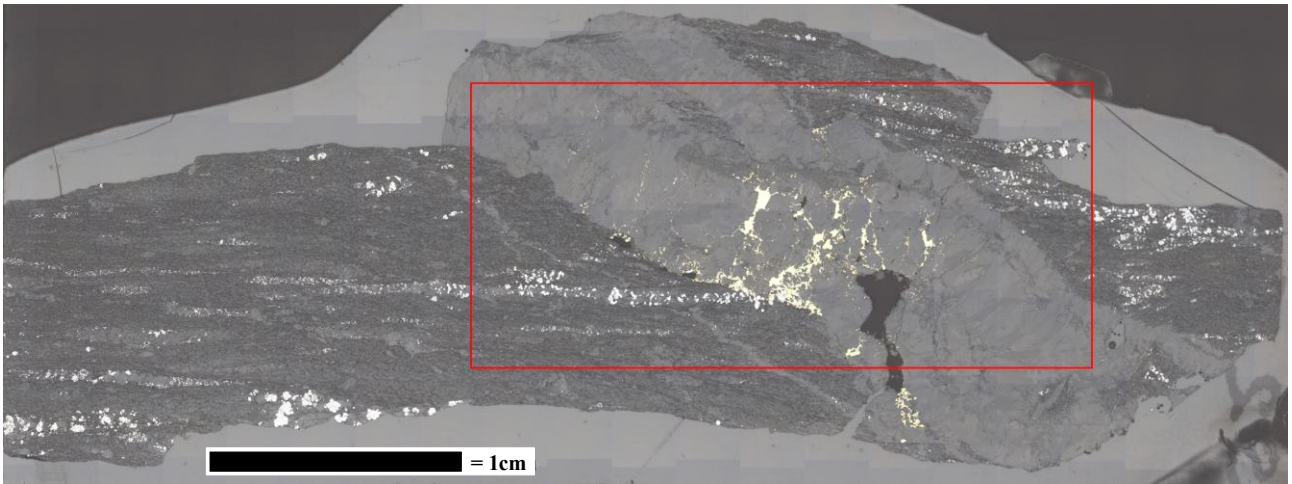


Figure 1. Reflected light image of thin section WSZA showing the interaction of two dominantly carbonate veins with a visible gold network (yellow). The white coloured grains in the wall rock are pyrite. The red box marks the area analysed by XRF presented in Figure 2.

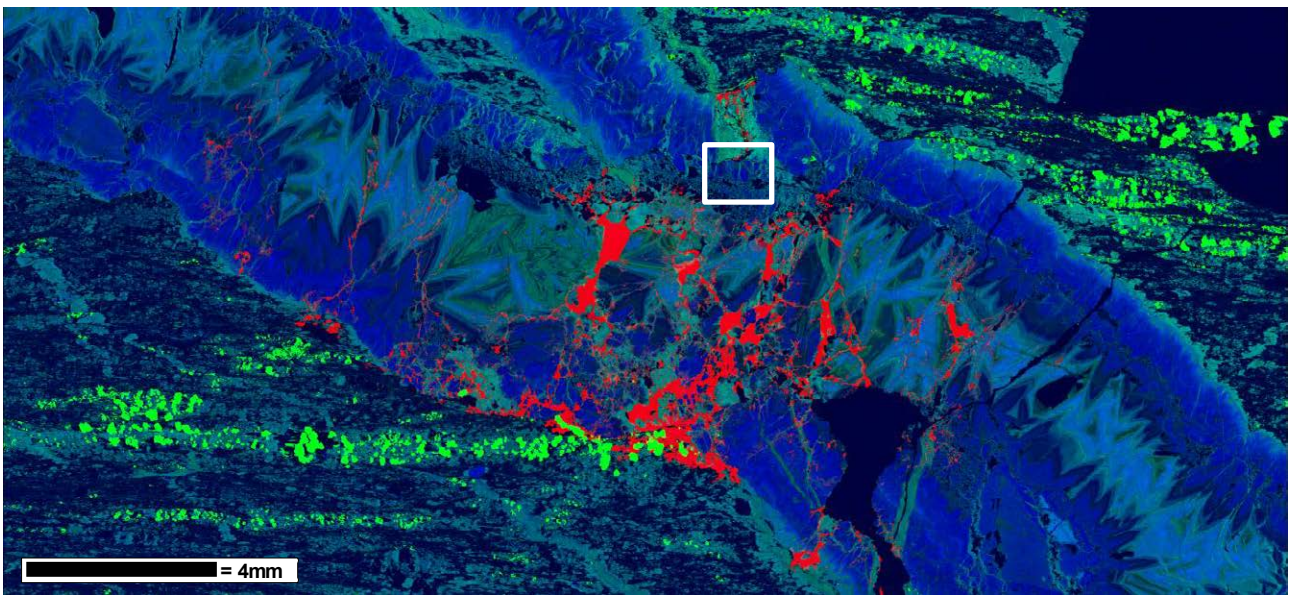


Figure 2. XRF image of WSZA collected at the Australian Synchrotron of a carbonate dominated vein with a visible gold network. Colour scheme is Au in red, Fe in green, and Sr in blue. The image shows systematic growth variations of Fe and Sr in the carbonate grains, but also a later Fe enrichment which is spatially linked with the gold mineralisation. The white box marks the area analysed by EDS and EBSD presented in Figures 3 and 4, respectively.

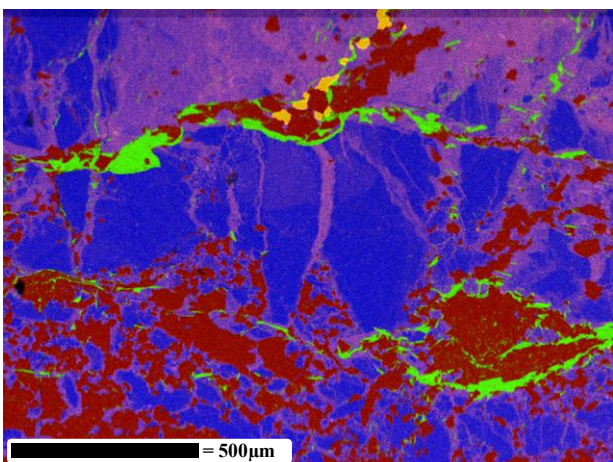


Figure 3. EDS map showing quartz in red, carbonate in blue, muscovite in green and gold in yellow. The pink shows relative levels of Fe enrichment in the carbonate.

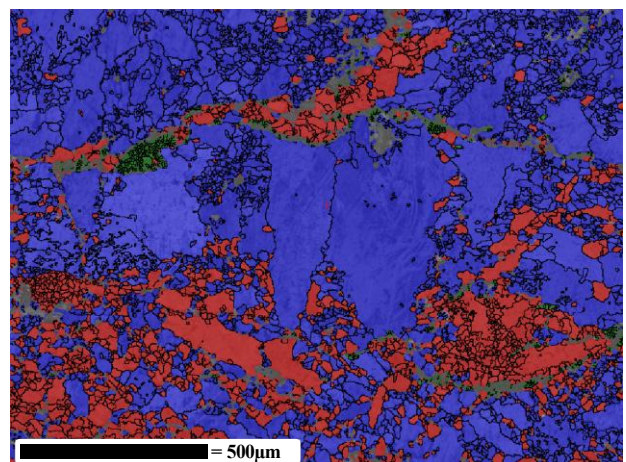


Figure 4. EBSD map plotting quartz in red, carbonate in blue and muscovite in green. Black lines represent high angle grain boundaries ($\geq 10^\circ$) and shows the large range of carbonate grain sizes.

5 Discussion and Conclusions

The data suggests that there have been two fluids involved in the hydrothermal alteration and mineralisation at Sunrise Dam and that these fluids had different sources and/or compositions. Another possibility is that the second fluid had an Fe-activity higher than the equilibrium activity of the first fluid which formed the carbonate veins. Therefore the chemical potential gradient would drive the Fe-rich alteration. The first fluid formed the carbonate vein and its composition fluctuated over time, resulting in Fe and Sr zonation (Fig. 2). The second was the main ore forming fluid, which utilised the permeability of the foliation to flow through the rock until it came into contact with the vein.

It is evident from Figures 1 and 2 that the gold is concentrated in the structurally complex part of the vein which has been brecciated by the cross-cutting of the second carbonate vein. This structural interaction zone has localised mineralisation; with the associated increases in local stress causing brittle fracture and dilation. The fracture system generated by this brittle deformation allowed the ore fluid to flow along grain boundaries and through the fracture system, cross-cutting individual carbonate crystals. The Fe-rich alteration of the carbonate crystals, around the sites of gold mineralisation, suggests that the ore fluid contained high concentrations of iron.

In summary the main conclusions so far are:

1. The mineralised fluids utilised the pre-existing permeability and porosity to flow through the host rocks.
2. Gold mineralisation is localised in the structurally complex regions within the carbonate veins.
3. Gold mineralisation began at the carbonate vein margin and then progressively penetrated and mineralised a fracture network across the vein.
4. Gold emplacement is associated with Fe enrichment of the surrounding carbonate.
5. Gold morphology is controlled by the shape of the voids created by brittle fracturing.

Acknowledgements

Permission from AngloGold Ashanti to publish these results is gratefully acknowledged. This research was supported by an Office of the Chief Executive (OCE) postdoctoral fund from the Commonwealth Scientific and Industrial Research Organisation (CSIRO). Part of this research was undertaken on the X-ray fluorescence beamline at the Australian Synchrotron, Victoria, Australia, grant number M4898 2012/2. The authors acknowledge the facilities, and the scientific and technical assistance of the Australian Microscopy &

Microanalysis Research Facility at the Centre for Microscopy, Characterisation & Analysis, The University of Western Australia, a facility funded by the University, State and Commonwealth Governments.

References

- Blewett RS, Czarnota K, Henson PA (2010) Structural-event framework for the eastern Yilgarn Craton, Western Australia, and its implications for orogenic gold. *Precambrian Res* 183:203-229. doi: <http://dx.doi.org/10.1016/j.precamres.2010.04.004>.
- Farla RJM, Fitz Gerald JD, Kokkonen H, Halfpenny A, Faul U, Jackson I (2011) Slip-system and EBSD analysis on compressively deformed fine-grained polycrystalline olivine. *Geol Soc Lon Spec Pub* 360:225-235. doi: 10.1144/SP360.13.
- Halfpenny A, Prior DJ, Wheeler J (2004) Using electron backscatter diffraction (EBSD) to measure misorientation between 'parent' and 'daughter' grains. Implications for recrystallisation and nucleation Recrystallization And Grain Growth, Pts 1 And 2. *Trans Tech Publications LTD*, pp 573-578.
- Halfpenny A, Prior D.J., Wheeler J (2006) Analysis of dynamic recrystallization and nucleation in a quartzite mylonite. *Tectonophysics* 427:3-14.
- Halfpenny A (2010) Some important practical issues for collection and manipulation of electron backscatter diffraction (EBSD) data from rocks and minerals. *J Vir Exp* 35:3. doi: 10.3809/jvirtex.vol.2010.037.
- Halfpenny A, Prior DJ, Wheeler J (2012) Electron backscatter diffraction analysis to determine the mechanisms that operated during dynamic recrystallisation of quartz-rich rocks. *J Struct Geol* 36:2-15. doi: 10.1016/j.jsg.2012.01.001.
- Halfpenny A, Hough RM, Verrall M (accepted) Preparation of samples with both hard and soft phases for electron backscatter diffraction: Examples from gold mineralisation. *Microsc Microanal*.
- Martin LAJ, Balleve M, Boulvais P, Halfpenny A, Vanderhaeghe O, Duchene S, Deloule E (2011) Garnet re-equilibration by coupled dissolution-precipitation: evidence from textural, major element and oxygen isotope zoning of 'cloudy' garnet. *J Metamorph Geol* 29:213-231. doi: 10.1111/j.1525-1314.2010.00912.x.
- Newton PGN, Gibbs D, Groves A, Jones CM, Ryall AW (1998) Sunrise-Cleo gold deposit In: Berkman DA, and Mackenzie, D.H. (ed) *Geology of Australian and Papua New Guinean Mineral Deposits*. The Australasian Institute of Mining and Metallurgy, Melbourne, pp 179-186.
- Prior DJ, Boyle AP, Brenker F, Cheadle MC, Day A, Lopez G, Peruzzo L, Potts GJ, Reddy S, Spiess R, Timms NE, Trimby P, Wheeler J, Zetterstrom L (1999) The application of electron backscatter diffraction and orientation contrast imaging in the SEM to textural problems in rocks. *Am Mineral* 84:1741-1759.
- Prior DJ, Bestmann M, Halfpenny A, Mariani E, Piazzolo S, Tullis J, Wheeler J (2004) Recrystallization and grain growth in rocks and minerals Recrystallization and Grain Growth, Pts 1 and 2. *Trans Tech Publications LTD*, pp 545-550.
- Prior DJ, Mariani E, Wheeler J (2009) EBSD in the earth sciences: applications, common practice and challenges In: Schwartz AJ, Kumar, M., Adams, B. L., Field, D.P. (ed) *Electron Backscatter Diffraction in Materials Science*. Springer Science + Business Media, pp 345-360.
- Ryan CG, Kirkham R, Siddons DP, Dunn PA, Laird JS, Kuczewski A, Moorhead G, De Geronimo G, Davey P, Jensen M, Paterson DJ, de Jonge MD, Howard DL, Hough RM (2010a) The Maia 384 detector array in a nuclear microprobe: A platform for high definition PIXE elemental imaging. *Nuclear Instruments and Methods in Physics Research Section B: Beam Interactions with Materials and Atoms* 268:1899-1902. doi: 10.1016/j.nimb.2010.02.052.
- Ryan CG, Siddons DP, Kirkham R, Dunn PA, Kuczewski A, Moorhead G, De Geronimo G, Paterson DJ, de Jonge MD, Hough RM, Lintern MJ, Howard DL, Kappen P, Cleverley J (2010b) The New Maia Detector System: Methods For High Definition Trace Element Imaging Of Natural Material In: Denecke MA, Walker CT (eds) *X-Ray Optics and Microanalysis, Proceedings*. pp 9-17.

Ore-forming processes in Reykjanes geothermal pipelines, Iceland

V Hardardóttir

Iceland GeoSurvey, Grensásvegur 9, 108 Reykjavík, Iceland

JW Hedenquist, MD Hannington

Department of Earth Sciences, University of Ottawa, Ottawa, K1N 6N5 Ontario, Canada

Abstract. The Reykjanes geothermal system has a reservoir liquid that originated as seawater and has reacted with the surrounding basalt at temperatures up to 340°C. As the fluid ascends in wells the pressure decreases which leads to boiling and the precipitation of sulfides. In surface pipelines the scales consist mainly of sphalerite, chalcopyrite with minor bornite, pyrrhotite, and pyrite. The bulk composition of the scales downstream of the orifice plate at ~22 bar is 45 wt% Zn, 15 wt% Cu, 3 wt% Fe, 30 wt% S, 2 wt% SiO₂, up to 950 mg/kg Au and up to 2.3 wt% Ag. The amount of scales formed in one year in three wells were up to 1.4 tonnes, consisting of 896 kg Zn, 284 kg Cu, 197 kg Fe, 22 kg Pb, ~ 5 kg Ag and 0.8 kg Au. The Reykjanes geothermal system is a subaerial analogue of high-temperature black smokers on the ocean floor, based on reservoir fluid compositions with high metal and trace element concentrations and the similar compositions of minerals that precipitate downhole and in surface pipelines.

Keywords. Reykjanes metal-rich scales, sulfide precipitation, geothermal fluids, black smoker analog

1 Introduction

The Mid-Atlantic Ridge surfaces on the Reykjanes Peninsula, SW Iceland, where it becomes a complex series of rift and transform zones as it crosses Iceland. Because the geothermal system at Reykjanes is recharged mainly by seawater, it is closely analogous to black smoker systems on the offshore ridge.

In the Reykjanes area high-temperature liquid of seawater composition up to 340°C is precipitating sulfide scales in wells utilized for geothermal power. The sulfides precipitate downhole and in surface pipelines in variable amounts depending mainly on pressure. Here we describe scales that have precipitated in surface pipelines and compare these with sulfides deposited in analogous seafloor hydrothermal systems.

2 Reykjanes Geothermal Field

Reykjanes geothermal system (Fig. 1) is located on the toe of Reykjanes peninsula, 50 km SW of the capital Reykjavík. The Reykjanes Peninsula is covered by young basaltic rocks of glacial, interglacial and post-glacial age (Jonsson 1978). Surface geothermal manifestations, mainly steam vents, mud pools and altered ground cover 1 km², but according to transient electromagnetic measurements (TEM) the extent of the thermal system is 10 km² at 800 m depth (Karlsdóttir

2005). Based on cuttings from 30 wells in the area the stratigraphy consists of hyaloclastite and breccias of reworked tuffaceous sediments to 100 m depth, all of tholeiitic composition, interbedded with basaltic lava flows, and pillow basalts at greater depths (Tómasson and Kristmannsdóttir 1972; Franzson et al. 2002).

The Reykjanes reservoir liquid, which has a seawater salinity, has reacted with the basaltic basement at elevated temperatures (270-340°C), becoming highly enriched in SiO₂, with Ca⁺² and K⁺ concentrations two to four times higher than seawater. SO₄⁻² and Mg concentrations of the reservoir liquid are two to three orders of magnitude lower than seawater. However, the concentrations of most metals in the reservoir liquid are significantly higher than in black smoker fluids with similar discharge temperatures (Hardardóttir et al., 2009): Cu ~15 mg/kg, Zn 5-25 mg/kg, Fe 10-140 mg/kg, Mn ~2.5 mg/kg, Pb 100-300 µg/kg, Ag 30-100 µg/kg and Au 1-6 µg/kg.

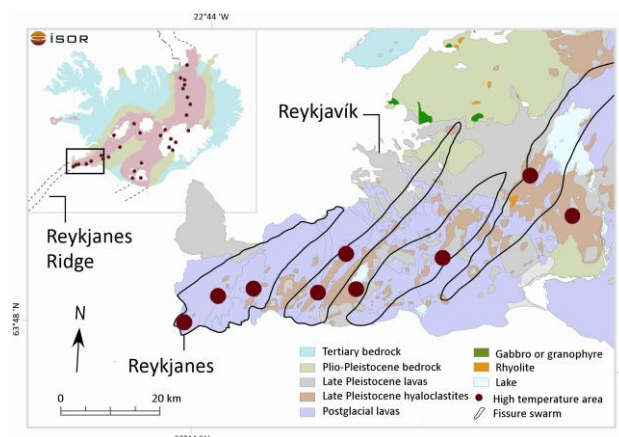


Figure 1. Location of Reykjanes geothermal system, SW Iceland (modified after Saemundsson and Jóhannesson 2004).

3 Mineralogy of the scales

Samples of scales in the surface pipelines were collected during cleaning of the pipes in 2000 and during maintenance in 2007 (Hardardóttir 2011). Scale samples were taken from the wellhead, as well as upstream and downstream of the orifice plate (with fluid-flow control valve; FFCV), in wells that had average wellhead pressures between 44 and 35 bar (257-244°C). At the orifice plates in these wells, the pressures decrease to at least 22 bar (220°C), resulting in precipitation of the sulfide scales.

Table 1. Mineralogy of scales from Reykjanes wells (RN) compared to TAG hydrothermal field

	Well RN-9			RN-12	TAG
	Well-head	4 m downst of OP	30 m downst of OP	Fluid-flow control valve	Black Smoker
Sphalerite	xxx	xxx	x	xxx	xxx
Chalcopyrite	xxx	xx	tr	x	xxx
Amorph. SiO ₂	tr	xxx	xxx	tr	x
Bornite	tr	tr		xxx	x
Digenite				xxx	
Galena	x	tr		xx	tr
Gold/silver	tr	tr		x	tr
Covellite	tr	x		x	tr
Pyrrhotite	tr			tr	x
Pyrite			tr	tr	xx
Anhydrite					xxx
Clay	tr	tr	tr		
Temp. (°C)	244	~188	~188	247-220	270-360

Downst; downstream, OP; orifice plate, TAG data are from Hannington et al. 1995 and Tivey et al. 1995



Figure 2. Photographs of scales in surface pipelines downstream of the orifice plate. The scale bar is 10 cm.

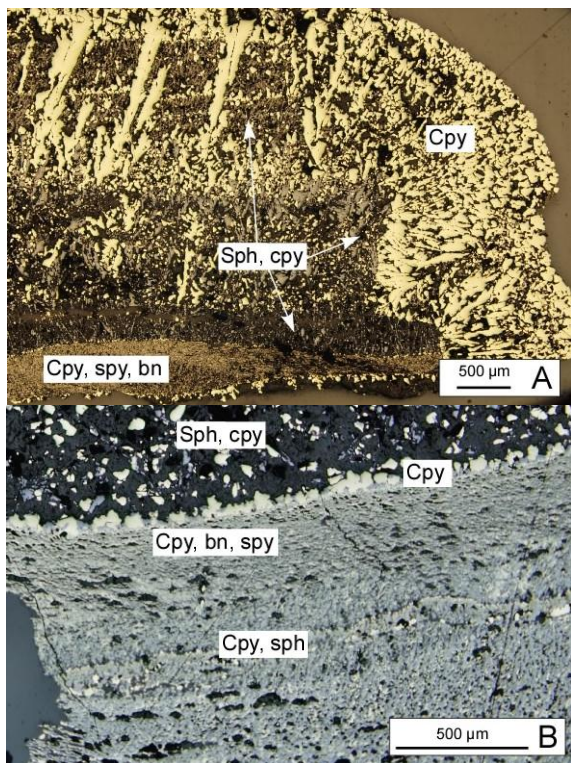


Figure 3. Reflected light photomicrograph of A) alternating bands of fine- and coarse- grained chalcopyrite (cpy yellow), sphalerite (sph gray), bornite (brownish) and galena. B) Two layers consisting mainly of sph (gray) + amorphous silica (black) and cpy (yellow) + minor bornite (brownish) with a band of mainly cpy. Samples upstream of well RN-9.

Upstream from the orifice plate, the scales are thin (<1 mm), but downstream the scales can be quite thick (Fig. 2), with the thickness depending on the pressure at wellhead. All of the scales are very fine-grained and hard, consisting mainly of sphalerite and chalcopyrite with minor bornite, digenite, galena, pyrrhotite, and pyrite (Table 1).

Chalcopyrite and sphalerite form alternating fine- and coarse- grained bands upstream of the orifice plate at high-pressure (~40 bar, 252°C) in well RN-9 (Fig. 3).

Gold occurs as interstitial grains between sulfides, as inclusions mainly in chalcopyrite, and in veins with silver in late-stage fractures seen in scales on the fluid-flow control valve (Hardardóttir et al. 2010). Where pressure decreases to 11 bar, (only well RN-9) amorphous silica is the main phase along with sphalerite and chalcopyrite. The amount of amorphous silica increases downstream of the orifice plate, reaching ~50 wt.% at distances of 4 to 30 m and ~80 wt.% at distances of 100 m.

4 Bulk composition – abundance of scales

The bulk compositions of the scales in the surface pipelines are shown for two wells in Table 2. The scales are dominated by Zn, Fe, Cu, S, and SiO₂, reflecting the major mineralogy. Zinc is the major metal deposited at all pressures. Cu concentrations are generally low at the same pressures (<5 wt%; Hardardóttir 2011) with the highest concentrations near the orifice plate (≤ 30 wt%) where the pressure decreases sharply. Iron generally ranges from 2 to 8 wt% upstream of the orifice plate but decreases sharply downstream of the orifice plate. Lead concentrations are generally highest downstream of the orifice plate and on the fluid-flow control valve, where they reach ~15 wt%.

Table 2. Bulk composition of scales from Reykjanes wells (RN) compared to TAG hydrothermal field

	Well RN-9			Well RN-23			TAG
	Upstr of OP	downst of OP	downst of OP	Upstr of OP	downst of OP	downstr of OP	
Pressure	40-30	11	11	43	22	22	
Zn %	17.9	17.7	10.2	57.5	44.6	44.9	0.4
Fe %	17.3	5.2	5.4	3.3	3.1	5.1	30.5
Cu %	20.7	13.7	5.4	1.4	13.8	13.8	23.0
Pb %	0.6	8.5	3.7	0.0	0.1	0.6	0.003
S %	29.8	16.8	9.3	32.8	30.6	29.8	34.5
SiO ₂ %	4.5	24.7	50.1	2.1	1.9	2.8	<0.5
Al ₂ O ₃ %	0.6	1.9	3.2	0.3	0.2	0.6	-
MgO %	1.1	0.2	0.2	0.3	0.2	0.3	-
LOI %	14.9	15.0	12.2	16.3	15.6	14.2	-
mg/kg							
Ag	667	6066	2740	161	1670	1290	6
Au	121	95	79	363	116	82.4	1

Upstr; upstream, downst; downstream, OP; orifice plate, - ; not available

The highest Au and Ag concentrations also occur near the orifice plate. Just downstream from the orifice plate the Au concentrations range between 50 to 950 mg/kg. At same location the Ag concentration commonly range between 450 to 7000 mg/kg with highest concentration on the fluid-flow control valve up to 2.3 wt%.

In well RN-9 the scales nearly filled the first 8 m of the ~ 350 m long pipeline (to the separation station), probably in <2 years. Only a 10-cm opening remained. The 0.4 m diameter pipeline, with a scale thickness of ~15 cm, contained a total of ~2865 kg scale. In the first year of production, from 2006-2007, three wells produced 2.4 tonnes of scales with ~1.405 tonnes of metals (Table 3).

Table 3. The amount of precipitation formed in Reykjanes (RN) surface pipelines

	RN-11, RN-22,	
	RN-9 ⁽¹⁾	RN-23 ⁽²⁾
Cu (kg)	147	284
Zn (kg)	435	896
Fe (kg)	135	196
Pb (kg)	112	22
Ag (kg)	10	5
Au (kg)	0.3	0.70
SiO ₂ +S+Mn (kg)	2026	1017

⁽¹⁾Precipitated in < 2 years, ⁽²⁾precipitated in 1 year

5 Discussion and conclusions

Geothermal liquid compositionally similar to the Reykjanes fluid, as well as scales precipitated from that liquid, have been observed in several geothermal systems (e.g., in the Fushime geothermal system: Akaku 1990, Akaku and Reed 1995). Similar scales have been documented in the Broadlands-Ohaaki and Rotokawa geothermal systems in New Zealand, which have much lower salinity than the Reykjanes wells (Cl between 1000 and 2000 ppm: Brown 1986; Hedenquist 1990; Simmons and Browne 2000; Reyes et al. 2002). In the Broadlands-Ohaaki system the hydrothermal fluid which enters the wells undergoes a pressure drops at >500 m depth that causes boiling, and Au (<10 to > 1,000 mg/kg) and Ag (<100 to > 10,000 mg/kg) are deposited on the back-pressure plates in surface pipelines. In Rotokawa pipelines the scales at the wellhead contain 5.6 wt.% Cu, 4.0 wt.% Ag, 3.0 wt.% Te, 1.5 wt.% Zn, 0.6 wt.% Pb, and Au 0.2 wt.% (Reyes et al. 2002). These geothermal systems are analogs of low-sulfidation epithermal systems (Simmons and Browne 2000).

The higher salinities of the reservoir liquids at Reykjanes have contributed to much higher base metal contents in the scales that more closely resemble the bulk compositions of sulfide at mid-ocean ridge black smoker vents (Table 2). Sulfide minerals in the chimneys at 21°N include, in order of abundance, sphalerite, pyrite and chalcopyrite, with minor marcasite, pyrrhotite, galena, and digenite. Traces of bornite, cubanite, covellite and chalcocite have also been

observed as well as amorphous silica an Mg-hydroxysulfate-hydrate (MHSH) intimately associated with anhydrite (Haymon and Kastner, 1981). In contrast to the scales in the Reykjanes pipelines, chimneys on the ocean floor typically contain abundant anhydrite formed by heating of seawater. The wells at Reykjanes are insulated from cold seawater and thus contain no anhydrite.

Acknowledgements

The permission from HS Orka HF and Iceland GeoSurvey (ISOR) to publish the data is acknowledged. This paper is financed by the National Energy Authority and GeoSurvey (ISOR).

References

- Akaku K (1990) Geochemical study on mineral precipitation from geothermal waters at the Fushime field, Kyushu, Japan. *Geothermics* 19: 455-467.
- Akaku K and Reed MH (1995) Chemical and physical processes occurring in the Fushime geothermal system, Kyushu, Japan. In: Kharaka YK, Chudaev OV (eds) *Water-Rock Interaction (WRI-8)*, AA Balkema, Rotterdam, pp. 489-492.
- Brown KL (1986) Au deposition from geothermal discharges in New Zealand. *Economic Geology* 81: 979-983.
- Franzson H, Thordarson S, Björnsson G, Gudlaugsson STh, Richter B, Fridleifsson GÓ, Thorhallsson S (2002) Reykjanes high-temperature field, SW-Iceland. *Geology and hydrothermal alteration of well RN-10. Proceedings, 27th workshop on Geothermal Reservoir Engineering*. Stanford University: 233-240.
- Hannington MD, Tivey MK, Larocque ACL, Petersen S, Rona PA (1995) The occurrence of gold in sulfide deposits of the TAG hydrothermal field, Mid-Atlantic Ridge. *Canadian Mineralogist*, 33: 1285-1310.
- Hardardóttir V (2011) Metal-rich scales in the Reykjanes geothermal system, SW Iceland: sulfide minerals in a seawater-dominated hydrothermal environment. PhD thesis, Graduate and Postdoctoral Studies, Department of Earth Science, University of Ottawa, 288 p.
- Hardardóttir V, Brown KL, Fridriksson Th, Hedenquist JW, Hannington MD, Thorhallsson S (2009) Metals in deep liquid of the Reykjanes geothermal system, southwest Iceland: Implications for the composition of seafloor black smoker fluids. *Geology*, 37: 1103-1106.
- Hardardóttir V, Hannington MD, Hedenquist JW, Kjarsgaard I, Hoal K (2010) Cu-rich scales in the Reykjanes geothermal system, Iceland. *Economic Geology*, 105: 1143-1155.
- Haymon R, Kastner M (1981) Hot spring deposits on the East Pacific Rise at 21°N: preliminary description of mineralogy and genesis. *Earth Planet. Sci. Lett.* 53: 363-381.
- Hedenquist JW (1990) The thermal and geochemical structure of the Broadlands-Ohaaki geothermal system, New Zealand. *Geothermics* 19, 151-185.
- Jonsson J (1978) Geological map of Reykjanes Peninsula. National Energy Authority Report No. OS JHD 7831: 303 p.
- Karlsdóttir R (2005) TEM-resistivity measurements at Reykjanes 2004 (in Icelandic). Iceland GeoSurvey report no. ISOR-2005/002, 23 p.
- Reyes AG, Trompeter WJ, Britten K, Searle (2002) Mineral deposits in the Rotokawa geothermal pipelines, New Zealand. *Journal of Volcanology and Geothermal Research* 119: 215-239.
- Saemundsson K, Jóhannesson H (2004) Geothermal map of Iceland, Reykjavík, Iceland GeoSurvey and Icelandic Energy Authority, 1:500,000.

- Simmons SF, Browne PRL (2000) Hydrothermal minerals and precious metals in the Broadlands-Ohaaki geothermal system: Implications for understanding low-sulfidation Epithermal environments. *Economic Geology* 95: 971-999.
- Tivey MK (1995) Modeling chimney growth and associated fluid flow at seafloor hydrothermal vent sites, *in* Humphris SE et al. eds, *Geophysical Monograph 91, Seafloor hydrothermal systems, physical, chemical, biological, and geological interactions*: 158-177.
- Tivey MK, Humphris SE, Thompson G, Hannington MD, Rona PA (1995) Deducing patterns of fluid flow and mixing within the TAG active hydrothermal mound using mineralogical and geochemical data. *Journal of geophysical Research* 100: 12,527-12,555.
- Tómasson J, Kristmannsdóttir H (1972) High-temperature alteration minerals and geothermal brine, Reykjanes, Iceland. *Contributions to Mineralogy and Petrology* 36: 123-134.

Comparison of metals in seawater-dominated fluids of Reykjanes, Iceland, and seafloor black smoker systems

V Hardardóttir

Iceland GeoSurvey, Grensásvegur 9, 108 Reykjavík, Iceland

JW Hedenquist, MD Hannington

Department of Earth Sciences, University of Ottawa, Ottawa, K1N 6N5 Ontario, Canada

Abstract. Reykjanes is a high-temperature subaerial geothermal system (275-340°C) with fluid compositions comparable to those discharged from black smokers on the ocean floor. The reservoir concentrations below 1350 m depth of trace metals, prior to boiling, were determined from downhole samples; they include 154-2431 μM Fe (9-140 mg/kg), 207-261 μM Cu (14-17 mg/kg), 79-393 μM Zn (5-27 mg/kg), 37-55 μM Mn (2-3 mg/kg), and 0.6-1.4 μM Pb (120-290 $\mu\text{g/kg}$), with 6-31 nM Au (1-6 $\mu\text{g/kg}$) and 250-960 nM Ag (28-107 $\mu\text{g/kg}$). By contrast, the discharge liquid at the surface has orders of magnitude lower metal concentrations due to precipitation caused by boiling and vapor loss during depressurization. The metals in similar seawater-dominated high-temperature discharges from ocean-floor black smokers are typically lower in concentration than the pre-boiled (and unmixed) fluids from Reykjanes wells. Some seafloor fluids have boiled before reaching the seafloor; more importantly they may have entrained cold seawater just before discharge. These processes resulted in metal deposition prior to sampling at the seafloor and as evidenced from the formation of now-eroded volcanic-hosted massive sulfide deposits.

Keywords: High-temperature, seawater-dominated, geothermal, sulfides, Au-rich, Ag-rich

1 Introduction

About one hundred high-temperature hydrothermal black smoker systems, some with polymetallic sulfide deposits, are known to vent along mid-oceanic ridges and in other tectonic settings, the latter including intraplate volcanoes, intraoceanic arcs, island arcs, back-arc basins, and rifted continental margins. The majority of the black smoker vents are found on fast-spreading ridges.

Reykjanes peninsula, SW Iceland, is an on-shore example of the oblique spreading zone of the Mid-Atlantic Ridge and is characterized by distinct areas of seismic activity. Where the diverging plate margin interacts with the Iceland plume, there is a complex pattern of rifting and transcurrent faulting; the Reykjanes Ridge is 30° to 40° oblique to the spreading direction, resembling faster spreading ridges, both in terms of topography and seismicity (Einarsson 2001). Present-day spreading is ~1 cm/year in each direction (Vine 1966, Einarsson 2008).

The Reykjanes geothermal system is located at the western tip of the Reykjanes peninsula (Fig. 1), and consists of seawater-dominated fluids at measured temperature up to 340°C. Downhole samples were collected from three wells at temperatures between 284-

295°C, below the boiling point at the collection depths of 1350 to 1500 m (Hardardóttir et al. 2009). This paper compares the metal concentrations, host rocks and tectonic settings of the seawater-dominated fluids of Reykjanes with some of the highest temperature and most metal-rich seafloor hydrothermal systems, TAG, 21°N, and 5°S.

2 Reykjanes hydrothermal system

Reykjanes geothermal system (Fig. 1) is located on the toe of Reykjanes peninsula, 50 km SW of Reykjavík capital. The Reykjanes Peninsula is covered by young basaltic rocks of glacial, interglacial and post-glacial age (Jonsson 1978). Surface geothermal manifestations, mainly steam vents, mud pools and altered ground cover 1 km², but according to TEM- measurements the extent of the thermal system is 10 km² at 800 m depth (Karlsdóttir 2005). Based on cuttings from 30 wells in the area the stratigraphy consists of hyaloclastite and breccias of reworked tuffaceous sediments to 100 m depth interbedded with basaltic lava flows, and pillow basalts at greater depths (Tómasson and Kristmannsdóttir 1972; Franzson et al. 2002).

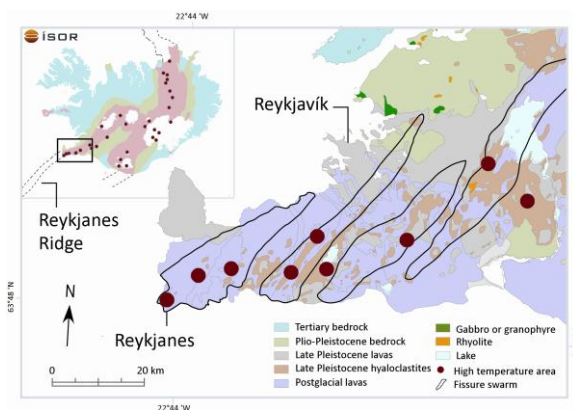


Figure 1. Location of Reykjanes geothermal system, SW Iceland (modified after Saemundsson and Jóhannesson 2004).

The Reykjanes reservoir liquid has a salinity (3.3 wt.%) that is similar to seawater (3.5 wt.%, Table 1); by contrast, the thermal fluid is greatly enriched in silica, and the concentrations of Ca⁺² and K⁺ are two to four times higher in the reservoir water compared to seawater. On the other hand, the concentrations of SO₄⁻² and Mg of the reservoir water are two to three orders of magnitude lower than seawater. The major metals Fe, Cu, and Zn in downhole samples from Reykjanes have a

narrow range in concentration, mainly between 10-25 mg/kg (100-450 $\mu\text{mol/kg}$, μM); Mn is 2-3 mg/kg (40-50 μM) and Pb is 100-300 $\mu\text{g/kg}$ (600-1400 nmol/kg, nM). The precious metals Au and Ag have a range of 1-6 $\mu\text{g/kg}$ (6-33 nM) and 30-100 $\mu\text{g/kg}$ (250-1000 nM), respectively (Hardardóttir et al. 2009). Boiling and gas loss causes precipitations of sulfides in various amounts in the wells as well as upstream and downstream of the orifice plate in the surface pipelines.

Table 1. Major and trace element concentrations from Reykjanes downhole (RN, average of 3 samples), surface fluids (RN, 3 wells), fluids of 21°N, TAG, Sisters Peak, and Turtle Pits, plus seawater

	RN Downhole average ⁽¹⁾	RN Surface average	21°N OBS ⁽²⁾	TAG ⁽³⁾	Sisters Peak 5°S ⁽⁴⁾	Turtle Pits 2006 ⁽⁴⁾	Sea- water ⁽⁵⁾
Sampling depth, m	1500	0	2600	3650	3000	3000	0
Temperature °C	284-296	284-296	350-273	366	400	407	2
pH	--	~4.8	3.4-3.8	3.4	--	--	7.4-8.5
Cl (mM)	521*	544	489	636	224	271	550
Na (mM)	393	422	432	557	209	237	468
K (mM)	39	36	23	17	7.4	8.6	10
Ca (mM)	44	41	16	31	11.6-17.4	8.8	10
SiO ₂ (mM)	11	11	18	21	14.4	11.6	0.07
Mg (mM)	0.21	0.03	0§	0§	0§	0	53.06
Br (μM)	796	855	802	--	392	482	838
Ba (μM)	74	64	8	19	--	--	0.14
Sr (μM)	103	101	81	99	35-52	--	92
B (μM)	704	733	509	--	591	547	416
Li (μM)	907	--	891	850	343	427	26
Al (μM)	55	3	--	--	--	--	0.04
Fe (μM)	1005	1.35	1664	5590	3380	3940	0.001
Cu (μM)	225	<0.01	35	140	110-374	9-76	0.01
Zn (μM)	220	0.2	106	46	50-155	28-69	0.01
Mn (μM)	46	20	1002	680	704	473	0.001
Ni (μM)	5	<0.01	--	<2	--	--	8.E-06
I (μM)	5	0.8	--	--	--	--	0.5
As (μM)	1.7	1.1	0.2	--	--	--	0.0049
Pb (μM)	1.1	<0.001	0.3	0.1	0.126-0.422	0.056-0.184	1.E-05
Cd (μM)	1.1	<0.001	0.2	0.066	--	--	0.00089
Cr (nM)	1092	3	--	--	--	--	6
Ag (nM)	510	--	38	51	--	--	1.9E-05
Sb (nM)	243	--	--	3.9	--	--	0.00197
Mo (nM)	206	93	--	5	80-270	15-57	104
Te (nM)	283	--	--	--	--	--	0.001
V (nM)	245	--	--	--	--	--	49
Tl (nM)	56	--	--	13	--	--	4.9E-05
W (nM)	59	--	--	--	--	--	0.54
Se (nM)	67	--	72	660	--	--	3
Au (nM)	15	--	0.2-1	--	--	--	2E-05
Sn (nM)	26	--	--	--	--	--	0.005
Hg (nM)	2	<0.01	--	--	--	--	5E-06

Note: surface fluids are recalculated to reservoir liquids conditions corrected for vapour loss, values are in mol kg⁻¹ H₂O, na; not analysed, * Cl; calculated from Na+K+Ca balance; §Mg assumed by authors to be 0 for calculation. ⁽¹⁾ Hardardóttir et al. (2009), ⁽²⁾ Von Damm et al. (1985), Von Damm (1990), ⁽³⁾ Douvill et al. (2002), Hannington et al. (2005), ⁽⁴⁾ Koschinsky et al. (2008), ⁽⁵⁾ Lide (1998).

3 Comparison with black smoker hydrothermal systems

The structure of the oceanic crust is recognized from seismic surveys, by analogy with ophiolites, and by direct sampling of the oceanic crust (Alt 1995). A sequence of volcanic basaltic rocks, a few hundred meters to 1 km thick, are overlain by pelagic sediments which are up to 1 km thick. The basaltic rocks are underlain by a sheeted dike complex of gabbroic composition, with average crustal thickness of 7 km (White et al. 1992).

The Trans-Atlantic Geotraverse field (TAG) lies on the Mid-Atlantic Ridge (MAR) at ~26°N and is dominated by a large cluster of black smoker vents near the intersection of a major transfer fault and the rift valley wall (Karson and Rona 1990). The full-spreading

rate is on the order of 2.4 cm/yr. The active black smoker complex sits atop a 200-m diameter and 50-m high mound at a seawater depth of 3670 m. The central black smoker complex discharges fluids up to 363°C (Table 1). The mound consists primarily of pyrite, chalcopyrite and sphalerite and late-stage amorphous silica (Rona et al 1993; Hannington et al. 2005); it has been constructed by intermittent hydrothermal activity over the last 140,000 years.

The 21°N field on the East Pacific Rise (EPR) is located in the axial rift zone at 2600 m depth. The axial rift is opening at a full-spreading rate of 6.2 cm/year and is dominated by linear fault-scarp topography and a central eruptive fissure zone with irregular relief up to 100 m high. The central zone of volcanic hills, ~2.5 km wide, is flanked by numerous open fissures several meters in width (Crane and Normark 1977). Fluids discharging from the highest temperature vents are up to 350°C (Table 1) and form chimneys of pyrrhotite, chalcopyrite and sphalerite. However, there are no large sulfide mounds.

The 5°S field occurs on the southern Mid-Atlantic Ridge, with a slow spreading rate of 3.2 cm/year and young volcanism in the area. Discharging fluids have temperatures up to 407°C at a depth of ~3000 m (Table 1). The black smokers occur in a flat, volcanically and tectonically active area 2 km across. Turtle Pits site is located within laminated and jumbled lava flows, whereas the Sisters Peak site is characterized by pillow lavas. The chimneys of both Sisters Peak and Turtle Pits are about 13 m high. Sisters Peak is composed of recrystallized massive sulfides, mainly chalcopyrite and pyrite, whereas Turtle Pits sulfides consist of a pyrite-chalcopyrite-isocubanite assemblage (Haase et al. 2007).

4 Discussion and Conclusions

The large range of metal concentrations in high-temperature mid-ocean ridge fluids sampled at the seafloor has been suggested to depend on temperature, pH, chlorinity, tectonic setting, and other factors (Von Damm 1995; Hannington et al. 2005).

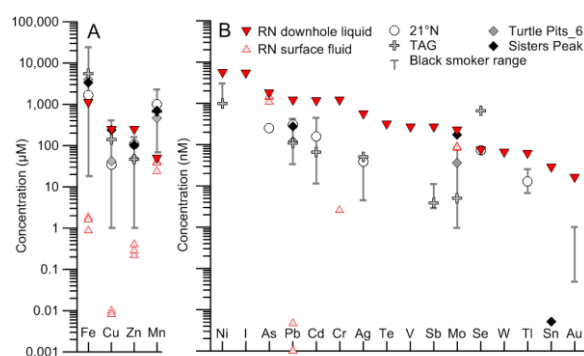


Figure 2. Metal and trace-element concentrations (in μM and nM) from three wells at Reykjanes (RN) compared to black smokers worldwide (Von Damm et al. 2003; Hannington et al. 2005; Gallant and Von Damm 2006), from 21°N EPR, TAG and 5°S MAR (Table 1).

A comparison of Reykjanes data and the seafloor compositions (Fig. 2) show that concentrations of Cu, Zn, and many trace elements in the downhole liquids

from Reykjanes are similar to or higher than those in highest-temperature black smoker discharges; there is a paucity of data for most trace elements from black smoker systems (Table 1, Fig. 2). Gold and Ag concentrations are one to two orders of magnitude higher at Reykjanes, whereas the downhole liquids are lower in Mn and Fe compared to the black smoker seafloor fluids.

All the systems considered here are situated along mid-ocean ridges and have a similar basaltic host rock composition. Previous papers have considered a host-rock source of trace elements via leaching by the heated seawater-dominated fluids (Von Damm 1990); this idea may be due to the evidence for control on the major-element composition via cation exchange with alteration minerals, in conjunction with the paucity of trace-element data. By contrast, de Ronde (1995) compiled evidence for magmatic contributions to seafloor hydrothermal systems, including the metals. Given the ubiquity of intrusive activity driving the high-temperature mid-ocean ridge systems, exsolution of fluids and their contained components from magmas must be also considered as a potential source, particularly of trace elements, in a manner similar to subaerial hydrothermal systems, both active and extinct (Hedenquist and Lowenstern, 1994).

Regardless of the fundamental origins of trace metals in these seawater-dominated hydrothermal systems, it is clear that deep fluids sampled prior to boiling and vapor loss at Reykjanes – and lacking any shallow mixing with cool seawater – have initial metal contents that are similar to or higher than the highest metal concentrations in the sampled seafloor systems.

The vent fluids from TAG and 21°N, as well as many other systems with lower metal contents, are depleted in metals compared to the downhole liquids at Reykjanes, likely due to deposition caused by shallow mixing with cold seawater and/or conductive cooling prior to sampling at the seafloor (Hardardóttir et al. 2009). Higher metal concentrations, with similar Cu, Zn, and Pb values to those at Reykjanes, are reported for fluid sampled from black smokers at Brandon (376°C) on the East Pacific Rise (Von Damm et al. 2003), in the Kairei (315-365°C) and Edmond vent fields (273-293°C) on the Central Indian Ridge (Gallant and Von Damm 2006), and at 5°S on the Mid-Atlantic Ridge (407°C; Koschinsky et al. 2008, Table 1). Lower than seawater Cl concentrations at 5°S (Table 1) indicate phase separation at depth, albeit at sufficiently high pressure that the buoyant (metal-rich) phase separated from a residual brine at depth at close to the critical point (Koschinsky et al. 2008).

These metal-rich discharges, particularly those associated with the highest temperature yet recorded on the seafloor at 5°S, may indicate relatively little metal deposition due to boiling and shallow mixing prior to seafloor discharge. Thus, the wide range in concentrations of trace elements – including metals – in black smoker fluids sampled at the seafloor may be due to a variable degree of depletion due to processes occurring beneath the seafloor. This is similar to the situation observed for fluids sampled at the surface from active volcanic fumaroles (Hedenquist et al. 1994) and

geothermal discharges (Simmons and Brown, 2006, 2007), compared to higher metal concentrations in erupted vapor and downhole samples, respectively. Volcanic-hosted massive sulfide deposits now exposed on land but formed in similar seafloor settings (Hannington et al. 2005) provide evidence for such shallow metal deposition prior to fluid discharge on the seafloor.

Acknowledgments

The permission from HS Orka HF and Iceland GeoSurvey (ISOR) to publish the data is acknowledged. This paper is financed by the National Energy Authority and GeoSurvey (ISOR).

References

- Alt JC (1995) Subseafloor processes in Mid-Ocean Ridge hydrothermal systems, *in* Humphris SE et al. eds, Geophysical Monograph 91, Seafloor hydrothermal systems, physical, chemical, biological, and geological interactions: 85-114.
- Crane K, Normark WR (1977) Hydrothermal activity and crestal structure of the East Pacific Rise at 21°N. *Journal of Geophysical Research* 83: 5336-5348.
- de Ronde CEJ (1995) Fluid chemistry and isotopic characteristics of seafloor hydrothermal systems and associated VMS deposits: Potential for magmatic contributions. *Mineralogical Association of Canada Short Course Series* 23: 479-509.
- Douvill E, Charlou JL, Oelkers EH, Bienvenu P, Jove Colon CF, Donval JP, Fouquet Y, Prieur D, Appriou P (2002) The Rainbow vent fluids (36°14'N, MAR): the influence of ultramafic rocks and phase separation on trace metal content in Mid-Atlantic Ridge hydrothermal fluids. *Chemical Geology* 184: 37-48.
- Einarsson P (2001) Structure and evolution of the Iceland hotspot; *Deutsche Geophysikalische Gesellschaft, Mitteilungs* 1/2991: 11-14.
- Einarsson P (2008) Plate boundaries, rifts and transforms in Iceland, *Jökull* 58: 35-58.
- Franzson H, Thordarson S, Björnsson G, Gudlaugsson STh, Richter B, Fridleifsson GÓ, Thorhallsson S (2002) Reykjanes high-temperature field, SW-Iceland. *Geology and hydrothermal alteration of well RN-10. Proceedings, 27th workshop on Geothermal Reservoir Engineering*. Stanford University: 233-240.
- Gallant RM, Von Damm KL (2006) Geochemical controls on hydrothermal fluids from the Kairei and Edmond vent fields, 23°-25°S, Central Indian Ridge. *Geochemistry, Geophysics, Geosystems* 6: 1-24.
- Hannington MD, de Ronde CEJ, Petersen S (2005) Sea-floor tectonics and submarine hydrothermal systems, *in* Hedenquist JW et al. eds, *Economic Geology 100th Anniversary Volume*, Society of Economic Geologists: 111-141.
- Hardardóttir V, Brown KL, Fridriksson Th, Hedenquist JW, Hannington MD, Thorhallsson S (2009) Metals in deep liquid of the Reykjanes geothermal system, southwest Iceland: Implications for the composition of seafloor black smoker fluids. *Geology* 37: 1103-1106.
- Haase KM et al. (2007) Young volcanism and related hydrothermal activity at 5°S on the slow-spreading southern Mid-Atlantic ridge. *Geochemistry Geophysics Geosystems* 8: 1-17.
- Hedenquist JW, Aoki M, Shinohara H (1994) Flux of volatiles and ore-forming metals from the magmatic-hydrothermal system of Satsuma Iwojima Volcano. *Geology* 22: 585-588.
- Hedenquist JW, Lowenstern JB (1994) The role of magmas in the formation of hydrothermal ore deposits. *Nature* 370: 519-527.
- Karlsdóttir R (2005) TEM-resistivity measurements at Reykjanes 2004 (in Icelandic). Iceland GeoSurvey report no. ISOR-

2005/002, 23 p.

- Karson JA, Rona PA (1990) Blocki-tilting, transfer faults, and structural control of magmatic and hydrothermal processes in the TAG area, Mid-Atlantic Ridge 26°N. *Geological Society of America Bulletin* 1102: 1635-1645.
- Koschinsky A, Garbe-Schönberg D, Sander S, Schmidt K, Gennerich HH, Strauss H-H (2008) Hydrothermal venting at pressure-temperature conditions above the critical point of seawater, 5°S on the Mid-Atlantic Ridge. *Geology* 36: 615-618.
- Lide DR ed (1998) *CRC Handbook of Chemistry and Physics* (78th edition, 1997-1998). New York CRC Press: 14.
- Rona PA, Hannington MD, Raman CV, Thompson G, Tivey MK, Humphris SE, Lalou C, Petersen S (1993) Active and relict sea-floor hydrothermal mineralization at the TAG hydrothermal Field, Mid-Atlantic ridge. *Economic Geology* 88: 1989-2017.
- Tómasson J, Kristmannsdóttir H (1972) High-temperature alteration minerals and geothermal brine, Reykjanes, Iceland. *Contributions to Mineralogy and Petrology* 36: 123-134.
- Saemundsson K, Jóhannesson H (2004) Geothermal map of Iceland, Reykjavik, Iceland GeoSurvey and Icelandic Energy Authority, 1:500,000.
- Simmons SF, Brown, K.L. (2006) Gold in magmatic hydrothermal solutions and the rapid formation of giant ore deposits. *Science* 314: 288–291.
- Simmons SF, Brown KL, (2007) The flux of gold and relate metals through a volcanic arc, Taupo Volcanic Zone, New Zealand. *Geology* 35: 1099–1102.
- Vine FJ 1966 (1966) Spreading of the ocean floor: New evidence. *Science* 154: 1405-1415.
- Von Damm KL (1990) Seafloor hydrothermal activity: Black smoker chemistry and chimneys. *Annual Review of Earth and Planetary Sciences* 18:173-204.
- Von Damm KL (1995) Controls on the chemistry and temporal variability of Seafloor hydrothermal fluids. *In* Humphris SE et al. eds, *Seafloor hydrothermal systems: physical, chemical, biological, and geological interactions*. Geophysical Monograph 91 American Geophysical Union: 222-247.
- Von Damm KL, Edmond JM, Grant B, and Measures CI, Walden B, Weiss RF (1985) Chemistry of submarine hydrothermal solutions at 21°N, East Pacific Rise. *Geochimica et Cosmochimica Acta* 49: 2197-2220.
- Von Damm KL, Lilley MD, Shanks III WC, Brockington M, Bray AM, O'Grady KM, Olson E, Graham A, Poskurowski G, and the SouEPR Science Party (2003) Extraordinary phase separation and segregation in vent fluids from the southern East Pacific Rise. *Earth and Planetary Sciences Letters* 206: 365-378.
- White RS, McKenzie D, O'Nions RK (1992) Oceanic crustal thickness from seismic measurements and rare earth element inversions. *J. Geophysics Research* 97: 19683-19715.

Reactive fluid flow and integrated fluxes recorded by tin-bearing greisens, Krušné hory (Erzgebirge) Mts., central Europe

Matylda Heřmanská, David Dolejš

Institute of Petrology and Structural Geology, Charles University, Prague, Czech Republic

Abstract. We use transport theory to evaluate integrated fluid fluxes responsible for the formation of tin-bearing greisens in the Western Krušné hory (Erzgebirge) granite pluton in central Europe. The pluton consists of multiple intrusive units of low- to high-Li-F-P biotite, two-mica, and topaz-zinnwaldite granites. Greisens form subvertical dyke swarms that have formed by constant-volume replacement (mica-quartz greisens, topaz-quartz greisens, monomineralic quartz greisens), followed by hydrofracturing (quartz veins). We use alteration reaction progress to assess the magnitude of chemical disequilibrium for infiltrating aqueous fluid and the time-integrated fluid flux necessary to reproduce the observed modal variations. The integrated fluid fluxes are 10^{2-3} m³ fluid per m² rock. Assuming the flow rate of 10^{-10} m s⁻¹, formation of a typical greisen vein requires 10^{5-7} m³ fluid phase. For 5 wt.% H₂O dissolved H₂O in granitic melt, the fluid would have exsolved from $3 \cdot 10^5$ - $2 \cdot 10^8$ m³ magma, that is, a reservoir with size of 80-700 m in each direction, which is comparable to the host intrusion.

Keywords. greisen, alteration, hydrothermal flow, fluid flux

1 Introduction

Advances in our understanding of thermodynamics of fluid-mineral interactions at elevated temperatures and pressures now permit calculation of time-integrated fluid fluxes and total fluid volumes to be estimated from petrological record in alteration or mineralization zones. By estimating mineral reaction progress from modal variations in zonal alteration sequence, we can balance respective fluid-mineral reactions and convert their progress into integrated fluid fluxes if the driving pressure and temperature gradients are known or can be reasonably well estimated. We illustrate application of this method to interpretation of mica-quartz and topaz-quartz greisen veins with cassiterite mineralization hosted by granites of the Krušné hory (Erzgebirge) batholith emplaced in the Saxothuringian zone of the Variscan orogen (360-310 Ma) in central Europe.

2 Geological setting

The Western Krušné hory (Erzgebirge) pluton is a discontinuous exposure, 70 by 30 km large, of biotite, two-mica and topaz-zinnwaldite granites (324-312 Ma). Traditionally, this suite of low- to high-Li-F-P granites is subdivided into an older, less evolved, intrusive complex (OIC) and a younger, highly evolved, intrusive complex (YIC) that is accompanied by extensive tin ± tungsten mineralization of the greisen type (Breiter et al. 1999).

Our study was conducted in the Horní Blatná

composite body, which forms a continuous outcrop 7 by 6 km large, accompanied by two stocks of extremely evolved, perphosphorous topaz-zinnwaldite granites (Fig. 1). The intrusive sequence consists of multiple intrusive units, which differ in their whole-rock and modal composition as well as in textural appearance. This granitic body is interpreted to represent an apical, moderately to highly evolved residual granitic melts emplaced beneath the roof of the batholith.

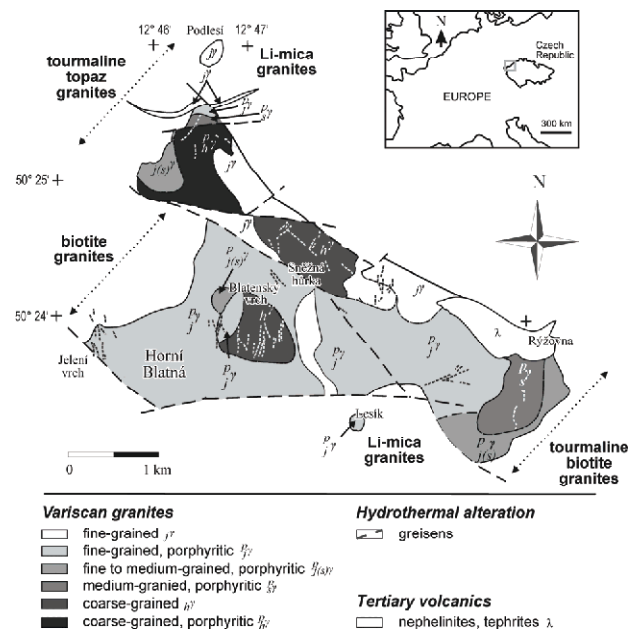


Figure 1. Geological map of the Horní Blatná composite body in the Western Krušné hory pluton.

The intrusive rocks correspond to the biotite or two-mica granites, locally with tourmaline, the topaz-lithian annite granites with tourmaline, and the topaz-zinnwaldite granites. The less evolved varieties are characterized by porphyritic texture with a fine-grained groundmass, the moderately evolved types are medium- to coarse-grained with microgranite bodies, and the extremely evolved granites are generally fine-grained and devoid of phenocrysts, although K-feldspar megacrysts forming solidification fronts (stockscheider) are locally present. All granites are chemically evolved (75-77 wt. % SiO₂; 12.5-15.0 wt. % Al₂O₃), moderately to strongly peraluminous (alumina saturation index, ASI = 1.1-1.2), with high concentrations of phosphorous (0.18-0.97 wt. % P₂O₅), lithium (0.05-0.28 wt. % Li₂O), and fluorine (0.20-1.45 wt. % F). Strong depletion in mafic constituents (2.7-0.8 wt. % MgO + FeO_{tot}; mg# = 0.49-0.04; 0.22-0.40 wt. % TiO₂) provides further

evidence for protracted magmatic fractionation. The major- and trace-element concentrations characterize the granites as continental collisional magmas derived from predominantly sedimentary precursors (Förster et al. 1999).

3 Hydrothermal alteration

Granites of the Horní Blatná composite body show increasing evidence for postmagmatic hydrothermal alteration: (i) pervasive tourmalinization and formation of tourmaline ± quartz-rich cavities in granites, (ii) focused tourmalinization in the surrounding phyllites leading to the formation of massive tourmalinites and tourmaline fracture fillings, with rare cassiterite mineralization, and (iii) widespread incipient greisenization, which becomes increasingly focused into vertical permeable zones leading to the formation of spatially zoned mica-quartz, topaz-quartz and monomineralic quartz greisens, with abundant cassiterite mineralization (Fig. 2). Greisens form subvertical veins and swarms up to 1.5 m thick, 400 m long, and 800 m deep that cross cut all compositional and textural granite types (Štemprok and Dolejš 2010).

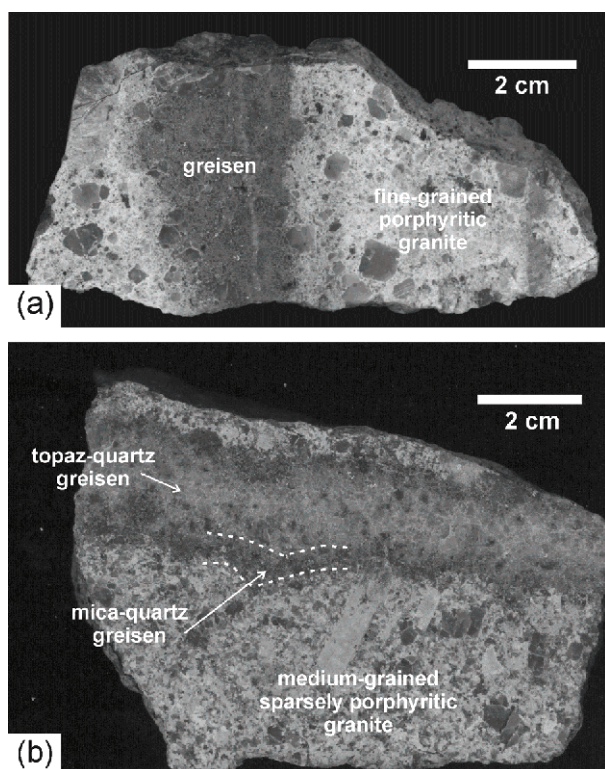


Figure 2. Greisen veins penetrating fine- to medium-grained granites. The continuity of primary magmatic textures as well as the distribution and preservation of quartz phenocrysts indicates that greisens have formed by granite replacement under constant volume.

4 Mineral chemistry

Chemical composition was analyzed using the TESCAN Vega scanning electron microscope with the EDS detector X-Max 50 (Institute of Petrology and Structural geology, Charles University in Prague). Measurements were carried out with an accelerating voltage of 15 kV,

beam current of 1.5 nA and the acquisition time of 100 s.

The granites are typical subsolvus granites with coexisting Na-rich plagioclase and K-feldspar. Their major element composition was recalculated to formula units on 8 oxygen equivalent basis. The K-feldspars are homogeneous or variably exsolved and exhibit perthite lamellae or albite rims and overgrowths. K-feldspar phenocrysts and matrix grains are frequently very pure ($Or_{98}Ab_{02}$) but some extend to Na-rich varieties ($Or_{69}Ab_{30}An_{01}$) until the alkali feldspar solvus has been reached. Plagioclase composition forms a linear trend originating at $Or_{03}Ab_{87}An_{10}$ and evolving towards pure albite ($Or_{01}Ab_{99}$). Rare plagioclase xenocrysts from incompletely assimilated metasediments contain up to 35 mol. % anorthite (Fig. 3).

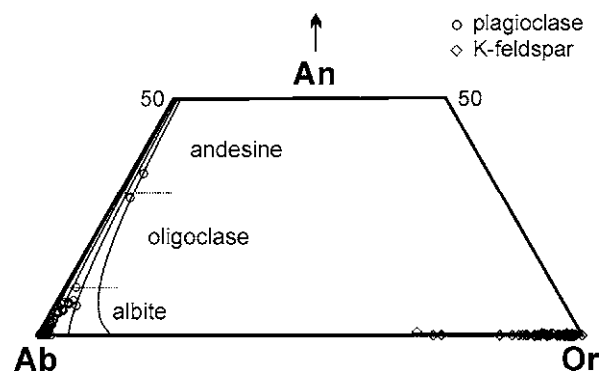


Figure 3. Chemical composition of feldspars in granites and greisens (present as relics). Abbreviations: Ab – albite, Or – orthoclase, An – anorthite. The solid curves are solvus isotherms at $T = 300, 400, 500$ and 600 °C, respectively, and $P = 1$ kbar.

Granites and greisens contain two micas (lithian annite and muscovite) or a single dark mica (zinnwaldite). Lithium in micas was calculated using the correlation relationships by Tischendorf et al. (2004): $Li_2O = 0.289 SiO_2 - 9.658$ and $Li_2O = 0.3935 F^{1.326}$ (in wt. %) for dark and white micas, respectively. The weight percentage concentrations were recalculated to formula units using 11 oxygen equivalents while assuming all iron to be present in the Fe^{2+} state. The composition of both micas varies strongly and correlates with the degree of magma geochemical evolution (Fig. 4). The dark micas are lithian annites through zinnwaldites and trilithionites, with $mg\# = 0.46-0.03$, 3.69-0.13 wt. % TiO_2 and 0.5-7.8 wt. % F. Correspondingly, the lithium concentrations reach up to 4.70 wt. % Li_2O . The white micas are lithian muscovites (up to 0.48 wt. % F, 4.87 wt. % Li_2O and 0.40 wt. % Na_2O), which evolved during greisenization to low-Li-F muscovites with declining proportions of the zinnwaldite and aluminoceladonite end-members.

Tourmalines in granites, greisens and tourmalinites hosted in phyllites are optically zoned, ranging from brown or greenish brown to blue varieties. The blue varieties appear to represent late hydrothermal growth zones or replacements. The tourmaline formula units were recalculated using the sum of tetrahedral and octahedral cations in the T, Z and Y sites to be 15 while allowing for octahedral vacancies associated with every three Ti atoms. All tourmalines are assumed to be Li-free

and contain only ferrous iron. Tourmalines in granites are close to schorl end-member (Fig. 5), but those from tourmalinites show greater variability (2.26-2.70 wt. % Na₂O; up to 0.70 wt. % CaO; mg# = 0.02-0.41). The deficiency in sodium is reflected in the partially vacant X site (up to 0.5 vpfu). The compositional trend of tourmalines corresponds to evolution from pure schorl to a mixture of foitite and oxy-dravite, corresponding to local derivation of Mg, Fe and Al from phyllites.

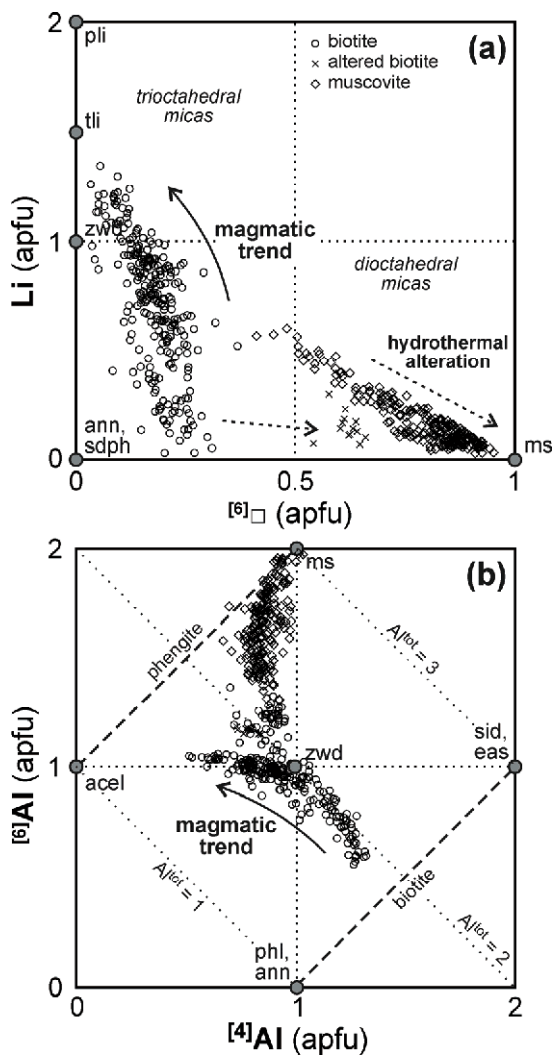
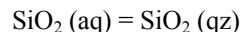
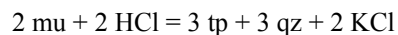
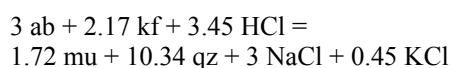


Figure 4. Chemical composition of micas in granites and greisens. Abbreviations: acel – aluminoceladonite, ann – annite, eas – eastonite, ms – muscovite, sid – siderophyllite, pli – polyolithionite, tri – trillithionite, zwd – zinnwaldite.

5 Alteration reactions and fluid transport

Greisen formation involves: (i) hydrolysis characterized by breakdown of plagioclase and K-feldspar, and formation of white mica with quartz, (ii) replacement of white mica by topaz and additional quartz, and (iii) silicification leading to the formation of monomineralic quartz greisens. At this stage, transition from volume-conserved replacement to open-space (fracture) filling occurs. Individual stages of greisen formation are summarized by the following reactions:



We propose a reactive-transport model to simulate the progress of alteration reactions and to estimate the fluid fluxes necessary for the formation of the spatial zoning. In this model we evaluate the disequilibrium fluid infiltration and the pressure–temperature gradient simultaneously. Using a series of initial conditions, from 650 °C and 1 kbar (magmatic fluid phase exsolving at the solidus) to 400 °C and 500 bar (conditions of greisen formation), the formation of muscovite-quartz greisens requires a time-integrated flux of $\sim 10^2$ to 10^5 m³ fluid per m² rock, whereas the formation of topaz-quartz greisens is predicted to occur at $\sim 10^2$ to $\sim 10^6$ m³ fluid per m² rock (Fig. 6).

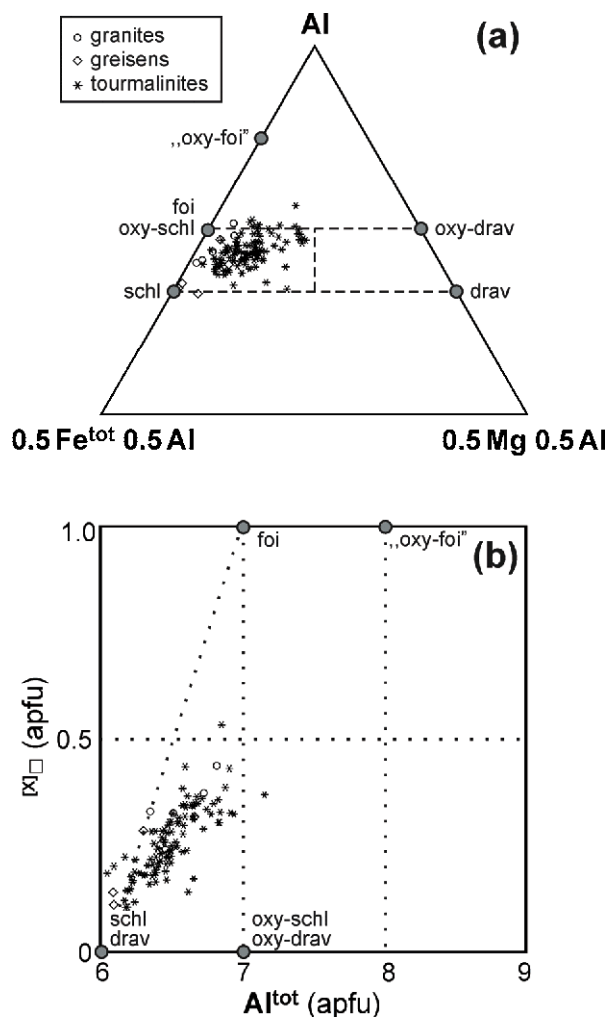


Figure 5. Chemical composition of tourmalines in granites, greisens and tourmalinites. Abbreviations: schl – schorl, drav – dravite, foi – foitite. The prefix “oxy” indicates oxy-varieties of respective end-members.

The fluxes can be further specified by constraining permissible modal variations and volume changes. For the volume-conserved replacement to occur, the integrated fluid flux could not have exceeded $\sim 10^3$ m³ fluid per m² rock. In addition, the incoming fluids must have been in disequilibrium with the host rocks (originating at $T = 480$ °C or higher) in order to produce

the topaz-bearing alteration assemblages. For a conservative estimate of the time-integrated fluid flux on the order of 10^2 to 10^3 m³ fluid per m² rock, the plausible flux rate is $\sim 10^{-10}$ to 10^{-8} m s⁻¹. Thus the formation of a single greisen vein with a typical volume of 10^3 to $5 \cdot 10^4$ m³ would require 10^5 - $3 \cdot 10^7$ m³ aqueous fluid. By using mass balance and an assumed 5 wt. % H₂O dissolved in a granitic magma, such amount of fluid phase would have exsolved from $5 \cdot 10^5$ to $3 \cdot 10^8$ m³ magma, or an intrusion measuring approx. 80 to 700 m in each dimension (Fig. 7). These estimates are comparable with dimensions of intrusive units of the Horní Blatná composite intrusion.

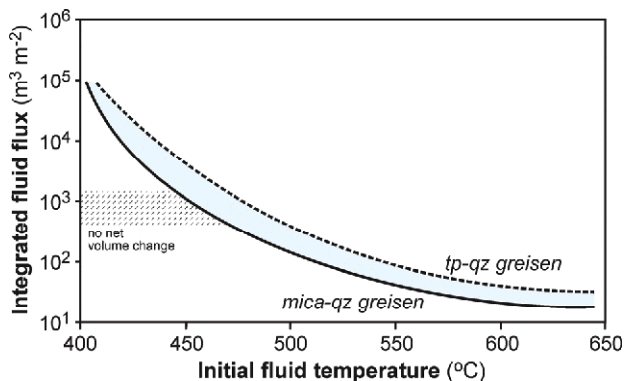


Figure 6. Integrated fluid flux vs. initial fluid temperature, responsible for the chemical disequilibrium at the inflow into the greisen formation site. The larger is the magnitude of initial disequilibrium, the lower fluid flux is necessary to reproduce the mineral assemblages of mica-quartz and topaz-quartz greisens.

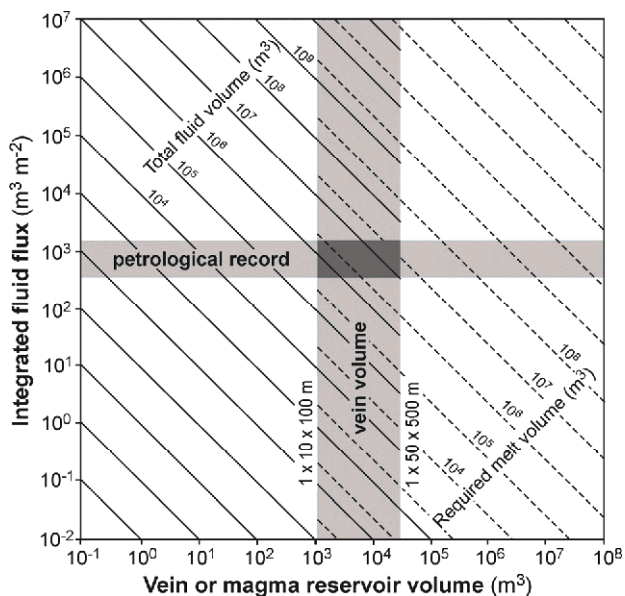


Figure 7. Relationship between the vein volume and the required magma volume necessary to produce the interpreted fluid fluxes (assuming 5 wt. % H₂O dissolved in a granitic magma).

6 Conclusions

The Western Krušné hory (Erzgebirge) batholith comprises a sequence of low- to high-Li-F-P biotite, two-mica and topaz-zinnwaldite granites that host tin-

tungsten mineralization of greisen type. Greisens form vertical vein swarms, which formed by hydrolytic replacement of the host granites but late-stage hydrofracturing lead to the formation of monomineralic quartz greisens. We propose a reactive-transport model, based on local equilibrium, embodied in the transport theory, to estimate time-integrated fluid flux necessary for the formation of observed spatial alteration zoning. By considering chemical disequilibrium of infiltrating fluid we estimate the time-integrated fluid fluxes approx. 10^2 - 10^3 m³ m⁻² in order to maintain constant-volume replacement with no net mass addition. This estimate is two to three orders of magnitude smaller than fluid fluxes published for focused fluid flow in brittle fractures or ductile shear zones. Furthermore, the calculated fluid fluxes are several orders of magnitude smaller than in local equilibrium models. However, the results indicate that no involvement of external (e.g., meteoric) fluids is necessary.

Acknowledgements

This work has been funded by the Czech Science Foundation (Project Nr. P210/12/0986).

References

- Breiter K, Förster H-J, Seltmann R (1999) Variscan silicic magmatism and related tin-tungsten mineralization in the Erzgebirge-Slavkovský les metallogenic province. *Miner Depos* 34: 505-521
- Förster H-J, Tischendorf G, Trumbull RB, Gottesmann B (1999) Late-collisional granites in the Variscan Erzgebirge, Germany. *J Petrol* 40: 1613-1645
- Štemprok M, Dolejš D (2010) Fluid focusing, mass transfer and origin of fracture-controlled greisens in the Western Krušné hory/Erzgebirge granite pluton, central Europe. *Zeitschr Geol Wiss* 38: 207-234
- Tischendorf G, Rieder M, Förster H-J, Gottesmann B, Guidotti CV (2004) A new graphical presentation and subdivision of potassium micas. *Miner Mag* 68: 649-667

Hydrothermally induced fluorine enrichment in metagranitoids of the Felbertal scheelite deposit (Austria)

Michael Kozlik and Johann G. Raith

Chair of Resource Mineralogy, Department of Applied Geosciences and Geophysics, Montanuniversitaet Leoben, 8700- Leoben, Austria, e-mail: michael.kozlik@unileoben.ac.at

Abstract. Biotite and titanite from the mineralised ~340 Ma K1-K3 orthogneiss in the Felbertal scheelite deposit have higher fluorine concentrations in comparison with barren Central gneisses in the distinct surroundings of the deposit. Elevated F concentrations in biotite correspond with lower TiO₂ contents and higher X_{Mg} values. In terms of F concentration and X_{Al} two generations of titanite, reflecting different physicochemical crystallisation conditions, can be distinguished too. Titanites low in F and Al₂O₃ and showing distinct growth zoning are interpreted as magmatic, whereas higher F and Al₂O₃ concentrations and patchy replacement structures suggest titanite formation by hydrothermal alteration. Similar to various other granite-related tungsten deposits, enrichment in F at Felbertal scheelite deposit can be related to late stage magmatic-hydrothermal processes. Fluids derived from the granitic protolith of the K1-K3 orthogneiss are proposed as a possible source of F.

Keywords. Felbertal scheelite deposit, fluorine enrichment, biotite, titanite, hydrothermal alteration

1 Introduction

The Felbertal scheelite deposit in the state of Salzburg (Austria) is one of the biggest producing tungsten mines in the world (annual production in 2011 was 423.000 t at 0.3 mass% WO₃). Despite several previous studies the genesis of the Felbertal deposit is still controversially discussed and further research is inevitable to clarify the origin of the tungsten mineralisation. For this purpose the chemical composition of biotite and accessory phases such as titanite were compared from an Early Carboniferous highly fractionated and mineralised metagranitoid (K1-K3 orthogneiss; cf. Briegleb 1987; Finger et al. 1985; Raith and Stein 2006) and from the barren Central gneisses of similar age exposed in the vicinity of the deposit.

This work presents data supporting a late to post-magmatic hydrothermally induced enrichment of fluorine, especially in the Variscan K1-K3 orthogneiss. The results are discussed in the context of the role of fluorine in granitic melts and their related types of tungsten deposits.

2 Geological setting

Within the central parts of the Penninic Tauern Window, the Felbertal scheelite deposit is located about 8 km south of Mittersill. Two major lithological units dominate the geology of the deposit: (1) Late

Proterozoic to Early Palaeozoic basement rocks, assigned to the Habach Complex, and (2) metagranitoids of Early Carboniferous to Early Permian age, referred as Central gneisses (e.g. Eichhorn et al. 2000).

Based on geological, petrographic and geochemical evidence, the pre-Variscan Habach Complex has been subdivided from bottom to top in the Basal Schist Formation, the Lower Magmatic Series (LMS), the Upper Magmatic Series (UMS) and an overlying sequence of clastic metasediments assigned to the Habach Phyllite Formation (Höll 1975).

The scheelite mineralisation is restricted to the lower parts of the LMS which consists of a sequence including fine-grained and coarse-grained amphibolites, hornblendites, hornblende-schists, prasinites, as well as Early Palaeozoic metagranitoids (Höll 1975). The pre-Variscan age for the LMS is confirmed by conventional and in-situ U-Pb zircon ages; the fine-grained amphibolites yielded 547 ± 27 Ma, the hornblendites 496 ± 2 Ma and the coarse-grained amphibolites 482 ± 5 Ma (von Quadt 1985; Eichhorn et al. 1999).

In the Early Carboniferous during the Variscan orogeny a lasting period of subduction-related magmatism caused in-situ crustal melting and produced collisional high-K calc-alkaline to shoshonitic I-type granitoids (Eichhorn et al. 2000). A second pulse of magmatic activity occurred during the Late Carboniferous until Early Permian generating I-type and to a minor extent S-type granitoids due to decompression and post-orogenic extension (Eichhorn et al. 2000).

A mineralised leucocratic orthogneiss (K1-K3 orthogneiss) is intercalated in the lithologies of the LMS at the upper levels in the western ore field of the Felbertal scheelite deposit. Conventional U-Pb dating of zircons revealed an intrusion age of 336 ± 19 Ma for this metagranitoid (Eichhorn et al. 1995).

Barren Central gneisses of predominantly Early Carboniferous age are exposed in vicinity of the deposit. They either form concordant planar intrusive bodies which can be traced over several kilometres (e.g. Felbertauern augengneiss, 340 ± 4 Ma; Knorrkogel gneiss, 334 ± 8 Ma) or dome-like structures (Granatspitz gneiss) (Eichhorn et al. 2000). For the latter Eichhorn et al. (2000) suggested a Permian crystallisation age (271 ± 4 Ma), although other studies proposed a Late Carboniferous age (314 ± 4 Ma, Kebede et al. 2005).

Variscan regional metamorphism reached amphibolite facies conditions and generated the pervasive fabrics observable in all lithologies of the deposit (Eichhorn et al. 1995). Young Alpine

compressional tectonics in the Felbertal area caused the development of discrete shear zones and thrust faults with northwards movement of the hanging wall rocks (Höll and Eichhorn 2000). It caused a greenschist facies regional metamorphic overprint. Crosscutting quartzveins and small scale thrust faults are distinct features of the Alpine deformation in the Felbertal scheelite deposit.

3 Mineral chemistry of F-rich minerals

3.1 Analytical methods

The chemical composition of F-rich minerals was measured using the JEOL JXA8200 electron microprobe of UZAG Steiermark at the Department of Applied Geosciences and Geophysics, Montanuniversitaet Leoben. For routine WDS-analyses an acceleration voltage of 15 kV and a beam current of 10 nA were chosen. To minimise possible matrix effects a synthetic F-rich phlogopite was used as reference material for F. The detection limit for fluorine was below 550 ppm and for chlorine below 200 ppm.

F-rich phases were analysed in the K1-K3 orthogneiss and in the barren Central gneisses (Felbertauern augengneiss, Knorrkogel gneiss, Hochweißenfeld gneiss, Weißeneck-Dichtensee gneiss). For details concerning the geological environment and magmatic evolution of mentioned Central gneisses see Finger et al. (1993) as well as Eichhorn et al. (2000) and references therein.

3.2 Biotite

Biotite from the different metagranitoids studied can be discriminated by means of its X_{Mg} [$=Mg/(Mg+Fe)$] and F-content (Fig. 1). The samples define different clusters in the X_{Mg} vs. F diagram. The highest F concentrations were measured in biotites from the ore deposit ranging from 0.20 to 2.85 mass% F. Very low concentrations in F (< 0.50 mass% F) correlate with low X_{Mg} ranging from 0.44-0.47 and most notably high TiO_2 (1.06-1.22 mass% TiO_2). The highest concentration of TiO_2 (1.55 mass% TiO_2) was measured in a sample having fluorine below the detection limit. In comparison F-rich biotites have X_{Mg} around 0.51-0.59 and TiO_2 near 0.70 mass%. Biotites from the Felbertauern augengneiss and Knorrkogel gneiss exhibit much lower F contents of 1.04-2.04 and 0.33-0.52 mass% F, respectively. Biotites from the Hochweißenfeld gneiss and Weißeneck-Dichtensee gneiss have F concentrations below the detection limit. Concentrations of Cl in biotites were analysed but they are always below the detection limit.

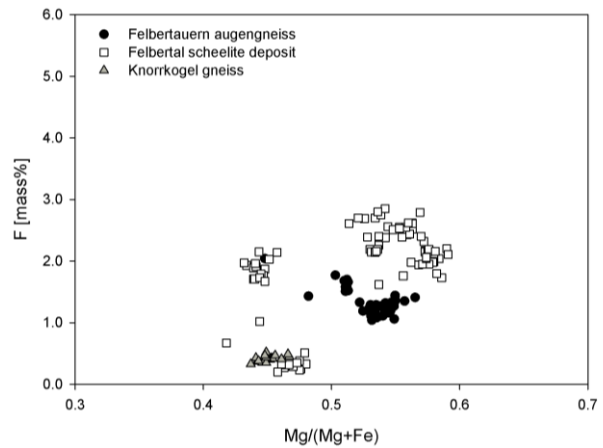


Figure 1. X_{Mg} vs. F [mass%] plot for metagranitoids in the Felbertal area. The highest F concentrations are observed in biotites from the Felbertal scheelite deposit

3.3 Titanite

Two generations of titanite can be distinguished based on backscattered electron images and variations in the chemical composition. Backscattered electron images of titanites from both the K1-K3 orthogneiss in the ore deposit as well as barren Central gneisses reveal distinct oscillatory as well as patchy chemical zoning. The μ m-thick oscillatory zones are formed parallel to the main crystal faces of titanite and are interpreted as magmatic growth zones. These crystals are characterised by euhedral shape, whereas titanite showing a patchy zoning exhibits both anhedral and euhedral crystal shapes. The patchy zoning is interpreted as a hydrothermal alteration texture formed under sub-solidus conditions. Magmatic titanites in the Felbertal scheelite deposit feature a small marginal zone with an irregular inner boundary which is attributed to dissolution and resorption processes due to hydrothermal alteration. Additionally, allanite inclusions in titanite are restricted to the observed alteration zones.

The magmatic and hydrothermal titanite generations can be clearly distinguished by their F contents and X_{Al} [$=Al/(Al+Ti+Fe^{3+})$] (Fig. 2). The magmatic titanites have X_{Al} between 0.03 and 0.05 and 0.001-0.030 F apfu. Patchy titanite and hydrothermal rims overgrowing magmatic titanite have elevated X_{Al} ranging from 0.09 to 0.20 and 0.040-0.097 F apfu.

The enrichment in Al_2O_3 is coupled with an increase in F concentration following the exchange vector $Al_1F_1Ti_{1-1}O_{-1}$ (Zabavnikova 1957). However, only half of the aluminium is compensated by fluorine (see Fig. 2) what indicates that another substitution must be operative. A combination of the exchange vectors $Al_1F_1Ti_{1-1}O_{-1}$ and $Al_1OH_1Ti_{1-1}O_{-1}$ would move the hydrothermal generation towards the 1:1 exchange line. Incorporation of OH (calculated as $OH=(Al+Fe^{3+})-F$) in magmatic titanite is attributed to the exchange vector $Fe^{3+}_1OH_1Ti_{1-1}O_{-1}$ (not shown here).

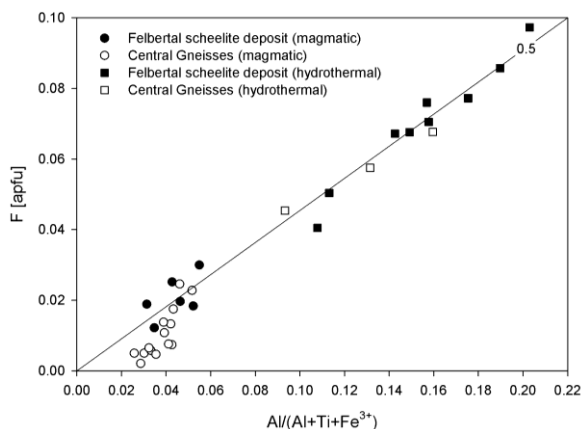


Figure 2. X_{Al} vs, F [apfu] of titanites from the K1-K3 orthogneisses in the scheelite deposit and from Central gneisses. Titanites crystallised under hydrothermal conditions are characterised by higher combined F and X_{Al} values

4 Discussion

Fluorine is recognised as an important constituent in mineralising hydrothermal fluids in Sn-W skarn systems and associated greisen (e.g. Lost River, Alaska, Dobson 1982; Moina, Tasmania, Kwak and Askins 1981; Cantung, Canada, Rasmussen and Mortensen 2013) and intrusion-related Cu-Mo-porphyry deposits (e.g. Henderson, USA, Gunow et al. 1980; Dawson Range, Canada, Selby and Nesbitt 2000). In most granitoid systems F behaves geochemically incompatible and is therefore enriched in the residual melt or fluids exsolved from such melts. The concentration of fluorine is among others controlled by the abundance of Ca in the melt and fluid phase, respectively (i.e. fluorite solubility) (Dolejš and Baker 2006). Subsequent partitioning of F into minerals precipitating from F-rich magmatic residual melts or hydrothermal fluids will result in an enrichment of fluorine in minerals such as biotite, apatite or titanite (see above); especially when not enough Ca is available to produce fluorite as it is in the case of highly fractionated Ca-poor and F-rich granites.

However, the F content of these phases is not a simple function of fluid composition, which itself is influenced by magmatic processes, interaction with the host rock (e.g. assimilation of crustal rocks), P - T conditions during crystallisation and sub-solidus alteration (Selby and Nesbitt 2000). It is also controlled by crystal chemical factors. A negative correlation of Fe and F contents is long known for biotite. It was termed Fe-F avoidance (Munoz 1984) and describes the ability of micas to incorporate more F with increasing X_{Mg} ratios. Because of the Fe-F avoidance in biotite, total mass% of F are not applicable to express the relative degree of fluorine enrichment in micas. Therefore the fluorine intercept value IV(F) was introduced to express the relative fluorine enrichment in micas at different X_{Mg} ratios. The IV(F) is a numerical but dimensionless number (Munoz 1984); small IV(F) values match higher degrees of fluorine enrichment

Table 1 shows that biotites in orthogneisses from the Felbertal scheelite deposit are enriched in F compared to the contemporary barren Central gneisses in the

Felbertal area. Only one out of five K1-K3 orthogneiss samples shows IV(F) values in the range of 2.1-2.5 which are not considered in the following tabular description.

	Felbertal deposit	Felbertauern augengneiss	Knorrkogel gneiss
IV(F) min	1.26	1.39	2.25
IV(F) max	1.84	1.81	2.70
Median	1.43	1.74	2.43

Table 1. IV(F) values of biotites from metagranitoids in the Felbertal area. IV(F) min shows the highest degree of F enrichment in each sample

There is other evidence of F enrichment in the Felbertal scheelite deposit. High F concentrations were reported for biotites (0.67-1.1 mass% F) and amphiboles (400-2.700 ppm F) of hornblendites and coarse-grained amphibolites from the eastern ore field (Schenk 1990). In addition, bulk chemical analyses of a mineralised metabreccia associated with the K2 orebody in the western ore field reveal high F contents of about 1.2 mass% F (Schenk 1990). Finally, fluorite is a commonly overlooked accessory mineral in the ores as known from the ore processing (flotation). Subsolidus decalcification of magmatic plagioclase by F-rich late stage fluids, similar to that observed in greisen type deposits (e.g. Haapala 1997), may explain formation of fluorite in hydrothermal scheelite-quartz veins

The fact that fluorine enrichment in Early Carboniferous orthogneisses of the central Tauern Window is either not identifiable (Hochweißfeld gneiss, Weißeneck-Dichtensee gneiss) or not pronounced (Knorrkogel gneiss) implies that the process responsible for concentrating fluorine in biotite, titanite and amphibole was restricted to the close surroundings of the Felbertal scheelite deposit. The moderate F-enrichment detected in biotite from the Felbertal augengneiss would be consistent with the hypothesis of such a rather local scale process because the mentioned orthogneiss body is exposed only a few kilometres south from the deposit.

High F contents in titanite are restricted to micro-domains where magmatic titanite is resorbed and overgrown by titanite with a patchy structure which is interpreted as hydrothermal. The occurrence of this second titanite type in the K1-K3 metagranitoids within the ore deposit suggest that F-enrichment is rather related to a late stage magmatic-hydrothermal event, causally linked to the intrusion of the Variscan K1-K3 orthogneiss than to regional metamorphic processes.

It was suggested that fluorine likely played a role in transporting tungsten, e.g. as WF_6 or $W_2O_2F_8$ (Schrocke et al. 1984). Evaluation of thermodynamic data, however, does not support this view (Wood and Samson 2000) but indicate that tungsten is rather transported as simple tungstate species (H_2WO_4 and its dissociation products). However, fluorine may affect the partitioning of tungsten in silicate melts and delay the exsolution of a W-bearing aqueous phase from a granitic melt (Wood and Samson 2000) due to the destabilisation of hydroxy complexes (Keppler and Wyllie 1991).

Although we currently favour a magmatic hydrothermal provenience of these F-rich fluids, re-equilibration of biotite and titanite with F-bearing metamorphic fluids cannot be excluded.

5 Concluding remarks

Biotite and hydrothermal titanite from the Early Carboniferous K1-K3 orthogneiss in the Felbertal scheelite deposit are relatively enriched in fluorine compared to barren Central gneisses of the same age in the proximity of the deposit. A possible source of F could have been magmatic-hydrothermal fluids that derived from highly fractionated granites, like the K1-K3 precursor. Such a close association of F and W is often recorded from granite-related tungsten deposits (skarn, vein-type etc.) elsewhere. These fluids infiltrated the lower parts of the Habach Complex where they formed a first-class stockwork-like tungsten deposit. Fluid influx was in part pervasive causing F-enrichment in biotite and amphiboles in the host rocks. It has to be verified in the future if fluorine can be used as a potential indicator element for scheelite exploration in the region.

Acknowledgements

The authors are much indebted to the following employees of Wolfram Bergbau und Hütten AG: Marie-Luise Pecher for her generous help with field studies in the underground mine, Steffen Schmidt for inspiring discussions and Alexander Mosser for handling the sample preparation. Moreover, we would like to thank Federica Zaccarini and Helmut Mühlhans at Montanuniversitaet Leoben for thin section preparation and help with microprobe analyses. An anonymous referee is thanked for his critical comments, which helped to improve this manuscript. This project is funded through FFG Bridge project 834149/30661.

References

Briegleb DD (1987) Geologische Verhältnisse im Bereich der Scheelitlagerstätte im Felbertal, Pinzgau, Land Salzburg. *Uni Akt Salzburg* 10:10-11

Dobson DC (1982) Geology and alteration of the Lost River tungsten-fluorine deposit, Alaska. *Econ Geol* 77:1033-1052

Dolejš D, Baker DR (2006) Fluorite solubility in hydrous haplogranitic melts at 100 MPa. *Chem Geol* 225:40-60

Eichhorn R, Schärer U, Höll R (1995) Age and evolution of scheelite-hosting rocks in the Felbertal deposit (Eastern Alps): U-Pb geochronology of zircon and titanite. *Contrib Mineral Petrol* 119:377-386

Eichhorn R, Höll R, Loth G, Kennedy A (1999) Implications of U-Pb SHRIMP zircon data on the age and evolution of the Felbertal tungsten deposit (Tauern Window, Austria). *Int J Earth Sci* 88:496-512

Eichhorn R, Loth G, Höll R, Finger F, Schermaier A, Kennedy A (2000) Multistage Variscan magmatism in the central Tauern Window (Austria) unveiled by U/Pb SHRIMP zircon data. *Contrib Mineral Petrol* 139:418-435

Finger F, Kraiger H, Steyrer HP (1985) Zur Geochemie des K1-Gneises der Scheelitlagerstätte Felbertal (Pinzgau/Salzburg) – ein Vorbericht. *Karinthin* 92:225-235

Finger F, Frasl G, Haunschmid B, Lettner H, von Quadt A, Schermaier A, Steyrer HP (1993) The Zentralgneise of the Tauern Window (Eastern Alps): Insight into an Intra-Alpine Variscan Batholith. In: Raumer JF, Neubauer F (ed) *Pre-Mesozoic geology of the Alps*, Springer, Berlin Heidelberg New York, pp. 375-391

Gunow AJ, Ludington S, Munoz JL (1980) Fluorine in micas from the Henderson molybdenite deposit, Colorado. *Econ Geol* 75:1127-1137

Haapala I (1997) Magmatic and postmagmatic processes in tin-mineralized granites: topaz-bearing leucogranite in the Eurajoki rapakivi granite stock, Finland. *J Petrol* 38:1645-1659

Höll R (1975) Die Scheelitlagerstätte Felbertal und der Vergleich mit anderen Scheelitvorkommen in den Ostalpen. *Bayer Akad Wiss, Math-Naturwiss KI* 157a, pp. 1-114

Höll R, Eichhorn R (2000) Tungsten Mineralization and Metamorphic Remobilization in the Felbertal Scheelite Deposit, Central Alps, Austria. In: Spry PG, Marshall B, Vokes FM (ed) *Metamorphosed and Metamorphogenic ore deposits*, Society of Economic Geologists, Boulder Colorado, pp. 233-264

Kebede T, Klötzli U, Kosler J, Skiöld T (2005) Understanding the pre-Variscan and Variscan basement components of the central Tauern Window, Eastern Alps (Austria): constraints from single zircon U-Pb geochronology. *Int J Earth Sci* 94:336-353

Kepler H, Wyllie PJ (1991) Partitioning of Cu, Sn, Mo, W, U, and Th between melt and aqueous fluid in the systems haplogranite-H₂O-HCl and haplogranite-H₂O-HF. *Contrib Mineral Petrol* 109:139-150

Kwak TAP, Askins PW (1981) Geology and geochemistry of the F-Sn-W(-Be-Zn) skarn (wrigglite) at Moina, Tasmania. *Econ Geol* 76:439-467

Munoz JL (1984) F-OH and Cl-OH exchange in micas with applications to hydrothermal ore deposits. In: Bailey SW (ed) *Micas*, Mineral Soc Am Rev Min, pp. 469-493

Raith JG, Stein HJ (2006) Variscan ore formation and metamorphism at the Felbertal scheelite deposit (Austria): constraining tungsten mineralisation from Re-Os dating of molybdenite. *Contrib Mineral Petrol* 152:505-521

Rasmussen KL, Mortensen JK (2013) Magmatic petrogenesis and the evolution of (F:Cl:OH) fluid composition in barren and tungsten skarn-associated plutons using apatite and biotite compositions: Case studies from the northern Canadian Cordillera. *Ore Geol Rev* 50:118-142

Schenk P (1990) Mikrothermometrische, gefügekundliche und geochemische Untersuchungen zur Genese der Scheelitlagerstätte Felbertal/Ostalpen. *Münchener Geol Hefte* 1, pp. 1-198

Schröcke H, Trumm A, Hochleitner R (1984) The transport of tungsten and the deposition of tungsten double oxides in fluid, aqueous solutions. *Geochim Cosmochim Acta* 48:1791-1805

Selby D, Nesbitt BE (2000) Chemical composition of biotite from the Casino porphyry Cu-Au-Mo mineralization, Yukon, Canada: evaluation of magmatic and hydrothermal fluid chemistry. *Chem Geol* 171:77-93

von Quadt A (1985) Geochronologische, geochemische und isotopengeochemische Untersuchungen an Gesteinen der Habachformation, der Scheelitlagerstätte und des angrenzenden Altkristallins im Felbertal (Land Salzburg, Österreich). Dissertation, ETH Zürich

Wood AW, Samson IM (2000) The hydrothermal geochemistry of tungsten in granitoid environments: I. Relative solubilities of ferberite and scheelite as a function of T, P, pH, and mNaCl. *Econ Geol* 95:143-182

Zabavnikova II (1957) Diadochic substitutions in sphene. *Geochemistry* 3:271-278

Cu-sulphides – native silver association in the Cu-Ag deposit, Lubin mine, Fore-Sudetic Monocline (SW Poland)

Gabriela A. Kozub

AGH University of Science and Technology, Faculty of Geology, Geophysics and Environmental Protection, al. A. Mickiewicza 30, PL-30-059 Krakow, Poland

Abstract. Silver is the second most important element in the Cu-Ag ore deposit at the Fore-Sudetic Monocline (SW Poland). The silver concentrates in the silver minerals, such as the native silver and silver amalgams, or Ag-Cu sulphides, or forms isomorphic substitutions in the copper minerals in the deposit. The aim of this study was to determine distribution of silver in the copper minerals forming association with the native silver and the silver amalgams, and to constrain conditions of precipitation of selected ore minerals. Textural observations in a microfield and electron microprobe chemical analyzes provided new insights into knowledge on the Ag distribution in the copper minerals from the Cu-Ag ore deposit at the Fore-Sudetic Monocline.

Keywords. Ag-Cu deposit, Ag-bearing minerals, distribution of silver, Fore-Sudetic Monocline

1 Introduction

Silver, next to copper, is the most important element in the Cu-Ag deposit at the Fore-Sudetic Monocline (Salamon 1979; Banaś et al. 2007; Piestrzyński 2007a; Kucha and Mayer 2007; Pieczonka 2011), and was determined in all types of the ore. The average content of silver in the profile of the deposit is 47 ppm, while in general, the Ag content in the deposit varies in a wide range from several ppm to several thousands ppm (Banaś et al. 2007). In the deposit, the silver forms isomorphic substitutions in chalcocite, bornite, chalcopyrite, tennantite, galena and sphalerite (Salamon 1979; Banaś et al. 2007; Kucha and Mayer 2007; Kucha 2007). Additionally, Ag minerals are represented by a native silver, silver amalgams and Cu-Ag sulphides such as stromeyerite, jalpaite and mckinstryite (Salamon 1979; Piestrzyński and Tylka 1992; Banaś et al. 2007; Kucha 2007; Piestrzyński 2007a). It should be noted, that the highest Ag concentration in the ore occurs in the Lubin mine area located in the eastern part of the deposit (Banaś et al. 2007). This study focuses on the Ag distribution between selected Cu sulphides occurring with native silver and silver amalgams in samples collected from the Lubin mine. The presented preliminary results allow for rough constraining conditions that controlled formation of selected ore minerals.

2 Geological setting

The Cu-Ag deposit at the Fore-Sudetic Monocline is a

world class deposit of stratabound type. The deposit is located in the western part of Poland, near the border with Germany. To the SW, the Fore-Sudetic Monocline is bordered with the Fore-Sudetic Block, to the NE – with the Szczecin-Łódź Synclinorium, to the W – with the Żary Pericline, and to the E – with the Silesian-Kraków Monocline (Kłapciński and Peryt 2007; Oszczepalski 1999; Pieczonka 2011). The pre-Permian basement of the Fore-Sudetic Monocline is built of volcanic rocks, granodiorites, gneisses and Carbon sedimentary rocks (Kłapciński and Peryt 2007; Pieczonka 2011). These are covered with Permian-Mesozoic sediments that form monocline dipping at low angle in the NE direction. The Permian-Mesozoic sediments are discordantly overlain by the Paleogene, Neogene and Quaternary sediments (Kłapciński and Peryt 2007; Pieczonka 2011).

The ore deposit is located in the SW part of the Fore-Sudetic Monocline, and borders with the Fore-Sudetic Block to the S (Kłapciński and Peryt 2007; Oszczepalski 1999; Pieczonka 2011). The other borders are designated on the basis of last positive drill holes (Pieczonka and Piestrzyński 2010). The Cu-Ag mineralization in the deposit occurs in the Permian sedimentary rocks (Rotliegend and Zechstein) in the following three lithological types of ore: the dolomite, the black shale and the sandstone (Pieczonka et al. 2008; Oszczepalski 1999; Pieczonka and Piestrzyński 2010; Pieczonka 2011). Beside of copper, the ore contains significant amounts of other elements, mainly metals such as Ag, Zn, Pb, Ni, Co, Re, Mo, Se, As, Hg and PGE (Salamon 1979; Oszczepalski 1999; Banaś et al. 2007; Piestrzyński 2007a; Kucha and Mayer 2007; Pieczonka et al. 2008; Pieczonka and Piestrzyński 2010; Pieczonka 2011).

3 Sample selection and analytical methods

Samples were collected from all types of the ore from the Lubin mine. Preliminary mineral identification was performed using optical polarizing microscope in the reflected light mode. Additionally, the chemical analyzes of the whole rocks were performed in the Acme Analytical Laboratory in Canada. Basing on the whole rock chemistry and optical microscope observations, samples with Ag content exceeding 100 ppm and containing native silver or silver amalgams were selected for further analyzes.

The textural observation and not standardized chemical analyzes of the minerals were performed utilizing a FEI QUANTA 200 Field Emission Gun

Scanning Electron Microscope equipped with the energy dispersive spectrometer (EDS) at the Faculty of Geology, Geophysics and Environmental Protection of the AGH-University of Science and Technology in Krakow, and a Hitachi S-4700 Field Emission Scanning Electron Microscope equipped with the energy dispersive spectrometer NORAN Vantage at the Laboratory of Scanning Microscopy with Field Emission and Microanalysis at the Institute of Geological Sciences, Jagiellonian University in Krakow.

The chemical analyzes of the copper and silver minerals were performed using a Cameca SX-100 electron microprobe (EMP) at the Inter-Institute Analytical Complex for Minerals and Synthetic Substances of the Warsaw University. The EMP was operated in the wavelength-dispersion mode at an accelerating voltage of 15 kV, a probe current of 20 nA, focused beam with a diameter of 2 μm for bornite, chalcocite, silver and silver amalgams and accelerating voltage 15 kV, a probe current of 10nA for stromeyerite. Counting times of 20 s on peak and 10 s on both (+) and (-) backgrounds were used. The following standards and lines were used: CuFeS_2 ($\text{SK}\alpha$, $\text{CuK}\alpha$), Ag_2Te ($\text{AgL}\alpha$), HgS-SPI ($\text{HgM}\alpha$), Fe_2O_3 ($\text{FeK}\alpha$) and ZnS ($\text{ZnK}\alpha$).

4 Results

Native silver and/or silver amalgams form association with copper minerals in all types of ore. Main minerals forming the association include bornite, chalcocite, stromeyerite, native silver, silver amalgams (Figs. 1, 4 and 6) and tennantite. These minerals form anhedral grains with size ranging from several to 1000 μm . The observed textural features indicate that the ore minerals replace terrigenous sediments, clay-carbonate cement in sandstones, and carbonate minerals in dolomites. These textures suggest that the mineralization is epigenetic.

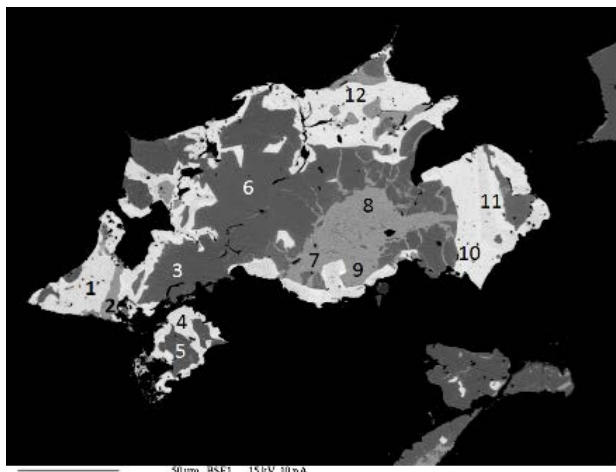


Figure 1. Intergrowth of bornite and stromeyerite with native silver. Analytical spots on the EMP-BSE (backscattered electrons) image correspond to the analyzes in Table 1. Scale bar 50 μm .

The native silver contains up to 99.24 wt.% Ag, <5.49 wt.% Hg, <1.11 wt.% Cu. Occasionally, the Hg content in silver minerals reaches 21.78 wt.%, with adequate lower Ag content (ca. 80 wt.%). Mineral phases

of such composition are named silver amalgams (Piestrzyński and Tylka 1992). The silver amalgams contain also trace content of copper, up to 0.5 wt.% (Table 1).

The most common mineral present in the association with the native silver is bornite. Silver content in the bornite is ranging from 0.98 to 15.85 wt.%. It has to be noted that the increased Ag content is subsequent with decreasing Fe content. The Cu concentration varies slightly depending on the Ag content (Fig. 2 and Table 1). There is no increase of Hg content in the bornite associated with the silver amalgams (Table 1). Although chemical composition of bornite varies, there are no structural features indicating presence of different generations.

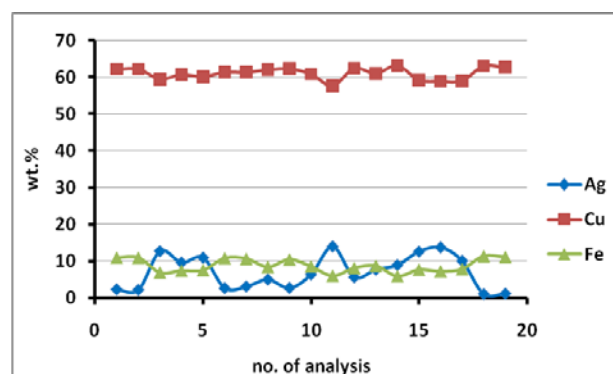


Figure 2. Concentrations of Ag, Cu and Fe in bornite [wt.%].

The chalcocite, present in the association with the native silver, contains from 1.65 to 7.25 wt.% Ag. Low concentrations of Fe in chalcocite are present (Fig. 3). Mercury concentration in the chalcocite rarely exceeds detection limit of the electron microprobe. Fine grains of stromeyerite forming an oleander leaves structures are commonly present in the chalcocite grains (Fig. 4). There is no evidence suggesting presence of different generations of chalcocite.

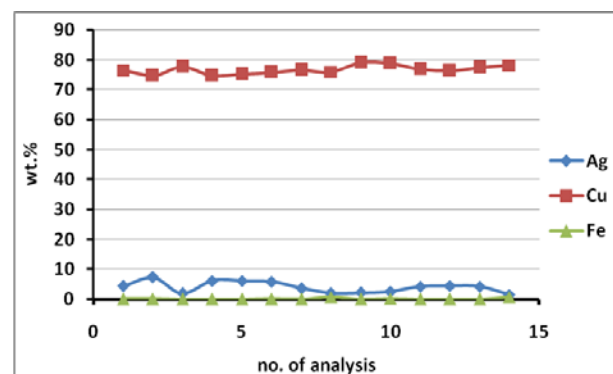


Figure 3. Concentrations of Ag, Cu and Fe in chalcocite [wt.%].

The stromeyerite is rarely present in the association, while compared to the minerals described above. The stromeyerite commonly fills interstices between grains of native silver or silver amalgams. The stromeyerite rarely forms irregular crystals or inclusions in the chalcocite and bornite grains, or partially replaces these minerals (Figs. 1 and 4). The Ag content in stromeyerite ranges from 47.71 to 54.70 wt.%, while Hg

concentration is below 1.7 wt.% (Fig. 5 and Table 1).

Table 1. Representative compositional electron microprobe analyzes of minerals forming the assemblage (in wt.%). The analyzes correspond to the analytical spots presented in Fig. 1.

Analysis	Mineral	S	Ag	Hg	Cu	Fe	Zn	Total
1	Native silver	0.02	97.73	1.48	0.52	b.d.l.	b.d.l.	99.76
2	Stromeyerite	15.55	52.07	0.13	31.26	0.26	b.d.l.	99.27
3	Bornite	23.02	9.50	b.d.l.	59.36	7.49	b.d.l.	99.37
4	Native silver	0.22	98.71	1.15	0.87	0.08	0.33	101.37
5	Bornite	24.75	3.48	b.d.l.	60.12	9.72	b.d.l.	98.07
6	Bornite	21.52	15.85	0.38	56.15	6.84	b.d.l.	100.74
7	Stromeyerite	15.95	48.75	0.07	34.84	0.35	0.01	99.99
8	Stromeyerite	15.82	47.71	0.02	35.17	0.29	b.d.l.	99.01
9	Stromeyerite	15.46	50.49	0.06	33.48	0.07	0.07	99.64
10	Silver amalgam	b.d.l.	92.28	7.88	0.27	b.d.l.	b.d.l.	100.44
11	Native silver	0.04	98.00	2.17	0.57	0.01	b.d.l.	100.79
12	Silver amalgam	b.d.l.	94.49	5.97	0.41	b.d.l.	b.d.l.	100.88

b.d.l. – below detection limit

The association includes replacement of chalcocite and bornite by stromeyerite, native silver and silver amalgams (Figs. 1, 4 and 6). The native silver and silver amalgams are present in the fractures formed in bornite and chalcocite (Figs. 1, 4).

The reaction zones are commonly present between grains of the native silver (or silver amalgams) and chalcocite or bornite. The fine grains (<4 μ m) of mineral with composition similar to stromeyerite are present in these reaction zones (Figs. 4 and 6).

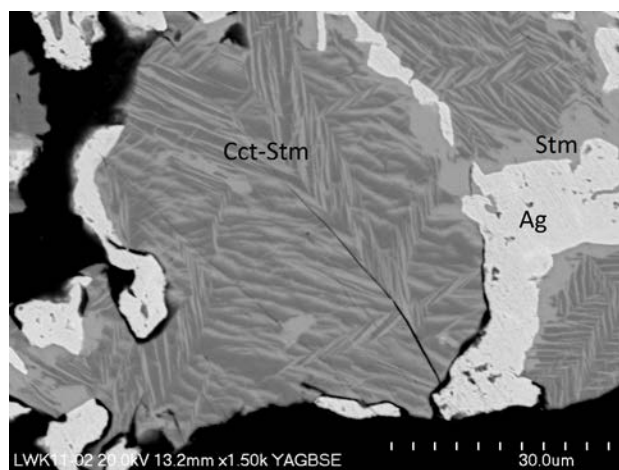


Figure 4. Microstructures of the stromeyerite (Stm) oleander leaves in chalcocite (Cct-Stm) crystals that form intergrowths with the native silver (Ag). SEM-BSE image. Scale bar 30 μ m.

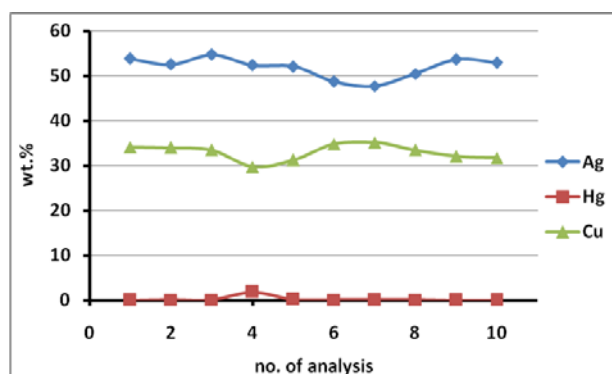


Figure 5. Concentrations of Ag, Cu and Fe in stromeyerite [wt.%].

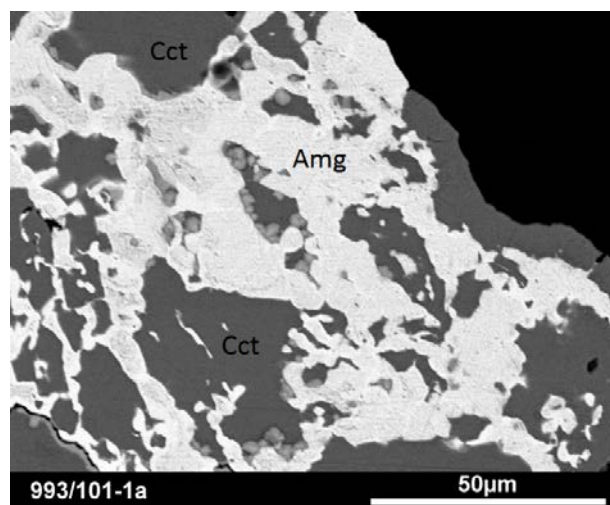


Figure 6. Intergrowth of chalcocite (Cct) with silver amalgam (Amg). Crystals of mineral with chemical composition similar to stromeyerite (light grey) are present at the border of silver amalgam and chalcocite. SEM-BSE image.

5 Discussion and conclusions

The distribution of Ag in copper minerals forming the association is irregular, which is indicated by presence of the native silver and silver amalgams intergrowths with Cu sulphides with variable Ag concentrations, bornite (from 0.98 to 15.85 wt.% Ag), chalcocite (from 1.65 to 7.25 wt.% Ag) or stromeyerite (from 47.74 to 54.70 wt.% Ag).

Lack of micro-inclusions of the native silver or silver amalgams in the copper minerals suggests that Ag is present mainly due to the isomorphic substitutions. According to previous works, Ag can substitute in copper minerals present in the association without modification of their crystallographic structure, reaching content of up to 49 wt.% Ag in mineral bornite and up to 1.8 wt.% Ag in chalcocite (Salamon 1979; Banaś et al 2007; Kucha 2007; Piestrzyński 2007a, Pieczonka 2011). Increased Ag concentration in the chalcocite is interpreted as resulting from crystallization of the chalcocite under conditions of migrating fluids with increased Ag content. The future extended work is required to determine potential modification of the crystallographic structure in the chalcocite due to the Ag substitution (ca. 7 wt.%).

Metasomatic alterations in the Cu sulphides with Ag substitutions, and reaction zones at the border between the Cu sulphides and native silver indicate unstable conditions during ore-forming processes. Formation of the described association suggests enrichment of the hydrothermal fluids with Ag or changes of the other factors, such as pH and temperature, that resulted in crystallization of the native silver and silver amalgams, as well as Ag substitution in the Cu sulphides that formed earlier. According to Piestrzyński (2007b), the Ag-bearing minerals formed during one event, simultaneously with the Cu sulphides, while the observed textural features indicate changes in the crystallization conditions. The temperature conditions of the formation of Cu sulphides were previously estimated to <103.5°C (Piestrzyński 2007b). Because stromeyerite is stable under temperature conditions of ca. 93°C (Fleet 2006), presence of the stromeyerite replacing bornite and chalcocite suggest that the replacement reactions occurred during cooling.

Acknowledgements

This work was supported by the National Science Centre research grant (No 2011/03/N/ST10/04619).

References

- Banaś M, Kijewski P, Salomon W, Pieczonka J, Piestrzyński A (2007) Associated metals in the copper ores deposit. [In:] Piestrzyński A (Ed) Monografia KGHM Polska Miedź SA., pp 214-228 (In Polish)
- Fleet ME (2006) Phase equilibria at high-temperature. [In:] Vaughan DJ (Ed) Reviews in Mineralogy and

- Geochemistry 61, pp 365-419
- Kłapcinski J, Peryt TM (2007) Geology of the Fore-Sudetic Monocline. [In:] Piestrzyński A (Ed) Monografia KGHM Polska Miedź SA., pp 3-11 (In Polish)
- Kucha H (2007) Mineralogy and geochemistry of the Lubin-Sierszowice orebody. Biuletyn PIG 423, pp 77-94 (In Polish)
- Kucha H and Mayer W (2007) Geochemistry. [In:] Piestrzyński A (Ed) Monografia KGHM Polska Miedź SA., pp 197-207 (In Polish)
- Oszczepalski S (1999) Origin of Kupferschiefer polymetallic mineralization in Poland. Mineralium Deposita 34, pp 599 - 613
- Pieczonka J (2011) Factors controlling distribution of ore minerals within copper deposit, Fore-Sudetic Monocline, SW Poland. 195 pp (In Polish)
- Pieczonka J and Piestrzyński A (2010) Mineral zonation in the Lubin – Sierszowice mining district, Kupferschiefer-type deposit, SW Poland. [In:] Barra F, Reich M, Campos E, Tornos F (Eds) Let's Talk Ore Deposits Proceedings of the 11th Biennial SGA Meeting, Antofagasta, Chile, Vol. I, pp. 43 - 45
- Pieczonka J, Piestrzyński A, Mucha J, Głuszek A, Kotarba M, Więclaw D (2008) The red-bed-type precious metal deposit in the Polkowice-Sierszowice copper mining district, SW Poland. Annales Societatis Geologorum Poloniae 78, pp. 151 - 280
- Piestrzyński A (2007a) Ore minerals. [In:] Piestrzyński A (Ed) Monografia KGHM Polska Miedź SA., pp 167-197 (in Polish)
- Piestrzyński A (2007b) Origin of the deposit. [In:] Piestrzyński A (Ed) Monografia KGHM Polska Miedź SA., pp 159 - 175
- Piestrzyński A, Tylka W (1992) Silver amalgams from the Sierszowice copper mine, Lubin-Sierszowice district, SW Poland. Mineralogia Polonica 23, 1, pp 17-25
- Salamon W (1979) Occurrence of the Ag and Mo in the Zechstein sediments of the Fore-Sudetic Monocline. Prace Mineralogiczne, PAN 62, pp 1–52 (In Polish)

Potential role of a buoyant CO₂ vapour phase in the formation of the Mount Isa copper ore deposit

Michael Kühn

GFZ German Research Centre for Geosciences, Section Hydrogeology, Telegrafenberg, 14473 Potsdam, Germany

Klaus Gessner

School of Earth and Environment, The University of Western Australia, 35 Stirling Highway, Crawley, WA 6009, Australia

Abstract. Fluids rich in H₂O and CO₂ transport energy and mass in Earth's crust and play a significant role during the deposition of mineral deposits. For a range of pressures, temperatures, and fluid compositions in the Earth's crust, a buoyant immiscible phase of CO₂ coexists with a higher-density aqueous liquid. The density difference between these phases can generate carbonic flow systems because buoyant CO₂ is driven to shallower levels in Earth's crust at higher rates than pressure gradients are able to drive aqueous liquids. Here we consider this effect to extend existing hypotheses of processes that formed the Mesoproterozoic Mount Isa Copper ore bodies in Queensland, Australia. We investigate the potential role of a buoyancy driven carbonic fluid in the formation of the Mount Isa deposit. Our numerical simulations show that a giant copper sulphide deposit is able to form by such a process within thousands of years. Comparable hydrodynamic scenarios may be relevant for other hydrothermal deposit types, where processes such as upward flow of an aqueous liquid driven by vertical pressure gradients or free thermal convection are unlikely to achieve realistic rates of flow and metal transport.

Keywords. ore deposit, Mount Isa, copper, CO₂, fluid flow, buoyancy driven flow

1 Introduction

Hydrothermal fluid flow systems in Earth's crust are characterized by the coupling between heat transfer, fluid flow, reactive transport and mechanical deformation. The challenge in understanding the formation of ore deposits is to account for the concentration of elements that generally occur in very low and thus uneconomical concentrations in rocks. To achieve the high metal concentration observed in ore deposits hydrothermal fluids need to transport metals extracted from rocks or melts in advective flow systems to the depositional site, where they precipitate due to changes in variables such as pressure temperature and chemical concentration, relative to the flow rate (Kesler 2005). In ore deposits that formed under metamorphic conditions within low porosity rocks, shearing and fracturing around steep fault zones generated the required permeability dynamically (Cox 1999 and references therein).

The compositions of fluid inclusions in mineralized rocks help constrain the composition of the mineralizing fluid, as well as the temperature and pressure conditions can be inferred (Sterner and Bodnar 1991). Fluids containing high concentrations of CO₂ in some cases up to a fraction of 0.9 of the total fluid, are a common

observation in structurally controlled gold and copper deposits (e.g. Ridley and Diamond 2000, Baker 2002, Fu et al. 2003, Heinrich et al. 1995, Beziat et al. 2008, Mumm et al. 1997).

Previous studies (Kühn and Gessner 2009a) have used coupled hydromechanical flow and reactive transport simulations to test conceptual models of how the Mesoproterozoic Mount Isa Copper mineralisation in Queensland, Australia, might have formed (Heinrich et al. 1995, Wilde et al. 2006). The numerical experiments had the specific focus to investigate whether fluid flow was driven by mechanical deformation, higher than hydrostatic fluid pressure gradients, or thermal buoyancy, and what the mechanism of ore deposition was. A distinct feature of the Mount Isa mineralising system is a massive silica-rich alteration that surrounds the copper ore bodies within the host formation of the Urquhart shale. This alteration envelope is likely to indicate upward flow of a cooling fluid saturated in SiO₂. This is emphasized by hydromechanical models which reveal that contraction and horizontal shear can produce a dilation pattern that favours upward fluid flow. In addition to that reactive transport models show that topographically driven flow is more likely to produce a realistic silica alteration pattern than free thermal convection, but neither process generated a flow pattern capable of precipitating copper at the appropriate location. Kühn and Gessner (2009a) proposed that gravity driven flow of a dense brine led to chalcopyrite mineralisation by fluid-rock reaction via a three step process: (a) upward flow of a basement fluid driven by either topography or by release from an overpressured reservoir at depth, followed by (b) gravity-driven downward flow of a dense oxidised basin brine along dilating faults and fracture zones and (c) fluid rock reaction. Matthäi et al. (2004) performed similar numerical simulations to test whether the deposit may have formed by forced fluid convection driven by progressive displacement on the Mount Isa fault zone and by mixing of a reduced fluid from overlying sediments and an oxidized fluid entering the host formation from the underlying system. Both investigated test cases outline feasible but fairly complex and time consuming processes during which pathways like faults and dilated rocks need to be open for as much as millions of years.

Here we discuss buoyant flow of CO₂ rich fluids as a potential driving mechanism for the Mount Isa Copper mineral system.

2 Mount Isa Copper System

The Proterozoic Mount Isa Inlier in Queensland, Australia is one of the most valuable regions for mineral resources in Australia (Solomon and Groves 1994, Murphy et al. 2011). Mesoproterozoic hydrothermal mineral deposits include shale hosted lead–zinc sulphides, Broken Hill-type lead–zinc–silver, as well as iron-oxide copper–gold and Mount Isa-type iron-sulphide copper deposits (Betts et al. 2006, Murphy et al. 2011). In addition to a large number of mines, there are hundreds of documented mineral occurrences, as well as ubiquitous evidence for potassic and sodic alteration zones and hydrothermal breccias. At Mount Isa approximately 22 million tonnes of copper precipitated as chalcopyrite during a hydrothermal brecciation event in the silicified portion of the multiply deformed Urquhart shale (e.g. Bell et al. 1988, Heinrich et al. 1995).

The chalcopyrite ore body is located in the partly brecciated, steeply dipping Urquhart shale (Fig. 1), which is separated from the metavolcanic Eastern Creek Volcanics by the Paroo fault. The widespread silica and quartz precipitation within the Urquhart shale and the large size of the alteration and ore system at Mount Isa suggest high permeability during the active phase of the hydrothermal system (Gessner et al. 2005; Gessner et al. 2009).

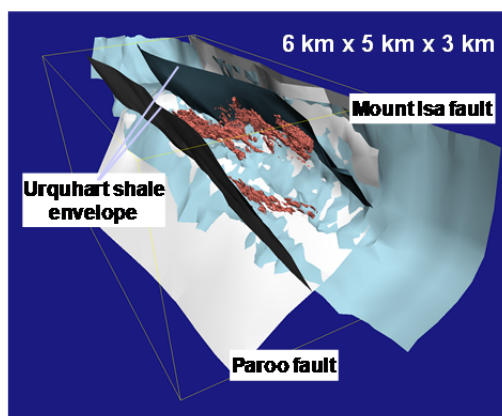


Figure 1. Geometry of the Mount Isa Copper deposit (red colour = Cu grade > 2.5 %) is hosted in Urquhart shale

3 Fluid Flow Driving Processes

Several possible drivers of regional groundwater flow exist, each of which is related to individual geological settings (Kühn and Gessner 2009b, Matthäi et al. 2004). These processes are deformation driven flow, topographically driven flow, free thermal convection, gravity driven flow or, as discussed here, buoyancy driven flow of an unmixed lower density phase.

3.1 Deformation driven flow

As shown by Gessner (2009) on the base of hydromechanical modelling, the change from contraction to strike slip (Bell et al. 1988, Wilde et al. 2006) had a considerable impact on the fluid flow

geometry within the Mount Isa system. Contraction driven upward flow is consistent with pre-copper quartz precipitation from a cooling metamorphic fluid (Wilde et al. 2006), while strike-slip has led to the dilation of the steeply dipping segments of the Paroo and the Mount Isa fault, and the Urquhart shale (Gessner et al. 2006, Gessner 2009). These steep fluid pathways may have provided access for brines from above or below the system with relations to the copper mineralisation (Wilde et al. 2006). However, they could have been just as significant for buoyancy driven flow of a CO₂ vapour phase.

Matthäi et al. (2004) followed the idea that the deposit may have formed by forced fluid convection driven by progressive displacement on the Mount Isa fault zone in the range of > 1 mm/yr which induced in the model regional fluid flow in a permeability-controlled convection system. Results are consistent with mineralogic and fluid-inclusion evolution, e.g. silica enrichment in the ore body.

3.2 Free thermal convection vs. topographically driven flow

As discussed by Kühn and Gessner (2009a) free thermal convection as well as topographically driven flow may have played a role during formation of the Mount Isa Copper mineral system. Kühn and Gessner (2009a) concluded that permeability controls the fluid flow direction and thus the temperature distribution in the system, for the case that free thermal convection occurs. As a consequence the resulting fluid flow controls the quartz precipitation pattern due to the temperature dependence of the quartz solubility. Further, it is important to take into account that precipitation of quartz reduces porosity and in turn permeability. This is in most cases going to affect the flow fields and finally the entire convection pattern.

What was found by Kühn and Gessner (2009a) is that both free thermal convection and topographically driven flow are capable of producing a realistic quartz precipitation pattern in the Urquhart shale, the formation that hosts the copper deposit. The authors were able to show that, even with a reduced permeability in the Urquhart shale, quartz precipitation patterns were very well reproduced in the case of topographically driven flow, but not in the free thermal convection models.

Flow velocities play an important role for quartz precipitation rates and the formation of the silica body. Either free thermal convection or topographically driven flow models require a quite long time of approximately 25 million years of continuous flow to increase the amount of quartz in the Urquhart shale from 40 wt% to 65 wt%, as estimated by Waring (1990). In any case on-going or repeated deformation is required to keep faults, fracture zones and the Urquhart shale permeable for a comparably long time period.

Kühn and Gessner (2009a) concluded that upward flow due to a vertical pressure gradient (forced flux, topographically driven flow) is more likely to be responsible for the observed quartz body within the Urquhart shale than free thermal convection. Only under unlikely conditions free thermal convection would be

able to produce a silica-rich alteration zone comparable with the field observations and these conditions may not be sustainable long enough to increase the quartz content from values of an unaltered Urquhart shale to amounts which have been sampled in the rocks.

3.3 Buoyancy driven flow

Fluids rich in H₂O and CO₂ transport energy and mass and play a significant role during the deposition of minerals. For a wide range of pressures, temperatures, and fluid compositions in the Earth's crust, a buoyant immiscible phase of CO₂ coexists with a higher-density aqueous liquid (Takenouchi and Kennedy 1964, Kaszuba et al. 2006, Liebscher and Heinrich 2007).

The density difference between these phases normally generates flow of CO₂ to shallower levels in Earth's crust at higher rates than pressure gradients are able to drive aqueous liquids. Here we propose that buoyancy driven carbonic fluids might have played a leading role in the formation of the Mount Isa Copper deposit.

Buoyancy forces are usually assumed to be directed vertically upwards, and its force is determined by density difference. The general assumption is that fluids lighter than water (such as CO₂) will rise vertically upwards. This requires steep structures to efficiently transport the CO₂ which are available in the Mount Isa system as discussed above (section deformation driven flow).

4 Mechanisms of Ore Deposition

According to Wilde et al. (2006) either wall rock reaction or fluid mixing are the most likely processes to have caused precipitation of chalcopyrite at Mount Isa. These findings were based on reactor-style and reaction path geochemical modelling. Matthäi et al. (2004) emphasize this scenario as well.

To understand if copper ore results from mixing of different fluids within the system the chemistry of the mixed fluids was considered. Since only the free thermal convection regimes produced mixing in the model, various scenarios were tested (Kühn and Gessner 2009a,b). In summary it can be said that although some convection modes may explain the occurrence of the silica-rich alteration zone, none of these models convincingly describes the formation of the observed chalcopyrite-only primary ore bodies.

We modelled various fluid flow driving processes to explain salient features of hydrothermal flow at Mount Isa. We found that two major convection modes can occur within the Mount Isa system under the premise that the Rayleigh number of the system exceeds the critical value (Kühn and Gessner 2009b). However, these flow systems require high permeability values within the host rock, the Urquhart shale, and it was shown that these values cannot be sustained for long enough to produce the actual concentration of quartz in the system, unless the system continues to dilate during the process. Furthermore free thermal convection is required to get fluids to mix in the Urquhart shale, and although fluid mixing is one chemical process leading to

the formation of the chalcopyrite ore body, the resulting copper distribution does not match the observations (Kühn and Gessner 2009a).

To illustrate the difference between an aqueous liquid driven by a pressure gradient versus a CO₂ vapour phase driven by buoyancy we compare transport rates in these scenarios for the Mount Isa copper. The ore at Mount Isa formed in a structurally controlled hydrothermal flow system in metamorphic rock with low intrinsic permeability. This flow environment is very similar to orogenic-type gold deposits for which water-based flow rates on the order of 0.1 kg m⁻² year⁻¹ (3×10^{-9} kg m⁻² s⁻¹, Cox 1999). CO₂ flux integrated across modern mountain belts is on the same order of magnitude – around 1.5×10^{-12} mol km⁻² Mio year⁻¹ (2×10^{-9} kg m⁻² s⁻¹) (Kerrick and Caldeira 1998). Potential CO₂ leakage from a 1000 m deep reservoir along a fault has been calculated at 10 kg s⁻¹ m⁻² (Pruess 2005). We consider density driven flow of CO₂ bubbles in a water column (Stokes flow) at 100 kg m⁻² s⁻¹ to represent the upper flow limit for CO₂ vapour in aqueous liquid. The time it takes to produce an ore deposit like Mount Isa is a function of the flow rate and the metal concentration in the fluid.

The amount of metals carried by liquid dominated fluids or brines is on the order of hundreds to thousands of ppm, and therefore around two orders of magnitudes higher than for CO₂-dominated fluids (Kesler 2005). Experiments have shown that in a two-phase system 1 % (0.2-0.6 ppm) of metals fractionate from brine into CO₂ vapour (Rempel et al. 2011a,b).

Assuming a scenario where brine containing 100 ppm Cu is driven across the ca. 250,000 m² fracture zone feeding into the deposition site by vertical pressure gradient driven flow with a rate of 0.1 kg m⁻² s⁻¹ (Cox 1999), it would take ca. 8 billion years to form the deposit. In comparison, buoyancy driven CO₂ carrying 1 ppm of copper at a flow rate of 10 kg m⁻² s⁻¹ (Pruess 2005) would only require thousands of years to form a deposit of this size. Furthermore, it has been shown that unmixing of CO₂ and H₂O fluids can have drastic consequences for the microphysical structure of the fluid mixture, as well as for its chemical properties. These changes can thus result in saturation of dissolved components such as metal ions, carbonate, or in silica and enhance precipitation of those minerals in veins (Kaszuba et al. 2006).

5 Conclusion

We have compared simulation results of coupled fluid flow, heat transfer, species transport, chemical reactions (Kühn and Gessner 2009a) and deformation (Gessner 2009) to evaluate processes driving fluid flow and causing mineralization in the Mount Isa Copper mineral system. We have shown that deformation concurrent with fluid flow is crucial to provide fluid pathways by dilating pre-existing structures and fracturing the Urquhart shale.

Reactive transport models showed that topographically driven flow is more likely to produce a realistic quartz precipitation pattern than free thermal convection. For copper precipitation, wall rock reaction

of a brine where it is driven into the fractured host rock by gravity appeared to be the most plausible scenario (Kühn and Gessner 2009a).

We propose here that CO₂ rich vapours, that have unmixed from a common 'aqua-carbonic mother-fluid' may be driven upwards in fractured rock mass by virtue of buoyancy. We argue that two-phase aqua-carbonic flow systems – similar to brine-steam systems in magmatic and epithermal ore systems – may represent an efficient means to transport mass and heat in hydrothermal systems in the absence of cooling magmatic bodies. In the chosen test case of Mount Isa Copper such a process would provide more realistic timeframes for ore body formation than previously proposed processes such as free thermal convection, vertical pressure gradient driven flow, or topographically driven flow. Two-phase aqua-carbonic flow systems may be of significance to other hydrothermal flow systems that comprise high xCO₂ and occur in pressure and temperature environments at or near aqua-carbonic phase separation conditions.

References

- Baker T (2002) Emplacement depth and carbon-dioxide-rich fluid inclusions in intrusion-related gold deposits. *Economic Geology* 97, 1109-1115
- Bell TH, Perkins WG, Swager CP (1988) Structural controls on development and localization of syntectonic copper mineralization at Mount Isa, Queensland. *Economic Geology* 83, 69–85
- Betts PG, Giles D, Mark G, Lister GS, Goleby BR, Ailleres L (2006) Synthesis of the proterozoic evolution of the Mount Isa Inlier. *Australian Journal of Earth Sciences* 53,187–211. doi:10.1080/081200905-00434625
- Beziat D, Dubois M, Debat P, Nikiema S, Salvi S, Tollon F (2008) Gold metallogeny in the Birimian craton of Burkina Faso (West Africa). *Journal of African Earth Sciences* 50, 215-233
- Cox SF (1999) Deformational controls on the dynamics of fluid flow in mesothermal gold systems. *Geological Society, London, Special Publications* 155, 123-140
- Fu B, Williams PJ, Oliver NHS, Dong GY, Pollard PJ, Mark GM (2003) Fluid mixing versus unmixing as an ore-forming process in the Cloncurry Fe-oxide-Cu-Au District, NW Queensland, Australia: evidence from fluid inclusions. *Journal of Geochemical Exploration* 78-9, 617-622
- Gessner K (2009) Coupled models of brittle-plastic deformation and fluid flow: Approaches, methods and applications to the Mesoproterozoic mineralisation at Mount Isa, Australia. *Surveys in Geophysics* 30, 211-232. doi: 10.1007/s10712-009-9062-6
- Gessner K, Jones PA, Wilde AR, Kühn M (2006) Significance of strain localisation and fracturing in relation to hydrothermal mineralization at Mount Isa, Australia. *Journal of Geochemical Exploration* 89(1-3), 129-132, doi: 10.1016/j.gexplo.2005.11.-048
- Gessner K, Kühn M, Jones PA, Wilde AR (2005) 3D numerical modelling of strain localization, fluid flow, and reactive transport related to hydrothermal mineralization at Mount Isa, Australia. *Geophysical Research Abstracts* 7, 00188 (SRef-ID: 1607-7962/gra/EGU05-A-00188)
- Gessner K, Kühn M, Rath V, Clauser C (2009) Coupled process models as a tool to analyse hydrothermal systems. *Surveys in Geophysics* 30, 133-162. doi:10.1007/s10712-009-9067-1
- Heinrich CA, Bain JHC, Mernagh TP, Wyborn LAI, Andrew AS, Waring CL (1995) Fluid and mass transfer during metabasalt alteration and copper mineralization at Mount Isa, Australia. *Economic Geology and the Bulletin of the Society of Economic Geologists* 90, 705-730
- Kaszuba JP, Williams LL, Janecky DR, Hollis WK, Tsimpanogiannis IN (2006) Immiscible CO₂-H₂O fluids in the shallow crust. *Geochemistry Geophysics Geosystems* 7, doi:10.1029/2005GC001107
- Kerrick DM, Caldeira K (1998) Metamorphic CO₂ degassing from orogenic belts. *Chemical Geology* 145, 213-232
- Kesler SE (2005) Ore-Forming Fluids. *Elements* 1, 13-18
- Kühn M, Dobert F, Gessner K (2006) Numerical investigation of the effect of heterogeneous permeability distributions on free convection in the hydrothermal system at Mount Isa, Australia. *Earth Planetary Science Letters* 244, 655–671. doi:10.1016/j.epsl.2006.-02.041
- Kühn M, Gessner K (2006) Reactive transport model of silicification at the Mount Isa copper deposit, Australia. *Journal of Geochemical Exploration* 89(1-3), 195-198. doi: 10.1016/j.gexplo.2005.11.076
- Kühn M, Gessner K (2009a) Testing hypotheses for the Mount Isa Copper mineralisation with numerical simulations. *Surveys in Geophysics* 30, 253-268. doi:10.1007/s10712-009-9064-4
- Kühn M, Gessner K (2009b) Coupled process models of fluid flow and heat transfer in hydrothermal systems in three dimensions. *Surveys in Geophysics* 30, 193-210. doi: 10.1007/s10712-009-9060-8
- Liebscher A, Heinrich CA (2007) Fluid-fluid interactions in the earth's lithosphere. *Reviews in Mineralogy & Geochemistry Volume* 65, 1-14, Mineralogical Society of America
- Matthäi SK, Heinrich CA, Driesner T (2004) Is the Mount Isa copper deposit the product of forced brine convection in the footwall of a major reverse fault? *Geology* 32(4), 357–360. doi: 10.1130/G20108.1
- Mumm AS, Oberthür T, Vetter U, Blenkinsop TG (1997) High CO₂ content of fluid inclusions in gold mineralisations in the Ashanti Belt, Ghana: A new category of ore forming fluids? *Mineralium Deposita* 32, 107-118
- Murphy FC, Kendrick MA, Ailleres L, Jupp B, McLellan J, Rubenach MJ, Laukamp C, Oliver NHS, Roy IG, Gessner K, Bierlein FP, Walshe JL, Cleverley JS, Hutton LJ (2011) Mineral system analysis of the Mt Isa–McArthur River region, Northern Australia. *Australian Journal of Earth Sciences* 58, 849-874
- Pruess K (2005) Numerical studies of fluid leakage from a geologic disposal reservoir for CO₂ show self-limiting feedback between fluid flow and heat transfer. *Geophysical Research Letters* 32, L14404. doi:10.1029/2005GL023250
- Rempel KU, Liebscher A, Heinrich W, Schettler G (2011a) An experimental investigation of trace element dissolution in carbon dioxide: Applications to the geological storage of CO₂. *Chemical Geology* 289, 3-4, 224-234. doi: 10.1016/j.chemgeo.2011.08.003
- Rempel KU, Liebscher A, Heinrich W, Schettler G (2011b) An experimental study of brine-CO₂ metal fractionation: Applications to the geological storage of CO₂. *Mineralogical Magazine* 75, 3, 1709
- Ridley JR, Diamond LW (2000) Fluid chemistry of orogenic lode-gold deposits and implications for genetic models. *Society of Economic Geologists Reviews in Economic Geology* 13, 141-162
- Solomon M, Groves DI (1994) The geology and origin of Australia's mineral deposits. Oxford University Press, Oxford, 951 pp
- Sternner SM, Bodnar RJ (1991) Synthetic fluid inclusions; Experimental determination of P-V-T-X properties in the CO₂ - H₂O system to 6 kb and 700 degrees C. *American Journal of Science* 291, 1-54
- Takenouchi S, Kennedy GC (1964) The binary system H₂O-CO₂ at high temperatures and pressures. *American Journal of Science* 262, 1055-1074
- Waring CL (1990) Genesis of the Mt. Isa Cu ore system. Ph.D. Thesis, Department of Earth Sciences Monash University, Clayton
- Wilde AR, Jones PA, Gessner K, Ailleres L, Gregory MJ, Duncan RJ (2006) A geochemical process model for the Mount Isa Copper orebodies. *Economic Geology* 101, 1547–1567. doi:10.2113/gsecongeo.101.8.1547

Cobalt-bearing structures of Tuva (Russia)

Vladimir I. Lebedev

Tuvianian Institute for Exploration of Natural Resources of Siberian Branch of RAS (ERAS TuvIENR SB RAS) 117-a Internatsionalnaya Street, Kyzyl, Republic of Tuva, Russia, 667000
Email: vil@mail.ru; vil@tikopr.sbras.ru

Irina G. Tretiakova

V.S. Sobolev Institute of Geology and Mineralogy SB RAS, 3, Koptyug av., Novosibirsk, Russia, 630090
Novosibirsk State University, 2, Pirogova st., Novosibirsk, Russia, 630090
Email: iritret@gmail.com

Abstract. The paper considers structures, which are spatially coincident with deep fault zones and limit fold-block structures of different age consolidation. They are characterized by high permeability of the Earth's upper mantle derivatives and distinctively fixed by gravity steps of the field; they control distribution of cobalt occurrences and manifestations of various formations. Each formational type has its specific set of ore-controlling factors, which are developed at most in ore clusters and fields. An analysis of cluster and local ore-controlling factors influence on distribution and location of proper cobalt deposits along with established age levels of intensive manifestation of arsenide nickel-cobalt and sulfoarsenide mineralization has permitted revelation of lateral rows of ore formations with relatively close ages.

Keywords: cobalt-bearing structures, ore controlling faults, ore clusters, genetic types, mineral parageneses, hydrothermal solutions.

1 Introduction

Cobalt mineralization on the territory of Tuva (fig. 1) is related (Unksov, 1954; Krutov, 1978; Ore associations of Tuva, 1981; Lebedev, 1986; 2003) mainly to two genetic types: hydrothermal and less frequent contact-metasomatic. The first is represented by nickel-cobalt arsenide, copper-cobalt sulfoarsenide, cobalt-copper sulfoarsenide-fahlore veined ore association; the second — by cobalt sulfoarsenide skarn, sulfoarsenide-magnetite cobalt-bearing skarn and sulfoarsenide cobalt-bearing listwanite-beresite ore associations. As a rule, deposits of cobalt ores are confined to interblock zones which mark activated zones of deep faults, or to basement fractures of rigid blocks. And rich arsenide nickel-cobalt ores of commercial interest are concentrated in ore clusters and fields in intersections of deep and large regional faults with long history of geological development, differentiated intrusive magmatism and intensive hydrothermal-metasomatic transformations (Distanov and Obolenskii, 1986).

2 Uvs-Nuur – Khovu-Aksy cobalt-bearing zone

In the Late Paleozoic – Early Mesozoic deposits of complex silver-gold-bismuth-copper-nickel-cobalt arsenide and sulfoarsenide-sulfosalt ores were being formed by ore-magmatic system, which spatially coincides with junction area of the East-Tannu-Ola anticlinal and West-Tannu-Ola synclinal fold systems along the Uvs-Nuur–Bayankol deep fault zone. This

metallogenic structure of the north-eastern strike is nearly 20 km width and 180 km length. It controls distribution of the Khovu-Aksy and Ulatai-Choza (fig. 2) ore clusters, which include Khovu-Aksy, Uzunoi, Boshtag, Kendei, Kara-Khem, Torgun, Teeli, Ulatai and other deposits and small ore objects.

Small intrusions including the two-phase Torgalyk intrusion complex (gabbro, gabbro-diabases, granophyres, granosyenite-porphyres) and dikes of different composition and ages (Lebedev, 1986, 2003) are also controlled by Uvs-Nuur – Khovu-Aksy zone. The zone is clearly noted in the gravitational fields in the 3–80 km depth interval. In spite of essential difference in structure both East- and West-Tannu-Ola fold systems contain this metallogenic zone.

The East-Tannu-Ola part is characterized by occurrence of Early-Middle Cambrian basalt and rhyolite formations and terrigene-carbonate deposits. Silurian marine terrigene-carbonate and Devonian-Carboniferous continental variegated once have less thickness and distribution.

The West-Tannu-Ola part is distinguished by the presence of deposits of the terrigene-carbonate and molassic rudaceous formations of the Ordovician, most completeness of stratigraphic section of Silurian, Devonian, Carboniferous, and Jurassic deposits. In total, the cobalt-bearing zone can be treated as a peculiar kind of metallogenic structure with indicators typical for adjacent areas (Kuznetsov, 1975). Contact-metasomatic, hydrothermally-altered rocks and faults occupy a significant place in the process of formation of ore clusters and fields within the zone. The postmagmatic rock alterations, associated with intrusion of the granodiorite-plagiogranite magma in the Middle Cambrian, produced wide fields of hornfels with biotite-feldspar, quartz-feldspar, and amphibole-pyroxene-feldspar composition. Contact-metasomatic formations, originated from replacement of terrigenous-tuffaceous-carbonate rocks by magnetite-andradite-epidote skarns, are of significant occurrence. The hydrothermal alterations are generally placed locally along faults and are presented by fields of secondary quartzites, sericite- and chlorite-containing rocks in the southern part of the zone and by vein-like zones of silicification and carbonatization in the central and northern parts.

The commercial cobalt concentrations, related with the Salairian tectono-magmatic cycle, have not been established and there are no prerequisites for their revealing. The Silurian and Devonian periods are characterized by movements of blocks of the Tannuola-

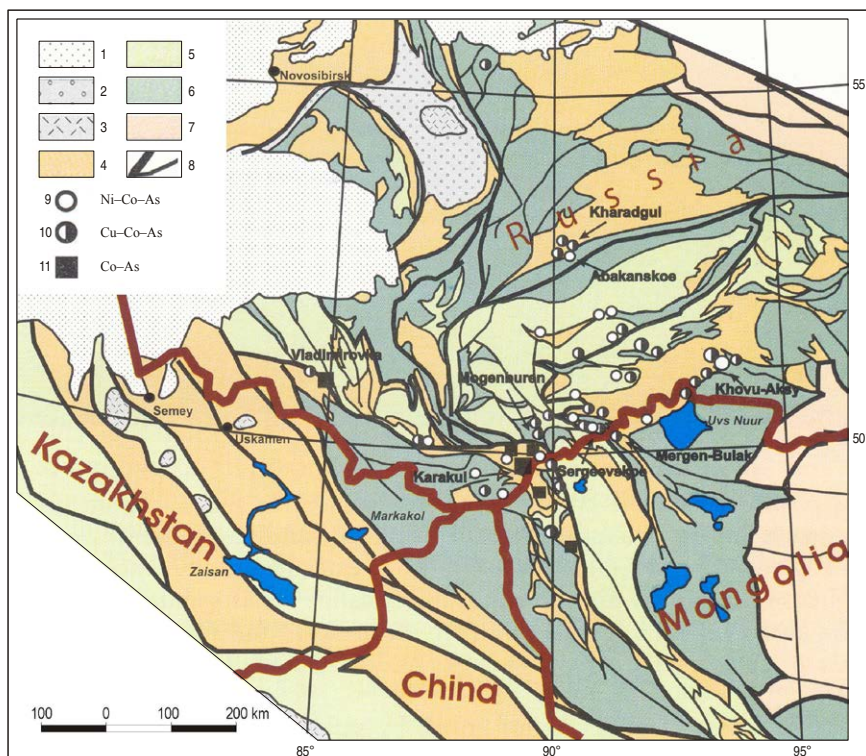


Figure 1. Location of cobalt mineralization in structures of Altai-Sayan folded region (Tretiakova et al., 2010). 1 – Mz-Kz sedimentary rocks of West Siberian Plate; 2 – Late Paleozoic-Triassic molasses of Kuznetsk trough (pull-apart basin); 3 – Late Carboniferous-Permian volcanic rocks; 4 – Devonian – Early Carboniferous volcanic-sedimentary rocks; 5 - Late Cambrian – Ordovician – Silurian sea molasses and flyschoid; 6 – Vendian-Cambrian flyschoid strata; 7 – Archean-Proterozoic metamorphic rocks; 8 – faults and geological boundaries; 9 – Ni-Co-As deposits; 10 – Cu-Co-As deposits; 11 – Co-As deposits.

Ondum island-arc system consolidated in the Late Cambrian-Ordovician. Intense volcanic eruptions of basalt, andesite-dacite, and trachyrhyolite lavas from volcanoes of the central type presumably occurred in the marginal part of the East-Tannu-Ola fold system in the zone of its conjugation with West-Tannu-Ola structure in the Early Devonian and Eifelian. In the endocontacts of subvolcanic piles of labradorite-bytownite porphyrites and gabbro-diabases hydrothermal alterations are locally noted. In the areas of development of quartz-ankerite stockworks and separated veins with the sulfide-sulfosalt mineralization, amygdales in plagiophyres and melanophyres intensely prehnitized contain an impregnation of native copper. At the end of the Upper Devonian epoch, the intense volcanic activity has been damped out and then salt-bearing piles have been accumulated in the southwestern and central parts of the zone. Terrigenous deposits were formed in the conditions of intermountain trough during stable subsidence. At the end of the Devonian and in the Early Carboniferous tectono-magmatic processes were activated, causing intruding basaltic magma along zones of a deep fault. The formation of small differentiated gabbro-syenite intrusions of the Torgalyk complex in the Uvs-Nuur – Bayankol zone of faults led to activation of supersaturated chloride and sulfate solutions buried in the post-Eifelian. These solutions disseminated through intensive fractured Silurian and Lower Devonian terrigenous-carbonate rocks in the conditions of elevated temperatures, resulted from Hercynian intrusion of subalkaline granites-granophyres, and formed contact-metasomatic chlorite-containing rocks (scapolite-garnet-pyroxene-amphibole skarns and pyroxene-prehnite-feldspar apokarns) (Shishkin, 1973; Lebedev, 2003). At this stage, the hydrothermal alterations of the host rocks

were intense chloritization and carbonatization of basic rocks and as silicification and partial baritization of Lower Devonian volcanogenic rocks. Within the ore fields, in local areas along fault zones, the many times repeated hydrothermal alterations caused formation stages and in some cases zonation in localization of hydrothermal rocks and ore mineralization. The cobalt mineralization of the considered zone is clearly associated with this step. The arsenide nickel-cobalt mineralization is controlled by a system of faults in the area of intersection of the Uvs-Nuur-Bayankol-Ungesh and Uvs-Nuur-Bayankol-Ulatai-Choza deep fault zones. Besides the Khovu-Aksy and Ulatai ore fields, the cobalt-nickel mineralization is present in ores of the Uzun-Oi deposit, Boshtag, Yush-Karasug, Kara-Khem and Mednyi ore points.

3 - North-Tannuola cobalt-bearing zone

This metallogenic structure is of regional fragmentary type; and is placed on adjacent area between Salairian-Caledonian Khemchik block, Chingekat uplift and Hercynian West-Tannuola trough. The main feature of development of this zone is that central part was relatively stable, but western and eastern blocks are characterised by high mobility, which can be caused by influence of tectonic movements along shear systems of Shapshal and Chazadyr-Karasug deep faults which control distribution of Vendian-Cambrian ophiolite association including massifs of chromite-bearing ultrabasites. Within the zone, stratified series are represented by metamorphic schists of the Late Proterozoic, ophiolite association of the Vendian, Silurian terrigene-carbonate deposits, Low Devonian andesite-dacites and their tuffs, tuffogenic- salt deposits

**SCHEME OF GEOLOGICAL SETTING
OF THE ULATAI-KHOVU-AKSY COBALT-BEARING ZONE**

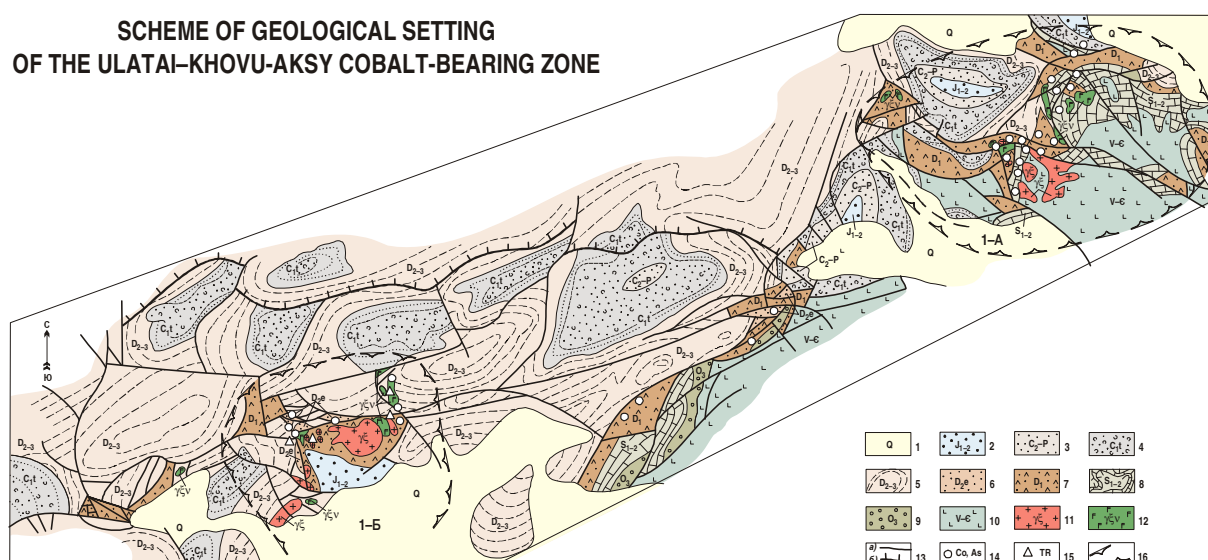


Figure 2. Geological scheme of the Ulatai-Khovu-Aksy cobalt-bearing zone.

1 – Quaternary deposits; 2 – Jurassic coal-bearing molasse; 3 – Carboniferous-Permian coal-bearing molasse; 4 – Tournaisian terrigenous-pyroclastic deposits; 5 – Givetian-Famennian alluvial-lake sandy-marly deposits; 6 – Late Eifelian carbonate-terrigenous-salt deposits; 7 – Early-Devonian effusive rifting midland molasse; 8 – Silurian organic coastal-marine and lagoonal deposits; 9 – Late-Ordovician red molasse; 10 – Vendian-Cambrian island-arc rifting-volcanogenic complex of basement sealed by plagiogranites; 11 – alkaline granites (D₂-D₃); 12 – sub-alkaline gabbroids (D₃-C₁); 13 – faults and zones of thrusts; 14 – ore objects of the five-element ore association; 15 – REE carbonatites deposits; 16 – Khovu-Aksy and Ulatai-Choza ore clusters.

of the Eifelian, and locally — by siltstone black-schist series of the Middle Devonian and coal molasse of the Jurassic. Pre-Cambrian and Low-Paleozoic formations underwent an intensive dynamometamorphism; they are folded, intruded by magmas of different composition, broken by multiple shears and thrust faults. Hercynian step of tectono-magmatic activation are known all around the zone. It produced formation of a belt of small separate intrusions of gabbro-syenite association, multiple dykes of basic composition, and zones of crumpling, layering and jointing. Spatially coincidental cobalt-bearing ore deposits and occurrences are concentrated in clusters, outlining fragmental character of the zone. Through fault systems, which traverse the North-Tannuola zone across the strike, had an important role in distribution of ore clusters. They are traced by chains of Late Paleozoic gabbroid intrusions. The Chergak, Akkhem and Ishtikhem ore clusters are confined to intersection areas. In general, the zone is characterized by the following features: many-acted interrupting tectono-magmatic processes; distinct influence of deep-seated tectonic structures and transverse faults of the basement, coincidental with the zone; close spatial connection between mineralization and Vendian – Low Cambrian ultramafites and Late Paleozoic gabbro-monzonitoid intrusions; fragmental character of mercury and copper-cobalt-antimony-arsenic mineralization.

4 – Khemchik - Kurtushibinskaya cobalt-bearing zone

This zone spatially coincides with the Sayan-Tuvian deep fault which separates West-Sayan fold system and Kurtushibinskii uplift from Khemchik-Systyg-Khem trough and has more than 300 km length and a band 10–

25 km width. Within the zone, there are Akol, Baitaiga, Shugur, Ezim and Upper Saianyk and other deposits of arsenide and sulfoarsenide ores. The zone is a trough with Vendian – Early Cambrian ophiolite association. It is characterized by a compound linear feathered structure which is clearly observed in magnet field by a narrow line of intensive maxima and gravity steps. The feature of the Khemchik-Kurtushibinskaya zone is its formation on the boundary of areas with different history of geotectonic development in Caledonian and Hercynian periods. The zone is a natural geotectonic boundary between Baikalian-Salairian-Caledonian West-Sayan trough and Tuvian Epialairian massif of the early consolidation. It is characterized by movements with relatively different ages resulted of formation of thick spilite-diorite series in the Low Cambrian, and amagmatic flyschoid-molassoid deposits – in the Upper Cambrian. The formation of Vendian – Low Cambrian ultrabasites with synchronous chromite and imposed chrysotile-asbestos mineralization was connected with initial stage of Salairides development, and the formation of Upper Cambrian gabbro-anorthozites, plagiogranites, granodiorites with synchronous iron ore mineralization, titanomagnetite and polymetallic mineralization — with its final stage. The coastal-continental Ordovician-Silurian molasse was formed in the Caledonian. The Late stage of the Caledonian is characterized by accumulation of relatively thin series of Silurian terrigenous-carbonate coastal-marine association. Low Devonian orogenic stage is expressed in formation of volcano-plutonic complexes of mainly acid composition and associated greisens and skarnoids with rare-earth mineralization. The next intrusions of subplatform fracture-type magmatism along deep fault zones can be results of Hercynian and Mesozoic activation periods which are

spatially and temporally coincidental with development stages of Gorny Altai palaeo-oceanic system. Hydrothermal and metasomatic alteration of host rocks and faults plays an important role in formation of structures of ore clusters and fields of the Khemchik-Kurtushibinskaya cobalt-bearing zone. Autometasomatic changes of ophiolite association rocks are connected with the Salairian stage. They have regional distribution and include serpentinization of ultrabasites and spilites, chloritization, hematitization and pyritization of effusives of basic-intermediate composition and their tuffs. The geochemical elements set was formed in this stage; it could serve in the following as one of sources for ore components of cobalt deposits. The formation of wide fields of quartz veins in series of Cambrian-Ordovician flysch is connected with the period of West-Sayan fold zone forming. The significant intensity and wide range characterize post-magmatic transformations of host rocks under influence of intrusions of alkaline-granite magma of the Caledonian late stage. They produced wide fields of hornfels of the biotite-feldspar and quartz-feldspar composition in Cambrian volcanogenic units and Cambrian-Ordovician terrigene deposits. Silurian sedimentary terrigene-carbonate rocks in exocontacts of these intrusions were transformed in epidote-garnet-pyroxene and garnet-epidote skarns. Connection of the most frequent hydrothermalites with the period of post-orogenic tectonomagmatic activation can be found by distribution of hydrothermalites along faults which traverse all complex of stratified and intrusive bodies including Eifelian rocks and Carboniferous gabbroids. Within the zone, hydrothermally altered rocks are represented by: aposepentinite listwanites in Vendian – Low Cambrian ophiolites with gold, cobalt and nickel; listwanites-like quartz-dolomite-calcite lodes in Silurian and Eifelian terrigene deposits with mercury and polymetals; zones of silicification, chalcidization and argillization in volcanogenic units of the Low Cambrian, Low Devonian and Eifelian; carbonatization, berestization and argillization zones in deposits of the Ordovician, Silurian and Low Devonian, in stocks of the Devonian, Carboniferous and Permian. Ore cluster with similar intensity and completeness of hydrothermal and metasomatic alteration are marked by presence of ore objects with similar mineral composition. In general, the cobalt-bearing zone is characterized by the multistep tectono-magmatic development, similar metasomatic and hydrothermal alterations of host rocks in adjacent areas of feathering fault zones, a repeating geochemical complex of ore components in separate clusters with leading gold-nickel-arsenic specialization. The tectono-magmatic development is fixed by sequence of three stages: Salairian which founded and formed an trough with typical Vendian-Cambrian ophiolite complex that includes basic mass of cobalt as accessory sulfides, arsenides and admixture elements in rock-forming minerals; Caledonian which produced flyschoid complexes and intrusion of granitoids accompanied by oxide, sulfide and sulfoarsenide mineralization in skarns and quartz veins; Late Paleozoic – Mesozoic which formed imposed basins during activation period of the deep fault zone with formation of a belt of subalkaline

mafic intrusions and fields of altered rocks with imposed arsenide nickel-cobalt veined and copper-cobalt sulfoarsenide-fahlore mineralization.

5 – Conclusions

1. The considered cobalt-bearing zones include deposits with similar mineral composition and conditions of hydrothermal ore formation.
2. Post-Devonian lowest age limit of mineralization has been established for the most of cobalt deposits; the upper age limit can be defined by early Mesozoic dykes of dolerites intersected by arsenide veins.
3. Within cobalt-bearing zones, ore fields are characterized by:
 - distribution in areas of intersection of regional deep faults characterized by long multi-stage development with distinct cobalt-arsenic geochemical mineralization;
 - location near areas of accumulation of salt deposits and control of their distribution by deep faults which were activated in the Late Paleozoic and Mesozoic;
 - association to relatively rigid structural blocks 15-20 km² in area; within them, intensity of folded forms is conditioned by influence of fault tectonics;
 - close spatial-structural connection of ore zones with small intrusions of subalkaline granitoids and fields of development of dykes of variegated composition.

Acknowledgements

The work is executed with the financial of RFBR by the projects №№ 10-05-00444, 11-05-10023, 12-05-10018.

References

- Borisenko AS, Lebedev VI, Tyulkin VG (1984) Forming conditions of hydrothermal cobalt deposits. Nauka, Novosibirsk.
- Borisenko AS, Obolenskiy AA, Lebedev VI, Obolenskaya RV, Pavlova GG, Goverdovskiy VA (1992) Silver-antimony ore formation. Nauka, Novosibirsk.
- Distanov EG and Obolenskii AA (1994) Metallogenic development of Central-Asian mobile belt in association with its geodynamic evolution. *Geologia i Geofizika*. Vol. 35, № 7–8; 252–269. (in Russian).
- Krutov GA (1978) Deposits of cobalt. In: *Ore deposits of the USSR*. V. 2. Moscow, pp. 77–99. (in Russian).
- Kuznetsov VA (1975) Central-Asian belt of Mesozoic tectono-magmatic activity and ore mineralization. In: *Regularity of localization of mineral resources*. Vol. XI. Moscow. pp. 190–199. (in Russian).
- Lebedev VI (1986) Ore-formation analysis, conditions of formation, and regularities of situation of cobalt deposits of Central Asia: PhD thesis. Novosibirsk. (in Russian)
- Lebedev VI (2003) Ore-magmatic systems of arsenide-cobalt deposits. TuvIENR SB RAS, Kyzyl. (in Russian)
- Zaikov VV, Lebedev VI, Tyul'kin VG et al (1981) Ore associations of Tuva. Novosibirsk. (in Russian)
- Shcheglov AD (1968) Metallogeny of regions of autonomous activation. Leningrad. (in Russian)
- Shishkin NN (1973) Cobalt in ores of USSA. Moscow. (in Russian).
- Tretiakova IG, Borisenko AS, Lebedev VI, Pavlova GG, Goverdovskiy VA, Travin AV (2010) Cobalt mineralization in the Altai–Sayan orogen: age and correlation with magmatism. *Russian Geology and Geophysics*. V. 51, I. 9, 1078–1090.
- Unkov VA (1954) Some features of metallogeny and geochemistry of cobalt. *ZVMO*. Issue 4, Part. 83. 23–30. (in Russian).

T-P-X evolution path of ore forming fluid in Qiangong polymetallic deposit, Tibet, China

Yingxu Li, Guangming Li, Li Zhang

Chengdu Centre of China Geological Survey, Chengdu, 610081, P.R. China

Yuling Xie, Baoshun Liu, Lamei Li

School of Civil and Environmental Engineering, University of Science and Technology Beijing, Beijing 100083, P.R. China

Abstract. Qiangong polymetallic deposit is genetically related to monzogranite porphyry. The mineralization styles include skarn type Fe(-Cu), distal vein type Pb-Zn-Ag(-Cu) and carbonate replacement type Pb-Zn-Ag. Based on field observation and petrographic results the ore-forming process in this deposit can be divided into at least six stages including garnet-magnetite stage (I), epidote-magnetite stage (II), quartz-hematite stage(III), fluorite-chalcopyrite stage (IV), calcite-galena-sphalerite stage (V) and calcite-quartz stage(VI). Petrographic, microthermometric and laser Raman microprobe results of fluid inclusions in quartz, garnet, epidote, calcite and fluorite from these six stages demonstrate that the pressure, temperature, density and salinity of the ore forming fluid decrease from early to later stage, and the fluid system change from early $H_2O-NaCl$ (I-II) via $H_2O-NaCl-FeCl_2-3\pm MgCl_2$ (III), H_2O-CO_2-NaCl (IV) to late $H_2O-NaCl-CaCl_2$ (V&VI). The deposition of Cu in Qiangong was triggered by the boiling of the ore-forming fluid of H_2O-CO_2-NaCl system from stage IV. Proton induced X-ray emission analyses show that the concentration of the metallic elements (such as Pb, Zn etc) in the fluid inclusions also decreased with the fluid evolution.

Keywords. Qiangong Polymetallic Deposit; Fluid Inclusions; Ore Forming Fluid Evolution; Porphyry-skarn-hydrotherm Mineralization System

1 Introduction

Qiangong together with Nazha, Jiangga, Jiugang, Sinongduo, Jiaduobule and Chazangcuo comprises a NNE trending skarn-belt along the Shenzha-Dingjie Rift in the Middle Gangdese metallogenic belt, but all these deposits have been rarely reported. And the ore genesis together with the ore potential of this belt is still questionably.

Qiangong Fe (Cu, Pb, Zn, Ag) polymetallic deposit is genetically related to a monzogranite porphyry which has a zircon U-Pb age of 68.8Ma (Xie et al., 2009a). Petrochemical results indicated a crustal source with mantle input for monzogranite porphyry and the mantle source magma upwells through the tearing window of the subducted Neo-Tethys slab (Li et al., 2011a; 2011b). The primary ore-forming fluid in Qiangong porphyry system is high temperature, high pressure and high salinity magmatic- fluid (Xie et al., 2009b). In this paper, we report some new fluid inclusion results and discuss the T-P-X evolution path of ore forming fluid and give a new understanding for the ore-forming process in the porphyry-skarn-hydrotherm mineralization system .

2 Geology

Qiangong deposit is located at 60km north of Xietongmen Country, Tibet, China, and is one of the skarn deposits genetically related to porphyry in the Middle Gangdese Metallogenic Belt, which has the same geographic location of the Lhasa Terrane (LT). LT has Proterozoic and Archean basement in the centre with accreted Phanerozoic crust in its both northern and southern edges (Zhu et al., 2011). LT had endured the subduction and roll back of the Neo-Tethyan seafloor and the collision between Indian and Asian continent during the Asia-India plate assembling (Pan et al., 2006; Hou et al., 2006).

Most area of Qiangong is covered by the Lower Cretaceous Takena Formation (K_1t), Lower and Middle Eocene Linzizong Group ($E_{1-2}L$) and granitic intrusions (Fig.1). The Takena Formation in the centre of this district is mostly limestone and partly siltstone. The Linzizong Group in the northern part of this area includes conglomerate, rhyolite, rhyolite porphyry, pyroxene andesite, dacite and tuff. Linzizong Group overlies unconformably on the Takena Formation as a result of the Indian-Asian continent-continent collision starting at no later than 65Ma (Mo et al., 2003; Hou et al., 2006).

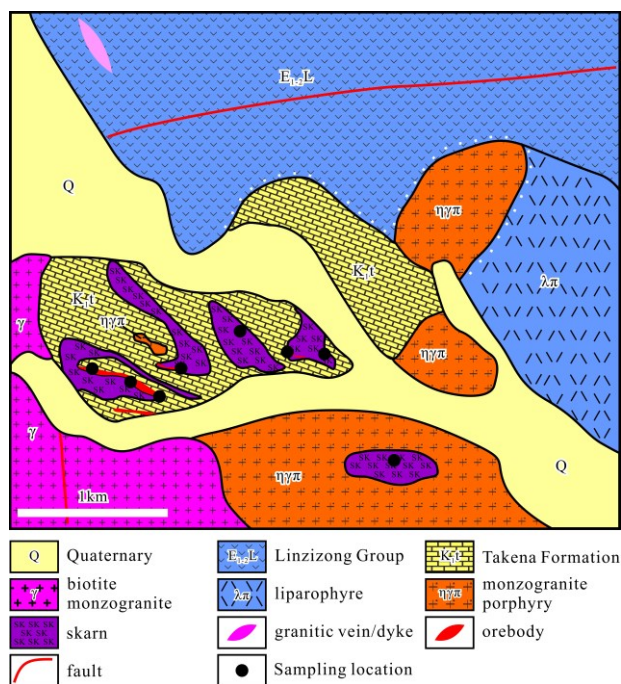


Figure 1. Geological map of Qiangong Polymetallic Deposit (modified and redraw from Xie et al., 2009a, based on Hubei Geological Survey, 2008)

The granitic intrusions include coarse biotite monzogranite outcropping in the south and west of the district, monzogranite porphyry mainly outcropping in the south part of the deposit, and quartz porphyry and aplite occurring as veins/dykes in biotite monzogranite and monzogranite porphyry. Monzogranite porphyry is also found occurring as a pophysis or stock along the NW trending fault in Takena Formation. The skarn occurs mainly in the contact zone between monzogranite porphyry and Takena formation implying a close genetic relationship between mineralization and monzonitic porphyry (Xie et al., 2009a). The biotite monzogranite, quartz porphyry and aplite semm t have little little benefit to ore forming.

The ore style in Qiagong can be divided into three types including skarn Fe (Cu), Pb-Zn-Ag(-Cu) vein type and carbonate replacement Pb-Zn-Ag. All the mineralization are spatially related to skarn alteration which was mainly controlled by faults and comprising a porphyry related skarn-hydrothermal mineralization system. The skarn type Fe(-Cu) occur in the contact zone between the monzogranite porphyry and the Takena Formation. The distal Pb-Zn-Ag(-Cu) mineralization occurs in the subsidiary fault and fracture and can be divided into vein type Pb-Zn-Ag(-Cu) and carbonate replacement type Pb-Zn-Ag.

Based on field observation and petrographic results, the ore-forming process in this deposit can be divided into at least six stages including garnet-magnetite stage (I) with mineral assemblage of garnet, wollastonite, diopside and magnetite; epidote-magnetite stage (II) with mineral assemblage of magnetite and epidote, quartz-hematite stage (III) with mineral assemblage of quartz, actinolite, hematite; fluorite-chalcopyrite stage (IV) with mineral assemblage of fluorite and chalcopyrite; calcite-galena-sphalerite stage with mineral assemblage of calcite, galena, sphalerite and quartz (V); and post mineralization calcite-quartz stage mainly calcite and quartz (VI).

3 Samples and Analytical Results

Fluid inclusion (FI) study samples are transparent minerals of the six stages, and include garnet(I), epidote(II), quartz(III, V&VI) fluorite(IV) and calcite(V&VI). Sampling locations are marked on Fig.1.

3.1 Classification of Fluid Inclusions

Been determined under microscope at room temperature, three different types of fluid inclusions (FIs) were classified by the phsaes they contain in this study. They are aqueous-vapour (AV) type, CO₂-bearing (AC) type and daughter mineral-bearing (ADV) type. Their petrographic characteristics are described as follow:

AV type: this type of FIs comprise aqueous and vapour phases, and the vapour phase take 10-25 vol.% of the inclusion. It is the most abundant type in quartz, calcite, fluorite and garnet. They occur as primary FIs in quartz (III, V&VI) and calcite (V&VI), and as secondary FIs in garnet(I), epidote (II) and fluorite (IV). In addition, secondary FIs in quartz (III, V&VI) and calcite (V&VI) are also AV type, but the occurence and

microthermometric results of the secondary FIs are different from the primary ones.

AC type: this type of FIs are primary FIs in fluorite (IV), and they offen occur as fluid inclusion assemblage (FIA) that comprises pure-CO₂ FIs, CO₂- rich FIs and CO₂-poor FIs (Fig.2). The variable liquid (aqueous phase) and vapor (CO₂ phase) ratios imply a heterogeneous trapping during fluid boiling (Carles et al., 2011).

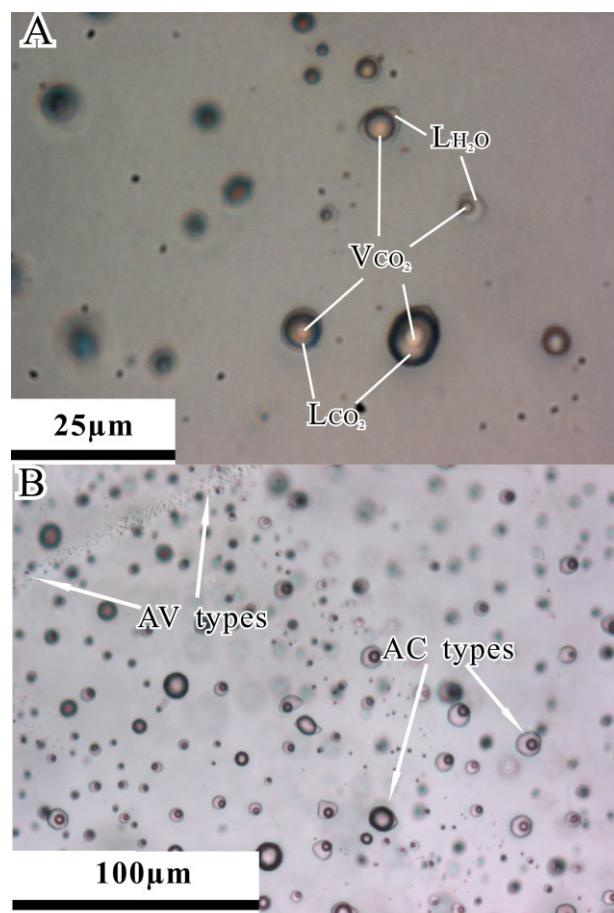


Figure 2. Primary AC type and secondary AV type fluid inclusions in fluorite from Qiagong

AC type FIs occur as unmixing FIA, and show variable liquid(aqueous phase)-to-vapor(CO₂ phase) ratios due to heterogeneous fluid trapping; some comprise aqueous phase, liquid and vapor CO₂ phase(A); AV type FIs distribute in a NE trending line "cut" the AC type unmixing FIA(B)

ADV type: this type of FIs are only found in some garnet(I) and epidote(II), and comprise one or two daughter minerals, aqueous and a vapour phase.

Laser Raman microprobe results show that the aqueous phases of all the these types of FIs are dominated by H₂O, and vapour phases in AV and ADV types FIs are also dominated by H₂O. CO₂ is detected in bubble phases of all AC type FIs and some ADV type FIs (Fig.3).

Petrographic study results show the fluid phase of the ore forming fluid in Qiagong is aqueous dominated, and types of fluid inclusions are different at each stage.

In early stages, such as garnet-magnetite(I) and epidote-magnetite(II), fluid inclusions are high in salinity, and most of FIs are ADV type. In later stages, such as fluorite-chalcopyrite(IV) and calcite-galena-sphalerite

(V), salinity of fluid are lower, and FIs are mainly AC type at stage (IV) and AV type at stage(V) and stage(III) respectively. At post mineralization stage(VI), their type is AV only. And their CO₂ concentration changed from very low early via high later and to low at last.

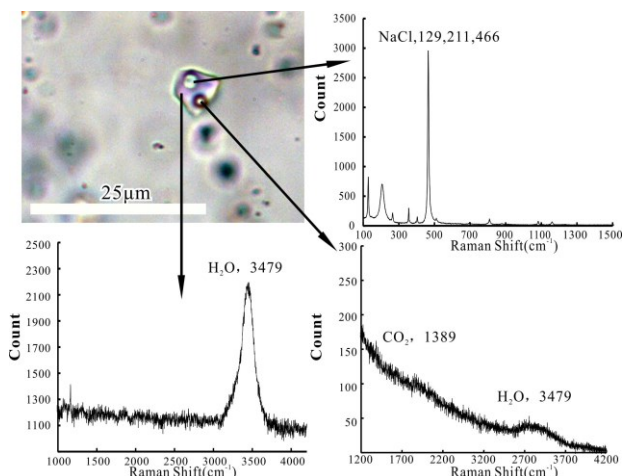


Figure 3. LRM spectroscopy of an ADV type fluid inclusion with a halite grain as daughter mineral, a little CO₂ in vapour phase and H₂O dominated aqueous phase

3.2 Microthermometry of Fluid Inclusions

Microthermometry on the three types FIs is done on Linkam® THMSG-600 at University of Science and Technology Beijing.

The microthermometric results of ADV type FIs show their homogenization temperature (Th_{l-v}) is 391-410°C, and their daughter minerals melt temperature (Tm) is 301-327°C, lower than Th_{l-v} .

Microthermometry on AC type FIs in fluorite(IV) only got poorly successful Th data as the CO₂-rich ones often explode at 230-260°C, and several FIs with CO₂ phase of 15-20 vol.% homogenised between 260-283°C and the clathrate melt temperature (Tm_{cal}) of these FIs range from 4.4-8.3°C. The CO₂ phases homogenised (Th_{CO_2}) at 24.5-29.1°C to liquid CO₂, and the melt temperature of solid CO₂ (Tm_{CO_2}) ranges from -56.9 to -59.6°C. Microthermometry on pure-CO₂ FIs got that their Tm_{CO_2} range from -56.6 to -56.8°C, and their Th_{CO_2} range from 23.2-25.7°C.

Microthermometric results of AV type FIs are complex as this type FIs are trapped at multiple stages, and they can also be product of necking.

Microthermometric results of AV FIs in quartz and calcite from stage (VI) show their Th_{l-v} range from 50-210°C, and mainly fall between 170 to 195°C. Their eutectic points (Te) range from -21.5 to -50.6°C in calcite and -21.3 to -52.3°C in quartz respectively. Their ice point (Tm_{ice}) range from -1.5 to -4.2°C.

Fig.4 shows the frequency of Th for AV FIs in calcite and quartz from stage V. The two frequency peaks of Th represent FIs of primary (200-220°C) and secondary (170-190°C) respectively. Their Te range from -20.8 to -21.6°C, and Tm_{ice} range from -2.6 to -5.1°C.

Primary AV FIs from quartz(III) have similar microthermometric results of some AV FIs occur in garnet(I) and epidote(II) as secondary. The Th_{l-v} range

from 272 to 318°C. Their Te has 2 ranges, and they are -21.9 to -22.7°C and -34.2 to -36.3°C respectively. Their Tm_{ice} range from -7.5 to -9.0°C.

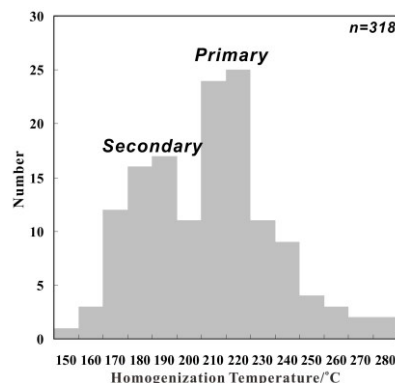


Figure 4. Homogenization temperature distribution histogram for AV type fluid inclusions in calcite and quartz of stage V in Qiaogong

Microthermometric results indicate that the temperature and salinity of ore forming fluid in Qiaogong came lower as it was evolving,

4 Discussion

4.1 Trapping Pressure and Temperature of Fluid Inclusions

AC type unmixing FIA give a good chance to estimate the trapping pressure and temperature, and the intersection point of iso- Th lines of the two fluid inclusion end members in unmixing on T-P diagram is the trapping pressure and temperature. But isometrics data for NaCl-H₂O-CO₂ system is insufficient for this study, so the trapping pressure and temperature are estimated by just extrapolating iso- Th lines of CO₂ to the homogenization temperature of the whole FI at 260-283°C, and the result is 90-110MPa. If use H₂O-NaCl system instead, the result is 125-137MPa at 395-410°C. The unmixing of ore forming fluid implies that Qiaogong mineralization system was turning from lithostatic pressure into hydrostatic pressure or the temperature went down. As most inclusions still have CO₂, the system might not be "open". Furthermore, decrease in salinity means meteoric water had contribution to the ore forming fluid.

Xie et al.(2009b) had reported the estimated pressure of ore-forming fluids derived from the exsolution of Qiaogong monzogranite porphyry, and it was about 200MPa. Li et al.(2011b) had reported the temperature of Qiaogong monzogranite porphyry magma determined by Ti concentration in zircon, which is about 600°C. And these data constrain the skarn forming fluid derived from Qiaogong monzogranite porphyry magma is below 600°C at temperature, and pressure is between 200 and 137MPa. Considering the microthermometric results of ADV type FIs, extrapolating on the isometrics of 40%wtNaCleq to the pressure 200-220MPa, its trapping temperature estimated is about 500°C.

Microthermometric results of AV type FIs from stage(V) are in accordance with many vein type Pb-Zn

deposit. This implies when Pb and Zn are depositing, Qiagong mineralization system was already under hydrostatic pressure, and trapping pressure and temperature correction may not be necessary.

4.2 T-P-X Evolution Path of Ore Forming fluid

Based on the estimation of trapping pressure and temperature, with Pb, Zn concentration analysed by PIXE and Xie et al.(2009) reported, T-P-X path of the fluid evolution was shown in Fig.5. It may also be a common evolution path for porphyry-skarn-hydrotherm mineralization system.

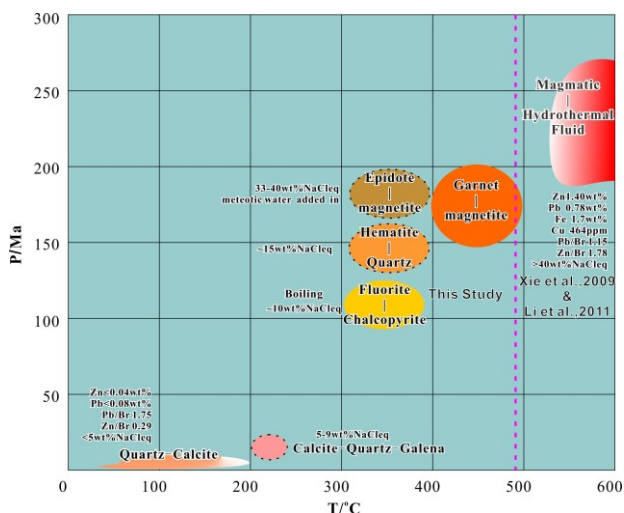


Figure 5. T-P-X evolution path of ore forming fluid in Qiagong polymetallic deposit. Data drawn on right side of the pink line in dash is from literature, on the left side is got in this study

Primary ore-forming fluid derived from monzogranite porphyry was high temperature(600-630°C), high pressure(200-220MPa) and high salinity (about 40wt%NaCl), and rich in Fe, Pb, Zn and Cu (Xie et al., 2009). Then skarn forming fluid "ejected" from the top of the magma chamber along the NW-NNW trending fault and metasomatized limestone of the Takena Formation, forming garnet and magnetite (I). Then, the temperature of fluid continued to decrease to about 350-400°C. As paragenetic minerals changed into enhydrite, activity of Si and Al was weakened, and the hydrothermal activity was mainly dominated by "water". Garnet was replaced by epidote (II), and abundance of magnetite deposited. As the fluid flow along the fault, meteoric water was added in, when hematite (III) deposited, the fluid system may be dominated by NaCl and FeCl₂₋₃ or/and MgCl₂. With the increasing input of CO₂ from wall rock and meteoric water, the pressure dropped to 90-137MPa, and the fluid temperature decrease and accompanied by fluorite-chalcopyrite (IV) deposition. With the increasing decrease of temperature and pressure, galena and sphalerite (V) deposited at 220-200°C and 10-20MPa. At last, the fluid cooled to 50-200°C, and decompress to 5-10MPa, forming only quartz and calcite at post mineralization stage(VI).

Qiagong is different from the Caicayén Hill style which has been reported by Franchini et al(2000). Pb-Zn mineralization in Qiagong formed at a lower temperature

and occur in NNW-NW trending faults. But Franchini et al(2000) only focus on the Cu mineralization. The gap in T-P-X evolution path between stage(IV) and stage(V) in Fig.5 with temperature 250-300°C and pressure 25-100MPa may mean more undiscovered ore reserves potential deeper in the NNW trending ore controlling fault.

Acknowledgements

This study has been financially supported by the "National Public Industry Research Special Fund of China" (No. 201011011-01), "National Basic Research Program of China" (No. 2011CB403105), "National Technology Plan of China" (No. 2006BAB01A04) and the Australian Research Council's Centre of Excellence in Ore Deposits (CODES). Many thanks to H.C. Zhao and G.M. Shuai of Taisheng Company for field work support.

References

- Carles C, Sara I F, Rosa M P L, Eduardo G P, Ruth E V E (2011) A model of boiling for fluid inclusion studies: Application to the Bolaños Ag-Au-Pb-Zn epithermal deposit, Western Mexico. *Journal of Geochemical Exploration*, 110: 118-125
- Franchini M B, Meinert L D, Montenegro T F (2000) Skarns related to porphyry-style mineralization at Caicayén Hill, Neuquén, Argentina: composition and evolution of hydrothermal fluids. *Economic Geology*, 95: 1197-1213
- Hou Z Q, Mo X X, Gao Y F, Yang Z M, Dong G C, Ding L (2006) Early processes and tectonic model for the Indian-Asian Continental Collision: Evidence from the Cenozoic Gangdese igneous rocks in Tibet. *Acta Geologica Sinica*, 80(9): 1233-1248. (in Chinese with English abstract)
- Hubei Geological Survey (2008) Assessment report of iron deposits along Qinghai-Tibet railway. (in Chinese)
- Li Y X, Xie Y L, Chen W, Tang Y W, Li G M, Zhang L, Li L M, Liu Y F, Liu X M (2011) U-Pb age and geochemical characteristics of zircon in monzogranite porphyry from Qiagong Deposit, Tibet, and their geological implication. *Acta Petrologica Sinica*, 27(7): 2023-2033
- Li Y X, Xie Y L, Dominy S C, Li G M, Zhang L (2011b) Geochemistry and petrogenesis of granites in the Qiagong skarn deposit, Tibet, China. 11th Biennial SGA meeting, 2011, Antofagasta, Chile: 40-42
- Mo X X, Zhao Z D, Deng J F, Dong G C, Zhou S, Guo T Y, Zhang S Q, Wang L L (2003) Response of volcanism to the India-Asia collision. *Earth Science Frontiers* 10(3): 135-148 (in Chinese with English abstract)
- Pan G T, Mo X X, Hou Z Q, Zhu D C, Wang L Q, Li G M, Zhao Z D, Geng Q R, Liao Z L (2006) Spatial-temporal framework of the Gangdese Orogenic Belt and its evolution. *Acta Petrologica Sinica*, 22(3): 521-532 (in Chinese with English abstract)
- Sibson, R H (2001) Seismogenic framework for hydrothermal transport and ore deposition. *Reviews in Economic Geology*, 14: 25-50
- Xie Y L, Li Y X, Chang Z S, Cooke D R, Dominy S C, Li G M, Zhang L (2009a) LA-ICP-MS zircon U-Pb dating of porphyries in the Qiagong iron skarn deposit, Tibet, China, Proceedings of 10th Biennial SGA meeting, 2009, Townsville, Australia: 303-305
- Xie Y L, Li Y X, Chang Z S, David R C, Chris G R, Jamie L, Bai J S, Liu Y F, Li G M, Zhang L (2009b) Magmatic evolution and characteristics of magmatic fluid in Qiagong porphyry system. *Acta Geologica Sinica*, 83(12): 1869-1886. (in Chinese with English abstract)
- Zhu D C, Zhao Z D, Niu Y L, Mo X X, Chung S L, Hou Z Q, Wang L Q, Wu F Y (2011) The Lhasa Terrane: Record of a microcontinent and its histories of drift and growth. *Earth and Planetary Science Letters*, 301: 241-255

Sulfur isotope composition of granite-molybdenum systems formed within a collided orogen setting: insights from the Newfoundland Appalachians, Canada

Edward P. Lynch^{1,5}, Martin Feely¹, David Selby², Derek H.C. Wilton³ and Anthony E. Fallick⁴

¹Earth and Ocean Sciences, School of Natural Sciences, National University of Ireland, Galway, Ireland

²Department of Earth Sciences, Durham University, Durham DH1 3LE, UK

³Department of Earth Sciences, Memorial University, St John's, Newfoundland and Labrador, A1B 3X5, Canada

⁴Scottish Universities Environmental Research Centre, East Kilbride, Glasgow G75 0QF, UK

⁵Geological Survey of Sweden (SGU), Villavägen 18, 75128 Uppsala, Sweden

Abstract. The $\delta^{34}\text{S}_{\text{V-CDT}}$ compositions of sulfides from several Paleozoic granite-molybdenum systems in the Newfoundland Appalachians were determined. The majority of sulfides have a narrow range from approximately 4 to 8‰. Paragenetic main-stage sulfides are more ^{34}S -enriched compared to late-stage mineralization. The $\delta^{34}\text{S}$ values indicate a single (magmatic) supply of sulfur during magmatic-hydrothermal mineralization. The primary sulfur source is inferred to be a lower to mid-crustal reservoir. Granitoid melts sequestered this sulfur, which was later transferred to the upper crust via late-orogenic transtensional faults. The addition of ^{34}S -enriched sedimentary sulfur may also have played a role.

Keywords. Sulfur isotopes, granite, molybdenum, Newfoundland, Appalachians

1 Introduction

Much of the world's metal is sourced from mineral deposits containing sulfide ore. The availability of sulfur species in mineralizing systems to complex metals therefore plays a fundamental role in the formation of sulfide deposits. An essential task in the study of sulfide-bearing deposits is to constrain the geological conditions controlling the source, supply and/or activity of sulfur during mineralization. Sulfur isotopes can retain a geochemical signature of depositional conditions during sulfide precipitation. Thus, sulfur isotope analysis can potentially constrain the history of sulfur within a mineralizing system, provide evidence of the sulfur reservoir(s) that may have been tapped, and offer insights into the broader physicochemical conditions that exist within a mineralizing magmatic-hydrothermal system (e.g., Ohmoto and Goldhaber 1997).

This study presents the results of a stable sulfur isotope investigation of granite-related molybdenum mineralization in the Paleozoic Newfoundland Appalachians (eastern Canada). The mineralization is generally associated with a suite of evolved, Late Devonian leucogranites that formed within a thickened, collided orogen setting, and includes various depositional styles such as magmatic disseminations, porphyry-type stockwork and greisen. The results shed some light on the source, availability and behaviour of sulfur in mineralizing magmatic-hydrothermal systems that develop during the concluding stages of a protracted, regional-scale, orogenic event.

2 Granitoid Geology and Mineralization

2.1 Geological setting

In the Newfoundland Appalachians, Early Paleozoic volcanosedimentary units and related structures record the sequential collision and accretion of oceanic and Gondwanan crustal components to the Laurentian craton during subduction of the Iapetus Ocean (e.g., Van Staal et al. 1998). Continued convergence into the Devonian produced voluminous, syn-collisional, granitoid magmatism within the core of the orogen known as the Central Mobile Belt (CMB, Fig. 1).

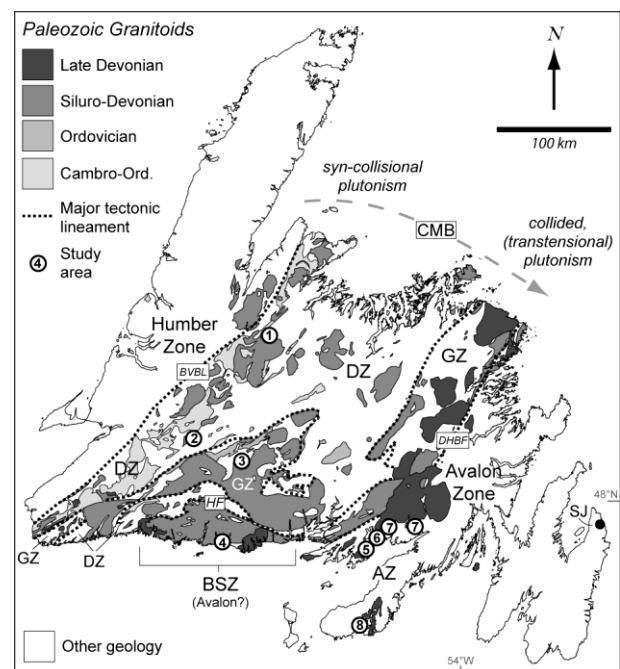


Figure 1. Paleozoic granitoid geology of Newfoundland. Study localities 1 – 8 are listed in Table 1. Abbreviations: AZ = Avalon Zone, BSZ = Burgeo Subzone, BVBL = Baie Verte-Brompton Line, CMB = Central Mobile Belt, DHBF = Dover-Hermitage Bay Fault, DZ = Dunnage Zone, GZ = Gander Zone, HF = Hermitage Flexure, SJ = St John's. Based on Coleman-Sadd et al. (1990) and Williams et al. (1988).

Granitoid plutons of the CMB encompass a broad range of mineralogical and geochemical types reflecting variable source regions, tectonic environments, emplacement mechanisms and magmatic

processes (e.g., Elias and Strong 1982; Kerr 1997). A first-order, regional-scale assessment of Newfoundland Paleozoic granitoids indicates that the plutons (broadly) young and evolve from northwest to southeast reflecting the tectonic and crustal evolution of the orogen with time (Fig. 1; cf. Strong and Dickson 1978; Williams et al. 1989). The culmination of this trend was the emplacement of a suite of evolved leucogranites in the Late Devonian that are associated with variable granophile mineralization (e.g., Strong 1980; Chatterjee and Strong 1982).

2.2 Late Devonian granites and mineralization

Late Devonian granites in Newfoundland (~ 385 – 374 Ma) form a relatively narrow, arcuate zone along the eastern and southern margins of the CMB (Fig. 1). In the east, the granites intrude along the Dover-Hermitage Bay Fault (DHBF, Fig. 1) separating the Gander and Avalon tectonostratigraphic zones (GZ and AZ, Fig. 1). In the south coast region (south of the Hermitage Flexure (HF), Fig. 1), evolved granites also occur within, and adjacent to, the wedge-shaped Burgeo Subzone (BSZ), which some workers regard as a lateral equivalent of the AZ (e.g., Dunning and O'Brien 1989). This regional emplacement pattern reflects transtensional movements along brittle-ductile shear zones in the upper crust which allowed passive magmatism to intrude steeply dipping fault conduits (D'Lemos et al. 1995). In mineralized areas, exposed plutons are interpreted to represent relatively shallow, structurally high, apical zones (e.g., Whalen 1980).

Petrologically, the suite consists of megacrystic and equigranular to locally porphyritic varieties of biotite granite and alkali feldspar granite (*s.s.*). Geochemical analyses indicate high-silica, alkali-rich, peraluminous to locally peralkaline compositions, enriched in large-ion lithophile and other incompatible elements. Granophile mineralization predominantly consists of hypogene intrusion- and vein-hosted molybdenum systems (i.e., Mo ± Cu, W; Table 1). The mineralization occurs as variable intragranitic disseminations and segregations related to late-stage magmatism (e.g., Ackley Granite, Harbour Breton), or as sulfide-bearing quartz veins related to magmatic-hydrothermal processes (e.g., Moly Brook). In the latter case, the stockwork may be detached from its causative magmatism (e.g., Moly Brook), or developed within a cogenetic pluton (e.g., at Granite Lake). Locally, metasomatic greisen and late-stage veins host minor Sn, W, Mo, Cu and Pb mineralization (Ackley, St Lawrence, Moly Brook). Fluorite also accompanies the mineralization. These general characteristics suggest a metallogenic affinity with intraplate, rift-related porphyry Mo systems (cf. Carten et al. 1993). Re-Os age constraints indicate granophile mineralization occurred as a temporally focused episode at ca. 380 Ma in southeastern Newfoundland (Lynch et al. 2012).

Table 1 lists the investigated areas and summarises the mineralization styles associated with the Late Devonian granites (no. 4 - 8) and older plutons located within the CMB (no. 1 – 3).

No.	Location	Mineralization ¹ ; style ¹ ; setting ²
<i>Avalon Zone (Late Dev.)</i>		
8	St Lawrence	Mo; late-stage qtz veins, greisen; granite-hosted
7	Ackley Granite	Mo±Sn; disseminated, qtz veins, greisen; granite-hosted
6	Belle Island	Mo±Cu; quartz veins disseminated; granite-hosted
5	Harbour Breton	Mo; qtz segregations & veins, disseminated; granite-hosted
<i>Avalon-BSZ (Late Dev.)</i>		
4	Moly Brook	Mo-Cu±W±Pb; qtz stockwork, country rock-hosted (G + MS)
<i>CMB (Late Ord. - Mid Dev.)</i>		
3	Granite Lake	Mo-W±Cu; qtz stockwork, disseminated; granite-hosted
2	Moly Peak	Mo-Cu; qtz stockwork; country rock-hosted (V)
1	Topsails	Mo; qtz stockwork; granitoid-hosted

¹Listed in decreasing abundance/significance

²Country rock abbrev.: G = granitoids, MS = metasediments, V = volcanics

Table 1. Summary of Paleozoic granite-related Mo mineralization in Newfoundland. Locations are listed (8 – 1) approximately youngest to oldest, and from east to west.

3 Sulfur Isotopes

Sixty seven samples (molybdenite, chalcopyrite, pyrite and galena), collected from eight mineralized areas, were analysed for their stable sulfur isotope compositions. 58 samples from five areas represent granophile mineralization linked to the evolved leucogranites previously described (i.e., Ackley Granite, Harbour Breton Granite, Belle Island, St Lawrence Granite and Moly Brook; locations 4 – 8, Fig. 1). A comparative set of 9 samples from three localities within the CMB represent earlier Late Ordovician to Mid-Devonian mineralization associated with syn-collisional granitoid magmatism (i.e., Granite Lake, Moly Peak and Topsails; locations 1 – 3, Fig. 1). Sulfur isotope compositions ($\delta^{34}\text{S}$) were determined at the Scottish Universities Environmental Research Centre (SUERC) and Memorial University using SO_2 extraction and in situ laser methods. Analytical precision is estimated to be $\pm 0.4\text{‰}$ (2σ) and results were determined relative to the V-CDT reference composition (0‰).

The sulfur isotope results are summarised as histograms in Figure 2. The data are grouped by area (Group 1 to 4) and individual analyses are classified into three broad mineralization styles (disseminated, early veins/segregations and late veins/greisen) reflecting a general paragenetic evolution. Results from the Ackley Granite (Group 1) and Moly Brook (Group 3) have been retained as separate datasets. This facilitates a comparison between hypogene disseminated mineralization within the Ackley Granite and the vein mineralization at Moly Brook that is inferred to have a genetic link to Ackley-type granitic magmatism (see Kerr et al. 2009). For the purpose of data presentation and discussion, the results from the Harbour Breton,

Belle Isl. and St Lawrence areas (within the AZ) have been grouped (Group 2). Likewise, the results from Granite Lake, Moly Peak and Topsails (within the CMB) are also grouped (Group 4).

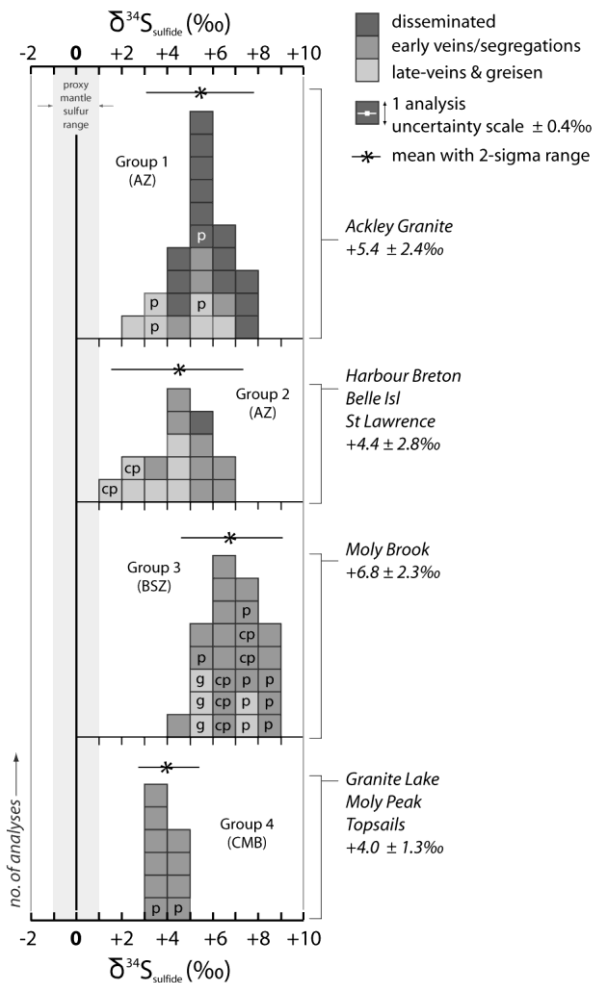


Figure 2. Sulfur isotope composition ($\delta^{34}\text{S}$) of granophile sulfides. Molybdenite was analysed except where labelled with cp (chalcopyrite), g (galena) or p (pyrite). Figure includes nine repeat analyses. Homogenous mantle sulfur range from Ohmoto (1986).

From east to west the results are as follows: In the Ackley Granite (Group 1), sulfide mineralization has an average ($\pm 2\sigma$) $\delta^{34}\text{S}$ value of $5.4 \pm 2.4\text{‰}$ ($n = 25$). Disseminated molybdenite has a relatively restricted range from 4.5 to 7.6‰. Vein and quartz-segregation molybdenite also falls within this range (4.8 to 6.6‰). Sulfides associated with quartz-topaz greisen and Sn mineralization have a wider range from 3.2 to 6.8‰. On the south coast (Group 2), sulfides have an average value of $4.4 \pm 2.8\text{‰}$ ($n = 16$). Disseminated and quartz-vein molybdenite values range from 3.7 to 6.7‰. Late-stage sulfide veins are isotopically lighter and range from 1.8 to 4.7‰. At Moly Brook (Group 3), vein-hosted sulfide mineralization has an average value of $6.8 \pm 2.3\text{‰}$ ($n = 25$) defining a relatively narrow range. Main-stage quartz-molybdenite-sulfide veins range from 4.5 to 8.5‰ and are relatively isotopically heavy. Late-stage galena and pyrite range from 5.2 to 7.5‰. The samples from the CMB (Group 4) have an average value of $4.0 \pm 1.3\text{‰}$ (n

= 10). Molybdenite in quartz-sulfide veins falls within a restricted range from 3.0 to 4.9‰.

4 Discussion and Conclusions

The $\delta^{34}\text{S}$ compositions display relatively narrow, overlapping ranges when viewed by the grouped datasets (Fig. 2). This indicates that for each group, a relatively consistent supply of ^{34}S -enriched sulfur was available during mineralization. This picture is comparable with the $\delta^{34}\text{S}$ compositions of granite-related sulfides from elsewhere in the Canadian Appalachians (e.g., Kontak 1990). The $\delta^{34}\text{S}$ compositions of granophile sulfides within the Avalon Zone (Groups 1 and 2) are similar to the values from the Moly Brook Mo-Cu deposit (Group 3) located in the Burgeo Subzone. This suggests similar causative processes and underlying geological controls for these mineralized areas, consistent with field and geochronological constraints. The $\delta^{34}\text{S}$ compositions of main-stage sulfides within the CMB (Group 4) overlap the values of other areas; however, they are marginally less ^{34}S -enriched.

Deviations in $\delta^{34}\text{S}$ values from the restricted ranges appear to have been influenced by local paragenetic change and mineralization style, rather than an additional sulfur source (e.g., wallrock-leached sulfur). For example, in Group 1 (Ackley Granite), main-stage sulfides (intragranitic disseminations and quartz-segregations) are ^{34}S -enriched and fall within a restricted range from ~ 4 to 8‰. However, late-stage greisen and vein sulfides are more ^{34}S -depleted and are somewhat more variable. A similar variation is visible for the Group 2 sulfides (Fig. 2). These isotopic fluctuations are likely due to changes in the physicochemical properties (i.e., T , pH , $f\text{O}_2$, $f\text{S}$) of the hydrothermal system as mineralization progressed (Ohmoto 1986).

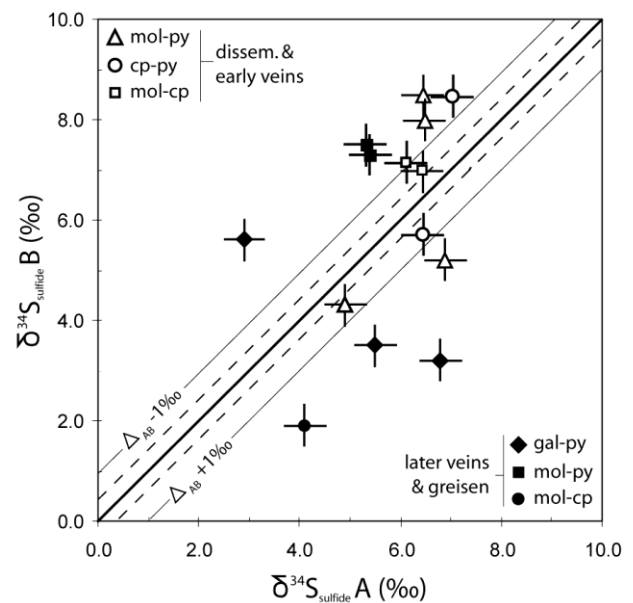


Figure 3. Sulfur isotope values of coexisting sulfide pairs. Thick line (slope = 1) indicates perfect equilibrium between pairs with dashed lines equal to the maximum analytical uncertainty. Disequilibrium of ± 1 per mil units also shown.

Variations in hydrothermal properties during mineral deposition can manifest itself as isotopic disequilibrium between coexisting sulfide pairs, as shown in Figure 3. In this study, isotopic equilibrium has been broadly maintained between sulfide pairs involved in early, main-stage mineralization, with an average isotopic fractionation (Δ_{AB}) of $\pm 1.2\%$. In contrast, sulfide pairs from late-stage veins and greisen display a greater degree of isotopic disequilibrium ($\Delta_{AB} = \pm 2.4\%$). This indicates a relatively stable magmatic-hydrothermal system prevailed during main-stage mineralization, while factors such as the availability of sulfur and/or changes in depositional redox state influenced the more variable $\delta^{34}\text{S}$ compositions of late-stage sulfides.

The $\delta^{34}\text{S}$ signature of Paleozoic granophile sulfides from Newfoundland is compatible with lower to mid-crustal sulfur that was sequestered by granitoid melts during orogenesis and transferred to upper crustal levels along shear zone fault systems (e.g., Sasaki and Ishihara 1979). Continued magma fractionation toward evolved granitic compositions provided a mechanism for progressive isotopic enrichment of the magmatic sulfur (cf. Poulsen et al. 1991). However, isotope studies of Ediacaran and Cambrian sedimentary sulfide from the Avalon platform suggest an upper crustal reservoir of ^{34}S -enriched sulfur potentially existed by the Devonian (e.g., Strauss et al. 1992, Canfield et al. 2007). Thus, the magmatic assimilation of sedimentary sulfur may also have played a role in the development of these ^{34}S -enriched granite-molybdenum systems.

Acknowledgements

We thank James Conliffe and Andy Kerr (GSNL) for assistance during field work. Chris Taylor and Craig Barrie are thanked for analytical help at SUERC. Mercator Minerals are thanked for access to the Moly Brook deposit. This study has been partly funded by a Thomas Crawford-Hayes research grant awarded to EPL by the School of Natural Sciences, NUIG.

References

Canfield DE, Poulton SW, Narbonne GM (2007) Late-Neoproterozoic deep-ocean oxygenation and rise of animal life. *Science* 315:92 – 315

Carten RB, White WH, Stein HJ (1993) High-grade granite-related molybdenum systems: Classification and origin. *Geological Association of Canada, Special Paper* 40:521 – 554

Chatterjee AK, Strong DF (1985) Review of some chemical and mineralogical characteristics of granitoid rocks hosting Sn, W, U, Mo deposits in Newfoundland and Nova Scotia. *Institute of Mining and Metallurgy, London*, 489 – 516

Colman-Sadd SP, Hayes JP, Knight I (1990) Geology of the island of Newfoundland. Newfoundland Department of Mines and Energy, Map 90-1, 1:1,000,000 scale

D'Lemos RS, Tribe IR, Pembroke, JW (1995) Emplacement and construction of Devonian 'posttectonic' granites, northeast Newfoundland Appalachians. Newfoundland Department of Natural Resources, Geological Survey, Report 95-1:221 – 235

Dunning GR, O'Brien SJ (1989) Late Proterozoic – early Paleozoic crust in the Hermitage Flexure, Newfoundland Appalachians: U/Pb ages and tectonic significance.

Geology 17:548 – 551

Elias P, Strong DF (1982). Palaeozoic granitoid plutonism of southern Newfoundland: Contrasts in timing, tectonic setting and level of emplacement. *Trans Royal Society Edinburgh Earth Sciences* 74:43 – 57

Kerr A (1997) Space-time composition relationships among Appalachian-cycle plutonic suites in Newfoundland. *Geological Society of America, Memoir* 191:193 – 220

Kerr A, van Nostrand TS, Dickson WL, Lynch, EP (2009) Molybdenum and tungsten in Newfoundland: A geological overview and a summary of recent exploration developments. Newfoundland and Labrador Dept of Natural Resources, Geological Survey, Report 09-1:43 – 80

Kontak DJ (1990) A sulfur isotope study of main-stage tin and base metal mineralization at the East Kemptville tin deposit, Yarmouth County, Nova Scotia, Canada: Evidence for magmatic origin of metals and sulfur. *Economic Geology* 85:399 – 407

Lynch EP, Selby D, Feely M, Wilton DHC (2012) The timing and duration of granite-related magmatic-hydrothermal events in southeastern Newfoundland: Results of Re-Os molybdenite geochronology. GAC-MAC 2012, St. John's, Canada. Programme and abstracts

Ohmoto H (1986) Stable isotope geochemistry of ore deposits. *Mineralogical Association of Canada, Reviews in Mineralogy*, 16:491 – 559

Ohmoto H, Goldhaber MB (1997) Sulfur and carbon isotopes. *Geochemistry of Hydrothermal Ore Deposits*, 3rd edn:517 – 611

Poulson SR, Kubilius WP, Ohmoto H (1991) Geochemical behavior of sulfur in granitoids during intrusion of the South Mountain Batholith, Nova Scotia, Canada. *Geochim Cosmochim Acta* 55:3809–3830

Sasaki A, Ishihara S (1979) Sulfur isotope composition of the magnetite-series and ilmenite-series granitoids in Japan. *Contributions to Mineralogy and Petrology*, 68:107 – 115

Strong DF (1980) Granitoid rocks and associated mineral deposits of eastern Canada and western Europe. *Geological Association of Canada, Special Paper* 20:741 – 769

Strong DF, Dickson, WL (1978) Geochemistry of Palaeozoic granitoid plutons from contrasting tectonic zones of northeast Newfoundland. *Canadian Journal of Earth Sciences*, 15:145 – 156

Strauss H, Bengston S, Myrow PM, Vidal G (1992) Stable isotope geochemistry and palynology of the late Precambrian to Early Cambrian sequence in Newfoundland. *Canadian Journal of Earth Sciences* 29:1662 – 1673

Whalen JB (1980) Geology and geochemistry of the molybdenite showings of the Ackley City batholith, southeast Newfoundland. *Canadian Journal of Earth Sciences*, 17:1248 – 1258

Williams H, Colman-Sadd, SP and Swinden, HS (1988). Tectonic-stratigraphic subdivisions of central Newfoundland. *Geological Survey of Canada, Paper* 88-1B:91 – 98

Williams H, Dickson, WL, Currie KL, Hayes JP, Tuach J (1989) Preliminary report on a classification of Newfoundland granitic rocks and their relations to tectonostratigraphic zones and lower crustal blocks. *Geological Survey of Canada, Paper* 89-1B:47 – 53

Van Staal CR, Dewey JF, MacNiocail C, McKerrow WS (1998) The Cambrian–Silurian tectonic evolution of the northern Appalachians and British Caledonides: History of a complex west- and southwest Pacific-type segment of Iapetus. *Geological Society of London, Special Publication* 143:199 – 242

Fault stepovers and gold mineralisation

Steven Micklethwaite

Centre for Exploration Targeting, The University of Western Australia, 35 Stirling Highway, Crawley, WA 6009, Australia

Abstract. The nucleation, growth and geometric properties of faults are critical to our understanding of fluid flow and mineralisation. Notably, many gold deposits have a spatial association with step-overs on large faults, although they tend to be hosted on subsidiary structures distributed away from the step-overs. Here, fault step-overs are examined from ancient, mineralised fault systems and compared to a control population of faults, comprising active fault systems and non-mineralised well-exposed fault systems. It is demonstrated that gold deposits are anomalously associated with underlapping fault step-overs. Underlap is typically rare in fault systems. The aspect ratios of underlapping mineralised step-overs may be scale-invariant across two orders of magnitude, similar to overlapping step-overs from the control population, though more data is required. Coulomb failure stress change calculations explain why underlap is necessary for the development of the observed distributions of gold deposits around step-overs. Field observations suggest that underlapping step-overs develop due to reactivation of pre-existing structures, or the presence of mechanical heterogeneities.

Keywords: step-over, jog, scaling, coulomb failure stress change, gold.

1 Introduction

Localised fluid flow through the Earth's crust is critically dependent on fault geometry and active deformation. In particular, fault stepovers are widely acknowledged to influence a broad range of phenomena related to fluid migration. These include fluid redistribution in the post-seismic period after an earthquake (Peltzer et al., 1996), the location of geothermal fields (e.g. Faulds et al., 2011), the migration of hydrocarbons (Fossen et al., 2010) and the distribution of ore grade mineralisation (e.g. Sibson, 1986; Connolly and Cosgrove, 1999; Ford et al., 2009; Micklethwaite et al., 2010; Zhang et al., 2012).

Given the association of hydrothermal ore deposits with step-overs it is somewhat surprising that no study exists systematically examining the detailed properties of step-overs associated with ore deposits. Connolly and Cosgrove (1999) used 2D photoelastic analogue experiments to investigate fluid flow around "dilatational" (releasing) step-overs. They modelled overlapping, neutral and underlapping fault geometries using mean stress as a proxy for fluid migration. Connolly and Cosgrove (1999) concluded fluid flow localised very close to large scale faults in the vicinity of step-overs. The experimental limitations at the time meant they were not able to account for the third dimension (and therefore vertical pressure gradients). Neither was data presented on the typical geometries of fault step-overs (e.g. Aydin and Schultz, 1990) and the experiments were not scaled. Weinberg et al., (2004) used simplified

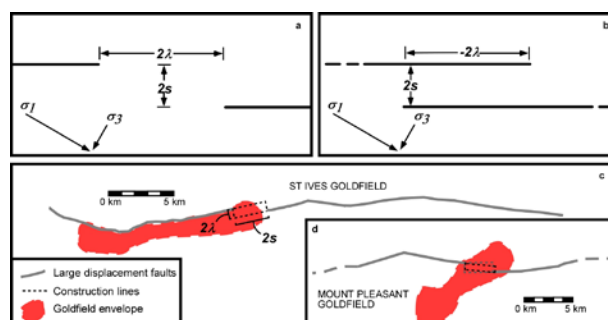


Figure 1. Parameters for field data analysis and model configuration. (a-b) Underlap and overlap fault configurations, for releasing step-overs with equivalent aspect ratios. Overlapping faults have a negative length dimension (-2λ). Separation ($2s$) is positive in both configurations. Inset is the maximum and minimum horizontal far-field principal stresses (σ_1 and σ_3 , respectively) applied to subsequent boundary element modeling. (c-d) Individual examples from the Mt Pleasant and St Ives goldfields respectively. (d) Two different sets of construction lines can be identified dependent on which fault tip dictates the orientation of the long-axis of the step-over.

1:500,000 scale fault maps of the Boulder-Lefroy shear zone (Archean Yilgarn craton, Western Australia), to identify correlations between geological complexity, shear zone trend and gold endowment. They concluded fluids were focused and gold deposits formed on the Boulder-Lefroy shear zone in dilatational sites of misorientation (e.g. releasing step-overs). Due to the scale of the study and the requirement for consistency in their source maps, data was not available for the detailed geometries of the mineralised step-overs. Neither of the studies outlined above explain the full range of characteristics of mineralised step-overs; including the location of deposits on second-order and third-order damage structures and the distribution of deposits >5 km away from the regional-scale structure and its step-overs.

In this study, published maps of step-overs associated with gold camps were compiled in order to analyse the geometries of step-overs. The aspect ratios and scaling properties of the step-over population were assessed and compared with equivalent, published data from non-mineralised fault systems (comprising non-mineralised active and inactive fault systems). A series of 3D boundary element numerical models are presented, based on a technique originally developed to assess the shear and normal stress changes occurring around fault slip events, which have a first-order control on secondary fracturing (c.f. Micklethwaite and Cox, 2004, 2006). The results provide a powerful explanation for the observed characteristics of mineralised step-overs. This study largely utilises data from greenstone-hosted mesothermal gold deposits (ie. orogenic-type) rather than other deposit styles (e.g. epithermal or porphyry).

2 Field Data

A number of characteristics are common, though not ubiquitous, in ore deposits from many different provinces. Deposits tend to cluster in camps associated with a regional scale structure. Deposits tend to be hosted in subsidiary structures (damage) adjacent to regional-scale structures and in association with a step-over. Deposit camps can be distributed >5 km away from the step-over.

In order to explore more fully the characteristics of mineralised step-overs, data were compiled from (1) fault maps of well-constrained ore camps, (2) previously published step-over studies of active fault systems (Aydin and Schultz, 1990; Wesnousky, 2008), and (3) published maps of inactive but well-exposed fault systems (e.g. Kim et al., 2004). Data pertain to fault systems mostly dominated by strike-slip movement. Figure 1 indicates the geometric parameters measured for the study, following a methodology modified from Aydin and Schultz (1990). For the purposes of this analysis, I used a convention such that the lengths of underlap fault configurations (2λ) have positive values and overlap configurations negative values (Figure 1). The data from the non-mineralised active and inactive fault systems were used as a control population for comparison with the mineralised population.

Three problems were encountered in quantifying the geometric properties of step-overs. First, small population statistics - only a limited number of published studies were of sufficient quality to provide appropriate information on mineralised step-overs. Second, the uniformity problem - published maps of non-mineralised fault systems are abundant but vary in accuracy. For these reasons, the data used for non-mineralised fault systems were either high-resolution (Kim et al., 2004) or employed strict mapping and quality control guidelines (e.g. Aydin and Schultz, 1990). Third, step-over linkage and the non-parallelism of adjacent fault segments introduce a degree of ambiguity during analysis. In this case, more than one length (2λ) and separation ($2s$) measure were taken from the step-over, determined by the orientation of each fault tip (e.g. Figure 1d). Measurements are straightforward for fault traces that are parallel (e.g. Figure 1c).

The aspect ratios of the step-overs (k) were measured using overlap length and separation (in metres). The modified form of the equation below prevents k tending to infinity in the special circumstance when adjacent fault segments align.

$$k = \frac{1 + 2\lambda}{1 + 2s}$$

Figures 2 and 3 derive from the Kalgoorlie greenstone terrane, Western Australia and the fault data compiled by Aydin and Schultz (1990). The following features of the mineralised and non-mineralised fault systems are shown. (1) Step-overs dominantly overlap, with only 9% of underlap (Figure 2; c.f. Aydin and Schultz, 1990). (2) There are more releasing than restraining overlaps but this relationship is marginally

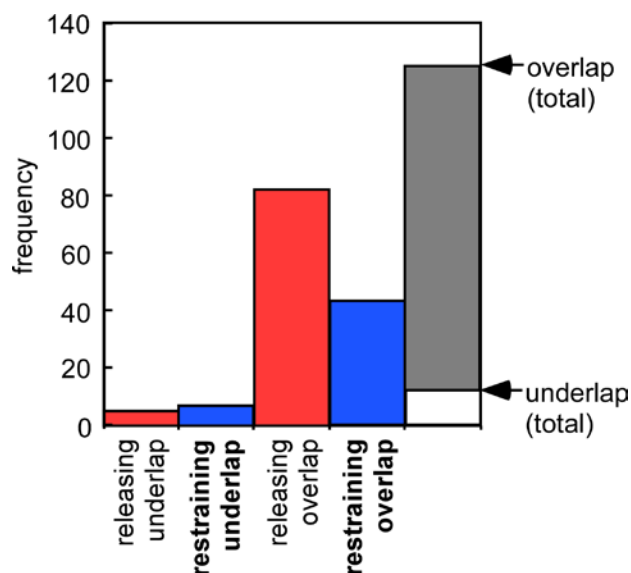


Figure 2. Relative frequencies of underlap and overlap fault configurations and their releasing/restraining characteristics (data from Aydin and Schulz, 1990).

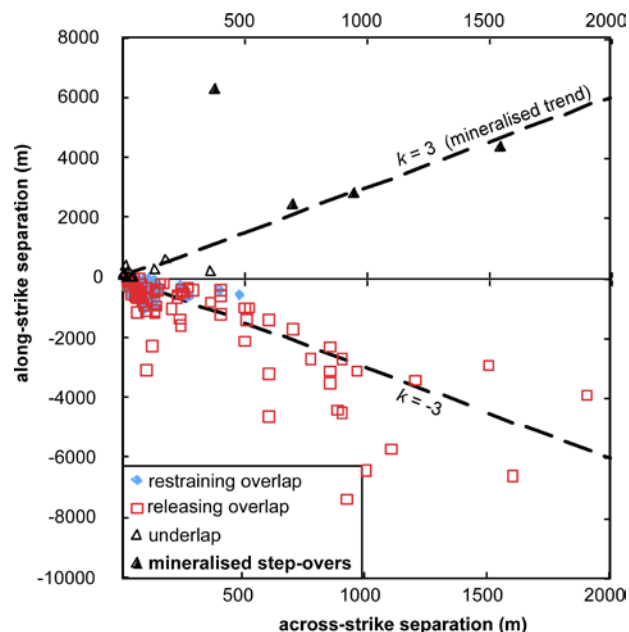


Figure 3. Plot of fault step-over length (2λ) and separation ($2s$). Data plotting above a separation of zero represents underlap step-overs. Mineralised step-overs from the fault systems analysed in this study anomalously underlap.

reversed for underlap configurations (Figure 2). (3) Overlap fault configurations follow a well-documented linear trend over several orders of magnitude (Figure 3; Aydin and Schultz, 1990; Soliva and Benedicto, 2004; Wesnousky, 2008). (4) The mineralised step-overs documented in this study are anomalously associated with underlap fault configurations (Figure 3). (5) Underlapping mineralised step-overs may also obey a linear scaling relationship over at least two orders of magnitude but more data is required.

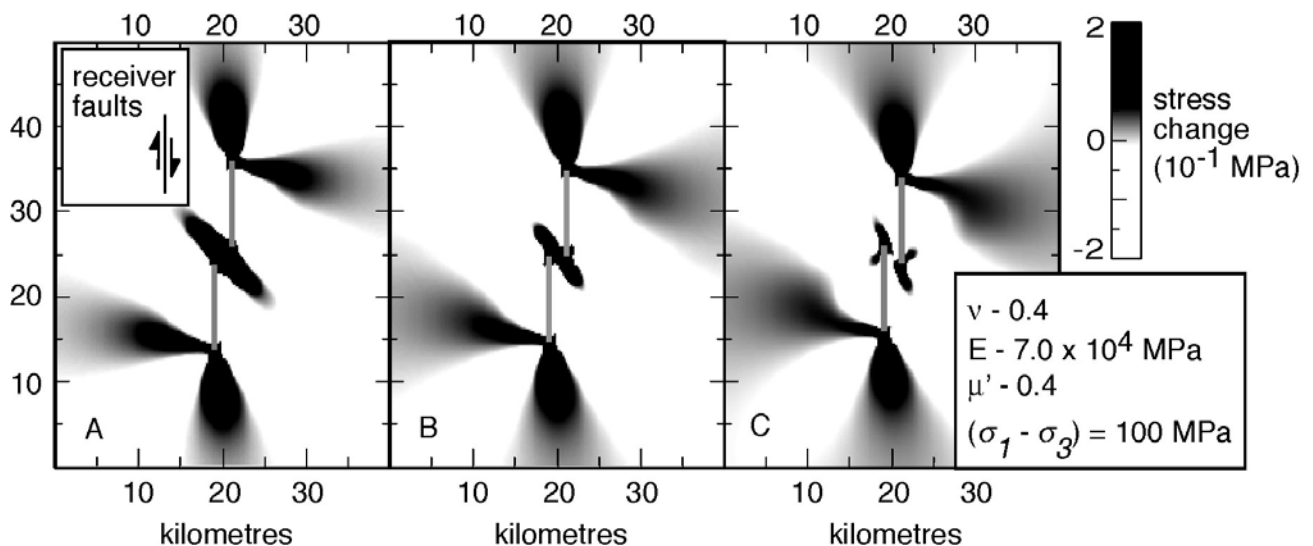


Figure 4. Coulomb failure stress change calculations, comparing the domains of triggering of second-order strike-slip faults in the vicinity of a releasing step-over. Positive stress changes are indicated by grey-scale. The step-over fault configuration changes in character from underlap, to neutral to overlap (left to right). ν – Poisson’s ratio, E – Young’s modulus, μ' – apparent friction.

3 Analysis

Incremental slip events on faults (e.g. earthquakes or creep events), alter the shear and normal stresses resolved on subsidiary structures. Coulomb failure stress change calculations are used to calculate this affect, and have been shown to correlate with the clustered distribution of near-field aftershocks in earthquake sequences (e.g. King et al., 1994; Hardeback, 2010), and the non-intuitive distribution of greenstone hosted, lode gold deposits around both releasing and restraining step-overs (Micklethwaite and Cox, 2006). The methodology is three dimensional and is fully described in King et al., (1994) and only briefly outlined here. Fault slip, with magnitude and distribution appropriate to an incremental slip event (earthquake or creep), is simulated as a dislocation in an elastic half-space and the static stress changes are quantified using a modified Coulomb failure criterion. The boundary parameters are friction, Poisson’s ratio, Young’s modulus, slip direction and the distribution and magnitude of slip on the modelled fault configuration (Figure 4).

I follow the configuration shown in Figure 1 and tested for Coulomb failure stress changes in both releasing and restraining step-overs that (1) underlap, (2) have zero length but a positive separation (e.g. neutral step-overs), and (3) overlap. The stress changes are calculated to test for activation of adjacent damage zone structures with reverse, normal and strike-slip fault characteristics. Figure 4 shows results for releasing step-overs with different length characteristics (underlap, neutral and overlap). The field of positive stress change differs dramatically from an underlap configuration to an overlap configuration, with the damage zone of triggered fracturing obtaining far greater dimensions around an underlap fault step-over. In the overlap scenario, the triggering of faulting is restricted to a small area around the step-over. By implication there is far greater potential

permeability enhancement in the underlap scenario and localised fluid migration can occur over a wider region.

4 Discussion

The observation that fault systems are dominated by overlap fault configurations is well known. Linear Elastic Fracture Mechanics (LEFM) provides a mechanical rationale suggesting linked overlap fault configurations are a natural outcome arising from interaction between two propagating fault segments, over geological time (Aydin and Schultz, 1990; Willemsse 1997). This study provides the first quantification of step-over configurations associated with gold deposits. Surprisingly, mineralised step-overs from the fault systems analysed are dominated by an association with the anomalous underlap fault configuration (Figure 3).

Coulomb failure stress changes have previously shown that the distribution of gold deposits around step-overs correlate with the regions where aftershocks, or creep-related microseismicity, are likely to have occurred after a large slip event (Micklethwaite and Cox, 2004, 2006; Micklethwaite et al., 2010). In this study the same approach explains why underlap fault configurations are favourable for high time-integrated fluid fluxes and the formation of gold deposits.

The remaining question that naturally arises is why do these underlap fault step-over configurations exist? In the example of the Kalgoorlie greenstone terrane, Western Australia, many world-class mesothermal lode goldfields are associated with regional scale strike-slip shear zones and step-overs. The Mount Pleasant goldfield (Micklethwaite and Cox, 2004) is located adjacent to a step-over on the Black Flag fault and is hosted in an antiform and a granodiorite intrusion. Along the Boulder-Lefroy fault zone both the supergiant Golden Mile deposit and the large New Celebration goldfield coincide with thick, folded intrusive bodies of

dolerite. The large St Ives goldfield, also along the Boulder-Lefroy fault zone is cored by the Kambalda anticline. In this latter example, the segmentation geometry of the large faults associated with the goldfield suggest that fold-limb thrusts were reactivated and linked as strike-slip faults during later deformation and mineralisation. These observations alone indicate that underlap fault configurations arise from the mechanical influence of pre-existing stratigraphy, or because fault geometry and propagation is dictated by reactivation of a pre-existing structural surface.

The results presented here have focused on gold mineralisation, particularly from greenstone hosted mesothermal systems but are likely to have wider application. For example, Ford et al., (2009) modelled faulting and fluid flow associated with Cu mineralisation in the Mt Isa inlier, Australia. On the basis of field observations they employed underlapping fault configurations to model the system. Sibson (1987) argued that clusters of epithermal deposits could be related to step-overs in large-scale strike slip fault systems. There is now a need to extend the results of this present study to a wider range of deposit types, and to examine whether different fault and fluid flow processes dominate mineralisation at different crustal levels, or whether there is a uniformity of process.

References

- Aydin, A, Schultz, R (1990) Effect of mechanical interaction on the development of strike-slip faults with echelon patterns: *Journal of Structural Geology* 12: 123-129
- Connolly, P, Cosgrove, J (1999) Prediction of static and dynamic fluid pathways within and around dilational jogs: *Geological Society of London Special Publications* 155: 105-121
- Faulds, JE, Hinz, NH, Coolbaugh, MF, Cashman, PH, Kratt, C, Dering, G, Edwards, J, Mayhew, B, McLachlan, H (2011) Assessment of favorable structural settings of geothermal systems in the Great Basin, western USA: *Geothermal Research Council Transactions* 35: 777-783
- Ford, A., Blenkinsop, TG, McLellan, JG (2009) Factors affecting fluid flow in strike-slip fault systems: coupled deformation and fluid flow modeling with application to the western Mount Isa Inlier, Australia: *Geofluids* 9: 2-23
- Fossen, H, Schultz, RA, Runhovde, E, Rotevatn, A, Buckley, SJ (2010) Fault linkage and graben stopovers in the Canyonlands (Utah) and the North Sea Viking Graben, with implications for hydrocarbon migration and accumulation: *AAPG Bulletin* 94: 597-613
- Hardebeck, J (2010) Aftershocks are well aligned with the background stress field, contradicting the theory of highly heterogeneous crustal stress: *Journal of Geophysical Research* 115: B12308, doi:10.1029/2010JB007586
- Kim, Y-S, Peacock, DCP, Sanderson, DJ (2004) Fault damage zones: *Journal of Structural Geology* 26: 503-517
- King, GCP, Stein, RS, Lin, J (1994) Static stress changes and the triggering of earthquakes: *Bulletin of the Seismological Society of America* 84: 935-953
- Micklethwaite S, Cox SF (2004) Fault-segment rupture, aftershock-zone fluid flow and mineralization. *Geology* 32: 813-816
- Micklethwaite S, Cox SF (2006) Progressive fault triggering and fluid flow in aftershock domains: Examples from mineralized Archean fault systems. *Earth and Planetary Science Letters* 250: 318-330
- Peltzer, G, Rosen, P, Rogez, F, Hudnut, K (1996) Postseismic rebound in fault step-overs caused by pore fluid flow: *Science* 273:1202-1204
- Sibson, RH (1987) Earthquake rupturing as a mineralizing agent in hydrothermal systems: *Geology* 15, 701-704, doi: 10.1130/0091-7613
- Weinberg, RF, Hodkiewicz, PF, Groves, DI (2004) What controls gold distribution in Archean terranes?: *Geology* 32: 545-548
- Wesnousky, S (2006) Predicting the endpoints of earthquake ruptures: *Nature* 444: 358-360
- Wesnousky, S (2008) Displacement and geometrical characteristics of earthquake surface ruptures: Issues and implications for seismic-hazard analysis and the process of earthquake rupture: *Bulletin of the Seismological Society of America* 98: 1609-1632
- Willemsse, EJM (1997) Segmented normal faults: Correspondence between three-dimensional mechanical models and field data: *Journal of Geophysical Research* 102: 675-692
- Zhang, Y, Schaub, PM, Sheldon, HA, Poulet, T, Karrech, A (2012) Modelling fault reactivation and fluid flow around a fault restraining step-over structure in the Laverton gold region, Yilgarn Craton, Western Australia: *Geofluids* in press

Pyrite trace element geochemistry of west and east Jiaodong gold district: insight into diverse metal sources in intrusion-hosted gold deposits

Stephanie E. Mills*, Andrew G. Tomkins, Roberto F. Weinberg
School of Geosciences, Monash University, Australia

Abstract. The Jiaodong gold district is located in northeast China, on the eastern margin of the North China Craton. Over 95% of mineralisation is hosted in Mesozoic granitic intrusions, which can be separated into east Jiaodong and west Jiaodong intrusive suites. Both suites host mineralisation. This study focuses on the trace element geochemistry and petrography of pyrite grains from east and west Jiaodong to identify differences in mineralisation style between the two areas. East Jiaodong pyrite grains are round in shape, inclusion-poor, have internal oscillatory zoning, and lack visible gold. Relative to west Jiaodong, east Jiaodong has elevated concentrations of As, Co, Cu, Mo, Sb and Se. West Jiaodong is characterised by large lath-like pyrite crystals that are inclusion rich and fractured. These lack internal zoning but host visible nuggety gold and electrum in fractures, along grain boundaries, and as inclusions. West Jiaodong Au mineralisation is strongly related to Ag, Bi, Pb and Te, and west Jiaodong pyrite grains host hydrothermal immobile element inclusions. The results from this study indicate that magmatism related to significant loss of lithospheric mantle in the eastern North China Craton preferentially influenced west Jiaodong, while convergent plate tectonics played a more important role in east Jiaodong.

Keywords. Jiaodong, pyrite, gold, trace element geochemistry

1 Introduction

The intrusion-hosted Jiaodong gold district is located on a 250km x 100km peninsula in the northeast Shandong Province of China (Fig. 1). With more than 100 gold deposits, ranging from 5t to 100t Au, the Jiaodong district has produced over 500t of gold as of 2010, contributing >20% to China's overall gold production (Zhou et al. 2002, Liqiang Yang pers. comm.). Over 95% of the Jiaodong gold deposits are structurally hosted along 2nd and 3rd order faults in Mesozoic granitoids, which intrude the Archean to Paleoproterozoic cratonic basement of the North China Craton (Qiu et al. 2002). The granitoids formed in two temporal pulses, the first at ~160 Ma, the second at ~130 Ma. Mineralisation ages across Jiaodong are 120 Ma ± 10 Ma. Traditionally, the Jiaodong district has been divided into three mineralisation belts: from west to east, these are the Zhao-Ye, Xixia, and Muping-Rushan belts (Qiu et al. 2002). Pyrite grains were collected from the largest belts, the Zhao-Ye and Muping-Rushan, both of which contain significant gold deposits hosted in Mesozoic intrusions.

This study focuses on the differences and similarities in pyrite morphology and trace-element geochemistry

between the Zhao-Ye belt (west Jiaodong) and the Muping-Rushan belt (east Jiaodong). There are significant variations between the two belts, reflecting heterogeneity in the processes that influenced mineralisation across Jiaodong. This is due to multiple tectonomagmatic events that affected the eastern North China Craton during the Phanerozoic, such as continental collision, trans-crustal faulting, oceanic subduction, and loss of cratonic lithospheric mantle. The variations in Jiaodong pyrite geochemistry provide insight into which of these major regional events affected the formation of the Jiaodong district.

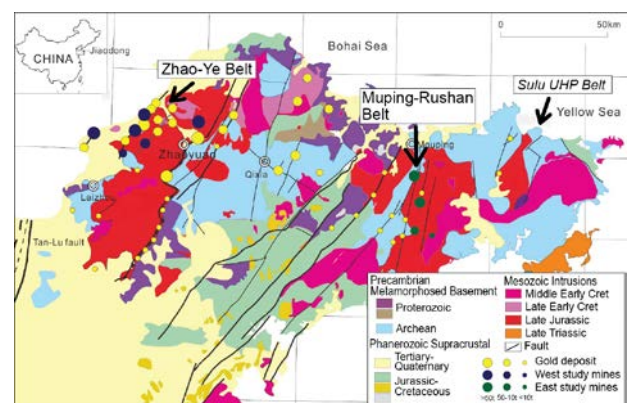


Figure 1. Geological map of the Jiaodong gold district (after Yang et al., submitted)

2 Methods

23 pyrite samples from 4 deposits (Jingqingding, Denggezhuang, Sanjia, Shicheng) were analysed for east Jiaodong, and 45 samples from 6 deposits (Xincheng, Jiaojia, Jiuqu, Wangershan, Sanshandao, Sizhuang) were analysed for west Jiaodong. Pyrite separates were picked by hand and crushed to a homogenised powder. The elements Ag, As, Ba, Be, Bi, Cd, Ce, Co, Cr, Cs, Cu, Ga, Ge, Hf, In, La, Li, Mn, Mo, Nb, Ni, P, Pb, Rb, Re, S, Sb, Sc, Se, Sn, Sr, Ta, Te, Th, Ti, Tl, U, V, W, Y, Zn, and Zr were analysed by ICP-AES and ICP-MS following a digestion by perchloric, nitric and hydrofluoric acids and leaching by dilute hydrochloric acid. Au analysis was done by atomic absorption spectroscopy (AAS) on a precious metal bead produced from a separate of the homogenised pyrite powder.

3 Pyrite Morphology

West Jiaodong pyrite grains are found as disseminated

mineralisation, veinlet mineralisation, and quartz-pyrite vein mineralisation. Pyrite grains in all styles of mineralisation are typically large (1-4mm), cubic to rectangular shaped, and inclusion-rich. They are also fractured, especially in disseminated mineralisation proximal to faults. Gold mineralisation occurs as macroscopic nuggets of gold in fractures, on the boundaries between pyrite grains, and as inclusions. Gold occurs as native gold or as electrum with up to 50% Ag. In disseminated mineralisation, gold occurs with galena and chalcopyrite and rarely sphalerite (Fig. 2). In veinlet and vein mineralisation there is a decrease in base-metal sulfides associated with Au mineralisation, often only galena or chalcopyrite, or none.

East Jiaodong pyrite grains typically have a pyritohedron rather than cubic crystal shape and can be completely rounded. They are generally less fractured and less inclusion-rich. There is no visible gold in the east Jiaodong pyrite grains, and while they rarely include other base metals sulfides, minor chalcopyrite inclusions have been observed. These pyrite crystals exhibit oscillatory zoning, which is absent in west Jiaodong pyrite grains (Fig. 2). As a whole, east Jiaodong has a much higher proportion of base-metal sulfide mineralisation, in some cases having economic concentrations of Cu mineralisation (Qiu et al. 2002). While this study focuses on pyrite geochemistry, east Jiaodong also has extensive chalcopyrite, galena, and sphalerite mineralisation, as well as occasional iron oxide minerals. The base metal sulfides appear to have formed mostly later than pyrite, though pyrite has been found to be co-genetic with chalcopyrite and (separately) with magnetite.

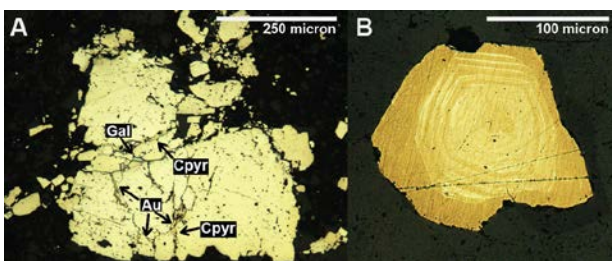


Figure 2. Comparison of pyrite from east and west Jiaodong (A) Fractured and inclusion-rich pyrite from west Jiaodong with fracture hosted Au, galena (Gal), and chalcopyrite (Cpyr) (B) Zoned east Jiaodong pyrite (zoning defined by surface oxidation).

4 Pyrite Trace Element Geochemistry

Selected results of pyrite geochemical analyses can be viewed as a comparison of east and west Jiaodong in Figure 3. West Jiaodong, relative to east Jiaodong, has higher concentrations of Au, Ba, Be, Cr, Ga, Hf, La, P, Rb, Sc, Sr, Ta, Ti, Th, Tl, U, W, and Zr. With minor exceptions, west Jiaodong also has higher concentrations of Bi, Ce, Nb, Pb, and Y. East Jiaodong has higher concentrations of As, Co, Cu, In, Li, Mo, Sb, and Se, as well as Ni and Zn with minor exceptions. Elements that did not show strong relative enrichment in west versus east include Ag, Cd, Cs, Ge, Mn, Re, S, Sn, Te, and V.

Element data for east and west Jiaodong were

analysed for correlations and trends within each district, especially with respect to Au mineralisation. This was done using self-organising map (SOM) analyses, based on vector quantisation methodology, followed by principal component analyses (PCA) of the SOMs.

In west Jiaodong, three distinct element correlation clusters are illustrated by SOM analyses with PCA overlay: (1) Au-Ag-Bi-Te, (2) Cd-In-Zn-(As-Sb), and (3) Be-Ce-Cs-Ga-Hf-La-P-Rb-Sc-Sr-Ta-Th-Ti-Tl-U-V-Y-Zr. Au clearly correlates with Ag, Bi, and Te, as well as Pb. Pb has two data populations, one correlated to the Au-Ag-Bi-Te cluster and one correlating to the Cd-In-Zn-(As-Sb) cluster. Cu has two data populations, one that relates to Sb and As, and one population that appears largely unique, but is most similar to Mo.

Using the same analyses within east Jiaodong, three element correlation clusters were defined: (1) Ag-Bi-Cd-Cu-In-Zn-(Pb), (2) Be-Ga-Ge-Rb-Tl, and (3) Hf-Nb-P-Ta-Th-Ti-U-V-W-Zr. Au appears to have two data populations: the larger population correlates with Te and Se, the smaller population with Ag-Bi-Cd-Cu-In and Pb. Pb also has a second population with no clear correlation, and As fails to correlate strongly with any element.

5 Discussion

Based on the work from Huston et al. (1995), it is generally accepted that elements in pyrite occur as (1) inclusions, (2) non-stoichiometric substitutions, and (3) stoichiometric substitutions. In the Jiaodong pyrite grains, we can expand “inclusions” to include metallic or metal-bearing inclusions and silicate inclusions. This is important as the main geochemical distinction of west Jiaodong pyrite grains is the higher relative concentration and correlation of immobile elements (LILEs, HFSEs, REEs). These pyrite grains are also more inclusion-rich, so it is likely that the immobile elements are largely controlled by silicate inclusions. In rare cases, pyrite has also been observed to have co-precipitated with monazite or contain zircon and apatite inclusions. Additionally, discrete zircon, apatite and rutile crystals are common as a hydrothermal phase (based on euhedral crystal shape in an otherwise cataclastic host rock and alignment along fractures) in disseminated mineralization. Metallic and metal-telluride inclusions have also been observed using SEM BSE imaging. These usually occur in Au-bearing pyrite grains and contain variable proportions of Ag, Bi, Sb, Pb, and Te. The presence of metallic inclusions, high Ag electrum, and galena associated with gold explain the correlation between Au-Ag-Bi-Te and Pb, particularly given that galena can contain significant Ag and Bi. The correlation of the Cd-In-Zn-(Sb-As) group is related to sphalerite, which occurs rarely but hosts In and Cd. The behaviour of Sb and As is still unclear, though only the Sanshandao deposit in west Jiaodong had significant quantities of both, which may present some data skewing.

Bulk rock compositions from west Jiaodong are depleted in immobile elements with respect to barren granites; hence, there is only relative, not absolute,

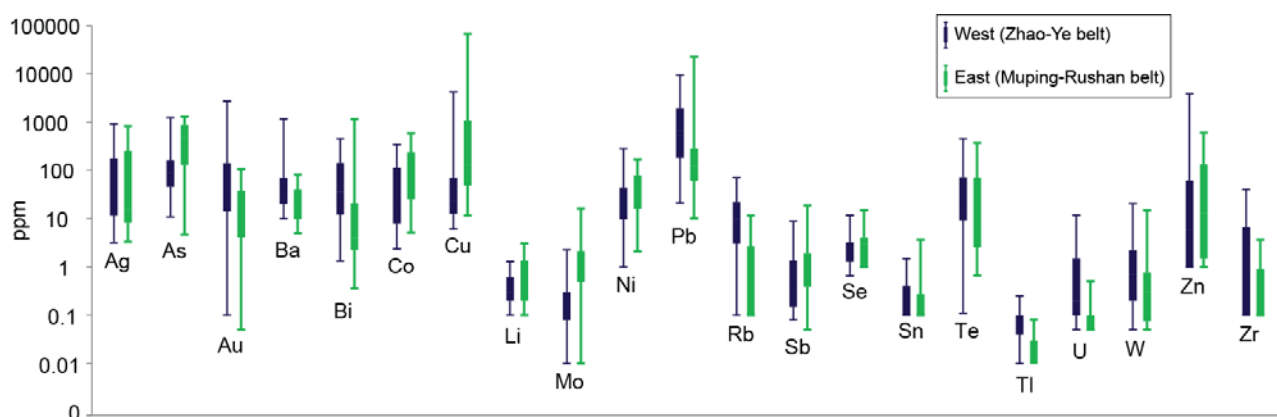


Figure 3. Box plot comparison of selected elements for east and west Jiaodong pyrite geochemistry. Boxes illustrate the combined middle two quartiles of data, with lines defining the maximum and minimum values.

enrichment of immobile elements in west Jiaodong pyrite grains. However, the presence of immobile elements in pyrite inclusions and discrete hydrothermal minerals requires a hydrothermal fluid capable of mobilising these elements. This would likely be a Cl⁻ or F⁻-rich fluid (e.g. van Dongen et al. 2010), characteristic of late stage felsic magmas. Enrichment of Au in the same magma could have been influenced by subducted oceanic slab, previously Au-enriched crust, or fertile mantle. The regional tectonic events capable of driving Au enrichment are (1) the onset of Pacific Plate subduction on the eastern margin of the North China Craton (Zhu et al. 2012) and (2) significant loss (>80km) of cratonic lithospheric mantle beneath the eastern North China Craton (Zheng et al. 2007), both of which are coeval with Jiaodong magmatism and mineralisation.

In the Pacific Plate subduction model, slab dehydration plus mantle wedge metasomatism and melting would modify the lithosphere and crust beneath Jiaodong, introducing Au into mantle-derived felsic magmas or hybrid magmas. However, there is still much debate on the location of the Pacific Plate subduction front through the Mesozoic, so it is unclear if the subduction front would have been close enough for Jiaodong to be affected by subduction-related processes.

Conversely, loss of over 80km of lithospheric mantle associated with extension, crustal thinning and asthenospheric upwelling, which is capable of generating high T metamorphism and associated crustal melting, is well documented to have occurred beneath Jiaodong (Zheng et al. 2007). This could account for Au enrichment if crustal melting occurred and scavenged gold from previously Au-enriched crust. Asthenospheric upwelling is also a process that could enrich Au in magma by addition of fertile mantle material. Asthenosphere will undergo decompression melting during upwelling, thereby adding mantle magma or releasing mantle volatiles into the lower crust. In an asthenospheric upwelling model, it is important to consider the Tan Lu fault, a major trans-crustal fault located 30km west of west Jiaodong. Seismic tomography shows mantle upwelling along the Tan Lu fault, and petrographic and geochemical studies of Cenozoic magmatism indicate that the Tan Lu served as a conduit for ascending asthenospheric magma during the Mesozoic (Wang et al. 2001, Xiao et al. 2010). The

mineralisation-controlling faults in west Jiaodong are thought to be related to the Tan Lu fault (Shandong Gold Group Co., Ltd. pers. comm.), so the Tan Lu may explain why crustal melting and/or fertile mantle upwelling influences west Jiaodong preferentially.

East Jiaodong pyrite grains lack the extensive inclusions and fractures observed in those from west Jiaodong, so element substitutions into pyrite are more important. East Jiaodong pyrite has higher As and Mo (non-stoichiometric substitutions) and Co, Ni, and Se (stoichiometric substitutions; Huston et al. 1995). East Jiaodong also has higher Cu, though chalcopyrite inclusions were rarely observed, so it is likely that instead Cu occurs as solid solution within pyrite. Higher As concentrations affect Au mineralisation, as higher As in pyrite facilitates increased Au precipitation (e.g. Reich et al. 2005 and references within). These authors also refer to common oscillatory zoning of As and Au, so although in situ geochemical analyses of the zoning of east Jiaodong pyrites are yet to be done, it is a reasonable hypothesis that the zoning is related to As and Au variations. However, the As-Au trend is not the same in all deposits, as only the Jingqingding deposit has a positive correlation between Au and As, whereas Sanjia and Denggezhuang have increasing As contents with constant Au. This may be due to a limited availability of Au, and likely accounts for the lack of As correlation with other elements. The correlations between Ag-Bi-Cd-Cu-In-Zn-(Pb) reflects the control of base metal sulfides, which are more common in east Jiaodong: Cd, In and Zn relate to sphalerite; Pb relates to galena which hosts Ag and Bi; chalcopyrite accounts for Cu.

Given the economic Cu in some deposits (Qiu et al. 2002), it is interesting to note that elevated Cu, Co, Mo, Ni, Sb, and Se in east Jiaodong pyrite grains bear a strong similarity to pyrite compositions in some porphyry Cu-Au deposits (Reich et al. 2013). The elevated As concentrations are analogous to orogenic gold deposits, which likely owe their high As contents to liberation of metamorphic fluids from metasedimentary crust (Pitcairn et al. 2006, Tomkins 2010). The similarity of the pyrite compositions to those in porphyry Cu systems as well as the elevated As concentrations are consistent with the involvement of subduction-related processes; these appear to have played a more significant

role in east Jiaodong than in west Jiaodong. Since east Jiaodong would be closer to an eastward-migrating Pacific Plate subduction front, it may have been in a more spatially favourable position to be influenced by subduction-related ore genesis.

Additionally, east Jiaodong is bordered to the southeast by the Sulu UHP terrane, which was formed by Triassic (~230-220Ma) continental collision of the Yangtze Craton and the North China Craton (Hacker et al. 2006). This collision resulted in the NNW-directed subduction of continental crust over 135km beneath the North China Craton (Hacker et al. 2006), including east Jiaodong, which is ~20 km from the Sulu UHP terrane. Although the subduction of Yangtze Craton continental crust predates mineralisation by ~100m.y., the proximity to east Jiaodong and significant depth of subduction make it possible that material released by metamorphism of the down-going crust was incorporated in the lithospheric mantle and/or crust beneath east Jiaodong, available for mobilisation by later events triggering mineralisation, such as Pacific Plate subduction. Although the extent to which Pacific Plate and Yangtze Craton subduction influenced mineralisation in east Jiaodong is debateable, it appears that being affected by two different styles of convergent plate tectonics and subduction produced noticeable differences in east Jiaodong with respect to west Jiaodong.

6 Conclusion

Pyrites from east and west Jiaodong gold district were analysed for trace element geochemistry to compare mineralisation styles in both areas of the district. Mineralisation across Jiaodong occurs in a restricted temporal pulse and is fundamentally similar for intrusion-hosted deposits; however, pyrite geochemistry indicates that east and west Jiaodong may have been differentially influenced by selected regional processes. West Jiaodong, with mobilisation of immobile elements and relative enrichment in Au, is likely to have been more affected by magmatic processes related to large-scale lithospheric mantle loss and asthenospheric upwelling. East Jiaodong is thought to be preferentially affected by convergent plate tectonics and subduction-related processes due to enrichment in As, liberated from subducting continental crust, as well as Cu, Co, Mo, Ni, Sb, and Se, which bears strong similarity to Cu porphyry mineralisation characteristic of convergent plate margins.

Acknowledgements

This research is supported by Monash University and grants from the Society of Economic Geology and IOM3. We thank Drs. Hongrui Fan and Liqiang Yang as well as Shandong Gold Mining Co., Ltd. for their invaluable support during field work.

References

Hacker BR, Wallis SR, Ratschbacher L, Grove M, Gehrels G (2006) High-temperature geochronology constraints on the tectonic

- history and architecture of the ultrahigh-pressure Dabie-Sulu Orogen. *Tectonics* 25:5.
- Huston DL, Sie SH, Suter GF, Cooke DR, Both RA (1995) Trace elements in sulfide minerals from eastern Australian volcanic-hosted massive sulfide deposits. *Econ Geol* 90:1167-1196.
- Pitcairn IK, Teagle DAH, Craw D, Olivo GR, Kerrich R, Brewer TS (2006) Sources of metals and fluids in orogenic gold deposits: Insights from the Otago and Alpine schists, New Zealand. *Econ Geol* 101:1525-1546.
- Qiu Y, Groves DI, McNaughton NJ, Wang LG, Zhou T (2002) Nature, age, and tectonic setting of granitoid-hosted, orogenic gold deposits of the Jiaodong Peninsula, eastern North China Craton, China. *Min Dep* 37:283-305.
- Reich M, Deditius A, Chryssoulis S, Li JW, Ma CQ, Parada MA, Barra F, Mittermayr F (2013) Pyrite as a record of hydrothermal fluid evolution in a porphyry copper system: A SIMS/EMPA trace element study. *Geochim Cosmochim Acta* 104:42-62.
- Reich M, Kesler SE, Utsunomiya S, Palenik CS, Chryssoulis SL, Ewing RC (2005) Solubility of gold in arsenian pyrite. *Geochim Cosmochim Acta* 69:2781-2796.
- Tomkins AG (2010) Windows of metamorphic sulfur liberation in the crust: Implications for gold deposit genesis. *Geochim Cosmochim Acta* 74:3246-3259.
- Van Dongen M, Weinberg RF, Tomkins AG (2010) REE-Y, Ti, and P remobilization in magmatic rocks by hydrothermal alteration during Cu-Au deposit formation. *Econ Geol* 105:763-776.
- Wang Q (2001) Rotational collision and the Tan-Lu transform fault, in: Briegel U, Xiao WJ (Eds.) *Paradoxes in Geology*. Elsevier Science, pp. 65-75.
- Xiao Y, Zhang HF, Fan WM, Ying JF, Zhang J, Zhao XM, Su BX (2010) Evolution of lithospheric mantle beneath the Tan-Lu fault zone, eastern North China Craton: Evidence from petrology and geochemistry of peridotite xenoliths. *Lithos* 117:229-246.
- Yang LQ, Goldfarb RJ, Zhang J, Gao BF, Wang ZL (Submitted for publication) 40Ar/39Ar geochronological constraints on the formation of the Dayingezhuang gold deposit: New implications for timing and duration of hydrothermal activity in the Jiaodong gold province, China. *Econ Geol*, submitted.
- Zheng JP, Griffin WL, O'Reilly SY, Yu CM, Zhang HF, Pearson N, Zhang M (2007) Mechanism and timing of lithospheric modification and replacement beneath the eastern North China Craton. *Geochim Cosmochim Acta* 71:5203-5225.
- Zhou T, Goldfarb RJ, Neil PG (2002) Tectonics and distribution of gold deposits in China: An overview. *Min Dep* 37:249-282.
- Zhu G, Jiang D, Zhang B, Chen Y (2012) Destruction of the eastern North China Craton in a backarc setting: Evidence from crustal deformation kinematics. *Gondwana Res* 22:86-103.

The Mariana-San Marcos vein system: shallow features of epithermal Au-Ag deposits, Cerro Negro District, Deseado Massif, Argentina

Conrado Permuy Vidal, Diego M. Guido and Sebastián M. Jovic

Instituto de Recursos Minerales (INREMI), Facultad de Ciencias Naturales y Museo, Universidad Nacional de La Plata, Paseo del Bosque s/n, B1900FWA, La Plata, Argentina.

Consejo Nacional de Investigaciones Científicas y Técnicas (CONICET). Buenos Aires, Argentina.

Gassaway Brown

Goldcorp Inc., Av. Apoquindo 4501, Las Condes, Santiago, Chile CP 7580125.

Abstract. The Mariana-San Marcos vein system is located in the Cerro Negro project, Deseado Massif province, Patagonia Argentina. Mineralization is characterized by low sulfidation type epithermal Au-Ag quartz veins with exceptional widths and length. During the last years, Au-Ag reserves have grown significantly at Cerro Negro to proven and probable reserves of 5.74 Moz Au, 49.36 Moz Ag at the end of 2012. Epithermal veins are hosted by Late Jurassic volcanic and/or intrusive rocks of andesitic to rhyodacitic composition, grouped in the Bahía Laura Complex. Cerro Negro epithermal veins are composed of eight mineralization stages grouped in 3 episodes with quartz-adularia crustiform-colloform banding textures and minor breccias. The highest Au-Ag grades are related to the early stages in clay-rich bands and/or in late tectonic-hydrothermal breccias. This system shows several diagnostic features of a shallow epithermal environment. These features may be grouped into textural (crustiform-colloform bandings and sulfide-rich “ginguro bands”); mineralogical (zeolites and truscottite), and geological (hydrothermal eruption breccia and hot spring deposits) features, comparable with other epithermal vein deposits such as Hishikari (Japan); Waihi, Golden Cross and Favona (New Zealand) and to active geothermal systems such as Yellowstone (USA) and Coromandel and Taupo Volcanic Zone (New Zealand). These shallow features related to high grade veins, should be considered in further exploration in the Deseado Massif metallogenial province.

Keywords. Shallow features, low sulfidation, epithermal, Jurassic, Deseado Massif, Patagonia.

1. Introduction

Epithermal deposits form in the shallow parts of high-temperature hydrothermal systems generally hosted by coeval and older volcanic rocks and/or underlying basement rocks and rarely by subvolcanic intrusions (Simmons et al. 2005). Shallow levels are characterized by several features including hydrothermal eruption breccias, sinter deposits, silicified finely laminated air-fall or lacustrine sediments, steam heated blankets and sheeted veins to the upper portions of some fissure vein system (Nelson and Giles 1985; Hedenquist et al. 2000; Corbett 2004; Simmons et al. 2005).

The Deseado Massif (southern Argentinean Patagonia) comprises a broad area of 60,000 km² with mainly Au-Ag low-sulfidation type epithermal deposits and numerous hot spring occurrences (Schalamuk et al. 1999; Guido and Schalamuk 2003; Echavarría et al.

2005; Fernández et al. 2008; Guido and Campbell 2011). Those deposits are related to a widespread Middle to Upper Jurassic volcanic-hydrothermal event of andesitic to rhyolitic composition and calc-alkaline affinity grouped in the Bahía Laura Volcanic Complex (BLVC). This volcanic succession is part of the Chon Aike Silicic Large Igneous Province (Pankhurst et al. 1998), developed in Argentinean Patagonia to Antarctica, and interpreted as a diffuse extensional back-arc setting associated with opening of the South Atlantic Ocean.

The region is an important gold and silver producer (3 Moz of gold and over 40 Moz of silver) from four operational mines (Cerro Vanguardia, Martha, Manantial Espejo and San José). In addition, two new mines are under construction, including Cerro Negro, and more than 50 epithermal projects are undergoing different levels of exploration. The Cerro Negro District is located at the western margin of the Deseado Massif comprising ~26,500 ha of mining property held 100 percent by Goldcorp since December 2010. Based on resource calculations, Cerro Negro will become a promising gold producer in the Deseado Massif with significantly expanding reserves and resources.

At the northwestern part of the Cerro Negro District mineralization consist of steeply dipping low-sulfidation Au-Ag epithermal veins with exceptional widths and length (Eureka, Marianas and San Marcos veins). The aim of this study is to recognize mineralogical, textural and geological diagnostic features of a shallow epithermal environment represented in the Mariana-San Marcos vein systems.

2. Cerro Negro District geological setting

The Cerro Negro veins lies within an Upper Jurassic thick volcanic sequence of the BLVC dated by U-Pb at 159-156 Ma (Lopez 2006). The stratigraphic sequence begins with andesitic lava flows interbedded with dacitic ignimbrites. These rocks are intruded by andesitic and dacitic subvolcanic bodies and late rhyolitic lava domes, flows and pyroclastic equivalents. The volcanic succession is topped by widespread fluviolacustrine and volcanoclastic deposits (Fig.1). During the last stages of BLVC volcanism a large hydrothermal system (~15 km² on surface) developed in the Cerro Negro area, creating low-sulfidation veins and

breccias, regional hydrothermal alteration and surface hot spring manifestations (Lopez 2006).

3. The Mariana-San Marcos epithermal vein system

The Marianas-San Marcos epithermal vein system is located in the central part of the Cerro Negro District and is characterized by mineralized structures occupying major normal faults and/or splays at the limits of a NNW striking half-graben structure. Veins are hosted in andesites and some of them are capped by hydrothermal eruption breccias and volcanoclastic deposits leaving restricted surface expression to few outcrops and quartz-bearing floats (Permuy Vidal et al. 2012; Fig. 1).

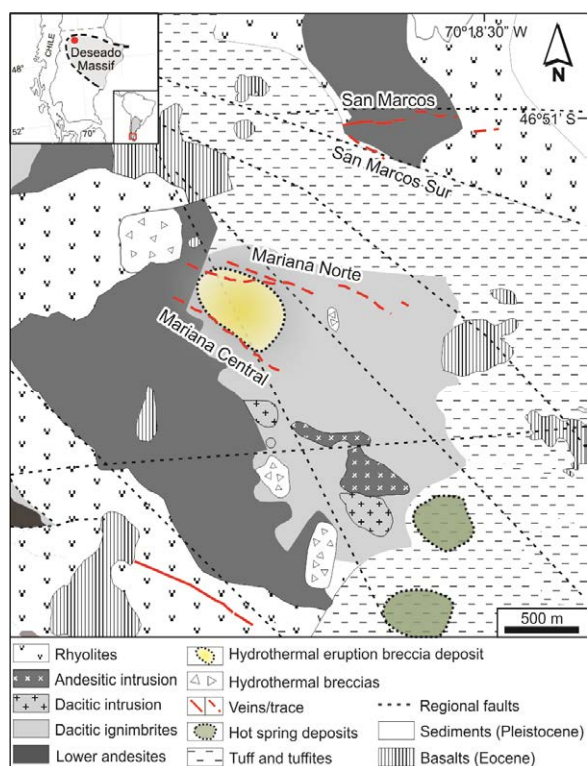


Figure 1. Geological map of the Mariana-San Marcos area with the location of the hydrothermal eruption breccia and hot spring deposits (modified from Guido and Campbell 2012).

To the south, the Mariana veins includes NW-WNW trending north steeply dipping structures (60° to 80°) with Mariana Norte vein at $N260^\circ$ and Mariana Central at $N305^\circ$ azimuths. Mariana Norte consists of a main tabular WNW trending structure with hanging-wall splays. Exploration drillings defined 850 m of strike length of the main structure, with mineralization reported down to 350 m below surface. The main structure average thickness is 3.5 m but can reach up to ~10 meters. Furthermore, Mariana Central is composed of a main thick structure, with sub-parallel discontinuous footwall and hanging-wall splays. The vein trend dimensions are 950 m long with an average of over 5 m thick, reaching a maximum thickness of 20 meters.

At the northern end of the district, the San Marcos

vein system comprised of the San Marcos Sur vein located in a regional NW striking and south-dipping major fault. Mineralization is mostly discontinuous within the fault zone extending 300 m in length and 300 m in depth. The currently more significant San Marcos vein is located at a dilatational E-W splay of the major San Marcos Sur fault with steep dips of $85-90^\circ$ to the north and south to the eastern margin. This structure has been explored along 800 m length and reported mineralization extends to 400 meters in depth with an average thickness of 4 m and a maximum of 15 meters.

3.1. Vein paragenesis

The Mariana-San Marcos vein systems are composed of quartz Au-Ag bearing epithermal veins characterized by several mineralization stages with crustiform-colloform banding textures and minor breccias. Carbonate replacement textures are observed locally but are not closely related with mineralization.

Eight mineralization stages were described and grouped into four main episodes. The first episode (E1 or high grade episode) is composed of crustiform-colloform banding textures and minor breccias with decreasing content of adularia, clay minerals (mainly smectites), zeolite group minerals (mordenite) and minor truscottite among quartz (after amorphous silica and/or chalcedony). High grade Au-Ag is related to early clay-sulfide rich bands or spots (“ginguro bands”), and/or disseminated in quartz bands. The second episode (E2 or barren episode) is the most voluminous, and consists of massive quartz, breccias and veinlets (fine comb quartz amethyst variety and carbonate pseudomorphs) with minor amounts of adularia and zeolites. E2 culminates with massive calcite with comb quartz filling in the remaining open space, as veinlets or breccias with crosscutting relationships over early stages. The third episode (E3) appears preferentially in WNW and E-W structures and it is locally composed of a locally hematite stained quartz (after chalcedony and amethyst variety) and colloform banding with disseminated sulfides. Lately E3 is composed by clay-rich matrix milled breccia with rounded clasts of the previous stages and locally displays erratic high silver contents associated with dark Ag-sulfosalts-rich matrix.

4. Evidence of a shallow depositional environment

Epithermal deposits form in the shallow parts of high-temperature mainly subaerial hydrothermal systems. Low-sulfidation epithermal type generally associated with bimodal (basalt-rhyolite) or intermediate in composition volcanism in a wide range of extensional tectonic settings (Sillitoe and Hedenquist 2003; Simmons 2005). These systems may be vertically zoned being hot spring gold type end-member with compelling field evidence for mineralization within the upper few hundred meters beneath the paleosurface (Nelson 1995).

The Mariana-San Marcos vein system is characterized by the presence of several diagnostic

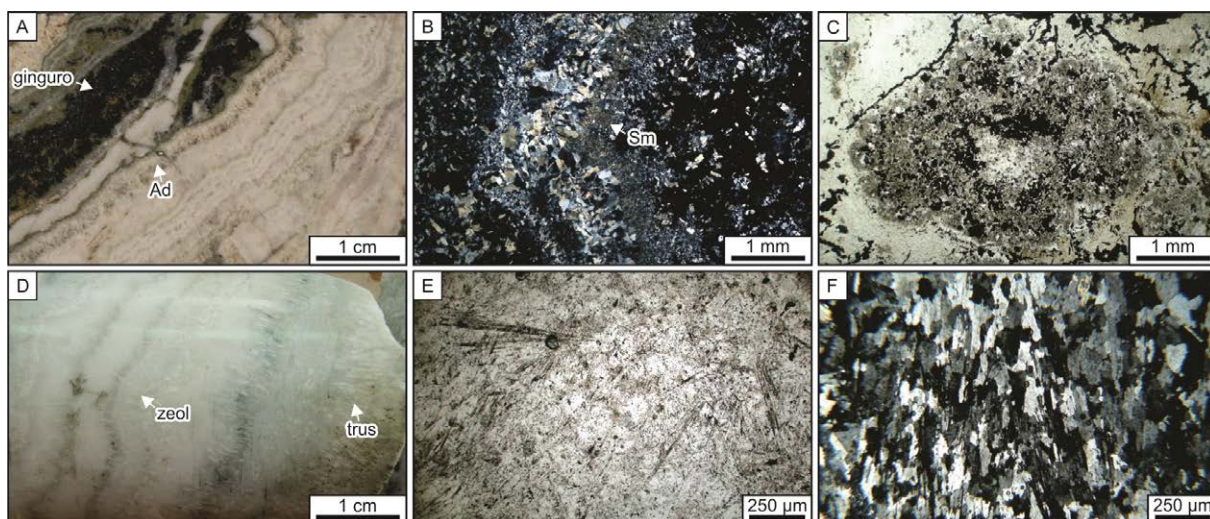


Figure 2. Shallow environment evidences for the Mariana-San Marcos vein system. a) Quartz-adularia (Ad) crustiform-colloform banding with early sulfide-rich “ginguro bands” associated with clay minerals. b) Microphotograph showing the alternation of quartz bands and euhedral smectites (X nicols). c) Microphotograph of recrystallization texture of quartz after amorphous silica with associated sulfides (// nicols). d) Crustiform-colloform banding texture with quartz replacement after radial fibrous minerals interpreted as zeolites (zeolites) and truscottite (trus). e) Microphotograph of the fibrous radial zeolites (// nicols) and f) truscottite (X nicols).

features of shallow formation conditions in the epithermal environment. These were grouped into textural, mineralogical and geological features.

4.1. Textural features

The mineralized veins are dominantly filled by quartz-adularia crustiform-colloform banding (Fig. 2a), a diagnostic texture of low-sulfidation vein deposits (Corbett 2004; Simmons 2005) also found in geothermal pipes at Broadlands-Ohaaki, active geothermal environment (Simmons and Browne 2000). Fine grained millimeter-scale quartz bands are characterized by recrystallization textures after amorphous silica or massive chalcedony (Fig. 2b and c), indicating low-temperature silica precursors (Dong et al. 1995).

Discontinuously, and interlayered with the quartz bands, high grade Au-Ag mineralization occurs as dark, sulfide-rich “ginguro bands” (Fig. 2a,b and c) composed mainly of sphalerite, chalcopyrite, acanthite, electrum, and, with minor amounts of galena, pyrite, pyrrargyrite and miargyrite. This term was originally used at the Hishikari world class deposit in Japan, and is also mentioned in other typical shallow epithermal deposits (e.g. Izawa et al. 1990; Brathwaite and Faure, 2002; Spörl and Cargill, 2011).

4.2. Mineralogical features

Crustiform-colloform banding presents a distinctive mineralogical assemblage within milky quartz bands, characterized by fibro-radiated acicular minerals partially replaced by quartz interpreted as zeolites (mordenite) and truscottite (hydrated Ca-Mn-Al silicate) (Fig. 2d, e and f). Zeolite minerals are commonly associated with low-temperature hydrothermal alteration assemblages. However, in Mariana-San Marcos veins they occur as gangue minerals also mentioned in some

deposits in New Zealand (Simpson and Mauk 2011). Truscottite was particularly found in association with high Au-Ag grades in the Hishikari deposit and reveals rapid cooling conditions after boiling and/or mixing with cold ground waters (Izawa et al. 1990).

Another mineralogical occurrence is the presence of clay minerals in the banding defined as euhedral smectites (Fig. 2b). These occur associated within ore minerals in “ginguro bands” and/or form discrete fine bands. Euhedral crystals of smectites are an evidence of direct precipitation from the hydrothermal fluid at low-temperature conditions (Faure 2002).

4.3. Geological features

The Marianas veins are capped by a hydrothermal eruption breccia deposits, extending to an area of ~0.2 km² and containing interlayered volcanoclastic deposits (Permuy Vidal et al. 2012). The overall cover extends to depths of 50 m and is characterized by intensely altered matrix breccia with major andesite host rock clasts and quartz-bearing banded fragments just above veins. Hydrothermal eruption breccias described in active geothermal environments and they form by the rapid expansion of depressurized geothermal fluids (e.g. Hedenquist and Henley 1985; Nelson and Giles 1985; Browne and Lawless 2001). Some of the eruption breccia systems cap sheeted veins (e.g. McLaughlin, USA), which extend into the breccia, while others cap mineralized fissure vein systems (e.g. Yamada, Japan; Favona, New Zealand).

Moreover, travertine hot spring deposits located about 1 km to the southeast of the Marianas veins and associated with two large ENE-WSW volcanic eruptive centers, were described and characterized by Guido and Campbell (2012). Those authors suggest that the diverse facies associations, size and other main characteristics of these deposits make them comparable to deposits as

the Yellowstone National Park (Wyoming, U.S.A.) and others.

5. Concluding remarks

The Mariana-San Marcos vein system represents an end-member of hydrothermal systems with several diagnostic features of formation in a shallow environment comparable with other deposits such as Hishikari (Japan); Waihi, Golden Cross and Favona (New Zealand) and to active geothermal systems such as Yellowstone (U.S.A.) and Coromandel and Taupo Volcanic Zone (New Zealand). Shallow characteristics were grouped into textural features including fine-grained quartz-adularia crustiform-colloform bandings, and dark sulfide-rich bands named “ginguro bands”. Mineralogical features relate to quartz replacement after fibro-radiated acicular minerals (zeolites and truscottite), intergrown within milky quartz bands, and the presence of euheudral clay minerals (smectites) in association with ore minerals and/or forming discrete bands. Finally the geological features observed correspond to hydrothermal eruption breccia deposit above some of the mineralized veins and travertine hot spring deposits at ~1km distance from vein system.

Low-sulfidation, hot spring gold type shallow deposits are enriched in precious metals with variable amounts of base metals. In that sense the Cerro Negro District high grade Au-Ag deposits are related to shallow epithermal features representing a new model for the Deseado Massif province, and must be considered in further exploration of the region.

Acknowledgements

This work is part of a PhD thesis carried out at the Universidad Nacional de La Plata (UNLP) and supported by Goldcorp Inc. The authors wish to thank the Cerro Negro staff for providing geological data and drill-cores.

References

Brathwaite RL, Faure K (2002) The Waihi epithermal gold-silver-base metal sulfide-quartz vein system, New Zealand: Temperature and salinity controls on electrum and sulfide deposition. *Economic Geology* 97: 269-290.

Browne PR and Lawless J (2001) Characteristics of hydrothermal eruptions, with examples from New Zealand and elsewhere. *Earth-Science Reviews* 52: 299-331.

Corbett G (2004) Epithermal and Porphyry Gold - Geological Models. In PACRIM 94 (The Australasian Institute of Mining and Metallurgy, Adelaide): 15-24.

Dong G, Morrison G, Jaireth S (1995) Quartz textures in epithermal veins, Queensland; classification, origin and implication. *Economic Geology* 90: 1841-1856.

Echavarría LE, Schalamuk IB, Etcheverry RO (2005) Geologic and tectonic setting of Deseado Massif epithermal deposits, Argentina, based on El Dorado-Monserrat. *Journal of South American Earth Sciences* 19: 415-432.

Faure K (2002) The Hishikari Au-Ag Epithermal Deposit, Japan: Oxygen and Hydrogen Isotope Evidence in Determining the Source of Paleohydrothermal Fluids. *Economic Geology*, 97: 481-498.

Fernández RR, Blesa A, Moreira P, Echeveste H, Mykietiuik K, Andrada de Palomera P, Tessone M (2008) Los depósitos de

oro y plata vinculados al magmatismo jurásico de la Patagonia: revisión y perspectivas para la exploración. *Revista de la Asociación Geológica Argentina* 63 (4): 665-681.

Guido DM and Schalamuk IB (2003) Genesis and exploration potential of epithermal deposits from the Deseado Massif, Argentinean Patagonia. In: Eliopoulos et al. (editors). *Mineral Exploration and Sustainable Development*. Balkema-Rotterdam, Vol I: 493-496.

Guido DM and Campbell KA (2011) Jurassic hot spring deposits of the Deseado Massif (Patagonia, Argentina): Characteristics and controls on regional distribution. *Journal of Volcanology and Geothermal Research* 203: 35-47.

Guido DM and Campbell K (2012) Diverse subaerial and sublacustrine hot spring settings of the Cerro Negro epithermal system (Jurassic, Deseado Massif), Patagonia, Argentina. *Journal of Volcanology and Geothermal Research* 229-230: 1-12.

Hedenquist J, Arribas R, Gonzalez Urien E (2000) Exploration for epithermal gold deposits. *Reviews in Economic Geology*, 13(1): 45-277.

Hedenquist JW and Henley RW (1985) Hydrothermal eruptions in the Waitapu geothermal system, New Zealand; their origin, associated breccias, and relation to precious metal mineralization. *Economic Geology* 80: 1640-1668.

Izawa E, Urashima Y, Ibaraki K, Suzuki R, Yokoyama T, Kawasaki K, Koga A, Taguchi S (1990) The Hishikari gold deposit: high-grade epithermal veins in Quaternary volcanics of southern Kyushu, Japan. *Journal of Geochemical Exploration* 36: 1-56.

Lopez RG (2006) Estudio Geológico-Metalogénico del área oriental al curso mediodel Río Pinturas, sector noroeste del Macizo del Deseado, provincia de Santa Cruz, Argentina. Unpublished PhD thesis, Universidad Nacional de La Plata, 226 p.

Nelson C (1995) Gold Deposits in the Hot Spring Environment. *Arizona Geological Society Digest* 20: 417-431

Nelson CE and Giles DL (1985) Hydrothermal eruption mechanisms and hot spring gold deposits. *Economic Geology* 80: 1633-1639.

Pankhurst R, Leat P, Sruoga P, Rapela C, Marquez M, Storey B, Riley T (1998) The Chon Aike province of Patagonia and related rocks in West Antarctica: a silicic large igneous province. *Journal of Volcanology and Geothermal Research* 81: 113-136.

Permyu Vidal C, Guido DM, Brown G (2012) The Marianas Epithermal Au-Ag vein system in the Cerro Negro district, Deseado Massif, Patagonia, Argentina. SEG 2012 Conference, Lima, Peru: "Integrated Exploration and Ore Deposits". ISBN: 978-1-934969-41-0.

Schalamuk IB, de Barrio R, Zubia M, Genini A, Echeveste H (1999) Provincia Auroargentífera del Deseado, Santa Cruz. In: *Recursos Minerales de la República Argentina* (Ed. E. Zappettini), Instituto de Geología y Recursos Minerales SEGEMAR, Anales 35: 1177-1188.

Simmons SF and Browne PR (2000) Hydrothermal Minerals and Precious Metals in the Broadlands-Ohaaki Geothermal System: Implications for Understanding Low-Sulfidation Epithermal Environments. *Economic Geology* 95: 971-999.

Simmons SF, White NC, John DA (2005) Geological Characteristics of Epithermal Precious and Base Metal Deposits, in: *Economic Geology, 100th Anniversary Volume*. Society of Economic Geologists: 485-522.

Simpson MP and Mauk JL (2011) Hydrothermal Alteration and Veins at the Epithermal Au-Ag Deposits and Prospects of the Waitekauri Area, Hauraki Goldfield, New Zealand. *Economic Geology*, 106: 945-973.

Sillitoe RH and Hedenquist JW (2003) Linkages between Volcanotectonic Settings, Ore-Fluid Compositions, and Epithermal Precious Metal Deposits. *Society of Economic Geologists, Special Publication Series* 10: 314-343.

Sporli K and Cargill H (2011) Structural evolution of a world-class epithermal orebody: The Martha Hill Deposit, Waihi, New Zealand. *Economic Geology* 106: 975-998.

Primary and secondary deposits from the Crisoleja area (Pb-Zn-Ag-Sn), La Unión, Murcia, Spain

Núria Pujol, Aleu Andreazini Sabaté, Stefania Schamuells, Sandra Amores Casals, Cristina Villanova-de-Benavent, Lisard Torró, Joan Carles Melgarejo
Departament de Cristal·lografia, Mineralogia i Dipòsits Minerals, Universitat de Barcelona, Barcelona, Catalonia, Spain

José Ignacio Manteca

Departamento de Ingeniería Minera, Geológica y Cartográfica, Universidad Politécnica de Cartagena, Murcia, España

Abstract. The Pb-Zn-Ag-(Sn) deposits of the central part of the Sierra de Cartagena formed by replacement of Triassic carbonate levels located in two Alpine thrust sheets. The replacement was produced by hydrothermal fluids associated with Miocene subvolcanic intrusives. Crisoleja, Agrupa-Vicenta, Cabezo Rajado and Pablo y Virginia mines are located in a proximal position, with regards to these intrusives. Primary mineral assemblages are replaced successively by greenalite, kaolinite, magnesian chlorite, ferric chlorite (associated with cassiterite, pyrite, quartz and minor amounts of uraninite, monazite and zircon) and finally Mn-siderite with cronstedtite, sphalerite, galena and bertrandite. Chlorites are enriched in Zn. This sequence, with late enrichment in Al, Sn and Be, may be interpreted as a result of the circulation of a magmatic fluid. In weathered zones, cassiterite remains unaltered and does not show variations in the composition. The other minerals are easily altered to goethite and to a sequence of minerals of the alunite supergroup.

Keywords. cassiterite, bertrandite, mineral sequence, supergene, alunite

1 Introduction

The mining area of La Unión, close to the city of Cartagena (Murcia, SE Spain), has been mined since ancient times until late 20th century. Some of the oldest mines are located in the central zone of the Sierra de Cartagena (S of La Unión town) and in the Cabezo Rajado hill (W of La Unión town). Nowadays some of the mining facilities have been restored with touristic purposes.

This district has been mined for Pb-Zn-Ag. The main ores define a zonation, already detected by Pavillon (1972; Fig. 1) and classified by Oen et al. (1975a) and Manteca & Ovejero, 1992). Tin-rich mineralizations are located in the central area of the Sierra, from the Crisoleja zone to the north. This metallogenetic distribution suggests the existence of felsic intrusive bodies at depth which represent potential sources of Sn.

As stated above, the deposits of La Unión were mined for base metals. However, the discovery of Sn in the central sector indicates that there might be other elements of economic interest which have not been mined before. The aim of this work is to evaluate the rare element content of the mineralization, both in primary and secondary ore deposits.

2 Geological setting

The Sierra de Cartagena constitutes the NE termination of the Béticas Range in the Iberian Peninsula, and it is parallel to the coast in an approximate E-W direction. In this range, two thrust sheets of Alpine age are distinguished, from the base to the top (IGME, 1974): the Nevado-Filábride complex, composed of series affected by medium grade metamorphism and the Alpujarride complex, formed by series affected by middle to low grade metamorphism. Both complexes are constituted by thick levels of carbonates inserted between detrital series.

The previous setting is discordantly covered by Miocene sediments. Also during the Miocene, a calc-alkaline magmas of acidic to intermediate composition intruded in this zone. Furthermore, it is possible to recognise a series of magmatic breccia, very extended in the Crisoleja and northern zone. These breccias indicate the proximity of the intrusive body.

3 Structure of the deposits

In the studied area it is possible to identify different types of deposits (Oen et al. 1975): a) deposits in different levels replacing carbonates in successive thrust sheets (i.e., Agrupa Vicenta mine); b) vein deposits, generally as small veinlets (i.e., Pablo and Virginia mine); c) zones with strong gossanization (i.e., Crisoleja mine).

Replacement deposits vary in size, have irregular morphology, and contain massive mineralization. In the central zone, relicts of the carbonate level are unusual, because replacement has been especially intense.

Veins may have highly variable sizes. Their width varies from a few mm to several metres. They are mainly subvertical but many other dipplings are observed, as well. These veins may appear associated to replacement mineralization. In that case, most contacts with the adjacent rock are sharp, although some are irregular.

Gossan zones occupy several km² in the Sierra de Cartagena south slope, as in the Crisoleja mine. They form as a result of weathering of some mineralized bodies outcropping as structural surfaces. In some zones the replacement of primary mineralization by supergene minerals is complet.

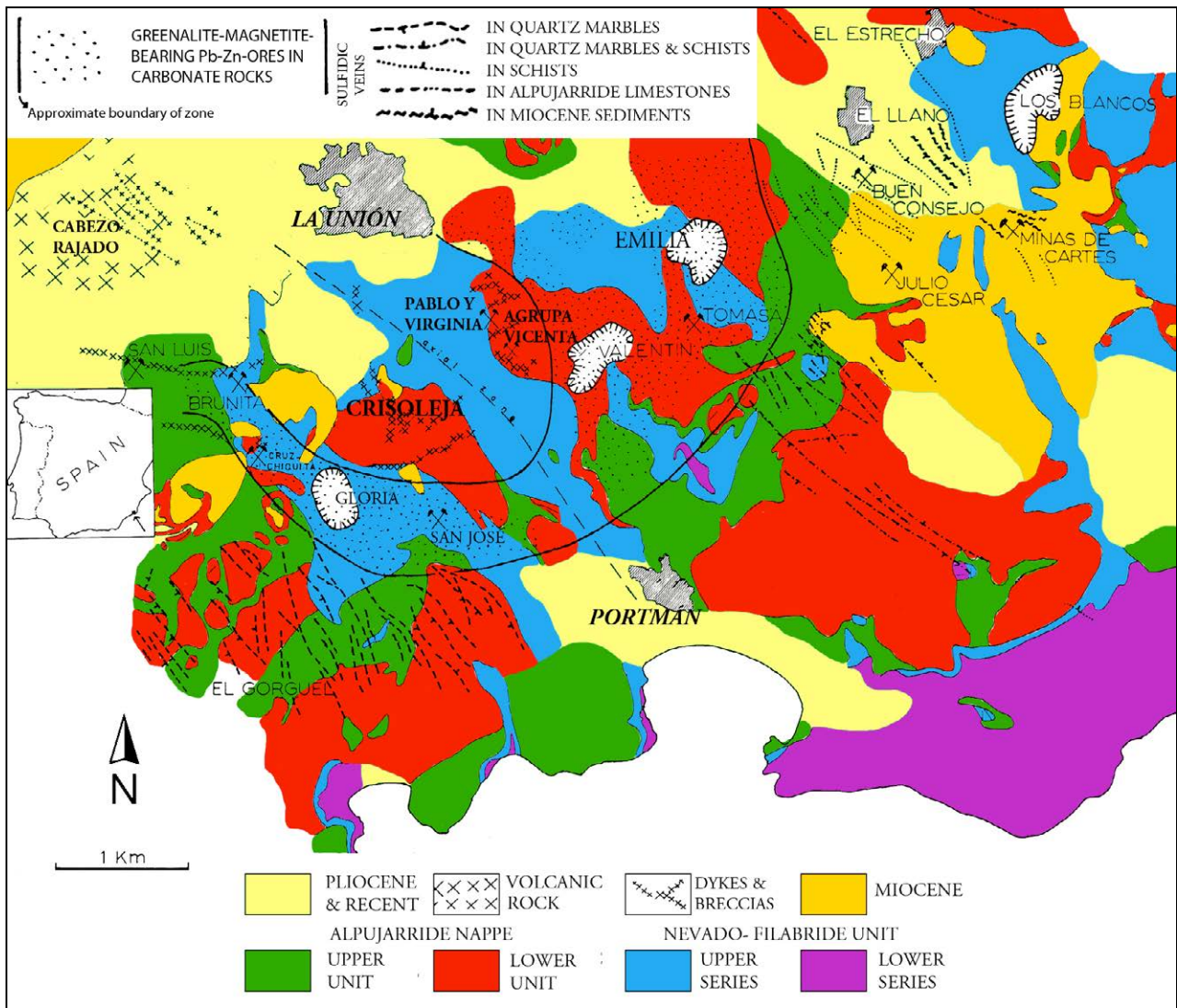


Figure 1. Geological map of the Sierra de Cartagena. Adapted from Pavillon (1972) and Oen et al. (1975a).

4 Mineralogy and textures

Fresh, primary ores are almost completely replaced by supergene associations in some areas, in particular, at the La Crisoleja locality.

Hydrothermal replacement can be observed in some non-weathered areas, as in Pablo y Virginia and Agrupa Vicenta mines, and consists of microcrystalline quartz aggregates, generally subhedral, coexisting with large amounts of euhedral pyrite (Fig. 2). Some interstitial porosity is filled by magnesian chlorite with kaolinite, which may be replaced by chamosite, siderite and small amounts of fine-grained cassiterite (Fig. 3).

The mineral sequences in non-weathered veins show similar patterns to those described in the replacement zones. Veins show a perfect symmetric structure, indicating open space filling, with comb or cockade textures (Fig. 4). According to the observations, there is a first generation of clinocllore followed by later kaolinite, and this in turn is replaced by chamosite. Associated to these phyllosilicates, a high concentration of cassiterite crystals is observed. Cassiterite forms euhedral prismatic crystals up to 20 microns in length. It may coexist with minor amounts of

zircon, monazite, xenotime and uraninite. All these mineral phases are very fine grained. Comb-shaped quartz grows over these mineral assemblages, developing euhedral crystals up to several centimetres in length. The centre of cavities is occupied by lenticular crystals of Mn-rich siderite, associated with millimetric to centimetric marmatitic sphalerite and galena crystals. Frequently these crystals are related to tabular hematite crystals, pseudomorphosed after magnetite (mushketovite) and bertrandite. Bertrandite displays tabular crystals up to 50 mm long, scattered in siderite; may be associated with barite (Fig. 5). The identification of bertrandite is confirmed by Raman spectroscopy. Finally, the latest cavity filling consists of cronstedtite tabular crystals, commonly forming radial aggregates.

The mineral assemblage is completely different in the weathered areas. In general, boxwork features are observed, formed by botryoidal goethite aggregates. Frequently, the boxwork porosity is filled by other secondary minerals. Minerals of the alunite group commonly grow over goethite. Some alunite crystals in Crisoleja display visible zonation, with initial hydronium jarosite and natrojarosite. Anglesite and/or cerussite precipitates normally in the final porosity.

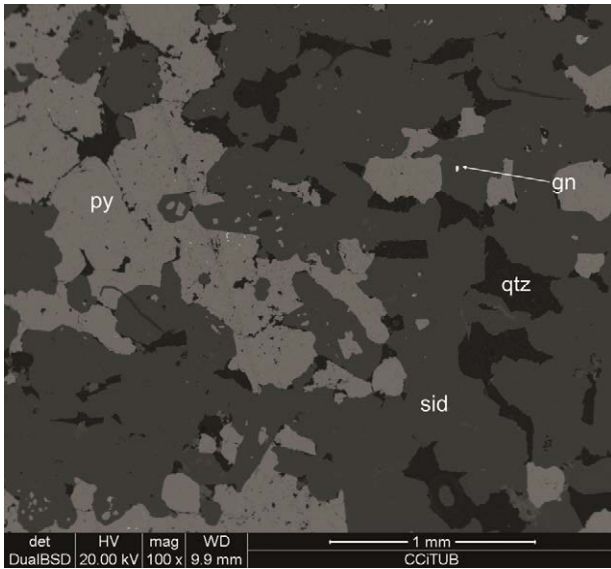


Figure 2. General aspect of the replacement bodies in Agrupa Vicenta mine. Note the porosity and occurrence of small galena (gn) grains in pyrite (py); the gangue mineral are quartz (qtz) and siderite (sid). SEM image, BSE mode.

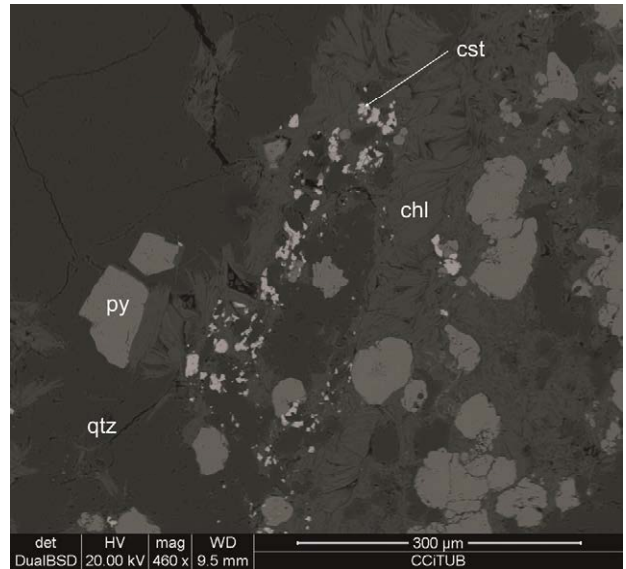


Figure 3. Drusical infilling of veins: cassiterite (cst), chamosite chlorite (chl), pyrite (py), and quartz (qtz). SEM image, BSE mode.

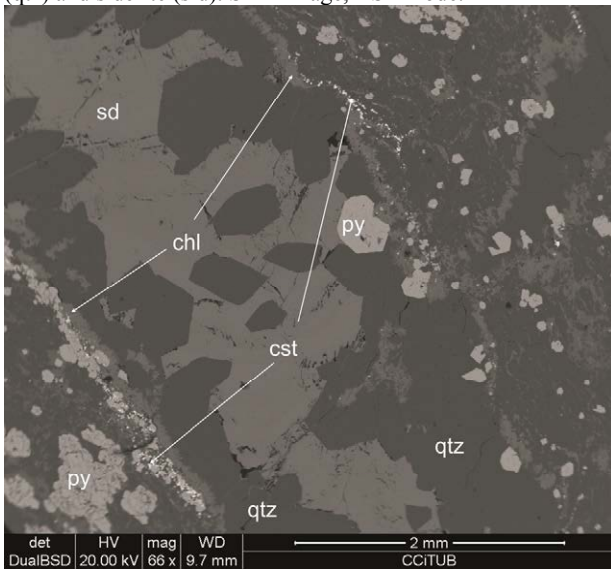


Figure 4. Drusical veins: cassiterite (cst), chlorite (chl), pyrite (py), siderite (sd), quartz (qtz). SEM image, BSE mode.

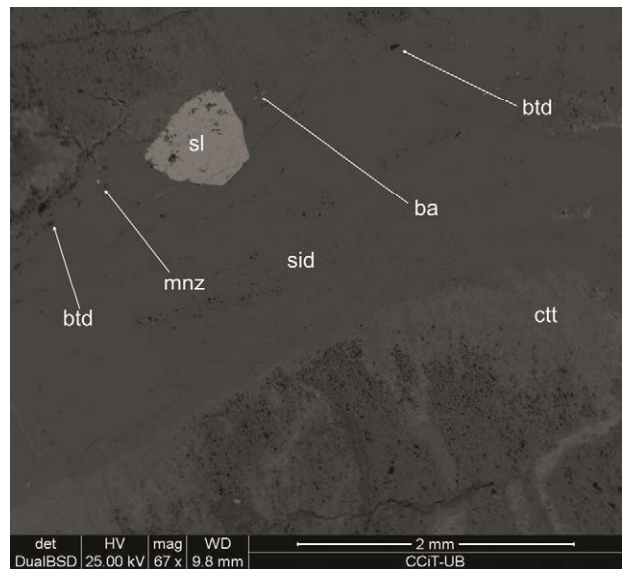


Figure 5. Late vein infillings: monazite (mnz), cronstedtite (ctt), sphalerite (sl), siderite (sid), barite (ba), bertrandite (btd). SEM image, BSE mode.

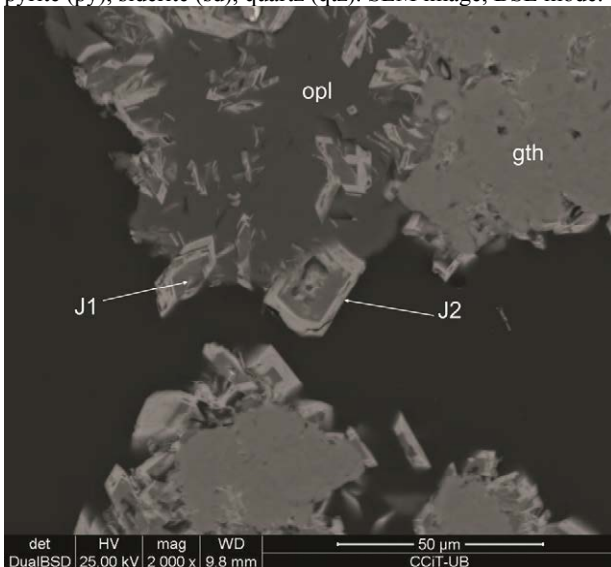


Figure 6. Typical sequence of gossan: goethite (gth), opal (opl) overgrown by natrojarosite (J1) and plumbojarosite (J2). SEM image, BSE mode.

5 Discussion and conclusions

The presence of Sn and Be suggest that the hydrothermal fluids may have an igneous origin. This is also supported by the presence of interstitial Al-rich minerals (such as chlorite and kaolinite) as products of hydrothermal alteration. However, Ta and Nb contents in cassiterite are low, indicating that the intrusive would be not much evolved. Significant In contents were not detected. In addition, no evidence of contact metamorphism was found. All these observations suggest that the studied mineralizations are in a distal position with regards to the possible intrusive.

Bertrandite origin is controversial. This mineral is relatively abundant in the late veins of Pablo y Virginia. Its concentration may be much higher than what has been observed, because it is not easily identified due to its fine-grained character. Oen et al (1975b) also detected bertrandite associated with grealite, but in

the intermediate zone of the Sierra de Cartagena. Thus, the presence of bertrandite spreads towards the most internal zone. This mineral phase is nowadays the main beryllium ore, and it is being mined in Spor Mountain (USA). In this case, the deposits formed by replacement of tuff levels under the influence of very fractionated intrusives, rich in topaz, rare elements, F and volatiles (Barton & Young 2002).

These differentiated magmas seem to be characteristic of anorogenic zones. Thus, this model is not applicable in the case of La Unión. In this context, the intrusives outcropping in the Sierra de Cartagena are calc-alkaline with intermediate compositions, related to convergent margins (IGME, 1974). Except for minor amounts of fluorapatite, significant concentrations of F-bearing minerals were not found in La Unión deposits. In relation to the transport of Be, from Beus (1966) most authors suggest F-rich fluids; and in absence of F, some authors explain that Be is transported as carbonate or sulphate complexes (Griffitts 1965). According to Barton (1986), bertrandite indicates a crystallization temperature below 450°C.

The presence of uraninite in the late stages, related to REE minerals, indicates redox processes during the precipitation of metals.

The alteration sequences found in the gossan of Crisoleja are different from those described for the zone of Cartagena by different authors. These references stated the presence of argentojarosite (Amorós et al. 1981, Lunar et al. 1981, 1982, Amorós et al. 1984, López García et al. 1988). However, the samples studied for this contribution show significant compositional variations at the centimetre scale in the same specimen. As a result, the mineral sequence formed in this environment depends on the availability of the different metals in the ores that are being altered. In the gossan, no differences are observed between cassiterite from the fresh zone and from the altered zone, which indicates that this mineral is stable in this context.

Acknowledgements

Samples were analyzed in the Centres Científics i Tecnològics of the University of Barcelona. Dr. X. Llovet helped in the microprobe calibration. Funding was provided by the Consolidated Research Group Grant SGR 444 of the Generalitat de Catalunya.

References

- Amorós JL, Lunar R, Tavira P (1981) Jarosite: A silver bearing mineral of the gossan of Río Tinto (Huelva) and La Unión (Cartagena). *Mineralium Deposita* 16: 205-213.
- Amorós JL, Lopez J A, Lunar R, Martinez J, Sierra J and Vindel E (1984) Chalcopyrite-sphalerite textures in same spanish syngenetic and epigenetic deposits: Guadarrama Mountain, Aznalcollar and La Union. In: Wauschkuhn et al. (Eds). *Syngeneses and Epigenesis in the Formation of Minerals Deposits*. Springer-Verlag Special volume, 18-27.
- Barton MD (1986) Phase equilibria and thermodynamic properties of minerals in the BeO-Al₂O₃-SiO₂-H₂O (BASH) system, with petrologic applications. *Am Mineral* 71: 277-300.
- Barton MD, Young S (2002) Non-pegmatitic deposits of beryllium: Mineralogy, geology, phase equilibria and origin: *MSA Rev. Mineral* 50, 591-691.
- Beus AA (1966) *Geochemistry of beryllium and genetic types of beryllium deposits*. W. H. Freeman & Co., San Francisco-London.
- Griffitts WR (1965) Recently discovered beryllium deposits near Gold Hill, Utah. *Econ Geol.* 60: 1298-1305.
- IGME (1974) Mapa geológico de España 1: 50,000, Sheets 978 Llano del Beal and 977 Cartagena: Inst. Geol. Minero España, Madrid.
- López García J, Lunar R, Oyarzun R (1988) Silver and lead mineralogy in gossan type deposits of Sierra de Cartagena (S.E. Spain). *Trans. Instn. Min. Metall. (Sect. B: Appl. earth sci.)* 97: 82-88.
- Lunar R, Amorós J, Tavira P (1980) The mineralogy and silver distribution of the gossan of Río Tinto (Huelva) and La Unión (Cartagena). Spain. 26th Congress Geologique International. Paris.
- Lunar R, Manteca JI, Rodríguez P, Amorós JL (1982) Estudio mineralógico y geoquímico del gossan de los depósitos de Fe-Pb- Zn de la Unión (Sierra de Cartagena). *Bol. I.G.M.E.* 93: 244-253.
- Manteca JI, Ovejero G (1992) Los yacimientos Zn, Pb, Ag-Fe del distrito minero de La Unión-Cartagena, Bética Oriental". *Recursos Minerales de España*. CSIC. Col Textos Universitarios, 15: 1085-1102.
- Oen IS, Fernández JC, Manteca JI (1975a) The Lead-Zinc and Associated Ores of La Union, Sierra de Cartagena, Spain. *Econ. Geol.* 70: 1259-1278.
- Oen IS, Uiterwijk BH, Voermans FM (1975b) Bertrandite and Be-enrichment in greenalitic Pb-Zn-ores, Sierra de Cartagena, Spain: *Pétrologie* 1: 121-124.
- Pavillon MJ (1972) Paléogéographies, volcanismes, structures, minéralisations plombo-zincifères et héritages dans l'Est des Cordillères Bétiques (zones internes): Thèse, Université de Paris, 623 p.

The mineral association in the Emilia and Brunita Pb-Zn-Ag-(Sn) deposits, La Unión, Murcia, Spain

Lara Sanmartí Rodríguez, Anna Gaya Manós, Carlota Molina Treviño, Sandra Amores Casals, Cristina Villanovade-Benavent, Lisard Torró i Abat, Joan Carles Melgarejo i Draper
Departament de Cristal·lografia, Mineralogia i Dipòsits Minerals, Universitat de Barcelona, Barcelona, Catalonia, Spain

José Ignacio Manteca

Departamento de Ingeniería Minera, Geológica y Cartográfica, Universidad Politécnica de Cartagena, Murcia, España

Abstract. The Pb-Zn-Ag-(Sn) deposits of the Emilia and Brunita mines were formed by replacement of Triassic carbonate levels that are part of an Alpine thrust sheet, by the circulation of hydrothermal fluids related to Miocene subvolcanic intrusives. Emilia and Brunita mines are located in a distal position by rapport to the intrusives. Primary paragenesis was replaced successively by greenalite, kaolinite, magnesian chlorite (with cassiterite, pyrite, quartz and minor amounts of uraninite, monazite and zircon) and finally Mn-siderite with cronstedtite, sphalerite, galena and marcassite. Phyllosilicates formed by replacement of sphalerite are enriched in Zn. The replacement sequence suggests that part of the Pb-Zn ores formed by remobilization of an early mineralization in the Triassic carbonate levels.

Keywords. greenalite, replacement, cassiterite, mineral sequence

1 Introduction

Emilia and Brunita mines are located in the mining district of La Unión, in the Sierra de Cartagena, in Murcia (Spain). This area holds a long-lasting mining tradition, started in the ancient Carthaginian colonization period, and it reached its maximum during the Roman Empire. The subterranean extracting activity evolved towards a larger-scale open pit exploitation during the second half of the 20th century. The main products were Pb, Zn and Ag. These mines have a certain economic significance, not only in this district, but also in the Iberian Peninsula, despite they remain inactive.

Some of the mines of La Unión district have characteristic mineral assemblages, including rare iron silicates discovered by Kager (1980), different from other Pb-Zn worldwide mineral deposits. The aim of this paper is to study these assemblages in detail and to evaluate their role in the formation of this deposit.

2 Geological setting

The Cartagena Ranges are located in the NE end of the Cordilleras Béticas in the Iberian Peninsula, and it extends parallel to the coast following an approximate E-W direction. In this Sierra, two Alpine thrust sheets are distinguished (IGME 1974; García Tortosa et al. 2000): a) the Nevado-Filabride unit (bottom), b) the Alpujarride unit (top). The first consists of series affected by medium grade metamorphism, whereas the

last is formed by series affected by middle to low metamorphic grade. Both units are composed by thick carbonate layers interstratified with detrital series. The mineralizations replacing the Triassic carbonate were mined both in Emilia and Brunita. Emilia is located in the upper sheet, whereas Brunita is in the lower. In Emilia mine some pre-mineralization diabase dykes crop out, hosted in the limestones.

These materials are covered discordantly by detrital Miocene sediments. In the central zone of the Sierra de Cartagena some calc-alkaline magmatic stocks intruded during the Miocene, in the vicinity of the studied mines. The magmas are of intermediate to rhyodacitic composition, and are accompanied by a set of dykes with magmatic breccias.

3 Structure of the deposits

Pavillon (1969, 1972), Oen et al. (1975; Fig. 1), Ovejero et al. (1976) and Manteca & Ovejero (1992) established a metallogenetic zoning in the Sierra de Cartagena, based on the mineral assemblages and the proximity to the intrusives.

At Emilia and Brunita, mining was performed in the deposits developed by replacement of the former carbonate levels in the successive thrust sheets (Kager 1980). The replacement is irregular, although relatively strata-bound. Circulation of fluids took place along small faults, stratification surfaces and joint networks. The size of veins is highly variable, and their thickness ranges from few mm to several metres. In general, veins dip subvertically and are displayed in many different directions. Veins may be related to replacement mineralization. In this case, the contact with the host rock is irregular; otherwise, and more frequently, the contacts are sharp.

Kager (1980) defined up to four episodes of mineralization, each presenting different and characteristic mineral assemblages.

4 Mineralogy and textures

The replacement zones of Emilia follow the contacts with the limestone, and are very irregular. In some cases they totally replace the limestone layer. On the basis of a petrographic study using scanning electron microscopy coupled with energy dispersive spectrometry (SEM-EDS), different replacement stages are identified:

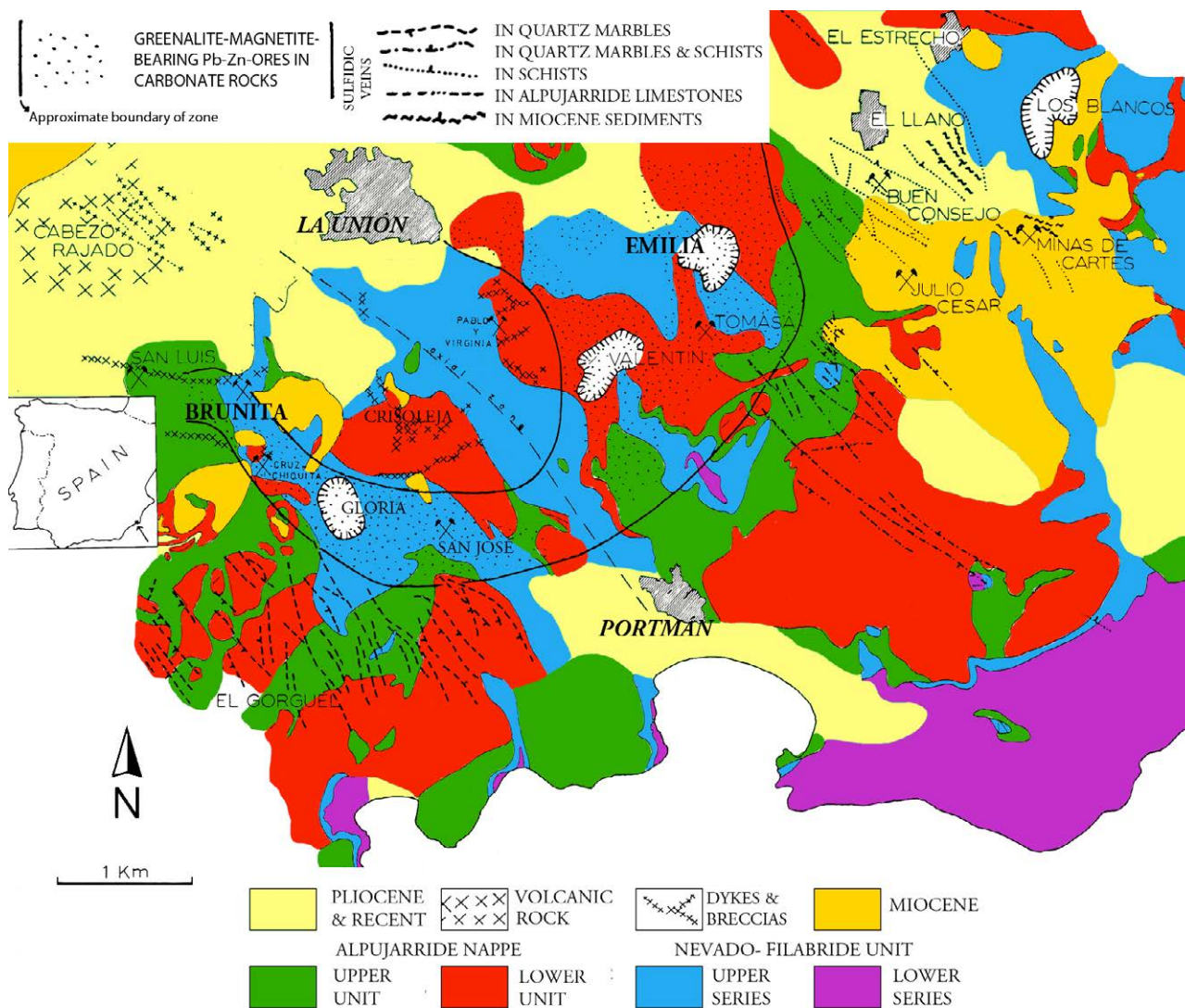


Figure 1. Geological map of the Sierra de Cartagena with the situation of the Emilia and Brunita mines. Adapted from Pavillon (1972) and Oen et al. (1975).

a) Replacement of the rock by greenalite, result of the reaction with hydrothermal fluids seeping through fractures and other discontinuities. The carbonate becomes strongly replaced by an assemblage consisting of greenalite, eventually associated with siderite and quartz. Also, early generations of galena and sphalerite crystals, previous to the greenalitization are systematically replaced. These crystals of galena and sphalerite are euhedral, with maximum diameters of 2 mm, and are scattered in the carbonate, which may have an ankeritic composition. Greenalite crystals clearly replace the rims and cleavage surfaces of sulphide crystals. In some cases, sulphides are completely replaced, leaving pseudomorph crystals (Figs. 2, 3). If greenalite replaces sphalerite, greenalite is enriched in Zn. The Zn content in greenalite is highly variable in the deposit, from 0 in greenalite replacing carbonates to 1,5 wt% in greenalite replacing sphalerite. Also, when siderite replaces sulphides, it is enriched in Pb and especially in Zn.

b) Replacement episode by kaolinite and chlorite. This

stage represents a less generalized replacement, compared to the one described in a), although it is relevant from metallogenetic point of view. In an early phase, clinocllore and quartz are formed, later replaced by kaolinite, and this in turn by chamosite (Fig. 4). As in the previous stage, chlorite may be in contact with galena or sphalerite crystals from earlier stages, may replace sulphides and become enriched in Zn (up to 0,13 wt%). Related to this stage, tiny prismatic crystals of cassiterite are also found (20 µm in length; Fig. 5). This cassiterite coexists with minor amounts of other minerals, forming micron-size crystals scattered in the phyllosilicates, such as uraninite, allanite, monazite, xenotime and zircon. In some cases, the proportion of these minerals is significant, thus representing important REE concentrations (Fig. 6).

c) Precipitation of siderite as zoned crystals, with a higher Zn content in the later stages. In an early stage, this siderite is related to quartz or chalcedony and tabular hematite, which is replaced by magnetite (mushketovitzation; Fig. 7).

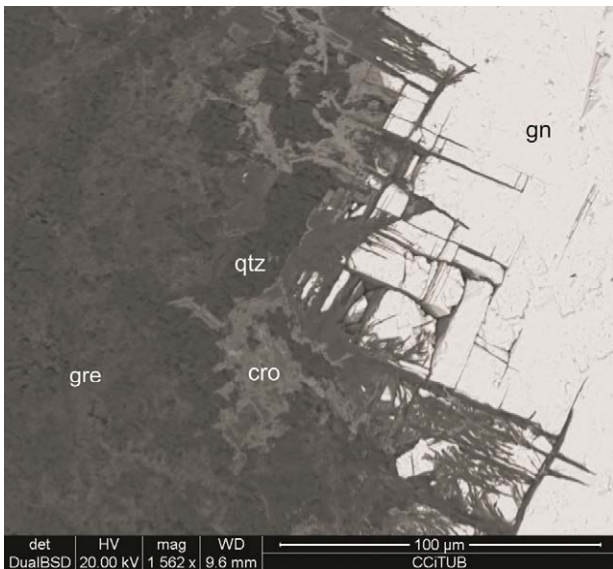


Figure 2. Greenalite (gre), quartz and cronstedtite (cro) replace galena (ga). Emilia open pit. SEM image, BSE mode.

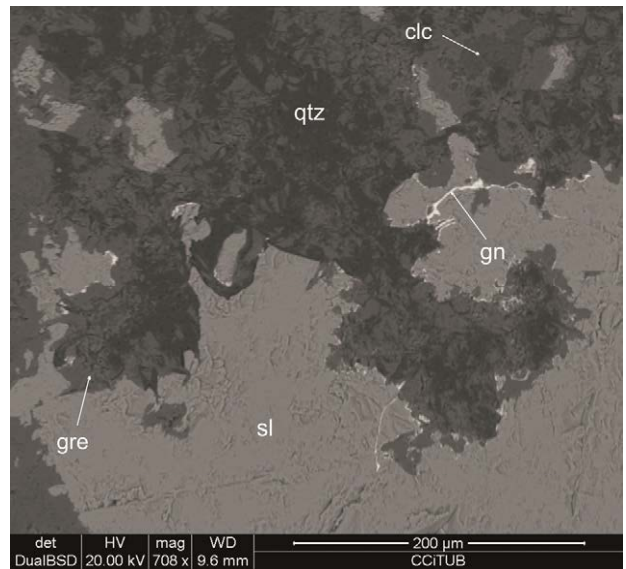


Figure 3. Greenalite (gre), clinochlore (clc), quartz (qtz) and galena (gn) replace sphalerite (sl). Emilia. SEM-BSE image.

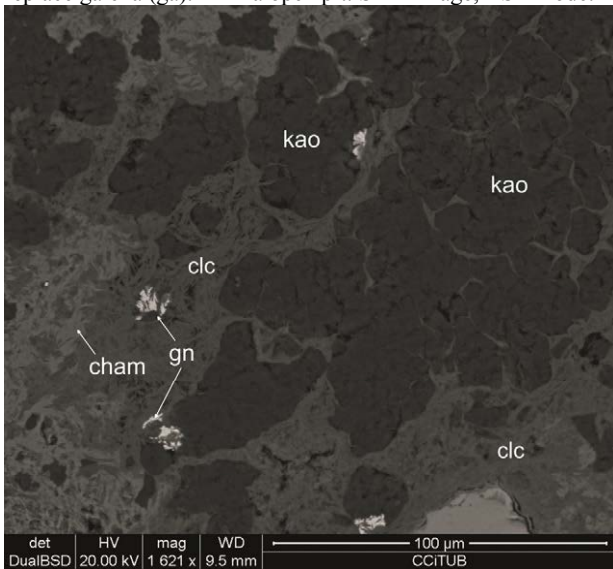


Figure 4. Fibrous aggregates of clinochlore (clc) and chamosite (cham) replacing kaolinite (kao) associated with galena (gn). Emilia mine. SEM image, BSE mode.

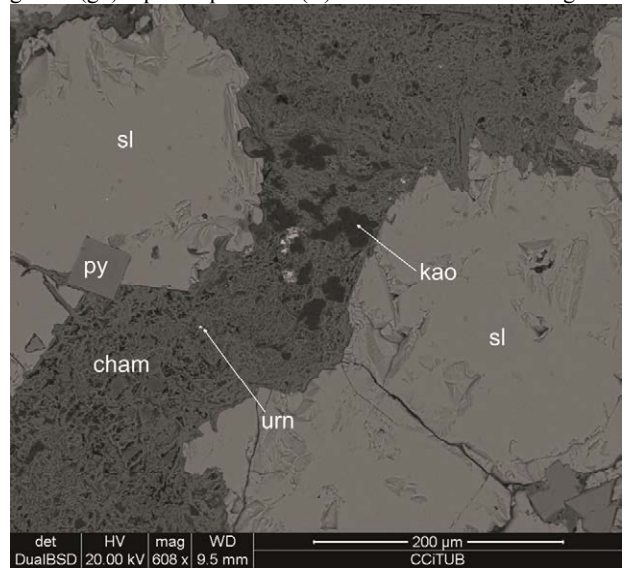


Figure 5. Pyrite (py) and sphalerite (sl) grains replaced by kaolinite (kao) and chamosite (cham) with uraninite (urn) and galena (gn). Brunita open pit. SEM image, BSE mode.

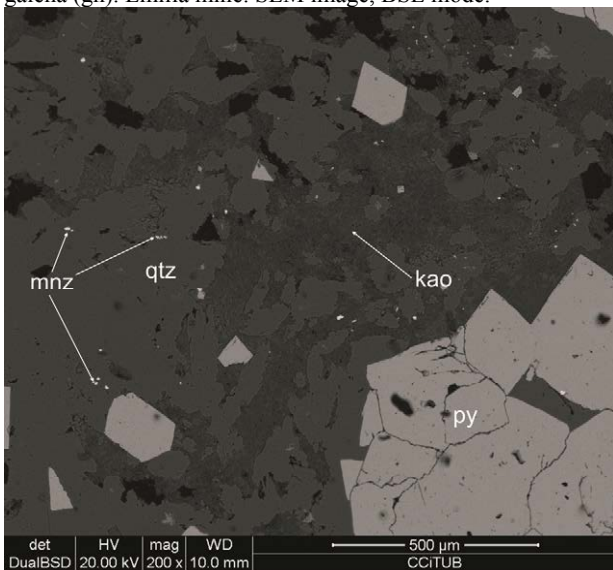


Figure 6. Monazite crystals (mnz), pyrite (py) and kaolinite veinlets (kao) in quartz (qtz). Brunita open pit. SEM image, BSE mode.

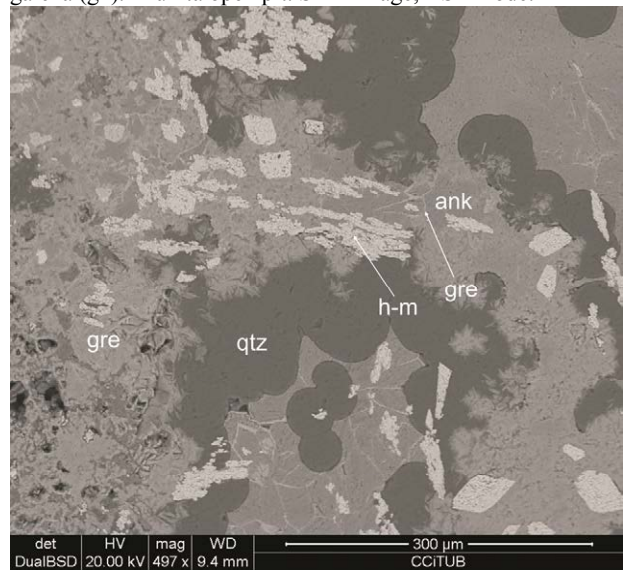


Figure 7. Platy hematite replaced by magnetite (h-m), accompanied with calcedony (qtz), ankerite (ank) and greenalite (gre). Emilia mine. SEM image, BSE mode.

d) Sulfide precipitation, associated with siderite. Early pyrrhotite is formed, although later replaced by pyrite, galena and marmatitic sphalerite. These sulphides are associated with geodic chalcedony, quartz and siderite.

5 Discussion and conclusions

The presence of sulfides replaced by successive stages of mineralization suggests that a pre-concentration of Pb-Zn existed in the Triassic sedimentary series previously to the circulation of the hydrothermal fluids associated with the Miocene intrusions.

However, there is an evidence of circulation of hydrothermal fluids with magmatic signatures. Cassiterite in association with chamosite and kaolinite is also found in the Sn deposits related to acidic magmatism in Bolivia (see Artiaga et al. 2013, this volume). These deposits have some similarities with IOCG, porphyry copper deposits and skarns, such as the development of tabular hematites later replaced by magnetite (mushketovization). This reducing mineral sequence has been interpreted as a result of the interaction between magmatic fluids with the host rock, at a low fluid/rock ratio and/or by mixing of the fluids with reduced seawater-derived fluids (De Haller & Fontboté 2009). In both oxidized and reduced sequences the redox state of the involved fluids converges at the rock buffer line during cooling as a result of wall-rock reaction and fluid mixing. Thus it explains why the later and lower temperature pyrite-chalcopyrite succession is shared by both mineral associations. Finally, the sequence hematite-magnetite-sulphides is widely documented in IOCG deposits worldwide as well as in skarn and porphyry copper deposits. This might be considered as a field evidence for mineralizing magmatic fluids (transporting metals and sulphur) having been released by oxidized I-type magmas (De Haller & Fontboté 2009).

As a consequence, the studied Pb-Zn mineralizations can be interpreted as having formed by remobilization of pre-existing deposits in the Triassic series, induced by hydrothermal fluids in equilibrium with granitic magmas.

Acknowledgements

The authors would like to thank Dr. X. Llovet, who kindly helped during the electron microprobe sessions (Centres Científics i Tecnològics of the University of Barcelona). Funding was provided by the Consolidated Research Group Grant SGR 444 of the Generalitat de Catalunya.

References

- De Haller A, Fontboté LI (2009) The Raúl-Condestable Iron Oxide Copper-Gold Deposit, Central Coast of Peru: Ore and Related Hydrothermal Alteration, Sulfur Isotopes, and Thermodynamic Constraints. *Econ. Geol.* 104: 365-384.
- IGME (1974) Mapa geológico de España 1:50,000, Sheets 978 Llano del Beal and 977 Cartagena: Inst. Geol. Minero España, Madrid.
- García Tortosa, F.J., López Garrido, A.C., Sanz de Galdeano, C. (2000). Las unidades Apujárrides y Maláguides entre Cabo Cope y Cabo de Palos (Murcia, España). *Geogaceta*, 28: 67-70.
- Kager PCA (1980) Mineralogical investigation on sulfides, Fe-Mn-Zn-Mg-Ca carbonates, greenalite and associated minerals in the Pb-Zn deposits in the Sierra de Cartagena, province of Murcia, SE Spain. Ph. D. thesis, University of Amsterdam. GUA Paper of Geology series. 1 (12): 230.
- Manteca JI, Ovejero G (1992) Los yacimientos Zn, Pb, Ag-Fe del distrito minero de La Unión-Cartagena, Bética Oriental. *Recursos Minerales de España. CSIC. Col Textos Universitarios*, 15: 1085-1102.
- Oen I., Fernández JC, Manteca, JI (1975). The Lead-Zinc and associated ores of La Unión, Sierra de Cartagena, Spain. *Economic Geology*, 70: 1259-1278.
- Ovejero G, Jacquin JP, Servajean G (1976) Les minéralisations et leur contexte géologique dans la Sierra de Cartagena (Sud-Est de l'Espagne). *Bull. Soc. Géol. France*, 18: 619-633.
- Pavillon MJ (1969) Les minéralisations plombo-cinzifères de Cartagena (Sud-Est de L'Espagne). Un exemple d'héritages successifs en metallogénie. *Mineral Deposita* 4: 368-385.
- Pavillon MJ (1972) Paléogéographies, volcanismes, structures, minéralisations plombo-zincifères et héritages dans l'Est des Cordillères bétiques (zones internes): Thèse, Université de Paris, 623 p.
- Sanz de Galdeano, C. (1990). Geologic evolution of the Betic Cordilleres in the Western Mediterranean, Miocene to Present. *Tectonophysics*, 172: 107-119.

The San José and Gloria Pb-Zn-Ag-Sn deposits, La Unión: An approach to the mineral sequence

Júlia Soler, Júlia Farré, Lena Portell, Sònia Jou, Omar Corrales, Sandra Amores, Cristina Villanova, Lisard Torró, Joan Carles Melgarejo

Departament de Cristal·lografia, Mineralogia i Dipòsits Minerals, Universitat de Barcelona, Barcelona, Catalonia, Spain

José Ignacio Manteca

Departamento de Ingeniería Minera, Geológica y Cartográfica, Universidad Politécnica de Cartagena, Murcia, España

Abstract. The mineral deposits of San José and Gloria (Pb-Zn-Ag) from the Sierra de Cartagena were formed by hydrothermal replacement of marble beds. The extensive development of mushketovite-siderite replacing an older Pb-Zn association suggests that a superposition of metallogenetic events exists in the Sierra de Cartagena area. This mushketovitization may be attributed to hydrothermal fluids equilibrated with the acidic intrusives of the area. Moreover, the widespread occurrence of molybdenite and cassiterite in association with kaolinite and chlorite also suggests the occurrence of a granitic source at depth.

Keywords. mushketovite, base metals, cassiterite, replacement

1 Introduction

The San José and Gloria mines are open-pit operations worked during the second half of the 20th century in the Portman area in the Cartagena Range. At the present moment these mines are closed. These mines are located at distal positions with regard to the intrusives of the area (Fig. 1), and differ from the proximal ones since they contain lesser amounts of iron silicates (Manteca & Ovejero 1992). The aim of this contribution is to establish the mineral sequence, in order to constrain the conditions of formation of the deposit.

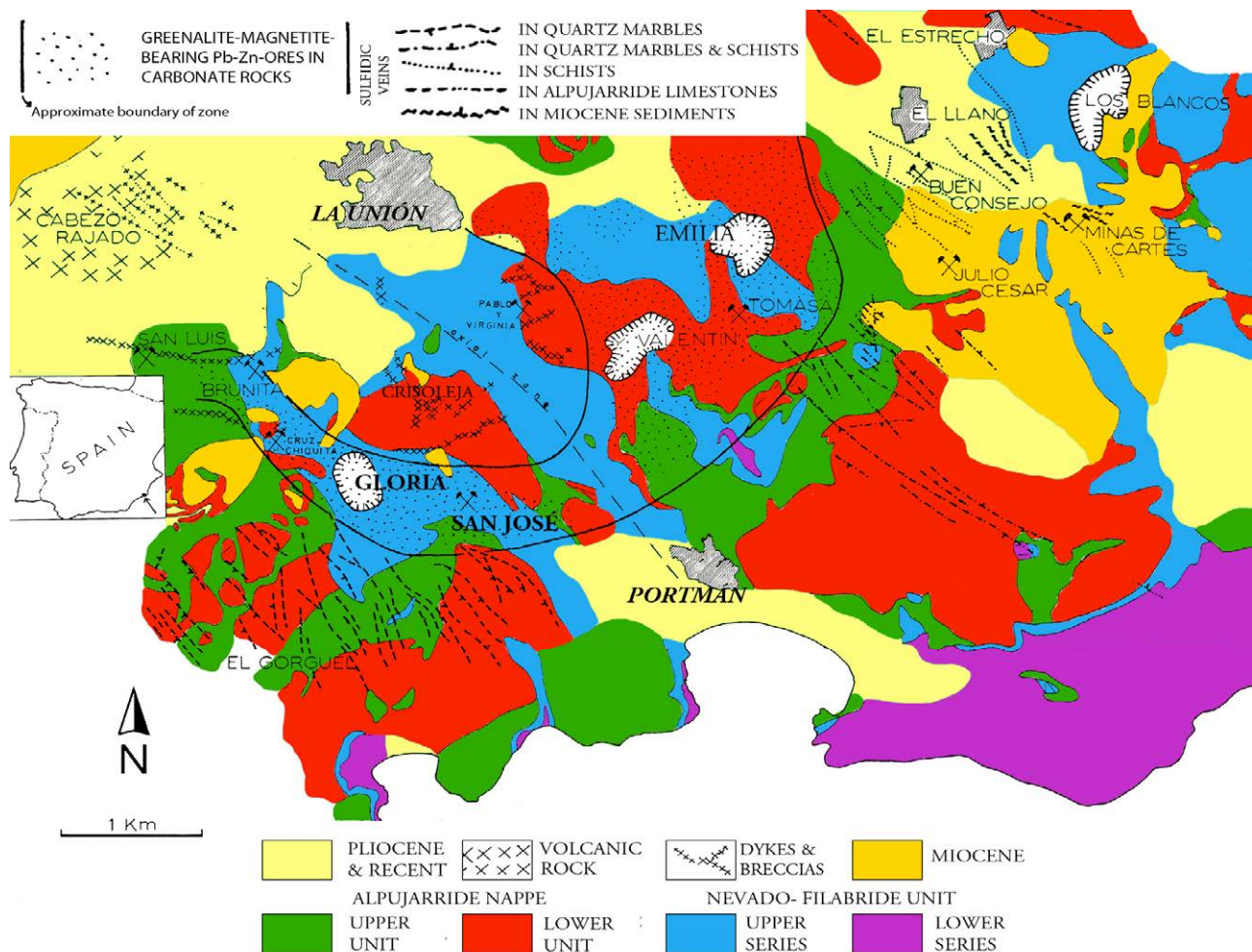


Figure 1. Geological map of the Sierra de Cartagena with the situation of the San José and Gloria mines. Adapted from Pavillon (1972) and Oen et al. (1975).



Figure 2. Ankeritized marbles crossed by randomly oriented magnetite veins (dark). San José open pit.

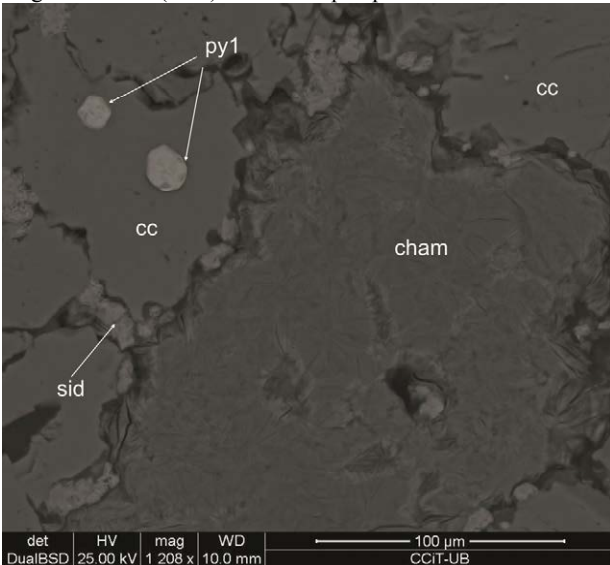


Figure 3. Rounded premetamorphic pyrite inclusions (py1) in calcite of the hosting marble (cc). Marble is replaced by siderite (sid) and chamosite (cham) in radial aggregates. San José open pit. SEM image, BSE mode.

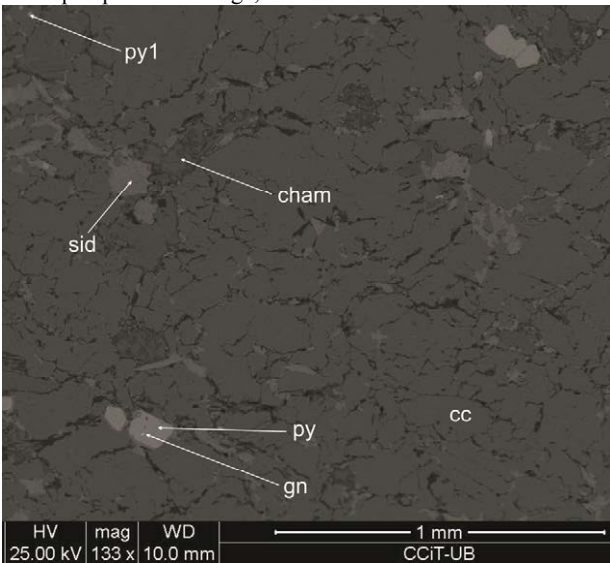


Figure 4. Calcitic marble (cc) with premetamorphic pyrite (py1) and galena (gn) replaced along grain borders by chamosite (cham), siderite (sid) and pyrite (py). San José open pit. SEM image, BSE mode.

2 Geology

The San José and Gloria deposits are in the south roof of the Cartagena range, between Portman and La Union mining towns (Fig. 1). These mountains represent the ENE termination of the Betic Ranges. The Betic Ranges are made up in this area of a pile of Alpidic thrusts. From the base to the top, the following materials can be distinguished (IGME 1974, García Tortosa et al. 2000): a) the Nevado-Filabride complex composed of series affected by medium grade metamorphism, b) the Alpujarride complex, composed of series affected by middle to low metamorphic grade. Both thrusts are composed of beds of marbles or limestones interbedded with detrital series. The ore bodies in Gloria and San José were formed by replacement of the marbles of the upper Nevado-Filabride formation (Kager 1980).

Miocene sedimentary sequences unconformably overlie the above materials. Miocene stocks of rhyodacitic subvolcanic rocks and an ensemble of dikes with magmatic breccias were emplaced in the central part of the Cartagena Range.

Oen et al. (1975) and Ovejero et al. (1976) defined the stratigraphy of these deposits. From bottom to top the following materials were observed: graphite bearing schists and quartzites of the Lower Nevado Filabride formation (more than 50 m); light coloured quartzites of the upper Nevado Filabride formation (up to 100 m), marbles of the upper Nevado Filabride complex (20-50 m); blue violet phyllites and quartzites of the San Ginés unit and platy blue limestones with detrital intercalations of the San Ginés unit.

The marbles were partly replaced by the ores, during several episodes. The shapes of the resulting bodies are very irregular (Fig. 2). The replacement is produced along several faults, joints and stratification. Hence, it is not rare to find barren areas inside the mineralized bodies.

3 Mineralogy and textures

The marbles of the San José mine are white in colour and have a foliated texture, which favoured the circulation of hydrothermal fluids. In the least replaced marbles, it is possible to observe slight replacements along the grain borders of the carbonate crystals.

The marbles have millimetric grain size, and the calcite grains have commonly inclusions of small rounded pyrite grains (Fig. 3). These grains can represent primary sedimentary pyrite from the host rocks and hence a possible source of S.

The first evidence of alteration in the marbles in the vicinity of the deposit is the occurrence of interstitial clinocllore among the calcite grains, accompanied by small amounts of pyrite, sphalerite and galena (Fig. 4). Clinocllore may be partly replaced by chamosite.

The existence of metasomatic fronts around veins in the San José mine can be observed at a thin section scale using a sequence of SEM-BSE images (Fig. 5). These veins are made up by quartz and siderite, and the width is centimetric. At the contact with the host rock, the rock has become strongly altered to magnetite, which forms skeletal millimetre-sized crystals. Magnetite is mixed

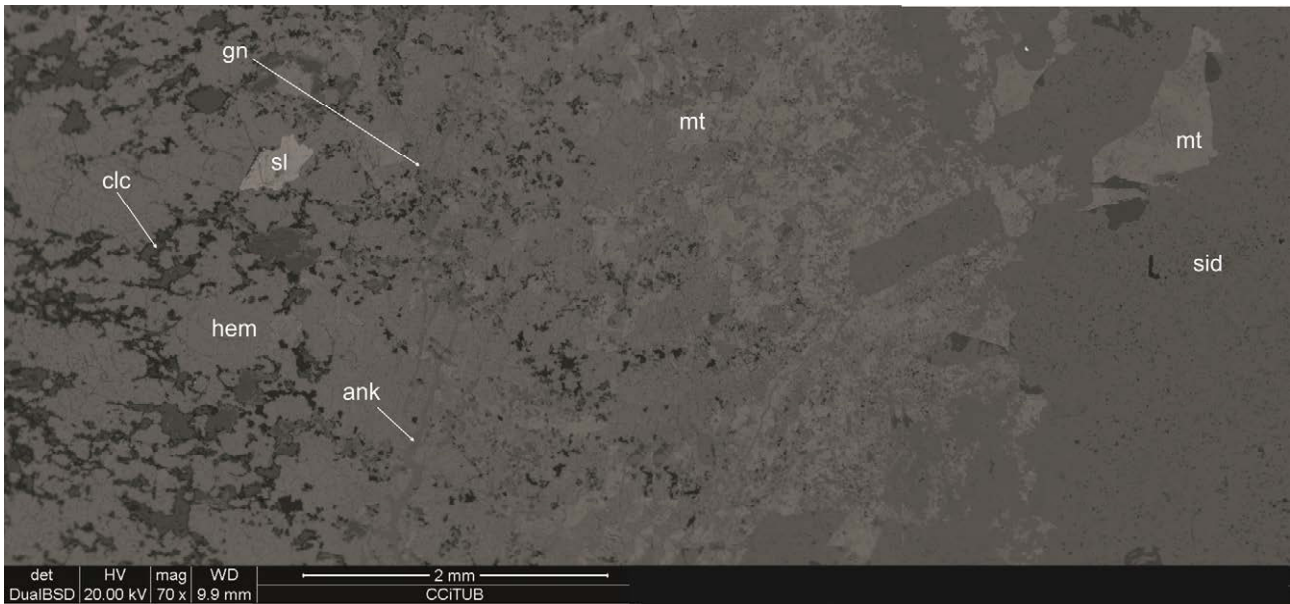


Figure 5. Sequence of metasomatic fronts around a siderite vein (sid; right of the image). At the contact with the vein, the host rock has been replaced by magnetite (mt) and siderite up to a distance of 2 mm. In a second metasomatic front up to 4 mm from the contact, the host rock was replaced by hematite (hem) and ankerite (ank); in this domain magnetite may replace the hematite plates (mushketovitzation). Further the rock is replaced by hematite and clinochlore (clc). Note that in this domain older sphalerite crystals (sl) are in part replaced by hematite and chlorite. San José open pit. SEM image, BSE mode.

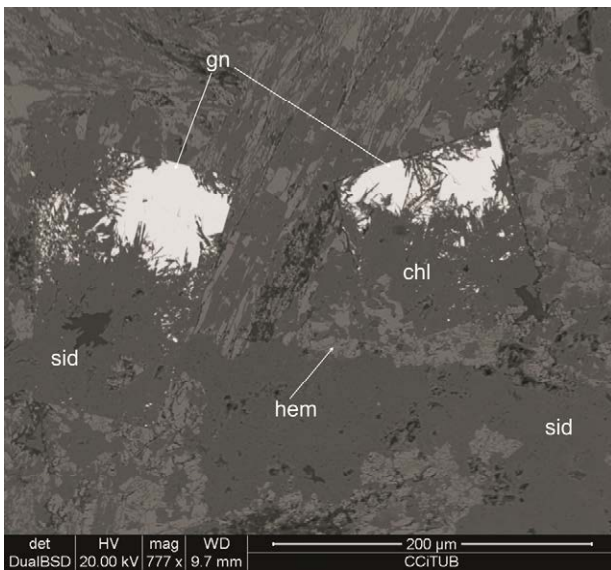


Figure 6. Pre-existing galena cubes (gn) rimmed by hematite plates (hem); a new venue of siderite (sid) and chlorite (chl) replaced the galena. Gloria open pit. SEM image, mode BSE.

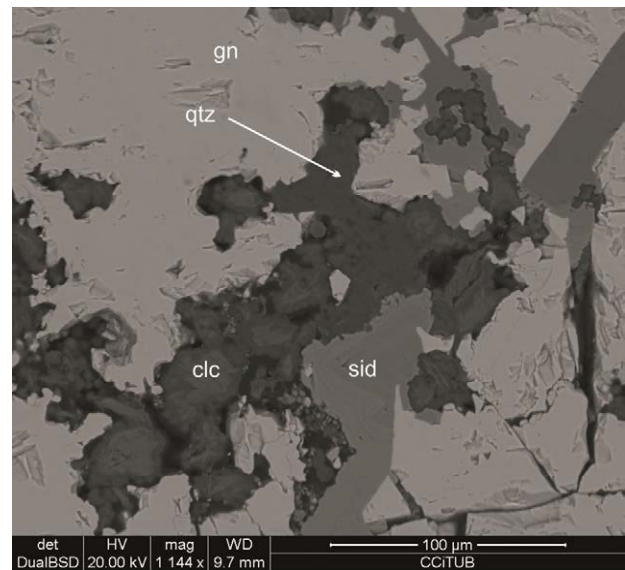


Figure 7 Galena (gn) replaced by clinochlore (clc), siderite (sid) and quartz (qtz). Clinochlore is enriched in Zn. Gloria open pit. SEM image, mode BSE.

with siderite in this domain. These minerals replace the host rock along the grain borders.

Millimetres far from the vein, magnetite becomes lesser common and gives rise to hematite platelets. Hematite is replaced by magnetite at the metasomatic front (mushketovitzation). At a distance of 1 cm from the vein the ankerite substitutes magnetite. Finally, relatively far from the vein, clinochlore forms instead of carbonate.

In the metasomatized domains some preexisting sulphides, as euhedral galena, are pseudomorphosed by later associations as mushketovite and siderite (Fig. 6); replacement of sphalerite by chlorite (Fig. 7) produces

Zn enrichments in the structure of chlorite (up to 1,8 wt% Zn).

The chloritized-silicified areas may be enriched in molybdenite and cassiterite. Molybdenite is common in these domains and occurs as small plates of several microns (Fig. 8).

Cassiterite is common and forms prismatic crystals, up to 20 µm in length. A core with ecandrewsite, a rare mineral of the ilmenite group (Fig. 9), is often observed. Cassiterite does not concentrate In, Ta or Nb in these occurrences.

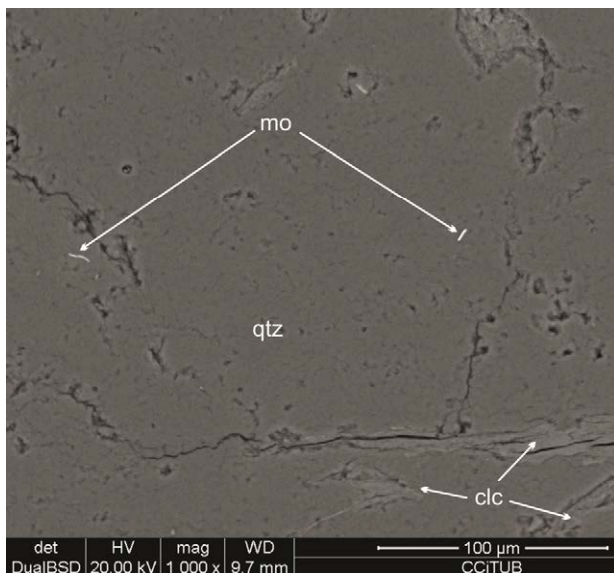


Figure 8 Molybdenite plates (mo) associated with quartz (qtz) and clinocllore (clc). Gloria open pit. SEM image, mode BSE.

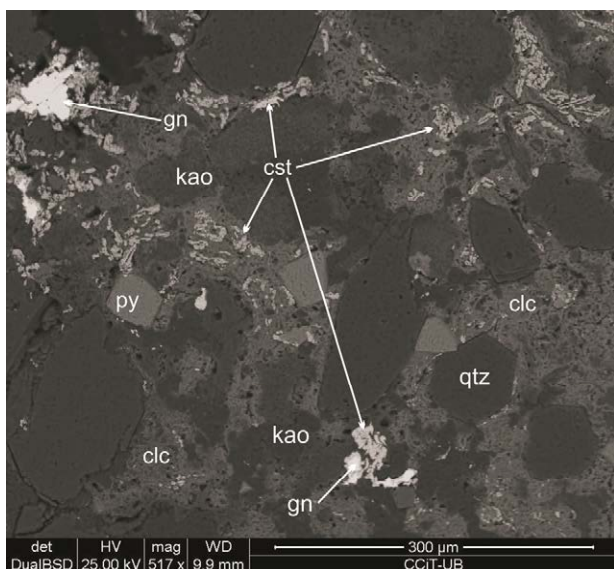


Figure 9 Abundant cassiterite crystals (cst) associated with chlorite (clc), pyrite (py) and kaolinite (kao) rimming euhedral quartz (qtz) and replacing galena (gn). Gloria open pit. SEM image, mode BSE.

4 Conclusions

The occurrence of large amounts of molybdenite and cassiterite is an argument to suggest a magmatic source for this stage of the ore formation. The common occurrence of mushketovite (hematite platelets pseudomorphosed by magnetite) also suggest that magmatic fluids interacted at low fluid/rock ratios with the host rock and/or mixed with reduced seawater-derived fluids (de Haller & Fontboté 2009).

On the other hand, the pseudomorphic replacement of galena and sphalerite suggests the existence of an older Pb-Zn mineralization in the area. Therefore, the possibility that at the least a part of the concentrations of metals in the area can be recycled from a MVT preconcentration cannot be ruled out.

Acknowledgements

Samples were analyzed in the Centres Científics i Tecnològics of the University of Barcelona. Dr. X. Llovet helped with the microprobe calibration. Funding was provided by the Consolidated Research Group Grant SGR 444 of the Generalitat de Catalunya.

References

- García Tortosa FJ, López Garrido AC, Sanz de Galdeano C (2000) Las unidades Apujárrides y Maláguides entre Cabo Cope y Cabo de Palos (Murcia, España). *Geogaceta*, 28:67-70.
- De Haller A, Fontboté LI (2009) The Raúl-Condestable Iron Oxide Copper-Gold Deposit, Central Coast of Peru: Ore and Related Hydrothermal Alteration, Sulfur Isotopes, and Thermodynamic Constraints. *Econ Geol* 104:365-384.
- IGME (1974) Mapa geológico de España 1:50,000, Sheets 978 Llano del Beal and 977 Cartagena: Inst Geol Minero España, Madrid.
- Kager PCA (1980) Mineralogical investigation on sulfides, Fe-Mn-Zn-Mg-Ca carbonates, greenalite and associated minerals in the Pb-Zn deposits in the Sierra de Cartagena, province of Murcia, SE Spain. Ph. D. thesis, University of Amsterdam. GUA Paper of Geology series. 1 (12): 230.
- Manteca JI, Ovejero G (1992) Los yacimientos Zn, Pb, Ag-Fe del distrito minero de La Unión-Cartagena, Bética Oriental. *Recursos Minerales de España*. CSIC. Col Textos Universitarios, 15: 1085-1102.
- Oen I, Fernández JC, Manteca JI (1975) The Lead-Zinc and associated ores of La Unión, Sierra de Cartagena, Spain. *Econ Geol*, 70: 1259-1278.
- Ovejero G, Jacquin JP, Servajean G (1976) Les minéralisations et leur contexte géologique dans la Sierra de Cartagena (Sud-Est de l'Espagne). *Bull Soc Géol France*, 18: 619-633.
- Pavillon MJ (1969) Les mineralisations plombo-cinzifères de Cartagena (Sud-Est de L'Espagne). Un exemple d'héritages successifs en metallogénie. *Miner Deposita* 4: 368-385.
- Pavillon MJ (1972) Paléogéographies, volcanismes, structures, minéralisations plombo-zincifères et héritages dans l'Est des Cordillères bétiques (zones internes): Thèse, Université de Paris, 623 pp.

Unconventional PGE mineralizations: a review

Bernhard Stribny

Federal Institute for Geosciences and Natural Resources (BGR)
 Stilleweg 2, D-30655 Hannover, Germany

Abstract. Platinum Group elements (PGE) are strategic raw materials. About 98% of the annual world production derives from just 5 mining districts. The failure risk for a continuous supply is the highest compared to other metals. Moreover, PGE cannot be substituted by other materials in many existing and emerging technologies due to their specific chemical and physical properties. Classic geologic environments mined for PGE are:

- 1) layered mafic-ultramafic intrusions and their contact zones,
- 2) Ni-Cu sulfide-bearing norite intrusions,
- 3) Ni-Cu sulfide-bearing dolerite sills,
- 4) placer deposits.

Unconventional PGE mineralizations occur in a broad variety of sedimentary, metamorphic and magmatic rocks. Even though, the classic PGE producers in South Africa, Russia, Canada, Zimbabwe and USA will continue to dominate the market in the next decades, unconventional PGE occurrences might help to diversify the supplier's base.

Keywords. Platinum group elements, unconventional mineralizations, Kupferschiefer, Ni-laterites, porphyry copper deposits, ophiolites

1 Introduction

In 2011 the world production reached 195 t of platinum (Pt) and 214 t of palladium (Pd) (Table 1). The mines operating in the South African Bushveld Complex are by far the world greatest producers with 145 t Pt or 85% of the total world production.

Table. 1 World mine production and reserves of Pt and

Pd in 2011 (modified after Loferski 2013). (†) Included in "other countries".

Mine Production	Pt (t)	Pd (t)	Reserves (t)
South Africa	145	82	63,000
Russia	25	86	1,100
Zimbabwe	11	8	(†)
Canada	7	14	310
United States	4	12	900
Colombia	1	-	(†)
Other countries	3	12	800
World total	196	214	66,110

At Noril'sk-Talnakh and on the Kola peninsula the Russian Pt production amounted in 2011 25 t or 13 % of the total world production. 11 t Pt were mined in the Great Dyke, Zimbabwe, 7 t Pt in Sudbury, Canada and 4 t Pt in the Stillwater complex, USA. 1 t Pt were panned in Colombian placer deposits.

It can be estimated, that about 1 t Pt and 1 t Pd are produced per year in unconventional PGM deposits worldwide.

Unconventional PGE mineralizations occur in a wide spectrum of sedimentary, metamorphic and magmatic rocks and their metallogeny is mostly related to complex and multi-stage processes with extreme enrichment factors (Figure 1).

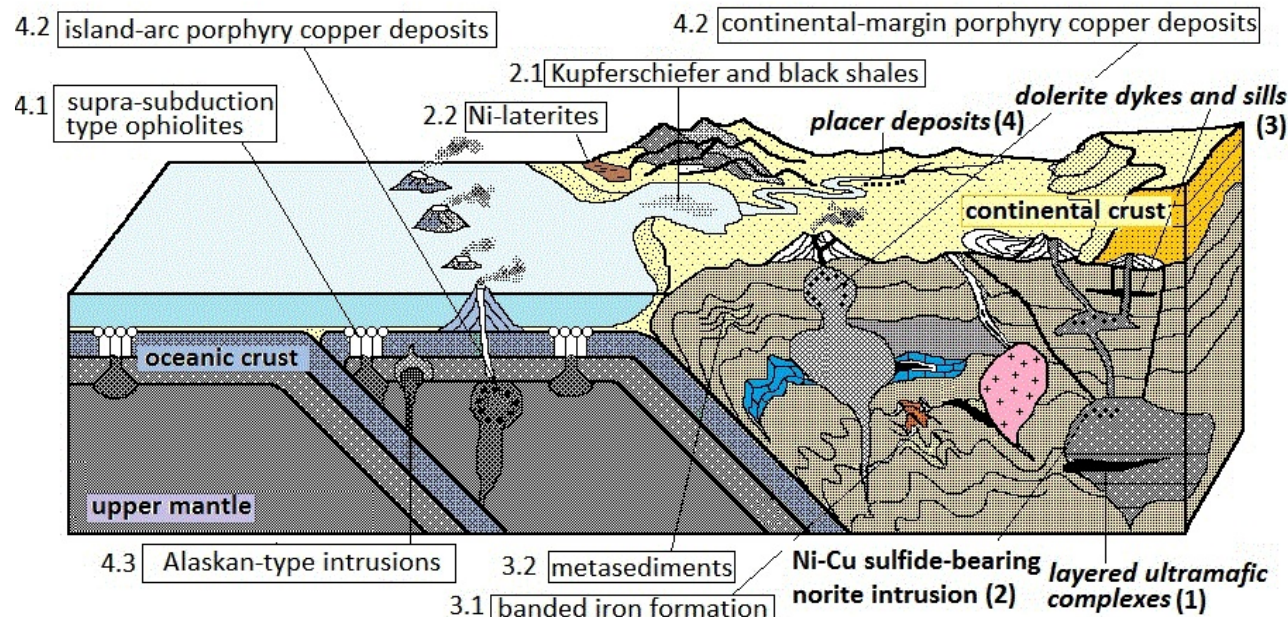


Figure 1. Sketch 3D-diagramm of the geologic setting of conventional PGE deposits (**bold italic**) in (1) layered mafic-ultramafic intrusions, representing 81 % of annual world production, (2) Ni-Cu sulfide-bearing norite intrusions (5 %), (3) Ni-Cu sulphide-bearing dolerite sills (12 %), (4) placer deposits (1 %) and unconventional PGE mineralizations in 2.1(chapter number in the text) Kupferschiefer and black shales, 2.2 nickel laterites, 3.1 banded iron formations, 3.2 metasediments, 4.1 ophiolites, 4.2 porphyry

copper deposits and 4.4 Alaskan-type complexes representing together 1 % of annual world production.

2 Unconventional PGM mineralizations in sedimentary rocks

2.1 Kupferschiefer and black shales

In the Fore-Sudetic monocline of SW Poland the Permian Kupferschiefer is mined in the Lubin-Sieroszowice mining district since more than 50 years. In 2011 KGHM produced 571,000 t Cu, 1,260 t Ag, 1 t Au and about 70 kg Pt+Pd in the copper anode refinery slime.

The zoned metal distribution in the Kupferschiefer is strongly controlled by the ascending “Rote Fäule” oxidation front (Figure 2). The maximum contents of Cu, S and C_{org} occur in the lowermost part of the Kupferschiefer. Platinum, Pd and Au are enriched directly on top of the front. Average contents of 48 Kupferschiefer samples are 255 ppb Pt, 94 ppb Pd, 2,400 ppb Au and 13,000 ppb Ag. Platinum and Pd show a positive correlation coefficient of $r=0.69$. Gold and Pt as well as Au and Pd are positively correlated too with coefficients of $r=0.68$ and $r=0.55$, respectively (Stribny et al. 2000). Comparable noble metal concentrations were described by Piestrzyński et al. (2002).

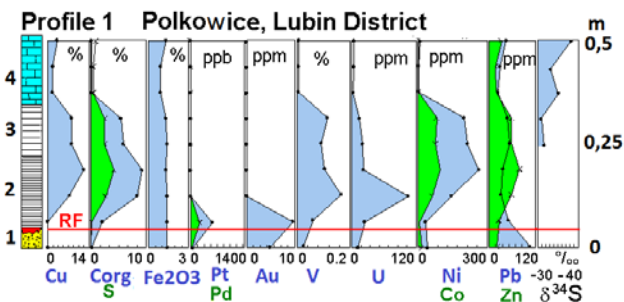


Figure 2. Element distribution in a representative Kupferschiefer profile of Polkowice mine. 1= Weissliegend sandstone, 2= Kupferschiefer, 3= dolomitic Kupferschiefer, 4= Zechstein limestone, RF= “Rote Fäule” oxidation front.

Upper Proterozoic metalliferous black shales with contents of 38 to 102 ppb Pd and 8 to 9 ppb Pt in the Bohemian Massif were described by Pasava (1991). Extreme enrichments of polymetallic Ni-Mo-PGE-Au ores in Lower Cambrian black shales occur in S China. The Huangjiawan ore district, located ca. 15 km west of Zunyi, Guizhou province, contains the thickest ore layer of up to 2 m (average 20 cm) and ore reserves of 240,000 t Mo and 150,000 t Ni. The metal grades are 5.5% Mo, 3.5% Ni and 1 g/t PGE + Au on average (Shao-Yong et al. 2007). The origin of this mineralization is explained by submarine volcanogenic hydrothermal processes.

2.2 Nickel laterites

PGE mineralizations in laterites were reported by Bowles (1986). In the Niquelandia Layered Complex in Goias, central Brazil, the mafic-ultramafic rock suites contain background Pt+Pd values below 20 ppb, but massive chromitites or sulphide-bearing pxroxenites

show content of 100-1,000 ppb (Walde et al. 2001). In the Jacuba mine up to 30 m thick weathering profiles are exposed with fresh pyroxenites at the bottom and saprolitic and clayey ferruginous layers on top with Pt+Pd contents of 900 to 1,500 ppb (Figure 3).



Figure 3. Sampling of Ni-laterites exposed in the open pit of the Corriola Mine, Niquelandia. The cude ore, mostly garnierite, contains up to 7.6 % Ni.

3 Unconventional PGM mineralizations in metamorphic rocks

3.1 Banded Iron Formation

Unusual Au-Pd alloys are described by Cabral (2006) from Palaeoproterozoic banded iron formations (BIF) of the Quadrilátero Ferrífero, Minas Gerais, Brazil. In the Gongo Soco mine Au-, Pd-, Ag- and Hg- aggregates are recovered from cross-cutting hematite-rich veins in itabirites. The gold grains are typically coated by Pd-O species and iron hydroxides, the so called *ouru preto* (black gold). In the Itabira world-class iron ore district Pd-rich gold and platinum group mineral (PGM) occur as fracture fillings intergrown with specular hematite in the BIF and adjacent placers and lateritic profiles.

3.2 Metasediments

In Pará, NE Brazil, the Serra Pelada Au-Pd-Pt deposit was worked from 1978-1992 by up to half a million of artisanal miners. In weakly metamorphosed sedimentary rocks of Late Archean age near surface bonanza ores were mined with palladiferous gold, Pd-Pt-Se, Pd-Se, Pd-Hg-Se and Pd-Bi-Se phases (Cabral 2006).

4 Unconventional PGM mineralizations in magmatic rocks

4.1 Ophiolites

Some unusual enrichments of Pt-Pd-Rh group metals have been reported from the Shetland ophiolite (Tarkian and Prichard 1987) and from the Zambales ophiolite, Philippines (Orberger et al. 1988). Near Bregu i Bibes in the Mirdita ophiolite, N Albania, a Pt mineralizations was investigated in supra-Moho cumulates in form of dunites, orthopyroxenites and olivine chromitites (Stribny et al. 2000). A Pt-Fe alloy, close to isoferroplatinum, Pt₃Fe, is the dominant PGM (Figure

4).

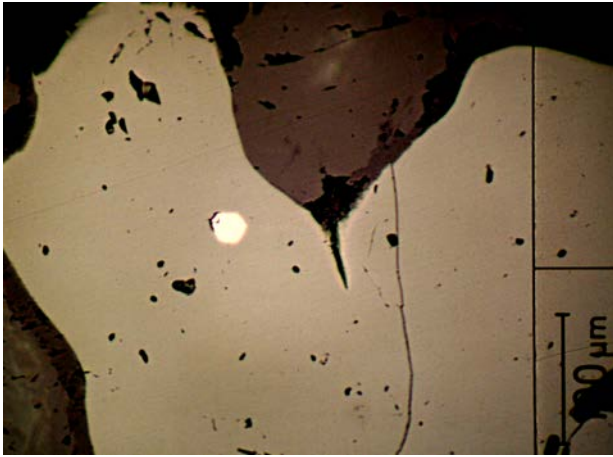


Figure 4. Pt-Fe alloy (white) in chromite (gray), polished section, reflected light, scale 100 μm, Bregu i Bibes, Albania.

Instrumental neutron activation analyses (INAA) of 51 channel samples (1 sample = 1 m section in trenches K7, K1, K1b and K2, see Figure 5) revealed contents of 0.01 to 4.3 ppm Pt (mean = 0.86) and 0.007 to 0.3 ppm Pd (mean = 0.06). The PGM are associated with chromite documented by a correlation coefficient between Pt and Cr of $r=0.93$.

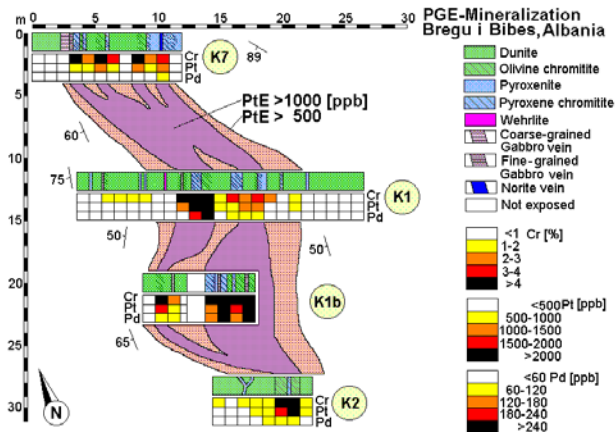


Figure 5. Geological sketch map and profiles of the 4 trenches K1, K1b, K2 and K7 across the central part of the Bregu i Bibes PGE mineralization. The positive correlation between Cr-, Pt- and Pd-contents is shown besides of the 2-dimensional distribution of Pt+Pd equivalent (PtE) contents >500 and >1,000 ppb PtE on the land surface which might be economically minable.

4.2 Porphyry Copper Deposits

PGE contents between 0.025 and 13.6 ppm Pt and 0.003 to 6.4 ppm Pd were described in rocks, ores and concentrates of Cordilleran alkaline suite porphyries in USA and Canada (Mutschler et al. 1985). Tarkian and Stribny (1999) published a reconnaissance study on PGE and PGM in concentrates of island-arc and continental-margin porphyry copper deposits. In order to find out whether porphyry copper deposits are potential hosts for PGE mineralizations as source for a profitable by-product, sulfide concentrates of 34 porphyry copper

deposits from all over the world were analysed by INAA. Only values lying 3 times higher than the detection limit of 8 ppb for Pt, Pd, Ru, Ir and Os were used for further statistical evaluation and interpretation. All 34 concentrates contain more than 130 ppb Au with maximum value of 40 ppm. Positive linear correlations exist between Au and Pd with a coefficient of $r=0.72$ (Figure 6) and between Pd and Pt with a coefficient of $r=0.61$. 58 % of the 34 concentrates contain Pd-contents between 24 and 1,900 ppb. 20 % of the samples carry Pt contents between 24 and 490 ppb (Stribny et al. 2000). Pt+Pd concentrations > 100 ppb were found in just 2 of 18 (11%) of the continental-margin porphyries, but in 7 of 14 (50%) of the island-arc porphyries.

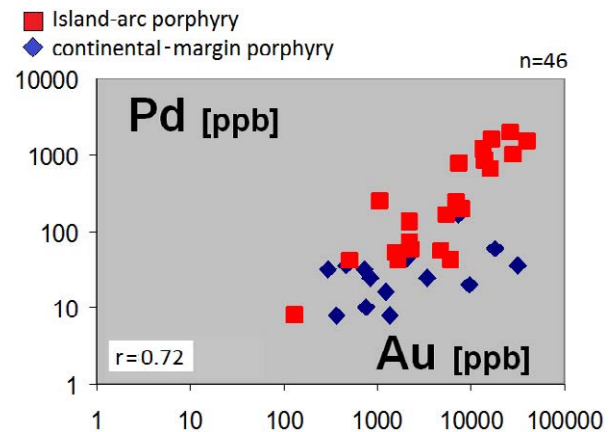


Figure 6. Correlation diagram of Pd and Au contents in 34 sulfide concentrates of island-arc and continental-margin porphyry deposits with a coefficient of $r=0.72$ (red and blue dots), implying comparable and common enrichments processes in both types. Lower Pd contents in continental-margin porphyries might be due to a higher probability of dilution of the magmas in this setting than in island-arcs.

Four concentrates have Pt+Pd content of >500 ppb, which might be a threshold of profitability if noble metal by-product bonuses are paid by the smelters. These 4 mines are Mamut, Malaysia (1860 ppb Pt+Pd), Santo Thomas, Philippines (1900 Pt+Pd), Elatsite, Bulgaria (1300 ppb Pt+Pd) and Ok Tedi, Papua New Guinea (827 ppb Pt+Pd) (Figure 8). Distinct PGM, mostly merenskyite, $PdTe_2$, (Figure 7), merenskyite-moncheite, $PdTe_2$ - $PtTe_2$, sperrylite, $PtAs_2$, and an unidentified Pd-Sb telluride were detected in the sulfide concentrates of Elatsite, Maidanpek, Mamut, Biga and Ok Tedi.



Figure 7. Inclusion of merenskyite, $PdTe_2$, white spot, in

chalcopyrite, yellow, polished section, reflected light, combined with the energy-dispersive X-ray spectrum showing Pd- and Te-peaks.

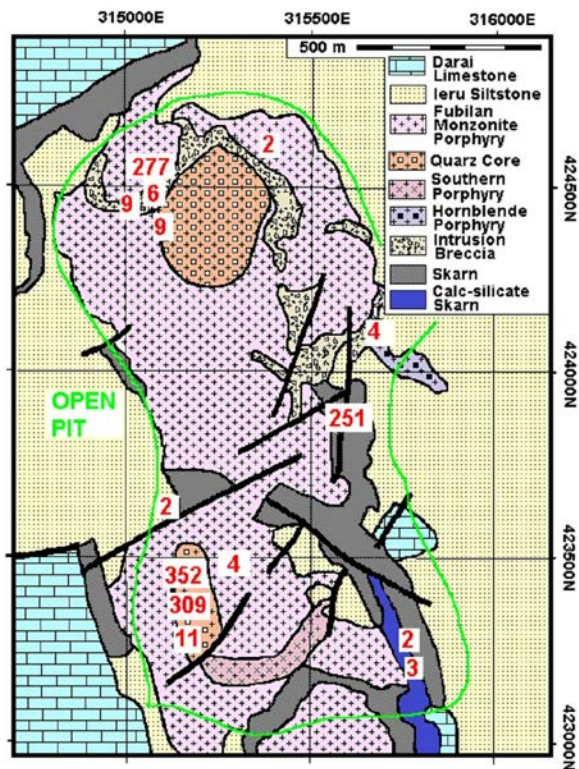


Figure 8. Geological sketch map of the Ok Tedi porphyry Cu-Au deposit with the sampling points and the Pd-analyses in ppb Pd (modified after Ok Tedi Mining Limited)

4.3 Alaskan-type complexes

PGM placers are mined in Colombia since precolonial times. Based on a “placer index” of $100 P t / (P t + I r + O s) > 90$, Cabri and Harris (1975) concluded, that the PGM derive from mafic-ultramafic Alaskan-type intrusions. Extensive panning of heavy mineral in the Rio Condoto traced the origin of PGM in the panning concentrates back to the dunitic core of the Alto Condoto intrusion (Stribny et al. 2000). PGM, mostly Pt-Fe alloys and rare cooperite (PtS), are associated with accessory chromite grains, but not with chromitite schlieren. Chondrite-normalized PGE patterns of the Alto Condoto intrusion are clearly distinct from those in layered complexes or in ophiolites.

5 Conclusions

Unconventional PGE mineralizations occur in a wide spectrum of sedimentary, metamorphic and magmatic rocks. Regardless the great differences in geologic setting, environment and age there are some common mineralogical and chemical features observable:

- 1) Between Pt and Pd, in general, linear positive correlations exist,
- 2) Pt and Pd are positively correlated with Au,
- 3) Pt and Pd often display a positive correlation to the main ore metal contents like Cr, Ni or Cu,
- 4) In sedimentary and metamorphic rocks the PGE are

linked to redox-reactions, highly oxidizing conditions (hematite stability field) or oxidation fronts,

- 5) PGM in placer deposits differ in many cases in size and composition from the PGE mineralization in the presumable source rocks in the hinterland,
- 6) Microscopic experiences show, that distinct Pt- and Pd-minerals are observable in polished sections if the Pt+Pd content of the hand specimen is >300 ppb.

In mafic-ultramafic layered intrusions, Alaskan-type complexes and in ophiolitic cumulates PGE are precipitated from silicate melt, immiscible iron sulphide melt or magmatic volatile fluids. PGE in cross-cutting veins of BIF or metasediments and in porphyry copper deposits were mobilized, transported as chloride- or bisulfide complexes and precipitated in physical and/or chemical traps. In sedimentary rocks (Kupferschiefer) metalliferous brines and an ascending oxidation front led to a remobilization and reprecipitation of disseminated PGE from underlying rocks on top or closely ahead of the front. PGM in Ni-laterites were formed by supergene weathering processes as residual components from pre-existing PGE contents in the ultramafic bed rocks.

Finally, it was a surprising observation, that many mines visited, did not carry out any investigation on noble elements and PGE in their rocks, concentrates or tailings.

References

- Bowles JFW (1986) The development of Platinum-Group minerals in laterites. *Economic Geology* 81:1278-1285
- Cabral AR (2006) Palladiferous gold mineralizations (ouro preto) in Brazil: Gongo Soco, Itabira and Serra Pelada. *Geol. Jb. SD* 8: 1-115
- Loferski PJ (2013) Platinum Group Metals: U.S. Geological Survey, Mineral Commodity Summaries 2009-2011: 120-121
- Mutschler FE, Griffin ME, Stevens DS, Shannon SS Jr (1985) Precious metal deposits related to alkaline rocks in the North American Cordillera – an interpretive review. *Trans Geol Soc S Afr* 88: 355-377
- Orberger B, Friedrich G, Woermann E (1988) Platinum-group mineralization in the ultramafic sequence of the Acoje ophiolite block, Zambales, Philippines. In: Prichard HM, Potts PJ, Bowles JFW, Cribb SJ (eds) *Geoplatinum 87*. Elsevier, London 361-380
- Pasava J. (1991) Comparison between the PGE distribution in black shales of the Bohemian Massif (CSFR) and other black shale occurrences. *Mineralium Deposita* 26: 99-103
- Piastrzyński A, Pieczonka J, Głuszek A (2002) Redbed-type gold mineralization, Kupferschiefer, south-west Poland. *Mineralium Deposita* 37: 512-528
- Shao-Yong J, Jing-Hong Y, Jing-Hong Y, Hong-Fei L, Yong-Quan C, Hong-Zhen F, Kui-Dong Z, Pei N (2007) Extreme enrichments of polymetallic Ni-Mo-PGE-Au in Lower Cambrian black shales and PGE geochemical investigation. *Palaeogeography, Palaeoclimatology, Palaeoecology* 254, 1-2: 217-228
- Stribny B, Wellmer FW, Burgath KP, Oberthür T, Tarkian M, Pfeiffer T (2000) Unconventional PGE occurrences and PGE mineralizations in the Grat Dyke: metallogenic and economic aspects. *Mineralium Deposita*: 35:260-281
- Tarkian M, Prichard HM (1999) Irarsite-hollingworthite solid-solution series and other associated Ru-, Os-, Ir- and Rh-bearing PGMs from the Shetland ophiolite complex. *Mineralium Deposita* 26: 178-184
- Tarkian M, Stribny B (1999) Platinum-group elements in porphyry copper deposits: a reconnaissance study. *Mineralogy*

Structural constraints on the formation of Cu-rich mesothermal vein deposits in the Repparfjord Tectonic Window, northern Norway

Espen Torgersen, Giulio Viola

Geological Survey of Norway, 7491, Trondheim, Norway (espen.torgersen@ngu.no)

Dept. of Geology and Mineral Resources, Norwegian University of Science and Technology, 7491, Trondheim, Norway

Jan Sverre Sandstad

Geological Survey of Norway, 7491, Trondheim, Norway

Holly Stein

AIRIE Program, Department of Geosciences, Colorado State University, USA

CEED Centre of Excellence, University of Oslo, Norway

Abstract. The Paleoproterozoic metasupracrustal sequence of the Repparfjord Tectonic Window (RTW) within the Caledonian Nappe System in northern Norway hosts several Cu-bearing mesothermal carbonate-quartz veins.

Structural analysis shows that the emplacement of the veins is geometrically and kinematically compatible with a phase of NW-SE shortening. Northwest- and southeast-dipping veins are related to brittle-ductile thrust faults, whereas sub-vertical E-W to NE-SW striking veins show a strong component of dextral strike-slip ductile shearing. It is proposed that the veins were emplaced under brittle-ductile conditions in a dextral transpressional shear corridor. Fluid overpressuring possibly led to fracturing of the host greenstones. The subsequent pressure drop led to metal precipitation. The newly-formed veins, which remained weaker than the surrounding metabasalts, localized subsequent fluid circulation and ductile strain increments.

Coaxial NW-SE compression is reported for both the Paleoproterozoic Svecofennian and the Silurian Caledonian orogenies. Re-Os analysis on sulfides is in progress and will provide constraints on the age of both vein formation and associated tectonic stress regime.

Keywords. Mesothermal, carbonate-quartz veins, Cu, structural control

1 Introduction

Mesothermal vein systems commonly form from fluids that were focused into- and transported along brittle-ductile shear zones. Vein geometry, orientation and spatial arrangement are a function of the properties of the stress field at the time of their emplacement. The opening of fractures that eventually act as fluid pathways, the deposition of vein material and in some cases even the precipitation of noble metals are structurally controlled and governed by the dominating stress state and its interplay with the local environmental conditions, not least fluid pressure (e.g. Sibson 1988, Weatherley and Henley 2013). It is therefore essential to constrain the structural boundary conditions of mesothermal vein systems in order to understand their formation and their genetic link to the regional geological evolution.

Greenstone-hosted mesothermal quartz-carbonate

vein systems are typically emplaced syntectonically, and are often associated with steeply-dipping shear zones developed under greenschist to amphibolite facies metamorphic conditions in a compressive to transpressive regime (e.g. Sibson et al. 1988, Dubé and Gosselin 2007). Quartz-carbonate vein systems are of great economic interest, especially because they can contain economic Au grades.

Numerous mesothermal carbonate (+/- quartz) veins are found within the Paleoproterozoic metasupracrustal rocks of the Repparfjord Tectonic Window (RTW) in northern Norway. The veins are mainly emplaced in deformed, greenschist facies tholeiitic metabasalts and are spatially related to a compressional imbricate stack of the Paleoproterozoic sequence. The RTW veins differ from typical greenstone-hosted quartz-carbonate veins because they are mainly carbonate-dominated, they lack economically viable Au concentrations, and are relatively Cu-rich (1-10% Cu).

Most of the Cu-vein deposits were exploited in the late 19th and early 20th century, with production ending in the 1930s. As a result, only a few geological investigations of the vein deposits have been carried out since then (e.g. Vokes 1956, Viola et al. 2008). Today, the known vein deposits in the RTW are only of sub-economic interest, mainly because of their small size.

In order to better understand the formation of the RTW vein deposits, constraints must first be placed on their structural characteristics and their age. In this paper, we explore the structural setting of these veins and try to frame the conditions leading to their formation in a regional tectonic context. Re-Os dating of sulfides is in progress to help establish the age of vein formation and the associated deformational episode.

2 Geological setting

The RTW is situated just north of the town of Alta and about 100 km south of North Cape, and is a culmination of Paleoproterozoic greenschist facies metasupracrustal rocks within the Caledonian Nappe System (CNS). The sequence is thought to represent the northern continuation of the Kautokeino greenstone belt, which in turn correlates with the Central Lapland greenstone belt in Finland (e.g. Pharaoh and Pearce 1984).

The Paleoproterozoic rocks of the RTW include

arkosic sandstones and conglomerates, ultramafic to rhyolitic calc-alkaline to tholeiitic volcanites and a sequence of stromatolitic dolomites and shales. Pharaoh et al. (1983) revised the original stratigraphy established by Reitan (1963) and defined four groups: the Holmvann Group (diverse volcanics), the Saltvann Group (clastic sediments), the Nussir Group (basaltic volcanics) and the Porsa Group (dolomites and shales). Some of these are crosscut by two plutonic suites: the ultramafic to gabbroic Rødfjell suite and the tonalitic to trondhjemitic Kvittfjell suite. A regional tectonometamorphic event at c. 1840 Ma (Svecofennian orogeny) produced long wavelength, upright folding along NE-SW trending axes associated with greenschist to lower amphibolite facies metamorphism (Pharaoh et al. 1983). The Paleoproterozoic RTW sequence is overlain by an autochthonous Neoproterozoic sedimentary unit, the Lomvann Formation. The NW-SE-directed Silurian emplacement of the CNS during the Caledonian orogeny produced large-scale compressional imbricate stacking of the Paleoproterozoic sequence in the western part of the window, as well as extensive deformation and greenschist-facies metamorphism of the autochthonous Lomvann Formation. The carbonate-quartz veins within the RTW are spatially associated with this imbricate and we tentatively assign them to this deformation episode.

In addition to the mesothermal veins, also larger sediment-hosted Cu deposits are found within the RTW (Sandstad 2012). These are the sandstone-hosted Ulveryggen (7.7 Mt at 0.81% Cu) and the dolomite-slate-hosted Nussir deposits (26.7 Mt at 1.13% Cu).

3 Characteristics of typical vein deposits

3.1 The Porsa deposit

The Porsa deposit is one of the largest vein-type deposits in the RTW, and the focus of this study. It consists mainly of two 1-5 m wide E-W oriented carbonate veins emplaced in weakly deformed to massive greenstones, with locally preserved pillow lavas and primary textures. The veins are arranged in an en-echelon pattern, with each individual vein segment being up to 100 m in length and tapering out at a depth of c. 100 m.

In the central part of the veins a pervasive mylonitic foliation is defined by alternating leucocratic carbonate-rich and melanocratic opaque-rich bands (Fig. 2). The foliation is oriented on average 180/85 (dip dir/dip) and parallels the veins. An E-W sub-horizontal mineral lineation is defined by stretched calcite crystals. On the regional scale, host greenstones have a variably developed NW-dipping foliation. At Porsa, this foliation is steep (85°), dips to the southeast and is progressively dragged into parallelism with the internal vein foliation, reflecting overall dextral strike-slip kinematics (Fig. 1). This kinematic interpretation is supported by the presence of quartz and greenstone sigma-clasts within the vein also indicating dextral shearing.

The main ore minerals are chalcopyrite, pyrite and magnetite, with minor hematite. Calcite, actinolite, albite, quartz and chlorite make up the gangue mineral assemblage. The wall-rock greenstones are affected by chloritisation, albitisation and carbonatisation reactions,

with alteration halos extending a few decimeters from the veins. Albitisation appears to pre-date the precipitation of calcite at several localities. Euhedral magnetite is abundant in nearby greenstones, whereas sulfides are absent. Sulfides and oxides occur both as coarse-grained irregular aggregates and lenses in the outer part of calcite veins and as fine-grained anhedral stringers in the foliated central part. Petrographic studies show that chalcopyrite in the outer parts of the veins tends to fill in cracks in coarse-grained euhedral pyrite and bladed magnetite (hematite pseudomorphs). In the foliated central parts chalcopyrite is frequently elongated parallel to the foliation (Fig. 4; similar texture at the Bratthammer vein). In pyrite-rich bands chalcopyrite is predominantly found as partial overgrowths on pyrite and magnetite. In some cases chalcopyrite even forms a coherent cement around the two.

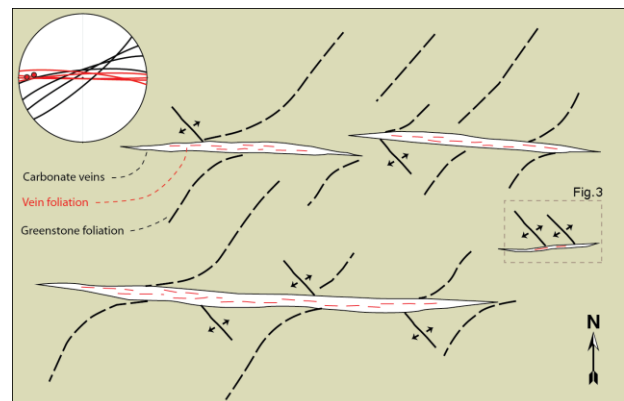


Figure 1. Sketch of the en-echelon arrangement of carbonate veins at the Porsa deposit, and of the relationship between internal vein foliation and external greenstone foliation. The sketch also illustrates the relationship between the Porsa veins and the NW-SE oriented pure extensional fractures. The stereonet plots the orientation of the two foliations (internal in red, external in black), as well as the associated mineral lineation.

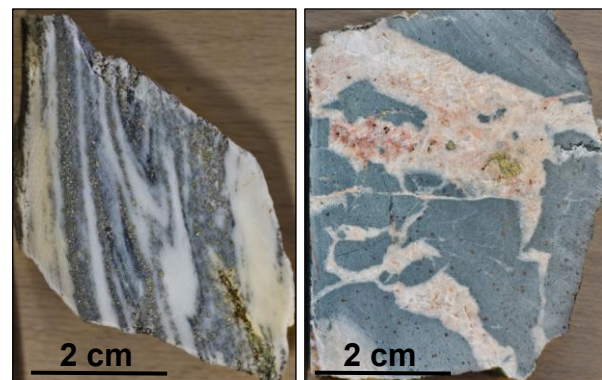


Figure 2. Hand specimens illustrating the clear textural difference between the strongly foliated core (left) and the outer, brecciated parts of the veins (right).

Along the vein contacts the greenstones are brecciated into angular fragments in an albite-quartz-calcite matrix (Fig. 2). Strongly altered sub-rounded greenstone clasts are abundant within the veins. The clasts become increasingly smaller and elongated in response to plastic deformation towards the centre of the vein, reflecting an increase in shear strain. A close genetic link between ductile deformation and

chalcopyrite morphology is observed in the central part of the veins. Chalcopyrite-bearing bands are isoclinally folded (Fig. 2) and chalcopyrite grains are elongated and strung-out parallel to the foliation.

Structural observations of minor faults and veins in the immediate vicinity of the deposit support the dextral strike-slip kinematics of the Porsa vein and help to constrain the orientation of the principal stress axes at the time of vein formation. At one locality (Fig. 3) a set of steep NW-SE striking extensional calcite-filled fractures intersects a discrete fault that parallels the Porsa veins and is itself locally Cu-mineralized. The extensional veins do not cut across the fault. Similarly to the main fault, the veins are in-filled by calcite, indicating that the dilation of the fractures was simultaneous with movement along the fault. As extensional fractures form parallel to the maximum and orthogonal to the least compressive stress, this indicates NW-SE compression with an horizontal NE-SW extension. This is also consistent with the stress field required to produce the opening of the Porsa veins and the dextral shearing along them.

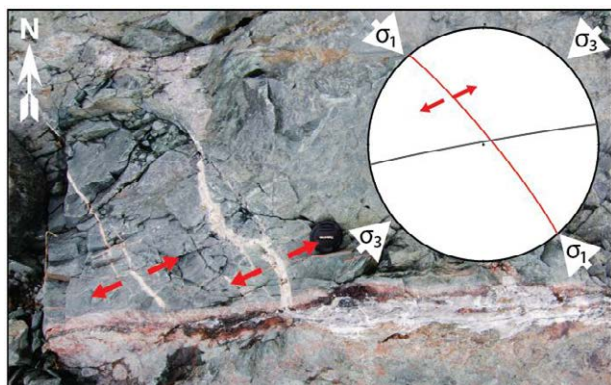


Figure 3. Steep NW-SE striking extensional calcite-filled fractures at Porsa are closely linked to the E-W striking dextral shear zones, such as the Porsa vein deposits. The stereonet shows the orientation of the extensional fractures (red) and the fault (black); arrows show the orientation of the associated greatest (σ_1) and least (σ_3) compressive stress.

3.2 The Bratthammer deposit

The Bratthammer deposit is a small (<1 m thick) Cu-rich carbonate vein that was mined in the early 20th century. It can be followed laterally for about 30 m, but down-dip it reduces in thickness to only 10 cm at 3-4 m below surface.

The Bratthammer vein shares many similarities with the Porsa deposit: it is also a sheared carbonate vein that cuts across foliated greenstones of the Holmvann Group, and it has an identical ore and gangue mineral assemblage. However, it differs from the Porsa deposit in terms of orientation and kinematic framework. At Bratthammer the vein dips moderately to the southeast (153/48), with moderately plunging stretching lineations (38→130). Small-scale duplexes and sigma-clasts indicate that the vein formed within a top-to-the NW thrust faulting regime.

Like in the Porsa veins, chalcopyrite is found either as small grains strung out parallel to the foliation or as partial overgrowths on pyrite and magnetite (Fig. 4).

Occasionally, chalcopyrite is found as coarser, sub- to euhedral grains with inclusions of subhedral pyrite (Fig. 4; left photo), indicating that at least some of the chalcopyrite precipitated after the pyrite.

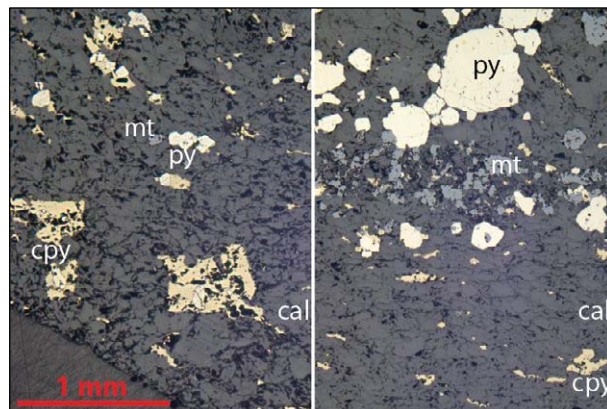


Figure 4. Two photomicrographs from the sheared part of the Bratthammer vein showing both fine-grained chalcopyrite strung out parallel to the foliation and coarse-grained sub- to euhedral chalcopyrite with pyrite inclusions. Reflected light. cpy = chalcopyrite, py = pyrite, mt = magnetite, cal = calcite

3.3 The Halsvatnet deposit

The Halsvatnet deposit is a quartz-dominated vein that was prospected for Cu for a short period during the early 20th century. The vein cuts greenstone conglomerates, is up to 4 m wide and extends laterally for at least 100 m. Its vertical extension, however, is not known. In the westernmost exposed part, the vein is at its thickest and dips moderately to the northwest (330/45). To the east the vein thins considerably, becomes steeper and changes in orientation to 358/75. The foliation in the adjacent greenstone conglomerates is oriented 310/80.

The Halsvatnet vein is different from the Porsa and Bratthammer deposits as it is *not* foliated. The lack of an observable central foliation possibly reflects the lack of calcite, which is only present as scattered and stretched lenses in between the quartz. In the western part of the Halsvatnet pit the foliation of the host greenstones is dragged asymptotically into the vein, indicating top-to-the E/SE thrust kinematics.

Chalcopyrite and magnetite are the main ore minerals, while quartz, calcite and chlorite define the gangue mineral assemblage. The precipitation of calcite and chalcopyrite appears to be coeval as they are often found together interstitially in the quartz, frequently infilling fracture networks. The amount of chalcopyrite is particularly high where the brecciation is most pronounced, indicating that chalcopyrite precipitation was associated with elevated fluid pressure.

4 Proposed model: Vein emplacement in a transpressive dextral shear corridor

The analysis of structural measurements from a total of 11 separate Cu-bearing veins in the RTW shows that the vein deposits can be sorted into three kinematically distinct groups (Fig. 5): 1) Sub-vertical E-W to NE-SW striking veins associated with dextral strike-slip movement, 2) NW or SE dipping veins associated with

dip-slip reverse faulting and 3) Sub-vertical NW-SE striking veins. The schematic 3D block in Fig. 5 illustrates the geometric and kinematic characteristics of the different groups.

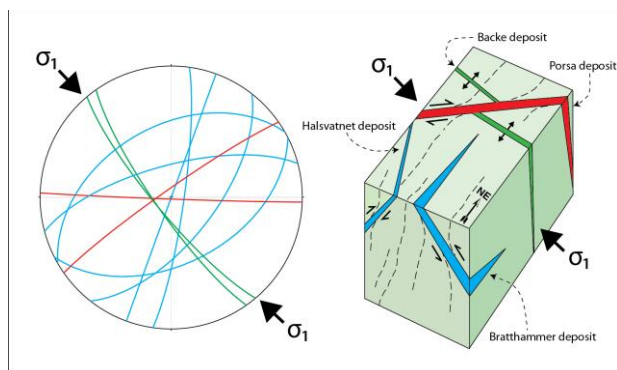


Figure 5. Compilation of structural measurements from the Cu-bearing veins in the RTW. The stereonet shows the orientations of the mineralized veins. The three different structural groups are color-coded in both figures. Small arrows in the block diagram indicate fault kinematics, while large arrows show the orientation of the largest compressive stress (σ_1).

The third group (sub-vertical NW-SE striking veins) includes the Backe and Bahrs deposits, where poor exposure prevents good structural observations. Nevertheless, the structural character of the NW-SE striking veins is demonstrated by a number of discrete extensional fractures and faults in the vicinity of the Porsa deposit. As seen in Fig. 3, these veins are purely dilatational. On a regional scale there is a predominance of sub-vertical NW-SE striking extensional fractures and a general lack of sub-horizontal ones. This implies that the least compressive stress (σ_3) must have been sub-horizontal, which is consistent with the stress state required for dextral strike-slip shearing along E-W to NE-SW striking veins. Dextral strike-slip deformation is also documented regionally within the RTW along non-mineralized NE-SW striking shear zones (Viola et al. 2008) and is confirmed by our study. In summary, the structural analysis suggests that the studied veins formed in a dextral transpressive shear corridor during a phase of overall NW-SE shortening.

The coexistence in the Porsa veins of structural features that can be ascribed to both plastic/brittle (breccias at the vein-host rock contact) and viscous/ductile (vein mylonitic cores) regimes, and the fact that the latter overprint the former, strongly suggests the reactivation of brittle precursors within an overall ductile environment. The embrittlement and mechanical failure of the host greenstones was, according to the Mohr-Coulomb criteria, possibly due to increased pore pressure locally exceeding the strength of the rock. This would result in the nucleation of fractures, localized dilatant brecciation and subsequent infill of the newly formed fractures with the vein material. Progressive crystallization and healing of the dilatant rupture zones would lead to strain hardening and accommodation of further deformation by viscous processes during the mylonitization of the veins' core.

In summary, we believe that initial fracturing and microcracking of the Nussir greenstones, possibly highly

enhanced by transient high strain rate or overpressured fluid phases, resulted in the pressure-dependent viscoplastic rheology of the Porsa shear zone corridor still under bulk viscous conditions, with only very limited overall loss of cohesion (e.g. Mancktelow, 2006).

NW-SE coaxial compression is reported for both the Paleoproterozoic Svecofennian and the Silurian Caledonian orogenies. In the RTW the Svecofennian orogeny caused long wavelength, upright folding along NE-SW trending axes, while the Caledonian orogeny produced a large-scale NW-dipping compressional imbricate stack in the western part of the window. From a structural point of view it is therefore difficult to assign the veins to either of the orogenic episodes. Traditionally, these deposits have been interpreted to be of Paleoproterozoic age, as similar vein deposits are not observed in the overlying CNS in the area. However, the spatial restriction of the veins to only the part of the window that is influenced by Caledonian imbrication may indicate that the veins are of Silurian age.

Ongoing Re-Os dating of a number of chosen sulfide samples will add valuable constraints to the proposed metallogenetic model of the RTW vein deposits and, in addition, will also strengthen our structural analysis by better constraining the age of the NW-SE shortening event.

Acknowledgements

Thanks to Håvard Smeplass for good discussions on the Bratthammer deposit.

References

- Dubé B, Gosselin P (2007) Greenstone-hosted quartz-carbonate vein deposits. In: Goodfellow WD (ed) Mineral Deposits of Canada: A Synthesis of Major Deposit-Types, District Metallogeny, the Evolution of Geological Provinces, and Exploration Methods. Geological Association of Canada. Special Publication 5:49-73
- Mancktelow, NS (2006) How ductile are ductile shear zones? *Geology* 34:345-348
- Pharaoh TC, Ramsey D, Jansen Ø (1983) Stratigraphy and structure of the northern part of the Repparfjord-Komagfjord window, Finnmark, Northern Norway. *Norges geologiske undersøkelse* 377:1-45
- Pharaoh TC, Pearce JA (1984) Geochemical evidence for the geotectonic setting of Early Proterozoic metavolcanic sequences in Lapland. *Precambrian Research* 25:283-308
- Reitan PH (1963) The geology of the Komagfjord tectonic window of the Raipas suite, Finnmark, Norway. *Norges geologiske undersøkelse* 221:1-71
- Sandstad JS (2012) N039 Alta-Repparfjord Cu-Au. In: Eilu, P. (ed.). Mineral deposits and Metallogeny of Fennoscandia. Geological Survey of Finland. Special Paper 53:122-127
- Sibson RH, Robert F, Poulsen KH (1988) High-angle reverse faults, fluid-pressure cycling, and mesothermal gold-quartz deposits. *Geology* 16:551-555
- Viola G, Sandstad JS, Nilsson LP, Heincke B (2008) Structural and ore geological studies in the northwestern part of the Repparfjord Window, Kvalsund, Finnmark, Norway. *Norges geologiske undersøkelse* Report 2008.029:93 p
- Vokes FM (1956) Some Cu sulfide parageneses from the Raipas formation of Northern Norway. *Norges geologiske undersøkelse* 200:74-111
- Weatherley DK, Henley RW (2013) Flash vaporization during earthquakes evidenced by gold deposits. *Nature Geoscience* 6:294-298

The Poopó Sn-Ag-Zn-Pb vein deposit, Bolivia: structure and mineralogy

Belén Torres, David Artiaga, Lisard Torró, Esperança Tauler, Joan Carles Melgarejo

Departament de Cristal·lografia, Mineralogia i Dipòsits Minerals, Facultat de Geologia, Universitat de Barcelona, Catalonia, Spain.

Oswaldo R. Arce

Colegio de Geólogos de Bolivia, C/ Federico Suazo 1673, Edificio SERGEOTECMIN

Abstract. The Poopó vein deposit in Bolivia is found on a regional fault. Deposition of the ore minerals is multiepisodic in association with the fault movement. A first generation of ore comprises pyrite, arsenopyrite, sphalerite and cassiterite. This ore formed contemporaneously with the fault activity and is brecciated. A second association is enriched in Sn-Sb-Pb-Ag-sulphosalts. These sulphosalts do not collect In, which is concentrated in the sphalerite structure. Despite these mineralizations would be linked with the Miocene intrusives of the area, the hosting Paleozoic black shales are suggested to have been a possible source of the metals.

Keywords. fault, vein, sulphosalts, Sn, Ag, In, Poopó deposit

1 Introduction

The Poopó deposit is located in the municipality of Poopó, 55 km SSE of Oruro city (Bolivia), and is part of the Sn-Ag belt of Bolivia (Ahlfeld, 1967; Turneure, 1971). The deposit has been mined since the 19th century. It is currently mined by local mining cooperatives, employing around 400 persons. The production of the ensemble of mines is around the 4000 t of ore per month. The ore is sold for refinement of Zn, Pb, Ag and Sn. However, no information exists on the rare metal content of the ore. The ore mineralization in these mines represents a great opportunity to study the behaviour of rare metals in a complex mineralization including a remarkable assortment of sulphosalts species. The aim of this contribution is to describe the mineral associations in the Poopó deposit and the distribution of rare metals among these mineral species.

2 Geological setting

The Poopó town is located close to the limit between the Bolivian Altiplano and the Central Ranges of the Eastern Cordillera, the so-called Poopó regional fault trending NNW-SSE (Fig. 1).

The Andean Eastern Cordillera is made up of polydeformed Ordovician to Cretaceous sedimentary sequences, comprising black shales, siltstones, limestones, sandstones, slates, and quartzites. The Andean orogeny produced regional faults and fold systems trending NNW-SSE, locally accompanied by thrusting (McQuarrie & DeCelles 2001). The ensemble has been affected by very low grade regional metamorphism.

Intrusions of Miocene felsic stocks and domes are found in the central part of the Eastern Cordillera, and are partly covered by ignimbrite sequences of Upper Miocene age.

The Altiplano is a continental foreland basin trending NNW-SSE along 850km with an average width of 130 km. The Cenozoic sedimentary basin infilling achieves more than 15 km in thickness, and is made up of detrital and evaporitic sediments (Lamb and Hoke 1997). Important lakes such as the Poopó Lake are developed in the plains.

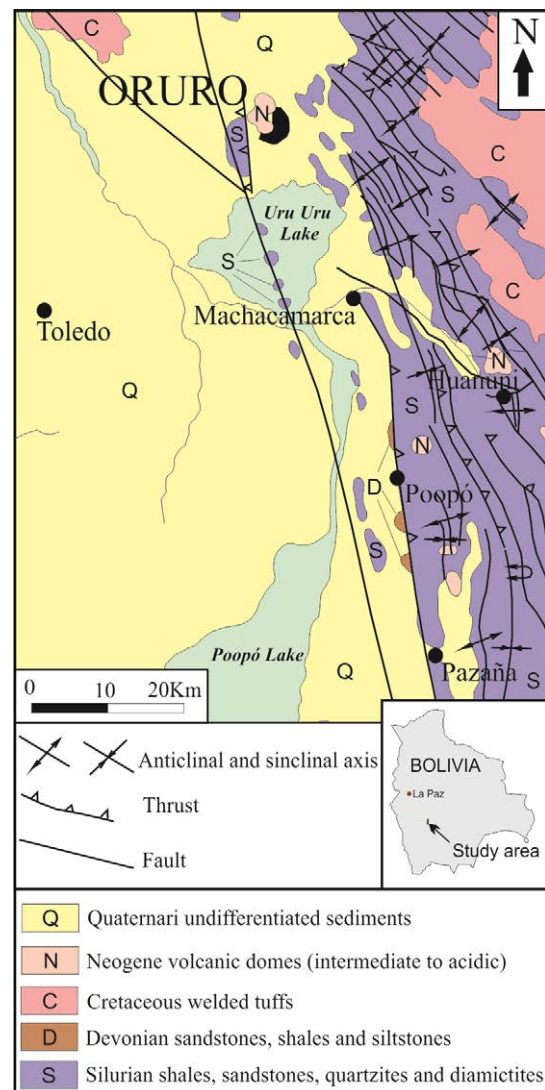


Figure 1. Geological map of the Poopó mining area, with indication of the main mines. Modified from SERGEOTECMIN (2001)

3 Structure of the deposit



Figure 2. Alignment of mining operations following the intercept of the Poopó fault with the topographic surface.

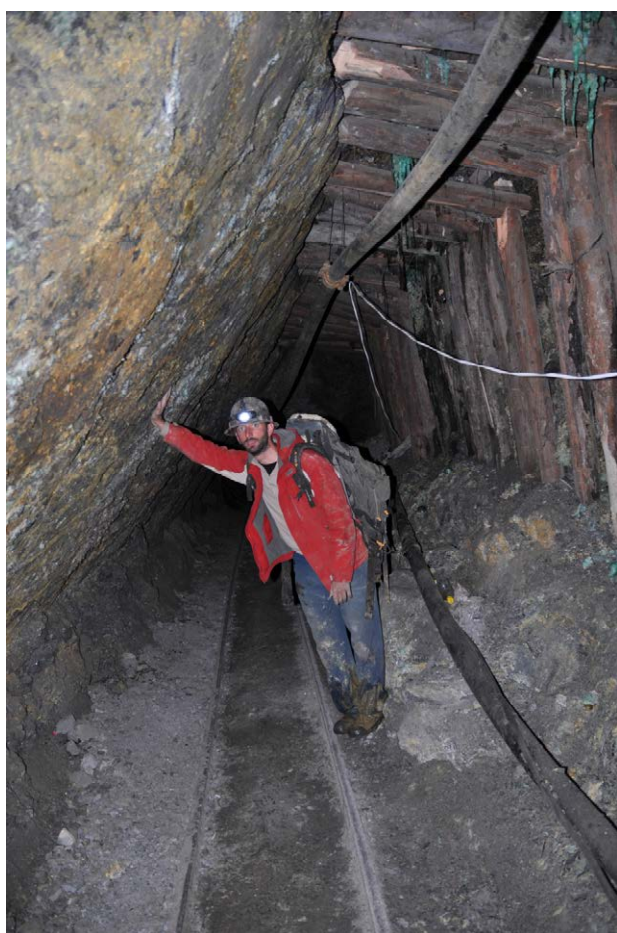


Figure 3. The Poopó fault plane in the San Francisco mine.

The Poopó mines are developed on a vein system hosted by the Poopó regional fault zone and their satellite structures (Ahlfeld & Schneider-Scherbina, 1964). The main vein is along the fault, and has a dipping of around 50-70° E. Some of the galleries are opened directly at the intersection of the fault plane with the topographic surface (Fig. 2). They are mainly mined using ramps descending directly following the fault plane. In other cases, as in the case of San Francisco mine, the fault surface is raised by horizontal galleries.

In addition to the main vein system associated with

the fault surface, there are many other veins that could represent joints in echelon associated with the fault plane. These veins, which can be more than 1 m wide, are currently under mining. Veins such as Calaveras and Santa Cruz are thought to belong to the latter.

The widths of the veins are generally of metric order, and have a complex internal structure suggesting many mineralizing pulses. In the San Francisco gallery the veins register evidences of having undergone cataclastic deformation with repetitive brecciation of the ores. The resulting fragments are cemented by quartz accompanied by late generations of sulphides and a large diversity of sulphosalts, poorly studied up to the present moment.



Figure 4. Evidences for multiphasic vein infilling in the veins of the Poopó fault system. The dark area is enriched in sphalerite and Sn sulphosalts and the clear area is filled by milky quartz. Total vein width is about 1,5 m.

4 Mineralogy and textures

The studied mineral associations in the deposit are remarkably complex. However, the mineral diversity is recognised to be very different in each part of the mines on an outcrop scale.

In the San Francisco section, the mineralization process comprise at least two main episodes.

The first episode resulted in an association of quartz, pyrite, arsenopyrite, sphalerite and cassiterite. These ores are generally fine-grained since they were deposited before or during the movement of the fault. Hence they are brecciated and have a cataclastic texture. The mineralizing process is thought to have been active during the periods of fault movement, as proved by the occurrence of complex brecciated fragments. That includes in turn several generations of fragments cemented by diverse pulses of ores (Figs. 5 and 6). The most common mineral in this stage is pyrite, accompanied by lesser amounts of Fe-rich, dark sphalerite. Pyrite and arsenopyrite tend to form small (less than 50 microns) euhedral crystals broken and recemented by the rest of minerals.

The second mineralising pulse took place after the climax of the activity of the Poopó fault. Delicate drusy crystal textures infilling cavities would be precipitated at later pulse. Comb and cockade textures are typical of this stage. The mineral association has also important differences with the first episode. A first vein infilling is

made up of quartz combs and geodes along with euhedral pyrite crystals. Stannite and a second generation of sphalerite are found replacing cassiterite. However, estannite is relatively scarce in this deposit, as already stated by Kelly and Turneure (1970). Alternatively to stannite, in most of the cases, the remaining porosity is filled by a sequence of euhedral Sn- sulphosalts. Teallite, frankeite, rhodostannite and cylindrite are particularly abundants (Figs. 7 and 8).

5 Mineral chemistry of the ores

Microprobe analyses were carried out in order to check the distribution of rare metals, in particular In and Ag, on the different mineral phases.

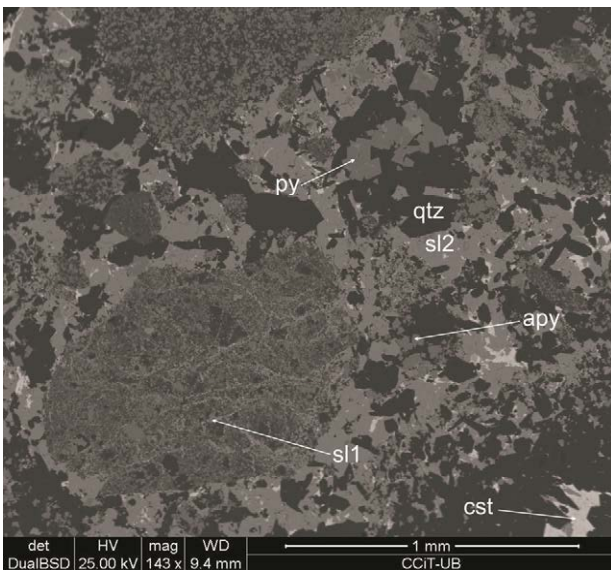


Figure 5. Brecciated ore including fragments composed of preexisting ore breccias. Note the cataclastic texture in the ores. Sl, sphalerite, py, pyrite, cst, cassiterite, apy, arsenopyrite. SEM image, BSE mode.

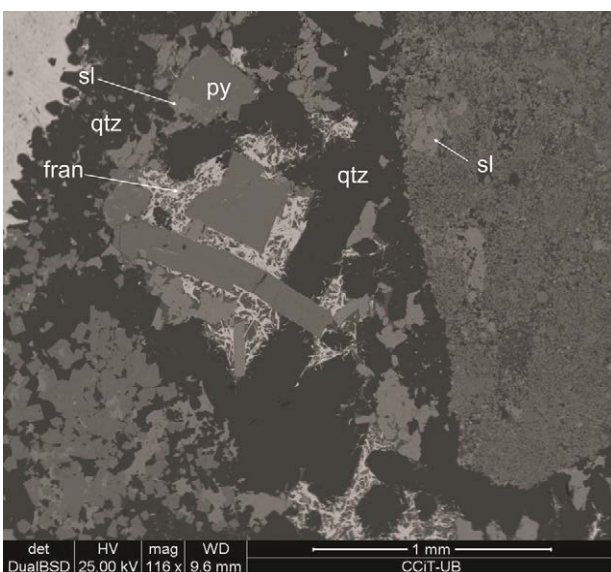


Figure 7 Brecciated ore of the first generation rimmed by euhedral quartz of the second generation. Sl, sphalerite, py, pyrite; fran, frankeite. SEM image, BSE mode.

5.1 Arsenopyrite

Arsenopyrite crystals are zoned due to the variations in the Sb contents, which is up to 5wt%. In contrast, Co and Ni contents are low. Nickel rarely exceeds 1 wt% concentrations.

5.2 Cassiterite

Cassiterite crystals are quite pure. The proportions of Fe and Ti are well below 1 wt % and no In enrichments was detected. Tantalum content is around 0,2 wt% in average. These values do not significantly differ from those reported on cassiterite from granites worldwide (i.e., Costi et al. 2000).

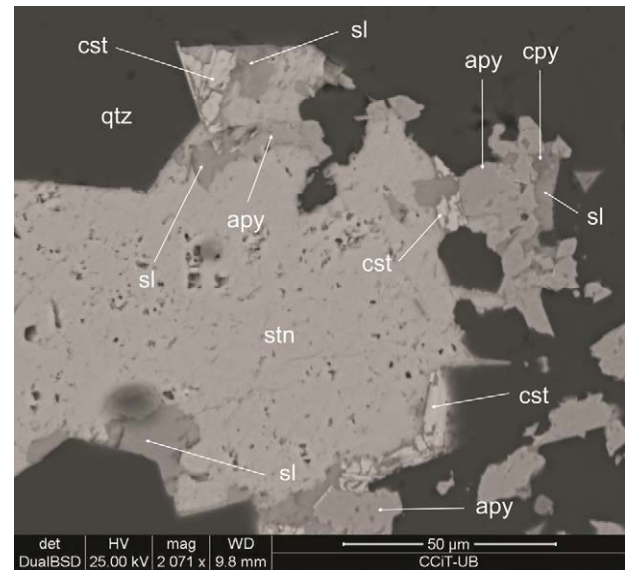


Figure 6. Drusy sequence of vein infilling during the post-tectonic stage (2) comprising quartz combs (qtz), along with arsenopyrite (apy), stannite (stn), chalcopyrite (cpy), cassiterite (cst) and sphalerite (sl). SEM image, BSE mode.

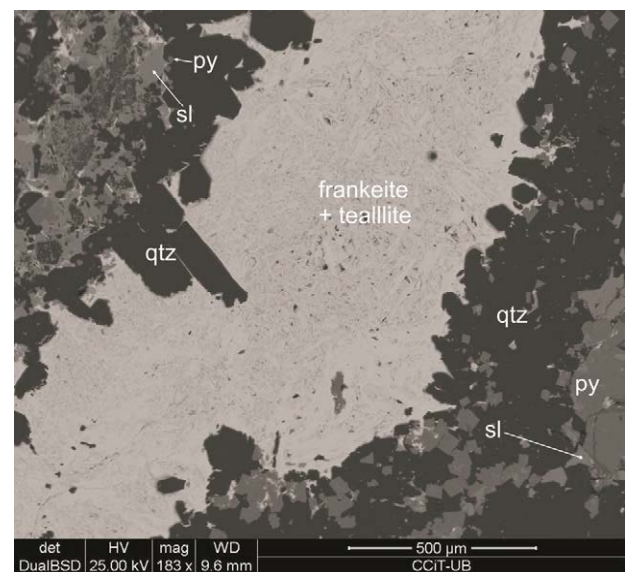


Figure 8. Drusy sequence of vein infilling during the post-tectonic stage 2 comprising euhedral quartz combs (qtz), accompanied by pyrite (py) and sphalerite (sl) and followed by a mixture of teallite and frankeite. SEM image, BSE mode.

5.3 Sphalerite

Sphalerite from Poopó has tenors of In of up to 0,5 wt%. However, the values are erratic and vary among the different sphalerite generations. Sphalerite from Poopó is also enriched in Cd, and achieves values higher than 1 wt% in the Santa Cruz vein. However these values are not high when compared with reference values worldwide (i.e., Ishiara et al. 2006; Cook et al. 2009). The Fe content is also low, less than 10 wt%. This feature is in good agreement with the relatively clear colour of the sphalerite in hand specimen.

5.4 Sulphosalts

The Poopó veins are enriched in sulphosalts. All the analysed samples are enriched in Ag. Franckeite from the Santo Toribio vein averages 1,1 wt% Ag, and appears along with Ag-rich rhodostannite (up to 4,6 wt% Ag, thus approximating to the compositions of toyohaite). These sulphosalts have a noticeable enrichment in Se, up to 0,17 wt% in analysed franckeite specimens. However, these sulphosalts do not concentrate significant amounts of In or Ge.

6 Discussion and conclusions

There are no outcropping intrusives that could be responsible for the generation of the Poopó deposit. In addition, evidence of contact metamorphism that could suggest the proximity of a plutonic intrusive is not detected. Alternatively, the Tertiary volcanic domes have been suggested as the activator for the metallogenetic processes (Turneure 1971). Similar situations occur in other parts of the Andean Cordillera, including Argentina (i.e., Jovic 2011). However, it should be taken into account that the Poopó vein, as well as other veins in Bolivia, is hosted by black shales of Paleozoic age. As it happens in other described cases in Bolivia, the possibility that the black shales could act as a preconcentrator for at least some metals such as Co, Ni, Ag, Zn, Mo and Pb cannot be ruled out. In this sense, the occurrence of large amounts of arsenides could be a favourable trap for the storage of Au and PGE in these mineralizations. Analogous situations in Catalonia allowed discovering PGE enrichments in löllingite and Ni- and Co- arsenides in unconventional PGE deposit styles (Canet et al. 2003).

Acknowledgements

The association of mining cooperatives in Bolivia (FENCOMIN) allowed us to visit the mines and to publish the results. Samples were analyzed in the Centres Científics i Tecnològics of the University of Barcelona. Dr. X. Llovet helped in the microprobe calibration. Funding was provided by the Consolidated Research Group Grant SGR 444 of the Generalitat de Catalunya and the AECID grant A3/042750/11.

References

- Ahlfeld F, Schneider-Scherbina A (1964) Los yacimientos minerales y de hidrocarburos de Bolivia. *Bol Dept Nac Geol La Paz* 5, 388 p.
- Ahlfeld F (1967) Metallogenetic epochs and provinces of Bolivia, *Miner Deposita* 2: 291–311.
- Canet C, Alfonso P, Melgarejo JC, Jorge S (2003) PGE-bearing minerals in Silurian sedex deposits in the Poblet area, southwestern Catalonia, Spain. *Can Mineral* 41: 581–595.
- Cook NJ, Ciobanu CL, Pring A, Skinner W, Shimizu M, Danyushevsky L, Saini-Eidukat B, Melcher F (2009) Trace and minor elements in sphalerite: A LA-ICPMS study. *Geochim Cosmochim Acta* 73(16): 4761–4791.
- Costi HT, Horbe AMC, Borges RMK, Dall'Agnol R, Rossi A, Sighnolfi G (2000) Mineral chemistry of cassiterites from pitinga province, Amazonian craton, Brasil. *Rev Bras Geoc* 30: 775–782.
- Ishihara S, Hoshino K, Murakami H, Endo Y (2006) Resource evaluation and some genetic aspects of indium in the Japanese ore deposits. *Res Geol* 56: 347–364.
- Jovic SM, Guido DM, Melgarejo JC, Páez GN, Ruiz, R, Schalamuk IB (2011) The Indium-bearing minerals of the Pinguino polymetallic vein system, Deseado Massif, Patagonia, Argentina. *Can Mineral* 49: 931–946.
- Kelly WC, Turneure FS (1970) Mineralogy, paragenesis and geothermometry of the tin and tungsten deposits of the eastern Andes, Bolivia. *Econ Geol* 65: 609–680.
- Lamb L, Hoke L (1997) Origin of the high plateau in the central Andes, Bolivia, South America. *Tectonics* 16: 623–649.
- McQuarrie N, DeCelles PG (2001) Geometry and structural evolution of the central Andean backthrust belt, Bolivia. *Tectonics* 20: 669–692.
- SERGEOTECMIN (2001) Mapa Geológico de Bolivia escala 1:1.000.000. La Paz, Bolivia.
- Turneure FS (1971) The Bolivian tin–silver province. *Econ Geol* 66: 215–225.

Gold metallogenesis of The Novo Mundo granite, eastern sector of the Alta Floresta Gold Province (MT), Amazon Craton

Verônica Godinho Trevisan, Roberto Perez Xavier, Rafael Rodrigues de Assis
Geosciences Institute, University of Campinas – UNICAMP, Campinas, Brazil

Antônio João Paes de Barros
Companhia Mato-Grossense de Mineração – METAMAT, Mato Grosso, Brazil

Abstract. The Novo Mundo granite represents one of the most important examples of disseminated and, more subordinately, gold mineralization in veins in granitic systems in the Paleoproterozoic Alta Floresta Gold Province. The Novo Mundo pluton hosts dozens of gold occurrences, such as Luizão, Dionissio and Basílio deposits. These deposits are hosted by granitic rocks strongly affected by hydrothermalism and that exhibits composition ranging from syenogranite-tonalite to monzonite. The hydrothermal system in each deposit evolved in a different way, but in general comprises pervasive alterations (potassic, sericitic, chloritic and propylitic alteration) as well as vein-type ones variable in composition. The ore zones are dominantly represented by gold-bearing pyrite, spatially and temporally related to intense sericitic/chloritic alteration, silicification and late-quartz veinlets. The ore precipitation can be attributed to decrease of temperature, increase of fO_2 and a decrease of pH. Furthermore, although the deposits have similarities and differences with general models such as porphyry gold and IRGS (Intrusion-related gold systems), these prospects do not fit into a single genetic model of deposit and therefore it is concluded that beyond the mineralization show spatial and genetic association with granitic plutons, it is located at greater depths than porphyry gold deposits.

Keywords. Alta Floresta Gold Province, Novo Mundo granite, gold, pluton-related deposits.

1 Introduction

The Alta Floresta Gold Province (AFGP, Mato Grosso State, Brazil), located in the south-central portion of the Amazon Craton, extends between the Ventuari - Tapajós (1.95 to 1.8 Ga) and Rio Negro - Juruena (1.8 to 1.55 Ga) geochronological provinces, which represents volcano-plutonic sequences generated in continental arc settings during the Meso- and Paleoproterozoic (Tassinari & Macambira 1999). This province hosts a significant number of Au ± Cu and Au-base metals deposits distributed along a NW-SW striking belt (Peru - Trairão belt) (Fig. 1). The primary deposits occur as veins, stockworks or disseminations mostly in tonalite/granodiorite and syenogranite/monzonite and display close temporal and spatial relationships with relatively oxidized (magnetite-bearing) I-type, calc-alkaline to sub-alkaline, medium to high K, metaluminous to peraluminous granitic rocks and, more subordinately, with volcanic sequences

(Souza et al. 2005, Paes de Barros 2007, Assis 2011).

Within this scenario occurs the Novo Mundo granite (1.970 ± 3 Ma – 1.964 ± 1 Ma; Paes de Barros 2007), which corresponds to one of the most important examples of disseminated and, more subordinately, gold vein mineralization in granitic systems in the province. Luizão (Paes de Barros 2007), Dionissio and Basílio are some of the major ore bodies hosted in the Novo Mundo granite. The first one is currently exploited by local prospectors (*garimpeiros*) whereas the last two still are under prospective studies.

In this work we characterize the host rocks, wall-rock alteration, ore association and fluid inclusions of some gold deposits hosted by the Novo Mundo granite to understand its metallogenic evolution such as in shedding more light on the genesis and exploration potential of gold-related granitic systems in the AFGP. For this, three gold deposits are presented as case studies: the Luizão, Dionissio and Basílio deposits.

2 Main types of deposits

2.1 Host rocks

Luizão, Dionissio and Basílio are the main representative mineralized systems within Novo Mundo pluton, a Paleoproterozoic oxidized I-type, calc-alkaline, high-K, meta- to peraluminous and magnesium granite, dated on 1970 ± 3 Ma – 1964 ± 1 Ma (Paes de Barros 2007).

The Luizão deposit is hosted by granitic rocks strongly affected by hydrothermal alteration, possibly of syenogranite, monzogranite and quartz-monzonite composition, however, the lesser altered portions are granodioritic (Paes de Barros 2007). This granite exhibits quartz crystal stretched and oriented at the same direction of NE-SW shear zones. On the other hand, Dionissio is hosted by rocks with composition varying from hornblende monzogranite to tonalite, whereas at Basílio the intrusion consists of biotite-hornblende granodiorite to tonalite (Fig. 2). Taken together, titanite, apatite, zircon, magnetite and monazite occurs as accessory phases. Basalt, andesite, gabbro and diorite dikes often crosscut the Novo Mundo granite. Additionally, aplite dikes also cross-cut the host rocks, especially at Dionissio and Basílio targets.

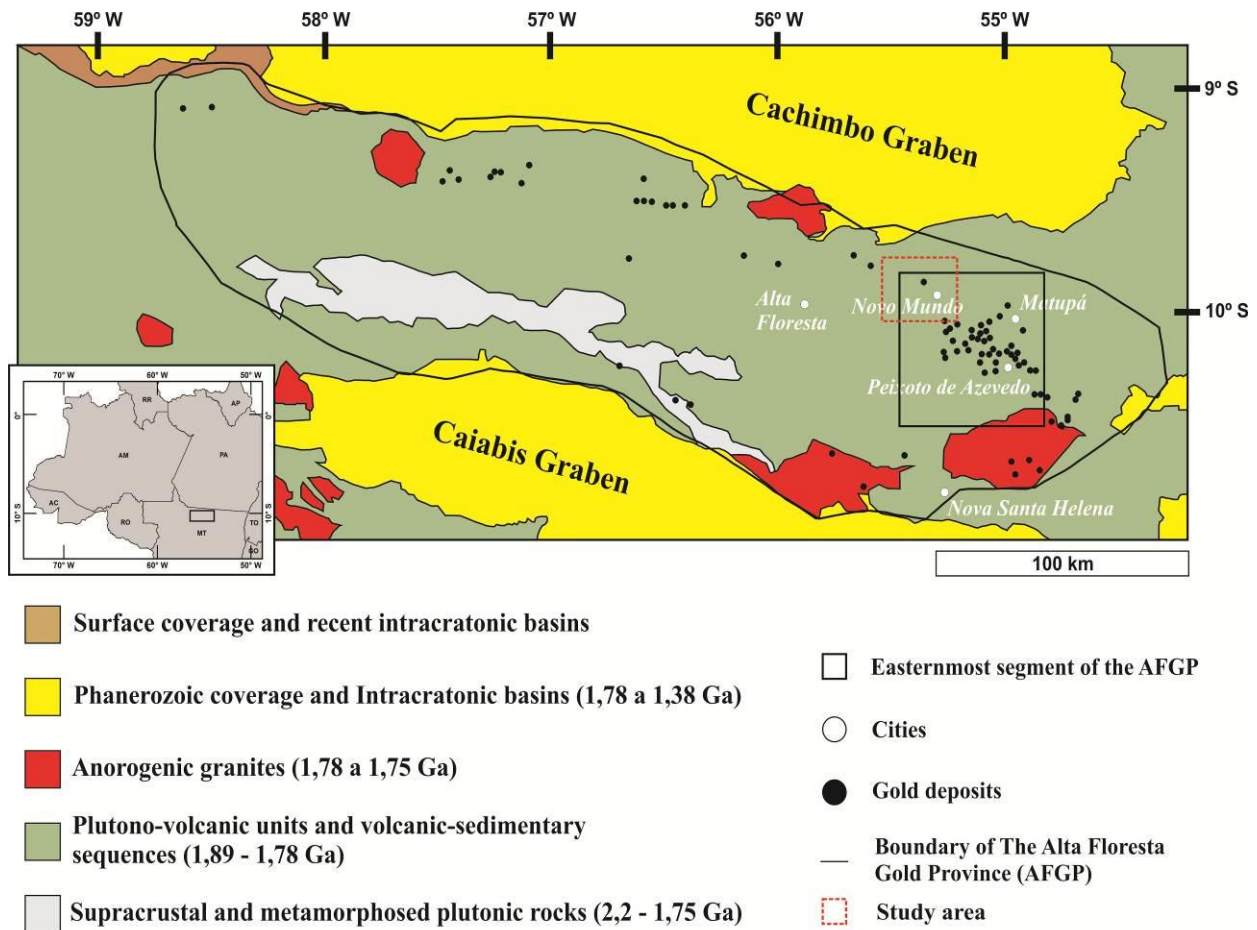


Figure 1. Simplified geological map of the Alta Floresta Gold Province (AFGP) showing the distribution of the gold deposits in the province (small black dots; modified from Paes de Barros 2007). The Luizão, Dionissio and Basílio gold deposits investigated in this work are located near Novo Mundo city (dotted red square).

2.2 Hydrothermal alteration

The host rocks in the Novo Mundo pluton are strongly affected by different types and styles of hydrothermal alteration.

In the case of Luizão deposit it has been temporally affected by the following hydrothermal alterations: (i) sodic alteration with albite; (ii) potassic alteration with microcline; (iii) sericitic alteration; (iv) chloritic alteration; (v) late epidote-apatite-dolomite-calcite vein-type (Paes de Barros 2007).

In the case of Dionissio deposit, the hydrothermal system follows the temporal sequence given by: (i) potassic alteration with orthoclase; (ii) early calcite-chlorite vein-type; (iii) silicification; (iv) phyllic alteration; (v) carbonatization; (vi) chloritic alteration; (vii) propylitic alteration with epidote-clinozoisite-calcite-chlorite-titanite-apatite-quartz; (viii) late calcite-epidote-quartz-chlorite-clinozoisite vein-type.

Finally, at the Basílio target the same hydrothermal alteration styles and types are found, nevertheless, in a different evolutionary path from Dionissio: (i) potassic alteration with orthoclase; (ii) carbonatization; (iii) sericitic alteration; (iv) chloritic alteration; (v) propylitic alteration with the same mineral association of Dionissio deposit; (vi) early calcite-chlorite vein-type; (vii)

silicification; (viii) late quartz-calcite-epidote-clinozoisite-chlorite-apatite vein-type.

2.3 Gold ore zones

The ore is disseminated and confined in veinlets within zones of intense sericitic/chloritic alterations, but also related to the silicification and late quartz-veinlets, especially for Dionissio and Basílio targets (Fig. 3).

The gold (Ag content = 4 to 45%) occurs dominantly as inclusions in pyrite, along with variable inclusions of chalcopyrite, sphalerite, galena, bornite, covellite and hematite, besides minor amounts of ilmenite, rutile, monazite, thorite, hessite (Ag_2Te), barite, matildite (AgBiS_2) and Bi-Te-rich phases.

Fluid inclusion assemblages in quartz reveal that the Luizão auriferous zones (Assis 2006) are dominated by two types of aqueous fluids: (1) a high salinity (33.6 – 37 wt% NaCl eq.) fluid represented by halite-bearing fluid inclusions with total homogenization temperature (Th) ranging from 200° to 280°C; and (2) a low-to-intermediate salinity (2.5 – 15 wt% NaCl eq.), lower temperature (Th = 95°C – 185°C) fluid represented by two-phase inclusions. Minimum pressure conditions of entrapment for these fluids are within 0.9 – 1.2 kb.

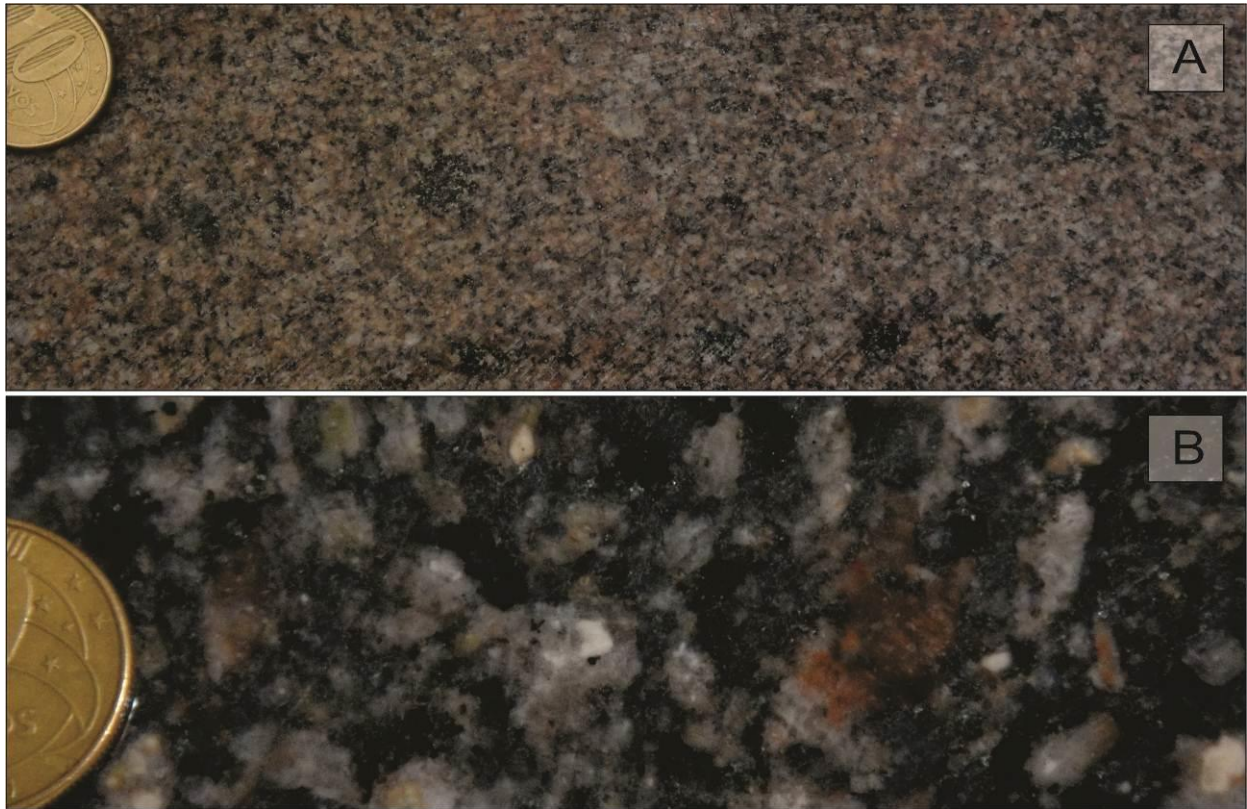


Figure 2. (A) Hornblende monzogranite to tonalite strongly hydrothermalized in a potassic alteration with orthoclase (Dionissio deposit); (B) Biotite-hornblende granodiorite to tonalite (Basilio deposit).

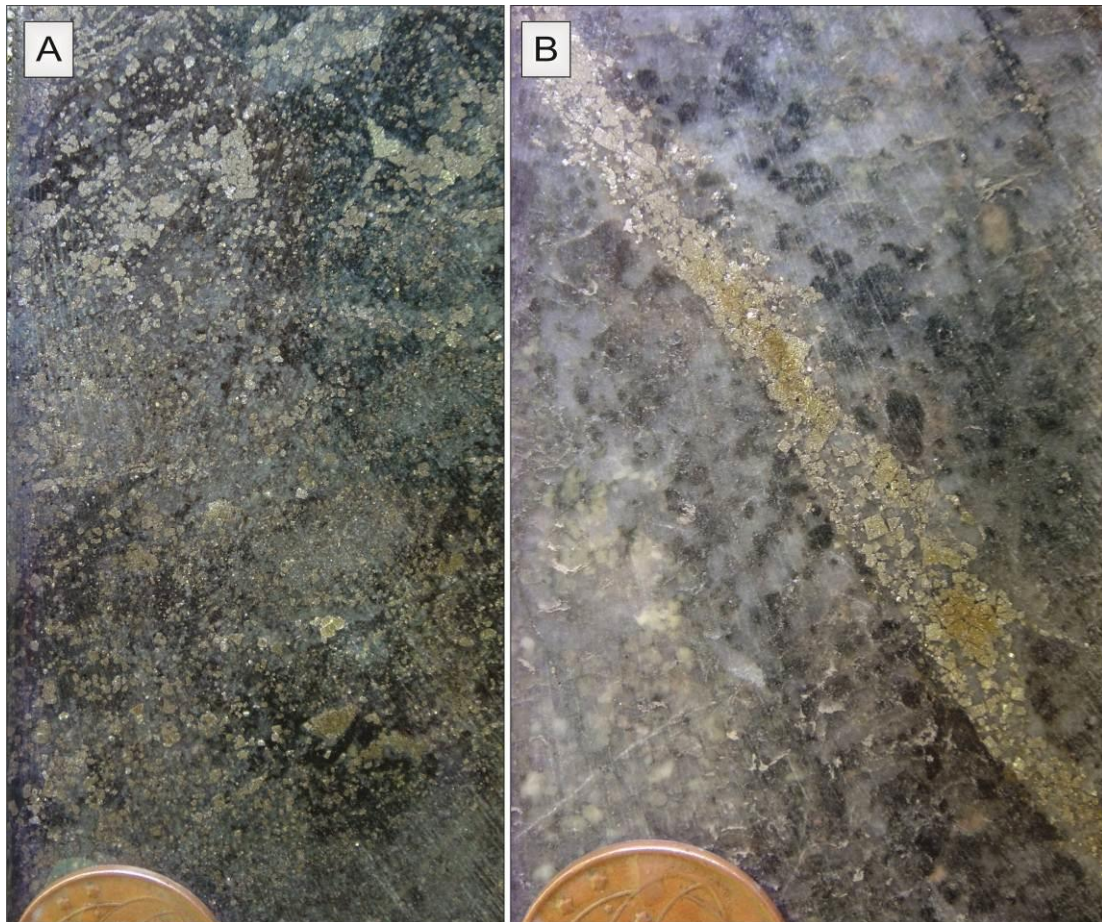


Figure 3. Gold ore zones dominantly associated with pyrite in intensely altered rocks: (A) Disseminated pyrite related to chloritic and sericitic alterations; (B) Fissural gold ore associated to late quartz-veinlets.

3 Discussions

A detailed characterization of the geological attributes of the Novo Mundo granite carried out in this study allowed complement the data obtained in previous studies (Paes de Barros 2007) on the Luizão deposit.

These data show that the host rocks of the Novo Mundo granite are mainly of granitic composition and even with the high fluid/rock ratios some original textures and composition of the protolith was preserved. The presence of shear zones in the NE and SW edges of the pluton may have facilitated both the rise of magma emplacement, due to the presence of stretched quartz in the matrix, and fluids from deeper crustal levels, which were responsible for producing these strongly altered rocks. Furthermore, the host rocks show a wide compositional variation, indicating the occurrence of different emplacement events (multiple intrusion stages?) or even a facies variation at the Novo Mundo granite.

The hydrothermal ore-forming paleosystem of the Novo Mundo granite encompasses pervasive hydrothermal alterations such as potassic alteration (with microcline and orthoclase), silicification, carbonatization, sericitic, chloritic and propylitic alterations, but also confined alteration with variable composition. These veinlets may indicate the incursion of later fluids or just a continuity in the evolution of the hydrothermal system of the pluton. Moreover, the ore precipitation is mainly related to the sericitic and chloritic alterations, but also to the silicification and later veinlets of quartz. Taking both the ore paragenesis and the fluid inclusions data together, the ore precipitation might have taken place due to an increase of fO_2 (hematite and barite precipitation), possibly due to influx of oxidizing external fluids (meteoric?) which triggered a temperature decreasing (mixing process?) plus a lowering in the pH of mineralizing fluid.

In this scenario, it is suggested that the deposits in the Novo Mundo granite show similarities and differences with general models such as gold-porphyry (Guilbert & Park, 1985; Pirajno, 1992; Sillitoe 1991; Corbett & Leach 1998; Seedorff et al. 2005; Candela & Piccoli 2005; Robb, 2006; Sinclair 2007; Sillitoe 2010) and IRGS (Intrusion-related gold systems; Lang & Baker 2001; Baker 2002; Thompson et al. 1999; Hart 2007). Nevertheless, the Au (\pm Cu) mineralization associated with these prospects do not fit into a single genetic model of deposit and therefore we can say that beyond the mineralization show spatial and genetic association with granitic plutons, it is located at greater depths than porphyry gold deposits.

Acknowledgements

We are very grateful to the Companhia Mato-Grossense de Mineração (METAMAT) for the continuous field support provided to our research group in the AFGP. This research was supported by the Instituto Nacional de Ciência e Tecnologia de Geociências da Amazônia (GEOCIAM) as well as Gráben Mineração S/A.

References

- Assis R R (2006) Estudo de inclusões fluidas nos depósitos auríferos de Novo Mundo e Santa Helena na região de Teles Pires - Peixoto de Azevedo (Mato Grosso), Província de Alta Floresta. Instituto de Geociências, Universidade Estadual de Campinas; Relatório PIBIC/ CNPq
- Assis R R (2011) Depósitos auríferos associados ao magmatismo granítico do setor leste da Província de Alta Floresta (MT), Cráton Amazônico: tipologia das mineralizações, modelos genéticos e implicações prospectivas. Instituto de Geociências; Dissertação de Mestrado
- Baker T (2002) Emplacement depth and carbon dioxide-rich fluid inclusions in intrusion-related gold deposits. *Economic Geology*, 97: 1111-1117
- Candela P A, Piccoli P M (2005) Magmatic Processes in the Development of Porphyry-type Ore Systems. In: Hedenquist J W, Thompson J F H, Goldfarb R J, Richards J P Society of Economic Geologists 100 th Anniversary Volume, pp 25-38
- Corbett G J & Leach T M (1998) Southwest Pacific gold-copper systems: Structure, alteration and mineralization. Special Publication 6, Society of Economic Geologists
- Guilbert J G, Park Jr C F (1985) *The Geology of Ore Deposits*. W. H. Freeman and Company, New York
- Hart C J R (2007) Reduced intrusion-related gold systems. In: Goodfellow, W D., *Mineral deposits of Canada: A Synthesis of Major Deposit Types, District Metallogeny, the Evolution of Geological Provinces and Exploration Methods: Geological Association of Canada, Mineral Deposits Division, Special Publication*, 5: 95-112
- Lang J R, Baker T (2001) Intrusion-related gold systems: the present level of understanding. *Mineralium Deposita*, 36: 477-489
- Paes de Barros A J (2007) Granitos da região de Peixoto de Azevedo – Novo Mundo e mineralizações auríferas relacionadas – Província Aurífera Alta Floresta (MT). Tese de Doutorado, Instituto de Geociências, Universidade Estadual de Campinas, Campinas
- Pirajno F (1992) *Hydrothermal mineral deposits. Principles and fundamental concepts for the exploration geologists*. Berlin, Springer-Verlag
- Robb L (2006) *Introduction to ore-forming processes*. Blackwell Publishing, Australia
- Seedorff E, Dilles J H, Proffett-Jr J M., Einaudi M T, Zurcher L, Stavast W J A, Johnson D A, Barton M D (2005) Porphyry deposits: characteristics and origin of hypogene features. *Economic Geology* 110th Anniversary volume, pp 251-298
- Sillitoe R H (1991) Intrusion-related gold deposits. In: Foster R.P. (ed.) *Metallogeny and exploration of gold*. Ed. Blackie, London, pp 164-209
- Sillitoe R H (2010) Porphyry Cooper Systems. *Economic Geology*, 105: 3-41
- Sinclair W D (2007) Porphyry deposits. In: Goodfellow, W.D. (ed.). *Mineral Deposits of Canada: A Synthesis of Major Deposit-Types, District Metallogeny, the Evolution of Geological Provinces, and Exploration Methods*. Geological Association of Canada, Mineral Deposits Division, Special Publication No. 5, pp 223-243
- Souza J P, Frasca A A S, Oliveira C C (2005) *Geologia e Recursos Minerais da Província Mineral de Alta Floresta*. Relatório Integrado. Brasília, Serviço Geológico Brasileiro, CPRM
- Tassinari C C G & Macambira M J B (1999) Geochronological provinces of the Amazonian Cráton. *Episodes*, 22: 174-182
- Thompson J F H, Sillitoe R H, Baker T, Lang J R, Mortensen J K (1999) Intrusion-related gold deposits associated with tungsten-tin provinces. *Mineralium Deposita*, 34: 323-334

Hydrothermal natrolite formation in the Fohberg phonolite, Kaiserstuhl volcanic complex, Germany

Tobias Björn Weisenberger

Department of Geosciences, University of Oulu, Oulu, Finland

Simon Spürgin

Hans G. Hauri Mineralstoffwerke, Bötzingen, Germany

Abstract. The subvolcanic Fohberg phonolite (Kaiserstuhl volcanic complex, Germany) is an economic zeolite deposit, formed by hydrothermal alteration of primary magmatic minerals. The Fohberg phonolite is mined due to the high (>40 wt%) natrolite content, which account for remarkable zeolitic physicochemical properties of the ground rock. It is used in the concrete industry as well as in many other applications. Natrolite formed during hydrothermal alteration under alkaline conditions and completely replaces feldspathoids in the matrix of the rock. In addition, veins and open fissures cut the intrusive body, wherein natrolite is precipitated, followed by apophyllite and calcite as younger generations. New mineralogical and geochemical studies are carried out a) to evaluate the manifestation of hydrothermal alteration, b) to constrain the physical and chemical conditions of the fluids, which promoted hydrothermal replacement, and c) to relate the hydrothermal overprint to the chronology and volcanic history of the Kaiserstuhl volcanic complex.

Keywords. Natrolite – Zeolite - Apophyllite - Hydrothermal alteration - Kaiserstuhl volcanic complex

1 Introduction

Zeolites are among the most common products of chemical interaction between groundwater and the Earth's crust during diagenesis, hydrothermal mineral alteration, and low-grade metamorphism. Natural zeolites form by reactions of aqueous solutions with volcanic rocks, and volcanogenic sediments. They occur in low-temperature (<250°C), low-pressure (<200 MPa), water saturated or fluid rich environments. The copious amounts of silica, aluminium, and alkali and alkaline-earth cations necessary for the formation of most zeolites are commonly derived from dissolution of volcanic glass and from the alteration of feldspar and feldspathoids.

Since the early days of its geological and mineralogical exploration, the Kaiserstuhl volcanic complex (KVC) is well known for its wealth in zeolites. A detailed description of zeolite distribution in relation to the host rock is given in Weisenberger and Spürgin (2009). Nevertheless, phonolite intrusions in the eastern KVC, namely the Fohberg phonolite, are the only local zeolite occurrences of economic interest. Therein natrolite is the predominant zeolite-group mineral. Today this rock is known for its excellent qualities in concrete and other applications, which are directly related to the high content of zeolites and their

physicochemical properties, e.g. cation exchange (Hauri 2006).

In this study we present new geochemical and mineralogical data and provide a genetic model for the hydrothermal replacement of primary magmatic phases by zeolite minerals.

2 Geological setting

The KVC is located in the central-southern segment of the Upper Rhine Graben, south-western Germany (Fig. 1), where it is the only larger volcanic edifice. Alkaline and carbonatitic rocks erupted along deep-rooting faults in a disrupted crustal segment (Bourgeois et al. 2007) at the intersection of two prominent fault zones (Hüttner 1996; Schreiner 1996). The KVC covers an area of 16 x 12 km northwest of Freiburg. A north-south oriented pre-volcanic horst structure in the eastern Kaiserstuhl, mainly comprising Paleogene marls, sandstones, and limestones, is partly overlain by effusive and explosive volcanics, and penetrated by subvolcanic intrusions (Fig. 1). Extrusive rocks of the KVC erupted from various volcanic centres and formed a complex stratocone or a volcanic field.

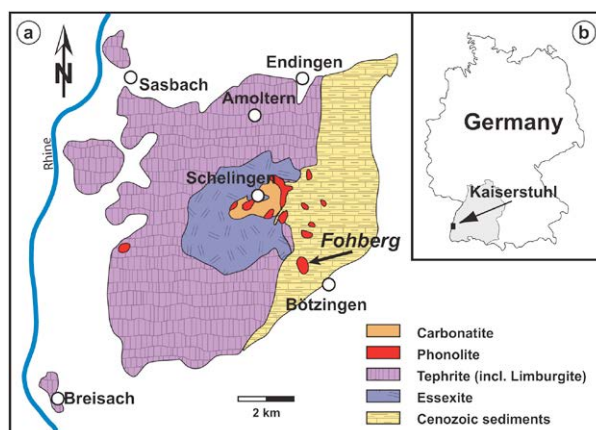


Figure 1. a Simplified geologic map of the Kaiserstuhl volcanic complex (after Wimmenauer 1963). The phonolite-hosted Fohberg zeolite deposit is shown with an arrow. b Outline of Germany

Phonolitic rocks of the KVC are derived from a hypothetical, initially fractionated K-basanite. This fractionates to rocks of a so-called essexitic family (essexites, tephrites), and a phonolitic family, e.g. phonolites, syenites, and evolved leucocratic dykes (Wimmenauer 1957, 1959, 1962).

Volcanism in the KVC lasted from 19.0-15.3 Ma. Activity started with the eruption of olivine nephelinites (19.0 ± 1.6 Ma, whole-rock K-Ar age; Baranyi et al. 1976), followed by the deposition of mainly tephritic rocks (18.2 – 16.5 Ma) and the emplacement of various subvolcanic intrusions and dykes during the volcanic main phase between 18.4 and 15.3 Ma (compiled in Wimmenauer 2003).

3 Petrography and field relations

3.1 Fohberg phonolite quarry, Bötzingen

The approximately 600 x 450 m large Fohberg phonolite in the southeastern Kaiserstuhl (Fig. 1) is a shallow subvolcanic stock, which intruded in Oligocene marls of the Pechelbronn Formation. Whole-rock K-Ar geochronology yields an age of 15.6 Ma (Lippolt et al. 1963). The main primary magmatic minerals are feldspathoid minerals, sanidine, aegirine-augite, wollastonite, and Ti-andradite (Wimmenauer 1962; Albrecht 1981). The rock is extensively altered. However, less altered portions of the rock show the primary porphyritic texture with phenocrysts (≤ 3 mm) of the mentioned minerals in a greenish-grey matrix. The phonolite stock is cut by a younger dike of porphyritic, black essexite.

3.2 The alteration assemblage

Alteration decomposed virtually all feldspathoid minerals to zeolites, which makes natrolite the major rock-forming mineral in the Fohberg phonolite (about 45 vol%; Albrecht 1981). Fibrous natrolite aggregates form pseudomorphs after feldspathoid minerals and therefore hinder the exact identification of the precursor mineral.



Figure 2. Alteration is most obvious along white natrolite veins and open mineralized fractures. The grayish rock matrix is also highly affected by zeolitization

In addition to the pervasive replacement of feldspathoid minerals by zeolite species, secondary mineralization occurs along joints and fissures, where massive portions of natrolite are formed, temporally followed by apophyllite and calcite (Fig. 2). Open

fractures are generally filled with euhedral needles or radial aggregates of natrolite several mm in length. Common fissure minerals younger and overgrowing natrolite are apophyllite (euhedral crystals varying from <1 to 5 mm in size), and calcite of variable size and shape.

Active mining of the Fohberg phonolite in the village of Bötzingen permits accessibility to a large portion of the intrusive body, and continuously provides excellent natrolite specimen.

4 Mineral chemistry

4.1 Natrolite

Natrolite ($\text{Na}_2[\text{Al}_2\text{Si}_3\text{O}_{10}]\cdot 2\text{H}_2\text{O}$) occurs as rock forming mineral in the phonolite matrix and as vein filling mineral. In the latter case, natrolite forms long, thin needles elongated along the c-axis, terminated by (111) faces, as well as radial aggregates and compact masses. It varies from colourless to white, and light yellowish to light reddish. Individual crystals can have a size up to 10 mm in length, but smaller needles (<1 mm) are more common.

Chemical analyses were obtained on colourless natrolite crystals from the Fohberg quarry (Fig. 3), which were precipitated as euhedral crystals in a vein together with apophyllite and calcite. Sodium is the main extraframework cation. Other extraframework cations, like Ca, K, Mg, and Fe occur only in traces. The average T_{Si} ratio is 0.599.

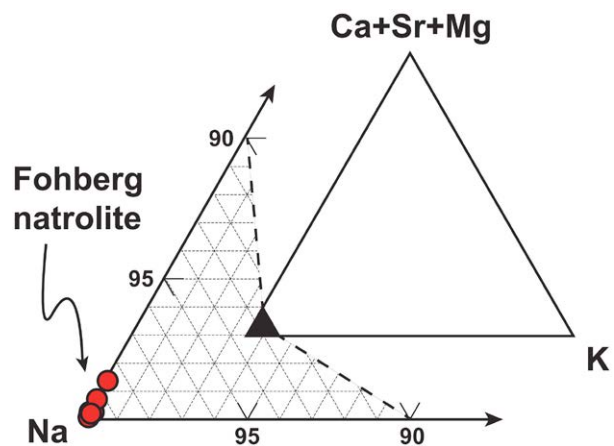


Figure 3. Composition of natrolite in the Na-Ca-K space, displaying extraframework cation occupancy. Fohberg natrolite is of nearly ideal composition.

4.2 Apophyllite

Apophyllite ($\text{KCa}_4\text{Si}_8\text{O}_{20}(\text{F},\text{OH})\cdot 8\text{H}_2\text{O}$) occurs as overgrowth on natrolite, forming transparent tetragonal pseudo-cubes of up to 1 cm in size. Common are four-sided crystals with truncated edges forming rhomboid faces that end in a pyramid. The apex can be truncated, in which case the appearance is cubic. The chemical composition of apophyllite is slightly variable with respect to OH-F exchange. Analyses range from 0.35 to 0.91 atoms per formula unit (apfu) for F content with an

average F content of 0.64 apfu. Nevertheless, individual crystals are chemically homogenous, with small variations of minor components concentrations such as Al and Na at average values of 0.14 and 0.05 apfu, respectively.

5 Genetic considerations

The conversion of an essentially anhydrous primary mineralogy to a zeolite-dominated and therefore water-rich assemblage (natrolite contains about 9.5 wt% H₂O) on the one hand, and the syn-deformative mineralization and healing of brittle fractures (Fig. 2) on the other hand, point to a hydrothermal regime at subsolidus conditions necessary for the observed zeolitization process. A likely scenario is hydrothermal overprinting of the Fohberg phonolite body during postmagmatic cooling.

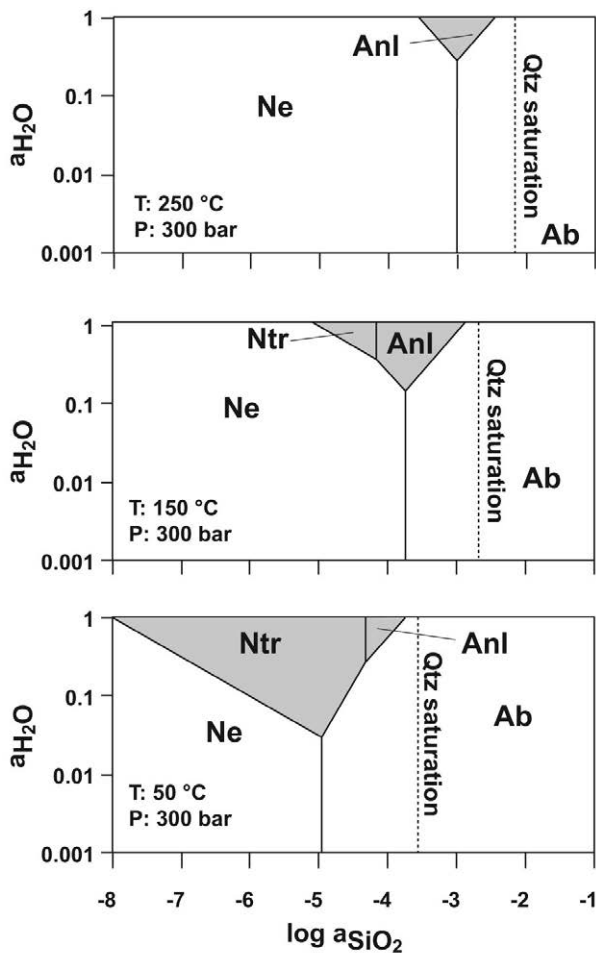


Figure 4. Quantitative $a\text{SiO}_2$ - $a\text{H}_2\text{O}$ diagrams for selected Na-Al silicates at constant pressure (300 bar) and different temperatures (50 °C, 150 °C, 250 °C). Gray areas are stability fields for zeolite species. Dashed lines represent the lower limits of quartz saturation. Ab: albite, Anl: analcime, Ne: nepheline, Ntr: natrolite. Qtz: quartz

Natrolite in the matrix of the Fohberg phonolite is obviously replacing feldspathoid minerals, forming pseudomorphs. The near-endmember composition of natrolite (Fig. 3), as well as its vast dominance in the fissure assemblage (beside calcite), implies that the

decay of primarily crystallized phases other than feldspathoid minerals play only a subordinate role for the composition of the percolating fluids. This is in agreement with textural observations, as other primary phases (sanidine, pyroxene, garnet) show no substantial decomposition patterns.

Figure 4 illustrates the change in fluid composition during the hydrothermal replacement as function of H₂O and aqueous silica activity, respectively, in the system Al₂O₃-SiO₂-Na₂O-H₂O. Phase equilibria between nepheline, albite, natrolite, and analcime allow the estimation of the activities of SiO₂ and H₂O at fixed pressure and temperature conditions. Diagrams were calculated using the thermodynamic properties and algorithms in the computer code SUPCRT92 (Johnson et al. 1992), by employing the slop98 database (<http://geopig.asu.edu/sites/default/files/slop98.dat>) and thermodynamic consistent data from Helgeson et al. (1978) and Neuhoff (2000).

At subsolidus temperatures of 250 °C, nepheline and albite buffer $a\text{SiO}_2$ to equilibrium values of ~ 0.005 and at $a\text{H}_2\text{O} \sim 0.5$, analcime is stable as the only zeolite mineral species. With decreasing temperatures, at ~ 150 °C, natrolite becomes stable at the expense of nepheline at the lower- $a\text{SiO}_2$ limit of the analcime stability field. At low-temperature conditions (~ 50 °C), natrolite is the dominant zeolite species, whereas the $a\text{H}_2\text{O}$ limit for natrolite stability decreases (Fig. 4).

Calculated saturation of quartz for the respective conditions plots at higher silica activities than the observed phase equilibria that buffer the activities of water and SiO₂. This is in agreement with the absence of quartz in the late-stage assemblages used for calculating Figure 4.

6 Outlook: Timing of the alteration

To constrain the replacement history in more detail, the crystallization age of the Fohberg phonolite will be determined on separates of titanite. The youngest episode of hydrothermal alteration is represented by apophyllite crystals growing on fissure natrolite.

The combination of magmatic titanite ages and ³⁹Ar/⁴⁰Ar ages of apophyllite will bracket the exact timing of the hydrothermal event and relate it to the volcanic activity of the KVC.

References

- Albrecht A (1981) Mineralogische Untersuchungen des Phonoliths vom Fohberg, Kaiserstuhl, mit besonderer Berücksichtigung der mafischen und akzessorischen Minerale. Diploma Thesis, Albert-Ludwigs-University Freiburg, 146pp
- Baranyi I, Lippolt HJ, Todt W (1976) Kalium-Argon-Altersbestimmungen an tertiären Vulkaniten des Oberrheingraben-Gebiets II. Die Alterstraverse vom Hegau nach Lothringen. *Oberrhein Geol Abh* 25: 41-62
- Bourgeois O, Ford M, Diraison M, Veslud CLC d, Gerbault M, Pik R, Ruby N, Bonnet S (2007) Separation of rifting and lithospheric folding signatures in the NW-Alpine foreland. *Int J Earth Sci* 96:1003-1031
- Hauri F (2006) Natural zeolites from southern Germany: Applications in concrete. In: Bowmann RS, Delap SE (eds).

- Zeolite'06 - 7th International Conference on the Occurrence, Properties, and Utilization of Natural Zeolites, Socorro, New Mexico, USA
- Helgeson HC, Delany JM, Nesbitt HW, Bird DK (1978) Summary and critique of the thermodynamic properties of rock-forming minerals. *Amer J Sci* 278-A:1-229
- Hüttner R (1996) Tektonik im Grundgebirge. In: Groschopf R, Kessler G, Leiber J, Maus H, Ohmert W, Schreiner A, Wimmenauer W (eds). *Geologische Karte von Baden-Württemberg 1:50000, Freiburg i.Br. und Umgebung, LGRB Baden-Württemberg, Freiburg*, pp 119-228
- Johnson JW, Oelkers EH, Helgeson HC (1992) SUPCRT92: A software package for calculating the standard molal thermodynamic properties of minerals, gases, aqueous species, and reactions from 1 to 5000 bar and 0 to 1000°C. *Comput Geosci* 18:899-947
- Lippolt HJ, Gentner W, Wimmenauer W (1963) Altersbestimmungen nach der Kalium-Argon-Methode an tertiären Eruptivgesteinen Südwestdeutschlands. *Jh Geol Landesamt Baden-Württemberg* 6:507-538
- Neuhoff PS (2000) Thermodynamic properties and parageneses of rock-forming zeolites, Ph.D. thesis, Stanford University, Stanford, CA, pp240
- Schreiner A (1996) Tektonik der Vorbergzone und der Oberrheinebene. In: Groschopf R, Kessler G, Leiber J, Maus H, Ohmert W, Schreiner A, Wimmenauer W (eds). *Geologische Karte von Baden-Württemberg 1:50000, Freiburg i.Br. und Umgebung, LGRB Baden-Württemberg, Freiburg*, pp229-241
- Weisenberger T, Spürgin S (2009) Zeolites in alkaline rocks of the Kaiserstuhl volcanic complex, SW Germany - new microprobe investigation and their relationship to the host rock. *Geol Belg* 12:75-91
- Wimmenauer W (1957) Beiträge zur Petrographie des Kaiserstuhls. Einführung und Teil I: Die Ergußgesteine und Tuffe. *N J Min Abh* 91:131-150
- Wimmenauer W (1959) Beiträge zur Petrographie des Kaiserstuhls. Schluß von Teil I: Die Ergußgesteine und Tuffe. Teil II. Die essexitisch-thermalitischen subvulkanischen Intrusivgesteine. Teil III: Die Ganggesteine der essexitischen Familie. *N J Min Abh* 93:133-173
- Wimmenauer W (1962) Beiträge zur Petrographie des Kaiserstuhls. Teil IV: Die Gesteine der phonolithischen Familie. Teil V: Die subvulkanischen Breccien. *N J Min Abh* 98:367-415
- Wimmenauer W (1963) Beiträge zur Petrographie des Kaiserstuhls: Teil VI: Die Karbonatite. Teil VII: Zur Petrogenese des Kaiserstuhls: *N J Min Abh* 99:231-276.
- Wimmenauer W (2003) *Geologische Karte von Baden-Württemberg 1:25000, Kaiserstuhl. LGRB Baden-Württemberg, Freiburg*, pp280

The REE distribution patterns in altered rocks: implications for the genesis of orogenic gold deposits

Olga V. Vikent'eva, Gennadii N. Gamyanin, Nikolay S. Bortnikov
IGEM, Russian Academy of Sciences, Moscow, Russia

Abstract. REE distribution patterns in the ore-related metasomatites from large orogenic gold deposits are considered. It is shown that the LREE enriched and relatively oxidized fluids were responsible for its formation. The multiple source of hydrothermal fluids is suggested; however contribution of magmatic fluid is significant. REE systematic combined with fluid inclusion and stable isotope studies indicate the origin of hydrothermally altered rocks and the source(s) of ore fluids.

Keywords. Gold deposit, metasomatite, REE, Eu anomaly, source of hydrothermal fluid

1 Introduction

Behavior of REE in hydrothermal process is useful for the reconstruction of composition and source of the ore-bearing fluid. Both REE mobility and immobility during hydrothermal fluid-rock interaction have been discussed for various types of mineralization (e.g., Bierlein et al. 1999, Jiang et al. 2004, Williams-Jones et al. 2000, van Dongen et al. 2010). We use the REE distribution patterns in metasomatic rocks from the large mesothermal gold deposits of the Middle Urals (Berezovsk) and the North-Eastern Russia (Nezhdaninsk, Nataka and Arkachan) as an additional guide for ore genesis.

2 Characteristics of gold deposits

The studied deposits of the North-Eastern Russia are mainly located in terrigenous rocks metamorphosed in the lower greenschist facies. Gold mineralization is



Figure 1. Location map of the studied deposits.

presented by veins, veinlets and mineralized zones, controlled by the regional faults and related faults of smaller order. Ore bodies are accompanied by haloes of hydrothermally altered rocks. It was suggested that the ore-forming processes on these deposits were polygenic and polychronic (Bortnikov et al. 2007, Goryachev et al. 2008). The comparative characteristics of the studied deposits are given in table 1; the Berezovsk gold deposit (Middle Urals) is also considered for comparison.

The Berezovsk ore field is located in the volcanogenic-sedimentary rocks of the Ordovician and Silurian, and intruded by granitoid dikes of the Carbon age. Gold-sulphide-quartz veins occur both in granitoid dikes (ladder-veins) and in host rocks and are accompanied by quartz-sericite-carbonate-pyrite metasomatites.

Two major deformation patterns accompanying metasomatic processes are recognized in the altered siltstones of Nezhdaninsk and Nataka deposits

Table 1. Characteristics of studied gold deposits

Deposit, region	Berezovsk Middle Urals	Nezhdaninsk South-Verkhoyansk	Nataka Kolima	Arkachan West-Verkhoyansk
Ore controlled structure	Regional submeridional fault zone, latitudinal minor faults	Regional submeridional deep-seated fault	Regional north-west fault	Fault zone of north-east direction
Host rocks	Volcanic-sedimentary (Silurian-Ordovician), gabbro, serpentinite, granitoid dikes (Carboniferous)	Sandstone, siltstone, shale (Permian)	Sandstone, siltstone, shale (Upper Permian)	Sandstone, siltstone, shale (Middle-Upper Carboniferous-Lower Permian)
Magmatic rock associations	Granite-tonalite	Granite, lamprophyre, gabbro-diorite	Granite, granodiorite, spessartite	Granite
Geochemical type	Gold-quartz-sulphide	Gold-silver-polymetallic	Gold-quartz lowsulphide	Gold-bismuth-siderite-polysulphide
Ore morphology	Veins	Mineralized brecciated zones, veins, vein zones	Veins, veinlets, linear stockwork zones	Linear stockwork zones
Wall rock alteration	Quartz-sericite-carbonate-pyrite			Carbonatization
Mineral composition of ores	Pyrite, fahlore, sphalerite, galena, quartz, aikinite, carbonates, Au (800-930)	Pyrite, arsenopyrite, galena, sphalerite, Ag sulfosalts, Au (560-900)	Quartz, arsenopyrite, pyrite, pyrrhotite, galena, calcite, Au (600-880)	Siderite, pyrrhotite, pyrite, arsenopyrite, chalcopyrite, bismuthine, Au (780-920)
Au reserves (av. C _{Au})	350 t (2.4 g/t)	470 t (5 g/t)	1760 t (1.7 g/t)	100 t (6 g/t)
$\delta^{18}\text{O}_{\text{H}_2\text{O}}$ (‰) ¹	+5.2...+8.1	+5.1...+10.4	+3.6...+8.8‰	+2.0...+9.4
PT conditions (ores)	295-285 °C; 1.8-0.9 kbar	387-129 °C; 2.0-0.7 kbar	363-280 °C; 2.4-1.1 kbar	385-261 °C; 1.8-1.1 kbar
Age, Ma	364	154-94	137-135	103-101

¹ - $\delta^{18}\text{O}_{\text{H}_2\text{O}}$ - oxygen isotope composition of fluid coexisted with ore quartz.

Decompression is marked by breccias and cataclastic structures. Compression is marked by clivage, schist bands and fault gouge. Compression and decompression result in different styles of metasomatic alteration. Under high stress pressure (compression) sericite replaces albite with partial or total silica loss, thus forming predominantly sericite metasomatites. Under decompression regime the metasomatic rocks become enriched in quartz due to silica precipitation.

3 REE distribution patterns

REE were analyzed by ICP-MS, the detection limit was 0.0n ppm. The Eu (Eu/Eu^*) and Ce (Ce/Ce^*) anomalies were calculated from the formulae $Eu/Eu^* = Eu_n / [Sm_n \times (Tb_n \times Eu_n)^{1/2}]^{1/2}$ and $Ce/Ce^* = Ce_n / [(2La_n + Sm_n)/3]$. REE contents were normalized to chondrite (Taylor and McLennan 1985) for comparison of altered terrigenous and igneous rocks.

3.1 Nezdansinsk deposit

The total REE content in metasomatites varies from 137 to 260 ppm. Under compression the HREE content increases from preore to synore metasomatites (Fig.2). The highest total REE concentration and La/Sm ratio (4.8) have been found in SiO_2 -poor sample from tectonic zone. Under decompression the HREE content and Eu/Eu^* slightly increase, but La/Yb decreases from 50 to 20 from preore to synore metasomatites. The highest La/Yb (50.7) and Gd/Yb (5.9) ratios occur in preore metasomatites. Both the terrigenous (La/Yb=7.6-11.3) and altered rocks (La/Yb=14-50.7) are enriched in LREE. Siltstones display weak negative Eu (0.8-0.9) and positive Ce (1.2-1.3) anomalies. The ratio of Eu/Eu^* is close to 1 for altered rocks.

3.2 Natalka deposit

The highest total REE content (117.4-151.2 ppm) has been found in preore metasomatites, while the lowest (4.4 ppm) occurs in a quartz vein very poor in carbonates and other minerals containing REE. All altered rocks are

enriched in LREE (La/Yb=6.3-18.6) (Fig. 2). Under decompression the highest La/Yb ratio was found in metasomatites with veinlets and sulfidization, and the lowest (6.3) – in preore metasomatites. La/Sm ratio is low in quartz veins. Gd/Yb is lower for pre-ore metasomatites and rises with the increasing degree of veining and sulfidization. The ratio of Eu/Eu^* is close to 1 for metasomatites and $Eu/Eu^*=1.25$ for quartz veins.

3.3 Arkachan deposit

The total REE content ranges from 156 to 202 ppm in altered terrigenous rocks; the highest Σ REE found in siltstones is 826 ppm. Siltstones are enriched in LREE (La/Yb=7.1-11.1). The REE patterns display weak negative Eu anomaly ($Eu/Eu^*=0.7-0.8$). The altered siltstones are weakly enriched in HREE. The altered sandstones, in contrast to siltstones, are enriched in both LREE and HREE. Total REE content is lowest in unaltered sandstone (87 ppm) and increases up to 198 ppm in altered rocks. The Eu/Eu^* value in sandstones with quartz veinlets and sulphides is 1.4. The total REE contents in altered granitoides (58-69 ppm) and quartz porphyry (62 ppm) are comparable.

3.4 Berezovsk deposit

The REE distribution in minerals (carbonates and silicates) from various metasomatic zones after gabbro, diabase and serpentinite has been studied. The REE distribution in altered diabase (6 zones) was also investigated. The composition of host rocks influences to the concentration and degree of REE differentiation in minerals. The highest total REE content was found in minerals from apodiabase metasomatites. The total REE content in carbonates varies from 15 to 50.8 ppm (diabase), from 4 to 9.8 ppm (gabbro) and from 2.6 to 5.2 ppm (serpentinite). The concentration of Ce and Eu decreases from apodiabase to apogabbro and to aposerpentinite metasomatites. All minerals are enriched in LREE. It is interesting that the behaviour of Au is similar to behaviour of HREE.

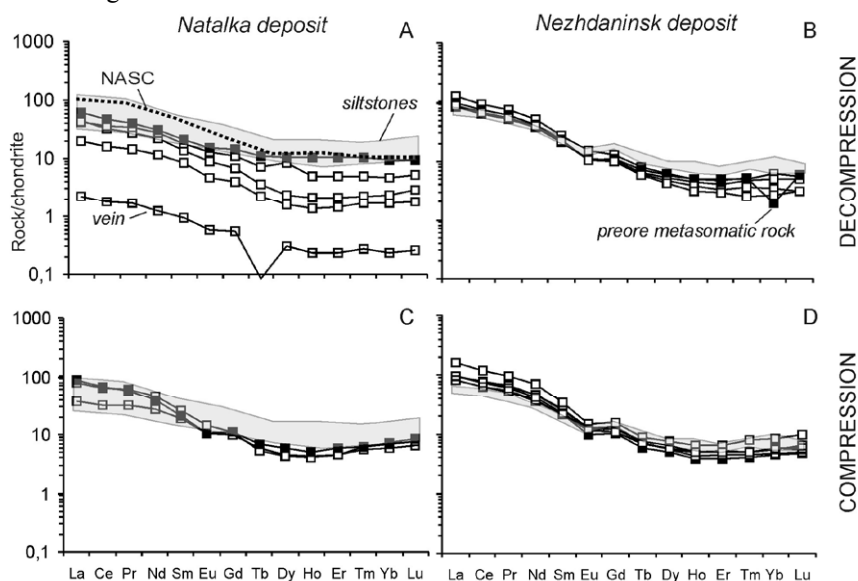


Figure 2. REE distribution patterns for metasomatic rocks formed under local decompression (A, B) and compression (C, D) for Natalka (A, C) and Nezdansinsk (B, D) deposits. Patterns for the unaltered siltstone (grey area) and early preore metasomatic rocks (black squares) are shown for comparison. NASC - North American Shale Composite.

4 Discussion

REE composition of fluids

The REE patterns in the studied metasomatic rocks show that all rocks are enriched in LREE, which suggests participation of LREE-rich fluid in their origin. The lowest Gd/Yb ratio was determined for preore metasomatites. This ratio rises in hydrothermally altered rocks with increasing amounts of veinlets and sulfides. The total REE concentration decreases with depletion in minerals-concentrators of REE. The differentiation of HREE (Gd/Yb) increases and the differentiation of LREE (La/Sm) decreases with increasing degree of rock alteration. This results from the variations in the REE mobility and stability of their complex compounds. The total REE content shows negative correlation with SiO₂ and Eu/Eu* and a positive correlation with TiO₂ and La/Sm in metasomatic rocks (Fig.3).

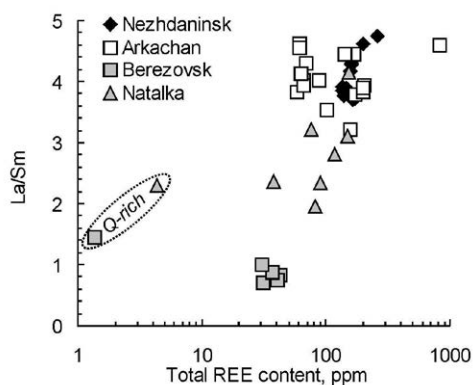


Figure 3. Correlation of the total REE content with La/Sm ratio in metasomatites from the studied deposits.

Eu and Ce anomalies

The REE patterns in the studied metasomatic rocks do not reveal pronounced Eu and Ce anomalies, either positive or negative, except for the Arkachan deposit. The Eu and Ce anomalies may be used to characterise the redox conditions in fluid because these elements occur in natural systems in two valence states. At $\text{Eu}^{3+} \ll \text{Eu}^{2+}$, the minerals precipitate from a relatively reduced fluid, and at $\text{Eu}^{3+} \gg \text{Eu}^{2+}$, from a relatively oxidized fluid. As is shown in Fig.4a, the Eu/Eu* values in the metasomatic rocks from all deposits studied are close to 1 and plot tightly along the diagonal line. These metasomatic rocks contain Eu predominantly as Eu^{3+} and should have formed from relatively oxidized fluids. Similar pattern is shown for minerals from various metasomatites of Berezovsk ore field (Fig.4b). The elevated Eu/Eu* ratio in samples of quartz vein may indicate a relatively reduced nature of the mineral-forming fluid (with a low $\text{Eu}^{3+}/\text{Eu}^{2+}$ ratio). Ce anomalies in the hydrothermally altered rocks are not expressed; the Ce/Ce* ratio is close to 1 ($0.96 < \text{Ce}/\text{Ce}^* < 1.05$). It seems likely that the rare Ce anomaly is due to the interaction of fluids with the host rocks containing Fe^{2+} . The negative Eu anomalies ($\text{Eu}/\text{Eu}^* = 0.65-0.80$) for the Arkachan deposit indicate that magmatic fluid participates in hydrothermal alteration. Negative Eu anomalies occur in fluid originated from Eu-depleted felsic magmas (Lüders et al. 1993).

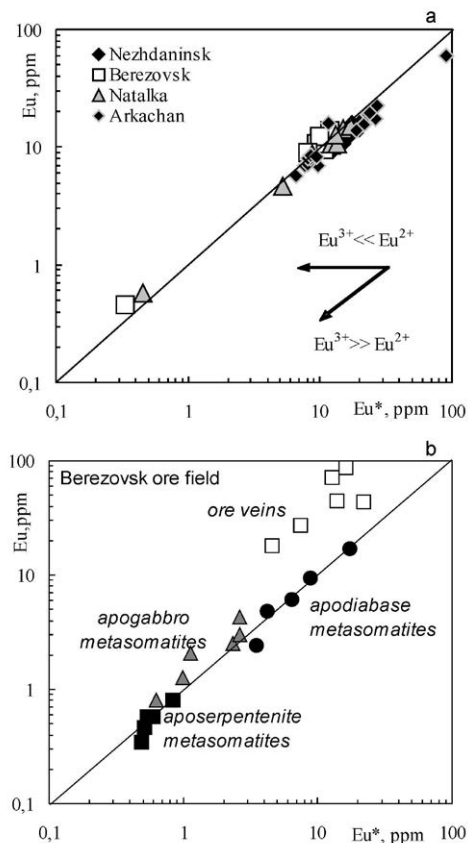


Figure 4. Eu versus Eu* for the metasomatites from the studied deposits (a) and for minerals from metasomatic zones of Berezovsk ore field (b).

Source of hydrothermal fluids

The REE patterns for the hydrothermally altered rocks demonstrate differences in REE distribution under regimes of compression and decompression. The lanthanides' content gradually decreases in altered rocks from host siltstones and preore metasomatic rocks to the vein of the Natalka deposit under decompression. The lower total REE content should be caused by two factors. First, by the dilution with silica added to the altered rocks during decompression accompanied hydrothermal alteration, and second, by leaching the REE out of the rocks by hydrothermal solutions. The progressive extraction of REE with increasing degree of alteration could be caused by fluids of magmatic (Lottermoser 1992) or meteoric (Taylor and Fryer 1982) origin. At the early stage, high-temperature postmagmatic fluids with predominant Cl^- , high pH, and low water/rock ratio produce mainly LREE dissolution. Recent experimental data of Migdisov et al. (2009) suggest that the LREE species are more stable than the HREE species in chloride-bearing solutions at elevated temperature. At the late stage, with decreasing temperature, pH of the solution and increasing water/rock ratio, fluids containing CO_3^{2-} , F^- , Cl^- , and PO_4^{3-} result in high mobility of all REE. LREE and Eu^{2+} under lower pH are the most soluble in chloride solutions, whereas HREE form complexes with CO_3^{2-} and F^- . The influence of meteoric water on rocks also leads to the leaching of all REE with increasing degree of alteration. However, in our case, the contribution of oxidized meteoric water is insignificant because Ce anomaly is absent in the

metasomatic rocks. The total REE content of the studied metasomatic rocks inversely correlates with the magnitude of the Eu anomaly (Fig.5). Such relationship is specific to igneous rocks and is not observed in metamorphic and sedimentary rocks (Vinokurov 1995), which suggests that magmatic fluid may have been involved in the formation of metasomatites.

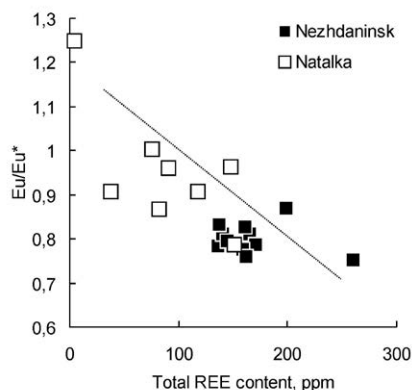


Figure 5. The total REE content versus Eu/Eu* in metasomatites.

Metamorphic fluid is generally enriched in LREE with Eu and Ce anomalies (Bau 1991, Jiang et al. 2004). The early fluid is enriched in REE with positive Eu and Ce anomalies, whereas the late fluid is poor in REE and Eu, and Ce anomalies become negative. The HREE content is stable. The distribution of REE in metasomatic rocks formed under decompression demonstrates the negligible role of the metamorphic fluid during its formation. The REE distribution in metamorphic fluid is similar to that of the shale. With increasing degree of alteration and silification, the REE pattern of metasomatic rocks departs increasingly from the REE pattern of the North American Shale Composite (NASC) and sedimentary host rocks. Assuming that the composition of the outer metasomatic zone is controlled by the initial rock composition and the composition of the inner zone is controlled by the fluid composition, the contribution of metamorphic fluid to the metasomatic alteration of rocks should be insignificant.

O and H isotope compositions of the mineral-forming fluid coexisting with metasomatites of Berezovsk ore field ($\delta^{18}\text{O} = +4.2\text{...}+7.6\text{‰}$ и $\delta\text{D} = -39\text{...}-63\text{‰}$) also suggest that magmatic fluid might play an important role in its formation.

5 Conclusion

1. The REE can become mobilized during hydrothermal alteration of host rocks during the formation of large orogenic gold deposits.

2. The relatively oxidized fluids enriched in LREE were responsible for the formation of the ore-related metasomatites. Continuous quartz precipitation in metasomatites (inner metasomatic zones) is accompanied by the increase in fluid reduction.

3. The main factor controlling the REE distribution in metasomatites from Berezovsk ore field was the pH of the mineral-forming environment. In acid environment the LREE (sometimes also the HREE) loss is observed, whereas in alkaline environment HREE are gained while

the LREE remain practically unchanged. Similar behaviour of HREE and Au may be used as a guide for Au mineralization search.

4. REE distribution in metasomatites suggests a multiple source of hydrothermal fluids, with a significant contribution of magmatic fluid.

Acknowledgements

This study was supported by Russian Foundation for Basic Research (Proj. 12-05-00623a) and the Earth Science Branch of RAS (Proj. "Ore Deposits"). The authors are much obliged to our departed colleagues (V.N. Sazonov and V.V. Alpatov), without them this paper hardly could be done. We also thank L. Aranovich and anonymous reviewer for helpful remarks.

References

- Bau, M (1991) Rare-earth element mobility during hydrothermal and metamorphic fluid-rock interaction and the significance of the oxidation state of europium. *Chem. Geol.* 93. 219-230
- Bierlein, FP, Waldron, HM, Arne, DC (1999) Behaviour of rare earth and high field strength elements during hydrothermal alteration of meta-turbidites associated with mesothermal gold mineralization in central Victoria, Australia. *Jorn. Geochem. Exploration* 67. 109-125
- Bortnikov, NS, Gamyagin, GN, Vikent'eva, OV et al. (2007) Fluid composition and origin in the hydrothermal system of the Nezhdaninsk gold deposit, Sakha (Yakutia), Russia. *Geol. Ore Deposits* 49. 87-128
- Goryachev, NA, Vikent'eva, OV, Bortnikov, NS et al. (2008) The world-class Nataalka gold deposit, northeast Russia: REE patterns, fluid inclusions, stable oxygen isotopes, and formation conditions of ore. *Geol. Ore Deposits* 50. 362-390
- Jiang, SY, Yu, JM, Lu, JJ (2004) Trace and rare-earth element geochemistry in tourmaline and cassiterite from the Yunlong tin deposit, Yunnan, China: implication for magmatic-hydrothermal fluid evolution and ore genesis. *Chem. Geol.* 209. 193-213
- Lottermoser, BG (1992) Rare earth elements and hydrothermal ore formation processes. *Ore Geol. Rev.* 7. 25-41
- Lüders, V, Moller, P, Dulskl, P (1993) REE fractionation in carbonates and fluorite. In: *Monograph Series on Mineral Deposits* 30. 133-150
- Migdisov, AA, Williams-Jones, AE, Wagner, T (2009) An experimental study of the solubility and speciation of the rare earth elements (III) in fluoride- and chloride-bearing aqueous solutions at temperatures up to 300°C. *Geochim.Cosm.Acta* 73. 7087-7109
- Taylor, RT, Fryer BJ (1982) Rare earth element chemistry as an aid to interpreting hydrothermal ore deposits. In *Metallization Associated with Acid Magmatism*, Wiley, New York 6. 357-365
- Taylor, SR, McLennan, SM (1985) *The continental crust: its composition and evolution*. Oxford, Blackwell, 312p.
- van Dongen, M, Weinberg, RF, Tomkins, AG (2010) REE-Y, Ti, and P remobilization in magmatic rocks by hydrothermal alteration during Cu-Au deposit formation. *Econ. Geol.* 105. 763-776
- Vinokurov, SF (1995) Geochemical significance of europium anomalies in the minerals of ore deposits. *Geochem. Int.* 32. 113-140
- Williams-Jones, AE, Samson, IM, Olivo, GR (2000) The genesis of hydrothermal fluorite-REE deposits in the Gallinas Mountains, New Mexico. *Econ. Geol.* 95. 327-341

Contrasting W and Sn mineralization events and related granitoids in Wangxianling-Hehuaping area, Nanling Range, South China

Rongqing Zhang, Jianjuan Lu, Rucheng Wang, Xiancai Lu, Jichun Guo, Fuchun Li

State Key Laboratory for Mineral Deposits Research, School of Earth Sciences and Engineering, Nanjing University, 210093 Nanjing, China

Bernd Lehmann

Mineral Resources, Clausthal University of Technology, 38678 Clausthal-Zellerfeld, Germany

Yuan Yao, Weiming Guo

Nanjing Institutes of Geology and Mineral Resources, CGS, 210016 Nanjing, China

Abstract. Wangxianling pluton is located in the central part of the Nanling Range, South China. According to zircon U-Pb dating, three phases of medium-grained two-mica granite, medium-grained muscovite granite and fine-grained muscovite granite were emplaced at 223.5 Ma, 224.9 Ma and 212 Ma, respectively. These granites are characterized by existences of magmatic muscovite and tourmaline, substantial inherited zircon cores and high W contents. Geochemical and Sr-Nd-Hf isotopic compositions indicate typical S-type granite signatures and were formed by partial melting of Paleoproterozoic metamorphic basement rocks. Hehuaping pluton (biotite granite) is situated to southeast of Wangxianling stock. It is a newly discovered buried pluton, which was emplaced at 155.6 Ma. Geochemical and isotopic compositions suggest that this biotite granite resembles aluminous A-type granite which was produced by partial melting of granulitized Mesoproterozoic metamorphic basement rocks with less addition of mantle-derived materials. Re-Os dating of molybdenites from two W deposits gives isochron ages of 228.1 Ma and 220.4 Ma, which are associated with the hydrothermal system of the Wangxianling pluton. In-situ cassiterite U-Pb dating results illustrate that mineralization ages of skarn and greisen type Sn deposits are 159.1 Ma and 155.5 Ma, which demonstrates that Sn mineralization is closely related to Hehuaping pluton, but not Wangxianling pluton as thought previously. Such a consideration can supply useful informations for prospecting for Sn deposits in the area.

Keywords. Radioactive isotope dating, Geochemistry, Granites, Wangxianling-Hehuaping, Nanling Range

1 Introduction

Tin and W are rare metal elements with several similar attributes. Both of them have high charge to ionic radius ratios and most of Sn and W deposits are related to granitoids. Tin exists in granitic melt as Sn^{4+} and Sn^{2+} . Sn^{4+} is a compatible element which can substitute Ti^{4+} in magnetite and titanite crystallizing in oxidized granitic melts, whereas Sn^{2+} behaves as an incompatible element in reduced melts (Taylor and Wall 1992). W^{6+} is the dominant oxidation state in oxidized granitic melts, even at moderately reduced conditions. Tungsten and Ti have similar crystal chemical properties and W^{6+} together with Fe^{2+} often substitutes Ti^{4+} in rutile and mica (Rice et al. 1998). Traditionally, Sn was supposed to coexist with W in the same deposit, such as W-Sn deposits related to

Mole granite in eastern Australia and Variscan silicic magmatism in the Erzgebirge Range and northern Portugal (Breiter et al. 1999; Audetat et al. 2000; Almeida et al. 2002). However, metallogenic diversities between tin and tungsten granites were mentioned by some researchers: granites related to W-dominant ores have lower degree of fractionation, but higher oxygen fugacity than those granites associated with Sn-dominant mines in the intrusive metallogenic provinces in eastern Australia (Blevin et al. 1996). In the Fairbanks-Circle area, Sn skarn-related granites are characterized by substantial F enrichment and early water loss induced by liquid-liquid fractionation, whereas scheelite granites are represented by relatively low F contents which decrease along with crystal-liquid fractionation from early to late stage (Newberry et al. 1990).

Wangxianling granitic stock is located to the west of Qianlishan stock in the central Nanling Range (southern belt of Qing-Hang suture zone), South China (Figure 1). According to Ar-Ar and single-grain zircon U-Pb chemical abrasion (CA-TIMS) dating, this pluton was emplaced in the Late Triassic. More than ten granite porphyry dykes occurred to the southeast of Wangxianling pluton, which are Middle Jurassic in age. Based on our field investigation and study on rocks from drill holes, a buried pluton with lithological features different from the Wangxianling granite was identified in the Hehuaping district. Several W and Sn deposits were discovered in the Wangxianling pluton and its adjacent area. However, the relationships between mineralization and granites are still unclear. Previous studies considered that the Hehuaping Sn-Pb-Zn deposit was a Late Triassic deposit related to Wangxianling pluton and no age data for orebodies closely associated to the buried pluton have been reported. This paper will confirm two mineralization events and study comparatively features between the buried Hehuaping and the Wangxianling plutons.

2 Geological setting

2.1 Geotectonic setting

An important NE-trending geotectonic belt passes through the study area. Gilder et al. (1996) named this belt as Shi-Hang zone (Shiwandashan basin and Gan-Hang rift). Yang and Mei (1997) called the zone

between the Yangtze and Cathaysia blocks Qin-Hang (Qinzhou Bay-Hangzhou Bay) suture zone with abundant non-ferrous metal resources, although the range of this juncture is much wider than the Shi-Hang zone. Wang et al. (2003) compared the coeval Mesozoic basalts on both sides of the Chenzhou-Lingwu deep fault and found out their systematic geochemical and isotopic differences, which might imply significant difference in crustal basement on both sides of the fault. They concluded that Chenzhou-Lingwu deep fault is the boundary between the Yangtze and Cathaysia blocks.

Nanling Range in Southern China is characterised by basin and range tectonics, extensively episodic granitoids, occurrence of non-ferrous and rare metal deposits such as W-Sn-Mo-Bi-Pb-Zn etc. The W and Sn mineralization have a large span, from Neoproterozoic to Cretaceous. The Middle to Late Jurassic and Late Cretaceous are the predominant W and Sn ore-forming periods. A few Late Silurian (S) and Late Triassic (T_3) ores are certified with precise dating, such as Zhangjialong (S, W), Niutangjie (S, W), Yuntoujie (T_3 , W-Mo), Liguifu (T_3 , W-Sn), Limu (T_3 , Sn-W-Nb-Ta) and Xian'tang (T_3 , W-Sn) mines. In the past three decades W-bearing and Sn-bearing granites are generally classified into transformation series granite (Xu et al., 1982). Zhu et al. (2008) investigated the geochemistry of granites associated with Sn and W mineralization in this zone within the Nanling Range and pointed out the existence of an important NE-trending Sn-W-bearing aluminous A-type granite belt with mixed mantle-crustal source of magmas. Recently, the differences between W-bearing and Sn-bearing granitoids in the Nanling Range attract attention of some researchers. Chen et al (2008) and Lu et al (2011, 2012) studied the geological and geochemical features of the W-bearing and Sn-bearing granites in the Nanling Range and subdivided them into S-type and A-type granites, respectively.

2.2 Geology of granitoids and associated ore deposits in Wangxianling-Hehuaping area

Figure 1 is a sketch map of the Wangxianling and Qianlishan plutons. The Wangxianling pluton with exposed area of 19.7 km² is located at the central part of the Nanling Range. It is composed of three phases which are medium- to coarse-grained two-mica (tourmaline) granite as central phase, medium-grained tourmaline muscovite (two-mica) granite as marginal phase, and fine-grained muscovite granitic dykes. Most of the central and marginal phase granites underwent greisenization. Preliminary data of mica Ar-Ar and single-grain zircon U-Pb chemical abrasion dating indicate that all of the three phases are Late Triassic (206~222.5 Ma) in age. Granite porphyry dykes and coarse-grained biotite granite are located to the southeast part of Wangxianling pluton. NNE and NE-trending granite porphyry dykes have an emplacement age of ~155 Ma with length and width of 200~1000 m and 15~80 m, respectively. They dip to southeast with slope angle of 50°~70°. Coarse-grained biotite granites can be predominantly identified below the depth of ~300 m in many drill holes, which are only exposed at Xijinling

and Yejiwo.

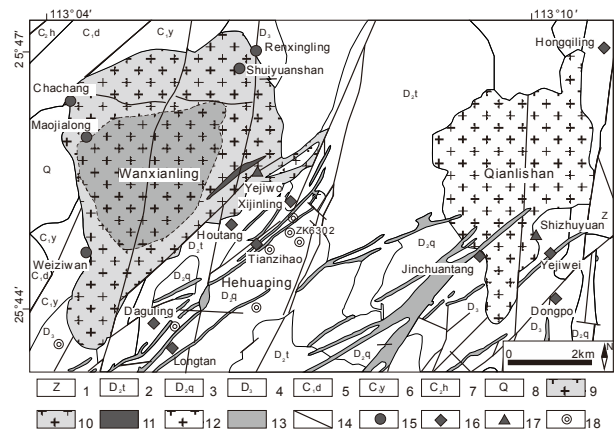


Figure 1. Sketch map of Wangxianling and Qianlishan plutons.

1-Sinian sandstone; 2-Middle Devonian Tiaomajian Formation sandstone; 3-Middle Devonian Qiziqiao Formation dolomitic limestone; 4-Upper Devonian Shetianqiao Formation limestone; 5-Lower Carboniferous Datang Formation sandstone; 6-Lower Carboniferous Yanguan Formation limestone; 7-Middle Carboniferous Huanglong Formation limestone; 8-Quaternary alluvium; 9-Medium- to coarse-grained two-mica (tourmaline) granite (T_3); 10-Medium-grained tourmaline-muscovite (two-mica) granite (T_3); 11-Fine-grained muscovite granite (T_3); 12-Biotite granite (J_3); 13-Granite porphyry (J_3); 14, Fault; 15-W deposit; 16-Sn deposit; 17-W-Sn deposit; 18-Drill hole.

EW, NNE and NE-trending faults developed in this region and cut through the Wangxianling pluton. Exposed sedimentary strata mainly consist of Devonian and Carboniferous sandstone, limestone and dolomitic limestone. Middle Devonian Tiaomajian Formation sandstone and Qiziqiao Formation dolomitic limestone, the Upper Devonian Shetianqiao Formation limestone are the predominant host rocks of Sn and W orebodies.

Several tungsten deposits occurred in the marginal phase of Wangxianling pluton, such as Shuiyuanshan quartz-wolframite vein and greisen scheelite type, Maojialong scheelite vein type, and Renxingling, Chachang and Weiziwan placer type tungsten mines, and Yejiwo greisen type W-Sn deposit. Tin mines dominantly occurred in Daguling, Longtan, Tianzihao, Houtang and Xijinling mineralized sections. Tin deposits (27.4 Mt @ 0.72% Sn) are hosted by Mg-skarns with Pb, Zn and Bi mineralization (0.162 Mt Pb+Zn ore, @ 2.9% Pb and 3.5% Zn). These tin deposits spatially associated to granite porphyry and biotite granite often occurred in the interlayer space of the Qiziqiao Member sandstone and Tiaomajian Member dolomitic limestone.

3 Age and rock geochemistry of granitoids

3.1 Wangxianling granite

Cathodoluminescence (CL) images of magmatic zircons from Wangxianling granites show bright inherited cores and dark rims. According to the zircon U-Pb dating results, the coarse-grained two-mica granite (central phase), the medium-grained tourmaline muscovite (marginal phase) and fine-grained muscovite granitic

dyke were emplaced at 223.5±1.8 Ma, 224.9±1.7 Ma, 212 Ma, respectively. Inherited zircon cores from these granites have an age span from 426 to 1760 Ma.

Both the central and the marginal phases, have similar textures, mineral assemblages and chemical compositions. Muscovite and tourmaline of magmatic origin are common minerals in these rocks. Accessory minerals are mainly zircon, apatite, monazite, thorite, rutile, xenotime, fluorite, wolframite and scheelite. As shown in Table 1, the Wangxianling granite is characterized by high P₂O₅ (0.22 wt%) and Al₂O₃ (14.37 wt%) contents. The average Li, Th, Y and Zr+Nb+Ce+Y concentrations are 68.2 ppm, 2.0 ppm, 2.2 ppm and 118.3 ppm, respectively. The P₂O₅, Th and Y contents decrease with the increase of SiO₂ content. The average zircon saturation temperature is 740°C. These rocks have low REE abundances (65.6 ppm), with LREE and HREE contents of 57.9 and 7.6 ppm, respectively. They have initial ⁸⁷Sr/⁸⁶Sr ratios of 0.7172 to 0.7305, εNd(t) values of -7.1 to -9.5 and εHf(t) values in situ zircon of -10.2 to -11.5, corresponding two-staged Nd and Hf model ages from 1.83~1.95 Ga and 1.5~2.0 Ga, respectively. All of the above chemical and isotopic compositions illustrate that Wangxianling granites belong to S-type granite.

Most of the granite samples are distinctly enriched in W with values from 5 to 174 ppm. Several greisenized granites have W contents of >300 ppm. Substantial wolframite and scheelite grains can be observed in the late-staged fine-grained muscovite granitic dykes (212 Ma), and they have W abundances from 3709 to 4856 ppm which could be mined as ore.

Table 1. Comparative features between Wangxianling and Hehuaping plutons

Pluton (ore type) Mineralization age	Wangxianling (W) 228.1~220.4 Ma			Hehuaping (Sn-Pb-Zn) 159.1~155.5 Ma	
	Central phase	Marginal phase	Dyke	Dyke	Buried pluton
Zircon U-Pb age (Ma)	223.5	224.9	212	155.6	154.7
Granite type	S-type	S-type	S-type	A ₂ -type	A ₂ -type
Magmatic tourmaline	Common	Common	Common	None	None
Magmatic muscovite	Common	Common	Common	None	None
Inherited zircon	Common	Common	Common	Rare	Rare
Al ₂ O ₃ (wt%)	14.37	14.04	15.07	12.25	12.91
P ₂ O ₅ (wt%)	0.22	0.21	0.13	0.04	0.04
Th (ppm)	11.2	13.2	2.0	71.1	45.6
W (ppm)	90.8	57.1	3153.6	9.7	7.6
Sn (ppm)	28.6	23.0	44.4	19.9	13.9
Zr+Nb+Ce+Y (ppm)	118.3	143.4	82.4	385.0	334.0
REE (ppm)	65.6	72.7	7.2	303.1	286.5
LREE (ppm)	57.9	65.0	6.0	265.7	233.5
HREE (ppm)	7.6	7.7	1.2	37.4	53.0
T _z (°C)	739.7	743.1	676.4	800.9	766.2
Initial Sr	0.7172 ~0.7305	-	0.7202	0.7079	0.7097 ~0.7305
εNd(t)	-10.2~-11.5	-	-14.4	-7.4	-5.1~-8.0
T _{DM2} Nd (Ga)	1.83~1.95	-	2.17	15.5	1.36~1.59
εHf(t)	-4~-12	-4.1~-17.3	-	-2~-10	-2~-10
T _{DM2} Hf (Ga)	1.5~2	1.51~2.34	-	1.4~1.9	1.4~1.8

3.2 Hehuaping granite

Zircon sample from the coarse-grained biotite granite from drill hole 6302 at depth of 300 m are typically colourless to pale yellow. CL images show that these zircon separates have clearly oscillatory zoning with few inherited cores. 15 spots yield a weighted mean ²⁰⁶Pb/²³⁸U age of 155.6±1.6 Ma with MSWD of 5.9.

Three zircons yield ²⁰⁶Pb/²³⁸U ages of 406 Ma, 830 Ma and 2322 Ma.

No magmatic tourmaline and muscovite were observed in Hehuaping biotite granite. Accessory minerals are mainly zircon, thorite, monazite, apatite, fluorite, rutile and parasite. Biotite granite resembles the granite porphyry in chemical and isotopic compositions. It is featured by relatively low P₂O₅ content (0.04 wt%) and Al₂O₃ content (12.91 wt%). Compared with Wangxianling granite the Hehuaping biotite granite has high Th, Zr+Nb+Ce+Y and total REE contents with their average values of 45.6 ppm, 334.6 ppm, 285.7 ppm, respectively (Table 1). Meanwhile, it has low LREE/HREE ratio and strongly negative Eu anomaly. Zircon saturation temperatures are >770°C. The biotite granite has low initial ⁸⁷Sr/⁸⁶Sr ratios (0.7097 to 0.7197), high εNd(t) values (-5.1~-8.0) and young Nd isotopic model ages (1.36~1.59 Ga). The εHf(t) values of zircons range from -2 to -10, with two-staged model ages of 1.4~1.8 Ga. According to the aforesaid chemical and isotopic features, Hehuaping biotite granite can be subdivided into aluminous A-type granite.

4 Mineralization ages

4.1 Molybdenite Re-Os Age

Eight quartz-molybdenite vein samples hosted in Wangxianling granite were collected from the Shuiyuanshan deposit. The Re and ¹⁸⁷Os contents of molybdenite separates range from 3.94 to 8.22 ppm and from 9.15 to 19.19 ppm, respectively. They have relatively concentrated Re-Os model ages from 218.5±3.3 to 222.5±3.2 Ma, with a weighted mean age of 220.6±1.1 Ma (MSWD=0.59). The samples yield a well-constrained ¹⁸⁷Re-¹⁸⁷Os isochron age of 220.7±4.1 Ma (MSWD=1.0).

Five quartz-tourmaline-molybdenite vein samples hosted in Wangxianling granite were sampled from the Yejiwo mine. The Re and ¹⁸⁷Os contents vary from 5.08 to 35.80 ppm and from 12.08 to 85.87 ppm, respectively. The molybdenite separates have relatively concentrated Re-Os model ages from 225.4±3.3 to 228.1±3.4 Ma, with a weighted mean age of 227.2±1.5 Ma (MSWD=0.58). These samples yield a well-constrained ¹⁸⁷Re-¹⁸⁷Os isochron age of 228.1±2.6 Ma (MSWD=0.9).

4.2 In-situ cassiterite U-Pb dating

Cassiterite is the most fundamental ore mineral in tin deposits. Cassiterite single-grain chemical abrasion U-Pb dating was firstly used to date mineral deposits by Gulson and Jones (1992). Afterwards, several researchers reported their achievements using cassiterite U-Pb dating, such as single-grain chemical abrasion by ID-TIMS (Liu et al. 2007) and in-situ MC-LA-ICPMS analysis (Yuan et al. 2011). In this research work, one greisen and one skarn tin ores were collected from Yejiwo and Daguling deposits, respectively.

The ²⁰⁴Pb isotopic ion signal was not precisely measured due to a combination of low ion signal and interference from small amounts of ²⁰⁴Hg in the Ar gas. Although ²⁰⁶Pb/²⁰⁷Pb ratios of 21 fractions of cassiterite

from Daguling skarn mine are in a large range (1.18~2.19), the common lead can be effectively corrected and these samples yield a reliable $^{206}\text{Pb}/^{207}\text{Pb}$ - $^{238}\text{U}/^{207}\text{Pb}$ isochron age of 159.1 ± 1.7 Ma (MSWD=1.3). 23 fractions of cassiterite from Yejiwo greisen mine also have large variational $^{206}\text{Pb}/^{207}\text{Pb}$ ratios (1.24~1.96) and yield a well-constrained $^{206}\text{Pb}/^{207}\text{Pb}$ - $^{238}\text{U}/^{207}\text{Pb}$ isochron age of 155.5 ± 4.7 Ma (MSWD=2.5).

5 Contrasting W and Sn mineralization events

Based on the mineral associations, chemical and isotopic compositions, Wangxianling granite is typical of S-type granite. It was formed at relatively low temperature and has substantial inherited zircon cores ranging from Silurian to Late Paleoproterozoic in age. Two-staged Nd and Hf model ages suggest that these rocks might be generated by partial melting of Paleoproterozoic metamorphic basement rocks induced by upwelling of asthenosphere in the post-collision event of Indo-Sinian and Sibumase blocks. The existences of scheelite and wolframite and obvious enrichment of tungsten in Wangxianling granite indicate that it is W-bearing granite, which is similar to most of the W granitoids in the Nanling Range. Molybdenite Re-Os dating results in Shuiyuanshan (220.7 ± 4.1 Ma) and Yejiwo (228.1 ± 2.6 Ma) tungsten mines are consistent with zircon U-Pb ages of Wangxianling granite (224.9 ± 1.7 Ma and 224.9 ± 1.7 Ma) within analytical errors, which demonstrates that both deposit types are closely related to Wangxianling pluton. Although Sn content in these rocks is not low, there is no corresponding tin mineralization.

According to the dating of samples for drill holes, mineral assemblages, geochemical and isotopic compositions, Hehuaping biotite granite is aluminous A-type granite which was formed at high temperature and emplaced in Jurassic (155.6 ± 1.6 Ma). Sr-Nd-Hf isotopes imply that they are produced by partial melting of granulitized Mesoproterozoic metamorphic basements with less addition of mantle-derived materials in response to subduction of Paleo-Pacific Block. Biotite granite is enriched in Sn (13.9 ppm) relative to W, which resembles the tin-bearing granitoids in the Nanling Range. In-situ cassiterite U-Pb dating results (159.1 ± 1.7 Ma and 155.5 ± 4.7 Ma) corroborate that economic Sn ores are related to the Jurassic buried biotite granite. The mineralization diversities between Wangxianling and Hehuaping plutons might be caused by their differences in ore elements contents of source rocks, forming process and addition of mantle-derived materials.

Acknowledgements

This study is supported by the Major State Basic Research Development Program of China (2012CB416702), the National Science Foundation of China (41230315, 41273053) and the Key Research Project of China Geological Survey (No. 1212011085407).

References

- Almeida A, Martins HC, Noronha F (2002) Hercynian acid magmatism and related mineralizations in northern Portugal. *Gondwana Res* 5:423-434
- Audetat A, Gunther D, Heinrich CA (2000) Magmatic-hydrothermal evolution in a fractionating granite: A microchemical study of the Sn-W-F-mineralized Mole Granite (Australia). *Geochim Cosmochim Acta* 64:3373-3393
- Blevin PL, Chappell BW, Allen CM (1996) Intrusive metallogenic provinces in eastern Australia based on granite source and composition. *T Roy Soc Edin-Earth* 87:281-290
- Breiter K, Forster HJ, Seltmann R (1999) Variscan silicic magmatism and related tin-tungsten mineralization in the Erzgebirge-Slavkovsky les metallogenic province. *Miner Deposita* 34:505-521
- Chen J, Lu JJ, Chen WF, Wang RC, Ma DS, Zhu JC, Zhang WL, Ji JF (2008) W-Sn-Nb-Ta-Bearing granites in the Nanling Range and their relationship to metallogenesis. *Geol J China Univ* 14:459-473 (in Chinese with English abstract)
- Gilder SA, Gill J, Coe RS, Zhao XX, Liu ZW, Wang GX, Yuan KR, Liu WL, Kuang GD, Wu HR (1996) Isotopic and paleomagnetic constraints on the Mesozoic tectonic evolution of South China. *J Geophys Res-Sol Ea* 101:16137-16154
- Gulson BL, Jones MT (1992) Cassiterite: Potential for direct dating of mineral-deposits and a precise age for the Bushveld Complex granites. *Geology* 20:355-358
- Liu YP, Li ZX, Li HM, Guo LG, Xu W, Ye L, Li CY, Pi DH (2007) U-Pb geochronology of cassiterite and zircon from the Dulong Sn-Zn deposit: Evidence for Cretaceous large-scale granitic magmatism and mineralization events in southeastern Yunnan province, China. *Acta Petrol Sin* 23:967-976 (in Chinese with English abstract)
- Lu JJ, Wang RC, Ma DS, Chen WF, Xie L, Zhang RQ (2012) Two contrasting Sn- and W-bearing granites in the Nanling Range, South China: evidence from Hf isotopes. *Mineral Mag* 76:A2036
- Lu JJ, Zhang RQ, Wang RC (2011) Two contrasting ore-bearing granites: Sn-bearing Qitianling granite and W-bearing Xintianling granite, Hunan province, China. *Mineral Mag* 75:A1359
- Newberry RJ, Burns LE, Swanson SE, Smith TE (1990) Comparative petrologic evolution of the Sn and W granites of the Fairbanks-Circle area, interior Alaska. *Geol Soc Am Sp Paper* 246:121-142
- Rice CM, Darke KE, Still JW, Lachowski EE (1998) Tungsten-bearing rutile from the Kori Kollo gold mine, Bolivia. *Mineral Mag* 62:421-429
- Taylor JR, Wall VJ (1992) The behavior of tin in granitoid magmas. *Econ Geol* 87:403-420
- Wang YJ, Fan WM, Guo F, Peng TP, Li CW (2003) Geochemistry of Mesozoic mafic rocks adjacent to the Chenzhou-Linwu fault, South China: Implications for the lithospheric boundary between the Yangtze and Cathaysia blocks. *Int Geol Rev* 45:263-286
- Xu KQ, Sun N, Wang DZ, Hu SX (1982) On the origin and metallogeny of the granites in South China. In: Xu KQ, Tu G (eds) *Geology of granites and their metallogenetic relations*. Proc Intern Symp Nanjing Univ. Beijing: Science Press, pp 1-3
- Yang MG, Mei YW (1997) Characteristics of geology and metallization in the Qinzhou-Hangzhou paleoplate juncture. *Geol Miner Resour South China* 3:52-59 (in Chinese with English abstract)
- Yuan SD, Peng JT, Hao S, Li HM, Geng JZ, Zhang DL (2011) In situ LA-MC-ICP-MS and ID-TIMS U-Pb geochronology of cassiterite in the giant Furong tin deposit, Hunan Province, South China: New constraints on the timing of tin-polymetallic mineralization. *Ore Geol Rev* 43:235-242
- Zhu JC, Chen J, Wang RC, Lu JJ, Xie L (2008) Early Yanshanian NE trending Sn/W-bearing A-type granites in the western-middle part of the Nanling Mts region. *Geol J China Univ* 14:16-21 (in Chinese with English abstract)

S 3.9

New developments in the understanding of IOCG deposits

Convenors:

Roberto Xavier & Brian Rusk

Vertical zoning and continuity in Fe oxide(-Cu-Au-Ag-Co-U-P-REE) (or 'IOCG') systems: Cordilleran insights

Mark D. Barton, David A. Johnson,* Douglas C. Kreiner* and Eric P. Jensen*

Lowell Institute for Mineral Resources, Dept. of Geosciences, University of Arizona, Tucson, Arizona 85721 USA
*now at Bronco Creek Exploration (Eurasian Minerals), Tucson, Arizona 85719, and Denver, Colorado 80125 USA

Abstract. Recent studies of Cordilleran Fe oxide(-Cu-Au-Ag-Co-U-P-REE) (or 'IOCG') systems demonstrate that they formed in the upper 8 km of terrestrial crust. Fe ± Cu mineralization extends from near or at the contemporary surface to depths of 1-4 km whereas related Na-Ca alteration (including metal leaching) spans paleodepths from 1 to 8 km. Many well exposed systems show systematic vertical zoning in Fe(-Cu) mineralogy from near-surface Hm-rich assemblages (including some syngenetic deposits) through Mt-dominated, sulfide-bearing zones (including Mt-rich, silicate-poor skarns in carbonate rocks) to sulfide-poor Mt(-Act/Cpx±Ap) mineralization (i.e., Kiruna or 'IOA' type), and ultimately with depth into Fe- and base metal-depleted intense Na-Ca alteration. This vertical zoning matches early syntheses of the IOCG clan, but differs from recent suggestions that IOA, Mt, and Hm styles necessarily represent distinct types of systems. Although there is considerable variation in the geochemically defined IOCG family, Cordilleran evidence demonstrates that these several styles typically form in regular, predictable patterns as part of zoned hydrothermal systems. Differences reflect depth, local host rocks, structural style, available S (for Cu precipitation), and composition of contemporaneous igneous rocks. These insights can apply directly to district- to regional-scale exploration.

IOCG, IOA, zoning, depth, Kiruna, Olympic Dam

1 Introduction

Many differences exist among deposit types within the Fe oxide(-Cu-Au-Ag-Co-U-P-REE) (or 'IOCG' *sensu lato*) clan (e.g., Williams et al., 2005; Barton, 2013). We follow the original definitions: voluminous Ti-poor, hydrothermal Fe oxides with a characteristic and eponymous suite of geochemically anomalous (but not necessarily economic) minor elements. As so defined, does this clan represent a part of a broad continuum of closely related systems as early syntheses suggested (e.g., Hitzman et al., 1992; Barton and Johnson, 1996, 2000)? Or, do the deposits reflect geochemically similar but geologically distinct types of systems? Clearly some IOCG family types, such as those intimately associated with regional metamorphic features do indeed differ in fundamental ways; nevertheless, the majority of systems share many features (Barton, 2013). Should one separate deposit families simply because they can be grouped as hematite- or magnetite-dominated (both with or without economic Cu±Au; Skirrow, 2010; Williams, 2010)? Also, should one create a separate classification for Kiruna-type (aka 'IOA') deposits with Mt/(Hm)±Act/Cpx±Ap or carbonate-hosted Mt/(Hm) replacement/skarn deposits both of which lack economic

Cu? These questions can be addressed by system-scale examination of well exposed IOCG family occurrences.

1.1 Models – geologically testable hypotheses

The integrated mineralization and alteration model for Fe oxide(-Cu-Au-U-REE-P) systems (Hitzman et al., 1992; Barton and Johnson, 1996, 2000) describes a pattern beginning with abundant, deep Na(-Ca) alteration which is also depleted in Fe and base metals. These metal-depleted zones grade upwards first into Mt-Ap-Act/Cpx (Kiruna-type) mineralization that is associated with varied and intense Na-Ca(-Fe-K) alteration, then into variably (some rich, some poor) sulfide-bearing Mt or Hm-rich mineralization associated with mixed K(-Ca-H⁺) alteration, and ultimately into intense hydrolytic (H⁺) alteration with Hm-dominated ore mineral assemblages. Sulfide abundances, including Cu-Fe sulfides commonly (but not universally) increase upwards from low contents in the Kiruna-type ores to higher values in Mt- and Hm-rich Cu ores. Variations on this theme include Mt(±Hm)-rich, silicate-poor "skarn" replacement in carbonate rocks and distal, low-T K-alteration in some coeval volcanic rocks. This model can be tested against observations in IOCG systems worldwide and against geochemical data and theory.

In this contribution we assess the above descriptive model through examination of districts where system-scale observations have been made in the Cordillera of South and North America (Table 1; see also Barton, 2009). We note evidence for formation in the upper few km of the crust and for systematic patterns across a range of geologic environments as well for Cu-rich vs. Cu-poor ores, and the possible use of this understanding for mineral exploration and for genetic interpretations.

2 Cordilleran IOCG Systems: Diversity and Vertical Zoning

Cordilleran IOCG systems show considerable diversity in form, mineralization, and geologic setting yet all exhibit the fundamental characteristics of voluminous low-Ti Fe oxides with anomalous quantities (compared to other elements) of Cu, Au, Co, U, P, and REE as well as a close association with voluminous Na-Ca-K(-Fe) hydrothermal alteration (Barton, 2009; Barton et al., 2011a; Chen, 2010; Sillitoe, 2003).

Table 1 summarizes key characteristics for a number of well exposed and well studied districts in the coastal cordillera of Chile and in the southwestern USA. Each of these districts exhibits considerable vertical exposure through a combination of structural and/or topographic relief and exploration and development.

2.1 Coastal Chile

In Chile, a complex tectonic history has juxtaposed different structural levels along and across the trend of the Middle Jurassic to Early Cretaceous arc. New regional- and district-scale alteration mapping coupled with hornblende barometry and stratigraphic reconstructions demonstrates that hydrothermal systems are concentrated in the upper half (depth range) of exposed crust which represents at least 10 km through upper part of the middle and late Mesozoic arc crust (Barton et al., 2012). These systems exhibit structural and stratigraphic controls, are intensely brecciated, and contain common coeval intermediate to felsic intrusions.

Most of the districts listed in Table 1 contain significant Cu(-Au-Fe) ore (ranging from 0.3 to 1.5 % Cu) with from >15 Mt (Ojancos Viejo) to >800 Mt (Candelaria). Mineralization occurs as Mt- to Hm-dominated breccias, veins and replacements. In the uppermost parts of these systems Hm-stable alteration consists of either intensely acid-altered tops (locally with S-poor advanced argillic assemblages, Productora,

Ojancos Viejo, Jesus Maria; Kreiner, 2011) or, in some cases, syngenetic features including banded Hm-rich jaspilites (Punta del Cobre, Candelaria).

At deeper structural levels (1-5 km depth) nearly all districts have produced at least some Fe from Mt-rich ores either as a major co-product (Candelaria, Santo Domingo Sur) or smaller amounts from Mt-rich(+Act+Epid±Ap) ores. The latter ores (Kiruna type) are present in all districts where they formed relatively deep within parts of the same district-scale hydrothermal system (e.g., Cerro Negro, Productora, Jesus Maria, Mantoverde). Where carbonate rocks are present, Mt-rich, Gar-bearing replacement deposits (skarns) formed; these have varied Cu contents. The deepest portions (2-8 km) of each of these districts contain intensely Na-Ca altered, Fe-depleted igneous rocks (intrusive ≥ volcanic). Deep alteration consists of scapolite or oligoclase plus actinolite or diopside with minor titanite. The deeper (>2-5 km) Fe ores differ little from those seen in the classic Kiruna-type deposits of the same region (e.g., Romeral, Algorrobo, Cerro Iman, Los Colorados) and which occur at similar paleodepths.

Table 1. Vertical zoning for selected igneous-related Cordilleran IOCG systems

District	Magmatism and host rocks	Hydrothermal alteration // Fe-Cu (deep to shallow)	Depth interval seen (km // evidence)	References
Coastal Chile				
Candelaria / Punta del Cobre, Chile	E Cret. basaltic andesitic hypabyssal & volcanic rocks	Na-Ca to K(-Ca-Fe) to K-H+ // Fe-loss to Mt(+Act±Ap) to Mt-Act-Epid(+Py+Cpy) to Hm(±Mt)+Cpy to syng. Hm	0-2 km // syng. Fe-Si, strat. reconstruction, fluid inclusions	Marschik and Fontbote (2001), Barton et al. (2011b), this study
Cerro Negro, Chile	E Cret. interm. compo. intrusions and volc. rocks	Na-Ca to K(-Ca-Fe) to K-H+ // Fe-loss to Mt(+Act±Ap) to Mt(+Py+Cpy) to Hm(±Mt)+Cpy	<1(?) - >4 km (Cu + Fe in upper 3 km); strat. + struct. reconstr.	Bonson (1998); this study
Jesus Maria, Chile	E Cret. interm. comp. plutonic and volcanic rocks	Na-Ca to Na(-Ca-Fe) to H+ // Fe-loss to Mt(+Act±Ap) to Mt(+Py+Cpy) to Hm(±Mt±Cpy)	<1 - 4 km (Fe + Cu in upper 2-3 km) // strat. + struct. reconstruction	Kreiner and Barton (2011), Kreiner (2011), this study
Mantoverde, Chile	E Cret. interm. compo. intrusions and volc. rocks	Na-Ca to K(-Ca-Fe) to K-H+ // Fe-loss to Mt(+Act±Ap) to Mt-Act(+Py+Cpy) to Hm(±Mt)+Cpy	<2(?) - >4 km (Cu + Fe in upper 1-3 km) // struct. + strat. reconstr.; fluid inclusions	Benavides et al. (2007); Rieger et al. (2010); this study
Productora, Chile	E Cret. interm. comp. intrusions and volc. rocks	Na-Ca to Na(-Ca-Fe) to H+ // Mt(+Act±Ap) to Mt(+Py+Cpy) to Hm(±Mt±Cpy)	<1(?) - >4 km (Cu + Fe in upper 3 km) // strat. and struct. reconstr.	Ray and Dick (2002); this study
Ojancos Viejo, Chile	E Cret. interm. comp. plutonic and volcanic rocks	Na-Ca to K(-Ca-Fe) to K-H+ // Fe-loss to Mt(+Act±Ap) to Mt(+Py+Cpy) to Hm(±Mt)+Cpy	<1 to 5 km (Cu + Fe in upper 2 km) // struct. reconstruction, fluid inclusions	Kreiner and Barton (2011), Kreiner (2011), this study
Santo Domingo Sur, Chile	E Cret. interm. comp. intrusions to volc. and sed. rocks	Na-Ca to Mt repl. and K(-Ca-Fe) to K-H+ // Fe-loss to Mt(+Act±Ap) to Mt+Act(+Py+Cpy) to Hm+Cpy	<1 - 4 km (Cu + Fe in upper 1-2 km) // strat. + struct. reconstruction	Daroch and Barton (2011), Rennie (2010)
Southwestern United States				
Iron Springs, Utah	Mioc. interm-felsic volc-intrusive complex in Mz. sed.	Na-Ca to K(-Ca) and Mt repl. to H+ // Fe loss to Mt(-Ap-Cpx) to Mt ± Hm (bx) to Hm+Qz (repl + syngenetic)	0 - 3 km (Fe + trace Cu in upper 2 km) strat. // struct. reconstructions	Barker (1995), Tobey (1976)
Cortez Mountains, Nevada	Jur. interm. to felsic intrusions in Mz volc; Pz carb	Na-Ca to K(-Ca) to H+ // Fe loss to Mt(-Ap-Cpx) to Mt(+Py) to Hm(+Mt+Cpy+Bn) to Hm±Apt+Qz (repl ± syngenetic)	0 - 7 km (Fe ± Cu in upper 3 km) // from struct. reconstruction	Johnson (2000); Barton and Johnson (unpubl. ms.)
Eagle-Palen Mountains, California	Jur. interm. to felsic intrusions in Mz volc; Pz carb	Na-Ca to Mg skarn and Fe(-Ca-K) to H+ // Fe-loss to Mt repl. and Mt(-Act-Ap) to Mt(+Py±Cpy) to Hm±Cpy	<1 - >5 km (Fe ± Cu upper 2-4 km) // strat. reconstr.	Barton et al. (2011), Kreiner (2011), JD Girardi, written comm.
Humboldt, Nevada	Jur. mafic volc-sed complex in Mes volc-sed section	Na-Ca to K(-Ca) to H+ // Fe loss to Mt(-Ap-Act) to Mt(+Py) to Hm(+Cpy+Bn) (bx) to Hm+Qz (repl + syngenetic)	0 - 5 km (Cu + Fe in upper 3 km) // strat. and struct. reconstruction	Johnson and Barton (2000), Johnson (2000)
Yerington, Nevada	Jur. interm. to felsic volc-plutonic complex in Mes. volc-sed. section	Na-Ca to Mt repl. and Fe(-Ca-K) to H+; // Fe-loss to Mt(-Act-Ap) to Mt(+Py±Cpy) to Hm±Cpy	0 - 7 km (Cu + Fe in upper 3 km) // struct. reconstruction	Proffett and Dilles (1995), Dilles et al. (2000), Ohlin (2010), Runyon and Barton (this volume)

2.2 Southwestern USA

In the southwestern USA, numerous Fe oxide-rich hydrothermal systems of Jurassic and Cenozoic age exhibit the features common to worldwide IOCG systems (Barton, 2009; Barton et al., 2011). As in Chile, many areas (Table 1) have good 3-dimensional exposures which resulted from combinations of structural complexity (notably tilted sections due to Cenozoic extension), topographic relief, and drilling.

A handful of districts have produced modest amounts of Cu(\pm Au), and several have major resources (e.g., >400 Mt, 0.6% Cu at Pumpkin Hollow, Nevada, Ohlin, 2010). Similarly, many districts (Table 1) have significant Kiruna-type and/or carbonate-hosted Fe resources associated with intense Na-Ca-K-Fe metasomatism. Also as in Chile, the patterns observed include deep (2-7 km depth), metal-depleted Na-Ca alteration grading upward (1-4 km) into Kiruna-type Mt(-Act-Ap) mineralization (present in all districts in igneous host rocks). Cu-Fe sulfide-bearing Mt(-Hm) breccias and replacement bodies (skarns in carbonates) occur in the upper few km (<1-3 km) with local syngenetic Fe-oxides at the surface (e.g., Humboldt, Iron Spring). Given these shared characteristics, which suggest a common process, it is noteworthy these systems formed across a broad range of tectonic settings (arc, back-arc, extension-related) and with diverse igneous compositions (mafic to felsic), thus implying distinct, independent mechanism for IOCG clan genesis.

2.3 Tops and bottoms: vertical extents, depths and implications

The vertical extent – from tops to bottoms – in the districts summarized in Table 1 ranges from 2-3 km to as much as 7-8 km. Such ranges resemble those for circulation of surface derived or basinal fluids, or the depth interval for vigorous release of magmatic fluids. There is no evidence for continuity to greater depths as implied by models calling on deep fluid sources.

Fe(\pm Cu) mineralization locally reached the surface and rarely extended deeper than 4 km as indicated by local syngenetic Fe deposits, barometry, stratigraphic (\pm structural) constraints, and evidence for phase separation (boiling) in fluid inclusions. In most districts, the Fe-rich interval was <3 km, with Mt(-Act \pm Ap) beneath Cu-rich intervals. The latter range from 0.5 to 1.5 km in vertical extent. Metal-depleted, Na-Ca altered bottoms formed within ~2 km to as much as 7 or 8 km below the surface. These features and their complex superposition plus other geochemical data indicate that cooling and mixing likely were important in metal precipitation in addition to the key role of wall rock reaction.

3 Comparison with other IOCG Regions

Many IOCG systems worldwide show similar patterns to those described here, including the evidence for deep to shallow Na-Ca to K(-Ca-Na) to H⁺ alteration, and the corresponding development of Hm- and/or Mt-

dominated variably sulfide(\pm Cu)-bearing mineralization overlying (or overprinting) sulfide-poor Mt(-Act/Cpx-Ap) mineralization (see Barton, 2013; Williams et al., 2005 for reviews). For example in South Australia Cu(-Au-U-Ag) Hm-dominated mineralization overprints and or overlies Mt-dominated assemblages with accessory Kf-Act-Ap-Bt (Skirrow, 2010). Similar patterns in alteration, ore mineral assemblages and general depth ranges can be inferred in the southern deposits of the Carajas district, Brazil (Xavier et al., 2010), and in the relatively Cu-poor domains of northern Sweden and SE Missouri (Hitzman et al., 1992). As is the case in South Australia exposures are limited, so vertical extents are difficult to establish, however geologic evidence and available drilling indicates significant zoning over intervals of <2 km. Alteration and, to an extent, metal ratios in these districts reflects the host rocks, with higher K/Na, Σ REE, F/Cl, and U in the more felsic systems (Barton and Johnson, 2000; Xavier et al., 2010).

4 Comparison with Fe(-Ti)-oxide-Apatite Systems

Kiruna-type (or 'IOA') mineralization is often compared with apatite-rich Fe-Ti oxide deposits. Cordilleran-type occurrences differ in fundamental ways: (1) hydrothermal alteration is intense and abundant, (2) as shown here, Mt(-Act/Cpx-Ap) ores form one part of clearly zoned systems with other ore and alteration types; (3) apatite contents are highly variable, typically 0.5-2% rarely exceeding 5 wt % over any appreciable volume (Barton and Johnson, unpubl. compil.), and (4) isotopic data demonstrate non-magmatic components (e.g., Sr and Os) in a number of Kiruna-type ores (Williams et al. 2010). In contrast, the Fe-Ti-oxide-apatite ('nelsonite') deposits, lack appreciable hydrothermal features, have relatively little pyroxene \pm amphibole but far more apatite (15-25 wt%, Kolker, 1982), and far better fit the experimental data on liquid immiscibility (Charlier and Grove, 2012). The Cordilleran evidence places Kiruna-type mineralization in a well-documented hydrothermal continuum with metal-depleted roots and varied tops, and not with a model which requires oxide-silicate melt immiscibility.

5. Concluding Remarks: Inferences from and Utility of Zoning Patterns

Understanding the IOCG clan remains a challenge, yet regular patterns emerge repeatedly when system-scale observations are made. In the relatively young and well exposed systems of the South and North American Cordillera, varied geologic settings yielded similar overall alteration and mineralization patterns like those described in early syntheses: vertical zoning goes from deep metal-leaching associated with intense Na-Ca alteration through a regular upward progression terminating in high-level hematite-rich and acid-altered assemblages. Such patterns are consistent with predicted reaction pathways for brine-rock interaction (Barton and Johnson, 2000). Likewise, differences are predictable: specific assemblages and accessory element contents should and do vary systematically with setting, notably

with rock compositions or, for Cu in particular, the availability of reduced sulfur.

The regular patterns observed in the Cordilleran IOCG clan constrain possible genetic models and may aid exploration. The similarity in vertical zoning given different geologic environments (e.g., magmas, host rocks, tectonic setting) requires an origin independent of these features and one that operates in the upper 5-8 km of the terrestrial crust (as evidenced by well defined, metal-depleted bottoms at such levels). These geologic observations when combined with other geochemical and petrological data support a key role in many systems for non-magmatic brines proposed by Barton and Johnson (1996) and discussed by many since then. This is not to conclude that other IOCG environments, especially in metamorph(ic/osed) terrains may have different fluid sources (Williams et al., 2010; Barton, 2013). Understanding these patterns can be particularly useful in guiding mineral exploration in covered or structurally complex IOCG-bearing terrains.

Acknowledgements

This paper reflects work done on IOCG projects over the last 15 years sponsored by industry (Phelps Dodge / Freeport-McMoRan, the UA-IMR Science Foundation Arizona consortium), USGS MRERP (08HQGR0060), the US National Science Foundation (EAR08-38157, EAR98-15032). I thank Simone Runyon and Roberto Xavier for helpful reviews.

References

- Barker DS (1995) Crystallization and alteration of quartz monzonite, Iron Springs Mining District, Utah: relation to associated iron deposits. *Econ Geol* 90:2197-2217.
- Barton MD (2009) IOCG deposits: A Cordilleran perspective. Proc. 11th Biennial SGA Meeting, 5-7.
- Barton, MD (2013) Iron oxide(-Cu-Au-REE-P-Ag-U-Co) systems. Chapter 20, *Treatise on Geochemistry* 13, in press.
- Barton MD, Johnson DA (2000) Alternative brine sources for Fe-oxide(-Cu-Au) systems: Implications for hydrothermal alteration and metals. *Hydrothermal iron oxide copper-gold & related deposits: A global perspective*. Aus. Min. Foundation, Adelaide, 43-60
- Barton MD, Dilles JH, Girardi JD, *et al.* (2011a) Jurassic igneous-related metallogeny of southwestern North America. In *Great Basin Evolution and Metallogeny* (eds. Steinger RL, Pennell B). *Geol. Soc. Nevada, Reno*:373-396.
- Barton MD, Kreiner, DC, Jensen, EP, Girardi, JD (2011b) Superimposed hydrothermal systems and related IOCG and porphyry mineralization near Copiapó, Chile. Proc. 11th Biennial SGA Meeting, 521-523.
- Barton MD, Kreiner DC, Girardi JD (2012) Multiple hydrothermal systems in coastal northern Chile and the footprints of IOCG systems: 34th Intern. Geol. Congr. p. 611.
- Belperio A, Flint R, Freeman, H (2007) Prominent Hill: A hematite-dominated, iron oxide copper-gold system; *Econ Geol* 102:1499-1510.
- Benavides JA, Kyser TK, Clark AH, Oates C, Zamora R, Tarnovschi R, Castillo B (2007) The Mantoverde iron oxide-copper-gold district, III Región, Chile: The role of regionally derived, nonmagmatic fluids in chalcopyrite mineralization. *Econ Geol* 102:415-440.
- Bonson CG (1998) Fracturing, fluid processes and mineralisation in the Cretaceous continental magmatic arc of northern Chile (25° 15'-27° 15'S). Unpubl PhD diss, Kingstom Univ, 357 p.
- Charlier B., Grove TL (2012) Experiments on liquid immiscibility along tholeiitic liquid lines of descent. *Contr Min Pet* 164:27-44.
- Chen HY (2010) Mesozoic IOCG mineralization in the central Andes: an updated review. In *Hydrothermal Iron Oxide Copper-Gold and Related Deposits: A Global Perspective* (Porter TM ed.). PGC Publishing, Adelaide. 3:259-272.
- Daroch G, Barton, MD (2011) Hydrothermal alteration and mineralization in Santo Domingo Sur iron oxide (Cu-Au) deposit, Atacama Region, Chile. Proc. 11th Biennial SGA Meeting, 488-490.
- Dilles, JH, Proffett, JM (1995) Metallogeneses of the Yerington batholith, Nevada: *Arizona Geol Soc Digest* 20:306-315.
- Dilles JH, Einaudi MT, Proffett JM, and Barton MD (2000) Overview of the Yerington porphyry copper district: Magmatic to non-magmatic sources of hydrothermal fluids, their flow paths, alteration affects on rocks, and Cu-Mo-Fe-Au ores. *Soc Econ Geol Guide Book Series* 32:55-66.
- Hitzman MW, Oreskes N, Einaudi MT (1992) Geological characteristics and tectonic setting of Proterozoic iron oxide (Cu-U-Au-REE) deposits. *Prec Res* 58:241-287.
- Johnson DA (2000) Studies of iron-oxide (Cu-REE-Au-Co-Ag-Ni-U) mineralization and associated sodic alteration in the Great Basin. Unpubl PhD dissertation, Univ Arizona, 277 p.
- Johnson DA, Barton MD (2000) Time-space development of an external brine-dominated, igneous-driven hydrothermal system; Humboldt mafic complex, western Nevada. *Soc Econ Geol Guidebook* 32:127-143.
- Kolker A. (1982) Mineralogy and geochemistry of Fe-Ti oxide and apatite (nelsonite) deposits and evolution of the liquid immiscibility hypothesis. *Econ Geol* 77:1146-1158.
- Kreiner DC (2011) Epithermal style iron oxide(-Cu-Au) (=IOCG) vein systems and related alteration. Unpubl PhD dissert, Univ Arizona, 659 p.
- Kreiner DC, Barton, MD (2009) Hydrothermal alteration and mineralization zoning in iron oxide (Cu-Au) vein deposits near Copiapó, Chile. Proc 10th Bien SGA Meeting, 635-637.
- Marschik R, Fontbote L (2001) The Candelaria-Punta del Cobre iron oxide Cu-Au(-Zn-Ag) deposits, Chile. *Econ Geol* 96:1799-1826.
- Ohlin H (2010) Geology of the Pumpkin Hollow Deposits, Lyon County Nevada: *Geol Soc Nevada 2010 Guidebook* 7:69-81.
- Ray GE, Dick LA (2002) The Productora prospect in north-central Chile: An example of an intrusion-related Candelaria type Fe-Cu-Au hydrothermal system. In *Hydrothermal Iron Oxide Copper-Gold and Related Deposits: A Global Perspective* (Porter, TM ed.). PGC Publishing, Adelaide, 2:131-151.
- Rieger A, Marschik R, Diaz M, Holz S, Chiaradia M, Akker B, Spangenberg J (2010). The hypogene iron oxide copper-gold mineralization in the Mantoverde district, northern Chile. *Econ Geol* 105:1271-1299
- Rennie DW (2010) Technical report on the Santo Domingo property, Region III, Atacama Province, Chile. A NI 43-101 Technical Report prepared for Far West Mining Ltd, 170 p.
- Sillitoe RH (2003) Iron oxide-copper-gold deposits: an Andean view. *Mineral Dep* 38:787-812.
- Skirrow RG (2010) "Hematite-group" IOCG ± U ore systems: Tectonic settings, hydrothermal characteristics, and Cu-Au and U mineralizing processes. *Geol Assoc Canada, Short Course Notes* 20:39-59.
- Tobey EF (1976) Geology of the Bull Valley intrusive-extrusive complex and genesis of the associated iron deposits: Unpubl. PhD diss, Univ Oregon, 244 p.
- Williams PJ (2010) Classifying IOCG deposits. *Geol. Assoc. Canada Short Course Notes* 20:23-38.
- Williams PJ, Kendrick, MA, Xavier, RP (2010) Sources of ore fluid Components in IOCG deposits. In *Hydrothermal Iron Oxide Copper-Gold and Related Deposits: A Global Perspective* (Porter, TM ed.). PGC Publ, Adelaide, 107-116.
- Williams PJ, Barton MD, Johnson DA, Fontbote L, de Haller A, Mark G, Oliver NHS, Marschik R (2005) Iron oxide copper-gold deposits; geology, space-time distribution, and possible modes of origin. *Econ Geol* 100th Anniv Vol, 371-406.

The Merlin high grade Mo-Re deposit, Cloncurry District, Australia

Joao Babo, Carl Spandler, Mike Rubenach, Nick Oliver

School of Earth and Environmental Sciences, James Cook University, Townsville, QLD 4811, Australia

Mat Brown

Exploration Manager, Regional Projects, Cloncurry Project, Ivanhoe Australia Ltd.

Abstract. The world's highest grade Mo deposit, Merlin, is hosted in Proterozoic metasedimentary rocks, 90 km south of Cloncurry, in the Mount Isa Block of northern Australia. The metasedimentary rocks consist of pelitic slates and phyllites interbedded with carbonaceous metapelites, then down to intensely altered calc-silicate rocks, and all structurally overlain by the 1516 ± 10 Ma Mt Dore Granite. The metasedimentary rocks host two main mineralization zones that partly overlap. The top zone is copper dominated, hosted primarily in the metapelites. The second zone is Mo-Re dominated, structurally controlled and hosted by the calc-silicates. Relatively early Na-(Ca) metasomatism is overprinted by strong potassic alteration and silicification. Petrography and LA-ICPMS sulfide analyses show the Cu mineralisation predates the Mo-Re mineralisation, and may have contributed to Mo mineralization by providing sulfur. Sulfur isotope studies show that Cu mineralization has magmatic signatures while the Mo-Re displays an additional sedimentary component. Re-Os geochronology places the Mo-Re mineralization concomitant with the A-type intrusives of the district. Different fluid systems drove the Cu and Mo. The Mo mineralization likely precipitated from a sedimentary-equilibrated fluid driven by intrusion and possibly precipitated by redox and/or pH changes due to wallrock interaction.

Keywords. Molybdenum, Rhenium, IOCG, Proterozoic

1. Introduction

In 2008 Ivanhoe Australia discovered the high grade Mo-Re deposit while drilling underneath the Mount Dore IOCG deposit, a historical copper resource (Fig. 1).

This discovery has had a profound worldwide effect on molybdenum geoscience and resources, and stimulated renewed exploration in the Eastern Fold Belt of the Mount Isa District. Although the Merlin deposit shares some of the characteristics of the IOCG deposits for which this area is renowned, there are many differences other than just the metal endowment, so a need for detailed petrography, geochemistry studies and geochronology has risen.

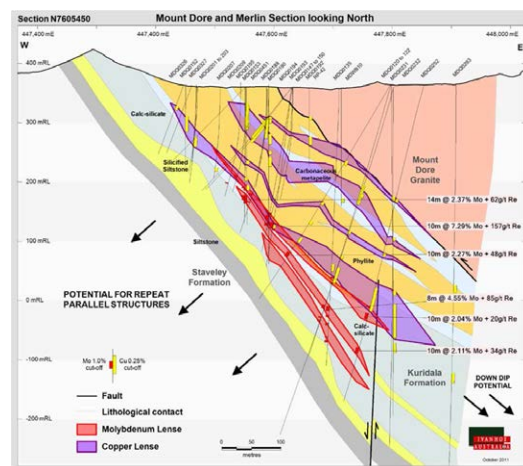


Figure 1. Merlin deposit cross-section looking north with copper and molybdenum lenses and high grade Mo-Re intervals. Courtesy of Ivanhoe Australia, Ltd.

2. Geological Setting

The Cloncurry district is part of the Mount Isa Inlier located in northwest Queensland, Australia. It displays a complex protracted Paleo- and Mesoproterozoic tectonic evolution. The Mount Isa Inlier is commonly sub-divided into three broad regions: the Eastern Fold Belt, the Kalkadoon-Leichhardt block and the Western Fold Belt. The Eastern Fold Belt, where the deposit is located, consists of a sequence of metasedimentary rocks and metavolcanics that were deposited during “far-field back-arc” rifting (Betts et al. 2006) and subsequently undergone several deformation events (Blake, 1987).

The Kuridala Formation, that hosts the deposit, is several kilometers thick, containing deep water turbiditic sediments and lower energy variably carbonaceous shales. The depositional age of the Kuridala Formation is no older than 1676 ± 5 Ma, from a tuff sample that is approximately 14km east of the study area (Page and Sun, 1998). The Kuridala Formation is also host for several mineral deposits and occurrences of copper and copper-gold.

Bedding parallel foliation is easily observed in the more pelitic metasedimentary rocks, and probably developed early during greenschist to amphibolite facies regional metamorphism, between 1650 and 1550 Ma (Rubenach et al., 2008). Intrusion of the Williams

Batholith (including the Mt Dore Granite), widespread metasomatism and mineralization, and some local shortening events (D_3 and D_4) dominated the late to post-orogenic stages from 1540 to 1500 Ma (e.g. Oliver et al. 2008; Rubenach et al. 2008). The D_4 deformation event was responsible for the thrusting of the granite on top of the metasedimentary package.

3. Geologic Units

The A-Type Mount Dore granite, (1516 ± 10 Ma; Pollard et al., 1997), of roughly 100 km^2 (Carter et al., 1961), shows uniform composition of equigranular K-feldspar, quartz, plagioclase (+ biotite + titanite) \pm zircon \pm hornblende. The bottom contact with the carbonaceous metapelites or phyllites is sharp and commonly brecciated, due to the thrust nature of the contact (Fig 1), whereas other contacts are intrusive and produce local contact metamorphic effects.

The pelitic shales and phyllites are composed of muscovite + K-feldspar + albite + quartz \pm andalusite \pm rutile and are strongly foliated and moderately folded. The interbedded carbonaceous metapelites show similar mineralogy although with graphite and no andalusite and rare albite. The relative proportions of quartz, muscovite and feldspar show lateral and vertical stratigraphic variations from more silica-feldspar rich to more pelitic.

The contact of these units with the underlying altered calc-silicate rocks is commonly brecciated and marks the location of the bulk of the Mo-Re mineralization. The calc-silicates are banded and consist of amphibole, plagioclase, K-feldspar, apatite, carbonates \pm titanite \pm magnetite. These metasedimentary rocks have a general metasomatic zoning profile from sodic dominated near the bottom of the sequence, to potassic dominated near the top, although fracturing and brecciation complicate the alteration geometry. The bottom part of the metasedimentary package consists of an intensely silicified rock that has been described historically as quartzite.

4. Mineralization

The indicated and inferred mineral resource of the Merlin deposit is 13 Mt at 0.8% Mo and 14 g/t Re, with a more recently identified pod of very high-grade Mo-Re mineralisation with an inferred mineral resource of 15,000 tonnes at 13% Mo and 160 g/t Re (Brown et al., 2010).

The Mo-Re mineralization occurs as infill of rounded clast matrix supported breccias (Fig 2) but also in small veins (commonly stylolitic) and disseminated. This mineralization is associated with Na alteration overprinted by potassic alteration and silicification (Fig. 2). The Re-Os

geochronology display similar ages to the A-type intrusives of the Williams Batholith in the district.

The copper mineralization can be divided into two zones. The upper zone is intensely weathered with cuprite, chrysocolla, chalcotrichite, pseudomalachite which gradationally becomes chalcocite dominated (Lazo and Pal, 2009). The lower Cu zone is mostly associated to the pelitic shales and phyllites and carbonaceous metasedimentary rocks in fractures with K-feldspar + quartz + sphalerite + tourmaline and in breccias with matrix of dolomite with fragments of pyrite + chalcocopyrite \pm sphalerite.

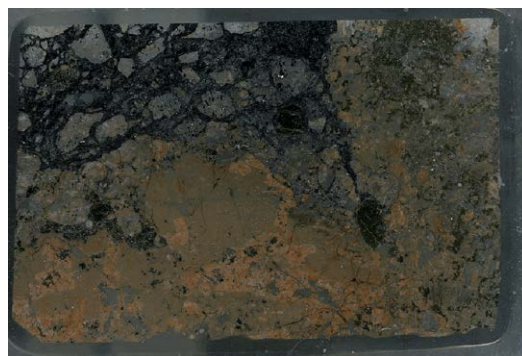


Figure 2. Example of Mo-Re mineralization occurring as infill of rounded clast matrix supported breccias. Polished section is approximately 4cm wide.

The style of occurrence of both the Cu and Mo dominated mineralization demonstrates a clear structural control on the deposit.

5. Sulfur Isotopes

The sulfur isotope analyses were conducted in molybdenite, chalcopyrite and pyrite of different mineralization styles and host units (Fig. 3).

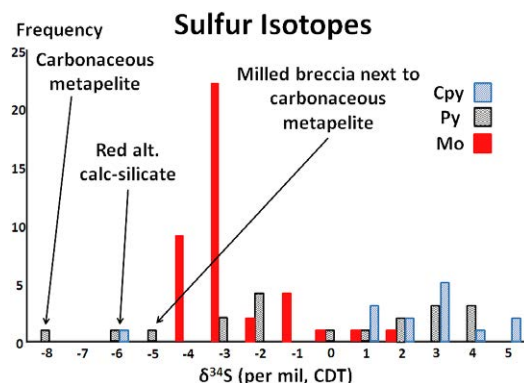


Figure 3. $\delta^{34}\text{S}$ values for mineral separates of pyrite ($\delta^{34}\text{S}_{\text{Py}}$), chalcopyrite ($\delta^{34}\text{S}_{\text{Cpy}}$) and molybdenite ($\delta^{34}\text{S}_{\text{Mo}}$)

The $\delta^{34}\text{S}_{\text{Mo}}$ values are mostly concentrated around -3‰, with a few heavier outliers. The $\delta^{34}\text{S}_{\text{Py, Cpy}}$ covers a larger range of values, but most fall between 0‰ and 5‰. We interpret these results to reflect sedimentary and magmatic

components to the Mo-Re and Cu mineralisation, respectively. The samples that overlap between these two main peaks probably result from the interaction of the molybdenite with the Cu and Py mineralization. The more negative values of Py are mostly due to their location in or closely associated to the carbonaceous metapelites and are interpreted to represent the syngenetic sediment sulfide signatures.

6. LA-ICP-MS Sulfide Analyses

Laser ablation ICP-MS analysis of sulfides was conducted on 11 samples of Mo-Re and Cu ore. For each sample, more than one sulfide type was analysed when possible, resulting in an extensive geochemical database of molybdenite, chalcopyrite and pyrite.

Laser ablation data interpretation coupled with sulfur isotope results show clear interaction between the Cu dominated and Mo dominated mineralization that has some correlation with sulfur isotope signatures (Fig. 4). Although not a perfect trend, the molybdenite samples with higher As and Co contents tend to have heavier sulfur isotope values, which we interpret to reflect interaction with Cu mineralization sulfides (e.g., pyrite). This correlation indicates that the younger Mo mineralization used, at least some, of the older Cu mineralization sulfur. It was also possible to define two to three different pyrite generations.

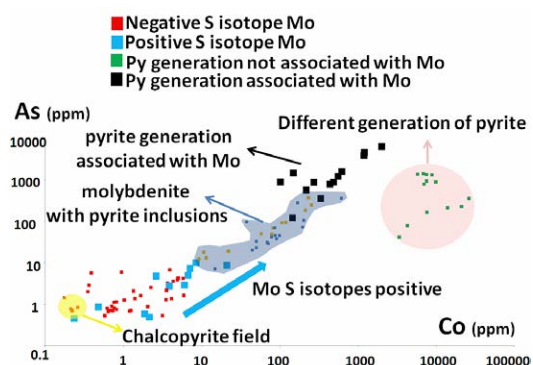


Figure 4. Trace element analysis of molybdenite (Mo) and pyrite (Py) by LA-ICP-MS. Chalcopyrite (Cpy) field is shown in yellow.

7. Discussion

The Merlin and Mount Dore deposits are multiphase hydrothermal deposits that have a complex genetic history, involving multiple fluid sources. We suggest that Cu mineralization was derived from a magmatic-hydrothermal fluid that used dilatational, brittle fractures in the pelitic metasedimentary rocks and was accompanied by potassic alteration.

The Mo-Re mineralization shows both magmatic and sedimentary signals. Part of the magmatic signal could have been derived from magmatic-hydrothermal fluids and/or by interaction with the previous Cu mineralization, but the Mo and some of the sulfur was derived by the passage of fluids through the broader metasedimentary sequence. The model of an igneous-derived fluid, moving up sequence through the calc-silicate package, mixing with a sedimentary equilibrated fluid is put forward. The igneous-derived fluid is from A-Type magmatism since the Re-Os dating places the Mo-Re mineralization at the same age as the Williams Batholith. The interaction of the sedimentary equilibrated fluid with the metapelitic package may be responsible for mobilising molybdenum and sulfur. The strong redox and/or pH change in the boundary between the metapelitic sequence and the calc-silicates provided a suitable chemical trap for Mo precipitation, and the rheological difference promoted brecciation and the very high grades of Mo-Re, which have no parallel with any other deposit worldwide.

Acknowledgements

Funding for this project was provided by Ivanhoe Australia Limited.

References

- Betts PG, Giles D, Mark G, Lister GS, Goleby BR, Aillères L (2006) Synthesis of the proterozoic evolution of the Mt Isa Inlier: Australian Journal of Earth Sciences 53: 187-211.
- Blake DH (1987) Geology of the Mount Isa Inlier and environs, Queensland and Northern Territory: Bureau of Mineral Resources Bulletin: 219.
- Brown M, Lazo F, Carter P, Goss B, Kirwin D (2010) The geology and discovery of the Merlin Mo-Re zone of the Mount Dore Deposit, Mount Isa Inlier, NW Queensland, Australia: SGA newsletter June: 27.
- Lazo F and Pal T (2009) The Merlin Mo-Re zone, a new discovery in the Cloncurry district, Australia: Biennial SGA Meeting, 10th, Townsville, Australia.
- Page RW and Sun SS (1998) Aspects of geochronology and crustal evolution in the Eastern Fold Belt, Mt Isa Inlier: Australian Journal of Earth Sciences 45: 343-361.
- Pollard PJ, Blake KL, Dong G (1997) Proterozoic Cu-Au-Co and Pb-Zn-Ag mineralization in the Cloncurry district, eastern Mount Isa Inlier, Australia: Constraints on fluid sources from mineralogical, fluid inclusion and stable isotope data: AMIRA P438 Cloncurry Base Metals and Gold Final Report, Section 7: 50.
- Oliver NHS, Butera KM, Rubenach MJ, Marshall LJ, Cleverley JS, Mark G, Tullemans F, Esser D (2008) The protracted hydrothermal evolution of the Mount Isa Eastern Succession: A review and tectonic implications: Precambrian Research 163: 108-130.
- Rubenach MJ, Foster DRW, Evins PM, Blake KL, Fanning CM (2008) Age constraints on the tectono-thermal evolution of the Selwyn Zone, Eastern Fold Belt, Mount Isa Inlier: Precambrian Research 163: 81-107.

The geology of the giant Pampa de Pongo magnetite skarn (S Peru) and its relationship with IOCG systems

Gustavo Calvo

Buenaventura Ingenieros, S.A. (BISA) Larrabure y Unanue 146, Lima 1, Peru. gcalvo@bisa.com.pe

Fernando Tornos

Consejo Superior de Investigaciones Científicas. CAB (CSIC-INTA). Ctra Ajalvir km. 4. 28850 Torrejon de Ardoz, Spain. f.tornos@csic.es

Francisco Velasco

Universidad del País Vasco, Dpt. Mineralogía y Petrología. Leioa, Vizcaya, Spain. francisco.velasco@ehu.es

Abstract. The Pampa de Pongo deposit forms part of the Marcona magnetite district (Peru), the zone with the largest iron resources of the American Cordillera, developed during a long lasting period of magmatic-hydrothermal activity in the Middle Jurassic-Early Cretaceous (177-95 Ma). Most of the magnetite-(Cu-Au) mineralization occurs within stratabound prograde magnesian skarns and an external aureole of dolomite-magnetite replacement. This orebody is capped by mineralized hydrothermal breccias and veins that crosscut the impermeable overlying andesite; these are most likely related to fluid overpressure and hydraulic fracturing synchronous with the underlying replacement. The geology and geochemistry are consistent with the mineralization being part of a large magmatic-hydrothermal system rooted on a hidden cupola of likely intermediate composition. This system was able to generate a large zone of hydrothermal alteration that included the skarn on the carbonate rocks and an alkaline-calcic, IOCG-like mineralization on the overlying andesite.

Keywords. skarn, IOCG, iron, Peru, Andes

1 Introduction

In southern Peru, the Coastal Cordillera hosts a world class iron ore district with several magnetite deposits, including Marcona (1,900Mt @ 55.4% Fe, 0.12% Cu) and Mina Justa (413Mt @ 0.79% Cu, 0.05g/t Au, 3.8g/t Ag). The recent discovery of the Pampa del Pongo deposit adds further interest to this emerging district.

The deposit is located 440 km SW of Lima and only 20 km from the Pacific coast. Pampa de Pongo is a blind orebody that was discovered in 1995 when Rio Tinto drilled a significant magnetic anomaly below a thick sedimentary cover. Currently, the project belongs to Jingzhao Mining Peru, which plans to start operations in the next future. Systematic drilling and resource evaluation carried by BISA have delineated more than 3,000Mt at 40% Fe, 0.1% Cu and 0.1g/t Au. There is little prior information on this deposit, with only a preliminary description by Hawkes et al. (2002) that described it as an IOCG-like mineralization.

The Pampa del Pongo deposit is probably one of the largest iron-rich magnesian skarn worldwide. With the Marcona and Mina Justa deposits forms a district with more than 5.5 Gt of magnetite ore, making it the largest iron cluster of the American Cordillera.

2 The geology of the Pampa del Pongo deposit

The deposit is hosted by the Marcona Fm (Carboniferous?), a thick carbonate sequence dominated by epigenetic dolostone with some lenses of quartz-rich sandstone supported and cemented by dolomite (Fig. 1). This unit is unconformable on shale, marl and diamictite

(Chiquerio Fm, Early Palaeozoic) and an older Neoproterozoic basement dominated by gneiss. The Marcona Fm itself lays unconformably below a thick early Mesozoic unit that includes andesite with interbedded volcanoclastic rocks, sandstone and limestone (>500 m; Rio Grande Fm, Middle Jurassic), grey limestone and calcarenite (Jahuay Fm, Late Jurassic) and quartz arenite, siltstone and volcanoclastic andesite (Yauca Fm, Early Cretaceous). As a major difference with the Marcona-Mina Justa area, the Rio Grande Fm in the Pampa del Pongo area is dominated by massive andesite flows and sills with only few volcanoclastic intercalations. The metamorphic grade of the Phanerozoic rocks is very low and consequently these rocks are virtually undisturbed. All the Neoproterozoic-Mesozoic sequence is adjacent and intruded by the Coastal Batholith, in this area dominated by diorite and quartz diorite. It has been dated in 109 ± 4 Ma (Vidal et al. 1990).

The mineralization occurs as: (1) magnesian skarn; (2) silicate-poor ores dominated by magnetite and dolomite; both styles of mineralization occur as large stratabound replacive bodies within the Marcona Fm; (3) discordant breccia pipes and veins that crosscut the overlying lithologies, from the Rio Grande to the Yauca formations. The skarn is the dominant lithology within the mineralization; it includes an early prograde assemblage with forsterite (fo_{95-96}), calcite and phlogopite replaced by forsterite and magnetite. When the protolith was more silica-rich, i.e., in the sandstone lenses, the skarn is dominated by a pyroxenitic skarn composed of diopside (di_{88-95}) with phlogopite and adularia. Locally, the pyroxenitic skarn evolved to more iron-rich rocks, including high-Fe diopside (hd_{19-48}) intergrown with magnetite and even grandite (ad_{53-97}); these rocks are interpreted to be equivalent to the calcic

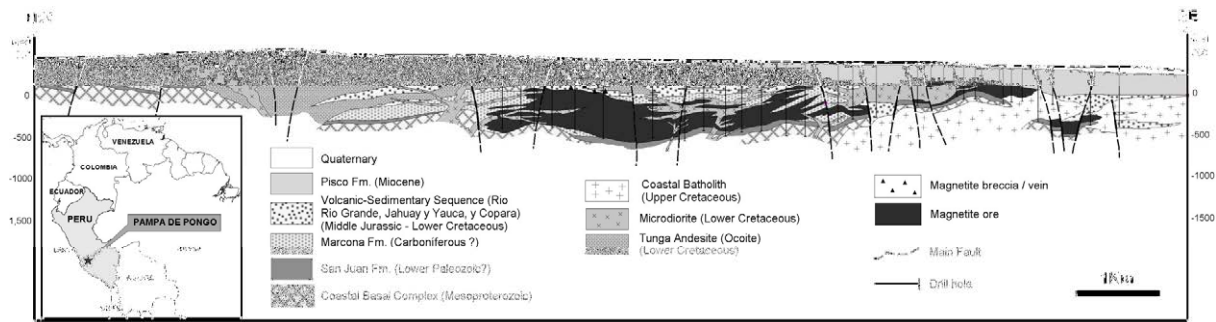


Figure 1. Longitudinal Section from Pampa de Pongo Fe-(Cu-Au) deposit

recurrences described by Einaudi et al. (1981). The superimposed retrograde skarn is accessory and includes tremolite (tr_{90-95}), magnetite, phlogopite (glimmerite), green biotite, vermiculite, calcite and clinocllore on the prograde magnesian skarn and epidote and actinolite on the calcic skarn. Furthermore, there is a late and widespread replacement of most of the forsterite by lizardite and chrysotile (Fig. 2); as a result, only accessory forsterite is found within the deposit.

The skarn is enclosed in a large aureole of silicate-poor hydrothermal replacement and made up of coarse-grained dolomite – later replaced by calcite – with variable proportions of magnetite and lesser amounts of ludwigite, hercynite and phlogopite. This magnetite-dolomite rock is interpreted as an external zone of hydrothermal alteration formed synchronously with the skarn, but due to the reaction of the early dolostone with the exhausted, silica-poor fluids.

The mineralization includes variable amounts of late stage sulphides, mostly as irregularly distributed veinlets or disseminations within the magnetite. The most common ones are pyrrhotite, pyrite and chalcopyrite; the assemblage includes trace amounts of sphalerite, galena, bornite, cubanite, arsenopyrite, löllingite, tennantite, gersdorffite, bismuthinite, native bismuth and marcasite. The pyrite includes minute grains of electrum (76% Au / 24% Ag) in fissures associated with hessite-tetradymite (Calvo et al. 2013). The magnetite of the prograde skarn and the magnetite-dolomite rocks shows exsolved lamellae of ilmenite, consistent with a high temperature of crystallization (>500°C).



Figure 2. Prograde magnesian skarn with magnetite and forsterite, the latter replaced by serpentine

Overlying the skarn and just above where the hydrothermal alteration is most intense, the early Mesozoic units are crosscut by a network of veins and breccia bodies. This type of mineralization includes ca. 10% of the total ore. The assemblage is similar to that found in the stratabound mineralization. The breccias include cm to m-sized fragments of the host rock, which are angular and with jigsaw textures near the edge of the pipes. The core of the breccias and veins is dominated by coarse grained dolomite and magnetite (Fig. 3). Here the fragments are rounded and polymictic, derived from the underlying lithologies – mostly from the Marcona Fm and the skarn. The fragments systematically show a cm-sized selvage of blue to yellow serpentine that replaces former forsterite.



Figure 3. Vein of dolomite-magnetite with a selvage of serpentine crosscutting andesite with alkali-calcic alteration

The volcanic and siliciclastic rocks above and below the deposit show a widespread hydrothermal alteration, better developed near lithologic contacts, fractures and within the most reactive/porous lithologies, like calc-silicate hornfels, limestone and volcanoclastic units. The andesite is replaced by a regional halo, some km wide, of potassic-calcic alteration with widespread fine grained biotite, K-feldspar, magnetite and actinolite. Locally there are zones of earlier albite-actinolite alteration. Superimposed on this early hydrothermal alteration or directly replacing the interbedded lenses of limestone and calc-silicate hornfels, there is a calcic skarn with intermediate clinopyroxene to hedenbergite and later grandite. No significant magnetite or IOCG mineralization has been found within these rocks.

The area has abundant dykes and sills of porphyritic andesite (ocoite) and microdiorite showing a pervasive hydrothermal alteration, similar to that of the volcanic rocks; however, equivalent dykes predate the hydrothermal alteration at Marcona (Chen et al. 2010). There are also some porphyry dykes of intermediate

composition with evidences of magma mingling and fluid exsolution, such as vesicles and tubes. These dykes show a high-temperature pervasive potassic-calcic alteration and are crosscut by veins with quartz, anhydrite and chalcopyrite.

The Coastal Batholith has enclaves of the skarn and the mineralization suggesting that the intrusion, at least of the dominant facies, postdated the formation of the skarn.

3 Geochemistry

The stable oxygen and strontium isotopes of the skarn ($\delta^{18}\text{O}_{\text{fluid}}$, 20.5-22.6‰; $^{87}\text{Sr}/^{86}\text{Sr}$, 0.7076-0.7086) and the magnetite + dolomite rock ($\delta^{18}\text{O}_{\text{fluid}} \approx 20.4$ -21.1‰; $^{87}\text{Sr}/^{86}\text{Sr}$, 0.7071-0.7076) are broadly consistent with these rocks being product of the interaction of a magmatic-hydrothermal fluid ($\delta^{18}\text{O}_{\text{fluid}} \approx 6$ -10‰; $^{87}\text{Sr}/^{86}\text{Sr}$, 0.7041-0.7066) equilibrated with the Coastal Batholith and the dolostone of the Marcona Fm ($\delta^{18}\text{O}_{\text{rock}} \approx 20.4$ -23.1‰; $^{87}\text{Sr}/^{86}\text{Sr}$, 0.7071-0.7076) at sub-magmatic temperatures (500-800°C). The unusually high $\delta^{18}\text{O}_{\text{magnetite}}$ values of the skarn (9.5-15.5‰) are consistent with the mineralization taking place at high temperatures and at low fluid/rock ratios. These isotope data also confirm that the magnetite-dolomite replacement was generated by the same fluids and at the same temperature that the prograde skarn.

However, there are evidences of equilibration with later fluids. The low $\delta^{18}\text{O}$ values of the dolomite within the mineralization (10.5-11.9‰) are in obvious isotopic disequilibrium with the associated magnetite and suggest re-equilibration of the carbonates with ^{18}O -depleted fluids at low temperatures. Furthermore, the fluids involved in the serpentinization are of unknown origin and age. The $\delta^{18}\text{O}_{\text{serpentine}}$ (14.9-16.2‰) values are likely inherited from the prograde skarn while the δD values (-92 to -75‰) suggest that the hydrogen was not of magmatic origin but equilibrated with low D waters of unknown origin, perhaps surficial waters related to the pervasive serpentinization.

Fluid inclusions are scarce but local euhedral crystals of diopside in the pyroxenitic skarn include FIA's with two types of inclusions, hypersaline aqueous brines having one to five daughter crystals, including magnetite, and low density inclusions with an aqueous vapour. They are here interpreted as derived from the heterogeneous trapping of coexisting immiscible fluids produced by the separation at low pressure of a magmatic intermediate density brine, as have been described in other magmatic-hydrothermal systems (e.g. Landtwing et al. 2005).

4 Discussion and genetic model

The crosscutting relationships indicate that the age of the Pampa de Pongo deposit is broadly similar to that of the nearby Marcona and Mina Justa deposits and the Coastal Batholith, i.e., early Cretaceous. Currently, there is no geochronological information of the deposit, but

the prograde alteration at Pampa de Pongo postdated the sedimentation of the Yauca Fm (<125 Ma) and the intrusion of the dykes of ocoite been dated at 137-118 Ma in Marcona (Chen et al. 2010). As quoted above, the mineralization is crosscut by the early facies of the Coastal Batholith (Hawkes et al. 2002), dated in 109±4 Ma (Vidal et al., 1990). Thus, the inferred age of the Pampa de Pongo deposit might be between ca. 125 and 109 Ma. If this proved to be true, the deposit should be younger than Marcona (ca. 162-154 Ma, Injoque et al. 1988; Chen et al. 2010) but older than Mina Justa (104-95 Ma Chen et al. 2010).

The Pampa de Pongo mineralization is interpreted here as a part of a giant magmatic-hydrothermal system rooted on a hidden sub-volcanic intrusion of intermediate composition. This magmatic-hydrothermal system developed a large replacement zone on the carbonate rocks characterized by a central core of magnesian and (accessory) calcic skarns and an external aureole of magnetite-dolomite replacements. The accompanying mafic volcanic rocks show a pervasive but irregularly distributed K-(Na)-Ca-Fe metasomatism. This late alteration is texturally and mineralogically similar to the sodic/potassic (alkaline)-calcic alteration described elsewhere in IOCG systems (Williams et al. 2005) and in Mina Justa (Chen et al. 2011). However, at Pampa del Pongo the mineralization is hosted by the skarn and scarcely by the IOCG-like alteration zone. The best interpretation is that the Rio Grande Fm was not permeable enough for hosting large fluid flow and IOCG mineralization, but capped the Marcona Fm forcing the lateral fluid flow and the formation of the skarn.

The breccias and veins overlying the mineralization are here interpreted as the product of the hydrothermal brecciation of the impermeable rocks capping the mineralization. The formation of such a large hydrothermal system involved the circulation of vast amounts of hydrothermal fluids. Also, the decarbonatization of the carbonate rocks during the formation of the skarn produced large amounts of immiscible CO_2 . These fluids migrated laterally or eventually accumulated below the impermeable Rio Grande Fm. The fluid pressure locally surpassed the lithostatic one leading to the hydrothermal brecciation and the formation of the mineralized pipes and veins.

Thus, the Pampa del Pongo-Marcona district represents a supergiant long-lived (>50 Ma) IOCG-like mineralizing event in which different types of mineralization formed in different structural and lithological traps such as calcic skarns (Marcona), magnesian skarns (Pampa del Pongo), IOCG deposits (Mina Justa) or magnetite-apatite veins (Acarí). Most of these deposits occur in an area with few outcrops suggesting that there is large potential for the discovery of new giant deposits belonging to the IOCG clan.

Acknowledgements

This study has been funded by BISA. We would like to acknowledge Antonio Delgado (CSIC, Spain) and Carmen Galindo (UCM, Spain) for the analyses of stable

and radiogenic isotopes, respectively.

References

- Calvo G, Rodriguez O, Serrano M, Tornos F, Rodriguez R, Velasco F, Contreras M, Ochoa J, Urbina M, Sapacayo M (2013) El skarn magnésico de Pampa del Pongo: un megayacimiento de hierro en la Cordillera de la Costa del Sur del Perú. Abstracts Congreso Peruano de Geología. Sociedad Geologica del Peru, Lima.
- Chen HY, Clark AH, Kyser TK, Ullrich TD, Baxter R, Chen YM, Moody TC (2010) Evolution of the Giant Marcona-Mina Justa Iron Oxide-Copper-Gold District, South-Central Peru. *Economic Geology* 105:155-185.
- Chen H, Kyser TK, Clark AH (2011) Contrasting fluids and reservoirs in the contiguous Marcona and Mina Justa iron oxide-Cu (-Ag-Au) deposits, south-central Peru. *Mineralium Deposita* 46: 677-706.
- Einaudi MT, Meinert LD, Newberry RJ (1981) Skarn deposits, In: *Economic Geology 75th Anniversary Volume*, pp 317-339.
- Hawkes N, Clark A, H., Moody TC (2002) Marcona and Pampa de Pongo: Giant Mesozoic Fe-(Cu, Au) Deposits in the Peruvian Coastal Belt In: Porter TM (ed) *Hydrothermal Iron Oxide Copper-Gold & Related Deposits: A Global Perspective*. PGC Publishing, Adelaide, pp 115-130.
- Injoque J, Atkin B, Harvey P, Snelling N. (1988) Mineralogía, geoquímica y geocronología del skarn geotermal de hierro de Marcona. *Boletín Sociedad Geológica Perú* 78: 65-80.
- Landtwing MR, Pettke T, Halter WE, Heinrich CA, Redmond PB, Einaudi MT, Kunze K (2005) Copper deposition during quartz dissolution by cooling magmatic-hydrothermal fluids: The Bingham porphyry. *Earth Planetary Science Letters* 235: 229-243.
- Vidal CE, Injoque-Espinoza J, Sidder GB, Mukasa SB (1990) Amphibolitic Cu-Fe skarn deposits in Central Coast of Perú. *Economic Geology* 85:1447-1461.
- Williams P, Barton MD, Johnson DA, Fontboté L, Haller Ad, Mark G, Oliver NHS, Marschik R (2005) Iron Oxide Copper-Gold Deposits: Geology, Space-Time Distribution, and Possible Modes of Origin In: Hedenquist JW, Thompson JFH, Goldfarb RJ, Richards JP (eds) *Economic Geology - One hundredth anniversary Volume*, pp 371-406.

Age constraints on the Merlin molybdenum-rhenium deposit, Cloncurry District, Queensland, Australia: are we dealing with a unique addition to the IOCG family?

Rob Duncan*

Mineral Deposit Research Group – Department of Earth, Ocean, and Atmospheric Sciences, University of British Columbia, Vancouver, British Columbia, Canada

Holly Stein

AIRIE Program – Department of Geosciences, Colorado State University, Fort Collins, Colorado, United States of America and CEED Centre of Excellence, University of Oslo, Norway

Murray Hitzman, Eric Nelson

**Department of Geology & Geological Engineering, Colorado School of Mines, Golden, Colorado, United States of America*

Abstract. Re-Os molybdenite model ages for the Merlin molybdenum-rhenium deposit in the Mount Dore-Selwyn corridor of the Cloncurry iron oxide-copper-gold (IOCG) district yield new information on the timing of molybdenite deposition and its relationship with nearby IOCG-style mineralization. The age data constrain mineralization at Merlin to ~1503 Ma. This age coincides with the emplacement of late highly fractionated anorogenic granitoids adjacent to the deposit and occurs ~10 myrs after the main phase of IOCG mineralization in the region. Molybdenite, pyrite, and chalcopyrite from Merlin yield $\delta^{34}\text{S}$ values of between -1.4 and +2.5 ‰ CDT which suggest a homogenized igneous sulfur source in contrast with previous data from the adjacent Mount Dore IOCG deposit. These relationships suggest a direct genetic association between the plutons and molybdenite mineralization. We propose that Merlin maybe more closely related to Climax-style porphyry mineralization than IOCG mineralization. More work is required to determine if Merlin represents a link between these systems.

Keywords. Cloncurry, iron oxide-copper-gold, porphyry transition, molybdenum, Merlin

1 Introduction

The Proterozoic Eastern Fold Belt (EFB) of the Mount Isa Inlier, northwest Queensland has experienced multiple deformation, metamorphic, and hydrothermal events between ~1870 and 1500 Ma (e.g., Oliver et al. 2008; Rubenach et al. 2008). This geodynamic evolution has resulted in the complex juxtaposition of fault blocks of varying age and lithology (e.g., Betts et al. 2006), and was ultimately responsible for large-scale metal fluxes within the crust over extended time periods (e.g., Oliver et al. 2004; 2008). Metals became concentrated in suitable structural and chemical traps throughout the EFB to form the spectrum of IOCG deposits recognized in the district (Williams 1998).

The Merlin Mo-Re deposit, immediately adjacent to the Mount Dore IOCG deposit, in the Southern Cloncurry district, appears to represent a fundamentally new style of Mo mineralization. Drilling at Merlin has defined a resource of 6.7 Mt at 1.4% Mo and 23.4 g/t Re (Ivanhoe Australia 2012). The small tonnage and high grade of Merlin is highly unusual in comparison with porphyry-related Cu-Mo, Mo-W, and Mo-only deposits.

Other Merlin-style mineralization has since been recognized in the EFB (e.g., Wilgar, Kalman, and Lanham's shaft occurrences), indicating that Merlin is not unique.

This study obtained Re-Os molybdenite model ages on paragenetically well-constrained samples from Merlin to investigate timing relationships with regional deformation, IOCG-related alteration and mineralization, and igneous activity. In addition sulfur isotopes on Merlin sulfides were measured to determine the likely source of sulfur in the system.

2 Geologic framework

A number of geochronologic studies throughout the Cloncurry district have identified two major periods of IOCG mineralization. One is associated with deformation during the (early) Isan orogeny and extends from ~1600 to peak metamorphism ~1570 Ma (e.g., Rubenach et al. 2008; Duncan et al. 2011) and the other is associated with the intrusion of the A-type Williams Batholith from ~1540 to 1500 Ma (e.g., Duncan et al. 2011; Rubenach et al. 2008; Perkins and Wyborn 1998). The Southern Cloncurry district contains several major IOCG systems, including SWAN-Mount Elliott, Mount Dore, and Starra, which are located within a two kilometre-wide zone adjacent to a major shear. The shear represents the contact between interbedded calcareous quartzites and metasilstones (Staveley Formation) and carbonaceous slates, schist, phyllite, and siltstone (Soldiers Cap Group), which were deposited in a series of intracontinental north-south elongate basins between ~1770 and 1710 and 1690 to 1650 Ma, respectively (Page and Sun 1998; Giles and Nutman 2003). The Staveley Formation was intruded by the Gin Creek Granite at ~1740 Ma (Page and Sun 1998). The sequence was multiply deformed during the Isan orogeny and intruded by the Squirrel Hills and Mount Dore granites from ~1515 to 1500 Ma (Pollard and McNaughton 1997; Page and Sun 1998).

2.1 Host rocks and structure

The Merlin resource as currently known occurs in a fault-bounded, north-striking and dominantly moderately

east-dipping, stratigraphic portion of the Toole Creek Volcanics (Soliders Cap Group) which consists of interbedded carbonaceous slate, metasiltstone, schist, and phyllite. The footwall of the mineralized package consists of a strongly silicified mylonitic zone which is typical of the regional expression of the Selwyn Shear. The host stratigraphy is cut off to the east by the Mount Dore Fault which structurally emplaces the Mount Dore Granite westwards over the metasedimentary rocks hosting the deposit.

2.2 Mineralization

The Merlin orebodies are located in the footwall of the Mount Dore 0.25% Cu equivalent ore shell. Mineralized zones at Merlin and Mount Dore are spatially distinct and have different geochemical signatures. Mineralization at Merlin is hosted in a series of moderately dipping stacked ore lenses that are distributed along thrust fault zones sub-parallel to the Selwyn Shear and Mount Dore Fault. Ultra-high grade molybdenite mineralization at Merlin, locally comprising up to 80% of the rock, occurs as a matrix replacement in poorly-sorted clast- to matrix-supported monolithic breccias that are dominated by poorly sorted, sub-rounded to sub-angular clasts. Some molybdenite crystals in these samples exhibit *durchbewegung*, kinked textures, and slickenside development which indicating post-mineralization deformation. Lower grade molybdenite mineralization occurs as fracture-fill, stylolitic infill, and disseminations. An excellent correlation between Mo and Re content in the ore shells at Merlin demonstrates that molybdenite is the predominant Re host mineral (Lazo and Pal 2009).

2.3 Hydrothermal alteration

Early alteration minerals at Mount Dore, which include hematite-stained albite, calcite, actinolite, and epidote, along with accessory biotite, magnetite, scapolite, garnet, titanite, epidote, and apatite, are restricted to calcareous metasiltstone units (Lazo and Pal, 2009). This sodic-calcic alteration assemblage formed prior to and during brecciation associated with the IOCG mineralizing event. A quartz-tourmaline assemblage overprints earlier alteration and is focussed near the granite-metasedimentary rock contact. A later potassic alteration assemblage (K-feldspar, quartz, and chlorite) appears as matrix infill to a crackle breccia and is cut by calcite veinlets. Although the majority of copper mineralization has been assigned to the potassic phase (Lazo and Pal 2009), significant amounts of copper were introduced during sodic-calcic alteration (Beardsmore 1992).

Molybdenite mineralization at Merlin overprints chalcopyrite. Alteration associated with molybdenite mineralization at Merlin appears to be associated spatially with chalcopyrite mineralization and intense K-feldspar-(chlorite-calcite) alteration (Lazo and Pal, 2009). Microscopically K-feldspar, chlorite, and calcite are intergrown with molybdenite in the matrix of mineralized breccias.

2.3 Existing age constraints

Molybdenites from Mount Dore yielded a weighted mean Re-Os model ages of 1503.3 ± 6.9 (MSWD = 2.8) inclusive of the error on the ^{187}Re decay constant (Duncan et al. 2011). These molybdenite aliquots are three to four times higher in Re than those analysed from IOCG deposits in the same study. The Mount Dore molybdenite samples included material from a pyrite-molybdenite-calcite vein in strongly K-feldspar-altered carbonaceous slate and a calcite-actinolite-diopside vein with disseminated molybdenite (Duncan et al. 2011). This model age constrains the age of early sodic-calcic and later potassic alteration assemblages. Although the accuracy of the ages cannot distinguish separate events because the ages are within 2σ error we suggest that both alteration events were essentially synchronous. This is not the case at the Mount Elliott-SWAN IOCG deposit where U-Pb titanite ages define the onset of sodic-calcic alteration spatially associated with mineralization to an earlier stage which began ~ 1530 Ma (Duncan et al. 2011).

The emplacement age for the south-east monzogranite portion of the Mount Dore granite of 1516 ± 10 Ma (Pollard and McNaughton 1997) is slightly older, but statistically indistinguishable from the molybdenite ages for Mount Dore. The close temporal relationship between mineralization at Mount Dore and granite emplacement have been used to suggest that late, evolved magmatic brines were involved in the mineralizing process. This interpretation is supported by previous stable isotopic data (Beardsmore 1992).

Younger ages associated with potassic alteration have been recorded at the small Lady Ella copper deposit (1487 ± 5 Ma; Re-Os molybdenite model age on a quartz-K-feldspar-biotite-chlorite breccia; Duncan et al. 2011), and the Jessie, Malakoff, Yellow Waterhole, and Wimberu Granites (strongly altered and brecciated samples; 1493 ± 8 Ma U-Pb zircon ages and 1465 ± 16 Ma $^{40}\text{Ar}/^{39}\text{Ar}$ on sericite; Page and Sun 1998, Perkins and Wyborn 1998).

3 Samples and analytical techniques

Two molybdenite samples were separated from a high grade intersection at Merlin (MDQ-119 413.3 m, part of a 20 m interval containing 6.25% Mo, 81.3 g/t Re, and 0.14% Cu from 408 m; Ivanhoe Australia 2009a). This interval is typical of breccia-hosted mineralization and is characterized by sub-rounded to sub-angular K-feldspar-quartz-calcite-altered metasiltstone and slate clasts of between 0.5 and 10 mm in diameter. Molybdenite predominantly occurs as replacements around clast rims, but also as disseminations throughout the breccia matrix (MDT-1264) where it is intergrown with K-feldspar, calcite, and chlorite. Molybdenite overprints pyrite in this sample. Molybdenite also occurs as vug infill in sample MDT-1266. The finer-grained matrix molybdenite exhibits *durchbewegung* textures around K-feldspar-altered breccia clasts.

Another sample was collected from a lower grade, relatively copper rich zone (MDQ-0218 440.7 m, part of a 6 m interval containing 0.71% Mo, 10.66 g/t Re, and

Table 1. Re-Os molybdenite data for Merlin and Mount Dore (from Duncan et al. 2011) and model age calculations

AIRIE Run #	Deposit	Drill Hole/Depth (m)	Re (ppm)	¹⁸⁷ Os (ppb)	Age (Ma)
MDT-877 ^a	Mount Dore	MDHQ-07-82/269.07	561.6 (9)	8915 (7)	1497 ± 6
MDT-884 ^a	Mount Dore	MDHQ-07-82/269.07 ^b	493.2 (2)	7849 (6)	1501 ± 5
MDT-908 ^a	Mount Dore	MDHQ-07-086/305.5	640.0 (6)	10232 (8)	1508 ± 5
MDT-909 ^a	Mount Dore	MDHQ-07-086/305.5 ^b	1001.1 (8)	15955 (12)	1503 ± 5
MDT-1033	Merlin	MDQ0218/440.7	643.4 (8)	10257 (8)	1503 ± 5
MDT-1264 ^c	Merlin	MDQ-0119/413.3	107.3 (3)	1710 (2)	1502 ± 7
MDT-1266	Merlin	MDQ-0119/413.3	375.4 (6)	6180 (5)	1552 ± 6

Notes. Unless otherwise noted, molybdenite mineral separates were created at AIRIE from drill core ^afrom Duncan et al. (2011), ^breplicate analysis of new mineral separate to optimize spiking and affirm accuracy ^cmolybdenite of similar occurrence was compiled from two grains to acquire sufficient material for analysis: Sample weights of 3-76 mg dissolved in Carius tube method with mixed-double Os spike Errors are 2σ and absolute for last decimal place indicated; assumed initial ¹⁸⁷Os/¹⁸⁸Os = 0.2 ± 0.1 Common Os was insignificant for all runs

0.21% Cu from 440 m; Ivanhoe, 2009b). In this sample molybdenite overprints chalcopyrite in a breccia in which clasts have been completely replaced by K-feldspar and quartz. Clasts are angular to sub-angular and very between 0.25 and 5 cm diameter. Molybdenite occurs as matrix replacement and clearly cross-cuts chalcopyrite (MDT-1033). Calcite is present as both late veinlets and vug infill.

Rhenium-Os molybdenite ages were derived using the analytical routines developed by the AIRIE Program at Colorado State University. Isotopic measurements were acquired by thermal ionization mass spectrometry using a Triton machine at AIRIE after Carius tube dissolution with a mixed-double Os spike. Sulfur isotope ratios in sulfide separates were measured on a GV instruments IsoPrime gas-sourced mass spectrometer at the Colorado School of Mines.

4 Results

Merlin molybdenites have a similar range of Re and ¹⁸⁷Os contents as those published previously (Table 1); sample MDT-1264 contained the lowest Re and ¹⁸⁷Os contents for mid-Proterozoic molybdenites from the EFB. Matrix and vug molybdenite from sample runs MDT-1254 and -1266 yielded 1552 ± 6 and 1502 ± 7 Ma ages, respectively. Molybdenite from sample run MDT-1033 gave an age of 1503 ± 5 Ma. The two younger ages are consistent with the previously published age for Mount Dore (Table 1; Duncan et al. 2011). Omitting run MDT-1266, a new weighted mean average of 1502.7 ± 3.7 Ma (MSWD = 1.7), inclusive of the ¹⁸⁷Re decay constant, has been calculated for the Mount Dore and Merlin data (*n*=6).

Bulk δ³⁴S isotope values for different molybdenite occurrences and associated chalcopyrite and pyrite (*n*=12) reveal a range between -1.4 and +2.5 ‰ CDT with a mean of 0.3 ‰ CDT. Data obtained on Mount Dore sulfides by laser ablation revealed two distinct populations (Duncan and Hitzman 2012); -10.0 to -2.5 ‰ CDT (sulfides associated with sodic-calcic alteration) and +4.0 to +6.5 ‰ CDT (vein-hosted sulfides in slate and schist).

5 Interpretation

Taking into account structural, overprinting, and mineral paragenetic relationships we interpret the majority of

mineralization at Merlin to have occurred at ~1503 Ma. This suggests that the previous molybdenite ages for Mount Dore may represent the formation of molybdenite-calcite veins peripheral to Merlin. This is supported by the high Re contents analyzed by Duncan et al. (2011). Further work is currently underway to determine the age of the calc-silicate hydrothermal alteration assemblages associated with the Mount Dore deposit to define if there was a significant period of time between formation of the base metal mineralization at Mount Dore and the formation of the Merlin system.

The older matrix age for Merlin is intriguing; it may reflect a pre-existing stage of mineralization at Merlin, potentially associated with calc-silicate alteration, or it could represent an erroneous old age determination caused by post-depositional fluid assisted deformation and recrystallization which may have preferentially leached Re and generated excess ¹⁸⁷Os (e.g., McCandless et al. 1993). Evidence in support of the latter explanation includes the recrystallization textures that are common in the finer-grained matrix-hosted molybdenite compared with the vuggy molybdenite infill. Although the ~1552 Ma age would represent a previously unrecognized mineralization event in the area, the age does correspond with the onset of A-type magmatism and sodic hydrothermal alteration (Oliver et al. 2004). If Merlin were of this age it would have been deformed by post-peak metamorphic deformation events (D₃ and younger). Although some molybdenite in the deposit does locally display ductile deformation features these are attributed late deformation in a shear zone (e.g., Cox 1987).

6 Genetic significance

The molybdenite ages from Merlin overlap with the crystallization age for the Mount Dore Granite. This close spatial and temporal relationship suggests that the late (~1500 Ma) phases of the Williams batholith may be responsible for the formation of the Merlin deposit. The distinct narrow range of Merlin sulfides represents a homogenised igneous sulfur source which is not reflected in the Mount Dore sulfur isotopic data. We propose that the Mount Dore Granite (and equivalents) represents the most likely source for metals and fluid at Merlin. The molybdenite sulfur isotopic data also preclude the possibility that molybdenum was derived from organic-rich slates within the host package to mineralization.

Wyborn (1998) presents field relationships and geochemical data that demonstrate the 1500 Ma portions of the Williams batholith are high SiO₂ leucogranites enriched in U, Th, F, and Rb. The characteristics are typical of Mo-bearing porphyry systems with highly fractionated magmas (e.g., White et al. 1989). It is likely that the Merlin deposit is genetically related to moderately saline, F-rich fluids that were exsolved from late stage portions of the crystallizing Mount Dore granite. It appears that Merlin-like systems have more in common genetically with Climax-type molybdenum deposits than with IOCG deposits.

Recent work on the Pb isotopic fluid composition responsible for mineralization at the Bingham Cu-Au-Mo deposit (and other Mo-rich porphyries of the

Colorado Plateau) demonstrated that the parental magma was derived by non-subduction related Cenozoic partial melting of the pre-existing metasomatized subcontinental lithospheric mantle that formed during a 1.8 Ga subduction event (Pettke et al. 2010). A similar scenario can be suggested for Mount Isa in which proposed northwards subduction of crust underneath the proto-Australian continent generated significant volatile and incompatible enrichment in the subcontinental lithospheric mantle (Giles et al. 2002; Oliver et al. 2008). This reservoir was then tapped by decompressive melting during intermittent extension events that are expressed as mafic extrusives within the sedimentary rock packages which are often cited as the likely source of metals within the Cloncurry IOCG systems (Oliver et al. 2004).

Zircon ϵ_{HF} values of 0 to +8 demonstrate that juvenile magmatic input was strong during the deposition of the Soliders Cap Group and the T_{DM} (minimum) model age for the source rocks was approximately 2.0 to 2.2 Ga (Griffin et al. 2006). Similar T_{DM} ages with zircon ϵ_{HF} values of ≈ 0 for the Williams batholiths imply that these magmas were probably generated by the melting of old crust that has been intruded by mantle-derived mafic magmas (Griffin et al. 2006) and was associated with the arrival of a north-trending hotspot (Giles et al. 2002). It was the protracted nature of the Williams igneous event along with the previous geodynamic history of the Mount Isa inlier which allowed non-subduction related, highly fractionated, magmas to evolve and eventually exsolve hydrothermal fluids which generated mineralization at Merlin.

The recognition that there are several Mo-rich mineral occurrences across the Cloncurry district indicates that Merlin is not a unique system. This work, along with that of Duncan et al. (2011), shows that molybdenite ages in the EFB range from ~ 1570 to 1490 Ma, indicating that molybdenite precipitation occurred over a protracted period which included metamorphic- and intrusion-related IOCG mineralization events, as well as Merlin-type mineralization and post-Williams Batholith hydrothermal events. More work is clearly required to understand how Merlin could potentially provide clues to link porphyry Mo and IOCG deposits.

Acknowledgements

Support for this study was sourced from Ivanhoe Australia and a MITACS Elevate Fellowship to RD. Two Re-Os analyses were funded by the AIRIE Program.

References

- Beardsmore TJ (1992) Petrogenesis of Mount Dore-style breccia-hosted copper-gold mineralization in the Kuridala-Selwyn region of northwestern Queensland. PhD thesis, James Cook University
- Betts PG, Giles D, Mark G, Lister GS, Goleby BR, Aillères, L (2006) Synthesis of the Proterozoic evolution of the Mt Isa Inlier. *Aust J Earth Sci* 53:187-211
- Cox SF (1987) Flow mechanisms in sulphide minerals. *Ore Geol Rev* 2:133-171
- Duncan RJ, Hitzman MW (2012) Tracking the source of metals in the Proterozoic Cloncurry Iron Oxide-Copper-Gold Belt, Mount Isa Inlier, Australia. Society of Economic Geologists 2012 Conference, Lima, Peru, 30
- Duncan RJ, Stein HJ, Evans KA, Hitzman MW, Nelson EP, Kirwin DJ (2011) A new geochronological framework for mineralization and alteration in the Selwyn-Mount Dore Corridor, Eastern Fold Belt, Mount Isa inlier, Australia: genetic implications for iron oxide-copper-gold deposits. *Econ Geol* 106: 169-192
- Giles D, Betts PG, Lister GS (2002) Far-field continental backarc setting of the 1.80-1.67 Ga basins of northeastern Australia. *Geol* 30: 823-826
- Giles D, Nutman AP (2003) SHRIMP U-Pb zircon dating of the host rocks of the Cannington Ag-Pb-Zn deposit, southeastern Mt. Isa Block, Australia. *Aust J Earth Sci* 50: 295-309
- Griffin WL, Belousova EA, Walters SG, O'Reilly SY (2006) Archaean and Proterozoic crustal evolution in the Eastern Succession of the Mt Isa district, Australia: U-Pb and Hf-isotope studies of detrital zircons. *Aust J Earth Sci* 53:125-149
- Ivanhoe Australia (2012) Merlin feasibility study completed. http://www.ivanhoeaustralia.com/i/pdf/IVA0065MR-Merlin_Feasibility_Study.pdf. Accessed 20 June 2012
- Lawley CJM, Selby D (2012) Re-Os geochronology of quartz-enclose ultrafine molybdenite: implications for ore geochronology. *Econ Geol* 107: 1499-1505
- Lazo F, Pal T (2009) The Merlin Mo-Re Zone, a New Discovery in the Cloncurry District, Australia. In: Williams PJ et al. (eds) Biennial SGA Meeting, 10th, Townsville, Australia, 17-20 August 2009, Proceedings, pp 56-58
- McCandless TE, Ruiz J, Campbell AR (1993) Rhenium behaviour in molybdenite in hypogene and near-surface environments: implications for Re-Os geochronometry. *Geochem Cosmochim Acta* 57: 889-905
- Oliver NHS, Cleverley JS, Mark G, Pollard PJ, Fu B, Marshall LJ, Rubenach MJ, Williams PJ, Baker T (2004) Modeling the role of sodic alteration in the genesis of the iron oxide-copper-gold deposits, Eastern Mount Isa Block, Australia. *Econ Geol* 99: 1145-1176
- Oliver NHS, Butera KM, Rubenach MJ, Marshall LJ, Cleverley JS, Mark G, Tullemans F, Esser D (2008) The protracted hydrothermal evolution of the Mount Isa Eastern Succession: A review and tectonic implications. *Precambrian Res* 163: 108-130
- Page RW, Sun S-S (1998) Aspects of geochronology and crustal evolution in the Eastern Fold Belt, Mt Isa Inlier. *Aust J Earth Sci* 45: 343-361
- Perkins C, Wyborn LAI (1998) Age and Cu-Au mineralization, Cloncurry district, eastern Mt. Isa inlier, Queensland, as determined by $^{40}\text{Ar}/^{39}\text{Ar}$ dating. *Aust J Earth Science* 45: 233-246
- Pettke T, Oberli F, Heinrich CA (2010) The magma and metal source of giant porphyry-type ore deposits, based in lead isotope microanalysis of individual fluid inclusions. *Earth Plant Sci Let* 296: 267-277
- Pollard P, McNaughton NJ (1997) U/Pb geochronology and Sm/Nd isotope characterization of Proterozoic intrusive rocks in the Cloncurry district, Mount Isa inlier, Australia. AMIRA P438 Cloncurry Base Metals and Gold Final Report, Section 4, 19 p
- Rubenach MJ, Foster DRW, Evins PM, Blake KL, Fanning CM (2008) Age constraints on the tectonothermal evolution of the Selwyn Zone, Eastern Fold Belt, Mount Isa Inlier. *Precambrian Res* 163: 81-107
- White WH, Bookstrom AA, Kamilli RJ, Ganster MW, Smith RP, Ranta DF, Steining RC (1981) Character and origin of Climax-type molybdenum deposits. *Economic Geology* 75th Anniversary Volume: 270-316
- Williams PJ (1998) Metalliferous economic geology of the Mt Isa Eastern Succession, Queensland. *Aust J Earth Sci* 45: 329-341
- Wyborn L (1998) Younger ca 1500 Ma granites of the Williams and Narku batholiths, Cloncurry district, eastern Mt Isa Inlier: geochemistry, origin, metallogenic significance and exploration indicators. *Aust J Earth Sci* 45: 397-411

Skarn alteration in iron oxide-copper-gold systems, the Pocheon magnetite deposit, Korea

Ji Su Go, Seon-Gyu Choi, Jieun Seo

Department of Earth and Environmental Sciences, Korea University, Korea

Jung-Woo Park

Research School of Earth Sciences, Australian National University, Australia

Sang-Tae Kim

School of Geography and Earth Sciences, McMaster University, Canada

Abstract. The Pocheon iron deposit district is located at the northwestern part of the Precambrian Gyeonggi massif in South Korea which is characterized by a distinct mineral assemblage of magnetite, anhydrite, acmite, diopside, garnet, epidote, amphibole and calcite. Sodic-calcic alteration is widely developed in the deposit, forming acmite and albite. In addition, the Pocheon deposit shows host rocks such as dolostone and limestone that are closely related to sodic-calcic, calcic, and magnesian skarn. In particular, the high grade iron mineralization occurs in the sodic-calcic skarn zone subdivided into prograde skarn and retrograde skarn based on the mineral assemblage. Prograde skarn is closely associated with magnetite, acmite, diopside, albite, garnet, and anhydrite while amphibole, epidote, magnetite, and chalcopyrite are shown in retrograde skarn. Mineral assemblage and composition of the magnetite ore indicate that mineralization in the Pocheon deposit occurred in a relatively oxidized environment.

Keywords. magnetite, sodic-calcic skarn, acmite, anhydrite, Pocheon

1 Introduction

The Pocheon deposit (PD), which is situated in the northern part of the Gyeonggi province, was one of the most important iron producers in South Korea (Figure 1). The past iron production amount was up to 650,000 tons with an average iron content of 56 wt.% Fe. No potential and economic Cu and Au mineralization has been identified.

The ore genesis of the PD remains enigmatic and controversial. The amphibolite with iron ores in the PD has been considered as products of contact metamorphosed contact products and alkali metasomatized meta-sediments or regionally metamorphosed iron-rich calcareous sedimentary rocks (Kim, 1977). One of the important lines of evidence that supports a sedimentary origin of the Pocheon ore is as banded magnetite-amphibole ores, which accompanies varying extent ore bodies and conformable layers, well foliated with the surrounding meta-sedimentary lime-silicate rocks and schists. (So, 1977). In contrast, Kanda (1969) suggested that it is a contact replacement skarn deposit.

However, a recent prospecting investigation showed that the PD has iron oxide-copper-gold (IOCG) type mineral assemblage composed of magnetite, acmite, albite, diopside, garnet, epidote, amphibole, anhydrite, and gypsum. Skarn zones in IOCG systems are

characterized by mineral assemblages of diopside, actinolite, calcic garnet, epidote, and scapolite (Williams, 2009). Some amphiboles and pyroxenes may have unusually high Na-content (Wang and Williams, 2001). The Ningwu deposits, located in the Yangtze River valley, China and has a quite similar mineral assemblage to the PD was reinterpreted as iron oxide apatite (IOA) type deposit (Yu, 2011). In this study, we present additional lines of mineralogical and geochemical evidence for IOCG-type mineralization in the PD.

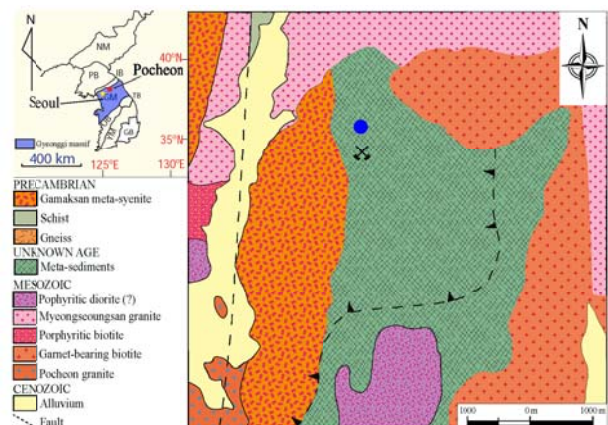


Figure 1. Geological map of the Pocheon iron deposit in Republic of Korea (the blue circle shows the drilling point).

2 Geological setting

The Korean Peninsula in the southeastern margin of the Sino-Korean platform is tectonically composed of two Precambrian massifs (the Gyeonggi and the Yeongnam massifs), two Phanerozoic mobile belts (the Permo-Carboniferous Imjingang and Paleozoic Okcheon Belt), and Cretaceous volcano-sedimentary basins. The Permo-Carboniferous Imjingang Belt is situated at the northern fringe of the Gyeonggi Massif and the Neoproterozoic to Paleozoic Okcheon Belt is flanked by the Archean to Mesoproterozoic Gyeonggi and Yeongnam massifs.

Recent tectonic models suggest that the Hongseong and Odaesan area located in the middle of Korean Peninsula is the eastern extension of the Late Paleozoic Dabie-Sulu collisional belt between the South and North China blocks. The collision between the North

and South China blocks began in the Korean Peninsula during the Permian (ca. 290 ~ 260 Ma) and propagated westwards until the Triassic (Songrim orogeny). Post-collisional Songrim igneous activity event occurred between ca. 250-230 Ma in the Gyeonggi massif during the extensional tectonic regime (Oh, 2006).

The Pocheon district consists of a stratum of metamorphosed subvolcanic rocks enclosed within a Precambrian gneiss complex intruded by Paleoproterozoic batholiths, Triassic (?) porphyritic diorite and Jurassic Pocheon granite (184.0 Ma), garnet-bearing biotite granite (164.5 Ma), porphyritic biotite granite (164.2 Ma), Cretaceous Myeongseoungsan granite (112 Ma), and Meta-sediments (unknown age) (Hwang et al, 2007). The structure of these rocks is conformable each other, representing a trend of foliation that strikes N-S with general dipping of 45° to 70°W, and the Pocheon iron ores are enclosed in meta-sediments of carbonate rocks, anhydrite, and gypsum (Figure 1).

3 Results

Skarns in the PD are subdivided into three groups based on mineral assemblages. The groups are described as sodic-calcic skarn, calcic skarn, and magnesian skarn as shown in Table 1.

Table 1. Mineral assemblages of the calcic, magnesian and sodic-calcic skarn from the Pocheon deposit.

Skarn type	Mineral Assemblage
Calcic	garnet, clinopyroxene, epidote, amphibole, calcite, phlogopite, sphene, magnetite, sericite
Magnesian	olivine, diopside, dolomite, amphibole, serpentine, apatite, quartz, magnetite, anhydrite
Sodic-calcic	I albite, acmite, diopside, magnetite, garnet, anhydrite, gypsum, calcite, sphene
	II albite, diopside, garnet, magnetite, amphibole, epidote, anhydrite, chalcocopyrite, gypsum

I = prograde skarn, II = retrograde skarn

Skarn development and ore mineralization in the PD are the results of prograde and retrograde stages of geochemical phenomena. Iron mineralization occurs as concordant to discordant layered, lenticular or massive magnetite-albite-acmite-anhydrite-gypsum, magnetite-garnet-diopside-albite, and magnetite-albite-epidote-garnet-amphibole ores. Chalcocopyrite is disseminated on the top of magnetite ore bodies.

Clinopyroxenes in the sodic-calcic skarn zone show a wide range of compositional variations from Mg-rich diopside core to Na-rich acmite rim. Clinopyroxenes in magnesian skarn zone show diopside (end-member) composition, whereas the calcic skarn zone shows intermediate compositions between diopside and hedenbergite.

Clinopyroxenes and garnets in the sodic-calcic skarn zone are Hd(CaFeSi₂O₆)₅₋₃₅ and Adr(Ca₃Fe₂Si₃O₁₂)₅₇₋₇₂ compositions, whereas clinopyroxenes and garnets from the Ca skarn zone are Hd₃₀₋₄₁ and Adr₃₀₋₄₅ composition. This indicates that the sodic-calcic skarn was formed under highly oxidized environments (Figure 2).

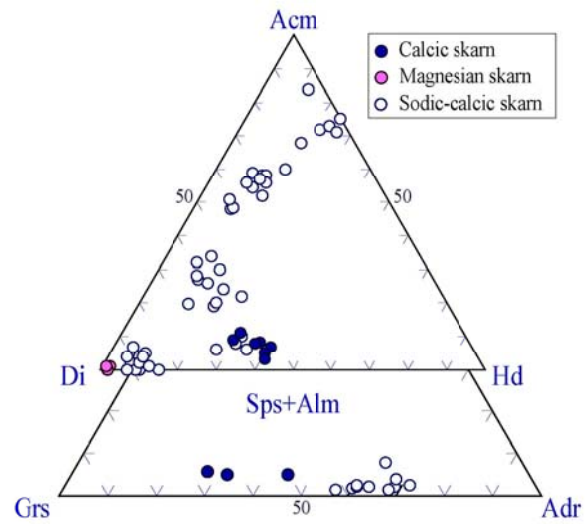


Figure 2. Chemical compositions of pyroxenes and garnets from the PD. Compositions of pyroxene are plotted on the acmite(Acm)-diopside(Di)-hedenbergite(Hd) diagram. Compositions of garnets are plotted on the spessartine(Sps)-almandine(Alm)-grossular(Grs)-andradite(Adr) diagram.

Carbon and oxygen isotope analyses were carried out on carbonate minerals from magnesian skarn, sodic-calcic skarn, bleached carbonate rocks, and dolostone. The dolostone has higher $\delta^{13}\text{C}$ and $\delta^{18}\text{O}$ values ($\delta^{13}\text{C}=1.0\text{‰}$, $\delta^{18}\text{O}=12.2\text{‰}$) high than the bleached carbonate ($\delta^{13}\text{C}=0.0$ to -3.5‰ , $\delta^{18}\text{O}=11.5$ ~ 5.7‰).

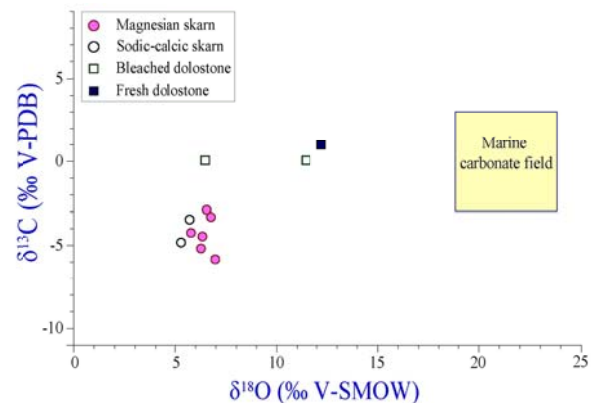


Figure 3. Carbon and oxygen isotope compositions of the carbonate minerals in the Pocheon deposit. The marine carbonate field is shown as a box in the figure.

4 Discussion and conclusions

Skarn types in the PD show calcic, magnesian, and sodic-calcic signature. Sodic-calcic alteration of the PD is a typical feature of IOCG-type deposit. The mineral assemblages of sodic-calcic skarn in the PD are divided into prograde and retrograde stage. Mineral assemblages of each stage in the PD are similar to the skarn alteration zone in the IOCG system (sodic clinopyroxene-diopside-garnet-scapolite-actinolite-sodic amphibole-epidote) (Table 1). IOCG skarns are commonly associated with large volumes of actinolite ± magnetite rocks as at the Sossego in Brazil (Monteiro et al, 2008) and the Raul-Condestable in Peru (De Halder et

al, 2006). Retrograde stage of sodic-calcic skarn in the PD shows a large volume of actinolite and tremolite. It was interpreted as amphibolite by So (1977). because of its banded and fold structures.

The paragenetic sequence of the PD shows sodic-calcic alteration accompanying Fe-mineralization. Given the fact that magnetite ores usually occur with acmite-albite-anhydrite-amphibole in the sodic-calcic skarn, we suggest that the retrograde sodic-calcic skarn is the main stage of Fe-mineralization. Calcic skarn occurred in the PD is just a subordinate Fe-mineralization event between the ore-fluids and carbonate-rich country rocks. As a result the PD needs to be reinterpreted as a skarn alteration zone in IOCG system.

Acknowledgements

This work was supported by National Research Foundation of the Korea (NRF) grant funded by the Korea government Ministry of Knowledge Economy (No. 2012R1A1A2005723).

References

- Corriveau L., Williams P.J., Mumin H. (2009) Alteration Vectors to IOCG Mineralization From Uncharted Terranes to Deposit, in Corriveau, L. and Mumin, A.H., eds., Exploring for iron oxide copper-gold deposit: Canada and global analogues: Geological Association of Canada, Short Course Notes, No. 20, p. 89-110
- De Haller, A., Corfu, F., Fontbote, L., Frank, M., and Zuniga, A.J., (2006) Geology and U-Pb geochronology of the Raul-Condastable iron oxide copper-gold deposit, central coast of Peru: *Economic Geology*, Vol. 101, p. 281-310
- Hwang J.H., Kihm Y.H. (2007) Geological report of the Jipori sheet. Korea Institute of Geoscience and Mineral Resources. p. 8
- Kanda Y. (1969) Geology and ore deposit of Pocheon Iron Mine, Korea. *Jour. Korean Inst. Mining Geol.*, vol. 2, p. 53-67
- Kim H.S. (1977) Mineralogy and petrology of the Precambrian iron deposits, Korea. *Jour. Geological Society of Korea*, vol. 13, No. 3, p.191-211
- Oh C.W. (2006) A new concept on tectonic correlation between Korea, China and Japan: Histories the late Proterozoic to Cretaceous. *Gondwana Research* 9, p. 47-61
- So C.S. (1977) Origin of the Strata-Bound Magnetite Ore from the Pocheon Iron Mine, Korea. *Jour. Geological Society of Korea*, Vol. 13, No. 4, p. 249-262
- Monteiro, L.V.S., Xavier, R.P., de Carvalho, E.R., Hitzman, M.W., Johnson, C.A., de Souza Filho, C.R., and Torresi, L. (2008) Spatial and temporal zoning of hydrothermal alteration and mineralization in the Sossego iron oxide-copper-gold deposit, Carajas Mineral Province, Brazil: paragenesis and stable isotope constraints: *Mineralium Deposita*, Vol. 43, p. 129-159
- Williams P.J. (2009) A Classifying IOCG deposit, eds., Exploring for iron oxide copper-gold deposit: Canada and global analogues: Geological Association of Canada, Short Course Notes, No. 20, p. 13-23
- Wang S. and Williams P.J. (2001) Geochemistry and origin of Proterozoic skarns at the mount Elliott Cu-Au (-Co-Ni) deposit, Cloncurry distric, NW Queensland, Australia: *Mineralium Deposita*, vol. 36, p. 109-124
- Yu J., Chen Y., Mao J., Pirajno F., Duan C. (2011) Review of geology, alteration and origin of iron oxide-apatite deposits in the Cretaceous Ningwu basin, Lower Yangtze River Valley, eastern China : Implications for ore genesis and geodynamic setting. *Jour. Ore Geology reviews*, Vol. 43 (2011) p. 170-181
- Zhang R., Zhang X., Hu S. (2011) Pyrite-anhydrite-magnetite-pyroxene-type deposits and coexisting hydrothermal fluids in Mesozoic volcanic basins, Yangtze River valley, China. *Jour. Ore Geology reviews*, Vol. 43 (2011) p. 315-332

Sulphur isotope geochemistry and ^{187}Re – ^{187}Os temporal constraints on the formation of polymetallic iron-oxide-dominated deposits in the Great Bear magmatic zone, NWT, Canada

Pedro Acosta-Góngora, Sarah A. Gleeson and Robert Creaser

University of Alberta, Department of Earth and Atmospheric Sciences, Edmonton, Alberta, Canada T6G 2E3

Bruce E. Taylor

Geological Survey of Canada, 601 Booth street, Ottawa, ON, Canada, K1A0E8

Iain M. Samson

University of Windsor, Depart of Earth and Environmental Sciences, Windsor, Ontario, Canada, N9B 3P4

Luke Ootes

Northwest Territories Geoscience Office, Yellowknife, Northwest Territories, Canada, NT X1A 2R3

Louise Corriveau

Geological Survey of Canada, 490 rue de la Couronne, Québec, QC, Canada, G1K 9A9

Abstract. The Great Bear magmatic zone (GBmz) contains several examples of iron oxide copper-gold (IOCG) mineralization including the Sue-Dianne and NICO deposits and other prospects like DAMP. The $\delta^{34}\text{S}$ values in pyrite, arsenopyrite and chalcopyrite from NICO range from 2.5‰ to 6.7‰; pyrite from DAMP varies from -0.1‰ to 5‰. Conversely, chalcopyrite from Sue Dianne $\delta^{34}\text{S}$ has a dominantly negative signature ranging from -7.7‰ to 1‰. The preliminary $\delta^{34}\text{S}$ data have values close to 0‰ suggesting an important magmatic contribution to the formation of IOCGs in the GBmz. However, some of the relatively ^{34}S -enriched (> 5‰) and -depleted (<-5‰) signatures could also indicate that some of the sulphur found in these systems is derived from non-magmatic sources. In addition, ^{187}Re - ^{187}Os dating of two molybdenite samples was carried out on NICO deposit. One sample represents a late stage of mineralization (NM3) within the main ore zone and has an age of ca.1865. The second sample formed ca.1877 and was collected from a U±Cu-Mo- rich zone within the Southern Breccia. The ^{187}Re - ^{187}Os molybdenite ages from NICO deposit also suggest a magmatic origin as they are correlative (within error) with plutonic events emplaced between 1866 Ma and 1875 Ma in this area.

Keywords. Sulphur isotopes, IOCG, Great Bear

1 Introduction

The discovery of the giant, polymetallic, iron oxide dominated Olympic Dam deposit, and other iron oxide dominant deposits (e.g. La Candelaria, Ernest Henry etc.) has led to a new classification of these systems as Iron Oxide Copper Gold (IOCG) deposits. These are an important exploration targets for mining companies due the potential for large tonnages and high ore metal grades. The IOCG deposits however, have many disparate features in terms of metal budgets, mineralization styles, alteration, age, and nature of the

host rocks. Also, globally, the origin of the hydrothermal fluids is poorly understood, but it has been suggested that there is a contribution of basinal brines (evaporites) (Barton and Johnson, 1996) and/or intermediate to felsic-alkaline magmatism-derived hydrothermal fluids (Pollard, 2000) in these polymetallic iron-oxide dominated systems.

The Great Bear magmatic zone (GBmz) in the Northwest Territories, Canada, is host to the NICO (Au-Bi-Co±Cu-W) and Sue Dianne (Cu-Au-Ag±U) deposits and other smaller iron-oxide dominated polymetallic systems (e.g. DAMP) that have comparable alteration and mineralization styles to the IOCG deposits in Chile, Brazil and Australia (e.g. Corriveau et al., 2010). Here we present preliminary sulphur isotope data from the NICO, Sue Dianne, and DAMP deposits and temporal constraints on the NICO deposit using ^{187}Re - ^{187}Os dating.

2 Regional Geology

The Wopmay orogen comprises three major zones, from east to west: the Coronation margin, the Great Bear magmatic zone (GBmz) and the Hottah terrane (e.g. Hildebrand et al., 1987). In the southern GBmz the Treasure Lake Group (TLG) represents the youngest component of the Hottah terrane (<1885 Ma, >1875 Ma; Gandhi and van Breemen, 2005) and is the host-rock for the iron-oxide dominated polymetallic NICO deposit. The younger GBmz intrudes the TLG in the study area and it is the host to the Sue Dianne deposit, the DAMP prospect, and a number of other mineralized prospects.

The TLG is a metasedimentary shallowing upward sequence consisting of four main units, from oldest to youngest: lower siltstone; calc-silicate; quartz-arenite; and upper siltstone based on a type section southeast of NICO property (Gandhi and van Breemen, 2005). The

lower siltstone (T1) is quartzo feldspathic. On top of the lower siltstone, the carbonate unit (T2) is dominated by marble, and in this study scapolite (meionite) has been recognized. This unit pinches out rapidly to the northwest at Lou Lake, where a bedded amphibole-magnetite-altered siltstone-argillite subunit occurs at the same stratigraphic level hosting NICO deposit. The top of the calc-silicate unit is interfingered with quartz arenite. The quartz-arenite (T3) grades into an upper zone of thin to thickly-bedded siltstone (T4), which locally has accessory fine-grained chalcopyrite and pyrite.

The <1875 Ma volcanic rocks of the GBmz are assigned to the MacTavish Supergroup (Hofman, 1980; Hildebrand et al., 1987). The volcano-sedimentary sequences have been divided into four groups from west to east across the zone, and from oldest to youngest: the age equivalent LaBine and Dumas groups in the north (e.g. Hoffman and McGlynn, 1977) the slightly younger Faber group in the central and south GBmz (e.g. Gandhi et al., 2001; Ootes et al., 2012). Of interest in this study is the Faber group. It consists mostly of andesite, dacite, ignimbrite, and rhyodacite (e.g. Gandhi et al., 2001). In the southern GBmz, the Faber group rests unconformably on the TLG and these rocks are intruded by a series of sodic to calc-alkaline felsic plutons at 1873 ± 2 , $1868^{+2.9}_{-2.4}$, $1867^{+1.6}_{-1.5}$, 1866 ± 2 and 1856^{+3}_{-2} Ma (Gandhi et al., 2001).

3 Iron oxide polymetallic mineralization at the GBmz

3.1 NICO deposit

The NICO deposit hosts economic Co-Au-Bi (\pm Cu-W) mainly in amphibolitic ironstones (Sidor, 2000). The most important discovery to date is the Bowl Zone (BZ; Goad et al., 2000). The mineralization in the BZ is contained within three ore lenses and it can be broadly divided into an early barren iron oxide \pm amphibole (PA1), early Co-As-Fe sulphide (NM2) and late Cu-Bi-Au sulphide stages (NM2). They are stratabound, and in veins and aggregates within the ore lenses.

The pre-ore alteration (PA1) is characterized by emplacement of magnetite and Fe-Ca rich amphibole \pm pyrrhotite as pervasive stratabound replacement, crosscutting veins and breccia infills. The early ore stage (NM2) overprints the PA1 and comprises the precipitation of cobaltite, loellingite, arsenopyrite, scheelite, magnetite, pyrite and lesser amounts of molybdenite, amphibole, biotite, quartz, potassic feldspar and fluorite. Textural and major element composition evidence suggests that cobaltite and loellingite have been re-crystallized to Co-rich arsenopyrite (>5%).

The Cu-Bi-Au introduction (NM3) occurs mostly as micro-veins (30-50 μ m thick) that crosscut and replaces the NM2. The NM3 starts with the precipitation of pyrite, chloro-potassichastingsite, magnetite, native Bi, bismuthinite, native Au and Au-tellurides, followed by the precipitation of hematite, emplectite, whittichenite and chalcopyrite.

One kilometer to the south of NICO a three kilometer long by five hundred meter wide corridor of brecciated albitite (Southern Breccia) hosts a series of uranium and polymetallic uranium mineralization (Corriveau et al., 2011). Geochronological and field crosscutting relationships constrain the formation of the Southern Breccia as syn-genetic with the formation of the NICO deposit (Corriveau et al., 2011). Molybdenite is associated with the precipitation of uraninite with or without pyrite-chalcopyrite within magnetite-K-feldspar \pm biotite-cemented breccias (Montreuil et al. in revision).

3.2 Sue-Dianne

The Cu-Au-Ag Sue Dianne deposit is located by the north arm of Dianne Lake and is hosted by a rhyodacite ignimbritic sequence of the Faber Group (Gandhi, 1989; Gandhi et al., 2001). The mineralization is hosted largely by an iron oxide (hematite-magnetite) matrix-rich breccia interpreted as a volcanic diatreme and limited in depth by a rhyodacitic porphyry (e.g. Goad et al., 2000). The pre-ore alteration (SDP) consists of pervasive potassic alteration. The early mineralization (SD1) starts with the precipitation of fluorite, epidote, magnetite, hematite, chlorite and accessory chalcopyrite and carrolite (CuCo_2S_4). The bulk of the Cu (\pm Bi) mineralization (SD2) is intergranular to SD1 and consists of chalcopyrite and minor emplectite. A later and less significant phase of mineralization (SD3) is represented by the precipitation of fine grained epidote micro-veins (10 to 100 μ m thick) crosscutting the SDP and SD1 minerals. Chalcopyrite, bornite, chlorite, fluorite, potassic feldspar and quartz are subordinate minerals occurring in variable amounts (1 to 15% of the vein material). At the shallower parts of the system chalcocite and covellite (along with hematite) occur as part of a supergene enrichment event.

3.3 DAMP

The Damp prospect is located in the central GBmz, is hosted by albitized rhyodacites and consists of polymetallic (Cu-U-Co-V \pm Zn-Pb) mineralization, contained within an extensive breccia zone. The early DM1 stage consists of the co-precipitation of magnetite, hematite, pyrite, potassic feldspar and minor amounts of quartz, calcite, albite and epidote. Brecciation continued after the deposition of DM1 as coarser pyrite grains are highly fractured and filled with chalcopyrite, carrolite (CuCo_2S_4), bornite, emplectite (CuBiS_2) and chlorite (DM2). Covellite and chalcocite replace chalcopyrite and bornite and are mostly associated with specular hematite.

4. Temporal constraints on NICO and Sue-Dianne

U-Pb zircon dating of felsic to intermediate intrusions at $1867^{+1.6}_{-1.5}$ and $1868^{+2.9}_{-2.4}$ Ma, from the Lou and Dianne lakes, respectively (Gandhi et al. 2001) have been used to infer the timing of mineralization at these locations (Ootes et

al. 2010; Sidor, 2000; Camier, 2002). However, unpublished U-Pb data from two porphyries emplaced within the NICO property (Davis et al., 2011), one altered by the NICO system and the other one crosscutting the ore lenses, more strongly support the timing of mineralization at 1870 Ma.

5 Analytical techniques

In situ $\delta^{34}\text{S}$ analysis of pyrite, chalcopyrite and arsenopyrite was carried out on the Micro In situ Laser Extraction System (MILES) at the Geological Survey of Canada in Ottawa. The values are reported relative to the Vienna-Cañon Diablo Troilite (V-CDT) standard. The ^{187}Re - ^{187}Os dating was carried out at the Radiogenic Isotopes Facility (RIF), University of Alberta, Edmonton, Canada.

6 Stable isotopes

$\delta^{34}\text{S}$ values from the NICO deposit (n=56) range from 2.5 to 6.7‰. The analysed sulphides include arsenopyrite and pyrite from NM2 and chalcopyrite from NM3. Most of the arsenopyrite, pyrite and chalcopyrite data are concentrated around 4‰ (Figure 1). Conversely, chalcopyrite from Sue Diane deposit (SD2; n=22) has lower values ranging from -7.7 to 1‰ with most values located between -3‰ and -6‰ (Figure 1). Pyrite crystals (DM1) from the DAMP prospect (n=6) has isotopic values that vary from -0.1‰ to 5‰ (Figure 1).

7 ^{187}Re - ^{187}Os molybdenite dating

Two ^{187}Re - ^{187}Os molybdenite analyses on molybdenite from the Bowl Zone (NM2 stage) and the U±Cu-Mo-rich zone of the Southern breccia yield model ages of ca. 1865 and ca. 1877 Ma, respectively.

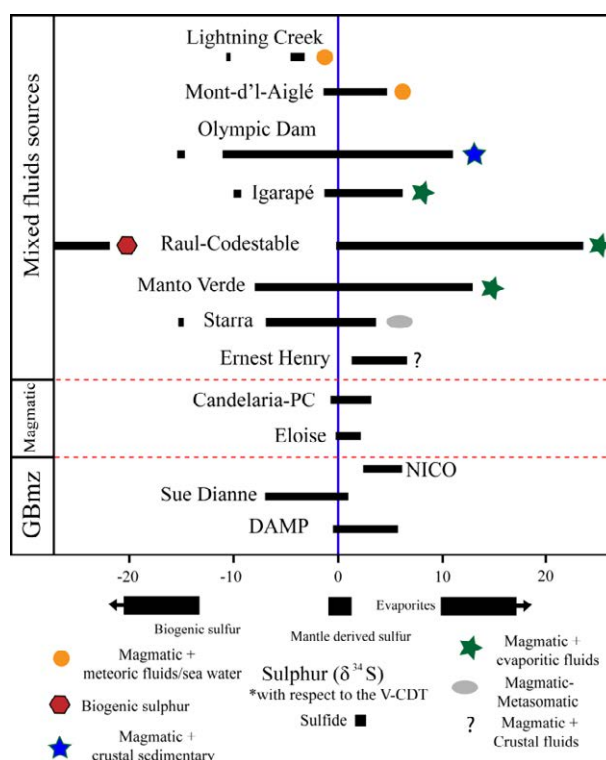
8 Discussion

8.1 Sulphur isotopes

Regionally, $\delta^{34}\text{S}$ values from the NICO and DAMP deposits exhibit a relative enrichment on the heavy isotope compared to that of Sue Dianne. There is no significant difference in $\delta^{34}\text{S}$ values of the NM2 to NM3 stages at NICO and, thus, the S may be derived from a common S source(s). Some of the data close to 0‰ for the three systems may be interpreted as having a magmatic origin. On the other hand, $\delta^{34}\text{S}$ values significantly greater (5‰-6.7‰; NICO-DAMP) and lower (-7.7‰; Sue Dianne) indicates the presence of a non-magmatic source of S. This is similar to other well-known IOCG systems (Fig 1) from the Peruvian Andes Australia, Brazil and Canada.

Contribution from magmatic fluids, especially in the early mineralization/alteration stages has been recognized in several IOCG deposits. However, fluid mixing with a non-magmatic derived fluid may have also played a significant role in the formation of these deposits. Bastrakov et al. (2007), Benavides et al. (2007), Dreher et al. (2008) and de Haller and Fontboté

(2009) recognized the presence of relatively ^{34}S -rich sulphides (with $\delta^{34}\text{S}$ values of mostly 5 to 11‰) and they suggest as possible sources of the heavy sulphur: i) seawater; ii) evaporitic water, and/or; iii) oxidized metasedimentary fluids. Some of the ^{34}S -depleted values from Olympic Dam (Titan prospect, -6.5 to -0.4‰; Bastrakov et al., 2007) are attributed to a metasedimentary source of sulphur. Although there is no evidence for the presence of evaporites in the TLG (or any other location in the GBmz), the presence of meionite in the carbonate unit (T2) indicate there could be an alternative source of oxidized sulphur for the NICO deposit. Equally, more reduced sulphur, perhaps from that within chalcopyrite and pyrite in the metasilstone unit T4 (and T1?) could be responsible for



some of the ^{34}S -depleted values in Sue Dianne.

Figure 1. Comparison of the GBmz $\delta^{34}\text{S}$ values with other IOCG deposits from Peru, Australia and Brazil. Symbols indicate the inferred fluid sources in deposits where fluid mixing is proposed. Data from Rotherham et al. (1998), Perring et al. (2000), Baker et al. (2001), Marschik and Fontboté (2001), Mark et al. (2005), Simard et al. (2006), Bastrakov et al. (2007), Benavides et al. (2007), Dreher et al. (2008) and de Haller and Fontboté (2009)

8.2 ^{187}Re - ^{187}Os dating

The uncertainties on the ^{187}Re - ^{187}Os dating of molybdenite from the NICO deposit make them statistically undistinguishable. Nonetheless, they imply a temporal association of NICO deposit with plutonic events of the GBmz occurring between ca. 1865 and ca. 1875 Ma as suggested by Sidor (2001), Camier (2002), and Ootes et al. (2011).

9 Summary

At a regional scale the isotopic signature of the GBmz is

consistent with a primordial magmatic origin of the sulphur. Nevertheless, contribution from other non-magmatic sources may account for some of the relatively ³⁴S-rich and -depleted signatures from NICO and DAMP and Sue Dianne, respectively. In addition, the magmatic origin for NICO deposit is also supported by the two Re-Os dates on molybdenite from the Bowl Zone and the Southern breccia zones that have ages correlative (within error) to the felsic intrusions in the region emplaced between ca. 1865 Ma and ca. 1875 Ma.

Acknowledgements

This work was funded by the IOCG-Great Bear project of the Geo-mapping for Energy and Minerals program of Natural Resources Canada, Research Affiliate Program agreement and funding from Natural Resources Canada and Funding of the Natural Science and Engineering Research Council of Canada to SG and IS. The project was also conducted through various collaborative agreements with Fortune Minerals Limited.

References

- Baker T, Perkins C, Blake KL, Williams PJ (2001) Radiogenic and stable isotope constraints on the genesis of the Eloise Cu–Au deposit, Cloncurry district, northwest Queensland. *Econ Geol* 96:723–742.
- Barton MD, Johnson DA (1996) Evaporitic source model for igneous-related Fe oxide-(REE-Cu-Au-U) mineralization. *Geol* 24:259–262.
- Bastrakov EN, Skirrow RG, Davidson GJ (2007) Fluid evolution and origins of iron oxide Cu-Au prospects in the Olympic Dam District, Gawler Craton, South Australia. *Econ Geol* 1415–1440.
- Benavides J, Kyser TK, Clark AH, Oates CJ, Zamora R, Tarnovschi R, Castillo B (2007) The Manto Verde Iron-oxide-Copper-Gold district, III Región, Chile: the role of regionally derived, nonmagmatic fluids in chalcopyrite mineralization. *Econ Geol* 102:415–440.
- Camier WJ (2002) Geology of the Sue-Dianne Proterozoic Cu-Ag-Fe oxide breccia complex, Mazenod Lake district, Northwest Territories. University of Western Ontario. Unpublished MSc. Thesis.
- Corriveau L, Mumin AH, Setterfield T (2010) IOCG environments in Canada: Characteristics, geological vectors to ore and challenges: In: Porter TM (ed) Hydrothermal iron oxide copper-gold and related deposits: A global perspective, vol 4. PGC Publishing, Adelaide, pp 311–343.
- Corriveau L, Mumin H, Montreuil J-F (2011) The Great Bear magmatic zone (Canada): Exposing the IOCG spectrum and related deposit types. SGA2011 - The 11th Biennial SGA Meeting of The Society for Geology Applied to Ore Deposits, Antofagasta, Chile, Transaction volume.
- Davis W, Corriveau L, van Breemen O, Bleeker W, Montreuil J-F, Potter E, Pelletier E (2011) Timing of IOCG mineralizing and alteration events within the Great Bear Magmatic Zone. 39th Yellowknife Geoscience Forum Program of Abstracts, November 2011, Yellowknife, NT, 97.
- De Haller A, Fontboté L (2009) The Raúl-Condestable iron oxide gold deposit, central coast of Peru: ore and related hydrothermal alteration, sulphur isotopes, and thermodynamics. *Econ Geol* 104:365–384.
- Dreher AM, Xavier RP, Taylor BE, Martini SL (2008) New geologic, fluid inclusion and stable isotope studies on the controversial Igarapé Bahia Cu-Au deposit, Carajás Province, Brazil: *Miner Depo* 43:161–184.
- Gandhi SS, Mortensen JK, Prasad N, van Breemen O (2001) Magmatic evolution of the southern Great Bear continental arc, northwestern Canadian Shield: Geochronological constraints. *Can J Earth Sci* 38:767–785.
- Gandhi SS (1989) Rhyodacite ignimbrites and breccias of the Sue-Dianne and Mar Cu-Fe-U deposits, southern Great Bear magmatic zone, Northwest Territories. *Geol Sur of Can. Pap* 89-1C:263–273.
- Gandhi SS, van Breemen O (2005) SHRIMP U–Pb geochronology of detrital zircons from the Treasure Lake Group – new evidence for Paleoproterozoic collisional tectonics in the southern Hottah terrane, northwestern Can. Shield. *Can J Earth Sci*, 42:833–845.
- Goad RE, Mumin AH, Duke NA, Neale KL, Mulligan DL, Camier WJ (2000) The NICO and Sue-Dianne Proterozoic, iron oxide-hosted, polymetallic deposits, Northwest Territories: Application of the Olympic Dam model in exploration. *Explor Mining Geol* 9:123–140.
- Hildebrand RS, Hoffman PF, Bowring SA (1987) Tectono-magmatic evolution of the 1.9-Ga Great Bear magmatic zone, Wopmay orogen, northwestern Canada. *J Volcanol Geotherm Res* 32:99–118.
- Hoffman PF, McGlynn JC (1977) Great Bear Batholith: a volcano-plutonic depression. In: WRA Baragar, LC Coleman and JM Hall (eds), Volcanic regimes in Canada. *Geol Assoc of Can Spec Pap* 16:170–192.
- Hoffman PF (1980) Wopmay orogen: A Wilson cycle of early Proterozoic age in the northwest of the Canadian Shield, in: Strangway, D.W., ed., The continental crust and its mineral Deposits: *Geol Assoc Can Spec Pap* 20:523–549
- Mark G, Williams PJ, Oliver NHS, Ryan C and Mernagh T (2005) Fluid inclusion and stable isotope geochemistry of the Ernest Henry Fe oxide-Cu-Au deposit, Queensland, Australia. *SGA Abs* 785-788.
- Marschik R and Fontboté L (2001) The Candelaria-punta del Cobre iron oxide Cu-Au(-Zn-Ag) deposits, Chile: *Econ Geol* 96:1799-1826.
- Montreuil JF, Corriveau L, Potter L (accepted with revision by Mineralium Deposita) Albitite-hosted uranium development within IOCG systems: the Southern Breccia, Great Bear magmatic zone, Northwest Territories, Canada.
- Ootes L, Davis W, Jackson VA, Acosta-Gongora P, and Shakotko P (2012) The Hottah – Great Bear stratigraphic continuum: implications for IOCG mineralization and plate interactions in the western Canadian Shield. 40th Yellowknife Geoscience Forum Program of Abstracts, Yellowknife, NT, November, 2012.
- Ootes L, Goff S, Jackson V, Gleeson S, Creaser R, Samson IM, Evensen N, Corriveau L, and Mumin H (2010) Timing and thermochemical constraints on multi-element mineralization at the Nori/RA Cu-Mo-U prospect, Great Bear magmatic zone, Northwest Territories, Canada. *Min Dep* 45: 549-566.
- Perring, CS, Pollard PJ, Dong G, Nunn AJ, and Blake KL (2000) The Lightning Creek sill complex, Cloncurry district, northwest Queensland: A source of fluids for Fe oxide-Cu-Au mineralization and sodic-calcic alteration. *Econ Geol* 95: 1067–1089.
- Pollard PJ (2000) Evidence of a magmatic fluid and metal source for Fe-oxide Cu–Au mineralization. In: Porter TM (ed) Hydrothermal iron oxide copper–gold and related deposits: a global perspective, vol 1. PGC Publishing, Adelaide, pp 27–41.
- Rotherham JF and Blake KL (1998) Stable isotope evidence for the origin of Mesoproterozoic Starra Au-Cu deposit, Cloncurry district, Northwest Queensland. *Econ Geol* 93:1435-1449.
- Sidor M (2000) The origin of the black rock alteration overprinting iron-rich sediments and its genetic relationship to disseminated polymetallic sulphide ores, Lou Lake, Northwest Territories, Canada. University of Western Ontario. Unpublished MSc thesis.
- Simard M, Beaudoin J, Bernard J, Hupé A (2006) Metallogeny of the Mont-de-l’Aigle IOCG deposits, Gaspé Peninsula, Québec, Canada. *Miner Depo* 41: 607-636.

The Oued Belif breccia (northern Tunisia): a Miocene representative of the (IOCG)-IOU class of deposits

Christian Marignac

Géologie et Gestion des Ressources Minérales et Energétiques - G2R (CNRS/Université Henri Poincaré, France)

Sophie Decrée, Thierry De Putter

Musée Royal de l'Afrique Centrale (Tervuren, Belgique)

Johan Yans

UNamur (Namur, Belgique)

Norbert Clauer

Laboratoire d'Hydrologie et de Géochimie de Strasbourg (CNRS/Uds, Strasbourg, France)

Jean-Marc Baele

UMons (Mons, Belgique)

Abstract. The Miocene Oued Belif ring-shaped breccia (hereafter OBB) is located in the Nefza mining district of northern Tunisia. The OBB encloses Triassic material (brecciated K-Mg altered pelites and siltites) within an extrusive diapiric structure reactivated in a late Miocene nappe emplacement episode. This deep-rooted structure drives the hydrothermal activity that caused the brecciation of the Oued Belif Breccia and the emplacement of two generations of shallow felsic magmatism. The matrix-supported OBB comprises clasts of altered Triassic material and others deriving from the regional substrate. Fine-grained, low-Ti, Si-Al-rich hematite (≥ 20 vol. %) is the main matrix mineral, along with REE- and U-minerals. A multi-phase alteration episode (K-Fe-(Mg)-metasomatism) slightly predates the Fe-LREE-U mineralization. The major brecciation event is coeval with the mineralization event and the emplacement of the Oued Belif rhyodacite intrusion. Except for its lack of economic level Cu and Au content, the OBB shares most typical attributes of the IOCG deposits. It may therefore be classified as either an "Iron-Oxide associated-Alkali Altered (IOAA)" or as an "Iron-Oxide Uranium (IOU)" mineral system. K-Ar dating of K-feldspar sets the OBB formation at 9.2 ± 0.25 Ma, which could make it the youngest presently known representative of this class of deposits.

Keywords. IOCG, IOU, REE, Oued Belif, Tunisia

1 Introduction

The IOCG concept was applied to an increasing diversity of hydrothermal deposits associated with Fe oxides, since the first definition of the iron oxide copper-gold (IOCG) class of deposits (Hitzman et al., 1992). The large diversity within this deposit family has made it necessary to better define and classify IOCG deposits, as several recent contributions have done (Williams et al. 2005; Corriveau and Mumin 2010; Williams 2010; Groves et al. 2010; Skirrow 2010 2011). In the Nefza region (Tellian domain of northern Tunisia), the Oued Belif breccias, with Fe-REE-U-(Cu-Au) mineralization, shares most IOCG attributes but lacks economic-level Cu-Au enrichment. The aim of this study is to describe the features of the OBB and suggest that it can be regarded as a member of the IOAA class (Porter 2010) or

of the IOU group (Skirrow 2011).

2 Geological setting

The Nefza mining district belongs to the Tellian "Nappe Zone" of northern Tunisia within the internal zone of the collisional Alpine Maghrebide belt. It is known both as a Late Miocene-Pliocene magmatic province and as a base metal and mercury metallic district. In this area, basement rocks are made of (1) limestone and marl from Late Cretaceous to Eocene age, occurring as autochthonous fm. or as thrust sheets (the Kasseb and Ed Diss thrust sheets), which are up to 1500m thick (Ould Bagga et al. 2006; and references therein), and (2) Oligo-Miocene sandstones that constitute the overlying Numidian nappe (Rouvier 1994).

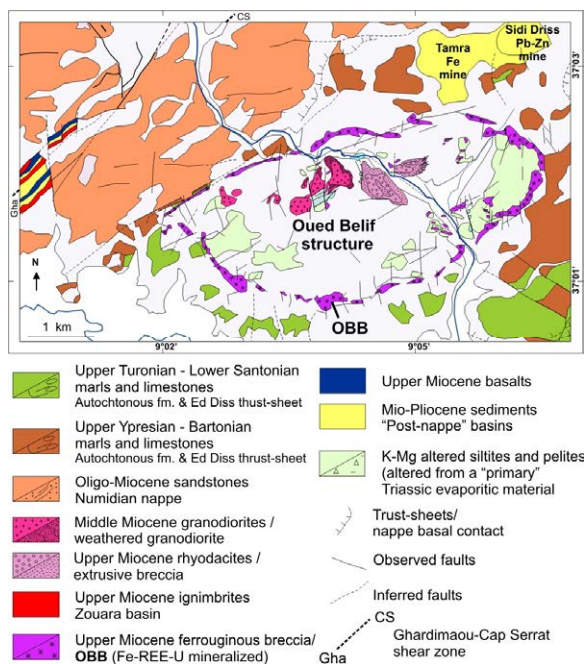


Figure 1. Simplified geological map of the studied area (modified and redrawn from Gottis and Sainfeld 1952, Rouvier 1987, Decrée et al. 2013)

The nappe pile is crosscut by the Oued Belif structure, a concealed magmatic-hydrothermal complex expressed at the surface as a prominent and discontinuous brecciated rim/ring (the OBB; 7 x 3 km; **Fig. 1**), which encloses K-Mg altered (and brecciated) Triassic sedimentary material and two generations of Miocene calc-alkaline subvolcanic intrusions (a 12.9 ± 0.5 Ma granodiorite and a 8.9 ± 0.2 Ma rhyodacite; Rouvier 1994; and references therein). In northern Tunisia, the post-collisional calc-alkaline magmatism involves a subcontinental lithospheric mantle (SCLM) source that was metasomatized during earlier subduction. Its ultimate origin is thought to be the rise of asthenospheric mantle through lithospheric delamination (Maury et al. 2000), possibly triggered by the Miocene reactivation of crustal scale faults inherited from the Variscan orogeny (Piqué et al. 2002). Such faults are present in the Nefza district (as the Ghardimaou-Cap Serrat shear-zone) and actually control magmatism and hydrothermal mineralizations.

3 The Oued Belif breccia: description

The OBB is a heterolithic and heterometric polyphase matrix-supported breccia, with hematitic cement (**Fig. 2**). The mostly angular to sub-rounded clasts range from a few millimeters to several decimeters. Metre-sized plate-shaped clasts of ferruginized marls are observed in the vicinity of the Ed Diss thrust sheets.



Figure 2. Ferruginized clasts comprised of K-feldspar rocks and phlogopites, the result of the alteration of siltites and pelites, respectively (from Decrée et al. 2013)

3.1 The OBB alteration

Most clasts are altered “Triassic” siltites and pelites, transformed into K-feldspar rocks, phlogopites and tourmalinites. These clasts are often ferruginized (with an iron-rich rim, **Figs. 2 & 3**) and re-brecciated. Locally, neoformed alteration minerals fill intra-clast fractures or form clast rims (**Fig. 3**), according to the sequence: K-feldspar-tourmaline-Fe-phlogopite and Fe-muscovite. All these minerals are also observed as broken and reworked clasts enclosed within later hematite cement. The K-Ar ages of the neoformed K-feldspar crystals are 9.1 ± 0.4 and 9.4 ± 0.4 Ma.

3.2 The OBB mineralization

Cement in the OBB predominantly consists of microgranular hematite with grains generally less than

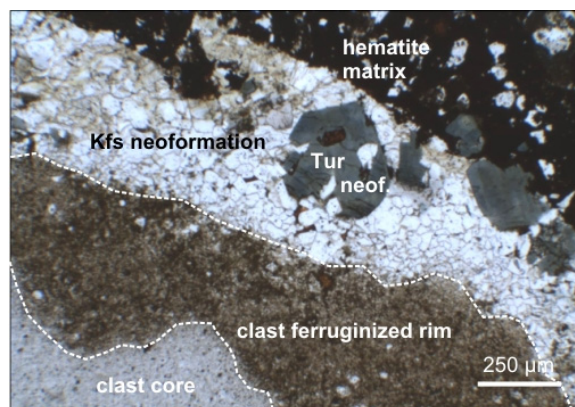


Figure 3. Photomicrograph using transmitted light: K-feldspar and tourmaline crystals lining the Hem 1 iron-rich rim of a K-feldspar-altered clast (from Decrée et al. 2013)

$1 \mu\text{m}$ in size. Several secondary minerals are genetically associated with hematite, either as late clast impregnation or as replacements after early clast ferruginization. These secondary materials include REE carbonates, namely bastnaesite $((\text{La,Ce,Nd})\text{CO}_3\text{F})$, Ca-bastnaesite $(\text{Ca}_x(\text{La,Ce,Nd})_{3-x}\text{CO}_3\text{F}_{3-x})$, and parisite $(\text{Ca}(\text{Ce,La,Nd})_2(\text{CO}_3)_3\text{F}_2)$, that are by far the most abundant mineral phases associated with hematite. Bastnaesite generally occurs as elongate laths or prisms (up to $30 \mu\text{m}$ in length or $10 \mu\text{m}$ in section) disseminated within the hematitic cement. Bastnaesite crystals most commonly show intergrowth with micrometer-thick parisite coatings. The OBB also includes large parisite and bastnaesite crystals (typically $200\text{--}300 \mu\text{m}$ long; **Fig. 4**) that are often intergrown with Ca-bastnaesite, and replaced K-feldspar-altered clasts.

Secondary minerals associated with hematite are euhedral monazite $((\text{La,Ce,Th,Nd})(\text{PO}_4))$; **Fig. 5**), uraninite (**Fig. 5**) and zircon.

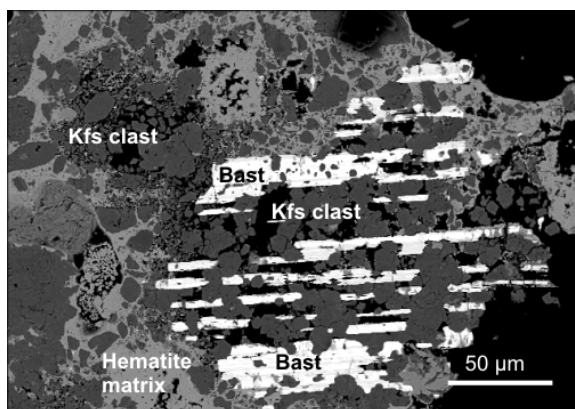


Figure 4. Backscattered electron images of a large bastnaesite crystals, intergrown with Ca-bastnaesite, replacing a former K-feldspar clast (from Decrée et al. 2013)

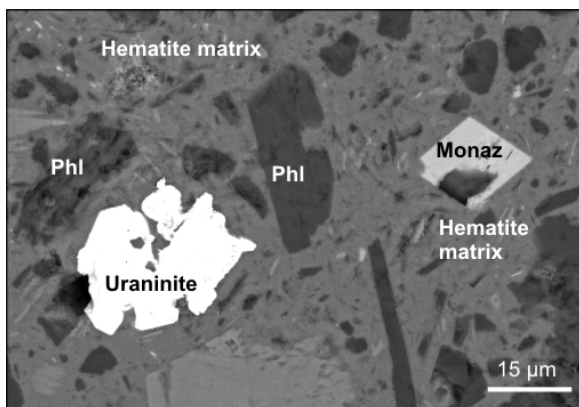


Figure 5. Backscattered electron images of well crystallized monazite, uraninite aggregates, and Fe-muscovite (Phl) crystals and laths within hematite cement (from Decrée et al. 2013)

4 Geochemical data

The OBB samples are significantly enriched in REEs (Σ REE: 363 up to 6000 ppm;), especially in LREEs ($17 < \text{La}_N/\text{Yb}_N < 391$). They also show significant enrichment in base (chalcophile) metals (e.g., from 153 ppm to 0.18 wt. % Cu, 1.0-15.7 ppm Ag, 151-3100 ppm Pb, 555-3950 ppm Zn); granitophile elements (e.g., 9-307 ppm W and 20 to >100 ppm Mo); and Au-related elements (up to 220 ppb Au, 20-542 ppm As, up to 71 ppm Bi), when compared to the MORB concentrations. These samples also show notable enrichment in Ba (up to 7886 ppm) and U (up to 489 ppm). Th, Ta, Nb, Zr and Sc are generally depleted in the OBB samples. Ti (0.06-0.56% TiO_2) and P (from 0.13 to 0.75% P_2O_5) may be enriched.

5 Paragenetic evolution

The following paragenetic evolution is suggested: Stage 1 represents a pre-brecciation K(+Mg) alteration event that strongly affected the regional rocks. "Triassic" pelites and siltites present in the Oued Belif structure were altered to K-feldspar rocks, ferroan phlogopite, and tourmalinite. In the OBB, this alteration event also led to formation of fluorite, apatite, barite and pyrite. Stage 2 is the main mineralizing event characterized by two brecciation episodes. A first brecciation event is associated with the beginning of K-Fe-rich fluid circulation, which caused the ferruginization of clast rims. It is followed by the dominant K-Fe alteration episode that resulted in the formation of K-feldspar, Mg-tourmaline, ferroan phlogopite, and muscovite either as clast coatings or filling voids and fissures within the clasts. This alteration predated the main (hydraulic) brecciation event and the circulation of a Fe + REE + Ca + P + Zr + U carbonate-rich mineralizing fluid that induced massive hematite precipitation as well as the formation of the breccia cement and the crystallization of a wide variety of REE-bearing minerals (monazite and REE-fluorocarbonates), zircon, and uraninite. Stage 3 corresponds to a late, post-brecciation Fe event.

6 IOCG deposit criteria

The OBB meets most of the criteria for an IOCG deposit (Williams et al. 2005; Corriveau and Mumin 2010; Williams 2010; Groves et al. 2010; Skirrow 2010 and 2011): (1) The OBB has a hydrothermal origin and is characterized by strong structural control that includes breccias and hydrothermal replacements. These breccias' hydrothermal origin can be seen in their matrix-supported nature; in their matrix of hydrothermal minerals; and in the high degree of disintegration of the Fe-metasomatized clasts. The OBB's structural control is evident, since the Oued Belif breccias are linked to a pre-existing structure. (2) Hematite is the dominant hydrothermal mineral in the OBB, seen either as a clast replacement or within a breccia matrix, with contents ≥ 20 vol. %. The OBB therefore resembles the Olympic Dam group of IOCG deposits (Williams 2010). (3) The OBB is significantly LREE enriched. The main LREE-bearing minerals in the OBB are fluorocarbonates (mostly bastnaesite) that are obviously synchronous with the main hematite stage, while there is no clear indication of a precursor. The LREE introduction was therefore contemporary with the Fe metasomatism in the OBB. Syn-hematite bastnaesite is recorded in other IOCG deposits such as Olympic Dam and Prominent Hill (Oreskes and Einaudi 1990; Belperio et al. 2007). (4) The Oued Belif structure is characterized by a dominant K-Fe alteration that would be developed at a very shallow depth, compared to the deep Na-(Ca) alteration (e.g., Hitzman et al. 1992; Baker et al. 2008; Corriveau et al. 2010). At Cloncurry, the fluids responsible for shallower K-metasomatism (associated with F and CO_2) and K-Fe alteration result from overpressured fluids breaking through a permeability barrier and inducing both brecciation and mineralization (Oliver et al., 2011). This phenomenon may also apply to Oued Belif. (5) As for the IOCG deposits, the OBB was formed under low silica activity, as demonstrated by the scarcity of quartz in the mineralized breccias. (6) The Oued Belif structure is temporally and spatially associated with felsic intrusions (the Ragoubet Es-Seid rhyodacite) whose root and feeder might be a $n \times 10$ km scale concealed intrusion (Jallouli et al. 2003).

7 Conclusions

The Oued Belif hematite-rich breccias (OBB) are the result of processes that include (i) two brecciation episodes (predating the Fe-REE-U mineralization) related to hydraulic fracturing coupled with a probable phreatomagmatism phase; (ii) two main alteration episodes, the first characterized by a K(-Mg) metasomatism accompanied by the introduction of F, P, Ba, and S, and the second, dated at 9.25 ± 0.25 Ma, comprised of K-Fe alteration; (iii) the mineralization event linked to the circulation of hot (Th up to 540°C and salinities ranging from ~30 to 59 wt. % eq NaCl in the fluorite; Talbi et al., 1999) and saline Fe + REE + Ca + P + Zr + U and F- CO_2 -rich mineralizing fluids. Its low Cu and Au levels as well as the high U contents might have been caused by the

felsic-dominated magmatic environment that lacks obvious mafic contribution, unlike most Cu-Au-rich IOCGs. Apart from the IOCG's Au and Cu economic criterion, the OBB displays most typical IOCG attributes. It could be therefore classified as an IOAA deposit (Porter 2010), which only possess subeconomic (or trace) copper and gold content, or, considering its significant U enrichment, as an IOU deposit (Skirrow 2011). Additionally, the OBB shares essential characteristics - extensional tectonic regime and the implication of a metasomatised SCLM through some kind of lithospheric delamination process - that are regarded as necessary for IOCG's (Skirrow 2010). Identifying the OBB as a member of the IOU-(IOAA)-IOCG family also opens new frontiers for prospection of IOCG deposits within the geodynamic environment of collisional belts.

Eventually, it is suggested that the Cu and Au economic criterion in the definition of IOCG's may be too restrictive and actually limit the understanding of the variability of these deposits and their efficient exploration

Acknowledgements

This research benefits from the 2008-2010 cooperation initiative between Tunisia and Wallonie-Bruxelles International entitled "Valorisation des géomatériaux de la région de Nefza-Sejnane (Nord-Ouest de la Tunisie)" as well as from the 2011-2013 TerMEX project entitled "Systèmes métallogéniques et géodynamique alpine : les minéralisations associées à l'évolution néogène des Maghrébides orientales. Relations avec la tectonique décrochante et le magmatisme post-orogénique". Louise Corriveau and Robert Skirrow are thanked for the constructive discussions.

References

- Baker T, Mustard R, Fu B, Williams PJ, Dong G, Fisher L, Mark G, Ryan CG (2008) Mixed messages in iron oxide-copper-gold systems of the Cloncurry district, Australia: insight from PIXE analyses of halogens and copper in fluid inclusions. *Miner Deposita* 43: 559-608
- Belperio A, Flint R, Freeman (2007) Prominent Hill: a hematite-dominated, iron oxide-copper-gold system. *Econ Geol* 102: 1499-1510
- Burrollet PF (1991) Structures and tectonics of Tunisia. *Tectonophysics* 195: 359-369
- Corriveau L, Mumin H (2010) Exploring for iron oxide-copper-gold (Ag-Bi-Co-U) deposits : case examples, classification and exploration vectors. In: Corriveau L, Mumin AH (eds) Exploring for iron oxide copper-gold deposits, Canada and global analogues, Geological Association of Canada, Short Course Notes 20, pp 1-12
- Corriveau L, Mumin AH, Setterfield T (2010) IOCG environments in Canada: Characteristics and geological vectors to ore. In: Porter TM (ed) Hydrothermal iron oxide copper-gold and related deposits, A global perspective, volume 4-advances in the understanding of IOCG deposits, Porter Geoscience Consultancy Publishing, Adelaide 4, pp 311-344
- Decrée S, Marignac C, De Putter T, Yans J, Clauer N, Dermech M, Aloui K, Baele JM (2013) The Oued Belif hematite-rich breccia: a Miocene iron-oxide Cu-Au-(U-REE) deposit in the Nefza Mining District, Tunisia. *Econ Geol*, accepted.
- Gottis Ch, Sainfeld P (1952) Les gîtes métallifères tunisiens : XIXème Congrès Géologique International, Monographies régionales, 2e série, Tunisie 2, p. 104
- Groves DI, Bierlein FP, Meinert LD, Hitzman MW (2010) Iron oxide copper-gold (IOCG) deposits through Earth history: implications for origin, lithospheric setting, and distinction from other epigenetic iron oxide deposit. *Econ Geol* 105: 641-654
- Hitzman MW, Oreskes N, Einaudi MT (1992) Geological characteristics and tectonic setting of Proterozoic iron oxide (Cu-U-Au-REE) deposits. *Precambrian Res* 58: 241-287
- Jallouli C, Mickus K, Turki MM, Rihane C (2003) Gravity and aeromagnetic constraints on the extent of Cenozoic rocks within the Nefza-Tabarka region, northwestern Tunisia. *J Volcano and Geotherm Res* 122: 51-68
- Maury RC, Fourcade S, Coulon C, El Azzouzi M, Bellon H, Coutelle A, Ouabadi A, Semroud B, Megartsi M, Cotten J, Belanteur O, Louni-Hacini A, Piqué A, Capdevila R, Hernandez J, Réhault JP (2000) Post-collisional Neogene magmatism of the Mediterranean Maghreb margin: a consequence of slab breakoff. *C R Acad Sci Paris* 331: 159-173
- Oliver NHS, Rusk BG, Blenkinsop TG, Rubenach MJ, Cleverley JS, Walshe JL, Cooke DR (2011) IOCG breccia hydrodynamics. In: Barra F et al. (eds) Let's talk ore deposits: Proceedings of the 11th Biennial SGA Meeting, Antofagasta, Ediciones Universidad Católica del Norte 2, pp 509-511
- Ould Bagga MA, Abdeljaouad S, Mercier E (2006) La "zone des nappes" de Tunisie : une marge méso-cénozoïque en blocs basculés modérément inversée (région de Tabarka/Jendouba, Tunisie nord-occidentale). *Bull Soc Géol France* 177 : 145-154
- Piqué A, Tricart P, Guiraud R, Laville E, Bouaziz S, Amrhar M, Ait Ouali R (2002) The Mesozoic-Cenozoic Atlas belt (North Africa): an overview. *Geodinamica Acta* 15: 185-208
- Porter TM (2010) Current understanding of iron oxide associated-alkali altered mineralised systems: Part I - An overview. In: Porter TM (ed) Hydrothermal iron oxide copper-gold and related deposits: A global perspective: Advances in the understanding of IOCG deposits, PGC Publishing, Adelaide 3, pp 5-32
- Rouvier H (1987) Carte géologique de la Tunisie, feuille n°10: Nefza: Service Géologique, Office National des Mines
- Rouvier H (1994) Notice explicative de la carte géologique de la Tunisie au 1/50000^e - Nefza, feuille 10: Office National des Mines, Direction de la Géologie, p. 48
- Skirrow RG (2010) "Hematite-Group" IOCGU systems: Tectonic settings, hydrothermal characteristics, and Cu-Au and U mineralizing processes. In: Corriveau L, Mumin H (eds) Exploring for iron oxide copper-gold deposits: Canada and global analogues: Geological Association of Canada, Short Course Notes 20, pp 39-58
- Skirrow RG (2011) Controls on uranium in iron-oxide copper-gold systems: insights from Proterozoic and Paleozoic deposits in southern Australia. In: Barra F et al. (eds) Let's talk ore deposits: Proceedings of the 11th Biennial SGA Meeting, Antofagasta, Ediciones Universidad Católica del Norte 2, pp 480-482
- Talbi F, Slim-Shimi N, Tlig S, Zargouni F (1999) Nature, origine et évolution des fluides dans le district minier de la caldeira d'Oued Bélif (Nefza, Tunisie septentrionale). *C R Acad Sci Paris* 328 : 153-160
- Williams P J (2010) Classifying IOCG deposits. In: Corriveau L, Mumin H (eds) Exploring for iron oxide copper-gold deposits: Canada and global analogues, Geological Association of Canada, Short Course Notes 20, pp 13-23
- Williams PJ, Barton MD, Johnson DA, Fontboté L, de Haller A, Mark G, Oliver NHS, Marschik R (2005) Iron oxide-copper-gold deposits: geology, space-time distribution, and possible modes of origin. In: Hedenquist JW, Thompson JFH, Goldfarb RJ, Richards JP (eds) Economic Geology 100 Anniversary Volume, Littleton CO, Society of Economic Geologists, pp 371-405

A new perspective on the giant Salobo IOCG deposit, Carajás Province, Brazil

Gustavo Henrique Coelho de Melo, Roberto Perez Xavier, Érika Suellen Barbosa Santiago
Geoscience Institute, University of Campinas – UNICAMP, Campinas, Brazil

Lena Virginia Soares Monteiro
Geoscience Institute, University of São Paulo – USP, São Paulo, Brazil

Antonio Fabricio Franco dos Santos, Axel Torres, Benevides Aires
VALE S.A.

Abstract. The giant Salobo deposit is the largest iron oxide-copper-gold deposit (IOCG) in the Carajás Province. It is hosted by least-altered gneiss and intensely altered rocks of uncertain origin. The latter comprises hastingsite-actinolite-, grunerite-almadine-biotite-(tourmaline)- and magnetite-rich rocks with disseminated bornite and chalcocite. The hydrothermal system evolved from early sodic-calcic (hastingsite-actinolite) alteration followed by a stage of iron-enrichment (grunerite-almadine-fayalite) and tourmaline formation. Subsequent potassic alteration I (bt) was superposed by magnetite formation, coeval with ore precipitation.

Post-ore alteration (potassic alteration II (kfs), propylitic alteration, and hematite formation) is also recognized at Salobo. It is spatially related to the Old Salobo Granite (2.547 ± 5.3 Ma) and overprints the IOCG hydrothermal alteration and mineralization. SHRIMP IIe U-Pb zircon dating for rocks affected by post-ore alteration yields ages of 2.950 ± 25 Ma and 2.857 ± 6.7 Ma, interpreted as crystallization and metamorphism ages of the host gneiss. This suggests that the Salobo deposit is hosted by extremely altered Mesoarchean basement rocks.

Keywords. Carajás, iron oxide-copper-gold, Salobo, SHRIMP U-Pb geochronology

1 Introduction

The Carajás Province represents an Archean nucleus in southeastern part of the Amazon Craton and hosts Archean and Paleoproterozoic world-class oxide-copper-gold (IOCG) deposits. Amongst these deposits, Salobo stands out as one of the most important of this class in the world due to its giant reserves of 1.112 billion tonnes @ 0.69% wt% Cu and 0.43 g/t Au (VALE, 2012).

The Salobo deposit occurs along the WNW-ESE-striking Cinzento Transcurrent Shear Zone located in the northern portion of the Carajás Province near to the limit with the Paleoproterozoic Bacajá Domain (2.26 – 1.90 Ga, Vasquez *et al.*, 2008).

Hydrothermal processes produced mineral assemblages with grunerite, tourmaline, almadine,

biotite, fayalite, and abundant magnetite associated with the copper-gold ore zones (Lindenmayer 1990; Lindenmayer 2003). However, the evolution of the Salobo deposit has been considered controversial, especially regarding the nature of the host rocks and the relationship of the alteration-mineralization with the 2.57 Ga Old Salobo Granite (Réquia *et al* 2003).

New geological, paragenetic and geochronological data presented for the Salobo deposit in this work intend to shed more light to these issues and lead to a new perspective for the evolution of the Salobo deposit.

2 Geology of Salobo deposit

The Salobo host rocks were strongly ductilely deformed in the Itacaiúnas (ca. 2.7 Ga) and Cinzento (2.555 ± 4 Ma; Machado *et al.* 1991) shear zones (Fig. 1). Basement gneissic rocks predominate in most of the Salobo area. However, least deformed gneisses are recognized only in the outskirts of the shear zones, whereas inboard they display a penetrative NW-SE subvertical mylonitic foliation and hydrothermal alteration.

The central zone of the deposit comprises intensely hydrothermally altered rocks variably mylonitised. Two granites crosscut the Salobo host rocks namely the Old Salobo (2.573 ± 2 Ma; zircon U-Pb; Machado *et al.* 1991) and the Young Salobo granites (1.880 ± 80 Ma; Rb-Sr; Cordani 1981).

Quartz mylonite has been identified in the southern part of the deposit by a crest in the relief. The origin of this lithotype remains uncertain; either it is a mylonitised quartzite or it is product of intense silicification within the shear zone.

2.1 Least-altered rocks

The gneiss is a foliated and banded rock with composition ranging from granodiorite to sienogranite. Proximal towards ore and shear zone, the gneiss shows mylonitic foliation and microstructures developed during shearing, such as

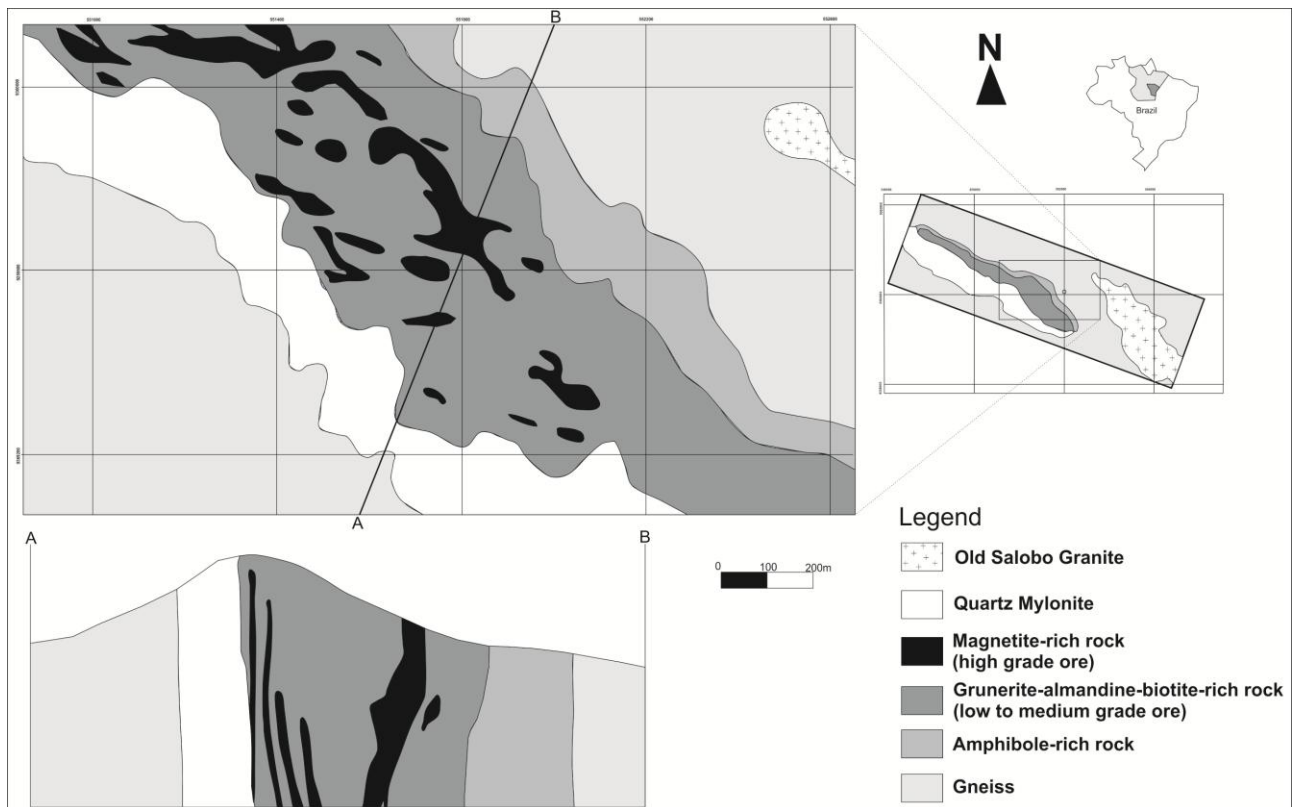


Figure 1. Geological map and profile of the Salobo deposit showing the least-altered and hydrothermally altered rocks of the deposit within a NW-SE-striking shear zone (modified from VALE).

quartz ribbon, deformation lamellae, undulose extinction, formation of subgrains in quartz, and deformation and bent twins in plagioclase, pointing to conditions over 400 °C up to 500 °C during deformation (Passchier & Trouw, 2005). The mafic minerals are hydrothermal phases represented by hastingsite, actinolite, and biotite.

The Old Salobo Granite is alkaline, mesozonal, metaluminous, and syn-tectonic (Lindenmayer 1990). It is represented by foliated rock in some portions, has granodioritic to tonalitic composition, and augite and hastingsite (Lindenmayer 1990) as the mafic minerals. It shows a distinct hydrothermal alteration pattern from the gneiss and the mineralization zones, characterized by potassic alteration II (kfs) with associated hematite, propylitic alteration and incipient chlorite formation.

The Young Salobo Granite is alkaline, metaluminous and anorogenic (Lindenmayer 1990). It is an isotropic rock with granodioritic composition that lacks hydrothermal alteration.

2.2 Hydrothermal alteration

The initial stage of the hydrothermal alteration at Salobo is only recognized in distal and very restricted portions of the deposit. Hastingsite formation may represent an early and incipient sodic-calcic alteration related to the first fluid pulses of the hydrothermal system. However, it was observed only where the gneiss has no mylonitic foliation.

A better developed and pervasive sodic-calcic alteration with actinolite associated with subordinated allanite, scapolite, and chalcopryrite has also been recognized in gneiss from distal portions of the deposit.

Although protolith textures may be locally recognized, the actinolite abundance accompanies the increase of intensity of hydrothermal alteration towards more deformed zones, where it gradually replaces primary minerals of the gneiss to form amphibole-rich rocks.

Quartz veins and pervasive silicification developed in several stages. Hydrothermal quartz shows undulose extinction, subgrain formation and ribbon texture, indicating its pre- to syn-tectonic crystallization.

The main hydrothermal alteration pattern can be recognized almost throughout the central zone of the Salobo deposit and encompasses iron enrichment revealed by the formation of Fe-rich amphibole (grunerite), which replaces the Ca-Na amphibole. Thus, it is possible to determine the evolution from the least altered hastingsite-(actinolite)-bearing gneiss to strongly hydrothermally altered grunerite-(actinolite)-rich rocks. In the latter, protolith characteristics have been completely obliterated. Fayalite also formed in the iron-rich alteration stage. It is restricted to proximal alteration zones in relation to orebodies, and commonly it has been replaced by greenalite.

In the iron-rich alteration zones, there is also a large concentration of hydrothermal almandine and tourmaline. In less deformed portions of the rock, these minerals occur as idioblastic porphyroblasts with up to 4 cm and 2 cm diameter, respectively, and commonly contain grunerite inclusions. Stretched almandine and tourmaline crystals with pressure shadows are common in foliated rocks, indicating that these minerals may have been formed mostly prior the development of the mylonitic foliation.

Potassic alteration I (bt) also represents an important hydrothermal alteration at Salobo. Biotite replaces primarily the grunerite crystals in the least-altered zones.

In strongly altered zones, biotite-rich rocks (over 60% of biotite) also contain almandine, tourmaline, and grunerite. There is a strong association of biotite abundance and the development of mylonitic foliation. Stilpnomelane occurs associated to the ore. Magnetite-rich rocks with more than 50% of magnetite are the locus of copper-gold mineralization. Magnetite crystals are idioblastic in less deformed zones or highly stretched in more deformed rocks.

The Salobo deposit also shows a post-ore alteration that clearly overprints the hydrothermal alteration related to the main copper-gold mineralization stage. This alteration is completely distinct from the previous stages. It is characterized by potassic alteration II (kfs) related to (i) an initial stage with potassium feldspar recognized in veins and veinlets; (ii) selective style resulting in replacement of garnet porphyroblasts by potassium feldspar; and (iii) intense pervasive alteration giving a strong red color for the altered rocks. Propylitic alteration formed epidote, chlorite, sericite, and carbonate. It is an incipient alteration commonly found either associated with veinlets or in selective style. The exception is chlorite, which is locally pervasive and locally replaces garnet porphyroblasts. Hematite is strongly associated with potassium feldspar as tiny inclusions, but also pseudomorphs garnet producing rocks variably enriched in hematite. This post-ore alteration pattern is very similar to that identified for the Old Salobo Granite and is spatially closely related to it.

2.3 Copper-Gold Ore

The copper-gold ore is disseminated and confined in some veinlets in the zones of intense potassic alteration I (bt) associated with iron-enrichment (grunerite, almandine, fayalite, magnetite). The concentration of the sulphides increases with the intensity of potassic alteration I (bt) and predominantly with the presence of magnetite. The ore is composed mainly of bornite and chalcocite commonly with myrmekitic-symplectite texture. Chalcopyrite, molybdenite, uraninite, ilmenite, graphite, Co-pentlandite, covelite, digenite, hematite, and native copper have been also identified in the ore (Lindenmayer 2003). Gold occurs as inclusions in bornite, chalcocite, and chalcopyrite.

3 Geochronology

SHRIMP IIe U–Pb zircon data for the Old Salobo Granite and host rock affected by late post-ore alteration have been acquired at the CPGeo, University of São Paulo.

3.1 Old Salobo Granite

Most of the zircon crystals of the Old Salobo Granite are murky pink, ranging from prismatic to rounded grains with eroded edges. All of the zircon grains are strongly metamict showing low luminescence in cathodoluminescence images. Thirteen zircon grains yielded a concordant age of 2.547 ± 5.3 Ma (MSWD = 0.26) and a discordant age with upper intercept of $2.551.3 \pm 9.0$ Ma (MSWD = 0.92) (Fig. 2).

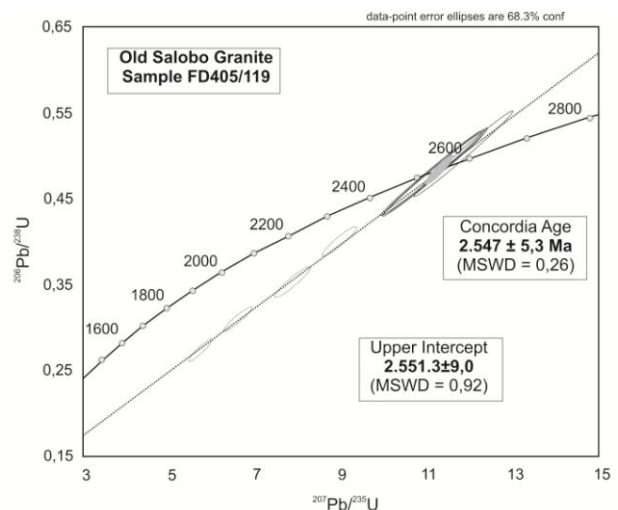


Figure 2. $^{206}\text{Pb}/^{238}\text{U}$ vs. $^{207}\text{Pb}/^{235}\text{U}$ diagrams for the Old Salobo Granite.

3.2 Host rock with post-ore alteration

Zircon occurs as prismatic euhedral grains with igneous oscillatory zonation or as rounded fragments without zonation in host rocks affected by post-ore alteration. Zircon crystals show low to moderate luminescence, as well as internal fractures in the backscattered images. Twelve analyzed zircon grains yielded two concordant ages of 2.950 ± 25 Ma (MSWD = 5.9) and 2.857 ± 6.7 Ma (MSWD = 0.00066) (Fig. 3). These two distinct ages reflect the differences among zircon grains: the older crystals show no zonation, whereas the younger zircon occurs as prismatic grains with oscillatory zonation.

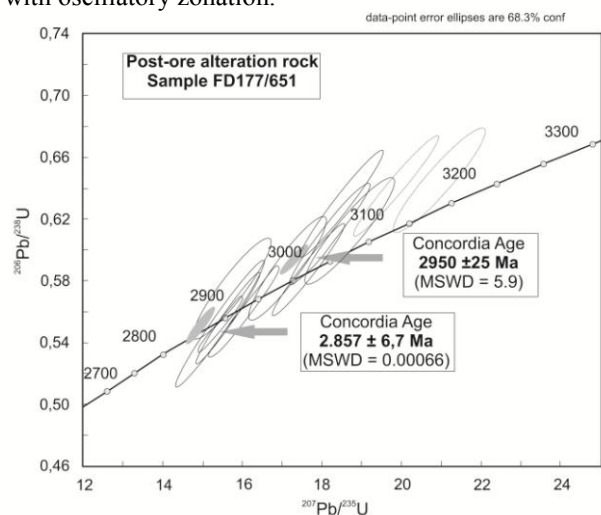


Figure 3. $^{206}\text{Pb}/^{238}\text{U}$ vs. $^{207}\text{Pb}/^{235}\text{U}$ diagrams for host rock with post-ore alteration.

4 Discussion

Previous studies attributed volcanic rocks of the ca. 2.76 Ga Igarapé Salobo Group, such as basalts and dacites, as the main hosts to the copper-gold mineralization in the Salobo deposit (Lindenmayer 2003; Réquia *et al.*, 2003). Detailed characterization of the host rocks carried out in this study, however, reveal the predominance of variably deformed quartzo-feldspathic rocks very similar to the basement migmatite-gneiss represented in the Salobo area by the Cascata and Upper Farias gneiss (Machado *et al.*, 1991). Therefore, it is

proposed that the Salobo deposit is hosted by basement rocks, which have been altered to rocks containing variable amounts of hastingsite-actinolite-, grunerite-almadine-biotite-tourmaline- and magnetite. These gneissic rocks are crosscut by a NW-SE-striking shear zone that may have played an important role in the evolution of the Salobo deposit, but postdates early hydrothermal alteration.

The strong hydrothermal alteration encompasses an initial and incipient sodic-calcic alteration stage, iron-enrichment, strong potassic alteration I (bt) and ore formation. The precipitation of the ore may have been temporally associated with the iron-enrichment alteration, but it was intensified during the potassic alteration I (bt) and magnetite formation. The evolution of Salobo IOCG system points to a decrease in the temperature, which can be one of the mechanisms that triggered the ore precipitation. This IOCG-related hydrothermal alteration lacks a clear relationship with any intrusion that occurs in the deposit and it is more likely associated with the shear zone development.

Post-ore hydrothermal alteration is distinct from the IOCG-related alteration. It is marked by potassic alteration II (kfs) (with hematite) and propylitic alteration, very similar to that described for the Old Salobo Granite, suggesting a genetic relationship with its emplacement. The post-ore alteration also points to increase of fO_2 conditions associated notably with zones enriched in hematite.

Host rocks affected by different hydrothermal alteration stages, including the post-ore alteration, show two zircon population dated in 2950 ± 25 Ma and 2857 ± 6.7 Ma. These concordant ages are consistent with those attributed to the basement rocks (2859 ± 2 Ma, Machado *et al.* 1991). These ages are interpreted as the timing of crystallization of the igneous protolith and of medium to high grade metamorphism possibly accompanied by anatexis, respectively. The geochronological data also evidences that the hydrothermal alteration and ore zones have been developed from basement rocks at Salobo.

New SHRIMP II geochronological data constrain the age of the Old Salobo Granite at 2547 ± 5.3 Ma, approximately the same age as previously obtained by Machado *et al.* (1991) (2573 ± 2 Ma; zircon U–Pb). These relatively distinct ages might reflect differences in the achievement of the data. Previous age (Machado *et al.* 1991) was obtained using ID-TIMS in which only two zircon crystals were analyzed through their dissolution. Moreover, the northern sector of Carajas Province shows a wide range of ages near ca. 2.5 Ga, as noted in previous studies regarding minerals along shear zones (e.g., Machado *et al.* 1991; Tassinari *et al.* 2003; Réquia *et al.* 2003). This likely reflects an important thermal event associated with the reactivation of the Cinzento Transcurrent Shear Zone.

The recognition of post ore alteration spatially related with the ca. 2.55 Ga Old Salobo Granite reveal overprinting of hydrothermal events and a more complex evolution for the Salobo deposit.

Acknowledgements

We are very grateful to VALE for the continuous support in the Carajás region. We are very grateful to VALE for the continuous support, especially to geologists Benevides Aires and to the technical geology Matheus Azevedo Alves. This research has been supported by the MCT/CNPq/CTMineral 555065/2006-5, CNPq 303359/2008-0, 472549/2009-0 and INCT Geociências da Amazônia (MCT/CNPq/Fapespa 573733/2008-2) and CNPq/UNICAMP scholarship.

References

- DOCEGEO (1988) Revisão litoestratigráfica da Província Mineral de Carajás - Litoestratigrafia e principais depósitos minerais. 35° Congr. Bras. Geol., Belém, SBG, Proceedings, pp 11–54
- Figueiredo, B (2000) Os sulfetos de cobre, in Minérios e ambiente, Campinas, pp. 73-85
- Lindenmayer ZG (2003) Depósito de Cu–Au do Salobo, Serra dos Carajás: Uma revisão. In: Ronchi LH, Althoff FJ (eds) Caracterização e modelamento de depósitos minerais. Editora Unisinos, São Leopoldo, pp 69–98
- Lindenmayer, Z.G., (1990) Salobo sequence, Carajás, Brasil: Geology, Geochemistry and Metamorphism; PhD thesis, University of Ontario, Canada, 407p.
- Machado N, Lindenmayer DH, Krough TE, Lindenmayer ZG (1991) U–Pb geochronology of Archean magmatism and basement reactivation in the Carajás area, Amazon Shield, Brazil. *Precambrian Res* 49:1–26
- Réquia K, Stein H, Fontboté L, Chiaradia M (2003) Re-Os and Pb-Pb geochronology of the Archean Salobo iron oxide copper-gold deposit, Carajás Mineral Province, northern Brazil: *Mineralium Deposita* 38: 727-73
- Passchier, CW.; Trouw, RAJ (2005) *Deformation Mechanisms*, in *Micro-tectonics*, second edition, Germany, pp. 25-63
- Vale (2012) Vale obtains operation license for Salobo. <http://saladeimprensa.vale.com/en/release/interna.asp?id=22000>. Accessed 04 february 2013
- Vasquez LV, Rosa-Costa LR, Silva CG, Ricci PF, Barbosa JO, Klein EL, Lopes ES, Macambira EB, Chaves CL, Carvalho JM, Oliveira JG, Anjos GC, Silva HR (2008) *Geologia e Recursos Minerais do Estado do Pará: Sistema de Informações Geográficas —SIG: texto explicativo dos mapas Geológico e Tectônico e de Recursos Minerais do Estado do Pará* Organizadores, Vasquez ML, Rosa-Costa LT. 1:1.000.000. CPRM, Belém.

Metallogenetic evolution of the Archean and Paleoproterozoic Iron oxide Cu-Au systems in the southern copper belt, Carajás Province

Carolina P. N. Moreto

Geoscience Institute, University of Campinas, Rua João Pandiá Calógeras 51, Campinas, Brazil

Lena V. S. Monteiro

Geoscience Institute, University of São Paulo, Rua do Lago 562, São Paulo, Brazil

Roberto P. Xavier

Geoscience Institute, University of Campinas, Rua João Pandiá Calógeras 51, Campinas, Brazil

Robert A. Creaser, Andy DuFrane

Department of Earth and Atmospheric Sciences, University of Alberta, Edmonton, Canada

Wagner S. Amaral, Marco A. D. Silva, Gustavo H. C. Melo

Geoscience Institute, University of Campinas, Rua João Pandiá Calógeras 51, Campinas, Brazil

Abstract. The Southern Copper Belt of the Carajás Province, Brazil, hosts the Sossego (Sequeirinho-Pista-Baiano and Sossego-Curral orebodies), Cristalino, Alvo 118, Bacuri, Bacaba, Castanha, Visconde, and Jatobá iron oxide–copper–gold (IOCG) deposits, which are situated within a WNW–ESE-striking shear zone. The host rocks of these deposits (e.g., porphyry, gabbro, mafic volcanic and meta-ultramafic rocks, granites and migmatites) were affected by Na, Na-Ca, K and chlorite alteration, followed by quartz, sericite, and epidote–calcite–chlorite formation. U-Pb LA-MC-ICPMS dating of hydrothermal monazite and Re-Os NTIMS in molybdenite indicate recurrence of IOCG events in the Southern Copper Belt. The Sequeirinho-Pista-Baiano orebodies, and the Bacuri, Bacaba, Visconde and Cristalino deposits were formed during 2.71–2.68 Ga, whereas IOCG genesis of the Sossego-Curral orebodies and the Alvo 118 deposit took place at 1.90–1.87 Ga. The Neoarchean IOCG event could have been triggered by hydrothermal fluid circulation related to the 2.7 Ga reactivation of main shear zones, due to the tectonic inversion of the Carajás basin. The Paleoproterozoic IOCG-forming event is possibly linked to heat sources associated with the emplacement of several A-type granites at the Carajás Province. Reworking of the Neoarchean IOCG deposits by the Paleoproterozoic fluids is suggested.

Keywords. IOCG deposits, Carajás Province, Southern Copper Belt, Re-Os NTIMS, U-Pb LA-MC-ICPMS.

1 Introduction

Most of the known IOCG deposits from the Carajás Province are situated in the Carajás Domain along or close to two distinct E-W and WNW-ESE-trending regional shear zones (>130 km-long), located at the northern and southern contacts between the ca. 2.76 Ga metavolcano-sedimentary rock units of the Itacaiúnas Supergroup (Carajás basin) and the Mesoarchean basement rocks. The Southern Copper Belt, which is the aim of this study, includes the Sossego, Cristalino and Alvo 118 deposits, and several other minor deposits, such as the Bacaba, Castanha, Bacuri, Visconde, and Jatobá IOCG deposits. Additionally, diverse barren massive magnetite bodies have also been recognized.

Succinctly, the deposits from the Southern Copper Belt were affected by sodic (albite–scapolite–iron oxide), sodic-calcic (actinolite-rich bodies) alteration, iron oxide formation, potassic and chlorite alteration, late sericite, epidote and carbonate formation (Monteiro et al., 2008a,b; Augusto et al. 2008; Moreto et al. 2011a; Pestilho 2011; Melo et al. Submitted). The marialitic scapolite alteration is particularly pervasive in the Bacaba, Bacuri, Visconde, Jatobá, and Castanha deposits, but is also present at the Pista orebody (Sossego deposit). Veins (>10 m wide) containing marialite (+ quartz, magnetite) are observed in drill cores. Furthermore, large magnetite- and actinolite-rich bodies (Na-Ca alteration) are widely recognized at the Castanha deposit and Sequeirinho orebody.

The types and distribution of hydrothermal alteration zones, fluid inclusion and stable isotope data (Monteiro et al. 2008a; Pestilho 2011; Torresi et al. 2012) suggest that the IOCG deposits from the Southern Copper Belt were formed at a range of depths, and that the hydrothermal fluids had variable sources.

However, a deeper comprehension and comparison between these deposits is limited by the scarcity of geochronological data that allows to define the ages of the alteration and IOCG mineralizing event(s).

This study presents new geochronological data, such as Re-Os in molybdenite and U-Pb LA-MC-ICPMS in hydrothermal monazite of the Sossego, Bacaba and Bacuri deposits aiming to determine the age interval(s) of IOCG formation. These results not only provide new insights into the timing of IOCG formation, but also give a clearer comprehension of the IOCG metallogenesis at the Southern Copper Belt.

2 IOCG deposits from the Southern Copper Belt

Detailed mapping in the central-west part of the Southern Copper Belt, where the Sossego, Bacaba, Castanha, Bacuri, and Visconde deposits are located, revealed the existence of felsic subvolcanic rocks, including the 2.74 Ga Castanha quartz-feldspar

porphyry, mafic intrusive and volcanic rocks, Mesoproterozoic to Neoproterozoic granitic rocks (e.g., Serra Dourada granite, Bacaba and Campina Verde tonalites, and Rio Verde trondhjemite), and migmatites (Xingu Complex). These rocks are isotropic to foliated close to several shear zones that cut the entire area. Additionally, diverse mylonitized meta-ultramafic rocks, represented by tremolite-talc schists, are tectonically imbricated along these discontinuities. Interestingly, there is a clear spatial relationship between the meta-ultramafic occurrences and Cu prospects (malachite) in the area.

The Bacaba and Bacuri deposits are both hosted by the 2.86 Ga Serra Dourada granite (Moreto et al. 2011a) and crosscutting gabbro. The 3.0 Ga Bacaba tonalite is also present in drill cores from the Bacaba deposit, whereas subvolcanic rocks of rhyolitic composition are recognized at the Bacuri deposit (Moreto et al. 2011a, Melo et al. Submitted).

The Sossego deposit, which is composed of two sets of orebodies (Pista-Sequeirinho-Baiano and Sossego-Curral) is hosted by the 3.0 Ga Sequeirinho granite (Moreto et al. 2011b), 2.96 Ga Pista felsic metavolcanic rock, and the 2.74 Ga Sossego gabbro and Sossego granophyric granite (Moreto et al. 2011b). The Pista metavolcanic rock contains lenses of intensively deformed meta-ultramafic rocks. The existence of gabbros and granites with the same age point to a bimodal character of the 2.74 Ga magmatism.

The Alvo 118 deposit is hosted by mafic and felsic metavolcanic rocks, gabbros, granites ($2,743 \pm 3$ Ma; Pb-Pb SHRIMP II zircon; Tallarico 2003) and rhyolitic porphyry dikes ($2,645 \pm 9$ Ma, Pb-Pb SHRIMP II zircon; Tallarico 2003).

In these deposits, high temperature ($> 550^\circ\text{C}$) sodic to iron-potassic hydrothermal alteration that was synchronous with ductile deformation was followed by lower temperature ($< 300^\circ\text{C}$) chloritic, carbonatic and hydrolytic alteration stages (Monteiro et al. 2008a,b). Copper-gold mineralization was associated with low-temperature alteration and hydrostatic brittle conditions (Monteiro et al. 2008a,b).

3 Timing of IOCG mineralization at the Carajás Province

Based on the geochronological data available in the literature, it is unlikely to assure a genetic link for all the IOCG deposits of the Carajás Province. Most of the data refers to the deposits located in the Northern Copper Belt (e.g., Salobo, Igarapé Bahia/Alemão, Igarapé Cinzento and Gameleira deposits), whereas less geochronological studies were conducted in the IOCG deposits from the Southern Copper Belt. Distinct methods have been used to date ore-related minerals and their host rocks, and considerably different ages were obtained, even in a single deposit. (e.g., Igarapé Bahia/Alemão, Gameleira, Salobo, and Igarapé Cinzento deposits). Re-Os in molybdenite (Salobo deposit; Rêquia et al. 2003) and U-Pb SHRIMP in hydrothermal monazite (Igarapé Bahia deposit; Tallarico et al. 2005) point to an important metallogenetic event at 2.57 Ga in the Northern Copper Belt.

In the Southern Copper Belt, U-Pb SHRIMP II in

hydrothermal xenotime from the Alvo 118 deposit (Tallarico 2003) suggests ore genesis at 1.88 Ga. The other available data were obtained by Pb-Pb systematic. Chalcopyrite from the Visconde and Cristalino deposits yielded Neoproterozoic ages of 2.74 Ga and 2.70 Ga, respectively, which were interpreted as the timing of mineralization at these deposits (Soares et al. 2001; Silva et al. 2012). At the Sossego deposit, chalcopyrite concentrates from the Sequeirinho and Sossego orebodies provided the 2.53 Ga and 1.59 Ga Pb-Pb ages, respectively, which were attributed to isotopic resetting due to subsequent thermal/ deformational events (Neves 2006).

4 U-Pb and Re-Os Geochronology

Re-Os molybdenite and U-Pb LA-MC-ICPMS monazite data for the Sossego (Sequeirinho, Pista, Sossego and Curral orebodies), Bacaba and Bacuri deposits were acquired at the Radiogenic Isotope Facility of the University of Alberta, Edmonton, Canada. Full descriptions of the analytical approaches are reported by Selby and Creaser (2004), Simonetti et al. (2005), and Markey et al. (2007).

4.1 Re-Os NTIMS

Three samples of molybdenite were selected for the Re-Os systematic, including two mineralized samples from the Pista orebody (Sossego deposit) and one from the Bacuri deposit. Samples SOS 364/76.84 and SOS 364/160.9 from drill cores of the Pista orebody were hosted by the 2.96 Ga Pista metavolcanic rock intensively affected by pervasive sodic alteration (albite) and silicification along mylonitic foliation, than cut by chlorite-rich zones. Sample SOS 364/76.84 has fine-grained (~1 mm) molybdenite crystals associated with chalcopyrite, chlorite and quartz, and yielded a Re-Os model age of $2,685 \pm 11$ Ma. Molybdenite crystals from sample SOS 364/160.9 are disseminated in quartz veinlets also containing chalcopyrite and albite. This sample reached a Re-Os model age of $2,710 \pm 11$ Ma.

Ore sample BRID 01/45 from the Bacuri deposit is hosted by foliated Serra Dourada granite affected by pervasive silicification and chlorite alteration. Fine-grained molybdenite and chalcopyrite are associated with calcite, and occur as centimeter-wide veinlet deformed along the mylonitic foliation. Molybdenite crystals produced a Re-Os model age of $2,758 \pm 11$ Ma.

4.2 U-Pb LA-MC-ICPMS

Hydrothermal monazite crystals were extracted from ore breccia of the Sequeirinho (SOS 259/270), Sossego (Min-Cp-SOS and SOS315/255.1) and Curral orebodies (SOS106/84) of the Sossego deposit, and from the Bacuri (BRID/115.42) and Bacaba (BACD25/229.25 and BACD15/237.4) deposits. A brief description of the samples and the U-Pb results, which yielded ages between ca. 2.72 to 1.89 Ga, are summarized in Table 1. Some of the U-Pb concordia diagrams for the Sossego, Bacuri, and Bacaba deposits are illustrated in Figures 1 and 2.

5 Discussion and conclusions

The geochronological data (Re-Os in molybdenite and U-Pb in hydrothermal monazite) presented in this study (Sossego, Bacaba and Bacuri deposits) combined with also reliable data from the Alvo 118 deposits (U-Pb in hydrothermal xenotime; Tallarico 2003) and Pb-Pb systematics (chalcopyrite) from the Cristalino and Visconde deposits (Soares et al. 2001; Silva et al. 2012) suggest that multiple Neoproterozoic and the Paleoproterozoic hydrothermal systems were responsible for alteration and/or IOCG ore formation at the Southern Copper Belt.

Multiple hydrothermal events took place at: i) 2.76 Ga, recorded in molybdenite from the Bacuri deposit, which predate the main stage of ore formation; ii) 2.71-2.70 Ga, registered in hydrothermal monazite from the Bacuri and Bacaba deposits, and Sequeirinho orebody, and molybdenite from the Pista orebody; iii) 2.68 Ga, obtained in hydrothermal monazite and molybdenite from the Bacaba deposit and Pista orebody, respectively; iv) 2.05 Ga, recorded in hydrothermal monazite from the Bacaba deposit; v) 1.90 Ga, evidenced by hydrothermal monazite grains crystallized at the Sossego orebody; vi) 1.88-1.87 Ga, suggested by hydrothermal monazite from the Sossego and Curral orebodies, and hydrothermal xenotime from Alvo 118 deposit.

Table 1. Synthesis of the results of U-Pb dating of monazite

Rock	Age (Ma)	MSWD
Sossego deposit		
<i>Sequeirinho orebody</i>		
Ore breccia (SOS 259/270)	2,712.3±4.7	1.6
<i>Sossego orebody</i>		
Ore breccia (Min-Cp-SOS)	1,878.9±4.1	1.3
Ore breccia (SOS 315/255.1)	1,904±5.2	1.2
<i>Curral orebody</i>		
Ore breccia (SOS 106/84)	1,889.8±8.5	2.7
Bacuri deposit		
Chlorite and scapolite altered rock (BRID 07/115.42)	2,703.0±5.8	3.9
Bacaba deposit		
Ore hosted by the Bacaba Tonalite (BACD 25/229.25)	2,681±11	3
	2,054.1±8.8	10.2
Albite altered and silicified Serra Dourada Granite (BACD 15/237.4)	2,716.4±8.4	2.4

The Pb-Pb ages from the Visconde ($2,747 \pm 140$ Ma, MSWD=12; Silva et al. 2012) and Cristalino ($2,700 \pm 29$ Ma, MSWD=656; Soares et al. 2001) deposits are very imprecise due to their large errors, and for this reason were not associated with any interval of a hydrothermal event as shown above. However, the data possibly indicate that the event(s) responsible for ore genesis likely took place in the Neoproterozoic instead of the Paleoproterozoic.

The 2.71-2.68 Ga and 1.90-1.87 Ga intervals are interpreted as the main episodes of IOCG ore formation at the Southern Copper Belt. Younger ages (< 2.05 Ga) evidence remobilization and overprinting of new

systems in previous altered zones. In this sense, recurrence of IOCG events, even at a single deposit scale, is suggested in the Southern Copper Belt.

The older 2.76 Ga hydrothermal event is contemporary with the deposition of the metavolcanic-sedimentary rock sequence that filled the Carajás basin. Hydrothermal fluids from the basin may have circulated through crustal weaknesses (e.g., previously active shear zones), close to the Bacuri deposit.

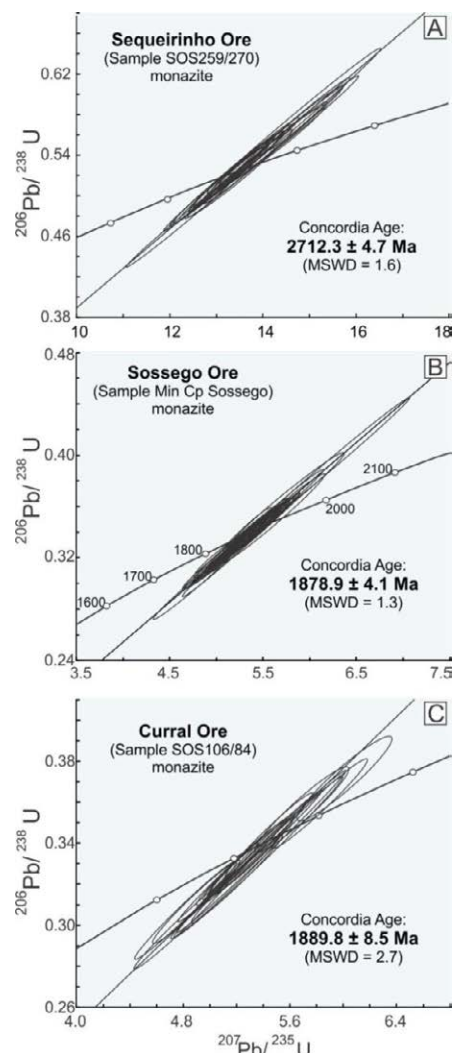


Figure 1. Monazite U-Pb diagrams for the Sossego deposit. A) Sequeirinho; B) Sossego; and C) Curral orebodies

Contrarily, the 2.71-2.68 Ga IOCG events are apparently not directly related to a magmatic event in the Southern Copper Belt. For this episode it is proposed that the circulation of the hydrothermal fluids, causing metal leaching from the country rocks and subsequent ore deposition, is related to the 2.7 Ga reactivation of the previously formed major crustal discontinuities, associated with the tectonic inversion of the Carajás basin. Alternatively, ore fluids may have ascended along these regional discontinuities.

The late Rhyacian (2.05 Ga) event, similarly to the ca. 2.70 Ga event, does not overlap in time with any magmatism so far recorded at the Carajás Province. This system could have also been triggered by heat sources related to another reactivation of the regional shear zones, linked to a weak tectonic inversion of the Carajás

basin between 2.0 to 1.8 Ga. Finally, with respect to the Orosirian (1.9-1.87 Ga) episode of IOCG formation, it is likely that the widespread 1.88 Ga anorogenic magmatism in the Carajás Province provided heat sufficiently high to cause the circulation of hydrothermal fluids at a regional scale, including the crustal discontinuities in the Southern Copper Belt.

The extensive zones of chlorine-bearing marialitic scapolite alteration in the rocks from the Southern Copper Belt may have played an important role in the episodicity of hydrothermal and ore systems. This type of sodic alteration is not only widely recognized in several deposits (e.g., Bacaba, Castanha, Bacuri, Sequeirinho; Monteiro et al. 2008a, Augusto et al 2008, Moreto et al 2011a; Pestilho 2011) but also widespread through the country and host rocks. Regional migration of hydrothermal fluids through areas with widespread marialite alteration possibly released chlorine and sodium to the hydrothermal fluid, increasing its total salinity and, therefore, the capacity of metal (Cu) transport.

These hot and saline fluids may have caused reworking of Neoproterozoic IOCG deposits, leading to remobilization and subsequent new ore deposition.

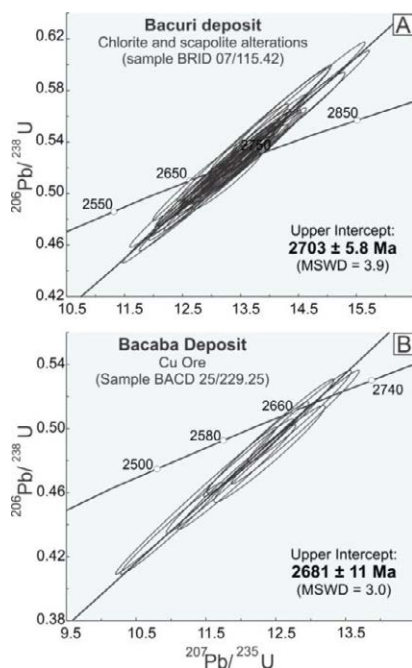


Figure 2. Monazite U-Pb diagrams for the A) Bacuri and B) Bacaba deposits

Acknowledgements

We are very grateful to the VALE Company, notably to Márcio Godoy, Benevides Aires and Cleive Ribeiro for their invaluable assistance. This research was funded by CNPq (555065 /2006-5, 472549 /2009-0 and 303359 /2008-0), INCT GEOCIAM (CNPq/ MCT/ FAPESPA 573733/ 2008-2), and Fapespa/VALE Grant. Carolina P. N. Moreto also thanks FAPESP (2009/ 18371-0) for the PhD scholarship.

References

Augusto RA, Monteiro LVS, Xavier R, Souza Filho CR (2008) Zonas de alteração hidrotermal e paragéneses do minério de cobre do Alvo Bacaba, Província Mineral de Carajás (PA). Rev

- Bras Geocienc 38(2): 263-277
- Markey RJ, Stein HJ, Hannah JL, Selby D, Creaser R (2007) Standardizing Re-Os geochronology: A new molybdenite Reference Material (Henderson, USA) and the stoichiometry of Os salts. *Chem Geol* 244:74-87
- Melo GHC, Monteiro LVS, Xavier RP, Moreto CPN, Silva MAD (Submitted) Bacuri copper deposit: host rocks, hydrothermal alteration and characterization of the copper ore, Carajás Province (PA). *Rev Bras Geocienc*, 15pp
- Monteiro LVS, Xavier RP, Carvalho ER, Hitzman MW, Johnson CA, Souza Filho CR, Torresi I (2008a) Spatial and temporal zoning of hydrothermal alteration and mineralization in the Sossego iron oxide-copper-gold deposit, Carajás Mineral Province, Brazil: paragenesis and stable isotope constraints. *Miner Depos* 43:129-159
- Monteiro LVS, Xavier RP, Hitzman MW, Juliani C, Souza Filho CR, Carvalho ER (2008b) Mineral chemistry of ore and hydrothermal alteration at the Sossego iron oxide-copper-gold deposit, Carajás Mineral Province, Brazil. *Ore Geol Rev* 34:317-336
- Moreto CPN, Monteiro LVS, Xavier RP, Amaral WS, Santos TJS, Juliani C, Souza Filho CR (2011a) Mesoarchean (3.0 and 2.86 Ga) host rocks of the iron oxide-Cu-Au Bacaba deposit, Carajás Mineral Province: U-Pb geochronology and metallogenetic implications. *Miner Depos* 46:789-811
- Moreto CPN, Monteiro LVS, Xavier RP, Kemp TIS, Souza Filho CR (2011b) In situ LA-ICPMS U-Pb zircon dating of the host rocks of the Sossego and Bacaba iron oxide-copper-gold deposits, Carajás Mineral Province, Brazil. *Proceedings of the 11th Biennial SGA Meeting*. Antofagasta, Chile
- Neves MP (2006) Estudos isotópicos (Pb-Pb, Sm-Nd, C e O) do depósito Cu-Au do Sossego, Província Mineral de Carajás. M.Sc. thesis, Universidade Federal do Pará, 116 p
- Pestilho ALS (2011) Sistemática de isótopos estáveis aplicada à caracterização da evolução dos paleo-sistemas hidrotermais associados aos depósitos cupríferos Alvo Bacaba e Alvo Castanha, Província Mineral de Carajás, PA. M.Sc thesis, Universidade Estadual de Campinas, 71 p
- Réquia, K., Stein, H., Fontboté, L., and Chiaradia, M., 2003, Re-Os and Pb-Pb geochronology of the Archean Salobo iron oxide copper-gold deposit, Carajás Mineral Province, northern Brazil: *Miner Depos* 38:727-738
- Selby D, Creaser RA (2004) Macroscale NTIMS and microscale LA-MC-ICP-MS Re-Os isotopic analysis of molybdenite: Testing spatial restrictions for reliable Re-Os age determinations, and implications for the decoupling of Re and Os within molybdenite. *Geochim Cosmochim Acta* 68:3897-3908
- Simonetti A, Heaman LM, Hartlaub RP, Creaser RA, Machattie TG, Bohm C (2005) U-Pb zircon dating by laser ablation MC-ICP-MS using a new multiple ion counting Faraday collector array. *J Anal At Spectrom* 20:677-686
- Silva ARC, Villas RNN, Lafon JM, Craveiro GS (2012) Idade da alteração e mineralização do depósito de Cu-Au Visconde, Província Mineral de Carajás (Pará), Brasil. 46^o Cong Bras Geol, Santos.
- Soares ADV, Macambira MJB, Santos MGS, Vieira EAP, Massoti FS, Souza CIJ, Padilha JL, Magni MCV (2001) Depósito Cu-(Au) Cristalino, Serra dos Carajás, PA: Idade da mineralização com base em análises Pb-Pb em sulfetos (dados preliminares): VII Simp Geol Amaz, SBG, Belém
- Torresi I, Bortholoto DFA, Xavier RP, Monteiro LVS (2012) Hydrothermal alteration, fluid inclusions and stable isotope systematics of the Alvo 118 iron oxide-copper-gold deposit, Carajás Mineral Province (Brazil): implications for ore genesis. *Miner Depos* 47:299-323
- Tallarico FHB (2003) O cinturão cupro-aurífero de Carajás, Brasil. Ph.D. Dissertation, Universidade Estadual de Campinas, 229 p
- Tallarico FHB, Figueiredo BR, Groves DI, Kositcin N, McNaughton NJ, Fletcher IR, Rego JL (2005) Geology and SHRIMP U-Pb geochronology of the Igarapé Bahia deposit, Carajás copper-gold belt, Brazil: an Archean (2.57 Ga) example of iron-oxideCu-Au-(U-REE) mineralization. *Econ Geol* 100:7-28

End-Permian Phreatomagmatic pipes of the Tunguska basin: IOCG deposits linked with the Siberian traps large igneous province

Polozov A.G.^{1,2}

¹Institute of Geology of Ore Deposits, Petrography, Mineralogy and Geochemistry, Russian Academy of Sciences (IGEM RAS), Moscow, 119017, Russia

²Center for Earth Evolution and Dynamics, University of Oslo (CEED), Oslo, 0316, Norway
a.g.polozov@mail.ru

Svensen H.²

²Center for Earth Evolution and Dynamics, University of Oslo, Oslo, 0316, Norway

Planke S.^{2,3}

²Center for Earth Evolution and Dynamics, University of Oslo, Oslo, 0316, Norway

³Volcanic Basin Petroleum Research AS (VBPR), Oslo, 0349, Norway

Abstract. The Tunguska Basin (Siberia) contains hundreds of volcanic pipes and three are currently mined for iron oxide mineralization. The pipes pierce sedimentary sequences composed of Late Proterozoic and Palaeozoic oil source rocks, evaporites, carbonates and terrigenous coal-bearing rocks. These phreatomagmatic pipes originated from magma–evaporites (brine) interaction during emplacement of the Siberian Traps (~252 million years ago). Iron oxides originated by iron liberation from dolerite alteration within the pipes. These deposits show classic features of the Iron Oxide – Copper – Gold (IOCG) deposit family.

Keywords.

Tunguska Basin, Siberian Traps, phreatomagmatic pipes, iron-ore deposits

1 Introduction

The Tunguska Basin in Siberia contains hundreds of pipe structures (up to kilometer-sized), many of which containing economic iron-ore deposits that are named in Russian literature as Angara-Ilim type (Fig. 1). More than forty pipes have been extensively explored in the 70s-80s for iron oxide mineralization and three of them (Korshunovsk, Rudnogorsk and Tatyansinsk) have been mined for decades. Pre-production reserves were about 490 Mt of ore (31.6 wt.% Fe_{tot}) for Korshunovsk[oe] deposit; about 270 Mt of ore (39.8 to 53 wt.% Fe_{tot}) for Rudnogorsk[oe] deposit and about 80 Mt (34.5 wt.% Fe_{tot}) for Tatyansinsk[oe] deposit (Soloviev 2010).

The magnetite ores were discovered in the mid-nineteenth century, but the origin of the deposits is still debated. A phreatomagmatic origin of the pipes with iron oxide mineralization was proposed (Geptner and Naumov 1986). Von-der-Flaass developed this hypothesis further (Von-der-Flaass 1992; 1997). However, conclusive evidence for a phreatomagmatic origin is missing. In this contribution we focus on new data from the pipes that strengthens the hypothesis of a phreatomagmatic origin, and provide evidence for the origin of the IOCG mineralization.

2 Geological Background

The Tunguska Basin sedimentary sequence is 2-4 km thick in the area of iron-ore bearing basalt pipes (Fig. 2). This sequence consists of Precambrian and Paleozoic evaporites, carbonates and terrigenous rocks. Permo-Triassic volcanoclastic rock overlies this sequence, and consists specifically of coal-bearing terrigenous rocks. Precambrian and early Paleozoic oil source rocks contain numerous high potential oil and gas fields. Palaeozoic evaporites contain rock and potassium salt deposits of commercial grade. Tunguska Basin evaporites are considered as a regional seal for the mineralizing brines.

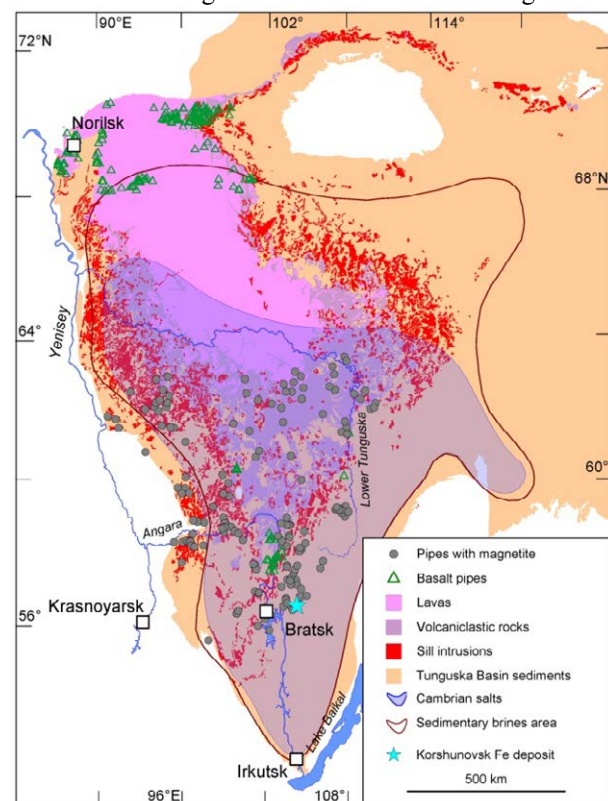


Figure 1. Iron-ore deposits in the Tunguska Basin. Areas of Cambrian salt and brines and locality of mining Korshunovsk Fe deposit are also shown.

Tunguska Basin has been intruded by the Siberian Traps Large Igneous Province composed of dolerite intrusions (sills), flood-basalts (lavas), volcanoclastic sediments (tuffs) and basalt pipes (diatremes).

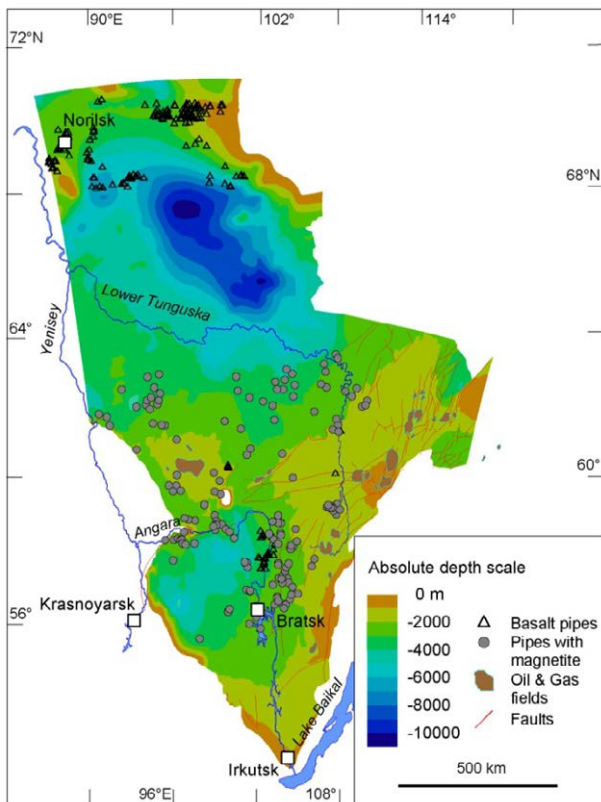


Figure 2. Iron-ore deposits position on the Tunguska Basin with oil and gas fields and thickness of sedimentary sequences expressed as depth of occurrences of the Tetera Formation top (Ediacaran). Modified from (Kontorovich et al. 2004)

Dolerite intrusions are surrounded by contact aureoles of thicknesses dependent upon sediment composition, dolerite thickness, depth of emplacement and the number of intrusive bodies. The basalt pipes are filled with breccias of magmatic, volcanoclastic and sedimentary rocks altered to varying extents. Zonation of alteration in basalt pipe breccias is less manifested than in dolerite contact aureoles. High temperature alteration minerals revealed at pipe depth (diopside, albite) change upward to high-medium temperature mineral association (garnet, epidote and feldspar). Chlorite, zeolite and calcite are dominated alteration minerals of upper diatreme interval.

The main magnetite ores in the pipes occur as breccias, veins, sub horizontal massive fine and coarse grained calcite-magnetite ores and bodies at footwall contact of dolerite sills. High temperature assemblage of olivine-magnetite-apatite with pyrrhotite and chalcopyrite occurs in the deep parts of some high-grade deposits. We hypothesize, that spectacular magnetite ores occurring in many of the iron-ore deposits (Fig. 3) are accretionary lapilli (previously interpreted as sedimentary oolites).

Pipes with iron oxide mineralization typically also contain low-grade minerals like zeolite, amethyst, jasper and calcite. Ore grade celestine, magnetite, and copper ores occur within crater sediments that still overlie some of the pipes.

3 Phreatomagmatic pipes

All large-scale deposits consist of one or two major and

up to three satellite pipes with crater deposits as round or elongate structures up to 2.3 km wide and 1.5 km depth.

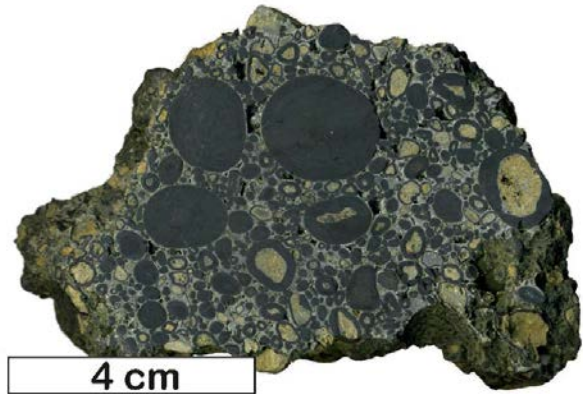


Figure 3. Spectacular "oolitic" magnetite ores of the Rudnogorsk iron-ore deposit are specific accretionary lapilli.

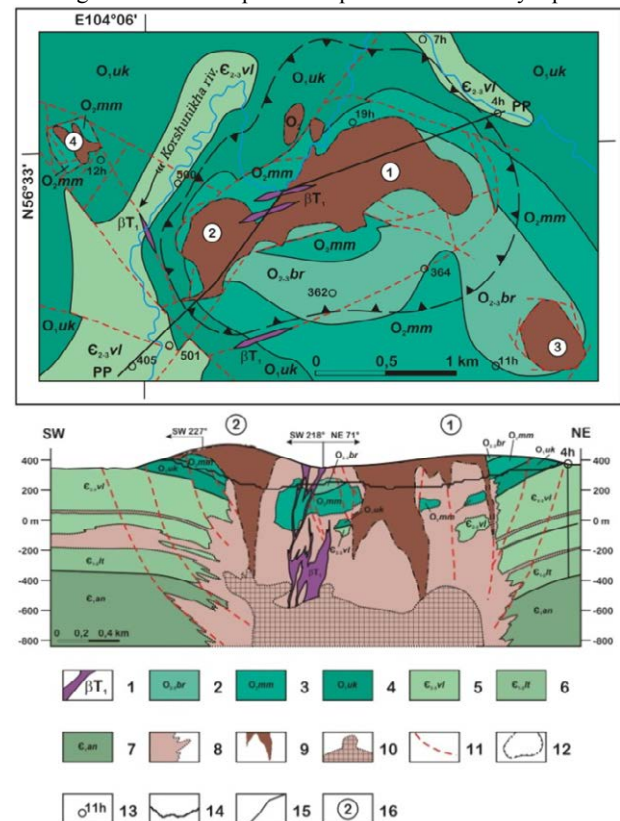


Figure 4. Korshunovsk iron ore deposit map and cross-section. 1 – Triassic basalt dikes; 2 – Middle-Upper Ordovician shales; 3 – Middle Ordovician silts and sandstones; 4 – Lower Ordovician terrigenous rocks; 5 - Middle-Upper Cambrian terrigenous rocks; 6 – Lower-Middle Cambrian dolomites; 7 - Lower Cambrian rock salts and dolomites; 8 – altered rocks with noncommercial magnetite mineralization; 9 – diatreme breccias with commercial magnetite mineralization at Intermediate Diatreme Zone; 10 – diatreme breccias with abundant dolerite and basalt fragments, cemented by rock salts at Lower Diatreme Zone; 11 – faults, 12 – depression of surrounding rocks; 13 – prospecting and hydrological (h) boreholes; 14 – contour of open pit; 15 – cross-section line; 16 – separate pipes; 1 – Rudnaya Gora 1 (Ore Mountain 1), 2 – Rudnaya Gora 2, 3 – Rudnaya Gora 3 and 4 – Zmeinnyaya Gora (Snake Mountain).

Intensive leaching and compaction of rock salts around some pipes results in the formation of depressions that can have diameters of 7-9 km and depth up to 350 m

(Fig. 4). Deposits with crater-shaped tops have paleo-lake depressions of 250-1600 m diameter and 200-700 m original depth. Blocky pipe fragments occupy the crater base whereas the upper part contains reworked volcanoclastic rocks and oxidized magnetite ores cemented by fine-grain hematite. Numerous tuffs horizons and intervals with carbonate cement occur in reworked volcanoclastic sediments.

The phreatomagmatic origin of the basalt pipes is supported by ubiquitous occurrence of volcanoclastic lapilli, corroded by brine during initial stages of magma-evaporite (brine) interaction. Corroded lapilli have rims of diopside, chlorine-bearing hornblende, apatite and magnetite (Fig. 5). Iron rich garnet is present on the tuff and glass fragments.

The age of the pipe mineralizations is geologically well constrained and are all related to Siberian Traps melt emplacement. A dolerite sill intruded into rock salt sequences of the Nepa potash deposit has a U-Pb zircon age of 252 ± 0.4 Ma (Svensen et al. 2009). Palynomorphic work in progress suggests a latest Permian age for the crater sediments (Visscher et al. 2008).

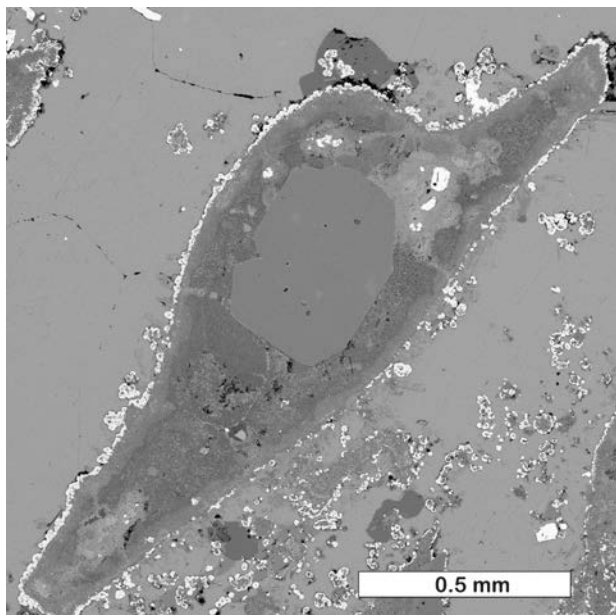


Figure 5. Basalt lapillus corroded and altered during magma-evaporite (brine) interaction. Lapillus encrusted by diopside, chlorine-bearing hornblende, apatite and magnetite (bright rim). The fragment derives from the Nepa potassium salt deposit, where the dolerite sills and basalt pipe pierce Cambrian evaporites.

Thus, our recent isotope dating, petrological, mineralogical and trace elements studies of the pipes confirm their temporary link with the Siberian LIP and their phreatomagmatic nature.

The structure and geometry of the Siberian pipes are similar to hydrothermal vent complexes present in volcanic basins elsewhere (e.g., the Vøring and Karoo basins). However, only the Siberian pipes contain major iron ore deposits.

Criteria of IOCG deposits (Table 1) show that both non-specific and specific features reflect magma-host sediment interaction that has been cited as a key

phenomenon for IOCG such as Olympic Dam (e.g. Hitzman et al. 1992). The pipe architecture, morphology of ore bodies, and element signature ($Fe \pm Cu \pm P \pm Sr \pm Ba$) is strongly dependent on the type of host rock and its fluid saturation at emplacement time.

We suggest the pipes were formed as a part of the Siberian Traps LIP when basaltic melt intruded into the Tunguska Basin about 252 million years ago. The pipes originated from magma-brine interaction around thick (>50 m) sill intrusions by explosive release of gases from contact aureoles shortly (tens of years) during and after sill emplacement.

IOCG Criteria	Non-specific	Specific
Age	●	
Tectonic Settings	●	
Magmatic Rocks	●	
Ore Minerals	●	
Alteration Style		▲
Brines		▲
Specific Elements		▲

Table 1. Criteria of non-specific and specific iron oxide copper-gold deposits, compiled from (Hitzman 2000; Hitzman et al. 1992; Williams and Skirrow 2000; Williams et al. 2005; Barton and Johnson 1996; Barton and Johnson 2000; Corriveau 2007).

4 Conclusion

Our studies suggest that basalt pipes with iron oxide mineralization originated from the Siberian Traps sills emplacement into brine-saturated host rocks. Magma-evaporite (brine) interaction resulted in the formation of phreatomagmatic pipes and iron liberation from magmatic (and sedimentary) clasts. These phreatomagmatic pipes belong to the class of IOCG deposits.

Acknowledgements

We express our thanks to Prof. F. Corfu for dating of the Siberian Traps dolerites and Dr. Muriel Erambert for the help with EMP analysis. AGP keeps a grateful memory of Dr. A.E. Vorontsov (deceased) and gives special thanks to Mr. P.F. Bedyuk, Prof. G.S. Von-der-Flaass and Mr. V.I. Nikulin, Russian geologists, for long discussions held during joint investigations of iron-ore deposits in Siberia.

References

- Barton MD, Johnson DA (1996) Evaporitic-source model for igneous-related Fe oxide-(REE-Cu-Au-U) mineralization. *Geology* 24:259-262. doi: Doi 10.1130/0091-7613(1996)024<0259:Esmfir>2.3.Co;2.
- Barton MD, Johnson DA (2000) Alternative Brine Sources for Fe-

- Oxide (-Cu-Au) Systems: Implications for Hydrothermal Alteration and Metals In: Porter TM (ed) Hydrothermal Iron Oxide Copper-Gold & Related Deposits: A Global Perspective. PGC Publishing, Adelaide, pp 43-60.
- Corriveau L (2007) Iron oxide copper-gold deposits: A Canadian perspective In: Goodfellow WD (ed) Mineral Deposits of Canada: A Synthesis of Major Deposit-Types, District Metallogeny, the Evolution of Geological Provinces, and Exploration Methods. Geological Association of Canada, Mineral Deposits Division, pp 307-328.
- Geptner AR, Naumov VA (1986) Composition of volcanoclastics of the Korbunchansk Series, Tunguska Syneclise. Lithology and Mineral Resources:169-181.
- Hitzman MW, Oreskes N, Einaudi MT (1992) Geological Characteristics and Tectonic Setting of Proterozoic Iron-Oxide (Cu-U-Au-Ree) Deposits. Precambrian Research 58:241-287. doi: Doi 10.1016/0301-9268(92)90121-4.
- Hitzman MW (2000) Iron Oxide-Cu-Au Deposits: What, Where, When and Why In: Porter TM (ed) Hydrothermal Iron Oxide Copper-Gold & Related Deposits: A Global Perspective. PGC Publishing, Adelaide, pp 9-25.
- Kontorovich AE, Belyaev SY, Kontorovich AA, Krasavchikov VO, Mandelbaum MM, Moiseev SA, Safronov AF, Sitnikov VS, Khomenko AV (2004) Tectonics of Vendian-Silurian strata in the Lena-Tunguska petroleum province (Siberian Platform). Geol Geofiz 45:100-109.
- Soloviev SG (2010) Iron Oxide Copper-Gold and Related Mineralisation of the Siberian Craton, Russia: 1 - Iron Oxide Deposits in the Angara and Him River Basins, South-Central Siberia In: Porter TM (ed) Hydrothermal Iron Oxide Copper-Gold and Related Deposits: A Global Perspective. PGC Publishing, Adelaide, pp 495-514.
- Von-der-Flaass (1992) Tuffites of subalkaline basaltoids and their role in formation of iron-bearing diatremes in the South Siberian Platform. Izvestiya - Akademiya Nauk, Seriya Geologicheskaya 8:98-112.
- Von-der-Flaass (1997) Structural and genetic model of an ore field of the Angaro-Ilim type (Siberian platform). Geol Ore Deposits 39 (8):461-473.
- Williams PJ, Skirrow RG (2000) Overview of Iron Oxide-Copper-Gold Deposits in the Curnomona Province and Cloncurry District (Eastern Mount Isa Block), Australia In: Porter TM (ed) Hydrothermal iron Oxide Copper-Gold & Related Deposits: A Global Perspective. PGC Publishing, Adelaide, pp 105-122.
- Williams PJ, Barton MD, Johnson D, Fontboté L, De Haller A, G. M, Oliver NHS, Marschick R (2005) Iron Oxide Copper-Gold Deposits: Geology, Space-Time Distribution, and Possible Modes of Origin. Econ Geol Bull Soc 100th Anniversary Volume:371-405.

Ore-forming brine-melts and fluids of the Karasug Fe-F-REE carbonatite deposit, Russia

Ilya R. Prokopyev

Institute of Geology and Mineralogy SB RAS, Novosibirsk, Russia; prokopyev_ilya@mail.ru

Andrey A. Borovikov

Institute of Geology and Mineralogy SB RAS, Novosibirsk, Russia

Galina G. Pavlova

Institute of Geology and Mineralogy SB RAS, Novosibirsk, Russia

Alexander S. Borisenko

Institute of Geology and Mineralogy SB RAS, Novosibirsk, Russia

Abstract. Brine-melt and fluid inclusions in minerals of ankerite-calcite and fluorite-barite-siderite carbonatites of the Karasug Fe-F-REE deposit in Russia have been studied using microthermometry, Raman spectroscopy, SEM and LA-ICP-MS. Results of brine-melt inclusion study show that the carbonatites were formed from the magmatic brine-melt at the initial temperature about 600°-650°C, pressure 250-300 MPa and water content 10-15 wt%. The salt components of the inclusions are NaCl and KCl, Fe, Ca, Mg, Sr, Ba, REE-carbonates and Na, Ca, Fe, Sr-sulphates. Carbon dioxide prevails in the gas phase of inclusions. The subsequent PTX-parameters alteration (temperature decrease from 400° to 300°C, pressure from 200 to 150 MPa and salt concentration from 80 to 40 wt%) demonstrates further evolution of chloride-carbonate melt and transition from the magmatic to hydrothermal stage of the ore-forming process. At the final hydrothermal stage temperature decreased from 300° to 130°C at a pressure less than 100 MPa and salinity of 30-25 wt%. The data obtained confirm a well-known evolution trend from ankerite to siderite carbonatites formation.

Keywords. Brine-melt, fluid inclusions, siderite carbonatite, Fe-F-REE, LA-ICP-MS

1 Introduction

The Karasug carbonatite deposit is situated in the Central Tuva region in southern Siberia, Russia. Its origin is linked with the formation of Late Mesozoic Central-Tuva carbonatite belt. Karasug is the largest deposit of Fe-fluorite-barite-REE ores in this area, which is still perspective for exploration. The estimated total reserves of the Karasug deposit are about 415 Mt with 1.1% REE₂O₃ (Bolonin, 2007). The Fe-F-REE siderite carbonatite is relatively rare among carbonatites, and high grade mineralization of this type occurs only in southern Siberia. Their magmatic or hydrothermal origin is still a matter of debate. To solve this question we performed a study of melt and fluid inclusions in carbonatite minerals using advanced fluid inclusion analytical techniques (Borisenko et al., 2011).

In this paper, we present data on the study of brine-melt and fluid inclusions in quartz and fluorite of the Karasug carbonatite deposit. We used traditional and more advanced techniques, such as Raman spectroscopy, SEM analysis, and LA-ICP-MS.

2 Geological and mineralogical settings

There are three ore districts with Fe-F-REE carbonatites in the Late Mesozoic Central-Tuva carbonatite belt: Chaylyukhem, Karasug, and Ulatay-Chozsk. There are two main types of carbonatites in the region, distinguished by their mineralogy: ankerite-calcite carbonatites and ore-bearing fluorite-barite-siderite (abbreviation: siderite) carbonatites. The area of the Karasug ore field is about 20 km² including 9 main ore bodies (Fig.1).

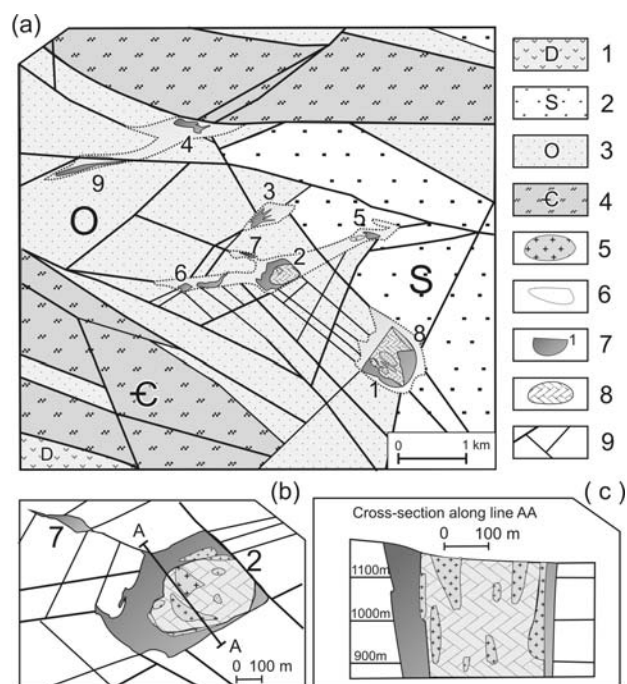


Figure 1. Geological map of the Karasug deposit (a), close-up of the second ore body (b) and cross-section through it (c) (modified after Mitropolsky, 1959 and Maximov, 1983).

1 - sandstones, siltstones, limestone, tuffs (D); 2 - sandstones, siltstones, (S); 3 - sandstones, siltstones, conglomerates (O); 4 - shales, sandstones, limestones (€); 5 - granitoids; 6 - fractured zones; 7 - ore bodies of fluorite-barite-siderite carbonatites; 8 - ankerite-calcite carbonatites; 9 - faults.

Carbonatites are localized in Early and Middle Paleozoic terrigenous host rocks (Cambrian, O-S, D).

Magmatic rocks in the ore districts are dolerite and lamprophyre (kersantite), syenite and syenite-porphyre dikes, and granosyenite stocks (Ontoev, 1984). The age of granosyenite is about 119 Ma by U-Pb (zircon) data (Bolonin et al., 2009), the age of carbonatite is 118 ± 1 (U-Pb, bastnaesite, Sal'nikova et al., 2010) and 118 ± 9 Ma (Rb-Sr, Nikiforov et al., 2005). $^{40}\text{Ar}/^{39}\text{Ar}$ dating of siderite carbonatites indicates the age of 117 ± 1.3 Ma (Institute of Geology and Mineralogy SB RAS, Novosibirsk).

Carbonatites form lenses, veins and tube-like diatremes (Fig. 1). They are composed of siderite, barite, fluorite, ankerite, calcite, hematite, magnetite, bastnaesite, parisite, Ba-celestite, apatite, monazite, K-feldspar, biotite, and rare sulfides. Siderite carbonatite cementing explosive breccia contains fragments of the host sandstones, schists, syenite-porphyre, granosyenites, and earlier ankerite-calcite carbonatite. At the surface the ores are strongly oxidized and replaced by goethite, hydrogoethite, and hematite.

2 Fluid and melt inclusion study

Brine-melt and fluid inclusions in trapped quartz and fluorite from ankerite-calcite and siderite carbonatites, and melt inclusions in apatite of granosyenite from the Karasug deposit are studied.

2.1 Methods

Heating and freezing experiments were performed using Linkam THMSG-600 to determine homogenization temperatures, salt and gas phase composition of inclusions. Data obtained were used to determine the concentrations of Na and K to use as an internal standard for the calculation of concentrations of other elements in the inclusions from the results of LA-ICP-MS analysis. Concentrations of ore elements (S, Fe, Cu, Zn, As, Sb, Mo, Ag, Th, U, REE etc.) and petrogenic elements (Na, K, Ca, Mg, Rb, Sr, Cs, etc.) in individual fluid inclusions were determined using LA-ICP-MS (X-series-2 with UP-213 Nd: YAG laser adapter). Raman spectroscopy was applied to determine the composition of the gas and solid phases in inclusions (Ramanor U-1000, Horiba DU420E-OE-323 detector Jobin Yvon, and Confocal Raman Microscope alpha300 R (WITec)). Scanning electron microscopy was used to determine the composition of solid phases in unsealed inclusions (LEO 1430VP microscope, OXFORD detector).

2.2 Petrography of inclusions

In the inclusions of minerals from carbonatites multiphase brine-melt inclusions, 3- to 5-phase water-salt fluid inclusions and gas-liquid fluid inclusions were found (Fig 2).

Primary multiphase brine-melt inclusions are found in idiomorphic bipyramidal crystals of quartz and in cubic crystals of violet fluorite (Fig. 2 a-c). Primary multiphase brine-melt inclusions in quartz are rare and

located in the growth zone or form clusters in the central parts of the crystals. In fluorite crystals primary multiphase brine-melt inclusions are located only along growth zones. Healed cracks in quartz and fractures in fluorite are traced by numerous of secondary and pseudo-secondary 3- to 5-phase water-salt and gas-liquid fluid inclusions (Fig. 2 d-e). Some of the secondary fluids are characterised by mainly gaseous composition (Fig. 2 f).

The average size of the multiphase brine-melt inclusions is about 30-50 microns, up to a maximum of 80 microns in some cases, whereas the size of water-salt and gas-liquid fluid inclusions is usually no more than 15-30 microns.

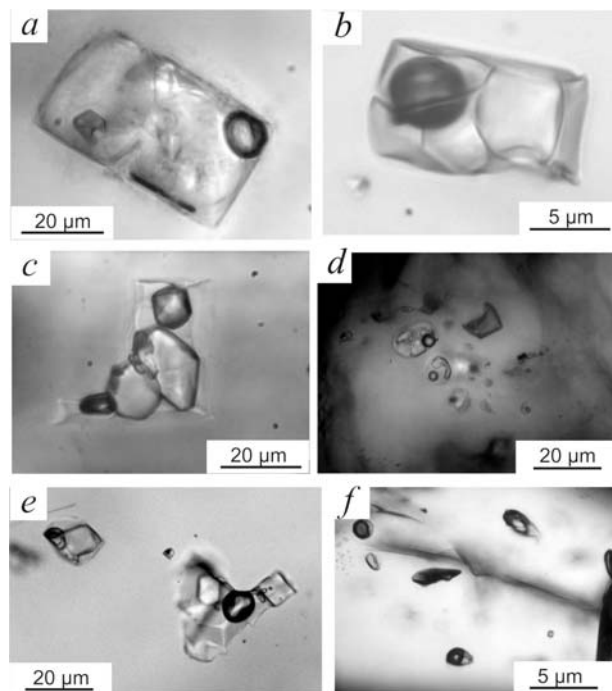


Figure 2. Inclusions in the carbonatites: primary multiphase brine-melt inclusions in quartz (a, b) and fluorite (c); 3- to 5-phase water-salt fluid inclusions in fluorite (d) and quartz (e); mainly gaseous fluids in apatite (f).

2.3 Raman-spectroscopy

Multiphase brine-melt inclusions in quartz and fluorite from carbonatites mostly contain a large cubic crystal of halite with violet tint and smaller sylvite crystal, which occupy the main volume. Usually 3 or 4 anisotropic crystalline phases and fine crystals of ore phases (hematite, etc.) occur in the inclusion. According to the Raman data, the gas phase of brine-melt inclusions contains CO_2 . The Raman-spectroscopy identified siderite FeCO_3 , thenardite Na_2SO_4 , anhydrite CaSO_4 , Cencylite $\text{Sr}(\text{Ce,Ca,La})[\text{CO}_3]_2(\text{OH})\cdot\text{H}_2\text{O}$, and Fe-copiapite $\text{Fe}_3(\text{SO}_4)_6(\text{OH})_2\cdot 20\text{H}_2\text{O}$ as solid phases (Fig. 3).

Water-salt 3- to 5-phase fluid inclusions in quartz are characterized by the CO_2 ($\pm\text{N}_2$) composition of the gas phase, and the solid salt crystalline phases are represented by hydrous Na and Ca carbonate gaylussite $\text{Na}_2\text{Ca}(\text{CO}_3)_2\cdot 5\text{H}_2\text{O}$ besides halite and/or sylvite.

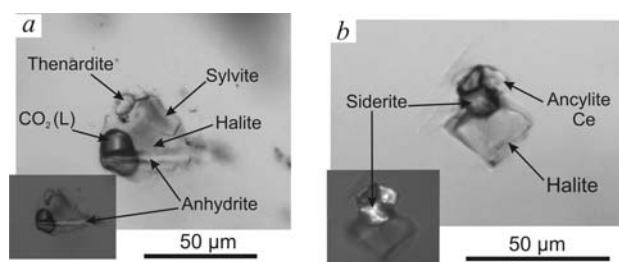


Figure 3. Multi-phase brine-melt inclusions in quartz.

2.4 Heating-freezing data

Heating-freezing experiments showed the range in temperatures of homogenization for the brine-melt multiphase inclusions from 400° to >650°C. In the inclusions in quartz sylvite dissolves at the temperature 220°-260°C and about 9/10 of halite volume dissolves at 480°-600°C with subsequent decrepitation of inclusions. Thus, the total salt content may be estimated to be at least 80 wt%. The concentration of NaCl is at least 40-50 wt%, while that of KCl is 27-30 wt%. The water-salt fluid inclusions in quartz have the temperatures of homogenization from 450° to 300°C at salinity of about 40-60 wt% NaCl eq. Secondary gas-liquid ± NaCl fluid inclusions have the temperatures of homogenization from 250° to 100°C at concentration of about <30 wt% NaCl eq.

Pressure estimated (Ontoev, 1984, Bredikhina and Mel'gunov, 1989) according to the values for density of carbon dioxide (1.3-1.4 g/cm³) was 250-300 MPa for brine-melt multiphase inclusions, with following pressure decrease for hydrothermal fluids from 75 to 50 MPa.

2.5 SEM analyses

The study of daughter minerals in unsealed multiphase brine-melt inclusions at the scanning electron microscope revealed REE-carbonate bastnaesite (Nd,Ce,La)CO₃·(F,OH), galena PbS, mineral with barite-celestite composition (Ba,Sr)SO₄, ankerite Ca(Mg, Fe)[CO₃]₂ and alumino-silicates (Fig. 4).

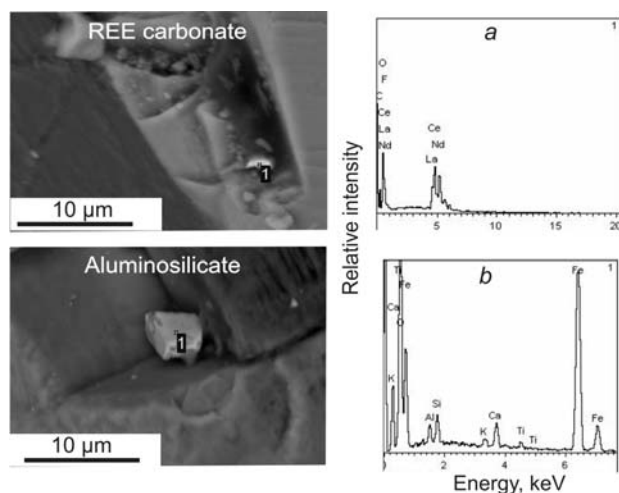


Figure 4. SEM results of determination of daughter minerals

in unsealed vacuoles of multiphase brine-melt inclusions in fluorite. Electron spectra of REE-carbonate (a) and aluminosilicate (d).

3 LA-ICP-MS data

LA-ICP-MS analysis of the multiphase brine-melt inclusions in trapped quartz and fluorite of the Karasug fluorite-barite-siderite carbonatites shows high concentrations of Fe, Sr, Ba, Mn from 0.1 to 1 wt%, and other ore elements typical for hydrothermal deposits Cu, Zn, Co, Mo, W, As, Sb, Bi, Pb, and rare-earth elements Y, La, Ce, Nd, Th and U from 1 to 100 ppm. Multiphase brine-melt inclusions in ankerite-calcite carbonatite are characterized by lower concentrations of ore elements, but higher Ca contents (Table 1).

Element	Concentration		
	Quartz I	Quartz II	Fluorite II
Na*, wt%	1.6 – 7.5	18 – 18.9	13.4 – 13.6
K*, wt%	1.3 – 8.05	15.6 – 14	5.4 – 7.1
Fe, wt%	0.26 – 6	2.6 – 4.9	3.55
Mn, wt%	0.13 – 1.1	0.05 – 0.13	0.045 – 0.32
Ca, wt%	2.7 – 14.6	0.001 – 0.014	0.01 – 0.013
Ba, wt%	---	0.2 – 0.8	0.014 – 1.2
Sr, wt%	---	0.28 – 0.7	0.43 – 2.7
Cs	---	10 – 130	1.4 – 16
Rb	---	80 – 1200	170 – 3800
Co	<i>nf</i>	3.3 – 95	340 – 2165
Cu	7.2 – 40	140 – 3200	140
Zn	170 – 2300	200 – 2300	1200 – 2700
Au	<i>f</i>	0.4 – 3.2	0.3 – 0.9
Ag	0.4	0.2 – 1.5	10 – 45
As	13 – 43	160 – 420	80 – 200
Sb	0.5 – 7.9	10 – 150	8 – 22
Mo	<i>nf</i>	0.3 – 34	10 – 12
W	---	0.3 – 1.8	4 – 22
Pb	200 – 760	200 – 760	150 – 200
Bi	0.15-15	0.4 – 6	0.6
La	4 – 5	30 – 60	460 – 1400
Ce	880 – 1100	15 – 70	2200 – 4700
Nd	---	5 – 30	4450
Th	---	0 – 55	0.2 – 0.6
U	---	2.5 – 35	10 – 35
Y	---	0.15 – 6	2800

Table 1. Concentration of elements in ppm (except where noted) in the multiphase brine-melt inclusions determined by LA-ICP-MS.

I – inclusions in quartz from the ankerite-calcite carbonatite; II – inclusions in quartz and fluorite from the fluorite-barite-siderite carbonatite; * - according to the thermometric data; --- not determined; (*nf*) - (not) found.

According to the LA-ICP-MS data ore-forming fluids in fluorite of fluorite-barite-siderite carbonatites contain higher concentrations of potassium and LREE (La, Ce, Nd) than brine-melt multiphase inclusions in quartz. Statistical processing of the geochemical data of LA-ICP-MS analysis allows to distinguish two groups of chemical elements with a high correlation (correlation coefficient >0.7) of their concentrations (within the

group): (1) - K, Fe, Zn, As, Sb, Pb, Bi; (2) - Ca, La, Ce, Nd, Y.

Based on the heating-freezing results together with calculations of solid phase, liquid and gas phase volumes in the brine-melt inclusions and LA-ICP-MS data, estimation of salt and fluid component contents has been carried out. Taking into consideration the density of salt phases, liquid and gas phases, the contents are approximately 85-70 wt%, 25-10 wt% and 5wt% of general inclusion content respectively. In addition, when inclusion solutions contain about 50% of dissolved chlorides, then common ratios of salt and fluid (H₂O, CO₂) components is about 90-80 and 10-20 wt% accordingly. It has been calculated that the carbonate phase of the inclusions in minerals of siderite carbonatite is about 15 wt%, and 45-50 wt% and more in ankerite-calcite carbonatite.

4 Conclusion

The research of the Karasug Fe-F-REE carbonatite ore field showed that its' formation is linked with the Cretaceous alkaline-mafic magmatism (117-120 Ma). The presence of intrusions of K-rich granosyenites, syenite and lamprophyres simultaneous with Fe-F-REE carbonatite in the Karasug ore field indicates the existence of magma chamber of alkaline-mafic melts in this region during Low Cretaceous time. During its evolution as a result of liquid immiscibility chloride-rich carbonate melt separated from the initial alkaline mafic magma. The carbonate content in this melt was not less than 50 wt. %. Ankerite-calcite carbonatites are formed from such melt. High contents of water, Cl, F and sulfates in the carbonatite melt (Keppler, 2003) provided a preferential accumulation of highly soluble salts in the residual melt at a temperature decrease that led to a brine-melt forming and at the final stage resulted in the formation of siderite carbonatite as lenses, veins and cement of explosive breccia in diatremes. Further evolution of the brine-melt resulted in the formation of hydrothermal fluid of sulfate-chloride composition that led to the late hydrothermal F-Ba-REE mineralization deposition. This model is consistent with a sequence of magmatic and mineralization processes in the ore field and is confirmed by the melt and fluid inclusions study.

Results of brine-melt inclusion study show that the Karasug deposit carbonatites were formed from magmatic brine-melt at initial temperature about 600°-650°C, pressure 250-300 MPa and water content 10-15 wt%. The main salt components of the chloride-carbonate melt are NaCl and KCl; Fe, Ca, Mg, Sr, Ba, REE-carbonates as siderite, calcite, strontianite, Cencylite, and gaylussite are also present, as well as Na, Ca, Fe, Sr-sulphates (anhydrite, barite-celestite, thenardite and Fe-copiapite). High contents of ore elements such as Fe, Mn, Ba, Sr, Cu, Co, Pb и Zn, As и Sb, REE, Th and U are a characteristic feature. Carbon dioxide with minor N₂ prevails in the gas phase of high temperature multiphase inclusions.

The temperature decrease from 600° to 400°C and subsequent alteration in PTX-parameters of the ore-forming fluid at the later stage (T decrease from 400° to

300°C, pressure from 200 to 150 MPa and salt concentration from 80 to 40 wt%) demonstrate further evolution of chloride-carbonate melt and transition from the magmatic to hydrothermal stage of the ore-forming process. At the final stage further temperature decrease occurred from 300° to 130°C at a pressure less than 100 MPa, and lowering of hydrothermal solution concentration down to 30-25 wt% have been traced. The data obtained confirm a well-known trend of the evolution from ankerite to fluorite-barite-siderite carbonatite (Bailey, 1995).

Acknowledgements

The work is supported by grant RFBR # 11-05-00662-a. We also thank to Alexei L. Ragozin and Irina V. Abornina from IGM SB RAS for analytical studies and our colleagues from Tuva Institute for Exploration of Natural Resources SB RAS: Prof. Vladimir Lebedev, Dr. Amina Sugorakova and Renat Kuzhuget.

References

- Bailey DK (1995) Carbonate magmas. Geological Society: London, Memoirs 16: 249-263.
- Bolonin AV (2007) Carbonatite complex ores of Central Tuva and the prospects for their development [in Russian]. Ores and metals 6: 16-26.
- Bolonin AV, Nikiforov AV, Lychin DA, Sugorakova AM (2009) The Chailag-Khem fluorite-barium-strontium-rare-earth carbonatite occurrence, The Western Sayan range, Russia. Geology of Ore Deposits 51 (1): 17-32
- Borisenko AS, Borovikov AA, Vasyukova EA, Pavlova GG, Ragozin A.L, Prokop'ev IR, Vladykin NV (2011) Oxidized magmatogene fluids: metal-bearing capacity and role in ore formation. Russian Geology and Geophysics 52: 144-164.
- Bredikhina SA, Mel'gunov SV (1989) Physicochemical parameters of formation of fluorite from fluorite-barite-iron-ore mineralization in the Tuva ASSR. Russian Geology and Geophysics 30 (10); 61-68 (56-62).
- Keppler H. (2003) Water solubility in carbonatite melts. American Mineralogist 88. (11-12): 1822-1824.
- Nikiforov AV, Bolonin AV, Lychin DA, Sugorakova AM, Popov VA (2005) Carbonatites of Central Tuva: geological structure and mineral and chemical composition. Geology of Ore Deposits 47 (4): 326-345.
- Ontonev DO (1984) Complex geology of rare earth deposits [in Russian]. Moscow: Nedra: 189.
- Sal'nikova EB, Yakovleva SZ, Kotov AB, Anisimova IV, Plotkina YV, Nikiforov AV, Yarmolyuk VV, Sugorakova AM (2010) Bastnaesite: a promising U-Pb geochronological tool. Doklady Earth Sciences: 430 (1): 134-136.

The isotopic record of sulphur from Archean and Proterozoic Cu-Au deposits in the Carajás Mineral Province, northern Brazil

Érika Suellen Barbosa Santiago, Roberto Perez Xavier
Geosciences Institute, State University of Campinas (UNICAMP), Brazil

Lena Virginia Soares Monteiro
Geosciences Institute, University of São Paulo (USP), Brazil

Steffen Hagemann
Centre for Exploration Targeting, University of Western Australia, WA 6009, Australia

John Cliff
The Centre for Microscopy, Characterisation and Analysis, University of Western Australia, Australia

Abstract. The $\Delta^{33}\text{S}$ and $\delta^{34}\text{S}$ compositions of chalcopyrite, pyrite, and pyrrhotite have been analysed by *in situ* Secondary Ion Mass Spectrometry to constrain sulphur sources in Archean and Paleoproterozoic Cu-Au hydrothermal systems of the Carajás Mineral Province (CMP). The Archean Castanha, Igarapé Bahia, Salobo, and Sequeirinho deposits show a narrow range of $\Delta^{33}\text{S}$ (-0.17‰ to +0.11‰) and variable $\delta^{34}\text{S}$ (-3.32‰ to +2.99‰) values. The Paleoproterozoic Sossego and Alvo 118 IOCG deposits exhibit similar $\Delta^{33}\text{S}$ values (-0.11‰ to +0.04‰) and variable $\delta^{34}\text{S}$ values (+2.46‰ to +4.68‰). The Paleoproterozoic intrusion-related Breves Cu-Au deposit is characterized by slightly positive $\Delta^{33}\text{S}$ values (+0.10‰ to +0.27‰) and $\delta^{34}\text{S}$ in the range of -0.4‰ to +3.83‰. The $\delta^{34}\text{S}$ values reflect magmatic sulphur, although the positive $\Delta^{33}\text{S}$ composition may imply contribution of sulphur from host pyrite-bearing sandstones. Although the $\Delta^{33}\text{S}$ values for most single analyses were very small compared to propagated uncertainties, 95% CI of most $\Delta^{33}\text{S}$ values fall outside our analytical uncertainty (± 0.054 ‰), leading us to conclude that MIF signatures are present in the investigated Cu-Au deposits from the CMP.

Keywords. Archean and Paleoproterozoic, IOCG and intrusion-related Cu-Au deposits, Carajás Mineral Province, sulphur isotopes, mass-independent fractionation

1 Introduction

Iron oxide-Cu-Au (IOCG) and intrusion-related Cu-Au (Mo-W-Bi-Sn) deposits are the main Cu-Au systems in the Carajás Mineral Province (CMP). The former are hosted by Mesoarchean tonalite and gneiss, Neoarchean metavolcanic-sedimentary, and mafic and felsic intrusive rocks. The latter are spatially and temporally associated with Paleoproterozoic A-type granitic intrusions.

Fluid inclusion studies combined with stable and radiogenic isotopes have indicated mixed sources for the ore-bearing fluids in Archean and Paleoproterozoic IOCG systems of the CMP (Dreher et al. 2008; Monteiro et al. 2008; Xavier et al. 2008, 2009). Potential sources have included: (1) nonmagmatic (e.g., evolved seawater, formation water, evaporative brines), (2) magmatic, or (3) hybrid magmatic-nonmagmatic sources. The intrusion-related polymetallic deposit, on

the other hand, have been interpreted as magmatic-hydrothermal (Xavier et al. 2004; Botelho et al. 2005).

In this work, we use multiple sulphur isotopes systematics (Farquhar et al. 2000, 2002) in an attempt to: (1) provide new insights into potential sulphur sources for Cu-Au systems of the CMP with implications to ore-forming processes; and (2) shed more light into the Archean-Paleoproterozoic sulphur cycling in the CMP. For this, Archean (Salobo, Igarapé Bahia, Sequeirinho, and Castanha) and Paleoproterozoic (Sossego and Alvo 118) IOCG deposits and the Paleoproterozoic Breves intrusion-related Cu-Au-(Mo-W-Bi-Sn) deposit were used as case studies.

2 Materials and methods

In situ sulphur three-isotope ratios ($\delta^{34}\text{S}$ and $\delta^{33}\text{S}$) were determined in 14 polished sections using a Cameca IMS 1280 multi-collector ion microprobe located at the Centre for Microscopy, Characterisation and Analysis (CMCA), University of Western Australia using methods similar to Farquhar et al. (in press). Rock fragments were cut from slabs and mounted with in-house SON-3pyrite standard and Ax3-4pyrrhotite standard for S-isotope analyses. Mass-independent fractionation (MIF) of ^{33}S was calculated as $\Delta^{33}\text{S} = \delta^{33}\text{S} - 1000[(1 + \delta^{34}\text{S}/1000)^{0.515} - 1]$. External precisions for $\delta^{33}\text{S}$, $\delta^{34}\text{S}$, $\Delta^{33}\text{S}$ Son-3 analyses were 0.09‰, 0.16‰, and 0.054‰ (2 SD), respectively, over seven analytical sessions (n=103). Twenty eight Ax3-4 analyses run as unknowns during sessions that included pyrrhotite analyses returned external precisions of 0.12‰, 0.17‰, and 0.07‰ (2 SD) for $\delta^{33}\text{S}$, $\delta^{34}\text{S}$, $\Delta^{33}\text{S}$, respectively. Pooled average values returned deviations in accuracy of less than 0.02‰ for $\delta^{33}\text{S}$ and $\delta^{34}\text{S}$, and less than 0.01‰ for $\Delta^{33}\text{S}$ compared with the Laser fluorination value. Error bars are propagated according to standard methods and contain components of internal and external precision, the uncertainty of the standard relative to V-CDT as well as additional uncertainty from calibrating chalcopyrite or pyrrhotite from pyrite. We consider here a sample to have a detectible MIF if the average $\Delta^{33}\text{S} \pm 95\%$ CI (confidence interval) for a single sample falls outside the analytical uncertainty of $\Delta^{33}\text{S} = 0 \pm 0.054$ ‰.

3 The Cu-Au deposits of the Carajás

Mineral Province

The Sequeirinho, Sossego, Castanha, and Alvo 118 IOCG deposits are located in the southern sector of the CMP, along an east-southeast-striking regional shear zone, close to the contact between the ca. 2.76 Ga metavolcano-sedimentary rocks of the Itacaiúnas Supergroup and the Mesoarchean basement.

Both Sequeirinho and Sossego orebodies belong to the Sossego mine. Host rocks of the Sequeirinho deposit include granite, gabbro, felsic metavolcanic rocks and minor meta-ultramafic rocks. These rocks have undergone regional sodic and sodic-calcic alteration. The latter is generally associated with massive magnetite-apatite bodies and envelops the Cu-Au ore (Monteiro et al. 2008). The Sossego deposit is confined to granophyric granite and gabbro. Early albitic and subsequent sodic-calcic alteration are poorly developed, whereas potassic alteration assemblages mark the onset of the Cu-Au mineralisation, and grades laterally outward to a widespread zone of chlorite and late hydrolytic alteration assemblages (Monteiro et al. 2008). In both cases, mineralisation is hosted by breccias and consists of chalcopyrite associated with magnetite, pyrite, native gold, siegenite, millerite, and hessite.

The Castanha IOCG deposit, located 7 km northeast of the Sossego mine, is hosted by the Castanha feldspar-quartz porphyry and gabbro (Pestilho 2011). Hydrothermal alteration is characterized by intense and widespread sodic metasomatism, potassic alteration (biotite and magnetite) along mylonitic foliation, and late chlorite \pm calcite \pm quartz \pm apatite + allanite \pm epidote that accompanies the Cu-Au mineralisation. This deposit comprises two distinct ore assemblages (Pestilho 2011): (I) chalcopyrite-pyrite \pm molybdenite, which occur associated with magnetite and actinolite bodies; (II) pyrrhotite-chalcopyrite-pyrite \pm sphalerite \pm marcasite.

Mafic and felsic metavolcanic rocks attributed to the Itacaiúnas Supergroup, together with ca. 2.74 Ga granite, ca. 2.65 Ga gabbro and porphyry dyke intrusions, comprise the main hosts to the Cu-Au ore at the Alvo 118 deposit. Progressively inwards towards the ore zones, alteration is defined by early and restricted albite-scapolite, a potassic assemblage dominated by biotite or microcline (\pm magnetite), pervasive and widespread chlorite spatially associated with quartz-carbonate breccia-hosted Cu-Au ore, and local post-ore quartz-sericite alteration (Torresi et al. 2012). The ore assemblage is generally composed of chalcopyrite, bornite, hematite, magnetite, and minor to trace amounts of native gold, chalcocite, galena, sphalerite, cassiterite and Bi-Te-Au-Ag minerals. SHRIMP II U-Pb dating on xenotime from massive and vein ore of the Alvo 118 deposit yielded ages of 1.86 Ga (Tallarico 2003).

The Igarapé Bahia and Salobo deposits lie in the northern sector of the CMP. The Igarapé Bahia deposit is hosted by a ca. 2.75 Ga breccia unit situated between chloritized basalt, with associated hyaloclastite, banded iron formation, and chert in the footwall and a dominantly siliciclastic sedimentary sequence in the hanging wall (Dreher et al. 2008). This deposit comprises four orebodies: Acampamento Norte (ACPN), Acampamento Sul (ACPS), Furo Trinta (FT) and

Alemão. The Cu-Au ore is characterized by disseminated to massive chalcopyrite and bornite with varying amounts of magnetite, chlorite, carbonate, amphibole, biotite, apatite, tourmaline, and quartz. Hydrothermal alteration are dominated by chlorite in weakly mineralised zones (e.g. FT and ACPN), whereas high grade ore zones (e.g. Alemão and ACPN) contain abundant assemblages of magnetite-siderite-Fe-amphibole-stilpnomelane. The mineralisation is Archean, but the precise age is contentious: \sim 2.76 Ga (Galarza et al. 2008) or \sim 2.57 Ga (Tallarico et al. 2005).

The Salobo deposit is confined to the NW-striking Cinzento shear zone where it is hosted by foliated rocks containing variable amounts of biotite, amphibole (hastingsite and grunerite), Fe-rich garnet, tourmaline, and magnetite (10 to $>$ 50%). These mineral associations are possibly products of high-temperature hydrothermal alteration, which precludes a more precise definition of their protoliths. The Cu-Au ore forms steeply dipping, irregular, lens-shaped and massive replacement bodies particularly associated with magnetite-rich rocks ("magnetic schists"). The mineralisation occurs as disseminations of bornite, chalcocite and chalcopyrite, associated with covellite, molybdenite, cobaltite, safflorite, native gold, and silver (Lindenmayer 1990). Post-mineralization alteration includes widespread chlorite, calcite, epidote, albite, sericite, quartz, greenalite, fluorite, and uraninite.

The Breves deposit is hosted by meta-sandstones and meta-siltstones of the Águas Claras Formation (minimum age of ca. 2.67 Ga) in the roof zone of a highly altered 1.88 Ga granite intrusion (Tallarico et al. 2004). The mineralisation is largely disseminated in the siliciclastic rocks and in crosscutting vein systems, with an alteration assemblage consisting of chlorite \pm muscovite-phengite \pm biotite \pm fluorite \pm tourmaline (Botelho et al. 2005). Copper mineralisation is dominated by chalcopyrite-pyrite-arsenopyrite-pyrrhotite \pm molybdenite \pm gold and the gangue assemblage includes fluorite-tourmaline \pm monazite \pm xenotime \pm chlorapatite \pm thorite \pm zircon \pm calcite \pm siderite \pm bastnaesite. Mineralisation is Paleoproterozoic and the age has been yielded at 1.87 Ga (SHRIMP II U-Pb monazite; Tallarico et al. 2004).

4 $\Delta^{33}\text{S}$ and $\delta^{34}\text{S}$ compositions of sulphides

Collectively, $\Delta^{33}\text{S}$ values for chalcopyrite, pyrite, and pyrrhotite from the Sossego mine (Sequeirinho and Sossego orebodies), and Castanha and Alvo 118 deposits are mostly negative and broadly confined between -0.17‰ and $+0.04\text{‰}$ (Figs. 1A-B and 1D). The range in $\Delta^{33}\text{S}$ compositions of the sulphides in each deposit have similar $\Delta^{33}\text{S}$ in spite of significant differences among these IOCG systems. The $\Delta^{33}\text{S}$ are: -0.17‰ to $+0.01\text{‰}$ and -0.11‰ to $+0.04\text{‰}$ for Sequeirinho and Sossego orebodies, respectively, -0.11‰ to -0.04‰ for Castanha, and -0.09‰ to -0.01‰ for Alvo 118.

The $\delta^{34}\text{S}$ signatures for the sulphides in these deposits reveal, on the other hand, important differences. At the Sossego mine, $\delta^{34}\text{S}$ values for chalcopyrite from the Sequeirinho orebody ($+0.75\text{‰}$ to $+1.37\text{‰}$) are distinct,

being lower than those for coexisting pyrite (+2.45‰ and +3.00‰). The latter are similar to the $\delta^{34}\text{S}$ range obtained in chalcopyrite from the Sossego orebody

(+2.20‰ to +2.75‰).

Chalcopyrite from the Castanha IOCG deposit defines

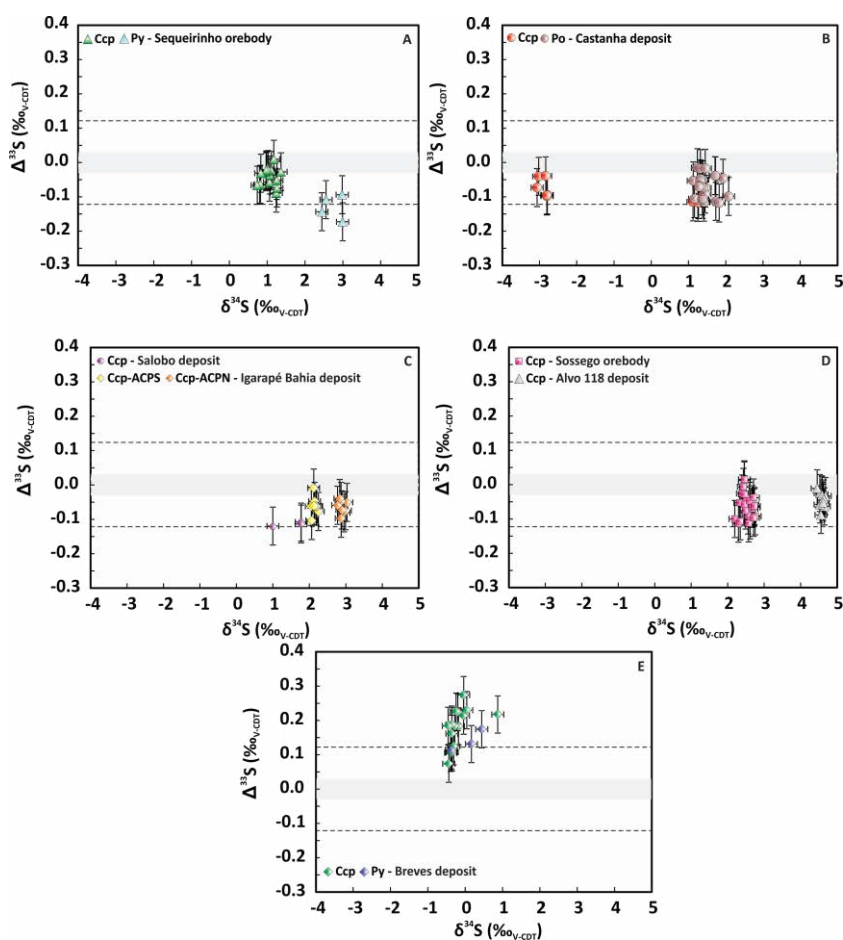


Figure 1. $\Delta^{33}\text{S}$ vs. $\delta^{34}\text{S}$ diagrams for chalcopyrite (Ccp), pyrite (Py) and pyrrothite (Po) from Cu-Au systems. Archean IOCG Sequeirinho (A), Castanha (B), Igarapé Bahia and Salobo (C) deposits; Paleoproterozoic IOCG Sossego and Alvo 118 (D) deposits; and Paleoproterozoic intrusion-related Breves (E). Gray bar and stippled lines indicate mantle-derived sulphur and Mass-dependent fractionation (MDF) intervals, respectively, based on Farquhar et al. (2000; 2002). Two standard deviation for $\Delta^{33}\text{S}$ values was $\pm 0.054\text{‰}$.

two distinct groups of $\delta^{34}\text{S}$ values (Figure 1B), one negative ranging from -3.07‰ to -2.80‰ and the other positive from +1.09‰ to +1.42‰ (Fig. 1A). The $\delta^{34}\text{S}$ data for pyrrothite from this deposit are mostly within the same range of $\delta^{34}\text{S}$ values (+1.10‰ to +2.04‰) of those recorded for the Sequeirinho chalcopyrite. Compared to Sossego and Castanha deposits, chalcopyrite from the Alvo 118 deposit displays the most positive $\delta^{34}\text{S}$ signature, with values clustering between +4.52‰ to +4.67‰ (Figure 1D).

Chalcopyrite $\Delta^{33}\text{S}$ values for the Igarapé Bahia and Salobo IOCG deposits are within the same range: -0.12‰ to -0.01‰. The Salobo chalcopyrite displays the lowest $\Delta^{33}\text{S}$ values (-0.12‰ and -0.11‰), whereas the Igarapé Bahia chalcopyrite the highest (-0.11‰ to -0.01‰) (Figure 1C).

The $\delta^{34}\text{S}$ signatures for Salobo (+1.00‰ to +1.77‰) are lower compared to the range displayed by Igarapé Bahia (+2.05‰ to +2.98‰). In addition, at Igarapé Bahia, the $\delta^{34}\text{S}$ values for the ACPN orebody (+2.76‰ to +2.98‰) are higher than those for the ACPS orebody (+2.05‰ to +2.24‰).

In comparison with the IOCG deposits, chalcopyrite and pyrite from the intrusion-related Breves deposit, yield remarkably contrasting $\Delta^{33}\text{S}$ values (Figure 1E). These values are positive and are in the range of +0.11‰ to +0.27‰. Similarly to the $\Delta^{33}\text{S}$ data, the $\delta^{34}\text{S}$ compositions for these sulphides show clear differences

compared to the IOCG deposits. In general, these values are within the range of -0.45‰ and +0.87‰, which are much lower than those obtained from the IOCG deposits.

5 Preliminary discussions

The $\Delta^{33}\text{S}$ values for the Archean (Salobo, Igarapé Bahia, Castanha, and Sequeirinho) and Paleoproterozoic (Sossego and Alvo 118) IOCG deposits are mostly negative and exhibit overlapping ranges that hardly distinguish them. In addition, lower $\Delta^{33}\text{S}$ values may suggest that the ore-bearing fluids have also contained a significant signature of sulphur assimilated from crustal reservoirs. Although the $\Delta^{33}\text{S}$ values for most single analyses were very small compared to propagated uncertainties, 95% CI of most $\Delta^{33}\text{S}$ values fall outside our analytical uncertainty ($\pm 0.054\text{‰}$), leading us to conclude that MIF signatures are present.

A recent study on multiple sulphur isotopes (Bühn et al. 2012) has indicated that the Sequeirinho and Salobo deposits do not record a MIF signature, the sulphur being derived from endogenic sources without interaction with surface sulphur reservoirs.

Similarly to the Archean equivalents, the Paleoproterozoic IOCG deposits may also show MIF effect, and their $\delta^{34}\text{S}$ values are in the magmatic range, however, slightly heavier sulphur isotope compositions

suggest that surface sulphur sources may have contributed to the sulphur budget of the ore-bearing fluids. Previous studies on Cl/Br vs. Na/Cl systematic in fluid inclusions from Sossego, Alvo 118 and Igarapé Bahia deposits and $\delta^{11}\text{B}$ on tourmaline from the Salobo, Igarapé Bahia and Sequeirinho deposits suggest that a combination of residual evaporative and magmatic brines may have been important sources for the fluids involved in the origin of the Cu-Au systems in the CMP (Xavier et al. 2008, 2009). These studies, coupled with our $\Delta^{33}\text{S}$ data, corroborate the involvement of surface reservoirs in the origin of Archean and Paleoproterozoic IOCG deposits.

The $\Delta^{33}\text{S}$ - $\delta^{34}\text{S}$ isotopic signature for sulphides from the Paleoproterozoic intrusion-related Breves deposit are in contrast to the IOCG deposits (Fig. 1E). The mineralising fluids at the Breves deposit may also have incorporated an input from surface sulphur. In contrast, the $\delta^{34}\text{S}$ signature shows a limited variation, closest to zero, implying a magmatic component (Fig. 1E).

Collectively, it could be suggested mixed sulphur sources for the Breves deposit, with both magmatic and surface sulphur as probable components. In addition, $\Delta^{33}\text{S} > 0$ values point to sedimentary sulphides of potential exogenic source. One possible contribution would be Archean pyrite-bearing meta-sandstones of the Águas Claras Formation. Nevertheless, $\Delta^{33}\text{S}$ data for these pyrites have shown no MIF signature or, at least, a minimal effect (Fabre et al. 2011, Bühn et al. 2012). On the other hand, the ~1.88 Ga Breves anorogenic granite, which shows a close spatial and temporal association with mineralisation, could be a significant magmatic source for the mineralising fluids including sulphur. However, previous studies on Cl/Br vs. Na/Cl in fluid inclusions have already revealed an involvement of bittern fluids in the Breves deposit (Xavier et al. 2009).

Acknowledgements

The authors are grateful to Vale for the continuous support provided to the UNICAMP researchers and students. Sincere gratitude is due to the facilities, and the scientific and technical assistance of the Australian Microscopy & Microanalysis Research Facility at the Centre for Microscopy, Characterisation & Analysis, of the University of Western Australia, a facility funded by the University, State and Commonwealth Governments. We wish to thank Dr. James Farquhar for his comments and suggestions which improved this paper. This research has been financially supported by the INCT - Geociências da Amazônia (GEOCIAM) (MCT/CNPq/Fapespa 573733/2008-2).

References

- Botelho NF, Moura MA, Teixeira LM, Olivo GR, Cunha LM, Santana UM (2005) Caracterização geológica e metalogenética do depósito de Cu ± (Au, W, Mo, Sn) Breves, Carajás. In: Marini OJ, Queiroz ET, Ramos BW (Eds.). Caracterização de depósitos minerais em Distritos Mineiros da Amazônia, ADIMB, pp 335-389
- Bühn B, Santos RV, Dardenne MA, Oliveira CG (2012) Mass-dependent and mass-independent sulfur isotope fractionation ($\delta^{34}\text{S}$ and $\delta^{33}\text{S}$) from Brazilian Archean and Proterozoic sulfide deposits by laser ablation multi-collector ICP-MS. *Chemical Geology*, 312-313: 163-176
- Dreher AM, Xavier RP, Taylor BE (2008) New geologic, inclusion and stable isotope studies on the controversial Igarapé Bahia Cu-Au deposit, Carajás Province, Brazil. *Mineralium Deposita*, 43:161-184
- Fabre S, Nédélec A, Poitras F, Strauss H, Thomazo C, Nogueira A (2011) Iron and sulphur isotopes from the Carajás mining province (Pará, Brazil): Implications for the oxidation of the ocean and the atmosphere across the Archean-Proterozoic transition. *Chemical Geology* 289:124-139
- Farquhar J, Bao HM, Thiemens M (2000) Atmospheric influence of Earth's earliest sulfur cycle. *Science*, 289: 756-758
- Farquhar J, Wing BA, McKeegan KD, Harris JW, Cartigny P, Thiemens MH (2002) Mass-independent sulfur of inclusions in diamond and sulfur recycling on early Earth. *Science*, 298: 2369-2372
- Farquhar J, Cliff J, Zerkle AL, Kamyshny A, Poulton SW, Claire M, Adams D, Harms B (in press) Pathways for Neoproterozoic pyrite formation constrained by mass-independent sulfur isotopes. doi: 10.1073/pnas.1218851110
- Galarza MA, Macambira MJB, Villas RN (2008) Dating and isotopic characteristics (Pb and S) of the Fe oxide-Cu-Au-REE Igarapé Bahia ore deposit, Carajás mineral province, Pará state, Brazil. *Journal of South American Earth Sciences*, 25: 377-397
- Lindemayer ZG (1990) Salobo sequence, Carajás, Brasil: Geology, Geochemistry and Metamorphism; PhD thesis, University of Ontario, Canada, 407 p
- Monteiro LVS, Xavier RP, Carvalho ER, Hitzman MW, Johnson CA, Souza Filho CR, Torresi I (2008) Spatial and temporal zoning of hydrothermal alteration and mineralization in the Sossego iron oxide-copper-gold deposit, Carajás Mineral Province, Brazil: paragenesis and stable isotope constraints. *Miner Depos* 43:129-159
- Pestilho ALS (2011) Sistemática de isótopos estáveis aplicada à caracterização da evolução dos paleo-sistemas hidrotermais associados aos depósitos cupríferos Alvo Bacaba e Alvo Castanha, Província Mineral de Carajás, PA. M.Sc. thesis, Universidade Estadual de Campinas, Brazil, 70p
- Tallarico FHB (2003) O Cinturão Cupro-Aurífero de Carajás, Brasil. PhD thesis, Universidade Estadual de Campinas, Brazil, 229 p
- Tallarico FHB, McNaughton NJ, Groves DI, Fletcher IR, Figueiredo BR, Carvalho JB, Rego JL, Nunes AR (2004) Geological and SHRIMP II U-Pb constraints on the age and origin of the Breves Cu-Au-(W-Bi-Sn) deposit, Carajás, Brazil. *Miner Depos* 39: 68-86
- Tallarico FHB, Figueiredo BR, Groves DI, Kositcin N, McNaughton NJ, Fletcher IR, Rego JL (2005) Geology and Shrimp U-Pb geochronology of the Igarapé Bahia deposit, Carajás Copper-Gold belt, Brazil: an Archean (2.57 Ga) example of iron-oxide Cu - Au-(U-REE) mineralization. *Econ Geol* 100:7 - 28
- Torresi I, Xavier RP, Bortholoto DFA, Monteiro LVS (2012) Hydrothermal alteration, fluid inclusions and stable isotopesystematics of the Alvo 118 iron oxide-copper-gold deposit, Carajás Mineral Province (Brazil): Implications for ore genesis. *Miner Depos* 47: 299-323
- Xavier RP, Wiedenbeck M, Trumbull RB, Dreher AM, Monteiro LVS, Rhede D, Araújo CEG, Torresi I (2008) Tourmaline B-isotopes fingerprint marine evaporites as the source of high-salinity ore fluids in iron oxide-copper-gold deposits, Carajás Mineral Province (Brazil). *Geology* 36(9): 743-746
- Xavier RP, Rusk B, Emsbo P, Monteiro LVS (2009) Composition and source of salinity of ore-bearing fluids in Cu-Au systems of the Carajás Mineral Province, Brazil. In: The 10th Biennial Meeting of the SGA, Townsville (Australia), Proceedings, 272-275

In situ U-Pb and whole rock Nd data for the Kiruna iron oxide apatite deposits and their host rocks, Norrbotten, Sweden

Anne Westhues, John M. Hanchar

Department of Earth Sciences, Memorial University of Newfoundland, Canada

Martin J. Whitehouse

Laboratory for Isotope Geology, Swedish Museum of Natural History, Stockholm, Sweden

Olof Martinsson

Department of Civil, Environmental and Natural Resources Engineering, Luleå University of Technology, Sweden

Abstract. The origin of the massive iron oxide apatite deposits in the Norrbotten region of northern Sweden, and similar deposits worldwide, has been debated for decades; magmatic vs. hydrothermal origins have been proposed. Combining in situ U-Th-Pb dating and tracer isotopes at whole rock and mineral scale is a promising approach for unravelling the origin of the Kiruna iron ore deposits.

In situ U-Pb geochronology of zircon and titanite confirms a previously documented event around 1880-1900 Ma in the Norrbotten region. However, U-Pb in monazite from one ore sample suggests a later event at 1624 ± 22 Ma. Sm-Nd isotopic whole rock data shows distinct differences between host rocks ($\epsilon_{\text{Nd}} \sim -6$), strongly altered host rocks (~ -3.5 to -4), and the ore ($\epsilon_{\text{Nd}} \sim -3$), possibly indicating a depleted mantle influence for the latter two. This difference in the Nd isotopic composition may be caused by the same event that is recorded by the U-Pb system in monazite within the ore. Further study is needed to confirm these findings and understand how the iron mineralization is related to the two events.

Keywords. Kiruna, iron oxide apatite deposit, IOA, IOCG deposit, U-Pb geochronology, Nd isotopes

1 Introduction

The Norrbotten region in northern Sweden hosts about 40 known iron oxide apatite (IOA) deposits (Bergman et al. 2001; Martinsson 2004). These deposits are some of the largest of this kind in the world. Several ore bodies occur around the town of Kiruna, including the huge Kiirunavaara mine, which led to the expression “Kiruna-type” deposits for this class of low-Ti apatite-rich iron ore deposits. The deposits in this part of Sweden have been mined intermittently since 1645 and continue to be an important source of iron and other elements. The three active mines Kiirunavaara, Malmberget and Gruvberget combined are estimated to contain ca. 2900 million tons of 45–57 wt.% Fe (Billström et al. 2010).

Iron oxide apatite deposits are either considered an end member of the iron oxide copper gold (IOCG) group of deposits (e.g., Hitzman et al. 1992; Barton and Johnson 1996), or as their own deposit type, unique from IOCG deposits *sensu stricto* (e.g., Groves et al. 2010). Despite the differences in Cu and/or Au contents, IOA and IOCG deposits share striking similarities, including abundant low-Ti Fe oxides, intense wall rock alkali

alteration (Na, K \pm Ca), an enrichment in rare earth elements (REE), especially LREE, and a temporal – but no close spatial – relation with magmatism (Groves et al. 2010). The most recent classifications (e.g., Porter 2010) tend to treat IOCG deposits and IOA deposits as separate deposit classes in the larger spectrum of iron oxide-alkali altered mineralized systems.

The main reason for this somewhat confusing classification scheme is the debated ore genesis of iron oxide-alkali altered mineralized systems. Some researchers argue for a magmatic origin, while others suggest the involvement of a hydrothermal ore forming fluid in models for the formation of IOCG and IOA deposits (e.g., Parák 1975; Frietsch 1978 for the deposits in the Kiruna area). The source of such hydrothermal fluids is unclear (Barton and Johnson 2004); and many IOCG deposits show evidence for the involvement of fluids from more than one source (Williams et al. 2010).

Constraining the timing of host rock emplacement, alteration, and mineralisation is crucial to understanding how IOA deposits form in nature. In the Adirondack Mountains, New York State, U-Pb geochronology of hydrothermal zircon crystals associated with magnetite showed that at least one stage of the IOA mineralization is 20 to 60 million years younger than the adjacent hydrothermally altered host rocks (Valley et al. 2009).

The IOA deposits in the Norbotten region are classic locations to undertake a fundamental research project combining high-resolution geochronology with tracer isotope studies as an example for IOA deposits worldwide. First results are presented that will help to clarify how these deposits form in nature, and how host rock formation, alteration and mineralisation are related.

2 Background and sampling

The IOA deposits in Norbotten are mostly hosted by Svecofennian metavolcanic rocks (Porphyry/Porphyrite group, ca. 1.91-1.88 Ga; Bergman et al. 2001). Their average content of Fe and P is 30-70% and 0.05-5%, respectively, and they are enriched in REE (Parák 1973).

The largest ore body Kiirunavaara is currently mined at ca. 1300 m below the surface, extends ca. 5 km in N-S direction, and is up to 100 m thick (Bergman et al. 2001). Kiirunavaara and Luossavaara occur at the contact between trachyandesitic lavas (footwall) and

pyroclastic rhyodacite (hanging wall). The Per Geijer and Tuollavaara ore bodies lie within the rhyodacitic unit (Fig. 1). A second underground iron mine in the Norrbotten region, Malmberget, can be found in the Gällivare district, ca. 80 km further to the southeast.

Previous geochronology work attempted to bracket the age of the main ore at Kiirunavaara; a U-Pb zircon age by Welin (1987) of 1882 ± 24 Ma from the hanging wall and a whole rock Sm-Nd isochron yielding an age of 1890 ± 90 Ma for host rocks (Cliff et al. 1990) are combined to suggest the broad period between 1900 and 1880 Ma for the ore formation. In a following study, ore samples from the Kiirunavaara mine resulted in a whole rock Sm-Nd isochron age of 1490 ± 130 Ma (Cliff and Rickard 1992) which they interpreted as a regional reset of the Sm-Nd system. Titanite grains dated by ID-TIMS from magnetite-titanite veins in the Kiruna area fall within error of the 1900 and 1880 Ma time frame (Romer et al. 1994). In the same study, titanite from an amygdale gives a slightly younger age of 1876 ± 9 Ma. Recently published LA-ICPMS U-Pb dates on titanite complicate the story by promoting an age of ca. 2050 Ma for the Kiruna host rocks, based on some analyses in titanite cores, while the majority of analyses agree with previously suggested time frame (Storey et al. 2007; Smith et al. 2009). Overall, until now, age constraints for the Kiruna area are based on (altered) host rocks or late phases; the ore itself has not been directly dated.

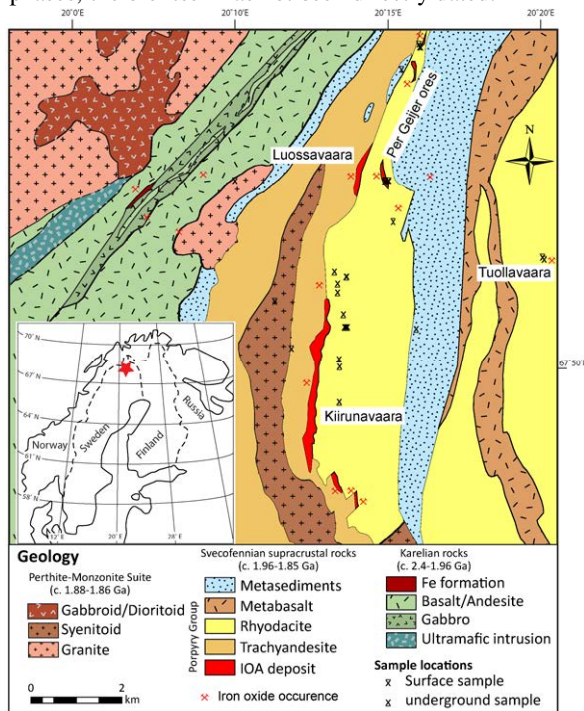


Figure 1. Geological map of Kiruna, N Sweden (simplified based on data provided by SGU) with sample locations. Underground sample locations at Kiirunavaara are projected to the surface and appear E of the ore, due to its eastwards dip.

2.1 Sampling

During two field seasons, host rocks, extensively altered host rocks, ore, and crucial intrusions at different locations within the Kiruna area were sampled for the

current study (Fig. 1). Further, samples from the two other active mines Malmberget and Gruvberget have been collected subsequently. Data presented here are from a high-phosphorous ore and host rocks from Kiirunavaara, a host rock from Tuollavaara, and variably altered host rock and ore from the Rektorn deposit (a Per Geijer deposit).

3 Accessory minerals and geochronology

Accessory minerals (zircon, titanite, monazite, and apatite) were separated using standard crushing techniques, magnetic, and heavy liquid methods, and then handpicked. The crystals were mounted in epoxy, and polished to reveal their centers and imaged using a FEI Quanta 400 scanning electron microscope (SEM) at Memorial University of Newfoundland.

Zircon is not abundant, but was found in a number of samples, most importantly in the high-P ore of Kiirunavaara. Zircon in this sample generally shows a zoned core and a rim dark in CL and rich in inclusions (Fig. 2b, c). The corresponding hanging wall contains zircon with a distinct internal growth zoning (Fig. 2a). Titanite is most common in the Kiirunavaara footwall (Fig. 2e) and Tuollavaara. Monazite is not common, but can be found in the ore samples either as single minerals, sometimes associated with apatite or as inclusion within apatite (Fig. 2d).

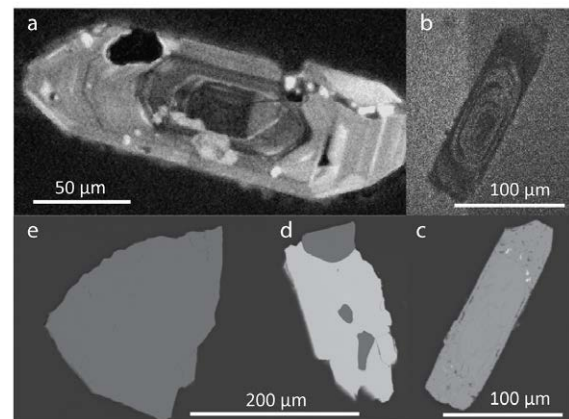


Figure 2. Cathodoluminescence (CL) and back-scattered electron (BSE) images of typical accessory minerals from the Kiirunavaara samples: a) CL image of zircon with oscillatory zoning from the hanging wall; b) CL image of ore zircon with zoned core and dark rim; c) BSE image of same ore zircon showing inclusion-rich rim; d) BSE image of ore monazite (light), associated with apatite (dark); and e) BSE image of featureless titanite from the footwall.

The U-Th-Pb mineral analyses were done using the Cameca 1270 ion microprobe at the Swedish Museum of Natural History (NordSIM facility) following the methods described by Whitehouse et al. (1999) and Whitehouse and Kamber (2005). Data reduction and common Pb correction was done using the Nordsim software written by Martin Whitehouse, and data regressions were done using Isoplot 3.0 (Ludwig 2003).

Zircon grains from the Kiirunavaara hanging wall and titanite from the footwall give Concordia ages of

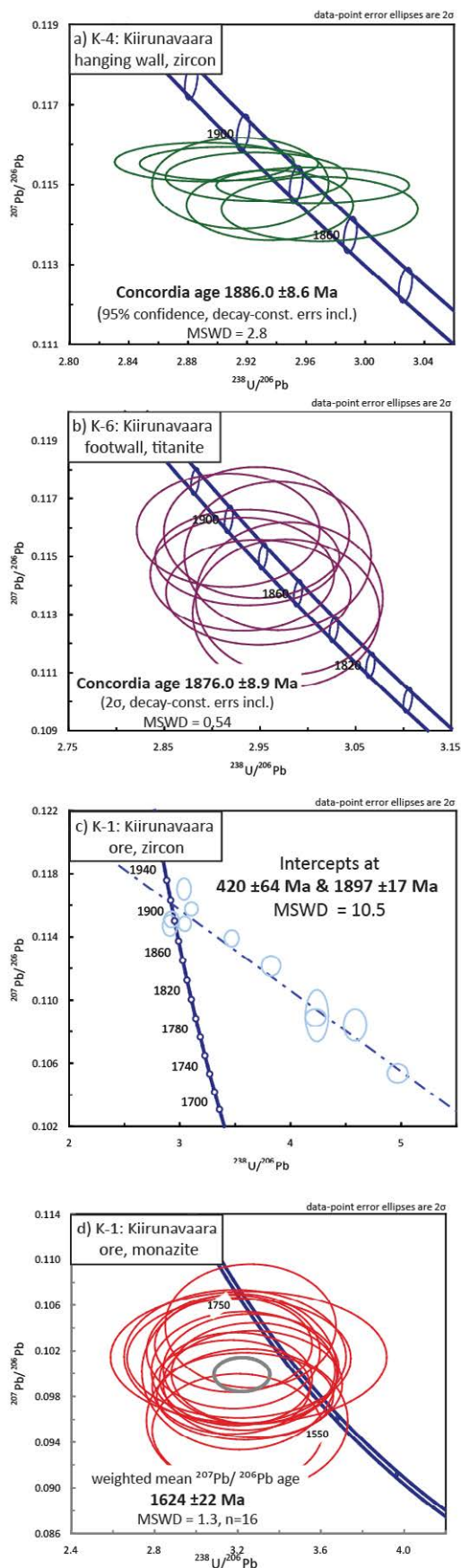


Figure 3. U-Pb data from the Kiirunavaara samples, plotted on Tera-Wasserburg concordia diagrams: hanging wall zircon (a), footwall titanite (b), high-P ore zircon (c) and monazite (d).

1886.0 ± 8.6 Ma and 1876.0 ± 8.9 Ma, respectively (Fig. 3a, b). Analyses within the cores of Kiirunavaara ore zircon form a discordia with an upper intercept of 1897 ± 17 Ma and a lower intercept of 420 ± 64 Ma (Fig. 3c). Analyses done in the zircon rims resulted in highly discordant data points. Lower U and Th concentrations of Kiruna monazite relative to the used standard complicate the Pb/U and Pb/Th age calculation. The data plot slightly below concordia, but form a coherent cluster (Fig. 3d). This shows that the system has not been disturbed and the calibration-independent $^{207}\text{Pb}/^{206}\text{Pb}$ age of 1624 ± 22 Ma for the Kiirunavaara ore is reliable.

4 Whole rock Nd tracer isotopes

For Sm-Nd analyses, whole rock powders were spiked with a $^{147}\text{Sm}/^{150}\text{Nd}$ mixed spike and dissolved in two stages ($\text{HF-HNO}_3 + 6\text{N HCl}$). Nd and Sm were isolated in a two-step cation exchange procedure and measured by thermal ionization mass spectrometer (TIMS).

Whole rock Sm-Nd isotopic data for two ores, five host rocks, and three extensively altered host rocks from Kiirunavaara, Rektorn, and Tuollavaara, are shown in Figure 4. ϵNd has been calculated at 1.88 Ga for comparison. Ore (ϵNd : -3.1, -3.3) and altered rocks (ϵNd : -3.5 to -3.9) have a less negative ϵNd signature than less altered host rocks (ϵNd : -5.8 to -6.7). The latter overlaps well with existing data for the volcanic (Cliff et al. 1990) and intrusive (e.g., Öhlander et al. 1993) rocks within the Kiruna area. In contrast, rocks with less negative ϵNd signature are more common in higher metamorphosed area around Malmerget, south Norrbotten region (e.g., Öhlander et al. 1993).

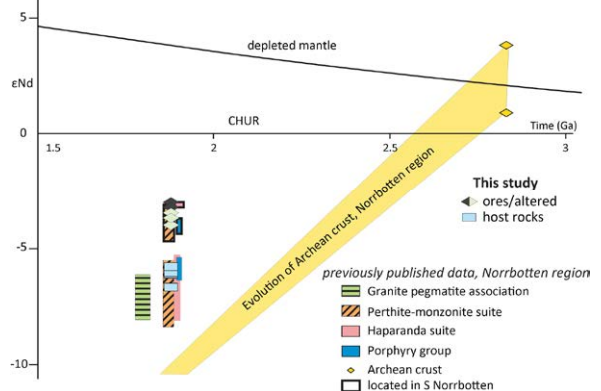


Figure 4. $\epsilon\text{Nd}_{(1.88 \text{ Ga})}$ composition vs. time for ores, host rock and altered samples from the Kiruna area, Norrbotten region, Sweden, compared to Svecofennian igneous rocks and Archean crust (Bergman et al 2001, and the reference therein). Depleted mantle curve is that of DePaolo (1981).

5 Discussion and conclusions

U-Pb ages from zircon and titanite presented here confirm a previously documented event around 1880-1900 Ma in the Norrbotten region (e.g., Cliff et al. 1990). No indication for an event at ca. 2050 Ma, as suggested by Storey et al. (2007), has been found. Instead, the

monazite U-Pb data suggests a younger event influencing the Kiirunavaara ore at ca. 1624 Ma. The lower intercepts of two samples fall within error in the period of the Caledonian orogeny. In general, the samples contained fewer datable grains than expected. Therefore, larger sample sizes are currently worked on to increase to number of suitable grains.

Ore samples and altered samples have distinctly different whole rock ϵNd values compared to the host rocks, possibly indicating different source regions of ore and host rocks. A similar difference in WR ϵNd values between ore and host rocks has been reported for the IOCG deposit Olympic Dam (Johnson and McCulloch 1995), and interpreted there as of mantle-derived influence on the ore. Also in Kiruna, host rock samples are closer related to the Nd signal of the Archean crust, while the extensively altered and ore samples are shifted towards the depleted mantle signature (Fig. 4). Detailed isotope geochemistry on mineral scale (Lu-Hf in zircon; Sm-Nd in monazite, apatite, titanite) is planned to follow up on this finding. Further investigation and data is needed to confirm the younger monazite dates: they may record a secondary event that is potentially related to the isotopic shift in the ore samples.

Acknowledgements

This abstract represents first results of the Ph.D. project of Anne Westhues, undertaken at Memorial University of Newfoundland (MUN) under the supervision of JM Hanchar. Great thanks are due to LKAB (Kiirunavaara operations) for financial and logistical support, especially K Holme for making the project possible, and many others for fruitful discussion and help during sampling. The project was financially supported by NSERC, MUN, SEG, and MAC. Numerous people are to thank for discussions and assistance in the labs including M Wilson, SJ Piercey, G Layne, GR Dunning, PJ Silvester, CM Fisher, S Strong, P King, and L Hewa at MUN, K Lindén and AS Bouvier at the Swedish Museum of Natural History, and J Anderson, A Hallberg, S Bergman, JA Perdahl and others of the Swedish Geological Survey.

References

Barton MD, Johnson DA (1996) Evaporitic-source model for igneous-related Fe oxide-(REE-Cu-Au-U) mineralization. *Geology* 24:259-262.

Barton MD, Johnson DA (2004) Footprints of Fe-oxide-(Cu-Au) systems. SEG 2004: Predictive Mineral Discovery Under Cover Centre for Global Metallogeny, Spec Pub 33:112-116.

Bergman S, Kubler L, Martinsson O (2001) Description of regional geological and geophysical maps of northern Norrbotten County (east of the Caledonian Orogen). Sveriges Geologiska Undersökning Ba 56. 110 pp.

Billström K, Eilu P, Martinsson O, Niiranen T, Broman C, Weihed P, Wanhainen C, Ojala J (2010) IOCG and related deposits of the Northern Fennoscandian Shield In: Porter TM (ed) Hydrothermal iron oxide copper-gold and related deposits: a global perspective, vol. 1. PGC Publishing, Adelaide, pp 415-426.

Cliff RA, Rickard D, Blake K (1990) Isotope systematics of the Kiruna magnetite ores, Sweden: Part 1. Age of the ore. *Econ*

Geol 85:1770 - 1776.

Cliff RA, Rickard D (1992) Isotope systematics of the Kiruna magnetite ores, Sweden: Part 2. Evidence for a secondary event 400 m.y. after ore formation. *Econ Geol* 87:1121-1129.

Depaolo DJ (1981) Neodymium isotopes in the Colorado front range and crust-mantle evolution in the Proterozoic. *Nature* 291:193-196.

Frietsch R (1978) On the magmatic origin of iron ores of the Kiruna type. *Econ Geol* 73:478-485.

Groves DI, Bierlein FP, Meinert LD, Hitzman MW (2010) Iron Oxide Copper-Gold (IOCG) Deposits through Earth History: Implications for Origin, Lithospheric Setting, and Distinction from Other Epigenetic Iron Oxide Deposits. *Econ Geol* 105:641-654.

Hitzman MW, Oreskes N, Einaudi MT (1992) Geological Characteristics and Tectonic Setting of Proterozoic Iron-Oxide (Cu-U-Au-Ree) Deposits. *Precambrian Res* 58:241-287.

Johnson JP, McCulloch MT (1995) Sources of mineralising fluids for the Olympic Dam Deposit (South Australia); Sm-Nd isotopic constraints. *Chem Geol* 121:177-199.

Ludwig KR (2003) User's manual for Isoplot 3.00, A geochronological toolkit for Microsoft Excel. Berkley Geochronology Center Special Publication 4:71 pp.

Martinsson O (2004) Geology and metallogeny of the northern Norrbotten Fe-Cu-Au province. Society of Economic Geologists, Guidebook Series 33:131-148.

Öhlander B, Skiöld T, Elming SÅ, Claesson S, Nisca DH (1993) Delineation and character of the Archaean-Proterozoic boundary in northern Sweden. *Precambrian Res* 64:67-84.

Parák T (1973) Rare-Earths in Apatite Iron-Ores of Lapland Together with Some Data About Sr, Th and U Content of These Ores. *Econ Geol* 68:210-221.

Parák T (1975) Kiruna iron ores are not 'intrusive-magmatic ores of the Kiruna type'. *Econ Geol* 70:1242-1258.

Porter TM (2010) Current understanding of iron oxide associated-alkali altered mineralised systems: Part I - An overview In: Porter TM (ed) Hydrothermal iron oxide copper-gold and related deposits: a global perspective, vol. 3. PGC Publishing, Adelaide, pp 5-32.

Romer RL, Martinsson O, Perdahl JA (1994) Geochronology of the Kiruna Iron-Ores and Hydrothermal Alterations. *Econ Geol Bull Soc* 89:1249-1261.

Smith MP, Storey CD, Jeffries TE, Ryan C (2009) In Situ U-Pb and Trace Element Analysis of Accessory Minerals in the Kiruna District, Norrbotten, Sweden: New Constraints on the Timing and Origin of Mineralization. *J Petrol* 50:2063-2094.

Storey CD, Smith MP, Jeffries TE (2007) In situ LA-ICP-MS U-Pb dating of metavolcanics of Norrbotten, Sweden: Records of extended geological histories in complex titanite grains. *Chem Geol* 240:163-181.

Valley PM, Hanchar JM, Whitehouse MJ (2009) Direct dating of Fe oxide-(Cu-Au) mineralization by U/Pb zircon geochronology. *Geology* 37:223-226.

Welin E (1987) The depositional evolution of the Svecofennian supracrustal sequence in Finland and Sweden. *Precambrian Res* 35:95-113.

Whitehouse MJ, Kamber BS, Moorbath S (1999) Age significance of U-Th-Pb zircon data from early Archaean rocks of west Greenland—a reassessment based on combined ion-microprobe and imaging studies. *Chem Geol* 160:201-224.

Whitehouse MJ, Kamber BS (2005) Assigning Dates to Thin Gneissic Veins in High-Grade Metamorphic Terranes: A Cautionary Tale from Akilia, Southwest Greenland. *J Petrol* 46:291-318.

Williams PJ, Kendrick MA, Xavier RP (2010) Sources of ore fluid components in the IOCG deposits In: Porter TM (ed) Hydrothermal iron oxide copper-gold and related deposits: a global perspective, vol. 3. PGC Publishing, Adelaide, pp 107-116.

Mineralogical and fluid characteristics of the Monakoff and E1 deposits, Cloncurry Region: implications for regional F-Ba-rich IOCG mineralisation

Megan R. Williams, David A. Holwell

Department of Geology, University of Leicester, University Road, Leicester, LE1 7RH, UK

Richard M. Lilly

Xstrata Copper Exploration, Oban Road, Mount Isa, Queensland, Australia

Iain McDonald

School of Earth & Ocean Sciences, Cardiff University, Cardiff, CF10 3AT, UK

Adrian J. Boyce

Scottish Universities Environmental Research Centre, Rankine Avenue, Scottish Enterprise Technology Park, East Kilbride, G75 0QF, UK

Abstract. The Eastern Succession of the Mount Isa Inlier is home to several significant and diverse Iron-Oxide-Copper-Gold (IOCG) deposits. Two of these, Monakoff and E1, represent a distinct style of IOCG within the Inlier, distinguished by high abundances of fluorite and barite. We show that these two independent, structurally variable deposits, situated ~25km away from each other, are analogous in terms of ore mineralogy and mineralising fluids, implying commonality of origin. This study includes the first investigation of REE concentrations within fluorite in the region. The two deposits show similar overall REE profiles, including a distinct positive Eu anomaly. New fluid inclusion data supports that both Monakoff and E1 formed from fluids within the temperature range 300–450°C and perhaps higher. Mineralogical relationships are consistent with the mixing of a low salinity, CO₂ rich and ultra high salinity, F-U-REE-bearing, fluid of probable magmatic source. Sulphur isotope signatures are similar to other IOCG deposits in the area and can be interpreted as being consistent with an evolving magmatic source for at least one of these fluids. This study highlights the extent of these distinctive mineralising fluids within the area and implies potential for similar deposits in proximity to the Williams and Naraku Batholiths.

Keywords. Fluorite, barite, IOCG, Mount Isa Inlier, fluid inclusions, fluorite REE.

1 Introduction

The Eastern Succession of the Proterozoic Mount Isa Inlier is one of the worlds' most productive mineral provinces, recognised worldwide for its diversity in Iron-Oxide-Copper-Gold (IOCG) styles, within a relatively small area. The Eastern Succession is host to several significant IOCG deposits, including Xstrata Copper's Ernest Henry Mining Operation and Monakoff and E1 deposits, with the Monakoff deposit containing reserves of 1.5 Mt at 1.39% Cu and 0.44g/t Au. Monakoff and E1, the focus of this study, represent a distinct style of IOCG within the Inlier, characterised by high abundances of barite and fluorite, plus a wide range of enriched elements such as REE, U, Pb and Zn. Fluorine-REE-U-rich fluids are recognised in some other IOCG deposits, notably the supergiant Olympic Dam, iron oxide Cu-Au-

U-REE deposit in the Gawler Craton of South Australia.

The E1 deposit is situated ~25km to the NNE of Monakoff and ~8km E of Ernest Henry, whilst Monakoff lies ~20km S of Ernest Henry and ~15km ENE of Cloncurry. This study characterises the style of mineralisation and the fluids which give rise to these assemblages at Monakoff and E1. This will help to constrain the distribution of these distinctive F-rich mineralising fluids and aid with exploration models in the region around Ernest Henry.

2 Regional Geology

Proterozoic aged (~1.74-1.66Ga) basement rocks form the majority of the Eastern Succession (Austin and Blenkinsop 2009), which have since been overlain by three major supracrustal sequences, in which the IOCG deposits occur. The Isan Orogeny was a major contractional deformation event at 1600-1490Ma (Austin and Blenkinsop 2009) and was coincident with the emplacement of the granitic A-type Williams and Naraku Batholiths between 1550-1500Ma. IOCG deposits within the area, including Ernest Henry, have been dated as being post-peak metamorphism, synchronous with the emplacement of these batholiths, thus compatible with a magmatic fluid source (Williams et al. 2005). However, several studies have shown that a magmatic source is not essential in the genesis of all IOCGs within the region (e.g. Oliver et al. 2008).

3 Field Relations and Mineralisation Style

3.1 Monakoff

The Monakoff deposit is hosted within the Proterozoic basement of the Soldiers Cap Group. This forms part of Cover Sequence Three, deposited between ~1655-1680Ma. The Soldiers Cap Group consists of a succession which is carbonate poor, younging from the Llewellyn Creek Formation, through the Mount Norna Quartzite Formation to the Toole Creek Volcanics (Davidson et al. 2002). Monakoff is located on the

northern, south dipping limb of the Pumpkin Gully Syncline. The mineralised zone is discrete (<15m wide), deformed and structurally controlled, formed within a dilational jog, in an E-W trending D₁ shear zone. This is thought to have facilitated the mixing of fluids during subsequent D_{2,5} deformation, which opened up dilations in the pre-existing D₁ shears (Davidson et al. 2002). The ore body has been documented as not being stratiform, occurring in a sub-vertical zone of dilation, associated with SW-orientated shortening (Austin et al. 2013). The ore zone is a linear, vertical sheet-like body composed of sulphides, magnetite, with fluorite-barite-calcite-quartz gangue. Mineralisation is hosted within sub-vertical meta-sediments between two more competent units; the Toole Creek Volcanics in the hanging wall (~1658Ma) and the volcanics of the Mount Norna Quartzite Formation in the footwall (~1654Ma).

3.2 E1 Deposits

The E1 deposit comprises three distinct copper-gold deposits, which share a similar mineralogy, but different structural setting and host rocks to Monakoff. E1 consists of E1 North, South and East, which have all been covered by 20-50m of Pliocene sands, gravels and Cretaceous siltstones, with a basement composed of altered mafic to intermediate volcanics, volcanoclastics and meta-sediments of the Soldiers Cap Group. These deposits all exhibit slightly different structural controls, however, the style of mineralisation within magnetite altered volcanoclastics and meta-sediments with late-stage fluorite, barite and sulphide bearing veins, is comparable between all three.

4 Monakoff Geochemistry

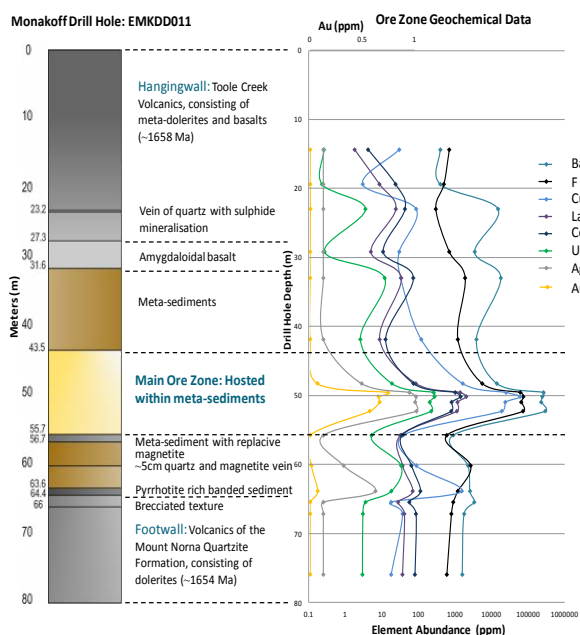


Figure 1. Log of Monakoff drill hole EMKDD011, displaying the main lithological units, coinciding with a graphical plot of elemental abundances, highlighting the ore mineralogy.

Figure 1 illustrates metal profiles across the ore zone and host rocks at Monakoff. Geochemically, the ore zone is

characterised by average concentrations of Au (0.66ppm), Ag (78ppm), Cu (1%), Pb (0.64%), Zn (0.81%), REE (Ce, La, Eu, Nd, Pr) (TREO 0.302%) and U (242ppm). This correlates with elevated concentrations of F (7%), BaO (21.4%) and MnO (2.33%), all occurring within a narrow <15m shear zone.

5 Ore Mineralogy

The ores of the two deposits are mineralogically diverse, but share remarkable mineralogical similarities (Fig. 2). Base metal assemblages in both deposits are dominated by magnetite, pyrite, chalcopyrite with associated galena, anglesite, sphalerite and accessory arsenopyrite and alloclasite (Co,Fe)AsS in a multistage paragenesis. Potassic alteration predates an early magnetite stage, which is overprinted by pyrrhotite and followed by the main ore stage. This main stage includes sulphides and major barite-fluorite-manganoo calcite-quartz gangue. REE and U minerals are associated with this F, Ba, Ca affluent stage. Accessory mineralisation is also analogous between Monakoff and E1. REE, U and precious metal minerals consist of richetite (Pb(UO₂)₄O₅·4H₂O), several U-silicates, La-Ce REE minerals, including bastnäsite-La ((La, Ce)(CO₃)F) and Ag-Bi-Pb sulphosalts (including treasureite (Ag₇Pb₆Bi₁₅S₃₂)).

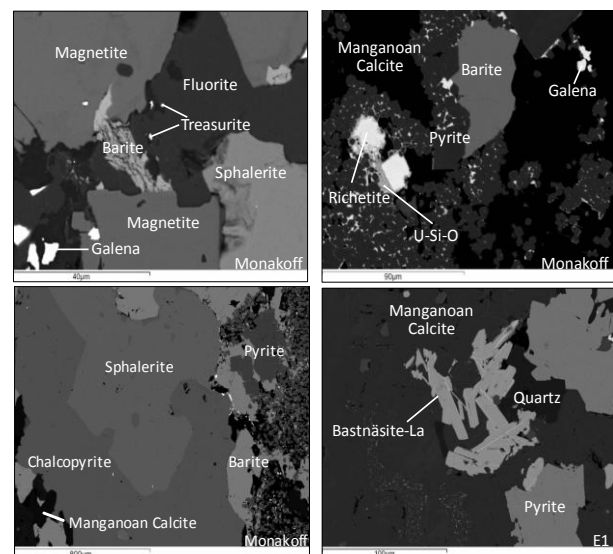


Figure 2. SEM images displaying the diverse ore mineralogy at Monakoff and E1.

Laser Ablation-ICP-MS work has revealed Au to be found predominantly as Ag-Au-Bi-Pb sulphosalts which are located within sulphides, particularly chalcopyrite, and fluorite in both deposits (Figs. 2, 3). In addition to this, Au has also been observed in solid solution within sulphides and as minor individual grains of electrum. The presence of gold as sulphosalts and in solid solution in pyrite contrasts with Au occurrence at nearby Ernest Henry and within many of the IOCGs of the region, where Au commonly occurs as electrum in association with sulphides (Mark et al. 2006).

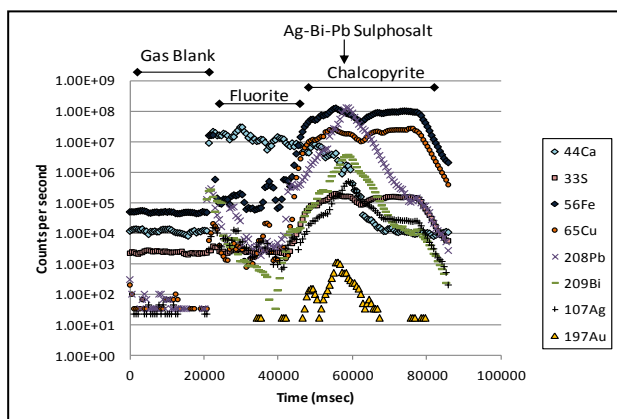


Figure 3. Time-resolved analysis spectra from a LA-ICP-MS line analysis of fluorite and chalcopyrite, with an Ag-Bi-Pb mineral, located within chalcopyrite, as the main Au carrier.

6 Fluid Characteristics

Fluid inclusion microthermometry conducted in fluorite is the first study of its kind at Monakoff and E1 and has highlighted the presence of at least three distinct fluid inclusion types at both Monakoff and E1:

1. Relatively pure CO₂-rich fluid inclusions.
2. Complex, high salinity, multi-phase, liquid-vapour-solid fluid inclusions. This group can be divided into lower temperature ($T_h \sim 317\text{-}370^\circ\text{C}$) and higher temperature ($T_h > 450^\circ\text{C}$) populations.
3. A low salinity, lower temperature, aqueous liquid-vapour fluid, with salinities in the range of $\sim 4\text{-}12$ wt% eq. NaCl (mean 6.06 wt% eq. NaCl) and T_h of $\sim 235^\circ\text{C}$.

These findings, therefore, are consistent with comparable fluid types at the two deposits. The presence of the multi-phase high salinity inclusions is analogous to many other IOCG deposits of the Cloncurry area (Williams and Skirrow 2000). Geochemical and mineralogical associations are consistent with the presence and mixing of at least two fluids: (1) an oxidised, U, REE, sulphate and F-rich fluid mixing with (2) a reduced Ba, Ca, Mn rich fluid. This is based upon the following parameters. Barium and sulphur can rarely be transported within the same fluid, due to the low solubility of barite (Mark et al. 2006). Ba and Mn also exhibit minimal solubility within oxidised fluids, therefore, transport of both Ba and Mn is enhanced under reduced conditions (Cooke et al. 2000). Similarly, due to fluorite's low solubility, transportation of fluorite and calcium requires division. Uranium transportation is often favoured by saline and oxidised fluids thus it has been purported to have been transported in fluid (1) (Hitzman and Valenta 2005). Mineralogical observations indicate that REE are linked with the fluorite rich stage and therefore, are likely to have been transported within the F-rich fluid. This is supported by Williams-Jones et al. (2000) who document REE transport within F-rich magmatic fluids, predominantly as fluid complexes. The mixing of these two fluids at the site of deposition would result in a sharp drop in the activity of F (due to Ca mixing), depositing fluorite and causing the destabilisation of REE fluoride complexes, resulting in

REE deposition. This mixing could also effectively account for synchronous barite deposition. This is analogous to the ore forming fluids at Olympic Dam, which were F-rich and had the capacity to transport diverse elements.

7 Sulphur Isotopes

Results from a pilot study of S isotope signatures of sulphides and sulphates from the two deposits give a range in $\delta^{34}\text{S}$ of -5.4 to -2.8‰ for Monakoff sulphides, with pyrite generally slightly heavier than chalcopyrite. Chalcopyrite from the main stage fluorite-barite-calcite-sulphide veins at E1 has a comparable $\delta^{34}\text{S}$ of -2.6‰ , whereas, coexisting barite displays $\delta^{34}\text{S}$ values of $+16\text{‰}$. This range in $\delta^{34}\text{S}$ of ore sulphides is consistent with other IOCG deposits in the Eastern Succession of the Mount Isa Inlier that generally have a range -6.5 to $+3.5\text{‰}$ (Mark et al. 2006) and is most comparable with the Starra deposit (Rotherham et al. 1998). The $\delta^{34}\text{S}$ signatures of pyrite within the host rock Toole Creek Volcanics and early pyrrhotite associated with pre-ore alteration in the meta-sediments is around 0 to $+1\text{‰}$, consistent with a magmatic signature. The similar ranges of sulphide and sulphate $\delta^{34}\text{S}$ at Starra have been interpreted to be from a single S source of magmatic-metasomatic origin under oxidised conditions (Rotherham et al. 1998). Davidson and Davis (2002), using sulphate-sulphide pairs from Monakoff, indicate that high temperature sulphate and sulphide had similar compositions, and in these cases, a magmatic rather than seawater S source was favoured. Further work on sulphide-sulphate pairs from E1 is ongoing to fully constrain the S source and provide temperature constraints that can be used to corroborate the fluid inclusion data.

8 REE Contents of Fluorite

The distribution of REE in fluorite is affected by ore forming processes due to the fractionation of Ce and Eu (Schwinn and Markl 2005). This study represents the first LA-ICP-MS investigation into the REE geochemistry of fluorite from any IOCG deposit within the Mount Isa Inlier.

Figure 4 displays the three fluorite REE chondrite-normalised patterns. Firstly, the Monakoff fluorite (Type 1) is characterised by a large positive Eu anomaly, a steep slope from La to Pr and a flat to arched HREE chondrite-normalised REE pattern. The E1 deposit displays two fluorite assemblages. The first one (Type 2) is associated with sulphides and displays a similar pattern to the Monakoff fluorite, albeit, with a smaller positive Eu anomaly. Type 3 represents a later vein stage, composed of fluorite and quartz. This fluorite is also characterised by a positive Eu anomaly, a steep slope from La to Pr and an enrichment in HREE (Tb, Dy, Ho and Er).

Although the magnitude of the Eu anomaly varies between Monakoff and E1, the overall profile shapes are similar, indicating that they are comparable. Positive Eu anomalies in fluorite require the presence of Eu^{3+} as this can substitute for Ca, whereas Eu^{2+} cannot

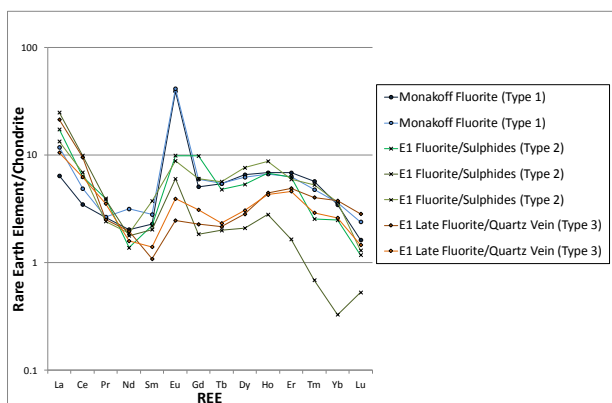


Figure 4. Chondrite-normalised REE patterns within fluorite from both Monakoff and E1.

(Constantopoulos 1988). Bau (1991) demonstrates that the temperature at which Eu^{3+} is reduced to Eu^{2+} increases with increasing oxygen fugacity. Thus, at elevated temperatures, a positive Eu anomaly can be preserved if the oxygen fugacity is sufficiently high. Our fluid inclusion data indicate a maximum temperature of $>400^\circ\text{C}$, and thus a minimum oxygen fugacity of formation can be estimated using the experimental work of Bau (1991). For such temperatures, Eu^{3+} is stable in oxidising conditions close to the sulphide-sulphate transition. This, together with the abundance of sulphide and sulphate in the ores, supports the presence of an oxidised fluid involved as one component in the ore genesis and deposition of fluorite at Monakoff and E1.

9 Conclusions and Exploration Implications

The ‘Monakoff’ style of IOCG mineralisation is characterised by high abundances of fluorite, barite, U and REE, which are related to the mixing of multiple fluids at temperatures of around $300\text{--}450^\circ\text{C}$. Gold is present predominantly within Ag-Bi-Pb sulphosalts, which is atypical for IOCG deposits in the area. Mineralisation is associated with structural features, including faulting and dilation jogs within shear zones, which have facilitated the fluid flow. This pathway is also enhanced by lithochemical contrasts. Monakoff and E1 share comparable ore mineralogies, fluid inclusion populations, S isotope signatures and similar REE profiles in fluorite, implying a commonality of origin. This stresses the presence of an extensive F-rich fluid system within the region. Moreover, it has been documented by Baker et al. (2008) that the Williams and Naraku Batholiths produced an ultrasaline, high temperature fluid, which may correlate with fluid inclusion Type Two. Pollard (2006) stated that this source would also explain the enrichment of elements including U, REE and F. The identification of this distinct style and further work on constraining the sources of the fluids will have implications for exploration of F-U-REE-bearing IOCGs in the region.

Acknowledgements

Sincere gratitude goes to Xstrata Copper Exploration, NW Queensland and Xstrata Copper Mount Margaret Mining for their funding towards the analytical

techniques used throughout this study and for their permission to publish these results. Gawen Jenkin is also thanked for his assistance with fluid inclusion work.

References

- Austin JR, Blenkinsop TG (2009) Local to regional scale structural controls on mineralisation and the importance of a major lineament in the eastern Mount Isa Inlier, Australia: Review and analysis with autocorrelation and weights of evidence. *Ore Geology Reviews* 35:298-315
- Austin J, Schmidt P, Lilly RM (2013) Anisotropy of Magnetic Susceptibility (AMS) and Paleomagnetism applied to the differentiation of the structural and metallogenic controls on Iron Oxide Copper-Gold (IOCG) mineralization: a case study from Monakoff, NW, Queensland. 23rd International Geophysical Conference and Exhibition, 11-14 August 2013
- Baker T, Mustard R, Fu B, Williams PJ, Dong G, Fisher L, Mark G, Ryan CG (2008) Mixed messages in iron oxide-copper-gold systems of the Cloncurry district, Australia: insights from PIXE analysis of halogens and copper in fluid inclusions. *Miner Deposita* 43:599-608
- Bau M (1991) Rare-earth element mobility during hydrothermal and metamorphic fluid-rock interaction and the significance of the oxidation state of europium. *Chemical Geology* 93:219-230
- Constantopoulos J (1988) Fluid Inclusions and Rare Earth Element Geochemistry of Fluorite from South-Central Idaho. *Econ Geol* 83:626-636
- Cooke DR, Bull SW, Large RR, McGoldrick PJ (2000) The Importance of Oxidized Brines for the Formation of Australian Proterozoic Stratiform Sediment-Hosted Pb-Zn (Sedex Deposits). *Econ Geol* 95:1-18
- Davidson GJ, Davis BK (2002) A decompression model of formation for some oxide Cu-Au deposit fluids—a hypothesis. *Geol Soc Australia Abstracts* 67:288
- Davidson GJ, Davis BK, Garner A (2002) Structural and Geochemical Constraints on the Emplacement of the Monakoff Oxide Cu-Au (-CO-U-REE-Ag-Zn-Pb) Deposit, Mt Isa Inlier, Australia. PGC Publishing:49-75
- Hitzman MW, Valenta RK (2005) Uranium in Iron Oxide-Copper-Gold (IOCG) Systems. *Econ Geol* 100:1657-1661
- Mark G, Oliver NHS, Carew MJ (2006) Insights into the genesis and diversity of epigenetic Cu – Au mineralisation in the Cloncurry district, Mt Isa Inlier, northwest Queensland. *Austral J Earth Sci* 53:109-124
- Oliver NHS, Butera KM, Rubenach MJ, Marshall LJ, Cleverley JS, Mark G, Tullemans F, Esser D (2008) The protracted hydrothermal evolution of the Mount Isa Eastern Succession: A review and tectonic implications. *Precambrian Research* 163:108-130
- Pollard PJ (2006) An intrusion-related origin for Cu-Au mineralisation in iron oxide-copper-gold (IOCG) provinces. *Miner Deposita* 41:179-187
- Rotherham JF, Blake KL, Cartwright I, Williams PJ (1998) Stable isotope evidence for the origin of the Mesoproterozoic Starra Au-Cu deposit, Cloncurry district, northwest Queensland. *Econ Geol* 90:1435-1449
- Schwinn G, Markl G (2005) REE systematics in hydrothermal fluorite. *Chemical Geology* 216:225-248
- Williams PJ, Barton MD, Johnson DA, Fontboté L, Haller AD, Mark G, Oliver NHS, Marschik R (2005) Iron Oxide Copper-Gold Deposits: Geology, Space-Time Distribution, and Possible Modes of Origin. *Econ Geol*, 100th Anniversary Volume:371-405
- Williams-Jones AE, Samson IM, Olivo GR (2000) The Genesis of Hydrothermal Fluorite-REE Deposits in the Gallinas Mountains, New Mexico. *Econ Geol* 95:327-342
- Williams PJ, Skirrow RG (2000) Overview of Iron Oxide Copper-Gold Deposits in the Curnamona Province and Cloncurry District (Eastern Mount Isa Block), Australia. In: Porter TM (ed) *Hydrothermal Iron Oxide Copper-Gold and Related Deposits: A Global Perspective*, PGC Publishing 1:105-122

Sources of mineralizing fluids in Cu-Au systems from the Carajás Mineral Province (Brazil): constraints from in-situ microanalysis of hydrogen and boron isotopes in tourmaline

Roberto Perez Xavier

Instituto de Geociências - UNICAMP, Campinas, Brazil

Robert B. Trumbull, Michael Wiedenbeck

GFZ German Research Centre for Geosciences, Potsdam, Germany

Lena Virginia Soares Monteiro

Instituto de Geociências - USP, São Paulo, Brazil

Abstract. Results of a pilot B- and H-isotope study using secondary ion mass spectrometry (SIMS) of hydrothermal tourmaline are reported from two contrasting Cu-Au deposits of the Carajás Mineral Province, northern Brazil: the Archean (2.76 or 2.57 Ga) breccia-hosted Igarapé Bahia iron oxide-rich copper-gold deposit and the Paleoproterozoic (1.88 Ga) intrusion-related Breves Cu-Au-(Mo-W-Bi-Sn) deposit. Tourmaline from the Igarapé Bahia deposit belongs to the intermediate Mg-rich schorl-dravite series and displays $\delta^{11}\text{B}$ and δD values ranging from 12.6‰ to 26‰ and from -89.1‰ to -69‰, respectively. The heavy $\delta^{11}\text{B}$ values combined with the calculated $\delta\text{D}_{\text{H}_2\text{O}}$ in the range of -30 to -10‰ (at 400°C) suggest an important involvement of non-magmatic fluids (e.g. evolved seawater, formation water or bittern fluids) in this hydrothermal system. The intrusion-related Breves tourmaline is near end-member schorl and yields much lower $\delta^{11}\text{B}$ (-4‰ to 2‰) and δD (-116‰ to -99‰) values. The calculated $\delta\text{D}_{\text{H}_2\text{O}}$ between -57‰ and -32‰ (at 400°C) and the lower $\delta^{11}\text{B}$ values are more consistent with a magmatic-derived fluid.

Keywords. Iron oxide-copper-gold deposits, Carajás Mineral Province, tourmaline, boron and hydrogen isotopes, SIMS.

1 Introduction

Tourmaline is commonly found in association with a variety of economically important Archean and Paleoproterozoic Cu-Au mineral systems of the Carajás Mineral Province (CMP), in the southeastern part of the Amazon Craton, northern Brazil. These systems are grouped, according to their geologic characteristics and metal endowments, into large-tonnage (100–789 Mt) Fe oxide-Cu-Au (IOCG) deposits (e.g., Salobo, Igarapé Bahia, Cristalino, Gameleira, Sossego and Alvo 118; Xavier et al. 2012) and Cu-Au-(Mo-W-Bi-Sn) deposits, generally of smaller tonnage (< 50 Mt; e.g., Breves, Águas Claras, Estrela; Tallarico et al. 2004).

In common with IOCG deposits elsewhere in the world, much controversy remains over genetic models for the Carajás deposits. Various proposed models involve contrasting syngenetic and epigenetic interpretations and point to evolution of the Carajás IOCG deposits in association with (1) nonmagmatic, (2) magmatic, or (3) hybrid magmatic-nonmagmatic

systems (Xavier et al. 2012). The Cu-Au-(Mo-W-Bi-Sn) deposits, on the other hand, generally show clear spatial and temporal relationships with Paleoproterozoic (1.88 Ga) granitic intrusions and, accordingly, have been interpreted as magmatic-hydrothermal polymetallic systems (Xavier et al. 2004).

This study compares the chemical composition and the combined boron - hydrogen isotope signature of tourmaline from iron oxide-rich-Cu-Au and intrusion-related Cu-Au-(Mo-W-Bi-Sn) systems from the CMP, using as case studies Igarapé Bahia and Breves deposits, respectively. These data demonstrate the feasibility of combined B-H measurements by SIMS and provide further insights into the evolution and sources of ore-bearing hydrothermal fluids, which were active during the Archean and Paleoproterozoic in the CMP.

2 Geologic Setting and Tourmaline Occurrence

2.1 Igarapé Bahia Fe oxide-Cu-Au deposit

The Igarapé Bahia deposit (219 Mt at 1.4 wt % Cu, 0.86 g/t Au; Tallarico et al. 2005) is confined to Archean (~2,75 Ga) volcano-sedimentary rocks of the Igarapé Bahia Group, Itacaiúnas Supergroup (DOCEGEO, 1988). The deposit is hosted by concordant, vertically dipping, polymictic and matrix-supported breccia bodies situated between chlorite-altered basalt with banded iron formation and chert in the footwall and a dominantly coarse- to fine-grained siliciclastic sedimentary sequence in the hanging wall. The breccia bodies are about 2 km long and 30 to 250 m thick, and comprise mainly coarse, angular to rounded basalt, BIF, and chert derived from the footwall unit (Dreher et al. 2008). Hydrothermal alteration assemblages are dominated by chlorite - carbonate in weakly mineralized zones, whereas strongly mineralized zones contain abundant Fe-K alteration minerals, including magnetite, biotite, siderite, Fe actinolite, and stilpnomelane (Tallarico et al. 2005; Dreher et al. 2008).

Mineralization is concentrated in the matrix of the breccia and consists of disseminated to locally massive, fine-grained chalcopyrite and bornite, with associated magnetite, Au, U, and light rare earth element (LREE)

minerals, cobaltite, pyrite, molybdenite, and varied amounts of chlorite, siderite, amphibole, biotite, apatite, tourmaline, ferropyrosmalite, scapolite, and quartz (Dreher et al. 2008). The mineralization is Archean, but the precise age is contentious: 2.76 Ga (Gallarza et al. 2002) or 2.57 Ga (Tallarico et al. 2005).

The most common occurrence of tourmaline is in the ore-breccia matrix, as disseminated bluish-green and beige hypidiomorphic grains particularly in chlorite-rich domains. In high-grade zones, tourmaline is either enclosed by chalcocopyrite or displays chalcocopyrite filling in fractured and brecciated grains (Fig. 1A). Collectively, these textural relationships suggest that precipitation of tourmaline was prior to the Cu-Au ore. Very subordinately, fine-grained deep blue-colored tourmaline crystals with fibrous arrangement also occur along discordant veinlets, together with carbonate, quartz and chalcocopyrite.

2.2 Breves Cu-Au-(Mo-W-Bi-Sn) deposit

The intrusion-related Breves Cu-Au (Mo-W-Bi-Sn) deposit is hosted by siliciclastic units of the Águas Claras Formation (2.64 Ga or 1.88 Ga), in the roof zone

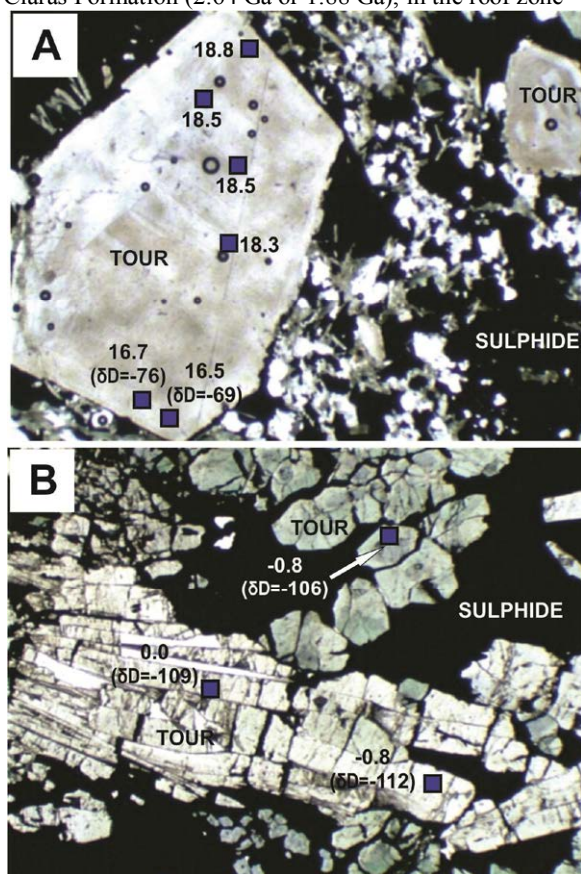


Figure 1. Photomicrographs of tourmaline (Tour) from the Igarapé Bahia (A) and the intrusion-related Breves Cu-Au deposits (B). Blue squares display in-situ boron isotope analysis, some of them coupled with hydrogen isotope values (in brackets).

of the apical part of a Paleoproterozoic (1.88 Ga) granitic intrusion (Tallarico et al. 2004). This largely disseminated mineralization occurs mainly in the

siliciclastic rocks and in cross-cutting vein systems. Ore minerals in the disseminated mineralization are dominated by chalcocopyrite, with very subordinate pyrite and arsenopyrite, whereas in the vein mineralization pyrite is the most abundant sulphide, accompanied by variable concentrations of arsenopyrite, chalcocopyrite, pyrrhotite, molybdenite, and minor amounts of ferberite, cassiterite and scheelite. Gold, together with native bismuth, bismuth-bearing tellurides, and cobalt-bearing arsenides, occurs particularly in the veins in association with arsenopyrite and, much less frequently, with chalcocopyrite. This sulphide-oxide paragenesis, both in the disseminated and vein-related mineralization, is frequently associated with an alteration assemblage consisting of chlorite ± muscovite-phengite ± biotite ± fluorite ± tourmaline (Xavier et al. 2004; Botelho et al. 2005). Mineralization is Paleoproterozoic and the age has been bracketed at 1.87 Ga (Tallarico et al. 2004).

Major concentrations of tourmaline are particularly common in veins or disseminated in the siliciclastic host rock. Tourmaline generally occurs as sets of green-colored, needle-like crystals, which form fibrous arrangement, or in aggregates of fine-grained crystals (Fig. 1B). Optical zoning is not commonly observed in thin section. It commonly appears in contact with pyrite, chalcocopyrite, arsenopyrite and molybdenite, suggesting to be syn-mineralization.

3 Tourmaline Chemistry and Boron - Hydrogen Isotopic Composition

The chemical and boron isotopic composition were determined for ore-related disseminated and vein tourmaline of the Igarapé Bahia deposit, whereas only vein tourmaline was analyzed for the Breves deposit.

Electron probe micro-analyses on tourmaline grains were measured using a CAMECA SX-100 instrument operated at 15 kV accelerating voltage and 10 nA beam current at the GeoForschungsZentrum (GFZ), Potsdam (Germany). Boron and hydrogen isotopic analyses were obtained on a Cameca ims 6f Secondary Ion Mass Spectrometry (SIMS), also at GFZ, by focusing a primary $^{16}\text{O}^-$ ion beam to a $\sim 5\mu\text{m}$ (for boron) or $\sim 25\mu\text{m}$ (for hydrogen) diameter on tourmaline grains in gold-coated, polished thin sections.

On a ternary Al-Fe-Mg diagram, the Igarapé Bahia tourmaline is mainly confined to the intermediate Mg-rich dravite-schorl solid-solution series (Fig. 2) and in compositional fields not related to granitic rocks. In contrast, Breves vein tourmaline is near end-member schorl and has compositions compatible with tourmaline derived from granitic sources (Fig. 2).

$\delta^{11}\text{B}$ values for the Igarapé Bahia tourmaline are mostly concentrated between 12.6‰ and 26.3‰, with a few in the 5.8‰ to 8.8‰ range (Xavier et al. 2008; Fig. 3A). Tourmaline δD values range from -89 to -69‰ (Fig. 3B), which correspond to calculated fluid δD compositions of -30‰ to -10‰ for the mineralization temperature of 400°C estimated from quartz/magnetite ^{18}O thermometry (Dreher et al., 2008).

Compared to the Igarapé Bahia, $\delta^{11}\text{B}$ values of vein tourmaline from the Breves deposit are considerably lower and confined within a more restricted range, from

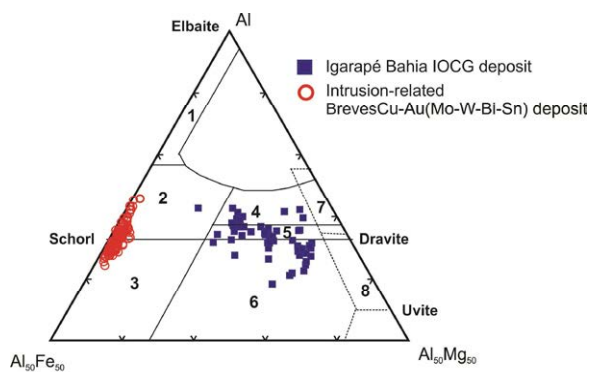


Figure 2. Chemical composition of tourmaline from Igarapé Bahia (Mg-rich intermediate schorl-dravite) and intrusion-related Breves Cu-Au (nearly pure schorl) deposits displayed on the Al-Fe-Mg ternary diagram of Henry and Guidotti (1985). (1) Li-rich granitoids and associated aprites and pegmatites; (2) Li-rich granitoids and associated aprites and pegmatites; (3) Fe³⁺-rich quartz-tourmaline rocks and hydrothermal altered granites; (4) Metapelites and metapsammites coexisting with an Al-saturating phase; (5) Metapelites and metapsammites not coexisting with an Al-saturating phase; (6) Fe³⁺-rich quartz-tourmaline rocks, calcisilicate rocks, and metapelites; (7) Low Ca metaultramafics and Cr, V-rich metasediments; (8) Metacarbonates and metapyroxenites.

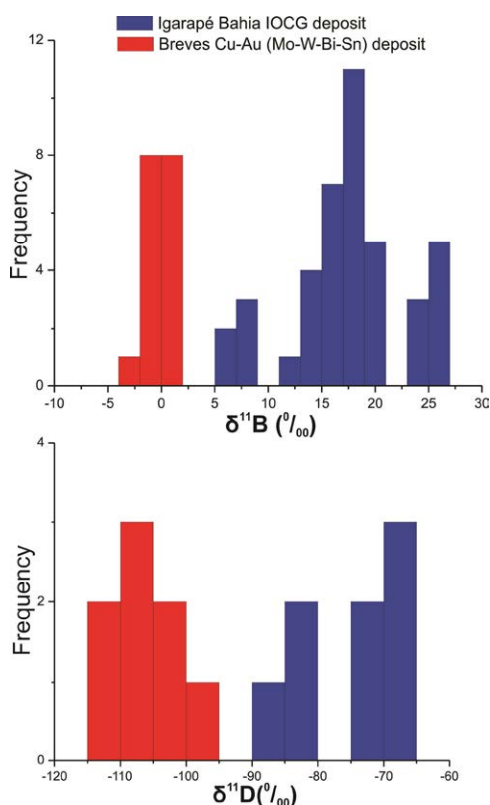


Figure 3. Boron (A) and hydrogen (B) isotope ratios of tourmaline from Igarapé Bahia and intrusion-related Breves Cu-Au deposits.

-3.6‰ to 1.8‰, with most values concentrated between -0.5‰ and 0.5‰ (Xavier et al., 2008; Fig. 3A). The corresponding δD values are -116 to -99‰ (Fig. 3B). Mineralization temperatures at Breves are estimated at 400°C from ¹⁸O thermometry of quartz and

biotite (Xavier, unpubl. data). For this temperature, calculated δD_{H₂O} is the range of -57‰ to -32‰.

4 Discussion

Igarapé Bahia and Breves represent contrasting types of Cu-Au systems in the CMP. The former is an iron oxide-rich hydrothermal system and by far one of the most controversial in the province. On the basis of the geological features, mineral paragenesis and geochemistry, Igarapé Bahia has been interpreted as an iron oxide-copper-gold (IOCG) deposit (Tallarico et al. 2005), but it was also compared to a magnetite-rich volcanic-hosted massive sulphide (VHMS) system (Dreher et al., 2008). The intrusion-related Breves deposit, on the other hand, represents a magmatic-hydrothermal system established during the emplacement of 1.88 Ga granitic magmas (Xavier et al. 2004; Botelho et al. 2005). Fluid regimes in both Cu-Au systems involve the interplay of Ca-rich highly saline (> 30 wt% NaCl eq.) brines and low salinity CO₂±CH₄-rich fluids (Xavier et al. 2005).

In this study we show that tourmaline from the Igarapé Bahia and Breves Cu-Au deposits have very distinct chemical compositions, as well as boron and hydrogen isotope signatures, indicating different ore-forming processes and fluid sources. The Mg-rich nature and the extremely heavy boron isotopic compositions of the Igarapé Bahia tourmaline require a major role of non-magmatic fluids of marine origin, (evolved seawater and/or marine evaporites), as a source of heavy boron and high salinity. The lower δ¹¹B values (5.8‰ to 8.8‰), may be attributed to mixing with other fluid(s) that had lighter boron (magmatic?) or a mixed boron source (Xavier et al. 2008).

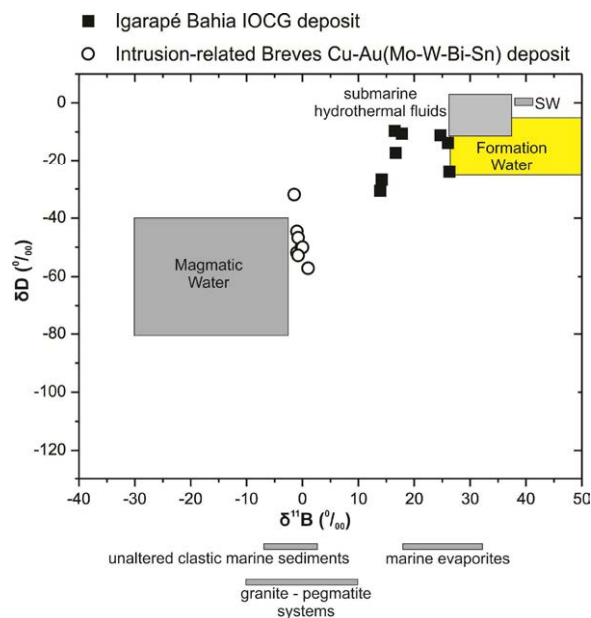


Figure 4. Boron and hydrogen isotope compositions of tourmaline from the Archean Igarapé Bahia and the Paleoproterozoic intrusion-related Breves Cu-Au deposits. δD values for the fluid calculated at 400°C using the fractionation factor of Kotzer et al. (1993). Fields representing the boron and

hydrogen isotope composition of magmatic fluids and sea water are from Barth (1993) and Taylor et al. (1999), respectively. Boron and hydrogen isotopic composition of formation waters are represented by saline formation waters from reservoirs of the Smackover Formation (Upper Jurassic), southwest Arkansas shelf, Gulf Coast sedimentary basin, USA (Moldovanyi et al. 1993). Note that boron isotope variations in rock reservoirs from Barth (1993) displayed at the bottom of the diagram.

Conversely, the Fe-rich composition of the Breves tourmaline coincides with those derived from granitic rocks and its lower $\delta^{11}\text{B}$ values are within the range reported for $\delta^{11}\text{B}$ of granites and magmatic tourmaline.

The development of these two Cu-Au systems from different fluid sources stands out when boron and hydrogen isotopes are combined (Fig. 4). The boron and hydrogen isotopes for the Igarapé Bahia tourmaline are heavier than expected for magmatic-derived fluid and support the involvement of evolved seawater and/or formation waters, with the participation of marine evaporites. This is in agreement with Cl/Br and Na/Cl ratios in inclusion fluids that plot close to the seawater evaporation curve, indicative of evaporative brines (e.g., bittern fluids; Xavier et al. 2009). The boron and hydrogen isotopes for the Breves tourmaline, on the other hand, are mostly consistent with magma-derived brines. Nevertheless, Cl/Br and Na/Cl ratios of the inclusion fluids from this deposit also suggest the incorporation of bittern fluids (Xavier et al. 2009). This may perhaps explain the slight displacement of the boron and hydrogen isotope values off to the right of the magmatic fluid box in Figure 4.

5 Conclusions

Tourmaline has proved valuable for the study of boron isotopic systematics related to hydrothermal ore formation. However, still more information is potentially available to constrain fluid sources from combined *in situ* analysis of boron and hydrogen isotope variations in tourmaline. This is demonstrated in this work using two contrasting types of Cu-Au systems from the Carajás Mineral Province, northern Brazil: the Archean Igarapé Bahia iron oxide-rich Cu-Au deposit and the Paleoproterozoic Breves Cu-Au (Mo-W-Bi-Sn) deposit.

The boron and hydrogen isotope data do not resolve whether the Igarapé Bahia deposit belongs to the IOCG class or not, but they reveal that highly saline non-magmatic fluids (e.g. evolved seawater, formation water or bittern fluids) were important components of the hydrothermal system. The low salinity, aqueous-carbonic fluids that commonly coexist with brines may represent the incorporation and mixing of a magmatic fluid in this hydrothermal system. The isotope data for the Breves tourmaline suggest, on the other hand, the involvement of magma-derived brines, although the results permit the possibility of mixing of these fluids with more ^{11}B -enriched non-magmatic sources. Mixing of different fluid sources, as suggested by the tourmaline boron and hydrogen isotopes, as well as by other isotope systems, may have been critical to Cu and Au precipitation in both deposits.

Acknowledgements

Research funded by FAPESP Grant # 04/02278-7, CNPq grant 302095/2011-0 and INCT-GEOCIAM.

References

- Barth S (1993) Boron variations in nature: A synthesis: *Geologische Rundschau* 82: 640–651.
- Botelho NF, Moura MA, Teixeira LM, Olivo GR, Cunha LM, Santana UM (2005) Caracterização geológica e metalogenética do depósito de Cu ± (Au, W, Mo, Sn) Breves, Carajás. In: Onildo João Marini; Emanuel Teixeira de Queiroz; Benedicto Waldir Ramos. (Org.). Caracterização de depósitos minerais em distritos mineiros da Amazônia.. 01 ed. Brasília: DNPM/CT-Mineral-FINEP/ADIMB, 2005, v. 01, 339-390p.
- Dreher AM, Xavier RP, Taylor BE, Martini SL (2008) New geologic, fluid inclusion and stable isotope studies on the controversial Igarapé Bahia Cu–Au deposit, Carajás Province, Brazil. *Mineralium Deposita* 43: 161-184
- Galarza MAT, Macambira MJB, Moura CAV (2002) Geocronologia e evolução crustal das seqüências vulcanosedimentares hospedeiras dos depósitos de Cu-Au Igarapé Bahia e Gameleira. In: SBG, Congr. Bras. Geol., 41, João Pessoa, PB, Anais, p. 519.
- Henry DJ, Guidotti CV (1985) Tourmaline as petrogenetic indicator mineral: an example from the staurolite-grade metapelites of NW Maine. *American Mineralogist* 70: 1 - 15
- Kotzer TG, Kyser T K, King RW, Kerrich R (1993) An empirical oxygen- and hydrogen-isotope geothermometer for quartz tourmaline and tourmaline-water. *Geochimica et Cosmochimica Acta* 57: 3421-3426
- Moldovanyi EP, Walters LM, Land LS (1993) Strontium, boron, oxygen, and hydrogen isotope geochemistry of brines from basal strata of the Gulf Coast sedimentary basin, USA. *Geochimica et Cosmochimica Acta* 57:2083 – 2099
- Tallarico FHB, McNaughton NJ, Groves DI, Fletcher IR, Figueiredo BR, Carvalho JB, Rego JL, Nunes AR (2004) Geological and SHRIMP II U-Pb constraints on the age and origin of the Breves Cu-Au-(W-Bi-Sn) deposit, Carajás, Brazil. *Mineralium Deposita*, 39: 68-86.
- Tallarico FHB, Figueiredo BR, Groves DI, Kositcin N, McNaughton NJ, Fletcher IR, Rego JL (2005) Geology and SHRIMP U-Pb geochronology of the Igarapé Bahia deposit, Carajás copper-gold belt, Brazil: An Archean (2.57 Ga) example of iron-oxide Cu-Au-(U-REE) mineralization. *Economic Geology* 100: 7–28
- Taylor B E, Palmer MR, Slack JF (1999) Mineralizing fluids in the Kidd Creek massive sulfide deposit, Ontario: Evidence from oxygen, hydrogen, and boron isotopes in tourmaline. *Economic Geology Monograph* 10, 389-414.
- Xavier RP, Araujo CEG, Dreher, AM, Nunes AR, Rêgo JL (2005) Fluid evolution in the Paleoproterozoic intrusion-related Breves Cu-Au-(Mo-W-Bi-Sn) deposit, Carajás Mineral Province, Northern Brazil. In: Horbe AMC. & Souza VS (eds) *Contribuições à Geologia da Amazônia, Sociedade Brasileira de Geologia – Núcleo Norte*, pp 129-137
- Xavier RP, Wiedenbeck M, Trumbull RB, Dreher AM, Monteiro LVS, Rhede D, Araújo CEG, Torresi I (2008) Tourmaline B isotopes fingerprint marine evaporites as the source of high salinity ore fluids in iron oxide-copper-gold deposits, Carajás Mineral Province (Brazil). *Geology* 36: 743 – 746
- Xavier RP, Rusk B, Emsbo P, Monteiro LVS (2009) Composition and source of salinity of ore-bearing fluids in Cu-Au systems of the Carajás mineral province, Brazil: Society for Geology Applied to Mineral Deposit (SGA) 2009, Biennial Meeting 10th, Townsville, Australia, Proceedings, p.272–274.
- Xavier RP, Monteiro LVS, Moreto CPN, Pestilho AI, Melo GHC, Silva MD, Aires B, Ribeiro C, Freitas e Silva FH (2012) The Iron Oxide Copper-Gold Systems of the Carajás Mineral Province, Brazil. Society of Economic Geologists, Inc. Special Publication 16 (in press)

S 3.10

Metallogenesis of collisional orogens in the Tethyside domain

Sponsored by IGCP/SIDA project 600

Convenors:

David Leach, Zengqian Hou & Mehraj Aghazadeh

Mineralization styles and orogen episodes in the Tethyan

Jeremy P. Richards

Dept. Earth and Atmospheric Sciences, University of Alberta, Edmonton, Alberta, Canada, T6 G 2E3

Abstract. Mineralization styles occurring within the Paleozoic Paleo-Tethys and Mesozoic–Cenozoic Neo-Tethys orogenic belts are reviewed. Few deposits are preserved relating to Paleo-Tethyan subduction, but numerous deposits are associated with closure of the Neo-Tethys ocean. Subduction-related porphyry and epithermal mineralization formed mainly in the late Mesozoic and early Cenozoic, whereas various styles of syn-, late-, and post-collisional porphyry and epithermal mineralization formed in the Neogene, with a peak in the Miocene of Iran, Pakistan, and Tibet.

Keywords. Porphyry, epithermal, subduction, collision

1 Paleogeography of the Tethyan ocean basins

The Tethyan orogen is a complex belt of collided, actively colliding, and still converging continental blocks that stretches from the Alps, through the Carpathians, Balkans, Turkey, Iran, Pakistan, Tibet, and southwards through Indonesia and Melanesia. The orogen formed in two main phases relating to formation and closure of the Paleo-Tethys in the Paleozoic, and the Neo-Tethys in the Mesozoic and Cenozoic.

The Paleo-Tethys ocean opened initially in response to Cambrian break-up of the Proterozoic supercontinent Rodinia, as Laurentia, Siberia, and Baltica separated from the Gondwana continents. Closure of the Iapetus and Rheic oceans to the south in the Silurian and Devonian was accompanied by widening of the Paleo-Tethys ocean towards the north as the North China block drifted away from Gondwana. By the Carboniferous and Permian, the Paleo-Tethys ocean was located at equatorial latitudes, but was slowly closing by subduction northwestwards beneath Euramerica and southwards beneath the Gondwana continents.

In the Late Permian, Paleo-Tethys subduction was initiated eastwards and northeastwards beneath the South China–Indochina and North China blocks, respectively. At the same time a group of continental microfragments known collectively as the Cimmerian continents (which included the Precambrian cores of Turkey, Iran, and Tibet) rifted from the northern margin of Gondwana to form the Neo-Tethys ocean. Northward migration of the Cimmerian continents during the Triassic ended with collision and accretion to the southern margin of Eurasia and final closure of the Paleo-Tethys ocean.

By the Early Jurassic, northeastward subduction of the Neo-Tethys ocean began beneath Eurasia and the accreted Cimmerian terranes, and the Gondwana continents began to move northwards. Cretaceous arc magmatism occurred extensively along the southern

accretionary margin of Eurasia, and is associated with typical arc-related porphyry and epithermal mineralization (Fig. 1).

Convergence between Africa-Arabia and Laurasia was advanced by the end of the Cretaceous, and collisional tectonism began with closure of small Neo-Tethyan ocean basins throughout the Carpathian–Balkans–Turkish section of the orogen. By the mid-Miocene, the Arabian plate collision had extended southeastward to Iran, with remnants of the Neo-Tethyan ocean remaining only in the eastern Mediterranean and the Indian Ocean. Numerous syn- to post-collisional porphyry and epithermal deposits formed in response to these complex tectonic readjustments.

Collision between India and Eurasia began at ~55 Ma and is ongoing, as is the slower Africa-Arabia collision, and an important belt of syn- to late-collisional magmatism and associated porphyry-type mineralization occurred during this period in Turkey, Iran, and Tibet.

Active subduction of Indian ocean lithosphere continues below the Makran accretionary prism in SE Iran and western Pakistan, and along the Indonesian and Melanesian arcs. Major porphyry Cu-Au and epithermal Au deposits formed in these Neogene arc systems.

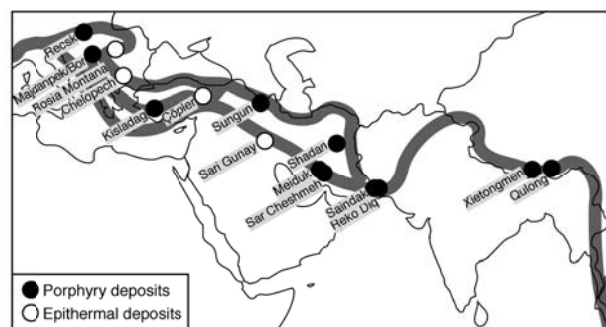


Figure 1. Locations of major porphyry and epithermal deposits in the Tethyan orogen; main suture zones are traced with dark grey lines.

2 Paleo-Tethyan Metallogeny

Few mineral deposits that may have formed during closure of the Paleo-Tethys ocean are preserved, but Goldfarb et al. (2001) and Yigit (2006) ascribe the formation of some mesothermal and listwaenite-hosted Au deposits in Europe and Turkey to this event, and Mo et al. (2005) describe a Middle–Late Triassic porphyry Cu belt (Zhongdian) that formed in Yunnan, China, in response to Paleo-Tethyan subduction. Mo et al. (2005) also describe some ophiolite-hosted VMS deposits that were formed during late Triassic rifting.

3 Neo-Tethyan Metallogeny

In contrast to the more deeply eroded Paleo-Tethyan orogenic belts, Neo-Tethyan arc and collisional orogenic belts are relatively well preserved, and host numerous porphyry and epithermal-style mineral deposits along their entire length (the Alpine–Balkan–Carpathian–Dinaride metallogenic belt of Heinrich and Neubauer, 2002).

3.1 Subduction-related ore deposits

Jurassic and Early Cretaceous subduction-related magmatism in the Pontides of Turkey, the Sanandaj–Sirjan zone and Alborz Mountains of Iran, and the Chagai belt of Pakistan is not known to be associated with major ore deposits. However, in Tibet, the recently discovered Xietongmen Cu–Au porphyry district occurs in Jurassic arc rocks in the Gangdese belt of Tibet (Tafti et al., 2009), and the Duolong porphyry Cu–Au deposit formed in the Early Cretaceous (Li et al., 2011). In addition, the large Dexing porphyry Cu deposit in SE China was formed during the Middle Jurassic by debated processes (Wang et al., 2006; Ge et al., 2007; Liu et al., 2012).

In contrast, Late Cretaceous subduction of the Neo-Tethys ocean generated important coupled porphyry Cu and high-sulfidation epithermal Cu–Au deposits in the Carpathians–Balkans, including the Bor and Panagyurishte Districts in the Banat–Srednogie arc of Serbia and Bulgaria (Lips, 2002; Lips, et al., 2004; von Quadt et al., 2005; Chambefort and Moritz, 2006; Kouzmanov et al., 2009).

In the Paleocene–Eocene, widespread calc-alkaline magmatism throughout the orogen is variably ascribed to subduction, slab rollback, back-arc, and early collisional processes, but associated mineralization is relatively restricted. Perhaps the largest deposit formed at this time is the Çöpler porphyry–epithermal Au–(Cu) deposit in central Turkey (44 Ma), which Imer et al. (2013) relate to back-arc extensional processes behind the south-facing Bitlis arc. The Shadan porphyry Cu deposit formed in the middle Eocene in the Lut block of eastern Iran (37 Ma; Richards et al., 2012), while the Dalli porphyry Au deposit formed in central Iran in the early Miocene (~21 Ma; Ayati et al., 2013). One small Eocene-age (~52 Ma) porphyry Mo deposit is reported in Tibet (Sharang; Zhao et al., 2012).

Porphyry Cu–Au–Mo mineralization related to ongoing subduction began in the Chagai belt of western Pakistan in the Eocene, but did not reach its peak in productivity until formation of the giant Saindak (22 Ma) and Reko Diq deposits (13–10 Ma) in the Miocene (Perelló et al., 2008; Richards et al., 2012).

3.2 Collision-related ore deposits

The Miocene marked a major flare-up of collision-related magmatism and ore formation along the length of the orogen. A major episode of Au mineralization occurred in the Carpathians of western Romania, with the largest deposit, Roșia Montană, forming at 12.7 Ma (Manske et al., 2006). The origin of this magmatic and

metallogenic event is not clear, but Neubauer et al. (2005) suggest that it relates to post-collisional crustal extension and slab rollback.

In Iran, the Miocene represents the main period of porphyry Cu and epithermal Au mineralization along the length of the Urumieh–Dokhtar magmatic arc. Porphyry deposits include Sungun (middle Miocene), Meiduk (12.2 Ma; Taghipour et al., 2008), and Sar Cheshmeh (13.6 Ma; McInnes et al., 2003), while the Sari Gunay epithermal Au deposit formed at 11 Ma (Richards et al., 2006). The timing of this magmatism appears to post-date the onset of collision between Arabia and Eurasia, which is estimated to have begun in the Oligocene or early Miocene (Gavillot et al., 2010; Okay et al., 2010; Karagaranbafghi et al., 2012). Richards et al. (2006) and Shafiei et al. (2009) have therefore suggested that these are syn- or late-collisional magmatic systems.

The Miocene was also an important time for late-collisional porphyry Cu–Mo deposit formation in Tibet. The origin of these magmas and related deposits is debated with models including subducted oceanic slab melting (Qu et al., 2004), lithospheric melting during post-collisional extension (Hou et al., 2004, 2009), and melting of subducted Indian continental crust (Xu et al., 2010). The largest deposits is Qulong, which formed at ~16 Ma (Yang et al., 2009; Xiao et al., 2012).

Elsewhere, in the southwest Pacific oceanic arcs of Melanesia and Polynesia, several large porphyry Cu–Au and epithermal Au deposits formed in the Miocene and Plio-Pleistocene in broadly post-subduction settings, such as subduction reversal, arc migration, and terrane accretion. Examples include the giant Grasberg (Pollard et al., 2005), Ok Tedi (van Dongen et al., 2010), and Panguna (Page and McDougall, 1972) Cu–Au porphyry deposits of Indonesia and Papua New Guinea, and the giant Porgera (Richards and Kerrich, 1993), Lihir (Müller et al., 2002), and Emperor (Ahmad et al., 1987) epithermal gold deposits of Papua New Guinea and Fiji.

4 Conclusions

The Tethyan orogenic belt reflects ocean lithosphere formation and destruction over most of the Phanerozoic. Paleozoic rock sequences related to subduction of the Paleo-Tethys ocean are not highly prospective for porphyry and epithermal-type mineralization, likely due to erosional loss of epizonal ore deposits. In contrast, Mesozoic and especially Cenozoic sequences related to subduction and collisional closure of the Neo-Tethyan ocean contain numerous examples of porphyry and epithermal deposits, including several giant systems. Many of these deposits have been formed in complex tectonic settings where a relationship to subduction magmatism may be indirect, or postponed to tectonic events involving lithospheric remobilization following collision.

Acknowledgements

I thank the SGA 2013 conference organizers for the invitation to present this paper. This work was supported by a Discovery Grant from the Natural Sciences and

Engineering Research Council of Canada, and is a contribution to IGCP/SIDA-600 project “Metallogenesis of Collisional Orogens in the East Tethyside Domain”.

References

- Ahmad M, Solomon M, Walshe J L (1987) Mineralogical and geochemical studies of the Emperor gold telluride deposit, Fiji. *Economic Geology* 82: 345–370
- Ayati F, Yavuz F, Asadi H H, Richards J P, Jourdan F (2013) Petrology and geochemistry of calc-alkaline volcanic and subvolcanic rocks, Dalli porphyry copper-gold deposit, Markazi Province, Iran. *International Geology Review* 55: 158–184
- Chambefort I, Moritz R (2006) Late Cretaceous structural control and Alpine overprint of the high-sulfidation Cu-Au epithermal Chelopech deposit, Srednogie belt, Bulgaria: *Mineralium Deposita* 41: 259–280
- Gavillot Y, Axen G J, Stockli D F, Horton B K, Fakhari M D (2010) Timing of thrust activity in the High Zagros fold-thrust belt, Iran, from (U-Th)/He thermochronometry. *Tectonics*, 29: TC4025, doi:10.1029/2009TC002484
- Ge W C, Wu F Y, Zhou C Y, Zhang J H (2007) Porphyry Cu-Mo deposits in the eastern Xing'an-Mongolian Orogenic Belt: Mineralization ages and their geodynamic implications. *Chinese Science Bulletin* 52: 3416–3427
- Goldfarb R J, Groves D I, Gardoll S (2001) Orogenic gold and geologic time: a global synthesis. *Ore Geology Reviews* 18: 1–75
- Heinrich C A, Neubauer F (2002) Cu-Au-Pb-Zn-Ag metallogeny of the Alpine-Balkan-Carpathian-Dinaride geodynamic province. *Mineralium Deposita* 37: 533–540
- Hou Z, Gao Y F, Qu X M, Rui Z Y, Mo X X (2004) Origin of adakitic intrusives generated during mid-Miocene east-west extension in southern Tibet. *Earth and Planetary Science Letters* 220: 139–155
- Hou Z, Yang Z, Qu X, Meng X, Li Z, Beaudoin G, Rui Z, Gao Y, Zaw K (2009) The Miocene Gangdese porphyry copper belt generated during post-collisional extension in the Tibetan Orogen. *Ore Geology Reviews* 36: 25–51
- Imer A, Richards J P, Creaser R A (2013) Age and tectonomagmatic setting of the Eocene Çöpler-Kabataş magmatic complex and porphyry-epithermal Au deposit, east central Anatolia, Turkey. *Mineralium Deposita in press*
- Karagaranbafghi F, Foeken J P T, Guest B, Stuart F M (2012) Cooling history of the Chapedony metamorphic core complex, Central Iran: Implications for the Eurasia–Arabia collision. *Tectonophysics* 524–525: 100–107
- Kouzmanov K, Moritz R, Quadt A, Chiaradia M, Peytcheva I, Fontignie D, Ramboz C, Bogdanov K (2009) Late Cretaceous porphyry Cu and epithermal Cu–Au association in the Southern Panagyurishte District, Bulgaria: the paired Vlaykov Vruh and Elshitsa deposits. *Mineralium Deposita* 44: 611–646
- Li J, Qin K, Li G, Xiao B, Zhao J, Chen L (2011) Magmatic-hydrothermal evolution of the Cretaceous Duolong gold-rich porphyry copper deposit in the Bangongco metallogenic belt, Tibet: Evidence from U–Pb and $^{40}\text{Ar}/^{39}\text{Ar}$ geochronology. *Journal of Asian Earth Sciences* 41: 525–536
- Lips A L W (2002) Correlating magmatic–hydrothermal ore deposit formation over time with geodynamic processes in SE Europe, in Blundell D J, Neubauer F, von Quadt A, eds., The timing and location of major ore deposits in an evolving orogeny. Geological Society, London, Special Publication 204: 69–79
- Lips A L W, Herrington R J, Stein G, Kozelj D, Popov K, Wijbrans J R (2004) Refined timing of porphyry copper formation in the Serbian and Bulgarian portions of the Cretaceous Carpatho-Balkan belt. *Economic Geology* 99: 601–609
- Liu X, Fan H R, Santosh M, Hu F F, Yang K F, Li Q L, Yang Y H, Liu Y (2012) Remelting of Neoproterozoic relict volcanic arcs in the Middle Jurassic: Implication for the formation of the Dexing porphyry copper deposit, Southeastern China. *Lithos* 150: 85–100
- Manske S L, Hedenquist J W, O'Connor G, Tămaş C, Cauuet B, Leary S, Minut A (2006) Roşia Montană, Romania: Europe's largest gold deposit. Society of Economic Geologists Newsletter, January 2006, 64, p. 1, 9–15
- McInnes B I A, Evans N J, Belousova E, Griffin W T, Andrew R L (2003) Timing of mineralization and exhumation processes at the Sar Cheshmeh and Meiduk porphyry Cu deposits, Kerman belt, Iran, in Eliopoulos et al., eds., Mineral Exploration and Sustainable Development (7th Biennial SGA Meeting, Athens, August 24–28): Rotterdam, Millpress, p. 1197–1200
- Mo X X, Yang K H, Wang L L, Dong G C (2005) Copper and gold metallogeny in the Tethyan domain in China, in Mao J, Bierlein F P, eds., Meeting the Global Challenge: Proceedings of the Eighth Biennial SGA Meeting, Beijing, China, August 18–21, 2005, Springer-Verlag, Mineral Deposit Research, v. 2, p. 1247–1250
- Müller D, Kaminski K, Uhlig S, Graupner T, Herzig P M, Hunt S (2002) The transition from porphyry- to epithermal-style gold mineralization at Ladolam, Lihir Island, Papua New Guinea: A reconnaissance study. *Mineralium Deposita* 37: 61–74
- Neubauer F, Lips A, Kouzmanov K, Lexa J, Ivascanu P (2005) Subduction, slab detachment and mineralization: The Neogene in the Apuseni Mountains and Carpathians. *Ore Geology Reviews* 27: 13–44
- Okay A I, Zattin M, Cavazza W (2010) Apatite fission-track data for the Miocene Arabia-Eurasia collision. *Geology* 38: 35–38
- Page R W, McDougall I (1972) Geochronology of the Panguna porphyry copper deposit, Bougainville Island, New Guinea. *Economic Geology* 67: 1065–1074
- Perelló J, Raziqie A, Schloderer J, Asad-ur-Rehman (2008) The Chagai porphyry copper belt, Baluchistan Province, Pakistan. *Economic Geology* 103: 1583–1612
- Pollard P J, Taylor R G, Peters L (2005) Ages of intrusion, alteration, and mineralization at the Grasberg Cu-Au deposit, Papua, Indonesia. *Economic Geology* 100: 1005–1020
- Qu X, Hou Z, Li Y (2004) Melt components derived from a subducted slab in late orogenic ore-bearing porphyries in the Gangdese copper belt, southern Tibetan plateau. *Lithos* 74: 131–148
- Richards J P, Kerrich R (1993) The Porgera gold mine, Papua New Guinea: Magmatic-hydrothermal to epithermal evolution of an alkalic-type precious metal deposit. *Economic Geology* 88: 1017–1052
- Richards J P, Wilkinson D, Ullrich T (2006) Geology of the Sari Gunay epithermal gold deposit, northwest Iran. *Economic Geology* 101: 1455–1496
- Richards J P, Spell T, Rameh E, Raziqie A, Fletcher T (2012) High Sr/Y magmas reflect arc maturity, high magmatic water content, and porphyry Cu=Mo±Au potential: Examples from the Tethyan arcs of central and eastern Iran and western Pakistan. *Economic Geology* 107: 295–332
- Shafiei B, Haschke M, Shahabpour J (2009) Recycling of orogenic arc crust triggers porphyry Cu mineralization in Kerman Cenozoic arc rocks, southeastern Iran. *Mineralium Deposita* 44: 265–283
- Tafti R, Mortensen J K, Lang J R, Rebagliati M, Oliver J L (2009) Jurassic U–Pb and Re–Os ages for the newly discovered Xietongmen Cu–Au porphyry district, Tibet, PRC: Implications for metallogenic epochs in the southern Gangdese belt. *Economic Geology* 104: 127–136
- Taghipour N, Aftabi A, Mathur R (2008) Geology and Re–Os geochronology of mineralization of the Miduk porphyry copper deposit, Iran. *Resource Geology* 58: 143–160
- van Dongen M, Weinberg R F, Tomkins A G, Armstrong R A, Woodhead J D (2010) Recycling of Proterozoic crust in Pleistocene juvenile magma and rapid formation of the Ok Tedi porphyry Cu–Au deposit, Papua New Guinea. *Lithos* 114: 282–292
- von Quadt A, Moritz R, Peytcheva I, Heinrich C A (2005) Geochronology and geodynamics of Late Cretaceous magmatism and Cu–Au mineralization in the Panagyurishte region of the Apuseni-Banat-Timok-Srednogie belt, Bulgaria. *Ore Geology Reviews* 27: 95–126
- Wang Q, Xu J F, Jian P, Bao Z W, Zhao Z H, Li C F, Xiong X L,

- Ma J L (2006) Petrogenesis of adakitic porphyries in an extensional tectonic setting, Dexing, South China: Implications for the genesis of porphyry copper mineralization. *Journal of Petrology* 47: 119–144
- Xiao B, Qin K, Li G, Li J, Xia D, Chen L, Zhao J (2012) Highly oxidized magma and fluid evolution of Miocene Qulong giant porphyry Cu-Mo deposit, southern Tibet, China. *Resource Geology* 62: 4–18
- Xu W C, Zhang H F, Guo L, Yuan H L (2010) Miocene high Sr/Y magmatism, south Tibet: Product of partial melting of subducted Indian continental crust and its tectonic implication. *Lithos* 114: 293–306
- Yang Z, Hou Z, White N C, Chang Z, Li Z, Song Y (2009) Geology of the post-collisional porphyry copper–molybdenum deposit at Qulong, Tibet. *Ore Geology Reviews* 36: 133–159
- Yigit O (2006) Gold in Turkey — a missing link in Tethyan metallogeny. *Ore Geology Reviews* 28: 147–179
- Zhao J, Qin K, Li G, Li J, Xiao B, Chen L (2012) Geochemistry and petrogenesis of granitoids at Sharang Eocene porphyry Mo deposit in the main-stage of India-Asia continental collision, northern Gangdese, Tibet. *Resource Geology* 62: 84–98

Bondar-e-Honza: An oldest and special porphyry copper (molybdenum) deposit in the Kerman porphyry copper belt, Iran

Mehraj Aghazadeh, Zahra Badrzadeh

Department of geology, University of Payame Noor, PO BOX 19395-3697, Tehran, Iran

Zangqian Hou

Institute of Geology, Chinese Academy of Geological Sciences, Beijing 100037, People's Republic of China

Abstract. Iran is part of Alpine-Himalayan orogenic and metallogenic belt and Kerman porphyry copper belt is main porphyry copper district in Iran, hosting Sar Cheshmeh world-class deposit. Intrusive bodies in the Kerman belt can be divided into old Jebal-e-Barez and young Kuh-e-Panj intrusions. It has been suggested that jebal-e-Barez type intrusions are barren and younger Kuh Panj intrusive are productive. Bondar-e-Honza is a porphyry copper deposit belongs to Jebal-e-Barez type intrusive. The deposit has 50 Mt ore with ~0.3% copper. Porphyry copper mineralization mainly developed as hypogene zone in a dioritic stock and potassic andesitic rocks and subordinately in a porphyry granodiorite. Alteration haloes mainly are potassic and propylitic. Potassic alteration developed mainly in the porphyry diorite, Eocene andesitic rocks and in the granodiorite porphyry stock. Actinolitic amphibole is main alteration mineral in the zone. U-Pb age dating on separated zircon grains from granodiorite porphyry yielded a 27.88 ± 0.48 Ma age at 95% conf. and MSWD = 3.3. This study results showed that Jebal-e-Barez type granitoids also have porphyry copper mineralization capability and Bondar-e-Honza is a typical and special porphyry copper mineralization belongs to these older intrusive in the Kerman belt.

Keywords.

Bondar-e-Honza, Porphyry copper deposit, Kerman, Iran

1 Introduction

Iran is part of the collisional Alpine-Himalayan orogenic belt which extends from Western Europe to Turkey, across Iran into Pakistan and China. Disappearance of the Neo-Tethys Ocean during Mesozoic and early Tertiary time and collision between Arabia and Eurasia caused formation of Zagros Orogen in Iran. The Zagros Orogen comprises the following sub-parallel tectonostratigraphic domains, from SW to NE: Zagros folded and thrust belt, Sanandaj-Sirjan magmatic-metamorphic zone (SSZ) and Urumieh-Dokhtar magmatic arc (UDMA). The UDMA hosts abundant Tertiary magmatic rocks, dominantly with arc (Berberian & Berberian, 1981) or island-arc affinity (Shahabpour, 2005). Volumetrically, volcanic rocks were mostly produced during Eocene and the oldest one date back to Early Eocene. Eocene pervasive volcanism followed by Oligo-Miocene plutonism in the belt (Berberian and King 1981). Porphyry copper

mineralization in the Zagros Orogen formed in different periods and belts (Aghazadeh et al., 2012). The UDMA in Iran is one of the main Cu-bearing regions in the world. There are several porphyry copper deposits in the southeastern, middle and northwestern parts of the UDMA (Aghazadeh et al., 2012). Kerman porphyry copper district (southeastern part of the UDMA) includes more than 20 porphyry copper deposits e.g. Sarcheshmeh a world-class deposit.

Kerman district is a NNW-SSE elongated mountain belt, 400 km long and 50 km wide. It is principally composed of a folded and faulted early Tertiary volcano-sedimentary complex (Fig. 1). Early Eocene onset of volcanic activity (Bahr Aseman complex) followed by mid-late Eocene basaltic-rhyolitic volcanoclastic sequences (Razak complex) and intrusion of Jebal-e-Barez type granitoids (Dimitrijevic 1973). Both the volcanic and intrusive suites show calc-alkaline and locally tholeiitic affinity (Ahmad and Posht Kuhi 1993) consistent with a subduction-related island arc setting (Shahabpour 2007). Subsequent magmatic activity generated the Oligocene Hezar volcanic complex and associated plutonic rocks with dominantly high-K calc-alkaline and shoshonitic rocks (Hassanzadeh, 1993; McInnes et al. 2003). Magmatism ceased between mid-late Oligocene and mid-Miocene times, and Eocene-Oligocene volcanoclastics and associated intrusive rocks are unconformably overlain by Late Oligocene-Miocene red beds and limestones (Dimitrijevic 1973). Magmatism resumed during the mid-late Miocene with a second episode of intrusive activity as Kuh Panj granitoids (McInnes et al. 2005) and continued into the Pliocene represented by sub-volcanic intrusions, two isolated stratovolcanoes, and few dacitic to rhyolitic domes and locally andesite, without mafic units in a post-collisional tectonic setting (Shafiei et al., 2009). Pliocene-Quaternary small volume alkali basalts and foidites represent the youngest magmatic activity (Dimitrijevic 1973; Hassanzadeh, 1993).

It has been suggested porphyry copper mineralization in the Kerman district associated with younger Kuh Panj type intrusives and earlier Jebal-e-Barez type granitoids are barren (e.g. McInnes et al., 2003; Shafiei et al., 2009). Shafiei et al., 2009 reported petrological and geochemical differences between Jebal-e-Barez and Kuh Panj type intrusives. Age dated

diorite porphyry and andesitic volcanic rocks and subordinately in the porphyry granodioritic stock. Actinolite, magnetite and alkali feldspar (albite) mainly develop during potassic alteration in the diorite porphyry. Secondary potassium feldspar and biotite are rare in the diorite porphyry. These last two minerals are more or less developed in the granodiorite porphyry. During potassic alteration different veinlet and vein formed the diorite porphyry and volcanic rocks and subordinately in the porphyry granodiorite. Phyllic alteration are locally develops in the porphyry granodiorite and primary minerals partially or totally replaced by sericite, silica and pyrite. Propylitic alteration develops in the host volcanic rocks and late dikes. Mineralization in the Bondar-e-Honza deposit mainly occurred as hypogene and supergene enrichment blanket and oxide zones are rare and limited to surface. In the hypogene zone chalcocopyrite, pyrite and molybdenite occurs as disseminated phase and in veinlets. In the potassic zone quartz-magnetite-amphibole, quartz-amphibole, quartz-magnetite, quartz-magnetite-amphibole-sulfide, quartz-amphibole-sulfide, quartz-molybdenite, quartz-sulfide and quartz veins and veinlets can be identified. Development of quartz-magnetite-amphibole -sulfide veins is dominant.

4 Age dating

The zircons analyzed in this study were separated, using standard heavy liquid and hand picking method, from 2-kg sample, collected from granodiorite porphyry outcrop. Zircon separates were sorted under binoculars with a purity of >95% and then mounted in epoxy resin and polished to expose their internal textures. All zircons were examined using a combination of cathodoluminescence and optical microscopy prior to analysis. The areas selected for analyses were free of visible inclusions and free of visible cores. SHRIMP U–Pb dating was carried out at the Chinese Academy of Geosciences. Pb/U ratios were corrected for instrumental inter-element fractionation using standard zircon TEM (age=417 Ma). U, Th and Pb contents were calibrated using the standard zircon SL13 (age=572 Ma and U=238 ppm). The two zircon standards were all provided by the Australian National University. Common Pb was corrected using determined ^{208}Pb by assuming concordance between $^{206}\text{Pb}/^{238}\text{U}$ and $^{208}\text{Pb}/^{232}\text{Th}$. Data were handled using the Ludwig SQUID 1.0 and ISOPLOT programs. The results are presented in U–Pb Concordia diagrams in Fig. 2. SHRIMP zircon U–Pb dating showed that among 21 spots from 21 zircons of the granodiorite porphyry yielded 27.88 ± 0.48 Ma age at 95% conf. and MSWD = 3.3. The $^{206}\text{Pb}/^{238}\text{U}$ age results of different grains vary from 26.6 ± 0.8 to 30.2 ± 0.6 Ma.

6. Discussion and conclusion

According to previous studies intrusive bodies in the Kerman district divided in to Jebal-e-Barez and Kuh-e-

Panj types (Dimitrijevic 1973). Jebal-e-Barez type intrusive is older than Middle-Late Miocene Kuh-e-Panj type intrusives. According to geochemical characteristics and age dating results it is stated that Jebal-e-Barez type intrusive have not susceptibility of porphyry copper mineralization while Kuh-e-Panj type intrusives have porphyry copper mineralization capability (Shafiei et al., 2009; McInnes et al. 2003; Dimitrijevic 1973). According to our new age dating results it is confirmed that Jebal-e-Barez type granitoids also show capability of porphyry copper mineralization and Bondar-e-Honza is a typical porphyry copper mineralization belongs to Jebal-e-Barez type intrusives. Although Jebal-e-Barez type intrusives include small and less abundant porphyry copper deposits but originally they have potential for porphyry type mineralization. Addition to differences in ages of both intrusives, porphyry copper deposits in the Jebal-e-Barez type intrusive represent potassic and propylitic alterations while porphyry deposits in Kuh Panj type represent typical Lowell and Gilbert model alteration halos include potassic, phyllic, argillic and propylitic alterations. Potassic alteration of porphyry deposits in the Kuh-e-Panj type intrusives include abundant secondary biotite and potassium feldspar while in the potassic alteration of the Bondar-e-Honza deposit actinolitic amphibole is the main mineral. Host intrusive in the Kuh-e- Panj type porphyry deposits mainly have felsitic (granodioritic) composition but in the Bondar-e-Honza deposit mineralization mainly associated with dioritic stock.

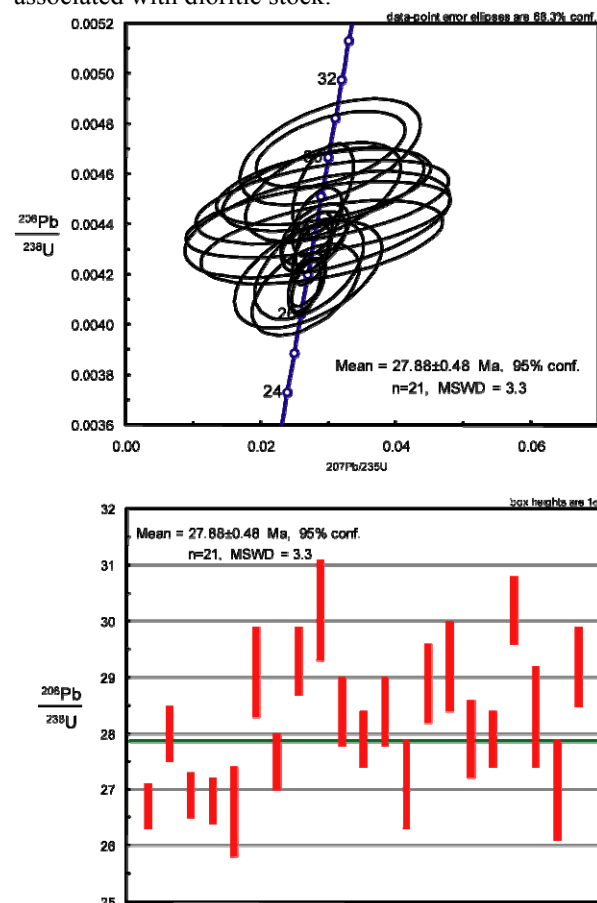


Figure 2. Concordia plot of SHRIMP U-Pb zircon results for granodiorite stock of Bondar-e-Honza deposit.

Acknowledgement

This study is financially supported by the IGCP/SIDA 600 project. Special thanks go to the exploration department of National Iranian Copper Industries Company (NICICO).

References

- Aghazadeh M, Hou Z-Q, Badrzadeh Z (2012) Porphyry copper mineralization in Iran: main metallogenic belts and ore-forming episodes, 34 international geological congress, Brisbane, Australia
- Ahmad T, Posht Kuhi M (1993) Geochemistry and petrogenesis of Urumiah–Dokhtar volcanic belt around Nain and Rafsanjan area; a preliminary study: treatise on the geology of Iran, Iranian Ministry of Mines and Metals, p 90
- Berberian F, Berberian M (1981) Tectono-plutonic episodes in Iran. In: Gupta, H.K., Delany, F.M. (Eds.), Zagros-Hindu Kush-Himalaya Geodynamic Evolution. Geodynamics Series, vol. 3. American Geophysical Union, Washington, D.C., 5-32
- Berberian M, King GC (1981) Toward a paleogeography and tectonic evolution of Iran. *Can J Earth Sci* 18:210–265
- Conrad G, Conrad J, Girod M (1977) Les formation continentals tertiaries et et quaternaries du block du lout (Iran): impottance du plutonisme et du volcanisme. *Memoire Hors-Serie N 8 de la Societe geologique de France* 8, 53-75
- Dimitrijevic MD (1973) Geology of the Kerman region. *Geol Survey Iran Rep* 52:334
- Ghorashizadeh M (1978) Development of hypogene and supergene alteration and copper mineralization patterns, Sarcheshmeh porphyry copper deposit, Iran. M.Sc thesis Brock University, Canada, p 223
- Hassanzadeh J (1993) Metallogenic and tectono-magmatic events in the SE sector of the Cenozoic active continental margin of Iran (Shahr e Babak area, Kerman province). Unpublished Ph.D. thesis, University of California, Los Angeles, p 204
- McInnes BIA, Evans NJ, Belousova E, Griffin WL (2003) Porphyry copper deposits of the Kerman belt, Iran: timing of mineralization and exhumation processes. *CSIRO Sci Res Rep* 41
- McInnes BIA, Evans NJ, Fu FQ, Garwin S (2005) Application of thermochronology to hydrothermal ore deposits. *Rev Mineral Geochem* 58:467–498
- Shafiei B, Haschke M, Shahabpour J (2009) Recycling of orogenic arc crust triggers porphyry Cu mineralization in Kerman Cenozoic arc rocks, southeastern Iran. *Mineralium Deposita*, 44, 265-83.
- Shahabpour J (2005) Tectonic evolution of the orogenic belt in the region located between Kerman and Neyriz. *J Asian Earth Sci* 24:405–417
- Shahabpour J (2007) Island-arc affinity of the Central Iranian Volcanic Belt. *J Asian Earth Sci* 30:652–665
- Shahabpour J, Kramers JD (1987) lead isotope data from the Sarcheshmeh porphyry copper deposit, Kerman, Iran. *Min Deposit* 22:278–281.

Hydrothermal alteration zones associated with Sargaz orebody, SE Iran

Zahra Badrzadeh . Mehraj Aghazadeh

Department of geology, University of Payame Noor, PO BOX 19395-3697, Tehran, Iran

Abstract. Sargaz was an underground mine in the southeastern part of the Sanandaj-Sirjan Zone, which contained 3 Mt of pyritic massive sulfide ore grading 1.34 wt.% Cu, 0.38 wt.% Zn, 0.08 wt.% Pb, 0.24 g/t Au, and 7 g/t Ag after ancient mining. The deposit is hosted within volcanic rocks of the Upper Triassic to Lower Jurassic volcanic and sedimentary sequence consists of Sargaz and Zaghu ore lenses. The mine sequence comprises of basaltic andesitic to rhyodacitic composition, and post-ore felsic to mafic dykes. The degree of hydrothermal alteration of basaltic andesitic host rocks has been quantified using mass change methods. The main alteration minerals are chlorite, quartz, and sericite. The alteration zones are interpreted as hydrothermal upflow or feeder zones. Haloes of quartz-chlorite are wider than the zones of quartz-sericite alteration, which occur around the ore lenses. Alteration zones below and around the ore lenses are characterized by large mass gains of FeO, MnO, MgO, and K₂O together with large mass gains or losses in silica. Identification of these alteration zones could provide an exploration guide to ore.

Keywords.

Hydrothermal alteration, zoning, Sargaz, SE Iran

1 Introduction

From a historical perspective, volcano-sedimentary sequence (VSS) in southern Sanandaj-Sirjan zone is one of the most significant VMS districts in Iran, which was re-discovered recently (Sabzehei and Youssefi 2000). The Sargaz area of southeastern Iran is covered by a well preserved, early Mesozoic submarine volcanic and sedimentary sequence. This sequence is host to massive sulfide mineralization. The massive Sargaz orebody is associated with stockwork stringer zones and footwall alteration pipes near the upper contact of the pillowed basalts with the overlying sequence of andesitic and rhyodacitic volcanoclastic and flows of probable Upper Triassic to Lower Jurassic age (Badrzadeh et al. 2011). Here we present the results of mineralogical and geochemical studies of hydrothermal alteration zones associated with the Sargaz pyritic Cu-Zn orebody.

2 Geological setting

The Zagros orogenic belt of Iran extends for about 2000 km in a NW-SE direction from the East Anatolian Fault of eastern Turkey to the Oman Line in southern Iran. This belt is considered to be a complex product of an early Mesozoic separation of the Iranian continental block from the rest of the Gondwana landmass followed by a NE-dipping subduction of the newly generated Neo-Tethyan oceanic crust below the Iranian microcontinent and subsequent collision between the Afro-Arabian and Iranian plates (e.g. Takin 1972; Berberian and King 1981; Sengor 1984; Dercourt et al. 1986). The belt consists of three tectonically related parallel zones which are from northeast to southwest: (1) the Urumieh Dokhtar Magmatic Arc, (2) the Sanandaj-Sirjan Zone and (3) the Zagros Fold and Thrust Belt (Fig. 1).

The Sanandaj-Sirjan zone (Mohajjel and Fergusson 2000) in Iran hosts several types of massive sulfide mineralizations with the Sargaz deposit, the most significant, and occurring in the easternmost part of this zone (Fig. 1). This zone is considered to be primarily either an accreted microcontinent that separated from Gondwanaland during the Early Jurassic (e.g., Stocklin 1968; among others) or an aulacogeosynclinal (intracontinental palaeo rift) basin (Sabzehei 1974) or a once-active margin of the Central Iranian block (e.g., Berberian and King 1981; Sheikholeslami et al. 2008).

Stratigraphically the early Mesozoic VSS regionally overlies Paleozoic (pre-Permian to lower Triassic) metamorphic basement rocks (Sabzehei 1974) and overlain by flysch-type sedimentary rocks and Upper Jurassic to Lower Cretaceous Calpionella limestone. They consist of mafic and felsic volcanic and volcanoclastic rocks overlain by shale, Fe-Mn bearing chert and limestone that were intruded by high-level subvolcanic gabbro-diorite to granitic rocks.

The mine sequence comprises flows and volcanoclastic units of basaltic andesitic to rhyodacitic composition, and post-ore granodioritic to mafic dykes. Lithostratigraphic units in the Sargaz area are, from oldest to youngest (Fig. 2):

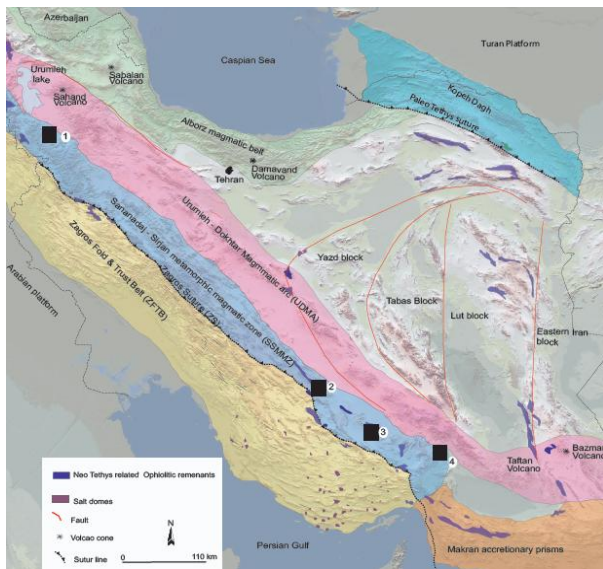


Figure 1. Tectonic map of Iran, showing the extent of the Sanandaj-Sirjan Zone (based on Stöcklin 1968) and locations of the massive sulfide mineralizations (black squares) of the Sanandaj-Sirjan Zone are also shown: (1) Barika; (2) Bavanat; (3) Chahgaz; (4) Sargaz

1. A Paleozoic metamorphic complex ranges in age from Upper Cambrian to Lower Triassic. This complex is unconformably overlain by pillowed mafic flows.

2. Basaltic pillowed flows of probable Upper Triassic age form the immediate footwall to the Sargaz massive sulfide deposit. The primary volcanic textures are obliterated near the stratigraphic base of the massive sulfide deposit where hydrothermal alteration effects are most intense.

The sulfide mineralogy of the interior of the Sargaz orebody is relatively simple and dominated by pyrite and chalcopyrite with minor sphalerite. Other primary minerals include tetrahedrite-tennantite and traces of galena. Bornite occurs mainly as oxidation products of chalcopyrite. Ore body composed of >70vol% sulfide and may be subdivided on a textural basis into massive sulfide, sulfide breccias, laminated sulfide and debris sulfides.

3. Along strike from the deposit, a jasper horizon lies stratigraphically at the contact between the footwall mafic rocks and the hanging wall andesitic rocks. Carbonate and barite beds underlie some of the jasper beds lateral to the deposit, and proximal to the massive sulfide lens they also overlie the massive sulfide lens.

4. Hanging wall andesitic volcanoclastic rocks and volcanic breccias that range from 500–1000 m in thickness.

5. A sequence of interbedded rhyodacitic flows, felsic volcanoclastics, shale, sandstone, radiolarian cherts, and Fe–Mn-oxide layer overlie the andesitic volcanoclastic rocks.

6. A regionally extensive, Middle Jurassic flysch-type sedimentary rocks is composed of sandstone, shale, conglomerate, and mafic tuff.

7. Jurassic to Neocomian calpionella-bearing limestones unconformably overlies the flysch-type

sediments.

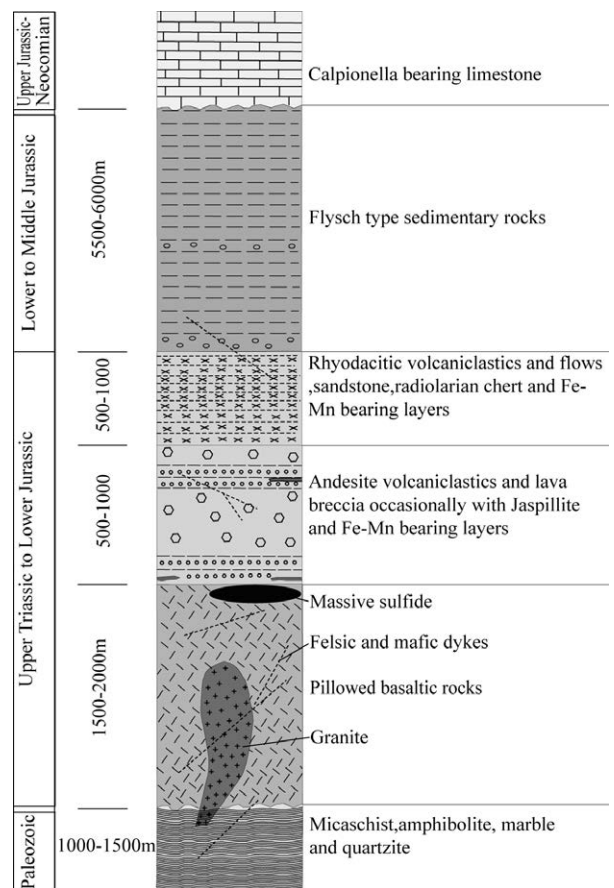


Figure 2. Schematic stratigraphic section showing setting of massive sulfide deposit in the Sargaz volcano-sedimentary sequence.

Important structural elements of the Sargaz area are north- and west-trending faults and northeast-trending folds. It is tightly disrupted by northeast-trending faults.

The bimodal nature of volcanism, the regional geologic setting and petrochemistry of the mafic and felsic volcanic rocks indicate that the massive sulfide mineralization in the VSS formed in a nascent ensialic back-arc basin related to the subduction of the Neotethys oceanic crust beneath the southeast part of Central Iranian microcontinent.

Massive sulfide formation in the Sargaz occurred during the waning stages of mafic volcanism within VSS. A continuous to discontinuous layer of jasper-barite-carbonate exhalite overlies the mafic volcanic sequence and the overlying massive sulfide mineralization (Badrzadeh et al. 2011).

3 Hydrothermal alteration zoning

The hydrothermally unaltered pillowed basalts have been affected by low temperature, subseafloor metamorphism and consist of mostly albitized plagioclase and chloritized clinopyroxene phenocrysts in a groundmass of albite, chlorite, epidote, calcite,

quartz, magnetite, and pyrite. The rocks show porphyritic, intersertal, and quench textures. They are amygdaloidal; the vesicles are <1mm in diameter and infilled with secondary minerals. Ore-related alteration, overprinting early semiconformable regional alteration has been characterized in detail in the footwall sequence of the Sargaz orebody. Type 1 alteration (central stockwork; quartz-sulfides veins and pervasive quartz-sericite-sulfide alteration) occurs in the central part of feeder zone (Fig. 3a); surrounded by Type 2 alteration that is the main part of the feeder zone. This alteration is plagioclase destructive and it typically constitutes a quartz-chlorite-sulfide assemblage (Fig. 3b). Type 3 alteration can be recognized by the occurrence of hydrothermal chlorite-quartz-sulfide assemblage (Fig. 3c). Type 4 alteration is a peripheral halo of alteration characterized by chlorite-sericite \pm hematite \pm epidote \pm leucosene assemblage (Fig. 3d) with dusting of hematite typically developed towards the base of the volcanic pile. Plagioclase and clinopyroxene have been replaced by chlorite, sericite, and pyrite. This alteration is most obvious in the form of vesicle infillings with chlorite-sericite, which commonly also contains sulfides. Chlorite in hydrothermal alteration halo is an Mg-rich variety and shows a decreasing Fe/Mg ratio toward the massive ore.

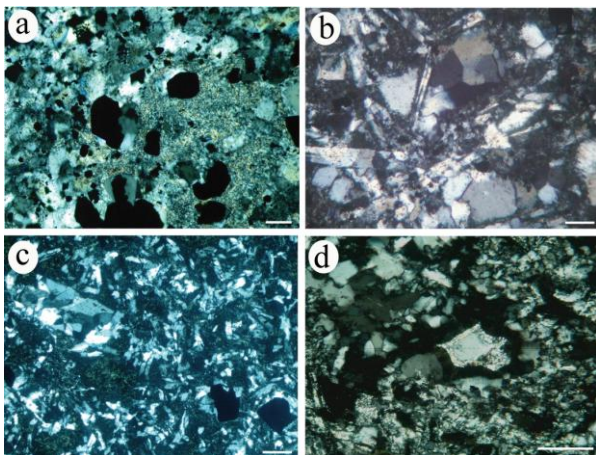


Figure 3. Representative photomicrographs of hydrothermally altered samples related to the massive sulfide mineralization occurrence. Scale bar is 100 μ m in all pictures. **a** The immediate footwall to the Sargaz orebody is characterized by quartz-sericite-pyrite alteration. Coarse grained quartz and pyrite is the dominant alteration mineral with minor sericite and rare chlorite. This alteration is the most pervasive and makes it impossible to visually determine the protolith; **b** quartz-chlorite alteration, which is the main portion of the Sargaz feeder zones, is plagioclase destructive and it typically constitutes a quartz-chlorite-sulfide assemblage; **c** chlorite- quartz alteration typically constitutes a chlorite-quartz-sulfide assemblage. This alteration characterized by plagioclase phenocrysts and groundmass which have been converted to chlorite, quartz and pyrite. This alteration is most obvious in the form of vein and vesicle infillings with chlorite and sulphides; **d** chlorite-sericite alteration in the deepest part of the feeder zone comprises a chlorite-sericite-sulfide \pm epidote \pm leucosene \pm hematite assemblage

4 Lithochemochemistry

Least-altered basaltic andesitic rocks display chemical features, which suggest that they are of tholeiitic to transitional affinity. All of the footwall basalts, regardless of degree of alteration show slight variation in its original composition over at least 100m under the deposit, judging by its near-uniform immobile-element ratios. This indicates that they have been derived from a chemically near homogenous precursor. In order to quantify hydrothermal alteration, we have used immobile-element techniques, following MacLean and Barrett (1993), and Barrett and MacLean (1994). Calculated mass changes for the mafic footwall reveal additions of K_2O to some parts of the alteration pipe. Near total losses of CaO and Na_2O and addition of MgO display breakdown of plagioclase and formation of chlorite during hydrothermal alteration. Silica was added to immediately below the orebody, but depleted from others (Fig. 4).

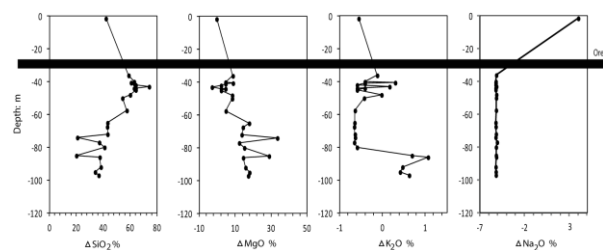


Figure 4. Downhole calculated mass changes for SiO_2 , MgO , K_2O and Na_2O . Mass changes (Δ values) are in absolute wt %.

5 Discussion and conclusions

Accumulation of pillowed basaltic to basaltic andesitic flows with mainly tholeiitic affinity took place in an incipient back arc setting. Hydrothermal fluid circulation resulted in a massive sulfide deposition and associated stockwork mineralization in the upper volcanic pile. Chlorite, quartz, sericite, and pyrite constituting the alteration pipe beneath the Sargaz deposit precipitated in a discharge zone from a highly reacted fluid of seawater origin. Replacement of primary minerals by Mg-chlorite in alteration pipe of Sargaz deposit may indicate drawdown of cold and fresh seawater into the discharge zone under deeper water conditions (e.g. Franklin 1986; Morton and Franklin 1987). The presence of a few percent hematite in the Sargaz alteration pipe may suggest a reduction of seawater sulfate (Mottl 1983).

In the Sargaz region the presence of Mg-rich chlorite together with strong enrichment in MgO , FeO and depletion in CaO and Na_2O together with different alteration types, their intensity and zonation can provide effective vectors to VMS mineralization in the southeastern part of the Sanandaj-Sirjan zone and appear to be useful guides in exploration for similar basaltic hosted deposits.

References

- Badrzadeh Z, Barrett TJ, Peter JM, Gimeno D, Sabzehei M, Aghazadeh M (2011) Geology, mineralogy, and sulfur isotope geochemistry of the Sargaz Cu–Zn volcanogenic massive sulfide deposit, Sanandaj–Sirjan Zone, Iran. *Miner Deposita* 46:905–923
- Barrett TJ, MacLean WH (1994) Chemostratigraphy and hydrothermal alteration in exploration for VHMS deposits in greenstones and younger volcanic rocks. In: Lentz DR (ed) *Alteration and alteration processes associated with ore-forming systems*. GAC Short Course Notes 11:433–467
- Berberian M, King GCP (1981) Towards a paleogeography and tectonic evolution of Iran. *Can J Earth Sci* 18:210–265
- Dercourt J, Zonenshain L, Ricou LE, Kasmin G, LePichon X, Knipper AL, Grandjacquet C, Sbertshikov IM, Geysant J, Lepvrier C, Pechersky DH, Boulin J, Sibuet JC, Savostin LA, Sorokhtin O, Westphal M, Bazhenov ML, Lauer JP, Biju-Duval B (1986) Geological evolution of the Tethys Belt from the Atlantic to Pamirs since the Lias. *Tectonophysics* 123: 241–315
- Franklin JM (1986) volcanic associated massive sulfide deposits— an update: *Irish Assoc. Econ Geol Spec. Pub* 4: 49–69
- MacLean WH, Barrett TJ (1993) Lithochemical techniques using immobile elements. *J Geochem Explor* 48:109–133
- Mohajjel M, Fergusson CL (2000) Dextral transpression in Late Cretaceous continental collision, Sanandaj–Sirjan zone, Western Iran. *J Struct Geol* 22: 1125–1139
- Morton JL, Franklin JM (1987) Two-fold classification of Archean volcanic-associated massive sulfide deposits. *Econ Geol* 82: 1057–1063
- Mottl MJ (1983) Metabasalts, axial hot springs, and structure of hydrothermal systems at mid-ocean ridges. *Geol Soc Am Bull* 94: 161–180
- Sabzehei M (1974) *Les melanges ophiolitiques de la region d Esfandagheh*. These, Universite de Grenoble, France, 303 p
- Sengor AMC (1984) The Cimmeride orogenic system and the tectonics of Eurasia. *Geol Soc Am, Spec Pap* 195
- Sheikholeslami MR, Pique A, Mobayen P, Sabzehei M, Bellon H, Emami MH (2008) Tectono-metamorphic evolution of the Neyriz metamorphic complex, Quri-Kor-e-Sefid area (Sanandaj–Sirjan Zone, SW Iran). *J Asian Earth Sci* 31:504–521
- Stöcklin J (1968) Structural history and tectonics of Iran: a review. *Am Assoc Petrol Geol Bull* 52:1229–1258
- Takin M (1972) Iranian geology and continental drift in the Middle East. *Nature* 235: 147–150

Collision- and subduction-related porphyry Cu deposits in Tibetan orogen: a possible genetic linkage

Zengqian Hou, Zhiming Yang, Yuanchuan Zheng

Institute of Geology, Chinese Academy of Geological Science, Beijing 100037, China

Juxing Tang, Zhusen Yang

Institute of Mineral Resources, Chinese Academy of Geological Sciences, Beijing 100037, China

Abstract. Source of metals for collision-type porphyry Cu deposits remains subjects of much debate. Previous models suggest that metals in such deposits were probably derived from subduction-modified lower crust, meaning that previous arc magmas underplated at the bottom of the lower crust probably provided an idealized source for late fertile magmas in collisional setting. However, the hypothesis has not been verified. Here we report Jurassic and Miocene mineralization events that form numerous giant porphyry Cu deposits in south Tibet, generated by subduction of Neo-Tethys in Jurassic and India-Asia collision in the early Cenozoic, respectively. Geochemical and Sr-Nd-Hf isotopic studies indicate that Jurassic fertile porphyries were derived from partial melting of a metasomatized mantle wedge in an arc setting and collisional fertile ones were generated by remelting of a juvenile mafic lower crust formed by underplating of Jurassic Cu-rich arc magmas. Involvement of abundant Jurassic Cu-rich primitive basaltic arc magmas into bottom of the original ancient lower crust was regarded to provide an idealized source for generation of Miocene fertile adakitic magmas in south Tibet.

Keywords. Porphyry Cu deposits, collisional setting, subduction-related, Tibet, adakites, source of metals

1 Introduction

Most porphyry Cu-Mo-Au deposits form in magmatic arc worldwide and are associated with hydrous, high- f_{O_2} , calc-alkaline magmas, derived from the mantle wedge metasomatized by subducted oceanic slab-fluids (Richard, 2003). Recently, such deposits have been documented to widely occur in collisional settings, and are associated with K-rich adakitic magmas generated during collisional process (Hou et al., 2004, 2009, 2011). Such collision-related magmas were regarded to have derived from remelting of previously subduction-modified arc lithosphere (Richards, 2009) or juvenile lower crust involved mantle components (Hou et al., 2004). This means that previous arc magmas underplated on the lower crust probably provided an idealized source for fertile magmas in collisional setting, implying a possible genetic linkage between subduction- and collision-related porphyry Cu deposits. However, there is no evidence to demonstrate this hypothesis.

Here we report Jurassic and Miocene mineralization events that form numerous giant porphyry Cu deposits in Himalayan-Tibetan orogen, formed by subduction of Neo-Tethys since Jurassic and subsequent India-Asia collision in the early Tertiary. Geochemical and Sr-Nd-Hf isotopic studies indicate that Jurassic fertile

porphyries were derived from the evolved mafic magmas produced by melting of the metasomatized mantle wedge in an arc setting and collisional fertile ones were generated by remelting of a juvenile mafic lower crust formed by underplating of the Jurassic arc magmas.

2 Subduction- and collision-related porphyry Cu deposits

The Himalayan-Tibetan orogen, formed by the Indian-Asian continental collision at early Tertiary, built on a complex tectonic collage composed of several accreted terranes, i.e., Songpan-Garzê, Qiangtang, and Lhasa (Fig. 1a; Yin and Harrison, 2000). The Lhasa terrane has undergone a complicated history of tectonic evolution from subduction of the Neo-Tethys at Jurassic (cf., Chung et al., 2005), which form the Indu-Yarlung suture, the Xigaze fore-arc basin (Dürr, 1996), and the Gangdese arc batholiths (184-70 Ma; Schärer et al., 1984; Chu et al., 2006; Zhu et al., 2011) from south to north, to India-Asia collision began at ~65Ma (cf., Mo et al., 2003; Ding et al., 2003), which resulted in crustal thickening (up to 70-80 km) and a 1500-km long transhimalayan igneous belt along its southern edge. At least two suites of porphyry systems have been recognized in the transhimalayan belt, i.e., Jurassic arc suite (184-158 Ma) associated porphyry Cu-Au, and post-collisional suites (26-10 Ma) associated with porphyry Cu-Mo mineralization, which comprise a 700-km long Gangdese porphyry Cu belt (GPCB) in Tibet (Fig. 1b). The Jurassic porphyry Cu-Au deposit, i.e., giant Xiongcu deposit at Xigaze, is located in western end of the GPCB, and yielded molybdenite Re-Os age of 177-170 Ma (Fig. 1a; Tang et al., 2010). The mid-Miocene porphyry Cu-Mo mineralization forms four giant and large-sized Cu-Mo deposits in whole GPCB, with molybdenite Re-Os ages of 18-14Ma (Fig. 1b; Hou et al., 2009; Yang et al., 2009), postdated subduction-related arc magmatism and mineralization at least by ~50 Ma.

3 Geochemistry and genesis of Jurassic fertile and barren arc magmas

The Jurassic arc intrusions, as product of northward subduction of the Neo-Tethys, mainly occur as numerous small-volume dioritic plutons, emplaced on southern edge of the Lhasa terrane. The majority of these plutons are barren due to lack of any hydrothermal alteration and mineralization. A few of porphyritic quartz dioritic stocks with intensely alteration were only discovered in

western end of a 600km-long arc magmatic belt, forming porphyry Cu-Au deposit (e.g., Xiongcun). The Jurassic arc rocks range in composition from dioritic (barren) to granodioritic (fertile), and mainly are calc-alkaline with minor tholeiitic. They are characterized by enrichment in LILE (i.e., K, Ba, Sr) and depletion in HFSE (i.e., Nb, Ta, Ti), similar to arc magmas. The fertile magmas have a limited range of high $\epsilon_{Nd(t)}$ (+5 ~ +6) and low ($^{87}Sr/^{86}Sr$)_i values (0.7040-0.7050) (Qu et al., 2007), identical to that of Jurassic arc basalt. All magmatic zircons of the fertile quartz-dioritic porphyries yield positive $\epsilon_{Hf(T)}$ values from +12 to +16 (Fig. 2), close to depleted arc lavas (Chu et al., 2011), suggesting that such magma was generated by partial melting of a depleted asthenospheric mantle. In combination with other geochemical characteristics such as young Hf model age and lack of any inherited zircons, we propose that the Jurassic rocks were formed in an island-arc setting, rather than continental arc setting as previously proposed by other authors (e.g., Yin and Harrison, 2000).

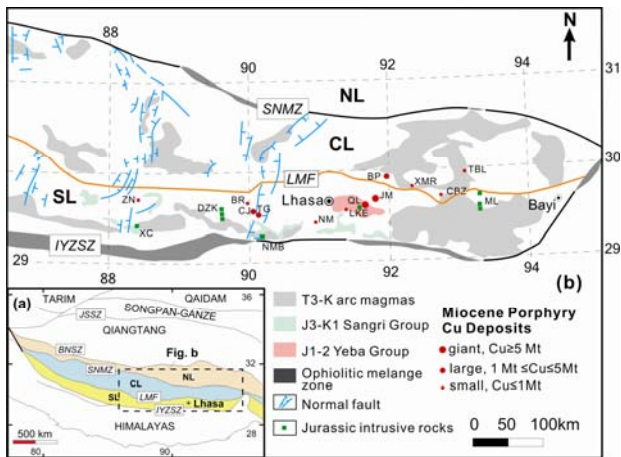


Figure 1. (a) Tectonic framework of the Tibetan plateau showing its structures and tectonic belts (after Yin and Harrison, 2000; Zhu et al., 2011). (b) Geological map of the southern and central Lhasa terrane showing the distribution of the Jurassic Xiongcun deposit and the Miocene Gangdese porphyry Cu belt (Z.M. Yang, unpublished data; compiled after Yang et al., 2011 and Zhu et al., 2011). Abbreviations: JSSZ=Jinsha suture zone; BNSZ=Bangonghu-Nujiang suture zone; SNMZ=Shiquan River-Nam Tso Mélange zone; LMF=Luobadui-Milashan Fault; JSSZ=Jinshajiang suture zone; IYZSZ=Indus-Yalung Zangbo suture zone; SL=southern Lhasa subterrane; CL=central Lhasa subterrane; NL=northern Lhasa subterrane. Miocene porphyry Cu deposits: ZN=Zhunuo, XC=Xiongcun, BR=Bairong, CJ=Chongjiang, TG=Tinggong, NM=Nanmu, LKE=Lakang'e, QL=Qulong, JM=Jiama, BP=Bangpu, XMR=Xiamari, CBZ=Cuibaizi, TBL=Tangbula. Jurassic intrusive rocks: XC=Xiongcun, DZK=Dazhuka, NMB=Nimu bridge, ML=Milin.

4 Geochemistry and genesis of mid-Miocene fertile and barren post-collisional magmas

The mid-Miocene porphyries in Tibet range in composition from granodioritic to granitic ($SiO_2 = 64\sim 73\%$). They are usually shoshonitic and high-K calc-alkaline with minor calc-alkaline. They yield relatively low content of Ni (2.4~23 ppm) and low $Mg^\#$ values

($Mg^\# = MgO/FeO+MgO: 0.32$ to 0.58), and are characterized by enrichment in LILE (i.e., K, Ba, Sr) and depletion in HFSE (i.e., Nb, Ta, Ti), close to that of Jurassic arc magmas, showing characteristic features of many subduction-related arc magmas (Rogers and Hawkesworth, 1989). However, their low Y (3.7~19.7 ppm) and Yb (0.27~1.47 ppm), coupled with high Sr/Y (12.2~201.5) and La/Yb (12.2~84.8) ratios, are the characteristics of most already-reported adakites (e.g., Defant and Drummond, 1990), indicating their adakitic geochemical affinity (Chung et al., 2003; Hou et al., 2004). However, in comparison with typical adakites generated by partial melting of oceanic-slab (e.g., Defant and Drummond, 1990; Peacock, 1993; Stern and Kilian, 1996), these collision-type adakitic rocks generally have higher initial $^{87}Sr/^{86}Sr$ ratios and lower ϵ_{Nd} values (see Hou et al., 2011 as a review).

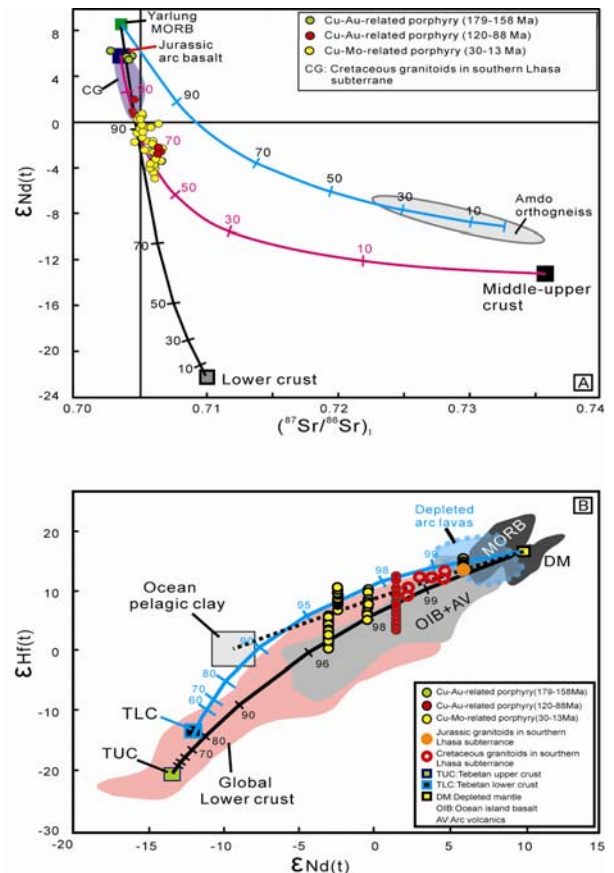


Figure 2. Plot of bulk-rock ($^{87}Sr/^{86}Sr$)_i vs $\epsilon_{Nd(t)}$ values (a); and plot of zircon $\epsilon_{Hf(t)}$ values vs bulk-rock $\epsilon_{Nd(t)}$ values (b) for felsic igneous rocks in the Lhasa Terrane. The rocks plotted include the Jurassic quartz dioritic porphyries (Cu-Au) and associated intra-oceanic arc volcanic rocks, Cretaceous granitoids and associated metaluminous granodiorite (Fe) and granodioritic porphyries (Cu-Au), and Oligocene-Miocene adakitic porphyries (Cu-Au), and Oligocene-Miocene adakitic porphyries (Cu-Mo, Mo-Cu) (after Z.-Q., Hou, unpublished data).

Although there are still some disputes, it's increasingly accepted that these collision-type adakitic rocks in south Tibet were derived from partial melting of thickened lower crust (Chung et al., 2003; Hou et al., 2004; Guo et al., 2007). The low anomalies of Nb, Ta, and Ti of the syenogranite porphyries on the primitive mantle-normalized diagrams further indicate such lower

crust has been modified by oceanic subduction (Guo et al., 2007). The relatively positive $\varepsilon_{\text{Nd}(t)}$ (~ 2.2), low $(^{87}\text{Sr}/^{86}\text{Sr})_i$ (Fig. 2a) and relatively young Nd model ages of some of these collision-type adakitic rocks suggests that the modification of oceanic subduction probably happened recently. Nearly consistent initial $^{87}\text{Sr}/^{86}\text{Sr}$ ratios, but much variable $\varepsilon_{\text{Nd}(t)}$ values ($+2.2 \sim -6.2$) of the fertile adakitic rocks result in distribution of these adakitic samples on the plot of $^{87}\text{Sr}/^{86}\text{Sr}$ versus $\varepsilon_{\text{Nd}(t)}$ (Fig. 2a) falling into mixing array between lower crust and Jurassic arc basalt. This suggests that the modification of the original ancient lower crust is probably related to Neo-Tethys subduction. Positive $\varepsilon_{\text{Hf}(T)}$ values (6.4-12.2) of magmatic zircons from the fertile porphyries lead to the distribution of the fertile porphyry samples falling in the field of global lower crust with Jurassic arc magmas on the $\varepsilon_{\text{Hf}(T)}$ versus $\varepsilon_{\text{Nd}(t)}$ plot (Fig. 2b), also supporting that juvenile characteristics of the lower crust was caused by modification of Jurassic Neo-Tethys subduction, during which basaltic arc magma generated by partial melting of mantle wedge would pool at the bottom of the subduction-modified lower crust and undergo MASH process (melting, assimilation, storage, and homogenization) (Hildreth and Moorbath, 1988).

5 Possible genetic linkage between the subduction- and collision-related porphyry Cu deposits

For the porphyry Cu deposits in collisional setting, source of metals has been poorly understood. Recently, Richards (2009) and Hou et al. (2011) proposed a plausible model to explain origination of metals (e.g., Cu and Au), in which they proposed that small to large amounts of sulfide (as melt or a crystalline phase) that originally precipitated during the ascent of arc magmas would expect to be present in the subduction-modified lower crust, and remelting of this sulfide may have provided metals for formation of porphyry Cu deposits in collisional setting. If the generation of porphyry Cu deposits in south Tibet are consistent with this model, the Jurassic arc magmas, which has ever been underplated at the bottom of the lower crust, should provide abundant metals for late formed Miocene fertile adakitic magmas.

As shown in Fig. 1b, outcrop area of the Jurassic intrusive rocks overlaps well with that of the Miocene porphyry Cu deposits, suggesting possible underplating of Jurassic arc magmas beneath the Miocene Gangdese porphyry Cu belt. Presence of economic Cu-Au mineralization (e.g., Xiongcu; Fig. 1b) associated with some Jurassic intrusive rocks indicates that contents of metals (e.g., Cu and Au) in such Jurassic arc magmas are high enough for generation of economic Cu deposits, implying a possible genetic linkage between subduction- and collision-related porphyry Cu deposits. Furthermore, such genetic linkage is verified by spatial association between Jurassic intrusive rocks and Miocene porphyry Cu deposits. As shown in Fig. 1b, the fertile Jurassic intrusions (e.g., Xiongcu) is spatially incompatible with the Miocene porphyry Cu deposits, whereas the barren Jurassic intrusive rocks are spatially compatible well

with the Miocene porphyry Cu deposits (Fig. 1b). According to above metal origin model for collision-type porphyry Cu deposits proposed by Richards (2009) and Hou et al. (2011), small to large amounts of sulfides should be precipitated from Jurassic arc magmas during MASH process for late generation of collision-type porphyry Cu deposits, which would reduce the possibility of formation of Jurassic porphyry Cu deposits and result in spatially overlapping between barren Jurassic intrusive rocks and Miocene porphyry Cu deposits. On the contrary, the possibility of formation of Jurassic porphyry Cu deposits (e.g., Xiongcu; Fig. 1b) would arise if sulfides were not precipitated during underplating of the arc magmas, which can explain well why the Jurassic Xiongcu Cu-Au being far from the dominant segment (east of 90°) of Gangdese porphyry Cu belt (Fig. 1b).

Possible contribution of metals in formation of collision-type porphyry Cu deposits by underplating of Jurassic arc magmas is also evident by comparison of geochemical characteristics between the Jurassic fertile and barren intrusive rocks. For example, the barren intrusions generally have higher bulk-rock $\varepsilon_{\text{Nd}(t)}$ value and very positive zircon $\varepsilon_{\text{Hf}(T)}$ values (Fig. 2), indicating that primitive arc basaltic magmas beneath Miocene porphyry Cu deposits solidified and emplaced quickly after their generation without intense fractional crystallization and/or assimilation (AFC). In this situation, Cu would expect to be free of transport to shallow by primitive basaltic magmas due to its incompatible behavior under high $f\text{O}_2$ condition (e.g., Richards, 2003). Original ancient lower crust modified with involvement of abundant such Cu-rich primitive basaltic arc magmas would provide an idealized source for generation late fertile magmas in collisional setting.

6 Conclusion

Similar geochemical features between Jurassic subduction- and Miocene collision-related ore-forming porphyries suggest their genetic linkage. Involvement of abundant Jurassic Cu-rich primitive basaltic arc magmas into bottom of the original ancient lower crust provides an idealized source for generation late fertile magmas in south Tibet.

Acknowledgements

This work was funded by National Basic Research Program of China (2011CB403104), the National Natural Science Foundation of China (41273051), the Ministry of Land and Resources of China (201011011), and IGCP/SIDA-600. We would like to thank Lianfeng Duan for his help in preparing the figures.

References

- Chu M F, Chung S L, O'Reilly S Y, Pearson N J, Wu F Y, Li X H, Liu D, Ji J, Chu C H, Lee H Y India's hidden inputs to Tibetan orogeny revealed by Hf isotopes of Transhimalayan zircons and host rocks. *Earth and planetary science letters* 307: 479-486
- Chu M F, Chung S L, Song B, Liu D, O'Reilly S Y, Pearson N J, Ji

- J, Wen D J (2006) Zircon U-Pb and Hf isotope constraints on the Mesozoic tectonics and crustal evolution of southern Tibet. *Geology* 34: 745-748
- Chung S L, Chu M F, Zhang Y, Xie Y, Lo C H, Lee T Y, Lan C Y, Li X, Zhang Q, Wang Y (2005) Tibetan tectonic evolution inferred from spatial and temporal variations in post-collisional magmatism. *Earth-Science Reviews* 68: 173-196
- Chung S L, Liu D, Ji J, Chu M F, Lee H Y, Wen D J, Lo C H, Lee T Y, Qian Q, Zhang Q (2003) Adakites from continental collision zones: Melting of thickened lower crust beneath southern Tibet. *Geology* 31: 1021-1024
- Defant M J, Drummond M S (1990) Derivation of some modern arc magmas by melting of young subducted lithosphere. *Nature* 347: 662-665
- Ding L, Kapp P, Zhong D, Deng W (2003) Cenozoic volcanism in Tibet: Evidence for a transition from oceanic to continental subduction. *Journal of Petrology* 44: 1833-1865.
- Dürr S (1996) Provenance of Xigaze fore-arc basin clastic rocks (Cretaceous, south Tibet). *Geological Society of America Bulletin* 108: 669-684
- Guo Z, Wilson M, Liu J (2007) Post-collisional adakites in south Tibet: Products of partial melting of subduction-modified lower crust. *Lithos* 96: 205-224
- Hildreth W, Moorbath S (1988) Crustal contributions to arc magmatism in the Andes of central Chile. *Contributions to Mineralogy and Petrology* 98: 455-489.
- Hou Z, Yang Z, Qu X, Meng X, Li Z, Beaudoin G, Rui Z, Gao Y, Zaw K (2009) The Miocene Gangdese porphyry copper belt generated during post-collisional extension in the Tibetan orogen. *Ore Geology Reviews* 36: 25-51
- Hou Z, Zhang H, Pan X, Yang Z Porphyry Cu (Mo-Au) deposits related to melting of thickened mafic lower crust: Examples from the eastern Tethyan metallogenic domain. *Ore Geology Reviews* 39: 21-45
- Hou Z Q, Gao Y F, Qu X M, Rui Z Y, Mo X X (2004) Origin of adakitic intrusives generated during mid-Miocene east-west extension in southern Tibet. *Earth and planetary science letters* 220: 139-155
- Mo X, Zhao Z, Deng J, Dong G C, Zhou S, Guo T Y, Zhang S Q, Wang L L (2003) Response of volcanism to the India-Asia collision. *Earth Science Frontiers* 10: 135-148 (in Chinese with English abstract)
- Peacock S M (1993) Large-scale hydration of the lithosphere above subducting slabs. *Chemical Geology* 108: 49-59
- Qu X M, Xin H B, Xu W Y (2007) Petrogenesis of the ore-hosting volcanic rocks and their contribution to mineralization in Xiongcu superlarge Cu-Au deposit, Tibet. *Acta Geologica Sinica* 81: 964-971 (in Chinese with English abstract)
- Richards J P (2003) Tectono-magmatic precursors for porphyry Cu-(Mo-Au) deposit formation. *Economic Geology* 98: 1515-1533
- Richards J P (2009) Postsubduction porphyry Cu-Au and epithermal Au deposits: Products of remelting of subduction-modified lithosphere. *Geology* 37: 247-250
- Rogers G and Hawkesworth C J (1989) A geochemical traverse across the North Chilean Andes: evidence for crust generation from the mantle wedge. *Earth and Planetary Science Letters* 91: 271-285
- Schärer U, Xu R H, Allègre C J (1984) U-Pb geochronology of Gangdese (Transhimalaya) plutonism in the Lhasa-Xigaze region, Tibet. *Earth and planetary science letters* 69: 311-320
- Stern C R, Kilian R (1996) Role of the subducted slab, mantle wedge and continental crust in the generation of adakites from the Andean Austral Volcanic Zone. *Contributions to Mineralogy and Petrology* 123: 263-281
- Tang J, Li F, Li Z, Zhang L, Deng Q, Lang X, Huang Y, Yao X, and Wang Y (2010) Time limit for formation of main geological bodies in Xiongcu copper-gold deposit, Xietongmen County, Tibet: Evidence from zircon U-Pb ages and Re-Os age of molybdenite. *Mineral Deposits* 29: 461-475 (in Chinese with English abstract)
- Yang Z, Hou Z, White N C, Chang Z, Li Z, Song Y (2009) Geology of the post-collisional porphyry copper-Molybdenum deposit at Qulong, Tibet. *Ore Geology Reviews* 36: 133-159
- Yang Z M, Hou Z Q, Jiang Y F, Zhang H R, Song Y C (2011) Sr-Nd-Pb and zircon Hf isotopic constraints on petrogenesis of the Late Jurassic granitic porphyry at Qulong, Tibet. *Acta Petrol. Sin* 27: 2003-2010 (in Chinese with English abstract)
- Yin A, Harrison T M (2000) Geologic evolution of the Himalayan-Tibetan orogen. *Annual Review of Earth and Planetary Sciences* 28: 211-280
- Zhu D C, Zhao Z D, Niu Y, Dilek Y, Mo X X (2012) Lhasa terrane in southern Tibet came from Australia. *Geology* 39: 727-730

The giant Jinding Zn-Pb deposit: ore formation in an evaporite dome, Lanping Basin, Yunan, China

David L. Leach

Institute of Geology, Chinese Academy of Geological Sciences, Beijing 100037, China; Centre for Exploration Targeting, University of Western Australia, Perth 6009, Australia

Yucai Song, Zengqian Hou, Tiannan Yang

Institute of Geology, Chinese Academy of Geological Sciences, Beijing 100037, China

Chuangdong Xue

Kunming University of Science and Technology, Kunming 650093, China

Abstract. The giant Jinding Zn-Pb deposit in SW China is hosted in sedimentary rocks in a dome that has been attributed to the effects of thrusting or a consequence of ascending mantle gases. New field observations show the ore deposit formed by halokinesis that produced a “salt dome” during the migration of evaporites along a thrust decollement during the Himalayan orogeny. The dome provided a reservoir for hydrocarbons and reduced sulfur providing a chemical trap for ascending Zn-Pb-rich sedimentary brines. A salt diapir origin for the Jinding dome is consistent with features present in other salt diapir deposits (e.g., Fedj el Adoum, Bou Grine deposits, Tunisia) and evaporite structures in the world. The evidence includes: the abundance of mega breccia, matrix supported evaporite tectonic breccia with fluid injection and flowage textures with clasts of sulphides and exotic rock lithologies, high fluid pressures indicated by fluidized sand injection features and the presence of abundant evaporite minerals in the dome. Jinding is best described as a “diapir Zn-Pb” ore deposit with ore-forming processes similar to Mississippi Valley-type (MVT) ores. Jinding is an exceptionally large deposit relative to similar diapir-related deposits in the world. This suggests that other giant Zn-Pb deposits may be present in the Lanping basin as well in other diapir belts in the world.

Keywords.

Jinding sediment-hosted Zn-Pb deposit, SW-China, evaporite dome, halokinesis, salt diapir

1 Introduction

The sediment-hosted Jinding Zn-Pb deposit is the largest Zn deposit in Asia (200 Mt ore with 6.1% Zn and 1.3% Pb; Xue et al. 2007). The genesis of the ore has remained enigmatic despite many studies on the deposit. It has been classified as a Zn-rich sandstone-hosted deposit (Kyle and Li 2002) or a syngenetic, SEDEX, epigenetic and as a unique “Jinding-type deposit” (see discussion in Xue et al. 2007). Ore is hosted in a dome that has been attributed to the effects of thrusting or a consequence of ascending mantle gases (Xue et al. 2007). In this paper, field observations are presented that show the ore deposit formed by halokinesis that produced a “salt dome” during the migration of evaporites along a thrust decollement developed from Cenozoic thrust loading.

2 Geological setting

The Jinding Zn-Pb deposit is located in the Lanping basin of the northern Lanping-Simao terrane, eastern Tibet (Fig. 1).

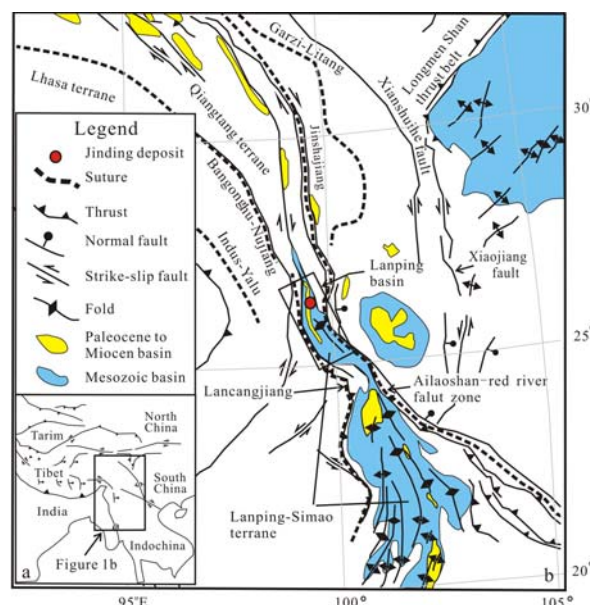


Figure 1. Location of the Jinding Zn-Pb deposit (modified from Wang et al. 2001)

During the Middle to Late Triassic, the early basin fill consisted of felsic magmatic rocks, bimodal volcanic rocks and marine-facies siliciclastics and limestone controlled by the closures of the Lancangjiang and the Jinshajiang sutures that produced post-collisional extension. The basin evolved into a foreland basin during the closure of the Bangonghu-Nujiang suture, and filled with marine, mixed marine-terrestrial and terrestrial red beds during Middle Jurassic to Cretaceous. Regional deformation during the Himalayan orogeny led to the formations of a strike-slip tensional and foreland basin. The basin was filled with terrestrial-facies red bed sequences including the Paleocene Yunlong Formation that contains several hundred meters of evaporites and evaporite-bearing sediments. During the Tertiary Himalayan orogeny, west to southwest thrusting juxtaposed the Mesozoic strata over the Cenozoic strata to form the current structural framework (He et al. 2009)

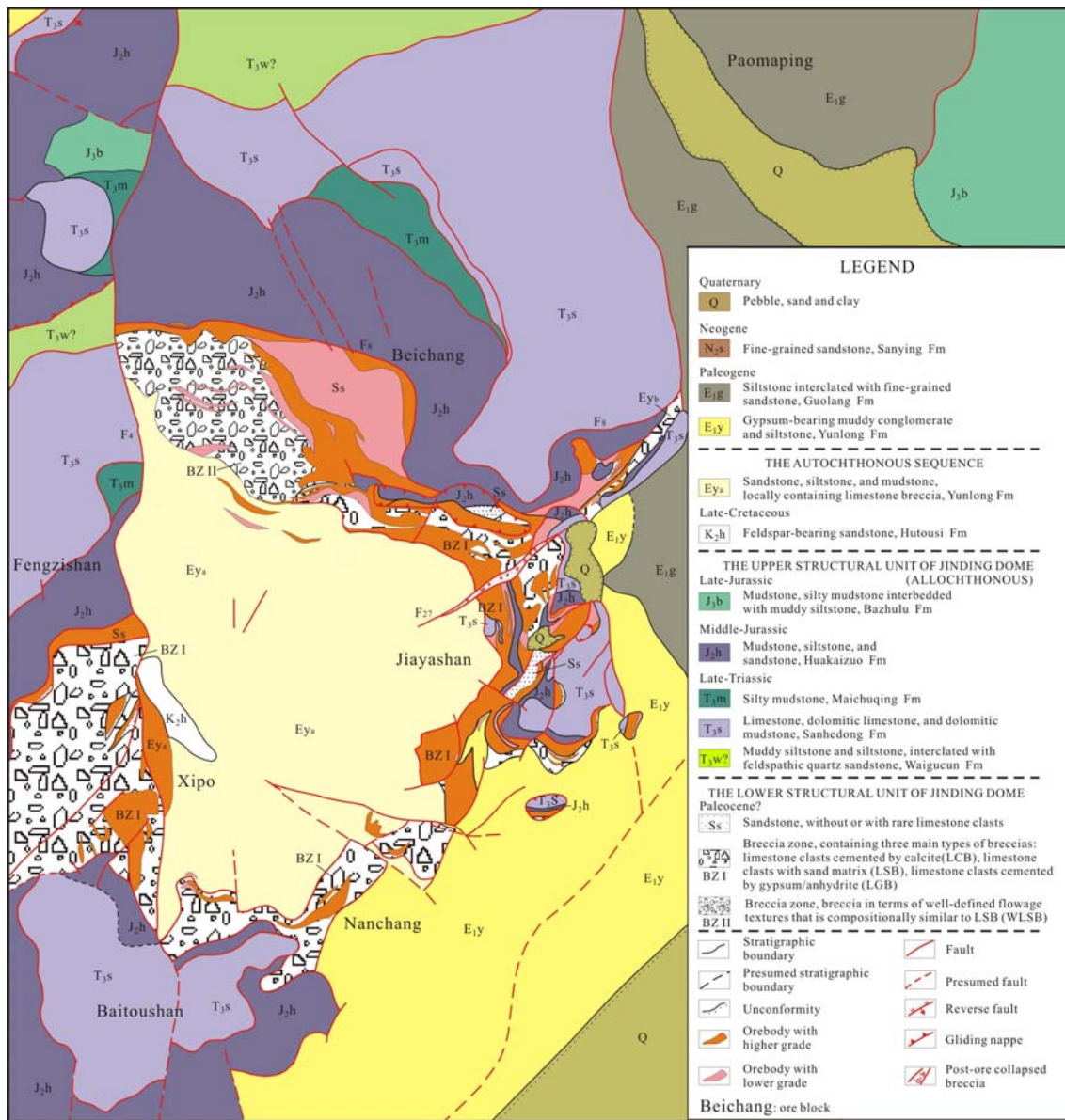


Figure 2. Geological map of the Jinding Zn-Pb deposit (modified from Third Team Geological Exploration 1984) and references therein).

3 Deposit Geology

The Jinding dome is developed on a normal autochthonous sequence dominated by Paleocene sandstone, siltstone, and mudstone (Fig. 2). It can be structurally divided into two main units. The upper unit is an allochthonous and overturned sequence that mainly consists of limestone (Late-Triassic Sanhedong Fm), dark mudstone (Late-Triassic Maichuqing Fm), and red mudstone and siltstone (Middle-Jurassic Huakaizuo Fm) (Fig. 2). The lower unit is located between the autochthonous sequence and the upper unit (separated by faults), and consists mainly of various types of breccia, sandstones and gypsum/anhydrite (Fig. 2).

Four major types of breccias are present in the lower unit that are similar to breccias in evaporite diapirs and other salt tectonic structures (e.g., Warren 2006 and references therein) that result from the migration and

intrusion of evaporites. These breccias contain clasts of host rocks supported by gypsum or anhydrite with calcite and or dolomite formed mainly from the alteration of the evaporative sulphate minerals. In addition to the mechanical transport and brecciation, dissolution of the sulphate minerals and sulphate reduction processes also contributes to development of the evaporite breccias.

The types of breccia in Jinding are described in terms of limestone clasts and the supporting matrix: limestone clasts cemented by calcite (LCB) (Figs. 3a, b, c), limestone clasts cemented by gypsum/anhydrite (LGB) (Figs. 3d, e), limestone clasts with sand matrix (highly variable sizes of clasts) (LSB) (Figs. 3f, h), sandstone matrix support breccia with well-defined flowage textures (Fig. 3g, h) and commonly with smaller limestone clasts (WLSB) that is compositionally similar to LSB (Figs. 3g). The LSB breccia can have clasts that are greater than tens of meters in diameter (Fig. 3d) that we compare to the “mega clasts” in some evaporite diapirs (Warren 2006).

In the lower unit, sandstone (Ss) (Fig. 3i), traditionally classified as or called Jinxing Formation (Lower-Cretaceous), occurs as tabular bodies below the Huakaizuo Fm. Gao et al. (2008) observed that the quartz sand grains of the sandstone (described here as Ss) appear to “intrude” into the hanging wall as “sand

veins”. Sandstone also occurs in breccia zones (BZ I in Fig. 2) as “intrusive bodies” or “sand injections” described by Chi et al. (2007). We interpret these sand injection features as a high-pressure injection of fluidized sandstones in the salt diapir environment.

In addition, massive gypsum and anhydrite bodies can

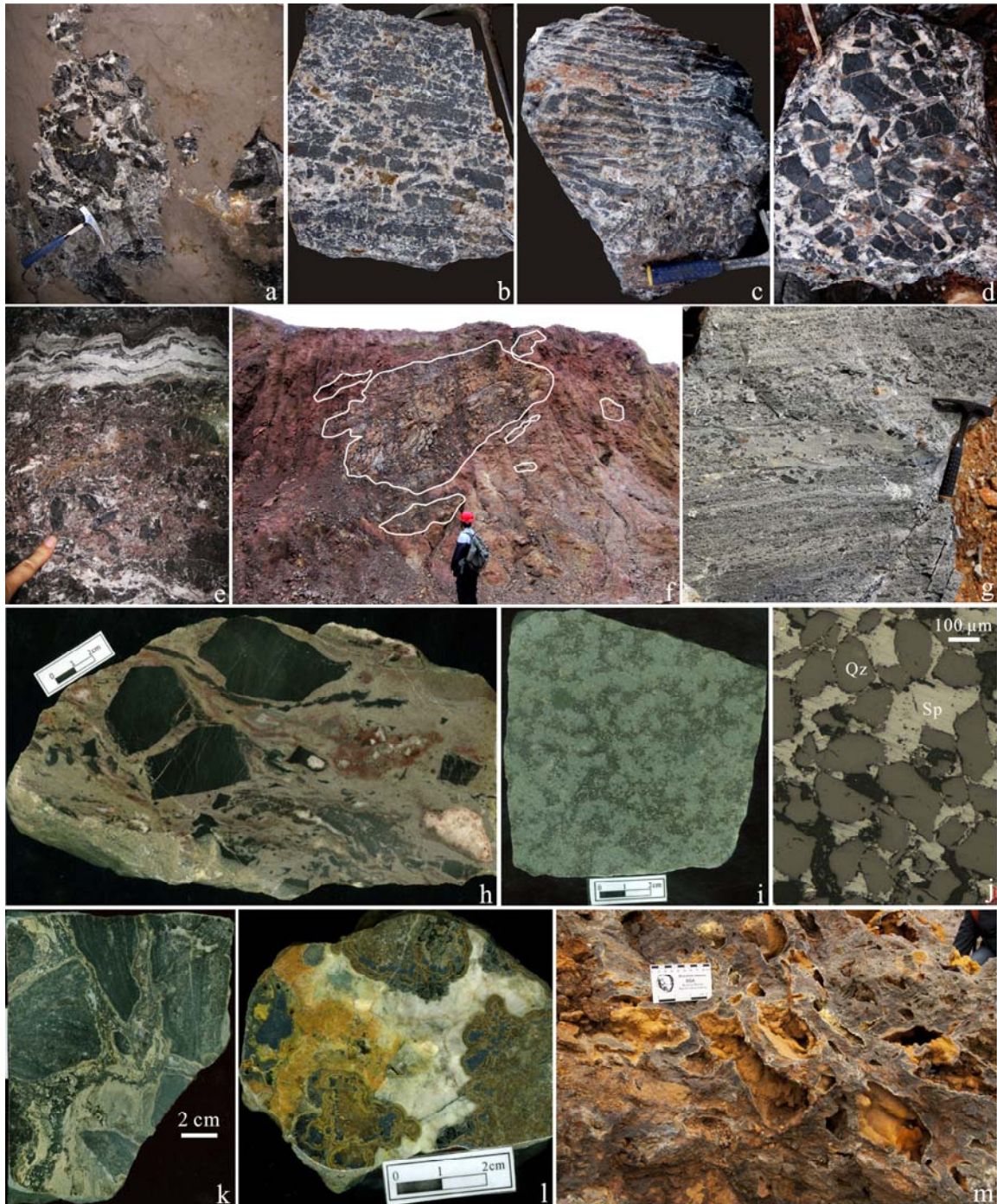


Figure 3. Photographs of rocks in the lower structural unit of the Jinding dome.

(a) breccia with angular and chaotic limestone clasts cemented by calcite (LCB); (b) breccia with a mosaic of limestone clasts cemented by calcite, a variation of zebra texture in c; (c) breccia with limestone clasts cemented by calcite, best described as zebra texture (LCB); (d) breccia with limestone clasts cemented by gypsum (LGB); (e) LGB and massive gypsum with flowage texture; (f) mega breccia with limestone clasts of highly variable size in sand matrix (LSB); (g) sandstone matrix support breccia with well-defined flowage textures (WLSB); (h) breccia with limestone clasts and matrix sand with flowage texture (LSB); (i) sandstone (Ss) with disseminated sulphides shown in j; (j) cement (sulphate or calcite?) between quartz grains replaced by sulphides with apparently abraded edges; (k) cements between limestone clasts replaced by fine-grained sphalerite with flowage texture; (l) ore as sulphides with colloform texture; (m) smithsonite -dominated oxidized LCB ores. Qz=quartz; Sp=sphalerite. These rocks and textures are interpreted in terms of halokinesis of evaporitic rock terminology: (a), (d), and (e) =evaporite tectonic breccia; (b)=evaporite breccia; (c)=zebra rock; (f) =mega breccia; (g), (h), and (k)=flowage breccia

be found in the lower unit. Most of the gypsum and anhydrite bodies, coexisting with LGB, occur in the Paomaping block (underground) and the Yunlong Fm (E₁y) in the Jiayahan block.

4 Mineralization

Primary sulphides account for about 60% of Jinding's global resource whereas the remaining is from oxidized ore derived mainly from the weathering of ores in the various types of carbonate-bearing breccia. Most of orebodies occur in the lower structural unit of the dome (Fig. 2). The most economically important sulphide orebody is tabular and hosted by sandstone and WLSB where sphalerite, galena and pyrite replaced calcite cements between detrital quartz grains (Fig. 3j). Minor sulphide orebodies are small, isolated, and irregular and are hosted by LCB where sphalerite, galena, pyrite, calcite, celestite, and minor marcasite and barite replace cements between limestone clasts (Fig. 3k). These hydrothermal minerals can also form the matrix of limestone clasts or form colloform texture in open-spaces of the breccias (Fig. 3l). The paragenetic sequence of the hydrothermal minerals is, from earlier to later stage, pyrite, marcasite, sphalerite, galena, calcite, celestite/barite, and bitumen. Oxidized ores are composed of smithsonite, cerusite, and Fe oxides and mainly occur in shallow levels of LCB (Fig. 3m).

Xue et al. (2007, 2009) provided compelling evidence from fluid inclusion studies, organic geochemistry and stable isotopes that the ore formed in a hydrocarbon reservoir or trap provided by the Jinding dome. Ore deposition resulted from the mixing of metal-rich sedimentary brines with reduced sulphur derived from bacterial reduction of sulphate trapped in the Jinding dome.

5 Salt Diapir interpretation

A salt diapir origin for the Jinding dome that hosts the Zn-Pb ore is consistent with features present in other salt diapirs and evaporite structures. The evidence includes: (1) abundance of mega breccia (Fig. 3f), characteristic of evaporite diapirs and evaporite intrusion features; Warren 2006) and matrix supported angular, transported and rotated clasts (Figs. 3a, b, c, d, e, f, g, h); (2) "flowage" textures of the clasts and matrix in the breccia bodies (Fig. 3e, g, h, k); (3) multi-lithologies of the clasts (including sulphide clasts); (4) high fluid pressures indicated by fluidized sand injection features (Fig. 3h, j) in the dome (Chi et al. 2007); (5) presences of evaporite minerals in the dome and breccia (Figs. 3d, e); and (6) evidence for ore formation in a hydrocarbon-rich dome.

The presence of salt diapirs and evaporite tectonic structures (Hudec and Jackson 2007) are common in thrust belts containing evaporite-rich sedimentary sequences. These evaporite structures provide traps for hydrocarbon resources and are known to host subeconomic Zn-Pb mineralization (e.g., the Gulf Coast of the United States and North Africa).

Some of the sandstone-hosted ore resulted from the

replacement of calcite cement. Another type of sandstone-hosted ore formed from the migration and flowage of evaporites containing entrained clasts of host rocks (Warren 2006; Hudec and Jackson 2007), sulphides and fluidized sandstone.

6 Research and Exploration Implications

The results from this study suggest that Jinding is not unique (Jinding-type) but rather is a "diapir Zn-Pb" ore deposit with ore-forming processes similar to Mississippi Valley-type (MVT) ores. Further research on Jinding can build from the knowledge acquired from previous studies of MVT ores. Although it is not unusual for Zn-Pb ores to form in salt diapir settings (e.g., Fedj el Adoum, Bou Grine deposits), Jinding is an exceptionally large deposit relative to similar deposits in the world. Therefore, there may be more large Zn-Pb deposits in diapir settings in the Lanping basin as well in other parts of the world.

Acknowledgements

This study is financially supported by the State Key Research Development Program of China (2009CB421008), the IGCP/SIDA 600 project, the Union Fund of USFC-Yunnan Province (No. U0933605), and the National Nature Science Fund (No. 41273050).

References

- Chi G, Xue C, Lai J, Qing H (2007) Sand injection and liquefaction structures in the Jinding Zn-Pb deposit, Yunnan, China: Indicators of an overpressured fluid system and implications for mineralization. *Econ Geol* 102: 739–743
- Gao L, Wang AJ, Liu JL, Xiu QY, Gao DH, Zhai YF (2005) New progress in study of superlarge Jinding Pb-Zn deposit: discovery of intrusive breccia and its geological implications. *Miner Depos* 24: 457–461 (in Chinese with English abstract)
- He L, Song Y, Chen K, Hou Z, Yu F, Yang Z, Wei J, Li Z, Liu Y (2009) Thrust-controlled, sediment-hosted, Himalayan Zn-Pb-Cu-Ag deposits in the Lanping foreland fold belt, eastern margin of Tibetan Plateau. *Ore Geol Rev* 36: 106–132
- Hudec M R, Jackson M (2007) Terra infirma: Understanding salt tectonics. *Earth-Sci Rev* 82: 1–28
- Kyle J K, Li N (2002) Jinding: a giant tertiary sandstone-hosted Zn-Pb deposit, Yunnan, China. *Soc of Econ Geol Newslett* 50: 9–16
- Third Team Geological Exploration (1984) The Jinding Pb-Zn deposit exploration report, Lanping Country, Yunnan Province. Yunnan Bureau of Geology and Mineral Resources, pp. 101–105 (in Chinese)
- Wang J H, Yin A, Harrison T M, Grove M, Zhang Y, Xie G (2001) A tectonic model for Cenozoic igneous activities in the eastern Indo-Asian collision zone. *Earth Planet Sci Lett* 188: 123–133
- Warren J K (2006) *Evaporites: sediments, resources and hydrocarbons*. Springer, Berlin, pp 455–566
- Xue C, Zeng R, Liu S, Chi G, Qing H, Chen Y, Yang J, Wang D (2007) Geologic, fluid inclusion and isotopic characteristics of the Jinding Zn-Pb deposit, western Yunnan, South China: A review. *Ore Geol Rev* 31: 337–359
- Xue C, Gao Y, Chi G, Leach D L (2009) Possible former oil-gas reservoir in the giant Jinding Pb-Zn deposit, Lanping, NW-Yunnan: the role in the ore accumulation. *J Earth Sci Environ* 31: 221–229 (in Chinese with English abstract)

Cu isotope fractionation during fluid evolution process in Qulong porphyry copper deposit, Tibet

Zhenqing Li

Institute of Mineral Resources, Chinese Academy of Geological Sciences, Beijing 100037, China

Zhiming Yang, Xiangkun Zhu, Zengqian Hou

Institute of Geology, Chinese Academy of Geological Sciences, Beijing 100037, China

Abstract. Three types of veins, A vein, B vein and D vein, were recognized in Qulong porphyry Copper deposit (Yang et al., 2008). A vein, formed during the earliest fluid stage, mainly included irregular Quartz-K feldspar vein, Quartz-Anhydrite vein and Biotite vein. B vein, come from the mid fluid stage, were mainly composed by Quartz-Anhydrite-chalcopyrite \pm molybdenite \pm pyrite vein and sericite-chlorite vein. D vein, the product of the latest fluid, were mainly plate chalcopyrite-pyrite vein and pyrite vein. Chalcopyrite was chosen for Cu isotope determine from the three types of veins. The range of $\delta^{65}\text{Cu}$ ratio of A vein is -0.47‰ to -0.1‰ , and cluster from -0.44‰ to -0.31‰ . The $\delta^{65}\text{Cu}$ of B vein is a little higher than A vein, with the range of $-.42\text{‰}$ to $+0.14\text{‰}$ and the average value of -0.18‰ , and cluster between -0.25‰ and -0.18‰ . D vein, having the highest $\delta^{65}\text{Cu}$ range (-0.27‰ to $+0.47\text{‰}$) and average value (-0.02‰), cluster -0.27‰ to -0.05‰ . Various type samples have significant Cu isotope fractionation, compare to early stage, later fluid relative enriched ^{65}Cu . The isotope fractionation among A vein, B vein and D vein maybe related to exsolution of the magma-fluid.

Keywords. Cu isotope; porphyry Copper deposit; Qulong; Tibet

1 Introduction

Qulong Copper deposit is the largest porphyry copper deposit in China. Many researches about the deposit were carried out in recent years (Hou et al., 2005, 2008; Zheng et al., 2004; Yang et al., 2006, 2008; Meng et al., 2006; Qu et al., 2006). As a whole, evolution processes of fluid and alteration zonality was clear in the deposit (Yang et al., 2008, 2009).

Following the application of ICP-MS, Cu isotope analytic technique is developed quickly in recent years. Many Cu isotope data were published about ten years (e.g. Maréchal et al., 1999, 2002; Zhu et al., 2000, 2002; Albarède et al., 2004; Luck et al., 2003; Jiang et al., 2001, 2003; Graham et al., 2004; Mathur et al., 2005, 2009; Li et al., 2009, 2010). The published data showed that there are variable Cu isotope composition ranges in various geological bodies. Which suggest that Cu isotope fractionation occurs during many geological processes including mineralization (Zhu et al., 2000, 2002; Graham et al., 2004; Ehrlich et al., 2004; Kierran et al., 2007; Li et al., 2009, 2010; Alvaro Fernandez et al., 2009; Wang et al., 2010). So, Cu isotope technique can be used to trace geological processes.

Whereas, the mechanism and fractionation of Cu

isotope are not very clear in many geological processes at present. This paper tries to investigate the Cu isotope composition and sum up the isotope fractionation of Cu during fluid evolution process in Qulong copper deposit.

2 Mmagmatism, hydrothermal alteration and fluid evolution in Qulong Cu deposit

2.1 Magmastism

Qulong porphyry Cu deposit lies on the eastern of the Gangdese porphyry Cu deposit zone. Differ to the island arc porphyry deposit, Qulong occurred in the continent collision environment. The strata belongs to Yeba formation (mid-Jurassic), were mainly composed of mid-acid volcanic rocks and volcanic clastic rock with a few sedimentary rock interlayers.

Four suits of magmatic rocks were developed in the mining area as following (Fig. 1):

Western porphyry ($182.3\pm 1.5\text{Ma}$): mainly distributed in the west of the mining area, and intruded into the Yeba formation of mid-Jurassic (Yang et al., 2008). Above 70% ore bodies were founded in granodiorite pluton ($19.5\pm 0.4\text{Ma}$), which was the host rock of ore. Eastern porphyry ($17.7\pm 0.3\text{Ma}$): distributed in the east of mining area, involved with mineralization. Diorite porphyrite ($15.7\pm 0.2\text{Ma}$): intruded after the mineralization, and had no relation with minimization.

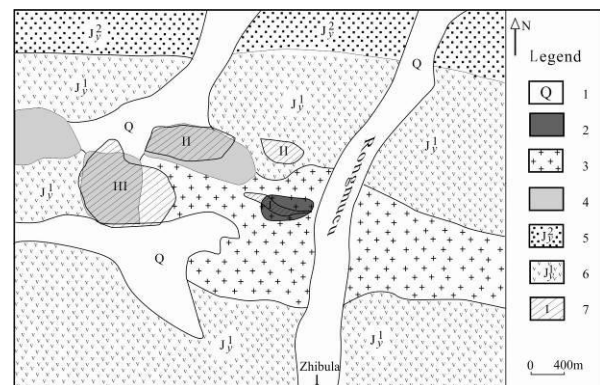


Figure. 1 Geology sketch map of Qulong copper deposit (after Yang et al.(2008), Zheng et al (2004)) 1— Quaternary; 2— Esatern porphyry; 3— Miocene granite; 4—western porphyry; 5— The 2nd section of Yeba formation; 6— The 1st of Yeba formation; 7— Ore bodies and their Number.

2.2 hydrothermal alteration

Hydrothermal alteration and vein, as product of fluid activity, were investigated to study the evolution of fluid. Three types of alteration were recognized.

- 1) Potassic alteration: is the early alteration, characterized by developing of quartz, potash feldspar, biotite, anhydrite, and carbonate minerals. Potassic alteration was divided into early potash feldspathization and later biotitization. Potash feldspathization pervades in the eastern porphyry and granodiorite. Biotitization, mainly developed in granodiorite pluton, is the main stage of copper-molybdenum mineralization.
- 2) Propylitic alteration: can be divided to 2 types according to wall rock. One is alteration of Yeba formation strata. The main mineral is epidote. The other is alteration of granodiorite, and chlorite, epidote, and carbonate minerals.
- 3) Feldspar-destructive alteration: overprint most of the potassic and part of the propylitic alteration. The alteration mineral is sericite-chlorite \pm clay minerals.

2.3 Type of vein

Three types of veins, A vein, B vein and D vein, were recognized in Qulong porphyry Cu deposit (Yang et al., 2008).

- 1) A vein: formed during the earliest fluid stage, mainly developed in porphyry rock and granodiorite nearby. A vein was consisting of irregular Quartz-K feldspar vein, Quartz-Anhydrite vein and Biotite vein. The inclusion of A vein is mainly present VL phase. The homogeneous temperatures various between 362°C and 525°C, and the salinity vary from 8.7wt%NaCl to 16.4wt%NaCl (Yang et al., 2009).
- 2) B vein, was mainly composed by Quartz-Anhydrite-chalcopyrite \pm molybdenite \pm pyrite vein and sericite-chlorite vein. The inclusion of B vein is also mainly VL phase. The homogeneous temperatures vary between 380°C and 585°C, and the salinity vary from 6.9wt%NaCl to 13.8wt%NaCl (Yang et al., 2009).
- 3) D vein, associates with feldspar-destructive alteration. The main minerals are quartz,sericite, chlorite and clay minerals, sulphide mineral is developed. The inclusion of B vein is mainly LV phase. The homogeneous temperatures various between 282°C and 395°C, and the salinity vary from 3.4wt%NaCl to 6.2wt%NaCl (Yang et al., 2009).

3 Cu isotope composition

Chalcopyrite was chosen for Cu isotope determine from the three types of veins and early potassic alteration zone. The range of $\delta^{65}\text{Cu}$ of early potassic alteration is -0.47‰ to -0.1‰, and the average value is -0.29‰. The $\delta^{65}\text{Cu}$ ratio of A vein is similar to potassic alteration in range and average value, and cluster from -0.44‰ to -0.31‰. The $\delta^{65}\text{Cu}$ of B vein is a little higher than A vein,

with the range of -0.42‰ to +0.14‰ and the average value of -0.18‰, and cluster between -0.25‰ and -0.18‰. D vein, having the highest $\delta^{65}\text{Cu}$ range (-0.27‰ to +0.47‰) and average value (-0.02‰), cluster -0.27‰ to -0.05‰ (Fig.2).

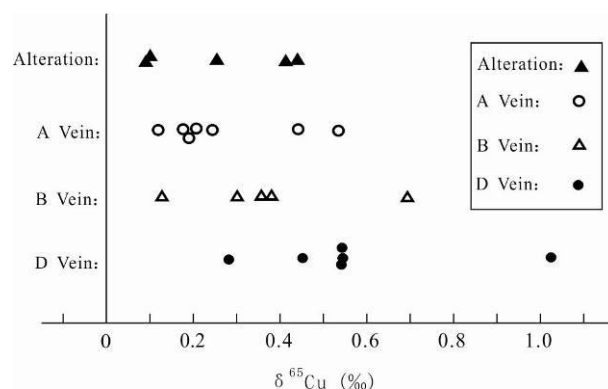


Figure 2. Variety in Cu isotope ratio of chalcopyrite from various stages in Qulong deposit region

4 Discussion and Conclusions

Cu isotope composition of different veins is significant various (Fig. 2). Chalcopyrite from A vein and potassic alteration has similar Cu isotope composition. Compare to early stage, later fluid relative enriched ^{65}Cu . In order to discuss the reason of variation of Cu isotope composition, feature of fluid and geology process may result in isotope fractionation must be considered.

In research of porphyry copper deposit, the critical homogeneous inclusion, usually is mid-salinity supercritical fluid (10wt% NaCl, Richards, 2005), can be considered to represent exsolution fluid from magma approximately (Roedder, 1984). Fluid of A vein (8.7-16.4wt% NaCl) and B vein (6.9-13.8wt%NaCl) can be considered exsolution fluid from magma. While fluid of D vein, with low temperature (282°C-395°C) and low salinity (3.4 - 6.2wt% NaCl), is mixture fluid of magma fluid and deep cycle rainwater (Yang et al., 2009).

Cu isotope composition should be homogeneous in the magma chamber. There differ between A vein fluid and B vein fluid is only the sequence of exsolution. Hence, exsolution of magma-fluid may result in the fractionation of Cu isotope.

The early exsolution occurred at high pressure (105 \pm 15 ~ 90 \pm 20 MPa) with a low density and riched gaseous phase fluid (Yang et al., 2009). According to the rule of isotope mass fractionation in an inorganic process, heavy isotope preference crystal lattice and valence bond band co-ordination (Bigeleisen and Mayer, 1947; Urey, 1947). So, light isotope (^{63}Cu) may come into gaseous phase with weak binding energy firstly. Following the 70% copper deposited at the early stage (Yang et al., 2009), a lot of ^{63}Cu escaped from magma chamber, and relict magma has poor ^{63}Cu relativity.

After the departing of early fluid with a lot of ^{63}Cu , fluid of B vein exsolved from relict magma with poor ^{63}Cu . Compare to A vein, B vein has poor ^{63}Cu and riched ^{65}Cu . Similarly, with the exsolution of fluid of B

vein, fluid of D vein has much ⁶⁵Cu.

Acknowledgements

Prof. Pan Fengchu in Xizang Geological Survey, geologists in Xizang Zhongsheng mining co. ltd are thanked for assistance with fieldwork and collecting of samples; we are grateful to Dr. Shizhen Li, Dr. Li Zhihong, Dr. Li Jin, Dr. Yan Bin, Prof Tang Suohan, Assistant Prof Wang Jinhui, Dr. He Xuexian, Dr. Qi Changshi for advice and help in the determining of Cu isotope. This study acknowledges support via IGCP/SIDA-600, Ministry of Land and Resources Public Industry Special 201011011, National Nature Science Fund 40730419 and 41040023.

References

- Albarède F (2004) The Stable Isotope Geochemistry of Copper and Zinc. *Reviews in Mineralogy & Geochemistry* 55:409-427
- Fernandez A, Borrok DM (2009) Fractionation of Cu, Fe, and Zn isotopes during the oxidative weathering of sulfide-rich rocks. *Chemical Geology*, 264:1-12
- Asael D, Matthews A, Oszczepalski S, Matthews MB, Halicz L (2009) Fluid speciation controls of low temperature copper isotope fractionation applied to the Kupferschiefer and Timna ore deposits. *Chemical Geology* 262:147-158
- Cooke DR, Hollings P, Walshe JL (2005) Giant porphyry deposits: characteristics, distribution, and tectonic controls. *Economic Geology* 100:801-818
- Borrok DM, Nimick DA, Wanty RB, Ridley WI (2008) Isotopic variations of dissolved copper and zinc in stream waters affected by historical mining. *Geochimica et Cosmochimica Acta* 72:329-344
- Ehrlich S, Butler I, Halicz L, Rickard D, Oldroyd A, Matthews A (2004) Experimental study of the copper isotope fractionation between aqueous Cu(II) and covellite, CuS. *Chemical Geology* 209:259-269
- Graham S, Pearson N, Jackson S, Griffin W, O'Reilly SY (2004) Tracing Cu and Fe from source to porphyry: in situ determination of Cu and Fe isotope ratios in sulfides from the Grasberg Cu-Au deposit. *Chemical Geology* 207:147-69
- Hou ZQ, Meng XJ, Qu XM, Gao YF (2005) Copper ore potential of adakitic intrusives in Gangdese porphyry copper belt: constrains from rock phase and deep melting process. *Mineral Deposits*, 24(2):108-121 (in Chinese)
- Hou ZQ, Yang ZM, Qu XM, Meng XJ, Li ZQ, Beaudoin G, Rui ZY, Gao YF, Zaw K (2009) The Miocene Gangdese porphyry Cu belt: Generated during post-collisional extension in the Tibetan orogen. *Ore Geology Review* 36:25-51
- Jiang SY (2003) Transition Metal Isotopes: Analytical methods and geological applications. *Earth Science Frontiers* 10(2):269-278 (in Chinese)
- Maher KC, Larson PB (2007) Variation in copper isotope ratios and controls on fractionation in hypogene skarn mineralization at corocochuayco and tintaya, Perú. *Economic Geology* 102: 225-237
- Kimball BE, Mathur R, Dohnalkova AC, Wall AJ, Runkel RL, Brantley SL (2009) Copper isotope fractionation in acid mine drainage. *Geochimica et Cosmochimica Acta* 73:1247-1263
- Larson PB, Maher K, Ramos FC, Chang ZS, Gaspar M, Meinert LD (2003) Copper isotope ratios in magmatic and hydrothermal ore forming environments. *Chemical Geology* 201:337-350
- Li WQ, Jackson SE, Pearson NJ, Alard O, Chappell BW (2009) The Cu isotopic signature of granites from the Lachlan Fold Belt, SE Australia. *Chemical Geology* 258:38-49
- Maréchal C, Albarède F (2002) Ion-exchange fractionation of copper and zinc isotopes. *Geochim et Cosmochim Acta* 66:1499-1509
- Maréchal CN, Télouk P, Albarède F (1999) Precise analysis of copper and zinc isotopic compositions by plasmasource mass spectrometry. *Chemical Geology* 156:251-273
- Meng XJ, Hou ZQ, Li ZQ (2006) Sulfur and lead isotope compositions of the Qulong porphyry copper deposit, Tibet: implications for the sources of plutons and metals in the deposit. *Acta Geologica Sinica* 80 (4):554-560 (in Chinese)
- Qu XM, Hou ZQ, Li YG (2002) Implications of S and Pb isotopic compositions of the Gangdise porphyry copper belt for the ore forming material source and material recycling with in the orogenic belt. *Geological Bulletin of China*, 21(11):768-776 (in Chinese)
- Rouxel O, Fouquet Y, Ludden JN (2004) Copper isotope systematics of the Lucky Strike, Rainbow, and Logatchev sea-floor hydrothermal fields on the Mid-Atlantic Ridge. *Economic Geology* 99:585-600
- Yang ZM, Hou ZQ, Song YC, Li ZQ, Xia DX, Pan FC (2008) Giant porphyry Cu deposit at Qulong, Tibet: geology, alteration and mineralization. *Mineral Deposit*, 27:279-318 (in Chinese)
- Yang ZM, Hou ZQ (2009). Genesis of giant porphyry Cu deposit at Qulong, Tibet: constraints from fluid inclusions and H-O isotopes. *Acta Geologica Sinica* 83(12):1838-1859(in Chinese)
- Zheng YY, Xue YX, Cheng LJ, Fan ZH, Gao SB (2004) Finding, characteristics and significances of Qulong superlarge porphyry copper (molybdenum) deposit, Tibet. *Earth Science* 29:103-108 (in Chinese)
- Zhu XK, Guo Y, Williams RJP, O'Nions RK, Matthews A, Belshaw NS, Canters GW, Waal EC, Weser U, Burgess, BK, Salvato B (2002) Mass fractionation processes of transition metal isotopes. *Earth and Planetary Science Letters* 200:47-62
- Zhu XK, O' Nions RK, Guo Y, Belshaw NS, Rickard D (2000) Determination of Cu-isotope variation by plasma source mass spectrometry: implications for use as geochemical tracers. *Chemical Geology* 163:139-149

Sediment-hosted Pb-Zn deposits controlled by facies transition in Tibetan orogenic belt: character and genesis – a case study of the Lalongla Pb-Zn deposit

YingChao Liu, ZengQian Hou
Institute of Geology, CAGS, Beijing 100037, China

ZhuSen, Yang
Institute of Mineral Resources, CAGS, Beijing 100037, China

Abstract. The Lalongla Pb-Zn deposit, located in the northeastern margin of the Tibetan orogen, is a subtype of MVT deposits controlled by thrust-nappe systems in ‘Sanjiang’ metallogenic belt, which is longer than 1000km. The Pb-Zn mineralization in the Lalongla deposit formed in the hanging wall of a thrust fault. The ore lenses are distributed along a facies transition between shale (T_3j) and limestone (T_3b), which type is first observed in the ‘Sanjiang’ metallogenic belt. Galena, sphalerite and smithsonite are the main ore minerals and breccia and mineral crust are the most common ore textures. The ore-forming hydrothermal fluids in the Lalongla deposit are from basin brines and regional fluids. The metals (and fluorine) were leached from regional strata including metamorphic basement and sediment-volcanic cap sequences. The ore-forming model of the Lalongla deposit can be summarized as follows: Regional migration was controlled by large-scale thrust activities and the metals were leached from regional strata. Reduced sulphur was produced by BSR after basin brine infiltrated into the host sequences. Metal-rich regional fluids mixed with a reservoir of basin brine rich in H_2S during regional structural extension. Ore minerals precipitated due to the mixing of the two distinct fluids.

Keywords. MVT; Sediment-hosted; Pb-Zn deposit; the Lalongla deposit; Character; Genesis; Tibetan orogen

1 Introduction

Over past decade, the metallogenesis in continent-continent collisional orogens became a research interest and researchers began to focus on the Tibetan orogen (Hou and Cook 2009 and references therein). Based on previous studies, a sediment-hosted Pb-Zn metallogenic belt longer than 1000km was defined in the northeastern margin of Tibetan collisional orogeny in a thrust-nappe belt named ‘Sanjiang’ belt (Hou et al. 2008). Most Pb-Zn deposits in this belt were classified as MVT-like deposits (Song et al. 2009; Liu et al. 2011). On the basis of ore-control factors several subtypes have been distinguished, including thrusting and salt related dome controlled (Jinding-type), uplift block controlled (Sanshan-type), thrusting related second order faults controlled (Fulongchang-type) and interlayer thrust faults controlled (Dongmozhazhua-type) (Hou et al. 2008). However, the authors found another subtype of Pb-Zn deposits with a new ore-control factor of facies

transition in the ‘Sanjiang’ Pb-Zn mineralization belt. Here, the character and genesis of this subtype deposits will be described for the Lalongla Pb-Zn deposit.

2 Geology of the Lalongla Pb-Zn deposit

The Lalongla Pb-Zn deposit is situated in the Changdu region, located at the change in direction from NE to SW of the ‘Sanjiang’ belt. Cenozoic thrust-nappe systems and strike-slip faults involved the basement strata composed of Proterozoic and Lower Ordovician metamorphic rocks and cap sequences comprised by Devonian-Carboniferous to Jurassic marine-volcanic sediments and Cretaceous to Neogene continental sediments. As a result of thrusting and strike-slip events, many pull-apart basins formed and accepted large gypsum sediments during their evolution. The Lalongla deposit lies in the middle to front belt of a thrust nappe system and along the same thrust fault with a Cenozoic basin.

The Pb-Zn mineralization of the Lalongla deposit formed in the hanging wall of a thrust fault (Fig. 1). The main ore bodies are lens shaped and are distributed along the facies transition between shale in Jiapela Formation (T_3j) and limestone in Bolila Formation (T_3b) underground and extending into the limestone (T_3b) on the surface (Fig. 2).

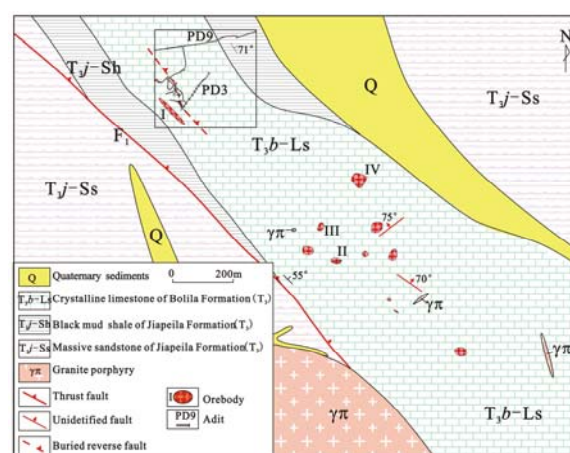


Figure 1. Geological sketch map of the Lalongla Pb-Zn deposit

Breccia and crust are main ore types (Fig. 3). Galena, sphalerite and smithsonite are main ore minerals and

calcite, pyrite, barite, fluorite and quartz are important gangue minerals. Weak calcite and fluorite mineralization of host rocks are located near the ore bodies. The ore-forming process can be divided into three periods: Period I consists of mainly coarse sulphides; Period II contains ore minerals mainly comprised by fine sulphides and Pb-Zn carbonates; and Period III consists of supergene oxides post-dating hydrothermal mineral deposition (Fig. 4).

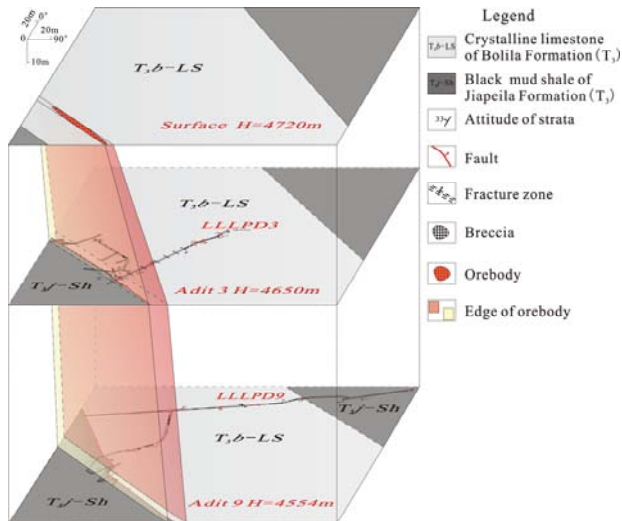


Figure 2. The stereogram of Ore-body I in the Lalongla deposit (see the rectangle in Fig. 1 for the location)

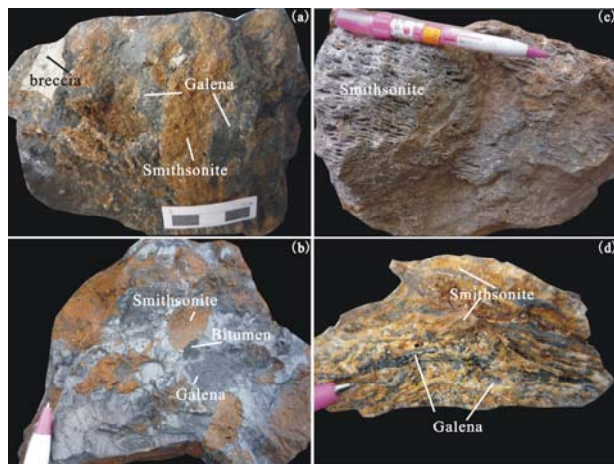


Figure 3. Typical ore types in the Lalongla deposit (a), (b)-Breccia ore; (c), (d)-crustification ore.

Mineral	Sulphide period (I)			Sulphide-carbonate period (II)			Supergene period (III)
	Sulphide-calcite-barite stage (I ₁)	Fluorite stage (I ₂)	Carbonate-quartz stage (II ₁)	Sulphate-carbonate stage (II ₂)	Pb-Zn carbonate stage (II ₃)	Calcite-barite stage (II ₄)	
Calcite	█						
Galena	█						
Pyrite	█						
Barite	█						
Fluorite		█					
Smithsonite			█	█	█	█	
Cerussite					█	█	
Quartz			█				
Sphalerite							
Siderite							
Sardinianite							
Marionite							
Natural sulphur							
Galapacite							█
Ledikite							█
Reinerite							█
Limonite							█

Figure 4. Paragenetic sequence of minerals in the Lalongla deposit

3 Fluid inclusions

Calcite and barite from Stage I₁ and fluorite from Stage I₂ in Period I (Fig. 4) were selected for fluid inclusion microthermometry. Calcite and barite from both Period I and II were selected for bulk ionic and gas composition analysis of fluid inclusions. Fluorite from Stage I₂ was selected for Raman microprobe analysis.

The results of analysis of hydrothermal fluids in Period I and II minerals indicate that ionic composition includes Ca²⁺, Mg²⁺, Na⁺, K⁺, SO₄²⁻, Cl⁻, F⁻ and NO₃⁻. In Stage I₁ of Period I, the composition of the vapour phases includes N₂, H₂O, CO₂ and O₂ and they were trapped at 190~210 bar and 700~750 m underground. The fluid inclusion microthermometry indicated low temperature (130~140 °C) and high salinity (23%~24% NaCl eq.) and a density of 1.10~1.12 g·cm⁻³, which are all similar to those of basin brines. In Stage I₂ of Period I, the geological condition changed to greater depths (950~1000m) and pressures (230~250bar) and more CO₂ and CH₄ were trapped in the fluid, which produced LV fluid inclusions with CO₂ and CH₄. The fluid inclusions have similar salinities but higher temperatures (170~180 °C) and lower densities (1.06~1.08 g·cm⁻³) than those in Stage I₁, indicating a kind of middle to lower temperature and higher salinity fluid overlapping with the basin brine in Stage I₁. The Na-K-Cl-Br contents of ionic composition show lower Cl/Br and Na/K molar ratios than those in normal seawater but similar to those in marine brines formed by seawater evaporation (Fontes and Matray 1993).

4 Isotope studies

For Period I and II, Calcite was selected for C and O isotope analysis, calcite and barite were selected for H isotope analysis of the ore-forming fluids, sulphide and barite from the Lalongla deposit and gypsum from regional Tertiary basin occurrences were selected for S isotope analysis, and galena was selected for Pb isotope analysis.

For both mineralizing periods, the C and O isotopic compositions of some calcites are similar to the regional carbonate rocks, while other calcites have descending values of δ¹⁸O_{V-SMOW} and increasing values of δ¹³C_{V-PDB}, indicating the hydrothermal carbon came from not only the dissolution of carbonate rocks in region (and ore field) (Liu and Liu 1997) but also from the region metamorphic fluid (Clark and Fritz 1997). The H and calculated O isotopic compositions (O'Neil et al. 1969; Lloyd 1968) of ore-forming fluids show characteristics of basin brines (eg. Kesler et al. 1997), evolved seawater and meteoric water with contributions of organic gases (Sheppard 1986).

The δ³⁴S values of sulphide in the deposit are negative which vary from -24.7‰ to -11.5‰, consisting with reduced sulphur reservoir produced by bacteriogenic sulphate reduction (BSR) (Machel 2001). This process is most effective at temperatures of 50~70 °C (Machel 2001), lower than the homogenization temperatures of fluid inclusions in the Lalongla deposit. Therefore, BSR likely occurred prior to the Pb-Zn

mineralization. The mixing of a fluid rich in H₂S with another fluid rich in metals (and fluorine) is the most plausible mechanism for mineral precipitation. The S isotope composition of barite in the deposit is similar to values for seawater S in late Carboniferous to late Triassic (Claypool et al. 1980), indicating that these sulphates might come from residual evaporites or connate seawater in the regional carbonate platform sequences. The values for S isotope composition of gypsum in the basin is between the S isotope composition of sulphide and sulphate in the deposit, giving additional evidence that the sulphur source for ores was S in gypsum dissolved in basin brine or connate seawater. Due to the large amount of S needed for ore deposition we suggest gypsum dissolved by the basin brine provided most of S for sulphide deposition.

The Pb isotope composition of galena in Period I and II are similar and along the evolution line of Pb isotope composition of strata in orogenic belts (Zartman and Doe 1981). Some Pb isotope values are discordant with those of regional carbonate rocks, indicating metals might come from both cap sequences comprised by sediment and volcanic rocks and basement comprised by metamorphic rocks. The later could also have provided fluorine.

5 Discussions and conclusions

According to the studies above, we propose that there were two sources of the hydrothermal fluid, including a low-temperature, high salinity basin brine and moderate temperature, high-salinity regional fluid comprised by evaporated-concentrated paleo-seawater in the strata and metamorphic water released from metamorphic rocks and meteoric water. The metals were probably derived from the sediment-volcanic cap sequences and metamorphic basement in the orogenic belt. By comparing the Lalongla deposit with other sediment-hosted Pb-Zn deposits in the 'Sanjiang' belt, we finally point out that the Lalongla deposit could be classified as MVT-like deposit controlled by facies transition in thrust-nappe belt.

The Pb-Zn mineralization in the Lalongla deposit happened at 35Ma which was got by Sm-Nd isochrone of calcite forming in the mineralizing periods. This age also accordance with the end of regional compression (Spurlin et al. 2005). Together with the Lalongla deposit, several other similar deposits are distributed in a cluster in Zhaofayong ore district nearly within the area of 800 km². Therefore, regional tectonic compression is the proposed fluid drive mechanism for the regional fluid. The detachment zone of regional thrusts and second faults formed during regional extension after compression could be the flow path for the regional fluid. The location with structure trap, facies transition and limestone would be the best place for ore precipitation. So, the mineralization model of the Lalongla deposit can be explained as follows (Fig. 5): Structural trap formed in the carbonate strata due to thrust nappe. The basin brine in Palaeogene basin descended, accumulated, and generated the local fluid reservoir rich in H₂S produced by BSR. The regional

fluid released by compressed deformation migrated along the main detachment zone of thrust nappes, leached ore-forming minerals and some halogen (e.g. fluorine) in strata and generated allochthonous fluid. Along extensional faults that formed during final movements of local thrust faults, the regional fluid ascended into the interface between limestone and shale, and mixed with a local fluid and led to deposition of Pb, Zn and F. Lenses of the ore formed along the facies transition of different rocks.

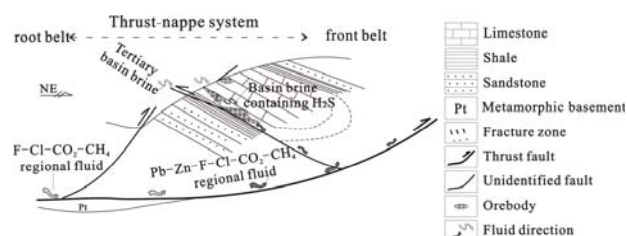


Figure 5. A model showing Pb-Zn metallogenesis of the Lalongla deposit

Acknowledgements

Funding for this research was provided through National Basic Research Program of China (2011CB403104 and 2009CB421007), the Union Fund of USFC-Yunnan Province (U0933605), the National Natural Science Foundation of China (41273035) and IGCP/SIDA-600.

References

- Clark ID, Fritz P (1997) Environmental Isotopes in Hydrogeology. Lewis Publishers, New York
- Claypool GE, Holser WT, Kaplan IR, Sakai H, Zak I (1980) The age curves of sulfur and oxygen isotopes in marine sulfate and their mutual interpretation. *Chem Geol* 28:199-260
- Fontes JC, Matray JM (1993) Geochemistry and origin of formation brines from the Paris Basin, France: 1. Brines associated with Triassic salts. *Chem Geol* 109:149-175
- Hou ZQ, Song YC, Li Z, Wang ZL, Yang ZM, Yang ZS, Liu YC, Tian SH, He LQ, Chen KX, Wang FC, Zhao CX, Xue WW, Lu HF (2008) Thrust-controlled, sediments-hosted Pb-Zn-Ag-Cu deposits in eastern and northern margins of Tibetan orogenic belt: Geological features and tectonic model. *Mineral Deposits* 27:420-441 (in Chinese with English abstract)
- Hou Z, Cook NJ (2009) Metallogenesis of the Tibetan collisional orogen: A review and introduction to the special issue. *Ore Geol Rev* 36:2-24.
- Kesler SE, Vennemann TW, Frederickson C, Breithaupt A, Vazquez R, Furman FC (1997) Hydrogen and oxygen isotope evidence for origin of MVT-forming brines, southern Appalachians. *Geochim Cosmochim Acta* 61:1513-1523
- Liu JM, Liu JJ (1997) Basin fluid genetic model of sediment-hosted microdisseminated gold deposits in the gold-triangle area between Guizhou, Guangxi and Yunnan. *Acta Mineralogica Sinica* 17:448-456 (in Chinese with English abstract)
- Liu YC, Hou ZQ, Yang ZS, Tian SH, Yang TN, Song YC, Zhang HR, Carranza EJM (2011) Formation of the Dongmozhu Pb-Zn deposit in the thrust-fold setting of the Tibetan plateau, China: Evidence from fluid inclusion and stable isotope data. *Resour Geol* 61:384-406
- Lloyd R (1968) Oxygen isotope behavior in the sulfate-water system. *J Geophys Res* 73:6099-6110
- Machel HG (2001) Bacterial and thermochemical sulfate reduction

- in diagenetic settings--old and new insights. *Sediment Geol* 140:143-175
- O'Neil JR, Clayton RN, Mayeda TK (1969) Oxygen isotope fractionation in divalent metal carbonates. *The Journal of Chemical Physics* 51:5547-5558
- Sheppard SMF (1986) Characterization and isotopic variations in natural waters. *Rev Mineral Geochem* 16:165-184
- Song YC, Hou ZQ, Li Z, Yang TN, Liu YX, Yang ZS, Tian S, Wang XH, Wang GH, Zhang HR, Liu YC, Liu CZ, Li LY, Wang GR, Wang Yk, Zhao CX, Liu Q (2009) The Chaqupacha Pb(-Zn) deposit in Tuotuo river: The production of basin brine in the continent-continent collision. *Acta Mineralogica Sinica* 29:186-187 (in Chinese)
- Spurlin MS, Yin A, Horton BK, Zhou J, Wang J (2005) Structural evolution of the Yushu-Nangqian region and its relationship to syncollisional igneous activity, east-central Tibet. *Geol Soc Am Bull* 117:1293-1317
- Zartman R, Doe B (1981) Plumbotectonics—The model. *Tectonophysics* 75:135-162

Mineralization of the Dalucao REE deposit at Himalayan Mianning–Dechang REE belt in the Eastern Indo-Asian collision zone, SW China

Yan Liu, Zengqian Hou

Institute of Geology, Chinese Academy of Geological Sciences, Beijing 100037, China

Zhusen Yang, Shihong Tian

Institute of Mineral Resources, Chinese Academy of Geological Sciences, Beijing 100037, China

Abstract. Mianning-Dechang (MD) REE belt is a giant belt located at eastern Indo-Asian collision zone, SW China. Fluid inclusions in coarse-grained fluorite, barite and calcite in Maoniuping deposit or veins bearing these minerals in Dalucao deposit have L-CO₂, melt, fluid-melt types of fluid inclusions and homogeneous temperature up to 550°C but bearing no mineralization. Ore samples have V-L fluid inclusions, which seems evolved from L-CO₂ fluid inclusions with homogeneous temperature at about 300°C. Syenite crystallization and mineralization of MD REE belt occurred at later- to post-collision of Indo-Asian. The Dalucao deposit is the only deposit in the southern segment of the MD REE belt. REE minerals in weathered ores from Dalucao deposit include bastnasite, monazite, parisite. REE minerals in Dalucao deposit contains bastnasite, parisite, cerous carbonate, britholite, spherulitic aggregation bearing REE and SiO₂, monazite. Alteration of wallrock is strong and ore vein imprinted in biotite-sericite.

Keywords.

Syenite, REE deposit, Indo-Asian collision zone, SW China, Dalucao

1 Introduction

The Dalucao REE deposit is the second largest in the MD REE belt, and contains about 0.76 Mt REO, grading 5.0% REO on average (Shi and Li, 1996). About 667 analytical samples outline the No.1 orebody with an average grade of 1.0–4.0% REO, 194 analytical samples outline the No.3 orebody with an average grade varying from 1.0% to 4.5% REO (Hou et al. 2009).

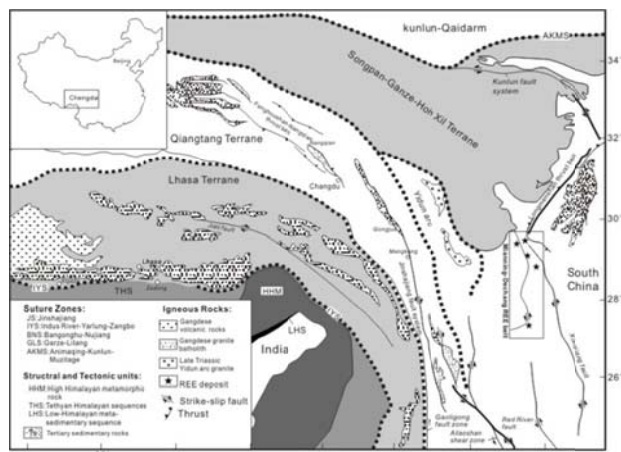


Figure 1. Simplified tectonic map of the Himalayan–Tibetan Orogen (modified after Yin and Harrison, 2000; Hou et al. 2003).

2 Geological Setting

The Himalayan MD REE belt is located on the western margin of the Yangtze craton (Fig. 1), a Cenozoic EIACZ. Available age date defines a Himalayan metallogenic epoch (40–10 Ma) for REE mineralization associated with Cenozoic carbonatite–alkaline complexes (Hou et al. 2006a). The basement of the Yangtze craton consists of Archaean high-grade metamorphic rocks, Proterozoic meta-sedimentary rocks and overlying Phanerozoic clastic and carbonate sequences (Cong, 1988; Luo et al. 1998). The Dalucao REE deposit is the second largest in the MD REE belt, and contains about 0.76 Mt REO, grading 5.0% REO on average (Shi and Li, 1996). About 667 analytical samples outline the No.1 orebody with an average grade of 1.0–4.0% REO, 194 analytical samples outline the No.3 orebody with an average grade varying from 1.0% to 4.5% REO (Hou et al. 2009).

3 Deposit Geology of Dalucao Deposit

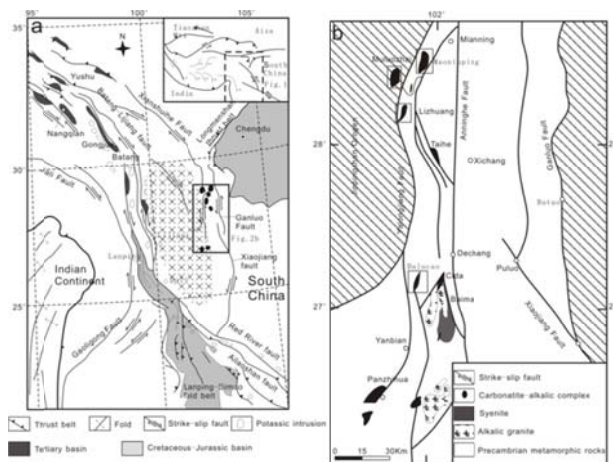


Figure 2. (a). Cenozoic tectonic map of eastern Tibet (Wang et al. 2001), showing the distribution of the Himalayan potassic rock belt (Chung et al. 1998; Zhang and Xie, 1997),

shoshonitic lamprophyre district (Guo et al. 2005), and carbonatite – alkalic complex belt (Yuan et al. 1995), which form a Cenozoic semi-discontinuous igneous province in the eastern Indo-Asian collision zone; (b). Sketch tectonic map showing distribution of the Himalayan carbonatite–alkalic complexes controlled by reactivated faults in western Sichuan (modified from Yuan et al. 1995).

The Dalucao deposit is located in the southern segment of the MD REE belt, and is controlled by the Dalucao strike-slip fault (Fig.2). Due to regional uplift, a Proterozoic quartz diorite pluton with a surface exposure area of 70 km² was exhumed. Jurassic sandstones outcrop in the eastern part of the district. The Himalayan nordmarkite and aegirine-augite syenite stocks mainly intrude the quartz diorite pluton and associated carbonatite sills intrude along structural fissures formed by strike-slip faulting (Fig.3). Two breccia pipes associated with REE mineralization were developed in the nordmarkite stock; their long-axial diameters vary from 200 to 400 m, short-axes vary between 180 and 200m, and the pipes extend downwards for 450 m. Clastic rocks in the breccia-pipes consist predominately of magmatic detritus and ore fragments hosted within a calcite-rich matrix with subordinate quartz and REE minerals. Post-ore strike-slip faulting led to displacement of the No.1 and No. 2 orebodies (Fig.3) (Hou et al. 2009).

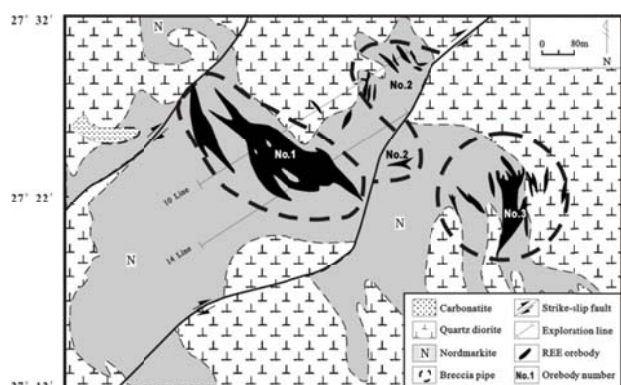


Figure 3. Sketch geological map showing the features of carbonatite-syenite complex and associated REE orebodies at Dalucao (Hou et al. 2009).

An alteration halo at Dalucao is developed mainly in the syenite stocks and associated carbonatite sills. Fenitization along fissures within quartz–diorite pluton is also observed. Fenitization is characterized by replacement of plagioclase and K-feldspar by albite, primary aegirine-augite by biotite, and by development of finegrained assemblages of aegirine-augite, albite and biotite overprinting the syenitic rocks. Within fissure zones in the quartz-diorite pluton, hydrothermal aegirine-augite occurs as dissemination and was locally replaced by biotite (Li, 2005). Minor bastnaesite occurs as dissemination associated with this fenitization in the alteration halo. Late alteration is dominated by intense carbonitization, which overprinted the early-formed fenitization halo, and is associated with REE mineralization.

The Dalucao deposit consists of two large ore lenses and numerous small orebodies (Fig.3). All assemblages occur as breccias, veinlets and as blocky and finely-

veined ores. Ore veinlets are usually transitional to mineralized breccia and brecciated ores, and are commonly enveloped by fine-veins and stringer zones with comparable mineral assemblages.

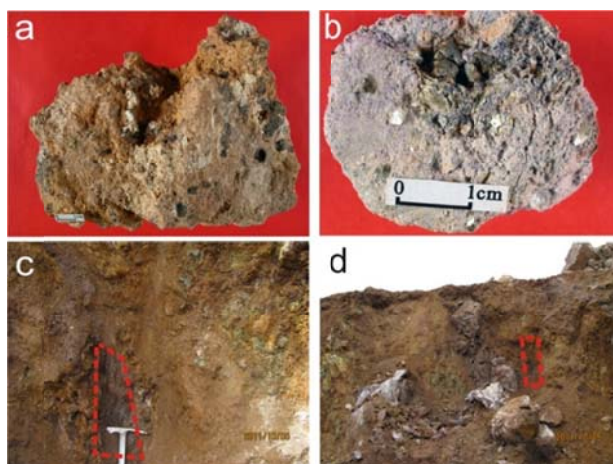


Figure 4. Typical ore samples from Dalucao REE deposits (a) Typical ore sample bearing fluorite from NO.1 deposit from Dalucao deposit; (b) Typical ore sample bearing muscovite and pyrite crystals from NO.3 deposit from Dalucao deposit; (c), (d) Typical weathered ore sample from NO.1 deposit from Dalucao deposit

Almost all orebodies at Dalucao have been outlined by drilling and chemical analysis. Orebody shape is mainly lenticular and pipe-like with minor veins. Breccia pipes in No.1 orebody are completely mineralized down to a depth of 450 m, with total thickness varying between 55 and 175 m. In the No.3 orebody, mineralization extends downward for N180 m with a total thickness of 14 to 58 m (Yang et al. 1998).

Four main ore types can be recognized. Brecciated ore is the most significant type (Fig.4a,b). The mineralized breccia is typically clast-supported, the clasts consisting largely of angular to rounded fragments of nordmarkite and carbonatite, and of calcite + fluorite + celestite assemblages. The matrix consists of an assemblage dominated by fine-grained calcite, quartz and extremely fine-grained bastnaesite (Hou et al. 2009).

Actually, in No.1 orebody, weathered ore are the main ore type, which was the main ore for exploration (Fig.4c, d). In this study, weathered ore samples were examined by X-ray powder diffraction and it is conclude that bastnasite, monazite, parasite are main REE minerals. The main ore type in the No 1 deposit is the weathering type of orebody with grades ranging from 5 to 60%.

3 Ages for Syenite and Mineralization

The Dalucao deposit is the representative of the southern part, while Maoniuping and Lizhuang are typical of deposits in the northern part. In Dalucao deposits, Sensitive High Resolution Ion Microprobe (SHRIMP) U-Pb zircon data for alkalic syenite and carbonatite samples indicate that they occurred at 14.5 and 13.0 Ma, respectively (Tian et al. 2008a). 40Ar/39Ar also suggests that No1 and No3 REE bodies developed at 13.5Ma and 12.9Ma, respectively (Tian et al. 2008b). Alkalic syenite samples from Maoniuping, Muluozhai and Lizhuang

REE deposits indicate that they occurred at 40.8 Ma, 31.2 and 27.1Ma, respectively, through methods of K-Ar, Ar-Ar (Yuan et al. 1995; Tian et al. 2006, 2008b). In this study, bastnaesite crystals were selected from Maoniuping, Lizhuang and Diaoloushan REE deposits for dating by LA-ICP-MS (Laser Ablation Inductively Coupled Plasma Mass Spectrometry) and ore formation ages were obtained of 32.5 ± 3.1 Ma, 31.8 ± 1.9 Ma and 29.6 ± 1.7 Ma, respectively. All these ages point to the fact that the entire MD belt occurred at post- and later collision setting.

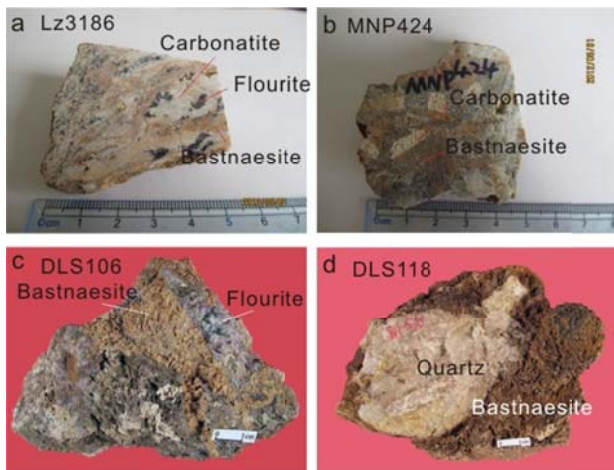


Figure 5. Photographs of bastnaesite crystals for ages examination by LA-ICP-MS.

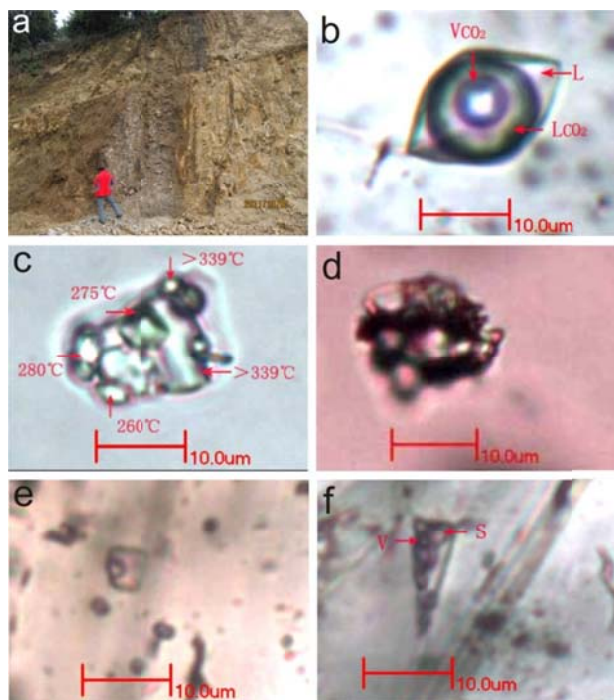


Figure 6. Photographs of fluid inclusions in coarse-grained minerals and minerals in ore samples. (a) fluorite-quartz-barite-calcite veins from Daluocao REE deposit; (b) L-CO₂ fluid inclusion from fluorite in fluorite-quartz-barite-calcite veins; (c) V-L+S fluid inclusion from fluorite in fluorite-quartz-barite-calcite veins; (d) melt inclusion from fluorite in fluorite-quartz-barite-calcite veins; (e) V-L fluid inclusion from bastnaesite from typical ore samples; (f) V-L+S fluid inclusion from bastnaesite from

typical ore samples; L-CO₂ fluid inclusion: three-phase inclusions contain liquid water plus CO₂ liquid and CO₂ vapor at room temperature (higher than 22°C); V-L fluid inclusion: two-phase liquid-vapor fluid inclusion; V-L+S fluid inclusion: three-phase liquid-vapor-solid minerals

4 Evolution of Ore-forming Fluids

Coarse-grained fluorite, quartz and barite, in addition to fluorite-quartz-barite-calcite veins, were found in the Maoniuping and Daluocao deposits (Fig.6a). However, no ore mineralization was observed around these minerals and veins. These coarse-grained minerals may, therefore, be representative of early crystallization of the fluid, as indicated by the L-CO₂ (Fig.6b), melt-fluid, V-L+S (Fig.6c) and melt (Fig.6d) fluid inclusions with high homogeneous temperatures up to 550°C found in these minerals. Fluid inclusions found in quartz, fluorite and bastnaesite in ore samples indicate that they are mainly V-L or V-L+S fluid inclusions with a small amount of L-CO₂ fluid inclusions. Transformation from melt, melt-fluid, V-L and L-CO₂ to V-L fluid inclusions indicates a process of decreasing temperature and non-mineralization to mineralization. Bastnaesite precipitation mainly occurs at temperatures below 300°C and up to 400°C in the Daluocao deposit.

5 Alternation of Wallrock

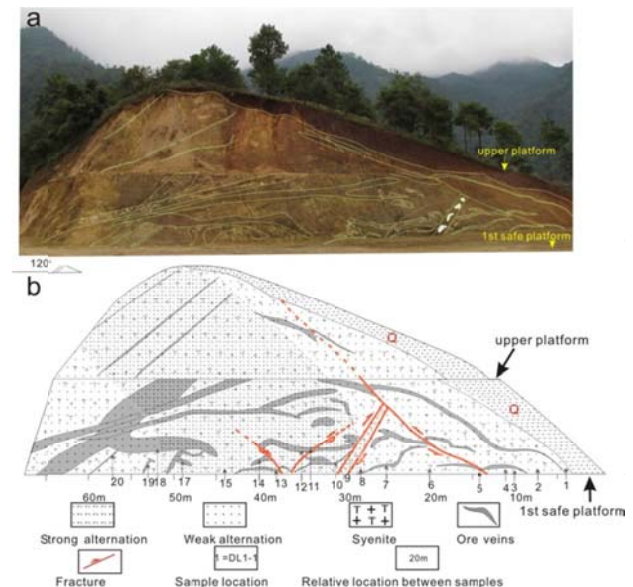


Figure 7. (a) The first safe platform cross section from examination of alternation; (b) Alternation, ore veins, syenite, fracture, samples location and relative location between samples of the cross section.

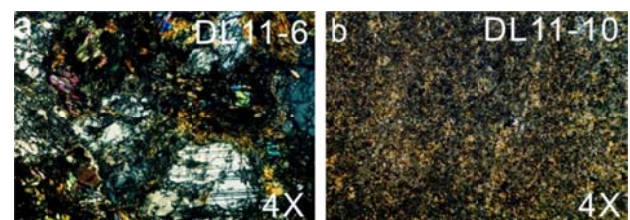


Figure 8. Photographs of syenite with weak alternation (a) and strong alternation (b).

Alteration of the wallrock in Dalucao REE deposit was less mentioned or studied and it was previously assumed that wall-rock alteration in the Dalucao deposit was weak (Yang et al. 1998). In this study, rock samples from one cross section were carefully examined. Wall-rock alteration was proved to be very strong (Fig.8) based on syenite in the deposit which turned into biotite-sericite rock-bearing ore veins. Based on the BSE images and microprobe observations, ore veins were found imposed on the biotite-sericite.

In the Dalucao deposit, only bastnasite REE mineral was reported. In this study, fine parisite, monazite, cerous carbonate and britholite crystals (less than 10 μ m) were found in ores under microscopic and backscattered electron (BSE) images (magnified 200-1000 times).

6 REE Minerals

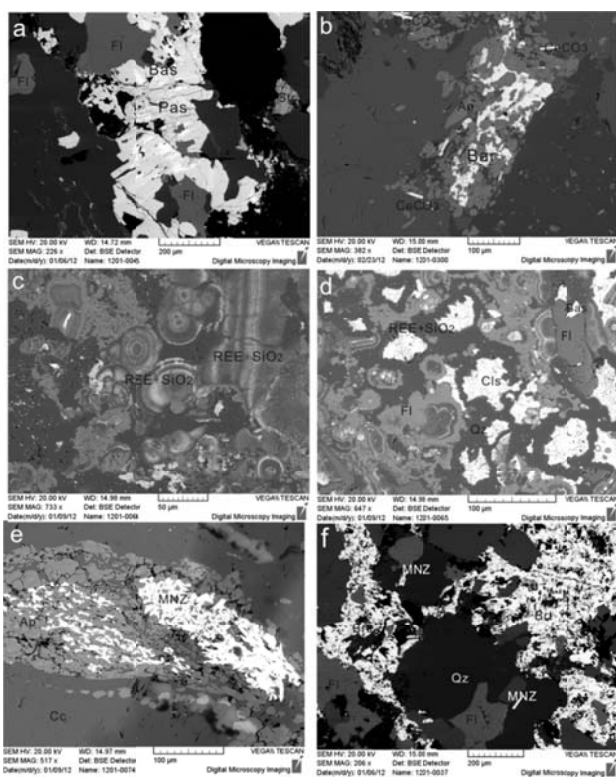


Figure 6. BSE images of REE minerals found in Dalucao REE deposit.

(a) bastnasite and parisite, staying with fluorite and barite occurring as breccia; (b) needle-like cerous carbonate staying with britholite and barite; (c) spherulitic aggregation bearing REE and SiO₂; (d) Oolitic aggregation bearing REE and SiO₂; staying with fluorite, barite and celestite occurring as breccia (e) veins bearing monazite, cerous carbonate and apatite cutting across calcite; (f) needle-like monazite and monazite aggregation staying with quartz, barite and fluorite. Qz=quartz; MNZ=monazite; Cc=calcite; Fl=fluorite; Bas=bastnasite; Pas=parisite.

7 Conclusions

According to this study, several lines of conclusions can be obtained: (1) REE minerals in weathered ores include bastnasite, monazite, parisite; (2) Fluid inclusion evolved from L-CO₂, melt, fluid-melt types to V-L fluids with transformation from non-mineralization to

mineralization; (3) Syenite and mineralization of MD REE belt occurred at later- to post-collision of Indo-Asian; (4) Alteration of wallrock is strong and ore vein imprinted in biotite-sericite; (5) REE minerals in Dalucao deposit contains bastnasite, parisite, cerous carbonate, britholite, spherulitic aggregation bearing REE and SiO₂, monazite

Acknowledgements

This study is financially supported by the State Key Research Development Program of China (2009CB421008), the IGCP/SIDA 600 project, and The Natural Science Foundation of China (Grant 41102039).

References

- Cong B L (1988) Formation and evolution of the Panxi paleo-rift. Beijing: Science Press. 1-427 (in Chinese with English abstract)
- Hou Z Q, Tian S H, Xie Y L, Yuan Z X, Yin S P, Yi L S, Fei H C, Zou T R and Bai G (2009) The Himalayan Mianning-Dechang REE belt associated with carbonatite-alkalic complex in the eastern Indo-Asian collisionzone, SW China. *Ore Geol Rev* 36: 65-89
- Hou Z Q, Tian S H, Yuan Z X, Xie Y L, Yin S P, Yi L S, Fei H C and Yang Z M (2006a) The Himalayan collision zone carbonatites in western Sichuan, SW China: Petrogenesis, mantle source and tectonic implication. *Earth Planet Sci Lett* 244: 234-250
- Li X Y (2005) Geological characteristics of Dalucao REE deposit in Dechang County, Sichuan Province. *Miner Depos* 24 (2): 151-160 (in Chinese with English abstract)
- Luo Y N and Yu R L (2001) Major features and dynamic model of the Himalayan tectonic-magmatism in the introcontinental orogenic belt in Longmenshan-Jinpingshan, Sichuan Province. In: Chen YC and Wang DH, eds. *Study on Himalayan Endogenic Mineralization*. Beijing: Seismological Press. 88-96 (in Chinese with English abstract)
- Shi Z M and Li X Y (1996) Geologic features and ore-forming conditions of alkali complex-hosted ore deposits of REE in Himalayan epoch in Panzhihua-Xichang region. *Sichuan Geol Acta*, 16 (1): 54-59 (in Chinese with English abstract)
- Tian S H, Hou Z Q, Yuan Z X, Chen W, Xie Y L, Fei H C, Yin S P, Yi L S, Zhou S (2006) ⁴⁰Ar/³⁹Ar geochronology of rocks and ores from the Muluozhai REE deposit in Mianning County, Sichuan Province. *Acta Petro Sin* 22, 2431-2436 (in Chinese with English Abstract)
- Tian S H, Hou Z Q, Yang Z S, Chen W, Yang Z M, Yuan Z X, Xie Y L, Fei H C, Yin S P, Liu Y C, Li Z and Li X Y (2008 a) Geochronology of REE deposits from the Mianning-Dechang REE belt: Constraints on the duration of hydrothermal activities and a tectonic model for the carbonatite-alkalic complexes in Sichuan, S W China. *Miner Depos* 27(2): 177-187 (in Chinese with English abstract)
- Tian S H, Hou Z Q, Yang Z S, Yang Z M, Yuan Z X, Wang Y B, Xie Y L, Liu Y C and Li Z (2008b) Zircon U-Pb ages, Hf isotopic compositions and geological significance: a case study of carbonatite and nordmarkite from the Dalucao REE deposit, Sichuan Province. *Acta Petro Sin* 24(3): 544-554
- Yang G M, Chang C, Zuo D H and Liu X L (1998) Geology and Mineralization of the Dalucao REE Deposit in Dechang County, Sichuan Province. Open file of China University of Geosciences, Wuhan, pp.1-89 (in Chinese)

The sediment-hosted Pb-Zn polymetallic deposits in Zhaxikang ore district, northern Himalayan metallogenic belt, Tibet, China

Guang-Ming LI, Yingxu-LI, Qing ZHOU, Sui-Liang DONG, Xiang-Biao XIA
Chengdu Centre of China Geological Survey, Chengdu, 610081, P.R. China

Abstract. The Zhaxikang ore district, located in the southern Tibetan detachment system (STDS) has been the site of recent intensive exploration that led to the discovery of several large Pb-Zn-polymetallic deposits, including Zhaxikang, Keyue, Suoyue and Zedang. These deposits are predominantly quartz-carbonate-sulfide vein systems in proximity to generally N-S trending faults that cut Jurassic to Cretaceous flysch strata. While sphalerite and galena are the dominant ores, important byproduct metals, including stibium, silver, indium and gallium are of potential economic significance. Preliminary estimates of reserves suggest that this emerging district may contain 3Mt combined Pb+Zn at average grade of 10% Pb+Zn. Some researchers have considered these systems to be primary or modified syndimentary to early diagenetic clastic sediment-hosted deposits based on texture and structure of some ores. However, our review of existing data and recent field investigations support a different genetic model. The ore bodies controlling fault formed later than flysch strata. We interpret these data and phenomena to indicate an epigenetic origin for base metal mineralization as a product of high heat flow, flysch melting and magma emplacement that facilitated hydrothermal circulation of basal brines in a system similar to core complex.

Keywords. Sediment-hosted Pb-Zn Deposits; Zhaxikang Ore District; Northern Himalayan Metallogenic Belt; Tibet

1 Introduction

The Northern Himalayan Metallogenic Belt (NHMB), parallel to the Gangdese Porphyry Copper Belt in Southern margin of the Lhasa Block (Hou et al, 2009), is also mainly formed by the metallogenesis of the Tibetan collisional orogen, and it has the same geographic location of Tethys Himalaya (THM) (Xu et al., 2006; Xu et al., 2011).

THM is the northern part of the Himalayan orogen (HMO) belonging to the southern Tibetan collisional orogen, and it lies to the south of the Lhasa Block with the Indus-Yarlu Suture (IYS) between them (Fig.1). The intense orogeny in southern Himalaya, which was caused by the continental collision of Indian-Asian started no later than 65Ma (Mo et al, 2003; Yin and Harrison, 2000), formed the south Himalayan thrust system, which consists of the Main Frontier Thrust (MFT), the Main Boundary Thrust (MBT), the Main Central Thrust (MCT), and the South Tibet Detachment Fault (STDF) successively from south to north (Yin, 2006). These faults separate Siwalik foreland basin of Indian Plate, Sub-Himaya, Lesser-Himalaya, Great-Himalaya and Tethys-Himalaya respectively (Wang et al., 2012; Xu et al, 2011). From Carboniferous to Paleogene, HMO was a passive continental margin before the collision began.

During the collision, HMO had been mainly controlled by N-S contraction regime. It experienced an early shorting and thrusting prior to 36-32Ma (Zhang et al., 2012). Between late 28.4-16.2Ma, the THM experienced widespread N-S extension, and the north-dipping STDS formed (Edwards and Harrison, 1997). At the same time, leucogranite, including two-mica granite and tourmaline granite (Visonà and Lombardo, 2002), sourced from partial melting of Great-Himalayan crystalline basement was emplaced. At about 23-13Ma, the N-S trending rift formed and cutted the STDS at Dingjie (Zhang et al., 2002).

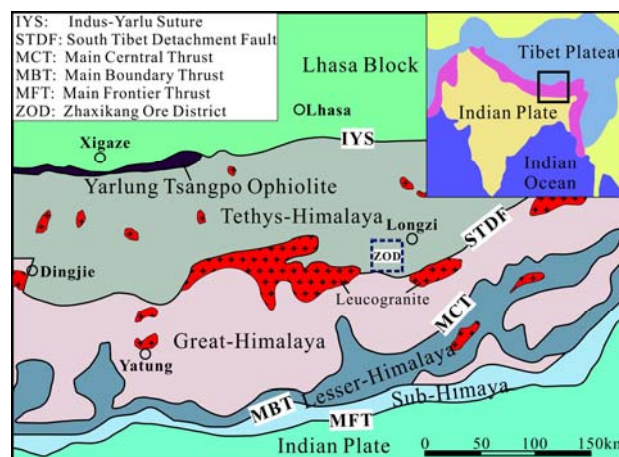


Figure 1. Tectonic Sketch Map of Zhaxikang Ore District (based on Wang et al., 2012 and Xu et al., 2011)

Up until now, the most famous and best studied metallic mineral resources in NHMB are post-collisional Sb-Au mineralization related to the STDS (Yang et al., 2009). But the newly discovered deposits also show huge lead and zinc resources potential in this belt, and one of the most important deposits is Zhaxikang, which is discussed in this abstract.

2 Geologic setting

The Zhaxikang deposit together with Keyue, Suoyue and Zedang comprises the Zhaxikang Ore District (ZOD), which is also a NNE-NS trending mineralization system share the same region of the southern Tibetan detachment system (STDS) near Longzi county, Tibet, China, and ore bodies in this system all are generally controlled by the NS trending high-angle fault zones (Fig.2). This district has recently been the focus of intensive exploration for Zn-Pb-polymetallic deposits.

In ZOD, area is mostly covered by Jurassic to Cretaceous flysch strata and magmatites. The flysch stratas in this district are mainly argillite and sandstone with a little limestone, and lie unconformity on the schist

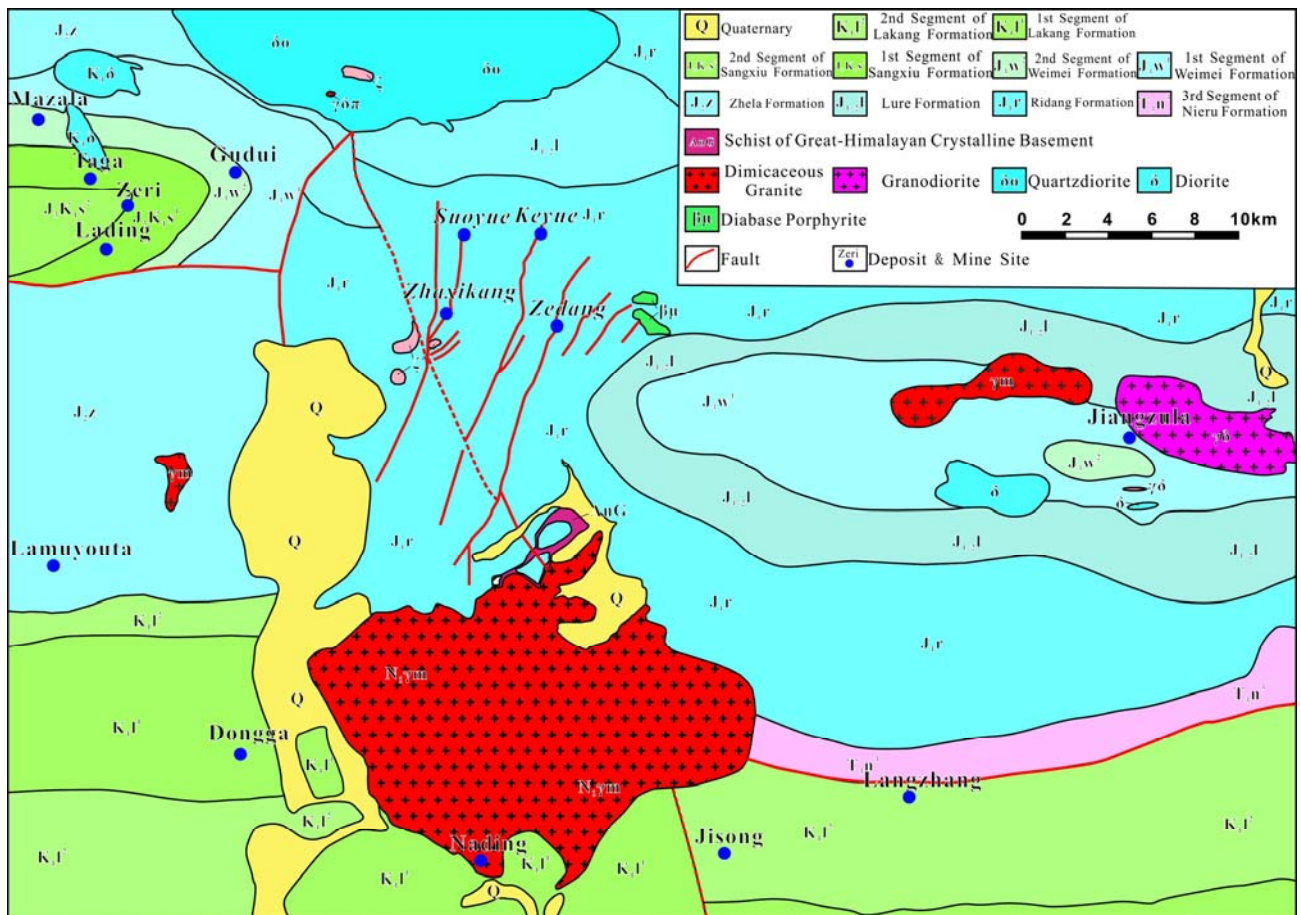


Figure 2. Geological map of Zhaxikang Ore District (modify and redraw from Xia et al., 2012)

of Great-Himalayan crystalline basement. Volcanics are only found in Jurassic Zhela Formation and Sangxiu Formation in this area.

The intense orogeny, which is controlled by N-S contraction, foliated and deformed the Jurassic to Cretaceous flysch strata, and formed several synclines, such as Jiangzhula and Zeri, and Dongga anticline.

Faults in the ZOD can be divided into two groups and both cut the Jurassic to Cretaceous flysch strata. The NWW to EW trending faults is mainly compressional, and formed early and are resultant structures of N-S contraction together with folds. They often has some extension character at their later period. The NNE to NS trending faults are caused by the E-W extension and N-S shearing. They extend from the north edge of the Cuonadong granite and cut the former group faults.

Magmatite in ZOD include basite, intermediate and acidite. Basite is mainly Jurassic, and often occurs as deformed veins. Intermediate are diorite and quartzdiorite outcropping mainly in the northern part of ZOD as apophysis. The largest area of acidite outcropping in ZOD is Cuonadong leucogranite, which consist of muscovitgranite in dominant and some luxulianite.

3 Pb-Zn-polymetallic deposits of the Zhaxikang district

Deposits and mine sites discovered in the ZOD could be grouped into two mineralization systems. The Au-Sb ones in the northwestern part, such as Mazhala and Gudui, belong to post-collisional Sb-Au mineralization

related to the STDS (Yang et al., 2009), and their ore bodies occur in the NWW to EW trending faults. The Pb-Zn-polymetallic deposits in the central part, specifically Zhaxikang, Keyue, Suoyue and Zedang, may belong to another, and their ore bodies are generally controlled by the NNE-NS trending faults. These four deposits have proven metal reserve of Pb+Zn 3Mt, Sb 0.25 Mt, Ag 3000t, and prospective reserves may get in future this district based on a preliminary estimation.

In the Zhaxikang deposit, there are five ore bodies with resource of Pb+Zn 1.5Mt, Sb 0.14Mt, Ag 2000t. The No.V orebody is now the largest of the five under presently being mined. It occurs from 4800m to at least 4400m deep at hight, and shapes an irregular vein or elongated lenticle in the fractured zone of the fault. It is greater than 1400m long, and 3.02m wide in average, with its ore grade at 2.96% Pb and 7.96% Zn in average, containing more than 70% of the reserves in Zhaxikang deposit. The boundary between the ores and wallrock is distinct. Metallic minerals in ores consist of pyrite, siderite, rhodochrosite, limonite, sphalerite, galena, arsenopyrite, jamesonite, boulangerite, stibnite, chalcopryrite, bournonite, argentite and cinnabar, and nonmetallic minerals are quartz, calcite, chlorite and clay. Furthermore, chemical analysis results also show economical indium and gallium. Vein, disseminated, stockwork and massive mineralization are the main types of ores. Near the boundary between ores and wallrocks, some breccia type ores are also found. Breccia in ores contains foliated and deformed flysch strata fragment, sphalerite and pyrite.

4 Historic geologic model

Zhaxikang was discovered at the end of 1990s as a Sb deposit belonging to the South Tibet Au-Sb metallogenic belt at first (Du et al., 1993). Until now, it has been considered to be part of the belt.

Nie et al. (2005) reported the geological settings in general, and synthesized the origin to be related to Late Yanshanian and Early Himalayan tectonism and high alkaline magmatism.

Yang et al. (2006; 2009) reported some H-O-S isotopic data of the Sb-bearing quartz veins. They found the $\delta^{18}\text{O}$ and δD value of the ore-forming fluid did not share the character of neither meteoric water nor magmatic hydrotherm. They considered the high $\delta^{34}\text{S}$ value of sphalerite (all at $\sim 10\%$) implies S may be from sedimentary rock. Hou and Cook (2006) reviewed the data, and explained the H-O isotopic might have been altered as a result of water-rock reaction.

Meng et al. (2008) reported the $\delta^{29}\text{Si}$, δD and $\delta^{18}\text{O}$ analyses of the Sb-bearing chert, and H-O isotopic data of the fluid inclusions in these chert. They concluded the ore forming fluid is mainly derived from hot-spring as H-O isotopic data plot in the area of Tibet hot-spring Zheng et al. (1982) reported, and it is different from that of other Au-Sb deposits in this belt. Furthermore, this article reported a quartz Electron Spin Resonance age (25-15Ma).

Zhang et al. (2010) reported Pb, He-Ar and more S, H, O isotopic data. The $\delta^{34}\text{S}$ value of pyrite, boulangerite, stibnite, galena and sphalerite are all greater than zero. Pb isotope ratios show a crust source. He-Ar isotope ratios in fluid inclusions suggest little mantle source as just 1 sample has a $^3\text{He}/^4\text{He}$ ratio of 1.305. So it come to the results that the ores sourced from earthcrust and Jurassic to Cretaceous flysch strata. However, Zhang et al. (2010) concluded that Zhaxikang deposit formed by replacement and filling along the SN fault zone, which belongs to a multi-stage replacement and hydrothermal vein type deposits.

Zhu et al. (2012) reported a more detailed fluid inclusions study result of this deposit, and estimated the densities of the ore forming fluid range from 0.65 to 0.86 g/cm^3 , with 2.07-12.50 wt% NaCl_{eq} salinity. In that paper, the ore formation occurred in two period and six stages: (I) Siderite-Sphalerite, (II) Quartz-Arsenopyrite stage, (III) Quartz-Galena-Sphalerite- Sulfosalt minerals stage, (IV) Quartz-Stibnite stage, (V) Quartz-Calcite stage and (VI) epigenesis oxidation. Considering the isotopic geochemistry data, Zhu et al. (2012) concluded the embryonic form that lead to the initial interpretation of the deposits as "sedex" or modified "sedex" systems.

Zheng et al. (2012) totally reviewed the published isotopic data, taking some newly discovered ore texture in small-scale and Ga/In ratio and Gd concentration in sphalerite into consideration, finally concluded that Zhaxikang is "the first super large deposit discovered in NHMB and first SEDEX modified by hot spring type Mn-Fe-Sb-Pb-Zn-Ag deposit discovered in China".

5 Magmatism-related model

Previous researchers did not pay enough attention to the

regional geological settings, and the spatial distribution of mineralization and ore texture are little mentioned in their published papers.

Our field investigations, coupled with existing data, led us to develop a different genetic model involving hydrothermal activity induced by emplacement of Miocene granites. Supporting evidence are the following:

- (1) The ores have texture similar to "SEDEX" is just some fault breccia binding or filling by quartz, calcite or sulphide. The clasts in the breccia consist of sphalerite, galena, fragment of slate and even fault breccia. The sulphide clasts have little deformation while the slate is foliated, thus orebodies formed later than the slate, and much later than the sedimentary rocks. So ores are not synsedimentary.
- (2) The ore bodies morphology is strictly controlled by NS to NNE trending faults that cut the Jurassic to Cretaceous flysch strata trending to NE, that means both the fault and ore bodies formed later than the deformation and formation of the sedimentary rocks. As the faults cut the flysch strata, ore bodies will not occur in a particular horizons or not be stratiform, thus the Zhaxikang deposit is not SEDEX type.
- (3) The published H-O isotopic data do not directly prove the ore forming fluid was derived from magma hydrotherm or sea water origin, but it could have provided thermal energy to the mineralization. Zhang et al. (2010) had mentioned the style, but it is not fully discussed in the conclusion.
- (4) In fact, Pb isotopic data Zhang et al. (2010) reported clearly show the Pb isotope composition is almost the same as the Great-Himalayan crystalline basement Zhao et al. (2007) had reported. Because leucogranite is derived from the partial melting Great-Himalayan crystalline basement, thus Pb may have been sourced from leucogranite, and mineralization may be genetically related to magmatism.
- (5) S isotopic data show high $\delta^{34}\text{S}$ values, which suggest the sulfur is from a sedimentary source. But $\delta^{34}\text{S}$ value of gas H_2S formed during magma degasification is also higher than that of magma (Zheng, 1990).
- (6) The ore forming fluid is middle-low salinity, low density and middle-low temperature, and may be the gas formed during degasification of magma, or the ore forming fluid is heated by the magma.
- (7) New field investigations show the fault controlled mineralization seems to be continuous along the fault. The mineralization has fluid inclusion temperatures higher in the south part, where is closer to the leucogranite. In the Cuonadong granite, outcrop of the potential Sn ores is indicated from geochemistry exploration, and remains undiscovered. These mineral occurrences comprise a system of ores similar to Dachang, Guangxi, which is comprised of deposits around Longxianggai intrusion (Cheng, 2011).

6 Discussion and Conclusions

Our revised model is: the active of STDF led to decompression of the Great-Himalayan crystalline basement under the sedimentary cover or deeper in the middle continental crust, which induced the partial melting and formed leucogranite magma. The magma

was emplaced in the upper crust or at shallow depths along faults, and dissolved fluid migrated along the NS trending fault. At location closed to the granite, Sn, W, Bi and other high temperature elements deposited ore bodies. At the same time, magma heated the wallrock, and the hydrothermal circulation of meteoric waters and/or basinal brines was migtarted, and metal, such as Zn, were extracted from the wallrock and carried in the fluid. As the temperature of these fluid decreased, metal sulfides were deposited in fault to make the Zhaxikang deposit is formed. In another way, Pb and possibly S were sourced directly from the magma.

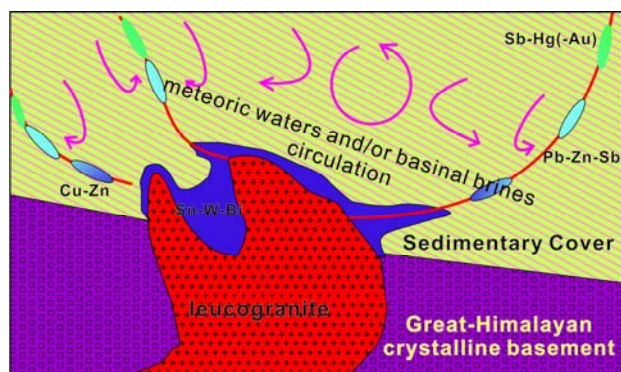


Figure 3. Preliminary mineralization model of Zhaxikang Ore District

This model explains the isotopic data and may be more consistent with the geological settings. Relating these deposits to other deposits in ZOD, will aid exploration by confirming the known ore forming temperature and paragenetic mineral, to predict ore metal. Further exploration along the NS trending fault may discover higher temperature metal elements.

Acknowledgements

This study was financially supported by the “National Basic Research Program of China” (No. 2011CB403105),

References

Cheng Y S (2011) Characteristics of granites and their relationship to mineralization, Dachang ore-field, Guangxi, China. *Procedia Earth and Planetary Science*, 2: 70-75

Du G S, Feng X L, Chen F Z (1993) *Geology of gold deposits in Tibet*. Southwest Jiaotong University Press, Chengdu, 1-177

Edwards M A, Harrison T M (1997) When did the roof collapse? Late Miocene north-south extension in the high Himalaya revealed by Th-Pb monazite dating of the Khula Kangri granite. *Geology*, 25: 543-546

Hou Z Q, Cook N J (2009) Metallogensis of the Tibetan collisional orogen: A review and introduction to the special issue. *Ore Geology Reviews*, 36: 2-24

Hou Z Q, Yang Z M, Qu X M, Meng X J, Li Z Q, Beaudoin G, Rui Z Y, Gao Y F, Zaw K (2009) The Miocene Gangdese porphyry copper belt generated during post-collisional extension in the Tibetan Orogen. *Ore Geology Reviews*, 36: 25-51

Meng X J, Yang Z S, Qi X X, Hou Z J, Li Z Q (2008) Silicon-oxygen-hydrogen isotopic compositions of Zhaxikang antimony polymetallic deposit in southern Tibet and its responses to the ore-controlling structure. *Acta Petrologica Sinica*, 24(7): 1649-1655 (in Chinese with English abstract)

Mo X X, Zhao ZD, Deng JF, Dong GC, Zhou S, Guo TY, Zhang

SQ, Wang LL (2003) Response of volcanism to the India-Asia collision. *Earth Science Frontiers*, 10(3): 135-148 (in Chinese with English abstract)

Nie F J, Hu P, Jiang S H, Li Z Q, Liu Y, Zhou Y Z (2005) Type and Temporal-Spatial Distribution of Gold and Antimony Deposits (prospects) in Southern Tibet, China. *Acta Geologica Sinica*, 79(3): 373-385 (in Chinese with English abstract)

Visonà D, Lombardo B (2002) Two-mica and tourmaline leucogranites from the Everest-Makalu region (Nepal-Tibet). Himalayan leucogranite genesis by isobaric heating? *Lithos*, 62: 125-150

Wang X X, Zhang J J, Liu J, Yan S Y, Wang J M (2012) Middle-Miocene transformation of tectonic regime in the Himalayan orogen. *Chinese Science Bulletin*, 58(1): 108-117

Xia X B, Dong S L, Zhou Q, Wu J Y, Li Y X, Lai Y, Qing C S, Yan G Q, Dong L (2012) Annual prospecting report of Zhaxikang Ore District, Shannan district, Tibet, China. Chengdu Centre of China Geological Survey and Huayu Mining Development co., LTD, Tibet, 1-139 (internal report, in Chinese)

Xu Z Q, Yang J S, Li H P, Ji S C, Zhang Z M, Liu Y (2011) On the Tectonics of the India-Asia Collision. *Acta Geologica Sinica*, 85(1): 1-33 (in Chinese with English abstract)

Xu Z Q, Yang J S, Qi X X, Cui J W, Li H B, Chen F Y (2006) India-Asia collision: A further discussion of N-S- and E-W-trending detachments and the orogenic mechanism of the modern Himalayas. *Geological Bulletin of China*, 25(1): 1-14 (in Chinese with English abstract)

Yang Z S, Hou Z Q, Meng X J, Liu Y C, Fei H C, Tian S H, Li Z Q, Gao W (2009) Post-collisional Sb and Au mineralization related to the South Tibetan detachment system, Himalayan orogen. *Ore Geology Reviews*, 36: 194-212

Yin A (2006) Cenozoic tectonic evolution of the Himalayan orogeny as constrained by along-strike variation of structural geometry, exhumation history, and foreland sedimentation. *Earth-Science Reviews*, 76: 1-131

Yin A, Harrison T M (2000) Geologic Evolution of the Himalayan-Tibetan Orogen. *Annual Review of Earth and Planetary Sciences*, 28: 211-280

Zhao Z D, Mo X X, Dong G C, Zhou S, Zhu D C, Liao Z L, Sun C G (2007) Pb isotopic geochemistry of Tibetan Plateau and its implications. *Geoscience*, 21(2): 265-274 (in Chinese with English abstract)

Zhang J F, Zheng Y Y, Zhang G Y, Gao S B, Ye X R, Zhang Z, Liu M Y, Li J Q (2010) Genesis of Zhaxikang Pb-Zn-Sb-Ag Deposit in Northern Himalaya: Constraints from Multi-Isotope Geochemistry. *Earth Science (Journal of China University of Geosciences)*, 35(6): 1000-1010 (in Chinese with English abstract)

Zhang J J, Guo L, Ding L (2002) Structural characteristics of middle and southern Xainza-Dinggye Normal Fault System and its relationship to South-ern Tibetan Detachment System. *Chinese Science Bulletin*, 47(13): 1063-1069

Zhang J J, Santosh M, Wang X X, Guo L, Yang X Y, Zhang B (2012) Tectonics of the northern Himalaya since the India-Asia collision. *Gondwana Research*, 21: 939-960

Zheng S H, Zhang Z F, Ni B L, Hou F G, Shen M Z (1982) Hydrogen and oxygen isotopic studies of thermal waters in Xizang. *Acta Scientiarum Naturalium Universitatis Pekinensis*, (1): 99 - 106 (in Chinese with English abstract)

Zheng Y F (1990) Comment on “Sulfur isotope ratios of the magnetite-series and ilmenite-series granitoids of the Sierra Nevada batholith - A reconnaissance study” by Ishihara and Sasaki. *Geology*, 18: 671-673

Zheng Y Y, Liu M Y, Sun X, Yuan E H, Tian L M, Zheng H T, Zhang G Y, Zhang L H (2012) Type, Discovery Process and Significance of Zhaxikang Antimony Polymetallic Ore Deposit, Tibet. *Earth Science (Journal of China University of Geosciences)*, 37(5): 1003-1014 (in Chinese with English abstract)

Zhu L K, Gu X X, Li G Q, Zhang Y M, Cheng W B, Bian X D (2012) Fluid Inclusions in the Zhaxikang Pb-Zn-Sb Polymetallic Deposit, South Tibet, and Its Geological Significance. *Geoscience*, 26(3): 453-463 (in Chinese with English abstract)

Genesis of fertile hydrous adakite-like melts in post-subduction porphyry Cu systems of Tibet

Yong-jun Lu, Robert R. Loucks, Marco L. Fiorentini

Centre for Exploration Targeting, Australian Research Council Centre of Excellence for Core to Crust Fluid Systems (CCFS), School of Earth and Environment, The University of Western Australia, Crawley, WA 6009, Australia

Abstract. Miocene post-subduction porphyry Cu deposits in Tibet are genetically associated with adakite-like intrusions, which have been widely attributed to partial melting of garnet-amphibolite and/or eclogite in a thickened lower crust. However, these fertile Tibetan porphyries are very hydrous with H₂O >9 wt%, which cannot be produced by dehydration melting of amphibolite and eclogite. The dehydration melting of amphibolites would likely exhaust hornblende before plagioclase and be unable to produce adakite-like melt with high Sr, Eu and Sr/Y ratios. To produce adakite-like melt by melting amphibolites, exogenous water must be added. Therefore, the current model for the post-subduction Tibetan porphyry Cu system may need revision.

Keywords. Porphyry Cu deposit, water, hornblende, adakite, Tibet

1 Introduction

Adakites originally were defined as sodic, aluminous, calc-alkalic rocks that were proposed to be derived from partial melting of hot, young (<20 Ma) subducted oceanic crust in the garnet stability field (Defant and

Drummond, 1990). However, it has now been widely recognized that adakite-like magmatism can be produced by various mechanisms other than slab melting. These adakite-like rocks are characterized by high Sr, Sr/Y and La/Yb ratios but low Y and Yb contents and no significant Eu anomaly, and are widely associated with porphyry Cu ± Mo ± Au deposits at convergent plate margins (Thiéblemont et al., 1997; Hou et al., 2004; Rohrlach and Loucks, 2005).

The Miocene post-subduction porphyry Cu deposits in Tibet are genetically associated with adakite-like intrusions, which have been widely attributed to partial melting of garnet-amphibolite and/or eclogite in a thickened lower crust (Chung et al., 2003; Hou et al., 2004; Guo et al., 2007; Xu et al., 2010; Li et al., 2011). However, there exist problems with regard to the generation of Cu-ore-forming magmas by dehydration melting of lower-crustal garnet-amphibolites and/or eclogite. In this contribution, we present evidence against dehydration melting of mafic lower crust for producing Cu-ore-forming magmas and propose alternative hypothesis to explain the genesis of fertile adakite-like melts in Tibet.

Table 1. Dacite experimental composition compared to some porphyry Cu ± Mo ± Au ore-forming intrusives

	Dacite starting composition	Oyu Tolgoi Mongolia	Yanacocha Peru	Bingham Canyon USA	Dexing E. China	Chongjiang S. Tibet	Jiama S. Tibet	Qulong S. Tibet	Nanmu S. Tibet	Tinggong S. Tibet
SiO ₂	67.51	67.85	68.38	67.96	68.73	69.89	68.69	67.86	67.81	67.54
Al ₂ O ₃	17.45	17.61	16.79	14.94	15.95	15.35	14.97	15.22	16.15	16.01
FeOT	2.20	2.14	2.30	3.27	4.33	2.40	1.34	2.77	3.20	3.78
MgO	1.19	0.62	0.58	2.13	3.08	1.41	1.30	1.37	1.38	0.79
CaO	3.52	2.32	3.87	3.45	2.14	2.15	2.03	3.23	3.10	3.37
Na ₂ O	3.90	4.52	4.35	3.80	2.36	3.84	2.33	3.89	4.45	3.35
K ₂ O	3.99	4.30	3.11	3.69	2.53	4.04	8.65	4.66	3.10	4.25
Sr		492	729	820	1318	726	282	788	1072	339
Zr		67	112	209	127	84	108	58	129	111
Sr/Y		41	146	59	132	88	51	130	154	66
Eu/Eu*		1.09	0.90	1.01	0.96	0.90	0.91	0.85	0.97	0.94
Ref.	Naney, 1983	Wainwright, 2008	Longo et al., 2010	Pulsipher, 2000	Wang et al., 2006	Xu et al., 2010	Hou et al., 2004	Yang, unpublished	Gao et al., 2007	Gao et al., 2007

Major elements are normalized to anhydrous basis.

2 Adakite-like porphyries in Tibet

Representative ore-related porphyries from the Tibetan porphyry Cu deposits are listed in Table 1 for comparison with other giant porphyry deposits in the world, such as Oyu Tolgoi in Mongolia, Yanacocha in Peru, and Bingham Canyon in USA. All of these

porphyries have high Sr (>400 ppm), Sr/Y (>20), and Eu/Eu* close to unity (Table 1). The Tibetan porphyries have nearly straight or listric-shaped heavy REE patterns, similar to Yanacocha and Oyu Tolgoi (Fig. 1).

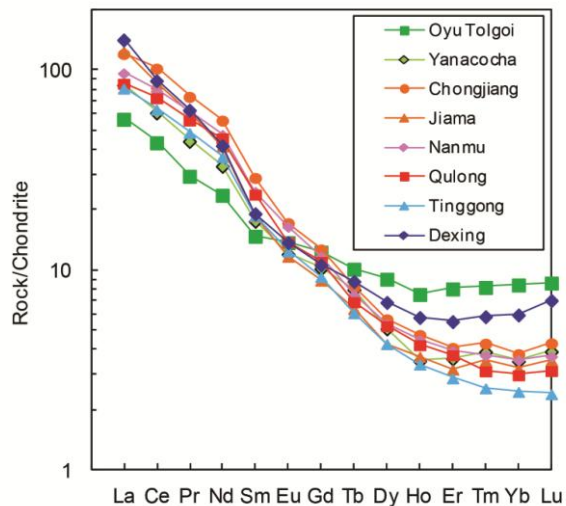


Figure 1. Chondrite normalized Rare Earth Element (REE) patterns for representative porphyry deposits listed in Table 1.

3 High water content in fertile porphyries

Water is the major factor affecting the Cu-ore-forming fertility of porphyry intrusions (Rohrlach and Loucks, 2005). To estimate the water contents in the fertile magmas at depth close to the lower crustal source, we compare these intrusions with equilibrium crystallization experiments on dacite at 8 kbar, equivalent to ca. 30 km depth (Naney, 1983; Fig. 2). These fertile porphyries have no Eu anomaly, which suggests no plagioclase segregates as cumulates or restites in the deep magma chamber before the melt was emplaced in the upper crust (Fig. 1). Therefore, these magmas apparently were at temperatures and H₂O contents above the plagioclase saturation curve on Fig. 2. The listric shaped HREE patterns of these porphyries suggest hornblende was a cumulate or restite in the deep magma chamber. Thus, these melts should plot below the hornblende saturation curve on Fig. 2. The fertile porphyries thus plot in the wedge enclosed by the vapour, hornblende and plagioclase saturation curves (Fig. 2).

The Zr contents of zircon-saturated melts can be used to estimate the temperature of the melt as Zr is mainly sensitive to the temperature and is insensitive to variations of pressure or dissolved H₂O content (Watson and Harrison, 1983). The Zr contents of fertile porphyries are mainly in the range 60-130 ppm (Table 1), which indicates a temperature range of ca. 750-850 °C for the fertile porphyries (Fig. 2). Therefore, the fertile porphyries should fall in the dashed triangle field on Fig. 2, which corresponds to dissolved water contents of 9-12 wt% at ca. 30 km depth.

A fully hydrated amphibolite has about 1 wt% H₂O bound as hydroxyl in amphibole. Dehydration melting of basaltic amphibolites or eclogite to a sufficiently advanced degree to produce dacitic-andesitic composition melts (69% SiO₂ or less) does not produce melts having enough dissolved H₂O to match the high H₂O contents (> 9 wt%) of the Tibetan porphyry Cu ore-forming magmas (Sen and Dunn, 1994; Wolf and Wyllie, 1995; Skjerlie and Patino Douce, 2002; Sisson

et al., 2005).

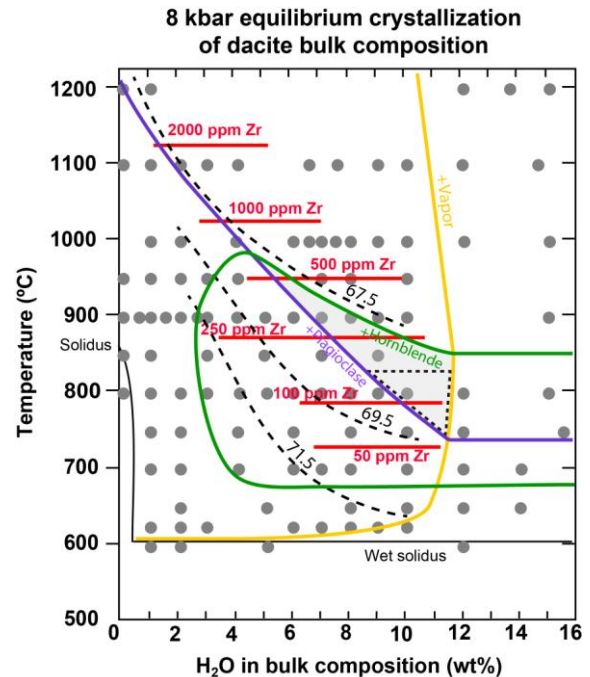


Figure 2. Zr contents of zircon-saturated melt are contoured (red) on a map of stable phase assemblages determined by melting/crystallization experiments on a dacitic composition at 8 kbar and varied wt% H₂O added to the starting composition. Each grey dot represents an experiment in which the stable phase assemblage was identified in run products by Naney (1983). Only the plagioclase (blue), hornblende (green) and vapour (orange) saturation curves are shown. Dashed black contours labelled with wt% SiO₂ in the initial melt (67.5%) or residual melt (69.5% and 71.5%, recalculated to an anhydrous basis) are based on electron-microprobe analyses of quenched melt (glass) in Naney (1983). At any given SiO₂ content, andesitic to dacitic melts that are more H₂O-rich are cooler and have lower Zr contents than less hydrous counterparts, because zircon solubility is mainly temperature-sensitive (Watson and Harrison, 1983). The light grey wedge enclosed by the hornblende, plagioclase and vapour saturation curves highlights the field in which hornblende crystallized earlier than plagioclase. The dashed triangle within the wedge is the approximate field of the ore-forming melts, estimated by the SiO₂ and Zr contents of the dacitic porphyries listed in Table 1. The H₂O contents in these ore-forming magmas are thus estimated to be at 9-12 wt% at 8 kbar, corresponding to ca. 30 km depth.

4 High Sr/Y in fertile porphyries

Figure 3 presents the stable phase assemblages and dehydration-melting relations of tholeiitic basalt corresponding to “average Archean tholeiite” as given by Condie and Hunter (1976). The dehydration melting of garnet-amphibolites (no fluid added) show that during heating from the solidus up to about 1100°C at 8-16 kbar, hornblende is exhausted at around 975°C before plagioclase at around 1040°C (Fig. 3). Sodic plagioclase persists to more than 1100 °C at 20 kbar (Fig. 3). The sodic plagioclase is very retentive of Sr and Eu, so the Sr and Eu abundances and REE patterns of these melts in equilibrium with restitic plagioclase cannot match the trace-element characteristics of Cu-ore-forming magmas in Tibet. Indeed, dehydration melting of amphibolite

with 1.5 wt% H₂O at 1.5 and 2 GPa, 850-1150 °C did not produce adakite-like melt having high Sr/Y ratios (Sen and Dunn, 1994). In addition, Wolf and Wyllie's (1994, 1995) dehydration melt of a basaltic amphibolite (67% hornblende, 33% plagioclase) at 850°C and 10 kbar produced a dacitic melt (65 wt% SiO₂) with ~5 wt% H₂O by 12% partial melting, with restite plagioclase (20%), hornblende (31%), garnet (4%), and minor augite and orthopyroxene. Hornblende was exhausted by 975°C and 40% melting, but plagioclase restite remained above 1000°C. A plagioclase-rich restite or cumulate at ~850°C cannot account for the high Sr and lack of Eu anomaly in the dacitic ore-forming magmas.

Production of adakite-like melts by melting amphibolite requires fluid addition substantially in

excess of the amount bound as hydroxyl in amphibolites. Several experimental studies that were aimed at reproducing the characteristics of Archean TTGs (which strongly resemble adakites) showed that at least 5 wt% H₂O must be added to a garnet-amphibolite of tholeiitic composition in order to produce a tonalitic melt at around 900 to 950 °C and 10-15 kbar in equilibrium with restitic hornblende, garnet and augite, and to selectively melt all or nearly all the plagioclase (Winther and Newton, 1991; Winther, 1996). Such melts match the major-element compositions of average Archean tonalite (andesite) and trondhjemitic (dacites) and should match their trace-element characteristics as well. However, it is critical to determine the trace elements of these hydrous experimental melt to prove this hypothesis.

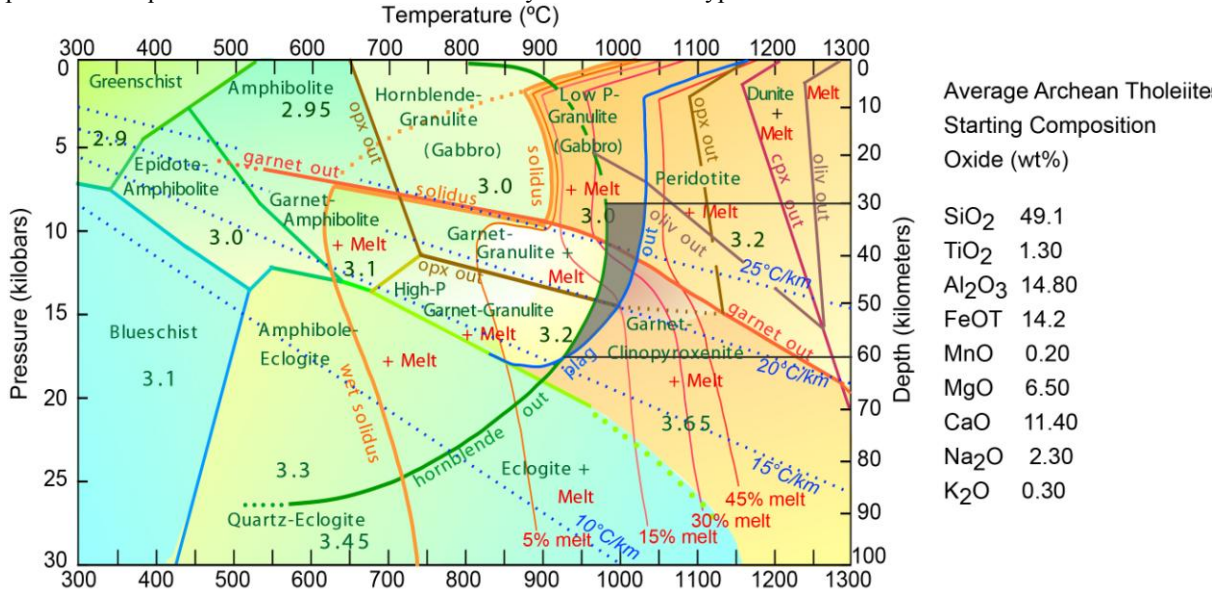


Figure 3. Stable phase assemblages and dehydration-melting relations of average Archean tholeiite with a bulk composition that is hydrated to a pyroxene-free, amphibole+plagioclase assemblage without excess (free) water at P-T conditions of the low-pressure amphibolite facies. Upon compression, garnet-forming, hornblende-consuming reactions release water that occurs as intergranular aqueous fluid at subsolidus conditions or dissolved in hydrous melt at super-solidus conditions, causing the solidus to shift abruptly down-temperature from fluid-undersaturated to wet across the garnet-stability boundary. Phase fields are based on experimental data compiled from Rushmer et al. (1991), Wolf and Wyllie (1994, 1995), Rapp (1995a, b), Rapp and Watson (1995), Springer and Seck (1997) and references therein. If more water were added incrementally to the bulk composition, the amphibolite fields would expand to higher temperatures, partially to completely consuming the granulite fields by converting plagioclase + pyroxene to hornblende, and the % melt contours (red) would shift down-temperature toward the wet solidus. The number (3.1, 2.95 etc) in each phase field represents the typical bulk-rock density in g/cc. The grey wedge highlights the field in which hornblende is consumed earlier than plagioclase at the depth of 30-60 km.

5 Discussion and conclusions

Dehydration melting of amphibolites and/or eclogites cannot produce melts having enough water to match ore-forming hydrous magmas in Tibetan porphyry systems with H₂O ≥ 9 wt%. Such dehydration melting of amphibolites would consume hornblende before plagioclase, thus be unable to produce adakite-like melt with high Sr, Eu and Sr/Y ratios.

To produce adakite-like melt by melting amphibolites or eclogites, significant additional water must be added. High H₂O content in the starting material and in the resultant partial melt stabilizes hornblende to higher temperature and depresses the upper temperature limit of plagioclase because the H₂O selectively hydroxylates Si and Na in the melt, which lowers their

thermodynamic activities in the melt and causes more plagioclase to melt until there is none left, while hornblende and garnet survive in the restite. However, the trace element composition of such hydrous experimental melts is still unquantified and needs to be systematically determined to constrain the crystal/melt partition coefficients of various minerals within very hydrous melts.

The next question is to understand how to flux the mafic lower crust in the absence of active subduction. The additional water may derive from the flow of metamorphic fluid from greater depth where prograde metamorphism caused dehydration reactions; alternatively, the underplating mafic magma from lithospheric mantle may provide additional fluid, such as hydrous lamprophyres or ultrapotassic-potassic mafic melts.

Given the similarity between Tibetan post-subduction

porphyry system and those in arc setting, the adakite-like fertile porphyries in Tibet may not due to melting of lower crust, but are instead associated with long-term (several tens of millions years) fractionation and replenishment in the lower crustal hot zone during a compressive regime, a scenario for arc porphyry deposits (Rohrlach and Loucks, 2005). Further work is needed to distinguish between these two end-member models of melting lower crust and long-term fractionation and replenishment of hydrous mafic melt.

Acknowledgements

This study is funded by foundation projects “Metal sources and transport mechanisms in the deep lithosphere” and “4D lithospheric evolution and controls on mineral systems” in the ARC Centre of Excellence for Core to Crust Fluid Systems (CCFS) and by the IGCP/SIDA 600 project. This abstract benefit from the constructive review of Dr. Zhiming Yang, which is greatly acknowledged.

References

- Chung SL, Liu DY, Ji JQ, Chu MF, Lee HY, Wen DR, Lo CH, Lee TY, Qian Q, Zhang Q (2003) Adakites from continental collision zones: Melting of thickened lower crust beneath southern Tibet. *Geology* 31: 1021-1024.
- Condie KC, Hunter DR (1976) Trace element geochemistry of Archean granitic rocks from the Barberton Regon, South Africa: *Earth and Planetary Science Letters*, 29: 389-400.
- Gao YF, Hou ZQ, Kamber BS, Wei RH, Meng XJ, Zhao RS (2007) Adakite-like porphyries from the southern Tibetan continental collision zones: evidence for slab melt metasomatism. *Contrib Mineral Petrol* 153: 105-120.
- Guo ZF, Wilson M, Liu JQ (2007) Post-collisional adakites in south Tibet: Products of partial melting of subduction-modified lower crust. *Lithos* 96: 205-224
- Hou ZQ, Gao YF, Qu XM, Rui ZY, Mo XX (2004) Origin of adakitic intrusives generated during mid-Miocene east-west extension in southern Tibet. *Earth and Planetary Science Letters* 220: 139-155
- Li JX, Qin KZ, Li GM, Xiao B, Chen L, Zhao JX (2011) Post-collisional ore-bearing adakitic porphyries from Gangdese porphyry copper belt, southern Tibet: Melting of thickened juvenile arc lower crust. *Lithos* 126: 265-277
- Longo AA, Dilles JH, Grunder AL, Duncan R (2010) Evolution of Calc-alkaline volcanism and associated hydrothermal gold deposits at Yanacocha, Peru. *Economic Geology* 105: 1191-1241
- Naney MT (1983) Phase equilibria of rock-forming ferromagnesian silicates in granitic systems. *American Journal of Science* 283: 993-1033
- Pulsipher T (2000) The correlation of Eocene extrusive block and ash flows to intrusions at the Bingham copper porphyry system, Utah. MSc Thesis, Brigham Young University, Provo, Utah
- Rapp RP (1995a) Amphibole-out phase boundary in partially melted metabasalt, its control over liquid fraction and composition, and source permeability. *Journal of Geophysical Research* 100: 15601-15610
- Rapp R (1995b) Recycling of hydrated basalt of the oceanic crust and growth of the early continents. *American Institute of Physics conference proceedings* 341: 261-269. “volatiles in the Earth and Solar system” K.A. Farley (Ed.) New York.
- Rapp RP, Watson EB (1995) Dehydration melting of metabasalt at 8-32 kbar: implications for continental growth and crust-mantle recycling. *Journal of Petrology* 36: 891-931
- Rohrlach, B.D., and Loucks, R.R., 2005, Multi-million-year cyclic ramp-up of volatiles in a lower crustal magma reservoir trapped below the Tampakan copper-gold deposit by Mio-Pliocene crustal compression in the southern Philippines: In Porter, T.M. (ed.), *Super Porphyry Copper & Gold Deposits-A Global Perspective*, PCG Publishing, Adelaide, v. 2, p. 369-407.
- Rushmer T (1991) Partial melting of two amphibolites: contrasting experimental results under fluid-absent conditions. *Contrib Mineral Petrol* 107: 41-59
- Sen C, Dunn T (1994) Dehydration melting of a basaltic composition amphibolites at 1.5 and 2.0 GPa: implications for the origin of adakites. *Contrib Mineral Petrol* 117: 394-409
- Sisson TW, Ratajeski K, Hankins WB, Glazner AF (2005) Voluminous granitic magmas from common basaltic sources. *Contrib Mineral Petrol* 148: 635-661
- Skjerlie KP, Patino Douce AE (2002) The fluid-absent partial melting of a zoisite-bearing quartz eclogite from 1.0 to 3.2 GPa: implications for melting in thickened continental crust and for subduction-zone processes. *Journal of Petrology* 43: 291-314
- Springer W, Seck HA (1997) Partial fusion of basic granulites at 5 to 15 kbar: implications for the origin of TTG magmas. *Contrib Mineral Petrol* 127: 30-45.
- Thieblemont D, Stein G, Lescuyer JL (1997) Epithermal and porphyry deposits: the adakite connection. *Comptes Rendus Acad. Sci. Paris, Se'rie 2, Sci. Terre Plan.* 325, 103-109.
- Wainwright A (2008) Volcanostratigraphic framework and magmatic evolution of the Oyu Tolgoi porphyry Cu-Au district, South Mongolia: Unpublished Ph.D. thesis, The University of British Columbia, 277 p
- Wang Q, Xu JF, Jian P, Bao ZW, Zhao ZH, Li CF, Xiong XL, Ma JL (2006) Petrogenesis of adakitic porphyries in an extensional tectonic setting, Dexing, South China: Implications for the genesis of porphyry copper mineralization. *Journal of Petrology* 47: 119-144
- Watson EB, Harrison TM (1983) Zircon saturation revisited: temperature and composition effects in a variety of crustal magma types. *Earth and Planetary Science Letters* 64: 295-304.
- Winther KT (1996) An experimentally based model for the origin of tonalitic and trondhjemitic melts. *Chemical Geology* 127: 43-59.
- Winther KT, Newton RC (1991) Experimental melting of hydrous low-K tholeiite: evidence on the origin of Archean cratons. *Bull. Geol. Soc. Den.*, 39: 213-228
- Wolf MB, Wyllie PJ (1994) Dehydration melting of amphibolite at 10 kbar: the effects of temperature and time. *Contrib Mineral Petrol* 115: 369-383
- Wolf MB, Wyllie PJ (1995) Liquid segregation parameters from amphibolite dehydration melting experiments. *Journal of Geophysical Research* 100: 15611-15621
- Xu WC, Zhang HF, Guo L, Yuan HL (2010) Miocene high Sr/Y magmatism, south Tibet: product of partial melting of subducted Indian continental crust and its tectonic implication. *Lithos* 114: 293-306.

Jurassic to Tertiary metallogenic evolution of the southernmost Lesser Caucasus, Tethys belt

Robert Moritz, Johannes Mederer, Maria Ovtcharova, Richard Spikings
Earth and Environmental Sciences, University of Geneva, Switzerland

Dave Selby
Department of Earth Sciences, University of Durham, United Kingdom

Rafael Melkonyan, Samvel Hovakimyan, Rodrig Tayan
Institute of Geological Sciences of the National Academy of Sciences of Armenia, Yerevan, Armenia

Alexey Ulianov
Institute of Mineralogy and Geochemistry, University of Lausanne, Switzerland

Vagif Ramazanov
Department of Mineral Resources, Baku State University, Baku, Azerbaijan

Abstract. Magmatic rocks and ore deposits of the southern part of the Lesser Caucasus were investigated by U-Pb dating of zircons, Re-Os dating of sulphides and $^{40}\text{Ar}/^{39}\text{Ar}$ dating of hydrothermal muscovite and alunite. The new isotope age data reveal an east to west progression of magmatic and mineralizing events, which can be correlated with different stages of the geodynamic evolution of the Tethys orogenic belt. Magmatic and intrusion-related ore deposit ages between 166 and 131 Ma in the Kapan block correspond to main island arc formation during Tethys subduction along Eurasia. Magmatism and porphyry-Cu-Mo deposits at 45-40 Ma in the Meghri pluton, followed Upper Cretaceous accretion of Gondwana-derived terranes with Eurasia, and are correlated with subduction of the western branch of the Neotethys as the Arabian plate was converging with Eurasia. Interruption of magmatism and ore-formation in the Meghri pluton at 40-30 Ma coincides with final closure of the Neotethys and Arabia-Eurasia collision. Renewed magmatism and ore formation between 31 and 22 Ma are post-collisional events. The world-class Kadjaran porphyry-Cu-Mo deposit was formed during this event.

Keywords: Lesser Caucasus, Tethys geochronology, intrusion-related, porphyry-Cu-Mo, epithermal

1 Introduction

The Lesser Caucasus extending from the Black Sea to the Caspian Sea is a key area to understand the metallogenic and geodynamic link between the western and eastern domains of the Tethys belt. In particular, the southern part of the Lesser Caucasus records a long lasting geologic and metallogenic evolution, from the Jurassic to the Cenozoic, well documented by magmatic rocks and ore deposits of the Kapan block and the Zangezur - Ordubad zone. We present LA-ICP-MS and TIMS U-Pb zircon ages of magmatic rocks, and Re-Os and $^{40}\text{Ar}/^{39}\text{Ar}$ ages of ore deposits, which allow us to constrain ore-formation and magmatism during progressive evolution from a subduction to a post-collisional setting, as Arabia and Gondwana-derived terranes converged with Eurasia (Sosson et al. 2010).

2 Regional Geological Setting

The southern Lesser Caucasus consists of two distinct tectono-magmatic zones, namely the eastern Kapan block and the western Zangezur-Ordubad zone. The Kapan block consists mainly of Middle Jurassic to Lower Cretaceous volcanic and volcano-sedimentary rocks with a dominantly andesitic composition, and subsidiary Mesozoic and Paleogene intrusions. Quaternary basalts unconformably cover older magmatic complexes (Shirinyan and Nahapetyan 1974). The magmatic rocks of the Kapan block have a calc-alkaline composition and were emplaced during subduction processes (Achikgiozyan et al. 1987; Mederer 2013). The Kapan block is generally considered as the southern extension of the Somkheto-Karabagh island arc, and both are regarded as parts of a discontinuous island-arc, segmented by roughly eastwest trending strike slip faults (Gabrielyan et al. 1989; Hässig et al. 2013).

The Zangezur-Ordubad zone is a component of the South Armenian block (Sosson et al. 2010; Hässig et al. 2013). It is an uplifted tectonic block (Tayan et al. 1976), consisting of the Tertiary Meghri pluton and Eocene volcano-sedimentary successions, respectively, intruding and overlying Devonian to Paleocene sedimentary and volcanic rocks (Belov 1968). The composite Meghri pluton was formed by successive pulses of intrusive rocks, with Eocene olivine gabbro, gabbro-monzonite, syenite and syenogranite, followed by Oligocene to Miocene monzonite, quartz-diorite, monzodiorite, syenogranite, granodiorite, and porphyritic granite (Tayan et al. 1976).

The contact between both tectonic zones is the location of the Ankhavan-Zangezur fault zone, locally named Khustup-Giratakh fault. It consists of a tectonic mélange, with ultramafic rocks, gabbro, andesite and radiolarite (Knipper and Khain 1980), interpreted as ophiolite slivers (Sosson et al. 2010), and correlated with the Sevan-Akera ophiolites (Hässig et al. 2013). The mélange is imbricated with Upper Precambrian to Lower Cambrian metamorphic rocks, and Devonian and Permian limestone and terrigenous rocks (Belov 1969).

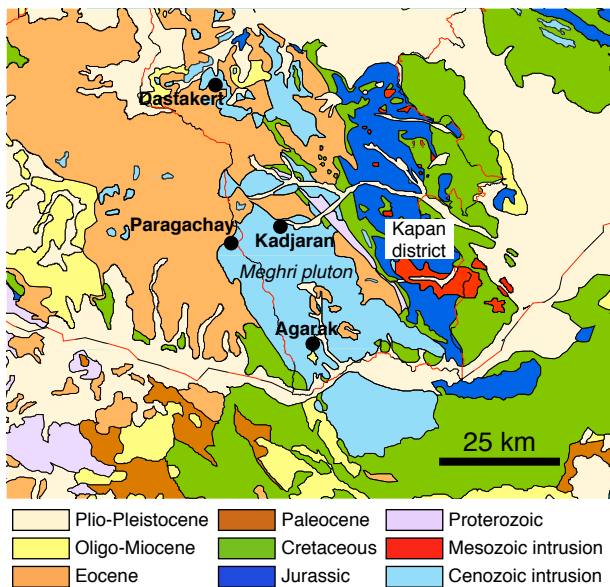


Figure 1. Geology of the southern part of the Lesser Caucasus and location of major ore deposits and ore districts (after Tayan et al. 1976; Babazadeh et al. 1990; Mederer 2013).

3 Ore Deposit Types

The most important ore deposits of the Kapan district (Fig. 1) are hosted by Middle Jurassic rocks, and are the Centralni West Cu-deposit, the Centralni East Cu-Au deposit and the Shahumyan polymetallic Cu-Au-Ag-Zn±Pb±Te deposit. The underground Shahumyan deposit remains the only active mine in the district. Based on a detailed petrographic and isotope study, the deposits are interpreted to be related to intrusion-related ore-forming processes, with predominantly magmatic intermediate- to high-sulphidation state fluids, and minor seawater or meteoric water participation during very late hydrothermal stages (Mederer 2013).

The Centralni West Cu deposit consists of steeply dipping E-W striking veins hosted by breccia lava, hyaloclastite and lava flow of basaltic to andesitic composition. Alteration consists of chlorite, carbonate and epidote, and sericite in the upper parts of the deposit. Chalcopyrite and pyrite are the main opaque minerals, with subsidiary sphalerite, tennantite-tetrahedrite and galena, and traces of tellurides and bismuth minerals in a gangue of quartz and carbonate (Achikgiozian et al. 1987; Mederer 2013). The Centralni East Cu±Au deposit consists of stockwork-type mineralization and vein-type orebodies. Silicification, phyllic alteration and residual quartz alteration with sericite, dickite and diasporite affect the andesitic to dacitic host rocks. The paragenesis is dominated by pyrite, colusite, tennantite-tetrahedrite, chalcopyrite, hematite and subsidiary luzonite and galena are the main ore minerals (Achikgiozian et al. 1987; Mederer 2013). Enargite, bornite, sphalerite, covellite, and tellurides were also reported. The Shahumyan polymetallic Cu-Au-Ag-Zn±Pb±Te deposit is hosted by a Middle Jurassic porphyritic subvolcanic quartz-dacite, and subsidiary hyaloclastite, and interlayered lava and ash fall deposits. The zoned veins

consist of an early barren quartz-pyrite stage, a polymetallic stage and a late carbonate stage. Pyrite, chalcopyrite, sphalerite, tennantite-tetrahedrite and galena predominate, and arsenopyrite, digenite, bornite, chalcocite and enargite are subsidiary. Most of the gold and silver is associated with tellurides. Phyllic alteration with sericite, quartz and pyrite prevails in proximity to the ore bodies. Alteration grades into argillic alteration at decreasing depth, with dickite, quartz, pyrite and ± sericite. Alunite, kaolinite and dickite are present in the northeastern part of the deposit.

Ore deposits of the Tertiary Meghri-Ordubad zone consist predominantly of porphyry-Cu-Mo deposits and spatially associated precious and base metal epithermal occurrences (Fig. 1). The spatial distribution of ore deposits and occurrences in the Meghri pluton is controlled by roughly north-south- and east-west-oriented regional faults (Tayan et al. 1976).

The porphyry-Cu-Mo deposits include the world-class Kadjaran and the smaller Agarak mine, the abandoned Paragachay deposit and numerous prospects, including Dastakert, Hankasar, Misdag, Lichk, Aygedzor, Qapujuk, and Diakhchay (Karamyan 1978; Babazadeh et al. 1990). Stockwork-type mineralization predominates, but vein-type and breccia-type ore is also encountered. The main opaque minerals are pyrite, chalcopyrite, molybdenite, magnetite, sphalerite, galena, and subsidiary sulphosalts, tellurides, and native gold, generally in a gangue of quartz, followed by late carbonate and sulfate. Ore formation is subdivided in different stages. (e.g. Karamyan and Faramazyanyan 1960), the economic stages being: quartz-molybdenite, quartz-molybdenite-chalcopyrite, and quartz-chalcopyrite.

Precious and base metal epithermal occurrences hosted by volcanic and plutonic rocks are spatially related to the same structures, which control the porphyry-Cu-Mo deposits in the Meghri pluton, but are generally of lesser economic interest. They consist of vein- or stockwork-type mineralization, and ore dissemination in altered wall rock. Alteration consists of silicification, sericite, clay minerals and carbonates. The occurrences contain in variable proportions native gold, pyrite, chalcopyrite, sphalerite, galena, sulfosalts, arsenopyrite and tellurides (e.g. Amiryan 1984; Babazadeh et al. 1990).

4 Geochronology

LA-ICP-MS U-Pb dating of zircons was undertaken on six intrusive rock samples of the Kapan district. One Middle Jurassic tonalite sampled from a pebble dike yielded an age of 165.6±1.4 Ma. Ages of four samples from plutons intruding the Kapan block are 137.7±1.6 Ma, 136.2±1.1 Ma, 133.6±2.2 Ma, and 131.5±2.1 Ma, and support the Upper Jurassic to Lower Cretaceous age of voluminous intrusive activity in the Kapan block. Finally, one Paleogene gabbro was dated at 50.82±0.51 Ma, and sets the onset of Tertiary magmatic activity in this part of the Lesser Caucasus.

Despite abundant petrography and mineral separation, especially of the immediate host rocks, and

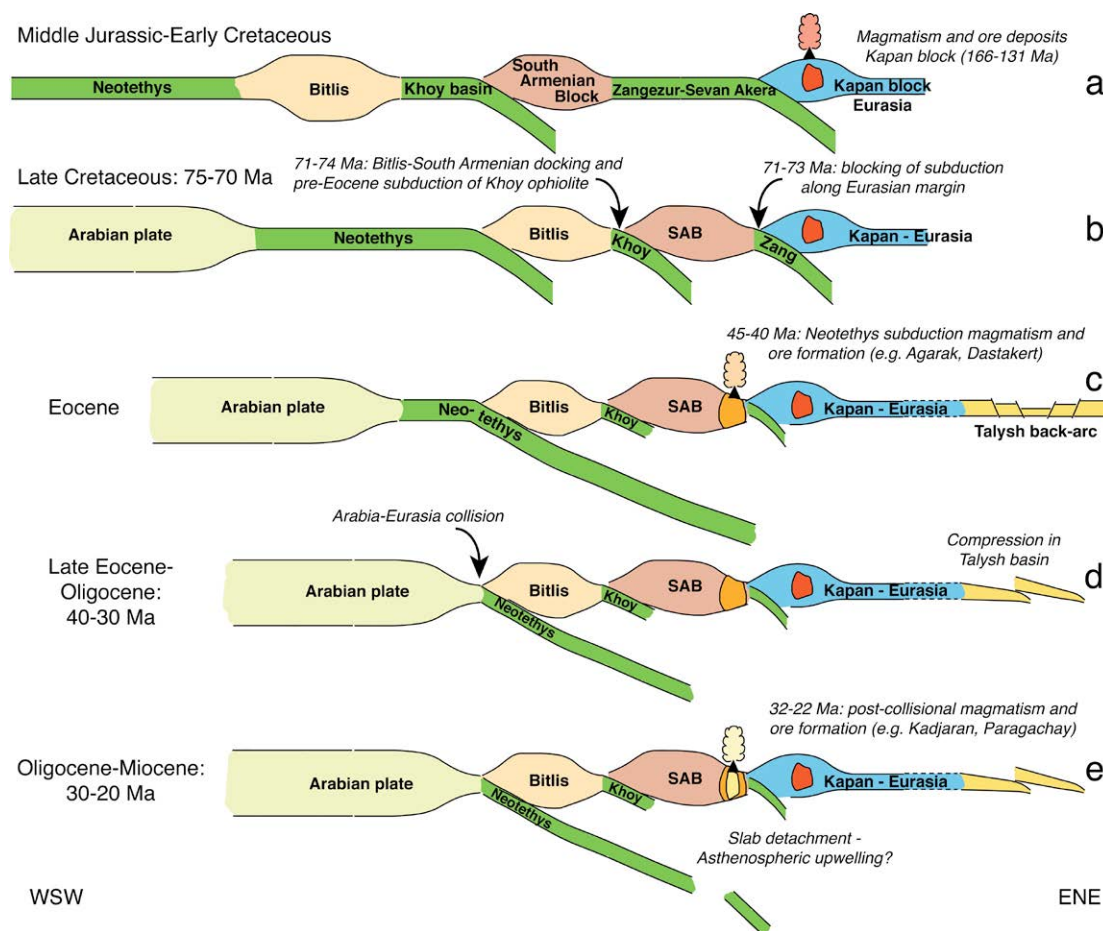


Figure 2. Magmatic and metallogenic events during progressive geodynamic evolution of the southern Lesser Caucasus.

dikes crosscutting ore bodies, only a few samples allowed us to constrain the timing of ore formation in the Kapan district. A hydrothermal muscovite from the Centralni West Cu-deposit has an $^{40}\text{Ar}/^{39}\text{Ar}$ weighted plateau mineralization age of 161.78 ± 0.79 Ma, and magmatic-hydrothermal alunite from the Shahumyan deposit yielded a 156.14 ± 0.79 Ma age. Both ages indicate that ore-formation occurred at the Middle-Upper Jurassic transition at Kapan, which is consistent with the local geological setting. Re-Os dating of pyrite from the Centralni West and East deposits yield weighted average model ages of 215.1 ± 4.3 and 146.0 ± 3.1 Ma, respectively. The 215.1 ± 4.3 Ma age is unreasonably old and is discarded, since it predates the host rock age.

TIMS U-Pb zircon ages were obtained for samples representing the different magmatic stages of the Tertiary Meghri pluton. One granodiorite from the southernmost part of the pluton yielded an age of 44.01 ± 0.11 Ma, which is consistent with Rb-Sr isochron ages between 45.3 ± 3.5 Ma and 38.3 ± 1.0 Ma obtained by Melkonyan et al. (2008, 2010). Re-Os ages of molybdenite obtained for four porphyry-Cu-Mo deposits fall in the Eocene age bracket, with Agarak at 44.2 ± 0.2 Ma, Hankasar at 43.14 ± 0.17 Ma, Aygedzor at 42.62 ± 0.17 Ma, and Dastakert between 40.22 ± 0.16 and 39.97 ± 0.16 Ma (four samples).

The monzonite complex hosting the Kadjaran deposit was dated by TIMS U-Pb zircon at 31.83 ± 0.02 Ma, which agrees with the a Rb-Sr isochron age of

30.0 ± 0.4 Ma reported by Melkonyan et al. (2008) for the same magmatic event, and a molybdenite Re-Os age of 31.00 ± 0.12 Ma from a pegmatite at Kaler.

A granodiorite located between the Kadjaran and the Agarak deposits (Fig. 1) at Djband yielded TIMS U-Pb zircon ages of 22.22 ± 0.02 and 22.34 ± 0.02 Ma, which agree with the Rb-Sr isochron age of 22.8 ± 2.1 Ma reported by Melkonyan et al. (2008) for a porphyry-like granitoid from the Kadjaran area. These ages coincide with a 22.87 ± 0.09 Ma Re-Os age of molybdenite impregnation in a late aplite granite.

Five molybdenite samples from the world-class Kadjaran deposit yielded consistent Re-Os ages between 27.2 ± 0.1 and 26.43 ± 0.11 Ma, which coincide with one molybdenite Re-Os age from the Paragachay deposit of 26.78 ± 0.11 Ma. These Re-Os ages are currently tested by TIMS U-Pb zircon dating of a dike crosscut by molybdenite mineralization at Kadjaran.

4 Discussion and conclusions

The absolute ages obtained in this study for the southernmost part of the Lesser Caucasus reveal an east to west progression of magmatic and mineralizing events, which can be correlated with different stages of the geodynamic evolution of the Tethys orogenic belt.

The magmatic and ore-forming events dated between 165.6 ± 1.4 and 131.5 ± 2.1 Ma in the Kapan block correspond to the construction of the island arc

during the Jurassic and Cretaceous along the Eurasian plate during subduction of the Tethys and progressive convergence of Gondwana-derived terranes (South Armenian and Bitlis blocks) with Eurasia (Fig 2a; Roland et al 2011).

Our data indicate that magmatism and ore formation in the southern Lesser Caucasus started during the Eocene, after blocking of the subduction along the Eurasian margin and accretion of the Gondwana-derived terranes at 71-74 Ma. This resulted in a subduction jump of the Neotethys to the west of the accreted Bitlis block (Figs 2b-c; Khalatbari-Jafari et al. 2004; Rolland et al. 2011).

According to our data, Eocene magmatic activity affected initially the Kapan block at 50.82 ± 0.51 Ma and then migrated westward across the Zangezur (Khustup-Giratakh) fault into the South Armenian block to form the initial stages of the composite Meghri pluton at about 45-40 Ma (Fig. 2c). This initial magmatic event is coeval with the generation of the first major porphyry-Cu-Mo event according to Re-Os geochronology (e.g. Agarak and Dastakert deposits). This Eocene magmatic and metallogenic event coincides with abundant and voluminous subduction-associated magmatism recorded in this part of the Tethys belt, in particular in Iran (Allen and Armstrong 2008; Agard et al. 2011). Therefore, we interpret this initial Eocene magmatism within the South Armenian block as related to progressive subduction of the Neotethys. This interpretation remains to be tested by geochemical investigations of the magmatic rocks.

The interruption of magmatic and ore-forming activity in the Meghri pluton, between about 40 and 30 Ma at the Eocene-Oligocene transition, corresponds to the collision of Arabia with Eurasia (Fig. 2d; e.g. Allen and Armstrong 2008; Agard et al. 2011).

Renewed magmatism and ore formation between 31 and 22 Ma, resulting in the world-class Kadjaran porphyry-Cu-Mo deposit, is clearly a post-collisional event. The processes at the origin of the Oligo-Miocene post-collisional magmatism and porphyry emplacement are still under study. Possible settings could be related to slab detachment and asthenospheric upwelling (Fig. 2e), but they need to be tested by geochemical investigations of the Oligo-Miocene magmatic rocks.

Acknowledgements

This project was funded by the Swiss National Science Foundation grants 200020-121519 and 200020-138130 and the SCOPES project IZ73ZO-128324. J. Mederer thanks the Augustin Lombard Foundation of the Geneva SPHN Society for a travel grant and the Hugh E. McKinstry Fund for a SEG student research grant.

References

Achikiozian SO, Zograbyan SA, Karapetyan AI, Mirzoyan HG, Sargisyan RA, Zaryan RN (1987) The Kapan Mining district: Armenian Academy of Sciences SSR, 198 p.
 Agard P, Omrani J, Jolivet L, Whitechurch H, Vrielynck B, Spakman W, Monié P, Meyer B, Wortel R (2011) Zagros

orogeny: a subduction-dominated process. *Geol Mag* 148: 692-725.
 Allen MB, Armstrong HA (2008) Arabia-Eurasia collision and the forcing of mid-Cenozoic global cooling. *Palaeogeol., Palaeoclim., Palaeoecol.* 265: 52-58.
 Amiryan SH (1984) Gold ore formation of Armenian SSR. Yerevan; Publishing House of the Academy of Sciences Armenian SSR, 304 p. (in Russian).
 Babazade VM, Makhmudov AI, Ramazanov VG (1990) Porphyry-copper and molybdenum deposits. Azerbaijan Publication, Baku, 377 p. (in Russian).
 Belov AA (1968) On the history of tectonic development of the northern margin of the Iranian Elibayk subplatform on Lesser Caucasus: *Izvestia of the Academy of Sciences of SSSR, volume geol. N10: 80-85* (in Russian).
 Gabrielyan AA, Nazaretyan SN, Ohannisyan ShS (1989) Deep fault of territory of Armenia. In *Nauka M* (ed) *Geodynamics of Caucasus*, p. 36-45 (in Russian).
 Hässig M, Rolland Y, Sosson M, Galoyan, Müller C, Avagyan A, Sahakyan L (2013) New structural and petrological data on the Amasia ophiolites (NW Sevan-Akera suture zone, Lesser Caucasus): Insights for a large-scale obduction in Armenia and NE Turkey. *Tectonophysics* 588: 135-153.
 Karamyan KA (1978) Geology, structure and condition of formation copper-molybdenum deposits of Zangezur ore region. Yerevan; Publishing House of the Academy of Sciences Armenian SSR, 179 p. (in Russian).
 Karamyan K, Faramazyan A (1960) The mineralization stages of Kadjaran copper-molybdenum deposit. The *Izvestia of Academy of Sciences Armenian SSR.*, the series of geology and geography, № 3-4 :65-88. (in Russian)
 Khalatbari-Jafari M, Juteau T, Bellon H, Whitechurch H, Cotten J, Emami H (2004) New geological, geochronological and geochemical investigations on the Khoys ophiolites and related formations, NW Iran. *J. Asian Earth Sci.* 23: 507-535.
 Knipper AL, Khain EV (1980) Structural position of ophiolites of the Caucasus. *Ophioliti* 2: 297-314.
 Mederer J. (2013) Regional Setting, Geological Context and Genetic Aspects of Polymetallic Hydrothermal Ore Deposits from the Kapan Ore District, Southern Armenia: a Contribution to the Mesozoic Island Arc Metallogeny of the Lesser Caucasus. Unpublished Ph.D. thesis, University of Geneva, Switzerland, 161 p.
 Melkonyan RL, Ghukasyan RKh, Tayan RN, Haroutiunyan MA (2008) Geo-chronometry of the Meghri pluton monzonites (Armenia) – results and consequences. *Nauki o Ziemle series journal of The Izvestia of the National Academy of Sciences of the Republic of Armenia.*, №2: 3-10.
 Melkonyan RL, Ghukasyan RKh, Tayan R N, Khorenyan RA, Hovakimyan S E (2010) The stages of copper-molybdenum ore formation in Southern Armenia (by the results of Rb-Sr isotope age estimations). *Izvestia NAN RA, Nauki o Zemle*, N 2: 33-40.
 Rolland Y, Sosson M, Adamia Sh, Sadradze N (2011) Prolonged Variscan to Alpine history of an active Eurasian margin (Georgia, Armenia) revealed by $^{40}\text{Ar}/^{39}\text{Ar}$ dating. *Gondwana Res.* 20: 798-815.
 Shirinyan KG, Nahapetyan LB. (1974) New type of basalts in Armenia. *Doklady AN ArmSSR*, 59: 45-50 (in Russian).
 Sosson M, Rolland Y, Müller C, Danelian T, Melkonyan R, Kekelia S, Adamia Sh, Babazadeh V, Kangarli T, Avagyan A, Galoyan G, Mosar J (2010) Subductions, obduction and collision in the Lesser Caucasus (Armenia, Azerbaijan, Georgia), new insights. In: Sosson M, Kaymakci N, Stephenson RA, Bergerat F, Starostenko V (eds) *Sedimentary basin tectonics from the Black Sea and Caucasus to the Arabian platform*. *Geol. Soc. London, Spec. publ.* 340, p. 329-352.
 Tayan RN, Plotnikov EP, Abdurakhmanov RU (1976) Some features of formation of geological structure of the Zangezur-Nakhichevan region of Lesser Caucasus. *Izvestia of National Academy of Sciences of Armenia, Nauki o Zemle*, № 4: 12-20.

Tectonic and structural setting of porphyry Cu-Au and epithermal Au mineralization of the Biga Peninsula, NE Aegean

Matias G. Sanchez

Mineral Deposit Research Unit, The University of British Columbia, Vancouver, BC, Canada, V6T 1Z4

Ken McClay

Fault Dynamics Research Group, Royal Holloway University of London, UK

Adrian King

Teck Resources Limited, General Manager Gold, Canada

Abstract. Epithermal gold and porphyry copper-gold mineralization of the Biga Peninsula in northwestern Turkey sits within a system of NE-trending back-arc extensional basins developed throughout Eocene, Oligocene and Miocene roll-back of the northward subducting African slab. We propose that porphyry style copper-gold mineralization is associated with granitoid intrusions in the footwall of detachment fault systems, as well as link to the processes of metamorphic basement exhumation by core-complex formation. We also document that high sulfidation style epithermal gold deposits are found in the hanging wall basins above the core complex detachment fault system, as well as forming major strata-bound silicified lithocaps fed by steep-dipping extensional faults and associated fractures above intrusions. Post-emplacment crustal extension resulted in “domino-style” block rotations and half-graben formation throughout the Miocene and Pliocene. Since the early Pliocene, the westward propagation of the North Anatolian Fault offsets a series of these deposits as a result of increased dextral transtension.

Keywords. Tethyan, Aegean, Tectonics, Epithermal, Porphyry

1 Introduction

The Biga Peninsula of northwestern Anatolia is part of the Tethyan Alpine-Himalayan orogenic belt and is located in the confluence of the Aegean Extensional Province (AEP) and the transtensional segment of the North Anatolian Fault (NAF) (Fig. 1; Stampfli and Borel 2004; Jolivet and Brun 2008; Armijo et al. 1999). The study area hosts several medium and small porphyry copper-gold and low and high sulfidation epithermal gold deposits of Late Eocene to Early Miocene age (Fig. 2; Yigit 2006, 2009; Yilmaz et al. 2010). This cluster of magmatic-hydrothermal ore deposits is part of the Cenozoic Serbomacedonian – Rhodope metallogenic zone (Neubauer 2002; Heinrich and Neubauer 2002) and of the broader Tethyan Metallogenic Belt (TEMB) which runs for more than 9000 km from the Alps to the West Pacific Metallogenic Belt in Indonesia (Jankovic 1997).

The northeast Aegean and northwestern Anatolian segments of the TEMB has undergone an initial “Andean Style” subduction phase followed by the continental collision and closure of the Vardar-Izmir-Ankara Ocean in the Late Cretaceous (Fig. 1; Ring et al. 2010; Brun and Faccenna 2008; Moix et al. 2008). A Cenozoic phase

of syn to post-orogenic extension developed as result of regional gravitational collapse, slab rollback or both processes acting in sequence (Bonev and Beccaletto, 2007; Brun and Sokoutis 2010).

We investigated the Cenozoic extensional structures and magmatic-related mineralization and propose a new tectono-stratigraphic evolution for the Biga Peninsula of northwestern Turkey. Based on geological and structural mapping, magnetometry analyses and Ar/Ar geochronology, this research focus on the link between mineralization and syn- to post brittle to ductile faulting and proposes a novel structural architecture and tectonic evolution.

2 Tectonic setting

The Biga peninsula sits within a system of back-arc extensional basins as a result of continental extension caused by slab roll-back of the northward subducting African slab during the Eocene, Oligocene and Miocene (Fig. 1; Jolivet and Brun, 2008; Brun and Sokoutis 2010; Bonev and Beccaletto 2007). Regional continental extension and crustal thinning followed the closure of the Vardar-Izmir-Ankara Ocean as the Pontides and Anatolides terranes collided in the Late Cretaceous (Fig. 1; Ring et al. 2010; Brun and Faccenna 2008; Moix et al. 2008; Okay and Tüysüz, 1999).

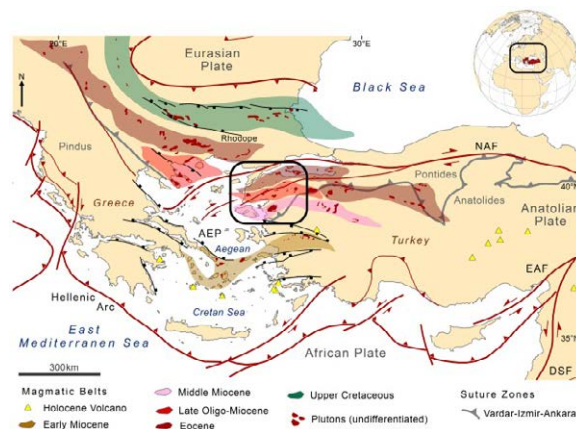


Figure 1. Tectonic map of the Aegean and western Anatolia. Magmatic belts, Late Cretaceous suture zone and major fault systems are shown.

Throughout the Early Cenozoic, a series of southward-youngening metamorphic core complexes, volcanic arcs and coeval magmatic-related ore systems developed in the northern Aegean and western Anatolia (Fig. 2; Agostini et al. 2010; Schefer et al. 2010; Harangi et al., 2006; Jolivet and Brun, 2008). The Middle Eocene to Early Miocene magmatic arcs of the Biga Peninsula (Bonev et al. 2009; Cavazza et al. 2008) produced porphyry type and epithermal style mineralization as part of a major NW to EW-trending arcuate magmatic-metallogenic zone running from the Dinarides and the Rhodopes to the Pontides of northern Turkey (Figs. 1 and 2; Yigit 2006, 2009; Heinrich and Neubauer 2002; Neubauer, 2002).

Since the Early Pliocene, the North Anatolian Fault (NAF) propagated westward through the Sea of Marmara, the Biga Peninsula and the northern Aegean generating increase extensional rates and dextral strike-slip offsets (Figs. 1 and 2; McClusky et al. 2000; Armijo et al. 1999; Taymaz et al. 2007).

3 Geology and intrusion-related mineralization of the Biga Peninsula

The geology of the Biga Peninsula is characterised by the NE-trending Kazdağ Massif formed by late Hercinian high grade gneiss and amphibolite grade metamorphic basement (Fig. 2; Cavazza et al. 2008; Bonev and Beccalotto, 2007). During the latest Oligocene, basement re-crystallization and granitoid plutonism was accompanied by metamorphic core complex exhumation and shallow-dipping detachment fault systems (Bonev et al. 2009; Cavazza et al. 2008; Okay and Satir, 2000).

The pre-Cenozoic hanging wall of the Kazdağ Massif is composed by Permo-Trassic metasediments (Karakaya Complex) and by Late Cretaceous ophiolites (Çetmi Mélange) (Okay and Satir, 2000; Cavazza et al. 2008). These are flanked by Oligo-Miocene extensional volcano-sedimentary basins (Altunkaynak and Genç, 2008; Donmez et al. 2005; Ercan et al. 1995) internally deformed by domino-style and ~NE-trending hanging wall extensional faults (Fig. 3).

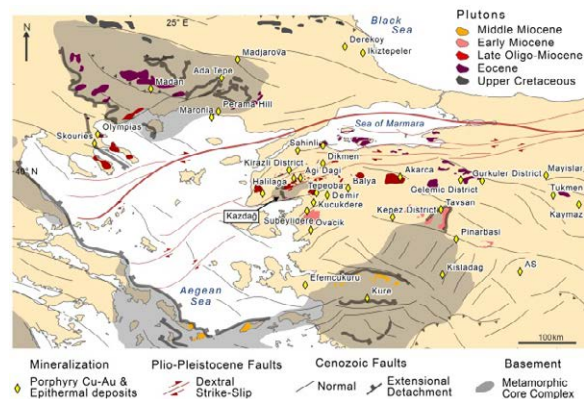


Figure 2. Simplified map showing the distribution of epithermal gold and porphyry copper-gold deposits, metamorphic core complexes and plutons.

Northwestern Turkey and the Biga Peninsula host a wide range of intrusion-related mineral deposits, such as, the high sulfidation style gold deposit of Kuşçayır (TV Tower) and Havran (Yılmaz, 2003; Koç et al. 2004), the low sulfidation style veins of Bergama (Yılmaz, 2007), the porphyry copper-gold stocks and breccias of Kuşçayır (TV Tower) and Tepeoba (Yılmaz 2003; Murakami et al. 2005), the base metal veins of Arapucan and Lapseki (Orgün et al. 2005; Yılmaz et al. 2010) and the skarn deposits of Evciler and Ayazmant (Öztürk and Helvacı, 2008; Oyman, 2010). These mineralized systems mainly respond to the development of a series of plutonic units with ages between 20.3Ma to 45.3Ma (Altunkaynak and Yılmaz, 1998; Delaloye and Bingöl, 2000; Genç, 1998; Karacık and Yılmaz, 1998; Okay and Satir, 2000).

4 Structural Implications for porphyry Cu-Au mineralization and epithermal Au mineralization

Field relations, ductile metamorphic and intrusive fabrics, as well as Ar/Ar geochronology, indicates that the latest Oligocene porphyry style copper-gold mineralization is associated with granitoid intrusions in the footwall of detachment fault systems (Fig. 3). These intrusions are link to ductile to brittle extensional faulting and metamorphic basement exhumation. North and south of the Kazdağ Massif metamorphic core complex, the ENE-trending Bayramiç-Çan and Edremit grabens host the Kestane (Halilaga) copper-gold Porphyry (~25 - 26 Ma) and Tepeoba copper-molybdenum-gold Breccia (Re/Os 25.6 Ma; Murakami et al. 2005) (Figs. 2 and 3). While the Kestane Porphyry (Halilaga) is located in the centre of the Bayramiç-Çan half-graben and is temporally related to the Evciler Pluton, the Tepeoba Breccia is emplaced along the northern flank of the Edremit Graben and in close relation to the Eybek Pluton (~25 Ma; Ar/Ar) (Fig. 3).

High sulfidation style epithermal gold deposits (e.g. AgiDagi, Demir, TvTower, etc), form major siliceous lithocaps and argillic alteration zones throughout the Biga Peninsula (Fig. 3). These mineralized systems are found above the ductile detachment fault systems and within the hangingwall basins, as well as in the vicinity or above Cenozoic plutons. Mineralization is locally controlled by steep dipping extensional faults and associated fractures. Higher gold grades commonly occurs at the intersection of steep dipping structurally controlled feeder zones (e.g. hydrothermal breccias in dilatational structures) and permeable pyroclastic layers. Barren stratabound silicified lithocaps results from the lateral migration of epithermal fluids within more permeable units and along the water table interface.

5 Discussion

The Biga Peninsula is characterized by prominent high sulfidation style alteration zones in which major siliceous lithocaps were formed in half-graben style

basins and exhumed along the footwalls of extensional fault systems (Fig. 3). At greater depths and higher pressure and temperature conditions, porphyry style copper-gold stocks and breccias occur in close association to plutonic bodies which intrude in the footwall of extensional faults (Fig. 3).

Late Oligocene to Miocene ENE- to EW-trending extensional detachments and steep dipping brittle faults played a major role in the emplacement and later disruption of both, porphyry and epithermal deposits (Figs. 2 and 3). These structures link to the processes of extensional exhumation of the Kazdağ Massif metamorphic core complex, as well as to Late Oligocene pluton and porphyry stock emplacement (Fig. 3). At shallow crustal levels steep dipping brittle structures, developed above the ductile fault systems, controlled the vertical fluid pathways for epithermal mineralization.

Post-emplacment crustal extension resulted in “domino-style” block rotations and increased half-graben subsidence throughout the Miocene and Pliocene (Fig. 3). Since the Early Pliocene, the westward propagation of the southern branches of the North Anatolian Fault offsets a series of these deposits (Fig. 3).

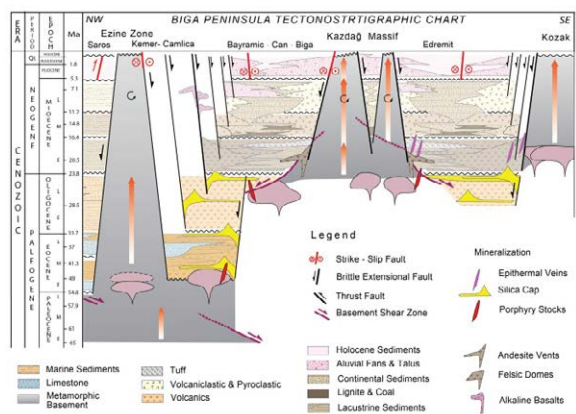


Figure 3. Tectonic and chronostratigraphic chart of central-south Biga Peninsula.

Acknowledgements

We thank Teck Resources in Canada and Turkey for the support given for this research. Most special appreciation to Tayfun Cerrah, Ugur Kiziltepe, Bayram Artun, Nuri Ceyhan, Mevlut Avsan, Chad Hewson, Ramazan Sari, Baris Yildirim and Anna Fonseca. We also thank the Mineral Deposit Research Unit (MDRU) and its Western Tethyan Metallogeny Project for their support on presenting this paper at the 12th SGA Biennial Meeting. The authors are also grateful to Thomas Bissig for helpful comments on this manuscript.

References

Agostini S, Doglioni C, Innocenti F, Manetti P, Tonarini, S (2010) On the geodynamics of the Aegean rift. *Tectonophysics* 488(1-4), 7-21
 Altunkaynak Ş, Genç ŞC (2008) Petrogenesis and time-progressive

evolution of the Cenozoic continental volcanism in the Biga Peninsula, NW Anatolia (Turkey). *Lithos* 102(1-2), 316-340
 Altunkaynak S, Yilmaz, Y (1998) The Mount Kozak magmatic complex, Western Anatolia. *Journal of Volcanology and Geothermal Research* 85(1-4), 211-231
 Armijo R, Meyer B, Hubert A, Barka A (1999) Westward propagation of the North Anatolian fault into the northern Aegean: Timing and kinematics. *Geology* 27(3), 267
 Bonev N, Beccaletto L (2007) From syn-to post-orogenic Tertiary extension in the north Aegean region: constraints on the kinematics in the eastern Rhodope Thrace, Bulgaria Greece and the Biga Peninsula, NW Turkey. *Geological Society London Special Publications* 291(1), 113-142
 Bonev N, Beccaletto L, Robyr M, Monié P (2009) Metamorphic and age constraints on the Alakeçi shear zone: Implications for the extensional exhumation history of the northern Kazdağ Massif, NW Turkey. *Lithos* 113(1-2), 331-345
 Brun J, Faccenna C (2008) Exhumation of high-pressure rocks driven by slab rollback. *Earth and Planetary Science Letters* 272(1-2), 1-7
 Brun JP, Sokoutis D (2010) 45 m.y. of Aegean crust and mantle flow driven by trench retreat. *Geology* 38(9), 815-818
 Cavazza W, Okay AI, Zattin M (2008) Rapid early-middle Miocene exhumation of the Kazdağ Massif (western Anatolia). *International Journal of Earth Sciences* 98(8), 1935-1947
 Delaloye M, Bingöl E (2000). Granitoids from western and northwestern Anatolia: geochemistry and modeling of geodynamic evolution. *International Geology Review* 42, 241-268
 Dönmez M, Akçay AE, Genç ŞC (2005) Biga yarımadasında Orta-Üst Eosen volkanizması ve denizel ignimbritler. *MTA Dergisi* 13, 49-61
 Ercan T, Satir M, Steinitz G, Dora A, Sarifakioglu E, Adis C, Walter HJ, Yildirim T (1995) Features of the Tertiary volcanism in the Biga Peninsula and in the islands of Gökçeada, Bozcaada and Tavşan adası (in Turkish). *Maden Tetkik ve Arama Dergisi* 117, 55-86
 Genç SC (1998) Evolution of the Bayramic magmatic complex, northwestern Anatolia. *Journal of Volcanology and Geothermal Research* 85(1-4), 233-249
 Harangi S, Downes H, Seghedi, I (2006) Tertiary-Quaternary subduction processes and related magmatism in the Alpine-Mediterranean region. *Geological Society, London, Memoirs* 32(1), 167-190
 Heinrich CA, Neubauer F (2002) Cu-Au-Pb-Zn-Ag metallogeny of the Alpine-Balkan-Carpathian-Dinaride geodynamic province. *Mineralium Deposita* 37(6), 533-540
 Jankovic S (1997) The Carpatho-Balkanides and adjacent area: a sector of the Tethyan Eurasian metallogenic belt. *Mineralium Deposita* 32(5), 426-433
 Jolivet L, Brun JP (2008) Cenozoic geodynamic evolution of the Aegean. *International Journal of Earth Sciences* 99(1), 109-138
 Karacik Z, Yilmaz Y (1998) Geology of the ignimbrites and the associated volcano-plutonic complex of the Ezine area, northwestern Anatolia. *Journal of Volcanology and Geothermal Research* 85(1-4), 251-264
 Koç Ş, Erdoğan S, Kaddioğlu K (1994) Epithermal mineralization potential of the volcanics in South East Havran (Balıkesir). *Mineral Res. Expl. Bull.* 116, 9-22
 McClusky S, Balassanian S, Barka A, Demir C, Ergintav S, Georgiev I, Gurkan O, Hamburger M, Hurst K, Kahle H (2000) Global Positioning System constraints on plate kinematics and dynamics in the eastern Mediterranean and Caucasus. *Journal of Geophysical Research* 105, 5695-5720
 Moix P, Beccaletto L, Kozur HW, Hochard C, Rosset F, Stampfli, GM (2008) A new classification of the Turkish terranes and sutures and its implication for the paleotectonic history of the region. *Tectonophysics* 451(1-4), 7-39
 Murakami H, Watanabe Y, Stein H (2005) Re-Os ages for molybdenite from the Tepeoba breccia-centered Cu-Mo-Au deposit, western Turkey: Brecciation-triggered mineralization. In *Mineral Deposit Research: Meeting the Global Challenge*, Springer Berlin Heidelberg

- Neubauer F (2002) Contrasting Late Cretaceous with Neogene ore provinces in the Alpine-Balkan-Carpathian-Dinaride collision belt. Geological Society, London, Special Publications 204(1), 81-102
- Okay AI, Satir M (2000) Coeval plutonism and metamorphism in a latest Oligocene metamorphic core complex in northwest Turkey. Geological Magazine 137(5), 495-516
- Okay AI, Tüysüz O (1999) Tethyan sutures of northern Turkey. The Mediterranean Basins: Tertiary Extension within the Alpine Orogen, 475-515
- Orgün Y, Gültekin AH, Onal A (2005) Geology, mineralogy and fluid inclusion data from the Arapucan Pb-Zn-Cu-Ag deposit, Canakkale, Turkey. Journal of Asian Earth Sciences 25(4), 629-642
- Oyman T (2010) Geochemistry, mineralogy and genesis of the Ayazmant Fe-Cu skarn deposit in Ayvalik, (Balıkesir), Turkey. Ore Geology Reviews 37(3-4), 175-201
- Ozturk YY, Helvacı C (2008) Skarn Alteration and Au-Cu Mineralization Associated with Tertiary Granitoids in Northwestern Turkey: Evidence from the Evçiler Deposit, Kazdağ Massif, Turkey. Economic Geology 103(8), 1665-1682
- Ring U, Glodny J, Will T, Thomson S (2010) The Hellenic Subduction System: High-Pressure Metamorphism, Exhumation, Normal Faulting, and Large-Scale Extension. Annual Review of Earth and Planetary Sciences 38(1), 45-76
- Schefer S, Cvetković V, Fügenschuh B, Kounov A, Ovtcharova M, Schaltegger U, Schmid SM (2010) Cenozoic granitoids in the Dinarides of southern Serbia: age of intrusion, isotope geochemistry, exhumation history and significance for the geodynamic evolution of the Balkan Peninsula. International Journal of Earth Sciences (3)
- Stampfli G, Borel G (2002) A plate tectonic model for the Paleozoic and Mesozoic constrained by dynamic plate boundaries and restored synthetic oceanic isochrons. Earth and Planetary Science Letters 196(1-2), 17-33
- Taymaz T, Yılmaz Y, Dilek Y. (2007) The geodynamics of the Aegean and Anatolia: introduction. Geological Society London Special Publications 291(1), 1
- Yigit O (2006) Gold in Turkey- a missing link in Tethyan metallogeny. Ore Geology Reviews 28(2), 147-179
- Yigit O (2009) Mineral Deposits of Turkey in Relation to Tethyan Metallogeny: Implications for Future Mineral Exploration. Economic Geology 104(1), 19-51
- Yılmaz H (2003) Exploration at the Kusçayırı Au (Cu) prospect and its implications for porphyry-related mineralization in western Turkey. Journal of Geochemical Exploration 77(2-3), 133-150
- Yılmaz H, Oyman T, Arehart G, Colakoglu A, Billor Z (2007) Low-sulfidation type Au-Ag mineralization at Bergama, Izmir, Turkey. Ore Geology Reviews 32(1-2), 81-124
- Yılmaz H, Oyman T, Sonmez FN, Arehart GB, Billor Z (2010) Intermediate sulfidation epithermal gold-base metal deposits in Tertiary subaerial volcanic rocks, Sahinli/Tespah Dere (Lapseki/Western Turkey). Ore Geology Reviews 37(3-4), 236-258

Mineral deposit model of the Duolong gold-rich porphyry copper deposit cluster in Gaize County, Tibet: evidence from zircon U-Pb dating

Guo Shuo

Faculty of Earth Sciences and Mineral Resources, China University of Geosciences, Beijing, China

Zhao Yuanyi

MLR Key Laboratory of Metallogeny and Mineral Assessment, Institute of Mineral Resources, Chinese Academy of Geological Sciences, Beijing, China

Li Xiaosai, Xu Hong, Liu Xiaofei

Faculty of Earth Sciences and Mineral Resources, China University of Geosciences, Beijing, China

Lü Lina

China Coal Geology Engineering Corporation, Beijing, China

Abstract: Duolong gold-rich porphyry copper deposit cluster is located on the north of the Bangonghu-Nujiang suture zone, at the south margin of Qiangtang Block and in Gaize County, North Tibet. It contains a super-large copper-gold deposit and has very good perspective. Our analyses of zircon SHRIMP U–Pb dating in Nadun, Bolong, Naruo, Tiegelong and Gaerqin indicate that the average metallogenic age is about 119 Ma. By comparing the characteristics of geochemistry, isotope, fluid inclusions and chronological data in different deposits of the cluster, we propose the mineral deposit model of the Duolong deposit cluster.

Key words: Geochronology, Deposit model, Zircon U-Pb age, Duolong deposit cluster

1 Geologic setting in region and deposit cluster

The Duolong deposit cluster is located on the north of Bangonghu-Nujiang suture zone and the south margin of Qiangtang Block. It has gold-rich porphyry copper deposits which are newly discovered and a super-large ore deposits (Qu et al., 2006; Li et al., 2007; Li et al., 2008b). They are pyromagma hydrothermal deposits related to intrusion of hypabyssal porphyry (She et al., 2006). There are more than 7Mt Cu with a grade of 0.46%-1.13% and more than 168.8t gold with a grade of 0.15-0.26g/t controlled in Duobuza and Bolong (China Geological Survey, 2008).

Duolong ore district has become a large porphyry copper deposit studied most thoroughly in Bangonghu-Nujiang metallogenic belt. But, it should be pointed out that these studies have often focused on Duobuza and Bolong, which has been taken as the representative of the whole ore district. There is no paper that introduces the relationship between various deposits in Duolong deposit cluster and develops a whole deposit model. This paper provides zircon SHRIMP U–Pb ages in Nadun, Bolong, Naruo, Tiegelong and Gaerqin, and proposes a mineral deposit model of Duolong ore district. This model will play a guiding role in exploring the deep part and periphery of Duolong deposit cluster and the same type deposits in

Bangonghu-Nujiang metallogenic belt.

Nadun, Bolong, Duobuza, Naruo, Tiegelong and Ge'erqin porphyry deposits are distributed, from the west to the east, in Duolong deposit cluster (Fig. 1). The copper reserves of Duobuza and Bolong deposits have reached the reserves of super-large deposits. In Duolong deposit cluster, exploration is underway in the classic porphyry deposits in the western section of Bangonghu-Nujiang metallogenic belt. Study of the deposit model is important.

The main strata exposed in the deposit cluster are: Member I of the Middle Jurassic Quse Formation (J_2q^1) and Member II of the same formation (J_2q^2). Member I of the Middle Jurassic Sewa Formation (J_2s^1) consists of shale intercalated with metamorphic thin-bedded feldspar lithic sandstone. Member II of the same formation consists of meta-quartz sandstone and meta-feldspar quartz sandstone intercalated with silty slate. The Lower Cretaceous Meirique Formation (K_1m) consists of andesitic porphyrite, andesitic basalt and pyroclastic rock. The Miocene Kangtuo Formation (N_1k) consists of brown-red clay and sandy gravel, and Quaternary residual material and slope wash (Q_4) (Fig. 1).

The deposit cluster is located in Duobuza tectonic-magmatic belt on the southern margin of Qiangtang-Sanjiang composite slab, where magmatic rocks are developed relatively, coordinate with the strike of the regional structure, and mainly occur in the intersection of EW with NW and NE trending structures, reflecting the well coupling relationship of magmatic rocks with structures in the area.

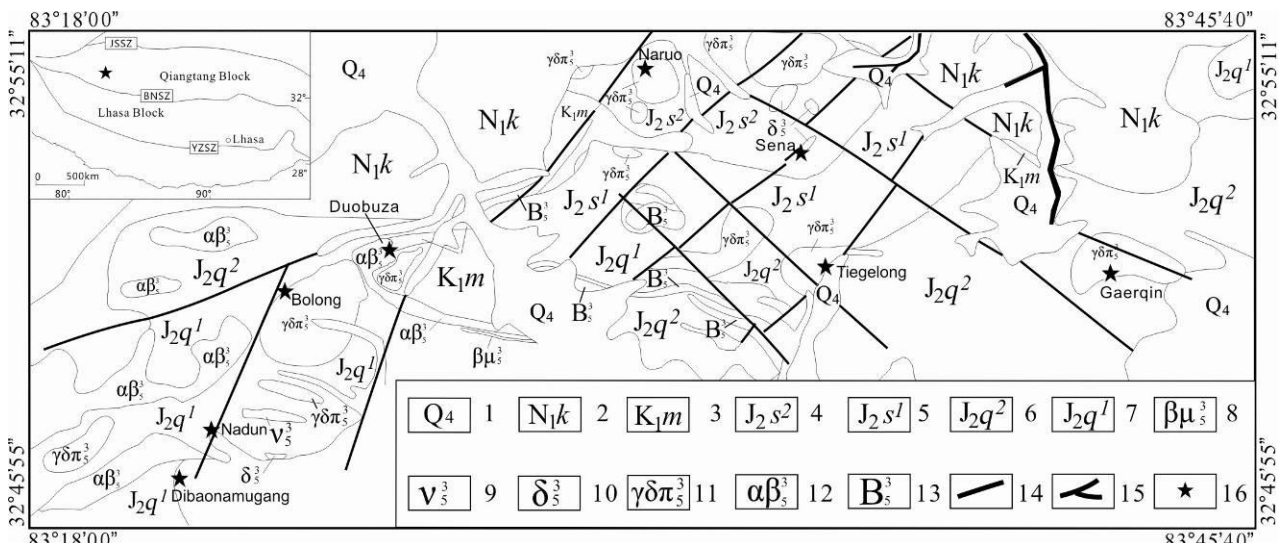
Bangonghu-Kangtuo-Cigedang fault in the south of Duolong deposit cluster is an ultra-crust fault that resulted in well developed secondary faults, including early nearly EW faults and later NE and NW faults. They form a rhombus framework, of which nearly EW faults are the main ore-bearing structure.

Granodiorite porphyry is the main ore-bearing rock (Xin et al., 2009). It occurs as two small stocks which are in the east and the west, respectively. The most common types of alteration are phyllic alteration, pyritization, potassium alteration and silicification. There are into three main alteration zones to be

1. Corresponding author: yuanyizhao2@sina.com

recognized around the porphyry body: from the inner to the outer, potassium silication-phyllitic alteration zone, phyllic alteration zone, and pyritization-hornfelsed zone. Within the porphyry body is the potassium

silication-phyllitic alteration zone where copper ores mainly occur (She et al., 2006). The ore minerals are chalcopyrite, pyrite and magnetite and a small amount of bornite, chalcocite, native gold and so on.



1-Quaternary; 2-Kangtuo Formation; 3-Meiriqie Formation; 4-Member II of Sewa Formation; 5-Member I of Sewa Formation; 6-Member II of Quse Formation; 7-Member I of Quse Formation; 8-Gray green diabase; 9-Shallow gray green diabase; 10-Diorite and quartz diorite; 11-Granodiorite porphyry; 12-Andesite; 13-Breccia; 14-Fault; 15-Placer gold; 16- Locations of mine areas

Figure 1. Geological map of Duolong Deposit Cluster (modified after Zhang et al., 2007)

2 Sample characteristics, analytic method and results

2.1 Sample characteristics

Our porphyry samples for zircon U-Pb dating were collected from Nadun, Bolong, Naruo, Tiegelong and Gaerqin deposits. Characteristics of the porphyry and zircons are shown in Fig.2. In the cathodoluminescence images, the zircons in the 4 samples from different districts show good columnar crystal morphology and clear oscillatory zoning, as is the case of magmatic zircon.

2.2 Analytic method and results

Zircons were extracted using conventional separation techniques and then handpicked under a binocular microscope with the purity of zircons up to 95%. Then, the zircon grains to be determined and the guide sample were mounted in epoxy and polished to expose the cores of the grains. Pictures were taken with reflection and transmission light microscopy and under cathodoluminescence (CL) using a scanning electron microscope. So we can select the measurement point to avoid cracks and inclusions. Cathodoluminescence (CL) images were completed by the laboratory of the Institute of Geology of Chinese Academy of Geological Sciences. U-Pb dating was performed on the SHRIMP II at the Beijing SHRIMP Center of Chinese Academy of Geological Sciences.

3 Discussion and conclusion

3.1 Significance of zircon U-Pb ages

Fig.2 gives the concordia plots of zircon SHRIMP U-Pb dating for Duolong deposit cluster. The results show that the surface age of each measuring point is concordant in the concordia diagram, it can represent the emplacement time of porphyritic intrusions. Thus, the weighted average age for Nadun is 115.54±0.70Ma, that for Bolong is 122.4±1.4Ma, that for Naruo is 119.45±0.61Ma, that for Tiegelong is 119.65±0.57Ma, and that for Gaerqin is 122.45±0.56Ma. Combined with the zircon U-Pb age of Duobuza district (~120Ma) in table 1, we conclude that the emplacement time of porphyry in the deposit cluster is about 119Ma and it proves that porphyry in the Duolong deposit cluster should be formed simultaneously.

In recent years, dating were carried out in Duolong deposit cluster using SHRIMP zircon dating, Re-Os molybdenite dating and K-feldspar (sericite) ⁴⁰Ar-³⁹Ar dating methods (Table 1). The Re-Os ages of Duobuza and Bolong are 118.0±1.5 and 119.4±1.3 respectively. They represent the ore-forming age, slightly later than magmatic emplacement age, but of consistency of age of the K-feldspar. The sericite ⁴⁰Ar-³⁹Ar age of Duobuza is 115.5±1.5Ma, representing the end of hydrothermal activity. In conclusion, the formation time of the porphyry in which ore deposits are hosted should be consistent with the formation time of ore deposits, belonging to the middle-late Yanshan period.

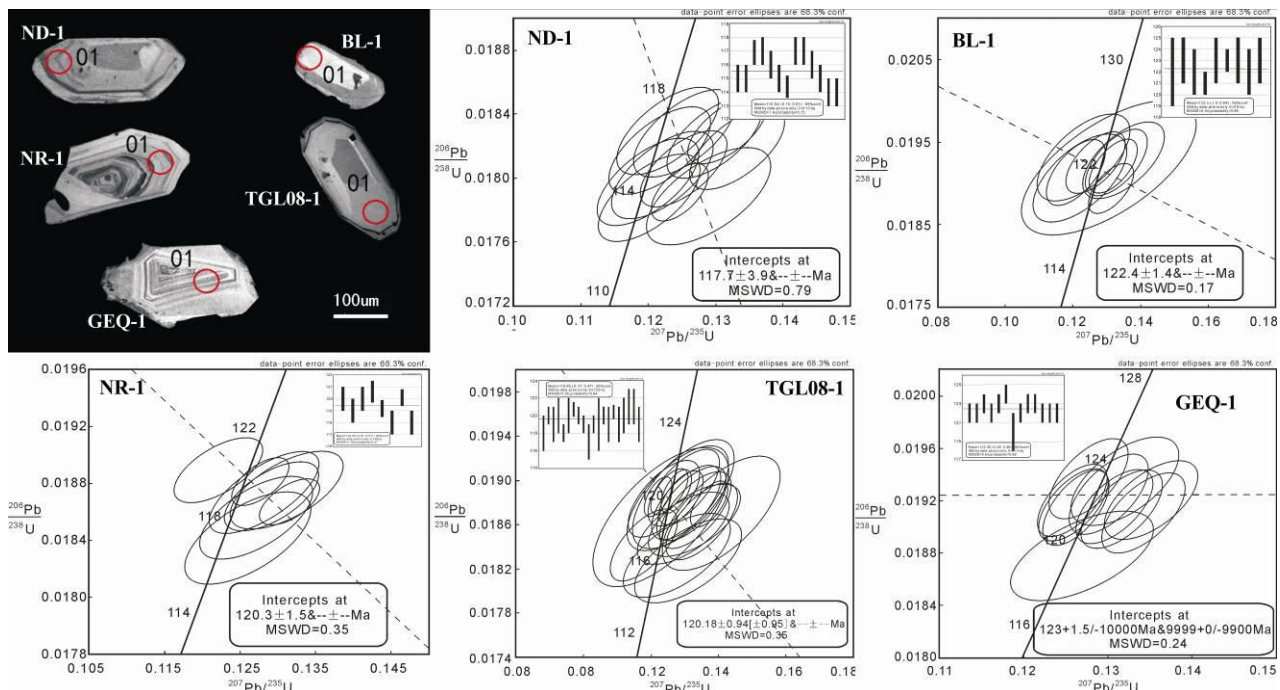


Figure 2. Cathodoluminescence (CL) images and concordia plots of zircon SHRIMP U-Pb dating in the Duolong deposit cluster

Table 1. Comparison of metallogenic ages of the Duolong deposit cluster

Sequence No.	Deposit	Age(Ma)	Test object/Method	Reference
1	Nadun	115.54±0.70	Zircons/SHRIMP U-Pb	This paper
2	Bolong	122.4±1.4	Zircons/SHRIMP U-Pb	
3	Bolong	119.4±1.3	Molybdenite/Re-Os isochron age	Zhu et al., 2011
4	Duobuza	121.6±1.9	Zircons/SHRIMP U-Pb	Li et al., 2008a
5	Duobuza	127.8±2.6	Zircons/SHRIMP U-Pb	Qu et al., 2006
6	Duobuza	120.9±2.4	Zircons/SHRIMP U-Pb	She et al., 2009
7	Duobuza	118.0±1.5	Molybdenite/Re-Os isochron age	
8	Duobuza	118.3±0.6	K-feldspar ⁴⁰ Ar- ³⁹ Ar	Zhu et al., 2012b
9	Duobuza	115.5±1.5	Sericite ⁴⁰ Ar- ³⁹ Ar	Li et al., 2011
10	Naruo	119.45±0.61	Zircons/SHRIMP U-Pb	This paper
11	Tiegelong	119.65±0.57	Zircons/SHRIMP U-Pb	
12	Gaerqin	122.45±0.56	Zircons/SHRIMP U-Pb	

3.2 Deposit model of the Duolong deposit cluster

Hou et al. (2008) developed a super-large gold-rich porphyry copper ore deposit metallogenic model of the Duolong cluster: in about late stage of early Cretaceous, neo-tethys subduction slabs carried a lot of ore-forming materials such as Cl, H₂O, Fe³⁺, Cu, etc., melted and replaced the overlying mantle wedge, making it melted partially, prompting the sulfide of the mantle melted, and finally resulting in all melting material rising to the upper crust, forming the first high-salinity ore-forming fluid of copper deposits in Duolong deposit cluster. High-temperature and high-salinity fluid inclusions in Duobuza are similar to those in many famous world-class porphyry copper mines, so this deposit cluster has potential to form a world-class copper deposit (She et al., 2006; Li et al., 2007).

The total amount of REE is between 9.369×10^{-6} - 1215.56×10^{-6} , LREE/HREE between 1.123 - 9.862 in the

Duolong deposit cluster. The δ Eu is between 0.428 and 1.266, and most of samples show negative anomaly. The δ Ce is between 0.755 and 1.563. The trace element spider diagram shows enrichment of LILE (Rb, Th, K) and depletion of HFSE (Nb, Ti, Sr).

S isotope distribution generally is relatively concentrated: $\delta^{34}\text{S}_{\text{V-CDT}}$ changes from 2.2‰ to 4.8‰ for pyrite, from 3.9‰ to 6.2‰ for chalcopyrite, and the variation range is not more than 6.2‰. The $\delta^{30}\text{Si}$ of quartz ranges between -0.5‰ and 0.3‰, and $\delta^{18}\text{O}$ ranges between 7.6‰ and 11.7‰. These suggest that S, Si and O mainly came from the magma. Pb isotopic composition of chalcopyrite and pyrite in Sena and Naruo indicates that it is from orogenic process (Lü et al., 2011).

The above evidences indicate that the geological characteristics of all deposits in the Duolong deposit cluster are similar, the deposits should be connected together in the shallow-deep part, and that it is likely to be a huge porphyry deposit (Fig. 3). Based on the

detailed field work and fluid inclusion experiment in Nadun and Dibaonamugang to the southwest of Nadun, we found that a large amount of limonite is developed on the surface. The main metal mineral includes chalcopyrite, tetrahedrite, covellite and a small amount of pyrite. The homogenization temperature of quartz inclusions in the major mineralization stage is about 280 Degrees Celsius, and the component of the inclusions is mainly CO₂, similar to Duobuza deposit (She et al., 2006). So Nadun and Dibaonamugang should be a good potential ore-prospecting area.

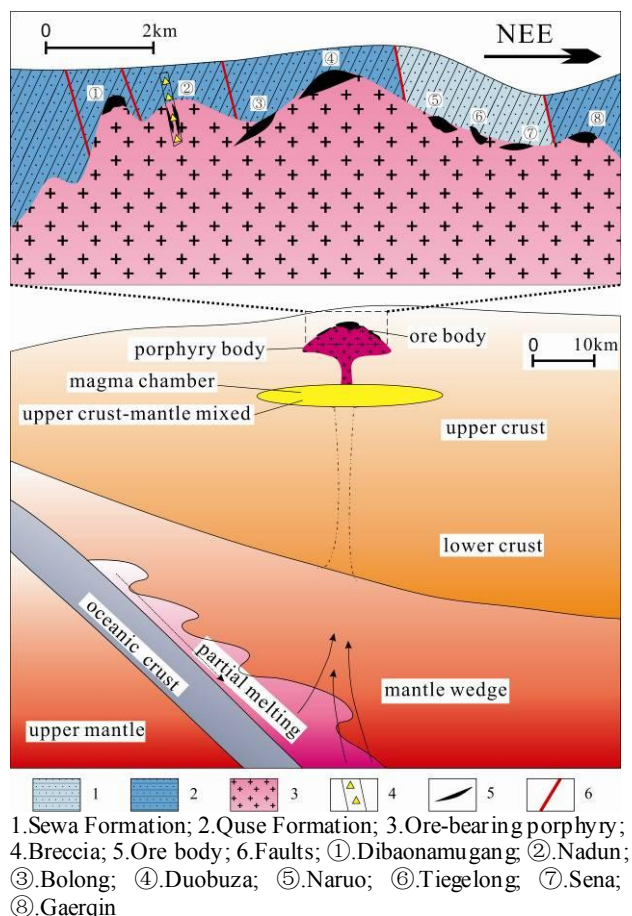


Figure 3. Deposit model sketch of the Duolong deposit cluster

Acknowledgements

This paper was financially supported by 973 programme (No. 2011CB403103), the National Scientific and Technological Support Program of China (No. 2006BAB01A05) and China Geological Survey Qianghai-Xizang special item (No. 1212010818097). We thank Li Yubin for his valuable help during our field investigations.

References

China Geological Survey (2009) The Important achievements of the mineral resources investigation and appraisal in 2009, 1-2
 Hou ZQ, Wang EQ, Mo XX, Ding L, Pan GT, Zhang Zhongjie (2008) Collisional orogeny and metallogenesis. Beijing: Geological Publishing House, 1-314 (in Chinese)
 Li GM, Li JX, Qin KZ, Zhang TP, Xiao B (2007) High temperature, salinity and strong oxidation ore-forming fluid at Duobuza gold-rich porphyry copper deposit in the Bangonghu tectonic belt, Tibet: Evidence from fluid inclusions. *Acta*

Petrologica Sinica 23: 935-952 (in Chinese with English abstract)
 Li JX, Li GM, Qin KZ, Xiao B (2008a) Geochemistry of porphyries and volcanic rocks and ore-forming geochronology of Duobuza gold-rich porphyry copper deposit in Bangonghu belt, Tibet: Constraints on metallogenic tectonic settings. *Acta Petrologica Sinica* 24: 531-543 (in Chinese with English abstract)
 Li JX, Qin KZ, Li GM, Xiao B, Zhang TP, Lei XG (2008b) Characteristics of rutiles from Duobuza gold-rich porphyry copper deposit in Bangong Lake Belt of northern Tibet and their significance. *Mineral Deposits* 27: 209-219 (in Chinese with English abstract)
 Li JX, Qin KZ, Li GM, Xiao B, Zhao JX, Chen L (2011) Magmatic-hydrothermal evolution of the Cretaceous Duolong gold-rich porphyry copper deposit in the Bangongco metallogenic belt, Tibet: Evidence from U-Pb and ⁴⁰Ar/³⁹Ar geochronology. *Journal of Asian Earth Sciences* 41: 525-536
 Lü LN, Zhao YY, Song L, Tian Y, Xin HB (2011) Characteristics of C, Si, O, S and Pb Isotopes of the Fe-rich and Cu (Au) Deposits in the Western Bangong-Nujiang Metallogenic Belt, Tibet and Their Geological Significance. *Acta Geologica Sinica* 85: 1291-1034 (in Chinese with English abstract)
 Qu XM and Xin HB (2006) Ages and tectonic environment of the Bangong Co porphyry copper belt in western Tibet, China. *Geological Bulletin of China* 25: 792-799 (in Chinese with English abstract)
 She HQ, Li JW, Feng CY, Ma DF, Pan GT and Li GM (2006) The high-temperature and hypersaline fluid inclusions and its implications to the metallogenesis in Duobuza porphyry copper deposit, Tibet. *Acta Geologica Sinica* 80: 1435-1447 (in Chinese with English abstract)
 She HQ, Li JW, Ma DF, Li GM, Zhang DQ, Feng CY, Qu WJ, Pan GT (2009) Molybdenite Re-Os and SHRIMP zircon U-Pb dating of Duobuza porphyry copper deposit in Tibet and its geological implications. *Mineral Deposits* 28: 737-746 (in Chinese with English abstract)
 Xin HB, Qu XM, Wang RJ, Liu HF, Zhao YY and Huang W (2009) Geochemistry and Pb, Sr, Nd isotopic features of ore-bearing porphyries in Bangong Lake porphyry copper belt, western Tibet. *Mineral Deposits* 28: 785-792 (in Chinese with English abstract)
 Zhang TP, Chen HQ, Li GR, Yan GD, Zheng YL (2007) Regional Geological map of Duolong deposit in Gaize county, the Tibet Autonomous Region (scaled by 1:50000). No.5 Geological Party, Tibet Bureau of Geology and Mineral Exploration and Development (in Chinese)
 Zhu XP, Chen HA, Ma DF, Huang HX, Li GM, Li YB, Li YC (2011) Re-Os dating for the molybdenite from Bolong porphyry copper-gold deposits in Tibet, China and its geological significance. *Acta Petrologica Sinica*, 27: 2159-2164 (in Chinese with English abstract)
 Zhu XP, Chen HA, Ma DF, Huang HX, Li GM, Liu CQ, Wei LJ (2012) ⁴⁰Ar/³⁹Ar Dating for K-feldspar from Duobuza Porphyry Copper-gold Deposit in Tibet, China and its Geological Significance. *Geoscience*, 26: 656-662 (in Chinese with English abstract)

Fluid inclusion and H, O, C, and Sr isotopes of Jinman-Liancheng vein Cu deposit in Lanping basin, Yunan, China: constraints on mineralization T-P-X conditions and source of the ore-forming fluid

Yucai Song, Zengqian Hou, Wang Guanghui

Institute of Geology, Chinese Academy of Geological Sciences, Beijing 100037, China

Chuangdong Xue

Kunming University of Science and Technology, Kunming 650093, China

Abstract. Various viewpoints on mineralization T-P-X conditions and source(s) of the ore-forming fluid have been proposed for the Jinman-Liancheng vein Cu deposit. New fluid inclusion (FI) and isotope studies indicate that the ore-forming fluid is a CO₂-bearing aqueous fluid system. It has the mineralization temperature of 180–260 °C and the salinity of 6–15 wt% NaCl eq. determined by homogeneously trapped FIs but not by heterogeneously trapped FIs that have the homogenization temperature of 184 to >300 °C. It estimates that the trapping pressure is lower than ~1150 bar and the CO₂/H₂O molar ratio is lower than ~0.05. The calculated $\delta^{18}\text{O}_{\text{SMOW}}$ values (2.4–10.1 ‰) of water from FIs basically match but the $\delta\text{D}_{\text{SMOW}}$ values (90–111 ‰) are lower than those of metamorphic water and “primary” magmatic water; The $\delta^{13}\text{C}_{\text{PDB}}$ values of -4‰ to -7‰ from hydrothermal carbonate are similar to those of CO₂ from magma, mantle, or metamorphic devolatilization of rocks; Initial $^{87}\text{Sr}/^{86}\text{Sr}$ values of 0.709426 to 0.713073 from the hydrothermal carbonates intersect with those of adjacent Paleogene granites at ^{87}Sr -rich end member. Synthetically, the isotopic compositions suggest that the ore-forming fluid originates from degassed (in open system) magmatic fluid from deep-seated Paleogene granites along Lancangjiang fault.

Keywords. Vein Cu deposit; fluid inclusions; Isotopes; mineralization conditions; source of ore-forming fluid; Jinman-Liancheng; Yunan

1 Introduction

Sediment-hosted (or metamorphosed) base metal vein-type deposits occur in many orogenic belts worldwide (Beaudoin and Sangster, 1992) but are poorly known in Himalaya-Tibet collision zone (HTCZ). The Lanping basin of the northern Lanping-Simao terrane in eastern HTCZ, hosts a number of sediment-hosted base metal vein-type deposits including the Jinman-Liancheng deposit (>0.2 Mt Cu metal with grade of 0.65–12.0%). Previous studies, mainly focused on the Jinman ore block, yield various viewpoints on mineralization T-P-X conditions and source(s) of the ore-forming fluid. This study performed fluid inclusion and systematic H-O-C-Sr isotope investigations for the Liancheng ore block as well as the Jinman ore block, aiming to give new insights into the mineralization conditions and the ore-forming fluid source(s).

2 Geological setting

Abundant quartz-carbonate-Cu sulphide veins are developed along the Lancangjiang fault in the western margin of the Lanping basin, western Yunnan. Wherein, the Jinman-Liancheng Cu deposit is the largest one so far. Sedimentation in the Lanping basin began with Middle- and Late-Triassic volcanic rocks and marine-facies sedimentary rocks, followed by Middle-Jurassic to Pliocene terrestrial-dominated red beds. Triassic and Paleocene to Eocene (55–38 Ma) granites are distributed along the Lancangjiang fault, which are metamorphosed into mylonite by followed ~N-S trending strike-slip shear (Zhang et al., 2010). Regional strike-slip also triggered 42–24 Ma high-potassic magmatic activities along the Jinshajing-Ailaoshan fault zone (east to the Lanping basin) (Wang et al. 2001).

3 Deposit Geology and Mineralization

The Jinman and the Liancheng ore blocks separate from each other about 3 km in the SSW-NNE direction. The former is about 500 m lower in elevation than the latter. Rocks in the Jinman-Liancheng deposit are composed of red clastics and slate of Middle-Jurassic Huakaizuo Formation and Bazhulu Formation. They are strongly deformed to form NNE-trending reversed folds with intense cleavages.

The NNE-striking and steeply W-dipping ore veins with thickness of < 1 centimetre to tens of centimetres are mainly filled in the cleavages as isolated tabular veins. Some ore veins are shown as echelon arrays and stockworks. Hydrothermal minerals in the veins include chalcopyrite, bornite, tennantite, and tetrahedrite, quartz, calcite, ankerite, sericite, and rare graphite.

Six molybdenite samples as alteration halos of Cu sulphide-bearing veins from the Liancheng block determine that the well-constrained Re-Os isochron is 49.0±1.3 Ma (MSWD=10.1) (Wang et al. 2009). It implies that Cu mineralization is ~49 Ma and hence is under the tectonic setting of Indian-Asian continent-continent collision (Hou and Cook 2009).

4 Fluid inclusion study

Abundant of CO₂-bearing fluid inclusions were found in hydrothermal quartz from the ore veins. They can be classified into two types: type A CO₂-bearing aqueous and type B CO₂ fluid inclusions (Fig. 1a). Type A fluid inclusions were trapped homogeneously (having approximate constant vapor/liquid ratio) (Fig. 1c) or heterogeneously (having variable vapor/liquid ratio) (Figs. 1a, b, d) in single fluid inclusion assemblage (FIA). CO₂, without other detectable nonaqueous volatiles, is identified by laser Raman analysis in the vapor phase of type A fluid inclusion, even in those having small vapor/liquid ratios. Microthermometric measurements obtain total homogenization temperature of 180/190-260 °C and the salinity of 6-15 wt% NaCl eq. for homogeneously trapped those in several FIAs (Fig. 2). Homogenization temperatures of heterogeneously trapped fluid inclusions vary from 184 to >300 °C but only the minimum temperature approximately represents their trapping temperature (Fig. 2).

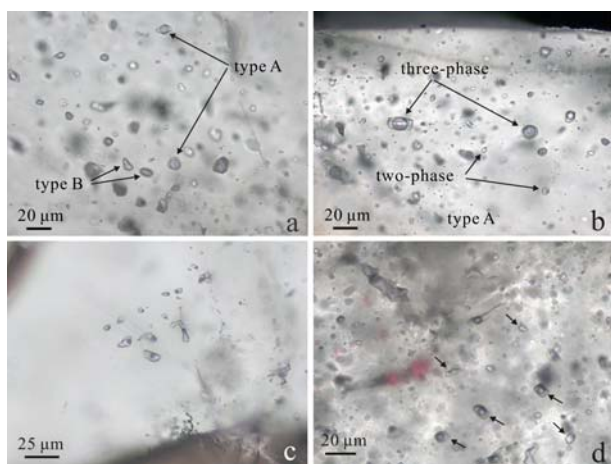


Figure 1. Photographs of fluid inclusions in hydrothermal quartz. (a) Type A CO₂-bearing aqueous fluid inclusions coexisting with type B CO₂ fluid inclusions; (b) two- and three-phase type A fluid inclusions. (c) clustered primary fluid inclusions having approximately constant vapor/liquid ratios; (d) clustered primary fluid inclusions having variable vapor/liquid ratios. Fluid inclusions in (a), (b), and (d) are interpreted to be heterogeneously trapped; those in (c) are interpreted to be homogeneously trapped

The homogenization temperature and the salinity, combining with several factors below, are used to estimate the trapping pressure and bulk composition of the ore-forming fluid. Firstly, microthermometric data of homogeneously and heterogeneously trapped fluid inclusions indicate that the fluid system is in liquid + vapor two-phase zone when temperature is lower than ~190 °C in the Liancheng block. The fluid system lies in the two-phase zone when temperature is lower than ~180 °C in the Jinman block, interpreted from our data and Chi and Xue's (2011) data. Secondly, the trapping pressure in the Jinman block is ~140 bar higher than that in the Liancheng block under lithostatic condition (Fig. 3). Under these conditions, the CO₂/H₂O molar ratio is ~0.03-0.04 and the trapping pressure is 794-1144 bar if the compositions of the ore-forming fluids are same for

both ore blocks. If the compositions are different, the geothermal gradient determines that the maximum CO₂/H₂O molar ratio is ~0.049 and the maximum pressure is ~1524 bar (Fig. 3).

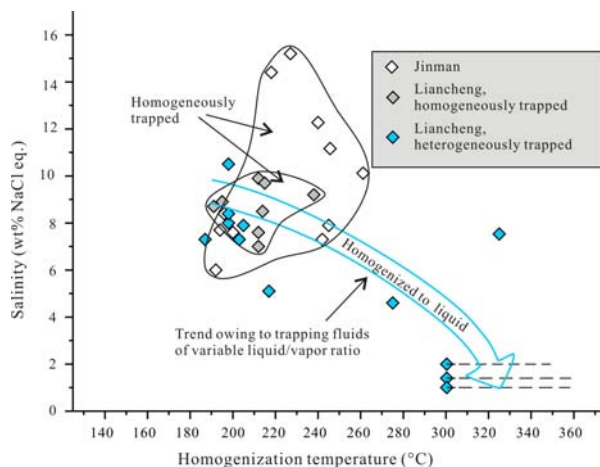


Figure 2. Diagram of salinity vs. homogenization temperature of type A fluid inclusions. Broken line extending from blue filled diamond means that the homogenization temperature is higher than the starting point. Owing to trapping fluids of variable liquid/vapor ratio, heterogeneously trapped fluid inclusions have highly variable salinities and homogenization temperatures where the minimum homogenization temperature approximately represents the trapping temperature

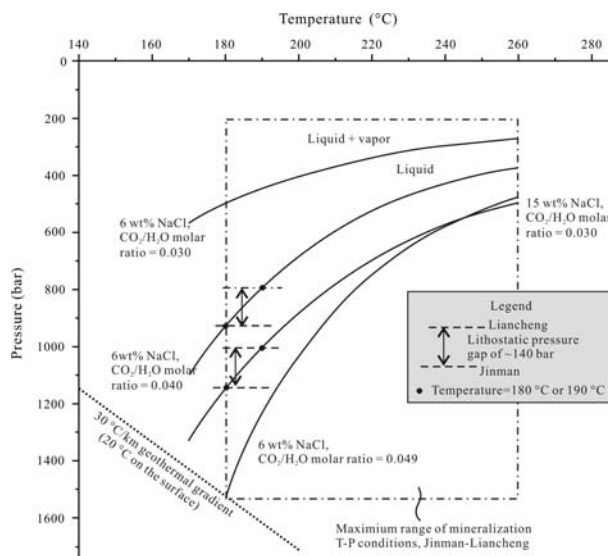


Figure 3. Solvus for a NaCl-H₂O-CO₂ system with different bulk compositions in P-T space. The solvus are determined using the model of calculating CO₂ solubility in aqueous NaCl solutions (Duan and Sun, 2003, <http://calc.geochem-model.org/Pages/Solubility.aspx>). The single-phase zone and the liquid + vapor two-phase zone are separated by the solvus. Temperature of the ore-forming fluid is normally higher than that of country rocks, so the T-P conditions are supposed to be above the geothermal gradient line in the diagram.

5 H-O-C-Sr isotopic study

This study obtains the δ¹⁸O_{SMOW} values of 15.4‰ to 17.2‰ and the δD_{SMOW} values of -90‰ to -111‰ for

hydrothermal quartz in both ore blocks. Assuming that the mineralization temperatures range from 180 °C to 260 °C, the calculated $\delta^{18}\text{O}_{\text{SMOW}}$ values of water are 2.4‰ to 10.1‰. The values are basically match but the $\delta\text{D}_{\text{SMOW}}$ values are lower than those of metamorphic water and “primary” magmatic water (Fig. 4); The $\delta^{13}\text{C}$ values (-4‰ to -7‰ relative to PDB) of hydrothermal carbonate minerals (mixtures of calcite and ankerite) are similar to those of CO_2 from magma, mantle, or metamorphic devolatilization of rocks but differ from those of reduced carbon, marine carbonates, or dissolution/decarbonation of marine carbonates; Initial Sr isotopic compositions of hydrothermal carbonates (0.709426 to 0.713073) intersect with those of adjacent Paleogene granites at $^{87}\text{Sr}/^{86}\text{Sr}$ -rich end member but apparently differ from those of Paleogene intrusions along Jinshajiang-Ailaoshan fault zone, host rocks, and potential pathway rocks (Fig. 5). Together, the isotopic systematics suggests that the ore-forming fluid sourced from degassed (in open system) magmatic fluid from deep-seated Paleogene granites along the Lancangjiang fault.

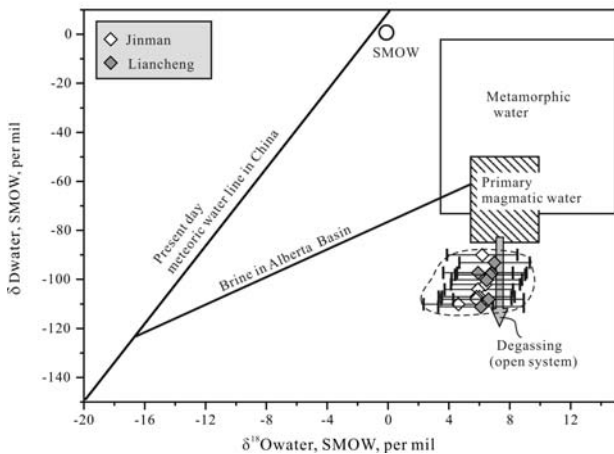


Figure 4. Plot of δD vs. $\delta^{18}\text{O}$ values of hydrothermal water. The field of metamorphic water is calculated for water in equilibrium with metamorphic silicate minerals at temperatures of 300-600 °C (Misra 2000). The field of primary magmatic water is calculated for water in equilibrium with “normal” igneous rocks at temperatures ≥ 700 °C (Taylor et al. 1974). The present meteoric water in China defines the compositions of meteoric water (Chen et al. 2004). The isotopic compositions of brine in the Alberta Basin are from Longstaffe (2000). SMOW represents standard mean ocean water. Uncertainties of the $\delta^{18}\text{O}$ values are caused by calculation using variable equilibrium temperatures (180-260 °C, homogenization temperatures of fluid inclusions)

6 Conclusions

The ore-forming fluid in the Jinman-Liancheng vein Cu deposit is characterized by a water- CO_2 -salt system that was homogeneously and heterogeneously trapped in fluid inclusions. It has the salinity of 6-15 wt% NaCl eq. and the mineralization temperature of 180-260 °C. It estimates that the trapping pressure is lower than ~1150 bar and the $\text{CO}_2/\text{H}_2\text{O}$ molar ratio is lower than ~0.05. The ore-forming fluid origins from degassed (in open

system) magmatic fluid from deep-seated Paleogene granites along the Lancangjiang fault.

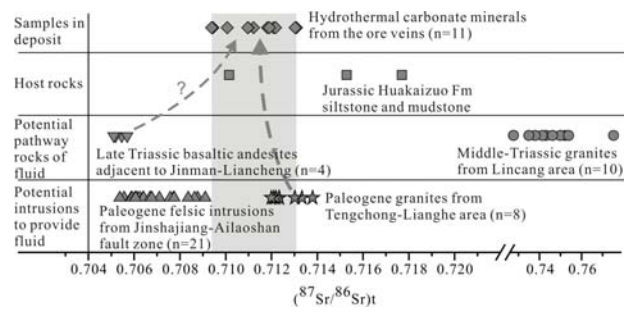


Figure 5. Initial $^{87}\text{Sr}/^{86}\text{Sr}$ ratios of hydrothermal carbonate minerals and regional rocks. n denotes numbers of samples. $^{87}\text{Rb}/^{86}\text{Sr}$ ratios of the Jinman and the Liancheng samples are calculated using maximum Rb/Sr ratio of hydrothermal carbonate minerals analyzed by Li and Pu (2000). $(^{87}\text{Sr}/^{86}\text{Sr})_t$ ratios of carbonate minerals in the Jinman and the Liancheng, Late Triassic andesites, Middle Jurassic Huakaizuo Fm clastics, and Middle Triassic granites were calculated assuming mineralization age of $t=45$ Ma. $(^{87}\text{Sr}/^{86}\text{Sr})_t$ ratios of Paleogene granites adjacent to the Lancangjiang fault represent the initial values where t ranges from 58.9 Ma to 41.8 Ma. $(^{87}\text{Sr}/^{86}\text{Sr})_t$ ratios of Paleogene felsic intrusions along the Jinshajiang-Ailaoshan fault zone are present day values ($t=0$ Ma), because Rb and Sr content data of whole rocks are partially lack. Data for Middle-Triassic granites from Lincang area, Paleogene felsic intrusions from Jinshajiang-Ailaoshan fault zone, and Paleogene granites from Tengchong-Lianghe area are collected from Zhang et al. (1990), Henning et al. (2009), Chen (1991), Yang et al. (2006, 2009), Hou et al. (2008), Zhang and Xie (1997), Zeng et al. (2002), and Dong et al. (2007)

Acknowledgements

This study is financially supported by the State Key Research Development Program of China (2009CB421008), the IGCP /SIDA 600 project, the Union Fund of USFC-Yunnan Province (No. U0933605), and the National Nature Science Fund (No. 41273050).

References

- Beaudoin G, Sangster DF (1992) A descriptive model for silver-lead-zinc veins in clastic metasedimentary terranes. *Econ Geol* 87(4): 1005–1021
- Chen Q-C (1991) Characteristics of Pb, Sr, isotopic compositions in west Yunnan granites discussion on the age and nature of the basement in west Yunnan. *Scientia Geologica Sinica* 2: 174–183 (in Chinese with English abstract)
- Chen Y, Pirajno F, Sui Y (2004) Isotope geochemistry of the Tieluping silver-lead deposit, Henan, China: a case study of orogenic silver-dominated deposits and related tectonic setting. *Miner Depos* 39: 560–575
- Chi G, Xue C (2011) Abundance of CO_2 -rich fluid inclusions in a sedimentary basin-hosted Cu deposit at Jinman, Yunnan, China: implications for mineralization environment and classification of the deposit. *Miner Depos* 46: 365–380
- Chi G, Xue C, Lai J, Qing H (2007) Sand injection and liquefaction structures in the Jinding Zn-Pb deposit, Yunnan, China: Indicators of an overpressured fluid system and implications for mineralization. *Econ Geol* 102: 739–743
- Dong F, Mo X, Yu X, Hou Z, Wang Y (2007) Trace elements geochemical and Nd-Sr-Pb isotopes characteristics of the Zhuopan alkaline complex in Yongping, Yunnan Province and

- its geological significance. *Acta Petrologica Sinica* 23:986–994 (in Chinese with English abstract)
- Duan Z, Sun R (2003) An improved model calculating CO₂ solubility in pure water and aqueous NaCl solutions from 273 to 533 K and from 0 to 2000 bar. *Chem Geol* 193: 257–271
- Hennig D, Lehmann B, Frei D, Belyatsky B, Zhao XF, Cabral AR, Zeng PS, Zhou MF, Schmidt K (2009) Early Permian seafloor to continental arc magmatism in the eastern Paleo-Tethys: U-Pb age and Nd-Sr isotope data from the southern Lancangjiang zone, Yunnan, China. *Lithos* 113: 408–422
- Hou Z, Cook NJ (2009) Metallogenesis of the Tibetan collisional orogen: a review and introduction to the special issue. *Ore Geol Rev* 36:2–24
- Hou Z, Wang E, Mo X, Ding L, Pan G, Zhang Z (2008) Metallogenesis of the Tibetan collisional orogen. Geological Publishing House, Beijing, pp 1–980 (in Chinese with English abstract)
- Li F, Fu W-M (2000) Geology of red-bed Cu deposits, western Yunnan. Yunnan University Press, Kunming, pp 1–133 (in Chinese)
- Longstaffe FJ (2000) An introduction to stable oxygen and hydrogen isotopes and their use as fluid tracers in sedimentary systems. *Mineralogical Association of Canada Short Course* 28: 115–119
- Misra KC (2000) *Understanding Mineral Deposits*. Kluwer Academic Publishers, London, pp 1–845
- Wang G, Song Y, Hou Z, Wang X, Yang Z, Yang T, Liu Y, Jiang Y, Pan X, Zhang H, Liu Y, Li Z, Xue C (2009) Re-Os dating of molybdenite from Liancheng vein copper deposit in Lanping basin and its geological significance. *Miner Depos*, 28: 413–424 (in Chinese with English abstract)
- Wang JH, Yin A, Harrison TM, Grove M, Zhang YQ, Xie GH (2001) A tectonic model for Cenozoic igneous activities in the eastern Indo-Asian collision zone. *Earth and Planet Sci Lett* 188: 123–133
- Yang Q-J, Xu Y-G, Huang X-L, Luo Z-Y (2006) Geochronology and geochemistry of granites in the Gaoligong tectonic belt, western Yunnan: Tectonic implications. *Acta Petrologica Sinica* 22:817–834 (in Chinese with English abstract)
- Yang Q-J, Xu Y-G, Huang X-L, Luo Z-Y, Shi Y-R (2009) Geochronology and geochemistry of granites in the Tengliang area, western Yunnan: Tectonic implication. *Acta Petrologica Sinica* 25:1092–1104 (in Chinese with English abstract)
- Zeng P, Mo X, Yu X (2002) Nd, Sr and Pb isotopic characteristics of the alkaline-rich porphyries in western Yunnan and its compression strike-slip setting. *Acta Petrologica et Mineralogica* 21: 231–241
- Zhang B, Zhang J, Zhong D (2010) Structure, kinematics and ages of transpression during strain-partitioning in the Chongshan shear zone, western Yunnan, China. *J of Struct Geol* 32: 445–463
- Zhang Y, Xie Y (1997) Geochronology of Ailaoshan-Jinshajiang alkali-rich intrusive rocks and their Sr and Nd isotopic characteristics. *Science in China Series D: Earth Sci* 40: 524–529
- Zhang Y, Xie Y, Wang J (1990) Rb and Sr isotopic studies of granitoids in Tri-river region. *Geochimica* 4: 318–326 (in Chinese with English abstract)

Rb-Sr and Sm-Nd isochron ages of the Dongmozhazhua and Mohailaheng Pb-Zn ore deposits in the Yushu area, southern Qinghai and geological implications

Shihong Tian

Key Laboratory of Metallogeny and Mineral Assessment, MLR, Institute of Mineral Resources, Chinese Academy of Geological Sciences, Beijing 100037, China; School of Earth Science and Mineral Resources, China University of Geosciences, Beijing 10083, China

Zengqian Hou, Yingchao Liu, Yucai Song

Institute of Geology, Chinese Academy of Geological Sciences, Beijing 100037, China

Zhusen Yang

Institute of Mineral Resources, Chinese Academy of Geological Sciences, Beijing 100037, China

Abstract. The Dongmozhazhua and Mohailaheng Pb-Zn deposits in the Yushu area of the Qinghai Province are representative Pb-Zn deposits of the Cu-Pb-Zn polymetallic mineralization belt in the northern part of the Nujiang-Lancangjiang-Jinshajiang area, which are in the front belt of the Yushu thrust nappe system. The age of the Dongmozhazhua deposit has been determined by the Rb-Sr isochron method for sphalerite, whereas the age of the Mohailaheng deposit has been determined by the Rb-Sr isochron method for sphalerite and the Sm-Nd isochron method for fluorite. The age of the Dongmozhazhua deposit is 35.015 ± 0.034 Ma ($(^{87}\text{Sr}/^{86}\text{Sr})_0=0.708807$) for sphalerite. The age of the Mohailaheng deposit is 32.22 ± 0.36 Ma ($(^{87}\text{Sr}/^{86}\text{Sr})_0=0.708514$) for sphalerite and 31.75 ± 0.28 Ma ($(^{143}\text{Nd}/^{144}\text{Nd})_0=0.512362$) for fluorite with an average of 32 Ma. Together with the regional geological setting during mineralization, a possible tectonic model for metallogeny of the Dongmozhazhua and Mohailaheng Pb-Zn deposits has been established. These two ages are close to the ages of the Pb-Zn deposits in the Lanping and Tuotuohe basins, indicating that it is possible that the narrow 1000-kilometer-long belt controlled by a thrust nappe system in the eastern and northern margins of the Tibetan Plateau could be a giant Pb-Zn mineralized belt.

Keywords. Rb-Sr and Sm-Nd isochron ages, thrust nappe system, tectonic model, Dongmozhazhua and Mohailaheng Pb-Zn deposits in the Yushu area, Qinghai Province

1 Introduction

Hou et al. (2008) infer that the northeast margin of the Tibetan Plateau developed a 1000-kilometer-long giant Pb-Zn-Cu-Ag metallogenic belt controlled by the Cenozoic thrust nappe structure (Fig.1). The formation mechanism of the mineralization, ore genetic types, metallogenic model, exploration model and the exact age of the mineralization have become an urgent need to address key scientific issues. In order to further constrain the mineralization age of the giant Pb-Zn metallogenic belt and identify the deposit genetic types of the Qinghai-Tibet Plateau, the Dongmozhazhua and Mohailaheng Pb-Zn ore deposits in the Yushu basin were chosen to carry out the study of Rb-Sr (sphalerite) and Sm-Nd (fluorite) geochronology.

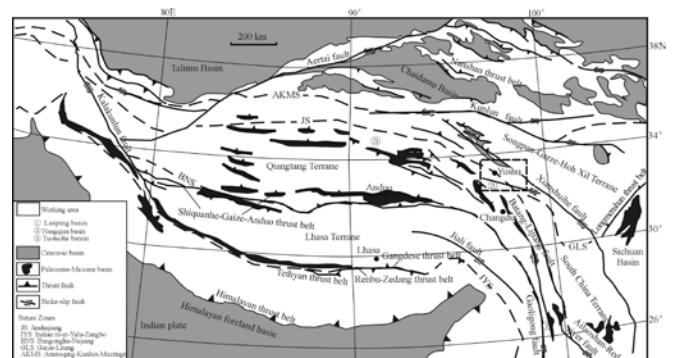


Figure 1. Sketch tectonic map of the Tibetan collision belt and locations of the study zones (Modified after Spurlin et al., 2005; Hou et al., 2008)

2 Geological setting

The Dongmozhazhua and Mohailaheng Pb-Zn ore deposits are located in the Yushu basin of the Qiangtang terrane, which is controlled by the north-east Qinghai-Tibet Plateau collisional orogen tectonics and the Jinshajiang and Bangonghu-Nujiang suture belts (Yin et al., 2000; Spurlin et al., 2005). The outcropping strata in the region include Paleozoic, Mesozoic, and Cenozoic units. The crustal shortening accompanied with the collisional orogeny resulted in thin-skinned deformation on the northern and eastern Tibetan Plateau, which is characterized by the thrusting nappe structure (Figure 1). Meanwhile, the Triassic and Jurassic-Cretaceous strata were thrust and/or placed on top of the Tertiary units. Major thrusting is separated into two episodes, at 55-50 Ma corresponding with the main collisional episode of the Qinghai-Tibet Plateau, and at 40-37 Ma corresponding with late collision (Hou et al., 2006a; 2006b; 2008). The thrust nappe structure is well developed in the Lanping, Yushu and Tuotuohe areas as a result of major tectonic deformation of the eastern and northern Tibetan Plateau. Mesozoic strata were cut by a series of thrust faults into tectonic slices successively stacked, and then pushed on top of sedimentary strata in the foreland basin, which controlled the formation and distribution of base metal sulphide deposits in the northern and eastern part of the plateau.

3 Deposit Geology

Dongmohazhua Pb-Zn ore deposit There are four known mineralized zones, and the amount of lead and zinc resources is up to 800,000 tons or more. The outcropping strata in the mine region are simple, including lower-middle Permian Kaixinling group, upper Triassic Jiezhaqun group and Quaternary cover. In the mine region, there are three trends of thrust or strike-slip faults (NWW, NE, NEE striking). Alteration related to mineralization includes dolomitization, carbonatization, pyritization, and silicification. The ore body geometry is stratiform and lenticular, with pinches and swells. Mineral assemblages are simple. The ore minerals include sphalerite, galena, pyrite, marcasite, with rare chalcopyrite and tennantite. The gangue minerals include barite, dolomite, calcite, quartz, sericite, halloysite, dickite, and asphalt. The ore textures include anhedral granular, colloform, euhedral granular, metasomatic, and re-crystallized textures. The mineralization styles include brecciated, disseminated, vein, and massive structures. Drilling catalog and petrographic studies indicate five stages of hydrothermal activity in the Dongmohazhua Pb-Zn ore deposit, including a dolomitization stage, baritization stage, polymetallic sulphide stage (pyrite-galena-sphalerite), calcite stage, and clay stage. The polymetallic sulphide stage is the main mineralization stage.

Mohailaheng Pb-Zn ore deposit There are also four known mineralized zones in the Mohailaheng deposit. The outcropping strata in the mine region only include a Lower Carboniferous group and Paleogene group. In the mine region, there are two sets of faults (NW, NE striking). Alteration styles related to mineralization include dolomitization, silicification, sericitization, baritization, fluoritization, pyritization, and carbonatization. The ore body shows stratiform and lenticular geometry, with pinches and swells. Mineral assemblages are simple. The ore minerals include sphalerite, galena, and pyrite. The gangue minerals include barite, fluorite, dolomite, calcite, quartz, sericite, halloysite, dickite, and asphalt. The ore textures include colloform, spherical, euhedral granular, euhedral-subhedral granular, and re-crystallized textures. The mineralization styles include disseminated, vein, massive, and brecciated structures. Drilling catalog and petrographic studies indicate five stages of hydrothermal activity in the Mohailaheng Pb-Zn ore deposit, including a dolomitization stage, baritization stage, polymetallic sulphide stage (pyrite-galena-sphalerite), calcite stage, and clay stage. The polymetallic sulphide stage is the main mineralization stage.

4 Results

Rb-Sr content and isotopic compositions of single sphalerite crystals from the Dongmohazhua Pb-Zn ore deposit have been analyzed. Figure 2A shows good positive correlation between $^{87}\text{Rb}/^{86}\text{Sr}$ and $^{87}\text{Sr}/^{86}\text{Sr}$. The Rb-Sr isochron age of sphalerite is 35.015 ± 0.034 Ma, the initial Sr isotope composition (I_{Sr}) is 0.708807, MSWD=3.8.

Rb-Sr content and isotopic compositions of single sphalerite crystals and Sm-Nd content and isotopic compositions of single fluorite crystals from the Mohailaheng Pb-Zn ore deposit have been analyzed. Figure 2B shows good positive correlation between $^{87}\text{Rb}/^{86}\text{Sr}$ and $^{87}\text{Sr}/^{86}\text{Sr}$. The Rb-Sr isochron age of sphalerite is 32.22 ± 0.36 Ma, the initial Sr isotope composition (I_{Sr}) is 0.708514, MSWD=2.9. Figure 2C shows very good positive correlation between $^{147}\text{Sm}/^{144}\text{Nd}$ and $^{143}\text{Nd}/^{144}\text{Nd}$. Sm-Nd isochron age of fluorite is 31.75 ± 0.28 Ma, the initial Nd isotope composition (I_{Nd}) is 0.512362, MSWD=1.07.

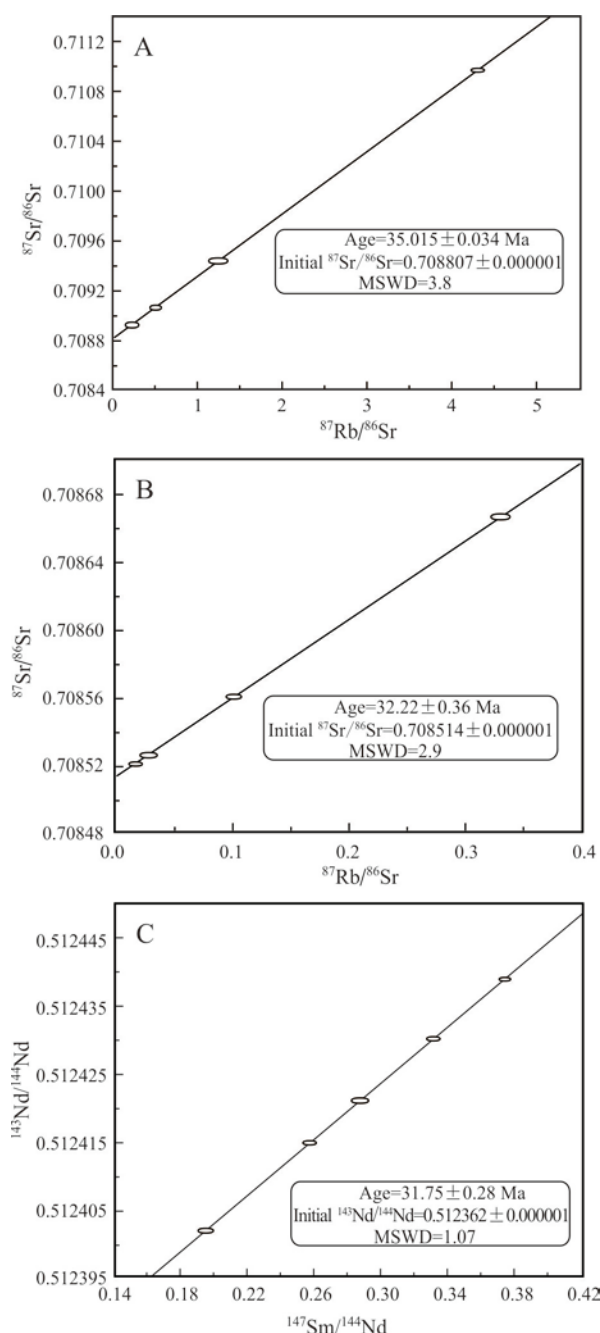


Figure 2. Rb-Sr isochron for sphalerite (A) from the Dongmohazhua Pb-Zn deposit, Rb-Sr isochron for sphalerite (B) and Sm-Nd isochron for fluorite (C) from the Mohailaheng Pb-Zn deposit

5 Discussions

Through five years of systematical research, the “India-

Asia collision zone mineralization” 973 project group has explained the Cenozoic orogenic processes of the Tibet Plateau in detail. The main collision stage was characterized by continent-continent collision and steep subduction from 65~41 Ma, the late collision stage characterized by intracontinental low-angle subduction and edge exchange orogeny from 40~26 Ma, and the post-collisional stage characterized by east-west extension and Zangnan detachment from 25~0 Ma (Hou et al., 2006a, 2006b, 2006c). The ore-forming ages of the Dongmozhazhua and Mohailaheng deposits show that they formed during the late collision stage of the Tibet Plateau, accompanied with intracontinental strike-slip, thrust nappe, and large-scale shearing. The metallogenic ages are just at the end of the large-scale thrust nappe period (40~37 Ma; Hou et al., 2006a), and the beginning of strike-slip faulting in Yushu in the Northeast Tibet Plateau (37 Ma; Spurlin et al., 2005). This indicates the close relationship between mineralization and regional thrust and strike-slip faulting.

The thrust nappe structure is significant to the formation and distribution of Pb-Zn and Ag polymetallic mineralization in Southern Qinghai Province (Hou et al., 2008). The thrust nappe structure can be divided into the root zone, middle belt, and front belt. These thrust faults dip south and gradually become shallower at depth to form a unified detachment zone, becoming the main channel and guidance system of the long distance migration of brines (Figure 3a). A Large-scale thrust nappe system not only provides a power source for the long distance migration of fluid, but also acts as the guidance system of ore-forming fluid migration and localization of metal aggregation and deposition. Long-distance migration of fluid is the premise of forming hydrothermal deposits (Oliver, 1986; Leach et al., 2005). This tectonic system also releases a large volume of fluid that reacts with carbonate rock, leaching metal in volcanic strata and forming fluid enriched in Pb and Zn during migration in tertiary basins. Ore-forming fluid entered into the Dongmozhazhua and Mohailaheng Pb-Zn ore district through thrust fault and strike-slip fault networks and mixed with pre-existing H₂S-rich fluid reservoirs, which led to precipitation of sulphide to form the ore near fractured and open space (Figure 3b).

6. Conclusions

- (1) The Dongmozhazhua and Mohailaheng Pb-Zn deposits are products of synchronous-isogenic mineralization and show consistent metallogenic ages of 35 Ma and 32 Ma, respectively.
- (2) Combined with the regional geological background, the ore-controlling structure model of the two investigated Pb-Zn ore deposits can be well established.

Acknowledgements

This study is financially supported by the State Key Research Development Program of China (2011CB403104, 2009CB421007, 2009CB421008), the IGCP/SIDA 600 project, the Union Fund of USFC-Yunnan Province (No. U0933605), and the National

Nature Science Fund (No. 41273035).

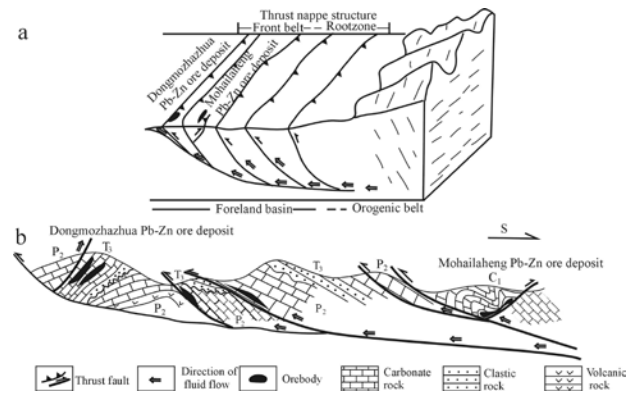


Figure 3. A tectonic model of metallogeny of Dongmo-zhazhua and Mohailaheng Pb-Zn deposits
a-A mineralization model diagram of Dongmozhazhua and Mohailaheng Pb-Zn deposits (Modified from Hou et al., 2008); b-A schematic diagram of metallogeny of Dongmozhazhua and Mohailaheng Pb-Zn deposits

References

- Hou ZQ, Pan GT, Wang AJ, Mo XX, Tian SH, Sun XM, Ding L, Wang EQ, Gao YF, Xie YL, Zeng PS, Qin KZ, Xu JF, Qu XM, Yang ZM, Yang ZS, Fei HC, Meng XJ and Li ZQ (2006b) Metallogenesis in Tibetan collisional orogenic belt: Mineralization in late-collisional transformation setting. *Mineral Deposits* 25: 521–543 (in Chinese with English abstract)
- Hou ZQ, Qu XM, Yang ZS, Meng XJ, Li ZQ, Yang ZM, Zheng MP, Zheng YY, Nie FJ, Gao YF, Jiang SH and Li GM (2006c) Metallogenesis in Tibetan collisional orogenic belt: Mineralization in post-collisional extension setting. *Mineral Deposits* 25: 629–651 (in Chinese with English abstract)
- Hou ZQ, Song YC, Li Z, Wang ZL, Yang ZM, Yang ZS, Liu YC, Tian SH, He LQ, Chen KX, Wang FC, Zhao CX, Xue WW and Lu HF (2008) Thrust-controlled, sediments-hosted Pb-Zn-Ag-Cu deposits in eastern and northern margins of Tibet anorogenic belt: Geological features and tectonic model. *Mineral Deposits* 27: 421–441 (in Chinese with English abstract)
- Hou ZQ, Yang ZS, Xu WY, Mo XX, Ding L, Gao YF, Dong FL, Li GM, Qu XM, Li GM, Zhao ZD, Jiang SH, Meng XJ, Li ZQ, Qin KZ and Yang ZM (2006a) Metallogenesis in Tibetan collisional orogenic belt: Mineralization in main collisional orogenic setting. *Mineral Deposits* 25: 337–358 (in Chinese with English abstract)
- Leach D L, Sangster D F, Kelley K D, Large R R, Garven G, Allen C R, Gatzmer J and Walters S (2005) Sediment-Hosted Lead-Zinc Deposit: A Global Perspective. *Economic Geology* 100th Anniversary Volume: 561–607
- Oliver J (1986) Fluids expelled tectonically from the orogenic belts: Their role in hydrocarbon migration and other geological phenomena. *Geology* 14: 99–102
- Spurlin MS, Yin A, Horton BK, Zhou JY and Wang JH (2005). Structural evolution of the Yushu-Nangqian region and its relationship to syn-collisional igneous activity, east-central Tibet. *GSA Bulletin* 117: 1293–1317
- Yin A and Harrison TM (2000) Geologic evolution of the Himalayan-Tibetan orogen. *Annual Review of Earth and Planetary Sciences* 28: 211–280

Metallogenesis of the Au-Ag Middle Palaeozoic Kedon Volcanic Belt of the Omolon Cratonic Terrane (Northeast Russia)

A. V. Volkov, A. A. Sidorov, V. Yu. Alexeev

Institute of Geology of Ore Deposits, Petrography, Mineralogy, and Geochemistry, Russian Academy of Sciences, Moscow, Russia

N. E. Savva

Northeastern Interdisciplinary Research Institute, Far East Division, Russian Academy of Sciences, Magadan, Russia

Abstract. Within the Omolon cratonic terrane the preaccretionary Kedon volcanic belt (KVB) is located, which was formed in the middle Paleozoic (D₂₋₃) on the continental crust. This belt composed of subaerial volcanic rocks extending ~ 400 km. The Kedon part of KVB is characterized by lateral zoning: porphyry Cu mineralization in the east, intrusion related Au and epithermal Au–Ag in the central area, and Au–Ag bearing jasperoides in the west. The important features of the metallogeny of the KVB are as follows: an unusually low sulfide content of Au–Ag epithermal ores (<0.5%); wide development of Au–Ag mineralization in jasperoids; the occurrence of Cu-mineralization in intrusion related Au deposits; and the absence of Sn ore deposits.

Keywords.

Volcanic belts, gold, silver, deposits, genetic features

1 Introduction

The KVB has attracted particular attention due to the discovery of the Kubaka gold deposit, one of the richest in

the world, within this belt. In the period 1998–2007, gold mining at this deposit reached 12–15 tons per year. However, by 2008, the gold reserves had been depleted; in total only 102 tons of gold and the same amount of silver were mined. We suggest that the questions raised in this work on the metallogenesis within the KVB are highly relevant for the prediction of new Kubaka type deposits.

2 Geological setting

According to (Egorov and Sherstobitov 2000) the KVB is a large fragment (400 × (80–130) km) of the Circum-Siberian marginal continental belt. However, the paleo reconstructions made by V.I. Shpikerman (Shpikerman 1998) show that the Kedon volcanic-plutonic belt formed on the margin of the Omolon-Okhotsk micro continent, detached from the Siberian plate. The fragments mapped of the belt preserved within the Okhotsk and Omolon cratonic terranes as well as on Shantar Islands point in favor of this conclusion. Within the Omolon terrane, a fragment of the KVB was studied well. Here, the volcanites of the KVB cover the Precambrian basement

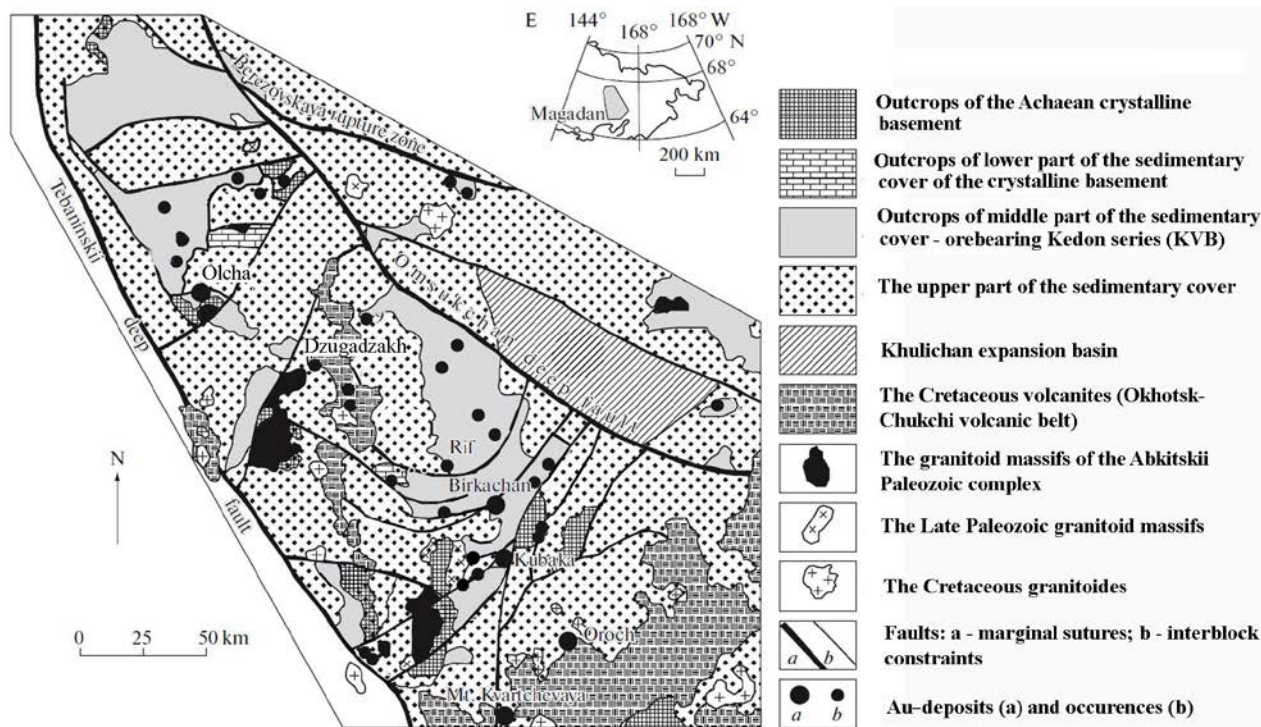


Figure 1. Scheme of gold metallogeny of the Omolon massif.

rocks and Phanerozoic sedimentary cover (Fig. 1). The KVB includes subaerial cover formations of the Kedon series and synchronous subvolcanic and extrusive massifs; its age ranges from the Devonian to the lower part of the early Carboniferous. According to the chemical composition, the volcanic rocks belong to calc-alkaline and moderately alkaline series.

Rocks of KVB lie on the underlying strata with a sharp angular unconformity and monoclinical plunge of no more than 5°–15°. The belt is characterized by the absence of large batholite like intrusions and essential predominance of acidic volcanic rocks. Within the KVB three volcanic areas (Kedon, Rassoshinsky and Tokur-Yuryakh) are distinguished from the southeast to the north. The total thickness of volcanic covers of the largest Kedon area is up to 1500–2000 m in the central area, narrowing in the marginal areas up to 500–1200 m. The age of the rocks of the Kedon complex is 334–377Ma (Kotlyar et al. 2001), according to the Rb–Sr age dating. In the middle Paleozoic ore mineralization typical of marginal continental volcanic plutonic belts was formed.

3 METALLOGENIC ZONING OF THE KVB

The locality of the ore mineralization is characterized by elements of lateral zoning (in modern coordinates): Cu-porphyry mineralization in the east, Au intrusion related and epithermal Au–Ag in the central area, and Au–Ag bearing jasperoides in the west. The KVB belt is characterized by absence of Sn deposits, which are widely developed within the Mesozoic belts.

Porphyry Cu–Mo–Au–Ag ore manifestations are common in the eastern part of the KVB, bordered by the Upper Omolon fault zone. Ore mineralization is located in exo- and endocontact zones of middle Paleozoic granitoid intrusions and subvolcanic rhyolite bodies of the Bulunskii complex, which are characterized by a higher potassium alkalinity. The intrusive rocks of the Bulunskii complex composed of quartz diorites, granodiorites, quartz monzonites, granosyenites, granites, and moderately alkaline granites are of porphyritic and porphyritic texture.

Intrusion related Au–Te–Bi mineralization was found in the Dzhugadzhakh ore field (Fig. 1). Among the sulfides, pyrite with breakdown relics of pyrrhotite and chalcopyrite, as well as chalcopyrite, are predominant. Perhaps we are dealing with transformed ancient Cu-sulfide mineralization, which is characteristic of basic rocks of crystalline Precambrian fundament. Paleozoic Au intrusion related mineralization is characterized by some specific features in comparison with its younger analogs (Table 1).

The major commercial components of ores are Au, Te, and Bi, among which native gold of high fineness

(average 914) is predominant. It intergrows with quartz and tellurides of Au and Bi, and rarely with chalcopyrite. Sometimes, native gold occurs as small inclusions in chalcopyrite. The Cu admixture in Au is >0.1%. Moreover, cuprous gold (Cu content of up to 15%) and native copper were identified in heavy concentrate aureoles.

Epithermal Au–Ag mineralization in the KVB is represented by two types: gold (Au/Ag from 1:1 to 1:5; Kubaka, Birkachan, etc.) and gold_silver (Au/Ag from 1 : 10 to 1 : 50; Yunoe, Ol'cha, etc.). A characteristic feature of both ore types is their low sulfide content (<0.1% and <0.5%, respectively) and poor mineral composition, which ensures high recovery of Au and Ag (95–97%) using a relatively simple technology of Au concentrating. It should be noted that in the ores of the most studied deposits of Kubaka and Birkachan, there are no other ore minerals except gold, electrum, and pyrite. For these deposits, a bimodal age of mineralization (Paleozoic and Mesozoic) (Kotlyar et al. 2001) and bimodal fineness of gold (Savva et al. 2008) were revealed. Ore bodies of some deposits (Kubaka, Birkachan, Yunoe, Burgali, and others) lie within volcanites of the Kedon series or subvolcanic bodies.

Within the deposits with Au–Ag mineralization (the gold type), differentiated volcanic activity (medium to acidic) of the moderate alkaline type (with a predominance of K₂O) over Na₂O is developed.

Structurally, the ore mineralization is confined to the local volcanic structures; typically, they are marginal zones of major depressions or basins, complicated by volcanic structures with subvolcanic bodies of acid composition, exposed in the central part. The metasomatic changes in ore-bearing rocks are as follows: pre ore areal low/medium temperature propylitization and argillization. Near ore quartz–sericite–hydromica and adular–quartz metasomatic rocks do not form large aureoles.

The peculiarities of the Paleozoic epithermal Au–Ag mineralization of the Omolon cratonic block are as follows: polychronic nature of mineralization; low to poor sulfide content in ores; a bimodal distribution of fineness of native gold; a low Au/Ag ratio; the deposition of arsenopyrite after sulfides, polymetals, and native gold; a wide distribution of copper and iron sulfides of the groups of mackinstitriite–yalpaite and shternbergite–shtromeyerite among silver minerals.

The low sulfide content and the presence of hematite in epithermal Ag–Au ore deposits in the KVB allowed us to include them into the ore complex presented by the Precambrian Au-bearing ferruginous quartzites and amphibolites, which are widespread in the Precambrian basement (Sidorov et al., 2009).

Table 1. Comparative characteristics of intrusion related Au deposits of different metallogenic epochs

Deposit	Locality	Age of an intrusion	Metasomatites	Geochemical features of ores	The fineness of native gold
Dzhugadzhak	Near-intrusive	D ₂	Pyrrotinization, epidote, hematite, chlorite	Fe–Cu, Au–Ag–Bi–Te	914
Chepakinskoe	Over-intrusive	J ₁	Greisens, muscovite, tourmaline	Au–As–W–Bi–Te	Invisible gold
Podgornoe	Near-intrusive	K ₁	Tourmaline, chlorite	Fe–Co–As, Ag–Bi–Te	680–800
Basugun'inskoe	Near-intrusive	K _{1–2}	Tourmaline, chlorite, muscovite	Fe–As–Sb, Te–Bi	680–940

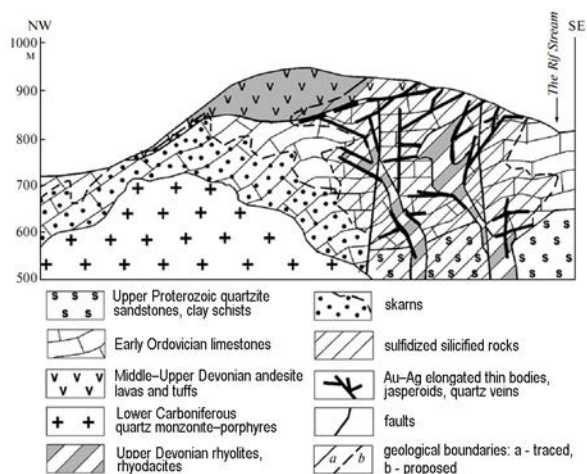


Figure 2. Geological cross-section of the Rif deposit.

Au-Ag bearing jasperoids (Rif, Yagelnoe, Ol'cha, etc.) are widespread only within the KVB, in its marginal parts, where they are controlled by basement uplifts (Fig. 2). Jasperoids formed under the cover of volcanic rocks. They are usually characterized by low (the first g/t) Au contents and highly anomalous Ag contents (from hundreds g/t to 1 kg/t). This is their primary difference from the “Carlin” gold-bearing jasperoides. Only within jasperoids of the Uschel'ninskoe ore field,

4 Discussion

The KVB metallogeny is essentially different from the Devonian volcanic belt of Central Kazakhstan, Kurama, Urals, and other Paleozoic belts in the southern periphery of the Siberian platform, which were formed mainly in the island arc setting (Kurchavov et al. 2002).

However, there are some similarities between the gold and silver metallogeny of the KVB and the Permian-Carboniferous volcanic belt of Eastern Australia (Morrison and Beams 1998). As noted above, the metallogenic characteristics of the KVB, in spite of the poor study of ore formations, are highly different from the Mesozoic volcanic-plutonic zones of northeastern Russia and the Cenozoic volcanic belts of Kamchatka. The latter are characterized by numerous deposits of native sulfur.

The absence of sulfides in ores of the Au–Ag deposits located in the KVB is probably due to deficiency of sulfur in the Archean crystalline rocks of the Omolon cratonic terrane basement.

5 Conclusion

In this work, the important features of the metallogeny of the KVB (northeastern Russia) are shown for the first time. They are as follows: an unusually low sulfide content of ores of the epithermal Au–Ag deposits (<0.5%); wide development of Au–Ag mineralization in jasperoids, overlapped by volcanic rocks, that allows us to predict the gold deposits of the “Carlin” type; the occurrence of Cu mineralization in gold deposits associated with granitoid intrusives; and the absence of Sn ore deposits. fluids and ore components, including Au and Ag, recovered from country rocks. The consecutive manifestation of geological events related to these causes resulted in the formation of inherited, rejuvenated, and often regenerated hypabyssal and near-surface (epithermal) deposits.

Acknowledgements

This study was supported by the Russian Foundation for Basic Research (project nos. 11-05-00006-a)

References

- Egorov VN, Sherstobitov PA (2000) The Kedon volcanic-plutonic association in the south-eastern Omolon massif. Magmatism and metamorphism of Northeast Asia. In Proceeding IV Regional. Petrograph. Conference on the Study of the North-East of Russia, Magadan, SVKNII DVO RAN, pp. 23–29
- Kotlyar IN, Zhulanova IL, Rusakova TB, Gagieva AM (2001) Isotope Systems of magmatic and metamorphic complexes of the North-East of Russia. Magadan, SVKNII DVO RAN, p 319
- Kurchavov AM, Grankin MS, Mal'chenko EG, Khamzin BS, Zhukovskii VI (2002) Metallogenic zonality of the Devonian volcano-plutonic belt in Central Kazakhstan. *Geology of Ore Deposits* 44:18–26
- Morrison GW, Beams SD (1998) *Economic Geology of Northeast Queensland*. Geol. Soc. Australia, Melbourne, pp. 7–38.
- Savva NE, Volkov AV, Sidorov A A (2007) Specific features of ore formation in the epithermal Kubaka gold-silver deposit, Northeast Russia. *Dokl. Earth Sci.* 417:79–83.
- Sidorov AA, Volkov AV, Chekhov AD, Alekseev V Yu (2010) On the metallogenic role of craton terrains in the marginal sea lithosphere. *Dokl. Earth Sci.* 430:523–528.
- Shpikerman VI (1998) Pre-Cretaceous minerageny of the North-East of Asia. SVKNII DVO RAN, Magadan, p 327

Geological and geochemical characteristics of Baiyangping lead-zinc polymetallic deposit in the Sanjiang Neo-Tethyan area, China

Xiao-Hu Wang

Institute of Geomechanics, CAGS, Beijing 100081, China

Zeng-Qian Hou, Yu-Cai Song, Hong-Rui Zhang

Institute of Geology, CAGS, Beijing 100037, China

Abstract. Among the deposits occurring in the collision setting of Tibetan plateau, the sediment-hosted Pb-Zn polymetallic deposits in Sanjiang Neo-Tethyan region is of great importance. We present the mineralization environment, fluid inclusions chemistry, geochemical characteristics, and mineralization age of the Baiyangping deposit. The results show that the deposit formed in a continental collision orogenic environment. The ore-forming fluid was a low temperature and high salinity basinal brine. The carbon was derived from the dissolution of carbonate rocks. Sulfur isotopic composition of sulfide and sulfosalts indicate a sulfur sourced from either thermochemical sulfate reduction or thermal decomposition of organic matter. The ore-forming metals were from basinal sedimentary strata. The Pb-Zn mineralization occurred about 30Ma ~ 29Ma.

Keywords. Geological characteristic; Geochemical characteristic; Baiyangping; Sanjiang-Tethys

1 The geological features

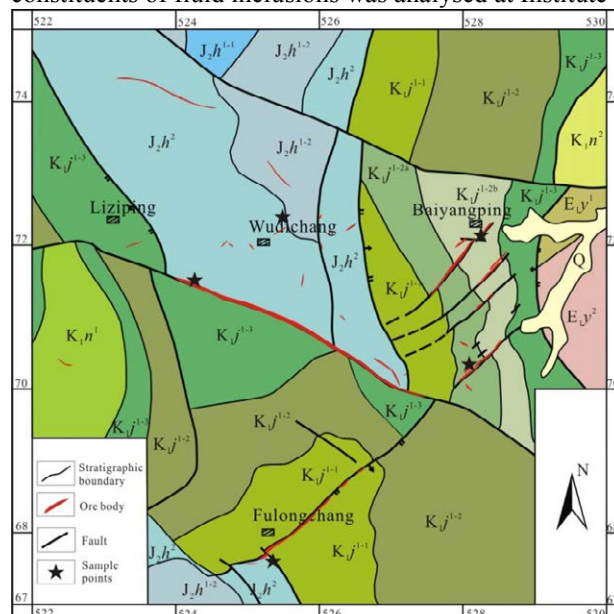
Observations on the deposit geology reveal that Baiyangping Pb-Zn polymetallic deposit in Lanping Basin consists of several ore veins, which can be divided into several ore blocks. The ore bodies in Baiyangping Pb-Zn polymetallic deposit are hosted in Mesozoic sandstone and carbonate rocks and occur in three sets of fault systems. These structural features are oriented nearly north-south, northwest-west and northeast-southwest. The orebodies are fault controlled and show no preference for specific stratigraphic lithologies. The orebodies primarily occur in fault zone, in fracture system, along the cleavage and within areas of wall rocks collapse (Fig.1). Ore textures include breccia, massive sulfide, and vein which indicate the epigenetic mineralization. In different ore blocks, mineral composition and elemental associations vary. In Liziping and Wudichang ore blocks the main minerals include sphalerite, gratonite, galena, jordanite, realgar and orpiment with a Pb-Zn-As-Sb association. In Fulongchang ore blocks the main minerals include sphalerite, jordanite, galena, tetrahedrite series minerals, bourmonite, argentite and kongsbergite, and a Pb-Zn-Cu-Ag association. In Baiyangping ore blocks, the main minerals include tetrahedrite series minerals, chalcocite, chalcopyrite, jordanite, cobaltine, siegenite cobalt-bearing arsenopyrite, galena, sphalerite, and a Cu-Co-As-Zn-Pb association.

2 The Geochemical Characteristics

2.1 Fluid inclusion chemistry

The fluid inclusions in Baiyangping deposit are small, and they have the form of round, oval, irregular shape, etc. Their sizes are generally less than 10 μ m and most of them are gas-liquid two phase inclusions. The

constituents of fluid inclusions was analysed at Institute



J₂h¹⁻¹: the first member of lower Huakaizuo formation;
J₂h¹⁻²: the second member of lower Huakaizuo formation;
J₂h²: the upper of Huakaizuo formation;
K₁j¹⁻¹: the first member of lower Jingxing formation;
K₁j^{1-2a}, K₁j^{1-2a}, K₁j¹⁻²: the second member of lower Jingxing formation;
K₁j¹⁻³: the third member of lower Jingxing formation;
K₁n¹: the lower Nanxing formation;
K₁n²: the upper Nanxing formation;
E₁y¹: the lower Yunlong formation;
E₁y²: the upper Yunlong formation;
Q: the Quaternary

Figure 1. The geological map and distribution of ore bodies in Baiyangping Pb-Zn polymetallic deposit

of Mineral Resources, Chinese Academy of Geological Sciences (CAGS). First, the sample of calcite and sphalerite single mineral particle size of 0.2mm to 0.3mm was selected under a binocular microscope, second, the sample was boiled for 3 to 4 hours with aqua regia at 70 degrees celsius to 80 degrees celsius, then, rinsed 20 times with double distilled water ultrasonic oscillation, placed in an oven at 70 degrees celsius to 80 degrees celsius baked for 4 to 5 hours. The gas chromatography analytical instruments was Shimadzu GC2010 from Japan, the carrier gas was He, the sampling temperature was 100 degrees celsius to 500 degrees celsius for decrepitated inclusions using thermal decrepitation furnace produced by Australia SGE company. The ion chromatographic analytical instrument was Japanese Shimadzu HICSP Super ion chromatograph, the sample handling was same as upside, after sample bursting, the sample was rinsed with

Millipure pure water under ultrasonic oscillations until the leaching lotion conductivity did not change, put into the ion chromatograph for analysis. The standard gas was from the National Standard Material Research Center, China. The minimum detection limit of the gas chromatogram and the cation is 10^{-6} , the anion minimum detection limit is 10^{-9} . Through the analysis of the composition of the fluid inclusions in mineralization stage calcite, the gas phase composition was H_2O , CO_2 , N_2 , O_2 and minor CH_4 , C_2H_2 , C_2H_4 , C_2H_6 , the liquid phase ion component mainly contains Mg^{2+} , Na^+ , K^+ , Cl^- , F^- . The positive ion composition of fluid inclusion in sphalerite was mainly Ca^{2+} , Na^+ , K^+ , Mg^{2+} , anion composed mainly Cl^- , F^- , NO_3^- .

The microthermometry of fluid inclusions was completed at Institute of Geology, CAGS, using Linkam THSMG-600, the determination of the temperature range of -200 degrees celsius to 600 degrees celsius. the data accuracy of freezing temperature and homogenization temperature were ± 0.1 degrees celsius and ± 1 degrees celsius. The freezing temperatures of fluid inclusions in sphalerite ranged from -24.5 to -9 degree celsius, an average of -20.2 degree celsius. The homogenization temperatures of fluid inclusions in sphalerite between 100 and 206.1 degree celsius, an average of 136.9 degrees celsius.

The salinity of the fluid inclusion in sphalerite ranged from 12.9 to 24.2 wt% (NaCl_{eq}), average 22.1 wt% (NaCl_{eq}), which is calculated according to previous formula (Hall et al., 1988; Chi et al., 2007). The density of ore-forming fluid in sphalerite fluid inclusions is between 1.025 and 1.11g/cm³, average 1.09g/cm³ by T-W- ρ phase diagram (Bodnar, 1983). Mineralization pressure is between 28.0MPa and 46.9MPa by Shao (1988) formula, the corresponding mineralization depths is between 1058m and 2452m via formula (Shepherd, 1985).

2.2 C and O isotope

The carbon and oxygen isotope compositions of calcite were analyzed by using a MAT-252 mass spectrometer at the State Key Laboratory for Mineral Deposit Research, Nanjing University. The specific method was same as McCrea (1950). the data accuracy was $\pm 0.2\%$. Our results and previous data (Chen, 2000; Xue et al., 2002; Yang et al. 2003; He et al., 2004; Liu et al., 2004; Zhao, 2006; Zeng, 2007) showed the $\delta^{13}C_{PDB}$ value of the mineralization stage calcite ranged of -4.16‰ to 3‰, an average of -2.09‰, the $\delta^{18}O_{SMOW}$ value ranged of -2.5‰ to 20.4‰, the average of 7.33‰. Carbon and oxygen isotope data which compared with the values of carbon and oxygen isotope compositions in different geological reservoir and strata (Ye et al., 1992; Clark and Fritz, 1997; Hoefs, 1997), indicated a single carbon source, and the carbon in hydrothermal calcite is derived from the dissolution of carbonate rock strata.

2.3 S isotope

The sulfur isotope measurements of sulfide were performed on powders made from ore samples from the Baiyangping deposit. Sulfide was extracted, and the sulfur isotope composition was determined based on the

method of Robinson and Kusakabe (1975). It was then analyzed with a MAT251EM mass spectrometer at the Stable Isotope Laboratory of Institute of Mineral Resources, CAGS. The sulfur isotope ratios were reported as $\delta^{34}S$ relative to the V-CDT, the analytical reproducibility was $\pm 0.2\%$. Previous published data (Pan et al., 2003; He et al., 2004; Wang, 2004; Li et al., 2005; Chen, 2006; Zhao, 2006; Zeng, 2007) and our test data of sulfide, the $\delta^{34}S_{V-CDT}$ value distribution of the Baiyangping Pb-Zn polymetallic deposits ranged of -10.2‰ to 11.2‰, the average of about 5.6‰, focused on 4‰ to 8‰. The research results showed that sulfur in sulfides is derived from thermochemical sulfate reduction, or the thermal decomposition of organic matter.

2.4 Pb isotope

The Pb isotope test work completed in the Yichang Center of Geological Survey, China Geological Survey. For lead isotope ratios, approximately 10 to 50 mg of sulfide samples was first leached in acetone to remove surface contamination and then washed by distilled water and dried at 60 °C in the oven. Washed sulfides were dissolved by double distilled mix solution of nitric acid and hydrochloric acid. Following ion exchange chemistry, the lead in the solution was loaded onto rhenium filaments using a phosphoric acid-silica gel emitter. The lead isotopic compositions were measured on MAT-261 mass spectrometer with the standard sample NBS 981. The isotope ratio of the absolute error is less than 0.01. In the mining area, the $^{206}Pb/^{204}Pb$ values ranged from 18.609 to 18.818, $^{207}Pb/^{204}Pb$ values ranged from 15.548 to 15.842, and the $^{208}Pb/^{204}Pb$ data ranged from 38.514 to 39.556. Comparing with the Pb isotope data of different formation of adjacent areas (Chen, 1991), reveals that it is likely that the lead is sourced from the sedimentary strata and basement, and that the mineralization had no directly association with magmatism.

3 The Metallogenic chronology

The Rb-Sr and Sm-Nd isotope compositions of sphalerite and calcite were analyzed by using a VG354 mass spectrometer at the Modern Analysis Center, Nanjing University. The specific method was same as Wang (2007). the $^{87}Rb/^{86}Sr$ and $^{147}Sm/^{144}Nd$ ratio relative error is 3% and the $^{87}Sr/^{86}Sr$ and $^{143}Nd/^{144}Nd$ ratio relative error is 0.03%. Sphalerite and calcite samples associated with the mineralization period were analysed by Rb-Sr and Sm-Nd dating methods respectively. The Baiyangping Pb- Zn mineralization age was about 30-29 Ma (Fig.2).

Acknowledgements

The study was funded by the National Natural Science of China (U0933605 to Z.Q. Hou) and we thank David Leach for guidance in field and Erin Marsh for modifying the manuscript.

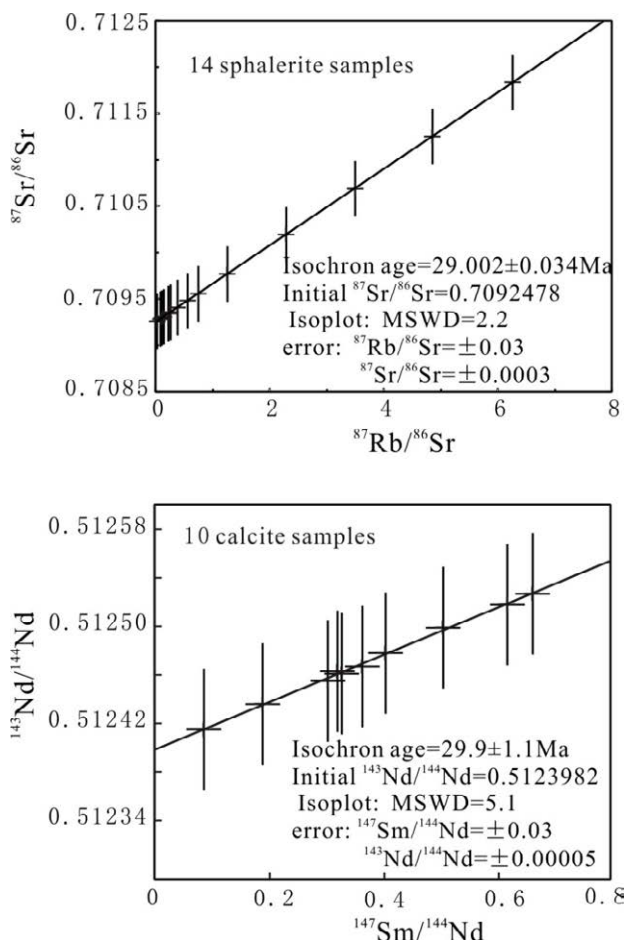


Figure 2. The Rb-Sr isochron diagram of sphalerite and Sm-Nd isochron diagram of mineralization stage calcite in Baiyangping Pb-Zn polymetallic deposit

References

- Bodnar RJ (1983) A method of calculating fluid inclusion volumes based on vapor bubble diameters and PVTX properties of inclusion fluids. *Econ Geol* 78:535-542
- Chen KX (2006) The forming mechanism of copper-silver polymetallic ore concentration area in the north of Lanping foreland basin in Yunnan Province. Dissertation submitted to China university of Geosciences for the Doctor's Degree of Science. China University of Geosciences, Wuhan. pp 1-160(in Chinese with English abstract)
- Chen KX, He LQ, Yang ZQ, Wei JQ, Yang AP (2000) Oxygen and carbon isotope geochemistry in Sanshan-Baiyangping copper-silver polymetallogenic enrichment district, Lanping, Yunnan. *Geology and Mineral Resources of South China* 4:1-8(in Chinese with English abstract)
- Chen SF, Liu YL, Bao YX, Meng JZ, Zou YB (1991) Research into metallogenic law, ore deposit types of Deqin-Xianguang lead-zinc ore zone. *Yunnan Geology* 10:119-144(in Chinese with English abstract)
- Chi GX, Ni P (2007) Equation of NaCl/(NaCl+CaCl₂) ratios and salinities from hydrohalite-melting and ice-melting temperatures in the H₂O-NaCl-CaCl₂ system. *Acta Petrol Sin* 23:33-37
- Clark ID, Fritz P (1997) *Environmental isotopes in hydrogeology*. Lewis Publishers, New York, pp 1-328
- Hall DL, Sterner SM, Bodnar RJ (1988) Freezing point depression of NaCl-KCl-H₂O solutions. *Econ Geol* 83:197-202
- He MQ, Liu JJ, Li CY, Li ZM, Liu YP (2004) Fluid mineralization mechanism of a large copper-lead-zinc ore-concentrated area in Lanping basin-Taking Baiyangping copper-cobalt polymetallic area as the example. Geological Publishing House, Beijing, pp1-117 (in Chinese)
- Hoefs J (1997) *Stable Isotope Geochemistry*. Springer, New York,

- pp 1-208
- Li ZM, Liu JJ, Qin JZ, Liao ZT, He MQ, Liu YP(2005) Ore-forming material sources of the Baiyangping copper-cobalt-silver polymetallic deposit in Lanping basin, western Yunnan province. *Geology and Prospecting* 41: 1-6(in Chinese with English abstract)
- Liu JJ, He MQ, Li ZM, Liu YP., Li CY, Zhang Q, Yang WG, Yang AP(2004) Oxygen and carbon isotopic geochemistry of Baiyangping silver-copper polymetallic ore concentration area in Lanping basin of Yunnan province and its significance. *Mineral Deposits* 23: 1-10(in chinese with English abstract)
- McCrea JM(1950) On the isotope chemistry of carbonates and a paleotemperature scale. *Jour Chem Phys* 18:849-857
- Pan GT, Xu Q, Hou ZQ, Wang LQ, Du DX, Mo XX, Li DM, Wang MJ, Li XZ, Hu YZ(2003) Archipelagic orogenesis, metallogenic systems and assessment of the mineral resources along the Nujiang-Lancangjiang-Jinshajiang area in southwestern China. Geological Publishing House, Beijing, pp 1-420(in chinese with English abstract)
- Robinson BW and Kusakabe M(1975) Quantitative preparation of sulphur dioxide, for 34S/32S analyses, from sulphides by combustion with cuprous oxide. *Anal Chem Res* 47:1179-1181
- Shao JL(1988) Prospecting mineralogy of gold deposit. China Univ Geosci Press, Wuhan, pp 38-45 (in Chinese)
- Sheperd TJ, Rankin AH, Alderton SHM (1985) A practical guide to fluid inclusion studies. Blackie Chapman and Hall, New York, pp 1-239
- Wang F (2004) The mineralization geochemical mechanism of Baiyangping silver polymetallic deposit. Dissertation submitted to Chengdu University of Technology for the Doctor's Degree of Science. Chengdu University of Technology, Chengdou, pp 1-77(in Chinese with English abstract)
- Wang YX, Yang JD, Chen J, Zhang KJ, Rao WB(2007) The Sr and Nd isotopic variations of the Chinese Loess Plateau during the past 7 Ma: Implications for the East Asian winter monsoon and source areas of loess. *Palaeogeography, Palaeoclimatology, Palaeoecology* 249:351-361
- Xue CJ, Chen YC, Yang JM, Wang DH, Yang WG, Yang QB(2002) Ore-forming Fluids Characteristics in Lanping Basin, Yunnan: Restricted by O- and C-Isotope Composition. *Mineral Deposits* 21(Supp): 1064-1067(in Chinese)
- Yang WG, Yu XH, Li WC, Dong FL, Mo (2003) The characteristics of metallogenic fluids and metallogenic mechanism in Baiyangping silver polymetallic mineralization concentration area in Yunan province. *Geoscience* 17:27-33(in Chinese with English abstract)
- Ye QT, Hu YZ, Yang YQ (1992) Regional geochemical background and gold, silver and lead-zinc mineralization in the Nujiang-Lancangjiang-Jinshajiang area. Geological Publishing House, Beijing, pp1-279(in Chinese with English abstract)
- Zeng R (2007) The Large-scale Fluid Ore-forming Process in the Lanping Basin--Taking the Jinding and Baiyangping deposits as the examples. Dissertation submitted to Chang'an University for the Doctor's Degree of Science. Chang'an University, Xi'an. pp 1-99(in Chinese with English abstract)
- Zhao HB (2006) Study on the characteristics and metallogenic conditions of copper polymetallic deposits in middle-northern Lanping basin, western Yunnan. Dissertation submitted to China university of Geosciences for the Doctor's Degree of Science. China University of Geosciences, Beijing. pp 1-110(in Chinese with English abstract)

Increased magmatic water content — the key to Oligo-Miocene porphyry Cu-Mo±Au formation in the Gangdese belt, Tibet

Rui Wang, Jeremy P. Richards

Department of Earth and Atmospheric Sciences, University of Alberta, Edmonton, Alberta, Canada T6G 2E3

Zengqian Hou, Zhiming Yang

Institute of Geology, Chinese Academy of Geological Sciences, Beijing 100037, PR China

Abstract. There is an uneven distribution of porphyry copper deposits in Gangdese belt, Tibet, over time in the Cenozoic. Such deposits are rare in association with Eocene rocks, but are abundant in the Miocene. The Eocene granitoids have intermediate $[La/Yb]_N$ ratios and intermediate-to-low Sr/Y ratios, are mainly composed of pyroxene, plagioclase, and quartz, with minor interstitial amphibole and biotite. In contrast, Oligo-Miocene granitoids have high $[La/Yb]_N$ ratios and high Sr/Y ratios, and their mineralogy consists of plagioclase, quartz, and amphibole. These features suggest that the Eocene magmas were relatively dry and evolved primarily by fractionation of pyroxene and plagioclase, whereas the Oligo-Miocene magmas were more hydrous and fractionated significant amounts of hornblende and lesser plagioclase prior to upper crustal emplacement.

The Eocene magmas were generated during the onset of collision between India and Asia, and record the final stages of subduction of oceanic lithosphere beneath Asia; their low water contents may reflect final dehydration of the remnant Neo-Tethyan slab. In the Oligo-Miocene, we suggest that upwelling asthenosphere mantle triggered partial melting of thickened, subduction-modified Tibetan lithosphere to generate hydrous hybrid melts. Such melts have a great potential to form porphyry-type deposits.

Keywords.

Magmatic water, Porphyry deposit, Miocene, Oligocene, Eocene, Gangdese, Tibet, Hornblende

1 Geological background

Gangdese magmatic belt that extends for more than 1600 km E–W preserves a complete magmatic record since the start of Neo-Tethyan oceanic subduction in the Late Triassic–Early Jurassic (Chung et al. 2009; Zhu et al. 2011) through to late-collisional plutonism. The India-Asia collision started at ~55 Ma and is ongoing (Allègre et al. 1984; Burg and Chen 1984; Rowley 1996). After initial collision, numerous small-sized Oligo-Miocene (~30 to 9 Ma) intrusive rocks with high Sr/Y and $[La/Yb]_N$ ratios formed in the Gangdese magmatic belt, and are locally associated with porphyry Cu-Mo±Au mineralization.

There are three episodes of porphyry-type mineralization associated with collision-related magmatism in the Lhasa terrane (Fig. 1), increasing in frequency and size from the Eocene to Miocene: (1) The Eocene featured only one deposit (the Sharang porphyry Mo deposit, Zhao et al. 2011); (2) Several deposits

formed in the Oligocene (e.g., the Nuri porphyry and skarn Cu deposit: 79.4 Mt @ 0.73% Cu; Chen et al. 2011; and medium- to small-sized porphyry and skarn Cu-Mo deposits such as Chongmuda, Mingze, and Kelu); (3) The largest deposits formed in the Miocene, and include the giant Qulong porphyry Cu-Mo deposit (1,420 Mt @ 0.5% Cu; Yang et al. 2009), and Jiama porphyry Cu-Mo-Au deposit (255.6 Mt @ 1% Cu; personal communication with Jiama mining company), large Bangpu porphyry Cu-Mo deposit and several medium- to small-sized porphyry Cu-Mo deposits and weakly mineralized stocks (Hou et al. 2011).

2 Changes in mineralogy and trace element contents over time

Eocene granitoids are mainly composed of pyroxene, plagioclase, and quartz, with minor biotite and amphibole forming as late interstitial phases or as replacements of pyroxene. These textures suggest that the magmas were relatively dry, with hydrous minerals only forming from late-stage residual melts. The samples have relatively low Sr/Y ratios (mostly <40), decreasing Sr concentrations over a wide range of SiO₂ from ~47 wt.% to 79 wt.%, and show increasingly negative Eu anomalies with SiO₂. These characteristics indicate that plagioclase fractionation occurred throughout the evolution of these magmas from mafic to felsic compositions. In contrast, the Y content of these rocks steadily increases until ~66 wt.% SiO₂ then decreases at higher silica contents, which suggests that hornblende (which preferentially partitions Y and MREE; Green and Pearson 1985; Rollinson 1993; Davidson et al. 2007; Müntener et al. 2001; Rooney et al. 2011) did not begin to fractionate until relatively evolved compositions were reached.

The Oligo-Miocene granitoids sampled are mostly intermediate to felsic in composition. These granitoids are mainly composed of amphibole, plagioclase, K-feldspar, and quartz. No samples of more mafic Oligocene rocks were found that could be compared with the Eocene mafic rocks, but the intermediate rocks have much higher Sr and Eu_n/Eu^* values (~1), and lower Y contents than Eocene equivalents, and both Sr and Y decrease with increasing SiO₂. These observations suggest that little plagioclase fractionation (or restite) occurred early in the evolution of these Oligocene magmas, whereas hornblende was an important early crystallizing or restite phase as indicated

by its abundance as phenocrysts in these rocks. The importance of hornblende as a crystallizing phase is reflected in the pronounced listric-shaped REE patterns of the Oligo-Miocene rocks, because hornblende preferentially partitions MREE. These features suggest that the Oligocene intermediate–felsic magmas were relatively hydrous (>4 wt.% H₂O), and fractionated abundant early hornblende with plagioclase (e.g., Moore and Carmichael 1998; Müntener et al. 2001).

3 Collisional magmatism and implications for metallogeny

The Paleocene–Eocene granitoids have calc-alkaline continental arc-like compositions, with enrichments in large-ion lithophile elements (LILE: Rb, Ba, Th, U, and K), and depletions in high field strength elements (HFSE: Nb and Ta). Their Sr and Nd isotope ratios ($(^{87}\text{Sr}/^{86}\text{Sr})_i = 0.704\text{--}0.707$; $\epsilon\text{Nd}(t) = +9.8$ to -0.5 ; Dong et al., 2006; Mo et al., 2007, 2008) are typical of continental arc magmas. The coeval Linzizong volcanic successions are interpreted to be the final products of Andean-type Neo-Tethyan continental subduction (Mo et al., 2007). The lower water contents of the Eocene magmas inferred from their mineralogy and geochemistry, might reflect the final dehydration of the remnant Neo-Tethyan slab.

Late-collisional calc-alkaline and high-K calc-alkaline Oligo-Miocene magmas were emplaced through this thickened crust along N–S normal faults (Williams et al., 2001), and intrude or crosscut the older Gangdese intrusive rocks and Linzizong volcanic successions. Sr–Nd composition ($(^{87}\text{Sr}/^{86}\text{Sr})_i = 0.705$ to 0.708 , $\epsilon\text{Nd}(t) = +5.5$ to -6.1 ; Fig. 2) of Oligo-Miocene magmas are similar to Paleocene–Eocene granitoids, reflecting crustal contamination upon emplacement (Wang et al., 2013, in prep.). Following Richards (2009) and Hou et al. (2011), we propose that hydrous calc-alkaline to mildly alkaline magmas with the potential to form porphyry Cu–Mo±Au deposits were generated during late collisional processes in the Indian–Asian orogen by partial melting of previously subduction-modified and thickened lithosphere. We suggest that break-off of Greater India slab triggered asthenosphere upwelling and underplating, which led to partial melting of subduction modified Tibetan lithosphere to generate hydrous melts. The high water contents and oxidation states of these remobilized arc magmas would have made them ideal transportation agents for chalcophile and siderophile elements, as for normal arc magmas (Candela and Holland 1984; Hamlyn et al. 1985; Richards 2009).

The Oligo-Miocene Tibetan porphyries demonstrate that deposits almost indistinguishable from normal arc porphyries can be generated in collisional orogenic belts tens of millions of years after subduction has ceased, by remobilization of fluids and metals previously introduced into the lithosphere by prior subduction events.

Acknowledgements

This study was funded by: a Discovery Grant from the

Natural Sciences and Engineering Research Council of Canada to Richards, and IGCP/SIDA-600 Project (China), a Student Research Grant from the Society of Economic Geologist Canada Foundation, a Student Research Grant from the Geological Society of America, a Student Travel Grant from the China Institute of the University of Alberta, and a Chinese Scholarship Council award to the first author.

References

- Allégre CJ, Courtillot V, Taponnier P et al (1984) Structure and evolution of the Himalayan-Tibet orogenic belt. *Nature* 307: 17–22
- Burg JP, Chen GM (1984) Tectonics and structural formation of southern Tibet, China. *Nature* 11: 219–223
- Candela PA, Holland HD (1984) The partitioning of copper and molybdenite between silicate melts and aqueous fluids. *Geochim Cosmochim Acta* 48: 373–380
- Chen L, Qin KZ, Li JX, Xiao B, Li GM, Zhao JX, Fan X (2011) Fluid Inclusion and hydrogen oxygen sulfur isotopes of Nuri Cu–W–Mo deposit in the southern Gangdese, Tibet. *Resour Geol* 62: 42–62
- Chung SL, Chu MF, Ji JQ, O'Reilly SY, Pearson NJ, Liu DY, Lee TY, Lo CH (2009) The nature and timing of crustal thickening in Southern Tibet: Geochemical and zircon Hf isotopic constraints from postcollisional adakites. *Tectonophysics* 477: 36–48
- Dong GC, Mo XX, Zhao ZD, Zhu DC, Song YT, Wang L (2006) Gabbros from southern Gangdese: Implication for mass exchange between mantle and crust. *Acta Petrol Sinica* 24: 203–210
- Green TH, Pearson NJ (1985) Experimental determination of REE partition coefficients between amphibole and basaltic to andesitic liquids at high pressure. *Geochim Cosmochim Acta* 49: 1465–1468
- Hamlyn PR, Keays RR, Cameron WE, Crawford AJ, Waldron HM (1985) Precious metals in magnesian low-Ti lavas: Implications for metallogenesis and sulfur saturation in primary magmas. *Geochim Cosmochim Acta* 49: 1797–1811
- Hildreth W, and Moorbath S (1988) Crustal contributions to arc magmatism in the Andes of central Chile. *Contrib Mineral Petr*, 98: 455–489
- Hou ZQ, Gao YF, Qu XM, Rui ZY, Mo XX (2004) Origin of adakitic intrusives generated during mid-Miocene east-west extension in southern Tibet. *Earth Planet Sci Lett* 220: 139–155
- Hou ZQ, Zhang HR, Pan XF, Yang ZM (2011) Porphyry Cu (-Mo-Au) deposits related to melting of thickened mafic lower crust: Examples from the eastern Tethyan metallogenic domain. *Ore Geol Rev* 39: 21–45
- Mo XX, Hou ZQ, Niu YL, Dong GC, Zhao ZD, Yang ZM (2007) Mantle contributions to crustal thickening during continental collision: Evidence from Cenozoic igneous rocks in southern Tibet. *Lithos* 96: 225–242
- Mo XX, Niu YL, Dong GC, Zhao ZD, Hou ZQ, Zhou S, and Ke S (2008) Contribution of syncollisional felsic magmatism to continental crust growth: A case study of the Paleogene Linzizong volcanic succession in southern Tibet. *Chem Geol* 250: 49–67
- Moore GM, Carmichael ISE (1998) The hydrous phase equilibria (to 3 kbar) of an andesite and basaltic andesite from western Mexico: Constraints on water content and conditions of phenocryst growth. *Contrib Mineral Petr* 130: 304–319
- Müntener O, Kelemen PB, Grove TL (2001) The role of H₂O during crystallization of primitive arc magmas under uppermost mantle conditions and genesis of igneous pyroxenites: An experimental study. *Contrib Mineral Petr* 141: 643–658
- Naney MT (1983) Phase equilibria of rock-forming ferromagnesian silicates in granitic systems. *Am J Sci* 283: 993–1033

- Richards JP (2009) Postsubduction porphyry Cu–Au and epithermal Au deposits: products of remelting of subduction-modified lithosphere. *Geology* 37: 247–250
- Rollinson H (1993) Using geochemical data: evaluation presentation interpretation. Pearson Education Limited Harlow, England
- Ridolfi F, Renzulli A, Puerini M (2010) Stability and chemical equilibrium of amphibole in calc-alkaline magmas: An overview new thermobarometric formulations and application to subduction-related volcanoes. *Contrib Mineral Petr* 160: 45–66
- Rooney TO, Franceschi P, Hall CM (2011) Water-saturated magmas in the Panama Canal region: A precursor to adakite-like magma generation? *Contrib Mineral Petr* 161: 373–388
- Rowley DB (1996) Age of initiation of collision between India and Asia: a review of stratigraphic data. *Earth Planet Sci Lett* 145: 1–13
- Wang R, Richards JR, Hou Z, Yang Z, DuFrane SA (2013) Increased magmatic water content—the key to Oligo-Miocene porphyry Cu–Mo±Au formation in the eastern Gangdese belt, Tibet, in preparation.
- Yang ZM, Hou ZQ, White NC, Chang ZS, Li ZQ, Song YC (2009) Geology of the post-collisional porphyry copper-molybdenum deposit at Qulong Tibet. *Ore Geol Rev* 36: 133–159
- Zhao JX, Qin KZ, Li GM, Li JX, Xiao B, Chen L (2011) Geochemistry and petrogenesis of granitoids at Sharang Eocene porphyry Mo deposit in the main-stage of India-Asia continental collision northern Gangdese Tibet. *Resour Geol* 62: 84–98
- Zheng YC, Hou ZQ, Li W, Liang W, Huang KX, Li QY, Sun QD, Fu Q, Zhang S (2012) Petrogenesis and geological implications of the Oligocene Chongmuda-Mingze adakite-like intrusions and their mafic enclaves, southern Tibet. *J Geol* 120: 647–669
- Zhu DC, Zhao ZD, Niu YL, Mo XX, Chung SL, Hou ZQ, Wang LQ, Wu FY (2011) The Lhasa terrane: Record of a microcontinent and its histories of drift and growth. *Earth Planet Sci Lett* 301: 241–255

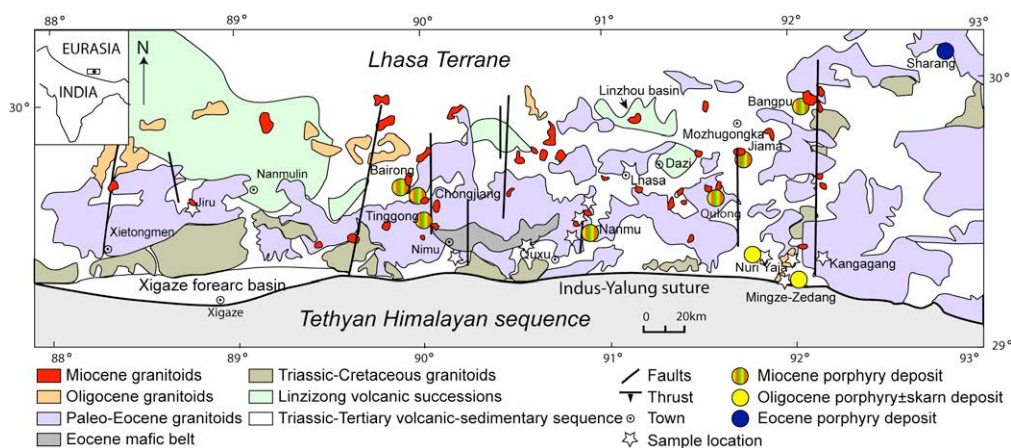


Figure 1. The eastern Gangdese magmatic belt on the southern margin of the Lhasa terrane (modified from Hou et al. 2004; Dong et al. 2006).

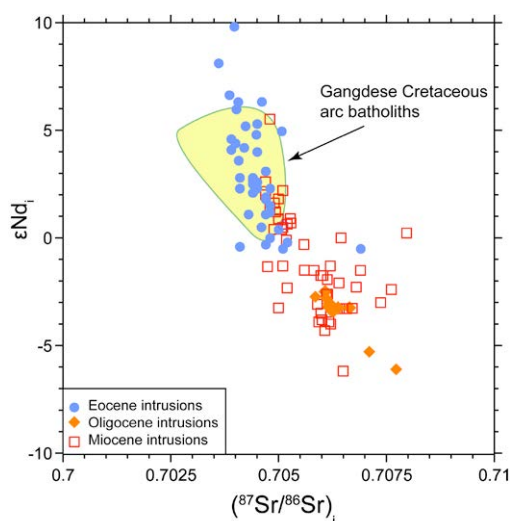


Figure 2. ϵNd_i vs. $(^{87}Sr/^{86}Sr)_i$ showing Sr-Nd compositions of the Eocene, Oligocene and Miocene intrusions in the Gangdese belt (Hou et al., 2004, 2011; Zheng et al., 2012), and Gangdese Cretaceous arc batholiths (Wen, 2007).

A model for carbonatite hosted REE deposits: Mianning-Dechang REE belt in Western Sichuan province, China

Yuling Xie, Yingxu Li

University of Science and Technology Beijing, Beijing 100083, China

Zengqian Hou

Institute of Geology, Chinese Academy of Geoscience, Beijing 100037, China

Simon C. Dominy

*Snowden Mining Industry Consultants Pty Ltd, PO Box 416W, Ballarat, VIC 3350, Australia;
WA School of Mines, Curtin University, GPO Box U1987, Perth, WA 6845, Australia*

David R. Cooke, Leonid Denyushevsky

CODES ARC Centre of Excellence in Ore Deposits, University of Tasmania, Private Bag 126, Hobart, TAS 7001, Australia

Abstract. The Mianning-Dechang REE belt in Sichuan province, China provides a good example for study of the genesis and ore deposit model of carbonatite REE mineralisation. The style of mineralization varies across different deposit as well as in different parts of same deposit. Styles include vein-stockworks, pegmatites, breccias and disseminated mineralisation. Based on geology, geochemistry and fluid inclusion results, this paper proposes a carbonatite hosted REE deposit model. The source carbonatite comes from unmixing between alkaline and carbonatite melts, which have a mantle origin. The ore-forming fluid derived from carbonatite magma is a high temperature, high pressure, high density, and high SO₄, REE supercritical fluid that underwent a distinctive evolution path. A dense carbonatite fluid and rapid evolution is disadvantageous for long distance migration and distal mineralization. Thus REE mineralization and related alteration, always occurs proximal to the source. Vein systems, pegmatites and carbonatite comprise a continuum. The vein system occurs at the top or at the outer zone of the carbonatite, followed by pegmatites, and disseminated ore in the carbonatite occurs at the lower level or inner zone of the system. A giant carbonatite body and deep magma chamber is not necessary for giant REE deposit formation.

Keywords. Carbonatite host REE deposit, Onsite mineralization, dense carbonatite fluid, Mineralization style

1 Introduction

Carbonatite, a special type of magmatic rock sourced from the mantle (Le Bas, 1987; Simonetti et al, 1995, 1998; Bell et al, 1999 and the reference there in) provides important information on mantle heterogeneity, mantle metasomatism (Lev et al, 1988; Amundsen, 1987) and the reaction between mantle and crust (Becker and Altherr, 1992). Carbonatite is often related to REE, U and Th mineralization worldwide and is also an important source of Nb, P, Cu and fluorite (Groves and Gwalani, 2004; Rakin, 2005). The causative carbonatite body, related to economically-significant giant REE and

Cu deposits worldwide, is usually relatively small (<0.1-1.2 km² in outcrop area) and with proximal mineralization. Key examples of carbonatite mineralized systems include the Palabora Cu deposit (Palabora Mining Company Limited Mine Geological and Mineralogical Staff, 1976) in South Africa, Mountain Pass REE deposit (USGS, 2010) in United State, Bayan Obo REE deposit in China (Yang et al, 2010; Yang et al, 2011) and Maoniuping REE deposit in China (Yuan et al, 1995; Hou et al, 2006). The Mianning-Dechang (MD) REE belt in Sichuan province of China provides a good example for study of the genesis and deposit models of carbonatite hosted REE deposits.

Although a number of studies on the geology and geochemistry of the REE deposits in the MD belt have been undertaken, the deposit model is still open to debate. Based on geological and geochemical results for key deposits in MD belt, this paper presents a deposit model and provides a new understanding for the ore-forming process and spatial distribution of varied mineralization styles in the carbonatite system.

2 Geological background

The Himalayan MD REE belt in western Sichuan, SW China, one of the most significant REE belts in China. It is approximately 270 km long, including one giant (Maoniuping, with 3.17Mt REO), two intermediate (Dalucao, with 82Kt REO; Muluo, with 100Kt REO) and a number of small REE deposits (e.g., Lizhuang, with 6kt REO) and REE occurrences. The belt is located in the western margin of Yangtze Craton (Fig.1) and sits along a Permian paleo-rift zone. Dating results of host carbonatite rocks and gangue minerals in REE ore define a Himalayan metallogenic epoch (Hou et al, 2009 and the reference there in). The western Yangtze Craton is involved in to eastern Indo-Asian collision zone during Himalayan stage. REE mineralization is associated with Himalayan carbonatite-alkalic complexes, controlled by a series of Cenozoic strike-slip faults. These complexes consist of carbonatitic sills or dykes and associated alkaline syenite stocks, which

intruded into Yanshanian granite or Proterozoic basement and Devonian-Cretaceous sedimentary sequences.

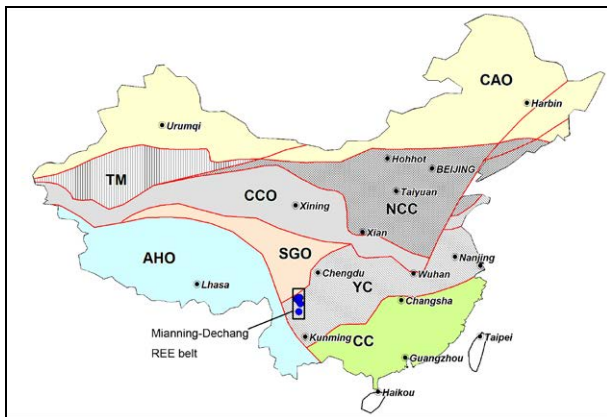


Figure 1. The location and tectonic setting of REE deposits in Mianning-Deang REE belt, China (Tectonic setting after Kusky et al, 2007); AHO – Alpine-Himalayan orogen; YC – Yangtze Craton; SGO – Songpan-Ganzi Orogen; CCO – Central China orogen; CC – Cathaysia Craton (South China Craton); Blue circle – location of REE deposit

3 The mineralization and alteration

Alteration in the key deposits of this belt is characterized by fenitization, which formed a fenite halo around the carbonatite and enveloped REE ore-bodies. Associated REE mineralization occurs mainly in the carbonatite bodies or as vein systems consisting of various veinlets, stringer and/or stockwork zones around the carbonatite. The REE ore bodies show various shapes from layer-like, lenticular to pipe-like in different districts. Ore types are dominated by pegmatitic, disseminated, brecciated, and stringer (stockwork) ores with mineral assemblages of barite, fluorite, aegirine-augite, quartz, calcite, microcline, and bastnasite, etc.

In Maoniuping, the pegmatite ore occurs mainly as large dykes at the top level of the carbonatite body and with vein/stockwork zones around them. Downward, mineralization becomes dominantly a disseminated ore type. Breccia ore occurs as the dominant ore type at Dalucao, and also occurs in Lizhuang and Maoniuping. The cross section at Lizhuang, shows a well-developed zonation from the outer breccia zone to an inner medium-grained carbonatite zone with numerous pegmatite pods and druses in it. At Dalucao, the breccia ore occurs at the top level of the deposit, because of the erosion of the upper stockwork zone. Disseminated ore occurs only in drill core at Maoniuping, but is dominant ore type in Lizhuang. No crosscutting relationships have been confirmed between the stockwork, veins, pegmatite and carbonatite styles. They are considered to be a continuum from the carbonatite body to various ore styles.

4 The inclusion results

Based on inclusion results for Maoniuping, Lizhuang, Dalucao and Muluo, a complex melt (M), melt-fluid (ML) and fluid inclusion assemblage exists in fluorite,

quartz, barite and bastnasite from carbonatite and REE ore. The net-like sulphate-bearing melt-fluid inclusions (ML-1) are most common in carbonatite host fluorite, which show an early crystallization character and contain a stable solid/aqueous/vapour ratio. This indicates that they are the most representative samples of the primary carbonatitic fluid (Xie et al, 2011). Quartz, barite and bastnasite contain a CO₂-rich fluid inclusion assemblage and show a later crystallization character than fluorite (Xie et al, 2009). The late alteration and unhomogenized trapping during evolution of the carbonatite fluid, causes a varied inclusion assemblage, such as melt and melt-fluid inclusions, solid-rich and solid-poor CO₂-rich fluid inclusions, and CO₂-rich and pure CO₂ fluid inclusion assemblages (Xie et al, 2011). Microthermometric results demonstrate that the ML-1 inclusions homogenized to an aqueous phase, displaying critical behaviour at 650-850°C and have a high trapping pressure (>350MPa). The heating of fluorite-hosted ML-1 inclusions displays a complex phase changing behaviour. Three immiscible liquid phases and some solid phases coexist in the inclusion from 335-350°C to 450-455°C, implying an unmixing and crystal fractionation process in the carbonatite fluid evolution (Xie et al, 2011). Reversing the heating process of ML-1 inclusions, the evolution path can be traced as phase separation of a critical fluid at 650-850°C, sulphate-melt exsolution from aqueous at 455 to 335 °C and sulphate crystallization at wide range of temperatures. The LA-ICP-MS results of ML-1 inclusions show high REE contents in the primary carbonatite fluid, as well as Pb, Zn, Sr Ba, etc. Exsolution of a sulphate melt and crystal fractionation of sulphate, may cause the enrichment of REE and base metals in the residual CO₂-rich fluid and hence ore deposition which was proved previously by the CO₂-rich inclusions in bastnasite and quartz (Xie et al, 2009). SEM and LRM analyses of solid phases in melt-fluid and solid-rich fluid inclusions, show that almost all the solid phases are sulphate, including syngenite (K₂Ca(SO₄)₂·H₂O), glauberite (Na₂Ca(SO₄)₂), apthitalite (K₃Na(SO₄)₂), mirabilite (Na₂SO₄·10H₂O), anhydrite (CaSO₄) and celestite (SrSO₄). Dominant SO₄ and H₂O in the aqueous phase and CO₂ in the vapour phase, is confirmed by LRM results (Xie et al, 2009). The LRM and SEM/EDS results imply a distinctive sulphate-dominated ore-forming fluid system and strong oxidizing conditions.

Microthermometric results of CO₂-rich inclusions in bastnasite and quartz, indicate that REE precipitation principally occurs in a medium-T stage (275~325°C) and during unmixing between CO₂ and aqueous phases, which may act as the most important mechanism for REE precipitation. The O-C isotopic data of gangue calcite, combined with δ¹³C_{V-PDB}, and δD of fluid inclusions in fluorite and quartz, further demonstrates that the ore-forming fluids were of orthomagmatic origin, but involving introduction of an external fluid during the late stage of fluid evolution (Hou et al, 2009).

5 Ore genesis and deposit model

5.1 Tectonic setting

The MD REE belt is located at western margin of the Yangtze Craton, which was involved in the eastern Indo-Asia collision zone during the Himalayan epoch (Hou et al, 2009). REE mineralization is associated with the Himalayan carbonatite-alkalic complexes, and was controlled by a series of Cenozoic strike-slip faults (Hou et al, 2009), which were constrained by the Permian paleo-rift zone. The India-Asia collision leads to reactivation of the Panxi paleo-rift and the eastern moving of thickened crust of the Qinhai-Tibet plateau. This leads to squeezing of the asthenospheric mantle and migration toward the western margin of the Yangtze Craton. The mantle derived alkaline-carbonatite magma upwelled and was emplaced into strike-slip faults, which occurs along the reactivated rift zone.

5.2 The genesis of the carbonatite

The alkaline carbonatite complexes in this area consist of carbonatitic sills, dykes, small stocks and associated alkaline syenite stocks. The main phase of host carbonatites are calcite carbonatites, which are extremely enriched in LILE (Sr, Ba) and light REE, but relatively depleted in high-field strength elements (Nb, Ta, Zr, Hf, Ti). Their $\epsilon\text{Nd}_{(t)}$ (-3.2 ~ -6.4), $(^{87}\text{Sr}/^{86}\text{Sr})_i$ (0.706020 ~ 0.707922), $^{18}\text{O}_{\text{V-SMOW}}$ (6.4 ~ 10.5 ‰) and ^{13}C values (-3.9 ~ -8.5 ‰) suggest a transitional source of enriched mantle, EM-I to EM-II (Hou et al, 2006, 2009). Associated alkalic syenites are dominated by nordmarkites, and show similar abundance patterns of trace elements normalized by primitive mantle and the Sr-Nd and C-O isotopic signatures, suggesting an immiscibility origin.

Because of the very low viscosity (Treiman and Schedl, 1983), the carbonatite magma can upwell at very high speeds and cause rapid exsolution and evolution of the carbonatite fluid.

5.3 Ore-forming fluid

Carbonatite can dissolve up to 10wt % water (Keppler, 2003). Rapid upwelling of a carbonatite magma causes a large decrease of pressure, and the exsolution of a carbonatite fluid. Large quantities of pegmatite pods and druses in carbonatite at Lizhuang, imply a dense carbonatite fluid and highly volatile solubility of in the carbonatite melt. This high density is consistent with the density estimate of a primary carbonatite fluid (2.4 g/cm³) (Xie et al, unpublished data).

The microthermometric, SEM/EDS, LRM and LA-ICP-MS results indicate a SO₄, CO₂, REE, Pb, Zn, Sr, Ba and Ca enriched distinctive fluid system, which is different from other ore-forming fluid systems.

5.3 REE precipitation

The calculated density of the primary carbonatite fluid is similar to the estimated density of carbonatite magmas by Wolff (1994). Although the carbonatite melt has a very low viscosity (Treiman and Schedl, 1983), the

dense carbonatite fluid is not easy to migrate upward to the top of the carbonatite. Fast evolution of the carbonatite fluid also is disadvantageous to long distance flow and distal mineralization. Alteration and mineralization thus occurs in or proximal to carbonatite dykes, sills and/or stocks.

Early degassing of CO₂ leads to large-scale precipitation of carbonate minerals, and mass fluid exsolution. The distinct exsolution of primary carbonatite fluid, including sulphate melt and CO₂ exsolution from the primary carbonatite fluid, causes REE enrichment in the residual fluid and minor REE precipitation. Unmixing between CO₂ and aqueous fluid, plays an important role in REE precipitation.

High water solubility in carbonatite magmas, low water in derived ore-forming fluids and high REE solubility in the fluid, implies that giant carbonatite bodies and deep carbonatite magma chambers are not necessary for giant REE deposits to form.

5.4 Deposit model

On the basis of geology and geochemistry, the authors propose a possible model for carbonatite-hosted REE deposit formation. This explains the distribution of various mineralization and alteration styles (Fig. 2).

- (1) Because of the Indian-Asian collision, the paleo Panxi rift was reactivated and formed a series strike-slip faults along the ancient rift zone. The carbonatite-alkaline complex was emplaced into the strike slip faults.
- (2) Geochemical results indicate an enriched mantle source for alkaline carbonatite complexes and an unmixing origin for syenite and carbonatite.
- (3) Rapid upwelling and pressure decrease of the magma, caused the rapid exsolution of carbonatite fluid. The exsolution of sulphate melt and CO₂ from the primary carbonatite fluid during fluid evolution, lead to the enrichment of REE in the residual fluid and REE precipitation. Further evolution of the fluid, including unmixing between CO₂ and aqueous, caused REE precipitation.
- (4) Giant carbonatite bodies and a deep magma chamber are not necessary for giant REE deposit formation, because of the high water solubility in the carbonatite magma and effective fluid exsolution and REE precipitation.
- (5) Dense primary carbonatite fluid and rapid evolution, is disadvantageous to long distance fluid migration and distal mineralization. Fenite alteration and REE mineralization occurs in or around carbonatite dykes, sills and/or stocks.
- (6) Stockwork, veins, pegmatites and carbonatite form a continuum in the carbonatite system, with normal zonation from an outer (upper) vein system, middle pegmatites and an inner (lower) mineralized carbonatite (Fig. 2). Breccias occur together with pegmatite or disseminated ore.

Acknowledgements

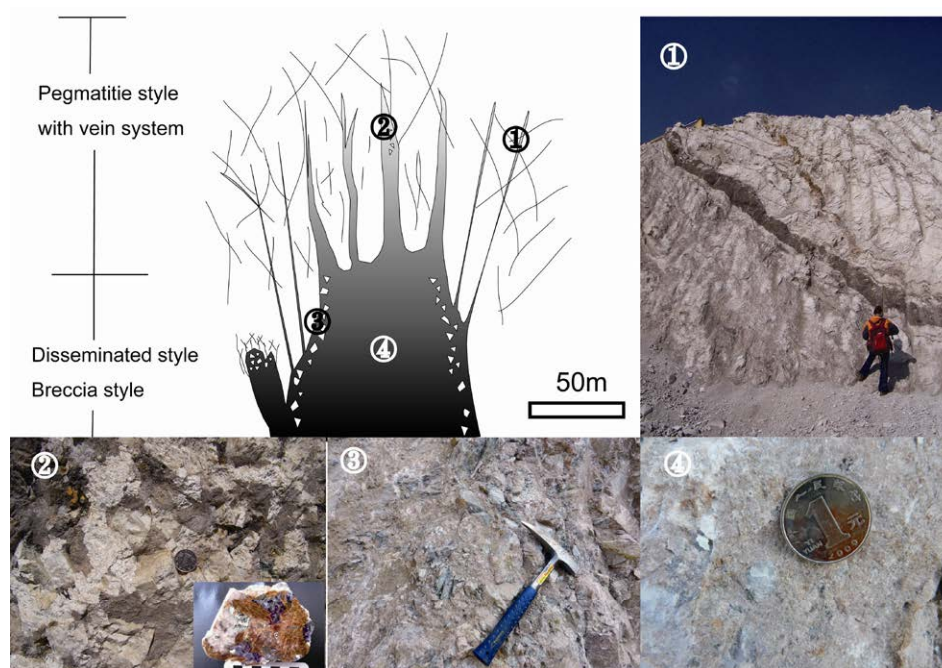


Figure 2. Carbonatite related REE deposit model and the mineralization style in different part of carbonatite system
 1-Vein system; 2-pegmatite style (microcline-calcite-barite) with insert pegmatite ore; 3- breccia sty; 4-disseminated style in carbonatite

This work was supported by the National Nature Science Foundation of China (No. 41072066) and IGCP-SIDA 600. We thank Shuping Yin, Longsheng Yi, Shihong Tian and Xiaoyu Li for their help in sample collecting. We thank the Jiangxi Copper Corporation for the help in field trip.

References

- Amundsen, H.F.F. Evidence for liquid immiscibility in the upper mantle. *Nature* 327, 692-695 (1987)
- Becker, H. and Altherr, R. Evidence from ultra-high-pressure marbles for recycling of sediments into the mantle, *Nature* 358: 745-748 (1992)
- Bell, K., Kjarsgaard, B.A., Simonetti, A. Carbonatites into the Twenty-First Century. *Journal of Petrology*, 39(11,12): 1839-1845 (1999)
- Groves D.I. and Gwalani G. Carbonatites and associated mineralization, *Mineralogy and Petrology*, 80: 123-126 (2004)
- Hou, Z., Tian, S., Yuan, Z., Xie, Y., Yin, S., Yi, L., Fei, H. and Yang, Z., 2006, The Himalayan collision zone carbonatites in western Sichuan, SW China: Petrogenesis, mantle source and tectonic implication: *Earth and Planetary Science Letters*, 244, 234-250.(2006)
- Hou, Z., Tian, S., Xie, Y., Yuan, Z., Yin, S., Yi, L., Fei, H., Zou, T., Bai, G. and Li, X., The Himalayan Mianning-Dechang REE belt associated with carbonatite-alkalic complex in the eastern Indo-Asian collision zone, SW China: *Ore Geology Reviews*, 36, 65-89
- Keppler H., Water solubility in carbonatite melts, *American Mineralogist*, 88 (11-12): 1822-1824 (2003)
- Kusky T., Li J., Santosh M., The Paleoproterozoic North Hebei Orogen: North China craton's collisional, suture with the Columbia supercontinent, *Gondwana Research*, 12: 4-28 (2007)
- Le Bas, M.J. Nephelinites and carbonatites. *Geological Society of London*, 30: 53-83 (1987)
- Lev, O., Sheintuch, M., Pisemen, L.M. & Yarnitzky, Ch., Mantle metasomatism by ephemeral carbonatite melts, *Nature* 336, 459-462 (1988)
- Palabora Mining Company Limited Mine Geological and Mineralogical Staff, The geology and economic deposits of copper, iron and vermiculite in the Palabora igneous complex: A brief review, *Economic Geology*, 71: 177-192 (1976)
- Simonetti A, Bell K, Viladkar SG Isotopic data from the Amba Dongar carbonatite complex, west-central India: evidence for an enriched mantle source. *Chem Geol (Isotope Geoscience Section)* 122:185-198 (1995)
- Treiman A.H. and Schedl A., Properties of Carbonatite Magma and Processes in Carbonatite Magma Chambers, *The Journal of Geology*, 91(4): 437-447 (1983)
- USGS, The Principal Rare Earth Elements Deposits of the United States—A Summary of Domestic Deposits and a Global Perspective, pp.96 (2010)
- Wolff, J.A. Physical properties of carbonatite magmas inferred from molten salt data, and application to extraction patterns from carbonatite-silicate magma chambers, *Geological Magazine*, 131 : 145-153 (1994)
- Xie, Y., Hou, Z., Yin, S., Dominy, S.C., Xu, J., Tian, S., and Xu, W., Continuous Carbonatitic Melt-Fluid Evolution for REE Mineralization System: Evidence from Inclusions in the Maoniuping REE Deposit in the western Sichuan, China: *Ore Geology Reviews*: 36: 90-105 (2009)
- Xie Y., Li Y., Cooke D.R., Kamenetsky V., Chang Z., Danyushevsky L., Dominy S.C., Ryan C., Laird J., Geochemical characteristics of carbonatite fluids at the Maoniuping REE deposit, Western Sichuan, China, proceedings of 11 th SGA Biennial Meeting (Let's Talk Ore Deposits): 196-198 (2011)
- Yang X, Zheng Y, Yang X, Zhang Le Bas P, M.J., A Geochemical Study of an REE-rich Carbonatite Dyke at Bayan Obo, Inner Mongolia, Northern China, *Acta Geologica Sinica*, 74(3): 605-612 (2010)
- Yang K F, Fan H R, Santosh M., Hu F F, Wang K Y, Mesoproterozoic carbonatitic magmatism in the Bayan Obo deposit, Inner Mongolia, North China: Constraints for the mechanism of super accumulation of rare earth Elements, *Ore Geology Reviews*, 40: 122-131 (2011)
- Yuan Z., Shi Z., Bai G., Wu C., Chi R. and Li, X., Rare earth element deposit in Maoniuping Mianning, Sichuan Province: *Geological Publishing House, Beijing*, 150 p. (1995)

Sandstone- and conglomerate-hosted Urogen Zn-Pb deposit, Xinjiang, NW China

Chunji Xue

State Key Laboratory of Geological Processes and Mineral Resources, Faculty of Earth Sciences and Resources, China University of Geosciences, Beijing, China, 100083

Guoxiang Chi

Department of Geology, University of Regina, Regina, Saskatchewan, Canada, S4S 0A2;

Abstract: The Urogen Zn-Pb deposit is hosted in sandstones and conglomerates of the Lower Cretaceous and argillaceous dolomite of the Paleocene in the Kashi sag, northwestern Tarim basin. It is characterized by mainly low grade (Zn+Pb ~ 3%) and large tonnage (potentially 10 Mt metals), with an average Zn/Pb ratio of about 5.8. The ore minerals mainly occur as replacement of cements, matrix and fragment grains of the host rocks and as open space filling to a lesser extent. The mineralization is interpreted to be epigenetic. The tightly clustered Pb isotopic values of ore minerals suggest a uniform fluid reservoir that supplied the metals, whereas the wide range of S isotopes are consistent with multiple sources of reduced sulfur including those from thermal sulfate reduction (TSR) and bacterial sulfate reduction (BSR). Mineralization probably resulted from mixing of a metal-rich fluid with multiple fluids carrying reduced sulfur from different sources.

Keywords: Sandstone-hosted, Zn-Pb deposit, Urogen, Meso-Cenozoic, Kashi, NW-China

1 Introduction

Compared to shale- and carbonate-hosted SEDEX and MVT deposits, there are only a few large Zn-Pb deposits that include the Jinding Zn-Pb deposit in China (Xue et al. 2007) and the Laisvall Pb-Zn deposit in Sweden (Rickard et al. 1979) in sandstones (Bjolykke and Sangster 1981; Leach et al. 2005). The Urogen deposit in Xinjiang, China represents a new example of large sandstone-hosted Zn-Pb deposits. The paper aims to provide an up-to-date summary of

the geologic characteristics of the Urogen deposit, and to discuss on its origin based on ore petrography, S and Pb isotopes.

2 Geology of Urogen Zn-Pb Deposit

The Urogen Zn-Pb deposit is located in the northwestern part of the Kashi sag in the western margin of the Tarim basin. The Kashi sag is a Meso-Cenozoic intracontinental basin developed between the Southern Tianshan and Western Kunlun Mountains. The strata hosting the Urogen Zn-Pb deposit includes, from older to younger, the Proterozoic Akesu Group, Lower Jurassic Kangsu Formation (J₁k), Middle Jurassic Yangye (J₂y) and Taerduo (J₂t) formations, Upper Jurassic Kuzigongsu Formation (J₃k), Lower Cretaceous Kezilesu Group (K₁kz), Paleocene Aertashe Formation (E₁a), Palaeocene-Eocene Qimugen Formation (E₁₋₂q), Eocene Kalataer (E₂k) and Urogen (E₂w) formations, Eocene-Oligocene Bashebulake Formation (E₂₋₃b), Oligocene-Miocene Keziluoyi Formation ((E₃-N₁)k), Miocene Anjuan (N₁a) and Pakabulake (N₁p) formations, and Quaternary Xiyu Formation (Q). The orebodies are hosted mainly in K₁kz and to a lesser extent in E₁a. The K₁kz is divided into five members. The E₁a consists of grey-white gypsum with intercalated grey, argillaceous dolomite.

The strata in the Urogen area are deformed into an east-west trending syncline plunging to the west. The orebodies are tabular and stratiform, and distributed on both limb of the Urogen syncline. The majority of the ore is hosted in grey-white sandy conglomerate of the fifth member of the K₁kz⁵, and a minor portion is

hosted in grey, argillaceous dolomite of the E₁a). The deposit is divided into the north ore zone and the south ore zone, distributed in the northern and southern limbs of the Uragen syncline, respectively. The north ore zone is developed along the bedding-parallel Wuheshalu fault, has an average thickness of 100m, Pb grades from 0.03 to 0.47 wt.%, and Zn grades from 2.24 to 3.41 wt.%. The south ore zone has an average thickness of 150 m, Pb grades from 0.23 to 0.89 wt.%, and Zn grades from 1.69 to 3.64 wt.%. A drill hole made in 2007 in the core of the Uragen syncline intersected Zn-Pb mineralization at a depth of 700m, suggesting that the two ore zones are connected at depth.

The Zn-Pb mineralization in the Uragen occurs as massive sulfides, patches and veinlets of sulfides in the host rocks, disseminations in the matrix and cements of sandstones, brecciated dolomite and conglomerates, and locally as veins of sulfides and celestine. The most important style of mineralization is dissemination in sandstones and conglomerates. Primary sulfide minerals are mainly sphalerite, galena, pyrite and marcasite, and supergene minerals include smithsonite, hydrozincite, anglesite, calamine, jarosite, and limonite. Primary sulfide minerals mainly occur as fine crystals filling interstitial space between fragment grains in sandstones and conglomerates, and replacing matrix, calcareous cements as well as framework grains. Open-space filling textures are locally developed, including colloform sphalerite filling vugs, followed by galena, and sphalerite and galena filling fractures.

3 Ore S and Pb-isotopes

The $^{34}\text{S}_{\text{V-CDT}}$ of sulfides in the ores vary widely from -27.9‰ to 14.6‰, whereas those of sulfates fall in a narrow range from 17.9‰ to 18.6‰. There is an apparent difference in $^{34}\text{S}_{\text{V-CDT}}$ between the North ore zone and the South ore zone, with those in the former ranging from -24.4‰ to -6.1‰ (average-15.2‰), and those in the latter from -27.9‰ to 14.6‰ (average -4.71‰).

The Pb isotopes of sulfides in the ores fall in a small cluster, with $^{206}\text{Pb}/^{204}\text{Pb}$ from 18.528 to 18.663, $^{207}\text{Pb}/^{204}\text{Pb}$ from 15.611 to 15.669, and $^{208}\text{Pb}/^{204}\text{Pb}$ from

38.616 to 38.839. The Pb isotopes of the host rocks fall in a slightly wider ranges, with $^{206}\text{Pb}/^{204}\text{Pb}$ from 18.362 to 18.629, $^{207}\text{Pb}/^{204}\text{Pb}$ from 15.594 to 15.662, and $^{208}\text{Pb}/^{204}\text{Pb}$ from 38.380 to 38.787.

4 Discussion

The Uragen deposit has been classified as different types of deposits by different authors, including syngenetic or SEDEX (Cai et al. 2002; Xie et al. 2003; Bai et al. 2008), reworked syngenetic (Li and Wang 2006; He 2007), epigenetic-basinal brine type (Ye et al. 1999; Gao et al. 2002; Li et al. 2005; Kang et al. 2009), and sandstone-hosted variant of MVT (Zhu et al. 2010; Zhang 2010). The fact that orebodies straddle across a hiatus in the host rocks (between K₁kz and E₁a) and the development of replacement and open-space filling textures and structures in the ores suggest that the mineralization at Uragen is of epigenetic nature. The stratiform shapes of the orebodies and the locally developed banded ore structures, which were used to support the SEDEX origin of the deposit (Cai et al. 2002; Xie et al. 2003; He 2007), can be formed by replacement and are not uncommon in epigenetic mineral deposits. In this aspect, the Uragen deposit is strikingly similar to the Jinding Zn-Pb deposit, which is also developed in Lower Cretaceous and Paleocene siliciclastic rocks, that was also proposed to be a SEDEX deposit based on the stratiform nature of much of the ore (Wang et al. 1992); Furthermore, various studies of the Jinding ore including isotopic dating suggest that the mineralization took place after the host rocks, therefore supporting an epigenetic origin of the deposit (Kyle and Li 2002; Chi et al. 2007; Xue et al. 2007).

The narrow ranges of Pb isotopes of ore minerals from the Uragen deposit suggest that the metals were well mixed in a fluid reservoir before being transported to the site of mineralization. It is unclear if this reservoir is located in the deeper part of the basin (the hydrothermal model) or on the surface, such as lakes in piedmonts (the groundwater transport model), both being compatible with continental or orogenic sources of lead. In contrast, the wide ranges in sulfur isotopes suggest that the sulfur involved in the mineralization may have been derived from multiple

sources. Similar sulfur isotopes characteristics have been observed for sandstone-hosted copper deposits in the area (Li et al. 2011; Wang et al. 2011). While the positive $\delta^{34}\text{S}$ values may indicate thermal sulfate reduction, the negative $\delta^{34}\text{S}$ values are likely related to bacteria participation in sulfate reduction. The absence of biodegradation of hydrocarbons suggests that the mineralization site was too hot for bacteria to survive. Therefore, the bacteria-related reduced sulfur may not have been generated in situ, but rather produced elsewhere and migrated to the site of mineralization. On the other hand, the positive $\delta^{34}\text{S}$ values suggest that some reduced sulfur may have been produced by in situ thermal sulfate reduction, which is consistent with the observation that organic matter at the site of mineralization appears to have been altered (oxidized). Such a reduced sulfur production mechanism is likely considering the abundance of evaporites in the host rocks (e.g., in the Fifth Member of the Lower Cretaceous Kezilesu Formation, and the Paleocene Artashe Formation).

In conclusion, the Urogen deposit represents a new example of large-scale zinc-lead deposit hosted in sandstones and conglomerates. The deposit is epigenetic and might form from hot brines (Zhu et al. 2010), which might have been derived from either deeper parts of the basin in a hydrothermal system, or descended from a near-surface groundwater system and became hot at burial conditions. The narrow range in lead isotope composition of the ores suggest that the metals were derived from a uniform fluid reservoir, whereas the wide range of sulfur isotopes indicate multiple sources of sulfur, including those related to bacteria activities and thermal sulfate reduction. At least part of the sulfur may have been generated through in situ thermal sulfate reduction, with organic matter at the site of mineralization as the main reducing agents. The participation of organic matter in mineralization is reflected by its reduced maturity relatively to those in the host rocks away from mineralization.

Acknowledgements

It is supported by NSFC (41072069) and the State Science-Technical Support Plan (2011BAB06B02).

References

- Bai H, Nian W, Quman G (2008) Geologic characteristics and exploration model of the Urogen lead-zinc deposit in Wuqia County, Xinjiang. *Nonferrous Metals of Xinjiang* 5: 1-4 (in Chinese with English abstract).
- Bjorlykke A, Sangster DF (1981) An overview of sandstone lead deposits and their relation to red-bed copper and carbonate-hosted lead-zinc deposits. *Economic Geology* 75th Anniversary Volume: 178-213.
- Cai H, Deng G, Zheng Y (2002) Genesis of the Urogen lead-zinc deposit in Xinjiang. *Mineral Resources and Geology* 16: 1-5 (in Chinese with English abstract).
- Chi G, Xue C, Lai J, Qing H (2007) Sand injection and liquefaction structures in the Jinding Zn-Pb deposit, Yunnan, China: indicators of an overpressured fluid system and implications for mineralization. *Economic Geology*, 102: 739-743.
- Gao Z, Liu J, Shu G, Kuang W, Hu J (2002) Geologic conditions and genesis of lead-zinc deposits in Wuqia, Xinjiang. *Journal of Central-South University of Technology* 33: 116-120 (in Chinese with English abstract).
- He H (2007) Geologic characteristics and preliminary genetic analysis of the Urogen lead-zinc deposit in Wuqia County, Xinjiang. M.Sc. thesis, Guilin Institute of Technology, 61 p (in Chinese with English abstract).
- Kang Y, Ouyang Y, Fan J, Liu W (2009) Origin of the Urogen lead-zinc deposit from hydrothermal brines, Wuqia, Xinjiang. *Geological Journal of Sichuan* 29: 400-405 (in Chinese with English abstract).
- Kyle JK, Li N (2002) Jinding: A giant Tertiary sandstone-hosted Zn-Pb deposit, Yunnan, China. *Society of Economic Geologists Newsletter*, no. 50: 8-16.
- Leach DL, Sangster DF, Kelley KD, Large RR, Garven G, Allen CR, Gutzmer J, Walters S (2005) Sediment-hosted lead-zinc deposits: A global perspective. *Economic Geology* 100th Anniversary Volume: 561-607.
- Li B, Wang J (2006) Lead-zinc deposits in Xinjiang. Geological Publishing House, Beijing, p. 55-63.
- Li F, Wang W, Yang J (2005) Geologic and geochemical characteristics of the Urogen lead-zinc deposit and its genesis, Wuqia County, Xinjiang. *Mineral Resources and Geology* 19: 335-340.
- Li Z, Xue C, Xin J, Wang S, Jia Z, Shi H, Dong X, Shao X (2011) Geologic characteristics and sulfur and lead isotope

- geochemistry of the Sareke copper deposit in Xinjiang. *Modern Geosciences* 25: 720-729 (in Chinese with English abstract).
- Rickard DT, Willden MY, Marinder N-E, Donnelly TH (1979) Studies on the genesis of the Laisvall sandstone lead-zinc deposit, Sweden. *Economic Geology* 74: 1255-1285.
- Wang J, Li C, Chen X (1992) A new genetic model for the Jinding lead-zinc deposit: Geological Exploration for Non-Ferrous Metals, 1: 200-206 (in Chinese with English abstract).
- Wang S, Xue C, Li, Z (2011) Geologic and S-Pb isotopes characteristics of the Jiashi sandstone type copper deposits in Xinjiang. *Modern Geosciences* 25: 219-227 (in Chinese with English abstract).
- Xie S, Mo J, Yang J, Yang J (2003) A study of the SEDEX origin of the Cenozoic Urogen lead-zinc deposit in Wuqia County, Xinjiang. *Mineral Resources and Geology*: 17: 11-16 (in Chinese with English abstract).
- Xue C, Zeng R, Liu S, Chi G, Qing H, Chen Y, Yang J, Wang D (2007) Geologic, fluid inclusion and isotopic characteristics of the Jinding Zn–Pb deposit, western Yunnan, South China: A review. *Ore Geology Reviews* 31: 337-359.
- Ye Q, Wu Y, Fu X, Chen M, Ye J, Zhuang D, Yang F, Bai H (1999) Mineralization conditions and prediction of nonferrous deposits in southwestern Tianshan. Geological Publishing House, Beijing: 129-140 (in Chinese with English abstract).
- Zhang S (2010) Geologic and geochemical characteristics and genesis of representative lead-zinc deposits in Southern Tishan. M.Sc. thesis, China University of Geosciences (Beijing), 90 p (in Chinese with English abstract).
- Zhu X, Wang J, Liu Z, Fang T (2010) Geologic characteristics and genesis of the Urogen lead-zinc deposit, Xinjiang. *Acta Geologica* 84: 695-702 (in Chinese with English abstract).

A preliminary study on geology of the post-collisional porphyry Mo-Cu deposit at Narigongma, Tibet

Zhiming Yang

Institute of Geology, Chinese Academy of Geological Science, Beijing 100037, China

Abstract. Post-collisional Narigongma deposit is associated with Eocene granitic intrusions that are hosted by a Permian volcanic–sedimentary sequence. A biotite granite stock (P1 porphyry) is the earliest Eocene intrusive unit, and was itself intruded by fine-grained granite porphyry stocks and post-ore diorite porphyry dikes. The main Mo–Cu mineralization is associated with the P1 porphyry.

Hydrothermal alteration around the deposits is characterized by concentric zones ranging from an inner potassic out to phyllic and argillic, and an outer propylitic zone. Potassic alteration is associated with quartz–K-feldspar and quartz–molybdenite veins, whereas phyllic alteration is related to pyrite±chalcopyrite-bearing veins.

Hypogene mineralization was characterized by early-stage precipitation of molybdenite during potassic alteration and late-stage deposition of chalcopyrite during phyllic alteration. Molybdenum mineralization is associated with quartz–molybdenite veins. Cu mineralization is related to pyrite–chalcopyrite-bearing veins. Deposition of molybdenite and chalcopyrite was both resulted from decreasing temperature. A high degree of crystallization of the P1 porphyry occurred prior to fluid saturation that produced Mo enrichment in the residual melt due to the incompatible behavior of Mo. However, compatible Cu was sequestered by the crystallizing phases and resulted in generation of a high-Mo/Cu magmatic–hydrothermal fluid and the final Mo±Cu mineralization assemblage.

Keywords.

Porphyry Cu deposits, Post-collisional setting, High-K adakite, Narigongma, Tibet

1 Introduction

Porphyry Cu deposits are mostly found in island and continental arc settings in association with subduction-related, calc-alkaline silicic magmas (Sillitoe, 2010). However, recent studies have discovered that such deposits are also found in post-collisional settings, such as the Eocene Yulong porphyry Cu belts (YPCB; Hou et al., 2003) in the Tibetan–Himalayan orogen. Although considerable research has recently been conducted on porphyry Cu systems in collisional settings, focusing on their geochronology and geochemistry, the geological characteristics of these deposits are still poorly documented.

The Narigongma deposit is a poorly studied Mo-rich porphyry Cu deposit located in southern Qinghai, Tibet, which is about 400 km northwest of the renowned YPCB. The deposit contains ~0.46 Mt of Cu with an average of ~0.32 wt.% Cu and ~0.25 Mt of Mo at an average grade of ~0.06 wt.% Mo. Preliminary research has mainly focused on the geochronology of mineralization-related granitic intrusions and Mo

mineralization in the deposit. These results have shown that the mineralization in the deposit occurred in the Eocene (43–40 Ma; Wang et al., 2008; Yang et al., 2008), which is coeval with the porphyry Cu deposits in the YPCB (Fig. 1a) and suggests that the Narigongma deposit is probably a northward extension of the YPCB. However, the reasons why the Narigongma Mo–Cu deposit has different ore assemblages as compared with the other porphyry deposits (Cu–Mo±Au) in the YPCB are still unclear and are a matter of debate. In this study, we present a preliminary geological investigation on the deposit, in order to: (1) document the geological characteristics of the deposit; and (2) identify the factors that led to Mo–Cu rather than Cu–Mo mineralization.

2 Geological setting

2.1 Regional geology

The Narigongma deposit is located in the Qiangtang terrane of the Himalayan–Tibetan orogen (Fig. 1a) on the northern edge of the Sanjiang metallogenic belt in eastern Tibet. The Qiangtang block comprises the eastern Qiangtang and western Qiangtang blocks, which are separated by the Early Triassic high-pressure Qiangtang metamorphic belt (Yin and Harrison, 2000). The Narigongma deposit has typically been considered to be bounded by the Jinshajiang suture (JSS) to north and the Bangonghu–Nujiang sutures (BNS) to the south (Fig. 1a).

Although the nature of the boundaries of the Qiangtang terrane are a subject of debate, it is generally accepted that the main oceans most likely to have been associated with the Qiangtang terrane as represented by the JSS, SHS, BNS, Garze–Litang suture (GLS) and Indus–Yalu suture (IYS) had closed before Cenozoic times (Yin and Harrison, 2000). After closure of these Paleo-, Meso- and Neo-Tethys oceans, the area became a post-collisional setting.

2.2 Ore deposit geology

Two main lithological units are present in the Narigongma district (Fig. 1b): (1) Middle–Late Permian volcanic–sedimentary rocks, which account for 80% of the surface outcrop across the whole area; and (2) Eocene intrusive rocks comprising mineralization-related biotite granite porphyry (P1 porphyry), fine-grained granite porphyry (P2 porphyry), and post-ore quartz diorite porphyry with an outcrop area of ~1.2 km².

The P1 porphyry is exposed in the east–central part of the deposit and is the largest intrusion in the region with an outcrop area of ~1.0 km² (Fig. 1b). The porphyry is NE–SW-trending, approximately 1.8 km in length along its long axis, and has variable width (0.4–1.0 km). The

P1 porphyry is typically granitic in composition, but locally grades to granodioritic compositions at its margins. The rocks are porphyritic in texture. In general, the phenocrysts range in abundance from 20–35 vol.%, and include variable amounts of plagioclase, K-feldspar, quartz, biotite, and minor hornblende. The groundmass of the P1 porphyry is quartzo-feldspathic in nature and consists of fine-grained quartz, feldspar, and biotite. Accessory minerals include apatite, rutile, zircon, and titanite. Emplacement of the P1 porphyry caused intensive contact metamorphism of the Permian volcanic–sedimentary sequence and formed a hornfels and localized skarns surrounding the intrusion. The P1 porphyry is cut by quartz veins and has experienced moderate to intensive potassic, phyllic, and argillic alteration, which may be related to the mineralization.

One NW–SE-striking and one NE–SW-striking fault have been recognized in the deposit. Field observations suggest that they are both normal faults. Emplacement of the P1 porphyry was controlled by the NE–SW-striking fault.

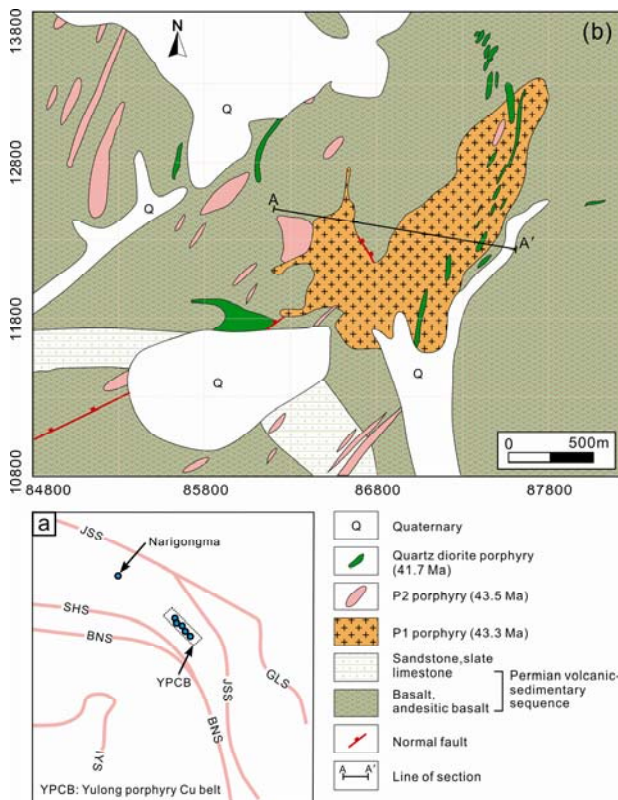


Figure 1. (a) Tectonic framework of northeast Tibet showing the distribution of the Narigongma deposit and the Yulong porphyry Cu (–Mo–Au) belts. (b) Geological map of the Narigongma deposit (modified after Yang et al., 2008). Sutures: BNS=Bangonghu–Nujiang suture, JSS=Jinshajiang suture, SHS=Shuanghu suture, IYS=Indus–Yalu suture, GLS=Garze–Litang suture.

3 Alteration and mineralization

3.1 Alteration

Potassic alteration: The earliest alteration is represented by potassic mineral assemblages developed pervasively and/or as veins in the P1 porphyry and wall rocks of the volcanic–sedimentary sequence surrounding the P1

porphyry. Potassic alteration is characterized by the formation of K-feldspar, biotite, and abundant quartz. The potassic alteration can be subdivided into two stages: early-stage K-feldspar alteration and late-stage biotite alteration (Fig. 2).

K-feldspar alteration took place before emplacement of the quartz diorite porphyry. This type of alteration is evident as veins, veinlets, and selective pervasive mineral replacement, and is mainly found within the P1 porphyry and, less commonly, in the volcanic–sedimentary sequence wall rocks. Vein- or veinlet-forming K-feldspar is the dominant style of K-feldspar alteration present at Narigongma and typically occurs at the internal contact of the P1 porphyry intrusion. These veins consist of quartz–K-feldspar and quartz–molybdenite±K-feldspar.

Biotite alteration is typically found in the wall rocks closely surrounding the P1 porphyry intrusion. Biotite alteration is characterized by the presence of abundant biotite, quartz, magnetite, and minor K-feldspar, and occurs in two main modes: (1) alteration haloes along quartz–molybdenite±K-feldspar and quartz–chalcopyrite veins; and (2) selective replacement of primary minerals such as biotite, hornblende, and feldspar. Quartz–molybdenite is the major vein type associated with biotite alteration at Narigongma. The veins are irregular to planar in form with variable widths (0.5–12 mm), and are characterized by the presence of disseminated or clots of molybdenite and K feldspar. Quartz in the quartz–molybdenite±K-feldspar veins is also granular in shape and lacks internal symmetry.

Propylitic alteration: Propylitic alteration has produced a mineral assemblage of chlorite+epidote+calcite, and is intensively developed at Narigongma due to the mafic nature of the wall rocks. The sulfide content is somewhat high in rocks close to the P1 porphyry intrusion, occurring mainly in pyrite. Propylitic alteration is irregularly developed and typically pervasive, apart from some small epidote veinlets.

The propylitic alteration zone surrounds the area of phyllic alteration and is mainly found in the wall rocks of the volcanic–sedimentary sequence. This alteration zone is approximately 4.5 km long and 2–3 km wide. Epidote±quartz±chlorite±calcite is the major vein assemblage associated with propylitic alteration.

Phyllic alteration: Phyllic alteration occurred pervasively or as haloes around pyrite-bearing veins, and has overprinted unaltered rocks and earlier alteration assemblages. Phyllic alteration assemblages are typically dominated by sericite, quartz, pyrite, and calcite, but chlorite and rutile are extensively present in the assemblage where the host rocks are the volcanic–sedimentary sequence. SWIR analysis showed that the sericite identified macroscopically or microscopically comprises muscovite and illite.

At the ore deposit scale, phyllic alteration has intensively overprinted the potassic and propylitic alteration (Fig. 2). Phyllic alteration has affected all the porphyry types, including the youngest quartz diorite porphyry, indicating that it largely post-dates all the major porphyry units. The main vein assemblages

associated with phyllic alteration are typically pyrite-bearing, and include quartz–pyrite–chalcopyrite, pyrite–chalcopyrite±quartz, pyrite±chalcopyrite±quartz, and pyrite±quartz.

Argillic alteration: Argillic alteration has affected all the rock units at Narigongma, but is mainly found in the central part of the P1 porphyry intrusion (Fig. 2), where it overprints unaltered rocks and earlier alteration assemblages. Argillic alteration is typically controlled by fractures or faults and occurs as a NE–SW-trending belt (0–20°) with a width of several to tens of meters over a length of tens to hundreds of meters (Fig. 2).

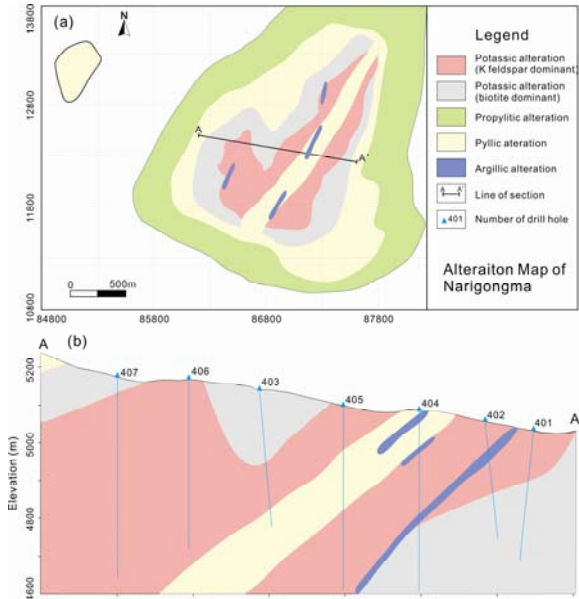


Figure 2. (a) Alteration map with the main alteration types. (b) Alteration distribution of the section A–A', inferred from logging of 7 drill holes along the sections. The biotite alteration is mainly developed in the wall rocks of volcanic–sedimentary sequence, whereas K feldspar alteration dominantly occurs in the P1 porphyry.

3.2 Hypogene mineralization

Molybdenum mineralization at Narigongma largely occurs in the P1 porphyry intrusion, and the main Mo-bearing mineral is molybdenite. Molybdenite is typically lamellar–columnar in shape and ranges in length from 100 to 500 μm . The molybdenite is disseminated along micro-cracks in quartz–molybdenite±K–feldspar veins. These micro-cracks are discontinuous and each is generally limited to one or two quartz grains, indicating they formed during growth of the quartz–molybdenite±K–feldspar veins. Alteration haloes of biotite and/or K-feldspar are observed within or along the margins of quartz–molybdenite±K–feldspar veins, suggesting that Mo mineralization at Narigongma took place during the potassic alteration stage.

Copper mineralization at Narigongma is also mainly within the P1 porphyry intrusion. The main Cu-bearing mineral in the deposit is chalcopyrite. Chalcopyrite occurs in disseminated form and infilling fractures. Disseminated chalcopyrite is irregular in shape and ranges in size from 50 to 200 μm , and may or may not be found with pyrite. Phyllic alteration is generally

associated with the disseminated chalcopyrite. Copper-bearing veins in the deposit mainly include quartz–pyrite–chalcopyrite, pyrite–chalcopyrite±quartz, and pyrite±chalcopyrite±quartz assemblages. All of these veins are associated with phyllic alteration, suggesting that most of the Cu at Narigongma was deposited during the phyllic stage.

Molybdenum and Cu concentrations are not correlated in the studied section at Narigongma (Fig. 3). The distribution of Mo is relatively uniform and high-grade ore (>0.06 wt.%) mostly occurs in the internal contact of the P1 porphyry, in close association with potassic alteration. The Mo grade decreases abruptly in rocks below the high-grade ore (Fig. 3a). However, the Cu distribution is relatively localized and high-grade (>0.3 wt.%), and is mainly found in the shallow or central part of the P1 porphyry intrusion in association with phyllic alteration. The Cu grade decreases abruptly with depth, even in areas where phyllic alteration is intensively developed (Fig. 3b).

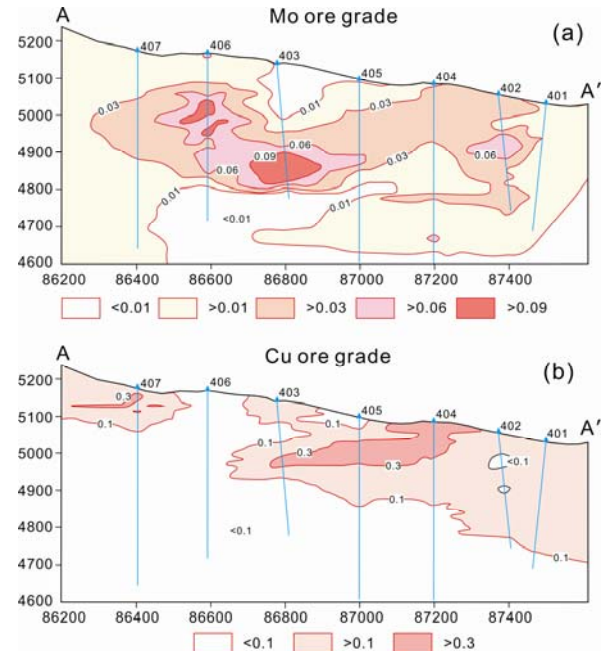


Figure 3. Ore-grade distribution along section A–A'. Molybdenum and Cu concentrations are not correlated in the studied section. Cu and Mo bodies show close correlation with the P1 porphyry.

4 Discussion and conclusions

4.1 Genesis of the Mo-rich characteristics of the Narigongma deposit

Narigongma is a Mo-rich porphyry Cu deposit with Mo/Cu ratio of ~0.2, which can be classified as a porphyry Mo–(Cu) deposit. The Mo-rich characteristics of the Narigongma deposit have been the subject of considerable attention (e.g., Wang et al., 2008; Yang et al., 2008), as an understanding as to why the deposit is Mo-rich might provide important constraints on regional metallogensis and future exploration strategies in this region. In general, Mo enrichment in porphyry Cu deposits has been explained by magmatic or magmatic–hydrothermal processes. For example, based on review

of geochemical data for Miocene porphyry intrusions at Gangdese in Tibet, Hou et al. (2012) noted that intrusions related to porphyry Mo or Mo-rich porphyry Cu deposits generally show a stronger geochemical fingerprint of ancient crustal materials. Hou et al. (2012) thus proposed that the formation of porphyry Mo or Mo-rich porphyry Cu deposits requires greater involvement of ancient crustal materials during magma generation. However, the origins of Mo enrichment at Narigongma are difficult to reconcile with this model, as samples from the Eocene intrusive suite in the deposit are more isotopically depleted than those from typical porphyry Cu deposits in the YPCB (Yang et al., 2008). This suggests that a more depleted mantle or juvenile crustal composition is involved in the magma genesis at Narigongma and leads us to propose that magmatic–hydrothermal processes played a key role in the Mo enrichment in this deposit.

A model for Mo enrichment during magmatic–hydrothermal processes was recently reviewed by Robb (2005). Porphyry Mo–(Cu) deposits like that at Narigongma commonly form in deeper settings than porphyry Cu–(Mo) deposits, and are related to magmas with slightly lower initial water contents. In general, these magmas need to undergo a greater degree of crystallization before fluid saturation is attained. The result of this is that Mo becomes enriched in the residual melt due to its incompatible behavior, whereas compatible Cu is likely to be sequestered by accessory sulfide and/or oxide phases, which results in higher Mo/Cu values in the melt. When saturation occurs, these melts will yield a magmatic–hydrothermal fluid with a high Mo/Cu ratio, giving rise to Mo–(Cu) porphyry-type mineralization. The Mo-rich characteristics of the Narigongma deposit are consistent with this model for the following reasons: (1) the presence of hornfels formed by contact metamorphism and absence of coeval hydrothermal alteration suggests that the initial water concentration of the mineralization-related magma was below the saturation water content at emplacement; (2) the P1 porphyry intrusion is moderately fractionated, with its margins being partly granodioritic and central part being granitic; and (3) the irregular margins of late-stage pyrite±chalcopyrite veins and the absence of typical planar B-type veins indicate that the P1 porphyry intrusion was emplaced at a significant depth (>4 km) where fluid pressures would probably not have been sufficiently high to result in rock fracturing.

4.2 Comparison between the Narigongma and other porphyry Cu deposits in the YPCB

The deposit at Narigongma, as well as other porphyry Cu deposits in the YPCB, reinforces some generalized characteristics of porphyry Cu deposits in arc settings (Sillitoe, 2010). For example, these deposits have similar hydrothermal alteration types and zoning pattern. However, there are also some obvious differences between the Narigongma and other porphyry Cu deposits in the YPCB. For example, the mineralization-related intrusion at Narigongma is moderately fractionated (granodioritic to granitic), whereas that in most porphyry Cu deposits in the YPCB is typically

monzogranitic in composition and generally unfractionated. Breccia pipes are commonly developed around the mineralization-related intrusions in the YPCB, but are not developed at Narigongma. Planar B-type veins that formed by open fracture filling (e.g., Gustafson and Hunt, 1975) are developed in the YPCB deposits, but are generally absent at Narigongma. Furthermore, the Mo/Cu ratio in the Narigongma deposit is relatively high (~0.2), whereas it is low (~0.1) in most porphyry Cu deposits in the YPCB.

The main reason for the differences between the Narigongma and other deposits in the YPCB is thought to be the different emplacement depths of the mineralization-related intrusions. The absence of typical B-type veins and breccia pipes at Narigongma indicates that the mineralization-related P1 porphyry was emplaced at greater depth (>4 km) than other porphyry Cu deposits in the YPCB (1–3 km; Hou et al., 2003), where fluid pressure would probably not be sufficient to fracture rock. The deeper emplacement of the P1 porphyry at higher lithostatic pressures would also enhance H₂O solubility in the mineralization-related magma, and require a greater degree of crystallization of the P1 porphyry before fluid saturation was reached. This may explain why the P1 porphyry at Narigongma is more fractionated than the other intrusions associated with the porphyry Cu deposits in the YPCB.

Acknowledgements

This work was funded by National Basic Research Program of China (2011CB403104 and 2009CB421004), the National Natural Science Foundation of China (41273051), the Ministry of Land and Resources of China (201011011), and IGCP/SIDA-600. We would like to thank Guiren Wang for his help with fieldwork.

References

- Gustafson LB, Hunt JP (1975) The porphyry copper deposit at El Salvador, Chile. *Economic Geology* 70: 857-912
- Hou Z, Ma H, Khin Z, Zhang Y, Wang M, Wang Z, Pan G, Tang R (2003) The Himalayan Yulong porphyry copper belt: Product of large-scale strike-slip faulting in eastern Tibet. *Economic Geology* 98: 125-145
- Hou Z, Zheng Y, Yang Z, Yang Z (2012) Metallogensis of continental collision setting: Part I. Gangdese Cenozoic porphyry Cu-Mo systems in Tibet. *Mineral Deposits* 31: 647-670
- Robb L (2005) *Introduction to ore-forming processes*. Wiley-Blackwell
- Sillitoe RH (2010) Porphyry copper systems. *Economic Geology* 105: 3-41
- Wang Z, Yang Z, Yang Z, Tian S, Liu Y, Ma Y, Wang G, and Qu W (2008) Narigongma porphyry molybdenite copper deposit, northern extension of Yulong copper belt: evidence from the age of Re-Os isotope. *Acta Petrologica Sinica* 24: 503-510
- Yang Z, Hou Z, Yang Z, Wang S, Wang G, Tian S, Wang Z, Liu Y, and Wen D (2008) Genesis of porphyries and tectonic controls on the Narigongma porphyry Mo (-Cu) deposit, southern Qinghai. *Acta Petrologica Sinica* 24: 489-502 (in Chinese)
- Yin A, Harrison TM (2000) Geologic evolution of the Himalayan-Tibetan orogen. *Annual Review of Earth and Planetary Sciences* 28: 211-280

Structural controls on carbonate-hosted Pb-Zn mineralization in the Dongmohazhua deposit, central Tibet

Hongrui Zhang, Tiannan Yang, Zengqian Hou, Yucai Song, Yingchao Liu
Institute of Geology, Chinese Academy of Geological Sciences, Beijing 100037, China

Zhusen Yang, Shihong Tian
Institute of Mineral Resources, Chinese Academy of Geological Sciences, Beijing 100037, China

Fuchun Wang, Wanwen Xue, Yubao Zhang
Qinghai Geological Survey, Xining 810012, China

Abstract. The structure deformation and ore texture were studied for the case of fault zones affecting lead-zinc mineralization in Dongmohazhua deposit, which is situated in central Tibet, approximately 100km west to Yushu. Two stages of deformation and two main types of ore textures are recognized through field mapping and micro-texture observations for the Dongmohazhua deposit. The second stage NW trending thrust and subsidiary extensional sites are related to mineralization. Sulfides precipitated at the extensional fractures formed during regional compression.

Keywords. Faults, Dongmohazhua deposit, Central Tibet, Pb-Zn

1 Introduction

Sediment-hosted Pb-Zn deposits are usually related to basinal brines, and formed in the passive margins or foreland basins in convergence setting with no spatial and temporal relationships to igneous activities (e.g. Bradley and Leach 2003; Leach et al. 2005, 2010). Recent studies on sediment-hosted Pb-Zn metallogenic belt in east-central Tibet have recognised that these deposits can occur in the hinterland of continent-continent (Indo-Asian) collisional orogeny (Hou et al. 2008; He et al. 2009; Liu et al. 2011). The mineralization is characterized by a metal suite that includes Pb-Zn-Cu-Ag and may be related to regional fold-thrust systems (Hou et al. 2008). But the controlling structures in these deposits, which are essential to reveal the ore forming process (e.g. Cox 2005; Mickelthwaite 2009; Caine et al. 2010), are poorly understood.

The Dongmohazhua deposit, situated in the Yushu area, central Tibet (Fig. 1), is one of six large-scale carbonate-hosted Zn-Pb deposits that have been discovered in the last decade (Zhang et al. 2013). It contains prospective reserves of >1.0 Mt metal, with average Pb and Zn grades of 0.76-1.49% and 2.10-2.62%, respectively. This paper describes the structural and mechanical controls associated with the Dongmohazhua carbonate-hosted deposit. The relationship between deformation and mineralization has revealed the ore bearing fluid flow and precipitation processes.

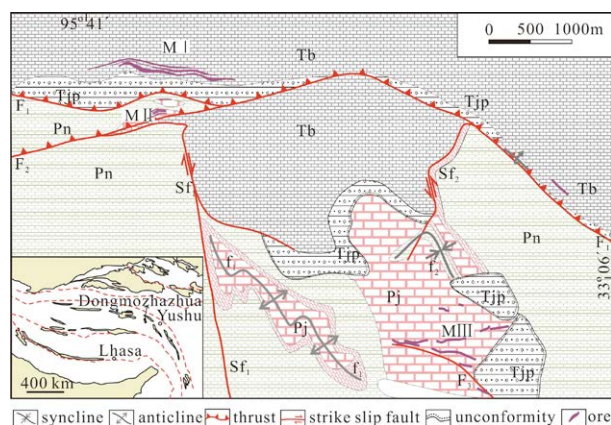


Figure 1. Geological map of the Dongmohazhua deposit. The inset shows the tectonic division of the Tibetan Plateau and the location of the Dongmohazhua deposit. Pj- the lower to middle Permian Jiushidaoban Formation limestone, Pn- the upper Permian Nayixiong Formation clastics; Tj_p- the upper Triassic Jiapeila Formation clastic rocks intercalated with volcanics; Tb- the upper Triassic Bolila Formation carbonate rocks, F₁- F₁ thrust, F₂- F₂ thrust, F₃- F₃ thrust, f₁- superimposed folds, Sf₁- strike slip fault, MI- MI mineralized zone, MII- MII mineralized zone, MIII- MIII mineralized zone

2 Geological framework

The earliest deformation recognized in Yushu area is characterized by NNE trending upright tight to isoclinal folds and high-angle reverse faults, which formed during the closure of Paleo-Tethyan oceans in Late Triassic (Yang et al. 2012). Large scale crustal shortening happened in the Early Tertiary in response to the Indo-Asian plate collision (e.g. Yin and Harrison 2000). Previously published studies have identified Fenghuoshan-Nangqian Fold Thrust Belt (FNFTB) in Yushu area (Coward et al. 1988; Horton et al. 2002; Spurlin et al. 2005). Thrusts in the FNFTB are mainly northwest-trending and place older Carboniferous to Triassic units over younger units (Spurlin et al. 2005).

The Dongmohazhua deposit is located at the northern margin of the FNFTB. Detailed geological mapping reveals four lithostratigraphic associations in Dongmohazhua area (Fig. 1), i.e., the lower to middle Permian Jiushidaoban Formation (Pj), consisting mainly of limestones; the upper Permian Nayixiong Formation

(Pn) composed of elastic and volcanic rocks; the upper Triassic Jiapeila Formation (Tjp) comprising elastic rocks intercalated with volcanics; and the upper Triassic Bolila Formation (Tb) of carbonate rocks. Between the Permian and Triassic is a regional angular unconformity, which is replaced locally by a nearly north-south trending thrust. The F_1 thrust fault in Dongmohazhua dips 40° - 50° to the north and juxtaposes Triassic carbonate and clastic sequence over Permo-Triassic strata. F_2 connects with the left-slip fault Sf_2 and right-slip fault Sf_1 , which makes the Triassic rocks in the footwall squeezed out. Located in the southeast part of Dongmohazhua deposit, the F_3 thrust develops mainly in Pj limestone, partly juxtaposes Permian limestone over Triassic clastics (Fig. 2a). The fault zone is about 5m wide, and composed of imbricated to lozenged breccias. Asymmetric folds and subsidiary extensional fractures are common near F_3 fault zone (Fig. 2b). Numerous superimposed folds are developed in the Permian-Triassic layered rocks (e.g. f_1 in Fig. 1). The curving hinge lines of those folds are common in the map and outcrop view.

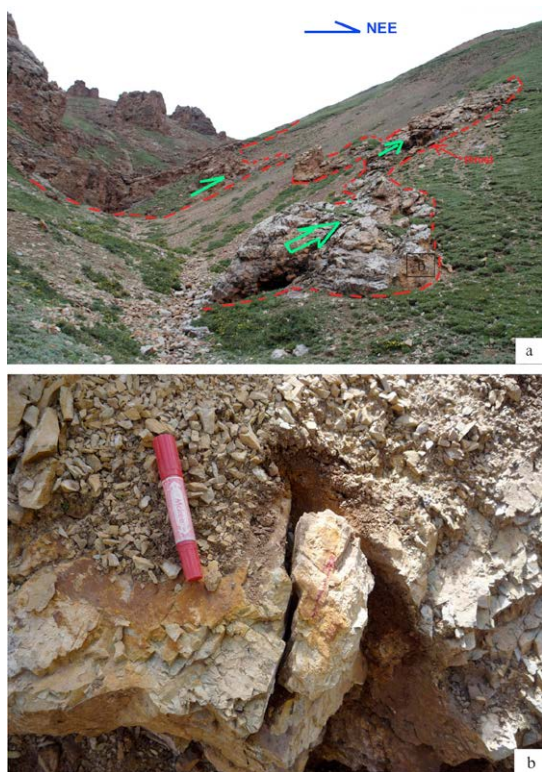


Figure 2. The F_3 thrust (a) and subsidiary extensional fractures (b)

3 Hydrothermal mineralization

The Dongmohazhua Pb-Zn deposit comprises three mineralized zones, i.e. MI, MII, and MIII (Fig. 1). All of them are hosted in carbonate rocks and situated in the hanging walls of thrust faults, such as the MI in the hanging wall of F_1 , the MII with F_2 , whereas the MIII with F_3 . Two main types of ore textures were recognized: disseminated and veinlet (Fig. 3). Disseminated ores, mainly occur in the MI mineralized zone, generally show hypidiomorphic-xenomorphic

granular textures. No obvious fracture is found even in thin section scale. Minerals are consisting of sphalerite + galena + pyrite + chalcopryite + dolomite + calcite + quartz and precipitated by replacement. Fluid inclusions in calcite have moderate homogenization temperatures (104 - 310°C) and salinities (8 - 18 wt% NaCl eq. Liu et al. 2011).

Veinlet ores mainly occur in the MII and MIII mineralized zones. Ore veins occur along the extensional fractures upon the thrust fault plane. All the extensional sites show vertical dips. Their E-W trending strikes are perpendicular to F_3 . The geometry of lodes suggests that they are subsidiary structure of F_3 . Minerals are deposited by open-space filling and consisting of sphalerite + galena + pyrite + chalcopryite + dolomite + calcite + barite. Sulfides occur as veins or cements between limestone breccias. Fluid inclusions in calcite have moderate homogenization temperatures (100 - 250°C) and high salinities (11 - 27 wt% NaCl eq.). The data in sphalerite show narrow range with homogenization temperatures of 100 - 140°C and salinities of 21 - 27 wt% NaCl eq. (Liu et al. 2011).

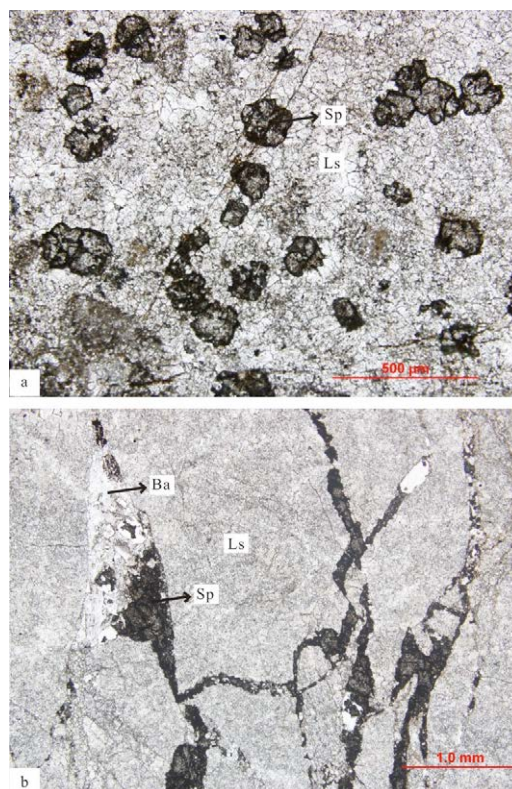


Figure 3. Photographs of ore texture. (a) disseminated ores; (b) veinlet ores. Sp- sphalerite, Ls- limestone, Ba- barite

4 Discussion

4.1 Deformation sequences

The existing of superimposed fold shows at least two stages of deformation in Dongmohazhua deposit. The NW thrust, such as F_1 , F_2 and F_3 , are the results of NE-SW contraction, they are belong to the FNFTB system. Sf_1 and Sf_2 only occur in the footwall of F_2 , and connect with NW thrust, we interpret they are subsidiary

structure of NW thrust. The superimposed folds axis is mainly parallel to NW trending faults, which implies that those folds are affected by NE-SW contraction. The extension part of F_1 cut 37 Ma granite of regional area (Zhang et al. 2013), this relationship indicates that the NW trending faults postdates 37Ma. The NW faults and their subsidiary structures are associated with crust shortening in Late Eocene during the Indo-Asian collision.

The earlier folds are badly superimposed by NE compression; we have no idea about the deformation time of this stage in deposit scale. Regional data show the earlier deformation formed during the closure of Paleo-Tethyan oceans in Late Triassic. Earlier folds in Dongmohazhua may be produced like this.

4.2 Mineralization during regional compression

It is notable that all Pb-Zn mineralized zones occur only in the hanging wall of the NW thrust. One explanation for this may be that high fracture density and connectivity in the hanging wall have enhanced permeability to localize fluid flow (Cox et al. 2001; Rowland and Sibson 2004; Cox 2005).

The structures described above for the veinlet ores demonstrate that mineralization occurred during regional compressional deformation. Despite the overall compressive strain regime, there are abundant extensional sites. These extensional sites developed locally within the hanging wall of the thrust. They are perpendicular to the fault and parallel to the regional stress. Hence, we conclude that Pb-Zn mineralization was initiated during the Indo-Asian collision. Ore-bearing fluids flow along the porous carbonate rocks and precipitate at the extensional sites upon the fault plane.

Based on regional geological evidence, Hou et al. (2008) proposed that the Pb-Zn mineralization at Dongmohazhua is 40-37 Ma. Recently, Tian et al. (2009) obtained 35 Ma age based on Rb-Sr and Sm-Nd isochron dating in sphalerite, pyrite and galena. Our deformation data show that NW thrust and related mineralization may be formed in the end of Eocene, which is coincides with others.

5 Conclusions

1. Two stage deformations can be recognized in Dongmohazhua deposit, D1 is characterized by early folds formed during the close of Paleo-Tethyan oceans in Triassic. D2 is consisted of NW thrust F_1 and related strike slip faults (Sf_1 and Sf_2), superimposed folds also formed during this compression. They are associated with Indo-Asian collision in Late Eocene during the Indo-Asian collision.

2. Two main types of ore textures were recognized: disseminated and veinlet. The ores are controlled by extensional fractures formed during regional compression.

Acknowledgements

This study was financially supported by the Ministry of Science and Technology of China (2009CB421001), the National Natural Science Foundation of China (NSFC) (41102040 and U0933605), and The International Geoscience Programme (IGCP/SIDA-600). Yongjun Lu and David Leach are thanks for their careful and thorough review and helpful comments.

References

- Bradley DC, Leach DL (2003) Tectonic controls of Mississippi Valley-type lead-zinc mineralization in orogenic forelands. *Miner Deposita* 38: 652-667
- Caine JS, Bruhn RL, Forster CB (2010) Internal structure, fault rocks, and inferences regarding deformation, fluid flow, and mineralization in the seismogenic Stillwater normal fault, Dixie Valley, Nevada. *J Struct Geol* 32: 1576-1589
- Coward MP, Kidd WSF, Yun P, Shackleton RM, Hu Z (1988) The structure of the 1985 Tibet geotraverse, Lhasa to Golmud. *Philos T R Soc A* 327: 307-333
- Cox SF (2005) Coupling between deformation, fluid pressures, and fluid flow in ore-producing hydrothermal systems at depth in the crust. In: Hedenquist JW, Thompson JFH, Goldfarb RJ, Richards JP (eds) SEG 100th Anniversary Special Publication. pp 39-75
- Cox SF, Knackstedt MA, Braun J (2001) Principles of structural control on permeability and fluid flow in hydrothermal systems. *Rev Econ Geol* 14: 1-24
- He L, Song Y, Chen K, Hou Z, Yu F, Yang Z, Wei J, Li Z, Liu Y (2009) Thrust-controlled, sediment-hosted, Himalayan Zn-Pb-Cu-Ag deposits in the Lanping foreland fold belt, eastern margin of Tibetan Plateau. *Ore Geol Rev* 36: 106-132
- Horton BK, Yin A, Spurlin MS, Zhou JY, Wang JH (2002) Paleocene-Eocene syncontractional sedimentation in narrow, lacustrine-dominated basins of east-central Tibet. *Geol Soc Am Bull* 114: 771-786
- Hou ZQ, Song YC, Li Z, Wang ZL, Yang ZM, Yang ZS, Liu YC, Tian SH, He LQ, Chen KX, Wang FC, Zhao CX, Xue WW, Lu HF (2008) Thrust-controlled, sediments-hosted Pb-Zn-Ag-Cu deposits in eastern and northern margins of Tibetan orogenic belt: geological features and tectonic model. *Miner Deposits* 27: 123-144 (in Chinese with English abstract)
- Leach DL, Sangster DL, Kelly KD, Large RR, Garven G, Allen CR, Gutzmer J, Walter S (2005) Sediment-hosted lead-zinc deposits: a global perspective In: Hedenquist JW, Thompson JFH, Goldfarb RJ, Richards JP (eds) SEG 100th Anniversary Special Publication. pp 561-607
- Leach DL, Bradley DC, Huston D, Pisarevsky SA, Taylor RD, Gardoll SJ (2010) Sediment-Hosted Lead-Zinc Deposits in Earth History. *Econ Geol* 105: 593-625
- Liu YC, Hou ZQ, Yang ZS, Tian SH, Yang TN, Song YC, Zhang HR, Carranza EM (2011) Formation of the Dongmohazhua Pb-Zn Deposit in the Thrust-Fold Setting of the Tibetan Plateau, China: Evidence from Fluid Inclusion and Stable Isotope Data. *Resour Geol* 61: 384-406
- Micklethwaite S (2009) Mechanisms of faulting and permeability enhancement during epithermal mineralisation: Cracow Goldfield, Australia. *J Struct Geol* 31: 288-300
- Rowland JV, Sibson RH (2004) Structural controls on hydrothermal flow in a segmented rift system, Taupo Volcanic Zone, New Zealand. *Geofluids* 4: 259-283
- Spurlin MS, Yin A, Horton BK, Zhou J, Wang J (2005) Structural evolution of the Yushu-Nangqian region and its relationship to syncontractional igneous activity, east-central Tibet. *Geol Soc Am Bull* 117: 1293-1317
- Tian SH, Yang ZS, Hou ZQ, Liu YC, Gao YG, Wang ZL, Song YC, Xue WW, Lu HF, Wang FC, Su AN, Li ZZ, Wang YZ, Zhang YB, Zhu T, Yu CJ, Yu YS (2009) Rb-Sr and Sm-Nd isochron ages of Dongmohazhua and Mohailaheng Pb-Zn ore deposits in Yushu area, southern Qinghai and their geological

- implications. *Miner Deposits* 28: 747-758 (in Chinese with English abstract)
- Yang TN, Hou ZQ, Wang Y, Zhang HR, Wang ZL (2012) Late Paleozoic to Early Mesozoic tectonic evolution of northeast Tibet: Evidence from the Triassic composite Western Jinsha-Garzê-Litang suture. *Tectonics* 31(TC4004): doi:10.1029/2011TC003044
- Yin A, Harrison TM (2000) Geologic evolution of the Himalayan-Tibetan orogen. *Annu Rev Earth Planet* 28: 211-280
- Zhang HR, Yang TN, Hou ZQ, Song YC, Yang ZS, Tian SH, Liu YC, Wang FC (2013) Structural deformation in the Dongmozhazhua deposit, northern segment of the Sanjiang belt. *Acta Petrol Sin*, 29: 1145-1155 (in Chinese with English abstract)

Magmatic-hydrothermal evolution of the Bolong porphyry copper deposit, Tibet, China

Xiangping Zhu, Guangming Li, Huaan Chen, Dongfang Ma
Chengdu Institute of Geology and Mineral resources, Chengdu 610081, China

Abstract. The Bolong porphyry copper deposit is a newly discovered deposit in the middle of Qinghai-Tibet plateau. Three granodiorite porphyry phases were distinguished in the Bolong porphyry copper deposit. Phyllic alteration is occurring on the surface of the Bolong deposit, and potassic alteration was found in the depth associating with granodiorite porphyries, and the copper mineralization is occurring mainly within the potassic alteration and strong phyllic alteration zone. Zircon U-Pb, molybdenite Re-Os and K-feldspar $^{40}\text{Ar}/^{39}\text{Ar}$ geochronology are applied to detect the magmatic-hydrothermal evolution of the Bolong deposit. Zircon U-Pb geochronology reveals that these granodiorite porphyry phases were emplaced at around 120 Ma. Re-Os data of four molybdenite samples from the potassic and phyllic hydrothermal alteration quartz-molybdenite veinlets yielded an isochron age at 119.4 ± 1.3 Ma, supporting a mineralization age of ca. 119 Ma. Hydrothermal K-feldspar from the potassic alteration zone was analyzed by $^{40}\text{Ar}/^{39}\text{Ar}$ dating technique. The plateau age of secondary K-feldspar is 118.31 ± 0.60 Ma, with a similar reverse isochron age of 118.49 ± 0.74 Ma, representing the potassic alteration age of the Bolong porphyry deposit. Therefore, the magmatic-hydrothermal process was persisted from ca. 120 Ma to 118 Ma, which is similar to the Duobuza porphyry copper deposit.

Keywords.

porphyry copper deposit, geochronology, thermochronology, magmatic-hydrothermal evolution

1 Introduction

The Bolong deposit is the secondly discovered porphyry Cu-Au deposit, which is neighbouring the Duobuza deposit. And the Bolong porphyry Cu-Au deposit is the largest deposit in the middle of Qinghai-Tibet plateau. Zircon U-Pb, molybdenite Re-Os and K-feldspar $^{40}\text{Ar}/^{39}\text{Ar}$ geochronology are applied to detect the magmatic-hydrothermal duration of the Bolong deposit.

2 Regional Geological Setting

Bolong deposit is located in the southern edge of Qiangtang block, north to the Tethyan Bangong-Nujiang suture. In Jurassic to Cretaceous, during Neo-Tethyan Bangong-Nujiang oceanic northward subduction (Guynn et al. 2006; Kapp et al. 2007; Zhu et al. 2012), in the west part of Qiangtang block, a set of accretionary prism were formed along the southern margin of Qiangtang block (Li et al. 2011). Volume magmas were also triggered within the Southwest Qiangtang accretionary prism, forming the Zhapu-Duobuza magmatic arc.

Bolong porphyry Cu-Au deposit is produced in the East of the Zhapu-Duobuza magmatic arc.

The Bolong porphyry Cu-Au deposit and the Duobuza porphyry Cu-Au deposit, together with some minor porphyry deposit compose the Dulong (Duobuza-Bolong) metallogenic district. The stratigraphy in the Dulong metallogenic district is mainly made up of the lower Jurassic Quse formation, the middle Jurassic Sewa formation and lower Cretaceous Meiriqiecuo formation, which are partly overlaid by Miocene Kangtuo group conglomerate and Quaternary. Four sets of major reverse faults go through the Dulong metallogenic district, i.e. north dipping thrust faults, north-east trending reverse faults, north-west trending reverse faults and south dipping thrust faults. All of these deposits in the Dulong metallogenic district are occurring along the north-east trending reverse faults and have close relationships to these porphyries, suggesting that the north-east trending reverse faults control the occurrence of mineralizing porphyry intrusions and deposits.

3 Deposit Geology

Bolong porphyry Cu-Au deposit is hosted by Lower Jurassic Quse formation interbedded sandstone and siltstone, which are strongly altered by silicification. Three granodiorite porphyry phases were emplaced into the lower Jurassic Quse formation. Phenocrysts in all of these granodiorite porphyry phases are similar and consisted of plagioclase, amphibole, biotite and quartz. The first and the second granodiorite porphyries can only be detected in drilling holes, and are associated with potassic alteration and Cu-Au mineralization, showing that they are syn-mineralization porphyries. The third granodiorite porphyry phase outcrops on the surface, and is associated with strong phyllic alteration.

4 Alteration and Mineralization

The Bolong porphyry Cu-Au deposit is weakly eroded, and its alteration zoning on the surface is not very obvious. On the surface of the Bolong deposit, alteration can be divided into two types, i.e. strong phyllic alteration and weak phyllic alteration. The phyllic alteration mineral association is sericite, quartz, chlorite, pyrite (replaced by limonite), while the strong phyllic alteration is accompanied by some quartz-pyrite (or limonite)-sericite veins. The strong phyllic alteration zone coincides with the alteration center of the Bolong porphyry deposit. In the alteration center of the Bolong

deposit, from the surface to the depth, the host rocks change from quartz sandstone to granodiorite porphyries, and the alteration type changes gradually from strong phyllic alteration to potassic alteration.

Copper and gold are the major valuable metal elements in the Bolong deposit, Cu-Au mineralization is closely associated with the first and the second granodiorite porphyries, and the Cu-Au ore body is occurring within the first and the second granodiorite porphyry phases and their contact zones with the quartz sandstones.

5 Zircon U-Pb Ages

Zircons for three granodiorite porphyries were all sampled from drilling holes in the Bolong deposit for LA-ICP-MS U-Pb dating. The first granodiorite porphyry phase sample has a zircon $^{206}\text{Pb}/^{208}\text{U}$ weighted average age of 120.2 ± 2.0 Ma, the second granodiorite porphyry phase yield a weighted mean zircon $^{206}\text{Pb}/^{238}\text{U}$ age of 119.5 ± 0.9 Ma, and zircons from the third granodiorite porphyry phase yielded a weighted mean $^{206}\text{Pb}/^{238}\text{U}$ age of 119.3 ± 1.3 Ma.

6 Molybdenite Re-Os Geochronology

Four molybdenite samples were selected from drilling holes in the Bolong deposit for Re-Os dating. Four samples plot along a linear array on the isochron diagram and form an isochron with an age of 119.4 ± 1.3 Ma.

7 $^{40}\text{Ar}/^{39}\text{Ar}$ Geochronology

Secondary K-feldspar sample selected from the potassic altered granodiorite porphyry was conducted $^{40}\text{Ar}/^{39}\text{Ar}$ dating. Heating of secondary K-feldspar from the Bolong porphyry copper deposit produced a weighted mean plateau age of 118.33 ± 0.60 Ma and formed an inverse isochron age is 118.49 ± 0.74 Ma, which represent the crystallizing time of secondary K-feldspar.

8 Discussion and Conclusion

Granodiorite porphyries were emplaced at ca.120 Ma, copper, gold and accessory metals mineralized at ca.119.5 Ma and the potassic alteration was occurring at ca. 118.5 Ma, suggesting that the duration of Magmatic-hydrothermal evolution of the Bolong deposit probably persisted from 120 Ma to 118.5 Ma, and prolonged for more than 1.5 Ma, and indicating that 120-119 Ma is an important metallogenic epoch in the Duolong district.

Porphyry Cu deposits usually show a marked tendency to occur in orogen-parallel belts ranging from a tens to hundreds and even thousands of kilometers long, and each belt is corresponding to a magmatic arc (Sillitoe 2010). Many felsic intrusions have similar tectonic setting, lithology, and intrusive ages, which may indicate that there might be some other porphyry copper metallogenic district occurring in the Zhapu-Duobuza

magmatic arc.

Based on the studies of Jurassic stratigraphy unconformity on the ophiolite and some igneous rocks, the final Lhasa-Qiangtang amalgamation is regarded occurring at 125-113 Ma (Kapp et al. 2007; Zhu et al. 2009, 2011, 2013) in the west part of the Bangong-Nujiang suture, and the magmatism, hydrothermal activity and mineralization of the Bolong deposit are within that interval, which probably suggest that the Bolong porphyry Cu-Au deposit formed near the end stage of Neo-Tethys Ocean northward subduction.

Acknowledgements

This study is financially supported by the State Key Research Development Program of China (No. 2011CB403105) and the National Nature Science Fund (No. 41202049, 41272091).

References

- Guynn J H, Kapp P, Pullen A, Gehrels G, Heizler M, Ding L (2006) Tibetan basement rocks near Amdo reveal "missing" Mesozoic tectonism along the Bangong suture, central Tibet. *Geology* 34: 505-508
- Kapp P, DeCelles P G, Gehrels G E, Heizler M, Ding L (2007). Geological records of the Lhasa-Qiangtang and Indo-Asian collisions in the Nima area of central Tibet. *GSA Bulletin* 119: 917-932
- Li G-M, Duan Z-M, Liu B, Dong S-L, Zhang L (2011) The discovery of Jurassic accretionary complexes in Duolong area, northern Bangong Co-Nujiang suture zone, Tibet, and its geologic significance. *Geological Bulletin of China* 30 (8): 1256-1260 (in Chinese with English abstract)
- Sillitoe R H (2010) Porphyry Copper Systems. *Economic Geology* 105(1): 3-41
- Zhu D C, Mo X X, Niu Y L, Zhao Z D, Wang L Q, Liu Y S, Wu F Y (2009) Geochemical investigation of Early Cretaceous igneous rocks along an east-west traverse throughout the central Lhasa Terrane, Tibet. *Chemical Geology* 268: 298-312
- Zhu D C, Zhao Z-D, Niu Y L, Dilek Y, Hou Z Q, Mo X X (2013) The origin and pre-Cenozoic evolution of the Tibetan Plateau. *Gondwana Research* 23(4): 1429-1454
- Zhu D C, Zhao Z D, Niu Y L, Mo X X, Chung S L, Hou Z Q, Wang L-Q, Wu F-Y (2011) The Lhasa Terrane: record of a microcontinent and its histories of drift and growth. *Earth and Planetary Science Letters* 301: 241-255

Miocene leucogranites, southern Tibet: geochemical characteristics and geodynamic significance

Song Xiaoqin, Zhong Kanghui, Chen Bo

College of Earth Science, Chengdu University of Technology, Chengdu 610059, China

Gou Jie

107 Geological Brigade of Chongqing Bureau of Geology and Mineral Resources, Chongqing 401120, China

Abstract. The Miocene granites of southern Tibet are mainly distributed in the Himalayas. The rock type is two-mica monzogranite, biotite monzogranite, tourmaline-muscovite granite. The major oxides composition of granites is of SiO₂ 65.66-75.35 wt%, Al₂O₃ 13.09-15.76 wt% and K₂O 3.42-5.92 wt% suggesting peraluminous and alkalic features. The samples mainly fall in S-type field with few in I-type field in the ACF plot. Miocene granites formed in the settings of large-scale extension and detachment in the post-collision stage of the Himalayas from evidence of existences of TTG Group, core complex and thrust instruction in this area.

Keywords.

southern Tibet, granite, TTG Group, geodynamics, extensional tectonic

1 Distribution of Granites in Southern Tibet

The Miocene granites are mainly distributed in the northern Himalayan tectonomagmatic belt and high Himalayan tectonomagmatic belt (Fig. 1).

The rock type in northern Himalayan tectonomagmatic belt is two-mica monzogranites,

biotite monzogranites, tourmaline-muscovite granites and granodiorites. Approximate 28 magma intrusions crop out as equiaxed shape or lumpy shape in this belt with a total area of 1049 km².

The rock type in high Himalayan tectonomagmatic belt is two-mica monzogranites and tourmaline-muscovite granites. Approximate 10 magma intrusions crop out as lumpy shape in this belt with a total area of 600 km².

2 Lithogeochemical Characteristics

Based on analysis of collected 42 major oxide data of granites from reports of 1:250000 scale regional geological survey in Wan Saga, Luozha and Dingjie county, southern Tibet, we found that leucogranites is characterized by limited range of major oxides composition (Table 1) with SiO₂ (65.66-75.35 wt%), and Al₂O₃(13.09-15.76 wt%), and K₂O(3.42-5.92 wt%). The samples mainly fall in alkaline series field with few in calc-alkaline series field (Fig. 2). Molar A/CNK ranges between 1.05 and 1.24 suggesting peraluminous character. Geochemical data indicates that it is typical S-type granite, which mainly fall in S-type field in the ACF plot (Fig. 3).

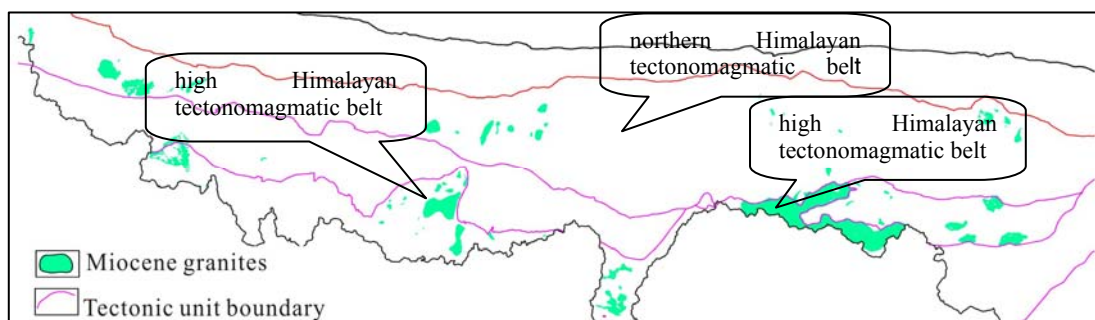


Figure 1. Distribution of granite in southern Tibet (modified from the geological map of Potential Evaluation of Tibetan Mineral Resources)

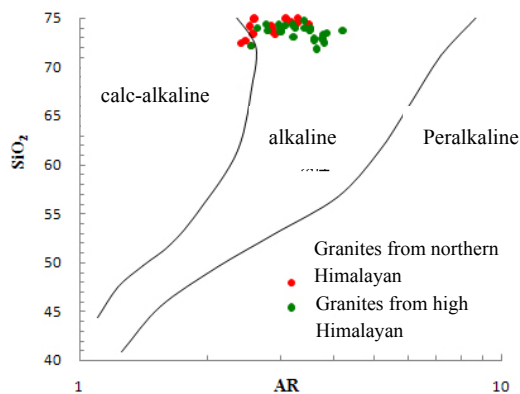


Figure 2. SiO₂-AR plot, (J.B Wright), 1969, showing calc-alkaline series to peralkaline series for granites

The samples are all in the granite field except one in the granodiorite field in the TAS classification and naming scheme. In the normative plot of albite, anorthite and orthoclase, 2 of 7 samples collected in the northern Himalayan tectonomagmatic belt fall in the granodiorite field, and the others fall in granite field; one of 24 samples collected in the high Himalayan tectonomagmatic belt fall in trondhjemite field, and the others fall in granite field (Fig. 4).

We could conclude that some of granites in the southern Tibet are with the characteristics of TTG groups.

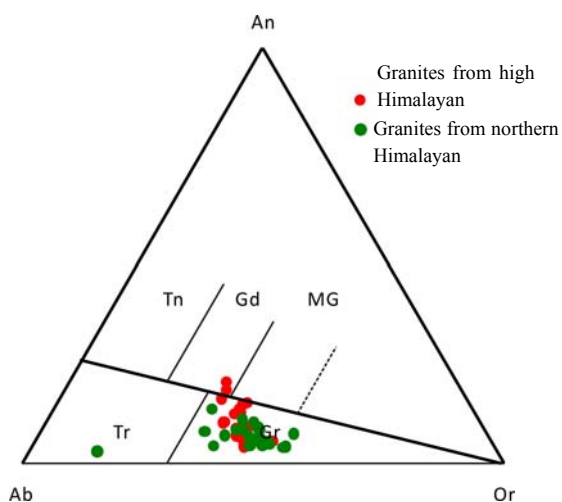


Figure 4. Plot of TTG and granite groups in the An–Ab–Or normative feldspar composition fields from O'Connor (1965) modified by Barker (1979) to account for K₂O present in biotite

3 Tectonic Setting and Geodynamics

The so-called TTG is composed of tonalite-trondhjemite-granodiorite, which formed in 'oceanic plate subduction' tectonic setting. The rock

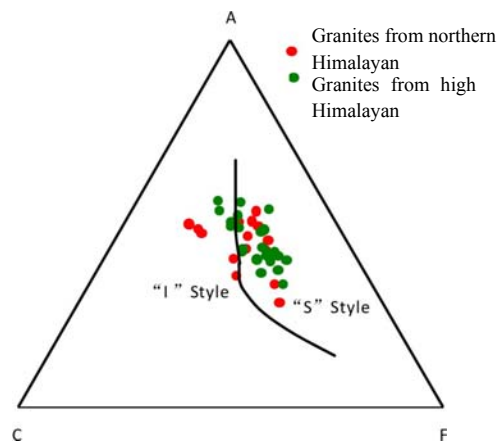


Figure 3. ACF plot (O'Connor, 1965), showing the genetic types for granites

group translates from T1T2 (tonalite-trondhjemite) to G1G2 (granodiorite-granite) along with the spatial transformation from ocean side to intracontinental side, which could indicate the direction of the subduction of the oceanic plate. That is to say TTG crops out at the side of ocean in the subduction zones.

Hou et al. (2006) concluded that the Yarlung Zangbo Ocean dived to north in the early Cretaceous Period, Simultaneously; the Indian Subcontinent and the Asian Subcontinent began to crash at about 65Ma ago. And the main collision period was from 65Ma to 41Ma, the late collision period was from 41Ma to 23Ma, and the later collision period was from 23Ma to 8Ma.

We could conclude that the 'subduction' had finished before Miocene, so the TTG group couldn't form in the 'Oceanic plate subduction' tectonic setting. How did it form? The author thinks the 'Subduction' direction and the formation mechanism of TTG rock group didn't only depend on the 'Oceanic plate subduction' tectonic setting, but the magma ratio of Si-Mg layers. T1T2 group appeared when the magma ratio of Si/Mg was higher than that of Si/Al. On the contrast, G1G2 group appeared. Therefore, the TTG group is of polarity from high magma ratio of Si/Mg to high magma ratio of Si/Al along with the subduction direction from ocean to continent.

The appearance of the TTG rock group in this area may be the result of high magma ratio of Si/Mg. The viewpoint that metamorphic core complexes in the southern Tibet formed in the extensional tectonic setting in late Cenozoic is generally accepted. So, some of granites originating in metamorphic core complexes in the northern Himalayan tectonomagmatic belt may form in the extensional

tectonic setting.

Table 1 Collected major elements analysis of granites in Himalayan tectonomagmatic belt

NO.	Samples No.	SiO ₂	TiO ₂	Al ₂ O ₃	Fe ₂ O ₃	FeO	MnO	MgO	CaO	Na ₂ O	K ₂ O	P ₂ O ₅
1	GS1301	73.26	0.2	14.82	0.1	1.58	0.034	0.62	1.16	3.62	4.08	0.1
2	GS01	73.36	0.13	14.29	0.08	1.24	0.022	0.24	0.97	3.72	4.2	0.1
3	GS2501	72.1	0.23	14.68	0.27	1.27	0.031	0.49	1.36	3.93	3.88	0.08
4	GS10002	73.16	0.11	14.53	0.4	0.9	0.022	0.22	0.7	3.8	4.63	0.09
5	GS504	73.84	0.16	14.2	0.06	1.39	0.025	0.4	0.84	3.12	4.9	0.15
6	GS12501	72.48	0.22	14.73	0.26	1.59	0.043	0.62	1.63	3.35	3.84	0.05
7	GS10001	73.16	0.1	14.62	0.23	1.02	0.022	0.17	0.62	3.8	4.63	0.08
8	D3207	71.49	0.26	15.56	0.22	1.54	0.04	0.67	1.78	4.01	3.52	0.08
9	D4327/1	71.7	0.22	14.81	0.07	1.78	0.06	0.84	2.39	3.59	3.53	0.1
10	D3227	72.14	0.24	15.07	0.19	1.57	0.04	0.66	2.06	3.72	3.54	0.07
11	D3514	65.66	0.45	15.22	0.92	2.41	0.08	2.16	2.72	3.54	3.46	0.16
12	D2018	72.64	0.16	14.93	0.27	0.67	0.03	0.42	1.07	4.07	3.42	0.1
13	D5022	73.45	0.07	14.9	0.22	0.8	0.03	0.22	1.2	3.36	4.6	0.06
14	D1030	73.01	0.12	14.83	0.24	0.95	0.03	0.22	0.85	3.42	4.54	0.14
15	D1031	72.76	0.17	14.92	0.3	1.04	0.04	0.4	1.18	3.36	4.67	0.14
16	D1033	72.68	0.18	14.88	0.32	1.09	0.03	0.37	1.37	3.3	4.36	0.12
17	D1041	72.97	0.17	14.96	0.27	1.02	0.03	0.43	1.4	3.36	4	0.11
18	D1159	73.44	0.14	14.39	0.03	1.87	0.04	0.19	0.83	3.46	4.85	0.12
19	D2001	73.24	0.13	13.97	0.24	1.67	0.03	0.16	0.73	3.28	5.75	0.15
20	D2168	72.58	0.19	15.06	0	1.48	0.04	0.25	1	3.76	5.31	0.14
21	D2179	73.12	0.13	14.48	0.12	1.58	0.04	0.2	0.97	3.86	5.13	0.14
22	D2202	73.24	0.15	14.68	0.24	1.32	0.05	0.18	0.76	3.73	5.33	0.12
23	D3027	71.49	0.26	15.56	0.22	1.54	0.04	0.67	1.78	4.01	3.52	0.08
24	D3278	74.16	0.1	14.32	0.06	1.48	0.04	0.1	0.7	3.59	4.6	0.13
25	D3296	73.41	0.08	14.49	0	1.94	0.08	0.09	0.66	4.38	4.06	0.08
26	D2216	72.88	0.12	14.99	0.2	1.8	0.04	0.13	0.86	3.87	5.08	0.08
27	D3008	73.47	0.09	14.94	0.19	0.71	0.02	0.12	0.96	3.68	4.65	0.09
28	DP12	75.35	0.08	14.52	0.05	1.02	0.05	0.06	0.4	6.14	1.52	0.02
29	D3315	71.78	0.19	14.91	0.16	1.64	0.03	0.24	0.86	3.67	5.52	0.11
30	D3318	72.74	0.15	14.82	0.23	1.82	0.05	0.18	0.76	3.58	5.45	0.09
31	D2189 - 1	71.62	0.2	14.79	0.03	2.57	0.04	0.27	1.1	3.13	5.92	0.1
32	D2189 - 2	73.32	0.13	14.55	0.21	1.5	0.05	0.14	0.79	3.15	5.39	0.22
33	D4045	72.38	0.11	15	0	1.94	0.07	0.16	0.98	4.16	4.23	0.06
34	D4046	73.55	0.1	14.54	0.08	1.57	0.04	0.11	1.14	3.76	4.52	0.06
35	DP13	73.3	0.05	14.97	0.27	1.3	0.03	0.11	1.13	3.78	4.24	0.08
36	B2606-1	74.33	0.4	13.09	0.16	1.7	0.02	0.61	1.15	3.35	4.23	0.08
37	B2576-2	73.3	0.17	15.15	0.01	1.07	0.02	0.51	1.34	3.57	3.59	0.14
38	B2574	74.18	0.11	14.61	0.03	0.68	0.02	0.33	1.83	3.32	3.94	0.06
39	B2608-1	74.11	0.07	14.36	0.23	1.03	0.08	0.32	0.87	3.55	4.21	0.1
40	B5119-2	74.32	0.1	14.48	0.04	0.75	0.02	0.35	1.84	3.25	3.99	0.05
41	B5118-2	73.57	0.05	15.08	0.02	0.47	0.01	0.26	1.65	3.72	4.29	0.02
42	B5118-1	73.26	0.06	15.27	0.01	0.53	0.01	0.22	1.64	3.87	4.25	0.03

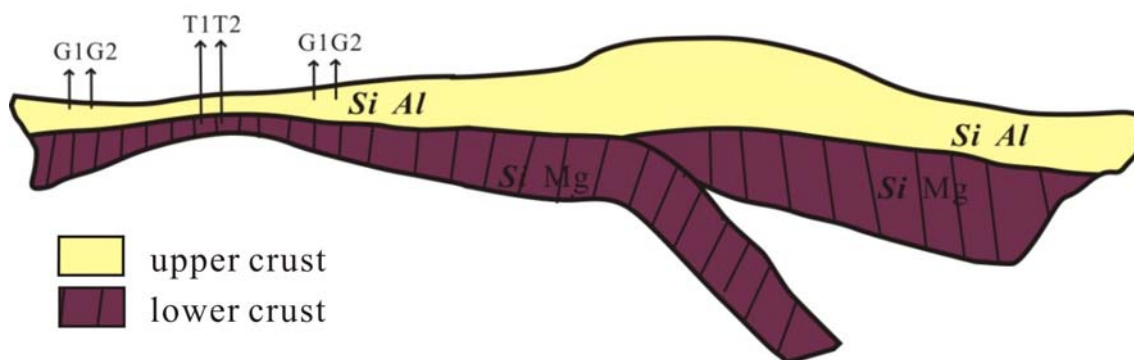


Figure 5. Scheme showing the formation of TTG group in southern Tibet

The huge detachment fault in the southern Tibet indicates that it had extended in south-north direction after Miocene in this area. Therefore, the author thinks the granites in the southern Tibet formed in the extensional tectonic setting. The Indian plate Dive into the Gangdise plate with the Yarlung Zangbo Ocean closing from the middle Eocene to Oligocene. And the Indian plate and the Asian plate began to splice with the proceeding of collisional orogeny.

The upper crust (Si-Al layer) becomes thinner along with the Si-Mg layer under the Indian plate making continuous subduction towards north. The magma ratio of Si/Mg was higher than that of Si/Al with the magma of the lower crust (Si-Mg layer) upwelling in the extensional and low-pressure conditions. So, TTG group formed (Fig. 5). Finally, the author concludes that the magma is mainly from upper crust and less from lower crust because the amount of GG group is more than TTG group.

continental margins[J]. *AJS*. 1974.,274:321-355.

DENG Jin-fu , XIAO Qing-hui , su shang-guo. Igneous Petrotectonic Assemblages and Tectonic Settings: A Discussion[J]. *Geological Journal of China Universities*, 2007, 13(3):392-402.

DENG Jin-fu , LUO Zhao-hua , su shang-guo. Petrogenesis, Tectonic Setting and Mineralization [M]. Geological Publishing House , 2004.

HOU Zeng-qian , WANG Er-qi , MO Xuan-xue. Collision Orogeny and Mineralization in Qinghai-Tibet Plateau[M]. Geological Publishing House , 2006.

Jakes P & WhiteJ R . Major and trace element abundances in volcanic rocks of orogenic areas[J].*GSA,Bull.* 1972.,83:29-40.

Miyashiro A. Volcanic rock series in island areas and active continental margins[J]. *AJS*. 1974.,274:321-355.

O,Co nnor J T. 1965. A classification for quartz-rich igneous rocks based on feldspar ratios [G]. *U.S. Geol. Surv. Prof. Papengchuper*, 525B, B79-B84.

Acknowledgements

The authors express their gratitude to reviewers to accept this paper.

References

O,Co nnor J T. 1965. A classification for quartz-rich igneous rocks based on feldspar ratios [G]. *U.S. Geol. Surv. Prof. Paper*, 525B, B79-B84.

Jakes P & WhiteJ R . Major and trace element abundances in volcanic rocks of orogenic areas[J].*GSA,Bull.* 1972.,83:29-40.

Miyashiro A. Volcanic rock series in island areas and active

SGU

Sveriges geologiska undersökning
Geological Survey of Sweden

Box 670
SE-751 28 Uppsala, Sweden
www.sgu.se

Uppsala 2013
ISBN 978-91-7403-207-9
Print: Elanders Sverige AB